TABLE OF CONTENTS

VOLUME I

OPENING ADDRESS & CONFERENCE SUMMARIES

INSTRUMENTS

Instruments: Posters

FUTURE MISSIONS

SOLAR SYSTEM

Solar System: Posters

STARS

Stars: Posters

STAR FORMATION

Star Formation: Posters

VOLUME II

INTERSTELLAR MEDIUM

Interstellar Medium: Posters

GALAXIES

Galaxies: Posters

COSMOLOGY

Cosmology: Posters

INTERSTELLAR MEDIUM

HEATING THE GAS IN PHOTODISSOCIATION FRONTS

B. T. Draine[1] **& Frank Bertoldi**[2,3]
[1]Princeton University Observatory, Princeton, NJ 08544, USA
[2]Max-Planck-Institut für Radioastronomie, Bonn, Germany
[3]Max-Planck-Institut für Extraterrestrische Physik, Garching, Germany

ABSTRACT

ISO has provided us with a new perspective on gas temperatures in photodissociation regions through measurements of line emission from rotationally-excited levels of H_2. The H_2 rotational level populations provide a thermal probe, showing that gas temperatures $T_{gas} \approx 500 - 1000\,\mathrm{K}$ prevail in a portion of the PDR where significant H_2 is present. Such high gas temperatures were unexpected. Theoretical models for the S140 PDR are presented. Possible mechanisms for heating the gas to such high temperatures are discussed.

Key words: Photodissociation fronts; molecular hydrogen.

1. INTRODUCTION

Photodissociation fronts play an important part in the global energetics of star-forming galaxies, as an appreciable fraction of the energy radiated by newly-formed stars is reprocessed in photodissociation fronts, resulting in H_2 and fine structure line emission. If we want to understand the emission spectra of star-forming galaxies, good theoretical models of photodissociation fronts are required.

ISO observations of line emission from rotationally-excited levels of H_2 have provided unequivocal evidence for gas temperatures in the $500-1000\,\mathrm{K}$ range in a portion of the photodissociation region (PDR) where the H_2 fraction is appreciable. These temperatures were higher than expected from current models of the heating and cooling processes in PDRs, and therefore require reconsideration of the physics of the gas and dust in PDRs.

In Sect. 2 we review the basic structure of photodissociation fronts, and in Sect. 3 we discuss how H_2 can be used as a thermometer to indicate the gas temperatures in PDRs. In Sect.4 we use the S140 PDR as an example. Theoretical models for the heating and cooling in PDRs are discussed in Sect. 5, and in Sect. 6 we stress some of the uncertainties in the modelling of PDRs. We summarize in Sect. 7.

2. WHAT IS A PHOTODISSOCIATION FRONT?

The term "photodissociation front" refers to the interface separating a region which is predominantly molecular, and a region where the ultraviolet energy density is sufficiently high so that the molecular fraction is $\ll 1$. Young O and B stars located near their natal (only partially-disrupted) molecular clouds produce conspicuous (i.e., high surface brightness) photodissociation fronts. A number of reviews of PDRs have appeared recently (Hollenbach & Tielens 1997, Sternberg et al. 1998, Walmsley 1998), including a comprehensive article by Hollenbach & Tielens (1998).

A photodissociation front is not a mathematical surface, but rather an extended "photodissociation region" (PDR). Figure 1 is a cartoon illustrating the different zones within the PDR.

The structure of the PDR is determined primarily by the attenuation of the far-ultraviolet (6 - 13.6 eV) radiation field, as one moves from the ionization front into the PDR. The H_2 abundance results from a balance between formation of H_2 on dust grains and photodissociation of H_2 by $912 < \lambda < 1110$Å photons. The photodissociation rate is determined by both H_2 self-shielding (Draine & Bertoldi 1996) as well as attenuation by dust. Because of this self-shielding, the H/H_2 transition occurs closer to the ionization front than the $C^+/C/CO$ or O/O_2 transitions. Atoms with ionization potentials lower than H (e.g. C) are photoionized in the PDR, whereas species with ionization potentials greater than H (e.g. O) are neutral in the PDR.

Ionization fronts and dissociation fronts are, in general, time-dependent structures (Bertoldi & Draine 1996). Under many circumstances, however, the structure can be approximated as being stationary in a frame moving with the dissociation front. Furthermore, if the dissociation front is advancing into the molecular gas with a propagation speed $v_{\mathrm{DF}} \gtrsim 0.3\,\mathrm{km\,s^{-1}}$ (Bertoldi & Draine 1996), advection terms can be neglected in the equations governing the thermal and chemical conditions: the temperature is effectively determined by a local balance between heating and cooling, and abundances by a local balance between formation and destruction. For most PDRs

Proceedings of the Conference "The Universe as seen by ISO", Paris, France, 20–23 October 1998 (ESA SP-427, March 1999)

this inequality is expected to be satisfied (Bertoldi & Draine 1996, Störzer & Hollenbach 1998), although time dependence may be important for some planetary nebulae (Hollenbach & Natta 1995).

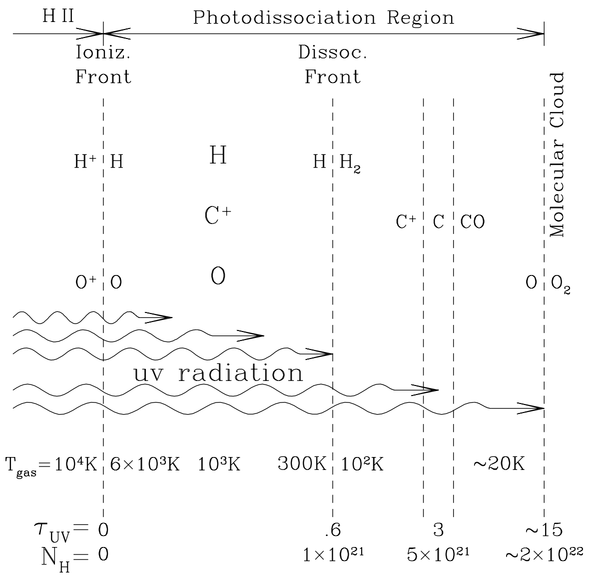

Figure 1. The structure of a PDR produced by radiation from a star which also emits enough ionizing photons to produce an HII region. The ionization front separates the HII region from the PDR. Typical values of the effective far-ultraviolet optical depth, and H nucleon column density are shown.

3. H_2 AS A THERMAL PROBE

The (v, J) rovibrational excited states of H_2 are populated by inelastic collisions

$$\mathrm{H}_2(v_1, J_1) + X \rightarrow \mathrm{H}_2(v_2, J_2) + X \pm KE \quad ;$$

by UV pumping:

$$\begin{aligned} \mathrm{H}_2(0, J_1) + h\nu &\rightarrow \mathrm{H}_2^*(v_1, J_1 \pm 1) \\ &\rightarrow \mathrm{H}_2(v_2, J_1 \pm 0, 2) + h\nu(\mathrm{UV}) \\ &\rightarrow \mathrm{H}_2(v_3, J_1 \pm 0, 2, 4) + h\nu(\mathrm{IR}) \\ &\quad \ldots \\ &\rightarrow \mathrm{H}_2(0, J_1 \pm 0, 2, 4, \ldots) \quad ; \end{aligned}$$

and by formation on grains:

$$\mathrm{grain} + \mathrm{H} + \mathrm{H} \rightarrow \mathrm{grain} + \mathrm{H}_2(v, J) + KE \quad .$$

At the densities $n_H \gtrsim 10^4\,\mathrm{cm}^{-3}$ of bright PDRs, collisions maintain the (v=0, J) levels of H_2 in approximate thermal equilibrium for $J \lesssim 5$. Therefore measurements with ISO of the quadrupole emission line intensities from levels $J \lesssim 5$ provide a good indicator of the gas temperature, while the emission from the higher J levels is sensitive to both the gas temperature and density. We do not expect the level populations to be characterized by a single "excitation temperature", but the "best-fit" excitation temperature characterizing a range of J values (e.g., J=3–5) should indicate the approximate gas temperature in the part of the PDR where these levels are predominantly excited.

The populations of very high J levels (e.g., J = 15) are potentially affected by UV pumping (the quadrupole decay cascade following a UV pump injects a small amount of H_2 into high J states) and formation on dust grains (some fraction of the newly-formed H_2 may be in high J states). Therefore excitation temperatures characterizing $J \gtrsim 10$ may not reflect gas temperatures.

4. THE S140 PDR

ISO obtained spectra of the photodissociation region where the S140 HII region abuts the L1202/L1204 molecular cloud (Timmermann et al. 1996); see Figure 2.

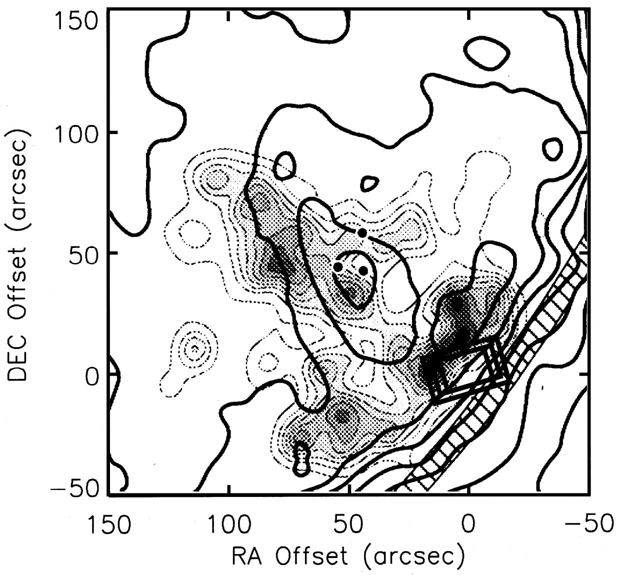

Figure 2. The S140 PDR, where radiation from the B0.5V star HD 211880 impinges on a dense clump in the L1202/L1204 molecular cloud. The ionization front is shown as a shaded region. The greyscale shows [CI]610μm emission (White & Padman 1991). Contours show CO(3-2) emission (Hayashi et al. 1987). The SWS apertures are shown as rectangles positioned just interior to the ionization front, where the photodissociation front is expected to be located, viewed approximately edge-on. The exciting star is located ~7 arcmin SW of the aperture. Figure taken from Timmermann et al. (1996).

Timmermann et al. (1996) reported measurements of line emission out of (0,J) levels with J as large as 9 (see Figure 3). The inferred column densities for $3 \leq J \leq 7$ are characterized by an excitation temperature $T_{\mathrm{exc}} \approx 500\,\mathrm{K}$; the emission from J = 8 and 9 suggest a higher temperature. How much of the PDR is characterized by such high temperatures? To address this question, Timmermann et al. (1996) considered an *ad-hoc* temperature profile, shown in Figure 4.

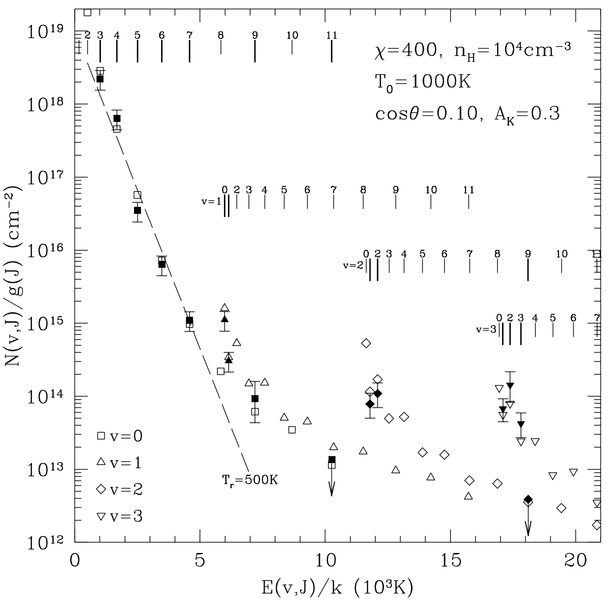

Figure 3. Observed (filled symbols) and model (open symbols) column densities in rovibrational levels of H_2 *along the line-of-sight. Observed intensities have been corrected for foreground extinction by dust with 0.3 mag of extinction at K. The PDR is assumed to be inclined with* $\cos\theta = 0.1$. *The broken line is a* $T = 500\,\mathrm{K}$ *thermal distribution, indicating that a significant amount of* H_2 *is located in regions where* $T_{gas} \gtrsim 500\,\mathrm{K}$. *Taken from Timmermann et al. (1996).*

With this *ad-hoc* temperature profile, the chemical abundances are computed by requiring steady-state balance between formation and destruction, using standard assumptions for the formation rate of H_2 on grains, and a detailed treatment of H_2 self-shielding. H_2 level populations were computed for a plane-parallel PDR, including both UV pumping and collisional excitation and deexcitation (Draine & Bertoldi 1996). The H nucleon density was assumed to be $n_\mathrm{H} = 10^4\,\mathrm{cm}^{-3}$ (as expected for pressure balance with the HII region), and the radiation field at 1000Å was assumed to be $\chi = 400$ times stronger than the Habing (1968) value (as expected for the $\sim 1.7\,\mathrm{pc}$ distance from the exciting B0.5V star).

The resulting model is shown in Figure 3, where it is assumed that $\cos\theta = 0.1$, where θ is the angle between the line-of-sight and the normal to the model PDR. It is seen that the level populations are in fairly good agreement with observations, although the model overestimates the $v = 1$ and 2 level populations, while underestimating the $v = 3$ levels. For this model, $T = 500\,\mathrm{K}$ at the point where $y \equiv 2n(\mathrm{H}_2)/n_\mathrm{H} = 0.2$, and $T = 150\,\mathrm{K}$ where $y = 0.5$.

Timmermann et al. (1996) also compared predicted and observed fine structure line intensities with those predicted by the model. Agreement is generally good, allowing for uncertainties in abundances of Si and Fe: [CI]609μm is close to the observed value, while [SiII]35μm and [FeII]26μm agree with observations if Si/H=1.5×10^{-6} and Fe/H=5×10^{-8}. The principal discrepancy is [OI]63μm, which the model predicts to be ~ 5 times stronger than observed.

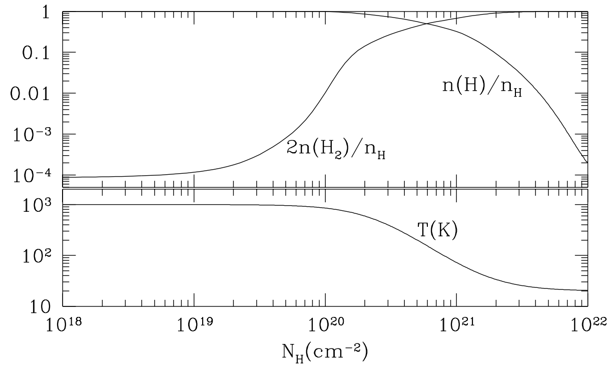

Figure 4. Ad-hoc temperature profile adopted for S140 PDR model. With this assumed temperature profile, the H_2 *abundances are computed by requiring a balance between* H_2 *formation and photodissociation. Taken from Timmermann et al. (1996).*

5. THERMAL BALANCE IN PDRS

The obvious question now is: what temperatures do we *expect* the gas to have in PDRs, if we assume that the gas temperature is determined by a balance between heating and cooling? The principal heating processes in PDRs are:

- Photoelectrons emitted from dust grains;
- UV pumping, followed by collisional deexcitation of rovibrationally excited H_2;
- Photodissociation (kinetic energy of H+H);
- H_2 formation (kinetic energy, collisional deexcitation);
- Photoionization of H, C, etc.

while the dominant cooling processes are:

- fine-structure line emission from [C II]158μm, [O I]63, 146μm, [Si II]35μm, [Fe II]25μm,...;
- H_2 quadrupole emission;
- CO rotational emission.

The grain photoelectric heating rate is quite uncertain. Here we show results assuming the photoelectric heating rate of Bakes & Tielens (1994).

The cross sections for collisional excitation and deexcitation of H_2 are also uncertain; for $T_\mathrm{gas} > 1000\,\mathrm{K}$ we use the H-H_2 inelastic rates of Martin & Mandy (1995) and Mandy & Martin (1995), while for $T_\mathrm{gas} <$

1000 K we extrapolate the Mandy & Martin rates using eq. (16) of Draine & Bertoldi (1996), but using $\theta = 1000$ K rather than 600 K as the transition temperature, as discussed by Draine & Bertoldi (1999).

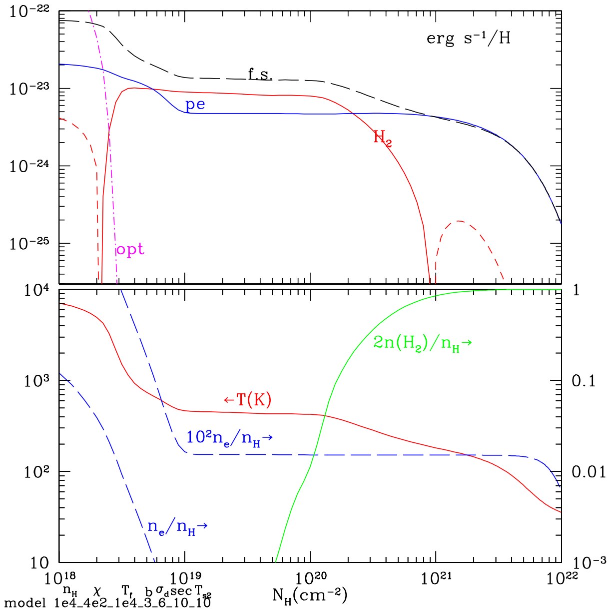

Figure 5. Thermochemical profile of S140 PDR model, with temperatures determined by thermal balance calculations. Lowel panel: gas temperature T, H_2 fraction $2n(H_2)/n_H$, and fractional ionization $n(e)/n_H$. Upper panel: heating (solid lines) and cooling (broken lines) due to grain photoelectric heating ("pe"), the H_2 molecule (including formation, collisional excitation and deexcitation, and photodissociation), fine structure line emission ("f.s."), and optical line emission ("opt"). Note that H_2 has a net heating effect in much of the PDR.

The fine-structure line emission is computed using standard collision rates, abundances characteristic of the gas toward ζOph (e.g., Si and Fe depleted by factors of 40 and 250, respectively). Some of the lines – in particular, [OI]63μm – can become optically thick. An "escape probability" approximation was used to estimate local cooling rates (Draine & Bertoldi 1999).

Figure 5 shows the calculated thermochemical profile, as well as showing the contributions of different processes to heating and cooling. Close to the ionization front the fractional ionization is a few percent, and $T_{gas} \approx 4000-6000$ K; in this region, optical line emission (e.g., [SII]6716,6739) dominates the cooling, but is unimportant when $T_{gas} \gtrsim 4000$ K. Emission from excited fine-structure levels dominates the cooling for $50 \lesssim T_{gas} \lesssim 4000$ K.

H_2 contributes net heating throughout much of the PDR. This heating arises mainly from collisional de-excitation of rovibrationally excited H_2 following UV-pumping or H_2 formation on grains, with a secondary contribution from the kinetic energy of newly-formed H_2 and H+H following photodissociation. The other major heating process is photoelectric emission from dust grains. Both H_2 heating and photoelectric heating are important for $N_H \lesssim 10^{21}\,\mathrm{cm}^{-2}$; beyond this point H_2 self-shielding has reduced the photodissociation rate (and therefore the H_2 formation rate as well) to very low levels, and photoelectric heating dominates.

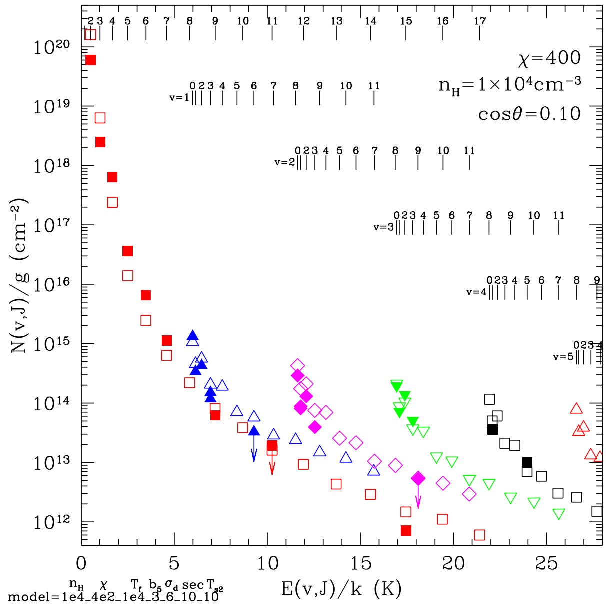

Figure 6. Column densities $N(v,J)$ along the line-of-sight, divided by level degeneracies $g(J)$. Solid symbols: observed values based on line intensities corrected for foreground extinction with $A_K = 0.2$mag, and internal extinction within the PDR, inclined with with $\cos\theta = 0.1$. Open symbols: model for S140 PDR with $\chi = 400$ and $n_H = 10^4\,\mathrm{cm}^{-3}$, with temperatures determined by thermal balance.

Figure 6 shows the observed column densities of excited states of H_2 along the line of sight toward the S140 PDR, corrected for an assumed extinction $A_K = 0.3$ mag. A number of H_2 line detections and upper limits were obtained subsequent to preparation of the Timmermann et al. (1996) paper on the S140 PDR; Figure 6 shows column densities obtained from the most recent data reduction (Bertoldi et al. private communication). Also shown are the column densities predicted by our model, which assumes an inclination of the PDR with $\cos\theta = 0.1$ – a factor of 10 "limb-brightening".

There are significant differences between the model H_2 level populations and those observed toward S140. The assumed factor of 10 limb-brightening leads to a good match for the vibrationally excited levels. However, the $v = 0$ column densities predicted by the model fall off too steeply – while the $J = 2, 3$ column densities in the model exceed the observed values by a factor ~ 2, the $J = 3-7$ column densities are too low by factors $\sim 2-3$. This presumably indicates that either the H_2 inelastic cross sections or the thermal profile are incorrect. Note, however, that the model appears to be able to reproduce the observed population of H_2 in $J = 15$, and thereby a high excitation temperature for the high$-J$ levels.

Somewhat better agreement can be obtained if the gas density and illuminating radiation field are both increased; in Figures 7 and 8 we show the result of increasing the illuminating radiation field to $\chi = 600$, and raising the gas density to $n_\mathrm{H} = 4 \times 10^4\,\mathrm{cm}^{-3}$. With the increased χ and n_H, a good fit to the observed H_2 line intensities is obtained for a limb-brightening factor $1/\cos\theta = 5$. However, the assumed value of χ is somewhat larger than expected from our knowledge of the exciting star, and n_H is larger than expected given our estimates of the pressure in the ionization front (Timmermann et al. 1996). It should also be noted that even with these values of χ and n_H, there are still noticeable discrepancies between model and observation. It is difficult to match the low observed line ratio between 0-0S(1) and 0-0S(2). Both lines are in the same size ISO aperture, so beam dilution differences could not be the cause of the mismatch. The model also overproduces $J = 15$, although this line was observed after ISO's helium boiloff, which made its flux calibration more difficult. Most other levels' column densities are well reproduced.

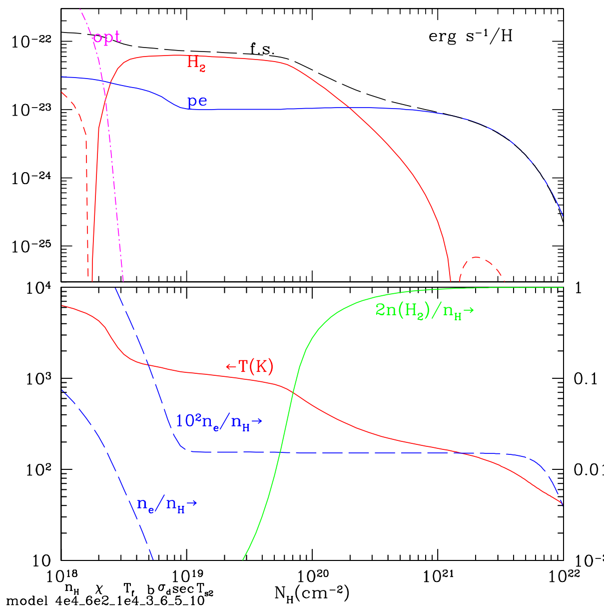

Figure 7. Same as Fig. 5, but for $n_\mathrm{H} = 4 \times 10^4\,\mathrm{cm}^{-3}$ and $\chi = 600$.

The high gas temperatures found in S140 are not unique. Early evidence for high gas temperatures in PDRs was obtained from H_2 $J = 3$–1 and 4–2 line observations by Parmar et al. (1991), who inferred $T_\mathrm{gas} = 1000 \pm 250\,\mathrm{K}$ at a position .0244 pc from the ionization front in the Orion Bar, and $T_\mathrm{gas} = 600 \pm 50\,\mathrm{K}$ another .0044 pc farther away from the ionization front.

High gas temperatures near the H/H_2 transition were inferred, based on ground-based spectra, for the reflection nebula NGC 2023 (Draine & Bertoldi 1996). ISO spectra of the reflection nebula NGC 7023 (Bertoldi et al. 1999) and the Orion Bar (Rosenthal et al., private communication), also show that some of the H_2 must be in a region of gas temperatures $T_\mathrm{gas} \gtrsim 600\,\mathrm{K}$.

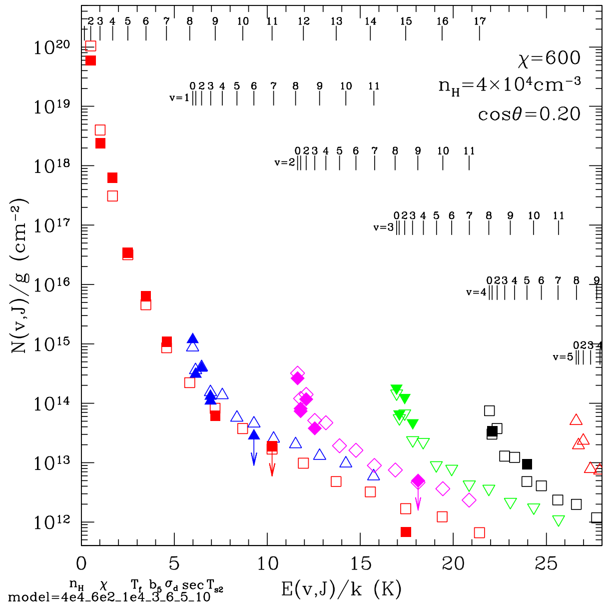

Figure 8. Same as Fig. 6, but for $n_\mathrm{H} = 4 \times 10^4\,\mathrm{cm}^{-3}$ and $\chi = 600$, and with the PDR assumed to be inclined with $\cos\theta = 0.2$.

6. WHAT NEEDS TO BE CHANGED IN THE MODELS?

Where do we stand on modeling the H_2 emission from PDRs? Considering that the emission arises from a region with a range of densities, one might take the point of view that we are doing pretty well – our constant density planar PDR models can approximately reproduce the observed level populations using ultraviolet pumping of H_2 plus collisional excitation/deexcitation, with gas temperatures obtained from a balance of heating and cooling. Nevertheless, it seems to us that the discrepancies between our best models and the observations are unacceptably large. The discrepancies may be due in part to our underlying assumptions of planar geometry and uniform density, but may also be due to poor approximations in our description of the local microphysics of heating, cooling, chemistry, and level excitation. Below we indicate some of the areas where existing models may require modification.

6.1. H_2 inelastic collision cross sections

The H–H_2 collisional excitation/deexcitation rates used here for $T_\mathrm{gas} \gtrsim 600\,\mathrm{K}$ are those of Martin & Mandy (1995) and Mandy & Martin (1995), which were obtained from quasi-classical trajectory calculations. These rates are thought to be accurate for $T_\mathrm{gas} \gtrsim 600\,\mathrm{K}$, but are likely to be increasingly inaccurate at low temperatures, where quantum calculations are required (Flower 1997, Forrey et al. 1997). Forrey et al. (1997) have recently reported accurate rates for $\Delta J = \pm 2$ transitions among the $v = 0$, $J = 0-5$ levels, for $100 < T_\mathrm{gas} < 1000\,\mathrm{K}$; our extrapolation from the Mandy & Martin (1995) results was adjusted to give good agreement with these newer rates.

While H-H_2 inelastic rates are generally larger than for H_2-H_2 collisions, the latter are important when the H fraction becomes small. Quantum calculations have recently been reported by Flower (1997).

6.2. Grain Photoelectric Heating Rate

The thermal models reported here employ a photoelectric heating rate recommended by Bakes & Tielens (1994) for heating by 6-13.6 eV photons:

$$\Gamma_{pe} = n_{\rm H}\sigma_{uv}u_{uv}c\ \epsilon$$

$$\begin{aligned}
\sigma_{uv} &= \text{dust EUV absorption/H} \approx 6\times10^{-22}\,\text{cm}^2\\
u_{uv} &= \text{EUV energy density} = \chi\times0.033\,\text{eV}\,\text{cm}^{-3}\\
\epsilon &= \text{photoelectric heating efficiency}\\
&= .049(1.+x/1925)^{-0.73}+\\
&\quad .037\,T_4^{0.7}(1.+x/5000)^{-1}\\
x &\equiv \chi(T/\text{K})^{0.5}/(n_e/\text{cm}^{-3})
\end{aligned}$$

Bakes & Tielens assumed a "MRN" power-law size distribution down to ultrasmall grains containing only ~ 30 carbon atoms (i.e., PAH molecules). Since we have only an imprecise understanding of the composition and size distribution of the grains, this heating rate is necessarily uncertain. Under the conditions of interest (e.g., the point where $2n(H_2)/n_{\rm H} = 0.1$ in Figure 5), we have $\chi \approx 400$, $n_e \approx 1.5\,\text{cm}^{-3}$, and $T \approx 350\,\text{K}$, so that $x \approx 5000$, and the heating efficiency $\epsilon \approx 0.021$, which increases further into the cloud to $\epsilon \approx 0.049$. Since photoelectric emission from grains is a dominant heating process in PDRs, its further study would be of value.

6.3. Dust-to-Gas Ratio

The dust grains play a crucial role in photodissociation regions. In particular, they determine the rate for formation of H_2 from H, and, as seen above, photoelectric emission from dust is a major heat source. Common practice is to adopt a "standard" dust-to-gas ratio and wavelength-dependent dust opacity in the PDR. However, Weingartner & Draine (these proceedings) have pointed out that the anisotropic radiation in a PDR can drive the grains through the gas at drift velocities which may be comparable to the flow velocity of the gas relative to the dissociation front, thereby leading to an *increase* in the dust-to-gas ratio in the PDR, at least for those grain compositions and sizes for which the grain-gas drift velocities are large. Increased dust concentrations in part of the PDR could alter the thermochemical properties of the PDR by increasing the H_2 formation rate (and therefore the local rate of UV pumping and photodissociation of H_2) and by increasing the grain photoelectric heating rate. As a result, we can expect that the gas temperature will be increased near the photodissociation front.

The anisotropic radiation incident on a dust grain results in a force which consists of the "ordinary" radiation pressure force due to absorption and scattering, plus additional forces due to anisotropic photoelectron emission (the "illuminated" side of the grain will emit more photoelectrons per second than the "dark" side) and anisotropic photodesorption (adsorbed H or H_2 can be photodesorbed, with a larger rate on the "illuminated" side of the grain). The recoil force from photoelectric emission and photodesorption can be several times larger than the "ordinary" radiation pressure (Weingartner & Draine in these proceedings).

Because the grains are charged, drift across the magnetic field lines will be inhibited. It will be of great interest to see the extent to which these effects will change the dust-to-gas ratio, and the grain size distribution, in the PDR, and how this affects the thermochemical profile of the PDR.

7. SUMMARY

ISO has opened a new window on photodissociation fronts, by allowing us to measure the populations of the rotationally-excited levels of the $v = 0$ state of H_2, thereby placing strong constraints on the gas temperature. The S140 PDR provides an excellent illustration of this capability.

The observed line emission from rotationally-excited levels of H_2 indicates that gas temperatures $T_{\rm gas} \gtrsim 500\,\text{K}$ prevail in part of the PDR where appreciable H_2 is present. Attempts to construct theoretical models of the PDR tend to fall short in terms of the populations of levels $J = 3-7$,

We discuss the uncertainties in the dominant heating and cooling mechanisms; the H_2 inelastic collision rates still have significant uncertainties, and the grain photoelectric heating rate is yet not well-established. In addition, it appears possible that the dust-to-gas ratio in PDRs such as S140 may deviate from the "standard" value since the anisotropic radiation field can drive the grains through the gas with significant drift speeds.

ACKNOWLEDGEMENTS

For their contribution to the recent S140 data analysis we are grateful to the MPE SWS group, and especially to H. Feuchtgruber and E. Wieprecht. This research was supported in part by NSF grant AST 96-19429 (BTD) and by the Deutsche Forschungsgemeinschaft (FB). B.T.D. wishes to thank Osservatorio Arcetri for its gracious hospitality during the completion of part of this work.

REFERENCES

Bakes, E.L.O., Tielens, A.G.G.M. 1994, ApJ, 427, 822

Bertoldi, F., Draine, B.T. 1996, ApJ, 458, 222

Bertoldi, F., Feuchtgruber, H., et al. 1999, in preparation

Draine, B.T., Bertoldi, F. 1996, ApJ, 468, 269

Draine, B.T., Bertoldi, F. 1999, in preparation

Flower, D.R. 1997, MNRAS, 288, 627

Forrey, R.C., Balakrishnan, N., Dalgarno, A., & Lepp, S. 1997, ApJ, 489, 1000

Habing, H.J. 1968, Bull. Astron. Inst. Netherlands, 19, 421

Hayashi, M., Hasegawa, D., Omodaka, D., et al. 1987, ApJ, 312, 327

Hollenbach, D.J., Natta, A. 1995, ApJ, 455, 133

Hollenbach, D.J., Tielens, A.G.G.M. 1997, ARA&A, 35, 179

Hollenbach, D.J., Tielens, A.G.G.M. 1998, Rev. Mod. Phys., in press

Mandy, M.E., Martin, P.G. 1995, ApJS, 86, 199

Martin, P.G., Mandy, M. 1995, ApJ, 455, L89

Parmar, P.S., Lacy, J.H., Achtermann, J.M. 1991, ApJ, 372, L25

Rosenthal, D., et al. 1999, private communication

Sternberg, A., Yan, M., Dalgarno, A. 1998, in *Molecules in Astrophysics: Probes and Processes*, ed. E. van Dishoeck, p. 141

Störzer, H., Hollenbach, D.J. 1998, ApJ, 495, 853

Timmermann, R., Bertoldi, F., Wright, C.M., et al. 1996, A&A, 315, L281

Walmsley, C.M. 1998, Astr. Lett. & Comm., 37, 1

White, G.J., Padman, R. 1991, Nature, 354, 511

SWS SPECTROSCOPY OF THE ORION PEAK 1 OUTFLOW: H_2 AND HD

D. Rosenthal[1], F. Bertoldi[1,2], S. Drapatz[1], & R. Timmermann[3]

[1]Max-Planck-Institut für Extraterrestrische Physik, Garching, Germany
[2]Max-Planck-Institut für Radioastronomie, Bonn, Germany
[3]Universität zu Köln, Köln, Germany

ABSTRACT

Using the Short-Wavelength-Spectrometer on board of ISO we obtained near- and mid-infrared spectra of Orion Peak 1, the brightest H_2 emission region in the sky. A wealth of emission and absorption features was detected, including some 80 H_2 ro-vibrational and pure rotational lines, the latter reaching to 0-0 S(25). We speculated upon the nature of the observed high-excitation tail in the H_2 level column density distribution, suggesting H_2 formation or high-velocity collisional excitation in C-shocks as its cause.

For the first time, an infrared emission line of HD was detected in the interstellar medium, the v =0-0 R(5) at 19.4305 μm. Assuming similar excitation conditions for H_2 and HD, and accounting for the subthermal excitation of HD, we were able to derive an abundance ratio $[HD]/[H_2] = (9.0 \pm 2.5) \times 10^{-6}$ in the Orion outflow. When we take into account that HD may be selectively depleted relative to H_2 in the warm, partially dissociated layers of C-shocks, we find a deuterium abundance of $[D]/[H] = (7.6 \pm 2.1) \times 10^{-6}$, which is on the lower end of abundances derived recently through UV absorption measurements.

Key words: ISO; Orion Peak 1; shock waves; H_2; HD

1. INTRODUCTION

At a distance of only 450 pc, the Orion Molecular Cloud (OMC) 1 has become the best studied region of ongoing low- and high-mass star formation (Genzel & Stutzki 1989). Deeply embedded in the dense cloud behind the Orion Nebula, a powerful outflow was found that originates within 5 arcsec from the bright infrared source IRc2 (Allen & Burton 1993). The interaction of this high-velocity outflow with the surrounding molecular cloud gives rise to hundreds of small peaks of H_2 emission. The brightest concentration of these emission peaks is located about 20 arcsec north of IRc2 and BN, and was named "Peak 1" from early observations that were unable to resolve the emission's fine structure (Beckwith et al. 1978).

ISO observations toward Peak 1 for the first time enabled the detection of H_2 emission arising from levels spaced over a very broad range of energies, thereby allowing a detailed study of the excitation conditions and mechanisms in the shocked, dense gas.

Emission from the deuterated hydrogen molecule, HD, has also been searched for with great effort in numerous shock and UV excited regions. An inferred measurement of the deuterium abundance is of great cosmological interest. Deuterium is continuously burned up in stars, and since no formation process is known, the present day deuterium abundance could provide a lower limit to its primordial value, which reflects the early baryon to photon density ratio. Possible spatial variations of the present deuterium abundance may in addition trace spatial variations in the star formation history.

2. OBSERVATIONS

2.1. Data reduction

We report on ISO-SWS observations of Orion Peak 1 in the full scan grating (SWS 01) and Fabry-Perot (SWS 07) modes, and in the single line scan grating mode (SWS 02). The full 2.3 to 45 μm SWS 01 spectrum was recorded in its slowest mode with the highest possible resolution. The data reduction was carried out using standard Off Line Processing (OLP) routines up to the Standard Processed Data (SPD) stage within the SWS Interactive Analysis (IA) system. Between the SPD and Auto Analysis Result (AAR) stages, a combination of standard OLP and in-house routines were used to extract the individual spectra. The in-house routines included an interactive dark-current subtraction for individual scans and detectors as well as for the removal of fringes. The flux calibration errors range from 5% at 2.4 μm to 30% at 45 μm. The statistical uncertainties derived from the line signal to noise ratio are for most detected lines smaller than the systematic errors due to flux calibration uncertainties.

Proceedings of the Conference "The Universe as seen by ISO", Paris, France, 20–23 October 1998 (ESA SP-427, March 1999)

2.2. Results

Figure 1 shows the larger part of the SWS 01 full grating spectrum, which contains a wealth of emission and absorption features. The spectrum is dominated by lines of molecular hydrogen. About 80 rovibrational and pure rotational H_2 lines were found; the latter range from 0-0 S(1) to 0-0 S(25) with corresponding upper level energies E(v, J)/k from 1015 K to 42,500 K.

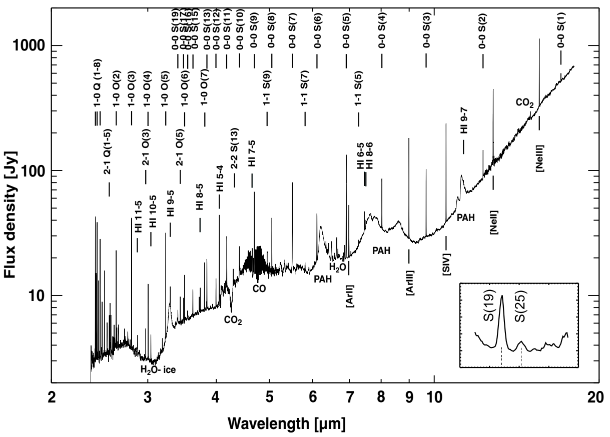

Figure 1. Part of the SWS 01 full scan grating spectrum, showing the richest forest of H_2 lines ever detected. The continuum flux levels were artificially adjusted to be continuous over band boundaries. The insert shows a SWS 02 spectrum of the H_2 0-0 S(19) and 0-0 S(25) lines.

Emission of H recombination, ionic fine-structure, of CO and H_2O lines, and of PAHs was detected. Besides the prominent water ice and silicate absorption features at 3.1 μm and 9.7 μm, CO_2, OH and probably CO are seen in absorption. For some of the lines, these spectra provide their first detection in the interstellar medium.

Because of their small Einstein coefficients, the electric quadrupole transitions of H_2 remain optically thin. This permits a straight forward calculation of the H_2 column densities in the respective upper levels

$$N(v,J) = \frac{4\pi}{h\nu}\,\frac{I_{\rm obs}(v,J\rightarrow v',J')}{A(v,J\rightarrow v',J')}\;10^{0.4A_\lambda}, \qquad (1)$$

where A_λ accounts for dust extinction at the transition's wavelength along the line of sight (see Section 2.3.). It is useful to plot the level column densities, divided by the level degeneracy, $g = g_{\rm s}(2J+1)$, against the level energy $E(v,J)/k$. The resulting excitation diagram is shown in Figure 2.

The distribution of column densities is very smooth, showing no hint of fluorescent excitation or for a deviation of an ortho-to-para degeneracy ratio of three. Fluorescently excited H_2 as seen in photodissociation regions (Timmermann et al. 1996) generally displays enhanced excitation in respectively higher vibrational levels, and ortho-to-para column density ratios lower than three in the vibrationally excited levels (Draine & Bertoldi 1996; Sternberg & Neufeld 1998). In

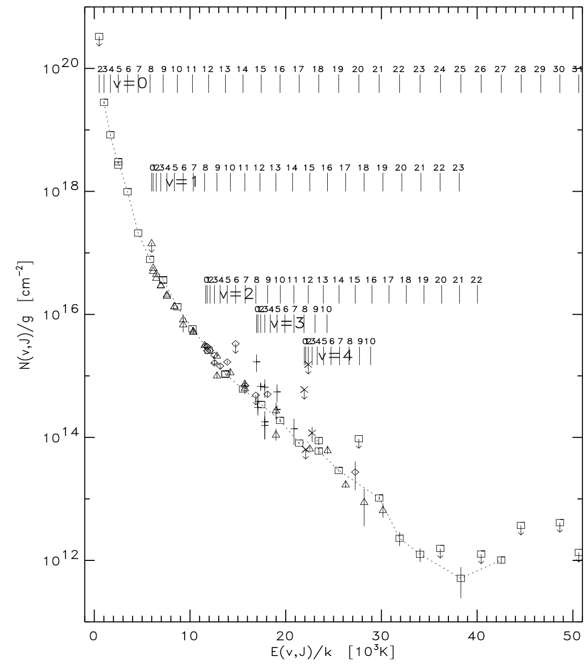

Figure 2. Observed, dereddened H_2 level column densities, divided by the level degeneracy, plotted against the level energy $E(v,J)/k$. Different vibrational levels are represented by separate symbols: squares, triangles, diamonds, +, and x, denote v =0, 1, 2, 3, 4, respectively.

Peak 1 however, the H_2 column densities (divided by g) appear to depend only on the level energy, not on the quantum number.

This might indicate that the molecules are thermally excited. The slope of the line which best fits $\ln[N(v,J)/g]$ as a function of $E(v,J)/k$ is the inverse of an excitation temperature, T_{ex}, at level energy $E(v,J)$. Near the lowest levels, $T_{ex} \approx 600$ K, which increases toward higher level energies to about 3000 K at $E(v,J)/k > 15,000$ K. Such excitation may be due to a superposition of emission from gas with a range of kinetic temperatures up to over 3000 K. To thermalize levels at $E/k > 15,000$ K even at kinetic temperatures above 3000 K requires densities way in excess of 10^5cm^{-3}. We infer from the excitation diagram that only a small fraction of the warm molecular gas is at such high temperatures. This may be somewhat difficult to reconcile with the expected smooth temperature profile in a C-type shock. However, during the initial establishment of a shock, when outflow material first hits a dense cloud, a J-shock is established within the C-shock, and here a relatively small column of gas may be heated to high enough temperatures (Chièze et al. 1998) to account for the high-temperature tail of the column density distribution.

In magnetic C-type shocks, which are believed to be responsible for most of the emission in Peak 1, some H_2 may also become highly excited through non-thermal processes in the magnetic shock precursor, where ions and neutrals collide at the shock speed of 20-40 km s^{-1}. The high-velocity inelastic collisions of H_2 with ions or with accelerated H and H_2 are responsible for the partial dissociation of the gas, and at the same time they should leave many of the surviving molecules in highly excited states (O'Brien & Drury 1996).

An alternative excitation mechanism for the high states is formation pumping, i.e., the population by newly-formed H_2. Although some of the 4.5 eV released in the formation of a new H_2 molecule is required to leave the grain, the remainder is somehow split into translation, rotation, and vibration of the released molecule. The exact level distribution of newly formed H_2 is yet unknown, but it could very well contribute to the observed excitation at intermediate energies, at $E/k \approx 10,000 - 30,000$ K.

The $J = 27$ level observed through the 0-0 S(25) line appears overpopulated by a factor of five over what would be expected from extrapolating the lower energy level populations. Unless we misidentified this line, it seems that a rather distinct mechanism may be populating this level, and possibly all of the very highest levels. The $J = 27$ level is 3.6 eV above ground and only 0.9 eV from the dissociation limit. H_2 that is newly formed on grains is unlikely to be able to populate states that high, because some fraction of the formation energy is lost to overcome the grain surface potential, and some goes to kinetic and vibrational excitation. The gas phase formation of H_2 via H^- might however be able to leave the new molecule in a high rotational state.

2.3. Extinction correction

In order to correct the derived fluxes for extinction we attempted to derive the extinction in the wavelength range $2\,\mu$m to $45\,\mu$m from the H_2 lines themselves (details are given by Bertoldi et al. 1998). Our inspection of the H_2 excitation diagram drawn from the line intensities *uncorrected* for extinction showed that the column densities follow a smooth distribution, with no dependence on vibrational quantum number, and no sign of an ortho-to-para column density ratio different from three.

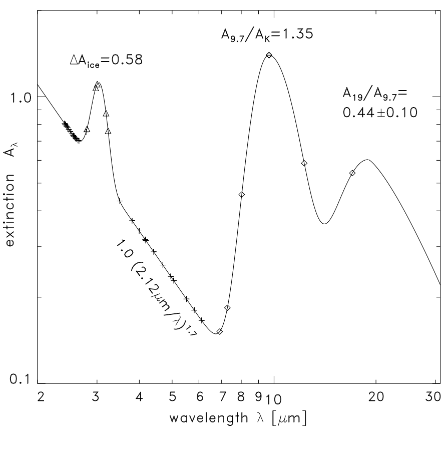

Figure 3. Adopted extinction curve.

Part of the dispersion in the columns is due to extinction, and we therefore tried to estimate the extinction by minimizing the dispersion around a least-squares fit to the level columns. We were thereby able to derive estimates for four parameters which describe our toy extinction curve (Figure 3): the absolute normalization of a $A_\lambda \propto \lambda^{-1.7}$ power law part from $2.4\,\mu$m to $6\,\mu$m, the width and depth of the water ice absorption feature at $3.1\,\mu$m, and the depth of the $9.7\,\mu$m silicate absorption feature. We adopted the width of the 9.7 and $18\,\mu$m silicate features from calculations by Draine & Lee (1984). The depth of the $18\,\mu$m feature was taken to be 0.44 times that of the $9.7\,\mu$m feature, which is an average of previous estimates.

2.4. Detection of HD

We also searched for seventeen HD lines toward Peak 1, and detected one of them, the 0-0 R(5) (i.e., $J = 6 \rightarrow 5$) dipole transition at an expected wavelength of 19.4305 μm (Bertoldi et al. 1998). Although the detection may seem marginal (Figure 4), the line does appear in two independent observations, and stands out well above the noise in the central wavelength range of the coadded scans. Its beam-averaged flux is $(1.84 \pm 0.4) \times 10^{-5}\,\mathrm{erg\,s^{-1}\,cm^{-2}\,sr^{-1}}$.

Since only one HD line was detected, the HD excitation could not be measured directly. To compute a total warm HD column density we therefore assumed that HD and H_2 underly similar excitation conditions, i.e., that they follow approximately the same density and temperature structure in the emitting region. The solid line in Figure 5b represents the least squares fit to the H_2 columns seen in Figure 5a, but normalized (i.e., vertically shifted) to the observed HD $v = 6$ level column.

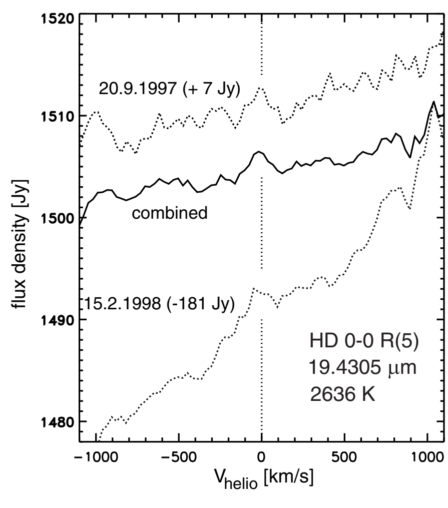

Figure 4. Detection of HD 0-0 R(5). The dashed lines are two independent AOT 02 observations, the solid line shows the coaddition. Note that the noise level rises toward the scan edges.

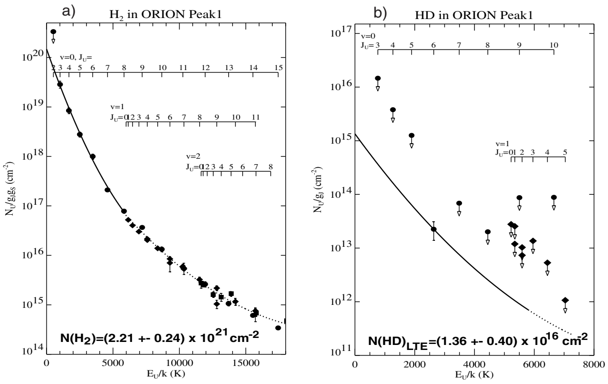

Figure 5. H_2 and HD excitation diagrams, showing the dereddened column densities plotted against level energy. The solid line in a) is a least squares fit, which is also shown in b), vertically shifted to match the observed HD $J = 6$ level column.

The total warm H_2 column density was derived from adding over all levels following the least squares fit to N/g, and we find

$$N(\mathrm{H_2}) = (2.21 \pm 0.24) \times 10^{21}\,\mathrm{cm^{-2}}. \tag{2}$$

The H_2 levels are most likely thermalized to excitation energies beyond 10,000 K. However, the HD dipole transitions are faster than the quadrupole H_2 transitions, so that the higher HD levels may be subthermally populated, and the column densities drop steeper with E/k than those of H_2. To assess the effects of non-LTE on the HD column densities we solved the equations of statistical equilibrium (see Timmermann 1996), including radiative decay, and excitation/deexcitation through collisions with He, H_2 and H. The result is shown in Figure 6a, where we plot the ratio between the non-LTE populations $n_{0\mathrm{J}}$ and those expected under LTE. For densities below $10^6\,\mathrm{cm^{-3}}$ the HD level population deviate significantly from LTE.

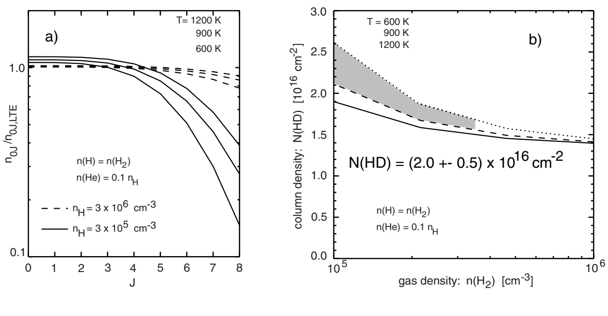

Figure 6. a): Deviations of the HD $v = 0$ level populations from LTE, as a function of rotational quantum number J, for two different gas densities, and three different kinetic temperatures in each case. $n_{0\mathrm{J}}$ and $n_{0\mathrm{J,LTE}}$ are HD densities in an individual level in non-LTE and LTE. b): Total HD column density in non-LTE as a function of H_2 density, for three gas temperatures. The shaded region covers the most likely density and temperature regime in Peak 1.

We account for these deviations in computing the total HD column,

$$N(\mathrm{HD}) = \frac{n_{06,\mathrm{LTE}}}{n_{06}} \sum_{v\,J} N_{v\,J} \, \frac{n_{v\,J}}{n_{v\,J,\mathrm{LTE}}}\ , \tag{3}$$

which now depends on both gas density and temperature. We illustrate this dependence in Figure 6b. For the range of temperatures expected to dominate in the Peak 1 shocks, 600 - 1000 K and the estimated H_2 densities of $(1 - 3.5) \times 10^5\,\mathrm{cm^{-3}}$, we compute

$$N(\mathrm{HD}) = (2.0 \pm 0.5) \times 10^{16}\,\mathrm{cm^{-2}} \tag{4}$$

2.4.1. Deuterium abundance

The derived H_2 and HD total column densities yield an abundance ratio of:

$$[\mathrm{HD}]/[\mathrm{H_2}] \;=\; (9.0 \pm 2.5) \times 10^{-6}\ . \tag{5}$$

How does this translate to a deuterium abundance? For this we need to consider that in a partly dissociative C-shock, HD is depleted somewhat more than H_2 because of an asymmetry in the exchange reactions

$$\mathrm{H_2 + D \rightleftharpoons HD + H} + \Delta H_0 \tag{6}$$

where $\Delta H_0/k = 418\,\mathrm{K}$ is the enthalpy difference. In the warmest layers of the shock, HD is thereby depleted by a factor two relative to H_2. Averaged over the warm shocked layer, where most of the observable emission arises, HD is depleted relative to H_2 by a factor ~ 1.7. Taking this depletion into account, we arrive at a deuterium abundance

$$[\mathrm{D}]/[\mathrm{H}] \;=\; (7.6 \pm 2.1) \times 10^{-6}\ . \tag{7}$$

which is at the low end of the range $(7 - 21) \times 10^{-6}$ measured through UV absorption observations toward nearby stars (Linsky 1998; Jenkins et al. 1999). This may indicate that the gas in the Orion molecular cloud has undergone much processing since its Big Bang nucleosynthesis.

REFERENCES

Allen, A., Burton, M. 1993, Nature, 363, 54

Beckwith, S., Persson, S., Neugebauer, G., Becklin, E. 1978, ApJ, 223, 464

Bertoldi, F., Timmermann, R., Rosenthal, D., Drapatz, S., Wright, C. 1999, A&A, submitted

Chièze, J.-P., Pineau des Forêts, G., Flower, D. 1998, MNRAS, 295, 672

Draine, B., Lee, H. 1984, ApJ, 285, 89

Draine, B., Bertoldi, F. 1996, ApJ, 468, 269

Genzel, R., Stutzki, J. 1989, ARA&A, 27,41

Jenkins, E., Tripp, T., Wozniack, P., et al. 1999, in preparation

Linsky, J. 1998, Space Science Review, 84, 285

O'Brien, I., Drury, L. 1996, MNRAS, 280, 550

Sternberg, A., Neufeld, D. 1998, ApJ, submitted

Timmermann, R., Bertoldi, F., Wright, C., Drapatz, S., Draine, B., Haser, L., Sternberg, A. 1996, A&A, 315, L281

Timmermann, R. 1996, ApJ, 456, 631

THE WATER VAPOUR ABUNDANCE AND ITS SPATIAL DISTRIBUTION IN ORION AND Sgr B2

J. Cernicharo[1], E. González-Alfonso[1,2], M.J. Sempere[1], S. Leeks[3] E. van Dishoeck[4], C.M. Wright[5], T. Lim[6], P. Cox[7] & S. Pérez-Martínez[1]

[1] CSIC. Instituto de Estructura de la Materia. Serrano 121. 28006 Madrid. Spain
[2] Univ. de Alcalá de Henares. Dpto Física. E-28871. Alcalá de Henares. Spain
[3] Queen Mary & Westfield College, London, E1 4NS, U.K.
[4] Leiden Observatory, Leiden, The Netherlands
[5] School of Physics, University College, Canberra ACT 2600, Australia
[6] Rutherford Appleton Laboratory, Chilton, Didcot, Oxon OX11 0QX, UK
[7] IAS, Orsay, France

ABSTRACT

We present our ISO open time results concerning the water vapour abundance and its spatial distribution in Orion-IRc2 and SgrB2. LWS grating and FP data have been obtained in both sources for H_2O and for the $H_2^{18}O$ and $H_2^{17}O$ rare isotopes. In Orion IRC2 we have observed more than 70 lines from the different isotopes of water vapour. As already probed by Cernicharo et al. in 1994 from ground based observations at 183.3 GHz, our LWS FP and grating maps of Orion show that water vapour is spatially extended in this cloud and has an abundance around 10^{-5} at large scale (ridge molecular cloud). The same abundance has been found for the extended water vapour absorption in the direction of SgrB2 where the 179.5 μm line of H_2O is detected over a region having a size of 80 pc.

In the direction of Orion IRC2 the data contain information on the different gas components associated to this prominent molecular cloud. The water vapour lines with wavelengths above 100 μm are in emission. However, for shorter wavelengths the lines arising from energy levels below 500 K present P-Cygni profiles while those arising from higher energies are in emission. All the lines observed with the SWS spectrometer are in absorption. The interpretation of the data is not obvious in view of the extremely large opacities of the water vapour lines and of the complex line profiles. We present radiative transfer models including dust and molecules simultaneously that predict several important effects in the water vapour lines intensities and line profiles. These models reproduce qualitatively and quantitatively the observed water vapour lines with the SWS and the LWS ISO spectrometers. A detailed fit to the data will require a more detailed knowledge of the geometry of the region and of the relative distribution of dust and H_2O. Water vapour abundances around 10^{-4} have been estimated for the shocked gas in IRC2.

Key words: Molecular Clouds; Orion-IRc2; Sgr B2; Molecules; Molecular Abundances.

1. INTRODUCTION

The determination of the abundance of water vapour is a long standing problem in astrophysics. Because water vapour is predicted to be an abundant molecule in the gas phase, a determination of its spatial extent, its distribution, and its abundance is crucial in modelling the chemistry and the physics of molecular clouds. In warm molecular clouds, water vapour could play a critical rôle in the cooling of the gas (Neufeld and Kaufman 1993) and, hence, in the evolution of these objects. Unfortunately, due to its high abundance in the terrestrial atmosphere, observations from the ground of the rotational, vibrational and electronic transitions of water vapour is particularly difficult. Some ground-based and airborne observations of water vapour have been performed, but most of observed transitions are maser in nature making very difficult the analysis of the data (Cernicharo et al. 1990; Menten & Melnick 1991). Even the observation of the $H_2{}^{18}O$ isotope gives only poor estimates on x(H_2O) due to contamination of the observed transitions by other molecular lines (Jacq et al. 1988, Gensheimer et al. 1996), or to the observation of only one line which avoids the correct determination of the population of the rotational levels of the ^{18}O isotopic species of water vapour (Zmuidzinas et al. 1995). HDO has been also observed (Jacq et al. 1990; Helmich et al. 1996b), but it is also difficult to derive the H_2O abundance from this rare isotopic species.

The 6_{16}-5_{23} masing transition of H_2O at 22 GHz, which arises from levels around 700K, has been used since its detection by Cheung et al. (1969), to trace high excitation gas around star forming regions and evolved stars. The size of the emitting regions at that frequency is typically of the order of a few milliarcseconds (a few 10^{13} cm at the distance of Orion). Hence, no information has been obtained on the rôle of water vapour at large spatial scales from this line. Other H_2O lines have been detected from ground or air-

Proceedings of the Conference "The Universe as seen by ISO", Paris, France, 20–23 October 1998 (ESA SP-427, March 1999)

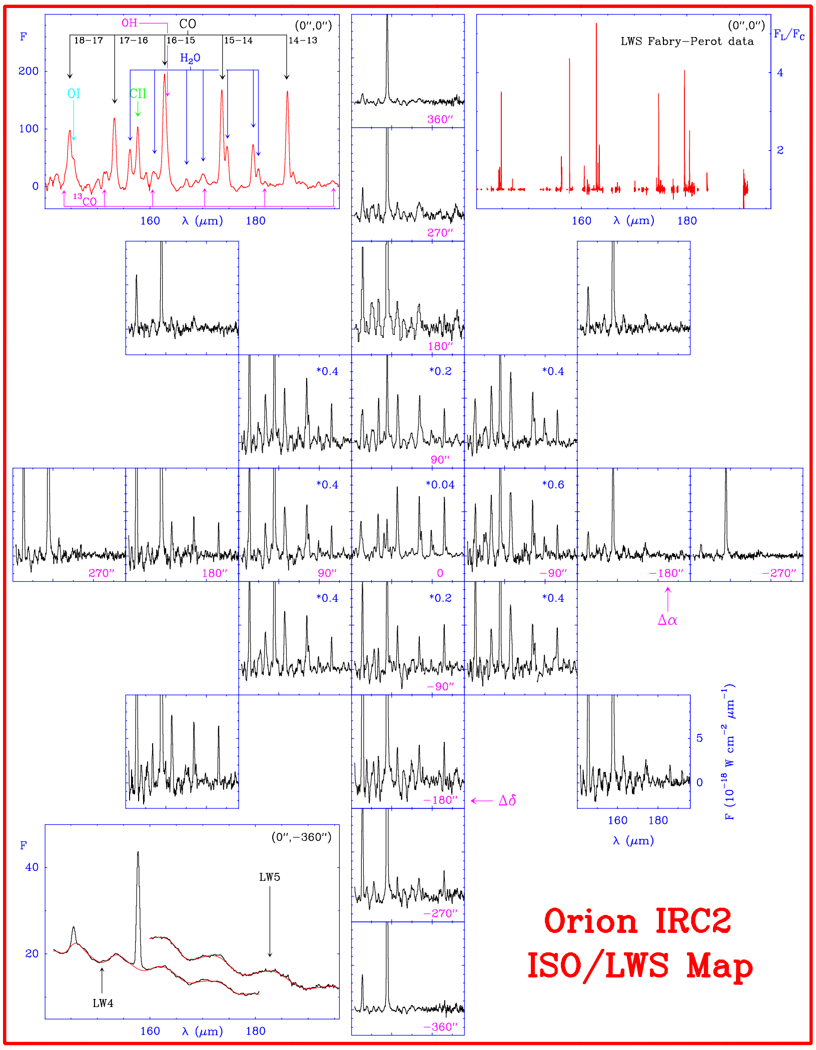

Figure 1. LWS raster of the Orion molecular cloud between 140 and 197 μm. Offsets, in arcseconds, are indicated in each box (in declination for the vertical strip and in right ascension for the horizontal one). Line identifications are given in the zoom to the central position in the top-right panel (see also Figure 2).

borne based telescopes like the 3_{13}-2_{20} transition at 183 GHz (Waters et al. 1980; Cernicharo et al. 1990, 1994, 1996; González-Alfonso et al. 1994, 1998), the 4_{14}-3_{21} transition at 380 GHz (Phillips, Kwan and Huggins 1980), the 10_{29}-$9_{3,6}$ transition at 321 GHz (Menten, Melnick and Phillips 1990a) and the 5_{15}-4_{22} transition at 325 GHz (Menten et al. 1990b). Among these lines only the 3_{13}-2_{20} transition at 183 GHz, for which the terrestrial atmosphere has good transmission under excellent weather conditions -see Cernicharo 1985, 1988; Cernicharo et al. 1990; Pardo 1996-, have been used to map the emission of water at very large spatial scale (Cernicharo et al. 1994, hereafter referred to as Cer94). The map of the Orion molecular cloud shown in Cer94 is 6 orders of magnitude larger than the size of the spots detected at 22 GHz and for the first time a water abundance estimation was derived for the different large scale components of the Orion molecular cloud.

The ISO satellite has provided the opportunity to observe thermal lines of water in the medium and far infrared (see the reviews by van Dishoeck 1997; Cernicharo 1997; and Cernicharo et al 1997a). Mapping of the SgrB2 molecular cloud by Cernicharo et al. (1997b) has definitely shown that water vapour is ubiquitous in molecular clouds with an abundance of 10^{-5}, i.e., similar to that derived by Cer94 from the masing line at 183 GHz. Maps of the emission of several H_2O lines in Orion IRc2 have been obtained by Cernicharo et al. (1997a, 1999). Observations of the central position have been also obtained by van Dishoeck et al. (1998), González-Alfonso et al. (1998) and Harwit et al. (1998). However, the ISO observations of H_2O have to be complemented with ground based observations, such as those obtained by Cernicharo et al. (1994) at 183.3 GHz, in order to disentangle the different spatial components of water vapour and to model correctly the emission of the different rotational lines. In this paper we discuss the available data at all wavelengths and we give an estimate of the water vapour abundance from detailed model calculations of the radiative transfer in molecular clouds having large dust opacities in the far-infrared domain.

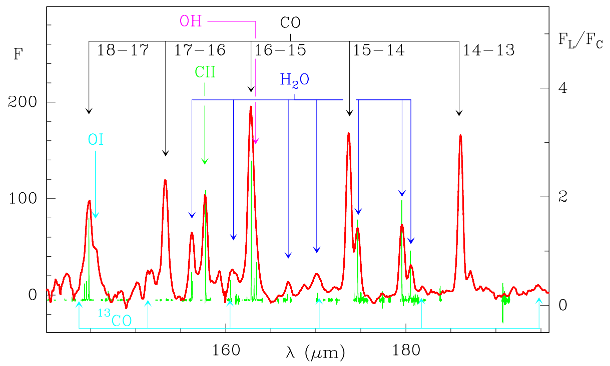

Figure 2. Grating and FP LWS spectra of the Orion molecular cloud towards IRc2. The continuum has been removed from the grating spectrum (left y-axis) while for the FP the line over continuum flux ratio is given in the y-right axis. A detailed analysis of the far-IR spectrum of Orion is given in the contribution by Cernicharo et al. these proceedings.

2. OBSERVATIONS

The severe absorption by the terrestrial atmosphere, even at airborne altitudes, limits the observation of water from the ground. Far-infrared/submillimetre astronomy from space alleviates this major obstacle. The spectrometers on board of ISO can provide a full spectrum of the near, middle and far infrared emission of bright molecular clouds. Unfortunately, the spectral resolution is limited and will produce strong line dilution in most sources. Nevertheless, towards prominent clouds, like SgrB2 (or very bright sources like Orion-IRc2 or other shocked regions), the linewidth can reach more than 100 $\mathrm{km\,s^{-1}}$, which will allow to detect the most abundant molecular species. In a previous paper (Cernicharo et al. 1997b) we have shown that the fundamental line of water vapour at 179.5 μm was detected in all observed positions of SgrB2. In order to determine the true spatial extent of H_2O in SgrB2 we have taken additional data with the ISO/LWS spectrometer (both grating and FP) at positions as far from the central position as $\pm$15 arcmin. A FP raster in H_2O and OH has been also performed and the data are presented in these proceedings (Cernicharo et al.).

In the direction of Orion we have previously presented FP observations towards the central position (Cernicharo et al. 1997a; see also Harwit et al. 1998). In this contribution we present a full map of Orion taken with the LWS grating spectrometer (a total of 24 positions have been observed -see Figure 1). Several lines of water vapour were also observed in a declination raster. More than 70 lines of water vapour have observed towards the central position with the LWS/FP spectrometer (including rare isotopes). A detailed description of the far-IR spectrum of Orion-IRc2 is giving in these proceedings by Cernicharo et al. The data of the grating spectra also show strong CO emission at all observed positions. These data are analyzed in the contribution by Sempere et al. (these proceedings).

3. ORION-IRc2

The grating data are shown in Figure 1. The central position has been analyzed in detail in the contribution by Cernicharo et al. (these proceedings). Some line identifications are given in the top panels of Figures 1 and 2. Figure 1 shows that the water vapour emission extends over several arc minutes around IRc2. Towards the central position all the lines of H_2O involving levels with energies below 2000 K have been detected in the grating spectrum. The water lines are typically 1/3 less stronger than the CO lines. In order to study in detail the excitation conditions of H_2O in a prototypical high-mass star forming region as Orion, we observed a large number of transitions of H_2O and its ^{18}O and ^{17}O isotopes. These data are shown in Figure 3. The line profiles show a complicated behaviour. The lines involving rotational levels at high energy appear in emission. However, those arising from levels of low and intermediate energy show P-Cygni profiles for $\lambda<100$ μm, while for longer wavelengths they appear in emission.

It is interesting to note that all the lines observed by van Dishoeck and collaborators (these proceedings) with the SWS-FP spectrometer are in absorption in front of the continuum source. Some of the lines they have observed have similar properties than those shown in Figure 3 for the shortest wavelengths. These lines show P-Cygni profiles with an important velocity range of the line in emission. That means that the filling factors for the molecular gas as seen by SWS and LWS beams are different, i.e., the emission observed with the LWS-FP spectrometer is arising from a larger surface than that observed with the SWS-FP instrument. We have mapped the thermal emission of water vapour in three rotational lines. A raster map of two of them is shown in Figure 4. As described by Cernicharo et al. (1994), the water vapour emission is very extended in Orion. They detected at least four different components : the extended molecular ridge, the high velocity wind, the "plateau" or wind of moderate velocity, and many narrow and very strong features which are probably associated with the small bullets observed at 22 GHz by Genzel et al (1981). These observations at 183.3 GHz are reproduced in Figure 5.

The ISO/LWS data suffer of a poor angular resolution. The "plateau" is clearly seen in almost all lines observed with the LWS-FP spectrometer (see Fig. 3). The extended molecular cloud around IRc2 is clearly visible in the raster shown in Fig. 4. The intensity of the lines outside Orion-IRc2 is 10-20 times less stronger than towards the center position and its contribution to the interpretation of the shocked H_2O emission is negligible. Figure 5 shows that the "plateau" gas extends over a region of 40$''$ in size. Depending of the orientation of the SWS-FP aperture the fraction of the emitting gas will be different than that of the more spherical aperture of the LWS spectrometer. Hence, the different behaviour of the lines seen with the SWS and LWS spectrometers can be easily understood. Nevertheless, the spatial extent of H_2O puts serious problems when trying to modelling the spatially unresolved data provided by the ISO instruments. The H_2O rotational transitions with P-Cygni profiles will change from cloud to cloud depending on the dust temperature and opacity. Also the different filling factors that gas and dust present

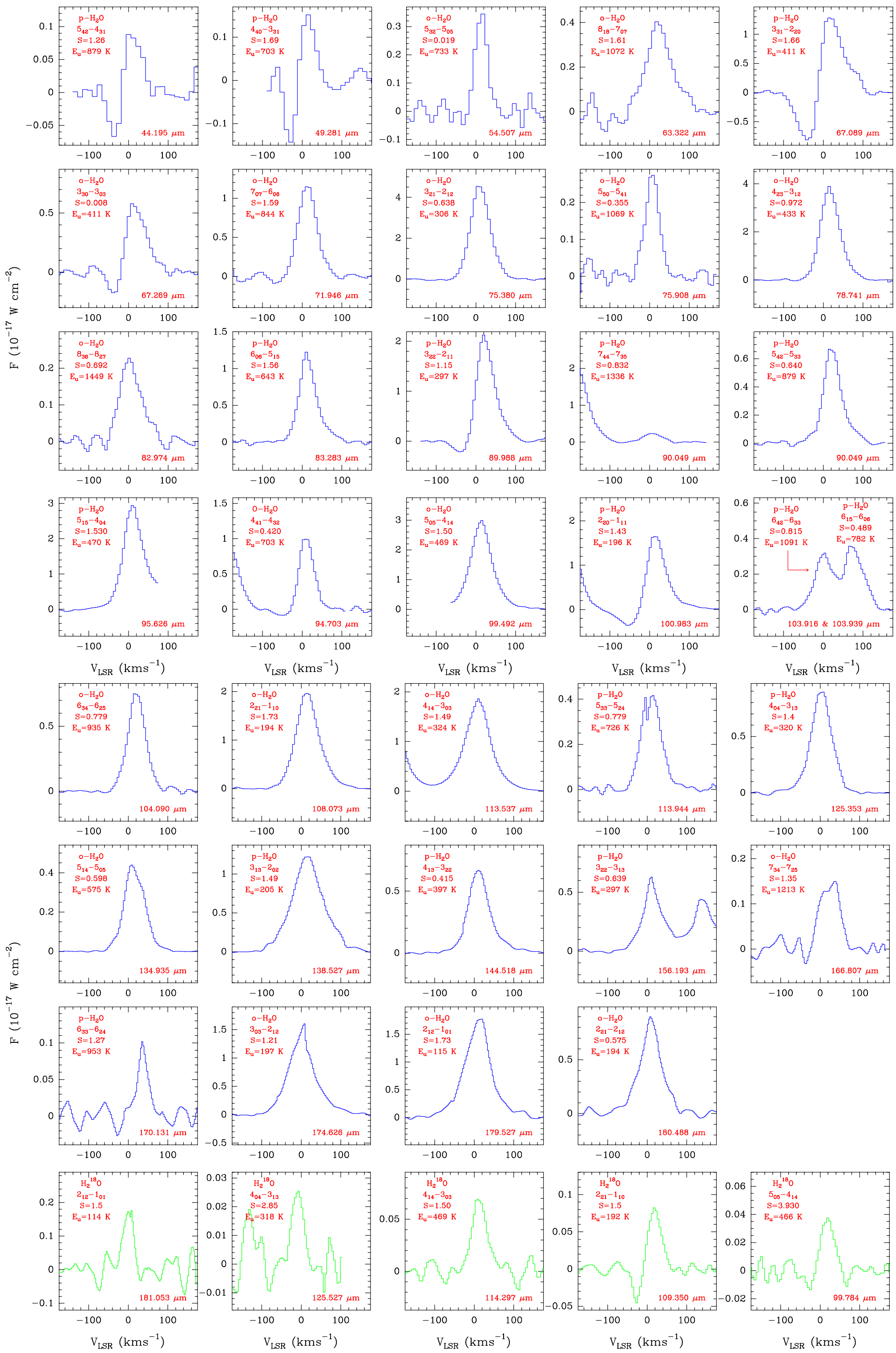

Figure 3. FP LWS spectra of rotational lines of H_2O in Orion. The continuum has been removed. Note the presence of P-Cygni profiles below 90 μm. The last row presents several lines of $H_2{}^{18}O$.

to the ISO apertures will affect the line shapes (e.g., one could think a model where dust emission arises from a larger region than that covered by H_2O; then, the continuum level that could be used to estimate the line opacities for P-Cygni profiles will be unknown from observations at limited angular resolution).

In order to model the H_2O emission in Orion we have used the data provided by the grating and FP LWS observations on CO and ^{13}CO. These data are useful to constrain the kinetic temperature, the CO column density and the size of the emitting regions. With these data as input we derived the H_2O column density and the H_2 volume density. An additional input was the dust temperature. The contribution of the extended emission of H_2O in the Orion molecular cloud has been also taken into account in the models. Dust and molecules are treated simultaneously (see, e.g., González-Alfonso et al. 1998). The models, which accounts for two regions of different temperature and density, reproduce qualitatively the P-Cygni profiles of H_2O and the fully absorbed lines observed with the SWS spectrometer. However, the results are very dependent on the assumed geometry and spatial distribution of the dust. Our calculations indicate that some lines will be redshifted due to self-absorption in the emitting layers and in the foreground gas, an effect that is observed for some H_2O lines. The comparison of the CO and H_2O emission allows to estimate an abundance ratio, x(CO)/x(H_2O), $\simeq$2-5 in the low velocity wind, and $\simeq$10-50 in the extended molecular cloud. The maser lines at 183.3 and at 325 GHz (Cernicharo et al. 1994, 1999) are well reproduced in our calculations. A detailed description of the models and the main results will be published elsewhere (Cernicharo et al. 1999).

4. Sgr B2

The grating ISO/LWS spectrum towards the central position of Sgr B2 shows a strong absorption at 179.5 μm corresponding to the water vapour 2_{12}-1_{01} transition (see Cernicharo et al. 1997b). The grating

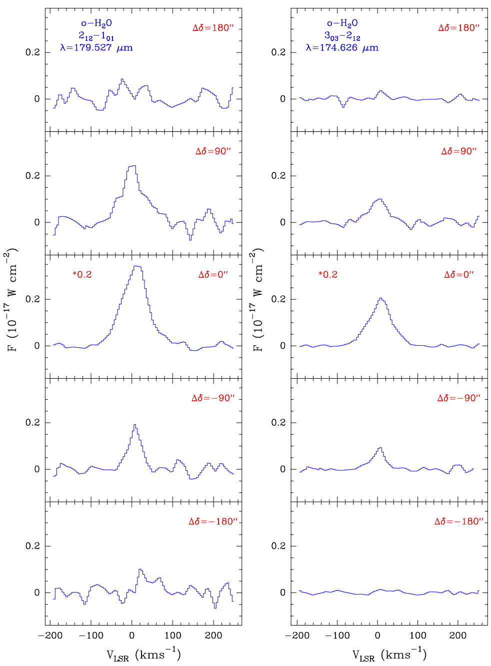

Figure 4. FP LWS spectra observed at several different declination offsets in the direction of Orion. The observed positions are indicated in each panel with the central panel showing the spectra in the direction of Orion-IRc2. The observed water vapour lines are the 2_{12}-1_{01} and 3_{03}-2_{12} at 179.5 and 174.6 μm respectively. The continuum emission has been removed.

spectra in different positions of the cloud are shown in Figure 6. The most striking result from the raster map is the presence of the water vapour 179.5 μm line in absorption in all directions (at least up to $\pm$830 arcsec, i.e., over 80 pc; see Figure 6). At the spectral resolution of the grating (i.e., $\simeq$ 1000 km s^{-1}), the absorption remains strong and roughly constant through the map. The absorption depth of $\simeq$15%, is consistent with saturated water vapour lines with a line width of $\simeq$150 km s^{-1}. Other H_2O transitions are detected in absorption: the 3_{03}-2_{12} H_2O line at 174.5 μm is also present in all the raster positions with an absorption depth of 1%. The absorption at 180.5 μm (also detected in all positions) could be a blend of the 2_{21}- 2_{12} H_2O transition at 180.488 μm, the CH line at 180.478 μm and the 2_{12}-1_{01} $H_2{}^{18}O$ line at 181.05 μm. Sensitive observations with the LWS-FP spectrometer of the lines of CH towards the central position of SgrB2 show that only the fundamental transitions of this species, around 149.5 μm, are detected (see contribution by Cernicharo et al. concerning the far-IR spectrum of SgrB2 in these proceedings). Therefore, the grating feature at 181 μm is not contaminated by CH and probably arises from $H_2{}^{18}O$. Nevertheless, we note that the inversion transition of H_3O^+ is exactly at the same frequency than the $H_2{}^{18}O$ line, and some contamination cannot be excluded. A preliminary analysis of other H_3O^+ lines seems to indicate that an important fraction of the absorption is due to $H_2{}^{18}O$. FP observations of some H_2O (including the rare $H_2{}^{18}O$ isotope) and OH are shown in Figure 7. Finally, note that the C[II] line is very strong in all observed positions but it decreases in intensity when approaching the center where it appears in absorption. Baluteau et al. (1997) have also found the O[I] line in absorption towards the central position while it is detected in emission in other positions through the cloud.

The main result from the present observations is that the far-infrared lines of water vapour are seen in absorption towards SgrB2, instead of in emission (Cernicharo et al. 1997b). This suggests that in SgrB2, where the continuum emission in the far-infrared is optically thick (see below), the H_2O lines arise in a region where the excitation temperatures are smaller than the dust temperature ($<$ 30 K). Nevertheless, the problem of H_2O line excitation is not simple because, apart from self-absorption and the possibility of collisional excitation, the excitation temperatures will also be affected by the continuum emission of the dust.

The role of dust is essential in the excitation of molecules such as H_2O which have transitions at far- and near-infrared wavelengths. If the transfer is dominated by infrared photons, the two transitions arising from the ground level of water vapour will determine how the higher levels will be populated. Even if collisions are important, the dust emission, which in the case of SgrB2 is optically thick around 100 μm (see below), will strongly affect the excitation temperatures of the H_2O transitions and must be taken into account in any realistic model. For a very thick cloud such as SgrB2, these conditions mean that the external layers of the cloud absorb not only the dust emission, but also the water line emission from the inner regions. In the following, a simple model is presented (see Cernicharo et al. 1997b) to define the conditions for which the far-infrared H_2O lines appear in ab-

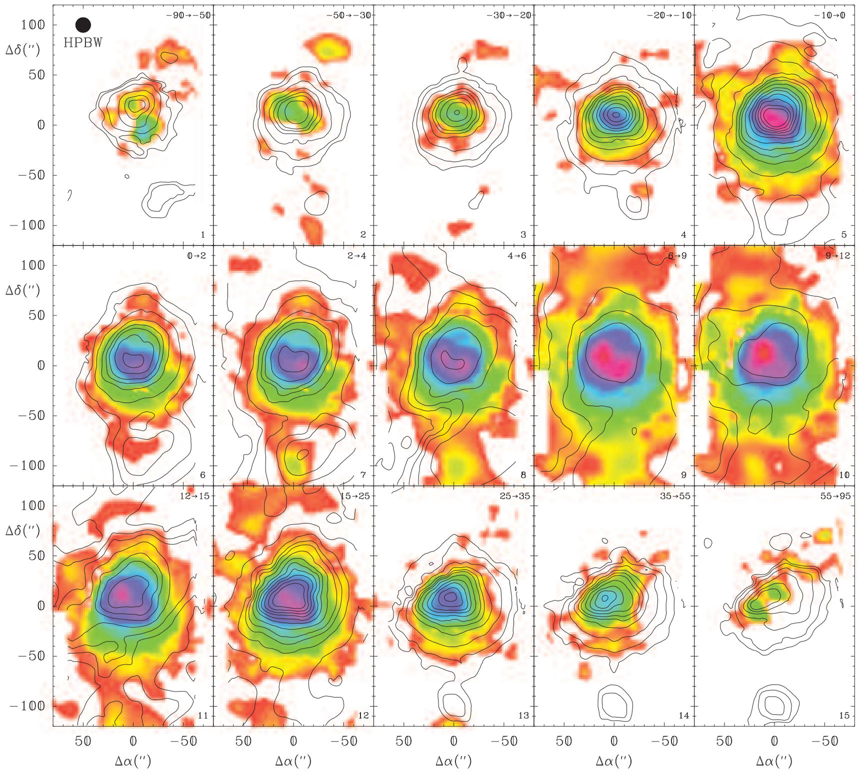

Figure 5. Water emission integrated intensity color maps for different velocity ranges in Orion-IRC2. The black contours correspond to the CO emission in the same velocity intervals. The CO data were observed simultaneously with the water emission with the 30-m IRAM radio telescope. The panels are labelled at their bottom-right corners, and the corresponding velocity intervals in km s^{-1} are given at their top-tight corners. The first color contour corresponds to 7.5 K km s^{-1} and the strongest value to 4200 K km s^{-1}. The CO contours are 3, 5, 10, 20, 30, 40, 60, 90, 120, 160, 200, 250 and 300 K km s^{-1}. For clarity, some CO low contours are not displayed in the panels 8-12; the first CO contours in these panels are 5, 40, 80, 10, and 5 K km s^{-1} respectively (from Cernicharo et al. 1994).

sorption and to quantify the depth of the absorption lines. The model assumes a uniform and spherical cloud, with the following physical parameters appropriate for SgrB2 (see Baluteau et al. 1997 and references therein): an H_2 column density of N(H_2)=10^{24} cm^{-2}, a dust to gas abundance of 10^{-2} by mass, a grain radius 0.1 μm, a dust temperature T_d=30 K, and a turbulent velocity V_{tur}= 10 km s^{-1}. The H_2 density, n(H_2), the kinetic temperature T_K, and the water abundance are free parameters. The dust continuum observed in the LWS wavelength range is well reproduced with the above parameters (Fig. 8). The continuum opacities are 3.5 and 1.9 at 100 and 180 μm respectively. The models compute the statistical equilibrium populations of the seven lowest levels of o- H_2O. The collisional coefficients are taken from Green et al. (1993) and the excitation by dust emission is treated by assuming that the dust grains and the water molecules are coexistent.

Figs. 8a and b display for the four lowest o-H_2O transitions, with wavelengths in the LWS range, the line over continuum flux ratio as a function of T_K for two values of n(H_2): 10^5 and 10^6 cm^{-3} and for an abundance of o-H_2O of 10^{-5}. All four lines are very thick across the cloud, with maximum opacities always greater than 10^3. The lowest lying 2_{12}-1_{01} line at 179.5 μm has an opacity greater than 5 10^4 and its line over continuum flux ratio varies significantly with T_K. Fig. 8 indicates that the H_2O lines are seen in absorption only if T_K is below 35 and 30 K for n(H_2)=10^5 and 10^6 cm^{-3}, respectively. Hence, the water vapour lines detected in absorption originate in the low density regions of SgrB2, i.e. the extended and tenuous envelope of the molecular cloud, and not in the inner regions with $T_K \simeq$100 K observed, e.g., in NH_3 (Hüttemeister et al. 1993), where the water lines would be expected to be in emission. Since these gas volume and column densities describe the moderate density envelope of SgrB2 observed in NH_3, we could expect to see the water vapour lines in emission. Consequently, the H_2O lines are probably formed in regions of much lower density, i.e., the extended and tenuous envelope of SgrB2 detected also in absorption in other molecular lines (e.g., Hüttemeister et al. 1995). With the grating resolution, and even when collisions are neglected, the absorption depths in our models for the 108.1, 174.6 and 180.5 μm lines are always lower than 1 %, due to the fact that the dust emission increases the line excitation temperatures to values close to T_d. This result is consistent with the Fabry- Perot observation of the 3_{03}-2_{12} line

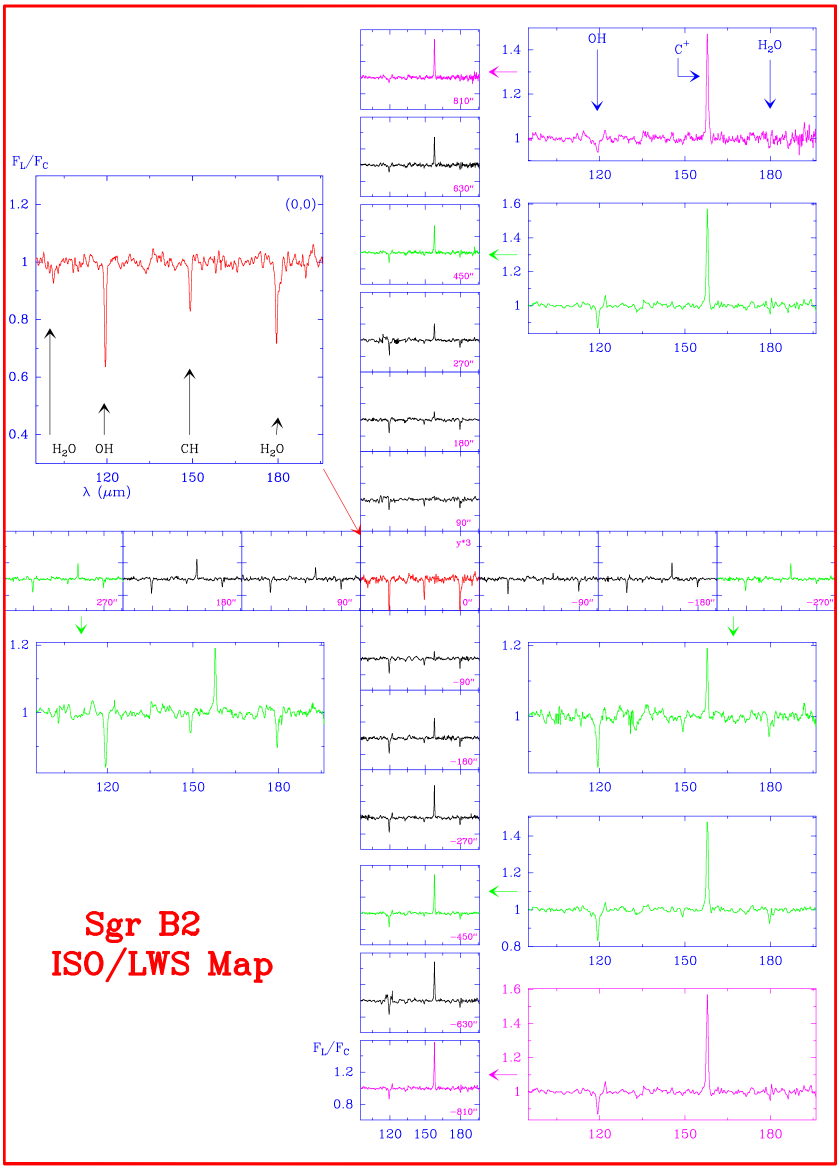

Figure 6. LWS raster of the SgrB2 molecular cloud between 100 and 195 μm. Offsets, in arcseconds, are indicated in each box (in declination for the vertical strip and in right ascension for the horizontal one). Line identifications are given in the zoom to the central position in the top-right panel. The adjacent panels show the spectra observed at selected positions -indicated by arrows. The line around 122 μm corresponds to N[II].

at 174.6 μm (see Figure 7), which shows an absorption of $\simeq$20 %. This is a result of the excitation by the dust emission which implies that the excitation temperature is always close to T_d. However, the absorption depth of the 2_{12}-1_{01} transition ($\simeq$15 % in the grating spectra) cannot be explained by this simple model. The reason is that the observed velocity coverage of this line is $\simeq$ 200 km s^{-1} (Figure 7), indicating that low excitation molecular clouds along the line of sight towards SgrB2 also contribute to the absorption. The excitation of the H_2O molecules in these intervening clouds must be low since the 3_{03}-2_{12} absorption line is not detected at velocities below 20 km s^{-1} (Figure 7). This is further confirmed by the lack of reemission of the 2_{12}-1_{01} line at those velocities. We have added to the previous model (with $n(H_2)=10^5$ cm^{-3} and T_K=20 K) an absorbing shell located between the observer and the SgrB2 model cloud. The parameters of this shell are the same as for the SgrB2 cloud except that $N(H_2)$ = 10^{21} cm^{-2} and V_{tur}=40 km s^{-1}. Since the absorbing shell is optically thin in the continuum, the excitation temperatures are low and there is only appreciable absorption in the 179.5 μm line. Figure 8c presents the resulting grating spectrum and the insert panel shows the line over continuum ratio around 180μm. For higher column densities in the absorbing shell, the excited H_2O levels begin to be appreciably populated and the optical depths at the other transitions are more pronounced.

The present observations confirm the previous results of Cernicharo et al. (1994) that water vapour ex-

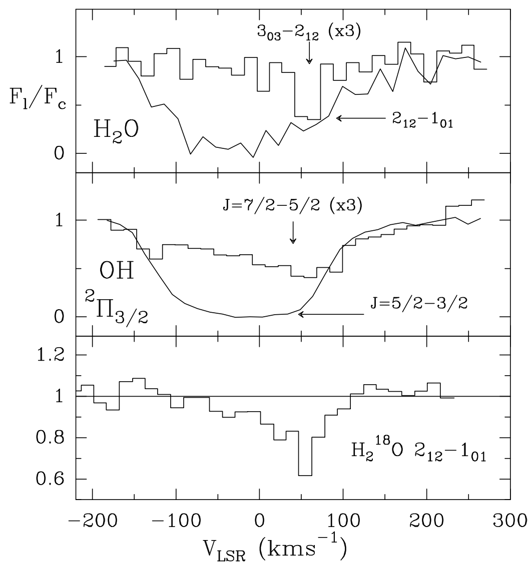

Figure 7. LWS Fabry-Perot observations of the central position of SgrB2. The abscissa is the VLSR in km s^{-1} and the ordinate corresponds to the line over continuum flux ratio. (a) The 2_{12}-1_{01} and 3_{03}-2_{12} lines of water at 179.52 and 174.6 μm, respectively; (b) the 5/2-3/2 and 7/2-3/2 lines of the $^2\Pi_{3/2}$ state of OH at 119 and 84 μm; (c) the 2_{12}-1_{01} $H_2{}^{18}O$ line at 181.05 μm. From Cernicharo et al. (1997b).

its in large amounts in the direction of molecular clouds, but the large opacity of the infrared H_2O lines detected in SgrB2 makes difficult any estimate of the water abundance. Our models indicate that the $H_2{}^{18}O$ 2_{12}-1_{01} line must also be thick in order to explain the line absorption at 181.05 μm. Nevertheless, we note that the depth of the absorption is still sensitive to the optical depth, even if the line is thick, because the velocity range where the line can absorb the continuum emission increases with the opacity. Hence, our simple models can derive the $H_2{}^{18}O$ abundance from the observed absorption depth at 181.05 μm. The value depends on the assumed velocity dispersion in the cloud. Adopting V_{tur}=20 km s^{-1}, N(H_2)=10^{23} cm^{-2}, n(H_2)=10^5 cm^{-3}, T_K=20 K, $H_2O/H_2{}^{18}O$=500 and neglecting collisional excitation, i.e. all the rotational levels are excited by infrared photons from the dust, we derive a lower limit for the water abundance in SgrB2 of 10^{-5}.

Finally, the $H_2{}^{18}O$ line profile in Figure 7 shows an absorption of 10% between −50 and 50 km s^{-1}. This absorption is produced in the low density gas associated with the molecular ring around the galactic center. Assuming that all the absorbing molecules are in the ground state, we derive N($H_2{}^{18}O$) $\simeq$ 5 10^{13} cm^{-2} and N(H_2O)$\simeq$3 10^{16} cm^{-2}. For gas column densities of 10^{21}-10^{22} cm^{-2} the water vapour abundance in the clouds along the line of sight of SgrB2 is $\simeq$0.1-1 10^{-5}.

In addition to the H_2O lines, the LWS grating spectra show the OH and CH lines across the cloud. The lines of OH arising from the J=3/2 $^2\Pi_{3/2}$ level and connecting with the J=5/2 $^2\Pi_{3/2}$ and J=1/2 and J=3/2 of the $^2\Pi_{1/2}$ level at 54, 80 and 119 μm are observed at many positions. The strength of the OH features, like for the water vapour lines, indicates that the lines are saturated.

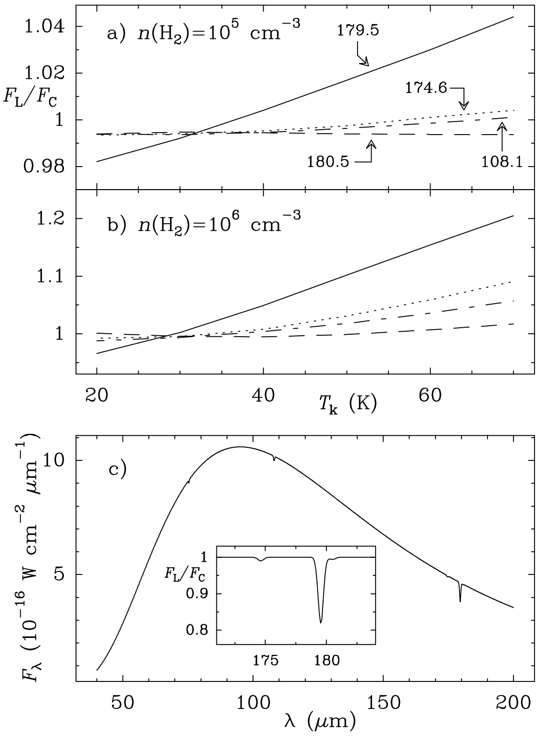

Figure 8. a) and b) Results of model calculations showing the line over continuum flux ratio of four o- H_2O transitions (labelled with their wavelengths) as a function of kinetic temperature. c) Model spectrum for a cloud with an external absorbing shell (see Cernicharo et al. 1997B for details).

CH absorption is also detected at several positions. The CH line profile obtained with the FP (see contribution by Cernicharo et al. on Sgr B2) is very similar to that observed with the KAO by Stacey et al. The absorption reaches about 20 % of the continuum. The column densities of CH in the J=1/2 level varies between 1-5 10^{15} cm^{-2} across the cloud. The lack of absorption from other lines of CH rather than those connecting with the ground level suggests that the molecule is only abundant in the external layers of the cloud where collisional excitation is unimportant.

ACKNOWLEDGMENTS

J. Cernicharo, E. González-Alfonso, and M.J. Sempere thank the Spanish Direccion General de la Enseñanza Superior for support through ACP96-0168, ESP96-2529-E, PB96-0883 and ESP98-1351.

REFERENCES

Baluteau, J.P., Cox P., Cernicharo J., et al. 1997, AA, 322, L33

Cernicharo, J. 1985, *ATM a program to compute atmospheric transmision between 0-1000 GHz*, IRAM internal report.

Cernicharo, J. 1988, Ph.D. Thesis, Université de Paris VII.

Cernicharo, J., Thum, C., Hein, H., John, D., Garcia, P., Mattioco F. 1990, A.&A., 231, L15.

Cernicharo, J., González-Alfonso, E., Alcolea, J., Bachiller, R., John, D. 1994 (Cer94), Ap.J., 432, L59.

Cernicharo, J., González-Alfonso, E., Bachiller, R. 1996, A.&A., 305, L5.

Cernicharo, J. 1997, "The Far Infrared and Submillimeter Universe", 15-17 April 1997, Grenoble, France. ESA SP-401, page 91.

Cernicharo, J., González-Alfonso, E., Lefloch, B., 1997a, "First ISO Workshop on Analytical Spectroscopy", 6-8 October 1997a. ESA SP-419, page 23.

Cernicharo, J., Lim, T., Cox, P., González-Alfonso, E., Caux, E., Swinyard, B.M., Martín-Pintado, J., Baluteau, J.P., Clegg, P.E. 1997b, A.&A., 323, L25.

Cernicharo, J., Pardo, J.R., González-Alfonso, E., Serabyn, E., Benford, D., Merringer, D., 1999, submitted to the ApJ Letters.

Cheung A.C., Rank D.M., Townes C.H., Thornton D.D., & Welch W.J. 1969, Nature, 221, 626

Genzel, R., Reid, M.J., Moran, J.M., Downes, D., 1981, ApJ, 244, 884

González-Alfonso, E., Cernicharo, J., Bachiller, R., Fuente, A. 1994, A.&A., 293, L9.

González-Alfonso, E., 1995, Ph.D., Universidad de Valencia (Spain).

González-Alfonso, E., Cernicharo, J., Alcolea, J., Orlandi, M.A. 1998, A.&A., 334, 1016.

González-Alfonso, E., Cernicharo, J., van Dishoeck, E.F., Wright, C.M., Heras, A. 1998, Ap.J., 502, L169.

González-Alfonso, E. and Cernicharo, J., ApJ, 1999 submitted.

Green S., Maluendes S., & McLean A.D., 1993, ApJS, 85, 181

Harwit, M. Neufeld, D.A., Melnick, G.J., Kaufman, M.J., 1998, ApJ, 497, L105.

Hüttemeister S., Wilson T.L., Henkel et al, 1993, A.&A., 276, 445

Hüttemeister S., Wilson T.L., Mauersberger R., Lemme C., Dahmen G., Henkel C., 1995, A.&A., 294, 667

Jacq T., Jewell P.R., Henkel C., Walmsley C.M., Baudry A., 1988, A.&A., 199, L5

Jacq T., Walmsley C.M., Henkel C., Baudry A., Mauersberger R., Jeweel P.R., 1990, A.&A., 228, 447

Menten, K.L, Melnick, G.J., Phillips, T.G. 1990a, Ap.J., 350, L41.

Menten, K.L, Melnick, G.J., Phillips, T.G., Neufeld, D.A. 1990b, Ap.J., 363, L27.

Menten K., & Melnick G.J. 1991, ApJ, 377, 647

Neufeld D.A., Kaufman M.J., 1993, ApJ 418, 263

Pardo, J.R. 1996, Ph.D. Thesis, Université Pierre et Marie Curie-Universidad Complutense de Madrid.

Phillips, T.G., Kwan, J., and Huggins, P.J. 1980, in *IAU Symposium 87 : Interstellar Molecules*, ed. B.H. Andrew (Dordrecht: Reidel), p 21.

Waters, J.W., Gustincic, J.J., Kakar, R.K., Kuiper, T.B.H., Roscoe, H.K., Swanson, P.N., Rodriguez Kuiper, E.N., Kerr, A.R., Thaddeus, P.1980, Ap.J., 235, 57.

van Dishoeck, E.F. 1997, "The Far Infrared and Submillimeter Universe", 15-17 April 1997, Grenoble, France. ESA SP-401, page 91.

van Dishoeck, F., Wright, C.M., Cernicharo, J., González-Alfonso, E., De Grauuw, T., Helmich F.P., VandenBussche, B. 1998, Ap.J., 502, L173.

Zmuidzinas J., Blake G.A., Carlstrom J., et al.:1995, ASP Conference Series, Vol. 73. Ed. M.R. Haas, J.A. Davidson and E.F. Erickson.

FAR-INFRARED COOLING LINES IN PRE-MS SOURCES

P. Saraceno[1], B. Nisini[1], M. Benedettini[1], A.M. Di Giorgio[1], T. Giannini[1,4], M.J. Kaufman[8], D. Lorenzetti[4], S. Molinari[1,9], S. Pezzuto[1], L. Spinoglio[1], E. Tommasi[10], E. Caux[3], C. Ceccarelli[5], P.E. Clegg[2], J.C. Correia[2], M.J. Griffin[2], S.J. Leeks[2], R. Liseau[6], H.A. Smith[7], & G.J. White[2]

[1]Istituto di Fisica dello Spazio Interplanetario - CNR, Roma, Italy
[2]Queen Mary & Westfield College, Mile End Road, London E1 4NS, UK
[3]CESR, BP4346, F-31028 Toulouse Cedex O4, France
[4]Osservatorio Astronomico di Roma, I-00040 Monteporzio, Italy
[5]Observatoire de Grenoble, BP 53 F-38041, Grenoble, France
[6]Stockholm Observatory, S-133 36 - Saltsjobaden, Sweden
[7]Smithsonian Center for Astrophysics, MA 02138 Cambridge
[8]Dept. of Physics, San Jose State University & NASA/Ames Research Center
[9]IPAC/Caltech, MS 100-22, Pasadena, California (USA)
[10] Agenzia Spaziale Italiana, Roma, Italy

ABSTRACT

We review the results of the observations in the 45–190 μm wavelength range with the ISO Long Wavelength Spectrometer of a sample of Class 0, Class I, Class II pre-Main Sequence objects. We briefly discuss the role of [OI] and of molecular lines in the cooling of these sources.

Key words: Stars: Circumstellar matter; Stars: Pre-main Sequence; Infrared: spectroscopy; Infrared: molecular lines.

1. CHARACTERISTICS OF THE SAMPLE

We used the Long Wavelength Spectrometer (LWS), (Clegg et al. 1996) on the ISO satellite to observe a sample of pre-Main Sequence sources (Class 0, Class I, Class II objects) selected for having a relatively strong submillimeter continuum and for being associated with relatively strong molecular outflows (Saraceno et al. 1996 and 1997).
The youth of the selected objects can also be seen by the ISO FIR colour temperature (Tc) ranging from Tc$\sim$27 K, for the youngest objects, (Class 0), to about 75 K in the most evolved Class II Herbig AeBe stars (see Pezzuto et al. these proceedings).

In Figures 1-2 a few LWS spectra representative of the different groups of objects are presented. Figure 1 shows the youngest objects of the sample: a Class 0 (L1448mm, Tc$\sim$35 K), a low luminosity (L$\lesssim 10^3$L$_\odot$) Class I (IC 1396N, Tc$\sim$35 K) and the high luminosity Class I W28 A2 (L$\sim 10^5$L$_\odot$, Tc$\sim$65 K a very young object with a dynamical time of $\sim$2000 years). Class 0 and low luminosity Class I sources have very rich spectra with several molecular transitions. In these objects (see Table 1) molecules are the major coolants of the gas. On the contrary, in the high luminosity Class I sources atomic lines are the major coolants and the spectra show weak or no molecular lines and have several intermediate ionization lines, as expected from sources with a very strong continuum (tens of kJy) and strong UV field.

Figure 2 presents the more evolved Class II sources: two Herbig AeBe (HAeBe) stars with quite different spectra, RCrA (Tc$\sim$40 K) and MWC 297 (Tc$\sim$75 K), and the TTauri star HL Tau (Tc$\sim$65 K). The HAeBe stars show a relatively large range of temperatures in the FIR colour-colour diagrams (Tc$\sim$ 35-75 K). The coolest objects are generally associated with an embedded cooler companion which probably dominates the FIR colours (in Figure 2 the FIR continuum of RCrA is similar to the one of a Class I); they often show molecular emission (weaker than the one in Class 0/I objects) explained by means of clumpy PDR models (see Giannini et al. 1998 and Giannini et al. these proceedings).
Finally, the observed TTauri stars present only the two fine structure lines ([OI] 63 μm and [CII] 158 μm) with the very important exception of TTauri itself, discussed by Spinoglio et al. in these proceedings.

2. [OI] EMISSION: PDRs AND SHOCKS

The [OI] 63 μm emission line is the strongest FIR line observed in YSOs. It is mainly originated by two physical processes: the excitation from photoionised and photodissociated regions (PDR, Tielens and Hollenbach 1985) and the shock excitation produced by the interaction of supersonic winds with the ambient medium.

Proceedings of the Conference "The Universe as seen by ISO", Paris, France, 20–23 October 1998 (ESA SP-427, March 1999)

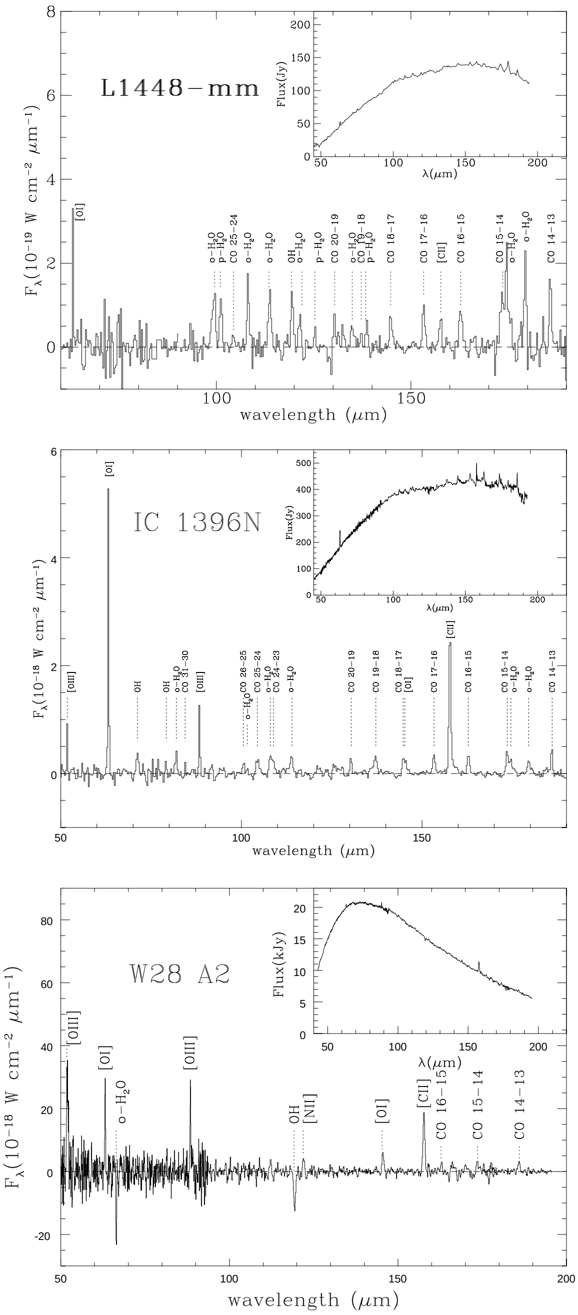

Figure 1. Spectra of the youngest objects: a Class 0 (L1448mm), a low luminosity Class I (IC 1396N) and a high luminosity Class I (W28 A2).

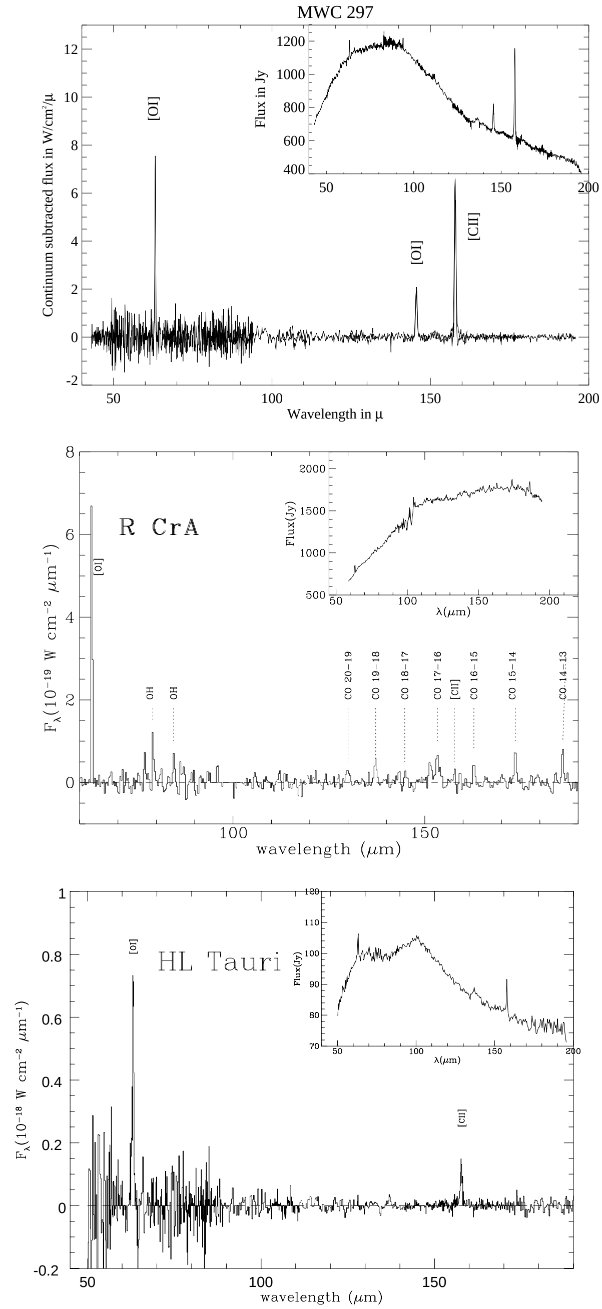

Figure 2. Spectra of Class II objects: 2 HAeBe stars (MWC 297 and RCrA) and a TTauri star (HL Tauri).

There are two kinds of shocks: dissociative "J" shocks (Hollenbach and McKee 1989), in which the temperature is relatively high, all molecules are dissociated and atomic lines are the dominant coolants of the gas and non-dissociative "C" shocks (Kaufman & Neufeld 1996; Draine 1983), in which molecules are the dominant coolants. [OI] 63 μm is the main coolant in dissociative "J" shocks; therefore Hollenbach (1985) suggested that the wind mass loss rate ($\dot{M}_{wind}$) should be proportional to the [OI] 63 μm line luminosity. $\dot{M}_{wind}$ can also be derived from the molecular mass loss ($\dot{M}_{mol}$) and its velocity (V_{mol}); therefore, assuming momentum conservation in the wind-molecular flow interaction, the following relation is valid: $\dot{M}_{wind}V_{wind} = \dot{M}_{mol}V_{mol}$. In the case of "J" shocks, the two $\dot{M}_{wind}$ determinations should be equal. Liseau et al. (1997) showed this equivalence for the [OI] detected in Herbig Haro (HH) objects.

This equivalence holds also for other objects of our sample, as shown in the upper panel of Figure 3, where the mass loss rate derived from the [OI] intensity is plotted versus the one obtained from the mole-

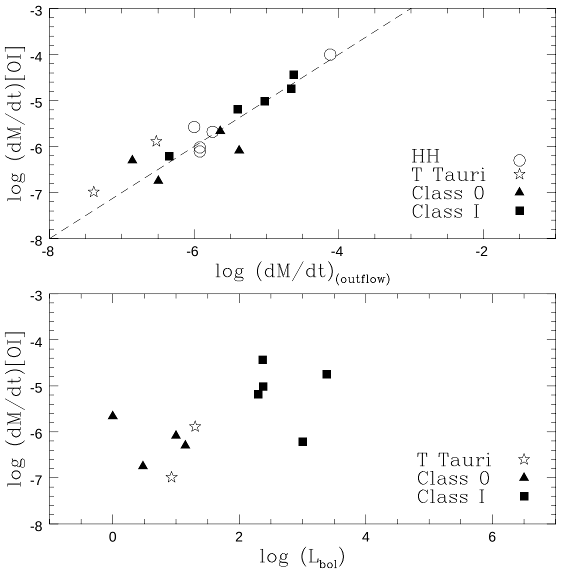

Figure 3. [OI] and molecular outflow mass loss rates determinations (upper panel) for Class 0, low luminosity Class I and TTauri stars; [OI] mass loss rate vs bolometric luminosity (lower panel) for the same objects.

cular flow observations. The dashed line represents equal values of the two mass loss rate determinations, as expected in "J" shocks. This figure contains the objects that lie on this line. They are all the HH objects, and all the Class 0 and low luminosity Class I (for TTauri stars the statistics is not conclusive).

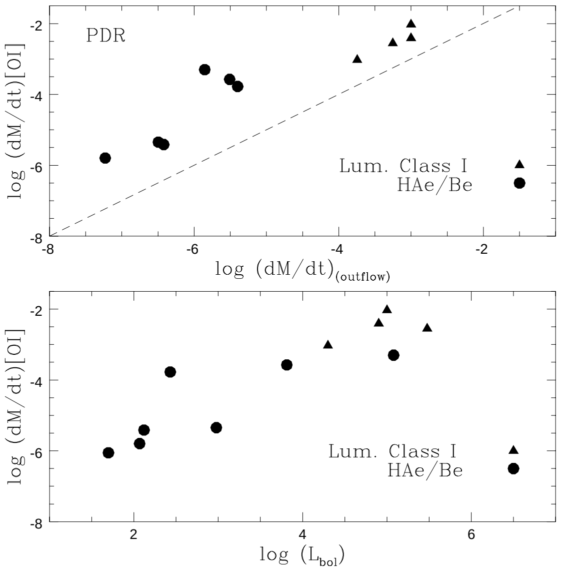

Figure 4. Same as Figure 3 but for Class I and HAeBe.

In the upper panel of Figure 4 the objects that do not lie on the line of equivalence are shown: they have an [OI] emission in excess of that predicted by "J" shock models. This means that a second and dominant component is added to the shock component, due to the presence of HII regions and PDRs, as expected for the objects in Figure 4: HAeBe stars, in which the [OI] emission is accounted for by PDR excitation (Lorenzetti et al. 1998), and high luminosity Class I sources ($L>10^4L_\odot$), which are embedded in HII regions and PDRs. The correlation shown by these objects is explained by the fact that, in HII regions and PDRs, the [OI] luminosity is proportional to the bolometric luminosity L_{bol}: in fact, for luminous young objects, L_{bol} is proportional to M_{mol}, while for Class 0 and low luminosity Class I this proportionality does not exist (Saraceno et al. 1996). This is clearly shown in the lower panels of Figures 3 and 4 where the mass loss derived from [OI] is shown as a function of L_{bol}. The objects of Figure 3 show a high dispersion while those of Figure 4 correlate. The effect is even more strong if we consider the distribution of the different classes of objects (Class 0, Class I, HAeBe) separately.

3. MOLECULAR LINE COOLING

Table 1 lists the objects of the sample for which it was possible to compute the molecular line intensities. Molecular lines have been detected in 2 HH objects out of a sample of 18, in 3 HAeBe stars out of a sample of 11 (Lorenzetti et al. 1998) and in one TTauri object out of a sample of 4. For the three categories listed above the table is statistically representative of the relevance of molecular lines. This is not the case of Class 0 and Class I sources: we observed about 20 objects and more than a half of them show molecular lines but at the present level of data analysis only for the 5 listed objects was it possible to compute the line cooling.

The table shows the importance of molecular cooling in Class 0 and Class I sources and the minor role that H_2O plays in the cooling of the shocked gas (with the exception of L1448mm). This is unexpected, because H_2O was foreseen to be the dominant FIR coolant of the gas around pre-MS objects. Water is produced by two processes: sublimation from grains, at T>100 K (van Dishoeck & Blake 1998), and gas-phase reactions ($O+H_2$)(Graff & Dalgarno 1987), which are very efficient when the gas reaches the threshold temperature of 300 K and all the oxygen not locked in CO is transformed into H_2O. These temperatures can be reached either by radiative heating close to the star, or in shocked regions, in particular by means of low velocity non dissociative "C" shocks (Kaufman & Neufeld 1996; Draine 1983).
The fact that we find $L_{H_2O}/L_{CO} < 1$ for most of the sources seems to exclude very efficient gas phase reactions and implies a gas temperature $T\lesssim 300$ K. From the fit of the CO lines we can estimate the temperature of the gas and (with the exception of L1448mm and IC 1396N) the models fit agrees quite well with $T_{CO}\approx 200$ K (Saraceno et al. 1998).

Is this scenario consistent with shock models ? Figure 5 shows the objects of Table 1 plotted in a L_{H_2O}/L_{CO} vs $L_{[OI]}/L_{CO}$ diagram together with "J" and "C" shocks models predictions. The "C" shock models foresee that between 10 and 20 km s^{-1} the threshold temperature for H_2O formation is reached (see Figure 3 of Kaufman & Neufeld 1996).

The observed spread in the distribution of the cooling luminosity ratios in Figure 5 shows that our sources must be close to the threshold temperature

Table 1. Line cooling

Source	Class	L_{bol}	$L_{[OI]}$	L_{CO}	L_{H_2O}	L_{OH}	L_{lines}	$\frac{L(mol)}{L([OI])}$	$\frac{L(lines)}{L(bol)}$
		Luminosities expressed in $L_\odot$							
B335 FIR	0	3	0.002	0.004	<0.001	...	0.006	2	2 E-3
IRAS16293	0	27	0.005	0.04	0.003	0.003	0.05	9.2	1.8 E-3
L1448mm	0	10	0 008	0.03	0.045	...	0.083	9.3	8 E-3
HH25mm	0	5	0.024	0.03	0.015	...	0.07	1.9	1.3 E-2
IC1396 N	I	235	0.1	0.63	0.17	...	0.9	8	3.8 E-3
TTau	II	28	0.013	0.01	0.01	0.02	0.05	6.6	2.0 E-3
R CrA	II	132	0.038	0.03	<0.002	0.01	0.078	1.05	5.9 E-4
IRAS12496	II	50	0.005	0.008	<0.001	...	0.013	1.6	2.6 E-4
LkH$_\alpha$234	II	270	1.68	0.5	...	...	2.18	0.3	8 E-3
HH54B	HH	-	0.026	0.01	0.002	0.001	0.039	0.5	...
HH26C	HH	-	0.022	0.025	0.02	...	0.067	2.04	...

for water formation and thus the factor 100 in the L_{H_2O}/L_{CO} ratio is fitted by an unlikely small range of velocities (12-16 km s^{-1} for the Draine models of Figure 5). Some model efforts are therefore needed to understand if it is possible to obtain lower temperatures allowing an higher range of velocities, by changing other parameters (as magnetic field and preshock densities).

The other hypothesis to explain at least those sources with the lower L_{H_2O}/L_{CO}, is that H_2O is mainly produced by sublimation of grain mantles (with a gas temperature below 300 K for not having efficient H_2O gas phase production). This hypothesis is supported by the fact that all the objects of Table 1 (except HHs) have only on-source H_2O detections, with inferred emitting regions of few hundreds of AU. If such a region is circumstellar the temperature necessary for grain sublimation can be easily reached. The sublimation of H_2O from grain mantles has been also suggested to explain the CO, H_2O, CO_2, and CH_4 abundances detected toward high luminosity sources, where the grains could be, at T$\lesssim$100 K, not fully thermalized with the gas (van Dishoeck 1998).

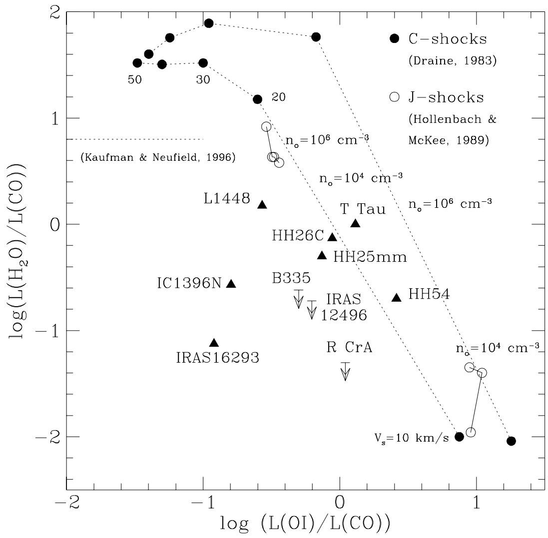

Figure 5. Cooling luminosity ratios for our sources with the predictions of shock models (Kaufman & Neufeld predictions are shown with a horizontal dashed line, since the [OI] line intensity is not given). Notice that "C" shocks models predict a jump in water cooling luminosity of 3 order of magnitude changing the velocity from 10 to 20 km s^{-1}

REFERENCES

Clegg, P.E., et al., 1996, A&A, 315, L38

Draine, B.T., et al., 1983, ApJ, 264, 485

Giannini, T., et al., A&A, 1998, submitted.

Graff, M.M., Dalgarno, A., 1987, ApJ, 317, 432

Hollenbach, D., 1985, Icarus, 61,40

Hollenbach, D., McKee, C., 1989, ApJ, 342, 306

Kaufman, M.J., Neufeld, D.A., 1996, ApJ, 456, 611

Liseau, R., et al., 1997, IAU Symposium N.182, 111

Lorenzetti, D., et al., 1998, A&A, submitted

Saraceno, P., et al., 1996, A&A, 309, 827

Saraceno, P., et al., 1997, in "Star Formation with the ISO", Yun J.L. & Liseau R. (eds), ASP Conf Ser., Vol.132, p.239

Saraceno, P., et al., 1998, 3rd Cologne-Zermatt Symposium, "The Physics and Chemistry of the Interstellar Medium", in preparation

Tielens, A.G.G.M., Hollenbach, D., 1985, ApJ, 291, 722

van Dishoeck, E.F., 1998, Faraday Discuss., 109, 31

van Dishoeck, E.F., Blake, G.A., 1998, ARAA, 36, 317

INTERSTELLAR AND CIRCUMSTELLAR PAHS

A.G.G.M. Tielens[1], S. Hony[2], C. van Kerckhoven[3], & E. Peeters[1]

[1]Kapteyn Astronomical Institute, PO Box 800, 9700 AV Groningen, The Netherlands
[2]Astronomical Institute, University of Amsterdam, Kruislaan 403, NL-1098 SJ Amsterdam, The Netherlands
[3]Institute voor Sterrekunde, K.U. Leuven, Celestijnenlaan 200B, 3001 Heverlee, Belgium

ABSTRACT

ISO has shown that the mid–IR spectra of almost all sources are dominated by narrow emission features collectively known as the UIR bands. These bands are carried by a family of aromatic hydrocarbon species containing about 50 C-atoms: PAH molecules. Other molecules such as C-chains as well as non-aromatic groups attached to the PAHs are much less abundant. ISO has revealed that the UIR spectrum is incredibly rich with a large number of weaker features, subfeatures, and shoulders; many, many of which were not known before. Some examples and the new insights they can provide are described. A systematic study of this spectral structure may well allow us to considerably narrow down the composition of the family of PAHs responsible for the observed emission. These studies have made it quite clear that the universe as seen by ISO is a molecular universe.

Key words: PAHs; infrared spectroscopy; dust; HII regions; Planetary Nebulae; post-AGB objects; galactic nuclei; interstellar medium; UIR bands.

1. INTRODUCTION

Ground–based and airborne observations through the 70's and 80's have shown that the IR spectra of bright sources with associated dust and gas are dominated by relatively broad emission features at 3.3, 6.2, 7.7, 8.6, and 11.3 μm, which always appear together (Gillett et al. 1973; Russell et al. 1977; Cohen et al. 1986; 1989; Geballe et al. 1985; Roche et al. 1989). Because the carriers of these bands remained unidentified for almost a decade, these bands have become collectively known as the Unidentified InfraRed (UIR) bands. The identification with an aromatic carrier is now universally accepted (cf. section 4) and this name is somewhat of a misnomer. Nevertheless, the abbreviation has stuck and is widely used.

The ISO mission was ideally suited to study these emission features: spectroscopically using the SWS spectrometer, ISOPHOT-S, and the ISOCAM-CVF and spatially with ISOPHOT and ISOCAM. Perusal of the posters at this meeting has really reinforced the ubiquitous nature of the UIR bands (section 2). They dominate the mid-IR emission in circumstellar regions, the local diffuse ISM, bright PDRs, nearby normal galaxies, and starburst regions in galactic nuclei. From a curiosity, the UIR bands have now developed into "mainstream" astronomy and, for example, they are now used to derive redshifts and as a diagnostic to separate AGNs from starbursters in the ULIRG population. Likely, these UIR bands are even a characteristic of the ISM of the starbursts in protogalaxies at $z \sim 5$. It is clear that if we want to understand the role of these features in the ecology of galaxies near and far, we have to study the physical and chemical characteristics and the origin and evolution of their carriers in the local universe. Fortunately, ISO has provided us just with the tools required for this endeavor.

2. THE UBIQUITOUS UIR BANDS

The SWS spectrometer on ISO has for the first time allowed to get complete 2.5–45 μm spectra of a great variety of bright ($\gtrsim$10 Jy) sources. Except for deeply embedded protostars, all of these spectra show the UIR bands. As an example, Figure 1 shows three spectra of C–rich post–AGB objects and PN (Hony et al. 1999). Representative SWS spectra of HII regions are shown elsewhere in these proceedings (Peeters et al.) and have also been published by Roelfsema et al. (1996) and Verstraete et al. (1996). Moutou et al. (these proceedings) show a breathtaking SWS spectrum of the reflection nebula, NGC 7023. The PAH emission features in the spectra of Herbig AeBe stars are shown in van Kerckhoven et al. (1999). Several of the brighter nuclei of starburst galaxies (eg., M82, NGC 253, circinus) have been observed in the mid IR by SWS as well and show bright UIR bands (cf., Rigopoulou these proceedings).

Much fainter sources ($\gtrsim$0.1 Jy) can be observed spectroscopically by ISOPHOT and ISOCAM. Besides bright PDRs such as those associated with HII regions (M17, Henning et al. 1998) and reflection nebulae (NGC 7023, Boulanger et al.1998a), at this level, it becomes possible to measure the mid-IR spectrum

Proceedings of the Conference "The Universe as seen by ISO", Paris, France, 20–23 October 1998 (ESA SP-427, March 1999)

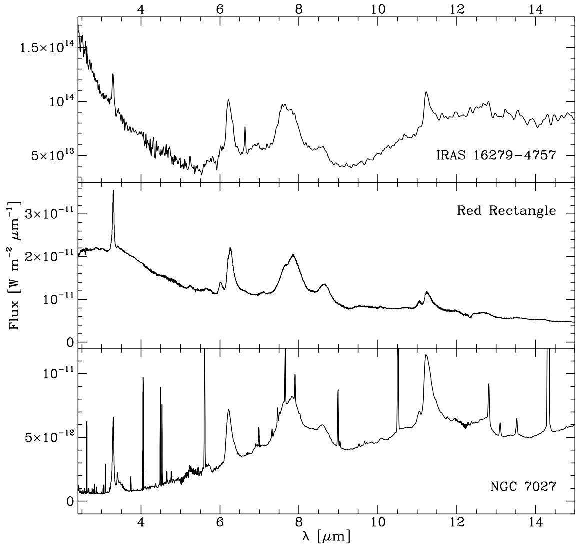

Figure 1. The 3–15 μm emission spectra of the post–AGB objects, IRAS 13428-6232 and the Red Rectangle, and the planetary nebula, NGC 7027 (Hony et al. 1999), illustrating the rich and variable UIR spectrum.

of the IR cirrus (Mattila et al. 1996) and surfaces of dark clouds (Boulanger et al. 1998b, Lemke et al. 1998) illuminated by the average interstellar radiation field. In agreement with earlier suggestions (Puget et al. 1985) based upon broad- and narrow-band photometry by IRAS (Low et al. 1984) and the AROME balloon mission (Giard et al. 1994; Ristorcelli et al. 1994), these spectra unambiguously demonstrate that the mid-IR spectrum of the ISM is dominated by the UIR bands. This is not only true for the Milky Way but, as demonstrated by the galaxy survey by Helou et al. (1999), is a general characteristic of the ISM in galaxies. A particularly nice example is given by the mapping of the IR spectrum in the edge-on "twin" of the Milky Way, NGC 891 (Mattila et al. these proceedings). Similar studies of (regions in) nearby bright galaxies have been performed for the LMC (Contursi et al. 1998), and M31 (Cesarsky et al. 1998). It is also possible to spectroscopically survey the nuclei of nearby ($z \lesssim 0.3$) starburst galaxies which all show bright UIR bands (Lutz et al. 1999; Bosselli et al. 1997). While the spectra of AGNs do not show the UIR bands – indeed that has been used as one observational diagnostic to separate true AGNs from starbursts (Genzel et al. 1999; Lutz et al. 1999) – that may merely reflect the high optical depth of the circumnuclear torus surrounding the central monster rather than a genuine absence of the carriers of the UIR bands.

3. THE INCREDIBLY RICH UIR SPECTRUM

The SWS spectra of bright sources obtained by ISO have revealed the incredible richness of the interstellar and circumstellar UIR spectrum. Besides the well-known UIR bands at 3.3, 6.2, 7.7, 8.6, and 11.3 μm, there is a wealth of weaker features: 3.4, 5.25, 5.65, 6.9, 10.5, 12.7 μm to mention some of them (Fig. 1; cf., Beintema et al. 1996). Moreover, many of the prominent bands show satellite bands (eg., 6.0, 11.0 μm) or break up into subfeatures (eg., 7.6 and 7.8 μm). A particular good example of this spectral richness is also provided by the high S/N, 7-9 μm spectrum of NGC 7023 where in this small wavelength range already about 10 subfeatures can be discerned (Moutou et al. these proceedings). The 11-15 μm region is another illustration of this spectral extravagance (cf. section 6).

It should be emphasized that not all sources show all of these emission components at the same time. Indeed, spectral variation is one important characteristic of the UIR spectrum. In particular, all sources show the 5 well-known features but their ratios can vary substantially and the 11.3/7.7 ratio in Fig. 1 provides a good example. More dramatic, some HII regions show a 8.6 μm feature and some Herbig AeBe stars show a 3.5 μm feature which dwarf the commonly much brighter 7.7 and 3.3 μm features, respectively (Roelfsema et al. 1996; Verstraete et al. 1996; van Kerckhoven et al. 1999). More subtle variations are provided by the ratio of the 7.6/7.8 components of the 7.7 μm feature among HII regions and planetary nebulae (Beintema et al. 1996; Roelfsema et al. 1996; Peeters et al. 1999). Also, often the features vary relative to each other with distance from the illuminating star within a single object (Geballe et al. 1989; Joblin et al. 1996; 1999). These spectral variations make each spectrum unique and imply that the carriers are sensitive to the local physical conditions.

4. THE AROMATIC NATURE OF THE EMITTERS

As first noticed by Duley & Williams (1981), the observed UIR spectrum is very characteristic for aromatic species[1] and this is not controversial at all anymore (cf., Allamandola et al. 1989 for a discussion of the spectroscopy of aromatic materials). Nevertheless, in the literature one may still sometimes find the bands attributed to such diverse species/materials as Polycyclic Aromatic Hydrocarbons (PAHs), hydrogenated amorphous carbon (HAC), Quenched Carbonaceous Composites (QCC), or Coal. In judging these assignments, it should be understood that any good spectral match is only provided by the aromatic structures within these materials. Except for the PAHs, these materials generally contain a substantial aliphatic component[2] as well and the spectral characteristics of the latter often dominates their IR spectra. However, when these materials have undergone substantial heat treatment to drive of any heteroatoms such as O or excessive H and to graphitize the C-skeleton, their IR spectra can provide great matches to the observed UIR spectrum; reemphasizing the aromatic nature of the carrier of the UIR bands. The spectra of heat–treated coals provide a telling example of this (Guillois et al. 1996).

[1] In aromatic structures, the C-atoms are arranged in planar hexagons (ie., a graphitic structure) generally decorated by H's at the edges.

[2] In aliphatic structures, the C-atoms are arranged on a tetrahedral network (ie., a diamond structure) again decorated with H's.

5. PAH MOLECULES AND THE UIR SPECTRUM

While the vibrational spectrum of any (almost) exclusively aromatic material can provide a good fit to the observed circumstellar and interstellar UIR spectrum, the UIR bands are generally attributed to small PAH molecules containing 50 C–atoms rather than coal, HAC, or QCC dust grains. The main evidence for this is an argument originally presented by Sellgren (1984) in connection to the mid-IR emission observed far from the illuminating star in reflection nebulae. Essentially, classical grains are not hot enough to emit at mid-IR wavelengths in these regions. This point has now been reinforced by the ISO observations of strong UIR bands in the diffuse ISM (Mattila et al. 1996; Boulanger et al. 1998). Specifically, the observed "color" temperature of the UIR bands in the ISM is $\sim$ 650 K. In contrast, classical dust grains with size, a, in radiative equilibrium with the average interstellar radiation field attain temperatures, $T_d \simeq 15\left[3000/a(\text{Å})\right]^{0.2}$ K and will not emit much shortwards of 60 μm (Draine and Anderson 1985). Kris Sellgren (1984) attributed the mid-IR emission therefore to small species which because of their limited heat capacity attain high temperatures upon absorption of a single FUV photon. The UIR bands represent then the cooling down of these highly excited species through emission in their vibrational modes. In this case, the temperature of a species with N_c carbon atoms is given by $T_{PAH} \simeq 1500\left[E_{FUV}(\text{eV})/N_c\right]^{0.5}$ K. With an absorbed FUV photon energy of, E_{FUV}=10 eV, the observed color temperature corresponds to a species containing about 50 C–atoms. Thus, the emitters are an aromatic hydrocarbon species with about 50 C–atoms; ie., PAH molecules such as hexabenzocoronene ($C_{48}H_{24}$) and circumcoronene ($C_{54}H_{18}$).

It has been speculated that an absorbed FUV photon might remain localized long enough in a single aromatic unit of (or perhaps loosely bound to) a solid grain that the emission would mimick that of an isolated PAH molecule (Duley & Williams 1988; Guillois et al. 1998). However, extensive laboratory and theoretical studies on the energy transfer within PAH crystals (ie., solids consisting of PAHs bound by weak van der Waals forces) have shown that the energy cascade from the vibrational energy of the PAH units to the phonon spectrum of the solid occur on a timescale of 10^{-9} s which is much shorter than the IR vibrational emission timescale ($\simeq$ 0.1 s; see Tielens 1993 and references therein). Hence, only ($\simeq 10^{-8}$ of the absorbed energy is expected as emission in the mid-IR, in stark contrast to the interstellar case where this fraction is $\gtrsim$0.05. To ISO–pundits, this is of course no mystery. The instruments on ISO were cryogenically cooled rather than radiatively decoupled by shrouding in a coal layer !

While the global observed spectra are consistent with PAHs as well aromatic carbonaceous solids, the observed high feature-to-continuum ratio ($\simeq$ 30 for the 3.3 μm in NGC 1333; Joblin et al. 1996) provides additional support for a molecular carrier (Geballe 1997). For small molecules, the (quasi-) continuum adjacent to the fundamental modes is due to intrinsically weak combination bands and overtones and hence the feature-to-continuum contrast is high. Carbonaceous solids such as coals or HAC have low feature-to-continuum ratios ($\simeq$ 0.5). These solids consist of PAH-like structures, of various sizes, bonded by aliphatic structures [the former gives rise to the 3.3 μm band the latter to the band at 3.4 μm]. The onset of the electronic transitions of a carbonaceous solid (or PAH) shift towards the (infra) red when the size of the aromatic domain increases. This closing of the bandgap implies that the 3 μm region is dominated by electronic transitions when the diameter of the typical connected aromatic structure reaches $\simeq$ 25 Å. For the type of solids under consideration, the 3.3/3.4 μm ratio (ie., the ratio of aromatics to aliphatics) is a measure of the size of the aromatic domain size and hence the bandgap. In a solid model, the observed interstellar 3.3/3.4 μm ratio would correspond to a high aromatic/aliphatic ratio and a strong continuum due to intraband transitions. Papoular and coworkers (Guillois et al. 1996; Papoular et al. 1996) are, in principle, correct when they point out that there are exceptions and that a carbonaceous solid can be "tailored" with a high aromatic feature to continuum ratio. Such a solid would have to consist of small PAH structures (large bandgap) bonded by weak van der Waals interactions (no 3.4 μm feature). A mothball (eg., a naphthalene crystal) would be a good example. However, highly disordered carbonaceous materials such as coals and HAC do not simultaneously give rise to a high feature to continuum ratio and a high 3.3/3.4 μm ratio and are therefore not good candidates for the carriers of the UIR from a spectroscopic point of view.

6. ISO SPECTROSCOPY AND INTERSTELLAR PAHS

The flood of high quality ISO spectra that is now becoming available will lead to new insights in the composition, origin and evolution of interstellar PAHs. The first results of this are now emerging and some examples are presented here.

Table 1. The overwhelming aromatic nature of the UIR bands.

Functional group	λ μm	fraction[a]
aromatic H	3.3	1
aliphatic CH_3	3.40	0.02
hydroxyl (OH)	2.77	< 0.002
amine (NH_2)	2.88-2.95	< 0.01
aldehydic (HCO)	5.9	0.006 (?)
nitrile (C≡N)	4.48	< 0.01
acetylenic (C≡CH)	3.03	< 0.003

[a]Fraction relative to aromatic hydrogen.

6.1. Aromaticity and the UIR bands

The availability of complete 2.5-45 μm spectra of the interstellar UIR bands allows a detailed search for the chemical structure of the carriers. In particular,

Table 2. Carriers of IR emission components.

carrier	IR emission component	N_c	a Å	f_C^a ppm
PAHs	UIR bands	20 – 100	4 – 10^b	14
PAH-clusters	plateaus	100 – 1000	10 – 20	8
very small grains	25 μm cirrus	$10^3 - 10^4$	20 – 30	7
small grains	60μm cirrus	$\sim 10^5$	50	16
classical grains	$\lambda > 100\ \mu$m		$\gtrsim$100	35^c ?

[a]Abundance of C locked up in these species in parts per million.
[b]Size corresponds to disk rather than sphere.
[c]The abundance of C locked up in dust grains is very uncertain (cf., Snow and Witt 1996).

interesting limits can be placed upon the presence of various sidegroups on the emitting PAHs. The abundance of various sidegroups determined from the observed spectra is summarized in Table 1. Structural formulae for these PAHs with sidegroups can be found in Geballe et al. (1989; their Figure 3). The overwhelming majority of the edge sites of the aromatic carrier of the UIR bands contain aromatic H with a minute amount of aliphatic CH_3 groups and possibly some aldehydic groups (HCO). This strongly reinforces the overwhelming aromatic nature of the UIR bands emphasized in section 4. Clearly, the carrier of the UIR bands does not consist of aromatic units bound by aliphatic chains in a three dimensional, coal–like or HAC–like structure. In principle, the spectroscopic evidence still allows a carrier consisting of PAH units bonded together in a three dimensional network by physical van der Waals forces. However, two 25 C–atom PAHs are bonded only by 0.6 eV and FUV photon absorption will rapidly breakdown such a cluster (Léger & Puget 1984).

6.2. PAH abundances

Models for the IR emission spectrum of the ISM have been developed by Draine and Anderson (1985), Désert et al. 1990; Schutte et al. 1993). All of these assumed, more or less, that the size distribution of interstellar dust extended smoothly into the molecular domain. The abundance of C, f_c locked up in interstellar PAHs can be derived from the ratio of the flux in the UIR bands to the total dust continuum emission, f_{IR}, and adopting standard dust parameters and measured UV absorption cross sections for the PAHs (Allamandola et al. 1989),

$$f_c \simeq 100\, \frac{6.3 \times 10^{-18}}{\sigma}\, \frac{f_{IR}}{1 - f_{IR}} \qquad \text{ppm} \qquad (1)$$

where σ is the absorption cross section per C–atom and the abundance is given in parts per million. Typical values for the abundance of PAHs in bright PDRs are given in Table 2. Very similar fractions of the carbon are locked up in PAH clusters of $\sim$ 400 C–atoms which carry the plateau emission underlying the UIR bands and in the very small grains (20–30 Å) which are responsible for the 25 μm cirrus. The abundance of small grains responsible for the fluctuating part of the 60 μm cirrus is slightly larger. Since the emission is at long wavelengths where there are few vibrational modes, these grains do not necessarily need to be aromatic. Boulanger et al. (1998) derived a somewhat larger fraction (70 ppm) of the C locked up in species responsible for the cirrus emission in the 2–15 μm region (corresponding to the PAHs and PAH clusters in Table 2). However, their estimate did not take the large visible component of the interstellar radiation field into account which can be reasonably well tapped by PAH cations (cf. section 6.4). Finally, the fraction of the elemental carbon locked up in larger dust grains is very unclear because the cosmic abundance of C is uncertain. Adopting B star C–abundances (1/2 of solar) leaves about 35 ppm for classical dust grains (Snow and Witt 1996). This small fraction of the carbon available for the interstellar grains responsible for visible extinction provides problems for all current dust models.

Table 3. Abundances of large interstellar molecules.

species	niche	abundance [H atom]$^{-1}$	f_C^a ppm^b
PAHs	the universe	10^{-7}	14
C–Chains	diffuse ISM	$< 6 \times 10^{-9}$	$< 3 \times 10^{-1}$
	molecular clouds^b	$\sim 10^{-8}$	8×10^{-2}
C_{60}^d	diffuse ISM	3×10^{-8}	2

[a]Abundance of C locked up in these species.
[b]Parts per million.
[c]For comparison, the estimated abundance of C–chains with more than 3 heavy atoms is also given for dark clouds (Irvine et al. 1987).
[d]Two absorption bands in the far–red have been attributed to C_{60}^+ (cf., Ehrenfreund & Foing 1997). For a search for IR emission by C_{60}, see Moutou et al. (these proceedings).

6.3. Large interstellar molecules

The available spectra can also be perused for the presence of other classes of molecules. Large hydrocarbon chains are of course of particular interest in view of the compelling suggestion that C_7^- is the carrier of some of the Diffuse Interstellar Bands (Tulej et al. 1998). IR spectroscopy of astrophysically relevant species are discussed in Allamandola et al. (1999a). Acetylenic C–chains such as C_7 will emit around 4.5 μm; e.g., C_5 absorbs at 4.61 μm (Heath et al. 1989). SWS spectra of bright PDRs associated with HII regions or PNe do not show a distinct feature at these wavelengths and hence the abundance of such species is small compared to that of the PAHs in these regions. Unfortunately, neither ISOPHOT-S, ISOCAM-CVF, or the spectrometers on board of the small Japanese satellite IRTS covered this wavelength region. We can however derive an upper limit to the abundance of C-chains in the diffuse ISM by combining ISOCAM and DIRBE data (Boulanger et al. 1998). Comparing these data, the emission in the M-band, and thus in C-chain vibrational modes, is observed to be less than 0.015 of that in the PAH modes and hence that is also the ratio of the UV absorbed by these species. For these molecules, the UV absorption will be dominated by their π–electron system with very similar intrinsic strength per C–atom, which results then in the values for C–chains in the diffuse ISM given in Table 3. This abundance is uncomfortably low compared to the abundance required to explain the DIBs of 4×10^{-8} (Tulej et al. 1998). This problem becomes even worse if one wanted to ascribe most of the DIBs to C–chains, since they all would have their main vibrational transitions in this same wavelength region.

As a molecular Darwinist, one may approach the problem from two opposite sides and consider that every molecule has a niche and each niche has its molecule. As is abundantly clear from the IR data presented at this meeting, the niche for PAHs is the whole universe (cf. section 2). It might not surprise us so much that C–chains are not very abundant in the diffuse ISM since such relatively small species are photochemically speaking rather fragile in the ISM. In that respect, larger C–rings, possibly bicyclic or tricyclic, might be better candidates for the carriers of the DIBs. But the same abundance limits would apply as derived above for the chains. In terms of the IR emission, it may be best to search for small chains in environments where they are rapidly formed such as C–rich stellar outflows rather than in the diffuse ISM. C_{60}^+ has tentatively been identified in the diffuse ISM through two far-red DIBs (Ehrenfreund & Foing 1997). Claire Moutou and Kris Sellgren and their collaborators have taken this Darwinistic approach and looked specifically for the IR signature of C_{60} in their spectra (Moutou et al. these proceedings).

6.4. Interstellar PAH iIons

While the peak positions of the UIR bands are very characteristic for PAHs, available laboratory spectra of neutral PAHs do not produce a good fit to the data in terms of relative strength of the features. In particular, the CH out-of-plane bending modes in the 11-15 μm region are intrinsically much too strong relative to the CC stretching modes in the 5–8 μm region. From the beginning, this difference has been ascribed to the effects of ionization on the intrinsic strength of these modes (Allamandola et al. 1985). The influence of ionization on the spectral characteristics of PAHs has been studied in depth in the laboratory (Hudgins & Allamandola 1995; Szczepanski & Vala 1993) and by theoretical quantumchemical calculations (Langhoff 1996; deFrees et al. 1993; Pauzat et al. 1997). Using this latest data, calculated spectra of (charged) PAH families are now in very good agreement with the observed interstellar UIR spectrum, both in peak position and in relative strength (cf., Allamandola et al. 1999b; Peeters et al. 1999; Bakes et al. 1999).

The PAHs charge depends on the ratio of the ionization rate to the recombination rate; i.e. $G_o T^{0.5}/n_e$ with G_o the intensity of the ambient radiation field, T the gas temperature, and n_e the electron density (Bakes and Tielens 1994). As a result, the emitted spectrum will depend on the local physical conditions and some of the variations observed (cf. section 3) may well reflect variations in the physical conditions, notably G_o. In particular, variations in the relative strength of the 11.3 and 8.6 μm bands with distance from the illuminating star in the NGC 1333 reflection nebula have been ascribed to variations in the degree of ionization of the PAHs involved (Joblin et al. 1996). Similarly, the variations in the 11.3 to the 7.7 μm bands in a sample of HII regions has also been attributed to variations in the charge distribution (Roelfsema et al. 1996; Peeters et al. 1999). The great strength of the 11.3 μm band in the ISM of the galaxy M31 (Cesarsky et al. 1998) may also reflect charge differences with the local solar neighborhood but now on a galaxy-wide scale.

Somewhat curiously, the UIR spectrum of galactic cirrus clouds is very similar to that observed in reflection nebula despite the large difference in $G_o T^{0.5}/n_e$ (Boulanger et al. 1998). While this seems at odd with the discussion above – a much larger neutral fraction is expected in the diffuse ISM (0.7) than in reflection nebulae (0.1; Salama et al. 1996) – it should be recognized that these environments also differ in the spectrum of the exciting radiation field. The interstellar radiation field has a large visible component and small neutral PAHs do not absorb in the visible but cations do. Thus, while cations are much less abundant in the diffuse ISM, they can still be important contributors to the UIR spectrum because they couple better to the total radiation field (Bakes et al. 1999). This emphasizes that the UIR carriers can be pumped by visible photons albeit at somewhat lower efficiency (Lu et al. 1996; Lequeux et al. 1998).

6.5. The C–H out-of-plane deformation modes

The 11–15 μm region of the spectrum has long been known to be very characteristic for the edge structure of the emitting aromatic species (Duley & Williams 1981; Cohen et al. 1985; Allamandola et al. 1989). While IRAS/LRS had already shown the presence of other bands than the strong 11.3 μm band, ISO/SWS has really unleashed the full power of IR spectroscopy on this problem. As illustrated by Fig. 2, this spectral region is rich in detail and, in the Red Rectangle, contains bands at 11.0, 11.3, 11.9, 12.8, 13.6, 14.2, and 14.8 μm plus a number of weaker shoulders.

This spectral region is characteristic for the C–H out-of-plane deformation mode. Due to coupling between the vibrating H–atoms, the exact peak position of these modes depends on the number of directly adjacent H–atoms (i.e. bonded to neighboring C atoms on

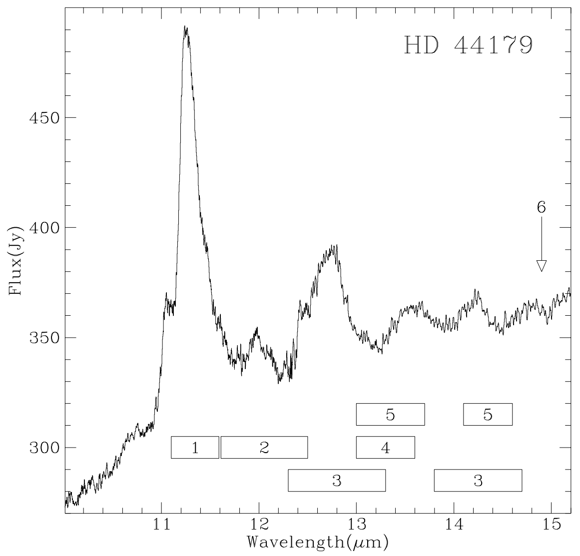

Figure 2. The 10–15 μm spectrum of the Red Rectangle. Bands in this spectral region are largely due to the C–H out-of-plane bending mode whose exact peak position is sensitive to the number of adjacent H–atoms involved. The boxes underneath the spectra give the ranges where neutral PAHs with the indicated number of adjacent H–atoms emit. The arrow labelled 6 indicates the position for Benzene.

a ring). The well–known 11.3 μm band is attributed to this mode for isolated H's in neutral PAHs. The 11.9 and 12.8 μm bands would then be due to 2's and 3's. Now, ionization shifts these ranges for the different number of adjacent H's to shorter wavelengths (Langhoff 1996). The 11.0 μm band is thus likely due to the "1" mode in cations and the 11.3 μm band might be 2's in PAH ions. However, an origin of the latter in neutral 1's should not yet be disregarded since this mode is so much more intense in neutral PAHs. A systematic study of this wavelength region for PAH neutrals and cations is presently underway at the Ames laboratory (Hudgins & Allamandola 1999) and, in combination with the ISO data now becoming available, this will be instrumental in settling these issues.

We also draw attention to the bands at 13.6 and 14.2 μm. These two weak bands are present in more spectra and seem to go together. It is therefore tempting to attribute them to phenyl (5's) groups; ie., one ring connected by a single bond to the rest of the PAH. In that case, the 14.2 μm band is actually a ring bending mode (cf. section 6.6). A phenyl group is likely very labile and hence the presence of these bands may signal the (photochemical) processing of the PAH family in these regions. Finally, in the spirit of Darwin, one might look for the smallest PAH, benzene, which has of course a unique peak position for its C-H out-of-plane bending modes. Indeed, there seems to be a band near this position (Fig. 2) and this may be worth looking into further.

6.6. Ring bending modes

Figure 3 shows a number of emission features in the 15 to 20 μm region of two Herbig AeBe stars (van Kerckhoven et al. 1999). The mid–IR spectra of these stars show prominent PAH emission features. The dust continuum emission in the spectra of these stars starts at longer wavelengths than in most other sources and hence these weak features in the 15–20 μm region are more readily recognized here. However, features in this wavelength region can be recognized in spectra of other sources as well. Even ISOPHOT spectra of sources associated with the galactic cirrus show indications for the onset of the 16 μm feature at the edge of their spectral range. Some of the features in these spectra repeat but, in general, the spectral structure seems to be more unique than in other wavelength regions. We also recognize a plateau of emission underlying the distinct peaks and some sources in our samples seem to show only this plateau in this wavelength region (van Kerckhoven et al. 1999).

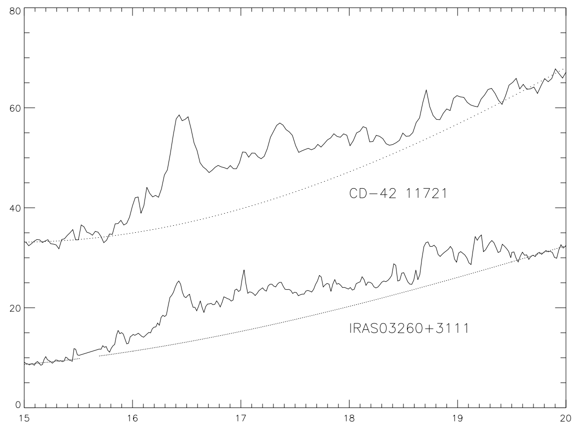

Figure 3. The 15-20 μm spectrum of two Herbig AeBe stars shows excess emission over the continuum. Various new UIR bands are present which can be attributed to ring bending modes.

The far–IR modes of PAHs have been studied in the laboratory by Moutou et al. (1996). In the mid–IR, the vibrational spectrum reflects nearest neighbor vibrations and as a result IR modes occur at very similar wavelengths. In contrast, in the far–IR, emission is due to in-plane and out-of-plane ring bending modes of the C–skeleton and hence these modes are more molecule specific. The IR spectrum of the collection of PAHs studied by Moutou et al. (1996) showed absorption bands throughout this wavelength region with distinct features at 16.2 and 18.2 μm where 20 and 50 % of the PAHs considered showed a band. A feature near 16.2 μm is present in our spectra but there is no sign of a distinct 18.2 μm band (cf. Figure 3).

In principle, this spectral region has great potential for the identification of specific PAH molecules. At present, analysis of most sources in this wavelength region is hampered by the onset of the strong dust continuum resulting in a low feature-to-continuum contrast but it is expected that, as data reduction techniques improve, features in those spectra can be extracted as well. Hopefully, the spectral detail in the different sources can be correlated and this may eventually lead to identification of specific PAH species.

6.7. Profiles

Based upon low resolution ISOPHOT and ISOCAM data, the observed UIR profiles have been fitted by Lorentzians whose width is attributed to the rate of exchange of energy between different modes in the PAH (Boulanger et al. 1998a,b; Mattila et al. 1999). However, high resolution SWS studies reveal that invariably the UIR bands show complex profiles with a variety of subpeaks and shoulders (cf. section 3) and such an approach has its limitations. Also, ground–based and airborne studies have already shown that often the 6.2, 7.7 and 11.3 μm bands are perched on a strong, broad emission plateau. Since in bright PDRs the latter has a different spatial distribution than the UIR bands themselves, the plateau has a different carrier. For various reasons, these plateaus are attributed to large PAHs or PAH clusters containing ~ 400 C–atoms (Bregman et al. 1989; Cohen et al. 1989).

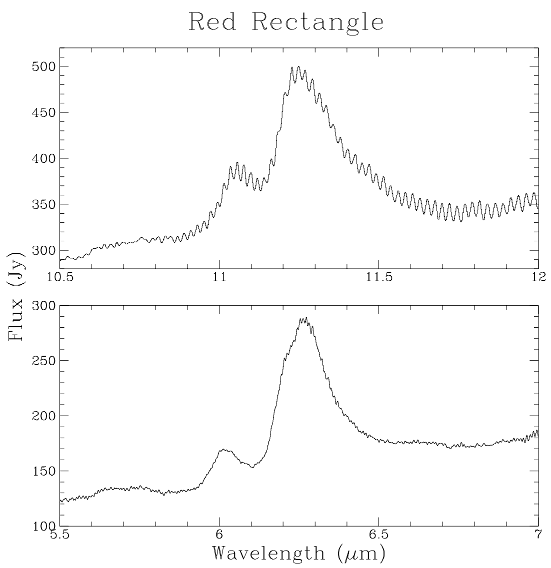

Figure 4. The 6.2 and 11.3 μm bands in the spectrum of the Red Rectangle. Note the asymmetric profile of these bands with a sharply rising blue side and a more gradual decrease in the red. This is a characteristic of the vibrational relaxation of a highly excited molecule (Barker et al. 1987). Note that the high frequency variations in the 11μm region are due to fringing in the SWS.

Finally, the emission process itself will lead to asymmetric profiles with a steeply rising blue side and a more gradual decrease in the red due to anharmonicity (i.e. emission in the 2-1 and 3-2 modes; Barker et al. 1987). Thermal emission in contrast will lead to more symmetric profiles. This emission profile is indeed beautifully observed for the 6.2 and 11.3 μm bands (cf. Figure 4). This observed profile is characteristic for emission during the vibrational cascade of a highly excited molecule and, in the eyes of these reviewers, this is a beautiful confirmation of the emission process. Moreover, the observed asymmetry is a measure of the excitation of the emitting carrier and a size of about 50 C–atoms seems to be indicated by the observations; in agreement with other size indicators (cf., Barker et al. 1987).

6.8. Continuum

Spectra of HII regions and some galaxies show smooth continuum emission throughout the mid–IR underlying the UIR bands ($\lambda > 5$ μm; Peeters et al. 1999; Helou et al. 1999). The origin of this continuum is unclear. Small species, which could get hot enough to emit at these wavelengths ($\lesssim$50 C–atoms), are expected to emit in vibrational bands (Léger & Puget 1984) and any quasi–continuum due to overtones and combination bands is intrinsically weak (Allamandola et al. 1989). Indeed, many well studied PDRs such as the Orion Bar show very weak continuum emission in the 9–10 μm region (Bregman et al. 1989). Perhaps, this emission is associated with a small amount of larger dust grains present in the ionized gas and heated by trapped Lyman alpha photons. The mid-IR emission of HII regions has traditionally been attributed to this process (Natta & Panagia 1978; Tielens & de Jong 1979). Spatial studies on the continuum and UIR bands in such regions might confirm this.

7. SUMMARY

ISO observations have shown that the UIR bands dominate the mid–IR spectra of almost all objects. The spectra show a rich variety of features; besides the well known 3.3, 6.2, 7.7, 8.6, and 11.3 μm bands there are plethora of weaker features, shoulders, and subfeatures. The detailed spectrum of UIR bands vary from source to another and often also within one nebula. Generally, these variations are small although in a few cases the spectra are radically different.

The UIR bands are very characteristic for aromatic hydrocarbon species. The ISO spectra allow us to place very stringent constraints on the presence of various side groups and the carrier is overwhelmingly aromatic. The strong mid–IR emission observed in the diffuse ISM and in nebula far from illuminating stars implies that the carrier is small ($\simeq 50$ C–atoms), transiently heated through the absorption of a single UV photon. Thus, a PAH molecule. While the fraction of C in the form of PAH molecules is about 14 ppm, about 45 ppm is in species which fluctuate (to some extent) in temperature (ie., all grain sizes $\lesssim$50 Å). The ISO spectra also allow us to search for other interesting molecular species such as C–chains and C_{60} and interesting limits have been derived. By far, PAHs dominate the molecular universe in the diffuse ISM.

ISO has allowed us to study the UIR spectrum in great detail and a number of new features have been observed. These include two features at 13.6 and 14.2 μm which we attribute to the CH out-of-plane bending modes in phenyl groups (ie., benzene groups attached through one bond to the rest of the PAH skeleton). New bands have also been observed in the 15–20 μm region which likely represent ring bending modes. While no identifications with specific molecules can be made at this point, this wavelength region holds great promise for the future. Finally, the 6.2 and 11.3 μm bands show a distinctly asymmetric profile with a blue side which rises more steeply than the red side, likely due to anharmonicity.

ACKNOWLEDGMENTS

We gratefully acknowledge Kris Sellgren, Claire Moutou, Kalevi Mattila, Kimmo Lehtinen, Dieter Lutz, Henrik Spoon, George Helou, Francois Boulanger, Diego Cesarsky, and Christine Joblin who shared their data and preprints with us. We thank Pierre Cox, Pjotr Roelfsema, Christoffel Waelkens, and Rens Waters for initiating these research programs, their continued support and encouragement and providing us with the means to dive into the circumstellar and interstellar PAH–bath. Lou Allamandola and Doug Hudgins shared their insight in the IR spectral characteristics of PAHs. Special thanks goes to the ISO-SWS instrument teams at Groningen, Leuven, and Vilspa for help in the data reduction.

REFERENCES

Allamandola, L.J., Hudgins, D.M., Bauschlicher, C.W., Langhoff, S.R., 1999a, ApJ, submitted

Allamandola, L.J., Hudgins, D.M., Sandford, S.A., 1999b, ApJ, in press

Allamandola, L.J., Tielens, A.G.G.M., Barker, J.R. 1985, ApJ 290, L25

Allamandola, L.J., Tielens, A.G.G.M., Barker, J.R., 1989, ApJS, 71, 733

Bakes, E.L.O., Tielens, A.G.G.M., 1994, ApJ, 427, 822

Bakes, E.L.O., Tielens, A.G.G.M., Hudgins, D., Salama, F., Allamandola, L.J., 1999, in prep

Barker, J., R., Allamandola, L.J., Tielens, A.G.G.M., 1987, ApJ, 315, L61

Beintema, D.A., et al. 1996, A&A, 315, L369

Bosselli, et al. 1997, A&A, 324, L13

Boulanger, F., Boissel, P., Cesarsky D., Ryter, C. 1998a, A&A, 339, 194

Boulanger, F., et al. 1998b, in Starformation with ISO, eds. J.L Yun, R. Liseau, (ASP San Francisco), 132, 15

Bregman, J., Allamandola, L.J., Tielens, A.G.G.M., Geballe, T.R., Witteborn, F.C. 1989, ApJ, 344, 791

Cesarsky, D., Lequeux, J., Pagani, L., Ryter, C., Loinard, L., Sauvage, M., 1998, A & A, 337, 35

Cohen, M., Tielens, A.G.G.M, Allamandola, L.J. 1985, ApJ, 299, L93

Cohen, M., et al. 1986, ApJ, 302, 737

Cohen, M., et al. 1989, ApJ, 341, 246

Contarsi , et al. 1998, A&A, 336, 662, 15

deFrees, D.J., Miller, M.D., Talbi, D., Pauzat, F., Ellinger, Y. 1993, ApJ, 408, 530

Désert, F.X., Boulanger, F., Puget, J.-L. 1990, A&A, 237, 215

Draine, B.T., Anderson, N. 1985, ApJ, 292, 494

Duley, W.W., Williams, D.A. 1981, MNRAS, 196, 269

Duley, W.W., Williams, D.A. 1988, MNRAS, 231, 969

Ehrenfreund, P., Foing, B. 1997, Adv Space Res, 19, 1033

Geballe, T.R. 1997, in From Stardust to Planetesimals, eds. Y. Pendleton & A.G.G.M. Tielens, (San Francisco; ASP), 119

Geballe, T.R., Lacy, J.H., Persson, S.E., McGregor, P.J., Soifer, B.T. 1985, ApJ, 292, 500

Geballe, T.R., Tielens, A.G.G.M., Allamandola, L.J., Moorhouse, A. Brand, P.W.J.L. 1989, ApJ, 341, 278

Genzel R., et al. 1999, ApJ, submitted

Giard, M., Lamarre, J.M., Pajot, F., Serra, G. 1994, A&A 286, 203

Gillett, F.C., Forest, W.J., Merrill, K.M. 1973, ApJ, 183, 87

Guillois, O., Nenner, I., Papoular, R., Reynaud, C. 1996, ApJ, 464, 810

Guillois, O., Ledoux, G., Nenner, I., Papoular, R., Reynaud, C. 1998, Faraday Discussions, 108

Heath, J.R., Cooksy, A.L., Gruebele, M.H.W., Schmuttenmaer, C.A., Saykally, R.J. 1989, Science, 244, 564

Helou, G., Lu, N. Y., Werner, M.W., Malhotra, S., Silbermann, N. 1999, ApJ, submitted

Henning, Th., Klein, R., Launhardt, R., Lemke, D., Pfau, W. 1998, A&A, 332, 1035

Hony, S., et al. 1999, in prep

Hudgins, D., Allamandola, L.J. 1999, in prep

Hudgins, D., Allamandola, L.J. 1995, J. Phys Chem, 99, 3033

Irvine, W.M., Goldsmith, P.F. and Hjalmarson, Å. 1987, in Interstellar Processes, eds. D.J. Hollenbach and H.A. Thronson, jr., (Reidel, Dordrecht), 561

Joblin, C., Tielens, A.G.G.M., Allamandola, L.J., Geballe, T.R. 1996, ApJ, 458, 610

Joblin, C., Geballe, T.R., Tielens, A.G.G.M. 1999, in prep

Langhoff, S.R. 1996, J. Phys Chem, 100, 2819

Léger, A., Puget, J.L. 1984, A&A, 137, L5

Lemke, D., et al. 1998, A&A, 331, 742

Low, F., et al. 1984, ApJ, 278, L19

Lutz, D., Spoon, H.W.W., Rigopoulou, D., Moorwood, A.F.M., Genzel, R. 1999, ApJ, submitted

Matilla, K., et al. 1996, A&A, 315, L353

Matilla, K., Lehtinen, K., Lemke, D. 1999, A&A, submitted

Moutou, C. C., Léger, A., d'Hendecourt, L. 1996, A&A, 310, 297

Natta, A., Panagia, N. 1976, A&A, 50, 191

Papoular, R., Conard, J., Guillois, O., Nenner, I., Reynaud, C., Rouzaud, J. 1996, A&A, 315, 222

Pauzat, F., Talbi, D., Ellinger, Y. 1997, A&A, 319, 318

Peeters, E., Tielens, A.G.G.M., Roelfsema, P.R., Cox, P., 1999, in these proceedings and in prep

Puget, J.L., Légerger, A., Boulanger, F. 1985, A&A, 142, L19

Ristorcelli, I., et al. 1994, A&A, 286, L23

Roche, P.F., Aitken D.K., Smith, C.H. 1989, MNRAS, 236, 485

Roelfsema, P.R., et al. 1996, A&A, 315, L289

Russell, R.W., Soifer¡ B.T., Willner, S.P. 1977, ApJ, 217, L149

Schutte, W.A., Tielens, A.G.G.M., Allamandola, L.J. 1993, ApJ, 415, 397

Sellgren, K. 1984, ApJ, 277, 623

Snow, T.P., Witt, A. 1996, ApJ, 468, L65

Szczepanski, J, Vala, M. 1993, ApJ, 414, 179

Tielens, A.G.G.M. 1990, in Submm astronomy, eds. G. Watt, A. Webster, (Dordrecht: Kluwer), 17

Tielens, A.G.G.M. 1993, in Dust and Chemistry in Astronomy, eds., T.J. Millar & D.A. Williams, (London:IOP), 103

Tielens, A.G.G.M., de Jong, T. 1989, A & a, 75, 326

Tulej, M., Kirkwood, D.A., Pachkov, Maier, J.P. 1998, ApJ, in press

van Kerckhoven et al. 1999, in these proceedings and in prep

Verstraete, L., et al. 1996, A&A, 315, L337

ISO–SWS OBSERVATIONS OF PROTOSTARS: THE RELEVANCE OF LABORATORY ICES SIMULATIONS

L. d'Hendecourt[1], M. Jourdain de Muizon[2,3], E. Dartois[1,4], K. Demyk[1], P. Ehrenfreund[5] & A. Heras[6]

[1]Institut d'Astrophysique Spatiale, Bat 121, Campus d'Orsay, F–91405 Orsay, France
[2]DESPA, Observatoire de Paris, F–92190 Meudon, France
[3]LAEFF–INTA, ESA Satellite Tracking Station, P.O. Box 50727, E–28080 Madrid, Spain
[4]IRAM, 300, rue de la Piscine, F–38406, Saint Martin d'Hères, France
[5]Leiden Observatory, P.O. Box 9513, 2300 RA, Leiden, The Netherlands
[6]Astrophysics Division of ESA, ESTEC, Postbus 299, 2300 AG, Noordwijk, The Netherlands

ABSTRACT

With its large wavelength coverage and a spectral resolution adequate for observations of solid state features, ISO is a unique and powerful tool. It allows not only to identify quantitatively simple and abundant molecular species frozen on grain surfaces but also to study their physico-chemical properties and their possible photochemical evolution towards molecular complexity. However, due to numerous and complicated solid state effects, the correct interpretation of the data requires the help of dedicated laboratory experiments, reproducing in a controlled environment "interstellar ice mixtures". These experiments, developed over the last 20 years, have allowed the detection of numerous icy solid state features even before ISO.

Here we present the originality of ISO spectroscopic data. The continuous wavelength coverage, especially in the $2.5 - 25\,\mu$m range, the molecular vibrational region of the spectrum, coupled to comparisons with laboratory data, gives a deep insight into the solid state molecular species and their gas phase counterparts, in particular toward a carefully selected protostellar object, RAFGL 7009S. To illustrate our topics, we concentrate on this object which presents very deep molecular absorption features. H_2O, CO, CO_2 and CH_4 are unambiguously identified. Other features are detected which are explained with further laboratory simulations involving photochemical and thermal processing of the ices as well as possible physical segregation of different ices made of large amounts of H_2O, CO_2 and CH_3OH. As evidenced by the proposed fits, the relevance of the laboratory approach to the interpretation of ISO–SWS data is fully demonstrated. Finally, the large amounts of molecules detected in the solid phase around massive protostars raise the problem of the intrinsic chemical evolution of interstellar matter within this cold solid phase as opposed to the evolution in gas phase, the only one generally considered in the scheme of the chemical evolution of our Galaxy.

Key words: interstellar ices, infrared spectroscopy

1. INTRODUCTION

Although the existence of interstellar ice had been proposed many years ago (Linblad 1935), its observation started with the advent of the first infrared astronomical spectroscopic data in the 70's. It is well known that laboratory simulations have been a key issue in interpreting the scarce data and validating the hypothesis from van de Hulst (1949) that the most abundant atomic species in the gas phase (O, C and N) should be found, in suitable environments, in the form of simple hydrides (H_2O, CH_4 and NH_3), frozen on cold interstellar grain surfaces. As an example, the first detections of the so-called $3.07\,\mu$m absorption feature, in the spectrum of dust obscured infrared sources (Gillett & Forrest 1973, Merrill et al. 1976) were not unambiguously attributed to water ice until the comprehensive laboratory work of Léger et al. (1979). They showed that a convincing identification of the band shape is possible if the interstellar ice is in an amorphous state. Hagen et al. (1980), following the ideas of van de Hulst (1949) and Greenberg (1976), not only confirmed this identification but proposed, on the basis of laboratory spectra of ice mixtures of simple hydrides and/or abundant and already known interstellar gas phase molecules (e.g. CO), that other bands might be observed, mainly in the infrared spectra of protostars. It was then not very long until new observations by Soifer et al. (1979) and, with a better suited resolution, Lacy et al. (1984), complemented by the theoretical work of Léger (1983) on the evaluation of the vapour pressure of condensed CO in an interstellar environment, detected the absorption of solid CO in the spectrum of W33A. In fact, there again, this achievement had been made possible by the use of extensive laboratory work illustrated in Hagen (1982) and Hagen et al. (1983). Moreover, in the same W33A spectrum, Lacy et al. (1984) emphasized the detection of an unknown broad solid state feature, located at $4.62\,\mu$m. Although not readily identified, the important point was that this feature, seemingly connected to the solid CO one, was present in the laboratory spectra of photolysed ice mixtures and more particularly the mixtures containing CO and NH_3. The quasi exact match of this interstellar band with laboratory data has led to numerous dedicated studies, which finally identified this feature with the molecular ion OCN^- (Grim & Greenberg 1987, Schutte & Greenberg 1997, Demyk et al. 1998).

Indeed, as early speculated by Greenberg (1976) and first investigated by Hagen (1982) and d'Hendecourt et al. (1982), interstellar ices, submitted to the constant bombardment of UV and/or cosmic rays, do display a rich chemistry, leading to the possible formation of abundant interstellar solid phase molecules such as CO_2, H_2CO, CH_3OH and other more complex species. The composition of interstellar grain mantles, calculated from grain surface reactions was theoretically investigated by Tielens and Hagen (1982). Molecular cloud chemistry including gas phase reactions and the interactive role of the grain chemistry was first considered by d'Hendecourt et al. (1985). These approaches clearly depicted the formation of large quantities of hydrides on grain mantles, mixed with the most abundant gas phase molecule, the well-known CO. Similar conclusions concerning the formation of H_2O/CO rich mantles were reached later on by Brown & Charnley (1990). In 1986, d'Hendecourt et al presented the results of the photolysis of realistic "astronomical mixtures" whose compositions were selected from the model calculations involving gas-grain interactions. The subsequent infrared spectra of the most abundant molecules and/or the strongest solid state transitions were depicted, most of them awaiting detection through airborne observations or space instruments such as those onboard IRAS and ISO.

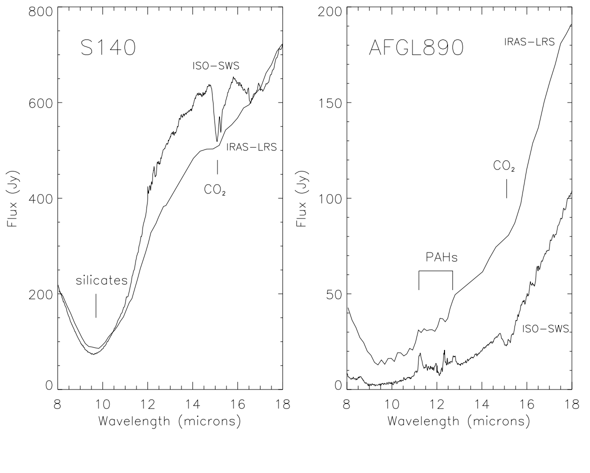

Figure 1. IRAS–LRS and ISO–SWS spectra (as indicated) of S 140 and AFGL 890. Resolutions are about 20 (LRS) and 300 (SWS). Substructures observed at high resolution in the 15.2 μm CO_2 band, permit to discuss the physical structure of the ice (see section 4.3) but the LRS data have allowed to derive reasonably accurate CO_2 column densities (d'Hendecourt & Jourdain de Muizon 1989).

2. THE CASE FOR SOLID CO_2

As emphasized by d'Hendecourt et al. (1986) and Sandford et al. (1988), CO_2 is a quite natural photoproduct in the photolysis of ice mixtures involving H_2O and CO, both molecules widely detected in interstellar spectra of protostars. Unfortunately, the active vibrations of CO_2, although very strong infrared transitions (located approximately at 4.27 μm, stretching mode and 15.2 μm, bending mode), are totally obscured from the ground due to the presence of atmospheric CO_2. Its detection in the interstellar medium is particularly significant for its potential implication on grain chemistry as well as on the relevance to the laboratory simulations currently able to produce large amounts of CO_2. Indeed, CO_2 is not an abundant gas phase molecule if one takes into account the results from various gas phase models (see for example, Herbst & Leung 1986).

Interstellar CO_2 was discovered by d'Hendecourt & Jourdain de Muizon (1989), who analysed data from the Low Resolution Spectrometer (LRS) onboard the IRAS satellite. They provided the first evidence for the presence of large quantities of solid state interstellar CO_2 measured through its 15.2 μm absorption band toward three protostars. As an example of the new possibilities offered 12 years later by the ISO–SWS instrument, we display in Figure 1 IRAS–LRS and ISO–SWS spectra of two sources, S 140 and AFGL 890. Even with the low resolution of the LRS, it was possible, thanks to the interpretation using laboratory experiments obtained at high and low resolution, to deduce the presence of large amounts of CO_2 for a certain number of objects. Numerous IRAS–LRS spectra of protostars and compact HII regions do display the same feature.

ISO was thus much awaited in order to confirm the IRAS discovery through the observation of the other, much stronger, CO_2 mode at 4.27 μm. The object RAFGL 7009S was selected from the IRAS–LRS data base as it presented this deep 15.2 μm absorption feature. The two absorption features from solid CO_2 at 4.27 and 15.2 μm were clearly detected in the ISO–SWS spectrum of this object, the first band being even saturated (d'Hendecourt et al. 1996). The detection of the two absorption bands from solid CO_2, in the ISO–SWS spectra of numerous interstellar objects, most of them embedded in molecular clouds (de Graauw et al. 1996), entirely confirmed not only the initial IRAS observations but also the early prediction on the high abundance of CO_2 in grain mantles obtained from the interpretation of the laboratory experiments (d'Hendecourt et al. 1986). Full confirmation of the importance of the CO_2 molecule as an abundant interstellar species comes from the detection of the 4.27 μm absorption feature using the low resolution spectral data obtained by the ISOPHOT–S instrument in many molecular clouds (Gürtler et al. 1996). This instrument proves to be very powerful as it reveals the 4.27 μm band in numerous weak sources, too faint to be measured by the SWS. Furthermore, the detection of gas phase CO_2 (van Dishoeck et al. 1996) in highly obscured massive protostars may help to understand the interactions between grain mantles and the gas phase chemistry. Finally, the recent detection of abundant quantities of solid-state CO_2 in a field star, Elias16

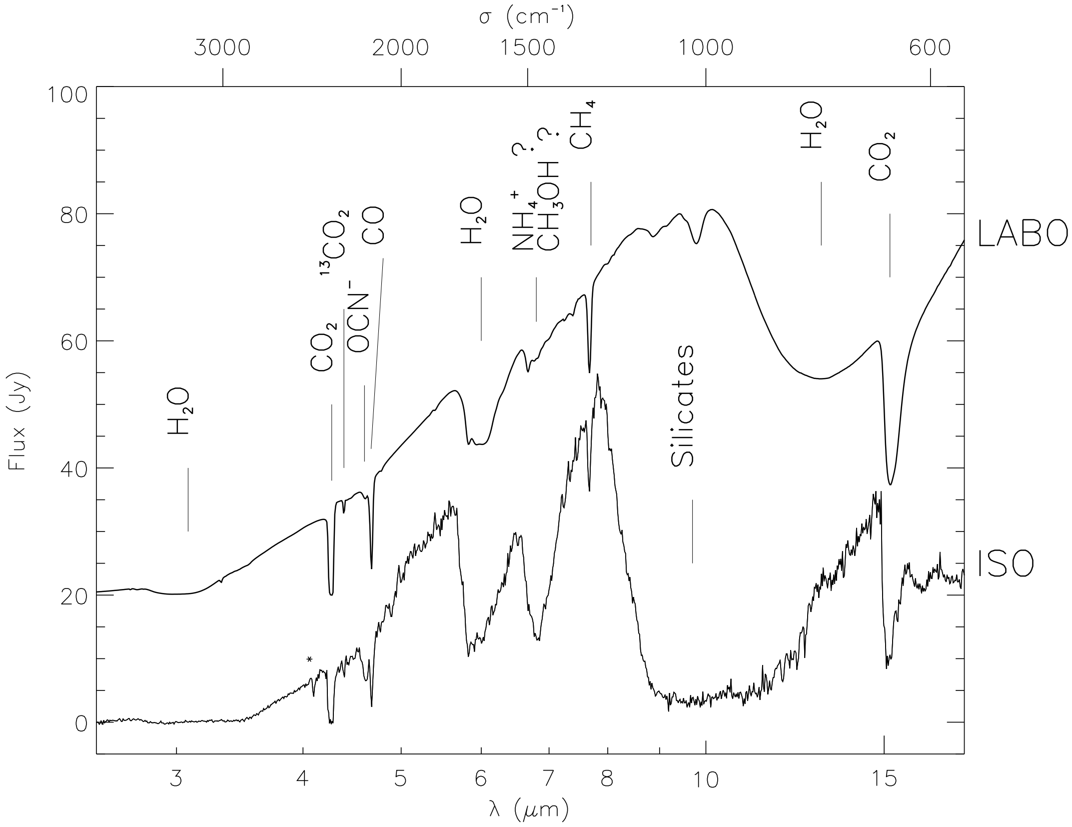

Figure 2. The 2.5 – 18 μm SWS spectrum of RAFGL 7009S (bottom curve). The spectrum of a U.V. photolysed mixture is multiplied by an estimated continuum of the source and shifted upwards for clarity. Identified solid state features are labelled above the spectra.

(Whittet et al. 1998) may shed some light on the formation path of this grain mantle molecule. Indeed, in such a quiet cloud, internal UV flux might be too low to explain the photoproduction of large quantities of CO_2, leaving room for an alternate route such as grain surface reactions between oxygen atoms and solid CO, a highly controversial reaction (Tielens & Hagen 1982, Grim & d'Hendecourt 1987).

Table 1. Solid phase column densities toward RAFGL 7009S.

Molecule	λ (μm)	N (cm^{-2})	% relative to H_2O
H_2O	6.0	1.2×10^{19}	100
CO	4.67	1.8×10^{18}	~15
CO_2	15.2	2.5×10^{18}	~21
$^{13}CO_2$	4.39	14.0×10^{17}	~0.33
CH_4	7.7	4.3×10^{17}	~3.6
OCN^-	4.62	4.4×10^{17}	~3.7
H_2CO	5.81	3.3×10^{17}	~3.0
OCS	4.9	4.9×10^{16}	~0.17
CH_3OH*	3.8/4.0	3.6×10^{18}	~30

*The CH_3OH is discussed in section 4.3.

3. MOLECULAR FEATURES IN RAFGL7009S: AN OVERVIEW

In the following, we focus on the interpretation of the solid state features observed toward the protostar RAFGL 7009S, first emphasizing the precious advantage given by the SWS instrument and second the role of the laboratory simulations for a deeper interpretation of the data. Figure 2 presents the SWS01 spectrum of RAFGL 7009S (lower trace) between 2.5 and 18 μm. For direct comparison, we have superimposed (upper trace) one of our laboratory spectra. To allow for easy comparison between the laboratory and the astronomical spectra, the laboratory one is simply multiplied by an assumed continuum of the source and slightly shifted upwards. This spectrum is the one obtained from an ice mixture containing H_2O:CO:CH_4:NH_3:O_2 = 10:2:1:1:1, photolysed with a vacuum-UV discharge lamp. The standard experiments involved are described elsewhere (see d'Hendecourt et al. 1996 and references therein). The choice of the mixture, corresponding roughly to the elemental cosmic composition, was selected from model calculations made by d'Hendecourt et al. (1985) in which the chemical evolution of the gas phase in a molecular cloud is calculated, taking into account the feedback from molecules produced on the grain surface.

We first note that the extinction toward the source is so large that three strong absorption features are quite saturated. These are, the silicate absorption band at 9.7 μm (whose reproduction is not attempted here), the 3.07 μm OH stretching mode from the ice band and, not surprisingly, the bending mode of CO_2 at 4.27 μm. The astronomical spectrum shows various solid state absorption bands: the 3.07 μm OH stretch of water ice (saturated), the 4.27 μm CO stretch of CO_2 (saturated), a strong 4.62 μm absorption band, the one first detected by Lacy et al. (1984) in W33A and further discussed in the next paragraph, the CO stretch of solid CO at 4.67 μm, a broad and large 6 μm feature which can be mostly attributed to the bending mode of H_2O, a very strong and broad absorption at 6.85 μm, a 7.7 μm band, attributed to CH_4, the 9.7 μm feature from silicates (saturated) and finally, the bending mode of CO_2 at 15.2 μm already discussed above. From the numerous laboratory simulations involving the spectroscopy of pure substances or various ice mixtures (see for example, Hudgins et al. 1993), it is possible to derive reasonably accurate column densities of the identified species. Since we observe absorption lines, this determination does not require any other knowledge than the absorption cross-sections of the molecules and an estimate of the underlying continuum. The derived numbers together with the proportions of water ice are given in Table 1.

At this stage, a few comments regarding our simulations and comparisons are worth making.

(i) the laboratory approach gives an easy access to the global chemical composition of the interstellar grain mantles in the molecular surroundings of the protostellar object. Line widths in the laboratory data are compatible to the first order, with those observed in the source. Line depths can be easily reproduced with the deposition of icy films of calibrated thickness and the simulation, involving photochemical evolution of the ices, produces new absorption bands compatible with the observations. This is particularly true for the CO_2 molecule.

(ii) most of the observed solid state features toward the astronomical object are immediately identified with no further hypothesis.

(iii) the laboratory spectrum, obtained from a photolysed mixture is fully compatible with the astronomical one. No other laboratory transitions are noted which conflict with the astronomical data.

(iv) two molecules, CO_2 and CH_4, are detected, which are unobservable from the ground and have no radio transitions. The role of these two molecules, present in numerous sources observed by ISO (Whittet et al. 1996, Boogert et al. 1996), has always been difficult to assess in the past in models of chemical evolution of molecular clouds, due to the lack of possible observations. One must however acknowledge here that the first detection of CH_4, at 7.7 μm was obtained from the ground by Lacy et al. (1991) and later confirmed by KAO observations (Boogert et al. 1997).

(v) detailed studies of line shapes and widths must be undertaken to obtain a more complete view of the nature of the ices observed. For example the CO_2 bending mode at 15.2 μm shows a complex peak structure which is not accounted for in the above experiment.

The SWS instrument has revealed the spectrum of interstellar ices over its full range. A rather good example of a spectrum similar to the one presented here is given for NGC 7538 IRS9 in Whittet et al. (1996) where the absorption features reveal also the presence of solid state H_2O, CO, CO_2 (and $^{13}CO_2$), CH_3OH, CH_4 and two absorption bands attributed to silicates (at 9.7 and 18 μm).

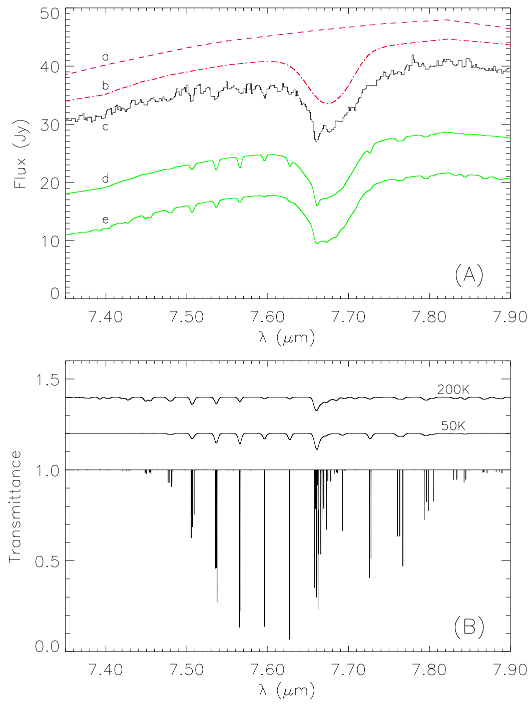

Figure 3. Gas phase CH_4 in the ν_4 region. Panel (A): (a) adopted continuum, (b) resultant spectrum with the CH_4 laboratory feature, (c) ISO spectrum of RAFGL 7009S, (d,e) spectra when the gas phase model ((d) 50 K and (e) 200 K) and laboratory ice spectrum are both taken into account. Even the broad absorption around 7.4 μm is well reproduced by the laboratory experiment. Panel (B): models spectra with T=200 K (top curve) and T=50 K (middle curve) (doppler parameter b=3 km s^{-1} and a column density of 10^{17} cm^{-2} at R=1800 for both models), the bottom curve shows the second model (T=50 K) at full resolution.

4. THE POWER OF LABORATORY SIMULATIONS

4.1. Gas phase and the gas-to-solid ratio

Higher resolution observations of RAFGL 7009S obtained with the SWS06 mode (R∼2000) have revealed sharper transitions superimposed on the broad solid phase absorptions. These lines are the gas phase counterparts to the ice constituents. These observations are largely reported in the literature for this source (Dartois et al. 1998) as well as for other similar sources (van Dishoeck et al. 1996, Helmich et al. 1996, Boogert et al. 1998). Despite the fact that the resolution is not fully suited to the gas phase rovibrational lines, we can nevertheless obtain a reasonable estimate for the gas excitation temperatures and column densities. This allows us to probe, with the same observational parameters, the gas and solid phases and derive the gas-to-solid ratios for many molecules. We choose to present here an example involving CH_4. Other gas phase molecules detected in this source are CO, H_2O and CO_2 (Dartois et al. 1998). Methane is inactive in its rotational ground state and thus not observable in the radio range. CH_4 can only be observed through the rovibrational modes such as the ones in the $\nu 4$ region, falling at 7.7 μm.

The CH_4 analysis, involving the solid and the gas phase is presented in Figure 3. In this figure, the only assumption is the adopted continuum (trace a, upper panel). The solid line obtained from a laboratory experiment is given (trace b, upper panel), whereas the ISO–SWS06 observation is on trace c. The presence of gas phase CH_4 is evidenced when a synthetic gas phase spectrum (lower trace, lower panel, shown at "infinite" resolution and at the SWS06 resolution) is multiplied by the laboratory spectrum (traces d and e, upper panel) to be directly compared with the astronomical data.

The same analysis has been performed for CO, H_2O and CO_2. The derived gas-to-solid ratios are given in Table 2 for these molecules. As can be readily seen from this table, CO is the only molecule more abundant in the gas phase than in the solid one. This may be due to the facts that this molecule is easily made in the gas phase, is very stable and that it is a very volatile species, all factors favouring a high gas phase abundance. Looking at the ratios from Table 2, we see that the solid phase abundances clearly dominate the gas phase ones in this source. Another striking aspect in this table is that the CO_2 appears depleted in the gas compared to the other abundant molecules present in the solid phase (H_2O and CH_4). This low gas-to-solid ratio, combined with the high production rate of CO_2 upon UV photolysis of the laboratory ice, tends to indicate that CO_2 is a typical grain reaction product and, when released to the gas phase, reacts or is destroyed by a specific mechanism (d'Hendecourt et al. 1986, Breukers et al. 1992). Similar results for CO_2 have also been presented by van Dishoeck et al. (1996) in the spectra of other massive protostars such as W33A and NGC 7538 IRS9.

4.2. Molecular ions in RAFGL 7009S

The 4.62 μm broad band has been observed for about twenty years in protostars (Soifer et al. 1979, Lacy et al. 1984).The almost exact match between the astronomical band and an unidentified one, produced in the photolysis of ice mixtures, particularly those containing CO and NH_3, has provoked intensive studies in various laboratories. The position of the band indicates that the molecule responsible for this feature

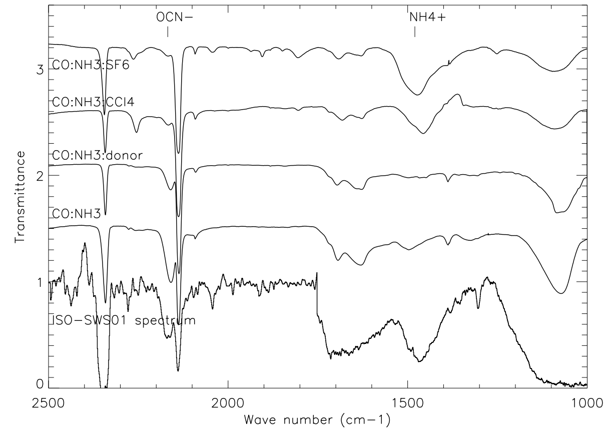

Figure 4. Comparison of the ISO–SWS spectrum of RAFGL 7009S with spectra of photolysed laboratory mixtures $CO:NH_3$ (1:1), $CO:NH_3:e^-$ donor (10:10:1), $CO:NH_3:SF_6$ (10:10:1) and $CO:NH_3:CCl_4$ (10:10:2). Position of the OCN^- and NH_4^+ bands in the laboratory ices have been indicated.

contains a C≡N bond and numerous molecules such as nitriles or isonitriles were proposed as the carrier of this band (Larson et al. 1985, d'Hendecourt et al. 1986, Bernstein et al. 1997). In 1987, Grim & Greenberg tentatively proposed that the negative ion OCN^- is the correct assignment. Since, in their experiments, this negative ion is produced together with a positive counterion, NH_4^+, via acid-base reactions, the astronomical detection of the main transition of NH_4^+ at 6.85 μm may provide a definite observational proof of this mechanism. Unfortunately, the position of the NH_4^+ falls in a region of the spectrum where all aliphatic hydrocarbons containing CH_2 and CH_3 groups also fall (Bellamy 1975), making a precise identification difficult. Again in this matter, laboratory simulations are crucial to decipher ISO–SWS data.

We have used the classical method of "matrix isolation" spectroscopy to study the behaviour of the two laboratory bands at 4.62 and 6.85 μm. The ionic nature of theses bands has been established, using electron donors and acceptors, as fully described by Demyk et al. (1998). This result confirms the previous identification given by Schutte & Greenberg (1997). A schematic presentation of the experimental results is given in Figure 4. The lower trace represents the ISO–SWS spectrum from 4 to 10 μm (2500 to 1000 cm^{-1}), to be compared with the upper traces, pertaining to different experiments (see figure caption). The position of the OCN^- band in the experiments is in very good agreement with the astronomical spectrum. As no other band in the $CO:NH_3$ mixture (second trace to the bottom) contradicts the ISO spectrum, OCN^-, unambiguously identified in the laboratory experiments, is also a good candidate for the interstellar 4.62 μm band. Furthermore, the abundance for OCN^- derived for this source (Demyk et al. 1998), is 4.7×10^{17} cm^{-2}, i.e. about 4 % of the water abundance, a reasonable quantity easily satisfying

Table 2. Gas-to-solid ratios observed in RAFGL 7009S.

Molecule	Densities(cm^{-2}) Gas	Solid	Gas/Solid
H_2O	$\geq 2\times10^{18} \leq 1\times10^{19}$ *	1.1×10^{19}	≥ 0.18
CO_2	$1.0^{+1}_{-0.5}\times10^{17}$	2.5×10^{18}	~ 0.04
CH_4	$1.2^{+0.5}_{-0.3}\times10^{17}$	4.3×10^{17}	~ 0.28
CO	$6.1^{1.7}_{-1.7}\times10^{18}$ *	1.8×10^{18}	~ 3.4

* values for the cold gas phase component.
Solid phase values are taken from d'Hendecourt et al. 1996.

cosmic abundances constraints. As no other ion has been identified in this source, NH_4^+ should be present in the ice. It then could participate to the 6.85 μm band but cannot produce the whole band depth. We estimate that NH_4^+ contributes to no more than 6-7 % to the interstellar feature. Finally, as noted from the laboratory experiments, the efficient production of the 4.62 μm band carrier (OCN^-) requires the presence of mixtures of CO and NH_3. Ammonia, the last simple hydride has recently been detected from ground based observations of NGC 7538 IRS9 (Lacy et al. 1998), in the wing of the silicate feature, there again, thanks to the precise location of this band obtained from laboratory simulations. In this object, ammonia has an abundance which is 10 % that of H_2O ice. Unfortunately, the very steep and deep silicate absorption band in RAFGL 7009S makes it impossible to detect ammonia in this source.

4.3. The shape of the 15.2 μm CO_2 band

The resolution achieved by the SWS instrument allows us to distinguish not only gas phase rovibrational lines of major species but also to examine precisely lineshapes and substructures in the solid absorption bands, in search for physical effects that may bring a different information about the structure of the interstellar ices. As a good example, specific attention may be drawn to the complex structure observed on the 15.2 μm band, the CO_2 bending mode. As also noted by de Graauw et al. (1996), for the infrared source NGC 7538 IRS9, this strong band presents a complex substructure, where up to four distinct absorption bands can be observed between 14.8 and 16 μm. A similar structure is observed in RAFGL 7009S, as well as in some other sources such as GL 2136, GL 2591, GL 4176 and S 140 (for this source, see Figure 1). Part of this structure is simply due to the presence of gas phase CO_2 on the line of sight, as evidenced in the work of Dartois et al. (1998).

We have looked for possible explanations for the remaining triple peak structure. Three explanations can be tested: (i) the presence, in the interstellar ices of other less abundant species, (ii) a particle shape effect modifying the lineshape, as suggested in de Graauw et al. (1996), (iii) a solid state effect involving the possibility of obtaining, within the ice, the formation of molecular complexes, for example due to the presence and interaction of two molecules in roughly equal abundances. The two first effects can be safely rejected. Due to the large and simultaneous wavelength coverage obtained with the SWS instrument, analysis of the whole spectrum of the source allows to scan over the entire vibrational spectrum towards shorter wavelengths, to detect possible additional features due to various species that may be also responsible for the presence of the observed substructures in the 15.2 μm band. We have not detected any transitions for various molecules considered as potentially abundant solid state interstellar molecules. The second solution, the effect of grain shape on the line structure can also be rejected. First of all, the precise fit of the solid state methane line (see Figure 3), obtained by comparing directly a thin film transmittance spectrum with the astronomical data confirms unambiguously that, even at 7.7 μm, the grains responsible for the absorption are very small compared to the wavelength of the observation. This applies even better at 15.2 μm and, for ices whose real index of refraction, n, is small (see for example Hudgins et al. 1993), no serious shape effects are ex-

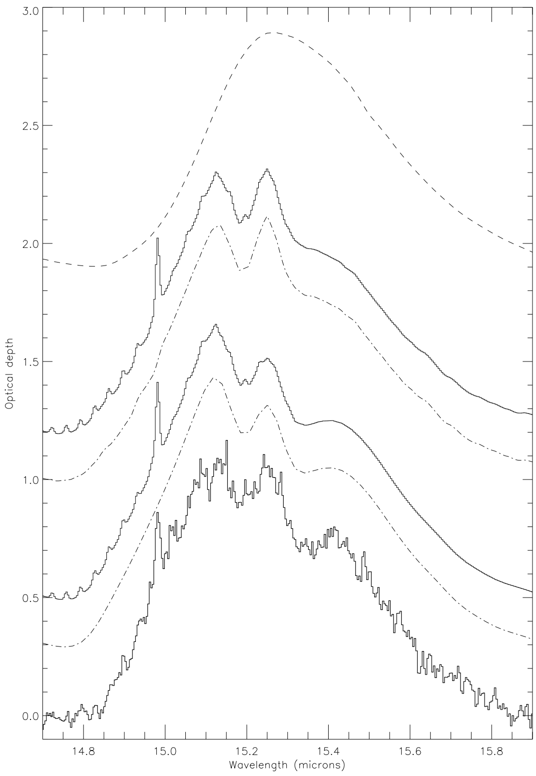

Figure 5. ISO–SWS06 spectrum of the CO_2 bending mode at 15.2 μm toward RAFGL 7009S compared with: (lower panel): a laboratory fit of a CO_2:C_2H_5OH (1:1) mixture heated to 90 K (dotted-dashed line), and a spectrum where the CO_2 gas phase contribution was added (solid line); (middle panel): a laboratory fit of an ice mixture containing equal amounts of H_2O, CH_3OH and CO_2 at 105 K (dotted-dashed line) and including the CO_2 gas phase contribution (solid line); (upper panel): a spectrum of a polar ice mixture H_2O:CH_3OH:CO_2 (10:1:2) at 105 K.

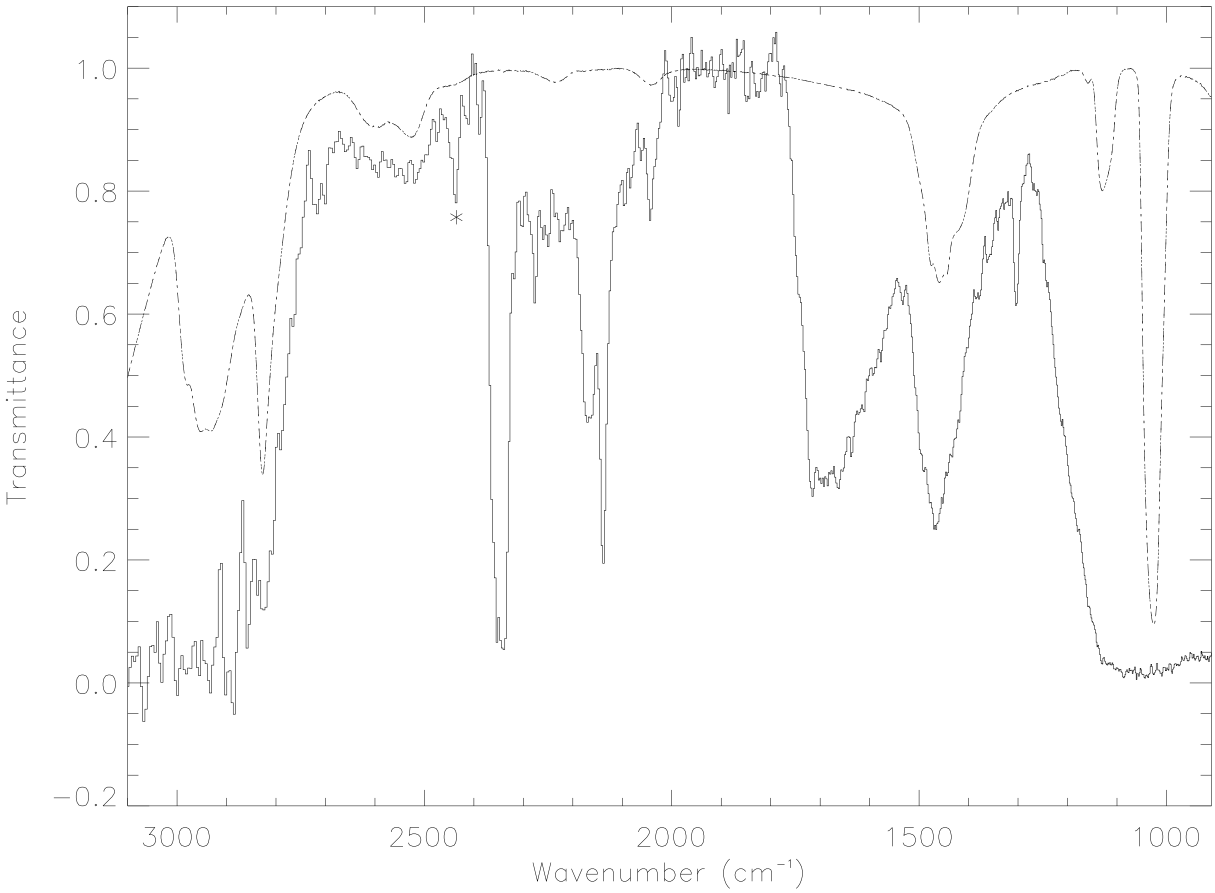

*Figure 6. Comparison of a pure solid methanol spectrum (dashed line) with the transmittance obtained from the analysis of ISO–SWS data of RAFGL 7009S between 3.3 and 10 μm (3000 and 1000 cm^{-1}). The methanol spectrum is normalised to the abundance of methanol derived from ground based observations (Dartois et al. 1999a). The symbol * indicates a spurious feature in the astronomical spectrum.*

pected on the absorption lines for grains which are obviously much smaller than the wavelength of observation.

The third solution we tested in the laboratory was to look for possible modification of the lineshape arising from molecular interactions within comparably abundant molecules trapped in the ice. Such an effect has been known for a long time, at shorter wavelengths. Indeed, solid CO_2 invokes particular interactions when mixed with polar or apolar molecules, which result in some spectroscopic diversity (Reed et al. 1986, Sandford & Allamandola 1990 and Ehrenfreund et al. 1997). This diversity has been used in the interpretation of astronomical data, to obtain information on the degree of mixing of CO with other molecules such as H_2O and CO_2, influencing the CO lineshape at 4.67 μm (see the review of Whittet & Duley 1991). We have thus performed specific experiments involving mixtures of plausible interstellar molecules, in particular water, carbon dioxide and alcohols. Some of our results are presented in Figure 5. The whole procedure is given in Ehrenfreund et al. (1998) and a full discussion of the molecular effects involved will be found in Dartois et al. (1999a). Figure 5 displays the ISO–SWS spectrum of RAFGL 7009S between 14.3 and 16 μm (bottom trace). Above this spectrum, lie three laboratory spectra (dashed lines) obtained from three different mixtures : H_2O:CO_2 (10:1, upper trace), H_2O:C_2H_5OH:CO_2 (1:1:1) and H_2O:CH_3OH:CO_2 (1:1:1). The gas phase CO_2 lines are readily accounted for with the sharp Q branch, located at 14.9 μm (Dartois et al. 1998). When taking into account the gas phase, the two solid lines give the final expected spectra for the alcohol containing mixtures, to be directly compared to the ISO–SWS spectrum at the bottom. The fit obtained demonstrates clearly that, in a molecular icy solid held by van der Waals forces, line shapes are entirely dominated by molecular interactions. Exception to this rule may be found towards short wavelengths where some scattering may alter the 3.07 μm ice band (Dartois 1998). Note however that this statement is only valid in the case of the protostars considered in this paper. The formation of the substructure can be understood in terms of the presence of the formation of molecular complexes between CO_2 and one of the alcohol molecules involved in our experiment as fully explained in Dartois et al. (1999b). Finally, complementary observations must be obtained in order to detect, if possible, which alcohol is truly responsible for the effect observed in the astronomical source. Such observations have been recently performed, using the far better sensitivity of the UKIRT instrument, in the 3 μm range where various vibrational features of alcohols can be searched for. Large quantities of methanol (up to 30 – 60 % of the abundance of H_2O ice) have been detected in two sources, W33A and RAFGL 7009S, there again by comparing laboratory mixtures spectra with astronomical data (Dartois et al. 1999b).

As a final example for the identification of interstellar species in the solid state, we display, in Figure 6, a full comparison of the spectrum of RAFGL 7009S (bottom trace) with a spectrum of a simple icy film of pure methanol, a molecule which shows a rich spectrum in the infrared. Surprisingly, one can see from this figure that not less than four methanol features are present in the astronomical spectrum. Among these features, the most important one is the 6.85 μm band, prominent in RAFGL 7009S. Note that, in this figure, the quantity of deposited methanol in the experiment has been chosen to be roughly the same than the one derived from the observation of the source with UKIRT (Dartois et al. 1999b). Thus methanol is a rather abundant species in this source, as well as in W33A, another massive protostar. High abundances of methanol have been tentatively derived from ground based observations in the 3 μm window (Allamandola et al. 1992). Methanol accounts for roughly 30 – 60 % of the 6.85 μm band, the uncertainty coming from the difficulty to determine an accurate baseline in this portion of the spectrum. As already mentioned above, the ammonium cation, NH_4^+, may fill up to 10 % of the band, leaving room for possible other candidates.

5. CONCLUSION

The ISO spectral data of deeply embedded objects prove to be extremely successful for the detection of abundant solid sate molecules that are unobservable from the ground and are, in some cases, radio-quiet (CO_2, CH_4). Although most of the solid state molecules known to date were detected prior to ISO, thanks to numerous and extensive laboratory simulations coupled to difficult infrared observations through patchy atmospheric windows or using the LRS spectrometer on board IRAS, the SWS instrument provides, for the first time, a large wavelength coverage and a resolution well suited for the observations of solid state features. A rather good example is provided by the CO_2 molecule which is now observed through its two active vibration modes at 4.27 and 15.2 μm, in a very large number of interstellar objects. From the data presented here, and because of its relative absence in the gas phase, CO_2 proves to be a useful tracer for icy grain mantle chemistry.

High resolution observations using the SWS AOT6 reveals the presence of gas phase counterparts to the most important solid state molecules. This may help to address the problem of the relationship between the gas and the grain chemistry. Moreover, this higher resolution reveals that some solid state features display peculiar lineshapes. The case for the triple substructure observed in the 15.2 μm band of the CO_2 bending mode has been analyzed here. Duplication of this band in the laboratory, as well as the reproduction of the CH_4 feature in the same object, show that lineshapes and widths are largely dominated by molecular interactions such as the formation of molecular complexes between CO_2 and an alcohol molecule. From complementary observations in the near infrared, using the UKIRT instrument, we have shown that this alcohol is methanol. This molecule thus becomes the second most abundant ice species in this source after water. The same situation also applies to W33A, another massive protostar. UV photolysis of laboratory mixtures does provide ample amounts of CO_2, as observed in RAFGL 7009S although it may not be the only source for this grain molecular species.

Other less abundant species are observed. H_2CO is marginally detected (no more than 3 % of H_2O). The ions OCN^- and NH_4^+ are unambiguously identified in the laboratory spectra. OCN^- is a serious candidate to reproduce the interstellar 4.62 μm line, based on the strong similarity between the laboratory and the astronomical bands. NH_4^+ is unfortunately hidden in the very strong 6.85 μm band observed in the source. The origin of this band comes partially from methanol (30 – 60 % of the band) and probably some NH_4^+ for no more than 10 %. Further observations in other evolved sources may help to understand the full nature of these two bands.

Finally, in spite of the originality and quality of the ISO–SWS data, one may regret that, due to the nature of the observed sources and the very high extinction in the 3.07 and 9.7 μm ice and silicate features, transitions of other molecules of astrophysical interest such as NH_3 still remain intrinsically difficult or impossible to observe.

ACKNOWLEDGMENTS

L. d'Hendecourt wishes to thank the continuous financial and scientific support of the "Programme du CNRS, Physico-chimie de la matière interstellaire (PCMI)".

REFERENCES

Allamandola, L.J., Sandford, S.A., Tielens, A.G.G.M., Herbst, T.M. 1992, ApJ 399, 134

Bellamy, L.J. 1975, in "The Infrared Spectra of Complex Molecules", Chapman and Hall, New York

Bernstein, M.P., Sandford, S.A., Allmandola, L.J. 1997, ApJ 476, 932

Boogert, A.C.A., Schutte, W.A., Tielens, A.G.G.M. et al. 1996, A&A 315, L377

Boogert, A.C.A., Schutte, W.A., Helmich, F.P., Tielens, A.G.G.M., Wooden, D.H. 1997, A&A 317, 329

Boogert, A.C.A., Helmich, F.P., Van Dishoeck, E.F., Schutte, W.A., Tielens, A.G.G.M., Whittet, D.C.B. 1998, A&A 336, 352

Breukers, R.J.L.H., d'Hendecourt, L.B., Greenberg, J.M, 1992, csim conf., Knudsen, p.273

Brown, P.E., Charnley, S.B. 1990, MNRAS, 244, 432

Dartois, E., d'Hendecourt, L., Boulanger, F., Jourdain de Muizon, M., Breitfellner, M., Puget, J.L., Habing, H.J. 1998, A&A, 331, 651

Dartois, E. 1998, PhD Thesis, University of Paris VI, France

Dartois, E. et al. 1999a, in preparation for A&A

Dartois, E., Schutte, W.A., Geballe, T.R., Demyk, K., Ehrenfreund, P., d'Hendecourt, L. 1999b, A&A, 342, L32

Demyk, K., Dartois, E., d'Hendecourt, L., Jourdain de Muizon, M., Heras, A., M, Breitfellner, M. 1998, A&A. 339, 553

van Dishoeck, E.F., Helmich, F.P., de Graauw, T. et al. 1996, A&A 315, L177

Ehrenfreund, P., Boogert, A.C.A., Gerakines, P.A., Tielens, A.G.G.M., van Dishoeck, E.F. 1997, A&A 328, 649

Ehrenfreund, P., Dartois, E., Demyk, K., d'Hendecourt, L. 1998, A&A 339, L17

Gillett, F.C., Forrest, W.J. 1973, ApJ 179, 483

de Graauw, T., Whittet, D.C.B., Gerakines, P.A. et al. 1996, A&A 315, 345

Greenberg, J.M. 1976, Astrophys.Sp. Sci. 39, 9

Grim, R.J.A., Greenberg, J.M. 1987, A&A, 181, 155

Grim, R.J.A., d'Hendecourt, L.B. 1987, A&A, 167, 161

Gürtler, J., Henning, T., Koempe, C., Pfau, W., Kraetschmer, W., Lemke, D. 1996, A&A 315, L189

Hagen, W. 1982, PhD Thesis, University of Leiden, The Netherlands

Hagen, W, Greenberg, J.M., Tielens, A.G.G.M. 1983, A&AS 51, 389

Hagen, W., Allamandola, L.J., Greenberg, J.M. 1980, A&A 86, L1

Helmich, F., van Dishoeck, E.F., Black, J.,H., et al. 1996, A&A 315, L173

d'Hendecourt, L.B., Allamandola, L.J., Baas, F., Greenberg, J.M. 1982 A&A 109, L12

d'Hendecourt, L.B., Allamandola, L.J., Greenberg, J.M. 1985 A&A, 152, 130

d'Hendecourt, L.B., Allamandola, L.J., Greenberg, J.M., Grim, R.J.A. 1986, A&A 158, 119

d'Hendecourt, L., Jourdain de Muizon, M., Dartois, E. et al., 1996, A&A, 315, L365

d'Hendecourt, L., Jourdain de Muizon, M. 1989, A&A 223, L5

Herbst, E.Leung, C.M. 1986, MNRAS, 222, 689

Hudgins, D.M., Sandford, S.A., Allamandola, L.J., Tielens, A.G.G.M. 1983, ApJS 86, 713

van de Hulst, H.C. 1949, "The solid particles in space", Drukkerij Schotanus and Jends, Utrecht, The Netherlands

Lacy, J.H., Baas, F., Allamandola, L.J., van de Bult, C.E.P., Persson, S.E., McGregor, P.J., Lonsdale, C.J., Geballe, T.R. 1984, ApJ 276, 533

Lacy, J.H., Carr, J.S., EvansII Neal, J., Baas, F., Allamandola, L.J., Arens, J.F. 1991, ApJ 376, 556

Lacy, J.H., Farji, H., Sandford, S.A., Allamandola, L.J. 1998, ApJ 501, L105

Larson, H.P., Davis, D.S., Black, J.H., Fink, U. 1985, ApJ 299, 873

Léger, A. 1983, A&A 123, 271

Léger, A., Klein, J., De Cheveigne, S., Guinet, C., Défourneau, D., Belin, M. 1979, A&A 79, 256

Linblad, B. 1935, Nature, 135, 133

Merrill, K.M., Russell, R.W., Soifer, B.T. 1976, ApJ 207, 763

Reed A.E., Wienhold, F., Curtis, L.A., Pochatko, D.J. 1986, J.Chem.Phys. 84, 5687

Sandford, S.A., Allamandola, L.J., Tielens, A.G.-G.M., Valero, G.J. 1988, ApJ 329, 498

Sandford, S.A., Allamandola, L.J. 1990, ApJ 355, 357

Schutte, W.A., Greenberg, J.M. 1997, A&A 317, L43

Soifer, B.T., Puetter, R.C., Russell, R.W., Willner, S.P., Harvey, P.M., Gillett, F.C. 1979, ApJ 232, L53

Tielens, A.G.G.M., Hagen, W. 1982, A&A 114, 245

Whittet, D.C.B., Schutte, W.A., Tielens, A.G.G.M., et al. 1996, A&A 315, L357

Whittet, D.C.B., Duley, W.W. 1991, A&A Rev 2, 167

Whittet, D.C.B., Gerakines, P.A., Tielens, A.G.-G.M., et al. 1998, ApJ 498, L159

COLD DUST IN THE INTERSTELLAR MEDIUM

R. J. Laureijs

ISO Data Centre, Astrophysics Division, ESA, Villafranca, Spain.

ABSTRACT

The presence of dust particles residing at very low temperatures ($T_d <$ 18 K) has been hypothesised for a long time. The predictions were based on assumed properties of dust particles in the infrared combined with plausible conditions of the ISM in dense regions. Nevertheless, our observational picture of the cold dust component in the ISM is still poor despite the accessibility of photometric windows in the far-infrared and sub-mm wavelength range where cold dust emission should be detectable. We review long wavelength observations ($\lambda > 100\ \mu$m) of the diffuse ISM, dense regions, cloud cores, and normal galaxies. A comparison is given between the different observations in terms of dust temperatures T_d and power in the far-infrared emissivity β.

Key words: ISM: dust, extinction – infrared: ISM: continuum – Galaxies: ISM

1. INTRODUCTION

Emission from dust grains responsible for the visual extinction can only be observed at wavelengths longward of 100 μm due to the low temperatures of these grains. With the availability of COBE data, ISO data, balloon-borne observations, and a new generation ground based sub-mm arrays, the interest in observing cold dust has increased in the last few years. There are several reasons to study the properties of dust in cold regions. Firstly, cold dust emission can trace the densest and most hidden parts of molecular clouds where the earliest stages of star formation take place. These regions are also detectable in molecular line emission such as $C^{18}O$, HDO, NH_3, etc. which provide important kinematic and chemical information. However, molecular line intensity depends strongly on the abundance of the molecule which in turn depends on the chemical history of the region. Dust continuum emission offers the possibility to obtain an independent view of these regions.

The second importance of cold dust is the observation of a "hidden" mass component. The detection of a low temperature dust component implies a large increase of the total dust mass of an object:

$$M_d = \frac{F_\nu D^2}{\kappa_\nu B_\nu(T_d)}, \qquad (1)$$

where T_d is the dust temperature, D is the distance to the object, κ_ν is the mass absorption coefficient which is proportional to area over mass, and B_ν is the Planck function. A significant detection of the flux density F_ν at a low temperature is usually sufficient to boost the total mass of an object. The total mass of an object as given in Eq. 1 depends on the assumed gas-to-dust ratio and the properties of the dust which are hidden in κ_ν.

The third reason to understand the properties of cold dust is to be able to properly decompose the far-infrared and sub-mm emission into separate emission components associated with the zodiacal, galactic, and extragalactic backgrounds.

Due to a limited amount of wavelength bands or due to a lack of sufficient spectral coverage, the spectral energy distribution of a given object is usually fitted according to the relation:

$$F_\nu \propto \nu^\beta B_\nu(T_d). \qquad (2)$$

This approach assumes a spectral energy distribution which is predominantly due to dust at a single temperature T_d and a power law dust emissivity proportional to ν^β. In the remainder of this review we will refer to β as the power in the emissivity. Following Cox et al. (1986) we speak of cold dust when the temperature of the dust is equal to or below the mean equilibrium temperature of the large dust grains in the local diffuse ISM. This temperature was predicted to be around 16 K for silicate grains and 20 K for graphite grains.

In this review the reality of cold dust in our Galaxy and in other galaxies is discussed. In Sect. 2 a summary is presented of observations of diffuse emission at high galactic latitudes. Studies in which the colder and denser regions are separated from the diffuse ISM are reviewed in Sect. 3. A discussion of temperature determinations of dense cloud cores is given in Sect. 4. Evidence for a relatively high amount of sub-mm emission with respect to the far-infrared in other galaxies is discussed in Sect. 5. In Sect. 6 we discuss the conditions that could lead to the presence of cold dust. Conclusions and future prospects are stated in Sect. 7.

Proceedings of the Conference "The Universe as seen by ISO", Paris, France, 20–23 October 1998 (ESA SP-427, March 1999)

2. OBSERVATIONS OF THE DIFFUSE ISM

The first results from the IRAS survey surprisingly showed that the surface brightness ratio $I_{60}/I_{100}\sim 0.2$ is significantly higher than predicted from classical dust models. The corresponding colour temperature is about 27 K assuming a $\beta = 2$ emissivity law. The high brightness ratio has been attributed to an additional warmer emission component in the 60 μm IRAS band. The warmer emission is most likely caused by non-equilibrium emission from very small grains (Draine & Anderson, 1986; Désert et al. 1990; Siebenmorgen & Krügel, 1992; Dwek et al. 1997 and references therein). This presence of at least two dust emission components makes it difficult - if not impossible - to derive the temperature of the large dust particles only from observations shortward of 100 μm.

In the recent years several groups have measured the spectral energy distribution of the high latitude sky longward of 100 μm. These observations were usually part of a larger scientific project to measure the cosmic microwave background. Table 1 summarizes the temperature measurements, and, if available, the inferred value of β. We have included the COBE result derived by Reach et al. (1995) obtained from a single temperature fit to the emission of regions with $b > 60°$ and the results obtained by Boulanger et al. (1996); see below for a full discussion of the COBE data.

Table 1. Summary of temperature determinations from far-infrared and sub-mm observations.

Experiment	T (K)	β	Reference
rocket	$16.4^{+2.3}_{-1.8}$	2^a	Kawada et al. 1994
COBE[b]	23.2±0.5	0.92±0.04	Reach et al. 1995
ARGO	20.1±1.2	1.5±0.2	Masi et al. 1995
MAX	18±3	1.4±0.4	Fisher et al. 1995
IRTS	18±1	2^a	Hirao et al. 1996
COBE[b]	17.5	2	Boulanger et al. 1996

[a]see text
[b]assumed

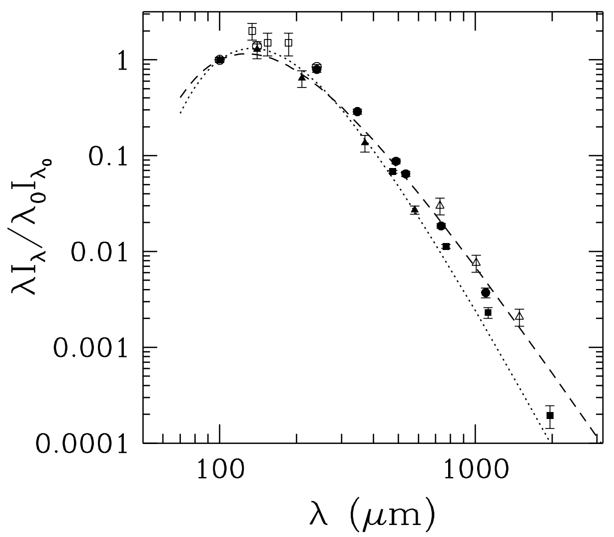

Figure 1. Compilation of the long wavelength observations of the diffuse emission at high galactic latitudes. All datasets have been normalized to $\lambda_\circ = 100\ \mu m$. Explanation symbols: open and filled circles: DIRBE and FIRAS data from the analysis by Boulanger et al. (1996), filled triangles: IRTS data for $b = 3.5°$ (Hirao et al. 1996), open squares: rocket observations (Kawada et al. 1994), closed squares: ARGO observations of Aries and Taurus regions (Masi et al. 1996), open triangles: MAX observations of the μPeg region (Fisher et al. 1995). The dotted and dashed lines give the spectra for modified blackbodies of 23.2 K with $\beta = 0.92$ and 18 K with $\beta = 2$, respectively.

The observations of the experiments listed in Table 1 have been plotted in Figures 1 and 2. Figure 2 contains the same data as Figure 1 but the data are presented in such a way that systematic differences between the data sets at the longest wavelengths are highlighted. All data have been normalized to 100 μm since all experiments except COBE have been calibrated against the IRAS 100 μm band (which was cross-calibrated with COBE).

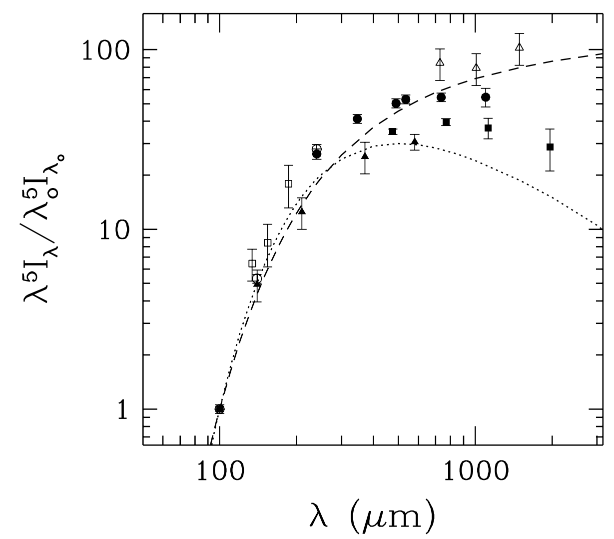

Figure 2. Same data as in Figure 1 but using the ratio ($\lambda^5 I_\lambda/\lambda_\circ^5 I_{\lambda_\circ}$) as ordinate, with $\lambda_\circ = 100\ \mu m$.

In case the dust follows an emissivity according to $\beta = 1$ the data displayed in Figure 2 should asymptotically rise to a constant level at the longest wavelengths. For larger values of β, the spectral energy distribution must show a turnover with a maximum at about 400–600 μm depending on the dust temperature. From the sub-mm datasets obtained by COBE, ARGO, and MAX, only ARGO exhibits a clear turnover suggesting $\beta > 1$ in the limit. The other datasets (COBE and MAX) indicate no maximum. From Figure 2, it can be concluded that a single power law emissivity with $\beta = 2$ poorly represents the longest wavelengths. Either the power in the emissivity is smaller than 2 or there is more than one emission component.

Masi et al. (1995) showed that the ARGO data (cf Table 1) can also be matched with a bimodal distribution of temperature components peaking at 14 K and 25 K, all components have $\beta = 1.3$. They conclude that a single temperature fit tends to overestimate the value of β compared to a multi-temperature fit.

The most comprehensive far-infrared and sub-mm data sets were provided by the DIRBE and FIRAS instruments of COBE. However, the interpretation of the spectral energy distribution is subject to debate. Wright et al. (1991) and Reach et al. (1995) showed that the FIRAS spectral energy distributions of high latitude lines of sight can be best fit by two temperature components of 16–21 K (the warm component) and 4–7 K (the very cold component) with $\beta = 2$ for both components. Reach et al. (1995) found that the two component fit gives a significantly better match to the observed spectra than a single temperature blackbody with $\beta = 2$ or a single temperature blackbody with β as a free fitting parameter. The very cold component varies little with galactic longitude and its temperature is not correlated with that of the warm component. But the optical depths of the two components are correlated. In case of single temperature fits with β as a free parameter they find for $|b| > 10°$ temperatures higher than 19 K and $\beta < 1.6$.

Evidence for a very cold dust component (4–7 K) was also given by the IRTS experiment where the 250/700 μm brightness ratio shows a significantly stronger decrease with increasing galactic longitude than the 150/250 and 250/400 μm brightness ratios (Hirao et al. 1996). One interpretation of this observation is that the dust temperature is constant with $T_d = 20$ K and β decreasing with latitude. Alternatively, there exists a cold component with $T_d = 5$–7 K for which either the temperature or optical depth increases with latitude. Proper comparison with the COBE results is difficult, since the IRTS observations cover only $-3.5° < b < +3.5°$, whereas the analysis by Reach et al. (1995) covers $b > 10°$.

The COBE findings by Reach et al. (1995) have been disputed by Boulanger et al. (1996) and Puget et al. (1996). They determined the spectral energy distribution of the high latitude cirrus component from the correlation of the FIRAS emission with the Leiden-Dwingeloo HI survey. After subtracting the HI cirrus component and after correcting the residual emission for the contribution of ionized hydrogen they obtained a significant residual emission which is isotropic. The presence of this residual emission has been confirmed by Fixsen et al. (1998) who applied several different foreground removal methods. Puget et al. (1996) attribute the isotropic component to sources at large redshift. In any case, Boulanger et al. (1996) conclude that the cirrus component (cf. Figures 1 and 2) does not show evidence for the presence of a 4–7 K very cold dust component. The results of their best fit ($T_d = 17.5$ K, $\beta = 2$) is included in Table 1.

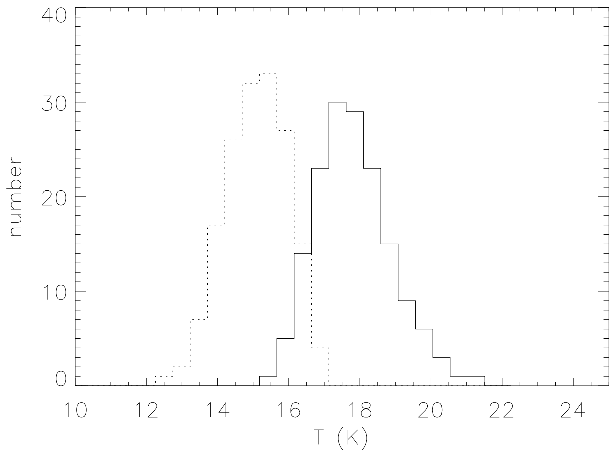

Figure 3. The temperature distribution in regions which show an emission component significantly colder than the diffuse ISM. These lines of sight can be decomposed in a cold - 60 μm deficient - ($T_d = 15$ K) and a diffuse ISM ($T_d = 17.5$ K) emission component. (Figure taken from Lagache et al. 1998.)

3. COLD REGIONS AT HIGH GALACTIC LATITUDES

The ratio I_{60}/I_{100} is generally constant in the diffuse ISM, but systematic variations over large regions on the sky has been inferred from the COBE observations (Lagache et al. 1998). In denser regions the constancy in the I_{60}/I_{100} ratio breaks down and becomes smaller. The difference $(I_{100} - I_{60}/\theta)$, where $\theta \approx 0.2$ is the mean value of I_{60}/I_{100} in diffuse regions, was found to be a good tracer of denser molecular material (Laureijs et al. 1991; Abergel et al. 1994; Cambresy et al. 1997). The absence of 60 μm emission provides an upper limit to the grain temperature. Using IRAS images with a spatial resolution of $\approx 5'$, Laureijs et al. (1991) derive $T_d < 13.8$ K assuming $\beta = 2$.

Since COBE measured also at the longer wavelengths, the actual temperatures can be determined of (1) the diffuse component associated with constant I_{60}/I_{100} and (2) the 60 μm deficient regions. Analysis of COBE observations of the high latitude sky by Lagache et al. (1998) showed that the regions with $I_{60}/I_{100} = \theta$ are associated with dust of a temperature $T_d = 17.5$ K ($\beta = 2$). The 60 μm deficient regions exhibit a temperature distribution peaking at 15 K, see Figure 3. These colder regions are associated with column densities in excess of $n_H > 2.5 \times 10^{20}\,\mathrm{H\,cm^{-2}}$. No evidence was found for the presence of a very cold dust component with $T_d < 12$ K.

Reach et al. (1998) separated the diffuse ISM from the denser regions by correlating the high latitude DIRBE maps with HI maps from the Leiden-Dwingeloo HI survey. The regions which exhibit an excess infrared emission with respect to the average IR/HI correlation give a mean temperature of 17±2 K, the known molecular clouds with excess infrared emission are at 15.5±2 K. The dust temperature in the atomic gas is found to be 19±2 K. The infrared excess clouds can be characterized by their lack of HI rather than lower temperature. Only when CO can be detected the temperature becomes significantly lower than the dust associated with atomic hydrogen. The resulting surface density of the infrared excess clouds is about 0.3 $M_\odot\,pc^{-2}$ which is comparable with the surface density derived from high latitude CO surveys.

4. OBSERVATIONS OF CLOUD CORES

Only few observations exist of cold cores longward of 100 μm which cover a significant part of the spectral energy distribution. Ristorcelli et al. 1998 measured with PRONAOS both the temperature and β of a newly discovered cold cloud in the Orion A complex. The inferred temperature is 12.5±3 K with β = 1.9±0.4. By combining ISO-LWS data with ground based sub-mm observations Lis & Menten (1998) were able to determine several parameters including dust temperature and emissivity law of a giant molecular cloud core. They find a temperature of 18 K and $\beta = 2.8$. It should be noted that the core is close to the Galactic Centre where the ISRF is different from that in the solar neighbourhood.

Other temperature determinations of (quiescent) cloud cores must assume a value of β due to a lack of spectral coverage beyond 100 μm or due to insufficient photometric accuracy. In Figure 4 the temperatures of dense cloud cores obtained by various observers have been plotted against the estimated size of the cores. The estimation of the core size suffers from large uncertainties, since it depends on the assumed distance and the adopted method to measure the projected size of a core. Nevertheless, it provides a useful crude estimate of the linear dimension of an object in the comparison of different temperatures. For all targets we assume that the cores are resolved and $\beta = 2$ unless otherwise stated.

Figure 4 shows that most of the cores reside in a narrow temperature range of 12-14 K. The smallest cores were observed by Ward-Thompson et al. 1994 with the JCMT (~18″ beam) and are the densest regions observed inside quiescent clouds. Two of these cores exhibit the lowest temperatures of 8 K of which one is the core of LDN183. On the other hand, ISO observations of LDN183 in the 100–200 μm range (~3′ beam) indicate a dust temperature of 12 K (Mattila, private communication). Figure 4 suggests no clear correlation with size, but with the caveat that the uncertainties are highest for the JCMT measurements. The cold giant molecular cloud close to the galactic centre measured by Lis & Menten (1998) resides in a radiation field with a higher energy density and is therefore likely to be warmer than an equivalent cloud in the solar neighbourhood.

The horizontal lines in Figure 4 represent the temperatures of the diffuse and cold regions at high latitude as measured with COBE, see Sect. 3. We see that measurements obtained with a higher spatial resolution enable detection of lower temperatures. The colder cores are probably embedded in the cold regions detected by COBE (Sect. 3). The sample of cloud cores in Figure 4 show no evidence for a large cloud fraction residing at very low dust temperatures ($T_d <$ 10 K). With an ISO resolution of about 3′, a resolved core of 0.1 pc corresponds to a distance of < 110 pc. Consequently, it will be very difficult to detect emission from cores with temperatures below ~12 K with ISO.

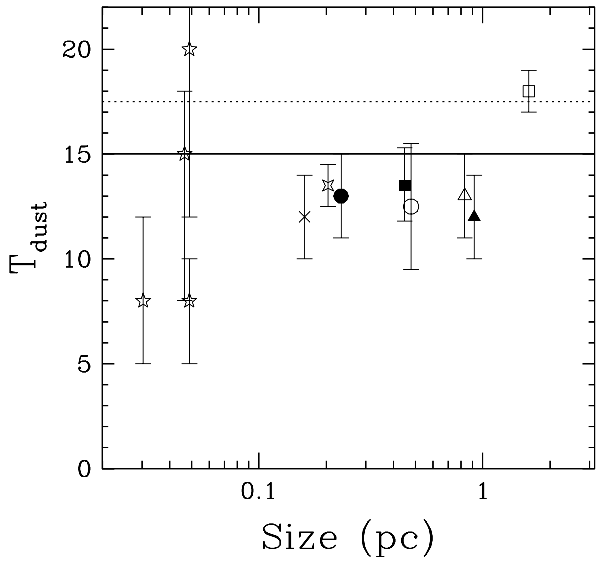

Figure 4. The temperatures of dense cores in clouds and globules as a function of linear size. The dotted line gives the temperature of the diffuse ISM in the solar neighbourhood, the solid line gives the mean temperature of the cold regions as derived by Lagache et al. (1998) from the COBE data (cf. Figure 3). The open square indicates the temperature ($\beta = 2.8$) of the giant molecular cloud core near the galactic centre obtained by Lis & Menten (1998). The open circle is the cold clump in Orion A ($\beta = 1.9$) observed by Ristorcelli et al. 1998. The pentagons are the starless cloud cores measured with the JCMT by Ward-Thompson et al. (1994). The remaining data are from Laureijs et al. (1996, filled square), Laureijs et al (1999, open circle), Lehtinen et al. (1998, starry cross), Keene (1981, only B133, open triangle), Toth et al. (1999, filled triangle), and Mattila et al. (1998, cross).

The analysis of extended structures in the ISOPHOT Serendipity Survey at 170 μm shows that the coldest structures which can be detected have temperatures of the order of 13 K (Tóth et al. 1999; Hotzel et al. 1999). These temperatures are derived from the ratio between the 100 μm IRAS and the 170 μm ISOPHOT emission.

5. COLD DUST IN OTHER NORMAL GALAXIES

With the availability of ISO and ground based sub-mm arrays, photometric data as well as maps of a growing number of galaxies at wavelengths $\lambda >$ 100 μm have become available. The emerging picture is that for non-active galaxies the dust temperature is significantly lower than the temperature derived from the IRAS 60 and 100 μm data alone. The presence of a colder dust component was suggested by Devereux

& Young (1990) on the basis of the high mean ratio (≈1000) between gas masses derived from HI observations and dust masses derived from the IRAS data at 60 and 100 μm.

The first long wavelength observations of a sample of non-active galaxies were carried out by Chini et al. (1986). In contrast to the active galaxies which can be characterized by one dust component of $T_d = 33\pm5$ K and $\beta = 1.9\pm0.3$ (Chini et al. 1989), the spectral energy distributions of the non-active galaxies are interpreted in terms of two dust components at about 16 and 53 K, and with $\beta = 2$ for both components. The cold component dominates in the wavelength range 100–1300 μm. This two component picture has been corroborated by more detailed observations of NGC 660 and UGC 3490 (Chini & Krügel, 1993) and a larger sample of 32 galaxies (Chini et al. 1995). It was found that the addition of 450 and 800 μm photometry to the IRAS data does not yield a unique temperature solution to the 2 component temperature model. For the cold component the average temperature ranges between 10 and 20 K. Both studies also indicate that the spatial extent of the cold component is comparable to the optical size of the galaxy.

Alton et al. 1998a found for a sample of 7 nearby spirals an average temperature $T_d = 18$ K ($\beta = 2$) from the IRAS 100 μm and ISOPHOT 200 μm photometry. This temperature is significantly lower than the IRAS 60 to 100 μm colour temperature ($T_d = 28$ K). The dust mass inferred from the $I_{100}(IRAS)/I_{200}(ISO)$ temperature is higher by more than a factor 20. The correspondingly lower gas-to-dust ratio found for the spirals is in better agreement with the value generally adopted for the solar neighbourhood.

By combining IRAS, ISOPHOT, and submillimetre observations Krügel et al. 1998 found evidence for a very cold dust component in 3 inactive galaxies. Similar to what was found in our own galaxy by Reach et al. 1995, Krügel et al. 1998 showed that the data could be best fit by a combination of a warm (~30 K) and cold (~10 K) component. For the active galaxies a single temperature fit (~30 K) gives an adequate match. An important consequence of the two component temperature model is that the inferred dust masses are 2–3 times higher than the estimated masses using a single temperature.

Observations with ISOPHOT of M31 show that most of the dust is situated in a ring at 10 kpc and has a temperature of 16±2 K assuming $\beta = 2$ (Haas et al. 1998). This component contributes to about 60% of the total FIR luminosity of the galaxy. The ISOPHOT temperature determination yields a total dust mass significantly higher than what was inferred from the IRAS observations at 60 μm and 100 μm, strongly supporting the view that the 60 μm band consists of an additional warmer dust component.

From the analysis of ISOPHOT and sub-mm data of NGC 205, one of the dwarf companions of M31, Haas, 1998 found evidence for a very cold dust component at $T_d = 8$ K with $\beta = 2$. This component contributes to the far-infrared spectrum together with a warmer component at $T_d = 22$ K ($\beta = 2$). The value $\beta = 2$ was favoured because smaller values of β cannot match the far-infrared spectral energy distribution in the range 60–200 μm. Similarly Alton et al. 1998b found for the edge-on spiral NGC891 a warm component of $T_d = 30$ K and a cold component of 15 K ($\beta = 2$) based on the IRAS and SCUBA 450 and 850 μm observations. They found that $\beta = 2$ gives the best fit to the data.

It should be noted that Krügel et al. (1998), Haas (1998) and Alton et al. (1998b) all include photometry at 60 μm in their analysis. Since the 60–100 μm range is contaminated by emission from small grains the fitting procedure is biased towards a "warmer" warm component and a more prominent cold component with $\beta = 2$. Alternatively, from the modelling of Arp 220 emission, Silva et al. (1998) found that the submm data are underpredicted by a factor 2–3 unless β is lowered from their initial value 2 to 1.6.

Pérez García et al. (1998) developed an inversion Bayesian method which assumes that the infrared spectrum can be composed of a continuum of modified blackbodies with $\beta = 1.5$. They used the method to recover the spectral energy distributions of 10 Seyfert galaxies which have been observed with ISOPHOT in the wavelength range from 16 to 200 μm. The resulting temperature distribution for each galaxy always shows peaks in three temperature regimes: (1) a 120–160 K component from the nuclear region, (2) a 40–50 K component from star-forming regions in the disk, and (3) a cold 15–20 K component from the diffuse ISM. The inversion method yields unexpectedly well-defined and sharp temperature components.

6. EMISSION FROM COLD DUST: GRAIN PROPERTIES AND MODELS

The equilibrium temperature of dust grains depend on their composition, size distribution, and shape, and also on the radiation field heating the dust. In the following sections we will review the effects of these parameters on the far-infrared and sub-mm dust emission.

6.1. Effect due to grain composition, size, and shape

Laboratory measurements combined with model calculations of spherical silicate particles have shown that their temperature is about 15–18 K in a standard radiation field. Graphitic grains attain higher temperatures of 19–22 K (Draine & Lee 1984). The model calculations were based on extrapolation of the optical properties of the materials to far-infrared and sub-mm wavelengths using the Kramers-Kronig relations. These relations impose an even and positive value of β in the $\lambda\to\infty$ limit.

Measurements of amorphous silicate grains at long wavelengths and under different temperature conditions carried out by Agladze et al. (1996) and Menella et al. (1998) suggest that the long wavelength absorption coefficient has a significant dependence on temperature. Agladze et al. (1996) find that for some of the amorphous silicate materials the value of β can vary between 2.5 for $T\sim10$ K and 2.0

for $T{\sim}20$ K. At temperatures below 10 K the value of β drops again. A different kind of amorphous silicate ($MgO{\cdot}2SiO_2$) shows a nearly constant β of 1.2. In addition, Agladze et al. (1996) find long wavelength emissivities for amorphous silicates that are several times higher than the values given by Draine & Lee (1984).

Amorphous carbon grains show smaller values of β compared to graphitic grains which have $\beta{\approx}2$. The value of β is smaller for materials that are more amorphous, with $\beta{\leq}1$ (Koike et al. 1994; Menella et al. 1995). Menella et al. (1998) find only a weak dependence on temperature with $\beta\approx$ 1.2 at 20 K for two kinds of amorphous carbons. These studies show that the far infrared properties of grains can be quite different from earlier predictions. The assumption that β should become 2 in the long wavelength limit does not necessarily apply to far-infrared and sub-mm wavelengths.

The effect of increasing grain size is generally to decrease the grain temperature under the same radiation conditions. For example, assuming the local ISRF, increasing the radius of an silicate sphere from 0.1 μm to 1 μm will decrease its temperature from 15.4 to 13.4 K and for an graphite sphere the corresponding drop in temperature is from 18.8 to 12.7 K (Draine & Lee 1984). In order to attain an equilibrium temperature below 10 K the size of a grain should be larger than 10 μm. In situ measurements by the Galileo and Ulysses spaceprobes of the mass distribution of grains show more grains with larger sizes ($a > 0.2\,\mu m$) than expected from a Mathis et al. (1977) power law size distribution (Landgraf & Grün, 1997). To explain the very cold dust component of 6 K, Reach et al. (1995) found that the inferred mass required in 100 μm size spheres is not excessive and can still satisfy the abundance constraint for silicate or carbon spheres.

Different from compact solid grains are the composite grains (Mathis & Whiffen, 1989) and fractal grains (Wright 1987). These types of grains consist of conglomerates of smaller particles with a high degree of porosity. Since these grains have a higher ratio surface area to volume, less material is needed to obtain the same extinction properties as compact grains in the visual (Mathis 1998). The porosity of these grains increases the opacity in the infrared leading to temperatures lower than in case of spherical grains of similar composition. Fogel & Leung (1998) computed the far-infrared properties of fractal grains and found that these type of grains are cooler than their spherical counterparts by 10–20%.

6.2. Dust temperatures in regions shielded from the ISRF

UV photons are important heating agents for dust grains, which, in turn, shield the inner cloud regions, if the cloud's opacity is sufficiently high. Dust temperature calculations involving a variety of cloud models, standard dust properties, and a standard radiation field (Lee and Rogers, 1987; Bernard et al. 1992) indicate that the temperature of a cloud drops quickly in the outer region, if the central opacity of the cloud is only a few magnitudes of A_V. However, further increment of the total cloud opacity has only little effect on the temperature in the centre of a cloud. The temperature in the cloud centre is maintained due to heating by photons at visible and red wavelengths which penetrate more deeply into a cloud than UV photons. The standard ISRF (Mathis et al. 1983) contains about half of the energy density in these photons. In addition, the penetration is also facilitated by a degree of forward scattering by the grains. The model calculations by Bernard et al. (1992) suggest that the heating by infrared photons due to re-radiation by dust particles inside the cloud provides only a minor contribution.

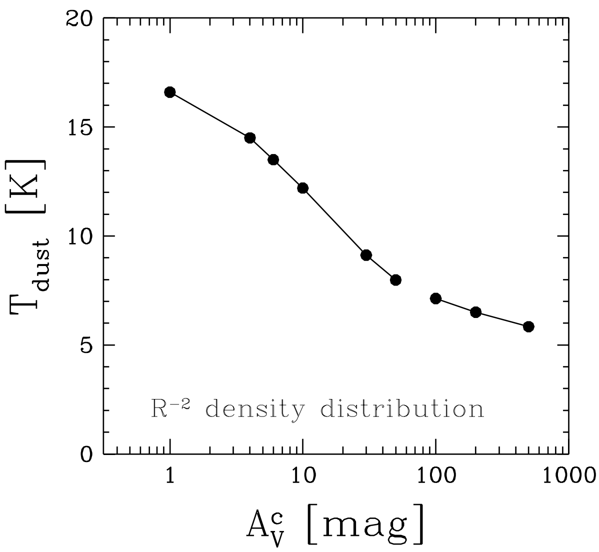

Figure 5. The temperature of dust in the centre of a cloud with R^{-2} density distribution as a function of total visible extinction through the cloud. The temperatures are from Bernard et al. (1992).

The central dust temperature of a set of cloud models with different central opacity computed by Bernard et al. 1992 is presented in Figure 5. The temperature is predicted to drop below 10 K, if the total opacity of the cloud exceeds A_V = 20 mag.

The models in Figure 5 assume clouds with a homogeneous structure and a radially symmetric density distribution. Alternative models which assume a clumpy cloud structure (e.g. Boissé 1990) indicate that the radiaton field can penetrate deeper into a cloud than one would expect from the line of sight column density. This implies that a realistic cloud structure tends to increase the temperatures predicted in Figure 5 provided that the dust properties inside dense clouds are not changing.

The observations presented in Sects. 3 and 4 indeed show that the dust temperatures in cloud cores are quite homogeneous. According to Figure 5 the emission that is detected for these cores corresponds to a shielding of about A_V = 10 mag at most. Only observations with the highest spatial resolution can detect regions as cold as 8 K which means a shielding up to A_V = 50 mag. It is unlikely that the very cold dust component (T_d < 10 K) suggested in the diffuse ISM and in non-active galaxies is due to shielding of the ISRF in view of the high column densities implied.

7. CONCLUSIONS AND PROSPECTS

We have reviewed the far-infrared and submm properties of the diffuse ISM in the solar neighbourhood (Sect. 2), more shielded dense regions (Sect. 3, and embedded cloud cores (Sect. 4).

Compilation of the observations of the diffuse ISM strongly suggests that the spectral energy distribution falls off less steeply towards the longest wavelengths than a single modified blackbody with $\beta = 2$ (cf. Figure 2). The question whether this is due to a discrete very cold dust component or due to an ISM dust property (causing $\beta < 2$) deserves further investigation. Cirrus mapping with a resolution of a few arcminutes (or better) at several infrared and submm wavelengths could clarify the issue. The structure of the diffuse ISM must be be used to isolate the diffuse ISM from other emission components. ISOPHOT surveys of low level regions and maps of diffuse clouds could be used for this purpose. Future space missions like the Far-Infrared Submm Telescope (FIRST) and Planck can provide decisive observational support.

The observation of a cloud core with β as large as 2.8 indicates that the properties of dust in a dense region can be significantly different from those of the diffuse ISM. The dust temperatures of quiescent cloud cores are predominantly in the range 12–14 K with some lower values for the smallest cores. There is no indication for the presence of large fractions of clouds residing at temperatures below 10 K. This picture is supported by model calculations of dusty clouds. ISOPHOT maps of dense cloud regions as well as the ISOPHOT Serendipity Survey can be used to find cold and dense regions in clouds which can be followed up in the submm to search for even colder cores with $T_d < 12$ K.

Observations of normal galaxies incorporating observations at $\lambda > 100\,\mu$m indicate dust temperatures ($10 < T_d < 20$ K) which are significantly lower than expected from the IRAS 60 and 100 μm fluxes. These temperatures yield mass estimates that are consistent with a galactic gas-to-dust ratio. This temperature component corresponds to the 18 K component seen in our Galaxy due to the diffuse matter heated by the ISRF.

Several studies reported on the presence of very cold dust ($T_d < 10\,K$, $\beta = 2$) in a number of quiescent galaxies. A better spectral coverage and more accurate photometry are necessary to confirm these results. ISO data in the 100–200 μm range in combination with ground based submm maps for more galaxies could clarify the issue. If real, the flux excess at submm wavelengths seen in these galaxies and in the diffuse ISM in the solar neighbourhood could have a common explanation.

ACKNOWLEDGEMENT

I would like to thank Ulrich Klaas for critical reading of the manuscript.

REFERENCES

Abergel, A., Boulanger, F., Mizuno, A., Fukui Y. 1994, ApJ 432, L59.

Agladze, N.I., Sievers, A.J., Jones, S.A., Burlitch J.M., Beckwith S.V.W. 1996, ApJ 462, 1026.

Alton, P.B., Trewhella M., Davies J.I., Evans R., Bianchi S., Gear W., Thronson H., Valentijn E., Witt, A. 1998a, A&A 335, 807.

Alton, P.B., Bianchi S., Rand R.J., Xilouris E.M., Davies J.I., Trewhella M. 1998b, ApJ 507, 125.

Bernard, J.P., Boulanger F., Desert F.X., Puget J.L. 1992, A&A 263, 258

Boissé, P. 1990, A&A 228, 483

Boulanger, F., et al. 1996, A&A 312, 256.

Cambrésy, L., Epchtein, N., Copet E., et al. 1997, A&A 324, L5.

Chini, R., Kreysa, E., Krügel E., Mezger P.G. 1986, A&A 166, L10.

Chini, R., Krügel E., Kreysa E., Gemünd H.-P 1989, A&A 216, L5.

Chini, R., Krügel E. 1993, A&A 279, 385.

Chini, R., Krügel E., Lemke R., Ward-Thompson D. 1995, A&A 295, 317.

Cox, P., Krügel, E., Mezger P.G. 1986, A&A 155, 380.

Devereux, N.A., Young J.S. 1990, ApJ 359, 42.

Désert, F.X., Boulanger F., Puget J.-L 1990, A&A 327, 215.

Draine, B.T., Anderson N. 1985, ApJ 292, 494.

Draine, B.T., Lee H.M. 1984, ApJ 285, 89.

Dwek, E., et al. 1997, ApJ 475, 565.

Fisher, M.L., Clapp A., Devlin M. et al. 1995, ApJ 444, 226.

Fixsen, D.J., Dwek E., Mather J.C., Bennet C.L., Shafer R.A. 1998, ApJ 508, 123.

Fogel, M.E., Leung C.M. 1998, ApJ 501, 175.

Haas, M. 1998, A&A 337, L1.

Haas, M., Lemke D., Stickel M., Hippelein H., Kunkel M., Herbstmeier U., Mattila, K. 1998, A&A 338, L33.

Hirao, T., Matsumoto T., Sato S., Ganga K., Lange A.E., Smith B., Freund M.M. 1996, PASJ 48, L77.

Kawada, M., Bock J.J., Hristov V.V. et al. 1994, ApJL 425, 89

Keene, J. 1981, ApJ 245, 115

Koike, C., Hasegawa H., Shibai H. 1994, MNRAS 268, 321.

Krügel, E., Siebenmorgen R., Zota V., Chini R. 1998, A&A 331, L9.

Lagache, G., Abergel A., Boulanger F., Puget J.-L. 1998, A&A 333, 709

Landgraf, M., Grün E. 1998, Proceedings of "The local bubble and beyond", Eds D. Breitschwerdt et al. in print.

Laureijs, R.J., Clark F.O., Prusti T. 1991, ApJ 372, 185.

Laureijs, R.J., Haikala L., Burgdorf M., Clark F.O., Liljeström, T., Mattila K., Prusti T. 1996, A&A 315, L317

Laureijs, R.J., et al. 1999, in preparation.

Lee, M.H., Rogers C. 1987, ApJ 317, 197.

Lis, D.C., Menten K.M. 1998, ApJ 507, 792.

Lehtinen, K., Lemke D., Mattila K., Haikala L.K. 1998, A&A 333, 702.

Mathis, J.S., 1998 A&A 497, 824.

Mathis, J.S., Mezger P.G., Panagia N. 1983 A&A 128, 212.

Mathis, J.S., Rumpl W., Nordsiek K.H. 1977 ApJ 217, 425.

Mathis, J.S., Whiffen G. 1989, ApJ 341, 808.

Mattila, K. et al. 1998 in Proc. of the Zermatt conference

Masi, S., Aquilini E., Boscaleri A., de Bernadis P., De Petris M., Gervasi M., Martinis L., Natale V., Palumbo P., Scaramuzzi F. 1995, ApJ 452, 253.

Mennella, V., Colangeli L., Bussoletti E. 1995, A&A 295, 165.

Mennella, V., Brucato J.R., Colangeli L., Palumbo P., Rotundi A., Bussoletti E. 1998, ApJ 496, 1058.

Pérez García, A.M., Rodríguez Espinosa, J.M., Santolaya Rey A.E. 1998, ApJ 500, 658.

Puget, J.-L., Abergel A., Bernard J.-P., et al. 1996, A&A 308, L5.

Reach, W.T., Dwek E., Fixsen D.J., et al. 1995, ApJ 451, 188.

Reach, W.T., Wall W.F., Odegard N. 1998, ApJ 507, 507.

Ristorcelli, I., Serra G., Lamarre J.M., et al. 1998, ApJ 496, 267.

Sodroski, T.J., Bennet C., Boggess N., Dwek E., Franz B.A., Hauser M.G., Kelsall T., Moseley S.H., Odegard N., Silverberg R.F., Weiland J.L. 1996, A&A 312, 256.

Siebenmorgen, R., Krügel E. 1992, A&A 259, 614

Silva, L., Granato G.L., Bressan A., Danese L. 1998 ApJ 259, 614

Ward-Thompson, D., Scott P.F., Hills R.E., André P. 1994, MNRAS 268, 276

Wright, E.L., Mather J.C., Bennet C.L., et al. 1991, ApJ 381, 200.

Wright, E.L. 1987, ApJ 320, 818.

ISO'S VIEW ON DUST IN COMETS AND CIRCUMSTELLAR MEDIA

C. Waelkens, K. Malfait, L.B.F.M. Waters[2], & Th. de Graauw[3]

[1]Instituut voor Sterrenkunde, Leuven, Belgium
[2]Astronomical Institute, Amsterdam, The Netherlands
[3]SRON Space Research Laboratory, Groningen, The Netherlands

ABSTRACT

The infrared spectrum of Comet Hale-Bopp obtained with the Infrared Space Observatory (ISO) presents astonishing similarities with those of the dusty disks surrounding young stars. The presence of crystalline silicates in comets, Herbig Ae/Be stars and the main-sequence star β Pictoris, is interesting in the context of the formation of comets and confirms that Herbig Ae/Be stars are evolutionary precursors of β Pictoris stars. The detection of hydrous silicates in both the spectrum of HD 142527 and in interplanetary dust particles (IDPs) strengthens the link between these dust disks and our own Solar System.

Key words: circumstellar disks; β Pic stars; Hale-Bopp; Herbig Ae/Be stars.

1. INTRODUCTION

The observation of comets contains important clues on the early evolution of our solar system. Their composition constrains the conditions in the solar nebula at the epoch of planet formation. A gratifying circumstance has been that ISO was operational when the dusty and extremely bright comet Hale-Bopp appeared in the sky, revealing a forest of crystalline silicates bands in the ISO-SWS spectrum.

On the other hand, during the last decade, there has been a growing interest in circumstellar dust disks surrounding young stellar objects. Observational evidence for the presence of crystalline silicates, hydrous silicates and water ice in the spectra of these disks is presented. Crystalline silicate features so far seem to be absent in spectra of the interstellar medium and in the disks of the youngest stellar objects. An attempt is made to confront these data with our understanding of the cosmic dust cycle and with stellar evolution.

2. β PICTORIS AND VEGA-TYPE STARS

The detection of IR excesses in normal main sequence stars was a spectacular result from the IRAS mission. It strongly influenced the studies of planet formation in the disks that are expected to surround all young stars. However, that distinctly evolved main sequence stars such as Vega and Fomalhaut are surrounded by a dust disk, while the expected lifetimes of circumstellar dust disks are much shorter, points to reprocessing of the dust.

A young member of the class of Vega-type objects is β Pictoris. It is situated close to the ZAMS (Crifo et al. 1997). Its dust disk has been imaged at optical and near-infrared wavelengths (Figure 1).

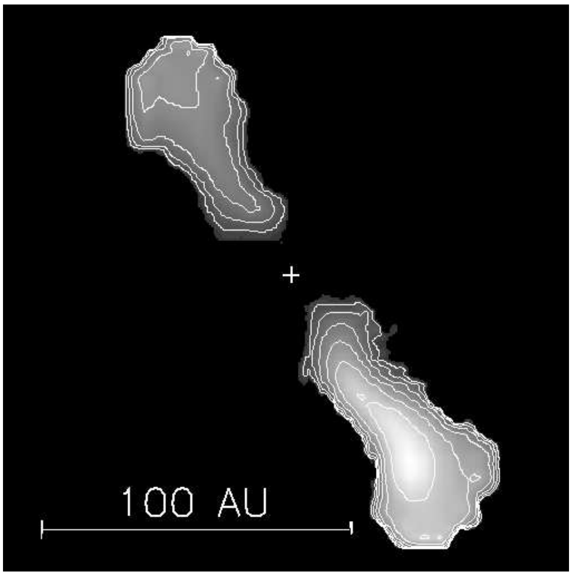

Figure 1. Dust density map at 10 μm of β Pictoris, deduced from the observed flux (courtesy E. Pantin), adopting a power-law distribution of silicate grains and the projected distance from the star (denoted by a cross) as a basis for the temperature calculation (Artymowicz 1997)

Proceedings of the Conference "The Universe as seen by ISO", Paris, France, 20–23 October 1998 (ESA SP-427, March 1999)

Frequent observations of variable absorption features in the UV (e.g., Lagrange-Henri et al. 1989) and the optical (e.g., Ferlet et al. 1993) spectra of β Pictoris are currently interpreted as due to impacts of cometary bodies. This hypothesis is strengthened by the unusual and cometary-like 10 μm silicate feature observed by Knacke et al. (1993).

3. HERBIG AE/BE STARS

Herbig Ae/Be stars are pre-main sequence stars with masses between 2 and 8 solar masses. These stars are the more massive counterparts of the T Tauri stars and were first discussed as a group by Herbig (1950). Recent reviews on Herbig Ae/Be stars have been written by Perez & Grady (1997) and Waters & Waelkens (1998).

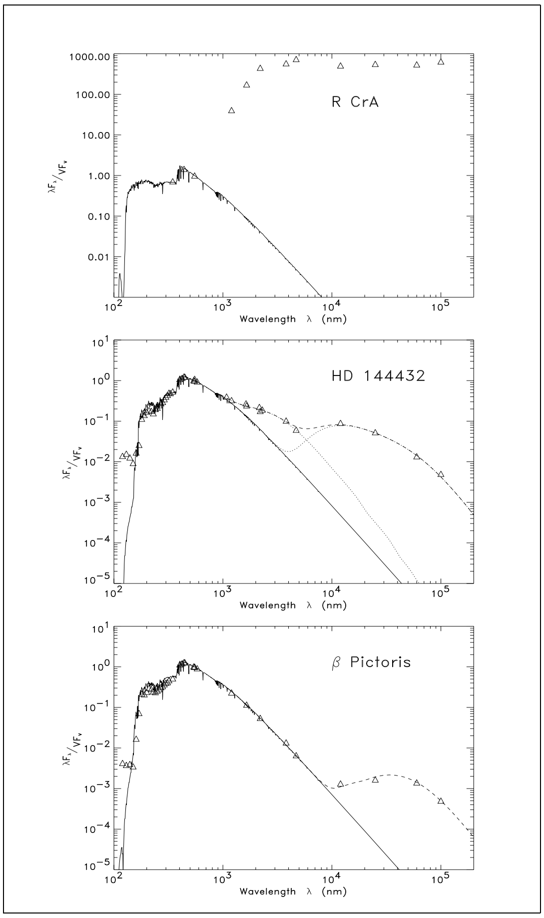

Figure 2. Evolution in the spectral energy distribution, with age. R CrA is an embedded Herbig Ae/Be star, HD 144432 on the other hand is an isolated Herbig Ae/Be star, while β Pictoris is situated close to the ZAMS (Malfait et al. 1998a).

Herbig Ae/Be stars are characterized by the presence of a strong IR excess, which is attributed to the presence of circumstellar dust. The youngest objects of this class are still embedded in the dust cloud they formed from, while somewhat older objects are surrounded by a dust disk, the shell being removed after the onset of bipolar winds. In our study we concentrate on isolated stars, some of which have already reached the main sequence. However, they exhibit a similar IR excess and optical emission lines and are therefore considered as true Herbig Ae/Be stars. The dust disks of Herbig Ae/Be stars are much more massive than the debris disks of main-sequence stars such as β Pictoris.

From photometric studies (e.g. Malfait et al. 1998a), it follows that the dust of Herbig Ae/Be stars is hotter than the β Pictoris like disks, which results in a substantial excess at near infrared wavelengths. However, where one might expect a gradual cooling of the dust disks with time, which would result in a shift in wavelength of the onset of the IR excess towards higher λ, one sees that where the youngest objects do exhibit a overall excess, the isolated Herbig Ae/Be stars often exhibit a two-component excess (of which the far IR excess resembles the excess of β Pictoris). A dip occurs at $\lambda \sim 10$ μm, which corresponds to a temperature comparable to that of the environment of Jupiter (Figure 2).

From the similarity in spectral type and from the apparent overlap in Hipparcos ages of β Pictoris (Crifo et al. 1997) and some isolated Herbig Ae/Be stars (van den Ancker et al. 1998), it is likely that Herbig Ae/Be stars are the progenitors of β Pictoris like objects. Spectroscopic evidence for infalling bodies (Grinin et al. 1994; Grady et al. 1997) is present for Herbig Ae/Be stars as well, which suggests that cometary activity starts in this early phase of evolution and continues on the main-sequence. The cleared inner gap in the dust disk (and the warp of the disk observed by Burrows et al. 1995) of β Pictoris may be caused by clearing due to a giant planet (Pantin et al. 1997). The breaking up of the excess of the isolated Herbig Ae/Be stars into a hotter and a cooler part may therefore be a sign that planets are forming in the circumstellar dust disks as well. However, it is also possible that the double excess that we see is caused by a temperature effect, the surface of an optically thick dust disk being directly heated by the star, while the inner part remains cool.

4. THE ISO REVOLUTION

Isolated Herbig Ae/Be stars are likely to be transition objects between the youngest embedded stars and main sequence objects such as β Pictoris. Their strong infrared excesses and circumstellar HI emission argue for a young age. Since they no longer occur inside a star-forming region (whether they have ever occurred inside one is another question, some might have formed from a local dense environment), they are ideal targets for IR spectroscopy. The isolated nature avoids confusion with the loose surroundings that occur for embedded sources.

We observed several Herbig Ae/Be stars with ISO, primarily using the Short Wavelength Spectrometer

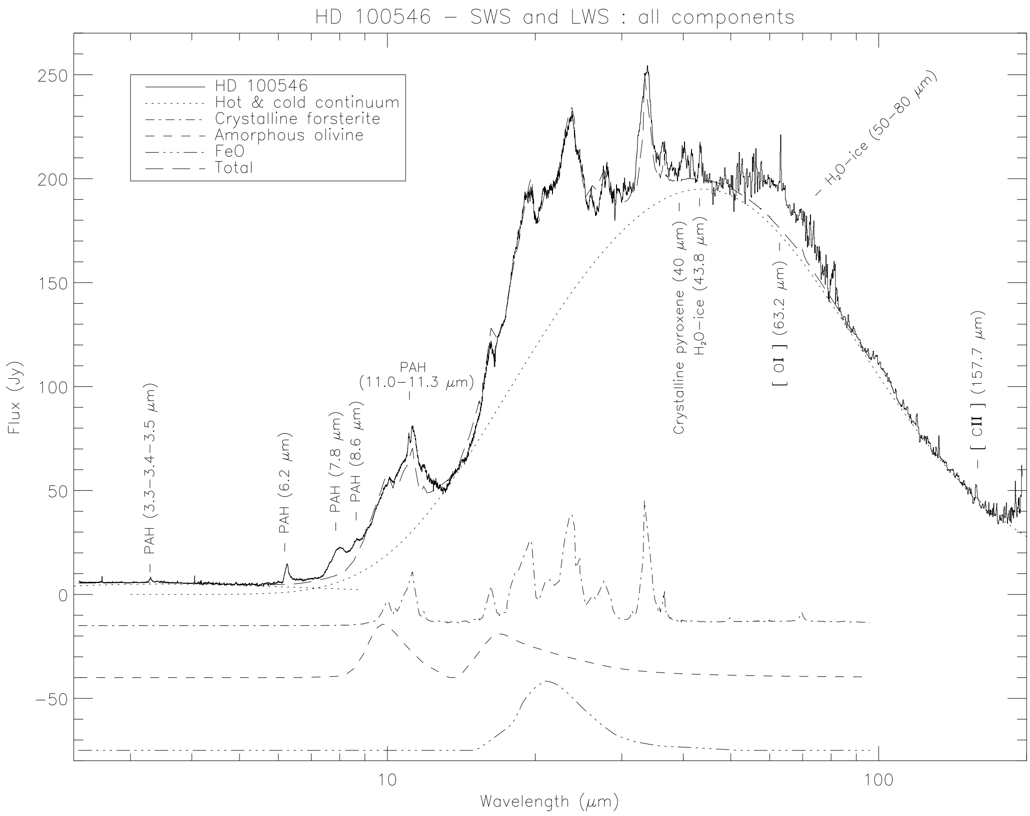

Figure 3. The full SWS-LWS spectrum and model for HD 100546.

(SWS) but for several objects, in addition to the 2.3-45 μm spectrum, we obtained the longer wavelength part (43-200 μm) using the Long Wavelength Spectrometer (LWS).

4.1. HD 100546

In Figure 3 we present the full SWS-LWS spectrum of HD 100546 (Malfait et al. 1998b). HD 100546 has spectral type B9V and from its Hipparcos distance, a main-sequence age slightly in excess of 10 Myr (van den Ancker et al. 1998) is suggested. The spectrum is characterized by a large variety of narrow and broad emission features superposed on a continuum. Next to the 3.29, 6.24, 7.9, 8.6 and 11.3 μm PAH bands, a series of mid-IR bands are very prominent. These are dominated by a crystalline olivine, namely forsterite (Mg_2SiO_4). Discriminating between this species and more Fe-rich olivines could be done by the detection of the forsterite band at 69 μm. The wavelength of this transition is very sensitive to the Fe/Mg ratio of the dust, and shifts to longer wavelength if Fe is included in the silicate.

In order to account fully for the spectrum, also amorphous silicates and a small amount of crystalline pyroxenes have to be included. The missing Fe is at least partially locked in FeO grains, responsible for a broad emission feature peaking around 23 μm and also contributing significantly to the excess at the shortest IR wavelengths.

In the LWS-range, a broad feature around 60-65 μm can be successfully reproduced by crystalline H_2O-ice with T $\leq$ 50 K. The presence of H_2O-ice is responsible for a high albedo of the dust, and thus makes the disk surrounding HD 100546 a good candidate to detect with high-angular-resolution observations.

The dust that causes the far-IR excess has a temperature ranging from 40 to 210 K, while a hot component (700-1500 K) is needed to explain the near-IR excess.

4.2. HD 142527

HD 142527 is a F-type emission-line star (spectral type F7IIIe), for which its Hα emission argues for a young age. It has a strong far-IR excess. Confronting the Hipparcos distance and the stellar evolution models of Palla & Stahler (1993), an age of only $\sim 10^5$ years could be derived, which is lower than the derived age for several embedded Herbig Ae/Be stars (van den Ancker 1998).

The full SWS-LWS spectrum is presented in Figure 4. Again, the infrared excess is composed of a hot and a cold component (Malfait et al. 1999). A very strong silicate emission at 10 μm occurs. There is no evidence for the presence of cold crystalline silicates (T $\leq$ 300 K), which would be reflected in the presence of solid state features at wavelengths of 20-40 μm. The 10 μm peak however, has a crystalline component in addition to the amorphous one, and this points to a high temperature of the crystalline dust.

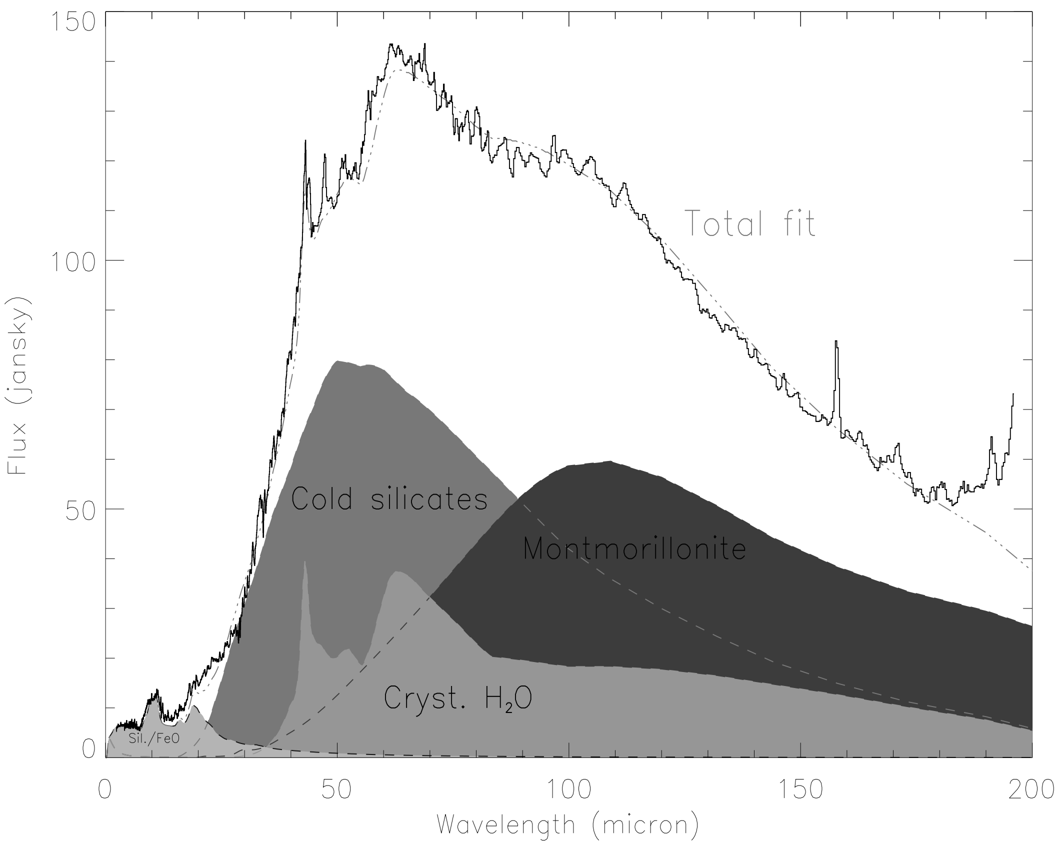

Figure 4. The full SWS-LWS spectrum and model for HD 142527.

If we consider the near-IR excess, we need FeO and a small amount of graphite in addition to the silicates (both amorphous and crystalline) to model the spectrum reasonably well. The cold dust component, on the other hand, takes off at $\lambda \sim 25$ μm, and is characterized by several solid state features, but also the atomic forbidden [CII] line at 158 μm can be identified. Crystalline H_2O-ice is the carrier of the sharp 43 μm peak and the broad bump centered at 65 μm. Modelling the continuum using an optically thin dust model (Waters et al. 1988) in which the dust is assumed to radiate as a blackbody, reveals another very broad solid state feature, centered at 100 μm (see Fig. 5). This feature cannot be attributed to H_2O-ice (Moore & Hudson 1994), but it has been seen in several evolved objects as well (Barlow 1998), and there it seems to be correlated with the H_2O-ice features (Barlow, private communication). Montmorillonite, a hydrous silicate (thus containing H_2O), with a temperature of 30-50 K emits at the corresponding wavelength and might as well explain the peaks at 47 and 52 μm (Malfait et al. 1999). We tried to model the spectrum using the radiative transfer code MODUST (de Koter & Bouwman 1999, in prep.). The dust mass calculated for the best model fit for the cold component, which is composed of 15 % montmorillonite, 25 % amorphous silicates and 60 % of H_2O-ice (of which 90 % is crystalline), is $5 \cdot 10^{-4}$ $M_\odot$, i.e. $\pm$ 10^6 more massive than the dust mass that was derived for the cold component.

4.3. HD 179218

HD 179218 has spectral type B9, and has an age comparable to the age of HD 142527 (van den Ancker 1998). Nevertheless, the ISO spectrum of HD 179218 is more similar to the one of HD 100546, being completely dominated by crystalline silicates. However, we should emphasize the fact that hydrous silicates such as montmorillonite do as well exhibit several mid-IR solid state features, which resemble those caused by and attributed to crystalline silicates, when the hydrous silicates have the appropriate temperature. In this case, it is likely that the cold dust surrounding this pre-main-sequence star is a mixture of all kinds of crystalline silicates, since identifications with both forsterite, clino- and orthopyroxene can be made (Figure 6). In a later paper, the spectrum of this object will be compared with that of HD 45677, a more massive Be star, which exhibits a rich forest of similar solid state features, mainly attributed to Mg-rich silicates (which are easier to form than Fe-silicates).

4.4. Evolutionary scenario

Next to the three specific objects mentioned above, a wide range of Herbig Ae/Be stars has been observed using ISO, from deeply embedded to isolated. Meeus et al. (these proceedings) arranged these spectra into 5 different categories, but found no correlation between several stellar parameters (such as effective temperature, E(B-V), photospheric abundances etc.) and this classification.

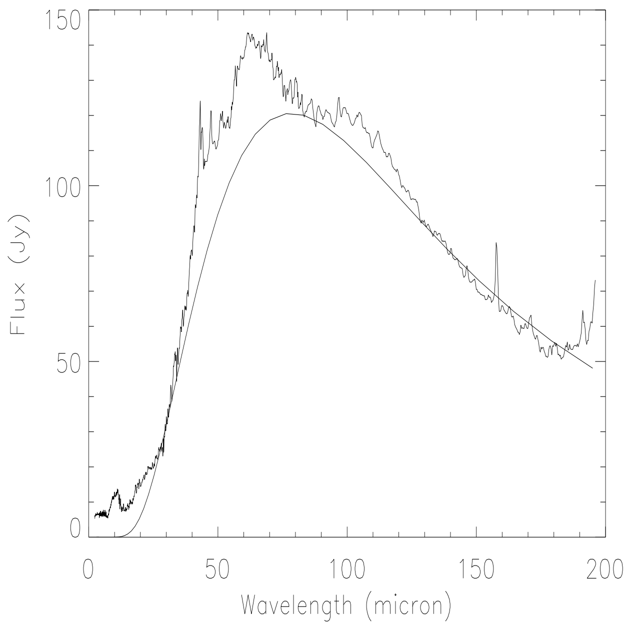

Figure 5. First try to model the far infrared excess of HD 142527, using an optically thin dust model (Waters et al. 1988). Next to the crystalline H_2O*-ice features (43, 65 μm), a broad bump at 100 μm persists.*

Still, some evolutionary trend is apparent. As the stars evolve from heavily embedded towards less and less embedded, the amorphous 10 μm feature evolves from an absorption towards an emission (optically thick vs. optically thin). The spectra of the embedded Herbig stars show ice bands (in absorption) in the near IR as well. No crystalline fingerprints are present, as can be seen in Figure 7.

In the spectra of the isolated stars (which have lost the envelope they were imbedded in as they formed), no ice absorption or silicate absorption is present. Crystalline silicate features pop up here and there. No clear correlation with age is present, since HD 142527 and HD 179218, two stars with similar ages, have very different dust characteristics. Whereas the crystalline silicates identified in HD 142527 have high temperatures, this is not the case for HD 100546, which is definitely the most evolved object, and not for HD 179218.

For crystalline silicates, the condensation temperature exceeds 1400 K, thus it is clear that the cold crystalline silicate dust in the environment of HD 100546 and HD 179218 cannot be processed from amorphous (as seen in the interstellar medium) to crystalline there, on the timescales that we are dealing with. The hydrous silicates of which the presence in the neighbourhood of HD 100546 cannot be ruled out (a small bump at 100 μm might be present), have condensation temperatures of $\sim$ 300 K. In the circumstellar environment of HD 142527, they are evidently located in a colder environment than the crystalline silicates, but their temperature suggests that they must have migrated outwards after condensation (T $\leq$ 60 K). This is also the case for the crystalline H_2O-ice which has a temperature of only 50 K in the environment of HD 142527, less than the temperature

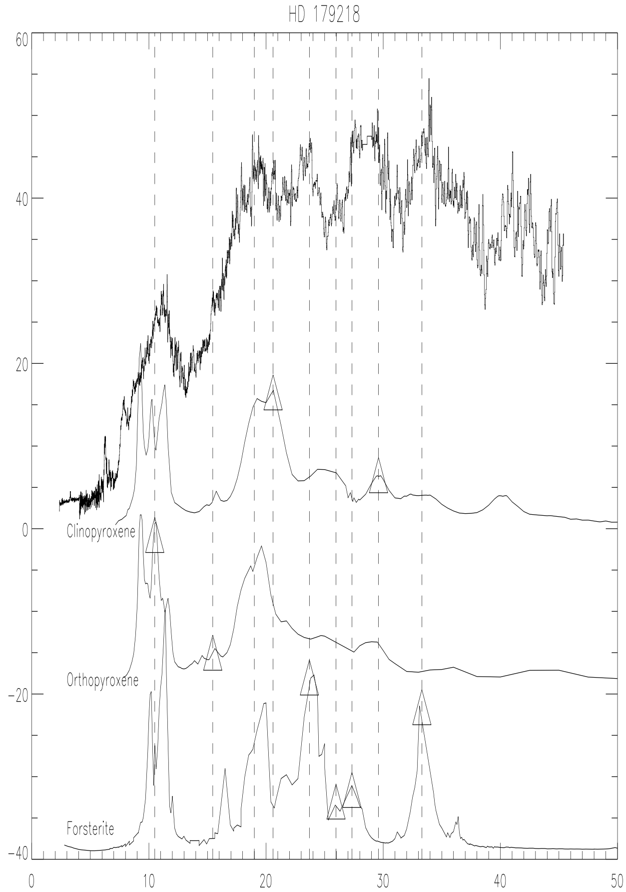

Figure 6. SWS-spectrum of HD 179218. No LWS-spectrum has been obtained for this Herbig Ae/Be star. The most prominent features could be identified by comparing with the optical constants of forsterite, clino- and orthopyroxene.

at which water ice with an ordered structure forms (120K, Smith et al. 1994). This migration process might as well cause the cooling of the crystalline silicates in a later stage of evolution, as seen in the other objects.

5. LINKS WITH OUR SOLAR SYSTEM

The detection of crystalline silicates in the circumstellar environment of young and old stars was not anticipated before ISO. 10 μm silicate spectra from comets were known to be different in shape from the so-called astronomical silicate, the crystalline nature of the dust was not fully understood, but its presence was clearly visible from the sharp peak at 11.3 μm amongst others. Since the spectrum of the young main sequence star β Pictoris exhibited a silicate signature of similar nature, and since the presence of a planet in the environment of this object has been indirectly inferred from imaging, it is considered to be a solar system, or to be forming one. Therefore, analogies between our own solar system and isolated Herbig Ae/Be stars, suspected to be the evolutionary precursors to β Pictoris stars, are very suggestive and strengthen the evolutionary picture outlined above.

The fact that comet Hale-Bopp, by far the most dusty comet that has approached the sun during the last

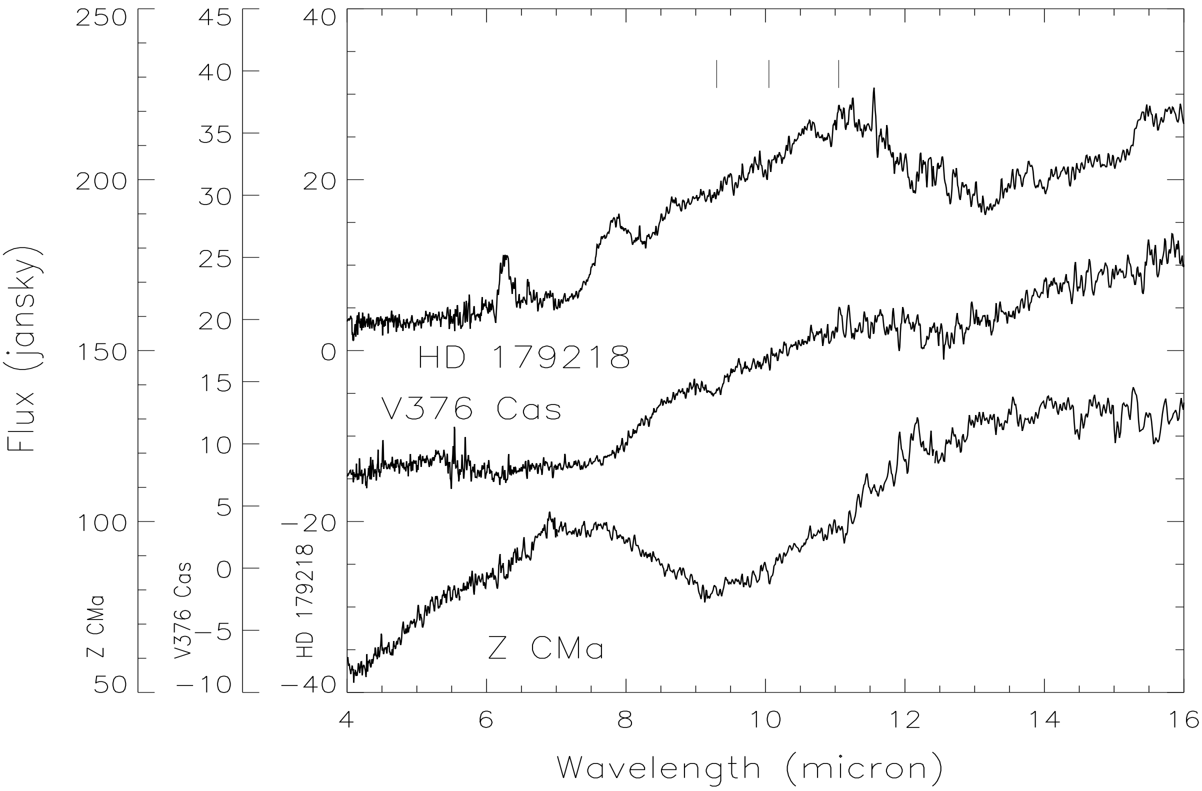

Figure 7. *Some typical spectra of Herbig Ae/Be stars. Z CMa is a heavily embedded star, which is reflected by a silicate absorption feature, resulting from optically thick dust surrounding this object. V376 Cas has a less dusty circumstellar environment, but no reprocessing has occurred yet, this results in an amorphous silicate emission. HD 179218 has a silicate feature dominated by sharp substructures, due to crystallinity. The peaks at 6.2, 7.8 and 8.6 μm are caused by PAHs. The features at 9.35, 10.05 and 11.05 (showed by the marks) are not real, but instrumental.*

decades, was visible during the observing lifetime of ISO was a very happy coincidence. The similarity between the spectrum of Hale-Bopp (Crovisier et al. 1997) and the spectrum of HD 100546 is extreme. Except for the PAH bands, which are not visible in the comet spectrum, the two observations look very alike (Fig. 8). The continuum of HD 100546 extends to longer wavelengths, due to the dust temperature range, while the dust in comet Hale-Bopp had a more uniform temperature, i.e. $\sim$ 210 K at the time this ISO-SWS spectrum was taken. The crystalline silicate features look very similar, and can be explained by pure forsterite, but in observations of the comet at smaller heliocentric distances, i.e. when the dust temperature was higher, also pyroxene features became apparent (Wooden et al. 1999).

Hale-Bopp is a comet originating from the Oort Cloud. The temperature out there is much too cold to have crystallized the comet. Either it must have become crystalline during close passages, where the temperature reached is high enough, or, the dust must have been crystallized before the formation of the Oort Cloud. Since the timescales resulting from passage models are quite short to crystallize the dust, the second possibility is preferred. The radiation of a very cold forsterite component (T $\sim$ 50 K) in the environment of HD 100546 (Malfait et al. 1998b) might therefore come from an Oort Cloud being formed presently around this star. On the other hand, not only objects that exhibit crystalline IR-bands have redshifted metallic lines in the UV (due to infall of 'large' comet-like bodies), thus not all comets that surround Herbig Ae/Be stars are composed of crystalline dust.

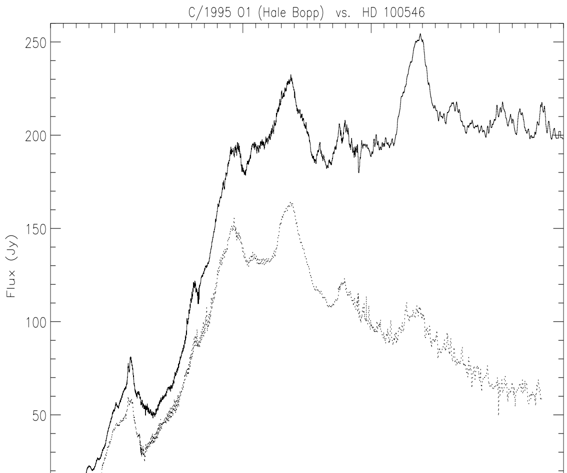

Figure 8. *Comparison between the ISO-SWS spectrum of comet Hale-Bopp (courtesy J. Crovisier, dashed line) and HD 100546 (full line)*

The Oort Cloud is supposed to have formed from gravitational ejection of inner solar system material due to the presence of giant planets (Fernandez 1978), so it is likely that the environment of HD 100546 is a solar system in formation, where a giant planet is already present.

Interestingly, ISO detected crystalline silicates in comet 103P/Hartley 2 as well (Crovisier et al., these proceedings). This comet originates from the Kuiper Belt, so both inner solar system dust (subsequently ejected to the Oort Cloud) and outer solar system dust (concentrated in the Kuiper Belt, which can correspond with the 210 K crystalline silicate component in HD 100546) incorporate crystalline silicates in their grains.

Another similarity between the circumstellar dust disk of HD 100546 and comet Hale-Bopp is highlighted in a recent paper by Lellouch et al. (1998). In this study of the LWS spectrum of Hale-Bopp, the presence of crystalline water ice (characterized by peaks at 43 and 65 μm), as it gets outgassed from icy grains in the coma, is revealed.

Hydrous silicates, of which montmorillonite is one example, are detected in the circumstellar environment of HD 142527. They are also known to be present in solar system matter. A study of interplanetary dust particles (IDPs) by Sandford & Walker (1985) shows that IDPs can be divided into three major families, the olivines, the pyroxenes and the layer-lattice (hydrous) silicates. Of the 26 particles they studied, 11 were composed of these layer-lattice silicates. From their isotopic study, it became clear that the IDPs must have been formed prior to the solar system formation, or even during the nebular-protostar phase. They also presented a fit to the spectrum of Comet Kohoutek using 50 % of pyroxene IDPS and 50 % of layer-lattice IDPs.

6. CONCLUSIONS

From a multiwavelength photometric study of Herbig Ae/Be stars, we learned that isolated Herbig Ae/Be stars are objects in an intermediate evolutionary stage between embedded Herbig Ae/Be stars and β Pictoris stars. ISO confirmed this picture. Some evolution in the infrared spectra can be seen: embedded objects have ice absorption bands, and amorphous silicates are present, either in absorption (most embedded sources) and emission. Some isolated Herbig Ae/Be show evidence for crystalline silicates in addition to their amorphous counterparts. These crystalline fingerprints have also been detected in the β Pictoris disk (Knacke et al. 1993).

The similarity between the spectrum of HD 100546, one of the most evolved Herbig Ae/Be stars, and comet Hale/Bopp is astonishing. Since the comet originates from the cold Oort Cloud, the dust must have been crystallized before it was ejected by Uranus and Neptune to its distant habitat, where the temperature is far too low to cause crystallisation. The very cold crystalline dust component of HD 100546 can analogously be a circumstellar Oort Cloud. From this we infer the likely presence of a giant planet in the planetary system that is forming around HD 100546.

In HD 142527, a F star that is more than 100 times younger than HD 100546, evidence for hot crystalline silicates is found. The cold dust of this star is dominated by very cold crystalline H_2O-ice. The silicates at large distances from the star are amorphous, though a not negligible fraction of the dust (15 %) is composed of hydrous silicates. Such hydrous silicates are also present in interplanetary dust particles, from which it is known that they must have formed in the very early stages of the formation of our Solar System (Sandford & Walker 1985).

The condensation temperatures for crystalline and hydrous silicates are respectively about 1400 and about 300 K (Larimer & Anders 1979), so it is impossible that the chemical structure of the dust changed to the ordered structure it has now at the location where it is situated at this moment. It is however logical that the crystalline silicates in the environment of HD 142527 are located at smaller distance from the star than the hydrous silicates.

Finally, the facts that no evidence for crystalline silicates has been found in the environment of the most embedded Herbig Ae/Be stars, nor in the ISM, but that crystalline silicates do occur in the environment of evolved objects (e.g. Waters et al. 1996) raise intriguing questions on the cosmic dust cycle. Mechanisms must be found to explain how crystalline silicates are hidden or even destroyed in the interstellar medium. A detailed study of a large number of ISO spectra will be needed to enable us to remove some of the question marks concerning this matters.

ACKNOWLEDGMENTS

The authors would like to thank the SWS and LWS dedicated instrument teams.

REFERENCES

Artymowicz, P. 1997, AREPS, 25, 175

Barlow, M.J. 1998, Ap&SS 255, 315

Burrows, C.J., Krist, J.E., Stapelfeldt, K.R. 1995, BAAS 187, 3205

Crifo, F., Vidal-Madjar, A. et al. 1997, A&A 320, L29

Crovisier, J., Leech, K. et al. 1997, Science 275, 1904

Ferlet, R., Lecavelier des Etangs, A. et al. 1993, A&A 297, L5

Fernandez, J.A. 1978, Icarus 34, 173

Grady, C.A., Sitko, M.L. et al. 1997, ApJ 483, 449

Grinin, V.P., Thé, P.S. et al. 1994, A&A 292, 165

Herbig, G.H. 1960, ApJS 4, 337

Knacke, R.F., Fajardo-Acosta, S.B. et al. 1993, ApJ 418, 440

Lagrange-Henri, A.M., Beust, H. et al. 1989, A&A 215, L5

Larimer, J.W., Amders. E. 1967, GeCoA 31, 1239

Lellouch, E., Crovisier, J. et al. 1998, A&A 339, L9

Malfait, K., Bogaert, E., Waelkens, C. 1998a, A&A 331, 211

Malfait, K., Waelkens, C. et al. 1998b, A&A 332, L25

Malfait, K., Waelkens, C. et al. accepted by A&A

Moore, M., Hudson, R.L. 1994, A&AS 103, 45

Palla, F., Stahler, S.W. 1993, ApJ 418, 414

Pantin, E., Lagage, P.O., Artymowicz, P. 1997, A&A 327, 1123

Perez, M.E., Grady, C.A. 1997, SSRv 82, 407

Sandford, S.A., Walker, R.M. 1985, ApJ 291, 838

Smith, R.G., Robinson, G. et al. 1994, MNRAS 271, 481

van den Ancker, M.E., de Winter, D., Tjin A Djie, H.R.E. 1998, A&A 330, 145

Waters, L.B.F.M., Coté, J, Geballe, T.R. 1988, A&A 203, 348

Waters, L.B.F.M., Molster, F.J. et al. 1996, A&A 315, L361

Wooden, D.H., Harker, D.E. et al. 1999, ApJ, in press

SPATIAL DISTRIBUTION OF DUST FROM CIRRUS TO DENSE CORES

A. Abergel[1], P. André[3], A. Bacmann[3], J.-P. Bernard[1], S. Bontemps[2], F. Boulanger[1], A. Coulais[1], F.X. Désert[5], E. Falgarone[4], A. A. Kaas[2], M. Huldtgren[2], M.A. Miville-Deschênes[1], L. Nordh[2], G. Olofsson[2], M. Pérault[4], & J.-L. Puget[1]

[1]Institut d'Astronomie Spatiale, 91405 Orsay Cedex, France
[2]Stockholm Observatory, S-133 36 Saltsjöbaden, Sweden
[3]Service d'Astrophysique, Centre d'Etudes de Saclay, 91191 Gif-Sur-Yvette Cedex, France
[4]Radioastronomie Millimétrique, Ecole Normale Supérieure, 24 rue Lhomond,75005 Paris, France
[5]Observatoire de Grenoble, BP 53, 414 rue de la piscine, 38041 Grenoble Cedex 9 France

ABSTRACT

Large scale mapping of several star forming regions in the interstellar medium has been conducted with ISOCAM in two broad-band filters (5-8.5 and 12-18 μm). The small scale (3-6 arcsec) extended mid-IR emission of dust at different stages of evolution and in a wide range of illuminations and densities has been revealed.
The structure of the infra-red emission of illuminated edges of nearby molecular clouds gives strong constraints on the penetration of UV radiations through these clouds and on their small scale density structure. For both the Horsehead nebula and the interface of the main cloud of ρ Ophiuchi, the edges of the molecular clouds strongly illuminated by B stars present extremely steep increases of column density, while the extinction of incident radiation inside the clouds appears compatible with homogeneous matter at small scale (typically below $\sim$ 0.01 pc).
Dense cores are seen as deep absorption structures against a diffuse background emission. The density profiles derived from the extinction profiles depart from a r^{-2} law due to a central flattening (typically for $r < 0.02$ pc). The steepest gradients in outer regions can be modelled with density profiles at least as steep as a r^{-2} law.
Finally ISOCAM data also allow to extend the statistical analysis of the spatial distribution of dust in the diffuse interstellar medium down to a few arcsec scales.

Key words: Interstellar medium, dust, extinction, density structure, PDR, dense cores

1. INTRODUCTION

Before ISO, the IRAS observations have given a complete view of the dust in our galaxy with an angular resolution of 4', within broad-band filters at 12, 25, 60 and 100 μm. The spectral coverage has been extended from the stellar scattered light (below 5 μm) to the millimeter emission by the the Far Infrared Absolute Spectrophotometer (FIRAS) and the Diffuse Infrared Background Experiment (DIRBE) on board of COBE, with a low angular resolution (7° and 40 arcmin respectively). The far IR emission together with the UV/visible interstellar extinction can be in the general case explained by three different components of interstellar particles (Désert et al. 1990, Dwek et al. 1997): (1) Large grains (of size $\geq$ 10 nm) in thermal equilibrium with the radiation field contribute to most of the sub-mm emission (T$\sim$17-20 K in cirrus clouds), (2) Large aromatic molecules explain the mid-IR emission features (Léger et al. 1989) and (3) Very Small Grains (VSGs) have a size intermediate between large grains and large molecules (Sellgren et al. 1985). Both large aromatic molecules and VSGs are transiently heated at high temperature each time they absorb a UV photon. They cool off radiating in the near and mid-infrared.
Images of the dust emission allow to study the spatial structure of clouds, the interaction of young stars with nearby dense gas, the propagation of radiation and more generally the evolution of dust within the interstellar medium. IRAS data have revealed IR emission everywhere in the galaxy, with a spectacular auto-similarity on a very wide range of scales and densities. An important result is also the variations of the colors of the IR emission (e.g. Boulanger et al. 1990) which imply local changes in the relative abundance of the different dust particles.
However IRAS was not able to spatially resolve individual structures, because of the limited angular resolution ($\sim$ 4'). In the interstellar medium, features as small as $\sim$1 arcsec (for nearby complexes: $\sim$200 AU or 10^{-3} pc) are detected with interferometric molecular observations (Falgarone et al. 1998), and structures of a few 10 AUs are revealed by absorption measurements (Diamond 1989, Marscher et al. 1993). Ground-based observations in the mid-IR can only be performed within limited spectral range and at high resolutions for very bright objects (for instance M17, Giard et al. 1994).
Part of the ISO guaranteed time program, the ISOCAM survey of nearby star forming regions has been conducted with the two broad-band filters LW2 and LW3 (5-8.5 and 12-18 μm, respectively) with an an-

Proceedings of the Conference "The Universe as seen by ISO", Paris, France, 20–23 October 1998 (ESA SP-427, March 1999)

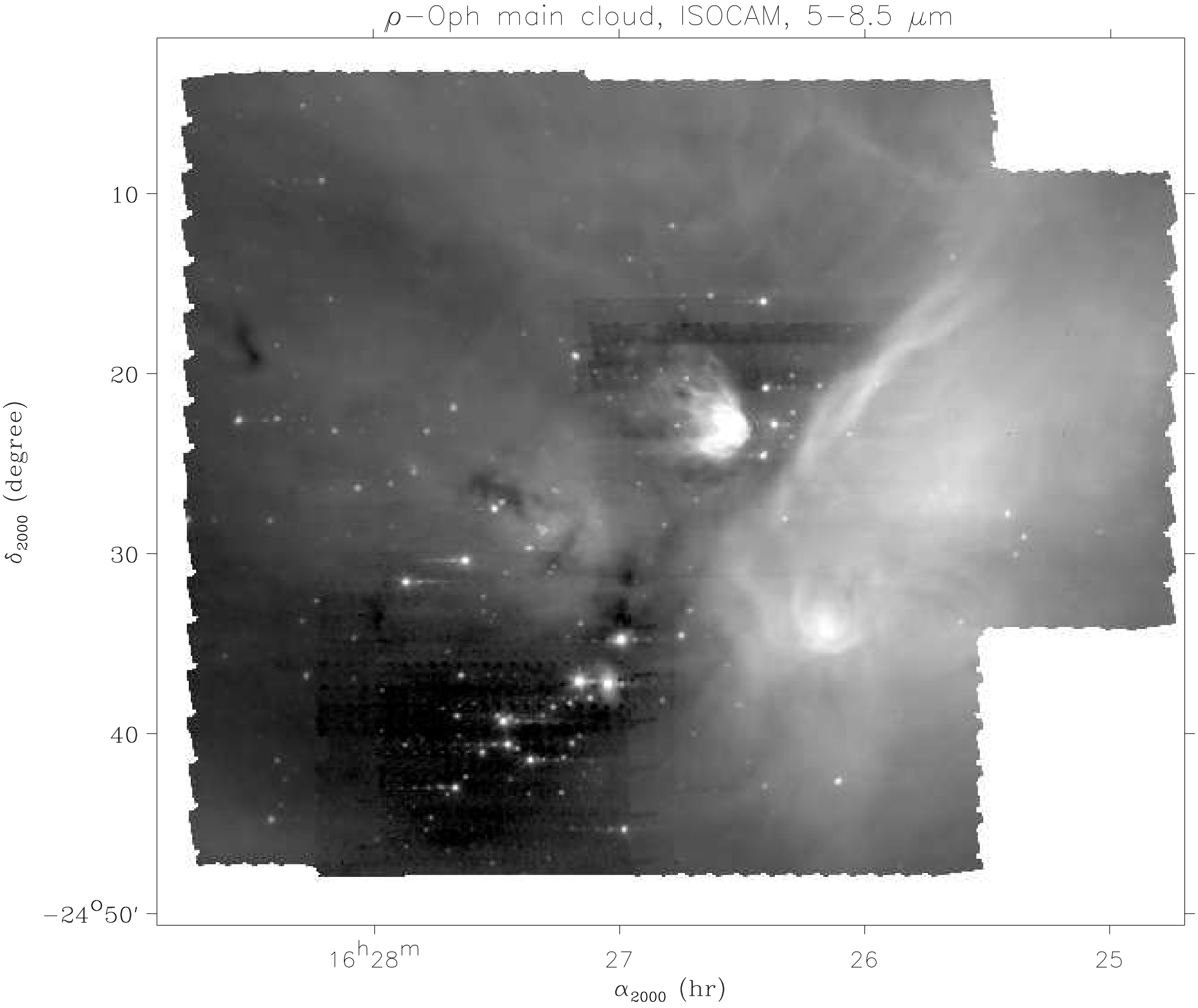

Figure 1. ISOCAM map of the ρ Ophiuchi main cloud with the LW2 filter (5-8.5 μm).

gular resolution of 3-6 arcsec. ISOCAM, SWS and ISOPHOT data have confirmed that, from cirrus to bright reflection nebulae, most of the emission within these two filters is due to emission features characteristic of C-C and C-H bonds in aromatic hydrocarbons (Boulanger et al. 1997, Mattila et al. 1996, Moutou et al. 1997). The intensity of these features globally scales with the UV radiation field (Boulanger et al. 1997). A continuum underlying the features, due to the same emitters and/or VSGs, may also contribute to the intensity measured within the two filters.
The observation strategy and the list of targets of the survey have been described by Olofsson et al. (1998). ISOCAM has an angular resolution and sensitivity of (Cesarsky et al. 1996) which greatly increases our ability to describe the small structure of the Interstellar Medium (e.g., Abergel et al. 1996). After discussing the actual status of the data reduction, we present some recent results.

2. DATA REDUCTION

Data were taken with the Long-Wavelengths (LW) channel of ISOCAM. The data reduction is made through a pipeline which filters all unpredictable events (essentially impacts of cosmic ray particles and long-term drifts), and inverts a model of the response (dark, transient effects, photometry). The accuracy of the processed data strongly depends (1) of the efficiency of the methods used to filter unpredictable events, and (2) on the accuracy of the model of the response.
Cosmic ray particles have continuously hit the detector. In the general case, the response of the affected pixels instantaneously increases (which produces a "glitch"), then recovers after one or two readouts. These events are discarded using a temporal median filtering which detect all pixels deviating from the running median value by more than a threshold value. Typically a few % of the data are affected. Impacts due to heavy ions are significantly less fre-

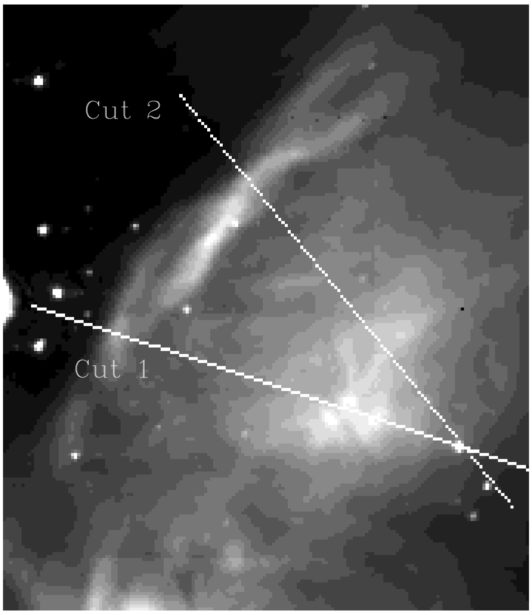

Figure 2. Bright filaments along the illuminated interface of ρ Ophiuchi main cloud (with the LW2 filter). The star HD147889 is at the intersection of the two slices (corresponding to cuts 1 and 2 of Fig. 3).

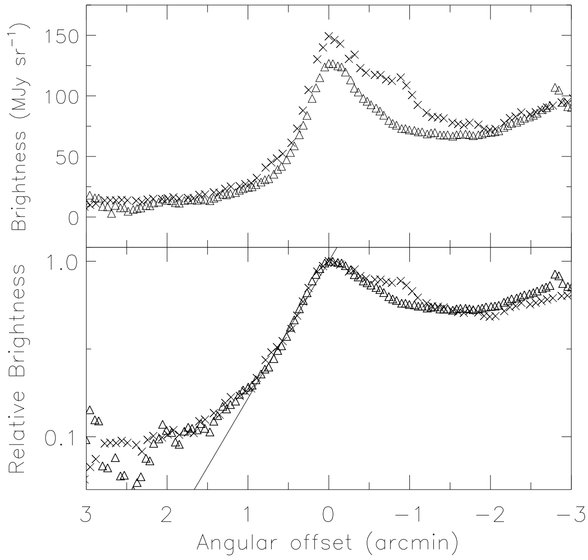

Figure 3. Upper panel: Brightness profiles (for the LW2 filter) along the two slices of Fig. 2 (Crosses: cut 1, Triangles: cut 2). Bottom panel: The same in relative and logarithmic scales. The solid line corresponds to the extinction law $I(z)= I_0\ e^{-Kz}$, with $K=$ 1.8 arcmin^{-1}.

quent, but produce glitches with significant memory effects (Désert et al. 1998). At the present time, they are not removed in the data of this survey, since actually no method allows to remove them systematically. However the time constant is large (typically more than several minutes) and part of the effects can be removed by applying a flat-field correction variable with the time (see below).

For each readout is subtracted a dark image computed using the estimator of the time behaviour of the dark signal (Biviano 1998). The detector presents systematic memory effects of the response which can bias the photometry by a factor of typically 40% (Abergel et al. 1999). The data of the survey have been processed two years ago using a simple empirical model (Abergel et al. 1996), with a final photometric accuracy of ∼10%. A new approach based on an analytical inversion of a physical model (Coulais & Abergel these proceedings) gives, for uniform illumination, an accuracy quite better (∼1%). We are currently testing this method for our images which generally contain strong gradients of illumination (point sources,...). Paradoxically, the signal to noise ratio is actually NOT better for strong sources than for faint sources because of the not proper correction of the transient response.

One flat-field image was extracted from each raster by computing the mean value of the lowest percentile (20%) seen by each pixel, excluding frames with strong emission above the zodiacal background. However large scale gradients of the sky brightness may contaminate this image. Therefore we use an iterative process to improve the flat-field correction and include a temporal dependence (Miville-Deschênes et al. 1999). Finally coadded images are projected on the sky map. A very long-term transient affects may affect typically 5-10% of the flux above the dark level during several hours. This effect, critical to study the large scale variations of brightness with low amplitude, is still not fully characterised (we do not know whether it is reproducible or not). Spectacular results are obtained using the redundancy of the observations, by comparing in an iterative process the flux measured for pieces of sky which has been observed at different times during the observations (Miville-Deschênes et al. 1999). In any case and at the present time, the data reduction to analyse the extended emission in the data of the survey is not yet definitive. Finally we remove the zodiacal emission at the time of the observations using the model of Reach et al. (1995) calibrated from the DIRBE/COBE data.

3. ILLUMINATED INTERFACES

3.1. The PDR of the ρ Ophiuchi main cloud

The ρ Ophiuchi main cloud L1688 is one of the nearest star forming complex (∼ 160 pc, Bertiau 1958). It contains a large number of Young Stellar Objects (YSOs) identified by ISOCAM (Bontemps et al. these proceedings) and previous surveys. The unusually high IR brightness is due to large column densities (A_v up to 100) combined with the presence of early type stars and YSOs. We have already shown (Abergel et al. 1996) that small scales spatial structures are mainly due to dust locally heated by embedded B stars, while large scale emission is due to external heating. The map discussed in Abergel et al. 1996 has been extended to the West (Figure 1) and now contains the B2V star HD147889 which illuminates the western interface. The star appears included in an empty cavity since it does not illuminate any dust located in its surrounding. A large fraction of the emission to the West of the map is due to dust

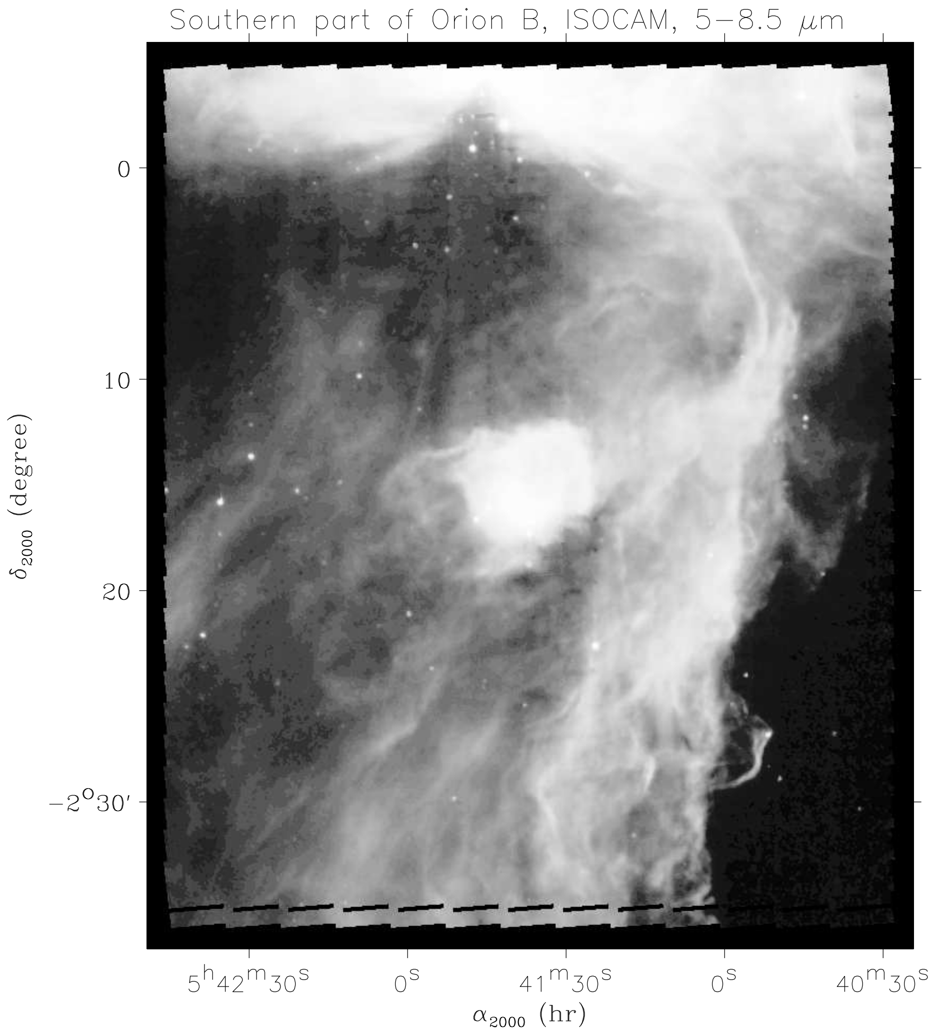

Figure 4. ISOCAM map of the Southern part of Orion B with the LW2 filter (5-8.5 μm). The contrast is so high that the bright structures in the reflection nebula NGC2023 in the central part and in the southern part of NGC 2024 to the north are not visible because of the limited grey scale.

illuminated by this star. The zone of interaction between radiation and dust is narrow, as suggested by the width of bright filaments in the region around $\alpha_{2000} \sim$ 16h26m, $\delta_{2000} \sim$ -24°22' (Figures 1 and 2). These filaments closely follow the western edge of the molecular cloud (Wilking & Lada 1976, Loren 1989). They do not necessarily correspond to filaments of dust, but to the illuminated edge of a dense cloud. The long axis of the filament appears on the ISOCAM image perpendicular to the projected star direction (Figure 2), confirming that the star is in this region the main heating source and at the center of a more or less spherical cavity. The filaments present interlaced structures likely due to an irregular shape of the edge of this cavity.

The brightness gradients across the filaments and along the projected direction of the star (Figure 3) are quite steep (within less than 1 arcmin or 0.05 pc). Most of the emission within the two filters LW2 and LW3 is due to emission features of aromatic hydrocarbons whose intensity globally scales with the UV radiation field (Boulanger et al. 1997). Therefore, at a first order, we can consider that the ISOCAM brightness is proportional to the column density of the emitting particles and the UV radiation field. IRAS data have shown that several dense clouds present a 12 μm limb–brightening effect at the edge with typical sizes of a few 10 arcmin, which may be due to an enhanced abundance of emitters (e.g. Bernard et al. 1993). However the width of the filament revealed by ISOCAM is ~1 arcmin, so we assume that the relative abundance of the emitters is constant. Starting from the star, the brightness increase is essentially due to a positive density gradient, while the brightness decrease in the direction opposite to the star is due to the extinction of incident UV radiation emitted by the star.

The peak emission I_0 can be written: $I_0 = \epsilon\ \eta\ N_H\ \phi_0$, where ϵ is the emissivity of the emitting particles, η their relative abundance and N_H the col-

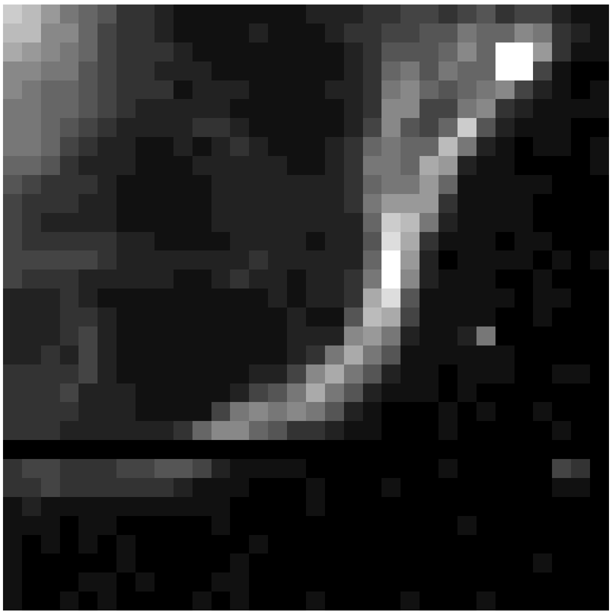

Figure 5. 32×32 image taken by ISOCAM with the LW2 filter of the edge of the Horsehead. This image has not been projected to avoid smoothing effects. North is up.

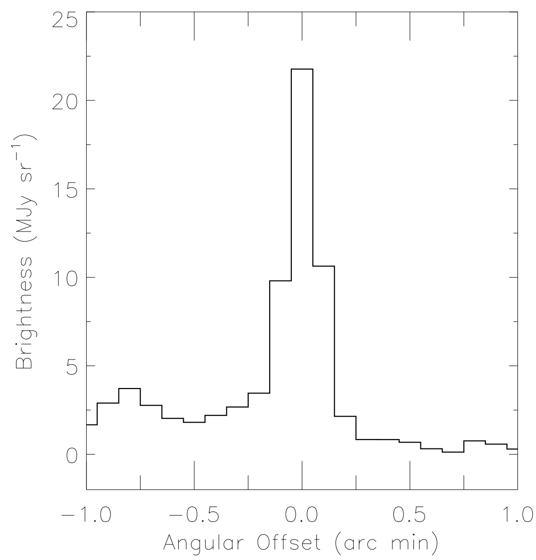

Figure 6. Horizontal profile (for the LW2 filter) along the brightest pixel at the edge of the Horsehead.

umn density. We assume that within the interface ϵ, η and N_H are constant. Adjusted with the law $I(z)= I_0\ e^{-Kz}$, the brightness decrease appears compatible with an extinction K= $\sim$1.8 arcmin^{-1}, corresponding to $\sim$38 pc^{-1} at a distance of 160 pc. If we assume that the medium is homogeneous and using standard conversion numbers (with τ_V/A_V= 1/1.096, A_V/N_H=1/1.9 10^{21} cm^{-2}, and τ_{UV}/τ_V= 2.8 from Roberge et al. 1981, we have: K= n $\times$ 4 10^{-3} pc^{-1}, n being the local density in units of cm^{-3}), we obtain a local density of $\sim 10^4$ cm^{-3}. This a lower limit since the observed gradients should be smaller than local gradients because of projection effects (the real shape of the interface is unknown). However it is remarkable to notice that the $C^{18}O$ emission at the western edge of the ridge ($\sim$ 2 K km s^{-1}, Wilking & Lada 1976) which closely follows the bright filaments also imply a local density of a few 10^4 cm^{-3}.

3.2. The PDR of the Horsehead in Orion B

ISOCAM observations reveal with the angular resolution of 6 arcsec the spatial structure of the southern part of Orion B (Figure 4 from Abergel et al. in prep). The measured emerging intensities of the CO (Kramer et al. 1996) and 158 μm C^+ lines (Jaffe et al. 1981) have indicated that the emissions arise from the surface of small clouds throughout the complex, and not only from a single layer at the edge. Except at the edges, most of the structures detected by ISOCAM are due to random superposition of individual clouds on the line of sights. Therefore the preliminary analysis we present in this paper concerns the Horsehead nebula, at the western edge of the complex (Abergel et al., in prep).
The Horsehead nebula is a dark cloud emerging from its parental complex L1630 due to UV eroding radiation emitted by the OB-systems ζ Ori to the north and σ Ori to the west (Reipurth & Bouchet 1984). Both systems are located at a projected distance of 0.5°, corresponding to $\sim$ 4 pc on the sky for a distance of 400 pc. However, Malin 1987 suggests that the ζ Ori system does not participate to the heating of the complex since it is located in the foreground, which is also confirmed by Hipparcos. The illuminated side of the Horsehead presents the sharpest IR filament detected in our Galaxy by ISOCAM (Figures 4 and 5), elongated toward the north-south direction. It is marginally resolve by ISOCAM, the FWHM being of the same order as the pixel size (6 arcsec). At a distance of 400 pc, 10 arcsec corresponds to $\sim$0.02 pc. The configuration is similar to the one revealed at the interface of ρ Oph, but the geometry is more simple: we only see an illuminated wall of matter, while for ρ Oph the interface appear more or less spherical. The increase of the emission on the illuminated side is due to an extremely steep increase of the column density, while the decrease on the east side is mainly due to extinction of the UV radiation emitted by σ Ori.
We use the same simple model as for ρ Oph. The illuminated edge is considered as a layer illuminated exactly edge-on. The decrease of the brightness toward the filament is compatible with an extinction coefficient K= 10 arcmin^{-1} (Figure 6), corresponding to $\sim$80 pc^{-1} at a distance of 400 pc. This is a lower limit, because of the dilution within the pixel field of view (the Point Spread Function is under-sampled for these observations). Using the relationship: K= n $\times$ 4 10^{-3} pc^{-1}, n being the local density assumed constant within the nebula (units: cm^{-3}), we obtain n= 2 10^4 cm^{-3}. Molecular observations (e.g. Kramer et al. 1996) have suggested that the average density in the nebula is within the range 1-3 10^4 cm^{-3}. We have assumed an infinite gradient at the illuminated edge which is unrealistic, as the simple modelisation

by an unique layer. However a lower density gradient and/or a more complex geometry would produce smoother brightness profiles because of projection effects.
These observations also allow to constrain the clumpiness of the material. For the same value of the average density, the UV radiation penetrates further in regions in which the material is clumped than in homogenous regions (Boissé 1990). Using the radiative transfer formalism developed by Boissé (1990) for two-phase clumpy regions, preliminary results (Abergel et al. in prep.) show that, at the edge of the Horsehead, the density contrasts between clumps and interclumps is strongly limited (typically lower than ~ 5).

3.3. Conclusion: Density structure of the interfaces

For the interfaces of ρ Oph and the Horsehead nebula, we reach the same conclusion. The brightness decrease can be explained by UV extinction within an homogeneous medium with a constant density derived from molecular observations, or a medium with limited density fluctuations at small scales (typically below 0.01 pc). Such a result may contradict the detection of very small molecular structures in several nearby clouds (e.g. Falgarone et al. 1998). However, the small scale density structure of the interfaces may be modified because of the strong illumination. Dense matter can be accumulated ahead of a shock (Loren & Wootten 1986) as suggested in ρ Oph by the coherence of the polarisation angle of IR absorption in this area (Vrba et al. 1976). The detection with ISOCAM of an extremely steep positive density gradient at the illuminated edge of the Horsehead supports this hypothesis.

4. DENSE CORES

In the theory of star formation, the dense starless cores are believed to be stellar progenitors. Opaque in the visible, they have been observed with different molecular lines such as NH_3, CS, $C^{18}O$, C_3H_2, DCO^+, HCO^+, or $H^{13}CO^+$ (e.g. Benson & Myers 1989, Butner et al. 1995). These observations give estimates of the central column density with assumptions about excitation and chemistry effects. However nothing was known about their density structure because of the limited angular resolution (at least a few 10"). Recent submillimeter and millimeter observations allow to detect the continuum emission emitted by dense cores (for instance at IRAM with an angular resolution of 11 arcsec, André et al. 1996, Motte et al. 1998). Assuming a constant dust temperature and a constant dust opacity in the core, the radial emission profiles appear consistent with a power law density n(r) α r^{-2} in the outer regions. At radii less than a few thousands AU, the profiles systematically flatten out near the center. None of the profiles appear consistent with a singular r^{-2} isothermal sphere (Shu 1977). However, the cores are heated from the outside and the physical properties of the dust likely vary within the cores, therefore the two assumptions (constant temperature and constant opacity) are questionable.

Several dense cores have been revealed by ISOCAM in the main cloud of ρ Ophiuchi as sharp and deep absorption structures against the diffuse background (Abergel et al. 1996). Several absorption features have also been found by ISOCAM in the galactic plane (Omont, in these proceedings) a nd in a survey of selected dense cores (Bacmann et al., these proceedings). In order to derive mass estimates and density profiles from absorption measurements, it is necessary to estimate as properly as possible the background and foreground emissions, and the local density outside of the core. For one core in ρ Oph (Oph D), we have shown in Abergel et al. 1997 that the total mass derived from ISOCAM measurements (typically 5-10 $M_\odot$) is in good agreement with measurements deduced from DCO^+ and 1.3 mm observations. This agreement is obtained for the two filters (5-8.5 and 12-18 μm) using the infra-red extinction law of Draine & Lee (1984). We have also confirmed the central flattening of the internal regions (typically for r < 0.02 pc). The external parts of the steepest brightness gradient are compatible with r^{-2} or r^{-3} profiles, depending on the assumed external density (in a range constrained by molecular observations). It is actually difficult to give any definitive conclusions, since the real shape of the core is not known.

5. POWER SPECTRUM OF THE ISM AT SMALL SCALES

Images of the ISM appear self-similar over a very wide range of scales and densities. The relationship between the apparent fragmentation at different scale can be quantified by computing the spectral index of the power spectrum of the emission. Gautier et al. (1992) have found a power spectrum P(k) α k^{-3} (k being the spatial frequency) for the IRAS emission at 100 μm, for angular scales going from a few degrees down to the angular resolution of IRAS, ~ 4 arcmin. For larger scales, the same power law has recently been obtained by Wright 1998 from the DIRBE data of the COBE satellite (at 100, 140 and 240 μm). Obviously, ISOCAM does not allow to observe the emission of the large grains component of the ISM which dominate the emission at these wavelengths. However, these grains are responsible of the infra-red extinction. ISOCAM observations of the main cloud of ρ Ophiuchi reveal a lot of structures seen in extinction, since it is illuminated on large scales from its far side by the Sco OB2 association (de Geus et al. 1989). Several dense cores are detected (see the previous section), but there are also absorption structures with a lower contrast which absorb the background emission, especially in the north-east part of the complex (Figure 1). In this region, likely most of the spatial fluctuations detected in the ISOCAM maps are due to extinction. This idea is also supported by the remarkable anti-correlation found between the ^{13}CO and the ISOCAM emissions. We have built power spectra of this region, and preliminary results for angular scales going from $\sim 0.1°$ down to ~ 6 arcsec indicates a k^{-3} law (Figure 7). By combining COBE, IRAS and ISOCAM data, we can conclude that the interstellar medium seems self-similar in diffuse regions for a range of angular scales going from several 10° down to a few arcsec.

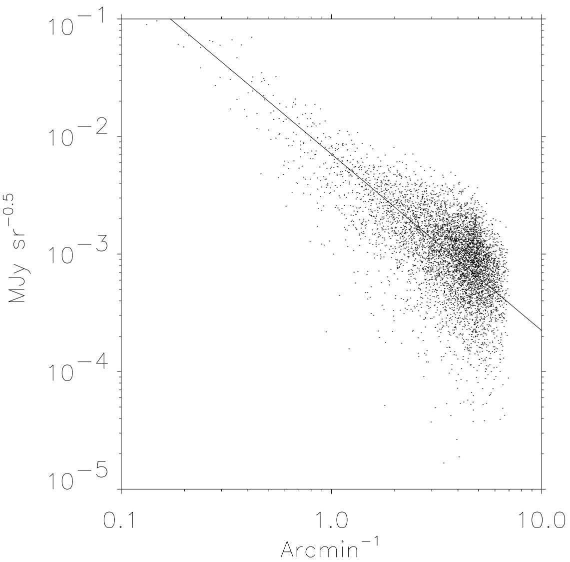

Figure 7. The square root of the two-dimensional power spectrum of the ISOCAM emission measured with the LW2 filter (5-8.5 μm). The solid line has a slope of -1.5, corresponding to a slope of -3 in the power spectrum.

6. CONCLUSIONS

The ISOCAM survey of different star forming regions has allowed to distangle between the contribution of embedded sources and extended emission. Individual structures can be analysed with an angular resolution of 3-6 arcsec.

The illuminated edges of the ρ Ophiuchi main cloud and of the Horsehead nebula presents bright and narrow filaments due to the interaction of incident radiation with the matter. These filaments can be explained by (1) steep density gradients at the interface and (2) the extinction of UV radiation within the dense clouds which appear homogeneous at small scales (typically lower than $\sim$ 0.01 pc for the Horsehead).

The spatial distribution of the column density of dense cores is revealed with unprecedented angular resolution and sensitivity. The density profiles depart from a r^{-2} law due to a central flattening of the internal regions (typically for $r < 0.02$ pc). The steepest gradients of extinction in outer regions can be modelled with a density profile at least as seep as a r^{-2} law.

The statistical analysis of the spatial distribution of dust in the interstellar medium is extended to angular scales unreachable before ISO (down to $\sim$ 6 arcsec). Preliminary results show that the interstellar medium seems self-similar in diffuse regions for a range of angular scales going from several 10° down to a few arcsec.

REFERENCES

Abergel A. et al. 1997, ASP 132, 220

Abergel A. et al. 1996, A&A, 315, L329

Abergel A. et al., 1998, Exp. Astron., in press

André P., et al. 1996, A&A 314, 625

Benson P.J., Myers P.C. 1989, ApJS 71, 89

Bernard, J.P., et al. 1993, A&A 277, 609

Bertiau F.C., 1958, ApJ 128, 533

Biviano, A., 1998 ESA report in prep.

Boisse 1990, A&A 228, 483

Boulanger, F., et al. 1990, ApJ, 364, 136

Boulanger F. et al. 1997, ASP, 132, 15

Butner H.M., et al. 1995, ApJ 448, 207

Cesarsky, C.J. et al., 1996, A&A 315, L32

de Geus E.J., et al. 1989, A&A 216, 44

Désert F. X., et al. 1990, A&A 237, 215

Désert F. X., et al. 1998, A&A, in press

Diamond, P.J., et al. 1989, ApJ, 347, 302

Draine B.T., Lee H.M., 1984, ApJ 285, 89

Dwek, E. et al. 1997, ApJ 475, 565

Falgarone, E. et al. 1998, A&A, 331, 669

Gautier III, T.N., et al. 1992, AJ, 103 (4), 1313

Giard, M., et al. 1994, A&A, 291, 239

Jaffe, D. et al. 1994, ApJ 436, 203

Kramer C., et al. 1996, A&A 307, 915

Léger, A., Puget, J.L. 1984, A&A, 137, L5

Loren R.B., 1989, ApJ 338, 902

Loren R.B., Wootten A., 1986, ApJ 306, 142

Malin, D., 1987, Sky & Telescope, 74, 253

Marscher, A.P., et al. 1993, ApJ 419, L101

Mattila, K. et al., 1996, A&A, 315, L353

Miville-Deschênes, M.-A. et al., 1999, in prep.

Motte, F. et al. 1998, A&A 336, 150

Moutou, C. et al. 1997, ASP, 132, 47

Reach W.T et al. 1995, Unveiling the cosmic infrared background. AIP press, New York, p. 37

Roberge, W.G et al. 1981, ApJ, 243, 817

Reipurth B., Bouchet P., 1984, A&A 137, L1

Sellgren, C. et al. 1985, ApJ 299, 416

Shu F. 1977, ApJ 214, 488

Vrba F.J., Strom S.E., Strom K.M., 1976, AJ 81, 958

Wilking B.A., Lada C.J., 1983, ApJ 274, 698

Wright, E.L. 1998, 496, 1

ISO OBSERVATIONS OF THE GALACTIC CENTRE

D. Lutz
Max-Planck-Institut für extraterrestrische Physik, Garching, Germany

ABSTRACT

This contribution discusses ISO spectroscopic observations of the Galactic Centre and the surrounding molecular ring, emphasizing the template role of the Galactic Centre region for extragalactic studies. An ageing starburst population is indicated by the low excitation fine structure line spectrum, consistent with results from the near-infrared stellar census. On closer inspection however, current stellar evolutionary tracks are found unable of accounting for ISO spectrum and near-infrared census.

The Galactic Centre region allows spatially resolved studies of the mid-infrared PAH emission features. While they are absent in the intense radiation field of the very center, PAH features are detected from the molecular ring, providing a template of a PAH spectrum suffering high foreground extinction.

Because of its well-known and fairly homogeneous foreground extinction, the Galactic Centre is uniquely suited for studies of the mid-infrared extinction law. Our results indicate significantly higher extinction in the 3-8 μm region than usually assumed.

Key words: Galaxy: center; galaxies: starburst; PAH features; extinction.

1. INTRODUCTION

By its brightness and its distance of only 8 kpc, the Galactic Centre offers the unique possibility for spatially resolved ISO studies of the central region of a galaxy. The central parsec of our Galaxy is powered by a cluster of young hot massive stars which formed a few million years ago, probably when a dense cloud fell into the center, was highly compressed, and became gravitationally unstable. Over the last decade, high angular resolution near-infrared photometric and spectroscopic observations have made it possible to carry out a detailed stellar census. This census can be confronted with global analyses that are based on ISO data, and used to test the validity of methods also applied to ISO data of spatially unresolved external galaxies. Here, we will focus on SWS observations, updating the results presented by Lutz et al. (1996) with new observations, and briefly discussing the role of PAH emission features in the Galactic Centre environment. An overview of the SWS 2.4-45 μm spectrum centered on Sgr A* is given in Figure 1.

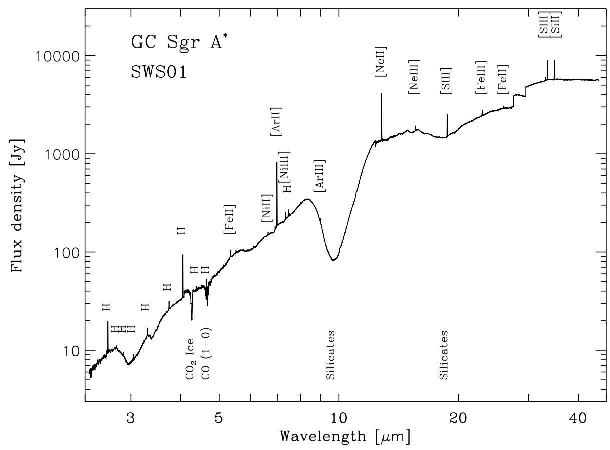

Figure 1. Full 2.4-45 μm SWS spectrum of the centre of our Galaxy

2. THE GALACTIC CENTER AS A STARBURST TEMPLATE

Fine structure line spectra are an extinction-insensitive tool for studies of stellar populations of H II regions and starburst galaxies. Ratios like [Ne III] 15.55 μm / [Ne II] 12.81 μm depend on the hardness of the ionizing continuum and can hence be used to constrain the hot star population. ISO observations of starbursts are consistent with stars forming up to masses well above 50 $M_\odot$ but suggest short star formation timescales and moderate ages, since the observed ratios of typically 0.1 to 1 are lower than expected for a very young population (Thornley et al. 1999). Previously it had been suggested on the basis of ratios like He I 2.06 μm / Br γ and [Ar III] 8.99 μm / [Ne II] 12.81 μm that the initial mass function starbursts may suffer sever upper cutoffs in the range ~30-35 $M_\odot$ (e.g. Doyon et al. 1992, Doyon et al. 1994, Puxley et al. 1989, Achtermann & Lacy 1995).

Proceedings of the Conference "The Universe as seen by ISO", Paris, France, 20–23 October 1998 (ESA SP-427, March 1999)

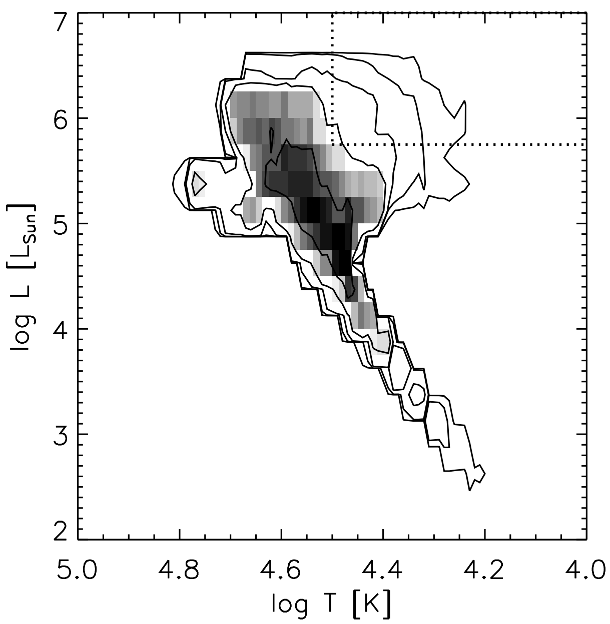

Figure 2. Contributions of different stellar types to the total Lyman continuum luminosity of a short starburst (t_{sc}=1Myr) at a burst age of 7 Myr. Contours are at 10^{-6}, 10^{-5}, etc. contribution of a Δ log L = 0.25, Δ log T=0.0125 bin to the total luminosity. The greyscale coded regions are above the 10^{-3} level and contribute more than 97 per cent of the total flux for this model. The box enclosed by a dotted line indicates the region which host stars contributing about 50 per cent to the ionizing luminosity of our Galactic Centre (Najarro et al. 1997).

The observed [Ne III]/[Ne II] ratio for the Galactic center (Figure 1, Lutz et al. 1996) is even lower than in most starbursts, despite the high ionization parameter log U = -1 derived for the spatially resolved ionized region, and the known presence of very massive stars. The picture of a short but ageing burst is supported by the direct stellar census (e.g. Genzel, Hollenbach & Townes 1998, Krabbe et al. 1995, Najarro et al. 1997) which suggests a star formation event centered around 7 Myr ago. The availability of both ISO data and stellar census provides an opportunity to test starburst models.

We have computed starbursts models tuned specifically to the Galactic Centre situation, using Geneva stellar evolutionary tracks and unified non-LTE hot star atmosphere models computed by the Munich group (Pauldrach, priv. comm.) to model the ionizing spectrum, and CLOUDY (Ferland 1996) to predict the fine structure line spectrum. We have assumed a single cluster with star formation timescale t_{sc}= 1 Myr, M_{up}=100, solar metallicity, and fixed log U = -1, n = 3000 cm^{-3} as derived by Lutz et al. (1996). The burst timescale is somewhat smaller than suggested by the stellar census and was chosen as a conservative assumption, since a shorter burst will produce softer radiation fields at late ages and thus minimize any need to invoke other effects for explaining the observed soft radiation field. At the age of 7 Myr preferred by the stellar census, the [Ne III]/[Ne II] ratio is still about 1 to 2, well above the extinction corrected value of 0.05 observed by Lutz et al. (1996). The model reaches the observed value only after more than 13 Myr which is difficult to reconcile with the presence of massive stars approaching 100 $M_\odot$ (Najarro et al. 1997, Ott et al. 1999). This discrepancy is new and was not found by Lutz et al. (1996) who were using Kurucz LTE and Sellmaier non-LTE atmospheres, both of which are no longer thought to be appropriate representations of O star ionizing continua.

Comparison to the near-infrared stellar census for the Galactic Centre gives a view which is largely independent of the adopted model atmospheres, through direct analysis of the contributions of different stellar types to the ionizing continuum. Figure 2 presents such a Hertzsprung-Russell diagram weighted by Lyman continuum luminosity, derived from the same starburst model for an age of 7 Myr. It is evident that most ionizing luminosity still originates in stars close to the main sequence at log T= 4.5 to 4.6, with smaller contributions by stars somewhat evolved towards lower temperatures and a population of hot Wolf-Rayet type stars to the left of the main sequence. This is in stark contrast to the finding by Najarro et al. (1997) that 7 of their stars, found at log T $<$ 4.5 and log L $>$ 5.75, contribute half of the ionizing luminosity of the Galactic center. The same region holds only less than 1 per cent of the ionizing luminosity for the model in Figure 2. Varying the age of this model, this fraction does never exceed about 1 per cent.

The fact that the discrepancy between 'hard' models and 'soft' observations is seen both in the ISO photoionization modelling and the near-infrared stellar census leads us to the conclusion that it is not primarily due to uncertainties in the hot star SEDs used for the photoionization models. Such uncertainties affect mainly the shape of the ionizing flux and thus the fine structure line ratios, but much less the total ionizing flux of the star and the census. Rather, we interpret the discrepancy as a failure of the adopted Geneva stellar evolutionary tracks (Schaller et al. 1992) to reproduce the large number of 20000 to 30000K supergiants seen in the Galactic center. The corresponding region is populated by these tracks but only for too short intervals, possibly because Wolf-Rayet stars rapidly move off to hotter regions in the tracks. The disagreement between tracks and observations may be related to the difficulty of defining mass loss, atmospheres, and effective temperatures for late stages of massive star evolution governed by strong winds. Our conclusions are unchanged when using evolutionary tracks with twice solar metallicity (Schaller et al. 1992) and higher mass loss (Meynet et al. 1994), which might be adequate for a somewhat higher metallicity in the Galactic center. The latter tracks in fact increase the disagreement by adding more very hot Wolf-Rayet types.

The case of the Galactic Centre has obvious implications for ageing starbursts with similar populations. If the current Geneva tracks indeed mispredict the post main sequence evolution of massive stars in the sense of postulating very hot stars where the Galactic Centre shows us a cooler luminous population, then starburst models will tend to predict too high values for ratios like [Ne III]/[Ne II]. Some of the need to invoke high ages or low upper mass cutoffs to explain soft radiation fields may be due to this effect.

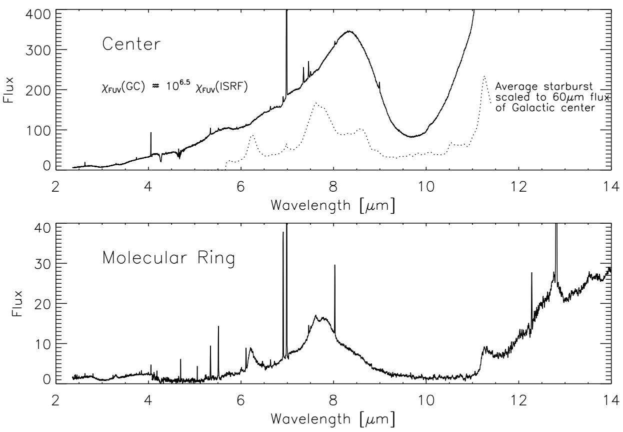

Figure 3. SWS spectra of the PAH features toward Sgr A and a position in the molecular ring*

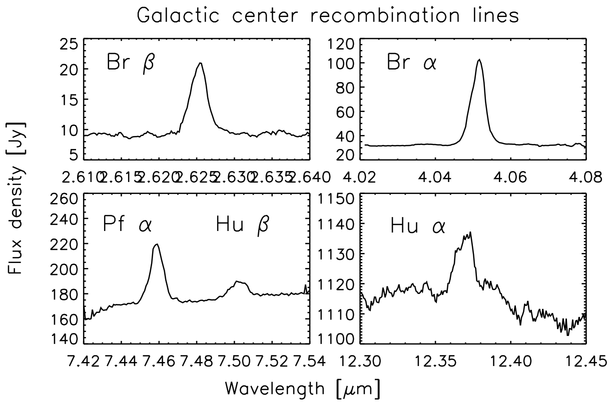

Figure 4. Examples of hydrogen recombination lines observed towards the Galactic center

3. PAH FEATURES IN THE GALACTIC CENTER REGION

At ISO sensitivities, the mid-infrared emission features commonly ascribed to polycyclic aromatic hydrocarbons (PAHs) are readily observed in a wide variety of galactic and extragalactic environments, from galactic cirrus (Mattila et al. 1996) out to ultraluminous infrared galaxies at moderate redshifts (Lutz et al. 1998). Again, the Galactic center can serve as a laboratory for phenomena which are also observed in more complex environments. The basic observational facts are presented in Figure 3 which shows SWS spectra towards the very centre and towards a position in the 'molecular ring', about 1 arcmin off the center.

No PAH features are detected towards Sgr A*. This is not just an effect of dilution by the unusually strong mid-infrared continuum - if PAH features were present at the same strength relative to the far-infrared (60 μm) continuum as in starburst galaxies, they would still be easily detectable. Most likely this indicates destruction of the carriers in the intense central radiation field ($\chi_{\rm FUV}$(GC) $\approx 10^{6.5}$ $\chi_{\rm FUV}$(ISRF)). The PAH features are clearly present in another spectrum taken towards the molecular ring, though they differ in relative strength from typical starburst values. The 11.3 μm feature appears faint, the 8.6 μm feature appears more as a shoulder at the long wavelength side of the 7.7 μm feature than as a separate feature, and on quantitative analysis also the 6.2 μm feature appears slightly suppressed with respect to the 7.7 μm one. This is readily explained as the effect of the $A_V \sim 30$ foreground extinction towards the Galactic Centre which tends to suppress the features at 11.3, 8.6, and 6.2 μm with respect to the 7.7 μm one. The same effect is seen in obscured ultraluminous galaxies (Lutz et al. 1998).

If we would observe our galaxy from above the galactic plane, thus eliminating the unusually high foreground extinction, and with a large aperture including center, molecular ring, and part of the bulge, the resulting spectrum would most certainly be PAH-dominated and very similar to PAH spectra of other normal and star forming galaxies. In this sense, the spectrum of the innermost 20 arcseconds as presented here is not representative.

4. THE MID-INFRARED EXTINCTION LAW

SWS spectroscopy of hydrogen recombination lines can be used to determine the previously poorly constrained extinction law at mid-infrared wavelengths. The centre of our Galaxy provides a unique laboratory for such studies since the extinction along this line of sight is high, well determined in the near-infrared K band (Rieke et al. 1989), and fairly homogeneous over the size of the SWS beam, thus approximating the ideal 'screen' case. Since the first analysis by Lutz et al. (1996), more observations of hydrogen recombination lines have been obtained. Figure 4 shows some examples including the Humphreys α transition which is extremely difficult to observe on the strong Galactic Centre continuum. Comparing the line fluxes to appropriate case B emissivities, we find that the extinction law (Figure 5 top) clearly lacks the deep minimum near 7 μm expected for standard graphite-silicate grain mixes as for example given by Draine (1989). Because of the decreasing line-to-continuum, our extinction law is less well determined at wavelengths beyond 10 μm. However, the silicate features are clearly present and likely strong, with $\sim$0.1 A_V or more in the peak of the 9.6 μm feature.

A simple test of the applicability of case B conditions can be obtained in regions where lines from different series are observed in a small wavelength interval. This is the case for the 4 μm region where we have data for the Brackett α line and for lines from the Pfund and Humphreys series, as well as the 7.5 μm region where Pfund α is close to a blend of Humphreys β and the 11-7 transition. The results for these lines are consistent, demonstrating that the population of the respective upper levels follows case B. In accordance with our results, L-band polarimetry of Galactic Centre sources finds higher polarization than expected from the extrapolation of shorter wavelength data (Nagata et al. 1994).

For external galaxies, the situation is less clear because of more scarce observations and the generally unknown dust configuration. A qualitative picture can be obtained, however, by simply plotting the observed ratios of the brightest hydrogen recombination lines (Figure 5 bottom). Note that Brackett β is not yet corrected for the contribution of the coincident

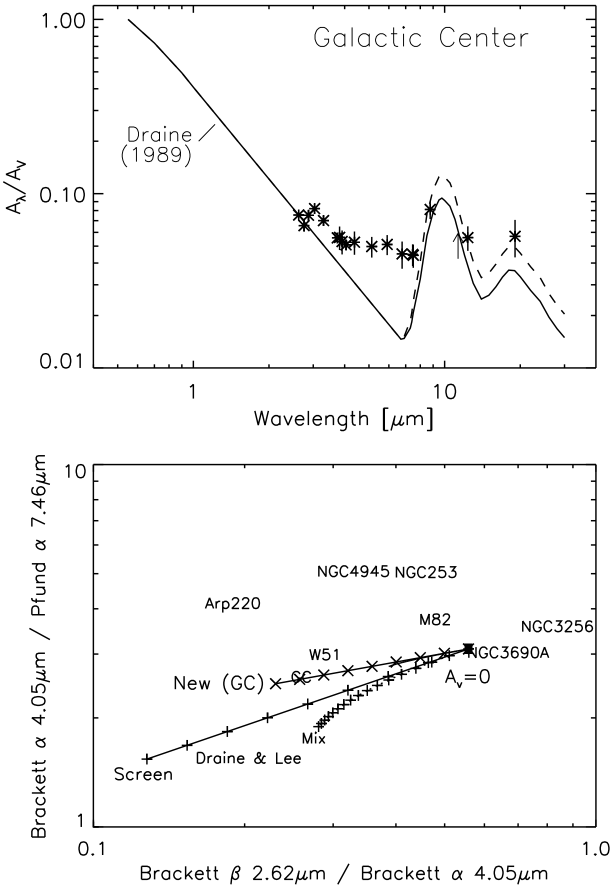

Figure 5. Top: Mid-infrared extinction law derived from hydrogen recombination line observations of the Galactic center, compared to the one given by Draine (1989). Bottom: Observed recombination line ratios in several galaxies and star forming regions compared to expectations for a standard extinction law

H_2 (1-0)O(2) line. For a standard extinction law, measurements should fall somewhere on or *below* the 'screen' line extending from the zero extinction point to the lower left, *irrespective of the precise dust configuration.* The location of the measured points is clearly inconsistent with such an extinction law and indicates significantly higher extinction at 7.5 μm.

Part of the increased extinction can be ascribed to features like the 3 μm OH stretch feature ('ice') which is clearly traced by the new Galactic Centre extinction law. Incomplete wavelength sampling, limited to those regions with useful H lines, and flux calibration accuracy do not allow to decide unambiguously whether the extinction at longer wavelengths has a similar origin in individual fairly localized features or whether, perhaps more likely, grain impurities change the shape of the silicate feature and introduce additional continuous absorption. The scatter in the observations of galaxies suggests a dependence on the properties of the specific line of sight.

ACKNOWLEDGMENTS

It is a pleasure to thank my collaborators H. Feuchtgruber, R. Genzel, Th. de Graauw, D. Kunze, A. Moorwood, A. Pauldrach, H.W.W. Spoon, A. Sternberg, E. Sturm, M. Thornley, and D. Tran. SWS and the ISO Spectrometer Data Centre at MPE are supported by DLR (DARA) under grants 50 QI 8610 8 and 50 QI 9402 3.

REFERENCES

Achtermann J.M., Lacy J.H. 1995, ApJ, 439, 163

Doyon R., Puxley P.J., Joseph R.D. 1992, ApJ, 397, 117

Doyon R., Joseph R.D., Wright G.S. 1994, ApJ, 421, 101

Draine, B. 1989, in proc. 22nd ESLAB Symp. on Infrared Spectroscopy in Astronomy, ed. B. Kaldeich, ESASP-290, 93

Ferland G.J., 1996, Hazy, a Brief Introduction to Cloudy, University of Kentucky Department of Physics and Astronomy Internal Report

Genzel R., Hollenbach D.J., Townes C.H. 1994, Rep. Progr. Phys. 57, 417

Krabbe A., et al. 1995, ApJ, 447, L95

Lutz D., et al. 1996, A&A, 315, L269

Lutz D., et al. 1998, ApJ, 505, L103

Mattila K., et al. 1996, A&A, 315, L353

Meynet G., Maeder A., Schaller H., Schaerer D., Charbonnel C. 1994, A&AS, 103, 97

Nagata T., Kobayashi N., Sato S. 1994, ApJ, 423, L113

Najarro F., Krabbe A., Genzel R., Lutz D., Kudritzki R.P., Hillier D.J. 1997, A&A, 325, 700

Ott T., Eckart A., Genzel R. 1999, ApJ, submitted

Puxley P.J., et al., 1989, ApJ, 345, 163

Rieke, G.H., Rieke, M.J., Paul, A.E. 1989, ApJ, 336, 752

Schaller G., Schaerer D., Meynet G., Maeder A. 1992, A&AS, 96, 269

Thornley M.D., et al. 1999, in preparation

COLD GMC CORES IN THE GALACTIC CENTRE

D.C. Lis[1], Y. Li[1], C.D. Dowell[1], & K.M. Menten[2]
[1]California Institute of Technology, MS 320-47, Pasadena, CA 91125, USA
[2]Max-Planck-Institut für Radioastronomie, Auf dem Hügel 69, D-53121 Bonn, Germany

ABSTRACT

We have used the Long Wavelength Spectrometer (LWS) aboard the Infrared Space Observatory in grating mode to map the far-infrared continuum emission (45–175 μm) toward several massive Giant Molecular Cloud (GMC) cores located near the Galactic center. These sources are observed in emission at far-infrared and submillimeter wavelengths (>100 μm). However, at mid-infrared wavelengths (<70 μm) they are seen in absorption against the general Galactic centre background. Gray-body fits to the observed far-infrared and submillimeter spectral energy distributions give low temperatures (∼13–20 K) for the bulk of the dust in all the sources. This indicates external heating of the dust by the diffuse ISRF and suggests that the cores do not harbor high-mass star-formation sites, in spite of their large molecular mass. In addition, the grain emissivity in these sources is a very steep function of frequency ($\beta > 2.4$). The high grain emissivity exponent is consistent with the presence of dust grains covered with thick ice mantles. Molecular line observations carried out with the Caltech Submillimeter Observatory (CSO) show a large velocity gradient across the most massive core, GCM0.25+0.11, indicative of streaming motions of the gas or of the presence of multiple, spatially overlapping velocity components. The observed gas kinematics may indicate that the GCM0.25+0.11 core is in an early stage of a cloud-cloud collision that may result in a future star formation episode. Recent MSX observations indicate that cold GMC cores similar to those studied with ISO are ubiquitous in the Galactic center and throughout the Galaxy. The observed intensities of the OI and CII fine structure lines imply a radiation field intensity of about 1000 times the standard ISRF intensity and a hydrogen density of about 1000 cm^{-3} for the diffuse gas component in the Galactic center.

Key words: Galactic center; star formation.

1. INTRODUCTION

The rate of current high-mass star formation in the Galactic center region (central ∼200 pc of the Milky Way; the region referred to as the nuclear disk, or the central molecular zone) has been a subject of controversy. Although the total FIR luminosity and the ionizing flux are consistent with a star formation rate per unit mass of molecular material comparable to that in the Galactic disk (see Güsten 1989), a number of studies suggest a decreased high-mass star formation rate in the central region. For example, Morris (1989) argues that star formation may be currently suppressed in the Galactic center as a result of the geometry and strength of the magnetic field in the central region, which arguably may inhibit cloud collapse. The high gas pressure implied by observations of diffuse X-ray emission also suggests that Galactic center GMCs may be held together by external pressure rather than self-gravity (Spergel & Blitz 1992). The gravitational collapse leading to the formation of high density cores may thus be suppressed in all but the most massive clouds.

Recent IR imaging observations have revealed several new high-mass star-formation sites in the Galactic center (e.g. Keck I observations of the Arches cluster, Serabyn et al. 1998, which show in excess of 100 main sequence stars with masses up to 120 M$_\odot$.) Nevertheless, large-scale star-formation patterns in the Galactic center still remain unestablished.

In an effort to identify possible sites of future star formation (namely high-density GMC cores) in the Galactic center, Lis & Carlstrom (1994) made an unbiased survey of the 800 μm continuum emission over a region ∼1.5° × 0.2° using the single pixel CSO bolometer. In this survey, in addition to the well known sources like Sgr B2, Sgr C, and the 50 and 20 km s^{-1} clouds in Sgr A, a number of compact GMC cores were detected, forming a long, clumpy ridge of dust emission (referred to as the 'Dust Ridge'), stretching from the radio Arc toward Sgr B2.[1] No evidence for the presence of embedded FIR sources or compact HII regions associated with the most massive GMC core in the Dust Ridge, GCM0.25+0.11, was found by Lis et al. (1994), and their VLA observations revealed the presence of only a weak H_2O maser associated with this source, suggesting the presence of some ongoing low-mass star formation.

[1]A much more sensitive, high-angular resolution 350 μm map of the same region has been recently obtained by Dowell et al. (1999) using the SHARC bolometer camera at the CSO.

Proceedings of the Conference "The Universe as seen by ISO", Paris, France, 20–23 October 1998 (ESA SP-427, March 1999)

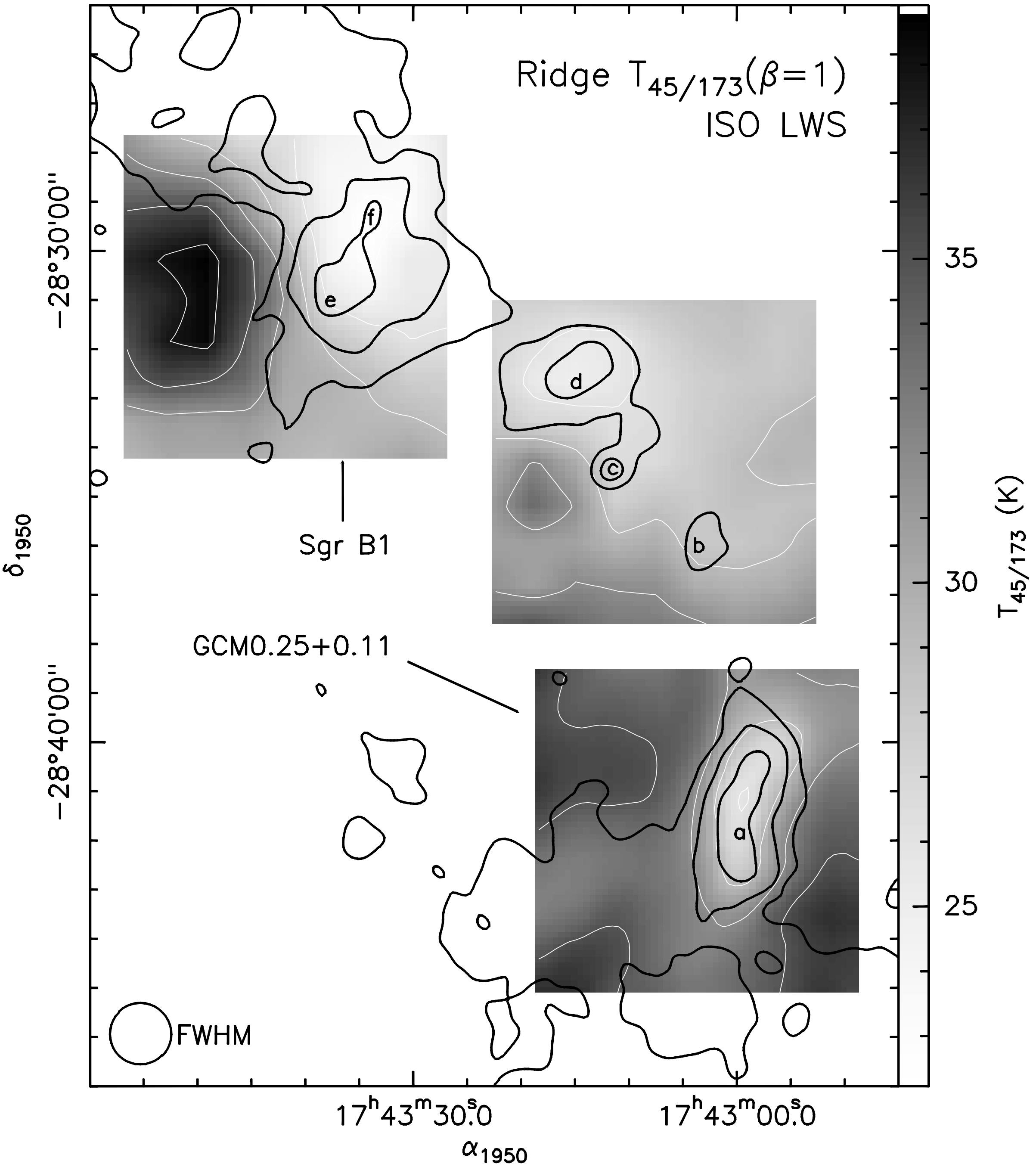

Figure 1. *Distribution of the 45/173 μm color temperature in the Dust Ridge calculated assuming a grain emissivity exponent $\beta = 1$ (appropriate for the diffuse dust component, but not for the dense cores; gray-scale and thin white contours). Black contours show the distribution of the 350 μm continuum emission at 30′′ angular resolution. The submillimeter sources appear as local minima in the color temperature. The coldest dust is located in the northern part of the Sgr B1 core (position 'f' in the map). Color temperature contour levels are from 23 to 38 K with an interval of 3 K. Note that the southern part of the Dust Ridge appears to be physically connected with the molecular cloud interacting with the non-thermal filaments in the radio Arc, indicating that these sources are in fact located in the Galactic center region.*

A detailed study of a submillimeter selected sample of cloud cores may provide new constraints for the magnitude of various dynamical effects invoked to explain the low rate of high-mass star formation in the Galactic center region. To better constrain the dust temperature and mass of the sources detected by Lis & Carlstrom (1994), we have obtained sensitive multi-wavelength images of the Dust Ridge with the LWS aboard ISO. Results for GCM0.25+0.11 have already been presented by Lis & Menten (1998). In the present paper we discuss the remaining sources in our ISO fields. Observational details are given in Lis & Menten (1998).

2. CONTINUUM RESULTS

The distribution of long-wavelength (173 μm) far-infrared emission in the Dust Ridge correlates well with that of the submillimeter continuum emission. However, at MIR wavelengths (<70 μm) the submillimeter sources are either invisible, or show up in absorption against the general Galactic center background. This has several interesting implications: (1) all the sources must be quite cold, significantly colder than the diffuse dust component, (2) they must have high continuum opacity at MIR wavelengths (and consequently high H_2 column density and mass), and (3) they must be located in front of the warm dust responsible for the diffuse MIR emission.

All the GMC cores in the Dust Ridge appear as depressions in the 45/173 μm color temperature map (Fig. 1). The upper limits to the dust temperature in the cores given by the color temperature are in the range 22–28 K. However, as discussed below, the actual dust temperature in these sources is significantly lower.

Owing to the complete spectral coverage afforded by our ISO and CSO measurements (45–800 μm), we can constrain the dust temperature in these GMC cores quite accurately. Two component gray-body models for GCM0.25+0.11 give a mean dust temperature of 18 K (Lis & Menten 1998). A small amount of warmer dust (35–40 K) is required to accurately reproduce the observed SED, but this warmer dust contributes only 1–3% of the total optical depth and most likely represents emission from the surface layer of the clouds. In addition, in order to reproduce the observed spectrum of this source a very steep grain emissivity exponent ($\beta = 2.8$) is required. As shown in Table 1, these results are typical for all the submillimeter sources in this region. The bulk of the dust in all the sources is quite cold (13–20 K) and is characterized by steep values of $\beta > 2.4$. The coldest dust is located in the northern part of the Sgr B1 core (see Fig. 1, position 'f').

The low dust temperature is a natural consequence of the absence of embedded heating sources in these cores – the dust is heated externally by the diffuse interstellar radiation field. The steep value of β has been interpreted by Lis & Menten (1998) as evidence for the presence of dust grains covered with thick ice mantles, consistent with the low dust temperature.

Our ISO observations firmly establish that the GMC cores in the Dust Ridge are different from the well studied Galactic center GMCs. However, the critical question is whether these sources are significant in terms of their mass and whether they are representative for the Galactic center GMC population.

Table 1. Source parameters

Position	T_d (K)	β
a	17	2.8
b	20	2.4
c	20	2.4
d	17	2.6
e	17	2.8
f	13	3.4

The mass determination depends critically on the knowledge of the 350 μm grain emissivity, that is not very well constrained. Lis & Menten (1998) estimated the value of Q_{350} in GCM0.25+0.11 by comparing the dust mass with the virial mass based on molecular line emission. The derived value of Q_{350} is 1×10^{-4}, consistent with that obtained by extrapolating the 125 μm value of Hildebrand (1983) with a ν^2 frequency dependence, as well as with the values derived by Goldsmith et al. (1998) at 800 μm for the Cep A and M17 clouds (again assuming a ν^2 frequency dependence). The resulting H_2 mass of GCM0.25+0.01 is $\sim 6\times 10^5$ $M_\odot$, only a factor of 3–4 lower than the mass of the Sgr B2 molecular cloud, the most massive star-forming GMC in the Galactic center. The combined mass of all the sources in the Dust Ridge is in fact comparable to the Sgr B2 mass, suggesting that these sources are not insignificant for the global mass balance in the Galactic center.

3. FINE STRUCTURE LINE EMISSION

In addition to the continuum SEDs, our LWS grating spectra cover the 63 μm fine structure line of OI and the 158 μm line of CII. Observations of these lines, together with the FIR continuum emission, allow determination of the physical conditions in the diffuse ISM in the Galactic center region, namely the gas density and the ISRF intensity, through PDR modelling.

Wolfire et al. (1990) calculated a grid of PDR models for a range of hydrogen densities ($n_{\rm H}$) and UV field intensities (G_o) and showed that the CII/OI and (CII+OI+SiII)/FIR intensity ratios can be used to distinguish between models with different values of $n_{\rm H}$ and G_o (see Fig. 2).[2] The gray points in Fig. 2 correspond to several lines of sight within our ISO maps, away from the dense cores, which cover a wide range of the 45/173 μm color temperatures. The points cluster around G_o=10^3 times the standard radiation field intensity and $n_{\rm H}$=10^3 cm^{-3}. The derived values of $n_{\rm H}$ and G_o are uncertain to within a factor of 2 owing to uncertainties in the optical depth of the fine structure lines. The value of G_o derived from the fine structure line observations will be used as an input parameter for detailed continuum radiative transfer modelling of the compact sources.

4. SUMMARY

Our ISO LWS observations imply low dust temperatures (13–20 K) in the GMC cores in the Dust Ridge. We find no evidence for ongoing high-mass star formation associated with these sources, in spite of their large molecular mass. As discussed by Lis & Menten (1998), molecular observations of GCM0.25+0.01 show complicated gas kinematics, possibly indicating an early stage of a cloud-cloud collisions. However,

[2] As discussed by Simpson et al. (1997), the intensity of the 35μm SiII line which is included in the plot of Wolfire et al. (1990) can be neglected, since Si is highly depleted in their models.

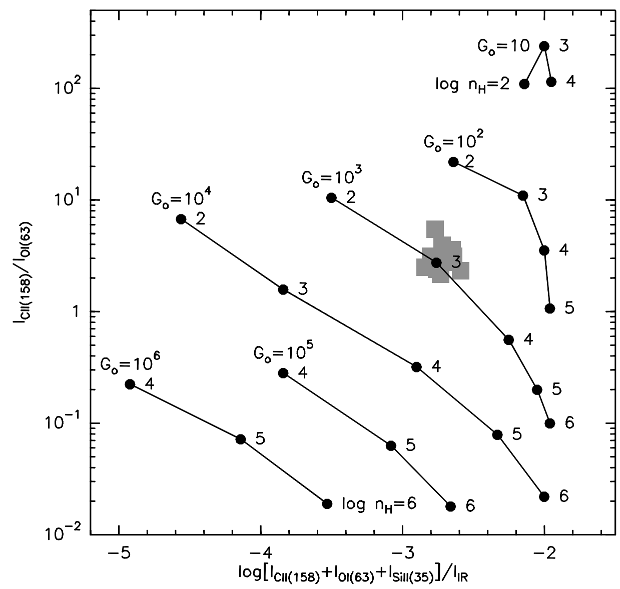

Figure 2. The CII/OI intensity ratio as a function of (CII+OI+SiII)/FIR for a grid of PDR models with a range of hydrogen densities and UV field intensities (from Wolfire et al. 1990). Gray squares correspond to several lines of sight in our ISO maps away from the submillimeter continuum sources.

the remaining sources appear to show a simpler velocity field. Follow-up high-angular resolution molecular observations are required to better constrain the kinematics of the gas.

Owing to the time constraints, we have been able to study in detail only a limited sample of sources with ISO. However, recent MSX observations (Egan et al. 1998; see also Egan et al. in these proceedings) indicate that a large number of presumably similar, cold dust sources are present in the Galactic center region and throughout the Galaxy. The GMC cores we have studied with ISO thus appear to represent 'typical' Galactic center GMCs, as opposed to the well studied star-forming clouds like Sgr B2, Sgr C, Sgr D, or the 50 kms^{-1} cloud in Sgr A. The latter sources were all identified because of their strong FIR and/or radio continuum emission, which are natural tracers of high-mass star formation. However, they do not appear to be representative for the Galactic center GMC population.

ACKNOWLEDGMENTS

This research has been partially supported by NASA and by the NSF grant AST 96-15025 to the Caltech Submillimeter Observatory.

REFERENCES

Dowell, C.D., Lis, D.C., Serabyn, E., Gardner, M., Kovacs, A., & Yamashita, S. 1999, in The Central Parsecs of the Galaxy, ed. H. Falcke et al. (ASP Conf. Series), in press

Egan, M.P., Shipman, R.F., Price, S.D., Carey, S.J., & Clark, F.O. 1998, ApJ, 494, L199

Goldsmith, P.F., Bergin, E.A., & Lis, D.C. 1998, ApJ, 491, 615

Güsten, R. 1989, in The Center of the Galaxy, ed. M. Morris (Dordrecht: Kluwer), 89

Hildebrand, R.H. 1983, QJRAS, 24, 267

Lis, D.C., & Carlstrom, J.E. 1994, ApJ, 424, 189

Lis, D.C., & Menten, K.M. 1998, ApJ, 507, 794

Lis, D.C., Menten, K.M., Serabyn, E., & Zylka, R. 1994, ApJ, 423, L39

Morris, M. 1989, in The Center of the Galaxy, ed. M. Morris (Dordrecht: Kluwer), 171

Serabyn, E., Shupe, D., & Figer, D.F. 1998, Nature, 394, 448

Simpson, J.P., Colgan, S.W., Cotera, A.S., Erickson, E.F., Haas, M.R., Morris, M., & Rubin, R.H. 1997, ApJ, 487, 689

Spergel, D. N., & Blitz, L. 1992, Nature, 357, 665

Wolfire, M.G., Tielens, A.G.G.M., & Hollenbach, D. 1990, ApJ, 358, 116

ISO SPECTROSCOPY OF DENSE REGIONS

P. Cox[1], P.R. Roelfsema[2], J.-P. Baluteau[3], E. Peeters[2], L. Martin-Hernandez[2], A.G.G. Tielens[2], B. Swinyard[4], T. Lim[4] & M.F. Kessler[5]

[1] Institut d'Astrophysique Spatiale, Bât. 121, Université de Paris XI, F-91405 Orsay, France
[2] Space Res. Org. of the Netherlands, P.O. Box 800, NL-9700 AV Groningen, The Netherlands
[3]Laboratoire d'Astronomie Spatiale, CNRS, BP 8, F-13376, Marseille Cedex 12, France
[4] Rutherford Appleton Lab., Chilton, Didcot, Oxon OX11 0QX, UK
[5] ISO Data Centre, Astrophysics Division, ESA, Villafranca, Spain.

ABSTRACT

The infrared satellite ISO has, for the first time, allowed us to obtain complete spectra from 2.5 to 196 μm together with detailed spectroscopy over this wavelength range for a variety of astronomical sources. This paper describes SWS-LWS ISO grating spectra of galactic dense star-forming regions. The diversity of the infrared spectra of compact H II regions is discussed and new results on the galactic abundance gradient are presented. The effects of absorption can be important even in the far-infrared as shown by the spectra of deeply embedded infrared sources and the data obtained on Sgr B2.

Key words: HII regions; abundances; dust bands; infrared lines.

1. INTRODUCTION

The launch in 1995 of the Infrared Space Observatory (ISO, Kessler et al. 1996) has had a profound impact on the study of the interstellar medium. It opened the *entire* 2.5–196 μm wavelength region for spectroscopic studies at spectral resolutions of $\frac{\lambda}{\Delta\lambda}$ from ~100 to ~500 with the Short Wave Spectrometer (SWS, de Graauw et al. 1996) and Long Wave Spectrometer (LWS, Clegg et al. 1996) grating instruments, and at spectral resolutions up to $\frac{\lambda}{\Delta\lambda} \sim 20,000$ with the SWS and LWS Fabry-Pérots. The availability of complete infrared grating spectra up to 196 μm for a great number of astronomical sources allows the study of all the components present at infrared wavelengths, i.e. the dust bands together with the infrared continuum, the atomic fine structure lines and molecular gas bands. This richness of information is one of the greatest achievements of ISO and part of what has been called the *ISO revolution.*

This paper summarises some of the results obtained with combined SWS and LWS grating spectra for compact galactic H II regions, as an example of the spectral diversity in the infrared wavelength domain. The main purpose of these observations is the study of the distribution of element abundances in the galaxy. First results on the variation of the abundances are presented. The effect of absorption at far-infrared wavelengths is shown to be important for some star-forming regions. The case of SgrB2 is discussed separately as it provides an extreme example of an infrared spectrum which is *entirely* dominated by absorption, including the [OI] and [CII] fine structure lines.

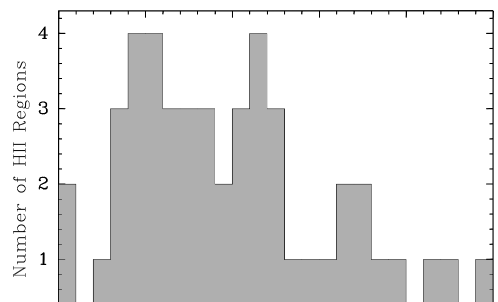

*Figure 1. Number of H*II *regions as function of galactocentric radius*

2. ISO SPECTRA OF COMPACT HII REGIONS

In order to study the distribution of elemental abundances in the Galaxy, infrared spectra from 2.5 to 196 μm have been measured for a sample of 46 compact H II regions in a series of ISO guaranteed time programs (see Roelfsema et al. 1998 for details). All the H II regions were observed with the LWS and SWS full AOT 01 scans yielding spectra with a resolution $\frac{\lambda}{\Delta\lambda}$ from ~100 to ~500. For some sources

Proceedings of the Conference "The Universe as seen by ISO", Paris, France, 20–23 October 1998 (ESA SP-427, March 1999)

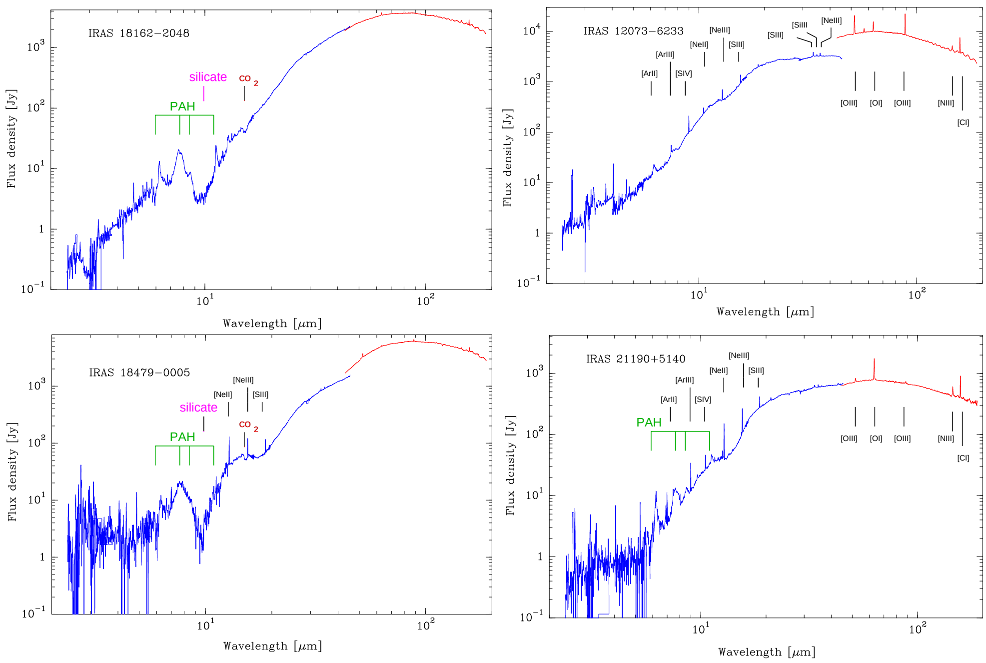

Figure 2. 2.5-196 μm SWS and LWS combined spectra of compact HII regions.

additional higher resolution data have been obtained to study in more detail the various dust and molecular features. The sources have a wide range in galactocentric distance ($0 \leq R_{gal} \leq 25$ kpc) and a relatively uniform distribution (Fig. 1) which will enable to study the galactic abundance variation over larger scales than in previous studies (e.g., Shaver et al. 1983, Afflerbach et al. 1997).

All data presented in this paper were calibrated using standard OLP6.0 or OLP7.0 calibration files and procedures (see de Graauw et al. 1996, Schaeidt et al. 1996, Swinyard et al. 1996). Further corrections for instrumental problems (e.g., de-fringing) were applied using the SWS and LWS interactive analysis packages. No corrections other than the standard calibrations were applied to match the spectral segments. With this method extremely good agreement was obtained between the two spectrometers; for true point sources, differences between SWS and LWS in the region of overlap are typically found to be less than 15%.

Presently all spectra are being re-calibrated in a uniform manner (e.g., all using OLP 7.0). Also a number of known instrumental effects (e.g., pointing errors, aperture sizes) are investigated for the individual sources. The fully calibrated data set (to be published as an atlas) will then be the basis for a detailed analysis of the physical properties (density, temperature, abundances) of the nebulae.

In Fig. 2, typical spectra of compact H II regions are shown. The diversity of the spectral content is clearly illustrated. For example, IRAS 18162−2048 presents a smooth continuum with prominent dust and molecular features and weak emission lines, whereas IRAS 21190+5140 has a very rich emission line spectrum, weak PAH bands and no indication of molecular features. Generally the data are very rich resulting in a lot of 'spin-off' science; PAH emission features (Roelfsema et al. 1996; Peeters et al. these proceedings), CO_2 (Boogert et al. in prep.) or H_2O ice (see Section 4).

The spectrum towards IRAS 12073-6233 illustrates one of the problems that may be found in combined LWS-SWS observations. In this case the spectrum shows some jumps, especially between the SWS and LWS parts of the spectrum. This indicates that this particular source is *not* a true point source for the two spectrometers. In such cases line fluxes have to be corrected for the size of the apertures.

In the mid-infrared, the spectra of compact H II regions display the series of well-known emission features at 6.2, 7.7, 8.6 and 11.3 μm which are commonly attributed to Polycyclic Aromatic Hydrocarbons or PAHs (e.g., Léger & Puget 1984 - see review by Tielens et al. in these proceedings). Figure 3 presents the spectra between 5 and 13 μm of a sample of H II regions. The spectra clearly show the characteristic C-C stretch (at 6.2 and 7.7 μm) and the C-H bending modes (8.6 and 11.3 μm) features of small aromatic compounds. The relative strengths of the bands vary significantly from source to source, in particular the 7.7/8.6 band ratio with values ranging from 0.6 to ∼ 6. In some cases the 6.2 μm band is very strong- see spectrum (j) in Figure 2. These variations are possibly due to different mixtures of neutral/ionized and compact/non-compact PAHs resulting from the different physical conditions in the

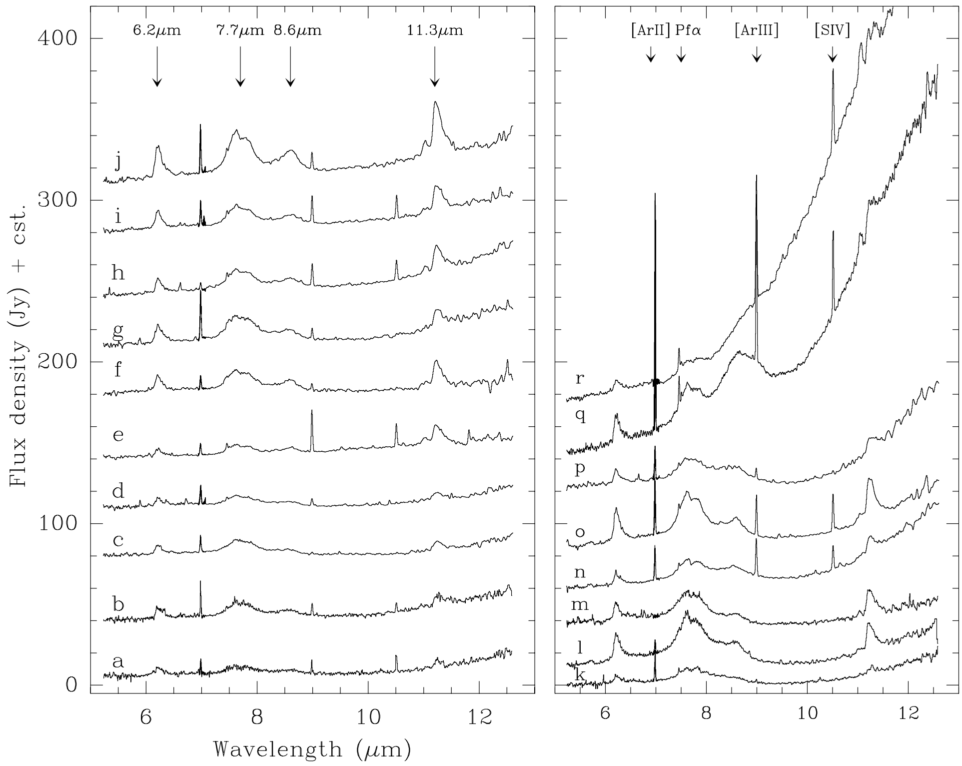

*Figure 3. The 5–13 μm SWS spectra of compact H*II *regions showing the shapes of the PAH features (identified in the figure) and variation of the relative intensities from source to source. No continuum has been subtracted. For display purposes additive factors have been used for each spectrum. The spectra are ordered by increasing strength of the continuum from bottom to top and from the left to the right panel. The sources are as follows: (a) IRAS 19207+1410, (b) IRAS 18502+0051, (c) IRAS 17279−3350, (d) IRAS 17221−3619, (e) IRAS 23030+5958, (f) IRAS 22308+5812, (g) IRAS 18116−1646, (h) IRAS 12063−6259, (i) IRAS 10589−6034, (j) IRAS 23133+6050, (k) IRAS 21190+5140, (l) IRAS 19442+2427, (m) IRAS 18162−2048, (n) IRAS 17455−2800, (o) IRAS 15384−5348, (p) IRAS 15502−5302, (q) IRAS 18434−0242, and (r) IRAS 12073−6233*

sources, such as the hardness of the radiation field (e.g., Roelfsema et al. 1996, 1998). As can be seen in Figure 3, the strongest 8.6 μm bands are present in the H II regions with the strongest mid-infrared continua and high excitation atomic fine structure lines ([SIV] and [ArIII]). Similar results are derived in the case of the H II region/Photodissociation interface in M 17 (Verstraete et al. 1996, Cesarsky et al. 1996).

3. RESULTS ON THE ABUNDANCE GRADIENT

The fine structure line of O^{++}, N^+, N^{++}, Ne^+, Ne^{++}, Ar^+, Ar^{++}, S^{++}, C^+, Si^+ and O^0 are detected in most sources allowing a precise determination of the abundances of oxygen, nitrogen, neon, argon and sulfur. The study of the last three species are prime diagnostics of the properties of the associated photodissociation regions.

For many of the sources reliable estimates have been obtained for the line intensities of Brα and several forbidden lines of various ionization stages of Ne, Ar, Si, O and N. A simplistic analysis based only on the line intensity ratios was carried out. As a result no conclusions with respect to absolute abundances can be drawn as yet. It should be noted that no corrections have been made for variations in the temperature or density which are expected to be small at infrared wavelengths.

Initial results concerning the abundances are shown in Figure 4. In the top and middle panels, the variations of the observed Ne^+ and Ar^+ intensities normalised to Brα are shown as a function of R_{gal}. These lines ratios should approximately indicate the behaviour of the ionic abundances of the species. A clear decrease is seen in both the neon and the argon ionic abundances towards the outer Galaxy (by a factor of 2 from 5 to 15 kpc). The bottom panel shows the ionic abundance ratio N^{++}/O^{++}, which is comparable to N/O for high-excitation sources, but is an upper limit to N/O for low-excitation sources (see Simpson et al. 1995). The present ISO sample together with previous results obtained with the KAO underscore the significant decrease of N^{++}/O^{++} with increasing $R_{\rm gal}$ out to large radii. The abundances of neon, argon and the N/O ratio all seem to decrease from the 4 kpc molecular ring to the central regions of the Galaxy. Due to the limited number of sources, this result should be confirmed by further data analysis.

The intensity ratios [NeIII] 15.56 μm/[NeII] 12.81 μm and [ArIII] 8.99 μm/[ArII] 6.99 μm are shown in

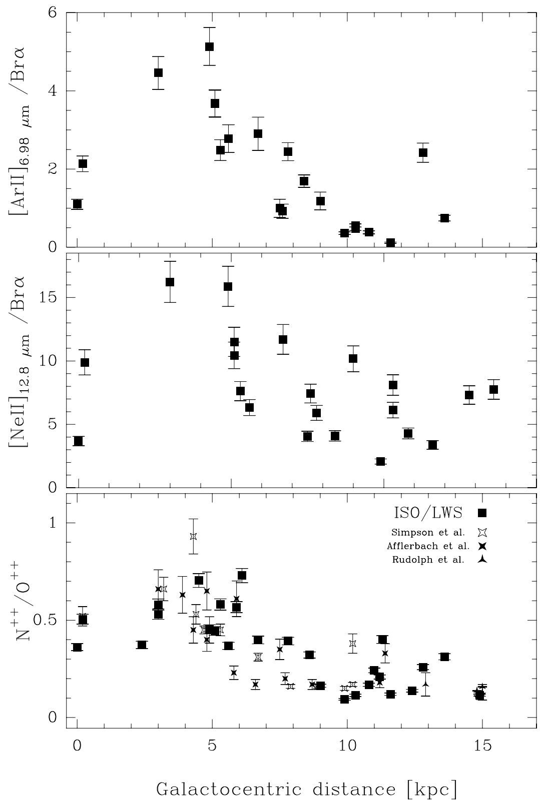

Figure 4. ISO results on the variations of the ionic abundances of Ne^+ and Ar^+ (normalised to Brα) and of the N^{++}/O^{++} *ratio as a function of galactocentric distance ($R_{\rm gal}$). In the bottom panel, the measurements of Afflerbach et al. (1997), Simpson et al. (1995) and Rudolph et al. (1997) are shown for comparison.*

Fig. 5. Both these line ratios are indicators for the degree of ionization of the observed nebula. The data show an increase in the hardness of the interstellar radiation field towards larger galactic radii.

4. SOURCES DOMINATED BY ABSORPTION

Depending on the geometry and/or the degree of evolution of the sources, the infrared spectra of compact H II regions can be entirely dominated by absorption bands. In one case, the source may be located behind a massive molecular cloud and observed through a large column density of molecular gas and dust, in another case, the young exciting star(s) is still embedded in its native environment and the small ionized region is surrounded by a large volume of dense molecular gas. The infrared spectra of embedded infrared sources have been important in the analysis of the refractory cores of dust grains (mainly the silicates) and have been the prime sources of information in deriving the chemical composition of the ice mantles which form around the dust cores in the cold regions deep inside molecular clouds (see, e.g. d'Hendecourt et al. in these proceedings).

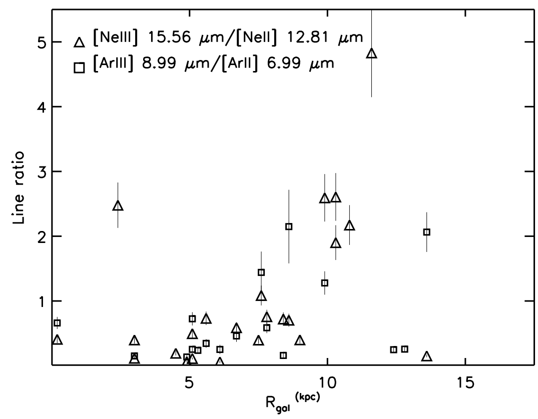

Figure 5. Line intensity ratios for ionization indicators as a function of galactocentric distance.

The combined SWS–LWS spectra of two embedded infrared sources, IRAS 18316−0602 and IRAS 19110+1045, have been presented by Dartois et al. (1998). Both are luminous protostars with luminosities of $10^{4.3}L_\odot$ and $10^{5.8}L_\odot$, respectively. IRAS 18316−0602 (also known as RAFGL 7009S) has been studied in detail by d'Hendecourt et al. (1996, and these proceedings) where the exceptional richness of its SWS spectrum has been reported. IRAS 19110+1045 is a young protostar associated with a dense, compact submillimeter source with evidence of infalling gas Hunter et al. (1997).

Figure 6 shows the SWS and LWS spectra of IRAS 18316−0602 and IRAS 19110+1045. No correction was applied to match the SWS and LWS portions of the spectrum. The good agreement in the overlap region of the two spectrometers (41–43 μm) confirms the high quality of the flux scale calibration of both instruments. Both spectra are dominated by a series of absorption bands which are identified in Fig. 6 – see the contribution of d'Hendecourt et al. in these proceedings for a description of the bands shortwards of 25 μm. Centred on the overlap region between the SWS and the LWS spectra, there is a broad absorption band at ∼ 44 μm which is identified with the transverse optical (TO) vibrational band of H_2O ice detected for the first time in absorption. There are differences in the band structure between the two sources which have been interpreted as due to different abundances of crystalline H_2O ice. A full description of these spectra and of the model shown in Figure 6 is given in Dartois et al. (1998).

These results clearly illustrate the importance of wide wavelength range spectroscopy even for the study of interstellar ices. All the well-known infrared embedded sources have been observed with ISO and it would be of great interest to make a systematic study of the combined spectra of these sources in order to investigate the changes in the shape of the 44 μm H_2O ice band as a function of the evolutionary state of the object.

The effects of extinction for some of the compact H II regions are also indicated in the far-infrared by molecular absorption bands of OH and H_2O. First

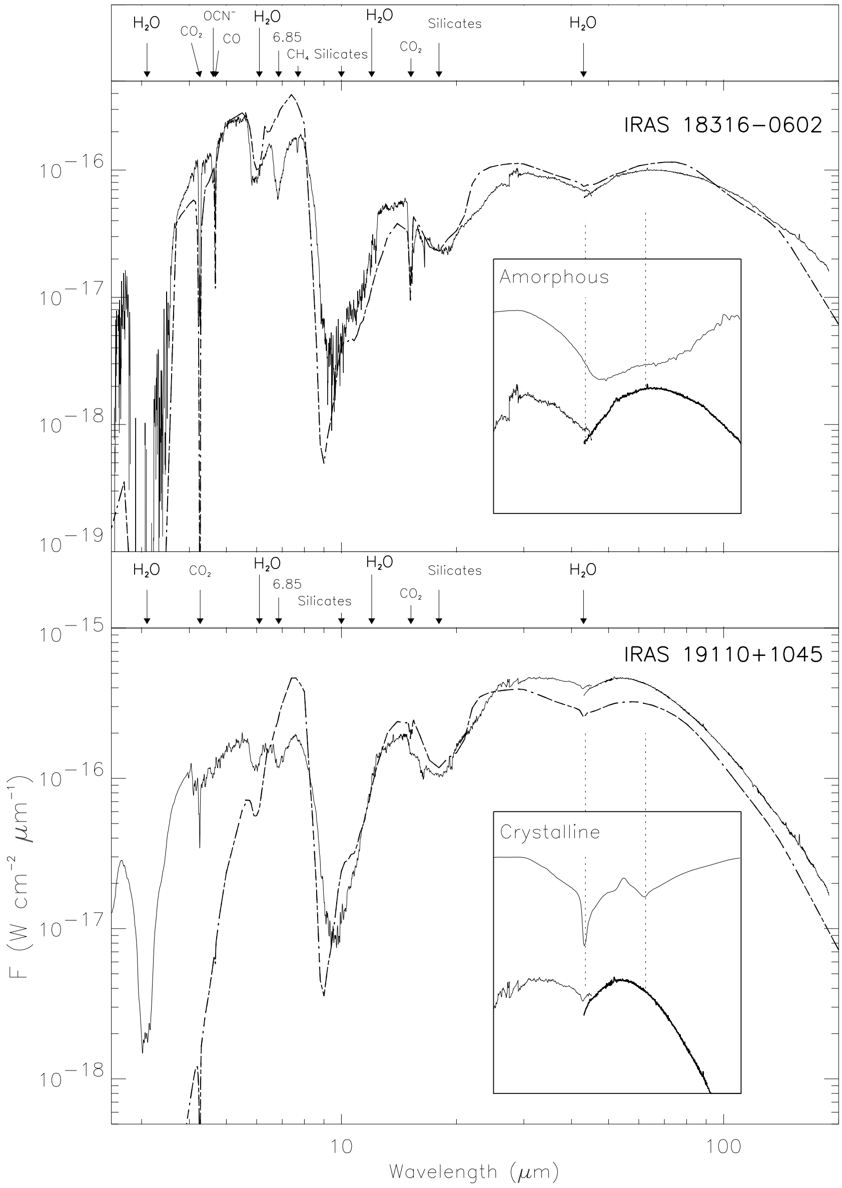

Figure 6. Combined SWS and LWS spectra of the embedded infrared sources IRAS 18316−0602 (RAFGL 7009) and IRAS 19110+1045. The position and the identification of the main absorption bands are given for each source. Note that the SWS and LWS spectra were calibrated independently and that no corrections were made to improve the match between the two instruments. The insert boxes display the transmittances of amorphous and crystalline water ices together with the source spectra - the intensity axis has been expanded for clarity purposes. The results of radiative transfer calculations (Dartois et al. 1998) are shown as dash-dotted lines.

analyses of the spectra of these sources show that the atomic fine-structure lines, in particular the [O I] and [C II] lines, might also be affected by absorption effects. The most spectacular case of the influence of absorption at far-infrared wavelengths is provided by the LWS spectrum of Sgr B2.

Sgr B2 is one of the most luminous star-forming regions in the Galaxy and consists of several compact H II regions embedded in a massive molecular cloud. The hydrogen column densities have been estimated to be a few 10^{24} cm^{-2} in the core of Sgr B2 and Harvey et al. (1977) derived an opacity of order unity at 100 μm. Figure 7 shows the LWS full grating spectrum of Sgr B2. The spectrum consists of a strong dust continuum (at 80 μm, the flux density is 34,000 Jy) with a series of lines and molecular bands *all* seen in absorption - see identification in Fig. 7. The signal-to-noise ratio being very high ($\sim$ 200) most of the features seen in the grating spectrum of Sgr B2 are likely real. At the resolution of the grating none of the atomic fine structure lines, such as the [O III] 52 μm, [O III] 88 μm, or [N III] 57 μm lines normally present in the spectra of compact H II regions, are detected. In addition, the [O I] 63 μm line is present in absorption and the usually dominant [C II] 158 μm line is not seen (Fig. 7). As discussed in Baluteau et al. (1997), the absorption of the 63 μm [O I] line implies a column density of atomic oxygen of the order of $(1-2) \times 10^{19}$ cm^{-2} and appears consistent with the fact that 40 to 100% of the interstellar oxygen is in atomic form along the line of sight to the Sgr B2 molecular cloud (see also J. Keene et al. in these proceedings).

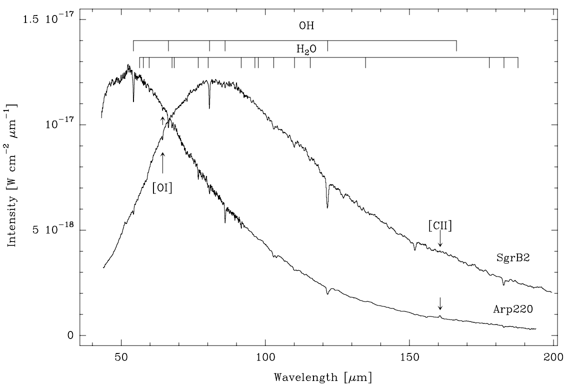

Figure 7. Comparison of the LWS spectra of SgrB2 and Arp220 (from Fischer et al. this conference). The spectrum of SgrB2 has been divided by a factor 115 and shifted to the redshift of Arp220. The main molecular absorption bands are identified together with the [OI] and [CII] lines.

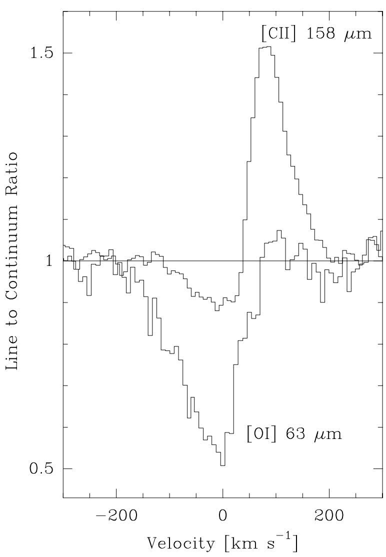

Figure 8. The LWS Fabry-Pérot spectra of Sgr B2 in [O I] 63.18 μm and [C II] 157.71 μm - from Swinyard et al. (in preparation).

It is interesting to compare the spectrum of Sgr B2 with that of Arp 220 which has been discussed by Fischer et al. (these proceedings). As in the case of Sgr B2, the spectrum of Arp 220 is dominated by molecular absorption bands, mainly from OH and H_2O, and shows the [O I] 63 μm line in absorption (see Figure 7). The [C II] 158 μm line is detected in emission but very weak. Whereas the explanation of the low [C II]/L_{FIR} ratio in galaxies with high dust temperatures (as measured by far-infrared colors $F_\nu(60\,\mu m)/F_\nu(100\,\mu m)$) is still debated, the above results indicate that extinction must play a role (see also Gérin & Phillips 1998), although high radiation fields per gas atom can lower the efficiency of the photoelectric heating and thus weaken the [C II] line intensity (see, e.g., Malhotra et al. 1997 and these proceedings). However, the fact that opacity effects are important is underscored by the LWS Fabry-Pérot spectrum of Sgr B2 which indicates that both the [O I] 63 μm and the [C II] lines are seen in absorption at negative velocities (Figure 8). At positive velocities, corresponding to Sgr B2, the [O I] line is not seen and [C II], which is seen in emission, is significantly reduced in intensity as compared to the prediction of standard PDR models (Swinyard et al. in preparation).

5. CONCLUSIONS

The possibility of making spectroscopic studies with ISO from 2.5 to 196 μm has opened up an entirely new field in the investigation of the properties of astronomical sources. This paper illustrates the potential of the combined SWS and LWS grating data and of detailed spectroscopy on dense galactic star-forming regions. It is clear that the rich harvest of spectra obtained during the ISO mission will provide for the years to come an important database to further study the physics and the chemistry of the interstellar gas and the nature of the interstellar dust grains and ice mantles.

Looking ahead, two major space missions will allow us to obtain complete spectra at infrared wavelengths. The Infrared Spectrograph (IRS) for the Space Infrared Telescope Facility (SIRTF) which enables low and moderate-spectral resolution spectroscopy from 4 to 40 μm (J.R. Houck et al. 1999, also M. Werner in these proceedings). On board the Far-Infrared Space Telescope (FIRST, see Bonnet at al. these proceedings), the heterodyne receivers, HIFI, which will cover at high spectral resolution the wavelength range from 200 to $\sim$ 600 μm Whyborn (1997), and the FTS imager of SPIRE which will allow uninterrupted spectro-imagery at variable spectral resolution between 20 and $\sim$ 1000 in the range 200 to 650 μm Griffin (1997).

REFERENCES

Afflerbach, A., Churchwell, E., Werner, M.W. 1997, ApJ, 478, 190

Baluteau, J.-P., et al. 1997, A&A, 322, L33

Cesarsky, D., Lequeux, J., Abergel, A., et al. 1996, A&A, 315, L309

Clegg, P.E., Ade, P.A.R., Armand, C. et al. 1996, A&A, 315, L38

Dartois, E., Cox, P., Roelfsema, P.R., Jones, A.P., Tielens, A.G.G.M., d'Hendecourt, L., Jourdain de Muizon, M., Schmitt, B., Lim, T., Swinyard, B., Heras, A. M. 1998, A&A, 338, L21

Gérin, M. & Phillips, T.G. 1998, ApJ, 509, L17

de Graauw, Th., Haser, L.N., Beintema, D.A. et al. 1996a, A&A, 315, L49

de Graauw, Th., Whittet, D.C.B., Gerakines, P.A. et al. 1996b, A&A, 315, L345

Griffin, M.J. 1997, in *The Far-Infrared and Submillimeter Universe* ESA SP-401, eds. M. Rowan-Robinson & G. Pilbratt, p.31

Harvey, P.M., Campbell, M.F., & Hoffman, W.F. 1977, ApJ 211, 786

d'Hendecourt L., Jourdain de Muizon M., Dartois E. et al. 1996 A&A, 315, L365.

Houck, J.R. et al. 1999, in *Astrophysics with Infrared Surveys: A Prelude to SIRTF*, eds. M. Bicay, R.M. Cutri, and B.F. Madore, to be published in the ASP Conference Series

Hunter T.R., Phillips T.G., Menten K.M. 1997 ApJ, 478, 283

Kessler, M.F., Steinz J.A., Anderegg M.E. et al. 1996, A&A, 315, L27

Léger, A., & Puget, J.-L. 1984, A&A, 137, L5

Malhotra, S. et al. 1997, ApJ, 491, L27

Roelfsema, P.R., Cox, P., Tielens A.G.G.M. et al. 1996, A&A, 315, L289

Roelfsema, P.R., Cox, P., Kessler, M.F., & Baluteau, J.-P. 1998, in *Star Formation with the Infrared Space Observatory*, ASP Conference Series, vol. 132, p. 76, J.L. Yun & R. Liseau (eds)

Rudolph, A.L., Simpson, J.P., Haas, M.R., Erickson, E.F., Fich, M. 1997, ApJ, 489, 94

Schaeidt, S.G., Morris, P.W., Salama, A. et al. 1996, A&A, 315, L55

Shaver, P.A., McGee, R.X., Newton, L.M., Danks, A.C., Pottach, S.R. 1983, MNRAS, 204, 53

Simpson, J.P., Colgan, S.W.J., Rubin, R.H., Erickson, E.F., Haas, M.R. et al. 1995, ApJ, 444, 721

Swinyard, B.M., Clegg, P.E., Ade, P.A.R. et al. 1996, A&A, 315, L43

Verstraete L., Puget J.L., Falgarone E., et al. 1996 A&A, 315, L337

Whyborn N.D. 1997, in *The Far-Infrared and Submillimeter Universe* ESA SP-401, eds. M. Rowan-Robinson & G. Pilbratt, p.19

ISO LWS OBSERVATIONS OF SGR B2: NH3 LINES

J-P. Baluteau[1], C. Ceccarelli[2], B.M. Swinyard[3], E. Caux[4], P. Cox[5], & S.D. Sidher[3]

[1]LAS, CNRS, Marseille, France
[2]LAOG, Grenoble, France
[3]RAL, Didcot, UK
[4]CESR CNRS-UPS, Toulouse, France
[5]IAS, Orsay, France

ABSTRACT

We report the observations of the pure rotational lines of NH_3 towards SgrB2(M). All lines are in absorption, the non-metastable lines being about a factor ten lower than the metastable lines. We discuss two possibilities: a) the non-metastable lines are radiatively pumped by the FIR source at ~ 1 pc which illuminates a tenuous (~ 1000 cm^{-3}) and hot (~ 400 K) gas or b) the non-metastable lines are collisionally pumped and originate in dense ($\sim 10^5$ cm^{-3}) and warm (~ 150 K) gas, whose column density is $\sim 6 \cdot 10^{15}$ cm^{-2}.

Key words: SgrB2; molecular lines

1. INTRODUCTION

The Long Wavelength Spectrometer (LWS: Clegg et al. 1996) on board the Infrared Space Observatory (ISO) offered an unique opportunity to completely explore the Far InfraRed (FIR) spectrum between 47 and 196 μm at both unprecedent high sensitivity and spectral resolution. Except for a few atmospheric windows accessible with the Kuiper Airborne Observatory (KAO), this spectral domain was essentially unexplored prior to ISO.

Cooling of the gas in the dense interstellar clouds takes place primarily at FIR and sub-mm wavelengths and depends on its chemical as well as physical conditions. Light molecules, mainly hydrides, believed to be the dominant coolants in many situations, have their rotational lines in the FIR, while heavier molecules emit mostly at mm wavelengths, which can in part be observed from ground. It is therefore of key importance to have an as complete as possible census of the lines emitted in the FIR range in order to understand the cooling mechanisms as well as the chemistry of the interstellar medium. Finally, absorption lines against strong continua have the advantage of allowing us to detect also relatively low density regions, unobservable with the "canonical" collisionally excited emission lines.

During the ISO Central Programme we carried out a systematic spectral survey in the direction of SgrB2, a dense star forming region molecular cloud close to the Galactic Center and one of the brightest known galactic IR sources. SgrB2 is a complex region which has been target of many studies. It is composed of more than fifty compact and ultra-compact HII regions, with the three brightest clusters named N (north), M (main) and S (south) respectively, roughly aligned in a N-S direction. These regions are embedded in a relatively dense ($\sim 10^5$ cm^{-3}) and warm (~ 100 K) medium which extends about 5 pc in the N-S direction and 2.5 pc in the W-E direction. Finally an hotter (~ 300 K) and tenuous (~ 1000 cm^{-3}) envelope extending for about 20 pc surrounds the entire SgrB2 complex (see e.g. de Vicente et al. 1997). This last hot component has been revealed by metastable NH_3 high-J inversion lines in absorption against the strong continua of M and N (Vogel et al. 1987; Hüttemeister et al. 1993). Here we report preliminary results of the observations of the rotational lines of NH_3, which allow a more complete view of the excitation mechanisms of this molecule.

2. OBSERVATIONS AND DATA REDUCTION

The region being very complex, more than one component will be inevitably be encompassed in the relatively large LWS beam (~ 80": Swinyard et al. 1998). In order to minimize the confusion we observed the position centered towards M, at 17^h 44^m 12.0^s, -28^o 22' 12" (1950), where neither N or S components enter in the LWS field of view. The observation consists of the complete spectrum between 47 and 196 μm, obtained at the highest spectral resolution possible with LWS, namely $\sim$8000. For this, we used the Fabry-Perot mode, namely the observation ISO AOT L03. L03 was the last LWS AOT to be commissioned and a partial description of its operation and calibration can be found in Clegg et al. (1996) and Swinyard et al. (1998). Mostly *ad hoc* routines were developed to reduce the data (see below). The complete spectrum was observed with 31 different AOTs between ISO revolution 476 (6 March 1997) and revolution 509 (8 April 1997), with a total target dedicated time

Proceedings of the Conference "The Universe as seen by ISO", Paris, France, 20–23 October 1998 (ESA SP-427, March 1999)

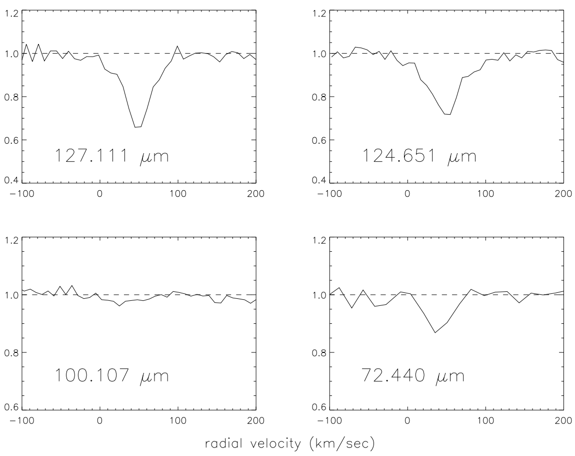

Figure 1. Selected ortho-NH_3 lines. Ordinates are the flux normalized to the continuum at each wavelength.

of 46.95 hours. Each mini-scan within any observation were repeated three times in order to get good confidence in the data. The integration time per individual data point was 0.5 sec.

The LWS FPs were calibrated by first setting the etalons to be parallel using strong, narrow emission lines. The wavelength calibration was then completed using various lines wavelength lines from a variety of sources. The wavelength calibration is accurate to within 15 km s^{-1}, or 1/2 a resolution element. There are some difficulties with establishing the instrument response function for the FPs as no lines are narrow enough that the response profile can be determined unambiguously. Similarly the transmission measurement of the FPs is also uncertain due to the same constraint. The calibration of the FP throughput is ongoing and new methods are being devised to solve this problem. The first level of pipeline processing of the LWS L03 data, i.e. converting the detector data from raw engineering values into photocurrent and providing the Standard Processed Data (SPD), is presently giving satisfactory results. The second level, Auto Analysis (AA) processing, which aims at converting from photocurrent into flux is still in progress. The present flux calibration depends critically on a few important parameters like the correct dark current level, the degree of contamination from adjacent FP orders, the correct position of the grating acting as a pre-filter. Some of these remaining problems will be solved in the next AA pipeline processing to be delivered soon.

The results presented here are believed to be quite well established. The new L03 pipeline will certainly allow more features to be detected, especially those which are faint and/or wider than the instrument profile. The data analysis is still in progress and specific publications, as regards the main molecular species, will appear in a near future. Fig. 1 shows a selection of four ortho-NH_3 lines. Given the limited space, in this contribution we will focus on the ortho-NH_3 lines only. Table 1 reports the list of NH_3 lines in the LWS wavelength range, with information about each line detection. The lines are centered at about 50 km s^{-1}, but the present uncertainty in the wavelength calibration cannot secure that our observations detected a component different from that seen in the radio at 65 km s^{-1}.

Table 1. List of NH_3 lines in the observed wavelength range. The central wavelength, Full Width Half Maximum, measured flux, energy of the upper level and the upper and lower states of the transition are in the first, second, third, fourth and fifth columns respectively.

λ (μm)	FWHM (μm)	Flux (W cm^{-2})	E_{up} (cm^{-1})	Transition
50.717		≤7e-19	790	(10,9)a-(9,9)s
55.814	0.005	-6.7e-19	656	(9,8)s-(8,8)a
56.340		≤6e-19	656	(9,8)a-(8,8)s
62.729	0.019	-4.2e-19	533	(8,7)s-(7,7)a
63.378	0.006	-2.6e-19	532	(8,7)a-(7,7)s
71.610	0.007	-1.9e-18	422	(7,6)s-(6,6)a
71.770		≤4e-19	463	(7,5)s-(6,5)a
72.440	0.012	-1.4e-18	422	(7,6)a-(6,6)s
72.526		≤5e-19	463	(7,5)a-(6,5)s
83.434	0.011	-3.1e-18	324	(6,5)s-(5,5)a
83.592		≤3e-19	357	(6,4)s-(5,4)a
83.712		≤3e-19	383	(6,3)s-(5,3)a
84.546	0.021	-2.5e-18	324	(6,5)a-(5,5)s
84.682		≤9e-19	383	(6,3)a-(5,3)s
99.952	0.013	-3.5e-18	239	(5,4)s-(4,4)a
100.107	0.011	-3.1e-19	265	(5,3)s-(4,3)a
100.215		≤3e-19	283	(5,2)s-(4,2)a
100.280	0.012	-2.4e-19	294	(5,1)s-(4,1)a
101.536	0.021	-5.9e-18	233	(5,4)a-(4,4)s
101.599		≤3e-19	264	(5,3)a-(4,3)s
101.645		≤4e-19	282	(5,2)a-(4,2)s
101.673		≤4e-19	293	(5,1)a-(4,1)s
124.651	0.024	-5.5e-18	166	(4,3)s-(3,3)a
124.799	0.023	-7.0e-19	184	(4,2)s-(3,2)a
124.887		≤4e-19	195	(4,1)s-(3,1)a
124.916		≤5e-19	199	(4,1)s-(3,0)a
127.111	0.019	-4.1e-18	165	(4,3)a-(3,3)s
127.156		≤3e-19	183	(4,2)a-(3,2)s
127.184		≤2e-19	194	(4,1)a-(3,1)s
165.601	0.024	-3.8e-18	105	(3,2)s-(2,2)a
165.733		≤4e-19	116	(3,1)s-(2,1)a

3. DISCUSSION

3.1. General considerations

As mentioned in the introduction, SgrB2 has been extensively studied in the ammonia inversion lines. Focusing on the 65 km s^{-1} component (probably that detected by our observations), the main results of these studies are the detection of:

a) several compact ($\sim 4''$), dense ($\geq 10^7$ cm^{-3}) hot ($\geq$ 300 K) cores (Gaume & Claussen 1990);

b) an extended ($\sim 4'$) region of emission of low J metastable transitions: the (1,1) and (2,2) maps show that the intensity of these lines peaks towards M and N. In contrast, metastable lines with $3 \leq J \leq 6$ are absorbed towards M and N and in emission elsewhere in the region. Finally, higher J (up to J=14) metastable lines are seen in absorption towards M and N (Hüttemeister et al. 1995, 1993).

c) A less extended region ($\sim 50''$ x $120''$) in which the (2,1) and (3,2) non-metastable transitions are seen in emission, with the peak of the (2,1) emission $10''$ west of M: towards M, non-metastable transitions with higher upper level energy show also a strong absorption around 50 km s^{-1}, while the emission component at 65 km s^{-1} vanishes (Hüttemeister et al. 1993) with increasing J.

Our observations revealed clearly *only absorption lines*, where, however, the non-metastable lines are at least a factor ten weaker than the metastable lines. Furthermore, the absorption *never reaches zero* indicating that either the lines are optically thin or they just cover 1/3 of the FIR source. The rotational diagram of the observed lines is shown in Fig.2. In the figure we also show the rotational temperature of the metastable lines, which has to be considered as lower limit to the kinetic temperature. The fact that the non-metastable lines are systematically lower in the rotational diagram suggests that the NH_3 lines are subthermally populated. In order to explain why the non-metastable lines are so weaker than the metastable lines, but still detected, there are two possibilities: either the non-metastable lines are radiatively populated by the strong FIR continuum or they are collisionally populated although they are far from LTE. In the following we will try to clarify the situation by means of an LVG model which includes the strong FIR continuum.

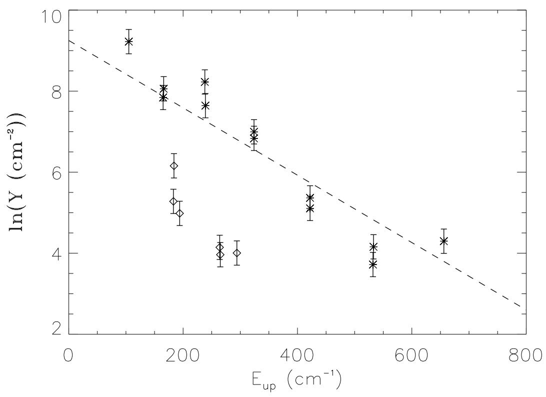

Figure 2. Rotational diagram of the observed lines. Asterisks refer to metastable lines and diamonds to non-metastable lines. The errors bars represent the calibration uncertainty only, ~ 30%. The dashed line is the best fit of the metastable lines and corresponds to a temperature of 120 K: if the point at 625 cm^{-1} -which has the largest statistical error- is not considered the rotational temperature is 95 K.

3.2. Modeling

The sketch of the model is shown in Fig.3. A FIR source, SgrB2(M), illuminates a slab of absorbing material: the distance between the slab and the FIR source is *dist*, while the distance between the slab and the observer is assumed to be 8.5 kpc. The intensity I_l of a line (either in emission or absorption) is given by the usual expression (e.g. Tielens & Hollenbach 1985):

$$I_l = \frac{1}{2\pi} \int_0^z dz' \; n_u \; A_{u,l} \; \beta_{u,l} \left(1 - \frac{P}{S}\right) \quad (1)$$

where n_u is the molecules in the upper level of the transition, $A_{u,l}$ is the spontaneous emission coefficient and $\beta_{u,l}$ is the probability that the photons escape absorption. S is the source function and P is

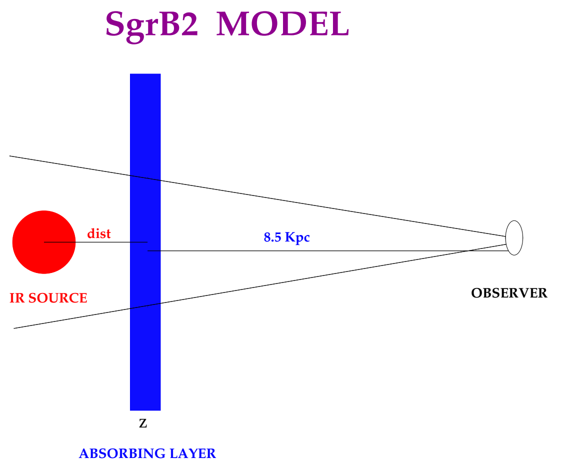

Figure 3. Sketch of the model: an absorbing layer of depth z lies between us and the FIR source SgrB2(M).

the observed intensity of the continuum emission at the wavelength of the transition. Eq. 1 implicitly assumes that the ratio S/P is constant over the solid angle. For absorption lines, when the source function and the stimulated emission can be neglected, Eq.1 gives the usual relation between the equivalent width and the column density (e.g. Spitzer 1968). When however the source function and the stimulated emission cannot *a priori* be neglected, one has to use Eq.1 and to solve the statistical equilibrium equations for the level populations to compute n_u and $\beta_{u,l}$:

$$n_u \sum_l (A_{u,l}\beta_{u,l} + B_{u,l}PW + C_{u,l}) = \sum_l n_l (A_{l,u}\beta_{l,u} + B_{l,u}PW + C_{l,u}) \quad (2)$$

where C are the collision coefficients, B the absorption coefficients and W is the dilution factor of the continuum emitted by the FIR source, which accounts for the angle within which the slab is illuminated by the FIR source:

$$W = \frac{1}{2}\left(1 - \sqrt{1 - \left(\frac{R_{FIR}}{dist}\right)^2}\right) \quad (3)$$

where R_{FIR} is 0.8 pc, assuming the distance of SgrB2 to be 8.5 kpc and the radial extent of the FIR source to be 40" (Goldsmith et al. 1990) at all considered wavelengths, a rough approximation of the reality. The escape probability β is function of the optical depth of the line and we used the relation valid in a planar slab (de Jong, Dalgarno, & Boland 1980). We assumed a linewidth of 15 km s^{-1}, as measured in the radio lines.

- Non-metastable lines radiatively populated

  Line intensity depends on the density, temperature and column density multiplied by the angular extent of the absorbing layer as well as on the distance between this layer and the FIR source.

  In practice, lines decaying towards metastable levels are rather insensitive to the last parameter, as their upper level populations depend mainly on the density and temperature of the slab: those lines can therefore be used to estimate the NH_3 column density multiplied by the

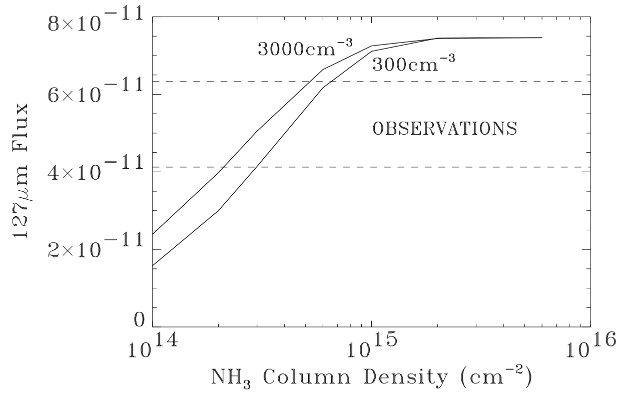

Figure 4. Flux (in erg s^{-1} cm^{-2}) of the (4,3)a-(3,3)s transition as function of the NH_3 column density, for two values of density. The curves are essentially the same varying the temperature from 200K to 500K.

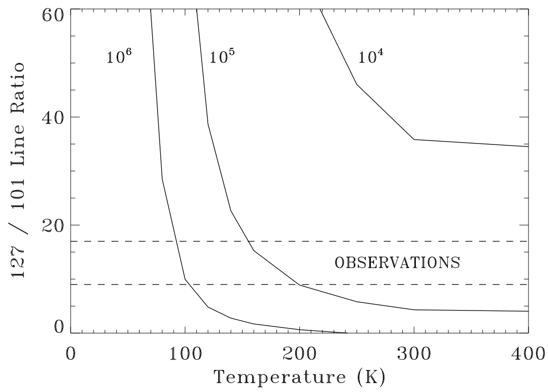

Figure 5. The (4,3)a-(3,3)s over (5,3)s-(4,3)a flux ratio as function of temperature for various densities.

layer angular extent, given a range of values for the density and temperature. Fig.4 shows the dependence of the 127.111μm (metastable) line flux as function of the NH_3 column density, assuming a (absorbing layer) filling factor equal to unity. The comparison of our observations with the predictions of Fig.4 suggests NH_3 column densities within 2 and 7 times 10^{14} cm^{-2}. The lines are predicted to be moderately optically thick ($\tau \sim 1$). In their study Flower et al. (1995) quoted NH_3 column densities about ten times higher than those we derived here, suggesting that the filling factor of our observations is less than unity, a fact also supported by the line absorption not reaching the zero level (see par. 3.1). However another possibility is that the LWS beam also probes a component in emission, which diminishes the strength of the absorption.

Non-metastable lines are very sensitive to the distance between the absorbing layer and the FIR source, as they can be populated by the FIR photons: they can therefore be used to estimate this parameter. Assuming N(NH_3)=$6{\cdot}10^{15}$ cm^{-2} and a filling factor equal to 0.1, we can derive an estimate of the distance (*dist*) by comparing the predicted 124.799 μm line flux with the observed one. We obtain a distance around 1 pc. *Therefore, a hot ($\sim$ 400K) and tenuous ($\sim$ 1000 cm^{-3}) gas at $\sim$ 1 pc from the FIR source can explain the FIR observations.*

- Non-metastable lines collisionally populated

The second possibility is that indeed the non-metastable lines are collisionally populated. Since apparently we detected only three non-metastable lines in absorption, at this stage of data analysis this argument can be used to put an upper limit to the density of the medium. Fig. 5 shows the 127.111 to 100.107 μm line ratio as function of temperature for densities between 10^4 and 10^6 cm^{-3} and N(NH_3)=$6{\cdot}10^{15}$ cm^{-2}. Fig.5 shows that also *a dense ($\sim 10^5$ cm^{-3}) and warm ($\sim$ 150 K) gas filling the LWS beam and whose column density is $\sim 6 \cdot 10^{15}$ cm^{-2} can explain the FIR observations.*

ACKNOWLEDGMENTS

We wish to warmly thank Malcolm Wamsley for insightful discussions, Pierre Valiron for providing us the electronic file for the NH_3 collisional coefficients and the entire LWS team, whose work made these observations possible.

REFERENCES

Clegg P.E. et al., A&A 315, L38, 1996

de Jong, T., Dalgarno, A., Boland 1980, A&A, 91, 68

de Vicente P., Martin-Pintado J., Wilson T. A&A 1997, A&A 320, 957

Flower D.R., Pineau des Forêts G., Wamsley M. 1995, A&A 294, 815

Gaume R.A., Claussen M.J. 1990, ApJ 351, 538

Goldsmith P.F., Lis D.C., Hills R., Lasenby J. 1990, ApJ 350, 186

Hüttemeister S., Wilson T.L., Henkel C., Mauesberger R. 1993, A&A 276, 445

Hüttemeister S. et al. 1995, A&A 294, 667

Swinyard B.M. et al. 1998, SPIE Vol. 3354, p. 888

Spitzer 1968, "Physical processes n the interstellar medium", eds. J.Wiley & Sons, Inc.

Tielens X., Hollenbach D. 1985, ApJ 291, 722

Vogel S.N., Genzel R., Palmer P. 1987, ApJ 316, 243

FIR CO LINE EMISSION OF PROTOSTARS IN NGC1333

E. Caux[1] C. Ceccarelli[2] A. Castets[2] L. Loinard[3], S. Molinari[4], P. Saraceno[5], H.A. Smith[6], & G.J. White[7]

[1]CESR, BP 4346, F-31028 Toulouse Cedex 04, France
[2]Laboratoire d'Astrophysique de l'Observatoire de Grenoble, B.P.53X, F-38041 Grenoble Cedex, France
[3]Institut de Radio Astronomie Millimetrique, F-38406 St. Martin d'Hères, France
[4]IPAC, California Institute of Technology, MS 100-22, Pasadena CA 91125, USA
[5]IFSI - CNR, Via G. Galilei, CP27, 00044 Frascati, Italy
[6]Harvard-Smithsonian Center for Astrophysics, 60 Garden Street, Cambridge MA 02138, USA
[7]Queen Mary & Westfield College, Mile End Road, London E1 4NS, UK

ABSTRACT

Using the Long Wavelength Spectrometer aboard ISO, we have observed three very young sources (Class 0 or I) in the molecular cloud NGC1333. We discuss in this contribution the FIR CO line emission observed towards the sources themselves and conclude that both a rather warm ($\sim$ 1500 K) and dense ($\sim 10^5$ cm^{-3}) gas or a colder ($\sim$ 300 K) and much denser ($\geq 10^8$ cm^{-3}) gas are consistent with the data. Based on this analysis only we cannot distinguish between the two cases and therefore assess whether the observed emission originates in a shock associated with the outflow or in the innermost, dense and warm regions of the envelopes that surround these sources.

Key words: molecular lines; star formation.

1. INTRODUCTION

The Long Wavelength Spectrometer (LWS) on board the Infrared Space Observatory (ISO) allowed for the first time to investigate the line emission from relatively low-luminosity sources in the FIR wavelength range. A handful observations have already been published (Liseau et al. 1996; Nisini et al. 1996; Saraceno et al. 1996; Ceccarelli et al. 1998a, 1998b, 1999a), showing intense CO emission from the high J rotational transitions in young low-luminosity sources (see also Saraceno et al. in these proceedings). The origin of the observed emission is still controversial, mainly because the relatively large beamwidth ($\sim$ 80″) and small spectral resolution ($\sim$ 250) of these observations does not allow to locate exactly where the emission originates. Ceccarelli et al. (1998a) suggested that the FIR CO lines originate in the same region traced by the J=6 transition (which is observed with ground based telescopes having much higher spectral and spatial resolution than ISO), and that probably originate in the shock caused by the interaction of the outflows with the surrounding medium. However, Saraceno et al. (these proceedings) considered a sample of five embedded very young sources in which molecular line emission was measured and concluded that current shock models fail to account for the observed emission. Finally, Ceccarelli et al. (these proceedings) suggested that the FIR water emission observed in the same sources originates in the innermost, dense and warm, regions of envelope.

In this contribution we present the ISO-LWS observations obtained towards three young embedded sources in NGC1333 and discuss some implications.

2. OBSERVATIONS AND RESULTS

The three sources IRAS2, IRAS4 and IRAS6 in NGC1333 were observed as part of the Guaranteed Time Program of the LWS. The observations were performed during revolutions 831 and 847, thanks to the extended lifetime of ISO. IRAS2 was observed on 5 positions, one on-source, and four on each side of the two perpendicular outflows. IRAS4 was observed on 3 positions, one on-source, and two on each side of the outflow. IRAS6 was only observed on-source. Fig. 1 shows the 1.3mm continuum map of the region and the observed positions.

In this contribution, we only discuss the origin of CO line emission observed on-source.

The ISO-LWS observations were performed using the AOT L01 (grating scans, spectral resolution $\sim$ 250 - Clegg et al. 1996, Swinyard et al. 1996) with an oversampling of 4. The integration time used on-source was $\sim$32 sec per spectral element. Fig. 2 presents six of the CO lines observed on the source IRAS6. The lines are fitted with gaussian profiles.

Table 1 lists the line fluxes measured towards each source.

Proceedings of the Conference "The Universe as seen by ISO", Paris, France, 20–23 October 1998 (ESA SP-427, March 1999)

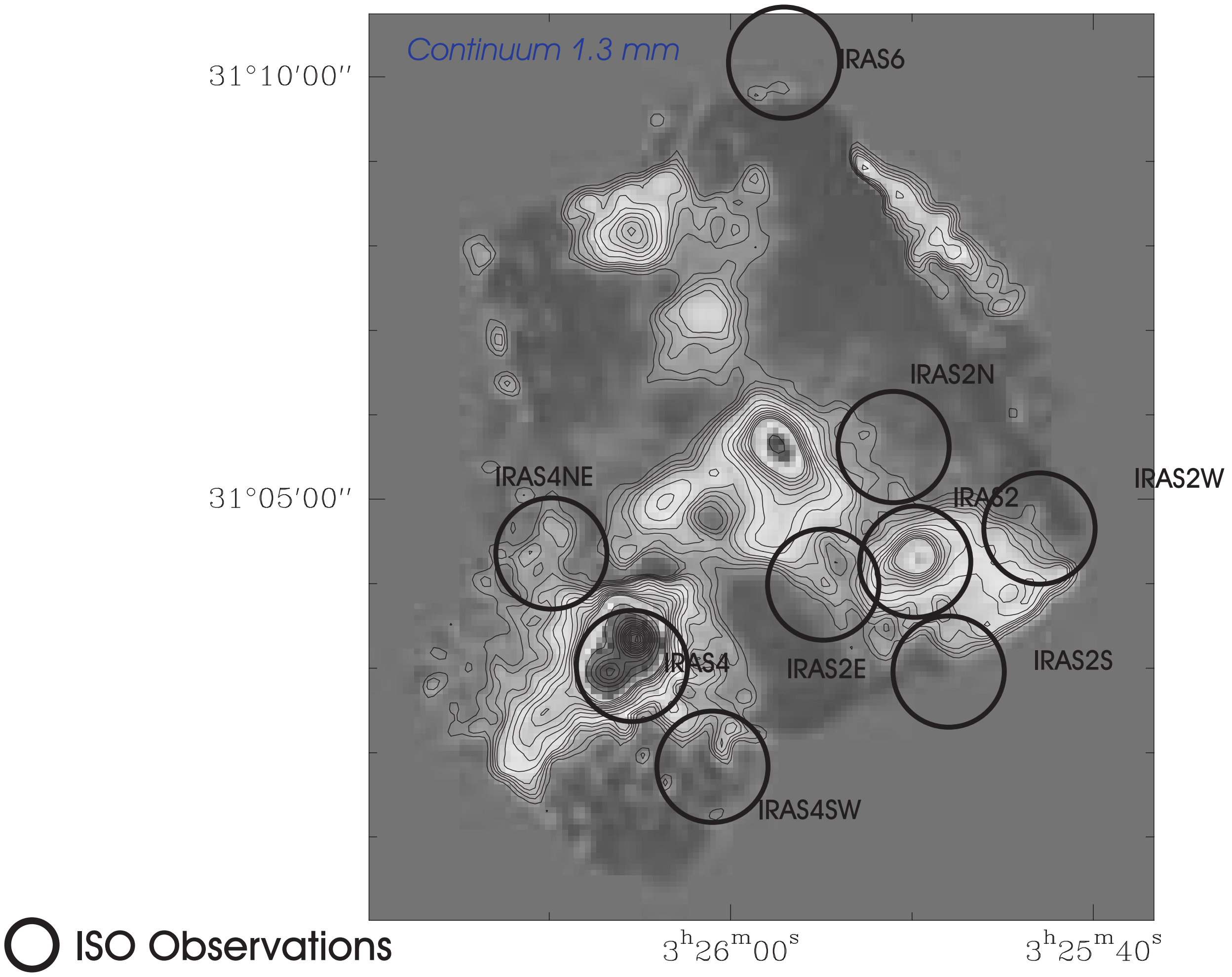

Figure 1. Observations of ISO-LWS of the molecular cloud NGC1333. The observed positions (circles) are overimposed to the 1.3mm continuum map (gray colours) obtained by Lefloch et al. (1998).

Table 1. Observed high J CO rotational lines on the sources IRAS2, IRAS4 and IRAS6 in NGC1333. Line flux unit: 10^{-12} *erg* s^{-1} *cm*$^{-2}$

CO line	IRAS2	IRAS4	IRAS6
(14-13)	0.43	1.72	0.58
(15-14)	0.32	1.54	0.58
(16-15)	0.32	1.44	0.55
(17-16)	0.22	1.28	0.46
(18-17)	0.24	1.20	0.43
(19-18)	nd	1.12	0.41
(20-19)	0.23	0.81	0.37
(21-20)	nd	0.62	nd

One can note that the CO line spectra of the three sources are remarkably similar, *the main difference being a mere multiplicative factor*. This is also what we found for the H_2O line spectra of these three sources, which show line ratios between the sources rather independent on the upper level of the transition (Ceccarelli et al. 1999a, see also Ceccarelli et al. in these proceedings). This characteristics implies that the excitation conditions, i.e. gas density and temperature, in the three sources are very similar.

3. DISCUSSION

To interpret the CO emission, we used a LVG model, applied to a slab geometry (see Ceccarelli et al. 1998a). This model considers the first 50 rotational levels (collisional excitation rates from McKee et al. 1982) and a ratio [CO]/[H2] = 10^{-4}. The free parameters of the model are the gas density, temperature and CO column density. Given the relatively large ISO-LWS beam also the source extent enters as a free parameter in modelling the absolute flux of the observed lines. Note that the two last parameters, the CO column density and source extent, are independent only if the lines are optically thick.

We used the ratio of the observed lines with the highest (J=20) and lowest (J=15) energy level to constraint the range of allowed temperatures and densities. As previously mentioned, the J=15 over J=20 line ratio is remarkably similar in the three sources, being 1.3, 1.5 and 1.9 in IRAS2, IRAS6 and IRAS4 respectively (the slight difference is within the calibration error of the fluxes, so it is not considered real). In Fig. 3, we report the J=15 over J=20 line ratio as function of density and temperature: as already known (Ceccarelli et al. 1998a) the FIR lines observed with ISO-LWS alone cannot efficiently constraint the two parameters. In this specific case either

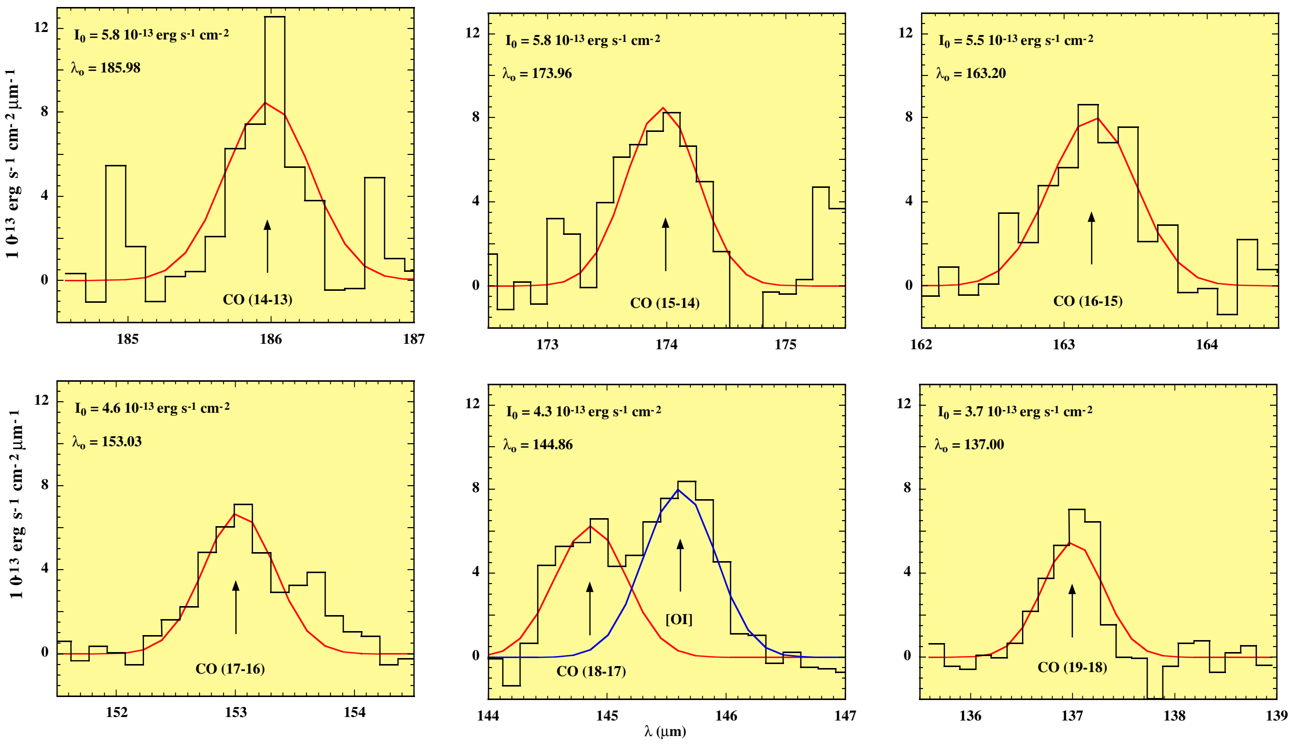

Figure 2. Observed CO lines on the source IRAS6

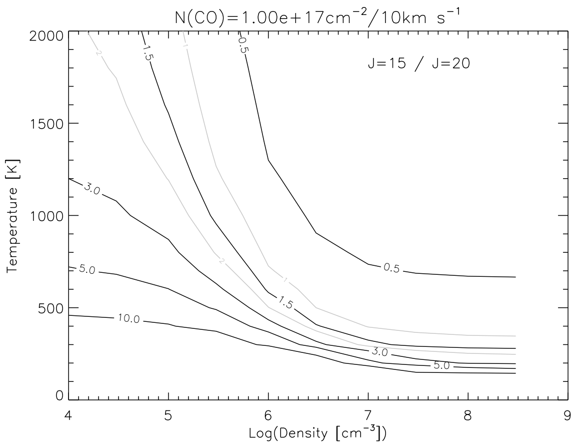

Figure 3. CO line J=15 / J=20 ratio as function of temperature and density. The range of observed values is marked by the grey lines. The CO column density is 10^{17} cm^{-2} with $\delta v = 10$ km s^{-1}.

a rather warm ($\sim$ 1500 K) and dense ($\sim 10^5$ cm^{-3}) gas or a colder ($\sim$ 300 K) and much denser ($\geq 10^8$ cm^{-3}) gas are consistent with the data.

This is also shown in Fig. 4, where the CO observed and computed spectra are reported for each source. The less dense case would probably correspond to a shock originated at the interface of the outflow with the surrounding medium (Ceccarelli et al. 1998a), while the extreme denser case may be explained either by a denser shock or in term of thermal emission from the surrounding envelope (Ceccarelli et al. 1999a and 1999b, these proceedings). At this stage of the analysis we cannot distinguish between these different hypothesis. Assuming a CO column density of N[CO] = 10^{18} cm^{-2}, the typical sizes of the emitting regions for the three sources are:
IRAS2: 6"x 6", IRAS4: 3"x 3", IRAS6: 5"x 5"
where we emphasize that, since the lines are predicted to be optically thin, *we can only constraint the product of the CO column density and the source extent.* Therefore the difference in the CO emission of the three sources has to be attributed either to a different CO column density or to a different angular extent of the emitting region.

Finally, we notice the striking difference between the CO line spectra of our sources when compared to that observed towards HH54B (Liseau et al. 1996). In HH54B the J=15 / J=20 ratio is larger than 10, implying a gas either colder or less dense (see Fig. 3) of that responsible of the CO emission in the three sources of our sample. In the HH54B case CO line emission was attributed to a low velocity, C-type shock. Clearly, if the origin of the observed CO emission in the sources of our sample is also a shock, it has to be a different shock than that seen in HH54B.

4. CONCLUSIONS

We obtained ISO-LWS spectra at low spectral resolution ($\sim$ 250) of three young protostars in the NGC1333 molecular cloud.

The on-source spectra are dominated by high-J CO rotational line emission detected from J = 14 up to J = 21. The three sources have a similar J=15/J=20 ratio ($\sim$ 1.5), implying similar excitation conditions. This ratio is definitely different from that observed

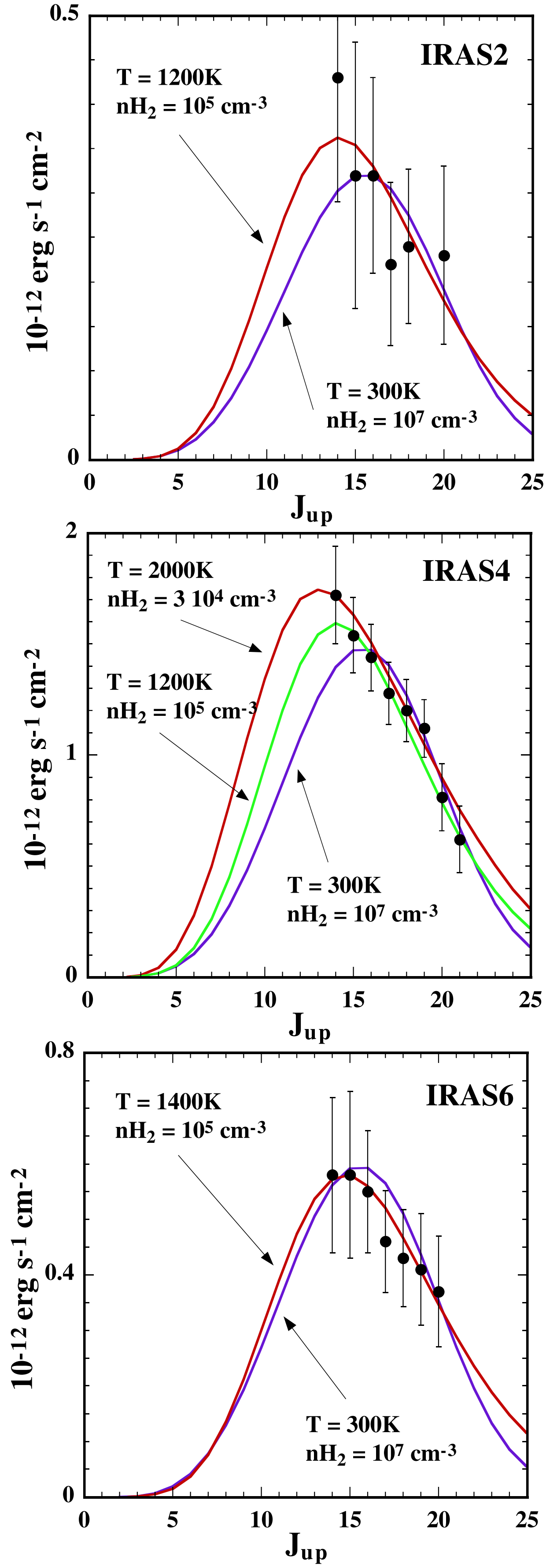

Figure 4. CO line spectrum of IRAS2 (top), IRAS4 (middle) and IRAS6 (bottom) as function of the upper level J.

toward HH54B (Liseau et al. 1996). In that case, the CO emission originates in a low velocity shock.

The observed line fluxes are consistent with either a high density ($\geq 10^8$ cm^{-3}) and a warm gas ($\sim$ 300 K), or a less dense gas ($\sim 10^5$ cm^{-3}) and warmer gas ($\sim$ 1500 K).

Since the lines are predicted to be optically thin, we can only estimate the product CO column density multiplied by angular extent of the sources. Then the difference in the absolute fluxes between the three sources has to be attributed either to a different column density or a different extent of the emitting region.

ACKNOWLEDGMENTS

We wish to thank the entire LWS team, whose dedication allowed the observations presented in this contribution.

REFERENCES

Ceccarelli C., Caux E., White G.J. et al. 1998a, A&A 331, 372

Ceccarelli C., Caux E., Wolfire M. et al. 1998b, A&A 331, L17

Ceccarelli C., Caux E., Loinard L. et al. 1999a, A&A in press

Clegg P., Ade P.M.S., Armand C. et al. 1996, A&A 315, L38

Lefloch B., Castets A., Cernicharo J., Loinard L. 1998, ApJ 504, L109

Liseau R., Ceccarelli C., Larsson B., et al. 1996, A&A 315, L181

McKee C.F., Storey J., Watson D., Green S. 1982, ApJ 259, 647

Nisini B., Lorenzetti D., Cohen M. et al. 1996, A&A 315, L321

Saraceno P., Ceccarelli C., Clegg P.E. et al. 1996, A&A 315, L293

Swinyard B.M., Clegg P.E., Ade P.A.R. et al. 1996, A&A 315, L43

WATER LINE EMISSION IN LOW-MASS PROTOSTARS

C. Ceccarelli[1], E. Caux[2], L. Loinard[3], A. Castets[1], A.G.G.M Tielens[4], S. Molinari[5], R. Liseau[6], P. Saraceno[7], H.A. Smith[8], & G.J. White[9]

[1]Laboratoire d'Astrophysique de l'Observatoire de Grenoble, B.P.53X, F-38041 Grenoble Cedex, France
[2]CESR-CNES, 9 Avenue de Colonel Roche, F-31029 Toulouse, France
[3]Institut de Radio Astronomie Millimetrique, F-38406 St. Martin d'Hères, France
[4]SRON, P.O. Box 800, 9700 AV, Groningen, The Netherlands
[5]IPAC, California Institute of Technology, MS 100-22, Pasadena CA 91125, USA
[6]Stockholm Observatory, S-133 36 - Saltsjobaden, Sweden
[7]IFSI - CNR, Via G. Galilei, CP27, 00044 Frascati, Italy
[8]Harvard-Smithsonian Center for Astrophysics, 60 Garden Street, Cambridge MA 02138, USA
[9]Queen Mary & Westfield College, Mile End Road, London E1 4NS, UK

ABSTRACT

Using the Long Wavelength Spectrometer on board ISO, we have detected far infrared rotational H_2O emission lines in five low-mass young stellar objects in a survey of seven such sources. The total H_2O fluxes are well correlated with the 1.3 mm continuum fluxes, but – surprisingly – not with the SiO millimeter emission originating in the outflows, suggesting that the water emission arises either in the circumstellar envelopes or in slow and dense shocks in the outflows. In this contribution we analyze in detail the case of NGC1333-IRAS4 and IRAS16293-2422, in which we measured several H_2O lines, and use their fluxes to put stringent constraints on the physical conditions (temperature, density and column density) of the emitting gas. Simple LVG modelling implies that the emission originates in a very small ($\sim$ 200 AU), dense ($\geq 10^7$ cm^{-3}) and warm ($\sim$ 100 K) region, with a column density larger than about 10^{16} cm^{-2}. The detected H_2O emission may be well accounted for by thermal emission from a collapsing envelope, and we derive constraints on the accretion rate and central mass of NGC1333-IRAS4. We also discuss an alternative scenario in which the H_2O emission arises in an extremely dense shock very close to the central object, perhaps caused by the interaction of the outflow with the inner regions of the circumstellar envelope.

Key words: molecular lines; star formation; young sources.

1. INTRODUCTION

In the quiescent ISM, most water molecules are believed to be frozen into the icy mantles of the dust grains (e.g. van Dishoeck & Blake 1998). However, if a phenomenon energetic enough to evaporate or destroy those mantles occurs, water can be released into the gas phase. In addition, at temperature larger than about 250 K, endothermic reactions in the gas phase can efficiently transform the oxygen not locked into CO molecules into H_2O molecules (Graff & Dalgarno 1987). Both effects can lead to high enhancements of the water gas phase abundance, and lead to intense emission in its far infrared rotational lines. Energetic phenomena and heating are known to occur near low-mass protostars: powerful outflows create strong shocks (e.g. Hollenbach & McKee 1989; Kaufman & Neufeld 1996), while in the infalling envelopes, heating due to the central source and/or to compression of the gas, may be sufficient to produce large over-abundances of water (Ceccarelli, Hollenbach & Tielens 1996).

Table 1. Basic parameters of the observed sources

Source	D (pc)	L ($L_\odot$)	Class	Cloud
IRAS16293	120	27	0	ρ Oph
16293-SE[1]	120	2	0	ρ Oph
EL29	120	36	I	ρ Oph
IRAS2	200	13	I	NGC1333
IRAS4	200	9	0	NGC1333
IRAS6	200	9	I	NGC1333
SSV13	200	27	I	NGC1333

2. OBSERVATIONS AND RESULTS

The sample consists of seven young (Class 0 or I) sources, all of which located in the ρ-Ophiuchus and NGC 1333 cloud complexes (Table 1). While the distance to ρ-Oph is fairly well known (120 pc – Knude & Hog 1998), the distance to NGC 1333 remains a

[1] 16293-SE is a recently discovered young source (Loinard et al., in prep.).

Proceedings of the Conference "The Universe as seen by ISO", Paris, France, 20–23 October 1998 (ESA SP-427, March 1999)

matter of debate. The distance commonly used is 350 pc, but Cernis (1993) recently proposed a somewhat lower value of 200 pc. The latter value will be used here, but we emphasise that most of our conclusions would stand essentially unaffected if 350 pc was used instead.

The H_2O spectra were obtained using the *Long Wavelength Spectrometer* (hereafter LWS) on board the ISO satellite in the LWS01 mode. They cover the spectral range from 45 to 200 μm at a resolution of about 250; the beamwidth is $\sim 80''$ (Swinyard et al. 1996). A more detailed description of the observations and data analysis is given in Ceccarelli et al. (1999a). Table 2 lists the observed sources and measured H_2O line fluxes towards each source.

3. DISCUSSION

Ceccarelli et al. (1999a) showed that the measured H_2O flux is not correlated with the SiO flux detected towards each source, while it seems to be correlated with the 1.3mm continuum flux. This situation suggests either that *water forms in low ($\leq$ 50 km s^{-1}) velocity shocks (which however do not occur where the high velocity shocks probed by SiO emission are found)* or that *water does not originate in shocks.* Furthermore, either *water emission is associated to the thermal emission from the envelopes themselves*, or *it originates in shocks where the shocked material belongs to the envelopes.*

3.1. Physical conditions of the emitting gas

The ratio between the H_2O line fluxes in IRAS16293 and IRAS4 are fairly similar in all the detected lines (Table 2), implying that the physical conditions in both sources (i.e. gas temperature and density) are similar as well. For the other sources, the small number of transitions detected does not significantly constraint the parameter space.

To constraint the physical conditions of the emitting gas, we modelled the H_2O lines using an LVG code. This model takes into account the first 48 rotational levels of ortho H_2O (the collisional excitation rates are from Green et al. 1993), but does not take into account the continuum emission. The spectroscopic data are taken from the JPL catalogue (Pointer & Pickett 1985). LVG predictions depend upon four parameters: the density and the temperature of the gas, the angular extent of the emitting region and the H_2O column density divided by the velocity gradient (which regulates the optical depth of the lines). The line ratios on the other hand depend mainly on the gas temperature and density, and to a smaller extent on the column density when the lines are optically thick. Hence, in the first step, we used the observed line ratios to estimate the temperature, density and H_2O column density of the gas, and later compared the absolute fluxes deduced from the model with the observed fluxes to infer the angular extent of the source.

The models were applied to IRAS16293 and IRAS4, and used the ratios between the 179, 174, 132 and 75 μm lines (which cover the widest range of upper level energies). Comparison between the model predictions and the observed line ratios (Fig. 1) shows that the emitting gas is dense (n $\geq 10^7$ cm^{-3}) and warm (T $\sim$ 100 K) and that the lines are optically thick. In particular, the lines at 132 μm and 75 μm set stringent constraints on the density. These depend on the actual H_2O column density, as shown in Fig. 2. Comparison of the observations with the predictions of Fig. 2 suggests that the H_2O column density is larger than $3{\cdot}10^{15}$ cm^{-2}.

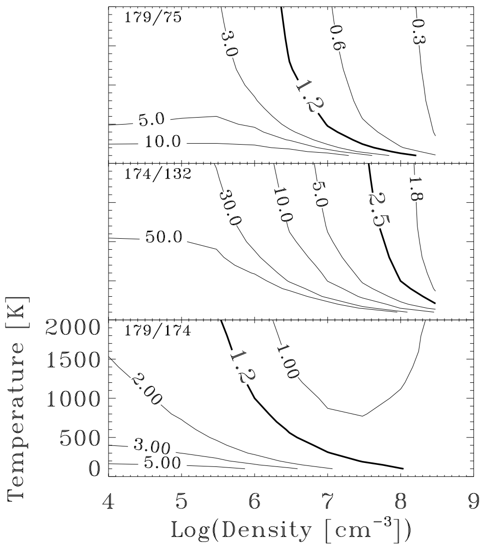

Figure 1. Ratios between the 179 and 174 μm lines (bottom), 174 and 132 μm lines (middle) and 179 and 75 μm lines (top), assuming N(H_2O)=10^{16} cm^{-2} and Δv=10 km s^{-1}. The observed values are shown by the thick lines.

One of the best fit to the IRAS4 data is obtained for n = $2 \cdot 10^8$ cm^{-3}, T = 200 K, and N(H_2O) = 10^{16} cm^{-2} (where we used a linewidth equivalent to Δv=10 km s^{-1}). The ratio between the predictions of this model and the observed values (top of Fig. 3) implies a beam filling factor of about $1/800\times \frac{\Delta v}{10\mathrm{km\ s^{-1}}}$. The corresponding angular size of the emitting region is therefore $\sim$ 2-3$''$, corresponding to a physical size of a few hundred AU. Slight discrepancies between the model and the observations occur systematically for the shorter wavelength lines, and may be a consequence of the lack of continuum background in our computations.

Finally, we note that the ratio between the 179 and the 174 μm lines is five times greater in HH54B than in all our sources. This indicates that the emitting regions are either much denser or much warmer (or both) in our sources than in HH54B, where the emission was ascribed to a mild shock (Liseau et al. 1996). In conclusion, the analysis of this paragraph and of the previous one lead to a rather clear situation and two possibilities to explain the observed H_2O emission: a) it is emitted in a very dense, warm and compact region, excited by a dense and relatively slow shock close to the central object, maybe caused by the interaction of the outflow with the inner regions of the circumstellar envelope, or b) to the thermal emission of these regions. We will consider in more detail these two possibilities in the next two paragraphs.

Table 2. Water line fluxes (in 10^{-12} erg s^{-1} cm^{-2}) detected towards the sources of the sample. The statistical errors are ~ 0.2 or less in these units.

Wavelength (μm)	Transition	16293	iras4	iras2	ssv13	iras6	16293-SE	EL 29
180.5	$2_{21}-2_{12}$	0.92	0.74	$\leq$0.3	0.4			
179.5	$2_{12}-1_{10}$	2.94	2.10	0.58	0.5	$\leq$0.6	$\leq$0.9	$\leq$1.5
174.6	$3_{03}-2_{12}$	2.55	1.66	$\leq$0.5	1.14	$\leq$0.6	$\leq$0.9	0.92
132.4	$4_{23}-4_{14}$	1.33	0.56	0.27	$\leq$0.3			$\leq$0.6
108.1	$2_{21}-1_{10}$		1.66	0.4				
99.5	$5_{04}-4_{14}$		1.02					
78.7	$4_{23}-3_{12}$		0.93					
75.4	$3_{21}-2_{12}$	2.66	1.56	$\leq$1	$\leq$1			
67.3	$3_{30}-3_{03}$		0.58					
138.5	$3_{13}-2_{02}$	0.94	0.86					
101.0	$3_{03}-2_{20}$	1.3	1.15					
90.0	$3_{22}-2_{11}$	0.47	1.76					

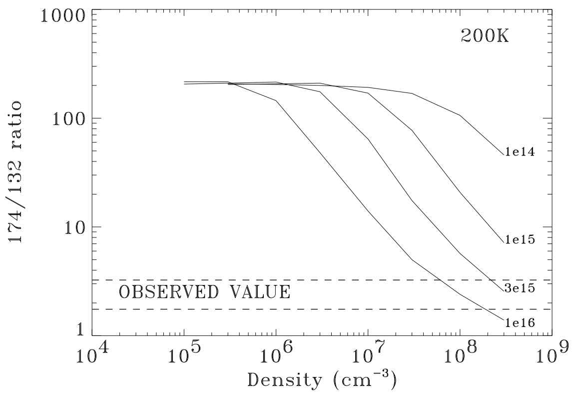

Figure 2. Ratios between the 174 and 132 μm lines as function of density for different H_2O column density values.

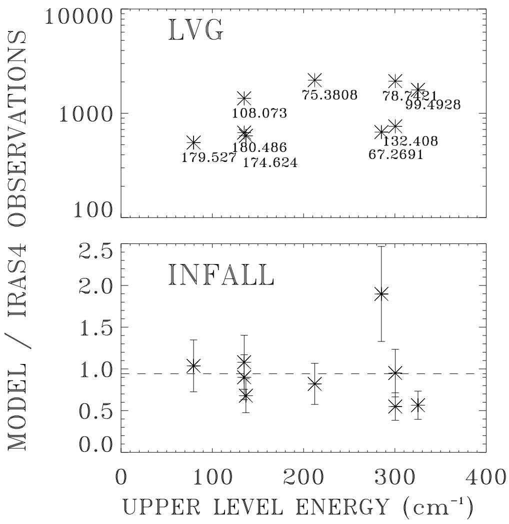

Figure 3. Ratio between LVG model (top) or "infalling envelope" model (bottom) and observations of IRAS4.

3.2. The dense shock hypothesis

As noted above, if the H_2O emission has to be attributed to a shock this is a shock totally different to those responsible for the SiO emission, implying a rather low velocity ($\leq$ 50 km s^{-1}). The presence of such a shock very close to the central object and due to the interaction of the outflow with the dense environment is suggested by the strong 22 GHz H_2O maser emission ($\sim 10^{-9}$ L_{bol}) with velocities ($\geq$ 7 km s^{-1}) in excess to the relevant keplerian velocities (e.g. Claussen et al 1996). The best-fit LVG model mentioned in the previous paragraph predicts a 22 GHz luminosity $\sim 4\cdot10^{-11}$ $L_\odot$, much lower than the mentioned observations. Moreover the masers in the IRAS4 and IRAS16293 differ by orders of magnitudes, whereas the H_2O FIR emission is very similar. This may suggest that the FIR emission is *not* related to the 22 GHz emission arising from the outflow.

3.3. The infalling envelope model

The second possibility is that the observed H_2O lines originate from a the warm inner region of the envelope. In order to test this hypothesis we used the model of an infalling envelope developed by Ceccarelli, Hollenbach & Tielens (1996), which self consistently computes the chemical composition, thermal balance and emerging far infrared line spectrum within the framework of the "inside-out" collapse (Shu 1977). The H_2O line fluxes observed towards IRAS4 can be well reproduced by this model for a central source mass of ~ 0.3 $M_\odot$ and a mass accretion rate of $\sim 3\cdot10^{-5}$ $M_\odot$ yr^{-1} (bottom of Fig. 3; see also Ceccarelli et al. 1999b). In this model, the H_2O emission originates $\leq$ 150 AU from the central source, where the density is $\geq 5\cdot10^7$ cm^{-3}, and the temperature high enough to evaporate the icy dust grain mantles. This infall model also predicts that the 22 GHz H_2O line should maser at a distance $\sim$ 80 AU from the central source, have a luminosity $\sim 3\cdot10^{-10}$ $L_\odot$, and a velocity close to the systemic velocity. Most of the components towards IRAS4 reported by Claussen et al. (1996) have velocities which differ from that of the source, and are likely to be associated with the outflow. However, one component at about the velocity of the source was detected (bottom of their Fig. 3) with an intensity in good agreement with the predictions of this model.

4. CONCLUSIONS

Water line emission was detected towards 5 of the 7 sources in our sample. In IRAS4 and IRAS16293, the fluxes of about ten lines could be measured; they show that the physical conditions (temperature and density) of the emitting regions are fairly similar in both sources. The H_2O emission flux does not correlate with the SiO emission associated with their outflows, but seems to be related to the 1.3 mm continuum flux of the sources. This suggests that the emission originates in the circumstellar envelopes rather than in the outflows. Simple LVG modelling of the line intensities shows that the H_2O emission originates in a compact ($\sim 2''$), dense ($n \geq 10^7$ cm^{-3}) and warm ($T \sim 100$ K) gas, with H_2O column densities $\sim 10^{17}$ cm^{-2}. Finally, the water lines observed towards IRAS4 can be successfully modelled within the framework of an infalling envelope (Ceccarelli et al. 1996), if the central source mass is $\sim 0.3\ M_\odot$ and the mass accretion rate $\sim 3 \cdot 10^{-5}\ M_\odot\ yr^{-1}$. However, we cannot exclude that some of the observed H_2O emission originates in a shock very close to the central object, the same responsible for most of the 22 GHz maser emission seen towards our sources.

ACKNOWLEDGMENTS

We wish to thank the entire LWS team, whose dedication allowed the observations presented in this contribution.

REFERENCES

Ceccarelli C., Hollenbach D.J., Tielens A.G.G.M. 1996, ApJ 471, 400

Ceccarelli C., Caux E., Loinard L. et al. 1999a, A&A in press

Ceccarelli C., Loinard L., Caux E. et al. 1999b, in "The Physics and Chemistry of the Interstellar Medium" ed. V. Ossenkopf

Claussen M.J., Wilking B.A., Benson P.J. et al. 1996, ApJS 106, 111

Cernis K. 1993, Baltic Astronomy 2, 214

Graff M.M., Dalgarno A. 1987, ApJ 317, 432

Green S., Malauendes S., McLean A.D. 1993, ApJS 85, 181

Hollenbach D.J., McKee C.F. 1989, ApJ 342, 306

Kaufman M.J., Neufeld D.A., 1996, ApJ 456,611

Knude J., Hog E. 1998, A&A 338, 897

Liseau R., Ceccarelli C., Larsson B., et al. 1996, A&A 315, L181

Pointer R.L. & Pickett H.M. 1985, Applied Optics 24, 2235

Shu F.H. 1977, ApJ 214, 488

Swinyard B.M., Clegg P.E., Ade P.A.R. et al. 1996, A&A 315, L43

van Dischoeck E. & Blake, G.A. 1998, ARA&A, 36, 317

THE FAR INFRARED SPECTRUM OF ORION-IRC2

J. Cernicharo[1], S. Pérez-Martínez[1], E. González-Alfonso[1,4]
S.J. Leeks[2], M.J. Sempere[1], T. Lim[3], B. Lefloch[1,5], & F. Najarro[1]

[1] CSIC. Instituto de Estructura de la Materia. Serrano 121. 28006 Madrid. Spain
[2] Queen Mary & Westfield College, London, E1 4NS, U.K.
[3] ISO Science Operations Centre, Villafranca, P.O. Box 50727, 28080 Madrid. Spain
(Now at Rutherford Appleton Laboratory)
[4] Univ. de Alcalá de Henares. Dpto Física. E-28871. Alcalá de Henares. Spain
[5] LAOG, Observatoire de Grenoble, France

ABSTRACT

We have observed the far-infrared emission of Orion Irc2 with the LWS spectrometer. The observations consist of 30 grating scans covering the full range 43-197 μm and 480 FP scans giving a total coverage of 100 μm. The spectrum is dominated by the rotational lines of H_2O and CO. Many other species, like NH_3, OH, CO isotopes, H_3O^+ and atomic fine structure lines contribute to the observed features. Rotational transitions of NH, SH, SH_2, NH_3, SO_2, OH^+, CH_2 and other light molecular species together with b-type transitions of slightly asymmetrical molecules like HCO, HNCO, $HOCO^+$ could contribute to the observed emission. The FP data show essentially the water vapour (H_2O, $H_2^{18}O$, $H_2^{17}O$), OH, and CO lines.

Key words: Molecular Clouds; Orion; Molecules; Molecular Abundances.

1. INTRODUCTION

The molecular content of warm molecular clouds is a key information for the study of their chemistry and dynamical evolution. The gas cooling depends on the emission of atomic and molecular lines which arise at millimeter, submillimeter and infrared wavelengths. The study of molecular clouds has been carried out in the last two decades through the observation of some molecular rotational lines, mainly CO, and in some cases other tracers like CS, HCO^+, HCN and NH_3. However, radio observations of warm molecular clouds provide a partial picture of their molecular content. Some molecules are observed from the emission of only one rotational line, others from a few, and most of the molecules that probably exist in these clouds are never observed. Some spectral sweeps have been performed in SgrB2 and Orion (Johansson et al. 1984; Sutton et al. 1985, 1991; Cummins, Thaddeus & Linke 1986; Blake et al. 1986; Turner 1989,1991; Greaves & White 1991; Ziurys & McGonagle 1993; Schielke et al. 1997; Nummelin et al. 1998) but with reduced frequency coverage. Mid and far IR absorption spectroscopy with ISO can provide a full description of the molecular content of the brightest molecular clouds of our Galaxy.

In this contribution we present the far-infrared spectrum of Orion-IRc2 as observed with the LWS spectrometer. The main goal of this frequency sweep is to study the molecular content, the chemistry and the main coolants of the Orion molecular cloud. Molecular abundances could be more easily derived than through radio observations because all the rovibrational lines of a given molecular band are observed. Moreover, all the fundamental transitions (in principle) of light molecules like CH, OH, CH_2, NH_2, H_2O, CH^+, OH^+, H_3O^+, ... could be detected. In addition, detailed mapping of the Orion molecular cloud will provide an important input to determine the physical conditions of the cloud at large spatial scale (see, e.g., the contributions by Sempere et al. and that of water vapour by Cernicharo et al. in these proceedings).

2. THE DATA

We present LWS-grating and LWS-FP data of the Orion molecular cloud. Five full LWS-grating rasters, centred on IRc2 and giving a total of 23 positions, have been obtained. The grating spectrum of the central position was consequently observed five times over two orbits. For each position of each raster, 6 scans between 43 and 197 μm were obtained. The data were reprocessed to remove non-linear effects and saturation problems using special procedures (see Leeks et al. in these proceedings). All the features present in the final averaged grating spectrum of the central position were detected in each individual scan. Although Orion-IRc2 is practically a point-like source for the LWS beam, residual fringes due to the extended Orion molecular cloud have been observed and removed using special data processing algorithms. The resulting spectrum together with

Proceedings of the Conference "The Universe as seen by ISO", Paris, France, 20–23 October 1998 (ESA SP-427, March 1999)

line identifications and the result of our models is shown in Figure 1. The full map obtained with the grating spectrometer is shown by M.J. Sempere et al. (these proceedings) which also gives details on the CO emission and modelling at large scale in the Orion molecular cloud (more information can also be found in the review by Cernicharo et al. in these proceedings).

A North-South raster with five positions was obtained with the FP in some lines of water vapour and OH. Finally, around 100 lines of water vapour (including many lines from $H_2^{18}O$ and $H_2^{17}O$) were observed with the LWS-FP spectrometer towards Orion-IRc2. Taking into account the extra data provided by the LWS-FP, we have covered a range of about 100 μm with a good signal to noise ratio (typically 12 scans per line). Figure 2 shows the FP scan with zooms to selected lines of OH, CO and water vapour. The grating scan is shown in this Figure in arbitrary units for comparison (green line in the central panel -see Figure 1). Details on the FP mapping of Orion IRc2 are given in Cernicharo et al. (these proceedings).

3. RESULTS

The far infrared spectrum of Orion IRc2 is dominated by the pure rotational transitions of CO and H_2O. However, at long wavelengths the emission of linear molecules like HCO^+, HCN, HNC, CN, CS, begin to be detectable as weak features compared to those of CO and water vapour. Other species, like H_3O^+, NH_3, SH_2 and SO_2 also contribute through the full frequency coverage of our data. The lines from O[III], O[I], C[II], N[II] are also detected. In addition to these features, it is clear that many other species contribute to the observed emission at low level. Among the potentially interesting carriers we have to consider the b-type transitions of slightly asymmetrical molecules like HCO, HNCO, $HOCO^+$, ... Many features remain unidentified and we have shown in Figure 1 different potential candidates for these lines. Other species like CH_3OH, $HCOOCH_3$, $(CH_3)_2O$ could also be present in the far-infrared spectrum of Orion.

The FP data show that the lines are very broad ($\simeq$60 kms^{-1}, often showing P-Cygni profiles, mainly at short wavelengths. The lines are formed in, at least, three different regions : the ridge, the plateau and the hot core. The ridge contributes to the extended water emission observed with ISO and with the 30-m radiotelescope by Cernicharo et al. (1994). The plateau is responsible for the broad emission in CO and H_2O. It contributes mainly to the lines above 80-90 μm. The hot core contributes to the lines involving high energy levels. The water abundance in the ridge is 10^{-5} while in the plateau and in the hot core it is around 10^{-4}, i.e., very similar values to those obtained from the 183.3 GHz ground based observations (Cernicharo et al. 1994).

A simple LVG model, which includes CO, H_2O, $H_2^{18}O$, and $H_2^{17}O$ is shown together with the grating spectrum in the Figures below (see Cernicharo et al. in these proceedings for further details). The agreement is reasonably good taken into account the large number of assumptions made in these calculations.

The far-infrared spectrum of Orion-IRc2 is particularly rich and many molecular species contribute to the observed emission. However, due to the poor spectral resolution of the grating spectrum and to the limited sensitivity of the FP scans we can not identify these species. Future satellite platforms, like FIRST, will provide a high spectral resolution and sensitivity and will give a unique view of the molecular content of the brightest molecular clouds in our galaxy.

ACKNOWLEDGMENTS

J. Cernicharo, E. González-Alfonso, B. Lefloch, S. Pérez-Martínez and F. Najarro thank the Spanish Direccion General de la Enseñanza Superior for support through ACP96-0168, ESP96-2529-E, PB96-0083 and ESP98-1351.

REFERENCES

Blake G.A., Masson C.R., Phillips T.G. Sutton E.C. 1986, ApJS, 60, 1

Cernicharo J. et al. 1994, ApJ, 432, L59

Cummins S.E., Thaddeus P., Linke R.A. 1986, ApJS, 60, 819

Greaves J.S., & White G.J. 1991, A&AS., 91, 237

Johansson L.E.B., Andersson C., Ellder J., Friberg P., Hjalmarson A., Hoglund B., Irvine W.M., Olofsson H., Rydbeck G. 1984, A&A, 130, 227

Nummelin A., Bergman P., Hjalmarson A., Friberg P., Irvine W.M., Millar T.J., Ohishi M., Saito S. 1998, ApJS, 117, 427

Schielke P., Groesbeck T.D., Blake G.A., Phillips T.G. 1997, ApJS, 108, 301

Sutton E.C., Blake G.A., Masson C.R., Phillips T.G. 1985, ApJS, 58, 341

Sutton E.C., Jaminet P.A., Danchi W.C., Blake G.A. 1991, ApJS, 77, 255

Turner B.E. 1989, ApJS, 70, 539

Turner B.E. 1991, ApJS, 76, 617

Ziurys L.M., & McGonagle D. 1993, ApJS, 89, 155

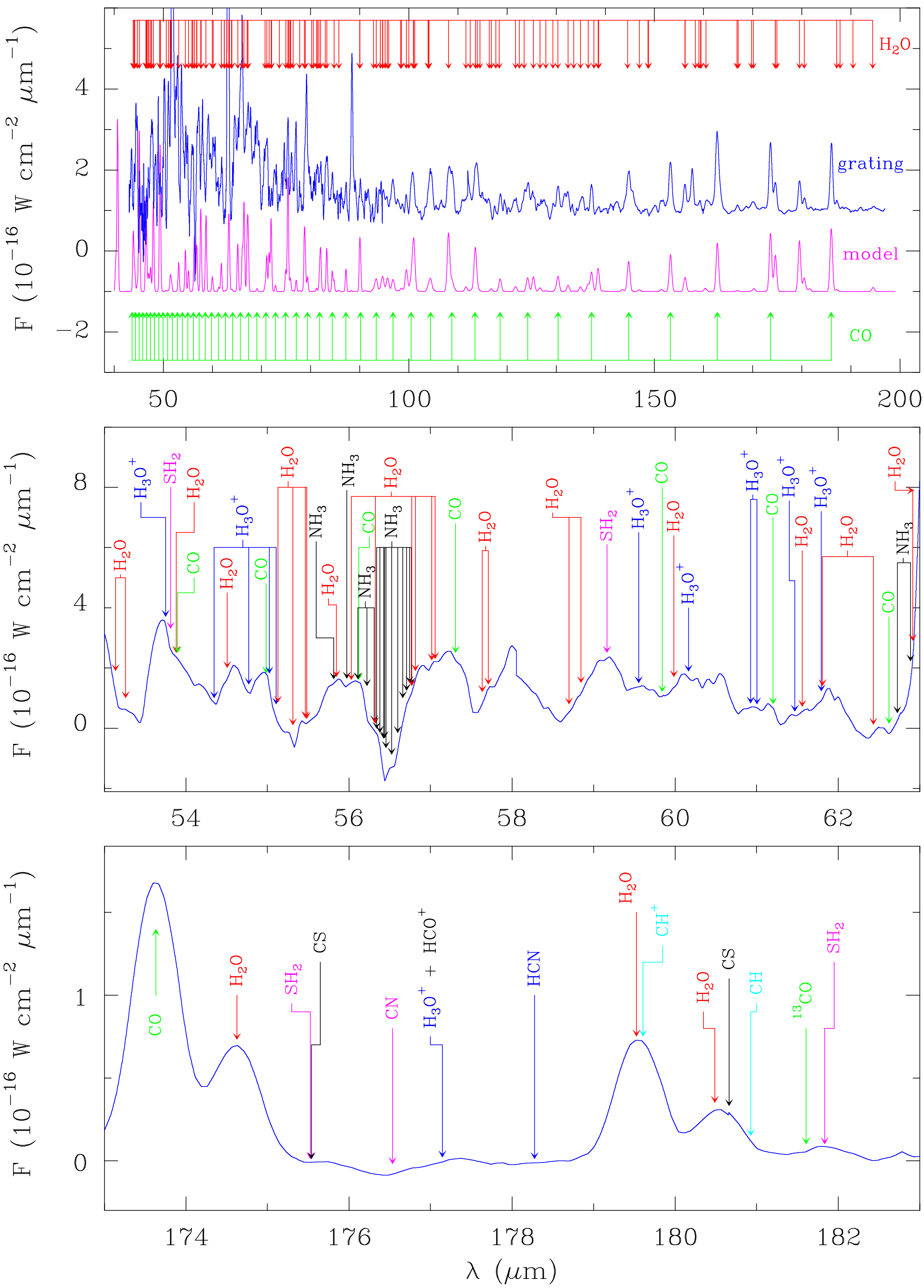

Figure 1. The grating spectrum of Orion-IRC2 observed with the LWS spectrometer between 44-197 μm (top panel). The CO and H_2O lines (those arising from levels below 2000 K and with line strength larger than 0.1) are indicated by arrows. The model includes the main and rare isotopes of CO and water vapour. The middle and bottom panels show select ranges of the grating spectrum with line identifications -see text.

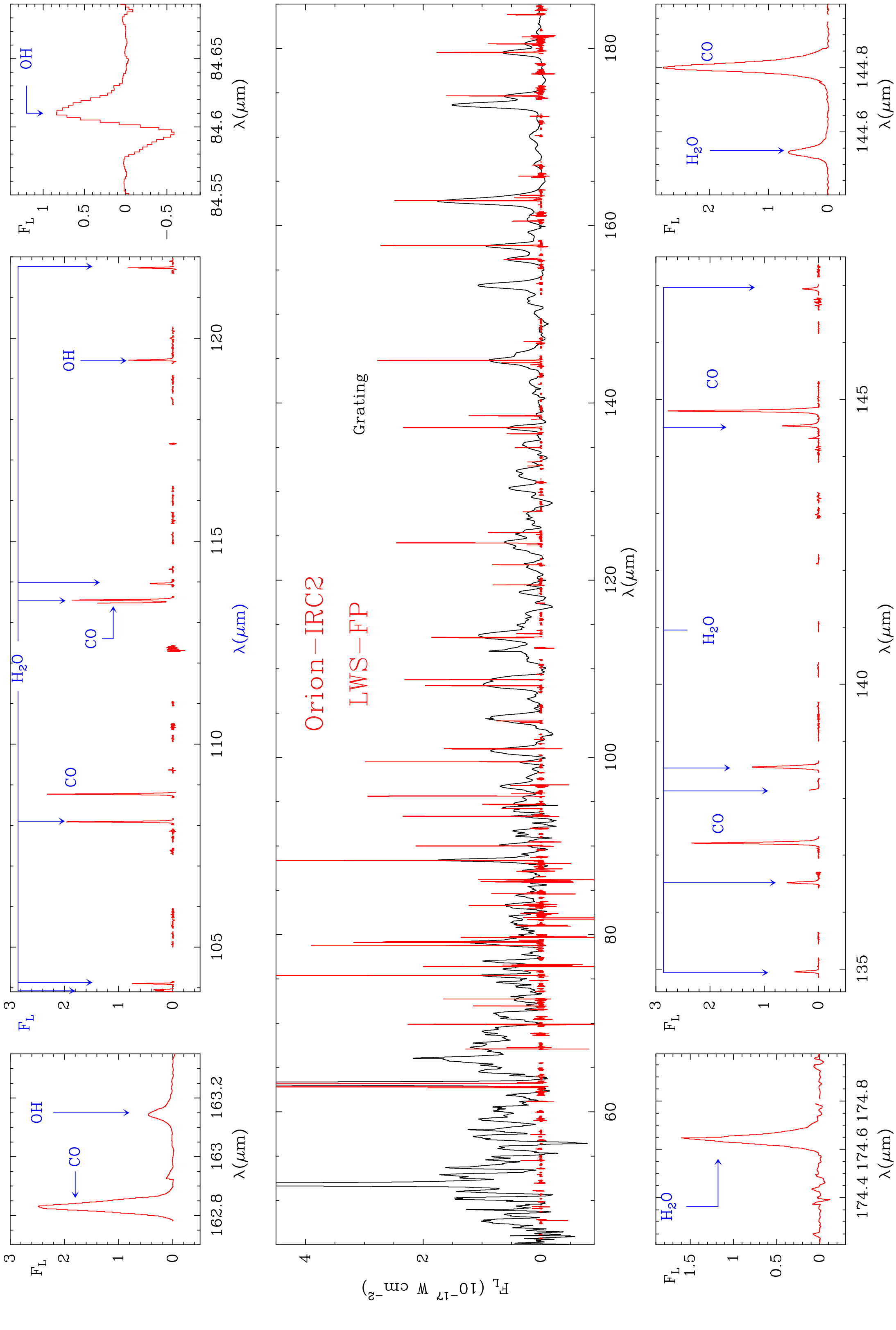

Figure 2. *The central panel shows the FP data together with the grating spectrum of Figure 1. The panels at top and bottom show selected ranges of the FP data. All strong lines in the FP are due to CO and water vapour. Some weak lines from NH_3, H_3O^+, and other species (see text) have been also detected.*

WIDESPREAD FAR-INFRARED ABSORPTION OF CH, OH AND H_2O IN SGR B2

J. Cernicharo[1], M.A. Orlandi[1], E. González-Alfonso[1,2], & S.J. Leeks[3]

[1] CSIC. Instituto de Estructura de la Materia. Serrano 121. 28006 Madrid. Spain
[2] Univ. de Alcalá de Henares. Dpto Física. E-28871. Alcalá de Henares. Spain
[3] Queen Mary & Westfield College, London, E1 4NS, U.K.

ABSTRACT

We present LWS-grating and LWS-FP data of the SgrB2 molecular cloud. Two full LWS-grating rasters, centred on SgrB2 and giving a total of 19 positions, have been obtained. In addition, a 7x7 position raster, with an angular separation of 90 arcsec, has been performed with the LWS-FP in the 179.5 μm line of H_2O and the 119.5 μm line of OH. Taking into account the H_2O map analysed by Cernicharo et al. (1997), the present data indicates that water vapour is abundant in the direction of SgrB2 in a region as large as half a degree (i.e., about 80 parsecs in size). In all observed positions there is a line in absorption at 181 μm that we believe to be the 2_{12}-1_{01} of $H_2^{18}O$ at 181.053 μm. The water abundance derived from these data is $\simeq 10^{-5}$. The FP map around SgrB2 indicates that the line profile changes from point to point suggesting important variations in the excitation conditions. The OH lines absorb completely the continuum emission in all observed positions. CH has been detected in all the positions observed with the grating. In addition, in the central position we have performed a search of several rotational lines of this molecule with the FP. Only the fundamental line was detected suggesting that CH is only abundant in the external parts of the cloud where collisions are not important enough to populate the high-J levels of CH. The averaged CH column density in our map is very similar to that found by Stacey et al. (1987) with the KAO in the direction of SgrB2. Several ro-vibrational lines of triatomic carbon, C_3, have been also detected towards the central position of the cloud.

Key words: Molecular Clouds; Sgr B2; Molecules; Molecular Abundances.

1. INTRODUCTION

The spectrometers on board of ISO can provide a full spectrum of the near, middle and far infrared emission of bright molecular clouds. Unfortunately, the spectral resolution is limited and will produce strong line dilution in most sources. However, towards prominent clouds, like SgrB2 (or very bright sources like Orion-IRc2 or other shocked regions), the linewidth can reach more than 100 kms^{-1} which will allow to detect the most abundant molecular species. In a previous paper (Cernicharo et al. 1997) we have shown that the fundamental line of water vapour at 179.5 μm was detected in all observed positions. A detailed modelling of the data allow us to estimate the water abundance at large scale to be $\simeq 10^{-5}$. In this contribution we present additional data and we analyze the main spectral features found in the LWS grating spectra of SgrB2.

2. RESULTS

The grating ISO/LWS spectrum towards the central position of Sgr B2 shows a strong absorption at 179.5 μm corresponding to the water vapour 2_{12}-1_{01} transition (see Cernicharo et al. 1997). The grating spectra in different positions of the cloud are shown in Fig. 1 (see also Fig. 1 of the review by Cernicharo et al. in these proceedings). The most striking result from the raster map is the presence of the water vapour 179.5 μm line in absorption in all directions (at least up to $\pm$830 arcsec, i.e., over 80 pc; see Figure 1). At the spectral resolution of the grating (i.e., $\simeq$ 1000 km s^{-1}), the absorption remains strong and roughly constant through the map. The absorption depth of $\simeq$15%, is consistent with saturated water vapour lines with a line width of $\simeq$150 kms^{-1}. Other H_2O transitions are detected in absorption: the 3_{03}-2_{12} H_2O line at 174.5 μm is also present in all the raster positions with an absorption depth of 1%. The absorption at 180.5 μm (also detected in all positions) could be a blend of the 2_{21}- 2_{12} H_2O transition at 180.488 μm, the CH line at 180.478 μm and the 2_{12}-1_{01} $H_2{}^{18}O$ line at 181.05 μm. Sensitive observations with the FP of the lines of CH towards the central position of SgrB2, show that only the fundamental transitions of this species, around 149.5 μm, are detected (see Figure 2). Therefore, the grating feature at 181 μm is not contaminated by CH and probably arises from $H_2{}^{18}O$. However, we note that the inversion transition of H_3O^+ is exactly at the same frequency than the $H_2{}^{18}O$ line, and some contamination can not be excluded. Nevertheless, a preliminary analysis of other H_3O^+ lines seems to indicate that an important fraction of the absorption is due to $H_2{}^{18}O$.

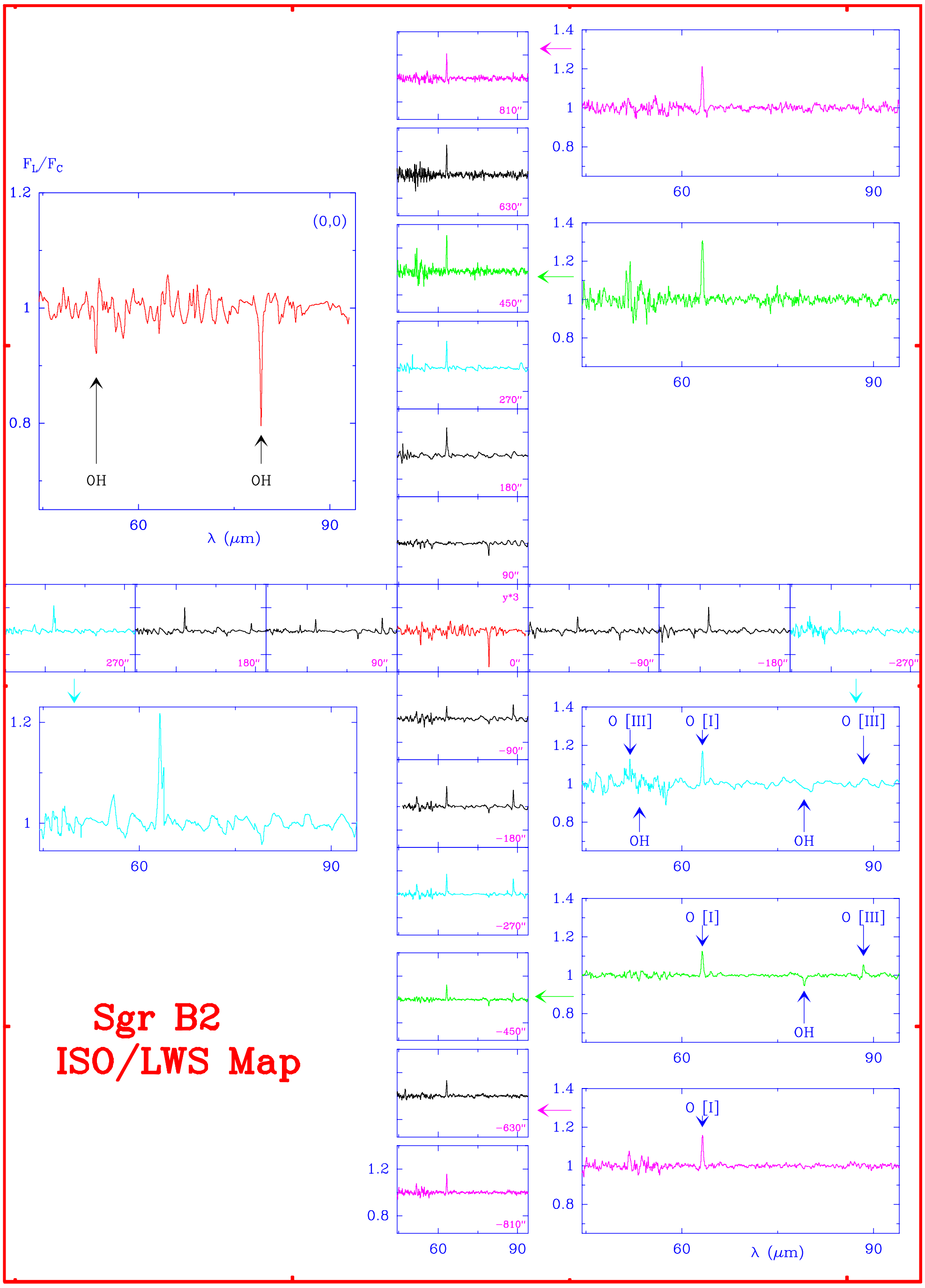

Figure 1. LWS raster of the SgrB2 molecular cloud between 45 and 95 μm. Offsets, in arcseconds, are indicated in each box (in declination for the vertical strip and in right ascension for the horizontal one). Line identifications are given in the zoom to the central position in the top-right panel. The adjacent panels show the spectra observed at selected positions -indicated by arrows.

The main result from the present observations is that the far- infrared lines of water vapour are seen in absorption toward SgrB2, instead of in emission as it is the case for Orion (Cernicharo et al. 1997). This suggests that in SgrB2, where the continuum emission in the far-infrared is optically thick, the H_2O lines arise in a region where the excitation temperatures are smaller than the dust temperature ($\simeq$30 K). The problem of H_2O line excitation is not simple because, apart from self-absorption and the possibility of collisional excitation, the excitation temperatures will also be affected by the continuum emission of the dust. The role of dust is essential in the excitation of molecules such as H_2O which have transitions at far- and near-infrared wavelengths, and must be taken into account in any realistic radiative transfer model. For a very thick cloud such as SgrB2, these conditions mean that the external layers of the cloud absorb not only the dust emission but also the water line emission from the inner regions. The lines could be in emission if the geometry of the cloud was such that the continuum sources were placed in front of the molecular cloud instead of behind it. This is the case for the Orion cloud (see the review by Cernicharo et al. in these proceedings). Finally, note that the C[II] line is very strong in all observed positions but it decrease is intensity when approaching the center where it appears in absorption.

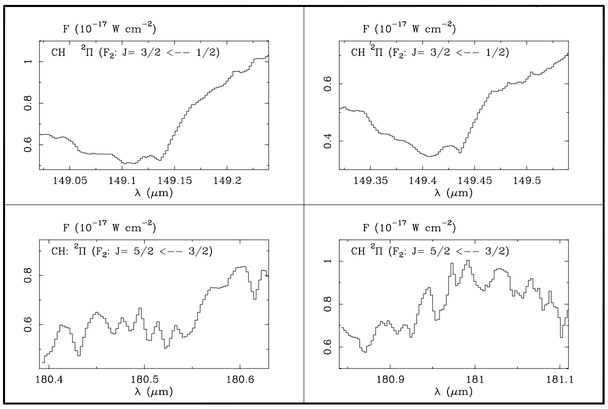

Figure 2. CH lines in SgrB2. The lines connecting the ground level with the first excited rotational level are detected in absorption (top panels - see also Stacey et al. 1987). The lines from the first excited rotational level are undetected within the S/N of the data.

In addition to the H_2O lines, the LWS grating spectra show the OH and CH lines across the cloud. The lines of OH arising from the J=3/2 $^2\Pi_{3/2}$ level and connecting with the J=5/2 $^2\Pi_{3/2}$ and J=1/2 and J=3/2 of the $^2\Pi_{1/2}$ level at 54, 80 and 119 μm are observed at many positions. Like for the water vapour lines, the strength of the OH features indicate that the lines are saturated. However, the relative intensity of the different features indicate that important radiative effects are affecting the population of the OH levels. FP observations of the 119.4 μm of OH (see Figure 3) clearly show that the line absorbs completely the continuum emission and covers a velocity range similar to that of H_2O. The ^{18}OH isotope has also been detected towards the central direction given an OH abundance of a 1-10 10^{-6}.

CH absorption is also detected at several positions. The CH line profile obtained with the FP (see Figure 2) is very similar to that observed with the KAO by Stacey et al. (1987). The absorption reaches about 20 % of the continuum. The column densities of CH in the J=1/2 level varies between 1-5 10^{15} cm^{-2} across the cloud. The lack of absorption from other lines of CH rather than those connecting with the ground level (see FP data above) suggests that the molecule is only abundant in the external layers of the cloud where collisional excitation is unimportant.

3. TRIATOMIC CARBON IN THE INTERSTELLAR MEDIUM

Among the carbon chain radicals, triatomic carbon has played an important role in astrophysics since its detection in cometary tails in the last century and its posterior identification in the laboratory by Douglas in 1951. The ν_2 bending mode at 62 cm^{-1} (90 K) is the only way to detect this molecule in the ISM because the flux of molecular clouds at the frequency of the stretching mode of C_3 is too low to allow systematic searches of C_3 or other polyatomic species. Only light species could have rotational transitions in the far-IR domain. The pure rotational transitions of the heaviest species involve high quantum numbers and, hence, very high energies. Polyatomic species, like C_3, C_4, C_5, C_4H_2, C_6H_2, ... have, however, vibrational bending modes at very low energy. The Q bands of these modes will contain absorption or emission from many lines and could contribute to the FIR spectrum of bright IR sources. Cernicharo et al. (1996) have reported a tentative detection of the bending mode of C_3 in IRC+10216 with the LWS grating spectrometer. Recently, Cernicharo and coworkers have detected two lines of C_3, R(2) and R(4), with the LWS/FP spectrometer in the same source and show that these lines arise from the external layers of the circumstellar envelope. In Fig. 4 we show the detection of four lines of C_3 in SgrB2 (see Cernicharo, González-Alfonso & Lefloch 1997). All the lines, except the R(2) are narrow and appear at the velocity of SgrB2. The R(2) line shows a broad absorption profile, like the 179.5 μm line of H_2O -see Cernicharo et al. 1997). Preliminary calculations indicate x(C_3)$\simeq 10^{-9}$.

ACKNOWLEDGMENTS

J. Cernicharo, E. González-Alfonso, and M.A. Orlandi thank the Spanish Direccion General de la Enseñanza Superior for support through ACP96-0168, ESP96-2529-E, PB96-0083 and ESP98-1351.

REFERENCES

Cernicharo J., Barlow M., González-Alfonso E., et al. 1996, A&A, 315, L201

Cernicharo J., Lim T., Caux E., et al. 1997, A&A, 323, L25

Cernicharo J., González-Alfonso E., Lefloch B., 1997, in *First ISO Workshop on analytical spectroscopy*, ESA SP-419, 23.

Douglas A.E. 1951, ApJ, 114, 446

Stacey et al. 1987, ApJ, 313, 859

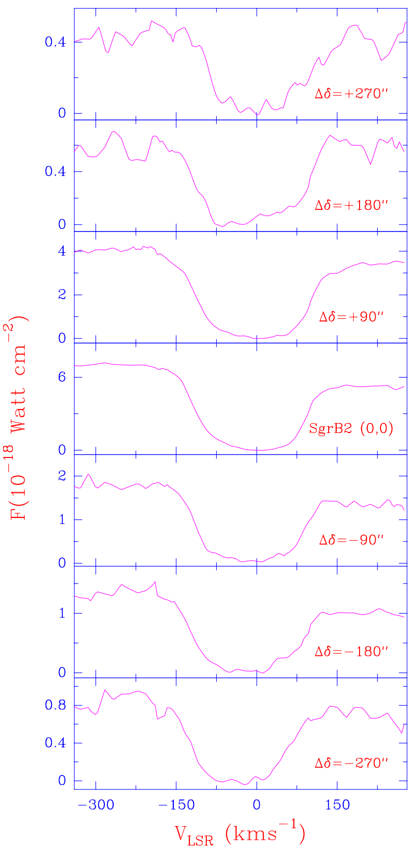

Figure 3. *OH line at 119.442 μm observed with the LWS/FP in a declination raster. Note that the line absorbs completely the continuum. Other lines of OH are detected also in absorption in the grating spectra.*

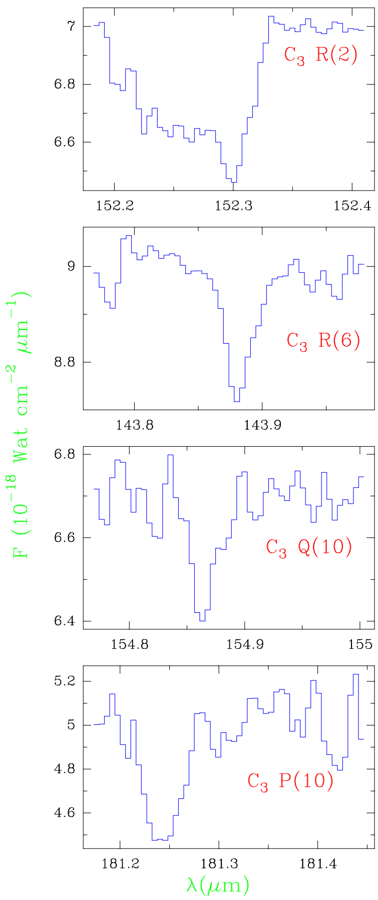

Figure 4. *Triatomic carbon (C_3) lines, detected in SgrB2. The R(2) line exhibits a broad absorption produced in the clouds lying the line of sight of SgrB2. Calibration of the data is preliminary.*

ISOGAL OBSERVATIONS OF MOLECULAR CLOUDS: THE S152/S153 COMPLEX

E. Copet[1,2] **& A. Zavagno**[3]

[1] DESPA - Observatoire de Paris, France
[2] Institut d'Astrophysique de Paris, France
[3] Observatoire de Marseille, France

ABSTRACT

ISOGAL (see Omont et al. these proceedings) is a detailed mid-infrared imaging survey of the inner Galaxy which combines ISOCAM observations at 7 and 15 μm with I, J and K_s DENIS data. The main goal of the project is to trace galactic structure and stellar populations, but several observations of HII regions of the bulge have been done.
We present here briefly the results of these observations on the S152/S153 complex.

Key words: HII region; S152/S153; UIB; ISOGAL.

1. INTRODUCTION

The S152/S153 complex is composed of two Sharpless HII regions associated with a CO cloud in the Perseus arm. The size of the S152 molecular cloud is about 1.5 pc for an adopted distance of 3.5 kpc (Cox et al. 1987).
Several observations have been done on this region (Heydary-Malayeri & Testor 1981; Tatematsu et al. 1985; Zinchenko et al. 1994). The exciting star has an O9V spectral type corresponding to Lyman continuum photon rate of N_{Lyc}=2.0910^{46} s^{-1}. According to the UBV photometry, the star has a visual magnitude of V=12.4 and a color excess E(B-V)=1.26, i.e. a visual extinction A_V=2.5 mag. (Crampton et al. 1978). The column density of the associated molecular cloud (estimated from CO data) is greater than 15 visual magnitudes, implying that most of the molecular material lies behind the exciting star.

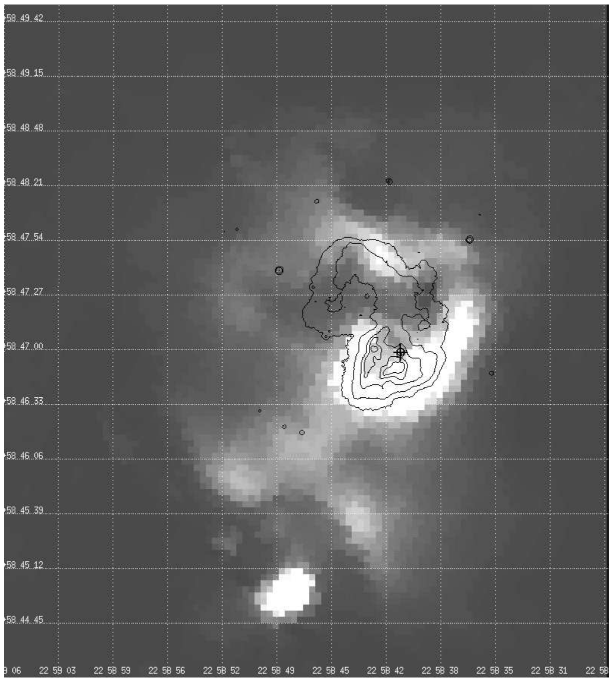

Figure 1. The central part of the S152 complex in the LW6 band (image) with the Hα emission (image courtesy of S. Darbon) shown as contours. The star responsible for the ionization is indicated by a cross.

2. OBSERVATIONS AND RESULTS

2.1. Observations

ISOGAL observations of this region have been done using the ISOCAM filters LW6 (7.7 μm) and LW9 (15.0 μm). The pixel field of view is 6×6 arcsec. The raster size which is $19.3' \times 19.3'$ contains both the S152 and S153 complexes. In addition, A. Zavagno has observed the central part of S152 using the ISOCAM CVF with broad band filters in the 3-12 μm range and pixels of 3 arcsec. We present here the result obtained with the narrow band filters.
The image processing was done using CIA (CAM Interactive Package). The inversion method was used, but some transients effects are still present on the images.

Proceedings of the Conference "The Universe as seen by ISO", Paris, France, 20–23 October 1998 (ESA SP-427, March 1999)

2.2. Morphology of the 7.7 μm emission

The S152 nebula is composed of two components in Hα: to the south, the bright and compact component A, and to the north, the component B, which is more elongated and contains two sub-regions (Heydari-Malayeri et al. 1981). These components are clearly visible on the contours plotted on Figure 1 which presents the 7.7 μm image of the S152 HII region and the Hα emission from an image taken by S. Darbon at Observatoire de Haute Provence (OHP). On this image, we see to the south, a bright arc-shaped nebulosity that surrounds the ionizing star (cross) and, to the north, component A which emission follows the edge of component B. We detect also south of the optical nebula, a bright compact region.
Since the projected size between the ionizing star and the peak of emission in LW6 filter is 0.3 pc, the 7.7 μm emission can not be considered as only thermal emission. If the component A is composed of gas, this spatial distribution indicates that the carriers of the 7.7 μm band are located outside the gaseous region, at the periphery of the neutral material.

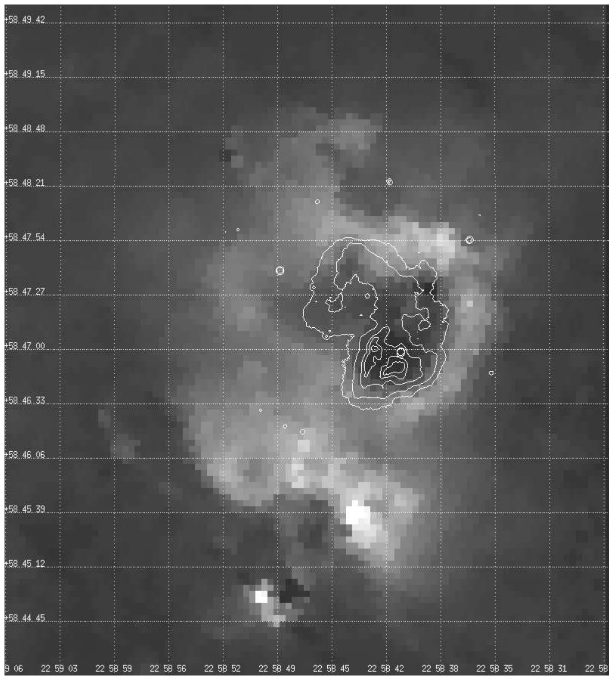

Figure 2. LW6/LW9 ratio map of S152 compared to the Hα emission (contours). North is up, East is left

2.3. The 7.7 μm emission

If we assume that most of the emission in the LW6 filter is due to the carriers of the 7.7 μm band, i.e. the Unidentified IR Band (UIB) plus continuum and that the LW9 filter is pure continuum, then the LW6/LW9 ratio should trace the 7.7 μm band emission alone.
Figure 2 shows the LW6/LW9 ratio map of the core of S152.
Clearly, we detect "a hole" of 0.3 pc diameter size in the spatial distribution of the LW6/LW9 ratio, which is centered on the ionizing star and encompasses the ionized region. The ratio is lower than 0.5 in the central part and larger than 2.0 at the edge of the hole. In fact the ratio LW6/LW9 follows the contours of the Hα emission. Several hypothesis could lead to this result:
A lack (or destruction ?) of dust responsible for the 7.7 μm emission towards the photodissociation region; and/or the presence of a strong thermal continuum emission in this area, as observed in SWS spectra of compact HII regions by Roelfsema et al. (1996); the 7.7 μm carriers are mainly in the molecular cloud and are excited by the radiation field on the outer surface of the HII region.
Note, that the previous observed bright source in the LW6 image exhibits high LW6/LW9 ratio.

2.4. The S152/S153 complex

Figure 3 presents both S152 and S153 nebulae in Hα emission, together with the LW6/LW9 ratio and the low resolution CS line intensity map from Zinchenko et al. (1994). The CS line is known to be a tracer of dense molecular material.
The highest ratio value (peak > 4.0) is observed along a bar located between the two regions (Figure 3). Since this bar corresponds to the peak of emission in the CS map, the bar could also correspond to an abundance maximum of the 7.7 μm UIB carriers. But since the maximum of the neutral material coincides with the peak of the LW6/LW9 ratio, we cannot disentangle if the bar is due the general increase of the column density of the molecular cloud, or if it is a local over-abundance of UIB carriers.
The compact region, not detected in the visible image, is well seen to the south of the bar but its nature remains unclear. Indeed its spectral energy distribution does not appear typical for IR embedded sources which normally are rising with wavelengths between 7 and 15 μm.

3. DISCUSSION

Clearly, the UIB carriers are located around the photon-dissociation region surrounding the HII region and at the edge of the molecular cloud. In the HII region and close to the ionizing star the 7.7 μm carriers disappear. The bar seen in the LW6/LW9 ratio, located between S152 and S153 could be due to a compression of the molecular material by the sources responsible for the two HII regions.

REFERENCES

Crampton, D., & Georgelin, Y.M. 1978, A&A, 66, 1

Cox, P., Deharveng, L., & Caplan, J. 1987, A&A, 171, 277

Heydary-Malayeri, M., & Testor, G. 1981, A&A, 96, 219

Roelfsema, P. et al. 1996, A&A, 315, 289

Tatematsu, K., Nakano, M., Yoshida, S., Wiramihardja, S., & Kogure T. 1985, PASJ, 37, 345

Zinchenko, L., Forsstrom, V., Lapinov, A., & Mattila, K. 1994, A&A, 288, 601

Figure 3. *Hα image of both S152 (north-west) and S153 (south-east) HII regions. (north is up and east left) The contours of the LW6/LW9 ratio (black solid lines, contour values: 0.3, 1.5, 2.7, 3.9) and CS line intensity map (white solid lines) are superimposed. Note the presence of a bar (also peak of the dust column density) at the interface between the two regions.*

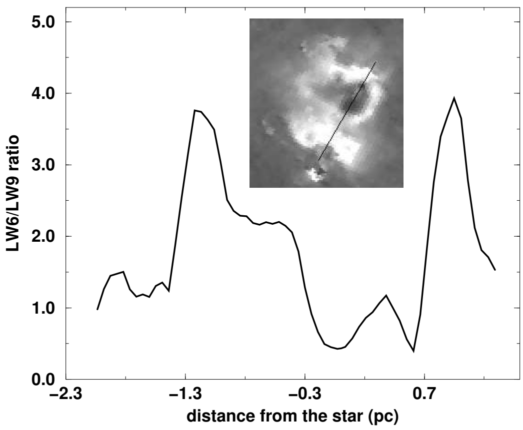

Figure 4. *Variation of the LW6/LW9 ratio along a cut passing through the exciting star (left, south-east point to right, north-west point seen as a black line on the image.)*

THE M17 INTERFACE OBSERVED BY ISOCAM: PAH AND OTHER NANO-PARTICLES

E. Crété[1], M. Giard[1], C. Joblin[1], A. Léger[2], D. Rouan[3], & I. Vauglin[3]

[1]Centre d'Étude Spatiale des Rayonnements, Toulouse, France.
[2]Institut d'Astrophysique Spatiale, France.
[3]Observatoire de Lyon, France.

ABSTRACT

We present high angular resolution ISOCAM observations (1.5 arcsec per pixel) of the M17 HII region/molecular cloud interface from 4.5 to 10 μm. These allowed us to map the 6.2 and 7.7 μm carbonaceous dust features together with the adjacent continuum. Compared with ground-based data at 3.3 μm and 11.3 μm, these data are analyzed in the frame of the PAH model. In addition to the classical PAH component which is located at the HII/molecular interface and is responsible for the classical emission features, our data show the presence of an additional component of nanometric particles emitting in the 8 to 10 μm range in the direction of the HII region.

Key words: UIB; M17 SW.

1. INTRODUCTION

M17 SW is a region of massive star formation. The HII region, powered by these young objects, erodes the South-West parent molecular cloud at an interface seen almost edge-on (Gatley et al. 1979). Due to this particular geometry, its relatively close distance of 2.2 kpc (Chini et al. 1980), and its bright infrared luminosity, it is one of the few regions which can inform us about the star formation mechanism. Thus, it has been then extensively studied. The dust, which couples the radiation field of the young stars with the gas is studied in its infrared emission. The nature and temperature of this dust have been a matter of debate. From the 10 μm continuum analysis Andriesse (1978) showed that this emission originates from very small particles, 10Å sized, out of thermal equilibrium, heated by single UV photons (Andriesse 1978; Sellgren 1984).

On the other hand, the Unidentified Infrared Bands (UIBs), attributed to various carbonaceous materials: PAH molecules (Léger & Puget 1984), PAH ions (Allamandola et al. 1985), or carbonaceous grains (Sakata et al. 1987; Duley & Williams 1988; Papoular 1988), have been shown to be ubiquitous in the interstellar medium. Near-infrared spectroscopy (Russel et al. 1977; Verstraete et al. 1996) and imaging (Giard et al. 1992; Giard et al. 1994; Cesarsky et al. 1996) of this region have revealed the presence of the UIBs there.

A good match of the UIBs is obtained with the absorption spectrum of coals (Guillois et al. 1996) with mild level of graphitization, but the grains must reach a high equilibrium temperature to emit, which raises the question of the heating mechanism. This is not the case for PAH molecules which emit out of thermal equilibrium and could account for the observed spectra in various conditions of excitation. Large PAHs (with $\sim$ 100 C atoms) seem to be the best candidates, but their laboratory spectrum has not yet been measured, and the spectral agreement with the observations still has to be proven.

Giard et al. (1992) have shown that, in M17 SW, the 3.3 μm feature emission was not correlated to the 3.2 μm and 10 μm continuum emission, concluding that the carriers of the UIBs were not responsible for the 10 μm continuum emission. The aim of this work is to map the 6.2 and 7.7 μm continuum and feature emissions in order to get new insights into the properties of their carriers.

2. OBSERVATIONS

The maps are presented in Figure 1. They have been taken with ISOCAM, in CAM 01 raster mode, and have a field of view of 2 $\times$ 2 arcmin^2. The angular resolution is the diffraction limit: 2.2 arcsec (4.5 μm) to 4.8 arcsec (9.6 μm) and the pixel size is 1.5 arcsec. Three spectra (Figure 2) of the region have been taken with the Phot-S instrument (field of view given by the squares in Figure 1b), and are used to calibrate the ISOCAM data. Additional maps of the features and adjacent continua at 3.3 μm (Giard et al. 1994) and 11.3 μm have been obtained with ground-based instruments at the CFH Telescope: the CIRCUS and C10μ (Observatoire of Lyon) cameras, respectively.

An interesting result is the different spatial extension of the 9.6 and 6.2 μm emission (Figure 3), the former following the HII region, the latter the molecular one.

Proceedings of the Conference "The Universe as seen by ISO", Paris, France, 20–23 October 1998 (ESA SP-427, March 1999)

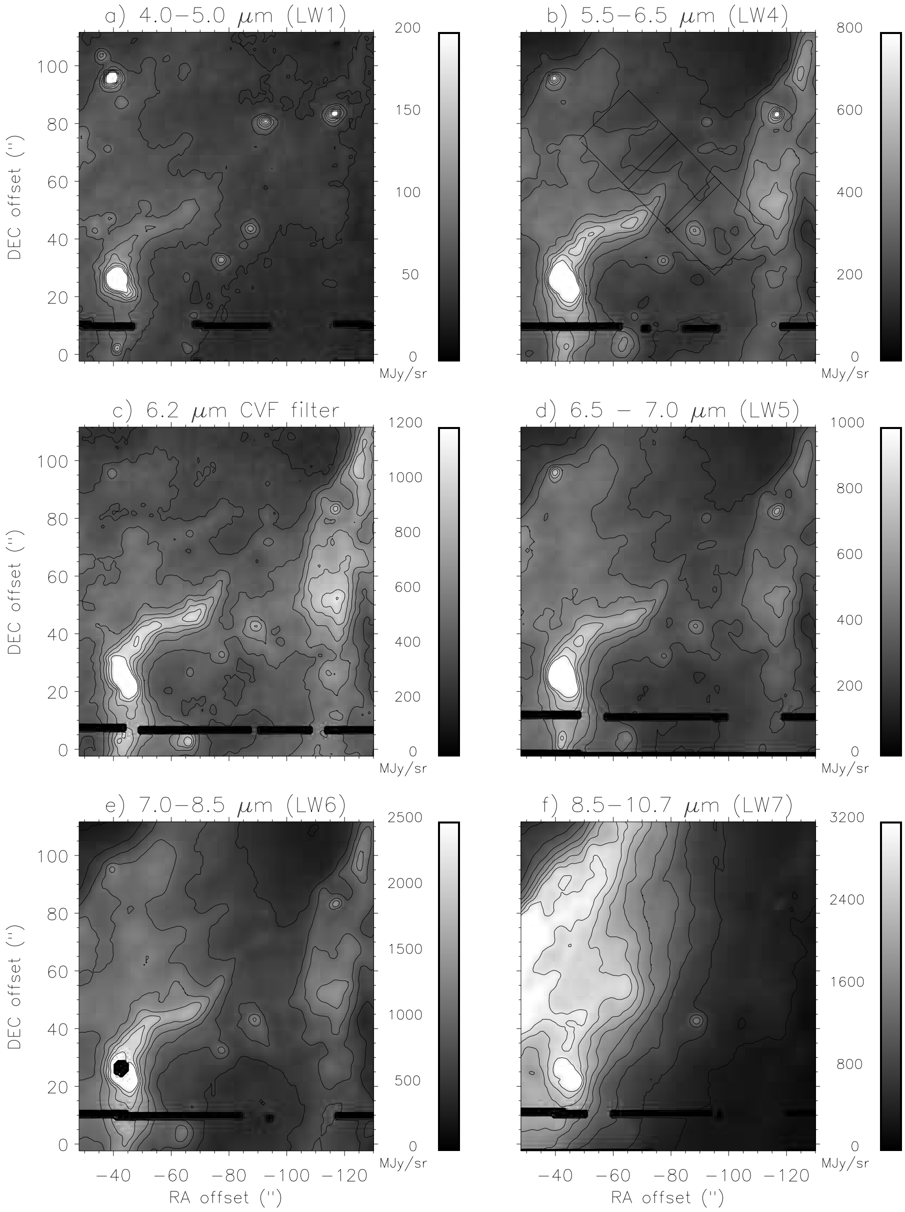

Figure 1. CAM data between 4.5 and 10.5 μm in different filters. Reference position is the star SAO 161 357 $\alpha(2000) = 18^h20^{mn}27.6^s$, $\delta(2000) = -16^o$ 12 arcmin 01 arcsec. The bright source at offsets of $\Delta\alpha = -40.5$ arcsec, and $\Delta\delta = 26$ arcsec is the Ultra Compact HII region UC1 (Felli et al. 1984), near the interface between the HII region (at the north-east), and the molecular cloud (at the south-west), especially seen in the 6.2 μm emission. First contour and contour step are 1/10 of the maximum. The squares in b) are the positions of the Phot-S field of view (Figure 2).

3. FEATURE EXTRACTION

As suggested by the three spectra (Figure 2), the continuum has been modelled as being linear between 5.5 and 7.7 μm and between 7.7 and 10 μm (3 parameters). The UIBs have been modelled with gaussians centered at 6.2, 7.7 and 8.6 μm. The 6.2 and 7.7 μm feature peak intensities have been left as two free parameters. The 8.6 μm intensity has been taken to be proportional to the 8.6 μm continuum intensity as in the three Phot-S spectra (Figure 2). The combined five parameter synthetic spectrum is used to fit the ISOCAM data for each pixel of the map, and then to derive the feature peak intensity of the 6.2 and 7.7 μm bands. They are compared with ground-based observations of the 3.3 μm band (Giard et al. 1994) and of the 11.3 μm band in Fig. 4 and 5, respectively.

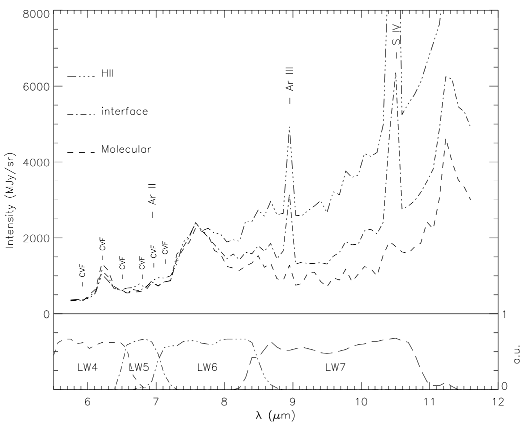

Figure 2. Phot-S spectra of the three regions delimited with squares in Figure 1b. The characteristics of the CAM filters which have been used in this study are also shown (LW large filter bandwidths and CVF positions).

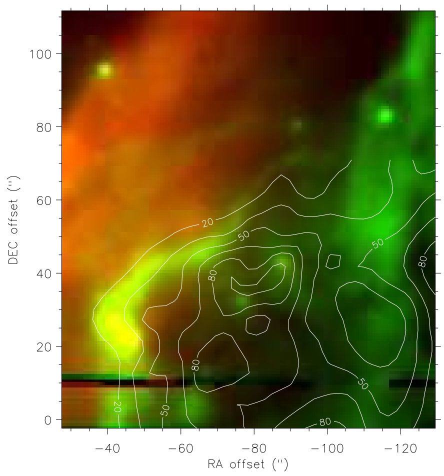

Figure 3. Total intensity in the LW7 (9.6 μm, red) and LW4 (6.2 μm, green) filters. The 6.2 μm emission traces the edge of the molecular cloud ($C^{18}O$ J=2→1 contours from Stutzki & Güsten (1990), units are $K\,km\,s^{-1}$), while the 9.6 μm emission is particularly intense in the HII region.

4. TWO COMPONENT MODEL (PAH AND NANOPARTICLES)

Comparison between the 3.3, 6.2, 7.7 and 11.3 μm feature emissions (Figures 4 and 5) shows a very good spatial correlation between the bands. On the other hand, the 9.6 μm continuum emission does not correlate with the UIBs, but with the HII region (Figure 3). Figure 6 a) shows that the spectral data cannot be explained by involving only one population of grain (graphite grains in the model of Désert et al. 1990). The fit of our data, together with the 50 and 100 μm data of Meixner et al. (1992) (Figure 6) shows that these observations are compatible with a model including, in addition to the classical big grain

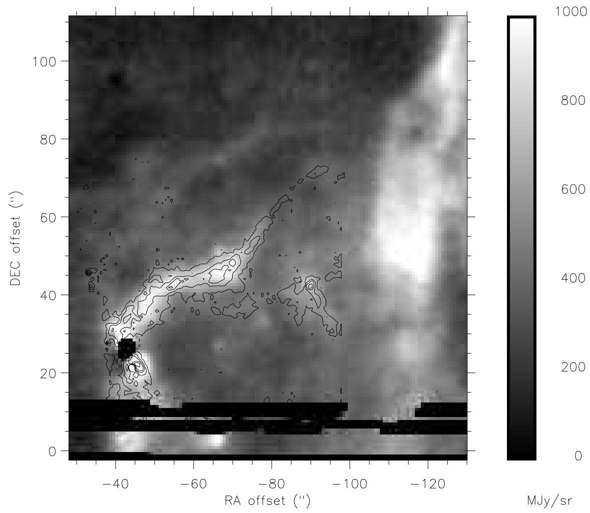

Figure 4. The 6.2 μm (greyscale) and 3.3 μm (contours, Giard et al. 1994) feature peak intensity emission measured by ISOCAM and the CIRCUS camera respectively. First contour is 100 MJy/sr and steps are 100 MJy/sr. No data are available at 3.3 μm in the north and east parts of the region.

component at thermal equilibrium, two populations of grains out of thermal equilibrium (Désert et al. 1990), which are supposed to be PAH and nano-sized particles. PAH are present in the whole region, but depleted by a factor ∼ 6 and with a larger size in the HII region compared to the molecular region. The nanoparticles represent 5 per cent of the dust mass in the HII region and less in the molecular region.

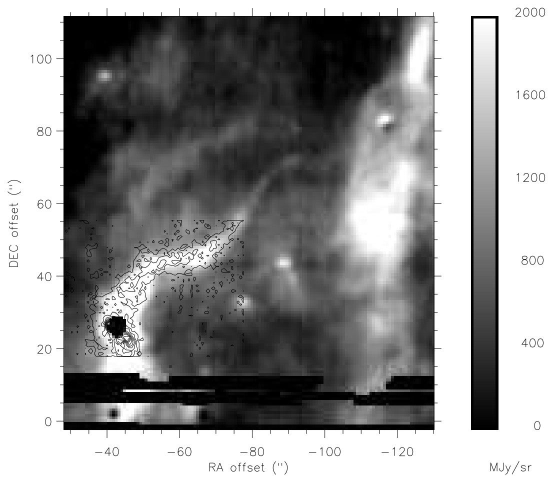

Figure 5. The 7.7 μm (greyscale) and 11.3 μm (contours) feature peak intensity emission measured by ISOCAM and by the C10μ camera at the CHFT respectively. The C10μ pixel size is 0.31 arcsec but the map has been smoothed to 1 arcsec. First contour of the 11.3 μm map is 1500 MJy/sr and steps are 1000 MJy/sr. No data are available at 11.3 μm in the north and east parts of the region.

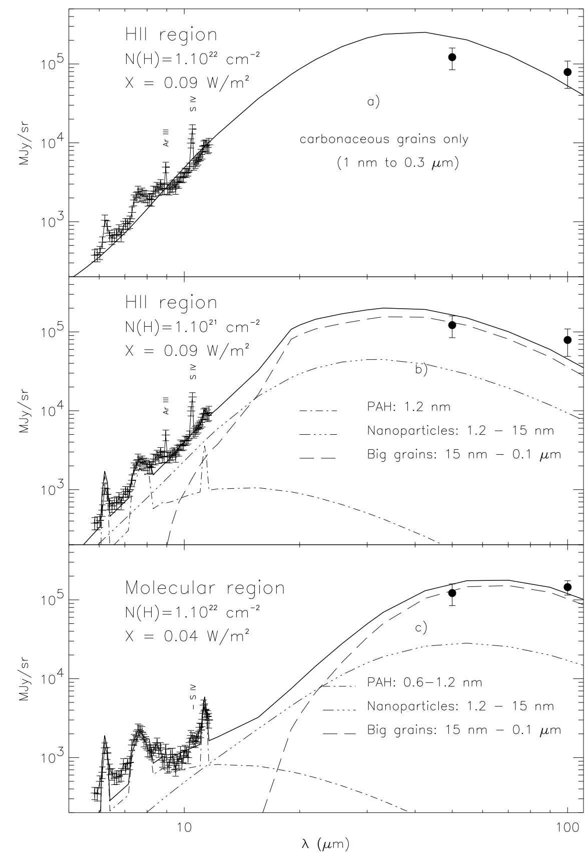

Figure 6. Fit of the observations with different grain components using the model of Désert et al. (1990). X is the integrated Interstellar Radiation Field (Giard et al. 1994). The points at 50 and 100 μm are from Meixner et al. (1992), and the measurements from 6 to 11 μm are from this work. a) best fit with graphite grains: the column density is enhanced by a factor 10 to fit the data. b) & c) Fit implying big grains, very small grains and PAH. The solid line represents the resultant synthetic spectrum. b) HII region: the nanoparticle emission dominates between 8 and 12 μm. The PAH and the nanoparticles are found to contain 0.001 and 0.005 of the total dust mass respectively. c) Molecular region: the PAH and big grain emissions are dominant. The PAH contain 0.006 of the total dust mass, the nanoparticles 0.04. In b) and c) the big grain mass abundance (relative to hydrogen) is $4.2 \pm 0.2\ 10^{-2}$.

ACKNOWLEDGEMENTS

The ISOCAM data presented in this paper was analysed using 'CIA', a joint development by the ESA Astrophysics Division and the ISOCAM Consortium. The ISOCAM Consortium is led by the ISOCAM PI, C. Cesarsky, Direction des Sciences de la Matière, C.E.A., France.

REFERENCES

Allamandola L. J., Tielens A. G. G. M., Barker J. R. 1985, ApJ 290, L25.

Andriesse C. D., 1978, A&A 66, 169.

Cesarsky D., Lequeux J., Abergel A., Perault M., Palazzi E., Madden S., Tran D. 1996, A&A 315, L305.

Chini R., Elsässer H., Neckel Th. 1980, A&A 91, 186.

Désert F–X., Boulanger F., Puget J-L. 1990, A&A 237, 215.

Duley W. W., Williams D. A. 1988, MNRAS 231, 969.

Felli M., Churwell E., Massi M. 1984, A&A 136, 53.

Gatley I., Becklin E. E., Sellgren K. & Werner M. W. 1979, ApJ 233, 575.

Giard M., Bernard J–P., Dennefeld M. 1992, A&A 264, 610.

Giard M., Bernard J–P., Lacombe F., Normand P., Rouan D. 1994, A&A 291, 239.

Guillois O., Nenner I., Papoular R., Reynaud C. 1996, ApJ 464, 810.

Léger A., Puget J-L. 1984, A&A 137, L5.

Meixner M., Haas M. R., Tielens A. G. G. M., Erickson E. F., Werner M. 1992, ApJ 390, 499.

Papoular R. 1988, A&A 204, 138.

Russel R. W., Soifer B. T., Merrill K. M. 1977, ApJ 213, 66.

Sakata A., Wada S., Onaka T., Tokunaga A. T. 1987, ApJ 320, L63.

Sellgren K. 1984, ApJ 277, 623.

Stutzki J. & Güsten R. 1990, ApJ 356, 513.

Verstraete L., Puget J–L., Falgarone E., Drapatz S., Wright C. M., Timmerman R. 1996, A&A 315, L337.

SPATIAL DISTRIBUTION OF UNIDENTIFIED INFRARED BANDS AND EXTENDED RED EMISSION IN THE COMPACT GALACTIC HII REGION SH 152

S. Darbon[1], A. Zavagno[2], C. Savine[1], V. Ducci[2], J.-M. Perrin[1], & J.-P. Sivan[1]

[1]Observatoire de Haute Provence du CNRS, 04870 Saint-Michel l'Observatoire, France.
[2]Observatoire de Marseille, 2 Place Le Verrier, 13248 Marseille Cedex 4, France.

ABSTRACT

We present visible and near IR images of the compact H II region Sh 152. Some of these images reveal the presence of Extended Red Emission (ERE) around 698 nm and emission from Unidentified Infrared Bands (UIBs) at 3.3 and 6.2 μm. Other images show the near infrared (7-12 μm) continuous emission of the nebula. The ERE emission is found to coincide with the ionized region and significantly differ from the UIBs location. Also some evidence is found in favor of grains as carriers for ERE.

Key words: H II regions, ERE, UIBs

1. INTRODUCTION

Extended red emission (ERE) is a continuous emission band observed in the red part (600–800 nm) of the spectrum of various astrophysical objects like reflection nebulae (Schmidt, Cohen & Margon 1980, Witt & Boroson 1990), planetary nebulae (Furton & Witt 1992), H II regions (Sivan & Perrin 1993, Darbon, Perrin & Sivan 1998), high-latitude galactic cirrus clouds (Szomoru & Guhathakurta 1998), the halo of the galaxy M82 (Perrin, Darbon & Sivan 1995) and also in the diffuse galactic interstellar medium (Gordon, Witt & Friedmann 1998). This emission can be attributed either to Hydrogenated Amorphous Carbon (HAC) grains (Watanabe, Hasegawa & Kurata 1982, Furton & Witt 1993) or silicon grains (Witt, Gordon & Furton 1998, Ledoux et al. 1998). A series of emission bands in the 3–16 μm range, the so-called UIBs, is also observed in dusty environments and commonly attributed to Polycyclic Aromatic Molecules (PAH)(Puget & Léger 1989, Allamandola, Tielens & Barker 1989) and/or carbonaceous materials (Papoular et al. 1989). In particular, the existence (or absence) of a spatial correlation between UIBs and ERE might be useful to put constrains on the nature of the carriers. Compact H II regions are bright and dusty objects well suited for this kind of study. This is the reason why we have carried out an observational program for imaging compact H II regions at visible and infrared wavelengths in order to detect and to map respectively ERE and UIBs. This paper reports on the results obtained for Sh 152.

2. OBSERVATIONS AND DATA REDUCTION

Infrared images of Sh 152 were obtained with ISOCAM in june 1997, during ISO revolution 563. These include UIBs images at 3.3 and 6.2 μm and four continuum images taken with the ISOCAM circular variable filter (CVF) at 6.911, 8.222, 10.52 and 12.00 μm. These observations and data reduction are described in Zavagno & Ducci (these proceedings). In particular, the 3.3 and 6.2 μm images presented in this paper were corrected for the adjacent continuum emission.

Visible images in the 500–850 nm range were obtained, in october 1997, with a 1024 $\times$ 1024 thinned back-illuminated Tektronix CCD camera mounted at the Newton focus of the 120 cm telescope of the Observatoire de Haute Provence. Four interference filters with a FWHM $\simeq$10 nm centered on 528.2, 612.0, 697.5 and 812.5 nm were used. These filters were chosen to isolate the continuum emission of Sh 152 and to avoid nebular and night sky emission lines. For each continuum filter, twenty-five 15 min exposure time frames were obtained and co-added, yielding a resulting image of six hours exposure time. Standard data reduction was performed using ESO-MIDAS software. It includes : dark current subtraction, flat fielding, airmass and interstellar extinction corrections, deconvolution by point spread function. According to spectroscopic observations of ERE in H II regions (Sivan & Perrin 1993), the emission excess in the 697.5 and/or 812.5 nm filters should be attributed to ERE. Actually the best contrasted results were obtained by making the difference between the 697.5 and 612.0 nm images. The resulting image was considered as giving the spatial distribution of ERE over Sh 152.

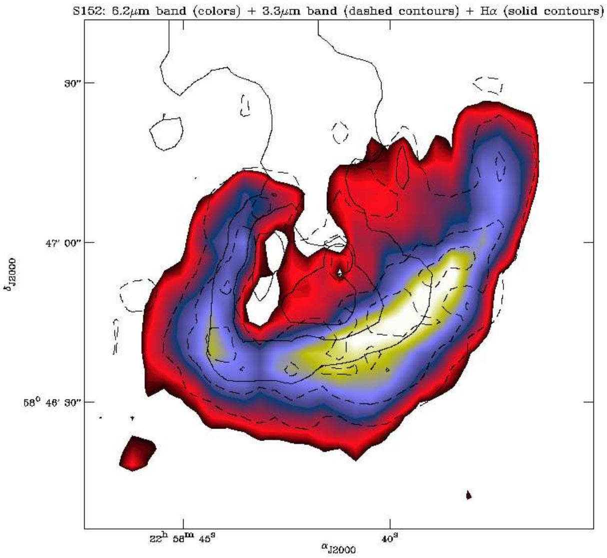

Figure 1. 6.2 μm (colors), 3.3 μm emission bands (dashed contours) and Hα emission (solid contours) in Sh 152

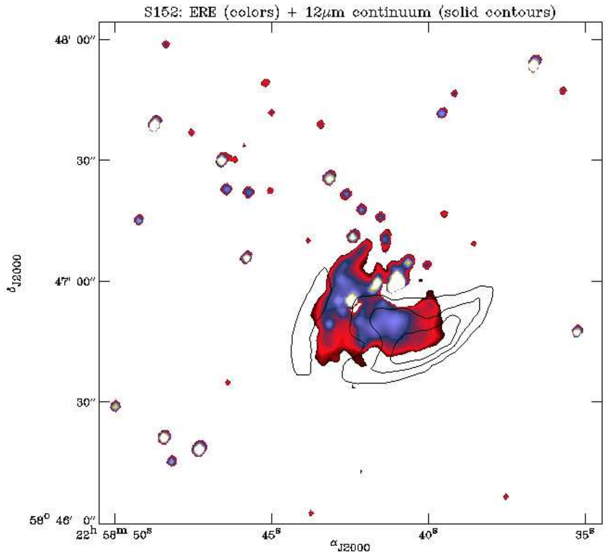

Figure 3. ERE distribution (colors) in Sh 152 and 12 μm continuum image (solid contours)

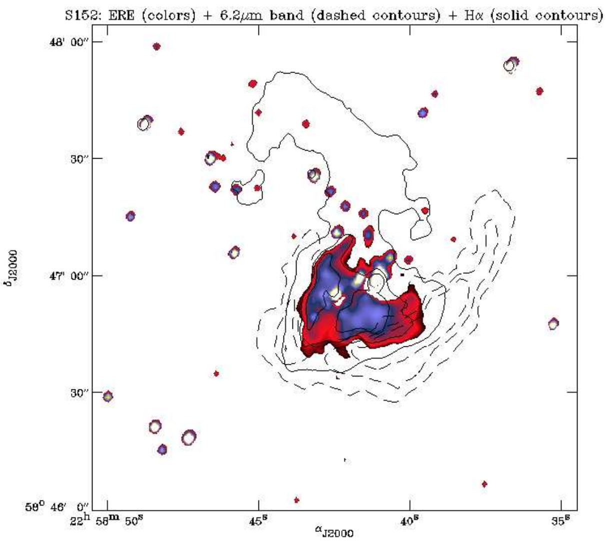

Figure 2. ERE distribution (colors), 6.2 μm emission band (dashed contours) and Hα emission (solid contours) in Sh 152

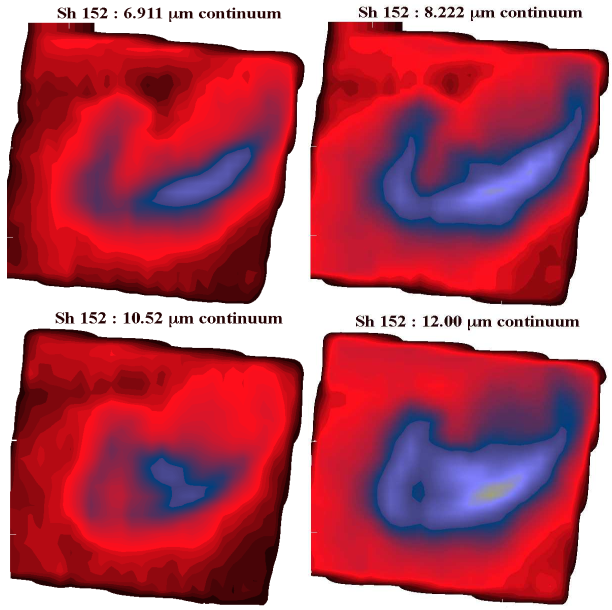

Figure 4. Continuum emission in Sh 152 observed with the ISOCAM CVF at 6.911, 8.222, 10.52 and 12.00 μm

3. RESULTS AND DISCUSSION

The 3.3 μm, 6.2 μm and Hα images of Sh 152 are displayed in Figure 1. It can be seen that the 3.3 and 6.2 μm emission bands have the same spatial distribution over the entire nebula. This suggests their carriers could be the same. Also, it appears from Figure 1 that the infrared emissions arise from regions located outside the ionized regions (traced by Hα emission).

Figure 2 presents the spatial distribution of ERE superimposed on the 6.2 μm band image and the Hα image. ERE is found to coincide with the Hα emission but significantly differs from that of the 6.2 μm emission band. Hydrogen environment and UV radiation are well suited to induce luminescence from HAC grains (Furton & Witt 1993).

Figure 3 presents the spatial distribution of ERE superimposed on a 12 μm continuum image. It can be seen that the 12 μm emission extends over the area where the ERE intensity reaches its maximum. This coincidence is in favor of grains as carriers of the ERE because (i) the 12 μm emission is thought to be the short wavelength part of a strong thermal emission from cold grains (see, for example, IR spectra of ultra compact galactic H II regions presented by Roelfsema et al. 1998) and (ii) because such cold grains can exist in Sh 152 at the distance from the exciting star where the observed coincidence occurs.

In effect, according to Lamy & Perrin (1997), the temperature of a dust solid particle located at a distance 10^4 $R_* = 2.10^2$ AU $= 10^{-3}$ pc from an O9.5 V star of radius $R_* \simeq 2.10^{-2}$ AU, would be of 200K for a silicate grain or 400K for a carbonaceous grain. The region in Sh 152 where ERE maximum and 12 μm emission coincide is in fact much farther from the star (about 0.2 pc, assuming a distance of 3.5 kpc for Sh 152 (Heydari-Malayeri & Testor 1981) than in the calculations so that, although the exciting star of Sh 152 is slightly hotter than an O9.5V star (Hunter & Massey 1990), we can assume that cold grains do exist in the area.

Figure 4 presents the four continuum images of Sh 152 at 6.911, 8.222, 10.52 and 12.00 μm taken with ISOCAM. In these images, the flux is normalized to the maximum observed in the LW6 filter, centered at 7.7 μm. At the location of the ERE maximum, the infrared images show flux values increasing with wavelength : this is in agreement with thermal emission from cold grains (note that the 10.52 μm flux might be contaminated by the [SIV] 10.54 μm emission line).

4. CONCLUSION

Visible and infrared images of Sh 152 allowed us to compare the spatial distribution of ERE and UIBs and to deduce basic physical properties. We found that :

- the spatial distribution of the two UIBs at 3.3 and 6.2 μm are the same, suggesting similar properties for their carriers
- the UIRBs emission peak is located at the border of the ionized region
- the ERE emission coincides with the ionized region and significantly differs from the UIBs location.
- the continuum emission observed between 10.5 and 12 μm is coincident with ERE emission and possibly due to cold grains, which is in favor of grains as carriers of the ERE.

Nevertheless, the exact nature of the ERE carriers will only be constrained using spectroscopic data and comparing the ERE band shape with laboratory experimental data (Darbon et al. in preparation)

REFERENCES

Allamandola, L.J., Tielens, A.G.G.M., Barker, J.R. 1989, ApJS 71, 733

Darbon, S., Perrin, J.-M., Sivan, J.-P. 1998, A&A 333, 264

Furton, D.G., Witt, A.N. 1993, ApJ 415, L51

Furton, D.G., Witt, A.N. 1992, ApJ 386, 587

Gordon, K.D., Witt, A.N., Friedmann, B.C. 1998, ApJ 498, 522

Heydari-Malayeri, M., Testor, G. 1981, A&A 96, 229

Hunter, D.A., Massey, P. 1990, AJ 99, 846

Lamy, P.L., Perrin, J.-M. 1997, A&A 327, 1147

Ledoux, G., Ehbrecht, M., Guillois, O., Huisken, F., Kohn, B., Laguna, M.A., Nenner, I., Paillard, V., Papoular, R., Porterat, D., Reynaud, C. 1998, A&A 333, L39

Papoular, R., Conard, J., Giuliano, M., Kister, J., Mille, M. 1995, A&A 217, 204

Perrin, J.-M., Darbon, S., Sivan, J.-P. 1995, A&A 304, L21

Puget, J.-L., Léger, A. 1989, ARA&A 27, 161

Roelfsema, P.R., Cox, P., Kessler, M.F., Baluteau, J.-P. 1998, in: Star Formation With The Infrared Space Observatory (ISO), eds. Yun, J.L., Liseau, R. (Lisbon: ASP Conf. Ser., 132), 76

Schmidt, G.D., Cohen, M., Margon, B. 1980, ApJ 239, L133

Sivan, J.-P., Perrin, J.-M. 1993, ApJ 404, 258

Szomoru, A., Guhathakurta, P. 1998, ApJ 494, L93

Watanabe, J., Hasegawa, S., Kurata, Y. 1982, Japanese Journal of Applied Physics 21, 856

Witt, A.N., Boroson, T.A. 1990, ApJ 355, 182

Witt, A.N., Gordon, K.D., Furton, D.G. 1998, ApJ 501, L111

THE DISTRIBUTION OF GALACTIC IR DARK CLOUDS FROM MSX SURVEY MAPS

M.P. Egan[1], S.J. Carey[2], S.D. Price[1],
R.F. Shipman[1], P. Feldman[3], & R. Redman[3]

[1]Air Force Research Laboratory, Hanscom AFB, MA, USA
[2]Institute for Scientific Research, Boston College, Chestnut Hill, MA, USA
[3]National Research Council of Canada, Dominion Astrophysical Observatory, Victoria, BC, CANADA

ABSTRACT

In quadrants I and IV of the Milky Way we have detected > 5000 Infrared Dark Clouds (IRDCs) using the MSX Galactic Plane Survey images at 8 μm. Follow-up observations of a sample of the IRDCs in the millimeter-wave and sub-millimeter regions of the spectrum confirm initial estimates of the high density ($>10^5$ cm^{-3}) and low temperature ($\sim$10 K) of the clouds. The distribution of the clouds maps known structures in the Galaxy (spiral arm tangents, the molecular ring).

Key words: ISM:clouds; IR:surveys.

1. INTRODUCTION

Pérault et al. (1996) reported that ISOCAM mid-IR images from the first ISOGAL survey field revealed the presence of numerous dark patches. They postulated that these are dense filaments which are optically thick at 15 μm, implying A$_V$>25.

From May 1996 through January 1997, the Midcourse Space Experiment (MSX) surveyed the Milky Way within $|b| < 5°$ at mid-IR wavelengths (6 colors between 4 and 22 μm). The MSX images show a population of these IR dark cores, >2000 within $|b| < 0.5°$ (Egan et al. 1998). From the 8 μm data, we estimated A$_V$>60. We also compared a number of the MSX image regions to IRAS 100 μm image maps. No emission or point sources were seen in the long wavelength IRAS data. Lis and Menten (1998) also note a lack of infrared emission at wavelengths less than 100 μm for their LWS observations of an infrared dark cloud located near the Galactic center. The lack of infrared emission (for $\lambda < 100$ μm) implies dust temperatures around $\sim$10K.

At present, we have examined the MSX Galactic plane survey data in quadrants I and IV, for Galactic latitudes within three degrees of the Galactic plane. In this region, (approximately 1000 square degrees) we have found 5566 IRDCs with diameters larger than 1.5 arc-minutes.

2. MM AND SUB-MM OBSERVATIONS

These estimates of the cloud physical conditions were confirmed by millimeter wave observations of H_2CO rotational lines, which trace high density gas, for ten infrared dark clouds. All ten clouds were detected in the $2_{12} - 1_{11}$ transition of H_2CO. There is good agreement between the mid-infrared extinction and H_2CO emission morphologies. Excitation analyses of the millimeter data indicate gas densities of $n > 10^5$ cm^{-3} and gas kinetic temperatures between 7 and 15 K for various clouds. Asymmetries in the observed line profiles suggest the presence of molecular outflows and/or infall. The distances estimated for the ten clouds observed are between 1.0-8.5 kpc resulting in cloud diameters of 0.5-15.0 pc. Details of these observations and derived parameters can be found in Carey et al. (1998).

Sub-millimeter continuum observations of 9 clouds have been made at 450 and 850 μm using the SCUBA instrument at the JCMT. We detected all 9 of the observed clouds. The sub-millimeter emission morphology agrees with the mid-infrared extinction and H_2CO emission morphologies and reveals considerable sub-structure in the IRDCs. Figure 1 displays a representative submillimeter scan map of a typical IRDC, G28.34+0.06. The IRDCs are strong submillimeter emission sources, with peak strengths of $\sim$1 Jy/beam (beamsize=13 arc-seconds FWHM). It is likely that the sub-millimeter emission peaks are due to protostellar or pre-protostellar condensations. These results also confirm the cold and dense nature of the dust.

3. SPATIAL DISTRIBUTION OF IRDCS

We have catalogued 5566 IRDCs larger than 1.5 arcminutes in diameter in quadrants I and IV of the Galactic plane (within $|b| \leq 3°$). For the most part, the spatial distribution of the Infrared Dark Clouds (IRDCs) is coincident with the molecular ring and spiral arms of the Milky Way. Nearly 80% of the clouds we have identified from the MSX images lie within $|l| \leq 30°$. In latitude, the clouds are also cen-

Proceedings of the Conference "The Universe as seen by ISO", Paris, France, 20–23 October 1998 (ESA SP-427, March 1999)

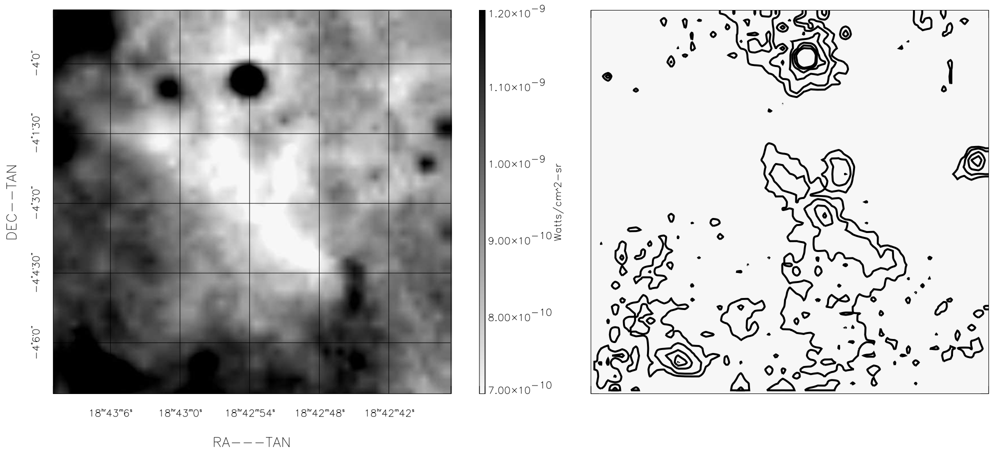

Figure 1. Left: MSX image of the cloud G28.34+0.06 at 8 μm. The IRDC is clearly seen as the white patch in the center of the image. The resolution of this image is 18 arcseconds. Right: Contour map of SCUBA 850 μm observations of the same region. The contour levels are 180, 360, 720, 1080 and 1440 mJy. The beamsize for a SCUBA bolometer is 13 arcseconds and the SCUBA data has been gridded with 9 arcsecond pixels.

trally condensed, with ~80% within |b| $\leq 1°$ - see Figures 2 and 3. This distribution makes physical sense, since most of the molecular material in the Galaxy is along these lines of sight. However, we identify these clouds in silhouette against the IR bright background of the Galactic plane; therefore, it is possible that selection effects influence this distribution. In addition, the complete distribution of IRDCs is difficult to ascertain as they can be shadowed both by foreground IRDCs as well as bright IR emission regions. The H_2CO line velocities observed are similar to recombination lines associated with HII regions within 0.5° on the sky, indicating that the clouds we identify in the IR are in the structures they appear superimposed on.

In the molecular ring and the arm regions, there are typically more than 15 IRDCs per square degree within $|b|\leq 1°$. The highest density of cores occurs at $l = 340°$, along the line of sight which intersects the molecular ring, the 3 kpc expanding arm, and the Norma tangent. Here there are up to 60 IRDCs per square degree.

4. SIZE DISTRIBUTION OF THE IRDCS

Figure 4 shows the size (projected area) distribution of IRDCs in quadrants I and IV (solid line) and the size distributions in two interesting regions. The plots are not cumulative, but show the number of clouds in each bin. Using a dotted line, we plot the size spectrum for the Cygnus region, while the dashed line shows the IRDC size distribution within 350°>l>330°. The second region, as noted above, encompasses the area of highest cloud density, and samples a line of sight through three distinct galactic components.

The overall distribution does not have a single distinct slope; however, the distribution of cloud areas in Cygnus has a slope of about -1 on this log-log plot. Plotting the size distribution of clouds near the Galactic center (|l|<10°) also yields a distribution with a slope of -1. The 350°>l>330° distribution shows a slope of -1 for clouds less than about 0.005 square degrees, but has an enhancement in the number of clouds near 0.01 square degrees. A similar enhancement in the distribution of clouds can be seen at 10°<l<30°. This line of sight is also complex, including the molecular ring and the Scutum tangent.

One way to interpret this data is to assume that the IRDCs are of a given physical size. In that case, if the clouds were uniformly distributed along a line of sight, we expect a slope of -1 on the logN-logA plot. We see this in the Cygnus and Galactic center distributions. The molecular ring data (the two samples centered on |l|=20°) suggests an enhancement in the number of clouds at a certain distance along lines of sight at both positive and negative Galactic latitudes. This is consistent with looking through the edge of the molecular ring, which is near ± 30°.

This interpretation also implies that the Cygnus clouds are intrinsically smaller than the molecular ring clouds and Galactic center IRDCs, given their relative distances (1 kpc for Cygnus, 4 - 6 kpc to the molecular ring). Different typical cloud sizes in different galactic structures may provide a clue to the formation mechanism of these clouds. If cloud-cloud collisions are important in IRDC formation, one might expect larger IRDCs in regions with a higher number density of giant molecular clouds.

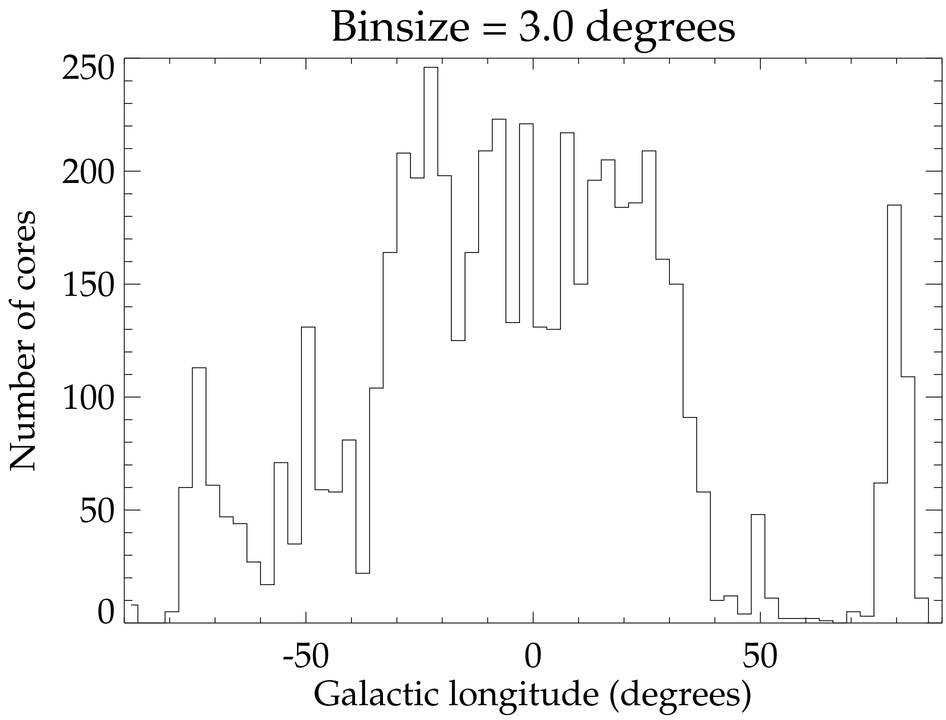

Figure 2. The distribution of the infrared dark clouds in Galactic longitude.

5. CONCLUSIONS

The ISO and MSX missions have identified a population of very dense, cold cores in the Galactic plane. The MSX Galactic plane survey has found > 5000 of these Infrared Dark Clouds larger than 1.5 arcmin in diameter (which is equivalent to 0.44 pc if a distance of 1 kpc is assumed) in quadrants I and IV of the Milky Way. The distribution of dark clouds traces spiral arms, the molecular ring and other regions of enhanced star formation. The infrared dark clouds are unusually large compared to typical molecular cloud cores which have diameters on the order of 0.1 pc. The combination of the infrared, millimeter, and sub-millimeter observations demonstrate that these large cores have high densities and low temperatures. The large column density and low kinetic temperatures of the infrared dark clouds make them ideal sites to probe grain surface chemistry and search for large carbon molecules with closely spaced rotational states. The H_2CO line profiles possibly suggest the presence of molecular outflow or infall. Also, the submillimeter maps indicate substructure in the clouds; however, the lack of infrared emission from these objects restricts any star formation activity to the earliest stages (protostellar class 0 or earlier).

The large number of dark clouds detected (comparable to the total number of giant molecular clouds observed in the Galaxy) suggest they are an important step in the star formation process. Further study of this population of objects is needed to understand how such a large number of extremely large molecular cores can form and remain in a pre-star forming state. It is puzzling that such a large number of objects are observed to be in the short lived pre-protostellar state. The close proximity of the infrared dark clouds to star forming sites and the filamentary shape of many of the clouds suggest that they may be formed by molecular cloud collisions or shocks from nearby star formation. It is possible that the infrared dark clouds have enhanced support against collapse and/or need external triggers to induce star formation. Higher resolution spectral line mapping is needed to examine the internal structure of these clouds as well as identify outflow/infall sources. Submillimeter polarimetry may be of use in determining whether magnetic field support is responsible for supporting the infrared dark clouds against collapse.

REFERENCES

Carey, S.J., et al. 1998 ApJ, 508, 721

Egan, M.P., et al. 1998 ApJ, 494, L202

Lis, D. C., & Menten, K. M. 1998, ApJ, 507, 794

Pérault, M. et al. 1996, A&A, 315, L165

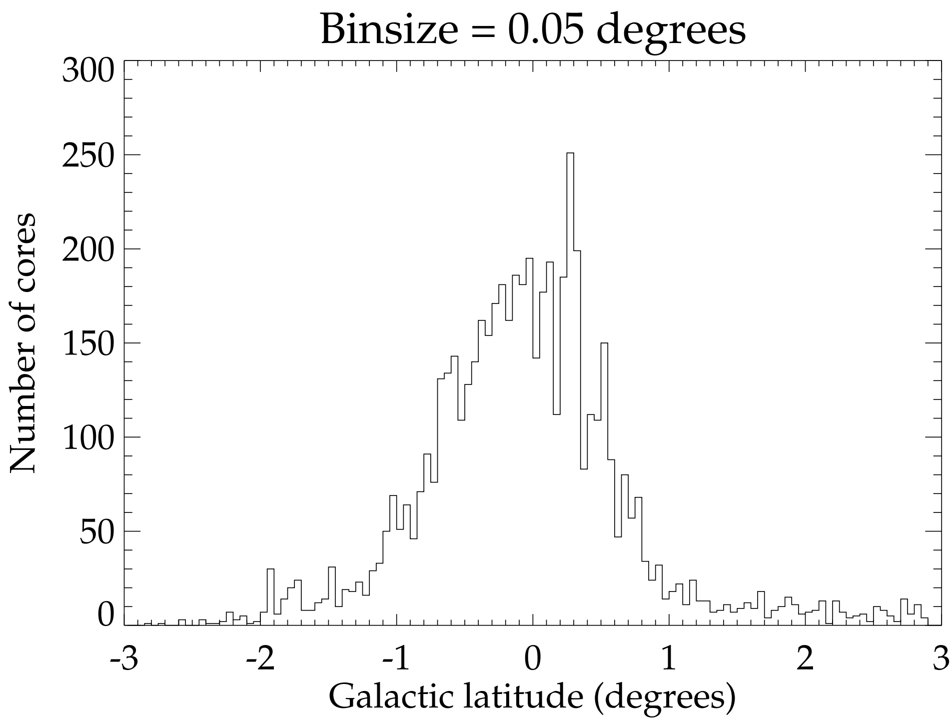

Figure 3. The distribution of the infrared dark clouds in Galactic latitude.

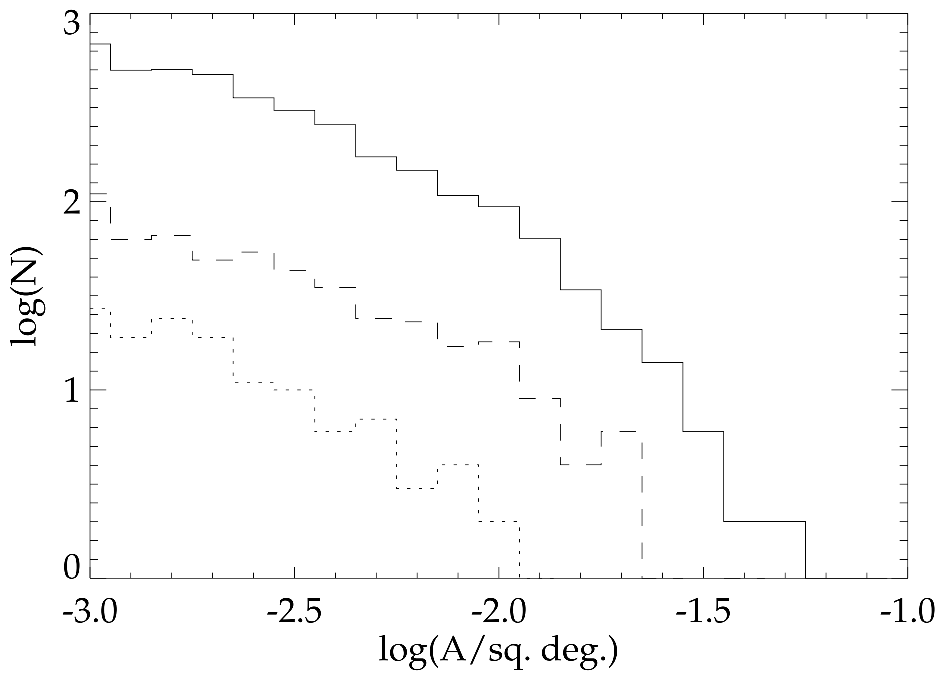

Figure 4. Size distribution of the infrared dark clouds. The solid line is the complete sample of clouds in quadrants I and IV. The dotted line is the population of clouds in the Cygnus region. The dashed line is the size distribution between -10 and -30 degrees Galactic longitude.

COLD SPOTS IN THE CHAMAELEON DARK CLOUDS

S. Hotzel[1], D. Lemke[1], L. V. Tóth[1,2]
M. Stickel[1], O. Krause[1], U. Klaas[1], S. Bogun[3],
M. F. Kessler[4], R.J. Laureijs[4], M. Burgdorf[4], C. A. Beichman[5],
M. Rowan-Robinson[6], A. Efstathiou[6], G. Richter[7], & M. Braun[7]

[1]Max–Planck–Institut für Astronomie, Königstuhl 17,
D–69117 Heidelberg, Germany
[2]Department of Astronomy, Loránd Eötvös University, Pázmány Péter sétány 1.
H–1117 Budapest, Hungary
[3]Data Management and Operations Division, ESO, Karl-Schwarzschild-Str. 2,
D–85748 Garching bei München, Germany
[4]ISO Data Centre, Astrophysics Division of ESA,
Villafranca, P.O. Box 50727, E–28080 Madrid, Spain
[5]Infrared Processing and Analysis Center, JPL, California Institute of Technology,
MS 100/22, Pasadena, CA 91125, USA
[6]Imperial College of Science, Technology and Medicine, The Blackett Laboratory,
Prince Consort Road, London SW7 2BZ, United Kingdom
[7]Astrophysikalisches Institut Potsdam, An der Sternwarte 16, D–14482 Potsdam, Germany

ABSTRACT

A method to detect very cold molecular cloud cores has been developed, using the ISOPHOT Serendipity Survey and the IRAS 100 μm data. As test case, three molecular cloud complexes in Chamaeleon have been investigated. Several cold spots ($T \approx 13$ K) have been detected in these fields, showing the success of the Serendipity Survey in locating cold cloud cores.

Key words: ISOPHOT Serendipity Survey ; ISM: cold dust; ISM: individual (Chamaeleon).

1. INTRODUCTION

The ISOPHOT Serendipity Survey is a far–infrared (FIR) survey at 170 μm, using the slewing time of the ISO telescope (Lemke et al. 1996). Altogether about 15 per cent of the sky is covered with an angular resolution (FWHM) of 2 arcmin (Bogun et al. 1996; for standard processing and calibration details cf. M. Stickel, these proceedings).

The long wavelength allows us to trace the cold dust of the interstellar medium. Standard dust models (Mathis et al. 1977) together with the average interstellar radiation field lead to typical grain temperatures of between $\sim$ 15 K and 19 K (Draine & Lee 1984). In Bok globules and molecular cloud cores somewhat lower temperatures are predicted and have been reported in many cases (e.g. Keene 1981, Lehtinen et al. 1998, Haikala et al. 1998). While the 60 μm IRAS data are still affected by the warmer very small grains, the FIR emission at 100 μm originates from the big grains alone (Désert et al. 1990), and so the comparison of the two bands at 100 μm (IRAS) and 170 μm (ISO) can determine the physical properties of the cold dust.

Ward–Thompson et al. (1998) reported the detection of cold cores in the Milky Way, which have been detected with ISOPHOT at 200 μm and 160 μm and in the mm and sub-mm range. Typically they remain undetected, or only weakly detected shortward of 100 μm. Temperatures of $\approx$ 13 K have been determined. These dense cores in molecular clouds are gravitationally bound but contain no embedded luminosity source. They represent the phase of star formation prior to the protostellar class 0 phase. With the 15 per cent sky coverage of the ISOPHOT Serendipity Survey it is possible for the first time to look for these objects in our Galaxy over a large fraction of the sky.

The region first investigated is Chamaeleon, containing the three molecular cloud complexes Chamaeleon I, II, and III. Several catalogues of optically opaque spots are available in this region of the sky (Vilas–Boas et al. 1994; Hartley et al. 1986), and the presence of some individual spots with cold dust is known (Haikala et al. 1998). Figure 1 gives an overview of the Chamaeleon region at 170 μm, pointing out the location of the investigated fields and showing the dense coverage of Chamaeleon with slews of the ISOPHOT Serendipity Survey.

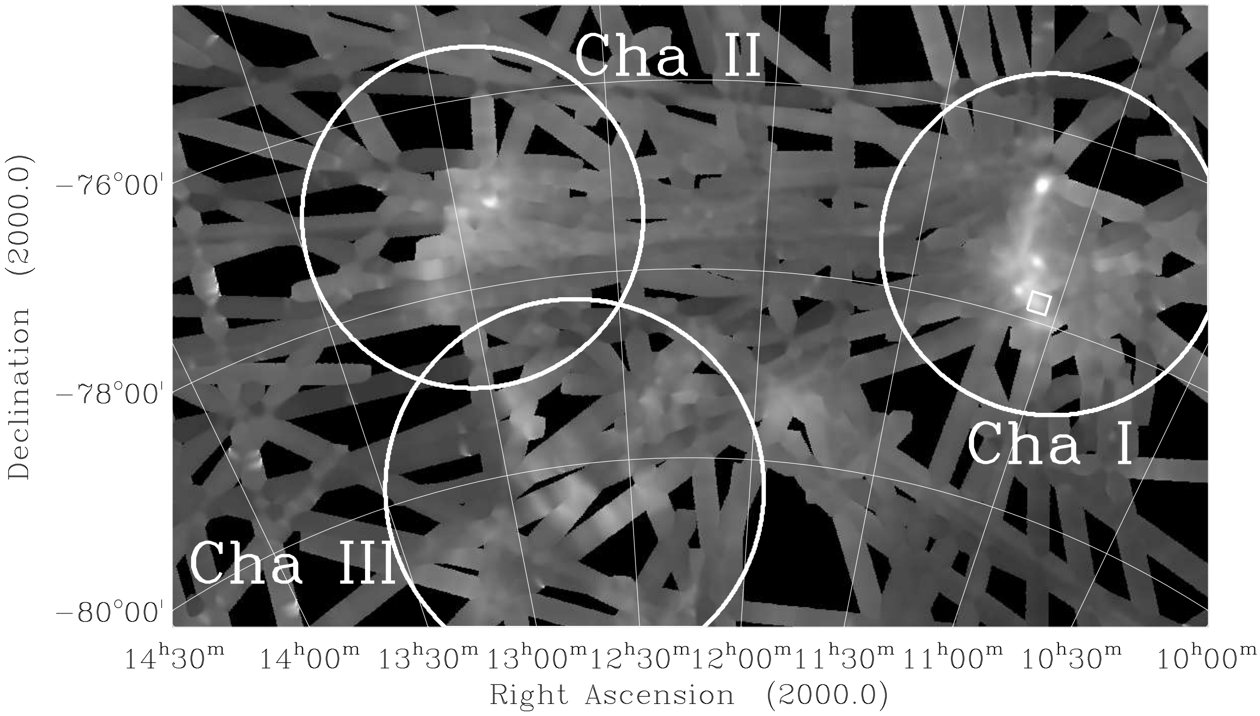

Figure 1. The Chamaeleon region at 170 μm. The map is a composite of the slews of the Serendipity Survey. It is smoothed to 4.5 arcmin resolution. The investigated (circular shaped) fields are indicated. The tiny square in Chamaeleon I marks the area covered by Figure 4.

2. THE METHOD

In order to derive dust temperatures, the 170 μm Serendipity data are compared with the 100 μm IRAS data. This is done in the following way:

After applying a deglitching algorithm (Stickel et al. 1998a, and these proceedings) all Serendipity slews are convolved one by one with a two-dimensional gaussian in order to match the IRAS resolution. As the information of the individual pixels becomes redundant at a resolution of 4.5 arcmin, the gaussian is always centred on the position of the detector centre instead of the positions of the four pixels. Thereby the data streams are reduced from 4 data points per sample (ramp) to 1 data point per sample.

The 100 μm intensity is read out of the ISSA maps along the Serendipity slews, i.e. at the detector centre position of all samples. The IRAS map pixel covering the position concerned, and all of the 8 adjacent pixels with distance dependent weight factors, are taken into account when calculating the IRAS 100 μm value of one sample.

The smoothed 170 μm slews are searched for intensity peaks. By definition, a peak is encountered where the intensity difference between two adjacent readouts increases compared to the preceding readouts. This can be quantified as a maximum in the second derivative of the intensity as a function of sky position. An increase of the intensity itself could be a background effect. To exclude that peaks are mimicked by noise, a lower limit of 1 MJy/sr for the peak intensity over the background is included. Figure 2

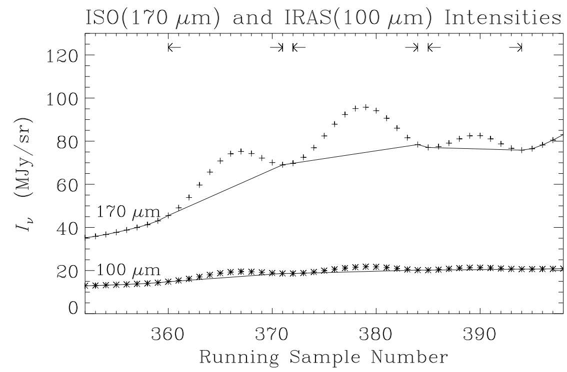

Figure 2. The course of the sky surface brightness at 170 μm (convolved Serendipity data, crosses) and at 100 μm (read out from ISSA maps, asterisks) is plotted against the sample number for a section of a slew. The solid lines represent the backgrounds. Here, 3 peaks are found as indicated below the top axis.

shows a section of a slew, where some peaks have been detected. The middle one will be followed further in Figure 3 and Figure 4.

Wherever a peak is encountered along the 170 μm slews, a linear background is defined for both ISOPHOT Serendipity Survey and IRAS data. As the peak in the 100 μm data might be small or even not detectable in the case of very cold dust emission, the extension of the source is assumed to be the same in both wavelengths (Figure 2).

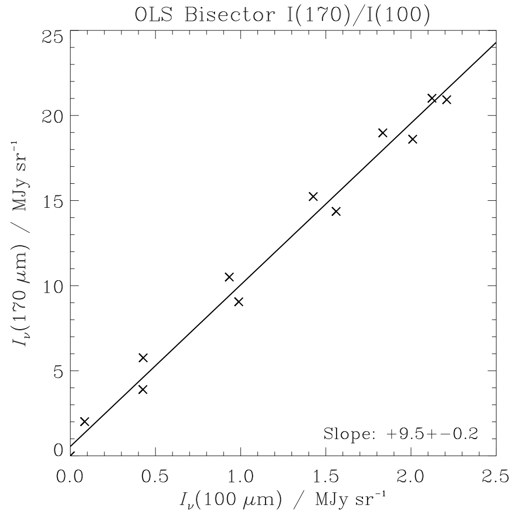

Figure 3. $I_\nu(170\ \mu m)$ versus $I_\nu(100\ \mu m)$ plot for the middle one of the peaks in Figure 2. A straight line is fitted to the data points, using the ordinary-least-squares bisector method. In this case, the slope of $I_\nu(170\ \mu m)/I_\nu(100\ \mu m) = 9.5$ corresponds to a colour temperature of $T \approx 12.5$K.

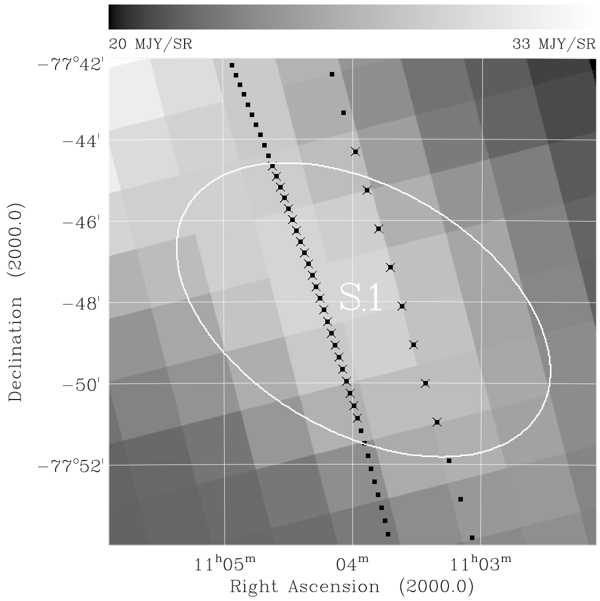

Figure 4. The area of the sky in which Figure 3 reveals the presence of a cold cloud core. The slews of the Serendipity Survey are plotted as small black dots on the IRAS 100 μm image. The samples belonging to the actual peaks are plotted as crosses. Both of the slews crossing this field have very high $I_\nu(170\ \mu m)$ to $I_\nu(100\ \mu m)$ ratio s. In this case, the slews detect a previously known molecular cloud core (indicated by the ellipse).

After subtracting the background, the $I_\nu(170\ \mu\mathrm{m})$ to $I_\nu(100\ \mu\mathrm{m})$ ratio is determined for each source. This is done by fitting a straight line to the $I_\nu(170\ \mu\mathrm{m})$ versus $I_\nu(100\ \mu\mathrm{m})$ plot (Figure 3), applying the ordinary-least-squares (OLS) bisector algorithm (Isobe et al. 1990). Although by using this procedure the absolute intensity levels at the two wavelengths are irrelevant for the intensity ratio, the background subtraction is necessary to account for a possible *slope* of the background underlying the source signal.

Finally, the dust colour temperature is calculated by modelling a modified Planck curve to the $I_\nu(170\ \mu\mathrm{m})$ to $I_\nu(100\ \mu\mathrm{m})$ ratio s. A ν^2 emissivity law is assumed, as calculated by Draine & Lee (1984) for interstellar graphite and silicate grains.

3. RESULTS

512 peaks of FIR emission have been found in the investigated region of 35 □°. About 5 per cent of these have $I_\nu(170\ \mu\mathrm{m})/I_\nu(100\ \mu\mathrm{m})$ ratios corresponding to dust colour temperatures as low as 13 K.

All sources with $T_{\mathrm{dust}} \leq 14$ K have been cross-checked against catalogues of optically opaque spots (Hartley et al. 1986, Vilas–Boas et al. 1994), molecular cloud cores (Vilas–Boas et al. 1994), and – for Chamaeleon I only – maxima of FIR dust emission as seen with ISOPHOT by Haikala et al. (1998). To do this, all slew sections concerned were projected back on the sky together with the catalogued objects. This way we can identify

- peaks in different slews that actually detect the same object
- detections in the ISOPHOT Serendipity Survey with objects known from other wavelengths.

This can be seen in Figure 4, which shows the location of the intensity peak presented in Figure 3. Here, actually *two* slews have almost parallel paths, and both have very high $I_\nu(170\ \mu\mathrm{m})$ to $I_\nu(100\ \mu\mathrm{m})$ ratio s. It is evident that the two findings belong to the same cloud core: it is the previously known molecular cloud core S1 (Haikala et al., 1998).

In areas where there is no object in the catalogues even though the Serendipity Survey detects cold dust, the Digitized Sky Survey has been inspected additionally by eye for putatively associated optical features.

It turned out that the vast majority of cores with $T_{\mathrm{dust}} \approx 13$ K have optical nebulosities associated, and that for a subset of these cores – where Vilas–Boas et al. (1994) measured $C^{18}O$ – the kinetic gas temperature is low. The full details of the findings will be presented elsewhere.

4. CONCLUDING REMARKS

In three test fields investigated in the Chamaeleon region, the method presented to detect cold dust in molecular clouds has proved successful. Despite the difference in data structure, the ISOPHOT Serendipity Survey and the IRAS 100 μm maps can be reliably used for finding cold dust anywhere within the

15 per cent of the sky covered by the Serendipity Survey. This was not possible before ISO, as the comparison of two IRAS bands alone cannot trace dust colour temperatures < 25 K.

In a next step we will expand the cold spot search to other regions, such as Orion, Taurus, Cygnus, Coalsack, Cepheus. Furthermore it is anticipated to make use of the full angular resolution of the ISOPHOT Serendipity Survey, while so far the Serendipity data have been smoothed to 4.5 arcmin. For selected fields this can be achieved by combining the Serendipity Survey with HIRES data instead of ISSA maps. By comparing these results with mm-wave spectroscopy data, which explore the gas content of the clouds, it will also be possible to examine the gas – dust relations in density and temperature in cold molecular cloud cores.

ACKNOWLEDGMENTS

The ISOPHOT project was funded by the Deutsche Agentur für Raumfahrtangelegenheiten (DARA, now DLR), the Max - Planck - Gesellschaft, the Danish, British and Spanish Space Agencies and several European and American institutes.
Members of the Consortium on the ISOPHOT Serendipity Survey (CISS) are MPIA Heidelberg, ESA ISO SOC Villafranca, AIP Potsdam, IPAC Pasadena, Imperial College London.
This research has made use of the Digitized Sky Survey, produced at the Space Telescope Science Institute, NASA's Astrophysics Data System Abstract Service, and the NASA/IPAC Extragalactic Database (NED) which is operated by the Jet Propulsion Laboratory, California Institute of Technology, under contract with the National Aeronautics and Space Administration.

REFERENCES

Bogun, S., Lemke, D., Klaas, U., et al. 1996, A&A, 315, L71

Draine, B.T., Lee, H.M. 1984, ApJ, 285, 89

Désert, F.X., Boulanger, F., Puget, J.L. 1990, A&A, 237, 215

Hartley, M., Manchester, R.N., Smith, R.M., Tritton, S.B., Goss, W.M. 1986, A&A Suppl. Ser., 63, 27

Haikala, L.K., Mattila, K., Lehtinen, K., Lemke, D. 1998, in "Star Formation with ISO", J.L. Yun & R. Liseau (eds.), ASP Conf. Ser. 132, p.147

Isobe, T., Feigelson, E.D., Akritas, M.G., Babu, G.J. 1990, ApJ, 364, 104

Keene, J. 1981, ApJ, 245, 115

Lehtinen, K., Lemke, D., Mattila, K., Haikala, L.K. 1998, A&A, 333, 702

Lemke, D., Klaas, U., Abolins, J., et al. 1996, A&A, 315, L64

Mathis, J.S., Rumpl, W., Nordsieck, K.H. 1977, ApJ, 217, 425

Stickel, M., Lemke, D., Bogun, S., et al. 1998a, in "Observatory operations to optimize scientific return", P.J. Quinn (ed.), Proc. SPIE 3349, p.115

Stickel, M., Bogun, S., Lemke, D., et al. 1998b, A&A, 336, 116

Vilas–Boas, J.W.S., Myers, P.C., Fuller, G.A. 1994, ApJ, 433, 96

Ward–Thompson, D., André, Ph., Motte, F. 1998, in "Star Formation with ISO", J.L. Yun & R. Liseau (eds.), ASP Conf. Ser. 132, p.195

THE INFRARED EMISSION FROM DUST IN THE M17-SW HII REGION: PARTIALLY CRYSTALLINE SILICATES IN THE ISM?

A.P. Jones, V. Frey, L. Verstraete, P. Cox, & K. Demyk

Institut d'Astrophysique Spatiale (IAS), Université Paris XI - Bât. 121, 91405 Orsay Cedex, France.

ABSTRACT

We present the results of models for the infrared dust emission observed in the M17-SW HII region by the ISO Short Wavelength Spectrometer. We interpret the observed spectra in terms of the thermal emission from amorphous carbon and silicate grains, and from Mg-rich crystalline olivine silicates. We estimate that of the order of a few percent of the silicate grain mass in the HII region could be crystalline. Stochastically heated small carbon particles must also be present, in order to explain the short wavelength emission, and we find that in the HII region there is an underabundance of the unidentified infrared band carriers (or PAHs), compared to the adjacent photo-dissociation region.

Key words: IR dust emission, HII regions, M17-SW

1. INTRODUCTION

The region M17-SW contains young massive stars that are irradiating a dense molecular cloud complex. Immediately around four of the central and brightest stars of type O4 V, O5 V and O8 V, which produce $\sim$ 70% of the ionising flux (Felli et al. 1984), there is an HII region with a radius of about 1 pc. Within and around this HII region the infrared (IR) emission from dust heated by the central stars was detected by the Short Wavelength Spectrometer (SWS) on board the Infrared Space Observatory (ISO) (Verstraete et al. 1996). In this paper we model this emission in terms of the thermal emission from large grains in thermal equilibrium with the radiation field and from transiently heated small carbonaceous grains.

2. OBSERVATIONS

The data that we use in this study were obtained as part of a guaranteed-time central program using SWS on board the ISO satellite. They were first described by Verstraete et al. (1996) where details of the original observational parameters and the data processing can be found.

In this work we consider the four SWS data positions towards the M17-SW HII region. SWS position 1 is approximately half way between the exciting stars and the HII region–molecular cloud interface, position 4 is at the interface 1 pc from the stars and the intervening two positions (2 and 3) are equi-distant between positions 1 and 4.

3. THE IR SPECTRA AND MODELLING

We have modelled the IR emission from the dust in the HII region by assuming that a major part of the dust mass is in thermal equilibrium with the local stellar radiation field. This radiation field is taken to be the sum of the radiation from the four closest stars (O4 V, two O5 V and O8 V) at their given distances from the centre of the HII region (Felli et al. 1984). In addition, we have also considered the IR emission from stochastically heated grains using the model of Désert et al. (1999).

Assuming that the dust within this region is composed of a mixture of amorphous carbons and amorphous and crystalline silicates we have adopted the optical constants of amorphous carbon (Rouleau & Martin 1991) and amorphous astronomical silicate (Draine 1985), and the transmittance of Mg-rich crystalline olivine, $(Mg_{0.8}Fe_{0.2})_2SiO_4$, measured in the laboratory at the IAS. In Figure 1 we show the temperatures of amorphous carbon and silicate grains as a function of distance from the centre of the HII region.

Figures 2 to 5 show the SWS observations and the modelled IR emission, assuming that the grains are in thermal equilibrium with the local radiation field. We find a good match to the observed emission spectra with amorphous carbon grain temperatures in the range 105–130 K, and silicate grain temperatures in the range 55–63 K (see Table 1). The derived amorphous carbon temperatures are consistent with the emission from 500 to 1500 Å radius grains at a distance of $\sim$1 pc from the exciting stars (Figure 1). However, the derived silicate temperatures are too cold because 500 to 1500 Å radius astronomical silicates grains have temperatures of the order of 100 K $\sim$ 1 pc from the exciting stars (Figure 1), the observed size of the HII region. This indicates that the emission properties of silicates in this region

Proceedings of the Conference "The Universe as seen by ISO", Paris, France, 20–23 October 1998 (ESA SP-427, March 1999)

are different from those of the amorphous silicates in the general diffuse interstellar medium (ISM). We are currently investigating the possible causes of enhanced silicate grain emissivity.

Table 1. Amorphous astronomical silicate and carbon grain temperatures (K) as a function of distance from the exciting stars at the SWS data positions.

SWS position	Distance (pc)	Temperature (K) Carbon	Temperature (K) Silicate
1	0.5	130	63
2	0.67	130	60
3	0.83	120	62
4	1.0	105	55

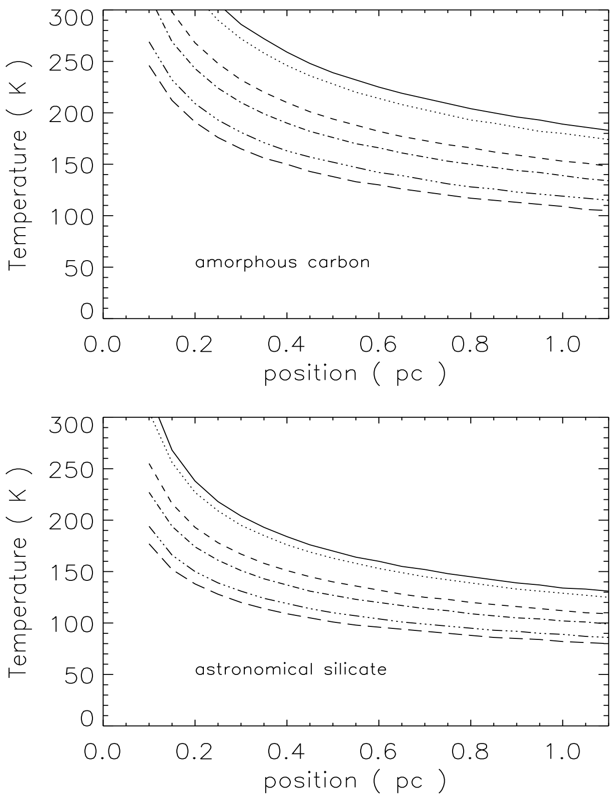

Figure 1. Dust temperatures as a function of distance from the exciting stars for amorphous carbon and astronomical silicate grains of radii 10 Å (solid), 100 Å (dotted), 300 Å (short-dashed), 500 Å (dotted-dashed), 1000 Å (triple-dotted-dashed), 1500 Å (long-dashed).

In the continuum-subtracted spectra of Figures 2 to 5 we note the good fit of the Mg-rich crystalline olivine 34μm band to the observed spectrum, and the presence of an, as yet unidentified, emission feature in the 20μm to 25μm region which decreases in intensity with distance from the exciting stars. We also note that the bands shortward of 15 μm are not well-matched by our model, we attribute them to emission from a carbonaceous grain component which may be associated with the unidentified IR band (UIB) carriers. The contrast between the UIBs, or so-called polycyclic aromatic hydrocarbon (PAH) bands, at 3.3, 6.2, 7.7, 8.6, 11.3 and 12.7 μm and the underlying continua increases with distance from the exciting stars. We conclude that the broad emission bands underlying the PAH bands are carried by a resilient grain component that survives in the high excitation regions where the PAH band carriers are destroyed (Allain et al. 1996). Alternatively, the UIB band carriers/PAHs may have been expelled by radiation pressure. Although, Cherchneff et al. (1991) found that PAHs couple less effectively to a radiation field than small amorphous carbon grains, and so band carrier destruction within the HII region may be the more plausible explanation.

We have also calculated the IR emission from the dust in the HII region using the model of Désert et al. (1999) for the emission from PAHs, very small grains (VSGs) and large silicate grains. In Figure 6 we present the results obtained using the Désert model for SWS position 1. In order to obtain a good fit to the emission shortward of 15 μm we found it necessary to decrease the abundance of the PAH component (the carrier of the UIBs in the Désert model) by an order of magnitude and to decrease the upper size limit for the VSG component to 100 Å. In this model we retained the 'standard' Désert et al. silicate size distribution. With this model (Figure 6) we are able to reproduce the short wavelength continuum which arises from stochastically-heated amorphous carbon VSGs. The broad feature in the 11–15 μm region which is not well-matched by the model is probably due to a carbonaceous grain component. This model also predicts amorphous silicate grain temperatures that are too hot, in agreement with the thermal equilibrium model results (see above). Clearly, the silicate grains in this region are different from those in the general diffuse ISM. We find similar results for all SWS positions within the HII region. We also note that in order to best fit the short wavelength emission within the region it is necessary to introduce a systematic decrease in the PAH abundance towards the centre of the HII region. This again seems to indicate small carbon grain destruction within the HII region.

4. DISCUSSION

The results presented here are particularly intriguing within the context of the evidence from ISO for partially crystalline silicates in both young and evolved stars (Waelkens et al. 1996; Waters et al. 1996; Malfait et al. 1998) and also in comets (Crovisier et al. 1996). We conclude that we may also be seeing crystalline silicates in the M17-SW HII region, an environment close to hot stars where the dust has been heated to temperatures of the order of 100 K for long periods, or may have been heated to higher temperatures earlier in the evolution of the region. In contrast, all evidence from the 10 and 18 μm silicate bands in the diffuse ISM indicates that the silicates are completely amorphous (e.g., Mathis 1990).

We must also also consider the possibility that, because the observed bands in the 20–40 μm region are rather weak with respect to the continuum, that they are due to some instrumental effect. We can neglect memory effects because the observed bands are too

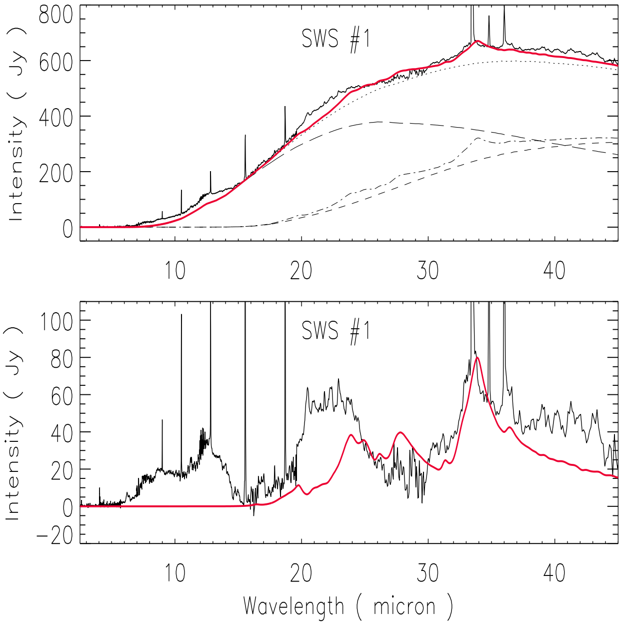

Figure 2. *Upper: observed and calculated emission spectra at SWS position 1 in M17-SW; SWS data ("noisy" solid line), and emission from 63 K amorphous silicate (short-dashed line), 63 K Mg-rich crystalline silicate (dashed-dotted line), 130 K amorphous carbon (long-dashed line), amorphous silicate and carbon (dotted line), and total calculated emission spectrum ("smooth" line). Lower: amorphous silicate and carbon continuum-subtracted SWS data ("noisy" line) and crystalline silicate emission ("smooth" line).*

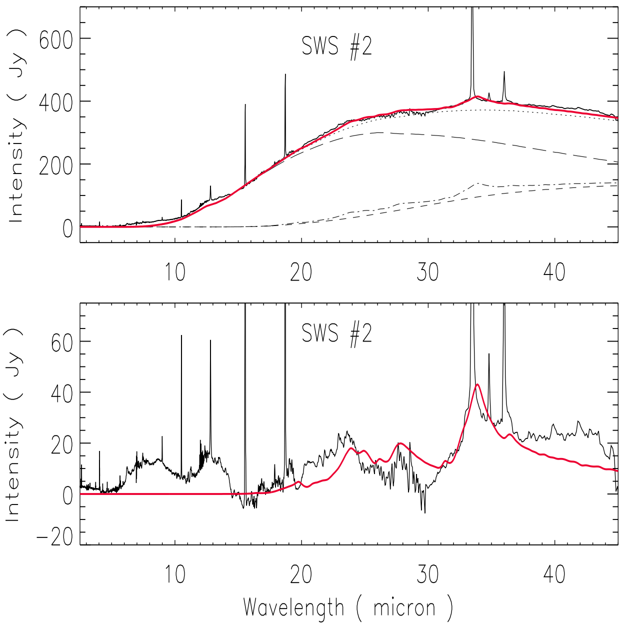

Figure 3. *SWS position 2 as per Figure 2; 60 K amorphous silicates (short-dashed line), 60 K Mg-rich crystalline silicates (dashed-dotted line), 130 K amorphous carbons (long-dashed line).*

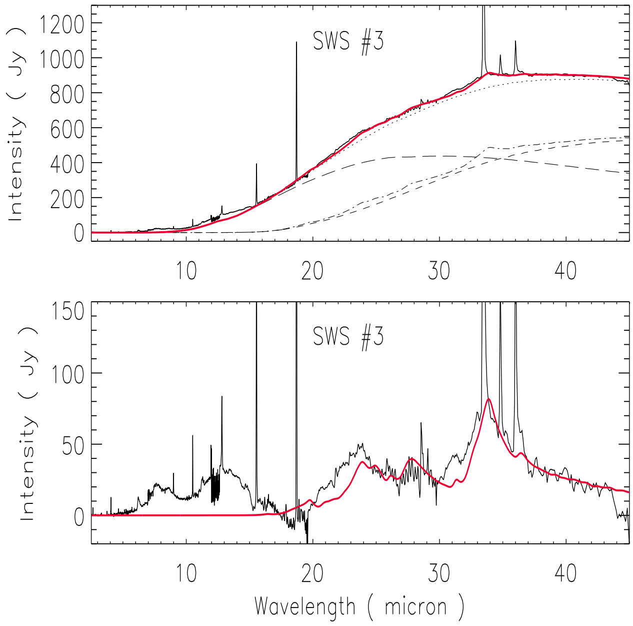

Figure 4. *SWS position 3 as per Figure 2; 62 K amorphous silicates (short-dashed line), 62 K Mg-rich crystalline silicates (dashed-dotted line), 120 K amorphous carbons (long-dashed line).*

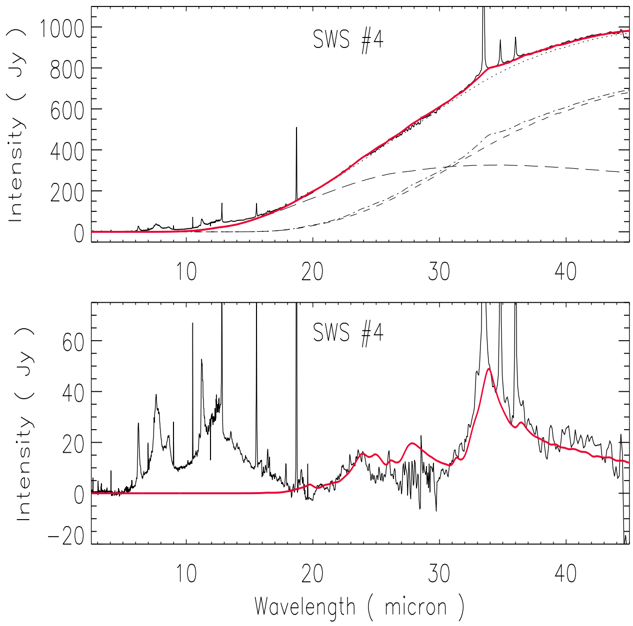

Figure 5. *SWS position 4 as per Figure 2; 55 K amorphous silicates (short-dashed line), 55 K Mg-rich crystalline silicates (dashed-dotted line), 105 K amorphous carbons (long-dashed line).*

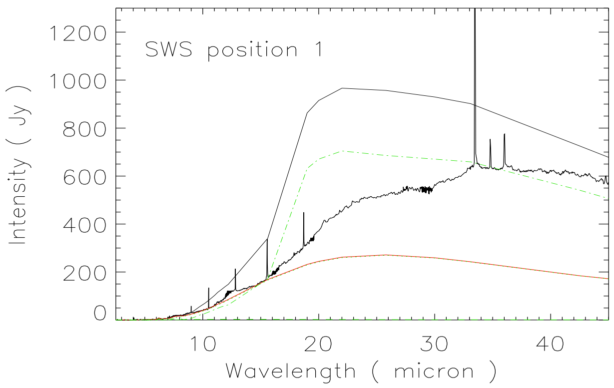

Figure 6. SWS position 1 emission spectrum ("noisy" solid line) and fit using the Désert et al. (1990) model. Note the good fit of the carbon VSG emission at short wavelengths (lower solid line) but the poor fits for the silicate (dotted line) and the total emission (upper solid line).

broad. We cannot entirely rule out an instrumental effect, but we do note the remarkable coincidence between the crystalline bands and several of the observed features. In support of this we note that at the SWS positions within the adjacent molecular cloud, with similar emission at 40 μm, we see no change in slope in the spectra at 34 μm.

The presence of a crystalline silicate component in an HII region seems to indicate the *in situ* partial crystallisation of amorphous silicates, or that the interstellar silicates incorporated into this region were not completely amorphous. We estimate that of the order of a few percent of the silicate mass could be crystalline. This is a small fraction of the total silicate mass and any crystalline silicate bands would, in *absorption*, be completely hidden by the broad and featureless amorphous silicate bands at 10 and 18 μm. Crystalline silicate dust may therefore only be observable in emission, as seen here in the M17-SW HII region.

Alternatively, it is possible that the silicates are annealed *in situ*. Can the heating of amorphous silicates at temperatures well below the glass temperature lead to the partial crystallisation of silicates? Current indications are that the crystallisation of silicates occurs only at temperatures above 1000 K for Mg-rich and above 1300 K for Fe-rich silicates (Hallenbeck et al. 1998).

It is interesting to note that, based on the expected emissivity of astronomical silicate, the silicates in this region appear to be too cold. Perhaps this is an indication that the silicate grain optical properties in HII regions exhibit enhanced IR emissivities.

5. CONCLUSIONS

We find that the IR emission from the dust within the M17-SW HII region is consistent with the presence of amorphous carbons and silicates, and Mg-rich crystalline silicates. However, the presence of crystalline silicates has yet to be confirmed by observations of other HII regions and/or by firmer data reduction. These observations imply that the heating of silicate dust in HII regions can lead to the partial annealing of amorphous interstellar silicates, or that the interstellar silicates incorporated into this region were not completely amorphous. From the temperatures that we derive it appears that the optical properties of the silicate grains in the M17-SW HII region are different from their interstellar counterparts, in that they appear to be more efficient IR emitters than the amorphous astronomical silicate of Draine (1985).

We also note a systematic depletion of the UIB carriers (PAHs) within the M17 HII region consistent with their destruction in the intense radiation field from the central stars, or their expulsion by radiation pressure. We suggest that band carrier destruction within the HII region is the most likely explanation for their underabundance. We also note that where the UIB/PAH bands are absent or very weak that there remains a broad underlying emission feature which we attribute to an amorphous carbonaceous grain component. Thus, the broad bands and superimposed narrower emission features at 3.3, 6.2, 7.7, 8.6, 11.3 and 12.7 μm may have different origins.

These observations, in conjunction with complementary observations from other HII regions, will help to constrain the nature, physico-chemical state and abundance of dust in HII regions. They will also allow a better understanding of the dust life cycle in environments where dust is formed and processed.

ACKNOWLEDGMENTS

A.P. Jones is grateful to the Société de Secours des Amis des Sciences for funding.

REFERENCES

Allain, A., Leach, S., Sedlmayr, E. 1996, A&A, 305, 602

Cesarsky, D., et al. 1996, A&A, 315, L309

Cherchneff, I., Barker, J.R., Tielens, A.G.G.M. 1991, ApJ, 377, 541

Crovisier, J., et al. 1996, A&A, 315, L385

Désert, F.X., Boulanger, F., Puget, J.L. 1990, A&A, 237, 215

Draine, B.T. 1985, ApJS, 57, 587

Felli, M., Churchwell, E., Massi, M. 1984, A&A, 136, 53

Hallenbeck, S.L., Nuth, J.A., Daukantas, P.L. 1998, Icarus, 131, 198

Malfait, K., et al. 1998, A&A, 332, L25

Mathis, J.S. 1990, ARA&A, 28, 37

Rouleau, F., Martin, P.G. 1991, ApJ, 377, 526

Verstraete, L., et al. 1996, A&A, 315, L337

Waters, L.B.F.M., et al. 1996, A&A, 315, L261

Waelkens, C., et al. 1996, A&A, 315, L245

ICE ABSORPTION FEATURES IN THE 5 - 8 μm RANGE

J. V. Keane[1], A. G. G. M. Tielens[1,2], A. C. A. Boogert[1,2], & D. C. B. Whittet[3]

[1] Kapteyn Astronomical Institute, P.O. Box 800, 9700 AV Groningen, The Netherlands
[2] SRON Laboratory for Space Research, P.O. Box 800, 9700 AV Groningen, The Netherlands
[3] Department of Physics, Applied Physics & Astronomy, Rensselaer Polytechnic Institute, Troy, NY 12180

ABSTRACT

ISO-SWS spectra (2 - 45 μm) have been obtained towards a large number of luminous young stellar objects. Here, we present a study of absorption features towards the two objects NGC 7538:IRS9 and Mon R2:IRS3, for the spectral region 5 - 8 μm. The shape of these features changes dramatically from source to source. The 6.0 μm feature varies as a result of the different H_2O ice temperatures and also as a direct consequence to the presence of additional absorption in this band for some sources. Furthermore, these new high resolution observations show that the peak position of the 6.85 μm varies from source to source. The observations draw attention to the fact that hotter sources (Mon R2:IRS3) have a 6.85 μm band position that is red shifted with respect to colder sources (NGC 7538:IRS9). This gives clues to the as yet unknown origin of this band

Key words: ISM: lines and bands; ISM: molecules; ISM: individual: NGC 7538 IRS9,Mon R2 IRS3.

1. INTRODUCTION

The 5 - 8 μm region probes the CH, NH, and OH bending and deformation modes. Two absorption features, at 6 and 6.85 μm, have been detected in this wavelength range (Merrill et al. 1976; Soifer et al. 1979). High spectral resolution observations ($\lambda/\Delta\lambda$=1600) have been obtained towards a large number of luminous young stellar objects (YSO's) for the 5 - 8 μm spectral region. The high signal to noise and high resolution of these observations facilitates the search for substructure and shifts in peak position that were not detectable with the earlier low resolution spectra (Tielens et al. 1984).

We focus here on two objects, NGC 7538:IRS9 and Mon R2:IRS3. These objects are massive protostars showing a wealth of ice absorption bands (Willner et al. 1982). NGC 7538:IRS9 has a significant amount of volatile ices (Tielens et al. 1991) whereas Mon R2:IRS3 shows no indication of such volatiles (Keane et al. in prep). Moreover, NGC 7538:IRS9 has mainly cold CO gas (Mitchell et al 1990) while Mon R2:IRS3 has an abundant warm gas component (Giannakopoulou et al. 1997). All indicating that these two sources have considerably different environments. These new observations give us the opportunity to conduct the first in depth study of the 6 and 6.85 μm absorptions bands.

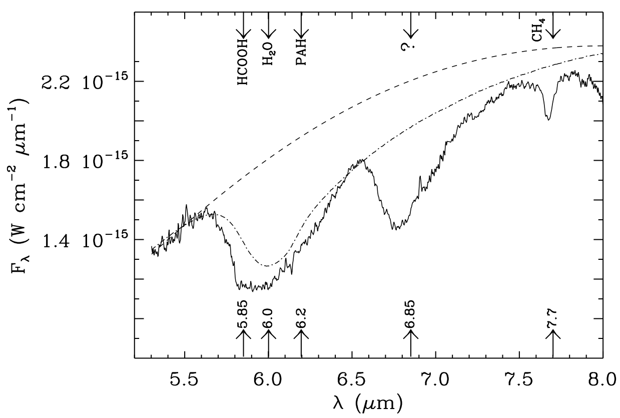

Figure 1. SWS AOT6 spectrum of NGC 7538:IRS9. The dashed line (- - -) is the blackbody continuum of 310K and the dashed-dot line (-.-) is the blackbody plus solid H_2O. The arrows at the bottom indicate the feature positions and the arrows at the top indicate the literature assignments for these features.

2. OBSERVATIONS & CONTINUUM

The latest version of the standard ISO-SWS reduction procedure and calibration files was applied (de Graauw et al. 1996). Treatment of the individual up and down scans is described in Boogert et al. 1996. The spectrum of NGC 7538:IRS9 is shown in Fig. 1.

For each source in our sample we have fitted blackbody or modified blackbody continua (cf. Fig 1) and derived profiles of the absorption features. The derived profiles are not very sensitive to the details of these continua (Keane et al. in prep.).

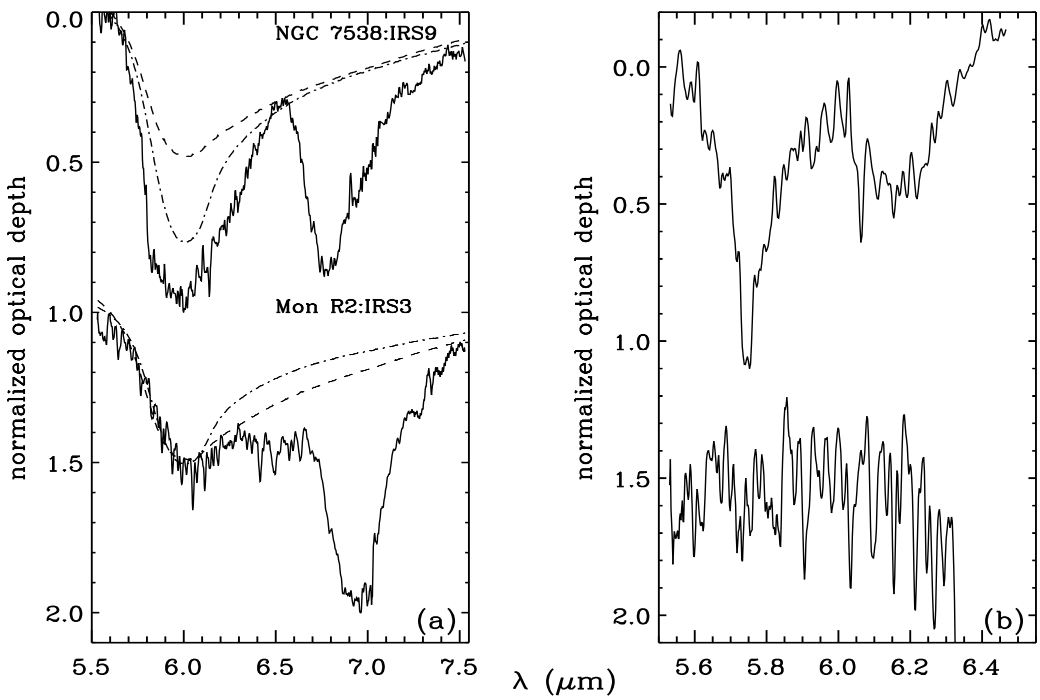

Figure 2. Optical depth plots obtained from the observations are shown on the left. The 6.0 μm feature is compared to solid H_2O at different temperatures. The dashed line (- - -) indicates solid H_2O at 80K and the dashed-dot line (-.-) indicates solid H_2O at 30K. On the right, the 6.0 μm displays the presence of additional components once the H_2O has been subtracted (see text).

3. ABSORPTION FEATURES

The 6.0 and 6.85 μm features dominate the 5 - 8 μm spectrum. A weak feature at 7.6 μm is also sometimes present. It is attributed to solid CH_4 (Boogert et al. 1996) and will not be discussed here. We also note the presence of weak structure in the 6.0 μm band around 5.85 and 6.2 μm. Additionally, between 5 - 7 μm in the spectrum of Mon R2:IRS3, narrow absorption lines are present which can probably be associated with H_2O vapor lines (van Dishoeck et al. 1996).

3.1. The 6.0 μm band

The 6.0 μm feature has long been ascribed to the bending mode of H_2O ice (Tielens et al. 1984). This assignment is supported by the presence of the H_2O stretching mode at 3μm. Laboratory inspection of the 6.0 μm band (Maldoni et al. 1998, Hudgins et al. 1993) show that the peak position is insensitive to temperature increase. However, the FWHM does increase with warm-up, a direct consequence to the deepening of the red wing resulting in the general broadening of the feature. In the case of NGC 7538:IRS9, comparing the observed 6.0 μm band with the H_2O at 30K shows reasonable agreement (Fig. 2a). Solid H_2O at higher temperatures do not provide satisfactory fits. It can be seen that while the position of the interstellar feature is well matched by H_2O, the observed band is considerably broader. This discrepancy cannot be remedied by warm-up of the ice. Therefore, in the case of NGC 7538:IRS9, additional components are contributing to the 6.0 μm band. Figure 2b illustrates that there are at least 2 additional components contributing to the 6.0 μm of NGC 7538:IRS9, centered near 5.85 & 6.2 μm. Schutte et al. (1996) assigned these excess features to C=O stretching mode in organic molecules and C-C stretching mode of aromatics, respectively. The 6.0 μm feature in Mon R2:IRS3 is fitted reasonably well by H_2O ice deposited at 80K (Fig. 2a). In contrast to NGC 7538:IRS9, there does not seem to be any additional components present in the 6.0 μm band. The fit of an 80K H_2O ice to Mon R2:IRS3 is in excellent agreement with Smith et al. (1989), who estimate ice temperatures from the 3.0 μm spectra of protostars.

In summary, the structure of the 6.0 μm absorption feature seems to vary from source to source, however amorphous H_2O ice is the dominant contributor to this band.

3.2. The 6.85 μm band

Due to the limited resolution of earlier observations, the spectra seemed to indicate that this band was constant in position (6.85 μm; Tielens & Allamandola 1987). However, with the recent ISO observations, it has become evident that the position of this band does indeed vary from source to source, by as much as 0.16 μm.

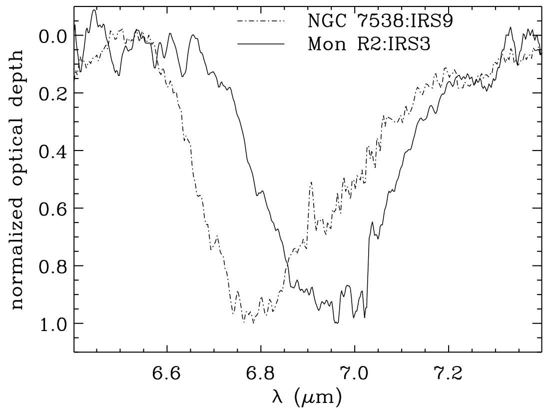

Figure 3. A comparison of the 6.85 μm peak positions for sources NGC 7538:IRS9 and Mon R2:IRS3. The variation of peak position of this feature is clearly illustrated.

Fig. 3 illustrates the shift in position of this feature , with NGC 7538:IRS9 centered near 6.79 μm and Mon R2:IRS3 centered near 6.95 μm. The other sources in our sample all lie in between these two extremes of peak position (Keane et al. in prep.). Furthermore, from Fig. 3, by comparing the profiles it is evident that there are structural variations from source to source and in fact all our sources can be fitted by a suitable combination of the profiles of NGC 7538:IRS9 and Mon R2:IRS3. There is a general trend amongst our sources, that those fitted by a hotter H_2O ice have a 6.85 μm position that is red shifted with respect to the sources fitted by a colder H_2O ice. It may be the case that the 6.85 μm carrier is one component which undergoes a shift with position due to thermal processing or that there are two components contributing, one of which is volatile due to its absence in the hotter source (Mon R2:IRS3)

The position of the 6.85 μm is indicative of the deformation modes -CH_2- & -CH_3- groups. However, methanol ice does not provide a good fit to the observed profiles. Furthermore, based upon the strong 6.85 μm, a CH_3OH/H_2O ratio of 0.5 would be expected (Tielens & Allamandola 1987). This would require strong absorption features at 3.54 & 9.7 μm. However, this is not observed and the weakness of these features indicates a much lower abundance of 0.05 (Grim et al. 1990). Here we emphasize that the carrier must also satisfy the constraint that the deformation mode at 6.85 μm must be stronger than any other absorption modes, including the 3.4 μm stretching mode.

4. CONCLUSION

In summary, ISO has revealed source to source variations in the shape of 6.0 μm feature. This is primarily attributed to the H_2O ice bending mode at different temperatures between the sources. Furthermore, some sources show evidence for additional absorption components contributing to this feature.

These new high resolution observations have shown that the peak position of the 6.85 μm varies from source to source. Furthermore the red wing of this feature is less pronounced in sources that have a larger fraction of volatile components.

ACKNOWLEDGMENTS

We are greatly indebted to the SWS Instrument Dedicated Team (SIDT) at VILSPA for their support in the calibration and analysis of SWS data.

REFERENCES

Boogert, A. C. A., Schutte, W. A., Tielens, A. G. G. M., et al. 1996, A&A 315, L377

de Graauw, Haser, L. N., Beintema, D. A., et al. 1996, A&A, 315, L49

Giannakopoulou, J., Mitchell, G. F., Hasegawa, T. I., Matthews, H. E., Maillard, J-P. 1997, ApJ, 487, 346

Grim, R. J. A., Bass, F., Geballe, T. R., Greenberg, J. M., Schutte, W. A. 1990, A&A, 243, 473

Hudgins D. M., Sandford, S.A., Allamandola, L. J., Tielens, A.G.G.M. 1993, ApJS, 86, 713

Keane, J. V., Tielens, A.G.G.M., et al. 1999, in preparation

Maldoni, M. M., Smith, R. G., Robinson, G., Rookyard, V.L. 1998, MNRAS, 298, 251

Merrill, K.M., Russell, R.W., Soifer, B.T. 1976, ApJ, 207, 763

Mitchell, G.F., Maillard, J-P., Allen, M., Beer, R., Belcourt, K. 1990, ApJ, 363, 554

Schutte, W. A., Tielens, A.G.G.M., Whittet, D. C., B., et al. 1996, A&A, 315, L333

Soifer, B.T., Puetter, R.C., Russell, R.W., Willner, S.P., Harvey, P.M., Gillett, F.C. 1979, ApJ, 232, L53

Smith, R.G., Sellgren, K., Tokunaga, A.T. 1989, ApJ, 344, 413

Tielens, A.G.G.M., Allamandola, L.J., Bregman, J., Goebel, J., d'Hendecourt, L.B., Witteborn, F.C. 1984, ApJ, 287, 697

Tielens, A.G.G.M., A., Allamandola, L.J. 1987, in *Physical Processes in Interstellar clouds*, eds. G. Morfill, and M. Scholer, (Reidel, Drodrecht), 333

Tielens, A.G.G.M., Tokunaga, A.T., Geballe, T.R., Bass, F., 1991, ApJ, 381, 181

van Dishoeck, E.F., Helmich, F.P., 1996, A&A 315, L177

Willner, S.P., Gillett, F.C., Heter, T.L., et al. 1982, ApJ, 253, 174

ATOMIC OXYGEN ABUNDANCE FROM THE DENSE ISM: ABSORPTION TOWARD GALACTIC HII REGIONS

J. Keene[1,2], D.C. Lis[1], T.G. Phillips[1], P. Schilke[3], M.W. Werner[2], & J. Zmuidzinas[1]

[1]California Institute of Technology, Pasadena, CA, USA
[2]Jet Propulsion Laboratory, Pasadena, CA, USA
[3]Max-Planck-Institut für Radioastronomie, Bonn, Germany

ABSTRACT

Using the ISO LWS Fabry-Perot, we have observed the [OI] 63 μm line toward nine Galactic HII regions which are bright in the far-infrared continuum and which have foreground cold clouds. In this way, we have detected OI absorption toward Sgr B2, W31C, W49, and W3(OH). These absorption lines show good correlation with the absorption lines of HI toward Sgr B2 and with absorption lines of molecular tracers such as CS and HCO^+.

Key words: Oxygen, abundances.

1. INTRODUCTION

A longstanding problem for our understanding of molecular clouds has been the difficulty of accounting for the gas phase abundance of carbon and oxygen. Since the first calculations of ion-molecule schemes there have been theoretical predictions indicating that the fundamental reservoirs of these elements are the molecular species CO, O_2 and H_2O. Initial assumptions are that oxygen has an abundance about twice that of carbon, as in the solar system, so nearly all carbon should be in CO, with plenty of oxygen left over for O_2 and H_2O. However, millimeter wave astronomy measurements have shown the strong presence of CO, but little H_2O, and there are strong detection limits on O_2. The observational evidence shows that the anticipated major oxygen molecular species are deficient by at least an order of magnitude.

In 1994 we proposed to use ISO to test whether the missing oxygen component was present in atomic form by means of absorption lines of OI at 63 μm. Using the ISO LWS Fabry-Perot, we have observed the [OI] 63 μm line toward nine Galactic HII regions which are bright in the far-infrared continuum and which have foreground cold clouds. The background HII regions were selected to have large line-of-sight velocity shifts (> 30 km s^{-1}) from the foreground clouds, enabling separation of the foreground OI absorption of the HII region continuum from the OI emission of the background HII regions by the 35 kms^{-1} resolution of the Fabry-Perot. In this way, we have detected foreground absorption toward Sgr B2, W31C, W49, and W3(OH). Our other five sources are all located in the Galactic Center region and show OI emission at all velocities, rather than the absorption we hoped to see.

From one absorption line feature it is not possible to deduce what fraction of the observed OI is associated with the molecular cloud, where complex molecules reside and where chemistry is driven by cosmic rays rather than UV illumination, and what fraction is associated with the PDRs at the surfaces, which certainly contain atomic oxygen. A further serious complication is the possibility of OI in the related HI regions, either outside the clouds, or inhomogeneously embedded within the clouds. The technique we propose, to measure several clouds of different molecular column density, should allow the test of correlation with the OI, to separate molecular cloud and other components, We need to know a lot about the various molecular and atomic tracers in these clouds, some of which material is presented below.

2. SGR B2 MAP

Baluteau et al. (1997) have shown that an OI map of Sgr B2 exhibits absorption at the peak of the HII region emission but emission elsewhere. We have reobserved not only the central Sgr B2 position with the ISO LWS Fabry-Perot but also two positions 180 arcsec north and south of the center. The spectra from these three positions is shown in Figure 1. These spectra show that strong OI absorption at the Sgr B2 peak is due mainly to cold line-of-sight clouds which have no associated emission. Away from the continuum emission peak, these clouds do not show up at all. However, the Sgr B2 cloud itself has an OI feature at about 60 km s^{-1} which shows up in emission at the off central positions. At the Sgr B2 peak, even this intrinsic feature shows up as a weak self-absorption, with intensity approximately that of the emission in the southern position. This indicates that the intrinsic Sgr B2 63 μm line must be optically thick.

Proceedings of the Conference "The Universe as seen by ISO", Paris, France, 20–23 October 1998 (ESA SP-427, March 1999)

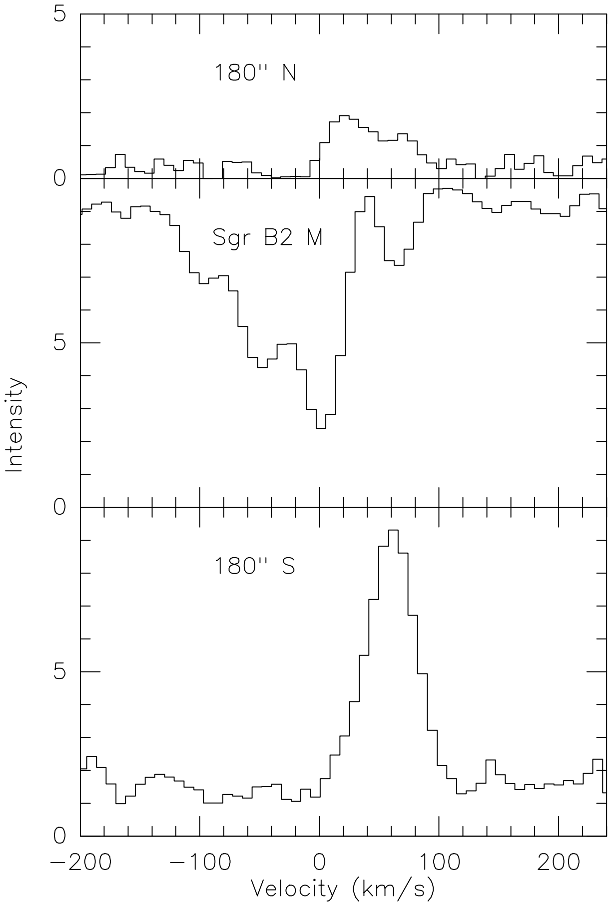

Figure 1. [OI] 63 μm from three positions toward Sgr B2. The OI absorption from the line-of-sight negative velocity and 0 km s^{-1} features appears only where the continuum emission is strong. The OI line intrinsic to the Sgr B2 region appears at velocities of 20–60 km s^{-1} in all three spectra, although, in the central position it appears as a weak self-absorption feature. In this and the following figures we have deconvolved the OI spectra using the known 35 km s^{-1} resolution of the LWS Fabry-Perot.

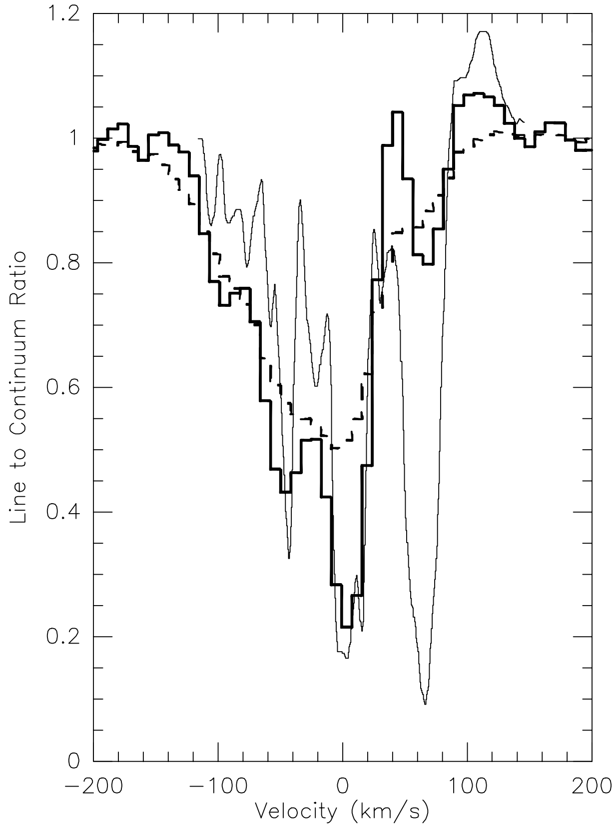

Figure 2. Comparison of [OI] 63 μm absorption (heavy lines) toward Sgr B2 M with the absorption line of HI (light line) in the same line of sight. The heavy dashed line shows the observed OI spectrum and the heavy solid line shows the OI spectrum as deconvolved by the known transmission of the LWS Fabry-Perot. It is clear the OI and HI show very similar features, except for the strength of the Sgr B2 cloud self-absorption at 60 km s^{-1}.

3. ASSOCIATION OF OI WITH ATOMIC AND MOLECULAR GAS

Sgr B2 has been observed in the HI absorption line by Garwood & Dickey (1989). Their spectrum is shown with our deconvolved spectrum of OI in Figure 2. The correlation of the features is strong with the largest discrepancy being the strength of the self-absorption feature of the Sgr B2 cloud at about 60 km s^{-1} . Of course, even with deconvolution applied to the OI spectrum, we cannot reproduce the wealth of detail seen in the HI spectrum. Our estimates of the OI column densities from the ISO data and HI column densities derived from their data are listed in Table 1. We have observed our target HII regions in molecular lines with the 30-m IRAM telescope and with the CSO. Some of the resulting spectra are shown in Figures 3 – 6. Here it is seen that molecular species also show a strong correlation with the OI absorption. In Sgr B2, the CS(2-1) spectrum particularly correlates well with OI.

4. OXYGEN ABUNDANCES

The column densities of atomic oxygen associated with foreground cold clouds are large (Table 1) and

Table 1. Column densities of atomic oxygen and hydrogen measured in absorption toward galactic HII regions. The uncertainties associated with these estimates are large (∼25 per cent) particularly for HI, because of its unknown spin temperature.

Background HII Region	LSR Velocity Range (km s^{-1})	N(OI) (10^{18} cm^{-2})	H(HI) (10^{21} cm^{-2})
Sgr B2	< -55	1.3	1.6
	−50 to −15	6.1	3.3
	−5 to 20	4.9	9.0
W 31C	18 to 50	5.0	
W 49A	30 to 80	6.7	
W3(OH)	−20 to 20	1.8	

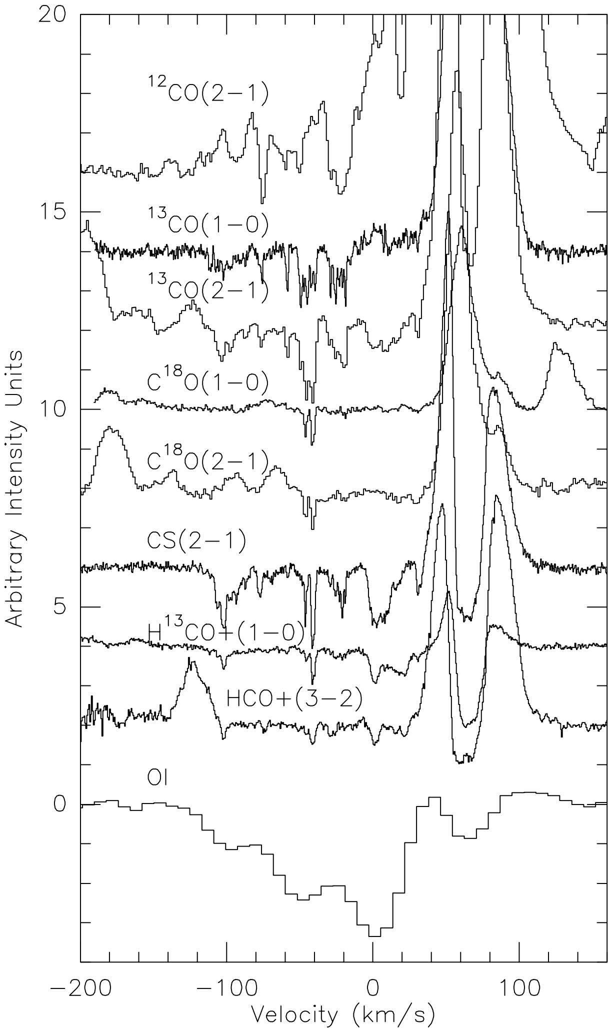

Figure 3. Comparison of [OI] 63 μm absorption toward Sgr B2 M with absorption lines of other species in the same line of sight. It is clear that the OI absorption shows features similar to CS(2-1), in that there are absorption features seen near –100, –50, 0, and 60 $km\,s^{-1}$.

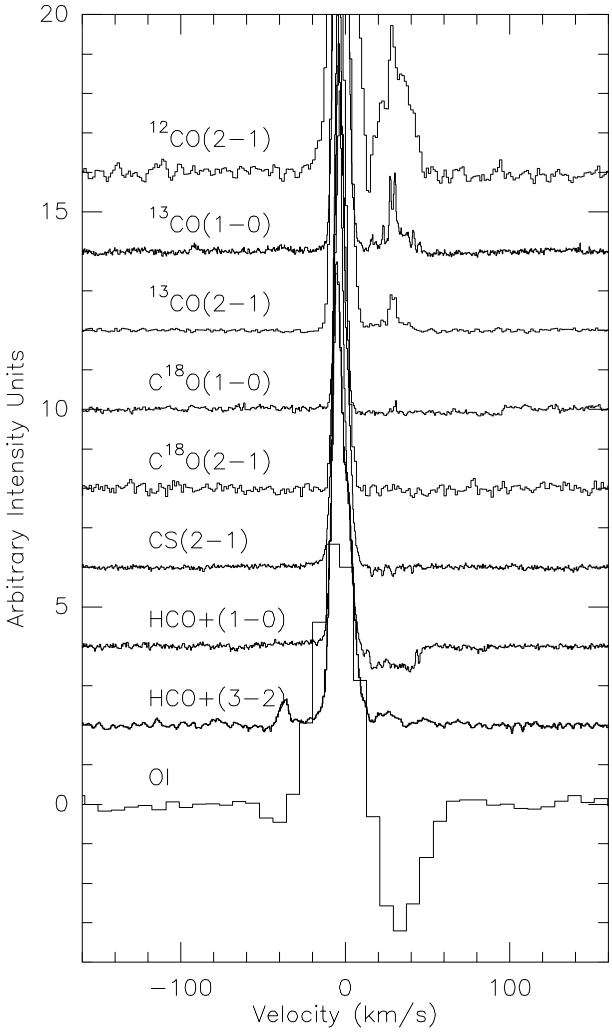

Figure 4. Comparison of [OI] 63 μm absorption toward W31 C with absorption lines of other species in the same line of sight. The line-of-sight cold cloud is seen most clearly in emission in ^{12}CO and ^{13}CO and in absorption in HCO^{+} (1-0).

could be consistent with a substantial fraction of the missing oxygen within molecular clouds being in the atomic form, if we use the as yet unsubstantiated assumption that OI absorption is associated only with the molecular clouds. Since we submitted our ISO proposal, OI absorption has been detected by 3 other groups - possibly in DR 21 by Poglitsch et al. (1996), in Sgr B2 by Baluteau et al. (1997) and in NGC 6334 by Kraemer et al. (1998). The atomic oxygen abundances which we infer could be consistent with the large values inferred by these groups.

ACKNOWLEDGMENTS

We would like to thank the IPAC staff, especially Steve Lord, for their help in obtaining and reducing these data. The ISO work is carried out under NASA contract NAG 5-3560. The CSO is supported by NSF contract AST 96-15025.

REFERENCES

Baluteau, J.-P., et al. 1997, A&A, 322, L33

Garwood, R.W., & Dickey, J.M. 1989, ApJ, 338, 841

Kraemer, K.E., Jackson, J.M., & Lane, A.P. 1998, ApJ, 503, 785

Poglitsch, A., et al. 1996, ApJ, 462, L43

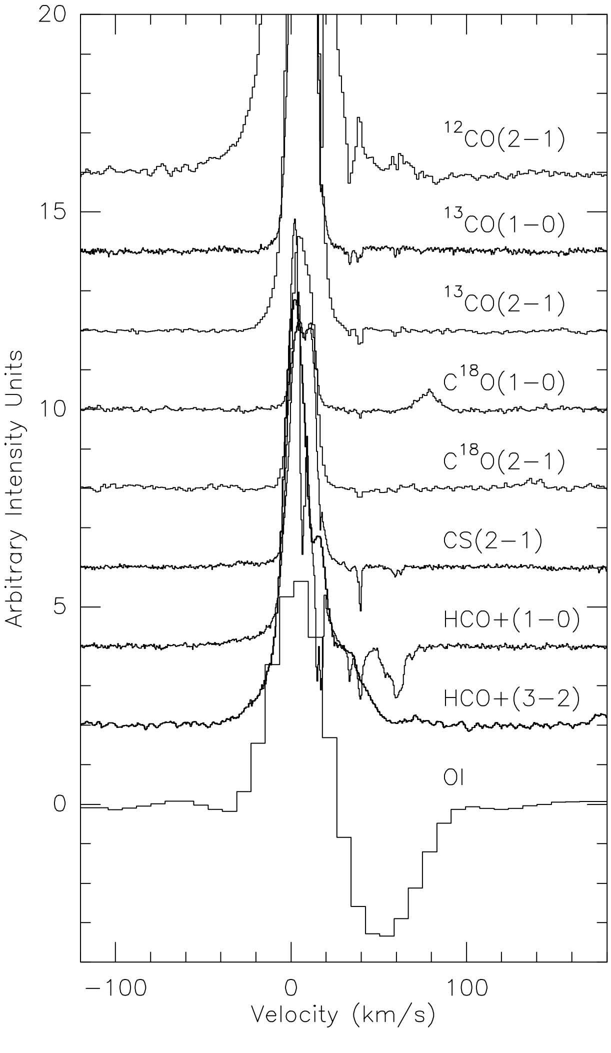

Figure 5. Comparison of [OI] 63 μm absorption toward W49 with absorption lines of other species in the same line of sight. The absorbing clouds are seen most clearly in ^{12}CO (2-1) emission and in absorption in the HCO^+ (1-0) line.

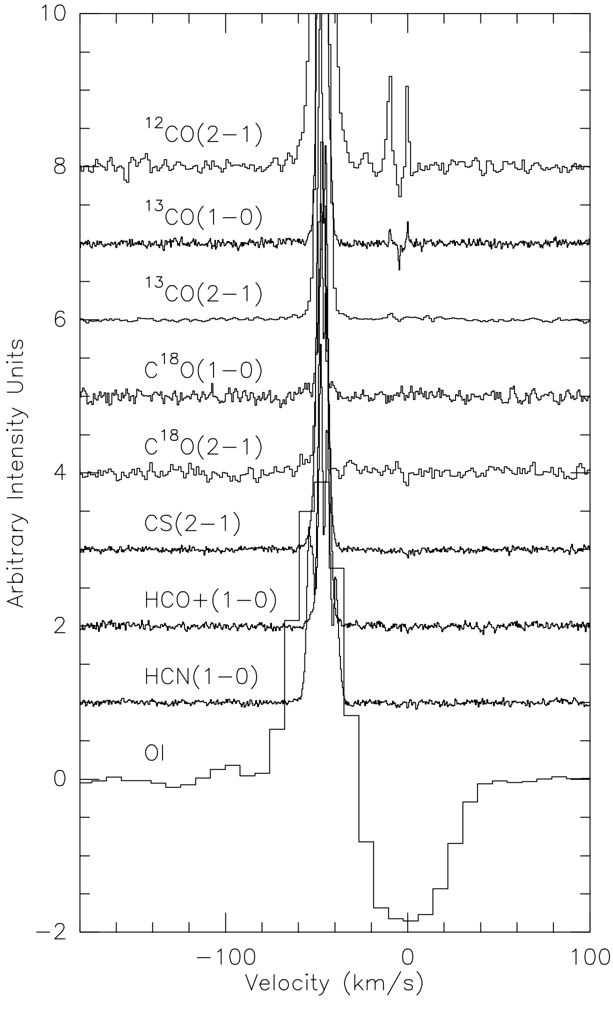

Figure 6. Comparison of [OI] 63 μm absorption toward W3 (OH) with absorption lines of other species in the same line of sight. In this case the line-of-sight cloud appears to be very diffuse as it is clearly seen only in the lines of ^{12}CO and ^{13}CO.

ISOCAM OBSERVATIONS OF THE CLOUD CORE M17-NORTH

R. Klein[1], **Th. Henning**[1], **& D. Cesarsky**[2]

[1]Astrophysikalisches Institut und Universitäts-Sternwarte (AIU) Jena, Germany

[2]Institut d'Astrophysique Spatiale, Université de Paris-Sud, France

ABSTRACT

We present spectro-imaging data of the molecular cloud core M17-North. The data have been obtained with the ISOCAM camera on board of the Infrared Space Observatory (ISO) using the circular variable filters (CVF). The spectra have a spectral resolution of about 40. They are dominated by polycyclic aromatic hydrocarbon (PAH) emission bands. A band at 16.6 μm is detected which is ascribed to the family of the PAH bands. Further, the PAH bands display clearly Lorentzian line profiles. The observations led to the detection of a new mid-infrared source with a very strongly rising continuum. Some information on the morphology of the H II region could be derived from the spatial distribution of the fine structure line emission by ionic species.

Key words: Star formation; Molecular Cloud: M 17-North; PAH bands.

1. INTRODUCTION

The cloud core M 17-North was detected by bolometer array observations at the IRAM 30 m-telescope at a wavelength of 1.3 mm (Henning et al. 1998, hereafter HKL). The cloud core M 17-North is located 10′ north of the optically bright H II region M 17, the Omega nebula. M 17 is located in the Sagittarius-Carina spiral arm at a distance of 1.3 kpc (Hanson et al. 1997).

The detection of a compact core in the millimetre continuum (mm core) made the object an extremely interesting target for the study of star formation and the properties of the dust and molecule population in a cloud core. Therefore, M 17-North was observed with all four instruments of the Infrared Space Observatory (ISO). The spectrometers detected a strongly rising continuum starting at about 20 μm superimposed with fine structure lines and the unidentified infrared bands (UIBs). First results from ISO spectroscopy and a comparison of ground-based near- and mid-infrared (NIR/MIR) data and the mm observations with the ISO data can be found in HKL. The UIBs were interpreted as emission from polycyclic aromatic hydrocarbon clusters (PAH). In this work we present the main results of recent ISOCAM observations of M 17-North. For further discussion the reader is referred to Klein et al. (1998).

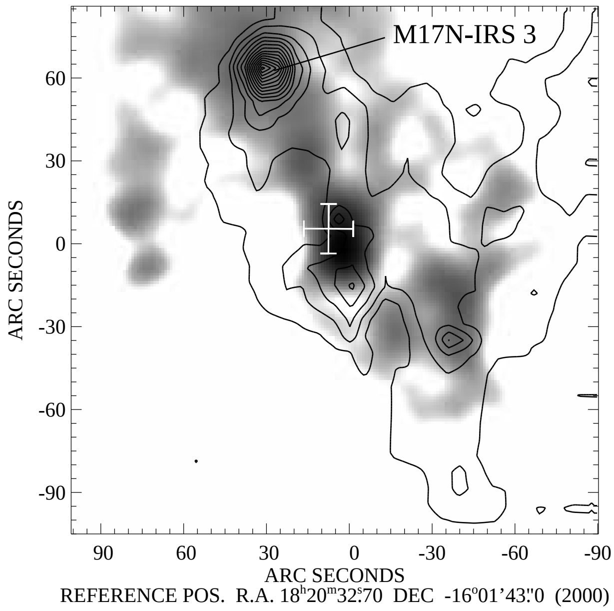

Figure 1. ISOCAM map at 15.1 μm (contours: 0.4, 0.5,... 1.9 Jy/pix) and the mm continuum map (logarithmic grayscale). The cross shows the H_2O maser position.

2. OBSERVATIONS

The data were obtained with ISOCAM (Cesarsky et al. 1996) on board of the ISO satellite (Kessler et al. 1996). We used this camera for spectro-imaging with the circular variable filters (CVF). A pointed observation towards the mm core at RA(2000): $18^h20^m32\overset{s}{.}7$, DEC(2000): $-16°01'43''$ was carried out in March 1998. Within one hour the full long-wavelength section (LW) of the CVF was scanned covering the wavelength range between 5 and 17 μm with a spectral resolution of about 40. The 32×32 detector array covered a field of $3'\times3'$. One pixel's field

Proceedings of the Conference "The Universe as seen by ISO", Paris, France, 20–23 October 1998 (ESA SP-427, March 1999)

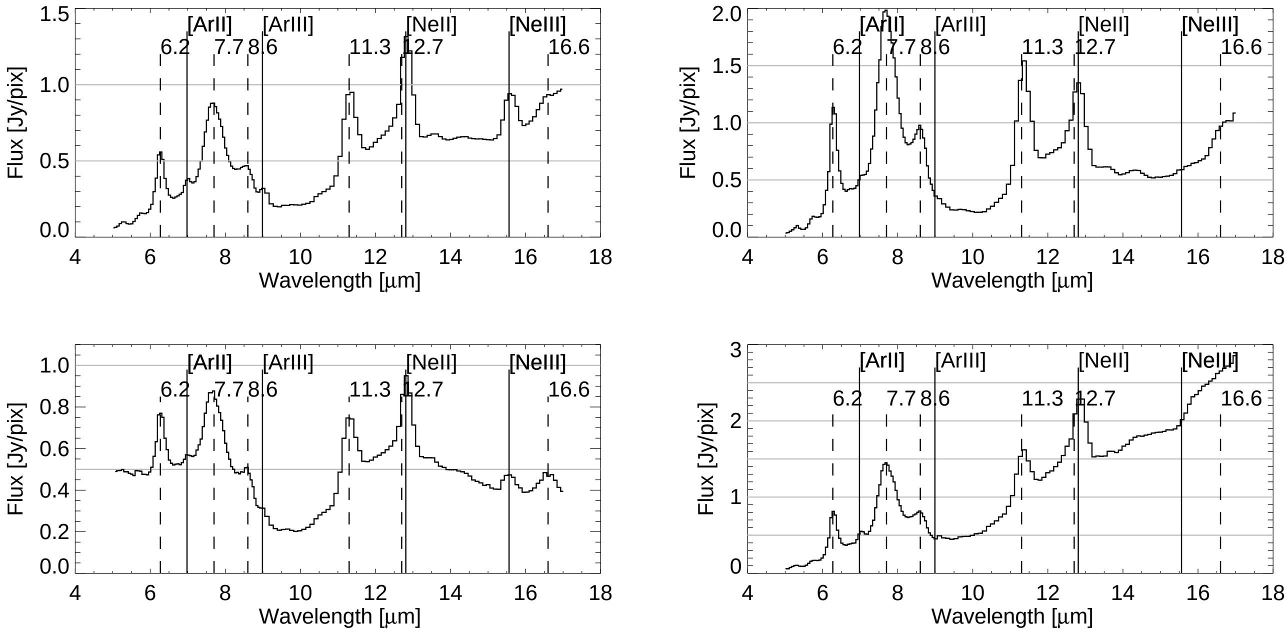

Figure 2. Four CVF-spectra: top left – the mm core, top right – strong PAH emission in the NW, bottom left – IRS 5, bottom right – IRS 3. The vertical lines indicate the position of some detected features (solid: PAH bands, dashed: fine structure lines). In order to make the different flux scales more apparent every 0.5 Jy/pixel a horizontal line is drawn.

of view (PFOV) is $6'' \times 6''$. The data obtained consist of 151 narrow-band images at wavelengths between 5 and 17 μm or in other words of 1024 spectra of this region. The data reduction was performed with the "CAM Interactive Analysis" software (CIA). The data for the missing column 24 was interpolated from the adjacent columns. We noticed a positional discrepancy of $12''$ between the ISOCAM images and our NIR images and shifted the ISOCAM data by that amount.

3. ANALYSIS

The main features of the M 17-North are visible in Fig. 1. The image displays the map at 1.3 mm with the mm core in the centre. The contours show the ISOCAM image at 15.1 μm representing the MIR continuum. The continuum emission at these two different wavelengths originate from the same region but the relative intensities are quite different. The ISOCAM images display a previously unknown strong MIR source (M 17 N-IRS 3). The bright mm core has no comparable counterpart in the MIR. The cross in Fig. 1 at the mm core indicates the position given by Jaffe et al. (1981) for the H_2O maser which was originally found by Cesarsky et al. (1978).

3.1. The sources

Four sources in the ISOCAM images have NIR counterparts. Their coordinates are compiled in Tab. 1 and marked in Fig. 3. One of these four sources is M 17 N-IRS 1. It was already mentioned together with M 17 N-IRS 2 in HKL. Both sources are located at the mm core and their NIR colour index is $m_{H-K'} > 1.7$ mag. They are probably embedded in the mm core.

Table 1. Coordinates of the named sources.

M 17 N-	RA(2000)	DEC(2000)	Comment
IRS 1	$18^h20^m32\overset{s}{.}8$	$-16°01'33''$	at mm core
IRS 2	$18^h20^m33\overset{s}{.}0$	$-16°01'48''$	at mm core
IRS 3	$18^h20^m34\overset{s}{.}6$	$-16°00'40''$	disk cand.
IRS 4	$18^h20^m31\overset{s}{.}4$	$-16°02'38''$	NIR star
IRS 5	$18^h20^m37\overset{s}{.}3$	$-16°03'10''$	NIR star

An outstanding source in the ISOCAM data is M 17 N-IRS 3. The most remarkable feature of this source is the strong rise of the MIR continuum (Fig. 2 bottom – right). A possible model for this continuum (13–17 μm) is 0.45 $M_\odot$ of circumstellar matter at a temperature of 160 K. No cold dust is present in IRS 3 as there is no sign of the object in the mm continuum map. It has a K′-band brightness of $m_{K'}$=11.9 mag and a colour index $m_{H-K'}$=1.15 mag. The reason for this moderate reddened H–K colour index, the surrounding warm dust, and no cold dust might be a warm disk seen face on.

In the NIR the two objects M 17 N-IRS 4 and 5 appear as bright stars (see Fig. 3). The ISOCAM spectra of IRS 4 and 5 are the only spectra which are flat or declining to longer wavelengths (Fig. 2 lower –left panel). It is tempting to explain the dip around 10 μm by silicate absorption but we do not observe

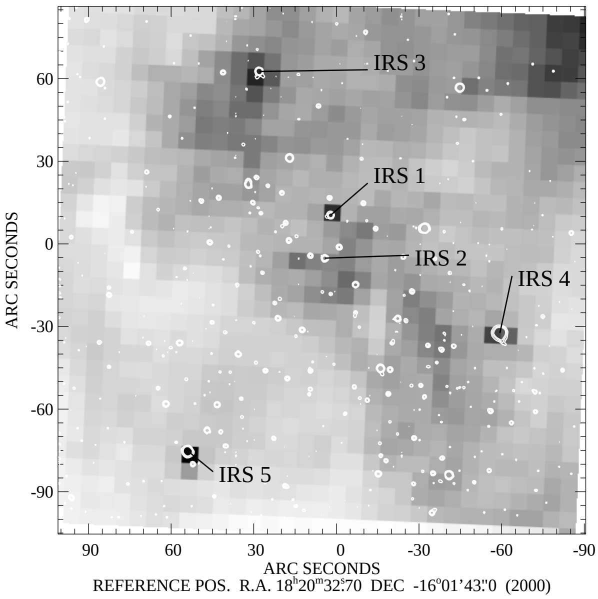

Figure 3. ISOCAM at 6.6 μm + K′-band contours.

silicate anywhere else in M 17-North. The reason for the dip may well be that the stellar spectra are seen on the one side of the spectra and the thermal emission by small grains on the other side.

3.2. The PAH bands

The first fact to mention is the dominance of the PAH emission in the ISOCAM spectra. In the wavelength range from 5 to 14 μm, the contribution of the PAH bands to the observed flux is at least 50% and 70% on average. The emission in the PAH bands is more extended than the continuum radiation. From the edge of the molecular cloud to the north-west, the PAH emission is continuously rising. It is very strong in the north-western part of the observed field while the underlying continuum is relatively weak. A spectrum of this region is displayed in the upper right panel of Fig. 2. Table 2 lists the detected features in the spectrum. Besides the known strong PAH bands and fine structure lines there is a new band at 16.6 μm. We ascribe it to the family of PAH bands because it seems to have a similar spatial distribution as the other UIB features. The band is at the edge of the wavelength range and, therefore, it is difficult to estimate the band's strength and width. A feature at 16.4 μm was already detected by Moutou et al. (1998) in NGC 7023 and was ascribed to large compact PAHs, possibly containing pentagons.

Table 2. Features in the ISOCAM spectra. Reliable estimates of the FWHM ($\Delta\lambda$) were possible only for the strong PAH bands.

PAH bands			others	
λ, $\Delta\lambda$ in μm		origin	wavel.	origin
5.3		C-H bend	7.0	[Ar II]
5.7		C-H bend	9.0	[Ar III]
6.261	0.15	C-C stretch	9.7	$H_2S(3)$
7.686	0.35	C-C stretch	10.5	[S IV]
8.567	0.19	C-H stretch	12.8	[Ne II][1]
11.34	0.31	C-H bend	15.6	[Ne III]
13.6		C-H bend		
14.3		C-H bend		
16.6		ring bend		

[1]blended with the PAH feature at 12.7 μm

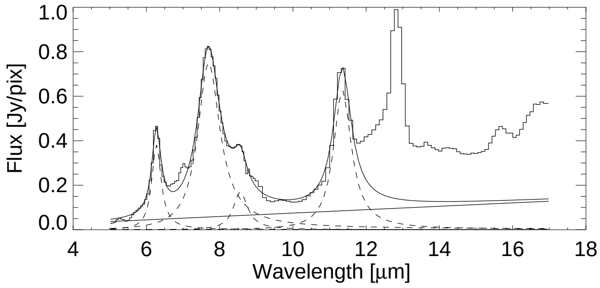

Figure 4. Example for a fit of the PAH bands with Lorentzians (pos.: +60″,+5″). The histogram is the original spectrum. The smooth line is the sum of the low continuum (straight line) and the four Lorentzians (dashed lines).

The PAH bands can be fitted by Lorentzian line profiles (Fig. 4). A fit of the bands with Gaussian profiles does not describe the data. It is remarkable that the broad wings of the Lorentzian lines account for the plateau between 6 and 9 μm. The low spectral resolution of about 40 or the intrinsic line profile of the CVF are not the reasons for the observed Lorentzian line profiles. The PAH bands in the SWS spectrum of M 17-North which has a resolution of about 200 are also better described with Lorentzian than with Gaussian line profiles and much of the plateau is explained with the broad line wings, too. A full discussion of the analytical fit to ISOCAM spectra can be found in the paper by Boulanger et al. (1998). They conclude that the Lorentzian line profiles of the PAH bands support the PAH hypothesis of large molecules heated by single photons.

3.3. Fine structure lines

Only the lines of [Ar II] at 7.0 μm, [Ne III] at 15.6 μm, and [Ar III] at 9.0 μm[1] are suitable for an analysis of their spatial distribution. The regions which emit these fine structure lines are displayed in Fig. 5. The emission region of [Ar III] is similar to [Ne III]. Both lines are strongest in the centre of the observed field where the mm core and the maser are located. Emission by [Ar II] mainly originates from a bar north of the region where argon is ionized twice but is found everywhere where also continuum emission is detected.

3.4. The H II region

The compact morphology of the ionized region with the mm core and the H_2O maser in the center indicates the presence of an ionizing source somewhere near its centre, but it is not seen. It cannot be deeply

[1]ordered by average in-band power

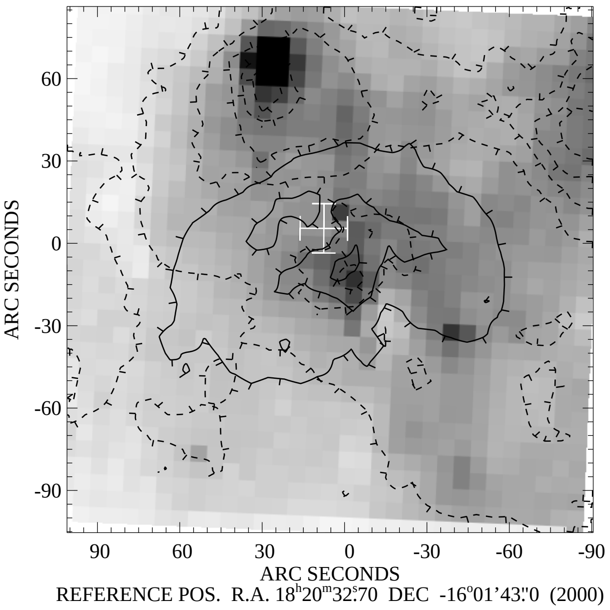

Figure 5. ISOCAM at 15.1 μm (MIR continuum) and contours for [Ar II] at 7.0 μm (dashed) and [Ne III] at 15.6 μm (solid). The contours are spaced by $5 \cdot 10^{-7} W m^{-2} sr^{-1}$ (tickmarks are pointing downward).

embedded in the mm core, because then it could not ionize such a large region as we see it. The ionizing source can be hidden behind the mm core producing the compact emission region of the doubly ionized noble gases and a shell of single ionized argon around. From a radiative transfer model HKL derived a visual extinction of $A_V = 80$ mag for the mm core. That would also mean that the H II region lies behind the mm core and that the mm core will absorb the fine structure line emission. In Fig. 5 this absorption can be seen for the [Ne III] line. There are two maxima and the mm core and the maser are located between them. The amount of the absorption is of the expected order of magnitude.

4. SUMMARY

The main results of the ISOCAM observations of M 17-North are:

1. The coincidence of the MIR emission and the mm continuum emission region. The emission at both wavelengths traces the extent of the molecular cloud but the relative intensities differ in the two maps.

2. The detection of the source M 17 N-IRS 3. The detected circumstellar matter may form a warm disk seen face on.

3. The fit of the PAH bands with Lorentzian line profiles. The fact that the Lorentzian line profiles account for almost all flux in the PAH band region supports the PAH hypothesis.

4. The detection of a band at 16.6 μm which is ascribed to the family of PAH bands.

ACKNOWLEDGMENTS

R. K. acknowledges support through the BMBF-Verbundforschung Astronomie / Astrophysik grant No. 50 OR 9414 9. The ISOCAM data presented in this paper were analyzed using "CIA", a joint development by the ESA Astrophysics Division and the ISOCAM Consortium. The ISOCAM Consortium is led by the ISOCAM PI, C. Cesarsky, Direction des Sciences de la Matière, C.E.A., France.

REFERENCES

Boulanger F., Boissel P., Cesarsky D., Ryter C. 1998, A&A 339, 194

Cesarsky C. J., Abergel A., Agnèse P., et al. 1996, A&A 315, L32, ISO special issue

Cesarsky C. J., Cesarsky D. A., Churchwell E., Lequeux J. 1978, A&A 68, 33

Hanson M. M., Howarth I. D., Conti P. S. 1997, ApJ 489, 698

Henning Th., Klein R., Launhardt R., Lemke D., Pfau W. 1998, A&A 332, 1035, (HKL)

Jaffe D. T., Güsten R., Downes D. 1981, ApJ 250, 621

Kessler M. F., Steinz J. A., Anderegg M. E., et al. 1996, A&A 315, L27, ISO special issue

Klein R., Henning Th., Cesarsky D. 1998, in preparation

Moutou C., Sellgren K., Léger A., et al. 1998, in: Star Formation with the Infrared Space Observatory, J. Yun and R. Liseau (eds.), Vol. 132 of *ASP Conference Series*, p. 47

ISOPHOT FAR-INFRARED OBSERVATIONS OF THE DARK CLOUD DC 303.8-14.2

K. Lehtinen[1], D. Lemke[2], & K. Mattila[1]

[1] Observatory, Tähtitorninmäki, P.O. Box 14, 00014 University of Helsinki, Finland
[2] Max-Planck-Institut für Astronomie, Königstuhl 17, D-69117 Heidelberg, Germany

ABSTRACT

We present an analysis of far-infrared observations of the dark cloud DC 303.8-14.2, made with the ISOPHOT instrument aboard ISO at 60, 100 and 200 μm. An IRAS source is located in the center of the cloud. This is a deeply embedded young stellar object (YSO). The purpose of this research is to study the properties of cold dust in the cloud, and to derive more reliable estimates of the evolutionary stage of the YSO. The dust temperature decreases towards the center of the cloud, where it is about 14 K. The circumstellar mass of the YSO is estimated to be about 0.2 $M_\odot$. We classify the YSO to be between the Class 0 and Class I evolutionary stages. We also compare the cloud DC 303.8-14.2 with the Thumbprint Nebula, a morphologically similar cloud which has no signs of star formation (Lehtinen et al. 1998).

Key words: dust, extinction; ISM:clouds; Infrared: stars.

1. INTRODUCTION

The globule DC 303.8-14.2 (Hartley et al. 1986) is located in the eastern part of the Chamaeleon II dark cloud complex. It harbours the IRAS point source IRAS 13036-7644, which possesses a spectral energy distribution (SED) typical for a young stellar object; the flux densities at 12, 25, 60 and 100 μm are 0.10, 1.08, 6.28 and 22.01 Jy, respectively (Prusti et al. 1992). Its coordinates are $\alpha(1950) = 13^h3^m41.4^s$, $\delta(1950) = -76°44'3''$, and the positional error ellipse has semi minor and major axes of 6 arcsec and 20 arcsec. The IRAS source is not detectable at near-infrared and shorter wavelengths.

In their continuum survey at 1.3 mm Henning et al. (1993) measured a flux density of 223 ± 49 mJy for this object. This emission is most probably thermal emission from cold circumstellar dust grains.

Lehtinen (1997) has observed DC 303.8-14.2 at millimeter molecular lines, and found that the high density tracers CS(J=2-1), CS(J=3-2) and $H_2CO(2_{12}$-$1_{11})$ show asymmetrical double-peaked profiles that are typical for a collapsing cloud. IRAS 13036-7644 is located at the center of a bipolar molecular outflow; thus it is probably the driving source of this outflow (Lehtinen 1997).

Chen et al. (1997) have calculated bolometric luminosities and temperatures (as defined by Myers & Ladd 1993) for YSOs in nearby molecular clouds. They find values of 0.47 $L_\odot$ and 63 K for IRAS 13036-7644. In a bolometric luminosity-temperature diagram of Chen et al. (1995) IRAS 13036-7644 is located near the division line between Class 0 and Class I sources. However, in the absence of flux measurements between 100 μm and 1.3 mm it has not been possible to deduce reliably the class of the IRAS source.

We have chosen the cloud DC 303.8-14.2 to be the comparison object for the Thumbprint Nebula, a morphologically similar cloud which has no signs of star formation (Lehtinen et al. 1998). By comparing these two clouds we wish to study, on one hand, the mechanisms that cause star formation, and on the other hand, the effects that star formation has on a small molecular cloud.

2. OBSERVATIONS AND DATA REDUCTION

The observations were performed on ISO revolution 719 and 723. The C100 camera (our 60 and 100μm observations) is a 3×3 pixel array, and the distance between the pixel centers is 46.0 arcsec. For the C200 camera (2×2 pixel array) the distance is 92.0 arcsec.

The size of the mapped area is about 23 arcmin^2 at 100 and 200μm, while at 60μm we have a single strip across the IRAS source. In the 100 μm map the distances of raster points in the in-scan and cross-scan directions are 135 arcsec (i.e. full detector width) and 90 arcsec (one pixel overlap). In the 200 μm map both the distances are 180 arcsec (full detector width). At 60μm the linear scan of 16 positions is approximately in the north-south direction, and the distance between raster positions is 50 arcsec.

Proceedings of the Conference "The Universe as seen by ISO", Paris, France, 20–23 October 1998 (ESA SP-427, March 1999)

The data analysis has been done using the PIA[1] (ISOPHOT Interactive Analysis) V 7.2. (Gabriel 1997). For the flat-field correction we have applied a statistical method; we correlate the value of the reference pixel, at each raster position, against other pixels. Instead of comparing the reference pixel only with a particular pixel located in the same raster position, we take a mean of two pixels located symmetrically around the reference pixel. In this way it is possible to reduce the scatter in the pixel-to-pixel relation caused by a surface brightness gradient in the image.

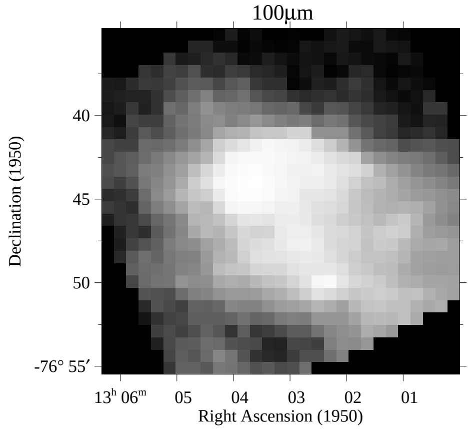

Figure 1. Grayscale image of the surface brightness at 100 μm

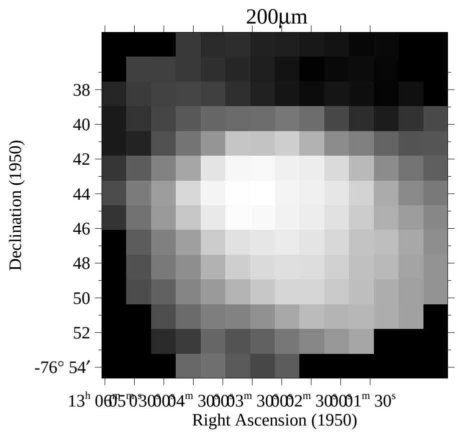

Figure 2. Grayscale image of the surface brightness at 200 μm

3. RESULTS AND DISCUSSION

In Fig. 1 and Fig. 2 are shown grayscale images of the surface brightness at 100 and 200 μm, respectively.

[1]The ISOPHOT data presented in this paper was reduced using PIA, which is a joint development by the ESA Astrophysics Division and the ISOPHOT Consortium (the ISOPHOT Consortium is led by the Max-Planck-Institute for Astronomy, Heidelberg)

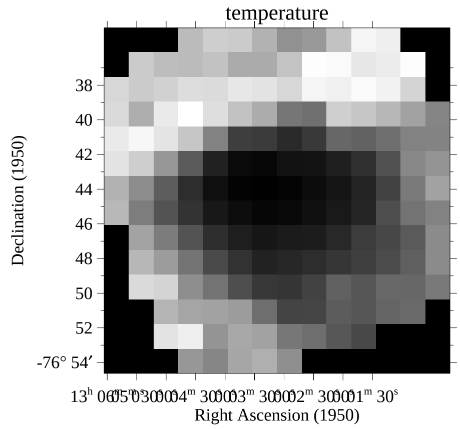

Figure 3. Temperature map as calculated by fitting the 100 and 200 μm surface brightness values with a modified blackbody. Darker areas are colder

The IRAS source is the bright pixel at the center of the image.

The temperature map is shown in Fig. 3, calculated by fitting the 100 and 200 μm surface brightness values with a modified blackbody, assuming an index -2 for the dust emissivity power law. We have not subtracted the background in this image. If we assume that the physical properties of the dust grains are the same all over the cloud, the Fig. 3 indicates that the temperature of the dust decreases towards the cloud center. At the cloud center the derived dust temperature (after subtracting the background) is about 14 K. This value is about the same as observed by ISO in the Thumbprint Nebula (TPN) (Lehtinen et al. 1998), which is a dark cloud of similar size and appearance, located in the Chamaeleon III region. The TPN is without any internal heat sources, and thus heated only by the interstellar radiation field. We can thus conclude that the radiation from the IRAS source is not able to warm up the whole cloud into significantly higher temperatures than a cloud without an internal energy source. The surface brightness values at the cloud center at 100 and 200 μm are about 50–100% higher than in the case of TPN. This is probably due to the higher optical depth of the DC 303.8-14.2.

The fluxes of the IRAS source are about 4.5, 19.5 and 43.3 Jy, at 60, 100 and 200 μm, respectively. The spectral energy distribution of the IRAS source is shown in Fig. 4. The emission at 100, 200 and 1300 μm wavelength is expected to originate from 'classical', large cold dust grains which are at an equilibrium temperature with the surrounding radiation field, thus we have fitted those flux values with a modified blackbody of the form

$$F_\nu = B_\nu(T_\mathrm{d})\,(1-\exp(-\tau_\nu))\,\Omega_\mathrm{s} \qquad (1)$$

where $B_\nu(T_\mathrm{d})$ is the Planck function at the dust temperature T_d, τ_ν is the optical depth which is assumed to vary with frequency as $\tau_\nu = (\nu/\nu_0)^\beta$, and Ω_s is the solid angle of the emitting region. We have tried different values of the opacity power-law in-

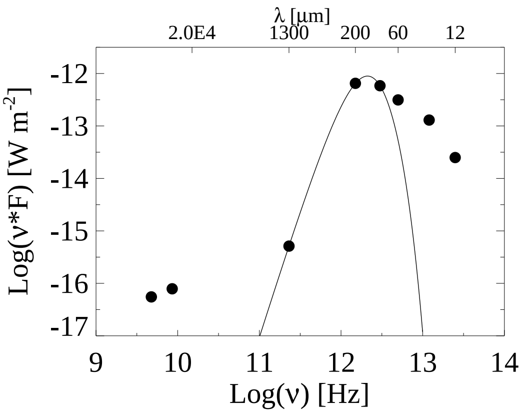

Figure 4. The spectral energy distribution of the IRAS source. The data points are, from shortest to longest wavelength, IRAS 12 and 25 μm, ISOPHOT 60, 100 and 200 μm, SEST 1.3 mm bolometer (Henning et al. 1993), and radio continuum 3 and 6 cm (Lehtinen & Higdon 1998) data. The solid line is a modified blackbody fit to the 100, 200 and 1300 μm data points

dex β between 1–2, and found that the value β=2 gives the best fit. The fitted values are $T_{\rm d} \approx$21.4 K, $\nu_0 \approx 184\,\mu$m (i.e. the wavelength where the optical depth is unity), and $\Omega_{\rm s} \approx 18\,$arcsec^2.

Clearly, the fluxes at wavelengths shorter than 60 μm are higher than accounted for by the emission of large grains at an equilibrium temperature, i.e. the fitted curve. The excess emission may come from transiently heated small grains, or from a disk region around the YSO.

Assuming a distance of 200 pc for the IRAS source and integrating under the fitted blackbody curve we obtain the bolometric luminosity of the cold dust $L_{\rm cd} \approx 1.1\,{\rm L}_\odot$.

At 1.3 mm wavelength the emission is optically thin, so we can estimate the circumstellar dust mass by using the flux at 1.3 mm and the derived dust temperature. Using the familiar formula for the circumstellar mass (e.g. Chini et al. 1987),

$$M_{\rm cm} = \frac{S_\nu D^2}{R \kappa_\nu B_\nu(T_{\rm d})} \tag{2}$$

where D is the distance, R is the dust-to-gas mass ratio and κ_ν is the mass absorption coefficient of the dust, we obtain (using $\kappa_\nu = 1\,{\rm cm}^2\,{\rm g}^-1$) $M_{\rm cm} \approx 0.2\,{\rm M}_\odot$.

We have estimated the bolometric temperature $\rm T_{bol}$ and bolometric luminosity $L_{\rm bol}$ of the IRAS source, as defined by Myers & Ladd (1993). We obtain the values $\rm T_{bol} \approx 59\,K$, and $L_{\rm bol} \approx 1.2\,{\rm L}_\odot$; the bolometric temperature is now slightly lower, and the bolometric luminosity is about two times higher than estimated by Chen et al. (1997). We can now estimate more firmly the evolutionary stage of the IRAS source. In a bolometric luminosity-temperature diagram of Chen et al. (1995) the position of the IRAS 13036-7644 is not much changed, it is still located near the division line between Class 0 and Class I sources. This is in accordance with the facts that some properties of the IRAS source are in favor of a Class 0 stage (e.g. non-detectability at wavelengths shorter than about 10 μm, detection of cm-wavelength continuum radiation) while some are not (e.g. the spectral energy distribution is not well fitted with a single blackbody curve).

ACKNOWLEDGMENTS

The work of K.L. and K.M. has been supported by the Finnish Academy through grant No. 1011055, which is gratefully acknowledged.

REFERENCES

Chen H., Myers P.C., Ladd E.F., Wood D.O.S. 1995, ApJ 445, 377

Chen H., Grenfell T.G., Myers P.C., Hughes J.D. 1997, ApJ 478, 295

Chini R., Krügel E., Wargau W. 1987, A&A 181, 378

Gabriel C., et al. 1997, Proc. of the ADASS VI Conference, eds. G. Hunt & H.E. Payne, pp. 108.

Hartley M., Manchester R.N., Smith R.M., Tritton S.B., Goss W.M. 1986, A&AS 63, 27

Henning Th., Pfau W., Zinnecker H., Prusti T. 1993, A&A 276, 129

Lehtinen K. 1997, A&A 317, L5

Lehtinen K., Lemke D., Mattila K., Haikala L.K. 1998, A&A 333, 702

Lehtinen K., Higdon J.L. 1998, submitted to A&A

Myers P.C., Ladd E.F. 1993, ApJ 413, L47

Prusti T., Whittet D.C.B., Assendorp R., Wesselius P.R. 1992, A&A 260, 151

BLOWING A CARBON-RICH BUBBLE IN THE GALACTIC CENTRE MEDIUM AROUND THE QUINTUPLET

D. Levine[1], M. Morris[2] & D. Figer[2]

[1]SIRTF Science Center, IPAC, Caltech/JPL, Pasadena, CA, USA
[2]University of California, Los Angeles, LA, CA, USA

ABSTRACT

The HII Region known as the "Sickle", follows the rim of a large scale ring of emission faintly visible at 20 cm and clearly visible in the mid-IR but undetected in CO surveys. We have taken SWS full range spectra at 3 points along the rim of the "bubble" and one point of relatively low emission to its interior. We detect several fine-structure lines and strong PAH features, but molecular lines are weak or absent.

Key words: Galactic Center

1. INTRODUCTION

The HII Region G0.18-0.04, also known as the "Sickle", follows the rim of a large scale (500 arcsec =20 pc) ring of emission faintly visible at 20 cm and clearly visible in the mid-IR (Egan et al. 1998) but undetected in CO surveys. IRAS HIRES data indicate a color temperature of ~100K, similar to AFGL5376 which has been explained as an extremely strong shock which dissociated the molecules behind the shock leaving only warm dust (Uchida et al. 1994).

2. OBSERVATIONS

We have taken spectra with the ISO Short Wavelength Spectrometer (SWS, de Graauw et al. 1996) at four locations around the large scale "bubble".

The locations of the four slit positions are indicated in Figure 1, shown overlaid on the 20 cm image from Yusef-Zadeh & Morris (1998). (The sickle itself, towards the northwest, has been observed in another program). The position called "SE_NTF_XNG" is a position on the rim to the southeast where the non-thermal filaments appear to cross the bubble in projection. This position shows enhanced emission at 20 cm. The position called "SSE" is a position along the rim to the southeast and the position called "SSW" is a position along the rim to the southwest towards the Galactic Center. The position called "OFF" is not a true off position, but is located away from the rim of the apparent bubble towards the interior, but away from the limb-brightened edge.

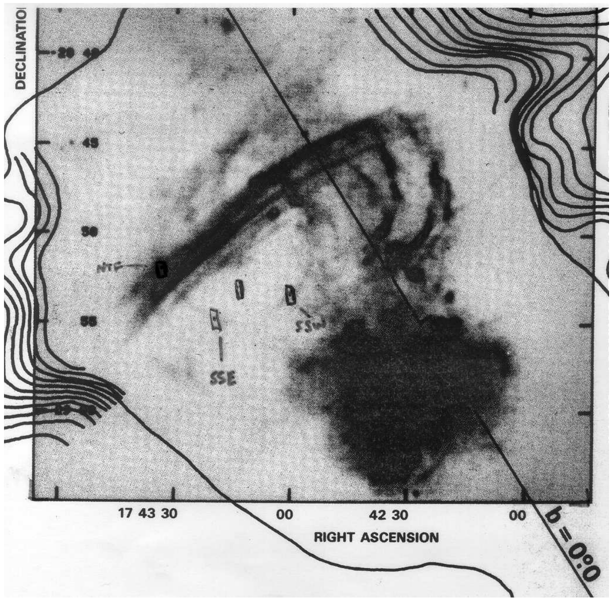

Figure 1. The 20 cm image with the 4 SWS slit positions overlaid

"SE_NTF_XNG and "SSW" are Speed 4 SWS01 observations; "SSE" and "OFF" were taken with the same AOT at Speed 3. The data presented here were reduced from the pipeline auto-analysis results (OLP6.x) using ISAP[1]

3. RESULTS

Figures 2-5 show the Band 2, 3 and 4 spectra for the 4 positions, with each section plotted on the

[1]The ISO Spectral Analysis Package (ISAP) is a joint development by the LWS and SWS Instrument Teams and Data Centers. Contributing institutes are CESR, IAS, IPAC, MPE, RAL and SRON.

same scale for all positions. The broad PAH features near 6.2, 7.7 and 8.6 μm are present in all pointings, but appear particularly strong in the SSW position. The fine-structure lines of [ArII], [NeII], [SIII], [FeIII], [SiII] are also present in all pointings except the "OFF" position where only the Band 4 lines of [SIII] and[SiII] are clearly detected. Other lines are present in some pointings but not in others and the relative strength of some features varies from pointing to pointing. Also, several strong features which have not been identified with known lines are present.

The fine structure lines are strongest in the position where the non-thermal filaments cross the structure and are relatively weak at the SSW position, which is the furthest of the 3 rim positions from the filaments. Both the continuum and the line-to-continuum ratio are also somewhat stronger at the SE_NTF_XNG position.

Table 1 summarizes the properties of the fine structure lines observed.

Table 1. High Signal-to-Noise Fine Structure Lines

Pointing	Flux (W/cm^2)	SNR	ID
OFF	7.80E-19±4.32E-20	13.1	[SIII]33.481
OFF	1.71E-18±6.66E-20	16.2	[SiII]34.815
SE_NTF_XNG	6.81E-19±8.04E-21	43.6	[ArII]6.985
SE_NTF_XNG	1.39E-18±3.94E-20	32.2	[NeII]12.813
SE_NTF_XNG	2.19E-19±1.12E-20	15.1	[NeIII]15.555
SE_NTF_XNG	6.44E-19±1.34E-20	38.5	[SIII]18.713
SE_NTF_XNG	1.24E-19±7.63E-21	14.4	[FeIII]22.925
SE_NTF_XNG	6.21E-18±4.87E-20	64.8	[SIII]33.481
SE_NTF_XNG	6.23E-18±3.69E-20	96.8	[SiII]34.815
SSE	7.02E-19±2.46E-20	14.1	[ArII]6.985
SSE	1.04E-18±7.72E-20	9.1	[NeII]12.813
SSE	4.80E-19±1.48E-20	23.8	[SIII]18.713
SSE	9.78E-20±7.25E-21	9.6	[FeIII]22.925
SSE	4.58E-18±9.08E-20	33.7	[SIII]33.481
SSE	6.27E-18±2.66E-20	159.7	[SiII]34.815
SSW	3.57E-19±9.01E-21	13.2	[ArII]6.985
SSW	7.14E-19±2.03E-20	29.5	[NeII]12.813
SSW	3.31E-19±1.61E-20	14.5	[SIII]18.713
SSW	1.48E-19±1.21E-20	8.1	[FeIII]22.925
SSW	7.86E-20±5.27E-21	10.8	[FeII]25.988
SSW	2.31E-18±3.02E-20	40.8	[SIII]33.481
SSW	2.89E-18±1.37E-20	118.2	[SiII]34.815

4. DISCUSSION

The "bubble" spectrum shows line emission similar to that seen in the GC spectrum of Lutz et al. (1996). However, it lacks any evidence of the absorption features seen there and it possesses strong PAH features reminiscent of those seen in carbon stars (Beintema et al 1996) and in starbursts and ULIRGs (Lutz et.al. 1998). The origin of these strong PAH features in the galactic center is somewhat puzzling in view of the fact that AGB stars near the galactic center tend to be oxygen-rich rather than carbon-rich (Jura, Yamamoto & Klein 1993).

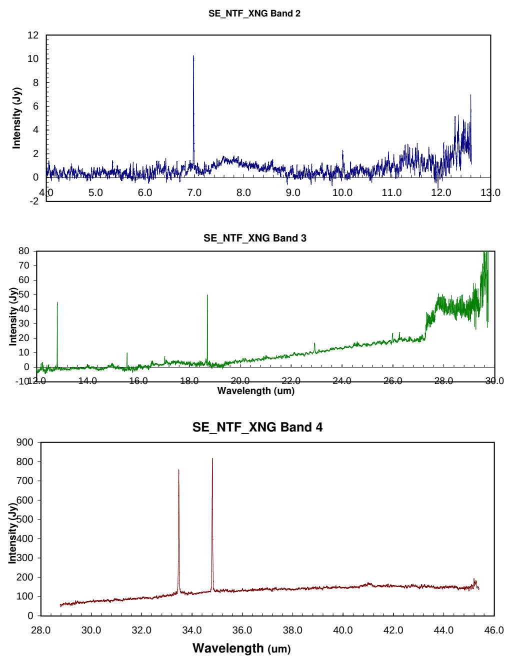

Figure 2. SWS bands 2-4 for the SE_NTF_XNG position

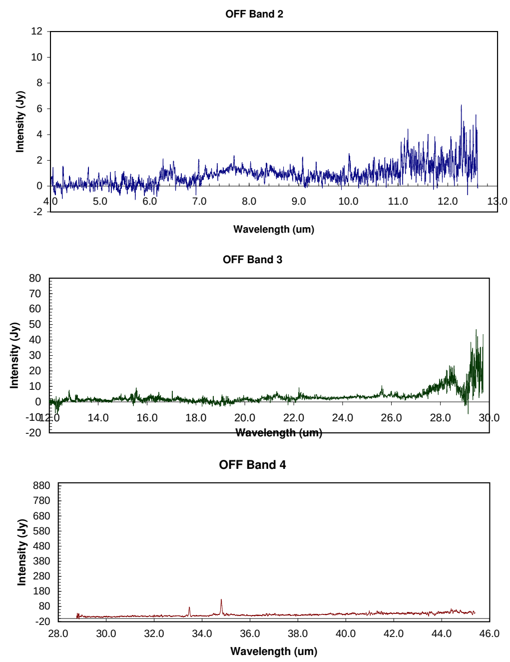

Figure 3. SWS bands 2-4 for the "OFF"position

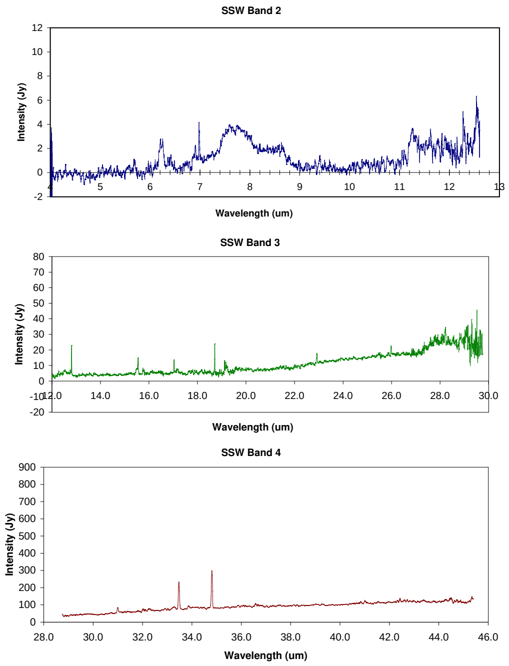

Figure 4. SWS bands 2-4 for the SSW position

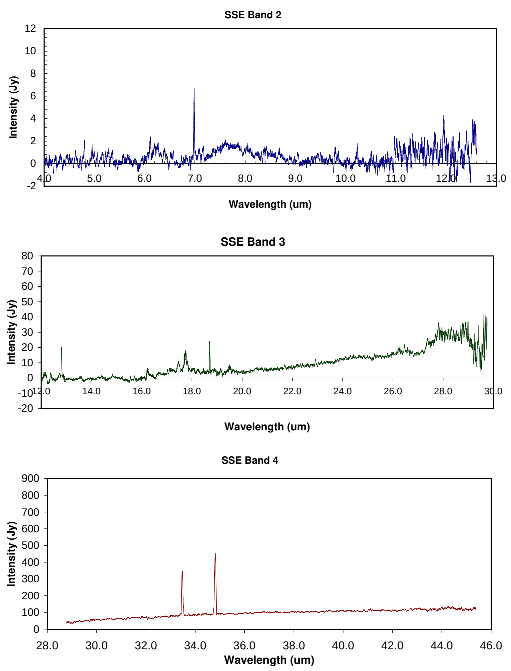

Figure 5. SWS bands 2-4 for the SSE position

REFERENCES

Beintema, D. et al. 1996, A&A, 315, L369

de Graauw, Th. et al. 1996, A&A, 315,L49

Jura, M., Yamamoto & Kleinmann, S. 1993, ApJ, 413, 298

Lutz, D. et al. 1996, A&A, 315, L269

Lutz, D. et al. 1998, ApJ, 505, L103

Egan, M., Shipman, R., Price, S., Carey, S., Clark, F. & Cohen, M. 1998, ApJ, 494, L199

Uchida, K. et. al. 1994, ApJ, 421, 505

Yusef-Zadeh, F. & Morris, M. 1988, ApJ, 329, 729

THE BEHAVIOUR OF THE [O I] 63 μm and [O I] 145 μm LINES IN THE ρ OPHIUCHI CLOUD

R. Liseau[1], G.J. White[2] & B. Larsson[1]

[1]Stockholm Observatory, Saltsjöbaden, Sweden
[2]Queen Mary & Westfield College, Dept. of Physics, London, UK

ABSTRACT

The dense cores B 1, B 2 and C North in the active star forming ρ Oph cloud have been observed with the ISO LWS (λ = 43–197 μm, $R = 140 - 330$). Detailed modelling of the FIR spectra shows that the emission originates in a PDR on the rear side of the cloud. However, the behaviour of the O I ground state lines ([O I] 63 μm, [O I] 145 μm) appears anomalous in the sense that observed flux ratios are too small compared to those predicted by theoretical models of O I excitation and line transfer. Based on the LWS data, we argue that self absorption in the [O I] 63 μm line by cool foreground material is not a viable explanation in the case of ρ Ophiuchi: the expected reduction in [O I] 63 μm flux towards the dense cores is not reflected by the data. In contrast, the [C II] 158 μm and [O I] 63 μm lines behave in accordance with model predictions. It seems likely, therefore, that it is not the [O I] 63 μm line being too weak, but that the [O I] 145 μm line is relatively too strong and we propose that slight masing in the [O I] 145 μm line is responsible for the observed line ratio anomaly.

Key words: ISM; Molecular Clouds; ρ Ophiuchi Cloud; PDRs; Star Formation.

1. INTRODUCTION

The relative strengths of the fine structure lines of atomic oxygen, viz. $O^0\,{}^3P_1$–${}^3P_2$ (63 μm) and $O^0\,{}^3P_0$–${}^3P_1$ (145 μm), are known to be difficult to predict theoretically for a number of astronomical sources (e.g., Tielens & Hollenbach 1985a & b; Saraceno et al. 1998). The ground state of O^0 is inverted, with the 145 μm line connecting the middle level with the upper level, more than 300 K above ground. The 63 μm transition, on the other hand, occurs between the middle level ($\Delta E/k \gtrsim 200$ K) and the lowest level at zero energy.

In several observed cases, 63 μm absorption (and/or scattering) by cool material along the line of sight towards the emitting source was directly suggested by the data (e.g., Baluteau et al. 1997). Such absorption could be expected to apply also to selected regions in the nearby (150 pc) ρ Oph cloud, harbouring a number of well studied dark and dense cores. In fact, the ρ Oph cloud could serve as a case study, since (1) the geometry of the emitting and of the putative absorbing regions is known, (2) the distribution of the volume and the column density is known, and (3) the spatial distribution and local strength of the UV-field (expressed in units of G_0, the integrated flux of the local interstellar field) is known from observation and theoretical modelling (Liseau et al. 1998, hereafter Paper I).

The regions ρ Oph B and ρ Oph C (Loren et al. 1990) appear as dark patches at wavelengths at least as long as 15 μm (see the ISOCAM image by Abergel at al. 1996). It is therefore most likely that the illuminating source (HD 147889, see: Paper I) is situated behind the bulk of the cloud and, consequently, that most of the PDR (Photon Dominated Region) emission originates at the rear side of the cloud. This scenario is in agreement with our detailed model presented in Paper I. In the present contribution, we examine the [O I] 63 μm and [O I] 145 μm observations with the LWS towards the dense cores ρ Oph B 1, B 2 and C 1 (C North).

2. OBSERVATIONS AND DATA QUALITY

In Fig. 1, the pointings of the ISO LWS (Kessler et al. 1996, Clegg et al. 1996) towards ρ Oph B are shown superposed onto a map in the emission of CS (J=5–4) (unpublished 15m SEST data of R. Liseau). The integrated CS line intensity traces the density distribution of the cloud. The high density clumps ρ Oph B 1 (south-west) and ρ Oph B 2 (north-east) are clearly revealed in this figure. The LWS data are spatially oversampled in the scan direction (Δ=40″, LWS-beam about 80″) and displayed in Fig. 2, where the positions of ρ Oph B 1 (b 4) and ρ Oph B 2 (b 11) are identified. The IRAS source IRS 37 (Wilking et al. 1989) is at b 6.

In Figs. 2 and 3, the positions of b 3 and c 6 are especially marked. The latter refers to a different scan (Paper I), which was obtained at a *different date*. The pointing towards c 6 was originally intended to coincide with b 3 for cross calibration checks. The actual angular distance between the two positions is only 25″, implying that these observations should

Proceedings of the Conference "The Universe as seen by ISO", Paris, France, 20–23 October 1998 (ESA SP-427, March 1999)

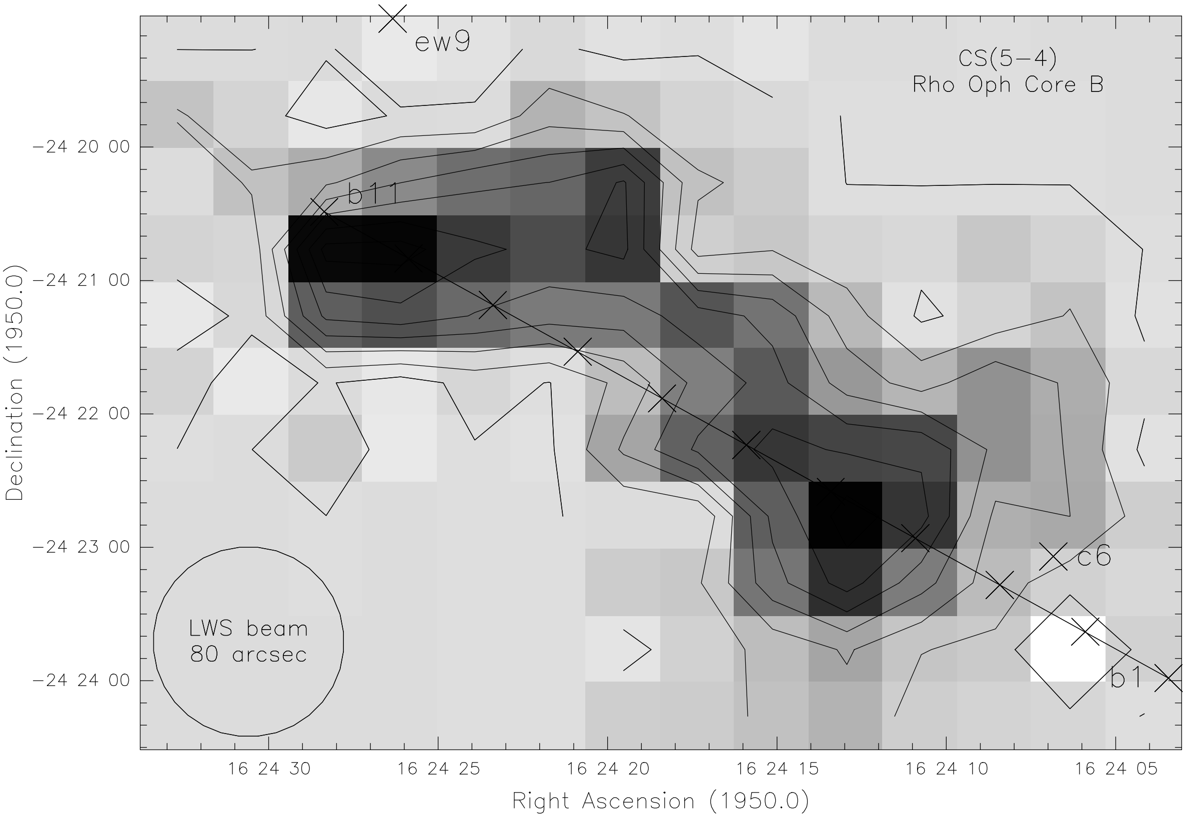

Figure 1. The positions of the LWS scan through the dense cores in ρ Oph B are shown and the first position, b 1, is identified. Offsets are 40″ and the shown beam of the LWS has a half power width of 80″. Also shown are two positions from different scans (c 6 and ew 9), the observations of which are separated in time. The LWS pointings have been overlayed onto a map in CS (5–4), obtained with the 15m SEST (R. Liseau, unpublished data). The CS data clearly reveal the cold and dense cores ρ Oph B 1 (south-west) and ρ Oph B 2 (north-east).

give nearly identical results (within the 30% accuracy of the absolute flux calibration; Swinyard et al. 1996). From Table 2 of Paper I one infers that the agreement is, in fact, excellent. Similar is true also for other cross-checks (e.g. b 11 and ew 9), although there the angular separations are larger. The good internal agreement of the LWS data, obtained at different dates, lends credence to their reliability.

Further, in Paper I, comparisons were made with *independent* observations, particularly with the KAO, which resulted in satisfactory agreement between the different data sets. Taken together, we regard it highly unlikely that the line line ratio anomaly discussed below is entirely of instrumental origin.

3. DISCUSSION AND CONCLUSION

In a scenario, where a small [O I] 63 μm/[O I] 145 μm line ratio (< 10) is caused by decreased 63 μm line flux due to self absorption in cool foreground material, one would expect the [O I] 63 μm flux to anticorrelate with the column density of the cold gas. Such behaviour is not observed anywhere in ρ Oph, however (see also Figs. 2 and 3). Surprisingly, rather the opposite seems to occur, viz. that the line strength appears to grow with the column density of cold gas (near their centres, the temperature of the cores is as low as below 10 K). Since G_0 is approximately constant over the core regions and the [O I] 63 μm emission is not optically very thick ($\tau_0 \sim 1 -$ a few, Paper I), the increase in line flux could reflect an increase in density in the emitting regions, i.e. in the PDR. Such increase could refer to either (1) an enhanced hydrogen density, for a constant (depleted) oxygen abundance or (2) an augmented abundance of atomic oxygen relative to hydrogen. The latter could be due to gas-grain chemical activity. However, on the basis of the available observational evidence we are not able to distinguish one possibility from the other. Alternatively, the IRAS source IRS 37 could contribute significantly to the [O I] 63 μm flux.

We recall the fact that the [C II] 158 μm and [O I] 63 μm lines behave in accordance with model predictions. It thus seems that the encountered difficulties are due to [O I] 145 μm alone and that the observed [O I] 63 μm/[O I] 145 μm line ratios in ρ Oph are not easily explained. In particular, self absorption of [O I] 63 μm seems to be ruled out. Should our comprehension of the source geometry be incorrect,

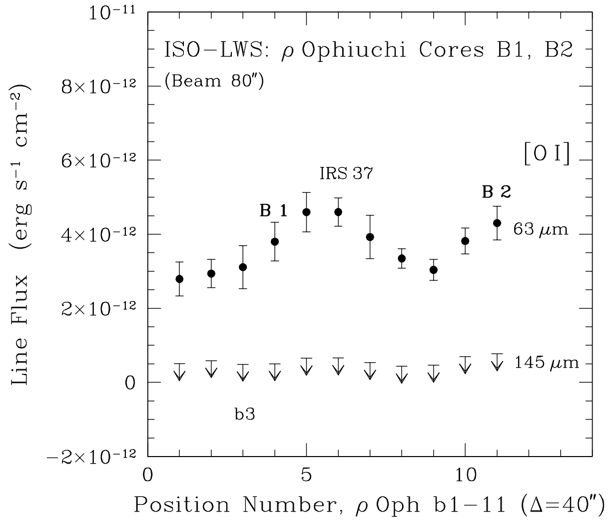

Figure 2. [O I] 63 μm and [O I] 145 μm data from the LWS-scan through the ρ Oph cores B 1 and B 2. Along the abscissa, the number of the individual pointings (b 1 to b 11) is given and along the ordinate the observed flux in the lines, corrected for continuum emission. The points are separated by 40″. The positions of the dense cores are indicated and the pointing b 3 is marked (cf. Fig. 3). No significant decrease in [O I] 63 μm flux towards the dense cores is discernible.

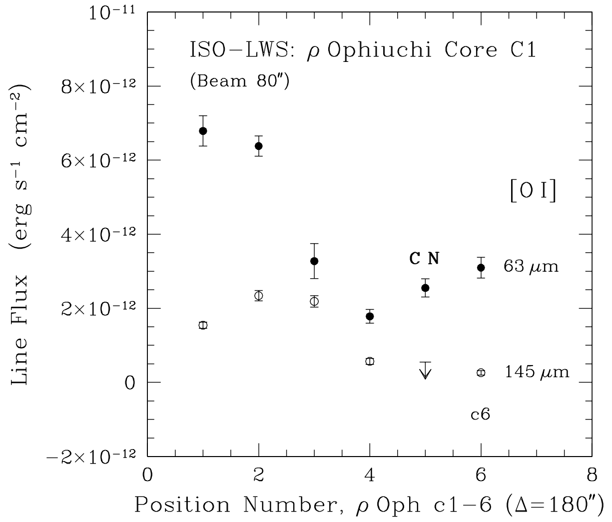

Figure 3. Same as Fig. 2, but for the LWS-scan through the ρ Oph core C 1, designated by CN (North), and with offsets of 180″. The [O I] 63 μm flux is not markedly reduced towards the dense core CN. The position c 6 is close to b 3 in Fig. 2, both showing identical flux. At positions, where both lines are clearly detected, the [O I] 63 μm/[O I] 145 μm flux ratio is smaller than ten.

the self absorption picture would suffer even further, since the PDR would then be on the side of the cloud facing the Earth and little, if any, foreground material to absorb or scatter 63 μm photons would be available. It seems more likely, therefore, that the causes of small line ratios are not external, but internal to the physics of O^0 excitation and/or line transfer. In Paper I, we have examined a large number of possible explanations and reached the conclusion that the hypothesis of slight masing in the [O I] 145 μm line seems most promising. A physical mechanism, accomplishing the maser action, should be investigated in more detail.

ACKNOWLEDGEMENTS

We thank A. Brandeker for his assistance with Fig. 1.

REFERENCES

Abergel A., Bernard J.P., Boulanger F., et al. 1996, A&A 315, L 329

Baluteau J.-P., Cox P., Cernicharo J., et al. 1997, A&A 322, L 33

Clegg P.E., Ade P.A.R., Armand C., et al. 1996, A&A 315, L 38

Kessler M.F., Steinz J.A., Anderegg M.E., et al. 1996, A&A 315, L 27

Liseau R., White G.J., Larsson B., et al. 1998, submitted to A&A (Paper I)

Loren R.B., Wootten A., Wilking B.A. 1990, ApJ 365, 269

Saraceno P., Nisini B., Benedettini M., et al. 1998, in: Star Formation with the Infrared Space Observatory, Yun J.L. & Liseau R. (eds.), ASP Conf.Ser., 132, p. 233

Swinyard B.M., Clegg P.E., Ade P.A.R., et al. 1996, A&A 315, L 43

Tielens A.G.G.M., Hollenbach D.J. 1985a, ApJ 291, 722

Tielens A.G.G.M., Hollenbach D.J. 1985b, ApJ 291, 747

Wilking B.A., Lada C.J., Young E.T. 1989, ApJ 340, 823

S106 : MORPHOLOGY AND EXCITATION OF PAH, H_2 AND H FROM ISO, C10μ AND BEAR

J.P. Maillard[1], C. Joblin[2], G.F. Mitchell[3], I. Vauglin[4], & P. Cox[5]

[1]Institut d'Astrophysique de Paris (CNRS), Paris, France
[2]Centre d'Etude Spatiale des Rayonnements (CNRS), Toulouse, France
[3]Astronomy and Physics Dept, Saint Mary's University, Halifax, Canada
[4]CRAL-Observatoire de Lyon, Lyon, France
[5]Institut d'Astronomie Spatiale, Orsay, France

ABSTRACT

A set of new data has been obtained on S106 with ISOCAM in CVF mode in the 6 to 9 μm range, with the ground-based mid-infrared camera C10μ and in spectro-imaging in the 2 μm region with BEAR an imaging FTS, both instruments having a 10 times better spatial resolution, i.e. $\sim 0.3''$. The latter data have been obtained in the Brγ and H_2 1-0 S(1) lines, at a spectral resolution of $\sim$ 15km s^{-1}. By comparing all these data the relation of PAH and H_2 can be studied. They have on large scale the same distribution but differ in the detail. BEAR maps in the H_2 and H lines show a very turbulent gas. With the velocity information provided by the BEAR data a picture of the 3D distribution of gas and dust in the S106 outflows can be built.

Key words: massive YSO; S106; PAH; molecular gas; imaging FTS.

1. INTRODUCTION

The infrared source S106IR (or S106-IRS4) is a typical massive young stellar object of high luminosity (2$\times$10^4 L$_\odot$), type O or early B (Eiroa et al. 1979), still embedded in its parent cloud (A$_v$ $\simeq$ 21). The isolation of this source and its relative proximity estimated at $\simeq$ 600 pc (Staude et al. 1982) make a detailed study of its environment possible. S106IR appears to be the unique source of excitation of the S106 molecular cloud, providing a good example of an interface between a photodissociation region (PDR) and an HII region. This environment has been mapped at many different wavelengths, from the visible to the centimeter waves (Gehrz et al. 1982, Felli et al. 1984, Aspin et al. 1990, Hayashi et al. 1990, Hodapp & Rayner 1991, Roberts et al. 1995). These broad-band images mainly illustrate the change of morphology with wavelength of an extended emitting region with a North-South bipolar extension. The infrared observations presented in this paper provide new information on the physical and chemical conditions of the YSO environment and on its kinematics. Images have been obtained in the "unidentified" infrared bands at 6.2, 7.7, 8.6, 11.3 and 12.7 μm, generally attributed to Polycyclic Aromatic Hydrocarbons (PAHs), using ISOCAM and a ground-based mid-infrared camera C10μ offering a high spatial resolution. At the same spatial resolution, and at a high spectral resolution the velocity profile of the 1-0 S(1) line of H_2 and the Brγ line of H have been obtained. These observations allow the building of a plausible tridimensional model of flows from a massive YSO.

2. OBSERVATIONS

The ISOCAM data (Joblin et al. 1999a) shown in Fig. 1 were obtained at 8.6 μm with the CVF, part of a spectral coverage from 6 to 9 μm, with a pixel size of 3 arcsec. This leads to a square field of 96$\times$96 arcsec, well adapted to cover the totality of the emitting zone, which exhibits the general bipolar shape seen in previous images of the continuum (e.g. Gehrz et al. 1982, Felli et al. 1984). The ISO data were complemented with ground-based observations with a mid-infrared camera using various filters to map the PAH bands at 8.6, 11.3, and 12.7 μm, and the nearby continuum at 10.6 μm. The 11.3 μm band has the advantage to be more intense than the 8.6 μm band, and thus is useful for tracing the PAH emission in detail. The emission at 8.6 μm common to the two sets of data was used for cross-calibration (Joblin et al. 1999b). These observations were conducted at the f/35 focus of the 3.6-m CFH Telescope in a run of July 1997 with C10μ. This 192$\times$128 Si:Ga camera has been developed by Lyons Observatory (Merlin et al. 1996), to work in the 5 - 15 μm range. This camera has the advantage of offering a pixel size (0.31 arcsec/pixel), about 10 times smaller than that of ISOCAM. While the useful field is thus only 59$\times$40 arcsec, it nonetheless covers the main part of the emitting regions of S106. In a run at the same focus in July 1997 and July 1998 with the BEAR spectrometer, a unique FTS imager (Maillard 1995), equipped with a 256$\times$256 NICMOS camera, with a scale comparable to that of C10μ (0.35 arcsec/pxl), a total field of 26×38 arcsec around S106IR was observed. This was obtained from the merging of two circular fields of 24 arcsec diameter, the size of the available field in one exposure. Spectro-imaging at a spectral resolution of $\sim$ 15km s^{-1} was obtained through narrow-band filters isolating H_2 2.12μm (Fig. 2) and H Brγ 2.16μm (Fig. 3) respectively. Previously reported spectro-imaging work had been made with a F-P etalon at a resolution of 130 km s^{-1} (Hayashi et al. 1990).

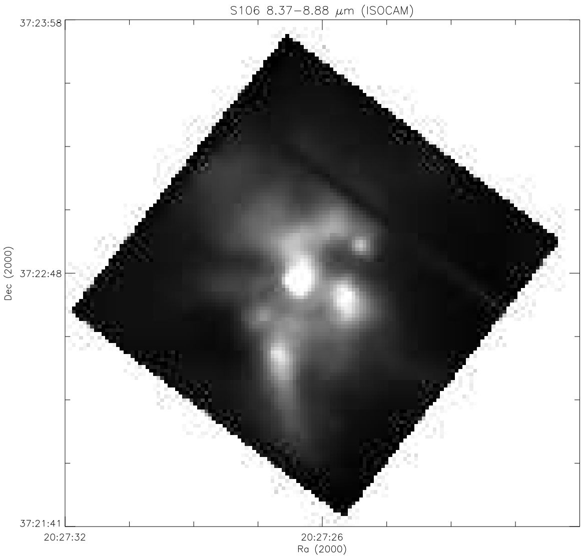

Figure 1. ISOCAM image of S106 in the 8.6μm PAH band obtained by summing the CVF positions in the 8.37 - 8.88μm range. The continuum is not subtracted.

3. LINE SHAPES

From the BEAR data the shape of H and H_2 lines can be analysed in all points of the field. The first striking difference is that the H_2 line is narrow and unresolved ($<$ 15 km s^{-1}) throughout the entire field, while for Brγ the line core is broad everywhere with FWHM equal to 35 km s^{-1}. Broad wings are observed in many positions (FWZI up to 130 km s^{-1}) and are often asymmetric. Surprisingly, a double line with a peak separation of 53 km s^{-1} is observed in a well-defined area in the southern flow (Fig. 3). A possible explanation for this profile will be discussed further down.

4. VELOCITY FIELD

These data also provide information on the velocity field of the gas. From a first analysis of the H_2 line, four separate structures (Fig. 2) can be seen with for each of them a specific velocity :

- a bright structure at the western edge of the field, oriented north - south, to the south of S106IR,
- a large, clumpy arc to the south
- an emission structure surrounding the YSO and extending generally southwest,
- a bright arc at the northern limit of the field.

The same four structures are present in the intensity distribution of Brγ (Fig. 3). Because of the larger linewidth they are less clearly separated in velocity. A complete mapping of the velocity field in the ionized gas with Brγ as tracer is required to show systematic velocity differences. Note that these structures are regions of enhanced emission, as the line is present everywhere, at low level between the bright regions.

The differences in velocity between each area in H_2 are only a few km s^{-1} (maximum difference 7 km s^{-1}), but are significant. Therefore, neither the H_2 nor the Brγ emission shows evidence for bipolarity from velocity measurements. This bipolarity is only revealed by the general distribution of gas and dust. This almost common velocity is indicative of flows in motion mainly in the plane of the sky. This conclusion had already been drawn by Solf & Carsenty (1982) from long-slit spectroscopy in the Hα line. This makes S106 useful for studying the structure of flows without projection effects.

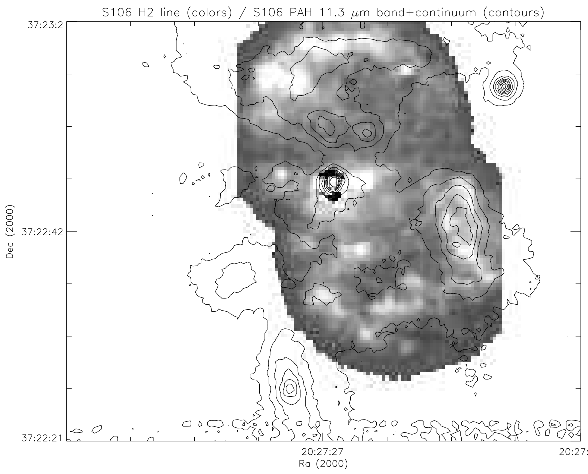

Figure 2. The 2.12μm H_2 emission integrated over the full velocity field from BEAR data (grey-scale) compared with the C10μ image of S106 in the 11.3μm PAH filter (contours).

5. COMPARISON BETWEEN GAS AND PAH EMISSION

In contrast to the ISOCAM image at 8.6μm (Fig. 1) where there is everywhere a continuous emission in the North and South flow, with some brighter areas corresponding coarsely to the structures identified in the BEAR images, these structures are clearly seen in the emission mapped with C10μ at 11.3μm, as expected given the higher contrast of this PAH band relative to 8.6μm, and the much higher spatial resolution. There are a few additional patches, in particular to the South-East of S106IR, a region not covered by the BEAR observations. Further discussion of the spatial distribution of the different PAH bands is reported elsewhere (Joblin et al. 1999a).

As an example, Fig. 2 compares the spatial distribution of the PAH 11.3μm band with that of the H_2 emission. Very interestingly, the H_2 emission follows very closely the same distribution, indicative of a good mixing between H_2 and the PAH grains in the same clumps. There is a remarkable exception for two bright blobs close to S106IR, just north of it, a region devoid of H_2. The obvious absence of H_2 at these positions can be ascribed to destruction by the intense UV field from the central source, while the locally dense dust has resisted destruction.

6. DISCUSSION : ORIGIN OF EMISSIONS

The narrow lines rule out a shock origin for the H_2 emission. Hayashi et al. (1990) suggested that a $7\,\mathrm{km\,s^{-1}}$ shock could explain the H_2 emission. If the surrounding gas is clumpy we might expect multiple shocks in the line of sight, broadening the line. As the H_2 line is everywhere unresolved, fluorescence in a PDR is more likely. ISO observations of fine structure of atomic lines (iron) in a SWS2 spectrum of S106 led to the same conclusion (van den Ancker et al. 1998). On the contrary, the Brγ line which is much broader than the H_2 line tends to indicate that H is representative of a shocked gas. The most plausible explanation to reconcile these facts is that, in these large clumps H results from the dissociation of H_2, but H and H_2 are spatially separated. A closer examination of the respective distribution of H and H_2 shows that the peaks of H are displaced with respect to the peaks of H_2, the latter being further away from the central source.

A tentative model which emerges is that, with S106, we witness the phase of disruption of the dense core in which the massive YSO formed, through the action of the presumably irregular stellar wind. We see large clumps of dust mixed with PAH and H_2 which are drifting apart as indicated by the velocity differences between clumps. This wind is not fully collimated, which is common for massive YSOs, with a main N-S direction in the plane of the sky. Note that the E-W dark lane seen in the images (Fig. 1, 2 and 3), which has often been interpreted as the signature of a large size disk (Gehrz et al. 1982) perpendicular to the flows might be a region devoid of material, the separation between the north and south clumps. This is in agreement with the fact that no such disk has been detected at any wavelength and that the dark lane is not centered on S106IR but is seen north of the source.

The double-peaked Brγ line seen in a rectangular zone (Fig. 3) formed by the edges of three clumps gives another indication on the spatial distribution of the flows. Remarkably enough, one of the components has the same velocity as the surrounding clumps while the other one is clearly redshifted. This latter component is indicative of emission coming from a region deeper in the same line of sight. It can be proposed that H is coarsely distributed in a open cone with its axis in the plane of the sky. The clumps which are seen are located in the forefront surface, blocking the emission from the background surface, only seen in this large hole. The high brightness of the North-South structure, on the western edge of this aperture, observed in the PAH band, in H_2 and in

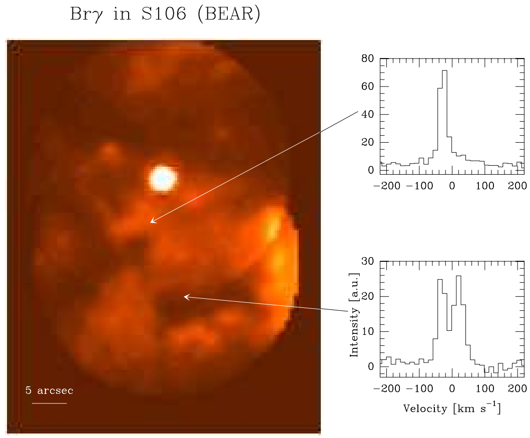

Figure 3. Distribution of atomic hydrogen traced with the Brγ line at 2.16μm from the BEAR data; obtained by summing planes representing a total velocity span of $150\,km\,s^{-1}$, with examples of velocity profile in two locations. The width of a velocity channel is equal to $14.3\,km\,s^{-1}$. H is present throughout the field, even in regions of low contrast. North is up, east is left.

Brγ lines, can then be explained as a limb effect from the conical distribution of emitting material. The most southerly North-South structure (Fig. 2) could mark the opposite limb and have the same origin. The projected expansion velocity of the cone in the radial direction can be estimated at $26\,\mathrm{km\,s^{-1}}$, half the peak separation, which means a much higher true expansion velocity. A value of $76\,\mathrm{km\,s^{-1}}$ had been inferred by Solf & Carsenty (1982) putting S106IR among the YSOs with high-velocity wind.

7. CONCLUSION

In conclusion, an image of the flow structure of a massive YSO like S106IR starts to emerge : an empty and bipolar widely open cone of ionized gas, in expansion, with the gas concentrated in patchy walls in which H_2, the dust and PAH grains are forming the most external layers. This structure in a later phase disperses in large clumps of material. This work is in progress. New data on the 11.3μm band through a CVF with C10μ and a systematic mapping of the velocity field in H_2 and Brγ should help to sharpen the facts already reported. A complementary discussion should consider the lifetimes of all the process.

REFERENCES

Aspin, C., Rayner, J.T., McLean, I.S., Hayashi, S.S. 1990, MNRAS, 246, 565

Eiroa, C., Elsässer, H., Lahulla, J.F. 1979, A&A, 74, 89

Felli, M., Staude, H.J., Reddmann, Massi, M., Eiroa, C., Hefele, H., Neckel, T., Panagia, N. 1984, A&A, 135, 261

Gehrz, R.D., Grasdalen, G.L., Castelaz, M., Gullixon, C., Morzukevitch, D., Hackwell, J.A. 1982, ApJ, 254, 550

Hayashi, S.S., Hasegawa, T., Tanaka, M., Hayashi, M., Aspin, C., McLean, I.S., Brand, P.W.J.L., Gatley, I. 1990, ApJ., 354, 242

Hodapp, K.W., Rayner, J. 1991, AJ, 102, 1108

Joblin, C., Vauglin, I., Tielens, A.G.G.M., Bregman, J., Merlin, P., Abergel, A., Vivarès, F. 1999a, *in prep*

Joblin, C., Vauglin, I., Abergel, A., Vivarès, F., Dubois, J.P. 1999b, *in prep*

Maillard, J.P. 1995, 3-D Spectroscopy with a Fourier transform Spectrometer, in *Tridimensional Optical Spectroscopic Methods in Astrophysics*, IAU Coll. 149, A.S.P. Conf. Series, ed. George Comte & Michel Marcelin, vol. 71, p. 316

Merlin, P., Sibille, F., Vauglin, I. 1996, User's Manual for the 10 micron camera C10μ, 1996, available at *httpp://www-obs.univ-lyon1.fr/ir*

Roberts, D.A, Crutcher, R.M., Troland,T.H. 1984, ApJ, 442, 208

Solf, J., Carsenty, U. 1982, A&A, 113, 142

Staude, H.J., Lenzen, R., Dyck, H.M., Schmidt, G.D. 1982, ApJ, 255, 95

van den Ancker, M.E., Wesselius, P.R., Tielens, A.G.G.M., Waters, L.B.F.M., in *ISO's View on Stellar Evolution*, ed. L.B.F.M. Waters, C. Waelkens, K.A. van der Hucht & P.A. Zaal, Kluwer:Dordrecht, 1998, Astrophys. & Space Sci., 255, 69

THE HOT GAS AND THE COLD DUST IN THE GALACTIC CENTRE CLOUDS AS SEEN BY ISO

J. Martín-Pintado[1], N.J. Rodríguez-Fernández[1], P. de Vicente[1], A. Fuente[1], T.L. Wilson[2], S. Hüttemeister[3], & D. Kunze[4]

[1]Observatorio Astrónomico Nacional, Apartado 1143, E-28800, Alcalá de Henares, Spain
[2]Max–Planck Institut für Radioastronomie, Postfach 2024, D 53010 Bonn, Germany
[3]Astronomische Institute, Auf dem Huegel 71, D-53121 Bonn 1, Germany
[4]MPE, Giesenbachstrasse 1, D-85748 Garching, Germany.

ABSTRACT

We present the first results of the LWS and SWS ISO observations of 18 molecular clouds in the Galactic centre (GC) region. H_2 emission from several rotational lines in the ground vibrational state is detected towards all molecular clouds. The rotational temperatures derived from these lines are between 150 and 500 K. Remarkably, the derived column densities of the hot H_2, $\sim 2\ 10^{22}$ cm^{-2}, are similar to those obtained for the cold gas. From the non-detection of the S(3) line at 9.7 μm, we derive that the hot gas must be located behind more than 30 mag of visual extinction of cold gas and dust. The LWS continuum spectra indicate that the cold dust has temperatures of 25-35 K and column densities similar to those required to explain the extinction of the H_2 emission. The observations of the J=2-1 and the J=1-0 line of $C^{18}O$ seem to sample only the cold (J=2-1/J=1-0 line ratios of 0.7-1.4) gas located in front of the hot gas. This indicates that the low J transition of $C^{18}O$ does not trace the total molecular gas in the GC. The LWS continuum spectra impose stringent limits ($\lesssim 1$ per cent) to the hot dust associated to the hot H_2. Towards most of the clouds we also detected emission from the fine structure lines of ionized species like SIII and NeII, and in some cases also from NeIII and OIII. In contract with the previous idea that the heating of the GC clouds is dominated by shocks, our data suggest that photoelectric heating by UV radiation can be the dominant mechanism. The effective temperature of the ionization radiation derived from the NeIII/NeII ratio is 35.000 K (typical of an O7 star). These ISO data when combined with the upper limits to the intensities of the recombination lines measured at millimeter wavelengths indicate that the UV radiation is very diluted. Cavities with sizes larger than 2 pc surrounding the ionizing star(s) are required to explain the mentioned dilution. The origin of the ionized cavities and the implications of these findings on the heating of the molecular clouds in the GC are briefly discussed.

Key words: Galactic Center; ISM; shock waves.

1. INTRODUCTION

The molecular clouds in the GC exhibit unusual characteristics with widespread high gas kinetic temperatures and relatively low dust temperatures (Güsten 1989). Unlike the warm and hot cores in the molecular clouds of the Galactic disk where the UV photons from young stars heat the grains and the gas is heated by dust-gas collisions, the low dust temperatures observed in the GC require a different heating mechanism which acts directly on the gas. So far, the main heating mechanism invoked to explain the particular properties of the molecular clouds in the GC is shocks (Wilson et al. 1982). The chemistry in the GC clouds seems also to be unusual. The abundance of refractory molecules like SiO is relatively large, supporting the shock scenario for the peculiar chemistry of the GC clouds (Martin-Pintado et al. 1997; Hüttemeister et al. 1998). Due to the large extinction towards this region most of our view of the GC clouds has been obtained from radio observations. Obviously, a complete picture of the energetics of these clouds will only be obtained when the main cooling lines in the IR are measured. We have used ISO to obtain a complete view of the ionized, hot and cold gas and dust in the GC clouds. These data will allow to fully characterize the GC clouds, and will help to understand the heating in the GC.

2. OBSERVATIONS, DATA REDUCTION AND RESULTS

We have observed 18 molecular clouds in the GC selected from the sample of Hüttemeister et al. (1993) and Martín-Pintado et al. (1997) with the LWS and the SWS of ISO. We have measured with the SWS several rotational line of H_2 (S(0), S(1), S(3) , S(4) and S(5)), the 18.7 and 33.5 μm lines of SIII, the 12.8 μm of NeII, and the 15.6 μm line of NeIII. The reduction of the SWS data was carried out with the Interactive Analysis programs at the ISO Spectrometer Data Centre at MPE. We also took full LWS spectra of all sources. Observations of the recombination line H41α and of the J=1-0 and J=2-1 lines of

$C^{18}O$ have also been obtained with an angular resolution similar to that of the SWS aperture using the IRAM 30-m telescope.

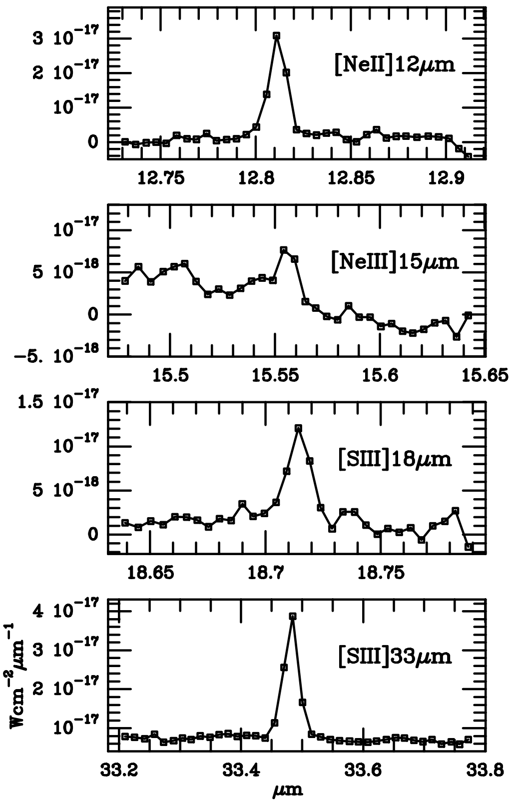

Figure 1. Fine structure lines observed with the SWS towards the cloud M+0.16-0.10. The spectra are averaged to one half of the instrument's resolution.

3. THE STRUCTURE IN THE GC CLOUDS

From the combination of all data a new picture of the GC clouds emerges. We find that all the sources in our sample show the presence of three different components: the ionized gas, the hot molecular gas and the cold gas and dust.

3.1. The ionized gas

Basically all the sources observed in the GC show emission from fine structure lines of ionized species like NeII and SIII (see Fig. 1). The ratio between the 18.7 and the 33.5 μm lines of SIII are $\leq$0.2, much smaller than the lower limit of 0.5 obtained from the excitation at very low density. This low ratio indicates that the ionized gas must be located behind more than 40 mag of visual extinction even in the case that the source of the ionized emission is extended. In the sources with the strongest NeII line, we also detect emission from the NeIII line. For those sources the ratios between the NeIII and the NeII lines, 0.05-0.2, suggest effective temperature for the ionization radiation of at least 35.000 K (Sellmaier et al. 1996), typical of an O7 star. This is in contrast with the recombination line data at millimeter wavelengths for which we measure an upper limit to the emission of $\sim$ 15 mK. Assuming the typical linewidths of $\sim$ 30 kms^{-1}, and a LTE electron temperature of 10.000 K, our upper limits indicates that the Lymann continuum photons in the SWS aperture must be $\leq$4 10^{47} s^{-1}, typical of a B0 star. The effective temperature of the ionization radiation derived from the NeIII/NeII ratio is inconsistent with ionization by main sequence OB starts exciting HII regions with sizes of $\leq$2 pc. As discussed in Section 4, the presence of large cavities surrounding the ionizing stars can explain the discrepancies.

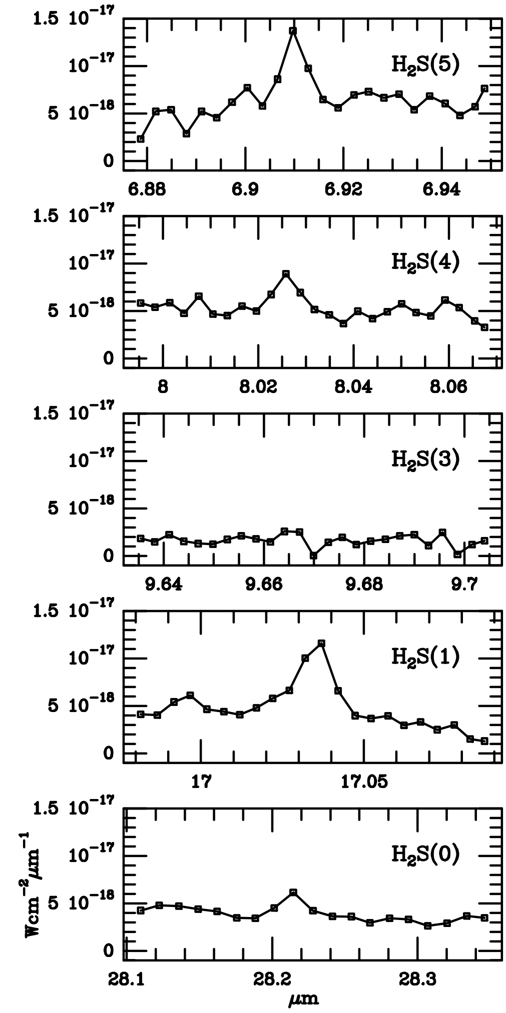

Figure 2. Pure rotational transitions of H_2 as observed with the SWS towards M+0.16-0.10. The spectra are averaged to one half of the instrument's resolution. Note that the S(3) line is not detected because of the absorption by the 9.7 μm silicates feature.

3.2. The hot molecular gas

All the clouds show emission in several rotational lines in the ground vibrational state of H_2 (see Fig. 2). In all sources the S(3) at 9.7 μm is weaker than expected pointing out that the hot gas is also behind of more than 30 mag of visual extinction. The rotational temperatures derived from the line intensity ratios varies from 150 K (S(1)/S(0)) to 500 K (S(5)/S(4)) (see Fig. 3) indicating large temperature gradients within the hot gas. Ortho-to-para ratios different than those in LTE will only change the kinetic temperature from 150 to 180 K.

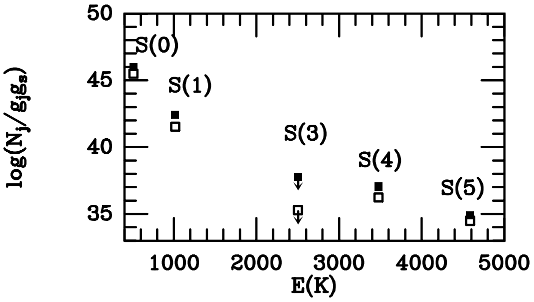

Figure 3. Rotational plot for H_2 rotational states J=2-7 obtained for M+0.16-0.10. The filled squares have been obtained after correcting the measured values (open squares) for 29 magnitudes of visual extinction using the extinction law of Draine 1989. The assumed ortho-to-para ratio is 3. Note that the values for the S(3) line are upper limits.

The total column densities of hot (150 K) H_2 corrected by extinction are at least 1-2 10^{22} cm^{-2}. These column densities of hot molecular gas must be considered as lower limits since the lowest kinetic temperatures sampled by the S(0) and S(1) lines are $\geq$ 140 K. If warm gas with kinetic temperatures of $\sim$ 80 K is present, the column densities of the hot gas will be increased by a factor of more than 5.

3.3. The cold molecular gas and dust

The line ratios between the J=2-1 and the J=1-0 lines of $C^{18}O$ towards all ISO sources are 0.7-1.4. This seems to be a general characteristic in the GC molecular clouds (see e.g. Hüttemeister et al. 1998) and indicates that the molecular gas sampled by these lines is relatively cold with kinetic temperatures much lower than the 140 K derived from the H_2 lines. The total H_2 column densities derived from the $C^{18}O$ emission towards the ISO clouds are 3-5 10^{22} cm^{-2}. These column densities are similar to those of the warm and the hot gas, but the measured line ratios of $C^{18}O$ are inconsistent with those expected for the hot gas, namely 3-4, suggesting that the $C^{18}O$ emission only samples the cold component. It is interesting to note that the column density of the hot component can be even larger than the column densities of the cold component measured from the $C^{18}O$ lines.

As mentioned in the previous section, the hot H_2 is located behind more than 30 mag of visual extinction. This material must be associated with relatively cold dust since it is outside of the region emitting the hot H_2. The corresponding H_2 column densities associated with the material in front of the hot gas are similar to the estimated from the $C^{18}O$ emission suggesting that both are associated. Further support for this idea comes from the spectrum measured with LWS. The continuum spectrum between 40 and 190 μm indicates that most of the luminosity in the FIR is emitted by cold dust with temperatures between 25 and 35 K, and H_2 column densities of 3-8 10^{22} cm^{-2}. The column densities and the temperatures derived from the dust emission are consistent with those derived from the low J $C^{18}O$ data.

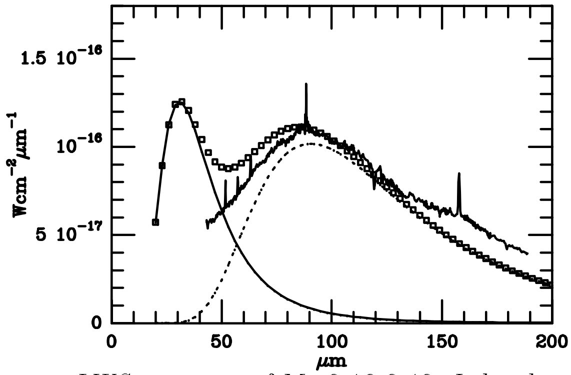

Figure 4. LWS spectrum of M+0.16-0.10. It has been superimposed a two component grey-body (squares) where a cold (33 K) dust component (dashed line) of N_{H_2} $\sim$ 3 10^{22} cm^{-2} is attenuating a warm (120 K) dust component with N_{H_2} 1000 times smaller (solid line). Note that even such an small amount of hot dust should have been detected.

From the continuum data at short wavelengths, we derive an upper limit to the column density of the hot dust with similar temperatures to that of the hot gas of $\leq 10^{20}$ cm^{-2}, more than 100 times smaller than that obtained from the H_2 lines (see Fig. 4). Our data support the previous idea that the dust associated to the hot gas is much colder than the gas.

4. DISCUSSION

Since the discovery of the relatively uniform high temperatures in the envelope of Sgr B2 and in other molecular clouds in the GC, a detailed understanding of the thermal balance in these molecular clouds has been a challenge. The most accepted idea is that shock heating explains the large column densities of hot gas associated with relatively cold dust (Wilson et al. 1982; Güsten 1989).

4.1. The heating mechanisms

Our ISO data show that the material along the line of sight towards the GC molecular clouds has a complex structure. The presence of an ionized component requiring an effective temperature for the ionization radiation of $\sim$35.000 K indicates that shock heating is not the only mechanism which heats the large column densities of hot molecular gas in the GC clouds. If only shocks are responsible for the heating, the presence of the NeII and NeIII lines would imply J type shocks with shock velocities $\geq$ 100 kms^{-1}. This is contradiction with the profiles of the ammonia lines arising from the hot and the cold gas (see

Hüttemeister et al. 1993) which do not show the displacement in radial velocities expected if the horty ammonia were heated by J-shocks. Furthermore, the ratio of the total line cooling rate to the FIR dust continuum is typically 0.006, far too low for the expected values from fast J shocks (Hollenbach & McKee 1989).

On the other hand, photoelectric heating will account for most of the observed characteristics of the ionized and the hot molecular components. For typical photodissociation regions (PDRs) in the Galaxy, photoelectric heating heats the gas to temperatures above those of the dust in a region with typical column densities of $\sim 3\ 10^{21}$ cm^{-2} (see Hollenbach & Tielens 1997). Several typical Galactic PDRs along the line of sight are then required to account for the large H_2 column densities of hot gas observed with ISO.

4.2. Wind blown ionized bubbles

Further support for the presence of several PDRs along the line sight of the GC comes from the inconsistencies between the Lyman continuum photons and the effective temperature of the ionization radiation. This can be reconciled if the ionized gas fills relatively large cavities surrounding the ionizing stars. Assuming a main sequence O star, our upper limit to the recombination line emission sets a lower limit to the size of the cavities of 2.5 pc. Hot (60-130 K) shells of molecular gas with sizes of 1-2.5 pc have recently been observed in the envelope of Sgr B2 molecular cloud (Martín-Pintado et al. 1999), and approximately 300 shells with sizes between 5 and 10 pc have been also identified from the CO survey of the GC (Hasegawa et al. 1998). From the number and the sizes of the shells detected in the GC, it is very likely that basically any line of sight towards the GC intersect at least two shells. In fact, Hasegawa et al. (1998) claim that the most likely occurrence of shells along the line of sight is ~ 20 shells. This would easily explain that the large column densities of hot H_2 observed with ISO can be produced by PDRs at the inner edges of a number of shells.

Although photoelectric heating can explain the ISO observations, the presence of a relatively large column density of hot ammonia ($\sim$ 30 per cent of the cold ammonia, see Hüttemeister et al. 1993) indicates that the Far UV radiation in not the only heating mechanism acting in the GC clouds. This is due to the fact that ammonia is a very fragile molecule and would be easily photo-dissociated in typical PDRs (Fuente et al. 1990). Martín-Pintado et al. (1999) have found that the hot ammonia shells in the Sgr B2 molecular cloud are expanding at relatively low velocities, 6-10 kms^{-1}. They proposed that the hot ammonia shells are produced by shocks associated with wind blown bubbles driven by evolved massive stars like Wolf-Rayets or Luminous blue variables. These wind blown bubbles will explain the large cavities around the stars, the rather high effective temperature of the ionization radiation, and the shock chemistry in the GC molecular clouds.

In summary, the ISO data show that the energetic of the GC molecular clouds is dominated by FUV radiation that ionizes and heats the gas by photoelectric effect and to less extent by low velocity shocks, caused by the wind of evolved massive stars, that contribute to the selective heating of the gas maintaining the dust at lower temperatures.

ACKNOWLEDGMENTS

We acknowledge support from the ISO Spectrometer Data Centre at MPE Garching, funded by DARA under grant 50 QI 9402 3. JM-P,NJR-F, PdV and A.F have been partially supported by the CYCIT and the PNIE under grants PB96-104 and ESP97-1490-E. NJR-F acknowledges a grant from Conserjería de Educación y Cultura de la Comunidad de Madrid.

REFERENCES

Draine B.T. 1989, in Proc. 22nd ESLAB Symp. on IR Spectroscopy in Astronomy, ed. B.H.Kaldeich, ESA SP-290,93

Fuente, A., Martín-Pintado, J., Bachiller, R., & Cernicharo, J. 1990, A&A, 237, 471

Güsten, R. 1989, in IAU Symposium 136, The Galactic Center of the Galaxy, ed. M. Morris, Kluwer Academic Publisher, p. 89

Hasegawa, T., Oka, T., Sato, F., Tsuboi, M., & Miyasaky, A. 1998, in 3rd Cologne-Zermatt Symposium, The Physics and Chemistry of the Interstellar Medium, de. V. Ossenkopf, Shaker Verlag, in press

Hollenbach, D., & McKee, C.F. 1989, ApJ. 342, 306

Hollenbach, D., & Tielens, A.G.M. 1997, ARA&A. 35, 179

Hüttemeister, S., Dahmen, G., Mauersberger, R., Henkel, C., Wilson, T. L., & Martín-Pintado, J. 1998, A&A, 334,

Hüttemeister, S., Wilson, T. L., Bania, T. M., & Martín-Pintado, J. 1993, A&A, 280, 255

Martín-Pintado, J., de Vicente, P., Fuente, A., & Planesas, P. 1997, ApJ, 482, L45

Martín-Pintado, J., Gaume, R., Rodríguez-Fernández, N.J., de Vicente, P., & Wilson T.L. 1999, ApJ, in press

Sellmaier, F.H., Yamamoto, T., Pauldrach, A.W.A., & Rubin, R.H. 1996, A&A, 305, L37

Wilson, T.L., Ruf, K., Walmsley, C.M., Martin, R.N., Pauls, T.A., & Batrla, W. 1982, A&A, 115, 185

ISOCAM OBSERVATIONS OF CIRRUS CLOUDS: CHAMAELEON RESULTS

M.-A. Miville Deschênes[1,2], F.Boulanger[1], A. Abergel[1], J.-P. Bernard[1], W.T. Reach[3] & C. Ryter[4]

[1]Institut d'Astrophysique Spatiale, Université Paris-Sud, Bât.121, 91405, Orsay, France
[2]Département de Physique, Université Laval, Sainte-Foy, Québec, G1K 7P4, Canada.
[3]IPAC, Caltech, Pasadena, USA
[4]DAPNIA/Service d'Astrophysique, CEA/Saclay, F-91191 Gif Sur Yvette Cedex, France

ABSTRACT

The cirrus cloud DC300-16 in Chamaeleon has been observed with ISOCAM in various bandpass filters and with the circular variable filter (CVF). Emission features characteristic of PAHs clearly appear in the average CVF spectrum. Furthermore there is a good spectral match between this spectrum and spectra taken in stronger radiation field environment, confirming the single photon excitation mechanism hypothesis. Imaging across the halo of the cloud with various filters reveals large scale color variations that could be explained by a decrease of C-H transitions (with respect to C-C transitions) inside the cloud. Small scale ($\sim$ 30 arc seconds) color variations are also observed, revealing regions where the emission properties are changing on small distance scale. These small scale color variations are significantly different from what is observed in brighter objects.

Key words: interstellar medium; infrared cirrus; PAH.

1. INTRODUCTION

An important goal of spectroscopic observations of the mid-IR emission from interstellar clouds was to verify that the 12 μm diffuse emission measured by IRAS was associated with the well known set of dust emission features at 3.3, 6.2, 7.7, 8.6, and 11.3 μm as originally proposed by Léger & Puget(1984), Allamandola et al.(1985) and Puget et al. (1985). These features are considered to be characteristic of C-C and C-H bonds in aromatic hydrocarbons (PAHs). ISO succeeded in detecting these emission bands in diffuse Galactic light (Mattila et al. 1996) and clouds heated by the Solar Neighborhood Interstellar Radiation Field (ISRF). Here we present observations of the Galactic cirrus cloud DC300-16 in Chamaeleon obtained with the ISO camera (ISOCAM). This cirrus has been targeted for its particularly bright halo in the 12 μm IRAS band. Part of the cloud has been mapped in various ISOCAM filters (LW2, LW3, LW4, LW6, LW7 and LW8) and a Circular Variable Filter (CVF) observation has been done in the brightest part of the cloud halo. The filter observations complement the spectroscopic observation in allowing to study the spatial variations of the spectrum.

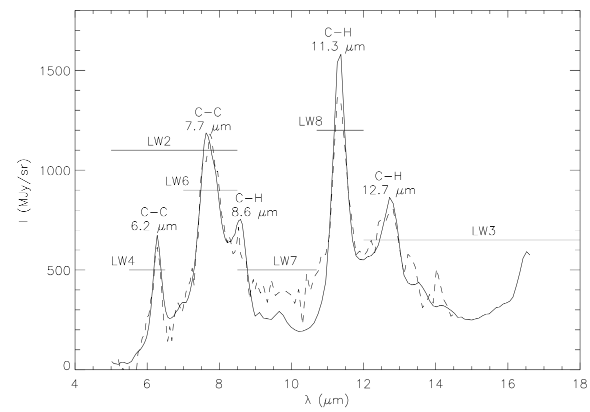

Figure 1. Comparison of the Chamaeleon and one NGC 7023 emission spectra. The Chamaeleon spectrum is the mean emission over the 3'x3' field of view of ISOCAM multiplied by 550. The NGC 7023 spectrum corresponds to the peak of the Northern PDR. The DC300-16 cloud has a molecular core with an overall opacity through its center of $A_V = 2$*; through the line of sight observed with ISOCAM the extinction is* $A_V = 1$.

2. MID INFRARED EMISSION SPECTRUM FROM CIRRUS CLOUDS

Two low resolution mid-infrared spectra taken with the CVF of ISOCAM are presented in Figure 1. Here the average spectrum of the Chamaeleon cirrus cloud is compared with one spectrum obtained with the same instrument in the reflection nebula NGC 7023 (Cesarsky et al. 1996). The PAH emission features appear clearly in the Chamaeleon spectrum. The

Proceedings of the Conference "The Universe as seen by ISO", Paris, France, 20–23 October 1998 (ESA SP-427, March 1999)

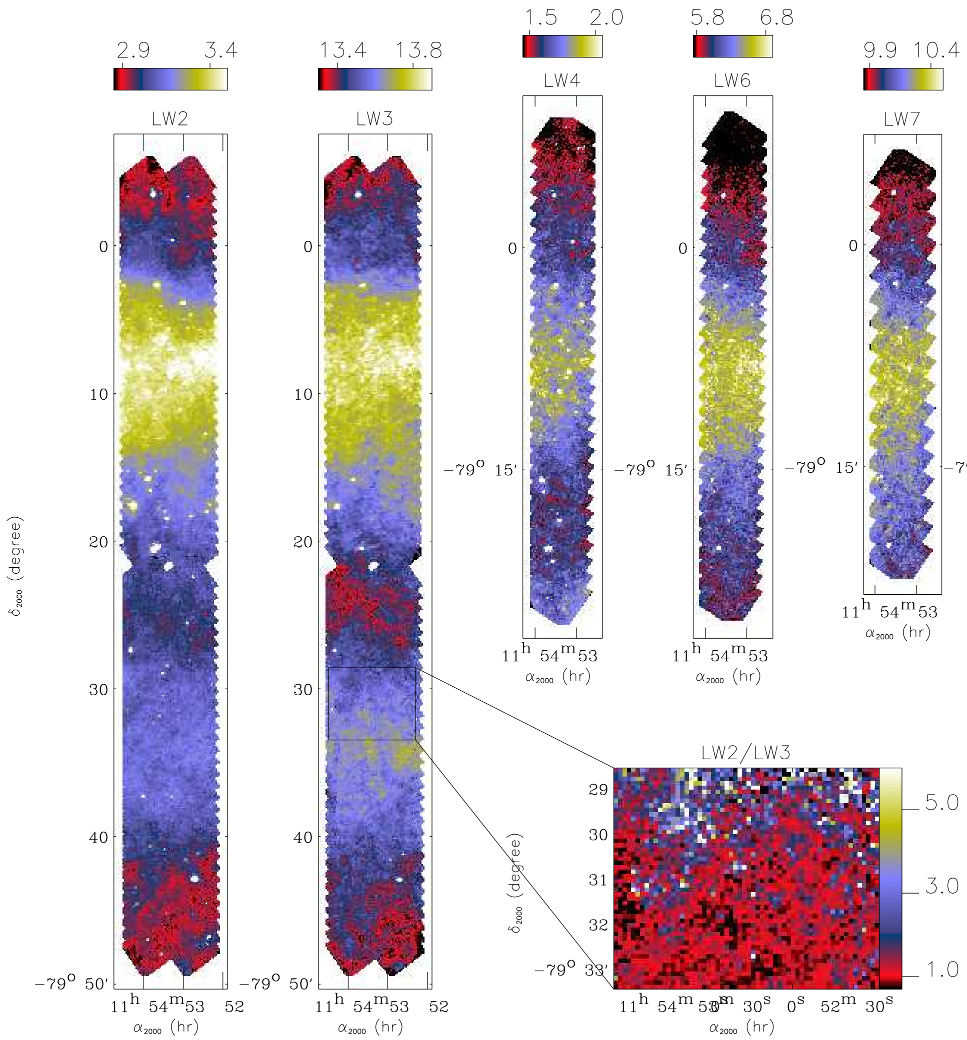

Figure 2. Maps (in MJy/sr) of the halo surrounding the Chamaeleon cloud in LW2, LW3, LW4, LW6, LW7 and LW8 filters (see Figure 1 for the wavelength correspondence of each filter). The extended emission of the halo is well detected in all filters. Many point sources are seen in the LW2 and LW4 maps. These maps have been used to build the average profiles across the halo shown in Figure 3. The LW2 over LW3 ratio of a sub-region of the southern halo is presented. Small scale LW2/LW3 variations are clearly apparent (particularly near α=11h54m, δ=-79° 30').

good spectral match between the two spectra, despite the three orders of magnitude difference in intensity, is a remarkable result confirming a strong prediction of the excitation of small particles by a single photon: the spectrum shape should be independent of radiation field intensity. Some of the dust features highlighted by the ISOCAM spectrum have also been detected in a cirrus cloud with narrow band filters using ISOPHOT (Lemke et al. 1998). The spectroscopic demonstration by ISO that the 12μm emission observed by IRAS in the diffuse interstellar matter is associated with the PAH emission features confirms the ubiquitous existence of small aromatic hydrogenated particles.

3. ABUNDANCE AND NATURE OF INTERSTELLAR PAHS

Current estimates of the abundance of carbon in small aromatic hydrocarbons are derived from the mean Solar Neighborhood 12 μm emission per hydrogen derived from the IRAS data (Boulanger & Pérault 1988). The ISO spectra validate the bolometric correction, used at that time, to estimate the emission in the 2 to 15 μm wavelength range from the 12 μm IRAS flux. Based on the ISOCAM spectra and the L band (3-4 μm) measurements of DIRBE (Bernard et al. 1994, Arendt et al. 1998), we find that $\mathrm{I}(2\text{-}15\,\mu\mathrm{m}) = 1.5 \times \nu \mathrm{I}_\nu(12\mu\mathrm{m}) = 1.6\,10^{-31}\,\mathrm{W/(H-atom)}$, very close to the value of $1.5\,10^{-31}\,\mathrm{W/(H-atom)}$ in Boulanger & Pérault (1988). The emission measured by DIRBE in the 3-4 μm wavelength range accounts for only 5 per cent

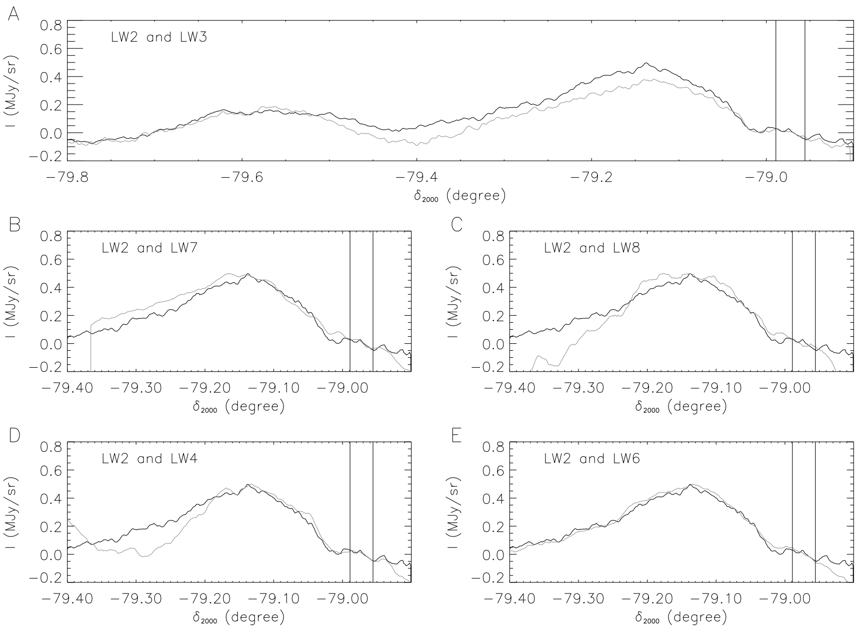

Figure 3. North-south average profiles in various filters (gray line) compared to the LW2 average profile (black line). The brightness of each profile have been set to zero at the edge of the cloud (between the two vertical lines). (A) Cut across the whole cloud in LW2 and LW3. (B-E) Cuts across the northern part of the cloud in LW7, LW8, LW4 and LW6. A multiplicative factor has been applied to each profiles to compare them to the LW2 cut.

of this integrated emission. From laboratory data, Joblin et al. (1992) computed the mean specific absorption of PAHs to be $2.3\,10^{-27}$ W/(C atom) for the Solar Neighborhood ISRF. Combining these numbers, we get an abundance of carbon in small aromatic hydrocarbons of $7.0\,10^{-5}$, or 19 per cent of the Solar abundance of carbon.

After absorption of a photon, a small particle is heated to a high temperature and emits most of its energy near that peak temperature. There is thus a rough correspondence between particle size and emission wavelength (Puget & Léger 1989). Most of the emission in the 5–16 μm range comes from particles of a few hundred atoms. For the 11.3 and $12.7\mu m$ features, particles with up to 1000 carbon atoms contribute. Such large particles might be 3 D aromatic hydrocarbon clusters rather than very large planar molecules. Molecules with less than 100 carbon atoms are necessary to account for the $3.3\mu m$ feature but they represent a minor fraction of the carbon in aromatic hydrocarbon particles. From the energy emitted in the 3-$4\mu m$ range, we estimate that the abundance of carbon in these molecules is only 1 per cent (5 per cent of the total abundance of carbon in aromatic hydrocarbons with less than 1000 C atoms). The interstellar aromatic hydrocarbons are thus on average larger than the molecules studied in the laboratory (e.g. Moutou et al. 1996) and modelled by quantum mechanics calculations (e.g. Pauzat et al. 1995). This difference may explain why none of the published laboratory spectra provide a good match to the interstellar spectra. Experiments on very large molecules and small carbon clusters are clearly needed to clarify the nature of the interstellar particles.

4. ISOCAM IMAGES OF CIRRUS CLOUDS

In addition to spectroscopy, imaging of clouds with ISOCAM and PHOT provides important information to understand the evolution of dust within interstellar clouds with respect to gas density, radiation field and velocity field (e.g., Abergel et al. 1996, Laureijs et al. 1996). Also, one can hope that some aspects of the evolution of dust can be sufficiently understood in order to use the spectral energy distribution of the dust emission as a diagnostic of physical conditions within interstellar clouds.

Mapping large regions in nearby clouds with various filters with ISOCAM allows to look for color variations at small scales and at brightness levels too low for CVF observations. Figure 2 shows such maps obtained across the halo surrounding cloud DC300-16 in Chamaeleon, where the PAH abundance is known from IRAS observations to be significantly larger than the solar neighborhood average (IRAS 12μm/100μm color 2.2 times higher than the solar neighborhood (Bernard et al. 1993)). The data processing done to obtain such low contrast ($\sim 3\%$) ISOCAM images of extended emission is detailed in Miville-Deschênes et al. (1999).

Average brightness profiles (mean brightness for each δ_{2000}) across the halo are shown in Figure 3. The brightness have been set to zero at the edge of the cloud. This figure shows that the colors in the outskirts of the halo are rather constant, but start to change toward inner regions of the clouds. The LW3 over LW2 ratio equals unity in the outer parts of the halo but seems to decrease at the center of the cloud. Figures 3 B-E show the average brightness profiles across the northern halo in the LW4, LW6, LW7 and LW8 filters, compared to the LW2 profiles. A multiplicative factor has been applied to each profiles, to compare them directly to the LW2 emission. Like in LW3, the LW8 profile drops at the center of the cloud. On the other hand the LW7 profile has an excess inside the cloud relative to the LW2 profile. The LW6 profile follows nicely LW2, confirming the important contribution of the C-C 7.7 μm PAH feature in the LW2 filter (see Figure 1). Finally, the LW4 profile has a not easily understandable shape. Roughly speaking, the variations observed are consistent with a decrease of the 11.3 and 12.7 μm feature emission (attributed to C-H transitions) with respect to the 7.7 μm feature in denser and radiation protected regions of the cloud. This is unlike what is observed in PDRs (e.g. NGC7023) where the ratio between the 11.3μm and 12.7 μm features on one hand and the 6.2μm, 7.7 μm and 8.6 μm features on the other hand increases towards the dense shielded molecular cloud behind the photodissociation region.

Beside systematic variations across the clouds, the broad band filters maps highlight small scale structures. Figure 3 shows the LW2 over LW3 ratio for a region in the southern halo. Significant sub-arc minute structures are observed in this map where LW2/LW3 is unusually high (>3) (particularly near α=11h54m, δ=-79°30'). In NGC 7023 this ratio ranges from 0.75 to 1.5. As these structures do not appear spherical, they could not be associated with embedded sources. These small scale color variations reveal regions where the emission properties may change on small distance scale.

REFERENCES

Abergel, A., Bernard, J. P., Boulanger, F., et al. 1996, A&A, 315, L329.

Allamandola, L. J., Tielens, A. G. G. M. & Barker, J. R. 1985, ApJ, 290, L25.

Arendt, R. G., Odegard, N., Weiland, J. L., et al. 1998, ApJ, 508, 74.

Bernard, J. P., Boulanger, F. & Puget, J. L. 1993, A&A, 277, 609.

Bernard, J. P., Boulanger, F., Desert, F. X., Giard, M., Helou, G. & Puget, J. L. 1994, A&A, 291, L5.

Boulanger, F. & Pérault, M. 1988, ApJ, 330, 964.

Cesarsky, D., Lequeux, J., Abergel, A., Perault, M., Palazzi, E., Madden, S. & Tran, D. 1996, A&A, 315, L305.

Joblin, C., Léger, A. & Martin, P. 1992, ApJ, 393, L79.

Laureijs, R. J., Haikala, L., Burgdorf, M., Clark, F. O., Liljestroem, T., Mattila, K. & Prusti, T. 1996, A&A, 315, L317.

Léger, A. & Puget, J. L. 1984, A&A, 137, L5.

Lemke, D., Mattila, K., Lehtinen, K., Laureijs, R. J., Liljestrom, T., Léger, A. & Herbstmeier, U. 1998, A&A, 331, L742.

Mattila, K., Lemke, D., Haikala, L. K., Laureijs, R. J., Léger, A., Lehtinen, K., Leinert, C. & Mezger, P. G. 1996, A&A, 315, L353.

Miville-Deschênes, M. A., Boulanger, F., Abergel, A. & Bernard, J. P. to be published, 1999.

Moutou, C., Léger, A. & D'Hendecourt, L. 1996, A&A, 310, 297.

Pauzat, F., Talbi, D. & Ellinger, Y. 1995, A&A, 293, 263.

Puget, J. L. & Léger, A. 1989, ARAA, 27, 161.

Puget, J. L., Léger, A. & Boulanger, F. 1985, A&A, 142, L19.

DETECTION OF EXTENDED LOW-DENSITY IONIZED GAS AROUND THE CARINA NEBULA

M. Mizutani[1], T. Onaka[1], & H. Shibai[2]

[1]Department of Astronomy, School of Science, University of Tokyo, Tokyo 113-0033, Japan
[2]Department of Physics, School of Science, Nagoya University, Nagoya 464-8602, Japan

ABSTRACT

We have made mapping observations of far-infrared spectroscopy of the Carina nebula, a very active region on the Galactic plane, with a spatial separation of 3 arcmin. The observations were made for the central 20 arcmin $\times$ 40 arcmin region of the Carina nebula with LWS01 (45 - 170 μm full grating scan mode). Several emission lines, such as [OI] 63, 145 μm, [OIII] 52, 88 μm, [NIII] 57 μm, [NII] 122 μm and [CII] 158 μm, have been detected at most observed positions. The electron density was derived from the [OIII] lines, and two distinct components can be seen in the electron density map. One is a component with a density of 100 - 150 cm^{-3}, which encloses two HII regions, Car I and Car II. The other is an extended diffuse component with a density of 30 - 60 cm^{-3}. The extension of the ionized gas in the line of sight direction has been estimated from the line intensity. It is about 10 pc for the central ionized region, suggesting the presence of spherical ionized gas centered at $l \sim 287°.55$ and $b \sim -0°.63$, while the extension is derived to be 1 - 2 kpc for the extended gas. The latter indicates that the diffuse ionized gas exists extensively around the Carina arm. The present LWS observations of the ionic lines indicate the presence of very low electron density gas ($n_e < 100\,\mathrm{cm}^{-3}$) extended over the Galactic plane in a scale of kpc unambiguously for the first time.

Key words: HII region; ELD ionized gas; Carina nebula.

1. INTRODUCTION

The Carina nebula is one of the most active regions on the Galactic plane and it covers an area of about 4 degree $\times$ 4 degree in visual wavelengths. The brightest region of the nebula has a triangular shape with two bright HII regions, known as Car I and II, which coincide with the radio emission peaks (Gardner et al. 1970). This region has several star clusters consisting of early-type stars and Wolf-Rayet stars. The most influential clusters are two OB star clusters, Trumpler (Tr) 14 and 16. These clusters contain numerous O-type stars. Tr 14 is a compact star cluster situated adjacent to the western dust lane and Tr 16 is an open cluster centered at vertex of the dust lane. An IR bright star η Car is also a member of Tr 16. It is generally believed that Tr 14 and Tr 16 are major heating sources in this region. According to a picture commonly accepted, Car I is excited by the open cluster Tr 14 and Car II by Tr 16.

The Carina nebula has been observed in various wavelengths and the spatial structure and kinematics of the nebular cloud have been studied. Molecular gas is concentrated in the dark lanes which cause optical obscuration (Gardner et al. 1970; de Graauw et al. 1981). Far-infrared emission associated with the dust lanes has also been observed (Harvey 1979; Ghosh et al. 1988). The velocity structure is explained by a model of molecular gas surrounding the ionized gas and expanding at about 7 km s^{-1} from a point 15 arcmin southwest of η Car (Dickel 1974). Optical observations show strong line splitting near Car II, suggesting that the ionized gas is expanding at 25 km s^{-1} (Deharveng & Maucherat 1975). The Carina complex is one of the most fascinating and puzzling objects in the Galaxy and it is suitable for the study of the physical conditions of diffuse interstellar medium associated with OB clusters.

In a guaranteed time observation, we have made mapping observations with the Long Wavelength Spectrometer (LWS) (Clegg et al. 1996) in order to investigate the nature of diffuse interstellar medium (ISM) of this region. Several fine structure lines have been detected. Here we report the results of two [OIII] lines (52, 88 μm) and one [NIII] (57 μm) line, and discuss the nebula properties derived from the analysis of these lines.

2. OBSERVATIONS

The observed region is a central rectangular area of the Carina region of $l = 287°.0 - 287°.65$ and $b = -0°.78 - -0°.23$. In the eastern part of the observed region ($l > 287°.3$), an HII region is located in front of molecular clouds, while in the western part the nebula is behind the molecular clouds. CO ($J = 2-1$) line observations show the spatial structure of an extended molecular cloud wrapped partly around bright HII regions (de Graauw et al. 1981).

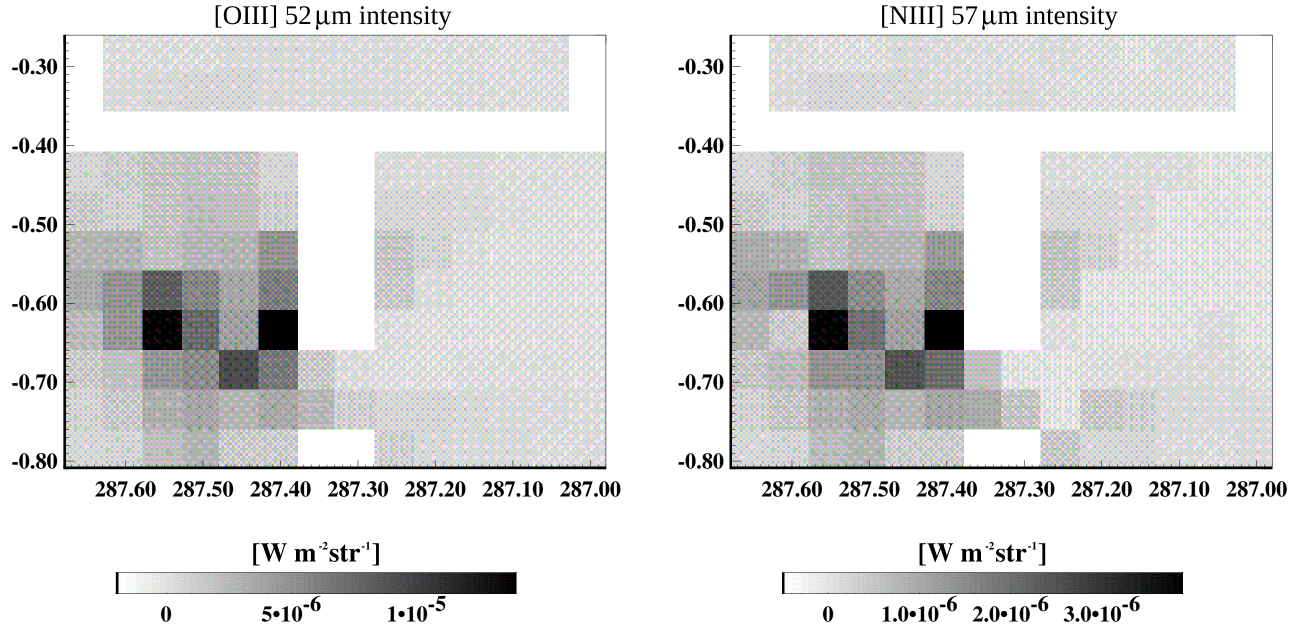

Figure 1. Line intensity maps of [O III] 52 μm (left) and [N III] 57 μm (right) plotted in the Galactic coordinates.

The distance to the Carina nebula is estimated as about 2.7 kpc (Grabelsky et al. 1988).

The observations were made with LWS on board ISO, in the full grating scan mode (LWS01: 45 - 170 μm). The spectral resolution is approximately 200 and the beam size is 80 arcsec (Burgdorf et al. 1997). To investigate the physical conditions of diffuse ISM, we have made mapping observations in a raster mode with 3 arcmin grid separation. In total observations were made at 132 positions. The exposure time for each grating position was 0.5 sec.

We have used the pipeline OLP.631 version products for most of the observed positions and partially used OLP.622 products. The spectra were defringed and fitted together by our own software, which was developed from the ISO Spectral Analysis Package (ISAP[1]) subroutines. The absolute level of the detectors was scaled to fit together. The detector signal for [OIII] 88 μm line was scaled by a factor of 1.2 at most relative to those for [OIII] 52 μm and [NIII] 57 μm in this procedure. In the reduction of the LWS spectrum, we adopted level scaling rather than level shifting because the uncertainty in the detector dark current is considered to be much less than the signals from the objects in the Carina nebula.

3. RESULTS

Several fine-structure lines, such as [OI] 63, 145 μm, [OIII] 52, 88 μm, [NIII] 57 μm, [NII] 122 μm, and [CII] 158 μm, have been detected in the observed spectra.

[1]The ISO Spectral Analysis Package (ISAP) is a joint development by the LWS and SWS Instrument Teams and Data Centers. Contributing institutes are CESR, IAS, IPAC, MPE, RAL and SRON.

We discuss here the [OIII] and [NIII] intensity distributions and electron densities derived from the analysis of these lines. The spectra were averaged over 5 scans. The baseline was assumed to be linear and the line intensities were derived from Gaussian fit of the line profile by the least-squares method.

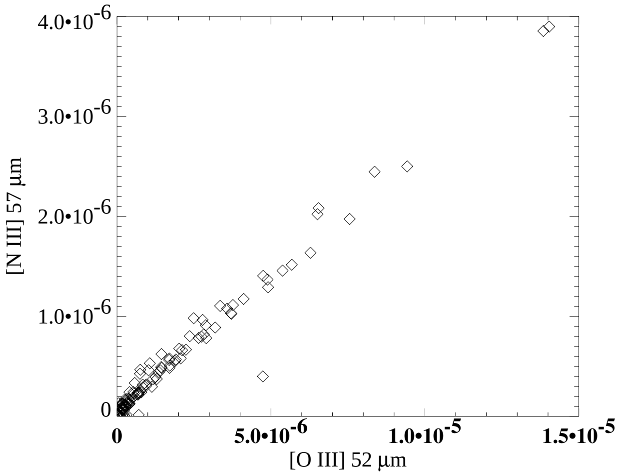

Figure 2. The correlation of the [O III] 52 and [N III] 57 μm line intensities.

Figure 1 shows the [OIII] 52 μm and [NIII] 57 μm intensity maps of the observed region. [OIII] 52 and 88 μm lines were detected in all of the observed points. They peak at the centers of Car I and II. A bright IR star η Car is located in the grid next left (east) of the Car II peak. Car I is believed to be excited by Tr 14 OB stars and there is an ionization front near the border between the HII region and molecular cloud. The Car I peak is located on the border. [NIII] 57 μm emission shows a very similar distribution to that of [OIII] lines. These ions are considered to have the same spatial extent with each other because of similar ionization potentials.

Figure 2 plots the [NIII] 57 μm intensity against the [OIII] 52 μm intensity. It is clearly seen that both intensities are proportional to each other fairly well for all the observed position. The linear slope gives the intensity ratio of [NIII] 57 μm to [OIII] 52 μm of approximately 0.28. A point largely deviated from the linear correlation is the data at the position closest to η Car.

The spatial distribution of [OIII] and [NIII] ionic lines indicates that there is an ionized region enclosing Car I and Car II. However, these lines have also been detected clearly outside the HII regions. They are observed even in the dust lane in the right hand side of the observed region which shows strong absorption in visual wavelengths, indicating the presence of extended ionized gas around the Carina nebula.

The electron density of the ionized gas where these ions are present can be derived from the ratio of the two [OIII] lines (Moorwood et al. 1980). The ratio does not sensitively depend on the gas temperature and we calculated the electron density assuming the gas temperature of 7500 K. No appreciable difference was obtained in the derived electron densities for $T_e = 5,000$K - $20,000$K. Figure 3 indicates the line ratio map and the derived electron density is shown in Figure 4.

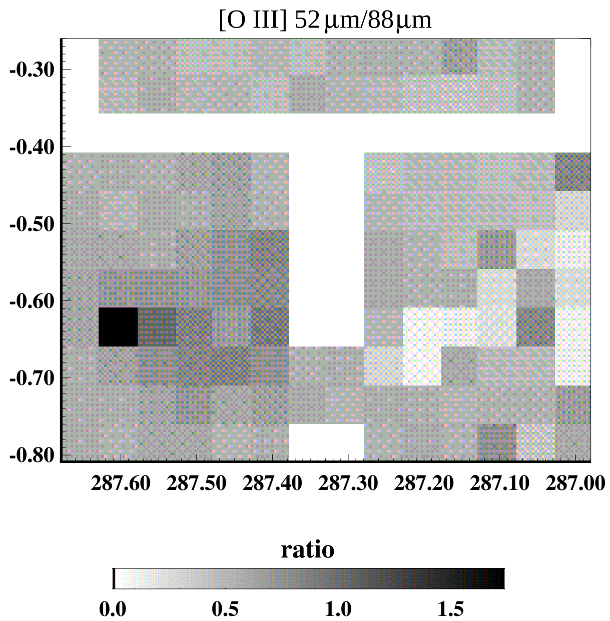

Figure 3. The intensity ratio of the [O III] 52 and 88 μm lines.

4. DISCUSSION

Two distinct components can be seen in Figure 4. One is the ionized gas enclosing Car I and Car II (we call this component "core ionized region"). The electron density derived for this component is 100 -150 cm^{-3} except the position closest to η Car. Previous

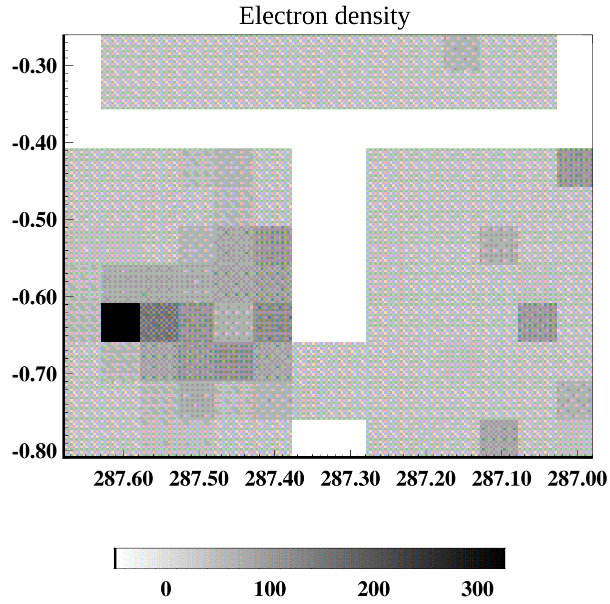

Figure 4. The electron density derived from the ratio of [O III] 52 μm/88 μm intensity.

far-infrared observations have shown that several HII regions, such as M17, W51 and NGC 7538, have electron densities of the order of 10^2 - 10^4 cm^{-3} (Watson et al. 1981; Moorwood et al. 1980). The electron density of the core ionized region is in the the lower end of the range, suggesting that the Carina nebula is an evolved diffuse HII region.

Using the derived electron density, we have calculated the extension of the ionized gas along the line of sight. The extension is required to be about 10 pc for the central ionized core. This value is about the same as the spatial distance between the positions of η Car and the center of Car I. Thus the core ionized region has a spherical structure, which is associated with Car I and II.

The other component is an extended low-density ionized gas all over the observed area. The electron density of this component is shown to be typically about 30 cm^{-3} (Figure 4). Even taking account of the uncertainty due to the level adjusting procedure, the value never exceeds 60 cm^{-3} since the intensity ratio is not very sensitive to the electron density in this range. The CO observations (de Graauw et al. 1981) indicate that the extinction is not significant in the far-infrared at all the observed positions except for a few points, where only [OIII] 52 μm line could be affected. In fact a few positions in the molecular cloud direction show intensity ratios less than the theoretical limit, 0.57. However, in other positions no serious extinction is expected and thus the low electron density of the extended component is a rather secure conclusion. The extension along the line of sight is estimated as about 1 - 2 kpc for the extended ionized gas. This is compatible with the geometrical distance of the observed region on the Carina arm ($\sim$ 2 kpc). Since this component is seen in all the observed area, it is suggested that there is very low density ionized gas extended over the Galactic plane.

The [NIII] 57 μm emission is also seen in the extended ionized gas. A simple calculation shows that the ratio of [NIII] 57 μm to [OIII] 52 μm is almost constant as long as the electron density is less than 200 cm^{-3}. Since the derived electron density is always less than 150 cm^{-3} except for the position closest to η Car, the line ratio should directly indicate the abundance ratio of N^{2+}/O^{2+}. This ratio is comparable to N/O for high-excitation sources, but is an upper limit to N/O for low-excitation sources (Simpson et al. 1995). A good correlation between [NIII] 57 μm and [OIII] 52 μm in all the observed positions indicates that N^{2+}/O^{2+} is approximately 0.2 both in the core ionized gas and the extended ionized gas. This value is in agreement with those obtained in compact HII regions at the galactocentric distance of 8 kpc (Roelfsema et al. 1998). The extended component is suggested to have a similar N^{2+}/O^{2+} abundance ratio to those in compact HII regions at a similar galactocentric distance.

The presence of low-density HII region on the Galactic plane has been predicted in previous works. The extended low density (ELD) HII region was first investigated in detail by Mezger (1978) to account for the extended radio continuum emission from the Galactic plane. He suggested that the ELD HII regions are created by overlapping of evolved and expanded photoionized regions surrounding early-type stars. He estimated the electron density as about 3 cm^{-3}. About 80 per cent of the total OB stars on the Galactic plane are needed to account for the exciting source of the ELD HII regions.

Shibai et al. (1991) have detected diffuse [CII] 158 μm emission on the Galactic plane by Balloon-Borne Infrared Telescope. They suggested the ELD HII region as one of the candidates for the source of the diffuse emission, while Heiles (1994) indicated that the ELD HII region is the most likely candidate of the source of the diffuse [CII] emission.

While the presence of the ELD regions has been suggested, physical conditions of the region have not yet clearly been understood. The present study shows the presence of low-density ionized gas directly by far-infrared spectroscopy and derived the electron density unambiguously for the first time. It clearly demonstrates the importance of far-infrared observations from cooled telescopes for the study of diffuse ISM. Further investigations including other lines are warranted to elucidate the nature of diffuse ISM.

ACKNOWLEDGMENTS

We would like to thank the LWS IDT in Rutherford Appleton Laboratory, particularly S. Sidher, for the LWS data processing. We thank K. Kawara, Y. Satoh, H. Okuda, and the Japanese ISO team for their continuous help and encouragement. This work is supported in part by grant-in-aids for Overseas Scientific Research from the Ministry of Education, Science, Sports, and Culture in Japan.

REFERENCES

Clegg, P. E., Ade, P. A. R., Armand, C. et al. 1996, A&A, 315, L38

Burgdorf, M., Clegg, P., Ewart, D. et al. 1997, in First ISO Workshop on Analytical Spectroscopy (ESA SP-419), 51

de Graauw, T., Lidholm, S., Fitton, B. et al. 1981, A&A, 102, 257

Deharveng, L., Maucherat, M. 1975, A&A, 41, 27

Dickel, H. R. 1974, A&A, 31, 11

Gardner, F. F., Milne, D. K., Mezger, P. G. et al. 1970, A&A, 7, 349

Ghosh, S. K., Iyengar, K. V. K., Rengarajan, T. N. et al. 1988, ApJ, 330, 928

Grabelsky, D. A., Cohen, R. S., Bronfman, J. et al. 1988, ApJ, 331, 181

Harvey, P. M., Hoffman, W. F., Campbell, M. F., 1979, ApJ, 227, 114

Heiles, C. 1994, ApJ, 436, 720

Kessler, M. F., Steinz, J. A., Anderegg, M. E. et al. 1996, A&A, 315, L27

Mezger, P. G., 1978, A&A, 70, 565

Moorwood, A. F. M., Salinari, P., Furniss, I. et al. 1980, A&A, 90, 304

Roelfsema, P. R., Cox, P., Kessler, M. F. 1998, ASP Conf. Ser. 132, 76

Simpson, J.P., Colgan, S.W.J., Rubin, R.H., et al. ApJ, 444, 721

Shibai, H., Okuda, H., Nakagawa, T. et al. ApJ, 374, 522

Watson, D. M., Storey, J. W. V., Townes, C. H. et al. 1981, ApJ, 250, 605

SPECTROSCOPY OF THE PISTOL AND QUINTUPLET STARS IN THE GALACTIC CENTRE

A. Moneti[1,2], J.A.D.L. Blommaert[1], F. Najarro[3], D. Figer[4], & S. Stolovy[4]

[1]ISO Data Centre, Astrophysics Division, ESA, Villafranca, Spain.
[2]On contract from SERCo F.M. B.V.
[3]IEM, Consejo Superior de Investigaciones Cientificas, Madrid, Spain.
[4]University of California, Los Angeles, CA, USA.
[5]Steward Observatory, Tucson, AZ, USA.

ABSTRACT

We present initial results of a spectroscopic study of the Pistol and of the cocoon stars in the Quintuplet Cluster. From ISOCAM CVF 5—17 μm spectroscopy of the field of the Pistol Star, we have discovered a nearly spherical shell of hot dust surrounding this star, a probable LBV. This shell is most prominent at $\lambda \gtrsim 12\,\mu$m, and its morphology clearly indicates that the shell is stellar ejecta. Emission line images show that most of the ionised material is along the northern border of this shell, and its morphology is very similar to that of the Pistol HII region (Yusef-Zadeh & Morris, 1987). We thus confirm that the ionisation comes from very hot stars in the core of the Quintuplet Cluster. An SWS spectrum of the Pistol Nebula indicates a harder ionising radiation than could be provided by the Pistol Star, but which is consistent with ionisation from Wolf-Rayet stars in the Quintuplet Cluster. The CVF 5—17 μm spectra of the cocoon stars in the Quintuplet do not show any emission feature that could help elucidate their nature.

Key words: Galactic Centre, Quintuplet, Pistol, LBVs

1. INTRODUCTION

The Quintuplet Cluster is one of the few young clusters known in the vicinity of the Galactic Centre. It took its name from five very luminous, $\sim 10^5\,L_\odot$ sources with very cool, 600—1200 K, energy distributions (e.g. Moneti, Glass, and Moorwood 1994, MGM94), henceforth the *cocoon* stars, and it is now known to contain several dozen hot stars (Figer, McLean, & Morris 1999, FMM99, and references therein for a detailed background) including several Wolf-Rayet stars, several OB supergiants, and at least one and probably two luminous blue variables (LBV; Figer et al. 1998, and references therein). One of these is located about 20 arcsec south of the cluster core and is now known as the *Pistol* star because of its location at the center of curvature of the G0.15–0.05 HII region (Yusef-Zadeh & Morris 1987), known as the *Pistol* because of its shape, and itself located half way between the cluster core and the Pistol star. The Pistol HII region was also detected in Br-γ (MGM), and was imaged in [ArII] (Nagata et al. 1996) and in Pa-α (Figer et al. 1999), confirming its thermal origin (as opposed to the non-thermal origin of the radio filaments which appear to cross it, Yusef-Zadeh & Morris 1987).

Early studies of the Pistol star indicated it had extremely high luminosity ($2\times10^6 L_\odot$, Figer, McLean & Morris 1995, FMM95, and $10^7 L_\odot$ Cotera et al. 1996). There have also been suggestions that the Pistol Star could be photoionising the Pistol HII region (e.g. Cotera et al. 1996), while FMM95 suggested that the HII region is material ejected from the LBV which is photoionsed by the hot stars in the Quintuplet Cluster. By modelling its IR spectral energy distribution (SED) and its IR line profiles, Figer et al. (1998) constrained the Pistol Star's luminosity to two classes of models, one with $L_* \approx 4\times10^6\,L_\odot$ and $T_{\rm eff} \approx 14,000\,$K, and the second with $L_* \approx 15\times10^6\,L_\odot$ and $T_{\rm eff} \approx 21,000\,$K. What remained unclear was why the ejecta was only seen to the north of the star.

The nature of the cocoon stars remains mysterious. Okuda et al. (1990) and MGM94 suggested they might be star-forming cocoons similar to BN or AFGL2591. FMM99 favour extremely dusty WC stars, but also suggests that they could form a new class of objects. Glass et al. (1999) report slight variability of two of the five cocoon stars at $2.2\,\mu$m, possibly inclining the balance toward the evolved nature of these stars. To date, no emission feature has been detected toward these stars that could help elucidate their nature, and the only absorption features are due to silicates and ices (Nagata et al. 1996), all of which are believed to be of interstellar origin.

Proceedings of the Conference "The Universe as seen by ISO", Paris, France, 20–23 October 1998 (ESA SP-427, March 1999)

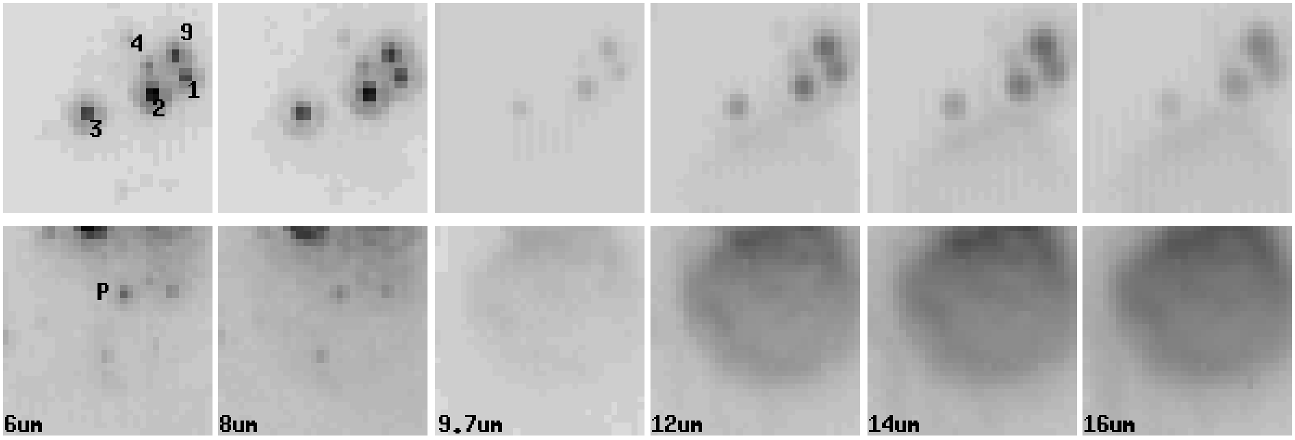

Figure 1. Continuum images of the Quintuplet Cluster (top) and of the Pistol Nebula (bottom). North is up, and east is to the left. The vertical stripes in the Quintuplet images are due to incomplete dark subtraction at the 0.28 sec on-chip integration time. Wavelengths corresponding to each frame are marked, and the Quintuplet and Pistol stars are identified.

2. OBSERVATIONS AND RESULTS

We have obtained ISOCAM-CVF scans of the Pistol and of the Quintuplet fields, covering the 5.0—17.1 μm spectral range. All scans were obtained with a pixel FOV of 1.5 arcsec, and the integration time was ~ 30 sec per CVF position, using the 2.1 and the 0.28 sec on-chip integration time on the Pistol and on the Quintuplet, respectively. Data reduction was performed with the CAM Interactive Analysis (CIA) package[1], and followed the standard steps of (i) dark subtraction, (ii) removal of cosmic ray events, (iii) averaging all valid images obtained at a given CVF position, (iv) flatfielding the results using library flats, (v) converting the average signal to physical units using standard conversion factors, originally derived from several standard stars. No transient correction was applied to the data presented here; given the brightness of the sources, the transient correction is very minor, below a few percent, and for the discussion presented here these deviations are not important.

Figure 1 shows a composite of continuum images of the Quintuplet and of the Pistol. They are scaled so that the intensities are proportional to the observed energy density, $\lambda F(\lambda)$, with the scaling for the Pistol being $5\times$ stronger than for the brighter Quintuplet Stars. Both datasets clearly reveal the deep 9.7 μm silicate absorption feature. The images of the Quintuplet Cluster are dominated by the cocoon stars, whose identification, following MGM94, is shown. Since images are diffraction limited, the FWHM of the images can be seen to increase with wavelength, and the first Airy ring can also be recognised. Also, the brightest stars at short wavelengths are no longer so at long wavelengths, showing their different colour temperatures. The Pistol Star is the point source located just above centre in the Pistol field, marked with a “P”. It is most clearly visible at short wavelengths, where other stars are also detected. The peak at the top edge of the frame corresponds to star no. 3 in the Quintuplet. Beyond the silicate feature the Pistol Star is lost in a nearly spherical centered on the Pistol star itself. The diameter of this Pistol Nebula is ~ 1.5 pc.

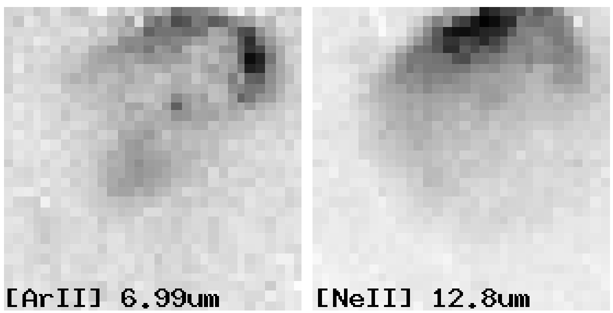

Figure 2. Line images of the Pistol Nebula.

Raw spectra extracted from the Pistol data cube show PAH emission at 6.2, 7.7, and 8.6 and 11.3 μm, and the fine structure lines of [ArII] 7.0 μm, [NeII] 12.8 μm, and [NeIII] 15.4 μm. Line images reveal that the PAH emission is uniform over the field, thus indicating that it is interstellar rather than local to the nebula, while the forbidden line emission is not. The spatial distribution of [ArII] and [NeII] is shown in Figure 2. The morphologies are similar, thought not identical, and they are also similar to the Pistol HII region (Yusef-Zadeh and Morris, 1987, see also Figer et al. 1998). Energy distributions of the northern, central, and southern parts of the Pistol Nebula are shown in Figure 3, together with the energy distributions of four of the cocoon stars. Photometry of these stars was obtained by measuring the flux within a 3 arcsec aperture and correcting for the aperture size using measurements of single stars. The Pistol Nebula spectra were extracted using 7×17 pixel synthetic aperture, and were normalised by the number of pixels. The background was determined from the southernmost region of the field, and subtracted. It

[1] CIA is a joint development by the ESA Astrophysics Division and the ISOCAM consortium. The ISOCAM consortium is led by the ISOCAM PI, C. Cesarsky, Direction des Sciences de la Matière, C.E.A., France

is clear from the energy distributions that the silicate absorption is much deeper in the cocoon stars than in the Pistol Nebula. Table 1 lists the measured optical depths, $\tau_{\rm sil}$, relative to a power-law continuum fitted through the spectral points at 8 and 13 μm. For comparison, from the Lutz et al. (1996) SWS spectrum of the Galactic Centre we derive $\tau_{\rm sil} = 2.0$. The difference in the depth of the feature in the Quintuplet Stars and in the Pistol is consistent with the results of Nagata et al. (1993).

Table 1. Silicate feature optical depths

Source	$\tau_{\rm sil}$
Q1	2.60
Q2	2.51
Q3	2.38
Q9	2.52
north	1.40
centre	1.32
south	1.08

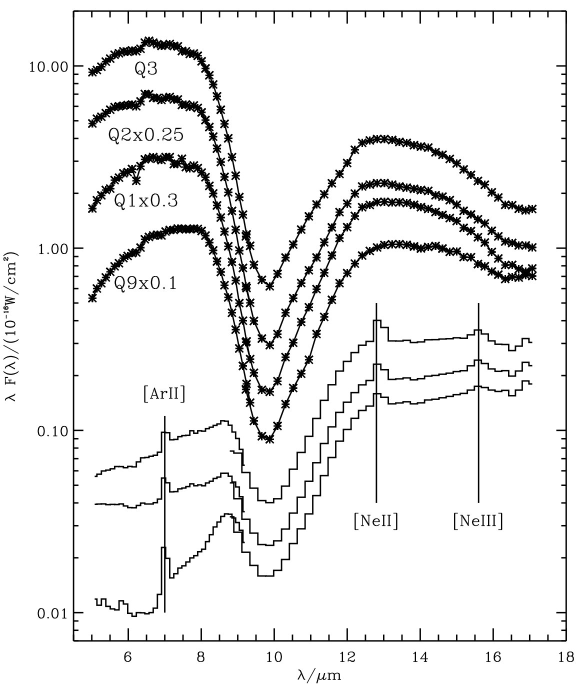

Figure 3. Spectral energy distributions of the northern, central, and southern part of the Pistol Nebula, shown with arbitrary normalisation, and of the cocoon stars.

An SWS spectrum covering the 2.3—47 μm range was obtained with the Pistol Star centered in the aperture. The AOT1-speed 4 mode was used, for a total integration time of $\sim$ 2 hrs. Pipeline-processed data was cleaned by removing data from noisy detectors, normalising each scan to the average of the complete dataset, and rebinning to a resolution of 1,000. This result was then defringed by finding and removing the strongest sinusoidal components. The final spectrum is shown in Figure 4; it shows a wealth of fine structure lines, many hydrogen recombination lines, and the standard absorption features of interstellar origin (silicates at 9.7 μm and 18 μm, water ice at 2.9 μm, hydrocarbons at 3.4 μm, and CO_2 ice at 4.3 μm) though the latter are not obvious in the representation given in Figure 4, which emphasises the emission lines. Preliminary analysis indicates that at $\lambda \lesssim 5\,\mu$m the continuum and the lines come primarily from the Pistol Star and its wind, while at longer wavelength they come primarily from the hot dust and the ionised gas in the HII region. A detailed analysis of the lines is in progress and will be presented in a future paper.

3. DISCUSSION

The discovery of a spherical nebula around the Pistol Star is the main result of this work presented at this workshop: our observations in the thermal IR have revealed the full shell of ejecta symmetrically distributed around the Pistol Star. Up until now, only the ionized part of the Pistol Nebula had been known, originally from radio continuum observations (Yusef-Zadeh and Morris, 1987), but subsequently also from near IR spectroscopy (see the Introduction). Many LBVs are known to be surrounded by shells of ejecta which is seen in reflection in the optical and near infrared (Nota et al. 1995) and via its thermal dust emission in the mid infrared (Trams et al. 1996, 1999). The size of the Pistol Nebula is comparable to that of other LBVs (Nota et al. 1995, Table 1), though unlike other LBVs, the nebular structure appears more as a full sphere than as a shell. Since the ejecta is not uniformly ionised, the ionisation probably does not come from the Pistol Star, which consequently must be relatively cool. This argues in favour of the cooler and lower luminosity class of models proposed by Figer et al. 1998. More likely, the ionisation come from other hot stars in the Quintuplet Cluster (FMM95, FMM99), of which there are several north of the ionised ridge. Other cluster stars (no. 76, 151, and 157 in FMM99) are located over the Pistol Nebula in projection, and two of these (no. 7 and 157) may be physically inside the nebula and could be responsible for the details of the structures seen in the ionised line images.

The relative strength of the high excitation lines in the SWS spectrum also indicates that the ionisation must come from stars stars much hotter than the Pistol Star. The ratios of [SIV]/[SIII], of [ArIII]/[ArII], and of [NeIII]/[NeII] in the Pistol spectrum are much stronger than in the Galactic Centre spectrum obtained by Lutz et al. (1996), from which these authors derive an average effective temperature of the ionising sources of 35,000 K. We deduce that at least some of the stars ionising the Pistol material must be hotter than 35,000 K, and the Wolf-Rayet stars in the Quintuplet Cluster are clearly indicated as the ionising stars.

The above scenario assumes that the Pistol Star and the cocoon stars are all members of the Quintuplet Cluster, though strictly speaking, this scenario involves only the Pistol Star and the hot stars in the cluster, and not the cocoon stars. In this context, the low silicate absorption optical depth of the the Pistol Nebula compared to the cocoon stars is puzzling. Either there is a steep gradient in extinction over the

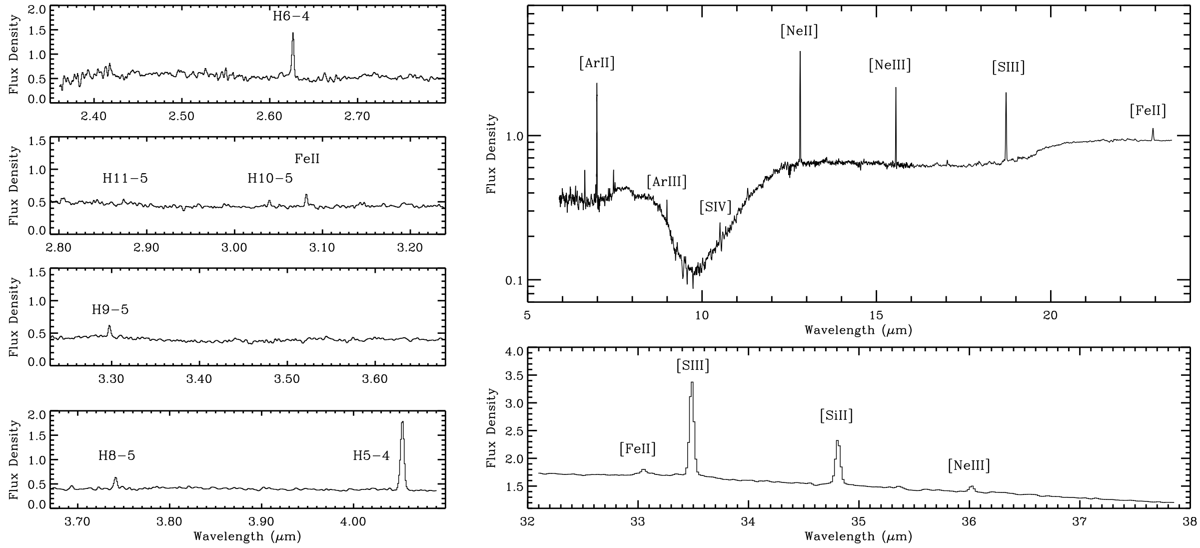

Figure 4. SWS spectrum of the Pistol Nebula. Different parts of the spectrum are plotted separately for clarity. The flux density is in units of $10^{-16}\,W\,cm^{-2}\,\mu m^{-1}$.

cluster, decreasing rapidly from north to south, or the extinction is spatially uniform, in which case the cocoon stars and the Pistol Star are at different distances along the line of sight. Alternatively, the silicate absorption of the cocoon stars is not entirely interstellar, but it is partly intrinsic. Figer et al. (1998) reviewed extinction estimates to the Quintuplet Cluster. They estimate $A_K = 3.28$ and adopt the Rieke, Rieke and Paul (1989) reddening law as the one that best characterises the reddening towards the hot stars in the Quintuplet. This gives $A_V = 29 \pm 2$ to the hot stars, and is an appropriate value for the Pistol Star, placing the whole group physically close to the Galactic Centre. Using $A_V = 29$, we obtain $A_V/\tau_{sil} = 20.5$ for the Pistol Nebula, a value comparable to that found by Roche and Aitken (1984) for nearby Wolf-Rayet stars and B supergiants. At the same time, the same A_V gives $A_V/\tau_{sil} = 11.6$ for the cocoon stars, a value more typical of sources in the Galactic Centre (Rieke and Lebofsky 1985). We do not offer a solution to this problem at this time.

In conclusion, we have solved one dilemma by discovering the full shell of ejecta around the Pistol Star, thus further confirming its LBV nature, but we have opened a new one by finding that τ_{sil} varies drastically between the Pistol Star/Nebula and the cocoon stars. These are only the first results from this data set; further analysis is in progress, and in an upcoming paper we will present a detailed analysis of the emission lines, which we will use to put constraints on the nature of the ionising radiation and of the extinction.

REFERENCES

Figer, D.F., McLean, I.S., Morris, M. 1995, ApJ, 447, L29

Figer, D.F., Najarro, F., Morris, M., Geballe, T.R., Ghez, A.M., & Langer, N. 1998, ApJ, 506, 384

Figer, D.F., McLean, I.S., Morris, M. 1999, ApJ, in press

Figer, D. F., Rich, R. M., Morris, M., McLean, I. S., Serabyn, E., Puetter, R., & Yahil, A. 1999, ApJ, in preparation

Glass, I.S., Moneti, & Moorwod, A.F.M. 1990, MNRAS, 242, 55p

Glass, I.S., Matsumoto, S., Carter, B.S., & Sekiguchi, K. 1999, MNRAS, in preparation

Lutz, D., Feuchtgruger, H., Genzel, R., et al. 1996, A&A, 315, L269.

Moneti, A., Glass, I.S., & Moorwood, A.F.M. 1994, MNRAS, 268, 194.

Nagata, T., Woodward, C.E., Shure, M.A., Pipher, J.L., & Okuda, H. 1990, ApJ, 351, 83

Nagata, T., Hyland, H.R., Straw, S.M., Sato, S., & Kawara, K. 1993, ApJ, 406, 501.

Nota, A. Livio, M., Clampin, M., Schulte-Ladbeck, R. 1995, ApJ, 448, 788

Nagata, T., Kawara, K., Onaka, T., Kitamura, Y., & Okuda, H. 1996, A&A, 315, L205

Okuda, H., et al. 1990, ApJ, 351, 89

Roche, P.F., & Aitken, D.K 1984, MNRAS, 208, 481

Trams, N.R., Waters, L.B.F.M., & Voors, R.H.M. 1996, A&A, 315, L213

Trams, N.R., van Tuyll, C.I., Voors, R.H.M, de Koter, A., Waters, L.B.F.M., & Morris, P.W. 1999, in IAU Coll. 169, in press

Rieke, G.H., Rieke, M.J, & Paul, A.E. 1989, ApJ, 336, 752

Yusef-Zadeh, F.V., & Morris, M. 1987, AJ, 94, 1178

THE RICH SPECTROSCOPY OF REFLECTION NEBULAE

C. Moutou[1], L. Verstraete[2], K. Sellgren[3], & A. Léger[2]

[1]Observatoire de Haute Provence, St Michel, France
[2]Institut d'Astrophysique Spatiale, Orsay, France
[3]Ohio State University, Columbus, USA

ABSTRACT

The ISO-SWS spectra of two bright reflection nebulae, NGC 7023 and NGC 2023, are presented. We discuss the emission of molecular hydrogen from these photodissociated interfaces. Details of the aromatic infrared band profiles as well as the continuum emission are also analysed. The ISO-LWS spectrum of NGC 7023 is also presented, at two positions in the nebula. The dust temperature at the brightest far-infrared position of NGC 7023 is estimated to be 45 K.

Key words: reflection nebula; dust emission bands; molecular hydrogen emission.

1. INTRODUCTION

ISO is providing us with high-resolution spectra of the Aromatic Infrared Bands between 3 and 13 μm (hereafter AIBs) in a wide variety of galactic environments. At the spectral resolution of ISOCAM-CVF ($\lambda/\Delta\lambda = 40$), the AIBs have been shown to be similar in interstellar regions with effective radiation fields ranging from 1 to 10^4 times the interstellar radiation field (Boulanger et al. 1998 and references therein). Using SWS data at higher spectral resolution, we show here that there are differences between the AIB spectra of two reflection nebulae, NGC 2023 and NGC 7023. The physical conditions of the gas, associated with the AIBs, are discussed through the analysis of the molecular hydrogen emission.

2. COMPARING THE SWS SPECTRA

2.1. Observations

The SWS spectrum of NGC 7023 was obtained with the AOT01 observing mode in 1996 and is fully described in Moutou et al. (1998) and Sellgren et al. (1999, in preparation). Its mean spectral resolution is $\lambda/\Delta\lambda = 1000$ (speed 4). A restricted part of this spectrum has been observed at higher spectral resolution (Moutou et al. 1999). The SWS spectrum of NGC 2023 was observed at a spectral resolution of $\lambda/\Delta\lambda = 500$ (AOT01, speed 3) in 1998. Data reduction has been done within the SWS-Interactive Analysis environment. Our observations have higher spectral resolution than previously published mid-IR spectra of NGC 7023 and NGC 2023 from the Kuiper Airborne Observatory (Sellgren et al. 1985) and of NGC 7023 with ISOPHOT-S and ISOCAM (Laureijs et al. 1996; Cesarsky et al. 1996).

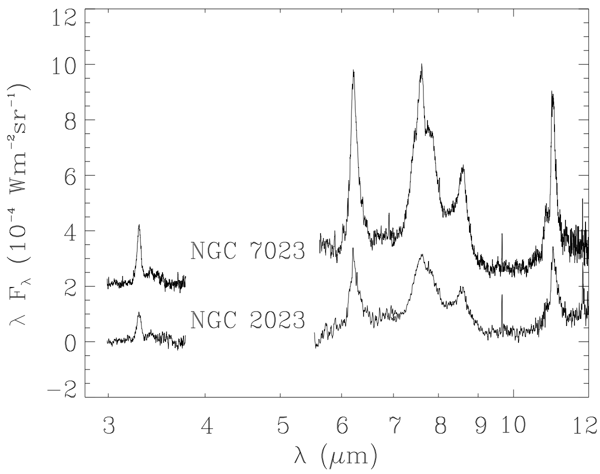

Figure 1. SWS01 spectra of the reflection nebulae NGC 7023 and NGC 2023. An offset of 2×10^{-4} W m^{-2} sr^{-1} is added to the spectrum of NGC 7023 (top) for clarity. The 3.5 to 5.3 μm region suffers of bad dark current measurements and is currently under processing.

NGC 7023 and NGC 2023 are two bright reflection nebulae irradiated by hot stars. The SWS aperture for NGC 7023 was centered 27″ W 34″ N (position 1) of HD 200775 (T_{eff}=17,000 K). For NGC 2023, the SWS aperture was 60″ S of HD 37903 (T_{eff}=22,000 K).

Figure 1 shows the mid-IR spectra of the two nebulae, with an offset added to NGC 7023 for clarity (see caption of Fig.1). The relative contribution of continuous emission and AIBs to the total emitted energy is comparable in both objects. More than 60% of the 3 – 20 μm energy is emitted in the AIBs. Reflection nebulae have a high feature-to-continuum ratio: this makes the study of faint details in the AIB profiles much easier than in more strongly irradiated sources where the AIBs are drowned by a strong mid-IR continuum (*e.g.*, planetary nebula, H II region interfaces).

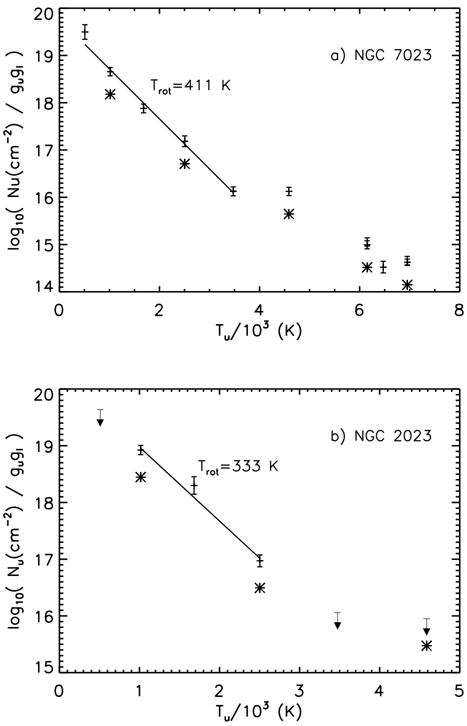

Figure 2. The excitation diagrams of H_2 in a) NGC 7023 and b) NGC 2023: N_u is the column density of the transition upper level, g_u is the degeneracy of the upper level, g_I the nuclear spin degeneracy and T_u is the upper level energy in Kelvin. The crosses with error bars indicate the values for R_{op}=1 (see text), while the asterisks show the case of R_{op}=3. The arrows show 3σ upper limits. The rotational temperatures have been estimated with R_{op}=1.

2.2. Molecular hydrogen emission

We detect many pure H_2 rotational lines in both nebulae as well as some ro-vibrational (or fluorescent) lines in NGC 7023. This emission comes from photodissociated gas lumped into filaments (Lemaire et al. 1996, Field et al. 1998). We derive excitation diagrams (Fig.2) from the line fluxes. In the case of NGC 7023, our upper level column densities (from the S(0) line at 28.22 μm through to the S(4) line at 8.02 μm) are well-fitted[1] by a single rotational temperature of 411 K if one adopts an ortho-to-para ratio (hereafter R_{op}) of 1. These results, although derived from observations with a much larger beamsize, are consistent with the findings of Lemaire et al. (1996). Indeed, the warm gas emission we detect is probably dominated by the filaments shown in the Lemaire et al. map. For NGC 2023, using the S(1) at 17.03 μm through to the S(3) at 9.66 μm lines, we find a rotational temperature of 333 K also with $R_{op} = 1$. While determining the rotational temperature, we have left aside higher levels ($T_u > 5000$ K) because their populations are strongly affected by the UV pumping (and subsequent radiative decay) of the H_2 molecule. Densities of about 10^5 cm^{-3} have been inferred for both nebulae (Lemaire et al. 1996; Field et al. 1998; Martini et al. 1997). At these high densities, the low rotational transitions (from upper levels with $T_u < 5000$ K) we are discussing here are collisionally thermalized and the rotational temperature is equal to the gas temperature, T_{gas}.

[1]We did not include the S(5) line at 6.91 μm in the fit because its profile is much broader than the other pure H_2 rotational lines suggesting contamination by another line.

Our low ortho-to-para ratio confirms earlier work (Chrysostomou et al. 1993 and references therein) on photodissociated interfaces. The H_2 molecule forms on the surface of dust grains and is expected to be rejected in the gas with a high vibration-rotation energy content and a R_{op} value close to 3. After formation, R_{op} can be changed by gas-phase spin exchange reactions of H_2 with atomic hydrogen and protons for $T_{gas} > 300$ K or by H_2-grain collisions for $T_{gas} < 300$ K. A value of $R_{op} = 1$ corresponds to an equilibrium temperature $T_{eq} \approx 80$ K (Burton et al. 1992). The fact that the dust temperature (≈ 40 K, see Sect. 3) and the gas temperature (300 - 400 K) are both very different from T_{eq} points at the importance of out-of-equilibrium effects; this point is also highlighted by the high R_{op} values (between 2 and 3) predicted by recent stationary models (Draine & Bertoldi 1996). We note that H_2 rotational populations in equilibrium at 40 K and 300 - 400 K correspond to $R_{op} = 0.15$ and 3 respectively.

Two scenarios have been proposed by Chrysostomou et al. (1993) to explain the observed low R_{op} values. First, if the newly formed molecular hydrogen resides long enough on the surface of the dust grain, R_{op} will be between 3 and the equilibrium value of 0.15 set by the grain temperature T_{dust}. To get $R_{op} = 1$, the residence time of H_2 on the dust grain should be approximately half the time required for the H_2 rotational populations to reach equilibrium at T_{dust} after formation (see Fig.9 in Chrysostomou et al.).

Alternatively, in cold gas, R_{op} is fixed at a low value by gas-grain interactions (0.15 for $T_{dust} = 40$ K). As the photodissociation front propagates into the molecular cloud at velocities of the order of 1 kms^{-1}, cold gas is advected through the hot (T_{gas} of a few 100 K) interface. In the hot gas, spin exchange reactions can drive the low R_{op} to the observed value.

The residence time of H_2 on the grain goes as $\exp(450\,\mathrm{K}/T_{dust})$ (Tielens & Allamandola 1987) while the rate for spin exchange reactions goes as $\exp(-3200\,\mathrm{K}/T_{gas})$. From photodissociation region models, variations of T_{gas} are expected to be much larger than those of T_{dust}: R_{op} should thus vary much more rapidly in the second scenario (cold gas advection) than in the former (modified H_2 formation). High spatial resolution observations yielding R_{op} profiles across photodissociated interfaces should help discriminate the 2 scenarios.

2.3. Band Profiles

We compare here qualitatively the AIB profiles of both nebulae. More quantitative results will be presented in a forthcoming paper (Sellgren et al. 1999). We remark that the AIB spectrum of NGC 2023 multiplied by 2.2 superimposes nicely to that of NGC 7023. As the AIB flux is proportional to the radiation field intensity (Sellgren et al. 1985), this suggests that the radiation field in NGC 7023 is twice as strong as that of NGC 2023 (at the positions given in Sect. 1). The two AIB spectra look very similar (width, position of the AIBs) as expected in view of the similar physical conditions (density, radiation field) derived for NGC 7023 (Lemaire et al. 1996) and NGC 2023 (Steinman-Cameron et al. 1997; Field et al. 1998). There are, however, significant spectral differences in the AIB profiles which we detail below. These differences reflect changes in the physico-chemical state of the AIB carriers.

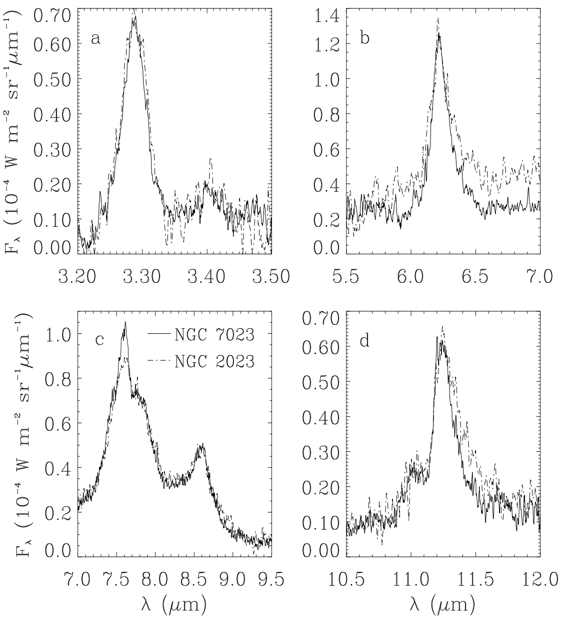

Figure 3. The profiles of the AIBs are shown for NGC 7023 (continuous line) and NGC 2023 (dot-dashed line). The intensity of NGC 2023 is multiplied by ~2.2 for comparison to NGC 7023.

Fig. 3a shows that the 3.3 and the 3.4 μm AIBs have identical profiles in both nebulae. The 3.4/3.3 μm band ratio remains thus the same while the radiation field intensity is multiplied by a factor 2.

Fig. 3b shows that the 6.2 μm AIB is asymmetrical and varies slightly between the two nebulae. Both profiles show a pronounced wing towards long wavelengths, which is interpreted as the consequence of anharmonic couplings during the cooling of the molecule (Barker et al. 1987; Joblin et al. 1995). In NGC 2023 the local continuum is more important, with respect to the 6.2 μm band, and has a steeper rise than in NGC 7023. This suggests that the underlying continuum has a different origin from the AIBs.

Fig. 3c demonstrates that the 7 – 9 μm range is the most complex. The main AIBs are at 7.6, 7.8, and 8.6 μm. The intensity of the 7.6 μm-component is stronger in NGC 7023 than in NGC 2023. Furthermore, the blue shoulder at 7.45 μm observed in NGC 7023 (see also Moutou et al. 1998) is not seen in NGC 2023. Roelfsema et al. (1996) and Verstraete et al. (1996) have shown that the profile of the "7.7" μm AIB and the distribution of energy between the 7.6, 7.8 and 8.6 μm AIBs varies with the radiation field. In the PAH model, the "7.7" μm AIB falls in the spectral range where the effects of ionisation are the most dramatic (Pauzat et al. 1997; Langhoff 1996). Such a prominent 7.6 μm feature as well as the 7.45 μm blue wing are unusual and have only been seen towards compact H II regions (Roelfsema et al. 1996) and towards the post-AGB star HR 4049 (Molster et al. 1996). These latter authors attributed the 7.45 and 7.6 μm new features to small ionized PAHs. Ionized PAHs have a strong 7.7/11.3 μm band ratio (Langhoff 1996). Since the AIB spectrum in NGC 2023 is scalable to that of NGC 7023 (see Fig.3), the 7.7/11.3 μm band ratio is the same for both nebula implying that the fraction of ionized PAHs is the same in both cases. From the absence of the 7.45 μm-band and the weaker 7.6 μm feature in NGC 2023, we conclude that the carriers of these bands are produced by other processes than photoionization (photochemical evolution, fragmentation...)[2].

Fig. 3d shows that the 11.3 μm AIB has a profile similar to the 6.2 μm band. A red asymmetry is observed, which again suggests strong anharmonic effects. We note that the red wing of the 11.3 μm band is more pronounced in NGC 2023. The 11.3 μm band also shows some weak sub-features within its profile. In particular, the 11.0 μm band (previously detected by Witteborn et al. 1989 and Roche et al. 1991) is clearly seen in both nebulae. The 11.0 μm band also appears in many objects with a similar ratio to the 11.3 μm band [3] (Molster et al. 1996; Roelfsema et al. (1996), Verstraete et al. 1996) while the 7.7/11.3 μm band ratio presents large variations (compare for instance the AIB spectrum of the M17-SW interface and that of NGC 7023). This again rules out photoionization as the cause of the 11.0 μm-band in moderately excited sources.

3. LWS SPECTRA IN NGC 7023

Finally, we show the complete LWS spectrum (AOT01 observing mode) of NGC 7023, at two nebular positions labelled 1 and 2. Unfortunately, we did not obtain any LWS spectrum of NGC 2023.

The LWS position 1 in NGC 7023 is the same as for SWS (see Sect. 1) and is close to the far-infrared peak of Whitcomb et al. (1981). Position 2 is located

[2] We also note that the 7.7/11.3 μm band ratio in HR 4049 is 4 times that of NGC 7023: such a variation points at very different fractions of ionized PAHs. The fact that the 7.45 and 7.6 μm features are seen in both spectra reinforces our conclusion that ionization cannot be the major way of producing these bands.

[3] This is not true for strongly irradiated regions where the AIB spectrum is deeply modified (strong 8.6 and 11.0 μm-bands).

100″N of the star. The LWS beam is 80″ in diameter, so the fields slightly overlap. Position 1 has been observed in the LWS guaranteed time program ISM IA and Position 2 was part of our open-time program on reflection nebulae. Both spectra are shown in Figure 4. The data reduction was done with the LWS-Interactive Analysis and ISAP software.

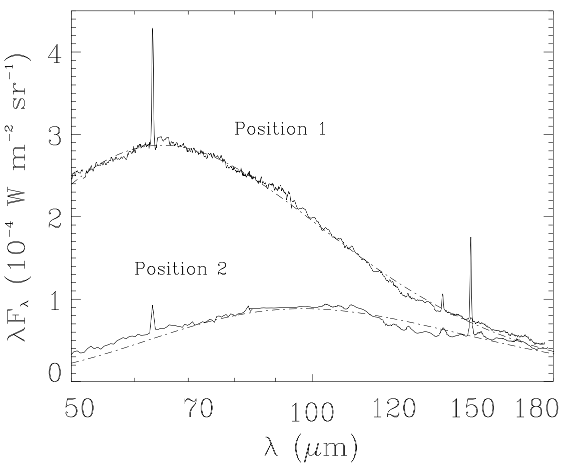

Figure 4. Complete LWS spectra of the reflection nebula NGC 7023, at two positions (see text). A modified blackbody fit is applied, which gives an effective temperature of 45K in Position 1 and 30K in Position 2. The narrow emission lines are due to atoms and ions of the gas (see text).

The LWS continuum emission is due to big dust grains in thermal equilibrium with the radiation field. We estimate the dust temperature by fitting a modified blackbody emission curve to the spectra with a dust emissivity law proportional to the frequency ν. The fits are shown on Figure 4. For Position 1, we also used the SWS spectrum of NGC 7023 (not shown here) to further constrain the fit. The effective temperature of dust grains at Position 1 is $T_{dust} = 45\pm$ 2K, while at Position 2, the temperature drops to $T_{dust} = 30\pm$ 2K. These temperatures are compatible with the temperature map obtained by Whitcomb et al. (1981). Poorer fits to the LWS spectra were obtained with a dust emissivity proportional to ν^2 (in this latter case, the above temperatures would drop by approximately 6 K). For a dust emissivity $\sim \nu$, the radiation field goes as T^5 and so the change in T_{dust} implies that the radiation field is stronger at Position 1 by a factor of 8 than at Position 2. Atomic emission lines accounting for the cooling of the gas are visible on both spectra, namely CII (158 μm), OI(63 μm) and NI (145 μm). They will be discussed elsewhere.

ACKNOWLEDGMENTS

We are very grateful to J.P. Baluteau for providing us the LWS spectra of NGC 7023. We acknowledge NATO Collaborative Research Grant 951347.

REFERENCES

Barker J.R., Allamandola L.J., Tielens, A.G.G.M. 1987, ApJ 315, L61

Boulanger, F. et al., 1998, A&A 339, 194

Burton, M.G., Hollenbach, D.J., Tielens, A.G.G.M. 1992: ApJ 399, 563

Cesarsky D. et al., 1996, A&A 315, L305

Chrysostomou, A., Brand, P.W.J.L, Burton, M.G., Moorhouse, A. 1993, MNRAS 265, 329

Draine,B.T., Bertoldi,F. 1996 ApJ 468, 269

Field D., Lemaire J. L., Pineau des Forêts G., Gerin M., Leach S., Rostas F. & Rouan D. 1998, A&A 333, 280

Joblin, C., Salama, F., Allamandola, L. 1995, J. Chem Phys. 102 (24), 9743

Langhoff S.R 1996, J. Phys. Chem. 100, 8, 2819

Laureijs R. et al. 1996, A&A 315, L313

Lemaire J.L., Field D., Gerin M., Leach S., Pineau des Forêts G., Rostas F. & Rouan D. 1996, A&A 308, 895

Martini P., Sellgren K. & Hora J.L. 1997, ApJ 484, 296

Molster F.J. et al. 1996, A&A 315, L373

Moutou C. et al. 1998, in *Star formation with the Infrared Space Observatory*, ASP Conf. Ser. 132, eds. Joao L. Yun and René Liseau, p. 47

Moutou C., Sellgren K., Verstraete L., Léger A. 1999, submitted to A&A

Pauzat F., Talbi, D. & Ellinger, Y. 1997, A&A 319, 318

Roche P.F., Aitken D.K. & Smith C.H. 1991, MNRAS 252, 282

Roefselma et al. 1996, A&A 315, L289

Sellgren K., Allamandola, L.J., Bregman, J.D., Werner, M.W. & Wooden, D.H. 1985, ApJ 299, 416

Steinman-Cameron, T.Y., Haas, M.R., Tielens, A.G.G.M. 1997 ApJ 478, 261

Tielens, A.G.G.M., & Allamandola L.J. 1987, in *Interstellar Processes,* ed. D. J. Hollenbach & H. A. Thronson (Dordrecht: Reidel), p. 397

Verstraete L., Puget J. L., Falgarone E., et al. 1996, A&A 315, L337

Whitcomb S.E., Gatley I., Hildebrand R.H., Keene J., Sellgren K. & Werner M.W. 1981, ApJ 246, 416

Witteborn F.C., Sandford S.A., Bregman J.D., Allamandola L.J., Cohen M., Wooden D.H. & Graps A.L. 1989, ApJ 341, 270

UNIDENTIFIED INFRARED EMISSION BANDS AND SUB-MICRON DUST GRAINS IN THE DIFFUSE INTERSTELLAR MEDIUM

T. Onaka[1], M. Mizutani[1], D. Tomono[1,2], H. Shibai[3], T. Nakagawa[4] & Y. Doi[5]

[1]Department of Astronomy, School of Science, University of Tokyo, Tokyo 113-0033, Japan
[2]Subaru Telescope, National Astronomical Observatory of Japan, Hilo, Hawaii 86720, U.S.A.
[3]Department of Physics, School of Science, University of Nagoya, Nagoya 464-8602, Japan
[4]Institute of Space and Astronautical Science, Kanagawa 229-8510, Japan
[5]Department of Earth Science and Astronomy, University of Tokyo, Tokyo 153-8902, Japan

ABSTRACT

Two H II regions, the Carina nebula and Sharpless 171, and the ρ Oph cloud region, have been mapped with PHT-S and LWS full grating scan (45–170 μm). The unidentified infrared (UIR) emission bands at 6.2, 7.7, 8.6, and 11.2 μm were detected at most observed positions. Their spatial variations are examined in relation to the far-infrared emission from the submicron dust grains. The temperature and optical depth of submicron grains are derived from the fit of the LWS spectra with modified blackbody. The strength of the incident radiation field in units of the solar vicinity value (G_0) is estimated from the dust temperature. The ratio of the UIR 7.7 μm band to the total far-infrared intensity (FIR) shows a similar trend in the two H II regions. It decreases as G_0 increases for $G_0 > 1000$. The ratio, however, stays constant in the ρ Oph region, even for $G_0 > 1000$. A more general relation is found if the ratio is plotted against [O III] 88 μm line intensity divided by FIR. The plot indicates that the UIR band carrier may be destroyed or the emission mechanism becomes inefficient in ionized regions. On the other hand, the relative band strengths among the UIR bands do not show any systematic trend with the radiation strength or ionization, indicating that the material properties of the UIR band carrier do not vary appreciably with the radiation field.

Key words: interstellar dust; unidentified infrared emission bands; H II regions.

1. INTRODUCTION

Recent space infrared observations by IRTS and ISO have clearly revealed that the diffuse galactic emission of 3–12 μm consists of the so-called unidentified infrared (UIR) emission bands (Tanaka et al. 1996, Onaka et al. 1996, Mattila et al. 1996). The major UIR bands are seen at 3.3, 3.4, 6.2, 7.7, 8.6, and 11.2 μm. They are thought to come from hydrocarbons with aromatic structures and several candidate materials have been proposed for the band carrier (see Tokunaga (1997) for a recent review).

Observations by balloons and IRTS have shown that the strengths of the UIR bands are linearly correlated with the IRAS 100 μm intensity quite well except for very active regions, indicating that the UIR band carriers are well mixed with submicron grains which emit the far-infrared radiation (Giard et al. 1989, Tanaka et al. 1996, Onaka et al. 1996). Investigations using the 155 μm data obtained by IRTS/FILM with the IRAS 100 μm intensity allow us to estimate the temperature and optical depth of submicron grains independently (Okumura et al. 1996, Okumura 1998). Correlation studies of the UIR band intensity with the properties of submicron grains have indicated that the strength of the UIR bands is proportional to the intensity of the incident radiation field for $1 < G_0 < 100$, where G_0 is the strength of the radiation field in units of the solar vicinity value. The relative strengths among the mid-infrared UIR bands seem to be constant for $1 < G_0 < 100$ in the diffuse galactic emission (Onaka et al. 1997, Onaka 1998, Okumura 1998).

The proportionality and the constancy of the spectrum are compatible with the theoretical interpretation that the UIR bands arise from temperature-fluctuating very small dust grains (Draine & Anderson 1985) or the infrared fluorescence of large molecules (Puget et al. 1985). Recently Boulanger et al. (1998) have suggested a similar proportionality based on the ISOCAM CVF observations of several individual objects with a possible deviation for $G_0 > 1000$.

In order to further study the variation in the UIR bands with various physical environments, we have analyzed the data of mapping observations of two H II regions (the Carina nebula and Sharpless 171) and the ρ Oph cloud region obtained in a guaranteed time observation program. The three regions have been mapped with PHT-S and LWS01 and the variation in the UIR band intensity derived from the PHT-S spectra is investigated in relation to the far-infrared emission obtained from the LWS spectra.

Proceedings of the Conference "The Universe as seen by ISO", Paris, France, 20–23 October 1998 (ESA SP-427, March 1999)

2. OBSERVATIONS

The Carina nebula is one of the most active regions on the galactic plane. It has a number of the most luminous stars in the Galaxy and constitutes a complex structure of H II regions and molecular clouds (e.g., de Graauw et al. 1981). The observations were made in a two-dimensional raster mode with a spacing of 3 arcmin for a rectangular area of 40 arcmin $\times$ 20 arcmin centered at $l = 287.25°$ and $b = -0.6°$. The observed area includes diffuse H II regions, Carina I and II, as well as molecular clouds. Strong [O III] 52 and 88 μm lines were observed in Carina I and II, but the ionic lines have also been observed from the diffuse medium all over the observed area (Mizutani et al. in these proceedings).

Sharpless 171 (S171) is a large H II region associated with star cluster Be 59 and molecular clouds. It is the main cloud associated with the Cepheus OB4 stellar association (Yang and Fukui 1992). S171 was observed in an one-dimensional raster mode from the center of Be 59 cluster to the molecular cloud complex with a spacing of 50 arcsec ($117.9° < l < 118.2°$ and $b = 4.98°$). Transition from the ionized region to the molecular phase can clearly be seen in the distributions of [O III] 52 and 88 μm lines and [O I] 63 μm line. The UIR bands are observed at all the observed positions but the vicinity of Be 59.

The ρ Ophiuchi dark cloud is a nearby low-mass star-forming region and is a C^+ region heated by embedded B-type stars (Yui et al. 1993). The observations were made in an one-dimensional raster scan, whose path includes the brightest star HD147889 (B2V) in the region at the center, with a spacing of 3 arcmin (Tomono et al. 1997). The UIR bands have been observed at the positions where the CO intensity is large and no [O III] lines have been detected.

All the three regions have been observed with PHT-S and LWS01 full grating scan mode (45–170 μm). The PHT-S data have been reduced by PIA version 7.2.2[1]. The intensity of the UIR bands has been estimated by assuming the local baseline determined from the neighboring continuum. The auto-analysis results (AAR) of OLP 6 have been used for the LWS observations. The spectra have been defringed and adjusted to the level of the SW3 detector.

3. RESULTS AND DISCUSSION

The total far infrared intensity from submicron dust grains, FIR, is supposed to be equal to the absorbed energy of incident radiation;

$$FIR = \tau_{abs} \cdot G_{\odot} \cdot G_0, \qquad (1)$$

where $G_{\odot}$ is the radiation intensity in the solar vicinity (1.6×10^{-6} W m^{-2}, Habing 1968), and τ_{abs} is the absorption optical depth averaged over the incident radiation spectrum. From the far-infrared emission spectrum FIR is obtained as

$$FIR = \tau_{100} \int (\epsilon_\lambda / \epsilon_{100}) B_\lambda(T) d\lambda, \qquad (2)$$

where τ_{100} is the optical depth at 100 μm, ϵ_λ and ϵ_{100} are the emissivity at λ and 100 μm, respectively, and $B_\lambda(T)$ is the Planck function of temperature T. Both optical depths, τ_{abs} and τ_{100}, are proportional to the column density of submicron grains. Assuming $\tau_{abs}/\tau_{100} = 700$, G_0 can be estimated from equations (1) and (2).

The observed LWS spectra are fitted with equation (2) and τ_{100} and T are derived. The beam size of LWS has not been determined accurately yet. In this paper, it is assumed to be 80 arcsec for all the LWS wavelengths (Burgdorf et al. 1997). The absolute values of the derived FIR and G_0 may have systematic errors due to the assumption of beam size, however, the relative values should not be affected since all the data have been analyzed with the same assumption.

Figure 1 shows a plot of the ratio of the UIR 7.7 μm band strength to FIR against G_0. In the study of the IRTS observations of the diffuse galactic emission for $1 < G_0 < 100$ the ratio stays in the range $0.02 - 0.05$ (Onaka 1998). Figure 1 indicates that the ratio in the three observed regions resides in a similar range to that in the diffuse galactic emission for $G_0 < 1000$, and that it starts decreasing for $G_0 > 1000$ in the two H II regions (open circles and crosses). The ratio in the ρ Oph cloud (filled circles), however, seems to stay constant even for $G_0 > 1000$.

In the ρ Oph cloud, the area where G_0 is larger than 1000 is located near the exciting star HD147889 and

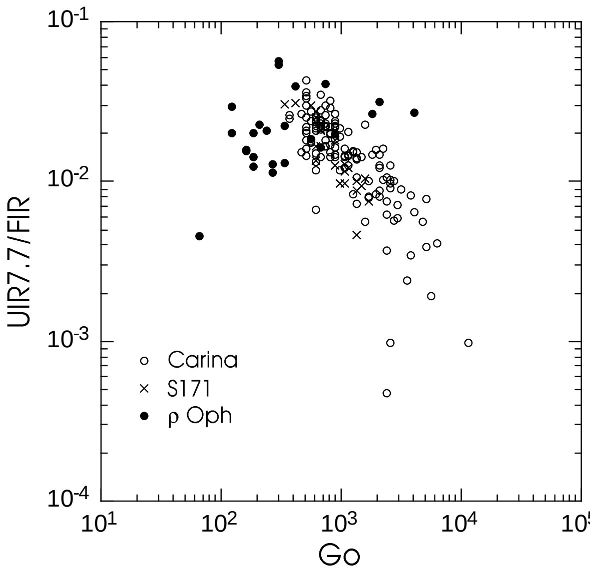

Figure 1. The ratio of the strength of the UIR 7.7 μm band to the total far-infrared intensity vs. the radiation field strength in units of the solar vicinity value. Open circles are for the Carina nebula, crosses for S171, and filled circles for the ρ Oph cloud.

[1]The PIA is a joint development by the ESA Astrophysics Division and the ISOPHOT Consortium. Contributing ISOPHOT Consortium institutes are DIAS, RAL, AIP, MPIK and MPIA.

the UIR bands are detected with sufficient signal-to-noise ratios. Ryter et al. (1987) made analysis of the IRAS data for the ρ Oph cloud and showed no systematic variation in the 12 μm intensity relative to the 100 μm intensity along a path through HD 147889. The constancy of the ratio in the observed region is observationally rather secure.

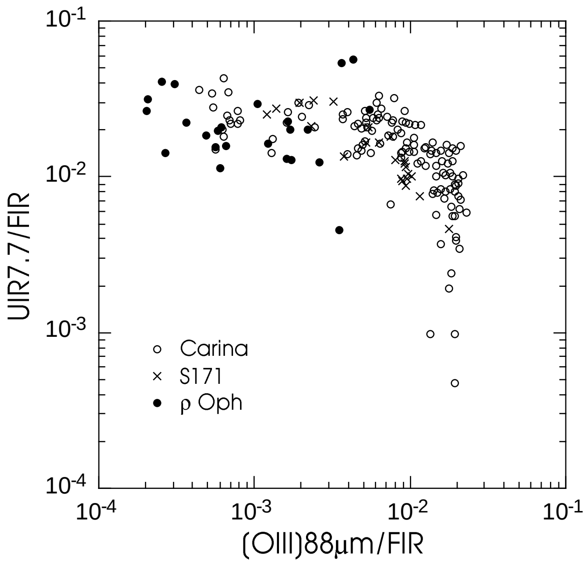

Figure 2. The ratio of the UIR 7.7 μm band strength to the total far-infrared intensity (FIR) is plotted against [O III] 88 μm line intensity divided by the FIR. Symbols are the same in Figure 1. Note that [O III] 88 μm line was not detected in the ρ Oph region and thus all the filled circles indicate only upper limits in the abscissa.

Figure 2 shows a plot of the ratio against [O III] 88 μm line intensity divided by FIR. In the ρ Oph cloud, no [O III] 88 μm line has been detected and thus the filled circles indicate only upper limits. Far-infrared [O III] lines are efficient coolants for the gas in H II regions and they are supposed to trace the ionized gas. Figure 2 suggests a more general trend than Figure 1. The UIR 7.7 μm to FIR ratio sharply decreases for [O III] intensity/$FIR > 0.01$. It is thus suggested that either the abundance of the UIR band carriers decreases relative to submicron grains or the UIR band emission mechanism becomes inefficient in the ionized region. The decrease seen in Figure 1 may have to be attributed to the presence of ionized region rather than the increase in G_0. Previous observations in near-to-mid-infrared spectroscopy have indicated that the UIR bands are weakened in ionized regions (e.g., Bregman et al. 1989). The present study clearly reveals that the decrease occurs relative to the far-infrared emission in ionized regions.

Figures 3 and 4 show the band strength ratios of the UIR 6.2 μm to 7.7 μm and 11.2 μm to 7.7 μm against G_0, respectively. Although the scatter is large, no clear trend is seen in the plot. A few data points of the ratio of the 11.2 μm to 7.7 μm bands in the Carina nebula may indicate a trend that the ratio increases in the ionized region, but it needs to be confirmed. The band ratio in the diffuse galactic emission, including cirrus clouds, does not change for $1 < G_0 < 100$ (Onaka 1998). The band ratios

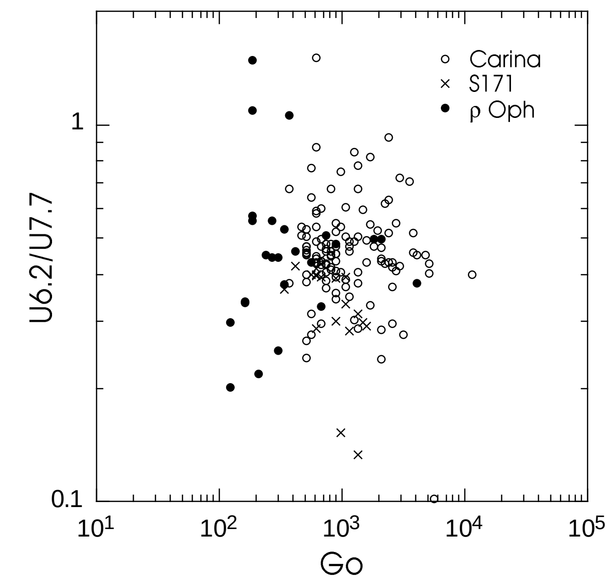

Figure 3. The UIR 6.2 μm to 7.7 μm band ratio against the radiation strength. Symbols are the same in Figure 1.

obtained in the present study are in the same range as in the IRTS observations. It is thus suggested that the constancy of the UIR band spectrum holds for $1 < G_0 < 10^4$. A similar result has also been indicated by ISOCAM CVF observations (Boulanger et al. 1998). On the other hand, observations of compact H II regions (Roelfsema et al. 1996, 1998) clearly shows variations in the UIR band spectra. Most recently Cesarsky et al. (1998) reported that quiet regions in M31 show only the 11.2 μm band, but do not have the 6.2, 7.7, and 8.6 μm bands. Spatial variations in the mid-infrared band ratios have also been seen in extended objects (e.g., Joblin et al. 1996).

The variations in the UIR band strengths definitely exist, but little variation is seen in spectra of most objects including the diffuse galactic emission which originates from general interstellar medium. Physical parameters which control the band strength have not yet been understood. A recent study for several individual objects by Lu et al. (1998) suggests a similar conclusion. Lu et al. (1998) also suggested that there is a trend between the band ratios of 6.2 μm/7.7 μm and 11.2 μm/7.7 μm, but the present data do not indicate any systematic variations among the band ratios.

4. SUMMARY

Three extended objects, the Carina nebula, S171, and the ρ Oph cloud, have been mapped with PHT-S and LWS01, and variations in the UIR bands are investigated in relation to the far-infrared emission. The present study estimates the far-infrared intensity from the full LWS spectra. It takes account of the emission for wavelengths longer than 100 μm and the variation in the dust temperature. Thus it should provide an accurate estimate of G_0, although the absolute value may have systematic errors.

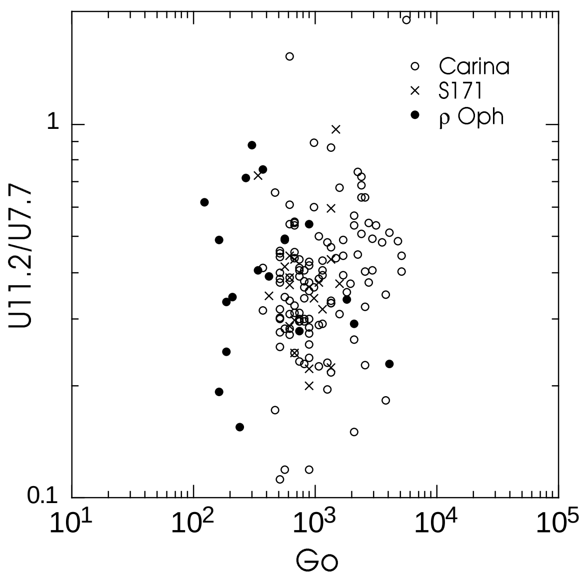

Figure 4. The UIR 11.2μm to 7.7μm band ratio against the radiation strength. Symbols are the same in Figure 1.

The UIR band strengths have been shown to be proportional to the incident radiation field strength as long as $1 < G_0 < 1000$. The band strengths show sharp decrease relative to the far-infrared emission when the ionic line [O III] 88 μm intensity exceeds about 1 per cent of the total far-infrared intensity. It is thus suggested that the the abundance of the UIR band carrier decreases relative to submicron dust grains in ionized regions or that the emission mechanism becomes inefficient when the UV radiation becomes strong. The deviation from the linearity of the UIR band strength for $G_0 > 1000$ may have to be attributed to the presence of ionized region rather than the increase in G_0.

The present study and the IRTS observations show that the relative strengths among the UIR bands do not vary systematically with G_0 for $1 < G_0 < 10^4$. Material properties of the UIR band emitters are suggested not to vary appreciably with the radiation field. The relative strengths of the UIR bands have been suggested to be a function of the size of the carriers, the ionization degree of the carrier, and the incident radiation field (Lu et al. 1998). Therefore it is suggested that neither the size distribution of the UIR band emitters nor the response to the incident radiation varies over a wide range of the environmental conditions. Parameters which cause the variation must be looked for other than the radiation strength. These results should provide important clues to the understanding of the band carriers and must be interpreted in future model analysis.

ACKNOWLEDGMENTS

We would like to thank the ISO project members for their efforts and help, and K. Kawara, Y. Satoh, H. Okuda, T. Tsuji, and other members of the Japanese ISO group for their continuous support. D. T. is supported by the JSPS Fellowship for young scientists. This work is supported in part by grant-in-aids for Scientific Research and Overseas Scientific Research from the Ministry of Education, Science, Sports and Culture in Japan.

REFERENCES

Boulanger, F., Abergel, A., Bernard, J.P., et al. 1998, ASP conf. 132, 15

Bregman, J.D., Allamandola, L.J., Tielens, A. G. G. M., Geballe, T.R., Witteborn, F.C. 1989, ApJ, 344, 791

Burgdorf, M., Clegg, P., Ewart, D., et al. 1997, Proc. First ISO Workshop on Analytical Spectroscopy, A. M. Heras et al. (eds.), ESA SP-419, 51

Cesarsky, D., Lequeux, J., Pagani, L., et al. 1998, A&A, 337, L35

de Graauw, T., Lidholm, S., Fitton, B., et al. 1981, A&A, 102, 257

Draine, B.T., Anderson, N. 1985, ApJ, 292, 494

Giard, M., Pajot, F., Lamarre, J.M., et al. 1989, A&A, 215, 92

Habing, H.J., 1968, BAN, 19, 421

Joblin, C., Tielens, A.G.G.M., Geballe, T.R., Wooden, D.H. 1996, ApJL, 460, L119

Lu, N.Y. 1998, ApJL, 498, L65

Mattila, K., Lemke, D., Haikala, L.K., et al. 1996, A&A, 315, L353

Okumura, K., Hiromoto, N., Okuda, H., et al. 1996, PASJ, 48, L123

Okumura, K. 1998, Ph.D. thesis, Univ. of Tokyo

Onaka, T., Yamamura, I., Tanabé, T., et al. 1996, PASJ, 48, L59

Onaka, T., the IRTS team 1997, ASP conf. 124, 170

Onaka, T. 1998, AdSpR, in press

Puget, J.-P., Léger, A., Boulanger, F. 1985, A&A, 142, L19

Roelfsema, P.R., Cox, P., Tielens, A.G.G.M., et al. 1996, A&A, 315, L289

Roelfsema, P.R., Cox, P., Kessler, M.F., Baluteau, J.-P., 1998, ASP. conf. 132, 76

Ryter, C., Puget, J.L., Péraut, M. 1987, A&A, 186, 312

Tanaka, M., Matsumoto, T., Murakami, H., et al. 1996, PASJ, 48, L53

Tokunaga, A.T. 1997, ASP conf. 124, 149

Tomono, D., Onaka, T., Yui, Y.Y., Nakagawa, T, Shibai, H. 1997, ASP conf. 124, 278

Yang, J., Fukui, Y. 1992, ApJ, 386, 618

Yui, Y.Y., Nakagawa., T., Doi, Y., et al. 1993, ApJL, 419, L37

SOLID CO_2 IN LABORATORY AND IN DENSE MOLECULAR CLOUDS

M.E. Palumbo, G.A. Baratta & G. Strazzulla
Osservatorio Astrofisico di Catania, Catania, Italy

ABSTRACT

We have studied by laboratory infrared spectroscopy the profile of the band due to the CO_2 bending mode in different H_2O:CH_3OH:CO_2 mixtures. Icy mixtures have been accreted on a substrate at 12.5 K inclined of 45 degrees with respect to the infrared beam of the spectrometer. Spectra have been taken with the electric vector of the infrared beam parallel (P polarized) and perpendicular (S polarized) to the plane of incidence. The samples have been warmed up and spectra have been taken at different temperatures. We have found that the profile of the band due to the CO_2 bending mode strongly depends on the temperature. Furthermore for the mixtures studied, the profile of this band is different in the two different polarization cases. In particular features not due to absorption appear in the P polarization case. Here we discuss the implications of these results in the astrophysical context.

Key words: carbon dioxide; laboratory; infrared spectroscopy; ices.

1. INTRODUCTION

Laboratory experiments and theoretical calculations had predicted and ISO observations have confirmed the presence of solid carbon dioxide (CO_2) in icy grain mantles in dense molecular clouds. It has been estimated that the CO_2 abundance is ~15-20% with respect to water ice. However the origin of solid CO_2 is not yet clear. Carbon dioxide is not predicted to have appreciable abundance in the gas phase in dense clouds so that its condensation on interstellar grains can be neglected. Thus its presence may be due to reaction of gas phase species on grain cores or to energetic processing such as UV and cosmic ray irradiation of ices. Indeed, laboratory experiments have shown that CO_2 is produced after UV and ion irradiation of astrophysical relevant ices (e.g., Gerakines et al. 1996; Palumbo et al. 1998).

The profile of the band due to the CO_2 bending mode observed towards several embedded objects (e.g., de Graauw et al. 1996; Ehrenfreund et al. 1997a) is characterized by a considerable structure with subpeaks. Preliminary comparisons of laboratory spectra of icy mixtures containing CO_2 with ISO spectra (de Graauw et al. 1996) have shown that it is not possible to find a single laboratory spectrum which fits the CO_2 observed bands and it has been suggested that the observed features are due to the sum of at least two independent components, namely CO_2 mixed in polar and non polar matrices. Alternatively, Strazzulla et al. (1998) have considered solid CO_2 produced after ion irradiation of ice mixtures containing C-bearing and O-bearing species. In particular they have fitted the bending mode of solid CO_2 observed towards the embedded source NGC7538 IRS1 with laboratory spectra of CO_2 produced by ion irradiation of CO at 10 K and warmed-up to 40 K and CO_2 produced in a H_2O:CH_3OH mixture. Recently, Ehrenfreund et al. (1998) have suggested that thermal processing which induces ice segregation is responsible of the observed features. In particular they have studied in the laboratory a H_2O:CH_3OH:CO_2=1:1:1 mixture and since the band due to the bending mode of CO_2 after warm-up well compares with the profile of the astronomical CO_2 bending mode they conclude that the observed profile is due to only this component.

Here we present the results of an experimental study of the profile of the band due to the CO_2 bending mode in different H_2O:CH_3OH:CO_2 ice mixtures as deposited at 12.5 K and after warm-up.

2. EXPERIMENTAL PROCEDURE

The infrared spectra here shown have been taken in the 4400-500 cm^{-1} (2.27-20 μm) range at the Experimental Astrophysical Laboratory of the Catania Astrophysical Observatory. A stainless steel vacuum chamber (shown in Figure 1) faces the spectrometer through KBr windows. Gases are accreted by a gas inlet on a silicon (or KBr) substrate inclined of 45 degrees with respect to the infrared beam of the spectrometer. The substrate is put in thermal contact with a closed-cycle helium cryostat whose temperature can be varied in the 10-300 K range.

In this experimental set-up it is possible to monitor the thickness of the film during accretion, by looking at the interference pattern (intensity versus time) given by a He-Ne laser beam reflected at an angle of 45 degrees both by the vacuum-film and film-substrate interfaces. For each sample, at all the examined temperatures, two spectra with the electric

Proceedings of the Conference "The Universe as seen by ISO", Paris, France, 20–23 October 1998 (ESA SP-427, March 1999)

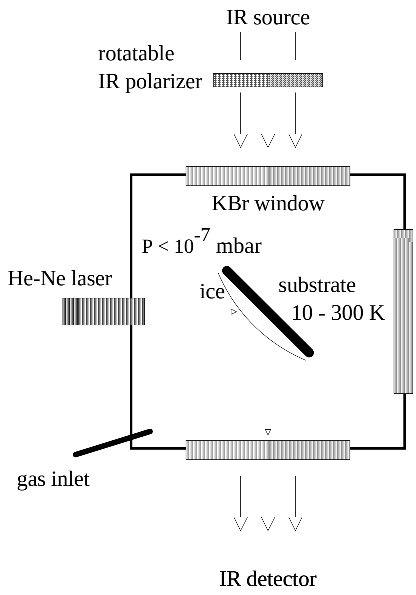

Figure 1. Schematic view of the vacuum chamber.

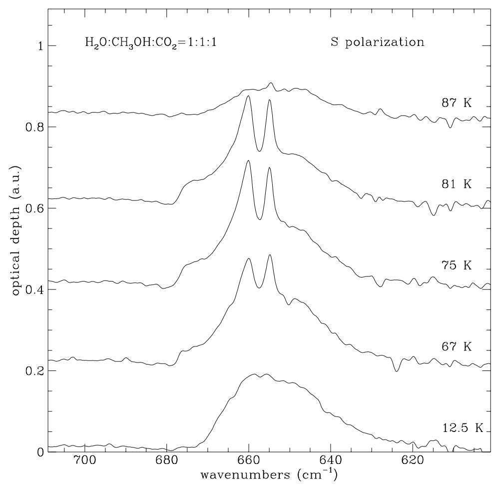

Figure 2. Infrared spectra of the CO_2 bending mode in a H_2O:CH_3OH:CO_2=1:1:1 mixture taken in S polarized light at 12.5 K and after warm-up. Spectra have been taken at a resolution of 1 cm^{-1} and sampling of 0.25 cm^{-1}. Spectra have been shifted upward by 0.2 in the optical depth scale, for clarity.

vector of the infrared beam parallel (P polarized) and perpendicular (S polarized) to the plane of incidence are taken where the polarization of the infrared radiation is changed by rotating a polarizer placed in the path of the infrared beam (Figure 1). All the spectra for a given polarization are ratioed to the corresponding spectrum of the background acquired before deposition.

3. ICE SEGREGATION STUDIES

We have studied the profile of the absorption band due to the CO_2 bending mode in different H_2O:CH_3OH:CO_2 ice mixtures as deposited at 12.5 K and after warm-up. The spectra have been taken in both P and S polarizations. In fact, Baratta & Palumbo (1998) have shown that when the sample is inclined with respect to the infrared beam, this procedure can clearly evaluate the contribution of reflection in the profile of the bands. Indeed reflection gives rise to features in the spectrum which are not due to absorption. This is the case for the stretching and bending modes of solid CO_2 and, in general, depends on the optical constants (n, k). It can be shown from theory and experiments that spectra taken in S polarized light are equivalent to those taken when the substrate plane is perpendicular to the infrared beam of the spectrometer (normal incidence).

Figures 2 and 3 show the spectra of the bending mode of CO_2 in S polarized light in two different ice mixtures namely H_2O:CH_3OH:CO_2=1:1:1 and 10:1:2. It is evident that in both mixtures after warm-up above 60 K the profile of the band changes. A double peak appears at 600 cm^{-1} and 655 cm^{-1}. The shoulder at 649 cm^{-1} is already present at 12.5 K. This modification of the profile indicates a change in the structure of the ice (referred to as segregation). The double peak disappears at about 85 K when most of CO_2 sublimates. According to Ehrenfreund et al. (1998) the shoulder is due to complexes formed between CO_2 and CH_3OH. The double peak is characteristic of pure or annealed CO_2 (Sandford & Allamandola 1990; Ehrenfreund et al. 1997b). Ice segregation has been observed in the two mixtures shown (1:1:1 and 10:1:2); no double peak has been observed after warm-up of more diluted mixtures (e.g., 20:10:1; see also Sandford & Allamandola 1990). The mixture H_2O:CH_3OH:CO_2=1:1:1 has already been studied by Ehrenfreund et al. (1998). Our results are qualitatively in agreement with these latter which are equivalent to the S polarization case. The main difference between the two sets of data is the temperature at which segregation is observed. A comparison between Figure 2 in this paper and Figure 1 in Ehrenfreund et al. (1998) shows that the difference is about 40 K. The reason of this difference is not yet clear and we are investigating on it.

Figure 4 shows the profile of the bending mode in a H_2O:CH_3OH:CO_2=1:1:1 ice mixture in the spectra taken in the two polarizations (S and P). It is evident that the P polarized spectra exhibit features that are not present in the S polarized spectra. It can be shown from theory and experiments that these features are also absent in spectra taken with the substrate plane perpendicular to the infrared beam of the spectrometer (normal incidence). Baratta & Palumbo (1998) have shown that these features are not due to absorption (k) but to the increased reflectivity corresponding to the region across the absorption band where $n < 1$.

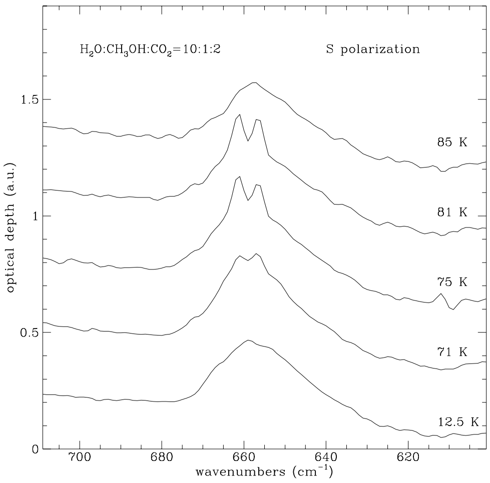

Figure 3. Infrared spectra of the CO_2 bending mode in a H_2O:CH_3OH:CO_2=10:1:2 mixture taken in S polarized light at 12.5 K and after warm-up. Spectra have been taken at a resolution of 2 cm^{-1} and sampling of 1 cm^{-1}. Spectra have been shifted upward by 0.3 in the optical depth scale, for clarity.

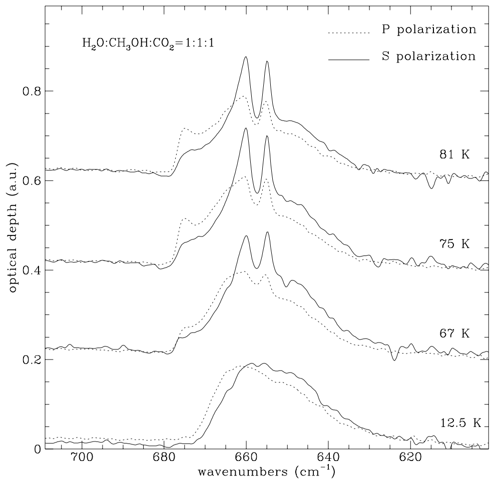

Figure 4. Comparison between the spectra of a H_2O:CH_3OH:CO_2=1:1:1 mixture taken in two different polarizations at 12.5 K and after warm-up. Spectra have been taken at a resolution of 1 cm^{-1} and sampling of 0.25 cm^{-1}. Spectra have been shifted upward by 0.2 in the optical depth scale, for clarity.

In molecular clouds, ices form as mantles on grains. Also in the case of light scattering by small particles, features not due to absorption similar to those observed in laboratory spectra (whose position however depends on particles shape) appear in addition to the absorption bands. A direct consequence of this result is that laboratory spectra taken at normal incidence (equivalent to the S polarization case) cannot be directly compared to the astronomical spectra. This result seriously questions the conclusion drawn by Ehrenfreund et al. (1998) that the profile of the band due to the CO_2 bending mode observed towards embedded objects is due to ice segregation and thermal processing of icy mantles which is based on a simple comparison of laboratory and astronomical spectra.

4. FINAL REMARKS

We have presented the results of a study of the profile of the CO_2 bending mode in H_2O:CH_3OH:CO_2 ice mixtures as deposited at 12.5 K and after warm-up. Our laboratory results are qualitatively in agreement with previous results presented by Ehrenfreund et al. (1998) which are equivalent to those we obtained in the S polarization case. In addition we have shown that when ice segregation occurs, features not due to absorption are present in the spectrum. This means that it is not possible to directly compare the spectra taken in the laboratory at normal incidence with the astronomical spectra. In order to perform this comparison, the extinction cross-sections for small particles must be derived. Small particles may give rise to multiple extinction peaks, where their number and position depend on the grain shape and on the $k^2 - n^2$ value across the band (see Ehrenfreund et al. 1997b). To perform this calculation reliable optical constants of the considered ice mixture must be known (Baratta & Palumbo 1998).

ACKNOWLEDGMENTS

This research has been financially supported by the Assemblea Regionale Siciliana (ARS), the Ministero dell'Università e della Ricerca Scientifica e Tecnologica (MURST), the Italian Space Agency (ASI) and the italian Consiglio Nazionale delle Ricerche (CNR).

REFERENCES

Baratta, G.A., Palumbo, M.E. 1998, J. Opt. Soc. Am., in press

de Graauw, Th., Whittet, D.C.B., Gerakines, P. et al. 1996, A&A, 315, L345

Ehrenfreund P., d'Hendecourt, L., Dartois, E. et al. 1997a, Icarus, 130, 1

Ehrenfreund P., Boogert, A.C.A., Gerakines, P.A., Tielens, A.G.G.M., van Dishoeck, E.F. 1997b, A&A, 328, 649

Ehrenfreund P., Dartois, E., Demyk, K., d'Hendecourt, L. 1998, A&A, 339, L17

Gerakines, P.A., Schutte, W.A., Ehrenfreund, P. 1996, A&A, 312, 289

Palumbo, M.E., Baratta, G.A., Brucato, J.R. et al. 1998, A&A, 334, 247

Sandford, S.A., Allamandola, L.J. 1990, ApJ, 355, 357

Strazzulla, G., Nisini, B., Leto, G., Palumbo, M.E., Saraceno, P. 1998, A&A, 334, 1056

PAHs IN COMPACT HII REGIONS

E. Peeters[1,2], A.G.G.M. Tielens[2,1], P.R. Roelfsema[1,2] & P. Cox[3]

[1]SRON, Groningen, The Netherlands
[2]Kapteyn Astronomical Institute, Groningen, The Netherlands
[3]Institut d'Astronomie Spatiale, Orsay, France

ABSTRACT

As part of the ISO guaranteed time program devoted to the study of compact HII regions in the Galaxy, ISO-SWS spectra covering the complete SWS wavelength range from a large sample of HII regions were obtained. The sample covers a large range in galactic radii from the galactic center out to a distance of ~25 kpc.

In addition to strong atomic emission lines, these data show a wealth of infrared emission features attributed to Polycyclic Aromatic Hydrocarbons (PAHs). The strength and shape of these features exhibit considerable variations in different lines-of-sight. These variations are thought to be a consequence of varying physical conditions of the emitting region (radiation field, density etc.).

Key words: ISM : dust; ISM : HII regions; ISM : molecules; Infrared : ISM : lines and bands.

1. INTRODUCTION

Since their discovery (Gillet et al. 1973), near- and mid-IR emission features have been seen in a variety of sources including reflection nebulae, HII regions, planetary nebulae, the ISM, etc. It is now generally accepted that these features can be attributed to PAHs, either neutral or ionized.

With the launch of the ESA's Infrared Space Observatory (ISO; Kessler et al. 1996) a unique opportunity arose to revisit the problem of galactic abundance gradients by using the Short Wavelength Spectrometer (SWS; de Graauw et al. 1996) and Long Wavelength Spectrometer (LWS, Clegg et al. 1996) to observe far infrared fine structure lines towards a sample of galactic compact HII regions (Cox et al. these proceedings). A sample of 45 compact HII regions uniformly distributed throughout the Galaxy were chosen (a catalogue of these data can be found in Peeters et al. (1999). The spectra of these HII regions also show PAH features. Here we present the spectra of four compact HII regions and analyze the PAH features.

2. OBSERVATIONS AND RESULTS

The data presented here are obtained by the SWS on board of ISO. The SWS-AOT6 spectra were reduced with the standard SWS Interactive Analysis (IA) reduction programs, using version 6 of the SWS off-line processing pipeline. The spectra were rebinned to a resolution of 1600 and are shown in figure 1 and 2.

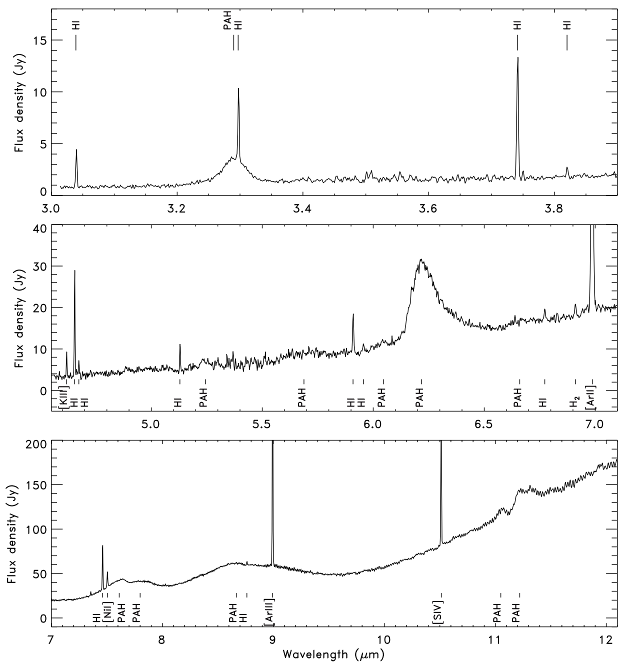

Figure 1. The SWS-AOT6 spectrum of IRAS18434-0242.

3. DISCUSSION

Figure 1 shows the SWS-AOT6 spectrum of IRAS18434-0242 in the wavelength range from 3-3.9 μm and from 4.55-12.1 μm. IRAS18434-0242 shows a

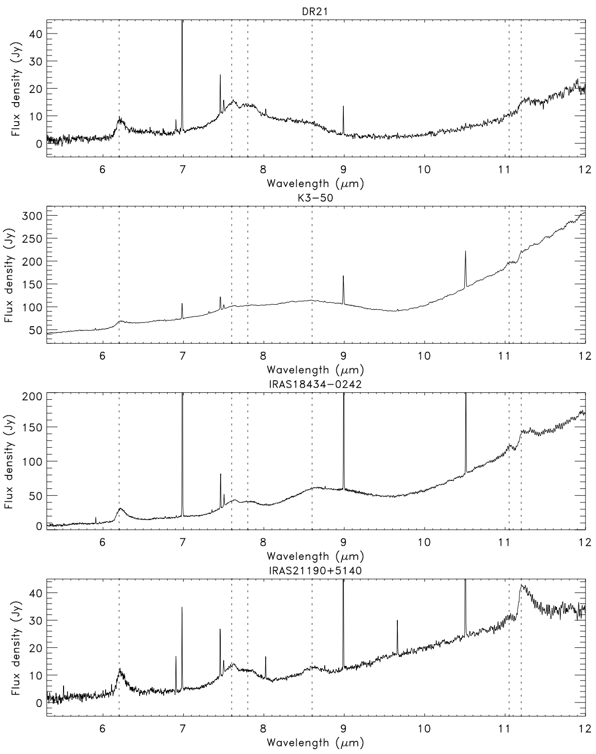

Figure 2. The SWS-AOT6 spectra of four compact HII regions; DR21, K3-50, IRAS18434-0242 and IRAS21190+5140 (from top to bottom).

very rich spectrum with intense atomic fine-structure lines, HI recombination lines (a detailed discussion of the atomic lines will be given in Martin et al. 1999), a few H_2 lines and strong emission bands of dust. The richness of the spectrum is characteristic for all sources in our sample.

Here, we want to elaborate on the PAH spectrum. One can clearly recognize the well-known 3.3, 6.2, '7.7', 8.6 and 11.3 μm features but also some minor PAH features are present at 5.24, 5.69, 6.05, 6.66 and 11.05 μm. At this resolution, the '7.7' breaks up into 2 components at 7.6 and 7.8 μm. In general, the IR features form a complex emission pattern with a variety of sub-peaks and spectral detail. Even for those features without obvious sub-peaks, the emission profiles are distinctly non-Lorentzian with a steep blue wing and a red tail, indicative of anharmonicity (Barker et al. 1987).

The SWS-AOT6 spectra of four compact HII regions, i.e. DR21, K3-50, IRAS18434-0242 and IRAS21190+5140, are shown in figure 2. Each of them reveal a spectral richness and, while subfeatures often repeat from one source to another, their relative intensity varies considerably. In particular, we note here the variation in the strength of the ratio of the C-H out-of-plane bending mode (11.3 μm) and the C-C stretching mode (7.7 μm) between IRAS21190+5140 and DR21 (for a more detailed analysis see Peeters et al. 1999b). This is in agreement with an earlier study of PAH features in HII regions (Roelfsema et al. 1996). In that study, large variations in relative intensities were reported for the 7.6 to 8.6, the 7.6 to 11.2 and the 11.04 to 11.2 μm bands while only subtle variations in relative strength of the 3.3 to 11.2 and 6.2 to 7.6 μm bands were found.

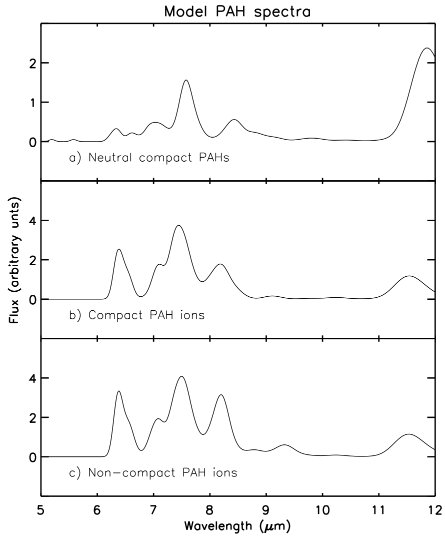

Figure 3. Emission spectra between 5-12 μm of compact neutral PAHs, compact PAH ions and non-compact PAH ions (from top to bottom - Roelfsema et al. (1996).

The spectral variations observed in our sample are consistent with emission from a family of related compounds whose composition is sensitive to the local physical conditions. This is illustrated in figure 3 for a sample of compact and non-compact PAHs. These have been calculated (Roelfsema et al. 1996) using the extensive database of laboratory spectra measured by Hudgins et al. (1994) and Hudgins & Allamandola (1995).

Comparison between panel a and panel b shows the effect of ionization of the excited PAHs on the spectrum. The ratio of the C-H out-of-plane bending mode (11-13 μm) to the C-C stretching modes (7.7 μm) is particularly sensitive to the degree of ionization. Hence the observed difference in the 11.3/7.7 ratio would suggest that PAHs are on the average more charged in DR21 than in IRAS21190+5140. The two sources have very comparable physical conditions (see Table 1) but the FUV field incident on the PDR is expected to be slightly higher in DR21 then in IRAS21190+5140. This might well cause charge variation of the level required (Bakes & Tielens 1994).

Differences in the relative strength of the features can also be caused by variations in the composition of the emitting PAH family. This is illustrated in figure 3 for compact and non-compact PAHs. The 8.6/7.7 ratio is particularly sensitive to those compositional variations. Such variations seems also to be present in our sample (Roelfsema et al. 1996).

Finally, we note that many of our sources show strong near-to-mid IR continuum emission. This emission is thus characterized by a high color temperature. Yet,

Table 1. Physical conditions of IRAS21190+5140 and DR21.

Source	IRAS21190	ref.	DR21	ref.
Size [pc]	0.14-0.06	a	0.06	b
n_e [cm^{-}3]	4.2 10^4	a	3 10^4	b
D [kpc]	6.8	c	3	d
L	1.4 10^5 $L_\odot$	c	5 10^5 $L_\odot$	e
G_0 [Habing]	2-10 10^5		20 10^5 *	

a: Scott & Harris 1978, b: Roelfsema et al. 1989,
c: Roelfsema et al. 1996, d: Campbell et al. 1982,
e: Colomé et al. 1995.
*: DR21 contains two prominent radio sources in the FIR beam. We have assigned half of the luminosity to each of them.

it cannot be due to small molecules ($\sim$ 50 C-atoms) since those would give rise only to a weak quasi-continuum in this wavelength region (Allamandola et al. 1989). Most of the emission will come out in discrete vibrational transitions (i.e. , the UIR bands). We attribute this continuum to a small fraction of dust in the HII region heated to high temperatures by resonantly scattered Lyman-alpha radiation.

4. CONCLUSIONS

The compact HII regions all show a very rich spectrum of atomic lines and strong emission bands of dust together with a continuum which can be attributed to Lyman-alpha heated dust.

The detailed profiles of the PAH features consist of a steep blue wing and a red tail. These characteristics are indicative of anharmonicity and therefore the PAH profiles are non-Lorentzian.

The spectral appearance of the PAH spectrum varies from source to source. These variations, in combination with a laboratory study of a wide variety of PAHs, will allow a detailed analysis of the PAH family. In particular, a correlation study may ultimately lead to the identification of the specific PAH species.

ACKNOWLEDGMENTS

We are greatly indebted to the SWS Instrument Dedicated Team (SIDT) at VILSPA for their support in the calibration and analysis of SWS data.

REFERENCES

Allamandola, L.J., Tielens, A.G.G.M., Barker, J.R. 1989, ApJS, 71, 733

Bakes, E.L.O. & Tielens, A.G.G.M. 1994, ApJ, 427, 822

Barker, J.R., Allamandola, L.J., Tielens, A.G.G.M. 1987, ApJ, 315, L61

Campbell, M.F., Niles, D., Nawfel, R. et al. 1982, ApJ, 261, 550

Clegg, P.E., Ade, P.A.R., Armand, C. et al. 1996, A&A, 315, L38

Colomé, C., Harvey P.M., Lester, D.F. et al. 1995, ApJ, 447, 236

de Graauw, Th., Haser, L., Beintema, D.A. et al. 1996, A& A, 315, L49

Gillet, F.C., Forrest, W.J. & Merril, K.M. 1973, ApJ, 183, 87

Hudgins, D.M., Sandford. S.A., Allamandola, L.J. 1994, J. Ph.Chem., 98, 4243

Hudgins, D.M. & Allamandola, L.J. 1995, J. Ph.Chem., 99, 3033

Kessler, M.F., Steinz, J.A., Anderegg, M.E. et al. 1996, A&A, 315, L27

Martin, L., Roelfsema, P.R., Tielens, A.G.G.M. et al. 1999, in preparation

Peeters, E., Roelfsema, P.R., Tielens, A.G.G.M. et al. 1999a, in preparation

Peeters, E., Tielens, A.G.G.M., Roelfsema, P.R. et al. 1999b, in preparation

Roelfsema, P.R., Goss, W.M., Geballe, T.R. 1989, A&A, 222, 247

Roelfsema, P.R., Cox, P., Tielens, A.G.G.M. et al. 1996, A&A, 315, L289

Scott, P.F., Harris, S. 1978, MNRAS, 182, 657

Smith, A., Jones, B. 1996, A&A, 555, 999

CAM-SW OBSERVATIONS OF THE 3.3 μm PAH FEATURE IN THE ORDINARY DIFFUSE ISM

D. Rouan[1], P. Le Coupanec[1], F. Lacombe[1], D. Tiphène[1]
P. Gallais[2], A. Léger[3], & F. Boulanger[3]

[1]DESPA, Observatoire de Paris–Meudon , Meudon, France
[2]CEA/DSM/DAPNIA Service d'Astrophysique, Gif-sur-Yvette, France
[3]Institut d'Astronomie Spatiale, Orsay, France

ABSTRACT

Beyond 5 μm, the ubiquitous presence of PAH-like emission features (UIBs) in all components of the ISM, including the diffuse weakly irradiated one, was fully demonstrated by ISO. The conclusion is less obvious regarding the 3.3 μm band, despite clear indications of such an universality exist. We present several observations performed at 3.3 μm with CAM-SW, pertaining to this question. The first two correspond to images through the diffuse ISM of edge-on spiral galaxies : the Milky Way on one side and NGC 891 on the other. The PAH band is detected in both cases, confirming the universal presence of the carrier of the band and, because the radiation field is weak, of its very small size, to allow for transient heating. In addition, we show that the sister band at 3.4 μm is especially enhanced in the galactic CVF spectrum, as was already predicted : if this result is confirmed, the hypothesis of alkyl groups substituted to H atoms, as the carrier of this band, would be strongly reinforced. The third set of data relates to the reflection nebula NGC 7023, where it is shown that the 3.3 μm band is found in filamentary structures that fit very precisely the filamentary structure observed in the near-IR H_2 rot-vib lines : this could be an indication of the efficiency of the mechanism of formation of H_2 on PAHs, proposed years ago.

Key words: Unidentified features; ISM; galaxies: individual: NGC 891, Galaxy, ISM: reflection nebulae: NGC 7023

1. INTRODUCTION

At $\lambda > 6$ μm, Unidentified Infrared Bands (at 6.2, 7.7 , 8.6, 11.3 μm) were detected with ISO in all components of the galactic and extragalactic ISM, including the diffuse moderately irradiated medium associated to molecular clouds or cirrus (Boulanger et al., 1996, 1998 ; Mattila, 1996). This discovery strongly supported the idea that only very small particles or big molecules could be the carriers of UIBs, emitting when transiently heated to high enough temperatures by a single UV photon, and this result advocates seriously in favour of the PAH hypothesis (Puget & Léger, 1989). Is the 3.3 μm band as ubiquitous as other UIBs in the diffuse ISM? This is one question that comes naturally to mind. The 3.3 μm band, clearly belonging to the same category of UIBs, is indeed observed in area of strong UV irradiation, such as starburst galaxies, HII regions or Planetary Nebulae, but was not as clearly identified in the more ordinary ISM, with the notable exception of wide field observations of the galactic plane (Giard et al., 1988; Tanaka et al., 1996; Onaka et al., 1997 ; Bernard et al., 1997). We present in the following a selection of observations at 3.3 μm, using CAM-SW (Cesarsky et al., 1996), of regions where the ISM is only moderately irradiated by the Interstellar Radiation Field. Since observations of the diffuse ISM generally means a low brightness, some tricks have to be used to reach a sufficient signal to noise ratio: one is to increase the column density by looking to lines of sight within the disk of the Milky Way or through edge-on external galaxies (Rouan et al. 1997), another one consists in looking at areas where the contrast of the emission is likely enhanced, such as in reflection nebulae.

2. NGC 891: AN EDGE–ON SPIRAL GALAXY

NGC 891 is a spiral galaxy of type Sb, with a strong bulge, which is sought to be very similar to the Milky Way. At a distance of 9 Mpc, it appears almost perfectly edge-on, so that a column density of the order of 10^{23}cm^{-2} should be probed. This galaxy has been already detected at 3.3 μm from the ground, but with a rather poor signal to noise ratio (Normand et al. 1994). Here, with CAM, two filters SW1 (broad) and SW2 (narrow) at 3.3 μm were used, at an integration time of 20 sec per image. Only the central 8 kpc were observed. Data were processed using the CIA package (Ott et al. 1998), with, in addition, a rather sophisticated attempt to cope with the transient effect of the detector (Tiphène et al. 1999). The continuum was evaluated and subtracted using the standard calibration data provided with the data set. A clear detection of the 3.3 μm band throughout the whole disk is apparent (see Fig. 1 for a com-

Proceedings of the Conference "The Universe as seen by ISO", Paris, France, 20–23 October 1998 (ESA SP-427, March 1999)

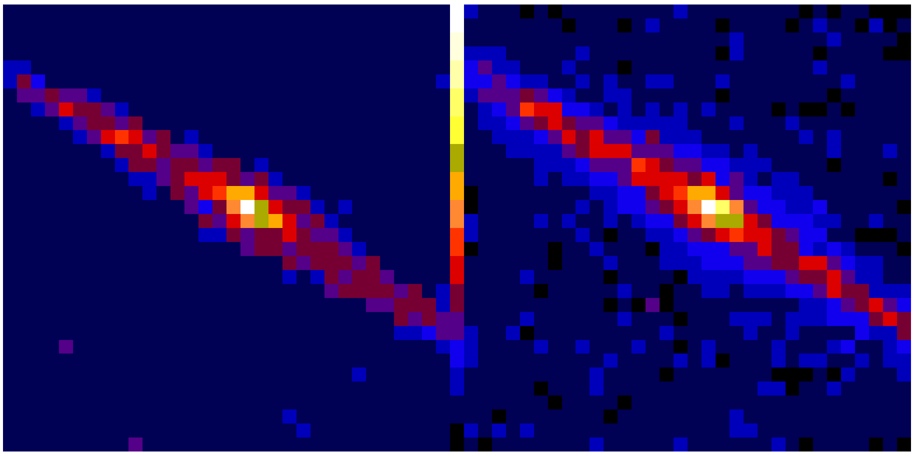

Figure 1. *Comparison of images at 3.3 μm of the edge-on galaxy NGC 891, obtained in the "continuum" (SW1) and in the 3.3 μm "PAH-band" (SW2). The emission in the band appears present at all location in the disk and in the bulge, with some enhancement at positions where arms are probably seen tangentially.*

parison of SW2 and SW1 images expressed in flux units). On top of the monotonic distribution which corresponds to a bright bulge and to a disk components, peaks of the 3.3 μm band are found at some places : comparisons with longer wavelengths data suggest that they are likely associated to star forming regions in spiral arms (see Le Coupanec et al. 1998). The intensity of the 3.3 μm band (f_ν(SW2) – f_ν(SW1)) appears on the average quite comparable, albeit somewhat smaller, to the one measured in the Milky Way (Giard et al. 1988), but this difference could reflect the photometric uncertainties, due to an unperfect correction of the transient effects. The level of the continuum, which is affected by a much less severe relative uncertainty, is remarkably similar to the Milky Way value (average of 12.7 MJy sr^{-1} versus 11.5 MJy sr^{-1} measured by Giard et al.). Excitation of the 3.3 μm emission requires high enough temperature of the carrier that cannot be reached by standard grains in the kind of medium we probe here : the unescapable conclusion is that, as in the Milky Way, the ISM of any external spiral galaxies must host an important population of extremely small aromatic compounds that are transiently heated by photons of the ISRF, PAHs molecules being one of the obvious candidates.

3. LOOKING THROUGH THE MILKY WAY

A quite ordinary line of sight through the galactic plane was selected at l_{II}=28.6 *deg*, b_{II}=0.8 *deg* and CVF scans performed from 3.1 to 3.8 μm, using the PFOV of 12 arcsec. Because of the weakness of the signal, the data sequence was affected by a strong transient effect which was processed as follows: (a) we selected pixels around the stars identified in the

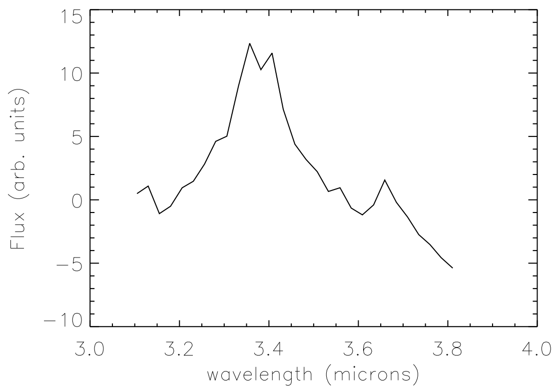

Figure 2. *3.1 to 3.8 μm spectrum of a selected area through the Milky Way, obtained with the CVF of CAM-SW. Only pixels around identified stars were selected in order to cope with the transient effect of the detector at low signal. A fit of the smooth transient effect is subtracted. The 3.3 μm band appears translated towards long wavelength, as if the 3.4 μm satellite band was becoming more important in the diffuse medium. This was recently predicted by Joblin et al. (1996), if -CH_3 groups are actually responsible of the 3.4 μm band.*

field (cross-identification with the Digitized Sky Survey was successful for several of them) allowing for a less severe lag effect ; (b) we used a fit of the unstabilized signal by a model which reveals to be very efficient (Tiphène et al. 1998) ; (c) we performed summation of all selected pixels in order to reach a sufficient signal to noise ratio. When the transient effect is correctly fitted to the underlying continuum and then subtracted, the resulting spectrum (Fig. 2), reveals a clear emission feature from 3.3 to 3.45 μm. One of the most conspicuous character of the feature is the shift of the band towards 3.4 μm. We do not exclude that this shift is due to an over-correction of the transient effect, but more likely it must correspond to an actual enhancement of the 3.4 μm band with respect to the 3.3 μm one. This is not unlikely since it was indeed predicted (Joblin et al., 1996) that the 3.4 μm feature could become stronger in conditions of low irradiation, if the band is due, as proposed by those authors, to the presence of the alkyl group ($-CH_3$) side group substituted to H at the periphery of PAHs. One note that we cannot pretend that we are measuring here the average emission of the diffuse medium : there may be some selection effect as we are looking only to matter surrounding ordinary stars within a typical radius of 0.5 pc (i.e. one pixel at 8 kpc), but anyhow, even in those conditions, the level of irradiation remains much lower than in reflection nebulae, for instance.

4. A REFLECTION NEBULA: NGC 7023

Finally we present observations at 3.3 μm of the archetype reflection nebula NGC 7023. Detection of the 3.3 μm band in this area is in fact known from years (Sellgren et al. 1985) but, here, the novelty is that we were able to observe it at a much smaller scale than previously done. Comparison of the two images in the SW2 and SW1 filters (Fig. 3) clearly reveals the detection of an emission in the 3.3 μm band, structured in twisted filaments to the north and to the south of the illuminating star HD200775. Those filaments, which have a typical thickness of 1000 AU, are obviously the exact counterpart of the H_2 (v=1–0, S(1)) filaments found by Lemaire et al. (1996) and in fact one can find a 3.3 μm correspondence to each of the H_2 filament. Despite their lower angular resolution, the features observed in the 6.2 and 11.3 μm bands (Cesarsky et al., 1996) clearly correspond to the same structured emission. We can derive several indications from those observations :

a) filaments should be actual density structures of high contrast rather than the projection of very thin shells, since this last interpretation (Field et al. 1994) was plausible in the case of excited H_2 (where the thickness of the slab is a result of the competition between UV excitation and UV dissociation), but is no longer meaningful for PAH excitation;

b) despite the likely high degree of ionisation of PAHs close to the exciting star (e.g. Rouan et al. 1992), the 3.3 μm band is still fairly intense : this does not agree with the theoretical prediction of a quasi-complete lack of 3.3 μm band emission for ionised species (DeFrees et al., 1993) and questions a current interpretation of 3.3 μm depletion in AGN or starburst (e.g. Normand et al. 1994);

c) there is apparently a very direct link between the presence of H_2 and the presence of excited PAHs. A plausible explanation would be that the surface of PAHs freshly expelled from grain mantles at the border of the molecular cloud, would be the place where H_2 would form through some chemi-sorbtion process (Omont 1986).

5. CONCLUSION

We have clearly detected the 3.3 μm band in three different components of the ISM where the interstellar radiation field is much lower than in regions where this band was classically observed: at a small scale in the reflection nebulae NGC 7023, across the galactic plane around normal stars and in the quiet spiral galaxy NGC 891. The band appears thus as ubiquitously found in the diffuse ISM as the other UIBs at longer wavelength, at least in the nearby Universe. Since UV photons in those regions are scarce, these observations strengthen the hypothesis of aromatic molecules (PAH-like) transiently heated by single photons, as the carrier of this band. Besides the confirmation of the widespread distribution of the carrier of the 3.3 μm band, our observations revealed that : *(a)* the 3.4 μm satellite band is enhanced with respect to the 3.3 μm feature in the ordinary diffuse medium, at least around normal stars, a result that would support the idea that alkyl groups are responsible of the 3.4 μm band ; *(b)* the emission in the 3.3 μm feature is a tracer of the very small scale structure of the medium, revealed under the form of thin twisted filaments ; the excellent coincidence with a same filamentary emission of excited H_2 suggests that H_2 molecules could could form efficiently at the surface of PAHs as proposed years ago.

REFERENCES

Bernard, J.P. et al. 1997, in “Diffuse Infrared Radiation and the IRTS”, ASP Conference Series, vol. 124, p. 161

Boulanger, F., Reach, W., Abergel, A., et al. 1996, A&A, 315, L325

Boulanger, F., Abergel, A., Bernard, J.P. et al. 1998, in “Star Formation with the Infrared Space Observatory”, 24-26 June 1997, Lisbon, Portugal, ed. Joao Yun and Rene Liseau, Publisher: ASP, as volume 132 of ASP Conference Series. p. 15

Cesarsky, C.J., Abergel, P., Agnèse P. et al. 1996, A&A 315, L32

Cesarsky, D., Lequeux, J., Abergel, A. et al. 1996, A&A 315, L305

DeFrees, D.J., Miller, M.D., Talbi, D., et al. 1993, ApJ 408, 530

Field, D., Gerin, M. , Leach, S., Lemaire, J.L. , Pineau des Forêts, G., Rostas, F., Rouan, D., Simons, D. 1994, A&A, 286, 909

Giard, M., Serra, G., Caux, E., Pajot, F., Lamarre, J. M. 1988, A&A, 201, L1

Joblin, C., Tielens, A.G.G.M., Allamandola, L.J., Geballe, T.R. 1996, ApJ 458, 610

Le Coupanec, P., Rouan, D., Gallais, P. et al. 1998, in these proceedings

Lemaire, J.L. , Field, D. , Gerin, M. , Leach, S., Pineau des Forêts, G. , Rostas, F. , Rouan, D., 1995 A&A 308, 895

Mattila, K., et al. 1996, A&A 315, L353

Normand, P., Rouan, D., Tiphène, D., Lacombe, F. 1994, Infrared Phys. Technol., 35, 383

Normand, P., Rouan, D., Lacombe, F., Tiphène, D. 1995, A&A 297, 311

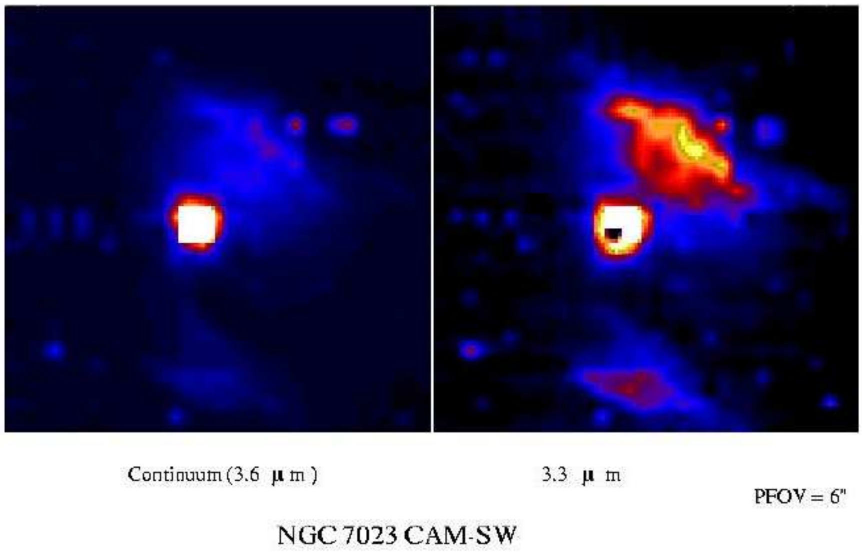

Figure 3. Comparison of 3.3 μm images of the reflection nebula NGC 7023, obtained in the "continuum" (SW1) and in the 3.3 μm "PAH-band" (SW2). The emission in the band appears located in filaments at NNW and S of the illuminating star (at center) that coincide exactly with the H_2 (v=1–0, S(1)) filaments seen at 2.16 μm. This suggests a direct link between the two emissions, may be an efficient formation of H_2 on PAHs freshly evaporated from grains mantles at the border of the molecular cloud.

Omont, A., 1986, A&A, 164, 159

Onaka, T. 1997, in "Diffuse Infrared Radiation and the IRTS", ASP Conference Series, vol. 124, p. 170

Ott, S., Gastaud, R., Abergel, A. et al. 1998, Astronomical Data Analysis Software and Systems VII, A.S.P. Conference Series, Vol. 145, R. Albrecht, R.N. Hook and H.A. Bushouse (eds.), p.275

Puget, J. L., Léger, A.1989, ARA&A 27, 161

Rouan, D., Léger,A., Omont, A., Giard, M. 1992, A&A 253, 498

Rouan, D., Le Coupanec, P., Lacombe, F., Tiphène, D., Gallais, P., Giard, M., Léger, A. 1997, in "Diffuse Infrared Radiation and the IRTS", ASP Conference Series, vol. 124, p. 170

Sellgren, K. et al. 1985, ApJ 299, 416

Tanaka, M., Matsumoto, T., Murakani, H., et al. 1996, PASJ, 48, L53

Tiphène, D., Rouan, D., Epstein, G., et al. 1998, Experim. Astron., in press

D/HD TRANSITION IN PHOTON-DOMINATED REGIONS

E. Roueff & T. Node-Langlois

[1]DAEC, Observatoire de Paris, Meudon, France

ABSTRACT

We consider the various formation/destruction and excitation processes associated to the deuterated hydrogen molecule in photon-dominated regions. The geometry of the cloud is assumed to be plane-parallel with an ultraviolet (UV) field impinging on one side of the cloud. The rotational equilibrium of the HD molecule is then obtained as a function of the visual extinction for various densities and values of the ultraviolet interstellar radiation field (ISRF). Prediction of the submillimeter rotational lines of HD is given.

Key words: interstellar medium; interstellar molecules; deuterium.

1. INTRODUCTION

The deuterium to hydrogen ratio is an important parameter for our knowledge of the universe formation and its observational determination is still subject to large uncertainties. In dense interstellar clouds, deuterium is probably mainly in molecular form whereas it is mainly atomic in diffuse clouds permeated by the UV ISRF. We consider the case of dense photon-dominated regions where the competition between photodissociation and formation processes leads to comparable atomic and molecular column densities. Section 2 gives the main features of our model, subsection 2.1 presents the input data of our model and we display in section 3 some typical results of our model. The recent detection obtained by the ISO satellite of the 112 μm line of HD in the Orion bar is in satisfactory agreement with the present model for the expected physical conditions.

2. PHOTON-DOMINATED REGION MODEL

We consider a steady state model of an interstellar cloud as an infinite slab of gas and dust illuminated on one side by the UV ISRF described by a multiplicative factor χ of the "standard" ISRF given by Draine (1978). The radiative transfer is solved by assuming a decoupling between continuum (due to dust absorption) and discrete lines due to the gas. The model is an extension of the model of Abgrall et al. (1992) and Le Bourlot et al. (1993) where the UV absorption lines of HD have been specifically introduced in addition to H_2 and CO. The resolution of the chemical equations and the energy balance is performed simultaneously and the temperature is then determined for different constant proton densities. Despite the fact that HD has the same electronic structure than H_2 , and that photodissociation of HD proceeds as in H_2 by the spontaneous radiative fluorescence towards the continuum of the ground state following an absorption in the Lyman and Werner discrete absorption, a number of significative differences should be mentioned concerning the physical processes involved:

- The HD molecule has a small permanent dipole moment due to the non coincidence between the center of mass and the center of charges (contrary to the H_2 molecule). Electric dipole rotational transitions may then occur inside the ground electronic state.
- The formation of HD on grains is less efficient than H_2 . The corresponding reaction rate coefficient is assumed to be given by that of H_2 divided by the square root of the mass ratio between both molecules.
- However, once the H_2 molecule is formed, HD is also efficiently produced in the gas phase through the reaction $D^+ + H_2 \longrightarrow H^+ + HD$

2.1. Molecular data introduced for HD

The various mechanisms involved in the UV pumping of the HD molecule are displayed on Fig. 1.

We have thus introduced in our numerical code

- the Lyman and Werner transitions of HD (whose transition probabilities have been calculated by including the rotational centrifugal terms) to calculate the UV absorption probabilities and photodissociation probabilities,
- the radiative dipolar cascades taking place inside the ground state (Abgrall et al. 1982)

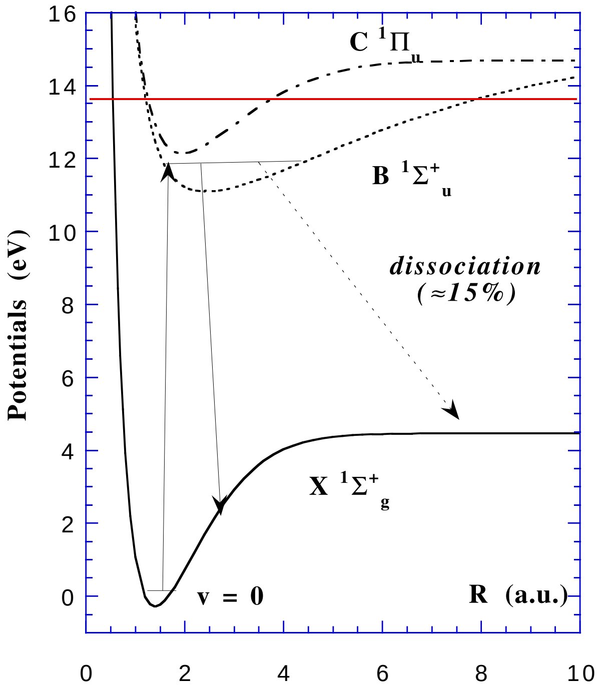

Figure 1. *Photodissociation mechanism and excitation of HD occurring after the absorption of an UV photon*

- the chemical formation/destruction processes on the grains and in the gas phase (Viala et al. 1988)
- the collisional excitation and deexcitation of rotational levels of HD due to H, He, H_2 and electrons. These latter data are presently not yet fully determined. The model calculations presented here have been performed with the available data, i.e. results of Schaefer (1990) for the rotational excitation of HD by He and H_2 and the excitation rates given by Viala et al. 1988 for the other perturbers[1]. 9 rotational levels of HD have been introduced, which implies some extrapolation of the rate coefficients which have been computed for smaller values of the rotational quantum number.

We have assumed a deuterium to hydrogen ratio of 2×10^{-5}.

3. RESULTS

Figure 2 displays the various photodissociation probabilities of H_2 , HD and CO as a function of the visual extinction for an interstellar cloud model in which $n_H = 10^6 cm^{-3}$ and $\chi = 10^4$.

As H_2 is much more abundant than HD, its self-shielding is more efficient as shown on Fig. 2. We have calculated the rotational equilibrium of HD by using the cascade formalism described in Viala et al. (1988) and deduced the emissivity of the dipolar

[1]We have computed the rotational excitation collision rates due to H and He since the model calculations have been performed (Roueff & Flower 1998 and Roueff & Zeippen 1998)

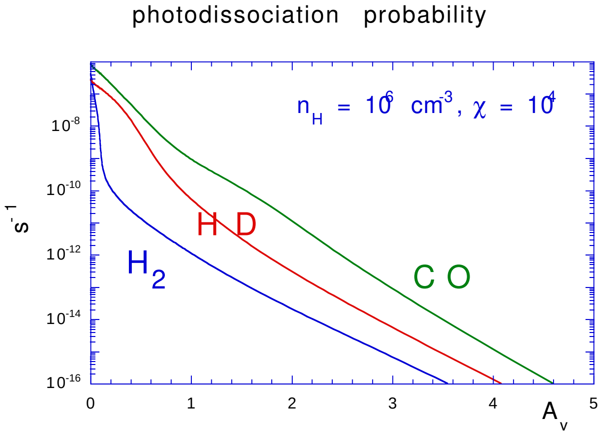

Figure 2. *The hierarchy of photodissociation probabilities of* H_2 *, HD and CO as a function of the visual extinction for a model in which* n_H *is equal to* $10^6 cm^{-3}$ *and the multiplicative factor of the radiation field is* 10^4 *.*

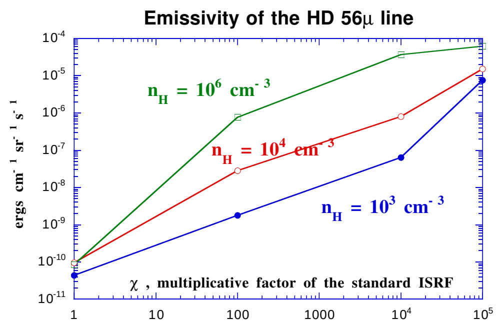

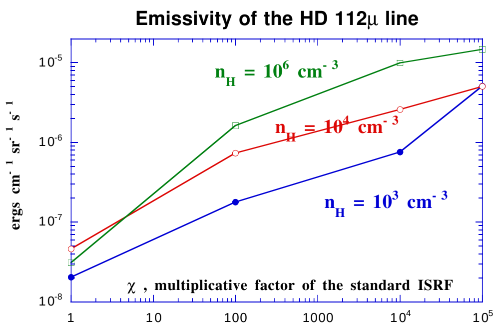

Figure 3. *The emissivity of the 1-0 and 2-1 lines of HD for a cloud of visual extinction of 10 with different densities and multiplicative factors of the ISRF.*

transitions emitted from the excited rotational levels which are in the wavelength range attainable by ISO. The corresponding values are displayed on Fig. 3 for a cloud with a visual extinction of 10 for different values of the densities and the ISRF. The values shown are in qualitative agreement with the determination of Wright et al. (1999) of the emissivity of the 112 μm line detected by ISO in the Orion bar region for the expected physical conditions ($n_H = 10^5$ and $\chi = 10^5$). The improvement of the data reduction facilities should allow other detections of HD with ISO. We now plan to introduce the new available collision rates (Roueff & Flower 1998) and Roueff & Zeippen (1998) in the model.

ACKNOWLEDGMENTS

We thank Dr Hervé Abgrall for his help in the calculations of the transition probabilities of the Lyman and Werner electronic transitions of HD.

REFERENCES

Abgrall, H., Roueff, E., Viala, Y. 1982, A&AS, 40, 505

Abgrall, H., Le Bourlot, J., Pineau des Forêts,G., Roueff, E., Flower, D.R., Heck, L. 1992, A&A, 253, 525

Draine, B. 1978, ApJS, 36, 595

Le Bourlot, J., Pineau des Forêts, G., Roueff, E., Flower, D. 1993, A&A, 267, 233

Roueff, E., Flower, D. 1998, MNRAS, in press

Roueff, E., Zeippen, C. 1998, A&A, in press

Schaefer, J. 1990, A&AS, 85, 1101

Viala, Y., Roueff, E., Abgrall, H. 1988, A&A, 190, 215

Wright, C.M.,van Dishoeck, E.F., Cox, P., Sidher, S., Kessler, M.F. 1999, ApJL, in press

THE IMPACT OF NEW IONIZING FLUXES ON ISO OBSERVATIONS OF H II REGIONS AND STARBURSTS

D. Schaerer[1] **& G. Stasińska**[2]

[1]Observatoire Midi-Pyrénées, Laboratoire d'Astrophysique, Toulouse, France; schaerer@obs-mip.fr
[2]DAEC, Observatoire de Meudon, Meudon, France; grazyna.stasinska@obspm.fr

ABSTRACT

Extensive grids of photoionization models have been calculated for single star H II regions and evolving starbursts. We illustrate the predictions for IR fine structure lines which are used to analyse the stellar content, and derive properties such as the age and IMF. The impact of recent ionizing fluxes on the IR lines are shown. First comparisons of our starburst models with IR-diagnostics and the ISO observations of Genzel et al. (1998) are also presented.

Key words: HII regions, galaxies: starburst.

1. INTRODUCTION

The analysis of fine structure lines is crucial to interpret IR observations of ultra-compact H II regions, giant H II regions and starburst galaxies in terms of their stellar content. Through photoionization modeling the nature of the ionizing sources of H II regions and properties of starburst regions such as the age and the IMF (slope, upper mass-cutoff) can in principle be determined. Considerable progress has been made in the recent year in this respect through the use of new stellar fluxes, spectral energy distributions appropriate for evolving stellar populations at different metallicities and including detailed observational constraints (e.g. Garcia-Vargas et al. 1995, 1997, Stasińska & Leitherer 1996, Stasińska & Schaerer 1997, González-Delgado et al. 1998). None of these studies have, however, focussed on IR observation which are now becoming widely available thanks to ISO.

In this contribution we present exploratory results regarding predictions of IR lines from two sets of recent photoionization models: *1)* Single star H II regions using the latest ionizing fluxes from non-LTE, line blanketed atmospheres including stellar winds (*CoStar* models, Schaerer & de Koter 1997) and, *2)* Photoionization models for evolving starburst populations based on the Leitherer & Heckman (1995) synthesis models. Detailed results from new photoionization models for starbursts including the *CoStar* models and updated stellar tracks will be presented elsewhere.

2. SINGLE STAR HII REGION MODELS

In Figure 1 we illustrate the behaviour of the line ratios of some important fine structure lines observable in the SWS range and with ISOCAM/CVF. This figure, based on the model calculations of Stasińska & Schaerer (1997, hereafter SS97), shows the dependence of the line ratios on the stellar temperature and – importantly – also on the ionization parameter. The comparison between the top and bottom row shows the differences obtained using either the recent *CoStar* atmosphere models or Kurucz plane parallel LTE models. Due to the harder spectrum predicted by the *CoStar* models above $\sim$ 35-40 eV (Schaerer & de Koter) a *higher excitation* is generally predicted for a given $T_{\rm eff}$ than with Kurucz models (see SS97).

Evidence supporting such an increase of the hardness of the ionizing flux comes from the KAO observations of Rubin and coworkers (cf. Simpson et al. 1995). Indeed, the *CoStar* models including stellar winds, non-LTE effects and line blanketing are thereby able to provide a satisfactory description of the Ne^{++}/O^{++} ionic fractions (see SS97, also Sellmaier et al. 1996).

Encouraged by these successes atmosphere models including the most relevant physical processes (stellar winds, non-LTE, blanketing) continue to be improved. See e.g. Pauldrach (1997) and Schaerer (1997) for recent progress reports. In addition more stringent tests using ISO observations of nebulae with well known ionizing sources would be extremely valuable. Detailed photoionization modeling including constraints on the nebular geometry and likely also their dust content will be necessary to achieve such a goal.

In Fig. 2 we plot the predictions for single star H II regions for some quantities of interest for the interpretation of integrated populations discussed later. The middle and right panels show the ratio of luminosity in the Lyman continuum (assuming an average photon energy of 16 eV) $L_{\rm Lyc}$ to the [Ne II] and [S III] line luminosity respectively. It is useful to understand the behaviour of the [Ne II]/[S III] 12.8/33.5 ratio (left) since either of these lines is sometimes used as a proxy in case the other line is unobservable (cf. Genzel et al. 1998). Indeed for a given $T_{\rm eff}$ one obtains a relatively small variation ($\sim$ 1 dex) of

Proceedings of the Conference "The Universe as seen by ISO", Paris, France, 20–23 October 1998 (ESA SP-427, March 1999)

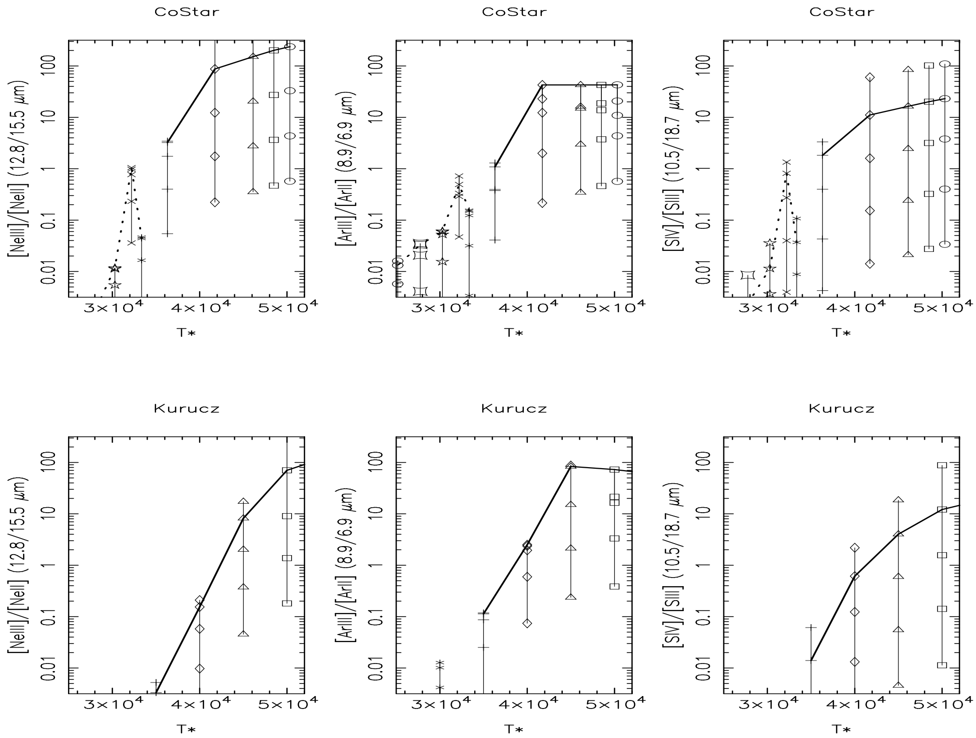

Figure 1. Top row: Photoionization models using CoStar *fluxes (dwarf models for $T_{\rm eff}$ > 35000 K, supergiant models otherwise. Bottom: same with Kurucz models. Models at solar metallicity with varying ionization parameter U over 4 dex (typically* $\log U \sim$ *-5 to -1). Solid lines connect models with U typical for giant H* II *regions or for bright single star H* II *regions ("reference model" of SS97).*

[Ne II]/[S III] with the ionization parameter. In all our "reference models" (constructed assuming a gas density of 10 cm^{-3}) we predict [Ne II]/[S III] < 1. For stars with $T_{\rm eff}$ > 36 kK the differences between the *CoStar* and Kurucz fluxes become non-negligible for [Ne II]/[S III]. Some implications of these finding are briefly discussed below.

3. PHOTOIONIZATION MODELS FOR EVOLVING STARBURSTS

IR fine structure lines provide a new tool to study the hot star population of obscured starbursts. Through comparisons with photoionization modeling this allows in particular to constrain the star formation history and the upper end of the initial mass function (e.g. Lutz et al. 1998). Empirical diagnostic diagrams based on IR lines also allow the distinction between starburst and AGN powered sources (Genzel et al. 1998). Theoretically these diagnostics remain, however, to be understood and quantified.

To address such questions photoionization models representing evolving starbursts at different metallicities are nowadays required. In the following we will briefly illustrate some predictions from such models for fine structure lines in the ISO LWS range. The predictions shown here are drawn from the models of Stasińska & Leitherer (1996, hereafter SL96, available by anonymous ftp from ftp.obspm.fr/pub/obs/grazyna/cd-crete). Detailed results from new photoionization models for young starbursts based on the most recent evolutionary synthesis models of Schaerer & Vacca (1998) including the latest Geneva stellar tracks and *CoStar* model atmospheres (cf. above) will be presented elsewhere.

In Figure 3 we show the computed temporal evolution of the line ratios of [Ne III]/[Ne II] 12.8/15.5 μm, [Ar III]/[Ar II] 8.9/6.9 μm, and [S IV]/[S III] 10.5/18.7 μm (all top row) for an instantaneous burst at 1/4 solar metallicity with a Salpeter IMF and $M_{\rm up}$ = 100 M$_\odot$ surrounded by a gas cloud of density n=10 cm^{-3}. Different symbols represent models with different (initial) ionization parameters: typically one has $\log U \sim -5$ (circles) to $\log U \sim -1$ (crosses). Note that in photoionization models of evolving starbursts, the dependence of U with time is a function of the adopted geometry, as stressed by Stasińska (1998). In the models of SL96, U decreases slightly with time.

As expected the excitation decreases with the age of the burst. It must, however, be reminded that the considered lines also strongly depend on the ionization parameter (see Fig. 3). Indeed the line ratios shown here vary typically by three orders of magnitudes for variations of U of 4 orders of magnitudes. For comparison a change of the upper mass-cutoff from 50 to 100 M$_\odot$ increases the same line ratios by less than one order of magnitude (e.g. Lutz et al. 1998). In general U is poorly constrained. Although optical spectra of H II galaxies can be reproduced with models covering only a fairly small range of U ($\sim$ 1 dex, SL96) this is not necessarily the case for

ISO observations of starburst galaxies. This question needs a careful analysis before meaningful results can be derived on the IMF, age etc.

Genzel et al. find an empirical value of [Ne II]/[S III] = 1.7 ± 1.3 (or 1.2 ± 0.6 excluding the two largest outliers) from their sample of 10 starbursts. The SL96 models constructed with a density of n=10 cm^{-3} typically predict [Ne II] < [S III] (this is true also for solar metallicity models, not shown here). However, the SL96 models with n= 10^4 cm^{-3} reach [Ne II]/[S III] of 1.5, due to collisional deexcitation of [S III]. The electron densities deduced from [S III] 18.7/33.5 for a subset of starburst galaxies from the Genzel et al. sample so it seems that collisional deexcitation is not sufficient to explain the large [Ne II]/[S III] observed. Among possible factors to reduce the discrepancy are an Ne overabundance (which however needs to be understood in more detail), or a softer ionizing radiation field. We conclude that the empirical value [Ne II]/[S III] ~ 1.7 for starbursts used in the diagnostic diagrams of Genzel et al. (1998) is theoretically not well understood yet.

For comparisons of the Lyman continuum luminosity $L_{\rm Lyc}$ to the bolometric luminosity of starbursts, ULIRGS, etc. it is interesting to be able to derive $L_{\rm Lyc}$ from the IR fine structure lines. This requires, however, some empirical calibration or the use of models. "Empirical" values of $L_{\rm Lyc}/L$([Ne II]) = 64 ± 37 and $L_{\rm Lyc}/L$([S III]) = 105 ± 61 are obtained from the starburst sample of Genzel et al. excluding NGC 5253, which shows much larger values. It must be reminded that $L_{\rm Lyc}$ is derived from the Brackett recombination lines assuming case B and an average photon energy of 16 eV, and neglecting the absorption of Lyc photons by dust.

Our model predictions show in Fig. 3 (mid/right bottom panels) for the instantaneous burst model show quite a wide range for the $L_{\rm Lyc}$/line ratios, depending on age and ionization parameter. Although these idealised models (instantaneous burst) are not necessarily representative for the average starburst population observed through the ISO aperture it is instructive to compare our predictions with the "observed" values of Genzel et al. In any case the predicted values of $L_{\rm Lyc}/L$([Ne II]) are systematically larger than the empirical starburst value even for the oldest age considered here. Using the *CoStar* model atmospheres will even further increase the predicted value given their harder energy distribution with respect to the Kurucz ones. The $L_{\rm Lyc}/L$([S III]) ratio shows a better agreement with the average value from Genzel et al. This is consistent with the discrepancy between the model predictions for [Ne II]/[S III] and the observations discussed earlier. Most probably, the Lyc luminosities derived from the observations are underestimated because they do not take into account dust absorption of Lyc photons. More detailed analysis are required to obtain consistent a consistent picture of the fine structure lines in such objects.

4. CONCLUSIONS

We have illustrated the impact of the recent *CoStar* ionizing fluxes on IR fine structure lines for single star H II regions and shown predictions of IR lines for evolving starbursts resulting from calculations of extensive grids of photoionization models (see SL96, SS97).

As shown earlier, ionizing fluxes from non-LTE, line blanketed atmospheres including stellar winds predict a harder spectrum (Schaerer & de Koter 1997) leading to higher excitation in the nebula. These predictions are supported by comparisons with optical and pre-ISO (KAO) IR observations of H II regions (SS97 and references therein). Detailed models of ultra-compact H II regions or H II regions with well-known stellar content based on ISO observations and other observational constraints will be extremely useful to better constrain the atmosphere models and probe the importance of other effects (e.g. dust) usually neglected in photoionization models. Such studies also provide important tests for our understanding of more complex objects like starbursts.

For starbursts we have illustrated the behaviour of line ratios which can in principle be used to constrain burst properties such as the age, IMF slope and upper mass-cutoff. We have also studied the behaviour of the [Ne II]/[S III] ratio and diagnostics of $L_{\rm Lyc}$ from fine structure lines extensively used by Genzel et al. (1998). We have shown that a thorough analysis of the properties of the *nebular* gas (ionization parameter, geometry, dust content, total amount of gas) is needed for reliable determinations of the *stellar* content of the nebulae observed by ISO.

ACKNOWLEDGMENTS

DS thanks the LOC for financial support.

REFERENCES

García-Vargas et al. 1995, A&AS,

García-Vargas et al. 1997, ApJ 478, 112

Genzel R., et al. 1998, ApJ 498, 579

González-Delgado et al. 1998, ApJ 495, 698

Leitherer C., Heckman T. 1995, ApJS 96, 9

Lutz D., et al. 1998, in "Star Formation with the Infrared Space Observatory", ASP Conf. Series 132, 89

Pauldrach A. 1997, in "Boulder Munich Workshop II: Properties of Hot Luminous Stars", ASP Conf. Series 131, 258

Schaerer D. 1997, in "Boulder Munich Workshop II: Properties of Hot Luminous Stars", ASP Conf. Series 131, 310 (astro-ph/9709225)

Schaerer D., de Koter A. 1997, A&A, 322, 598

Schaerer D., et al. 1996, A&A, 312, 475

Schaerer D., Vacca W.D. 1998, ApJ, 497, 618

Sellmaier F., et al. 1996, A&A 305, L37

Stasińska G. 1998, in "Dwarf Galaxies and Cosmology", Eds. T.X. Thuan, C. Balkowski, V. Cayette, J. Tran Than Van, Editions Frontières (Gif-sur-Yvette, France), in press

Stasińska G., Schaerer D. 1997, A&A, 322, 655

Stasińska G., Leitherer C. 1996, ApJS, 107, 66

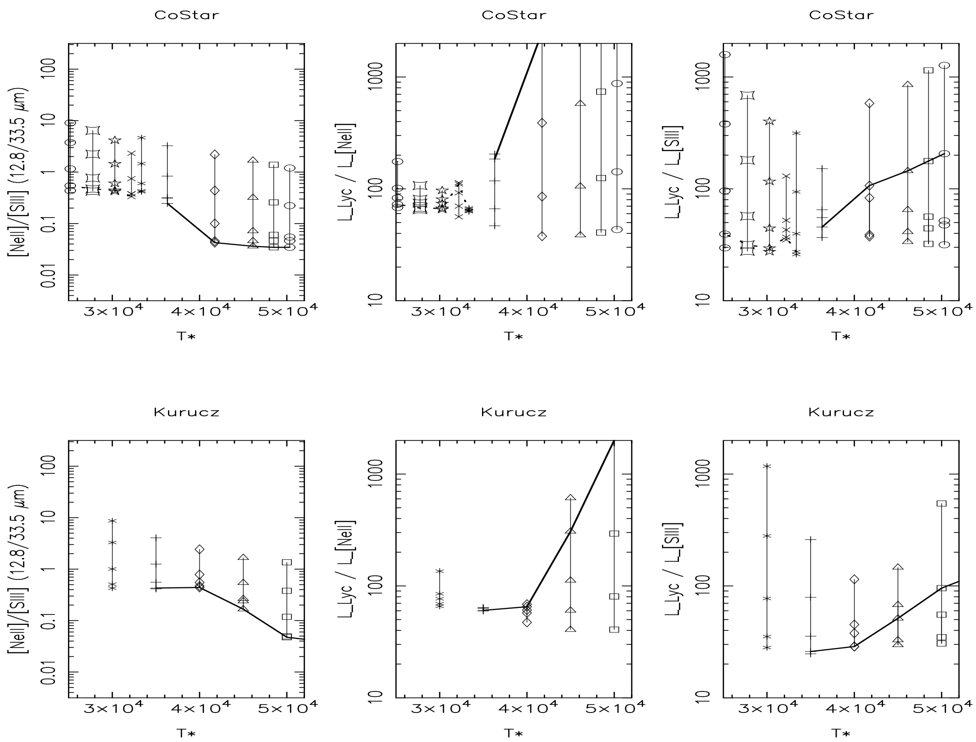

Figure 2. Same conventions as Fig. 1.

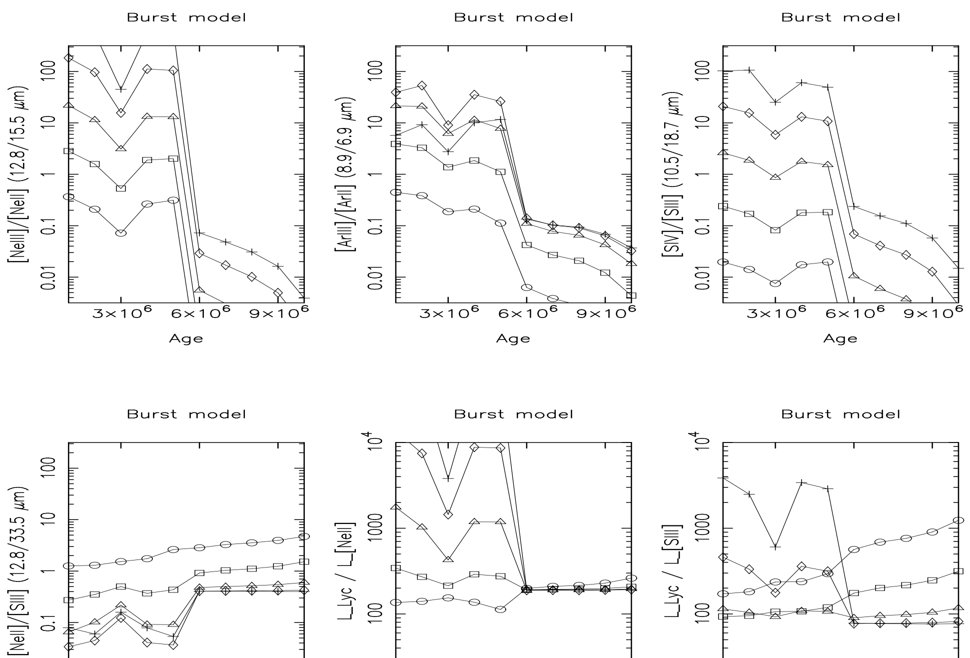

Figure 3. Photoionization models for evolving starburst (instantaneous burst, Salpeter IMF, $M_{\rm up}$ =100 $M_\odot$, $Z = 1/4 Z_\odot$) and varying ionization parameters ($\log U \sim$ -5 to -1, circles to crosses).

SUBMM- AND FIR OBSERVATIONS OF THE S106 PHOTON DOMINATED REGION

N. Schneider[1,2], **C. Kramer**[1], **R. Simon**[1], **J. Stutzki**[1], **& G. Winnewisser**[1]

[1] I. Physik. Institut, Universität zu Köln, Köln, Germany
[2] Observatoire de Grenoble, Université Joseph Fourier, Grenoble, France

ABSTRACT

Mapping of the S106 region in the [CII] 158 μm and [OI] 63 and 145 μm fine structure lines, using the KAO, and the ^{13}CO J=6$\rightarrow$5 line with KOSMA, revealed that the PDR around the exciting star S106 IR is extended on a size scale of $10' \times 3'$. The [CII] 158μm/[OI] 63μm line ratio in a 55″ beam centering S106 IR accounts for a gas temperature of 500 K and a density around 10^5 cm^{-3}. The cold molecular gas component was mapped in isotopomeric J=1$\rightarrow$0 and 2$\rightarrow$1 lines in the 'on-the-fly' mapping mode at the IRAM 30m telescope. The data reveal the fragmented structure of the region with a pronounced eastern peak, coinciding with the maximum of [OI] emission. Channel-maps of the ^{12}CO 2$\rightarrow$1 emission reveal the eastern peak at blueshifted velocities between –8 and –3.5 km s^{-1} to be due to strong and highly localized outflow emission. The red wing is much weaker and more dispersed.

Key words: Submm astronomy; FIR astronomy; PDRs; Molecular Clouds.

1. INTRODUCTION

The clumpy and filamentary nature of molecular clouds leads to a deep penetration of UV photons into the cloud. The radiation dissociates and ionizes molecular and atomic species, creating Photodissociation Regions (PDRs) on the surfaces of individual clumps. The UV-heated PDR gas cools via characteristic FIR and submm lines, e.g. the [CII] 158 μm and [OI] 63 μm and 145 μm fine structure lines and the mid- to high-J CO lines, which are studied in order to reveal the impact of PDRs on the physics and chemistry of molecular clouds. We present here observations of these PDR tracing lines as well as low-J CO molecular lines, characterizing the colder molecular gas component, in the Sharpless 106 region.

2. THE S106 REGION

The HII region S106 in Cygnus is a prominent bipolar emission nebula, associated with a molecular cloud. The optical and radio emission of the nebula is formed in two lobes with a linear extent of $3'$, seperated by a dark bar which is devoid of optical and radio continuum emission. The bar was initially interpreted as a large-scale molecular gas disk around the exciting star S106 IR (Bally 1982) but more recent interpretation assume that the PDR lines and CO emission arises from a clumpy molecular cloud and/or the fragmented remnants of a molecular torus around S106 IR.
The nebula is most likely excited only by a single O9 star (S106 IR), which created a bright PDR (Tielens et al. 1985). But though S106 has been extensively studied in various optical and radio lines as well as in continuum emission, there are only few observations of typical PDR tracers or extended molecular line maps at higher angular resolution. Therefore, we started a multiwavelength study of S106 in various fine structure lines, using the Kuiper Airborne Observatory (KAO) and the Infrared Space Observatory (ISO) for these observations, and molecular lines, using the IRAM 30m and KOSMA 3m radio telescopes.

3. OBSERVATIONS AND RESULTS

3.1. FIR fine structure lines

We observed S106 in the [CII] 158 μm and [OI] 63 and 145 μm fine structure lines with the MPE/UCB Fabry-Perot Interferometer FIFI (Poglitsch et al. 1991) onboard the KAO. The [CII] 158 μm map at an angular resolution of 55″ (Fig. 1) covers an area of $10' \times 3'$ with peak emission at the exciting star S106 IR at RA(1950)=$20^h22^m33.8^s$ and DEC(1950)=$37°12'50''$. The overall structure is similar to the 25″ resolution ^{12}CO 6$\rightarrow$5 map obtained by Harris et al. 1987, indicating that the PDR extends deep into the molecular cloud. The higher angular resolution [OI] observations at 22″ show more structure, a pronounced peak of [OI] emission is located 20″ east of S106 IR, coinciding with an eastern CO peak found in the IRAM CO-maps.
The [CII] 158μm/[OI] 63μm line ratio in a 55″ beam centering S106 IR is 0.1, which accounts for a gas temperature of 500 K and a density around 10^5 cm^{-3} (Tielens et al. 1985).

Proceedings of the Conference "The Universe as seen by ISO", Paris, France, 20–23 October 1998 (ESA SP-427, March 1999)

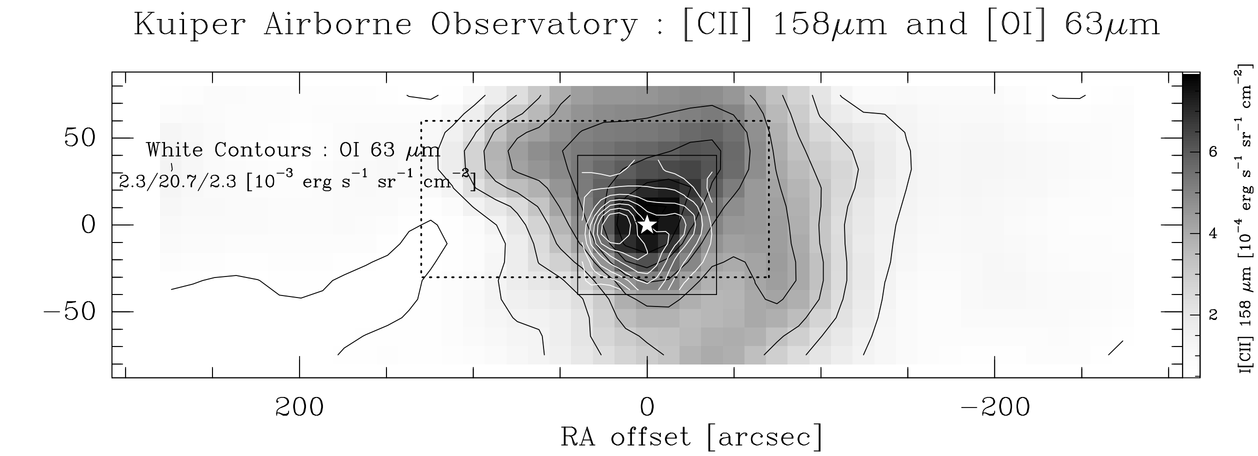

Figure 1. The extent of the PDR region of S106 is outlined by the integrated [CII] 158 μm emission (55″ angular resolution), the major cooling line for UV heated gas at densities around 10^3 cm^{-3} and temperatures around 100 K. The [CII] emission peaks at S106 IR (marked with a star), in contrast to the higher resolution (22″) [OI] 63 μm observations, which show peak emission at the eastern CO-clump. The contour levels both start at the σ-level (0.5×10^{-4} erg s^{-1} sr^{-1} cm^{-2} for the [CII] data in steps of 2σ). The region observed in the ^{13}CO 6→5 line with KOSMA is indicated with dashed lines.

The ISO observations concentrate on two positions within the PDR region. The observations constitute an LWS01 scan between 45 and 195 μm, including the [CII] and [OI] lines obtained with the KAO, and SWS data on the H_2 S(0), S(1) and S(2) lines at 28, 17 and 12 μm, the SiII line at 34.8 μm, the FeII and SI lines between 25 and 26 μm and OIII between 52 and 88 μm. Data reduction and analysis is on its way.

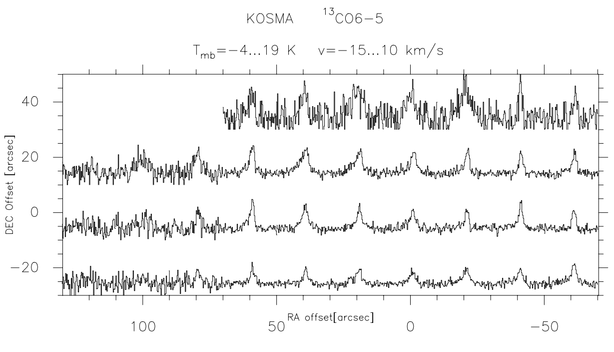

Figure 2. The ^{13}CO 6→5 spectra, recently obtained with KOSMA, show non-gaussian line profiles with a broad underlying component and pronounced wing emission at blueshifted velocities in the region around S106 IR (0,0).

3.2. Submillimeter CO-lines

The extend of the warm, molecular gas component of the PDR was determined by observations of the ^{13}CO 6→5 line at the KOSMA 3m-telescope in February 1998. The observatory has recently been equipped with a new telescope (including pedestal, backstructure, main reflector and wobbling secondary) with a surface accuracy of about 30 μm to date for the main dish (Kramer et al. 1998). A total of 37 positions (Fig. 2), centering on S106 IR, was mapped fully sampled. The HPBW was 38″ and the main beam efficiency 0.48 at 660 GHz. A preliminary analysis indicates that the 6→5 emission is extended on a (main beam brightness) temperature scale of 3 to 12 K. A two-component gaussian fit gives a low intensity (3–6 K), broad (FWHM typically around 6 km s^{-1}) component at –2.5 km s^{-1} and a higher intensity line (8–12 K) with a FWHM around 2 km s^{-1} at –1.4 km s^{-1}. The peak intensity of around 12 K is found at offset (60″,0), close to the [OI] emission peak and still in a region with significant [CII] emission, whereas in the outskirts of the PDR, indicated by a strong gradient of decreasing [CII] emission, the CO line is reduced to about 6 K.

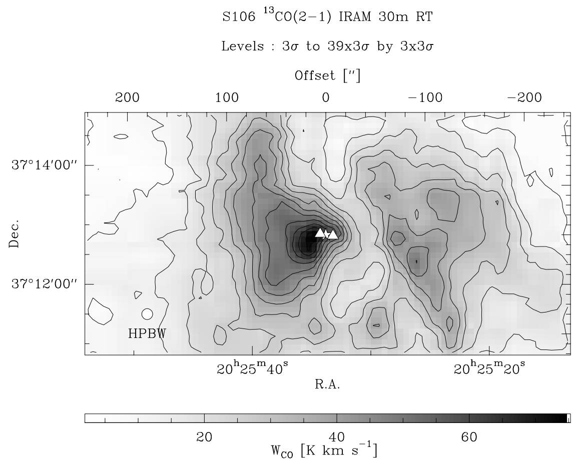

Figure 4. The distribution of the line integrated (–8 to 5 km s^{-1}) ^{13}CO J=2→1 intensity, obtained with the IRAM 30m telescope, shows the double peak structure of the molecular cloud.

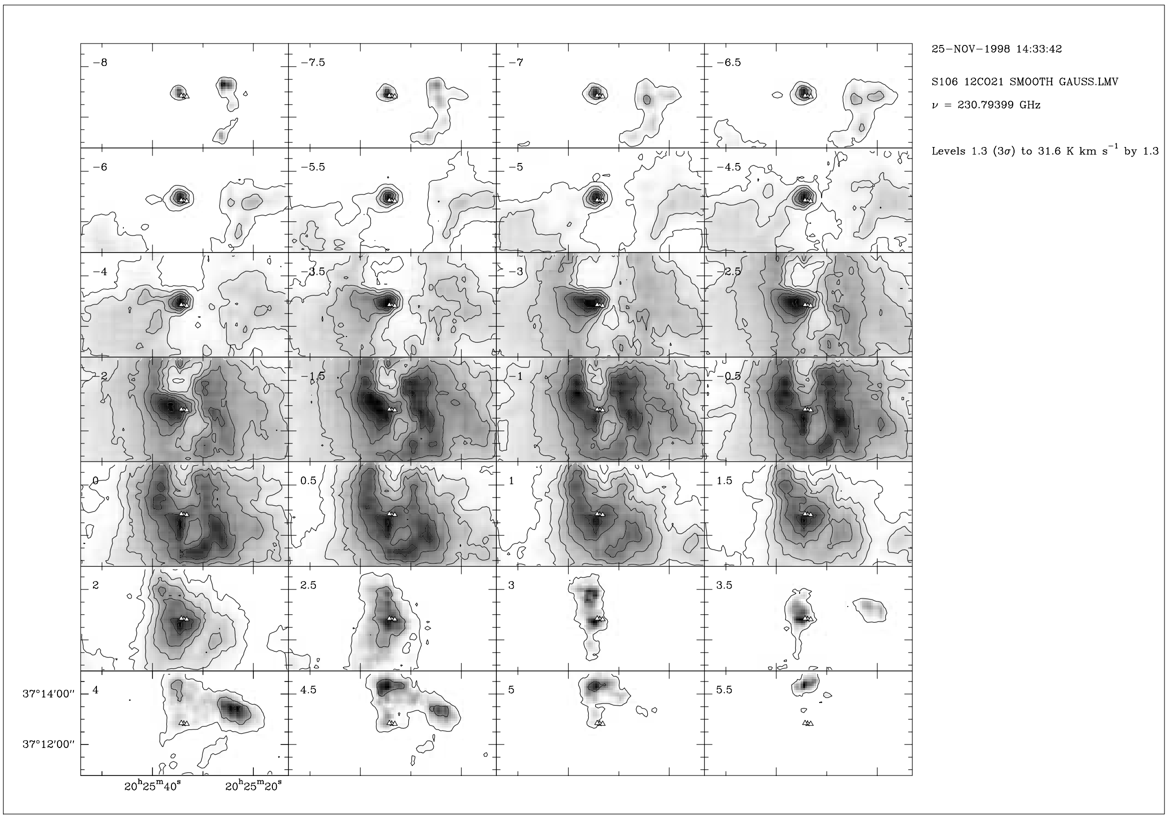

Figure 3. The channel maps of ^{12}CO 2→1 emission, obtained with the IRAM 30m telescope with an angular resolution of 11″, show the highly localized blue outflow emission between –8 and -3.5 km s^{-1}. At higher velocities (–2.5 to 2 km s^{-1}), the bulk emission of the molecular cloud is concentrated in a pronounced western and eastern part (with regard to S106 IR) and a southern clump at the border of the ionization front. A red lobe of the outflow source can not unambigeously identified, it may constitute the emission above 2 km s^{-1} in the region of S106 IR.

3.3. Millimeter CO-lines

From low angular resolution molecular line maps, the extent of the molecular cloud is determined to be $20' \times 25'$ with two maxima of emission separated by $3'$ east and west of S106 IR. The whole cloud has a mass of $\approx 10^3$ M$_\odot$ and an average density of 1.4×10^3 cm^{-3} at a temperature of 40 K (Bally 1982).

Our ^{13}CO 2→1 map (Fig. 4), recently obtained in the 'on-the-fly' (OTF) observing mode at the IRAM 30m telescope, shows a pronounced eastern peak (15″ east of S106 IR) which is a superposition of the bulk emission of the molecular cloud and the CO-outflow, and somewhat weaker, clumpy emission west and south of S106 IR. The HII region is nicely outlined by a lack of CO emission.

Channel-maps of the ^{12}CO 2→1 emission (Fig. 3, IRAM 30m OTF-data), reveal the eastern peak at blueshifted velocities between –8 and –3.5 km s^{-1} to be due to strong and highly localized outflow emission. In the channel-maps, as well as in the ^{12}CO 1→0 spectra (Fig. 5), it gets obvious that the blue wing is more pronounced than the red wing, which shows up at velocities around 2 km s^{-1} with a rather dispersed emission distribution.

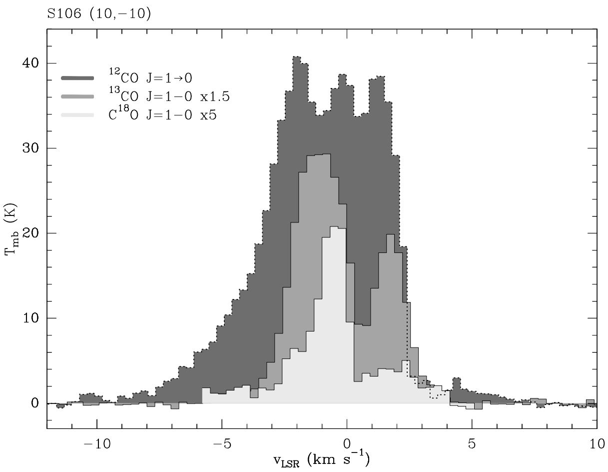

Figure 5. These ^{12}CO, ^{13}CO and C^{18}O 1→0 spectra, extracted from the OTF observation with the IRAM 30m telescope at the position (10″,-10″) relative to S106 IR, reveal the complex structure of the lines in that region.

A dip in the spectra close to S106 IR (Fig. 5) is due to self-absorbtion effects: the optically thick ^{12}CO line is self-absorbed at velocities around –1 km s^{-1} due to colder foreground gas, since the ^{13}CO and – though slightly shifted – the C^{18}O emission are peaking there. At 2 and 4 km s^{-1} individual components can be identified, representing different clumps in the line of sight. The blue wing due to outflow emission is prominent in the ^{12}CO 1→0 line.

REFERENCES

Bally J., Scoville N. 1982, ApJ 255, 497

Harris A. et al. 1987, ApJ 322, L49

Kramer C. et al. 1998, SPIE 1998, Kona/Hawaii

Poglitsch A. et al. 1991, Intern. J. IR–mm Waves, 12, 859

Tielens A.G.G.M. et al. 1985, ApJ 291, 722

FAR-INFRARED CO ROTATIONAL LINES IN THE ORION MOLECULAR CLOUD

M.J. Sempere[1], B. Lefloch[1], J. Cernicharo[1], E. González–Alfonso[1], S. Pérez–Martínez[1], S.J. Leeks[2], & F. Najarro[1]

[1]Instituto de Estructura de la Materia (CSIC), Madrid, Spain.
[2]Queen Mary & Westfield College, London, U.K.

ABSTRACT

We present a high signal–to–noise grating spectrum between 43–196.9μm of the Orion molecular cloud towards the massive star–forming region IRc2, obtained with the Long Wavelength Spectrometer (LWS) on board ISO.

CO lines up to J=20–19 have been detected around Orion-IRc2, while in the central position higher quantum numbers have been found. Lines of the ^{13}CO isotopic species have also been observed in several directions. In addition, high quality LWS-FP observations of some CO lines have been performed towards IRc2.

The data analysis suggest that at least two regions of Orion-IRc2 contribute to the observed CO emission: the ridge, responsible of the spatial extension, and the *plateau*, dominating the line flux observed towards the center of the map.

CO emission through the Orion molecular cloud has been studied in terms of temperature, column density and H_2 volume density, using and Large Velocity Gradient (LVG) model. We find that the flux ratio of the several CO lines can not be explained in terms of an homogeneous source, but a gradient in temperature and density must be involved.

Besides the CO lines, several molecular and fine–structure atomic lines have been detected in all observed positions. A detailed discussion of other molecular species rather than CO (H2O, OH...) can be found in Cernicharo et al. (1999).

Key words: Interstellar medium; molecules; Orion-IRc2.

1. THE ORION-IRc2 REGION

The Orion nebulae is a well-known region of massive star formation in the Galaxy. Its proximity and spectacular nature has made from the Orion nebulae the main target for most of the pioneering observations at infrared and millimeter wavelengths, which have played an essential role in our understanding of the birth and evolution of massive young stars and their surrounding interstellar medium.

Several components have been identified in the central region of the Orion-IRc2 cloud: a shocked dominated region produced by the powerful outflow emanating from the new born star(s), a hot core centered at ∼2 arcsec south of IRc2 composed of hot and dense clumps which are optically thick in the near– and mid– infrared continuum; an extended ridge of quiescent, warm and dense gas extended in the NE–SW direction, and an HII region and a neutral photon–dominated region (PDR) produced by the irradiation of the Trapezium stars.

There are some abundant and important molecular and atomic species, in particular CO and H_2O, that irradiate the bulk of the emission at infrared wavelengths, so that the ISO mission provides a unique opportunity to study the physics and chemistry of star forming regions.

2. RESULTS

A total of 23 positions around IRc2, with an angular separation of 90 arcsec (∼ beam size), were observed (see Figure 2a). The obtained spectra are shown in Fig. 1 of the review by Cernicharo et al. (these proceedings).

All the features present in the final averaged grating spectra were detected in each individual scan. Among the molecular species detected in Orion, CO appears to be the most widespread. At angular distances higher than ∼ 180 arcsec from the central region the CO lines weaken, and the spectra are dominated by the [O I] (146 μm) and [C II] (158 μm) fine-structure lines originated in the PDR region. The LWS grating spectra for 15 selected positions between 140 and 197μm are shown in Fig. 1.

Four CO pure rotational lines have been detected in the LWS grating between 160–186μm. The flux values for external positions are listed in Table 1.

Proceedings of the Conference "The Universe as seen by ISO", Paris, France, 20–23 October 1998 (ESA SP-427, March 1999)

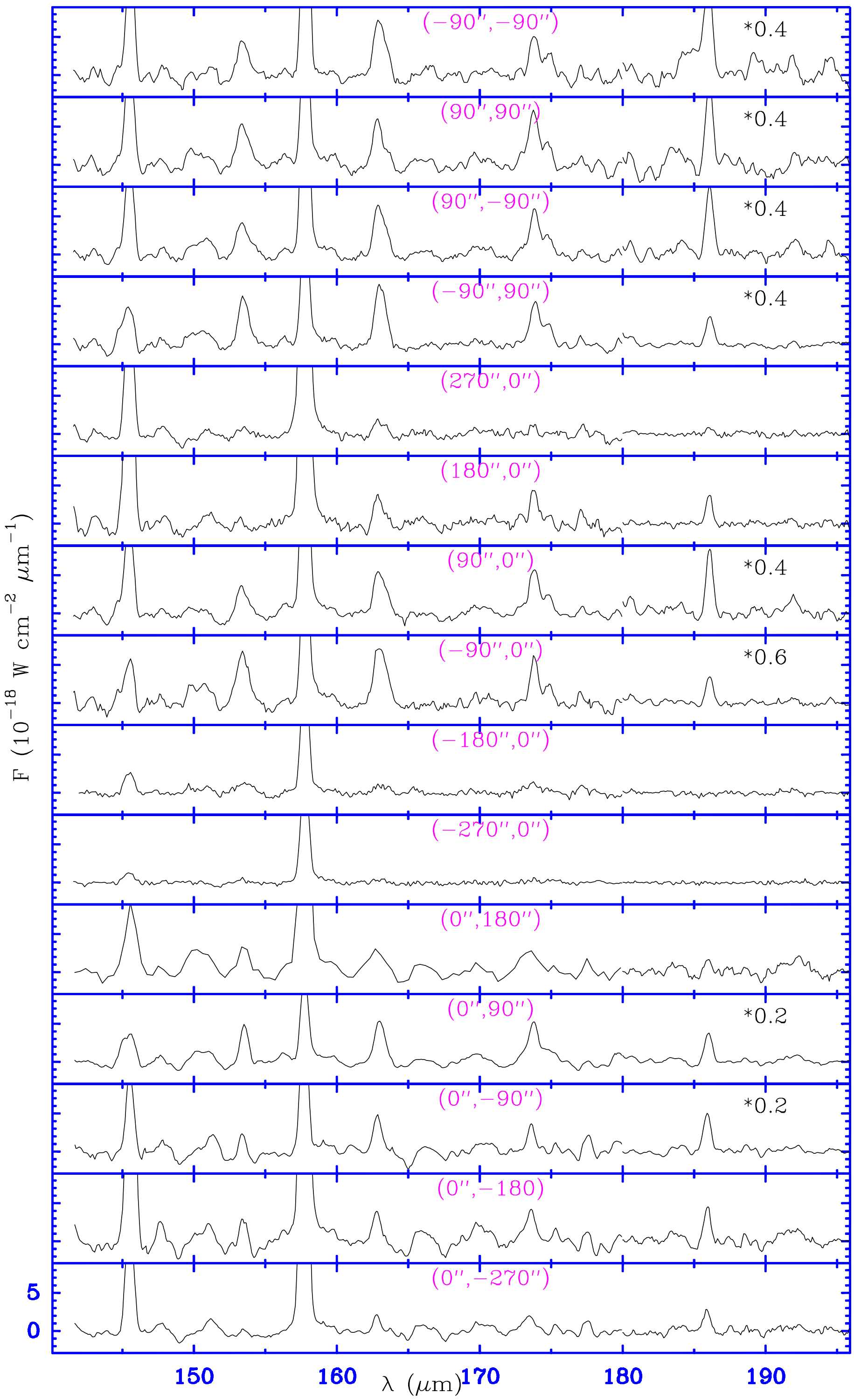

Figure 1. LWS grating spectra from selected positions around IRc2 between 140 and 197 μm. The CO rotational transitions identified in this range are listed in Table 1.

3. PHYSICAL PROPERTIES OF THE CLOUD

We have estimated the temperatures necessary to account for the fluxes of the different rotational lines identified in the LWS bands (see Table 1) across the whole Orion-IRc2 cloud. CO line profiles in the millimeter and infrared range were calculated using a Large Velocity Gradient (LVG) code.

Our model is based on the simple following hypothesis:

- Temperature and density are uniform along the line of sight.
- The CO column density is N(CO)=$10^{19}\,cm^{-2}$ (Blake et al 1987).

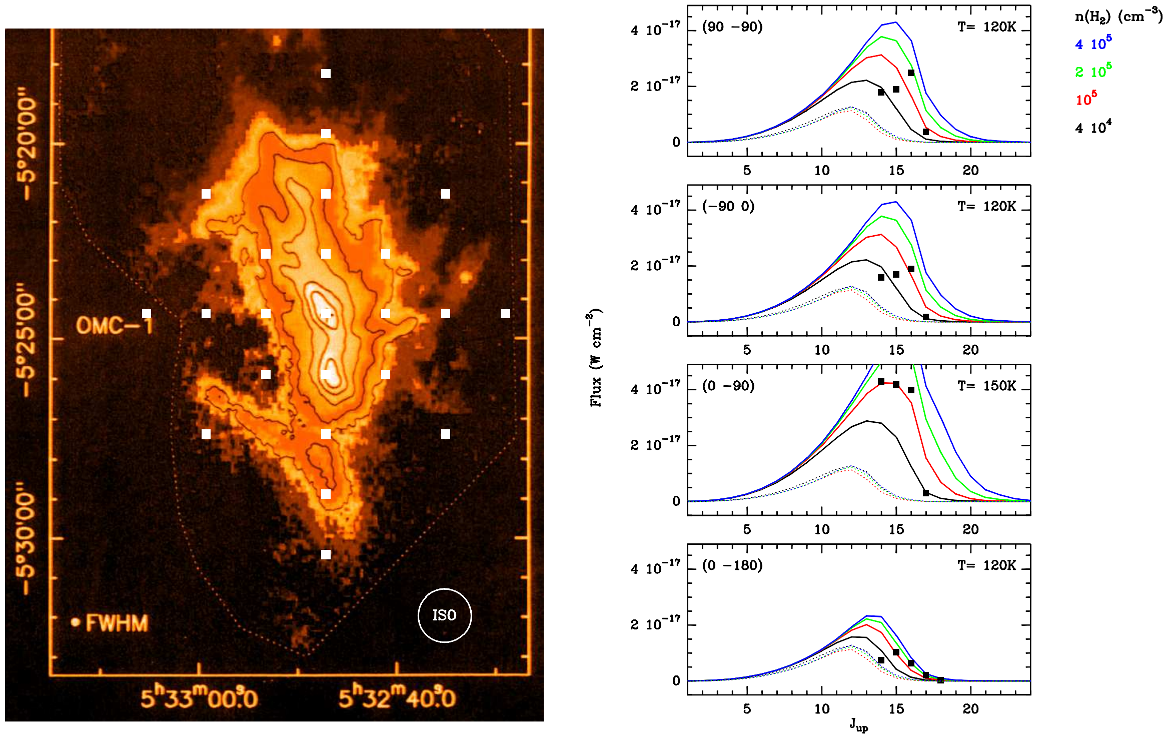

Figure 2. Left: Positions observed with ISO (black squares) superimposed upon the 350μm image observed with SHARC (Lis et al 1998). Right: Expected flux in an 80″ lobe (ISO) for kinetic temperatures comprised between 60 and 150 K assuming an average density $n(H_2) = 10^5 cm^{-3}$ and a CO column density N(CO)= $10^{19} cm^{-2}$. We show the CO transitions observed at (-90″,90″).

Table 1. Integrated CO lines intensities in Orion–IRc2

Levels $\lambda(\mu m)$	*J=14-13* 185.999	*J=15-14* 173.631	*J=16-15* 162.812	*J=17-16* 160.305	
Position	Flux (W cm^{-2})				T(K^o)
(0″, -270″)	$4.9\,10^{-18}$	$4.6\,10^{-18}$	$1.7\,10^{-18}$	$2.2\,10^{-19}$	–
(0″, -180″)	$7.5\,10^{-18}$	$1.0\,10^{-17}$	$6.5\,10^{-18}$	$2.2\,10^{-18}$	80
(0″, -90″)	$4.3\,10^{-17}$	$4.2\,10^{-17}$	$4.0\,10^{-17}$	$3.0\,10^{-17}$	150
(0″, 90″)	$3.2\,10^{-17}$	$4.8\,10^{-17}$	$3.8\,10^{-17}$	$4.0\,10^{-18}$	120
(0″, 180″)	$2.8\,10^{-18}$	$4.5\,10^{-18}$	$2.7\,10^{-18}$	$1.3\,10^{-18}$	80
(-270″, 0″)	$8.0\,10^{-19}$	$2.2\,10^{-18}$	$3.3\,10^{-19}$	$3.0\,10^{-19}$	–
(-180″, 0″)	$1.9\,10^{-18}$	$1.3\,10^{-18}$	$1.3\,10^{-19}$	–	60
(-90″, 0″)	$1.6\,10^{-17}$	$1.7\,10^{-17}$	$1.9\,10^{-17}$	$1.9\,10^{-18}$	120
(90″, 0″)	$1.6\,10^{-17}$	$1.8\,10^{-17}$	$1.5\,10^{-17}$	$3.9\,10^{-18}$	100
(180″, 0″)	$7.1\,10^{-18}$	$7.0\,10^{-18}$	$4.5\,10^{-18}$	$2.3\,10^{-18}$	80
(270″, 0″)	$2.7\,10^{-18}$	$3.0\,10^{-18}$	$6.4\,10^{-19}$	–	–
(-90″, 90″)	$1.6\,10^{-17}$	$2.3\,10^{-17}$	$2.5\,10^{-17}$	$6.2\,10^{-18}$	100
(90″, -90″)	$1.8\,10^{-17}$	$1.9\,10^{-17}$	$2.5\,10^{-17}$	$3.8\,10^{-18}$	120
(90″, 90″)	$1.7\,10^{-17}$	$1.8\,10^{-17}$	$6.7\,10^{-18}$	$2.5\,10^{-18}$	80
(-90″, -90″)	$1.9\,10^{-17}$	$2.9\,10^{-17}$	$2.7\,10^{-17}$	–	100

- The linewidth is Δv=10 km s^{-1} for positions close to the center (±90″, ±90″). For distant points from IRc2 the adopted linewidth is Δv=5 km s^{-1}.

which provides us with a full temperature description of the cloud at 80 arcsec resolution.

Throughout the *whole* cloud we find T≥80–100 K, (Figure 2b), which probably arises from two contributions : the hot gas of the PDR and the molecular gas.

Around the central position (±90″, ±90″) we find evidence for hot gas with T≥100 K. Across the whole cloud the typical densities are of the order of ∼

$10^5\,cm^{-3}$, with higher values at (0″,-90″) (coincident with a star forming core: S6, in Schmid–Burgk et al 1990).

The most severe limitation of these data comes from the contamination of the CO lines by strong adjacent features (e.g. OI at 145.6 μm, OH at 163.2 μm , H_2O). In practice the flux for J$\geq$18 transitions could not be directly measured in a reliable way.

More accurate analysis estimating these contributions and adopting a more realistic density distribution are on going.

REFERENCES

Blake, G. A., Sutton, E.C., Masson, C.R., Phillips, T.G. 1987, ApJ, 315, 621.

Cernicharo, J. et al.. 1999, (in preparation).

Lis, D.C., Serabyn, E., Keene, J., et al. 1998, ApJ (in press).

Schmid–Burgk, J., Güsten, R., Mauersberger, R. et al. 1990, ApJ, 362, L25.

A RING OF ORGANIC MOLECULES AROUND HD 97300

R. Siebenmorgen[1], A. Natta[2], E. Krügel[3] & T. Prusti[1]

[1] ISO Data Centre, Astrophysics Division, ESA, Villafranca, Spain.
[2] Osservatorio Astrofisico di Arcetri, Largo E. Fermi 5, I-50125 Firenze
[3] MPIfR, 69 Auf dem Hügel, D-5300 Bonn, Germany

ABSTRACT

This paper presents spectro-photometric images of the pre–main–sequence Herbig AeBe star HD 97300 in the mid-IR obtained with ISOCAM on board of ISO. The images show extended emission, an elliptical ring structure of size about 0.045×0.03 pc as well as two peaks of emission, separated by about 3″ (240 AU). One of the two peaks coincides with the position of HD 97300, while the other may be an embedded companion. The data show that the emission in this region is dominated by the infrared emission bands centered at 6.2, 7.7, 8.7, 11.3 and 12.5 μm, with a very small contribution from continuum emission at longer wavelengths. We fit the spectra with a dust model including organic molecules such as polycyclic aromatic hydrocarbons, very small graphite and very small silicates, as well as large grains. The fit to the ISOCAM data is very good if one applies a classical oscillator model for the infrared emission bands. Our fitting procedure allows us to estimate the total mass of the ring, which is $\sim$0.03 $M_\odot$. Its possible origin is briefly discussed.

Key words: star formation, Herbig AeBe stars, dust bands.

1. INTRODUCTION

We present the results of imaging spectroscopy of the pre-main–sequence star HD 97300, obtained with the infrared camera (ISOCAM, Cesarsky et al. 1996a) and circular variable filter wheel on board of the infrared space observatory (ISO, Kessler et al., 1996). The data presented here are the first results of a program aimed at investigating the nature of the mid-infrared emission associated to Herbig AeBe stars (Siebenmorgen et al., 1997, 1998). The young star HD 97300 is located in the Chamaeleon I cloud (Whittet et al. 1997), at distance $D \sim 188$ pc.

We report the detection of an extended, ring-like structure around HD 97300, whose emission is dominated by the infrared emission bands at 6.2, 7.7, 8.7, 11.3 and 12.5 μm (hereafter IEBs) observed in our own and other galaxies wherever neutral matter is exposed to UV radiation (see for example, the review by Allamandola et al. 1989 and the many papers presenting CVF and SWS spectra in the special issue of *Astronomy and Astrophysics* on ISO published in November 1996 and also these proceedings).

2. RESULTS

Fig. 1 shows the images of HD 97300 obtained in the four CAM narrow-band filters centered at 6.0 μm (lw4), 6.8 μm (lw5), 11.3 μm (lw8) and 14.9 μm (lw9). The morphology of the object is very similar in the four filters: we can see extended emission centered on the star and an elliptical ring of size $\sim$50×36″ around it. This same morphology is also seen in the CVF images at all frequencies, with very similar characteristics.

The ring is not symmetric around the star, but is much more extended in the SE than in the NW direction. The off-center location of the star with respect to the ring may be the effect of a density gradient in the SE–NW direction in the outer region of the Chamaeleon I cloud where HD 97300 lies. The position of the star in our images coincides with the emission peaks seen near the center in lw4 and lw5, and with the secondary peak of the emission seen in lw8, roughly at the same position. In the lw8 and lw9 filters we detect a second peak of emission, about 3″ (240 AU) north of the star.

Fig. 2 shows CVF spectra between 5.8 and 13.8 μm in 8 positions roughly aligned along P.A. = 142.4°. This line intersects the star, as well as the emission minimum and the ring seen in the SE direction. The location of the 8 positions is indicated in Fig. 1. In all positions, we detect strong IEBs over a weak continuum.

3. THE IEBs CARRIERS

To acquire a better understanding we fit the spectra of Fig. 2 using the three component dust model

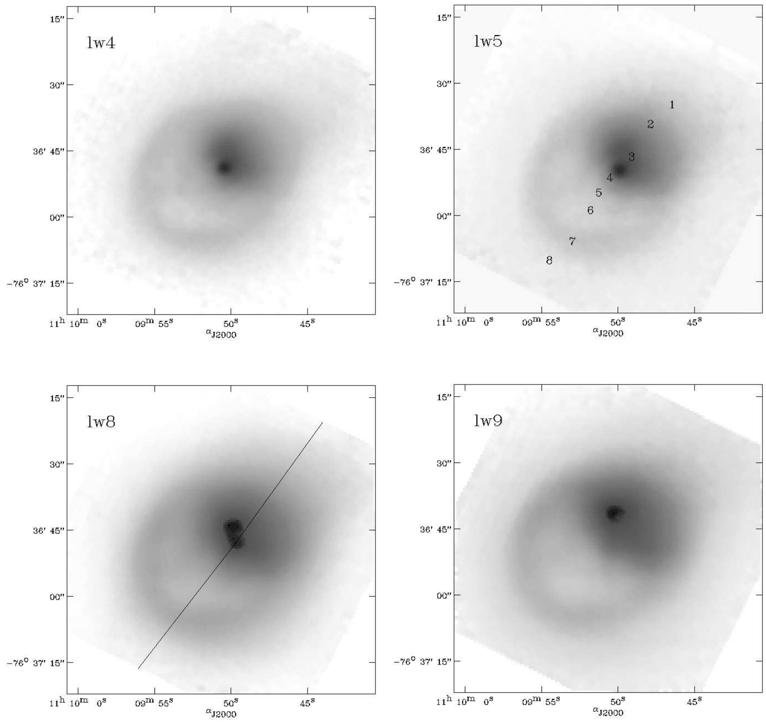

Figure 1. Logarithmic grey scale images of HD 97300 of the four narrow-band filters. The images are re-sampled to 0.5″ pixel scale. The numbers in the lw5 image indicate the positions of the CVF spectra shown in Fig. 2. The full line in the lw8 image at P.A. =142.4° gives the direction along which the spectra have been measured.

of Siebenmorgen & Krügel (1992). This model computes the emission per unit mass of dust heated by radiation of known intensity and spectral distribution; we use $T_\star$ =10700 K and luminosity $L_\star$=35 $L_\odot$. The computed spectra are smoothed to the CVF spectral resolution and adjust only the gas column density $N_{\rm H}$ until a satisfactory fit is obtained.

The simplest picture we can construct to model the band shapes is to consider that the bands can be described by classical oscillators. The absorption coefficient (σ_ν; Schutte et al. (1993)) of such a driven damped oscillator is a Lorentzian profile

$$\sigma_\nu \;=\; \frac{\sigma}{2\pi}\cdot\frac{\gamma}{(\omega-\omega_0)^2+(\gamma/2)^2}\;, \qquad (1)$$

where $\omega = 2\pi\nu$.

Note that an excited level in an atom has an average lifetime $t_{\rm L} = A^{-1}$, where A is the Einstein coefficient for spontaneous transition, the probability to find the atom there decays like e^{-At}. Because of Heisenberg's uncertainty principle $\Delta E\cdot\Delta t \geq \hbar$, the energy of the upper level is then only defined to an accuracy $\Delta E = A\hbar$. This leads naturally to a Lorentzian emission profile, and A may be identified with the damping constant, $\gamma = A$. In this picture, the line width is determined by the timescale Δt. For PAH resonances with a width of $\simeq 0.1\mu$m, the characteristic time Δt would be 10^{-12} s. This would imply immense values for A ($10^{12}\,{\rm s}^{-1}$) as well as for the associated dipole moment $\mu \sim 10^5$ Debye because $A \propto \mu^2\omega^3$. A way out of the dilemma would be to assume that the IEBs arise from a superposition of many narrow lines.

4. MASS OF CIRCUMSTELLAR MATERIAL

An interesting possibility opened up by our observations is to derive the mass of circumstellar material from the observed intensity of the PAH features.

We know the geometry of the emitting region, i.e., the approximate distance of the grains from the star. For a given distance and stellar luminosity, the integrated 6 to 14 μm flux is directly proportional to the number of C atoms in PAHs. This is because the PAHs account for the total emission in this spectral region (Fig. 2). The fraction of C atoms in PAHs is known to within a factor of three, so we can directly convert the carbon column density $N_{\rm C}$ derived by fitting the feature intensities into a hydrogen column density $N_{\rm H}$. The uncertainty on $N_{\rm H}$ is probably comparable to the uncertainty that affects its determination from sub-millimeter continuum observations (see, for example, Krügel & Siebenmorgen, 1994). The mass of gas and dust can then be computed from the values of $N_{\rm H}$ averaged over the region of interest.

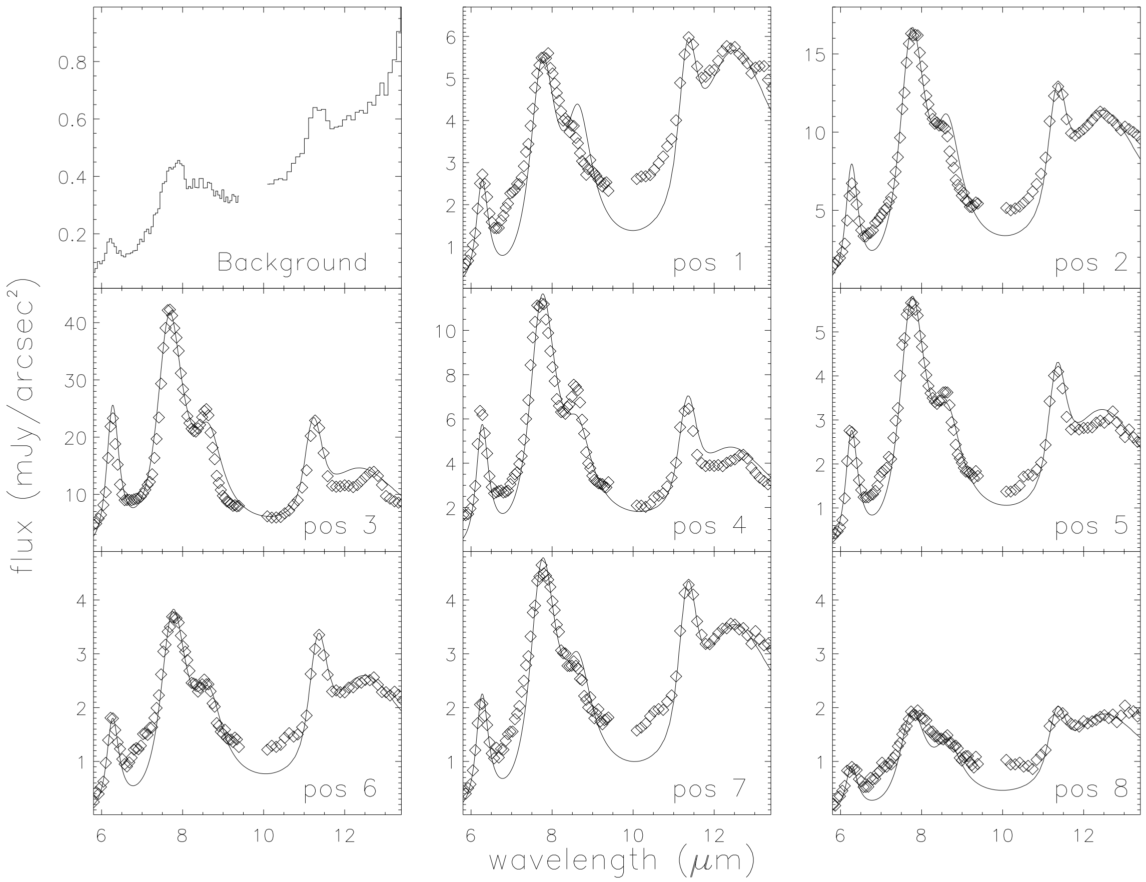

Figure 2. CVF spectra of HD 97300 in the 8 positions shown in Figure 1. Position 4 is closest to the star; Position 6 coincides roughly with the minimum of emission seen in the images; position 7 with the ring. The background emission has been measured in the upper-left corner of the imaged area. Each spectrum has been measured over a single pixel, i.e., over an area of 3″ × 3″. The uncertainties are typically smaller than a few %. Data are shown by diamonds and the best-fit models by the full lines.

We derive a total mass of the circumstellar material in a region of about 0.03 pc radius (33″) of about 0.07 $M_\odot$ of which 0.03 $M_\odot$ is in the elongated ring structure and only 0.003 $M_\odot$ in the central region of ∼1600 AU radius. Our estimates agree with the upper limit $\lesssim$0.015 $M_\odot$ in a region of size 23″ (2000 AU radius) derived from the 1.3mm flux (< 91 mJy; Henning et al. 1993).

5. THE ORIGIN OF THE RING

The presence of PAHs in the ring indicates that it is made of interstellar matter, rather than of matter ejected from the star. Its morphology suggests that the ring structure has been created by the interaction of the star with the surrounding matter.

It is possible that the ring results from the interaction of a stellar wind with the environment. In this hypothesis, the material in the ring is swept-up gas. The ring coincides with the inner wall of a three-dimensional cavity created by the wind. If we take a ring radius ∼0.02 pc and an average ambient density $\sim 2 \times 10^4$ cm^{-3} (as derived from the column densities in position 8; see Table 2), the swept-up mass is ∼0.015 $M_\odot$, comparable to the estimated ring mass. Since there is no evidence of a stellar wind at the present time, the ring formation must be due to a recent, sporadic episode of mass-loss. Assuming that the ring is expanding at 10 km s^{-1} (there is no dynamical information available), we estimate the momentum in the ring to be $\sim 6 \times 10^{37}$ gr cm s^{-1}. If the mass-loss episode was characterized by rate 2×10^{-8} $M_\odot$ yr^{-1} (Nisini et al. 1995) and velocity 300 km s^{-1} (Finkenzeller and Mundt 1984), as typical of winds in Herbig Ae/Be stars, the duration of the episode must have been $\sim 5 \times 10^4$ yr.

A second possibility is that the ring is due to the action of the radiation pressure from the star. The radiation pressure at the ring ($\sim L_\star/(4\pi$ c R^2)) is $\sim 10^{-10}$ erg cm^{-3}, comparable with the thermal pressure of the ambient medium $nkT \sim 1.4 \times 10^{-10}$, with $n \sim 2 \times 10^4$ cm^{-3} and $T \sim 50$K, the typical temperature of the large grains at the distance of the ring.

The ring is not centered on the star, which is closer to the NW edge than to the SE. This asymmetry may be related to a density gradient in the ambient medium, if the density is higher to the NW than to the SE. Since HD 97300 is very likely located near the front edge of the Chamaeleon I cloud, the best tracer of its immediate environment is an optically thick molecule such as ^{12}CO. The ^{12}CO map of Mattila et al. (1989) shows an enhancement of the radiation temperature just to the NW of HD 97300.

Finally, it is interesting that HD 97300 is not the only Herbig AeBe star with a ring. A similar structure (although about 3.5 times larger) is seen in scattered light in the younger and more deeply embedded star LkHα198 (Leinert et al. 1991). In that case also the ring has an elliptical shape and the exciting star is shifted from its center. In LkHα198, there is a CO outflow (Levreault 1988), roughly aligned with the reflection nebulosity, whose association to LkHα198 itself is, however, uncertain. We do not know if there is PAH emission associated with the LkHα198 ring.

REFERENCES

Cesarsky C., Abergel A., Agnèse P. et al. 1996a, A&A 315, L32

Henning Th., Pfau W., Zinnecker H., Prusti T. 1993, A&A 276, 129

Finkenzeller U., Mundt R. 1984, A&AS 55, 109

Kessler M.F., Steinz J.A., Anderegg M.E. et al. 1996, A&A 315, L27

Krügel E., and Siebenmorgen R. 1994, AA 288, 929

Leinert Ch., Haas M., Lenzen R. 1991, A&A 246, 180

Levreault R.M. 1988, ApJ 330, 897

Mattila K., Liljeström T., Toriseva M. 1989, in: *Low Mass Stars Formation and Pre-Main Sequence Objects*, B. Reipurth ed., ESO Workshop Proceedings n.33, p.153

Nisini B., Milillo A., Saraceno P., Vitali F. 1995, A&A 302, 169

Schutte W.A., Tielens A.G.G.M, Allamandola L.J. 1993, ApJ 415, 397

Siebenmorgen R., Krügel E. 1992, A&A 259, 614

Siebenmorgen R., Natta, A., Krügel E., Prusti A. 1997, 'The energetics around Herbig Ae/Be stars', Proc. First ISO Workshop on Analytical Spectroscopy, ESA SP-419, Eds. Heras et al., p. 229.

Siebenmorgen R., Natta, A., Krügel E., Prusti A. 1998, A&A 339, 134

Whittet D.C.B., Prusti T., Franco G.A.P., Gerakines P.A., Kilkenny D., Larson K.A., Wesselius P.R. 1997, A&A 327, 1194

WEAK H_2 EMISSION FROM DIFFUSE AND TRANSLUCENT CLOUDS

W.F. Thi[1], E.F. van Dishoeck[1], J.H. Black[2], D.J. Jansen[1], N.J. Evans[3], & D.T. Jaffe[3]

[1]Leiden Observatory, P.O. Box 9513, 2300 RA Leiden, The Netherlands
[2]Onsala Space Observatory, S–43992 Onsala, Sweden
[3]Department of Astronomy, University of Texas, Austin TX 78712, USA

ABSTRACT

We present the first results of a survey for the lowest pure-rotational lines of H_2 with the ISO-SWS in a number of well-studied low-density diffuse and translucent clouds. The data are compared with those of the high-density PDR IC 63, for which H_2 lines up to S(5) are detected, and of the "cool" PDR Cederblad 201. Searches for the S(0) line at 28.218 μm and the S(1) line at 17.035 μm have been performed for the diffuse cloud along the line of sight toward ζ Oph, the translucent clouds toward HD 94413 and HD 154368, the high-latitude cloud MBM 55D, as well as the translucent outskirts of the S 140 molecular cloud. The lines are not detected in diffuse clouds down to ~0.3–0.5 Jy (2σ). They are weakly observed in the peripheral regions of S 140, where their intensities are more than an order of magnitude less than at the peak of the PDR. The observations are compared with available physical models based on optical absorption and/or millimeter emission line data, and, in the case of ζ Oph, with H_2 observations in the ultraviolet. The models include both collisional excitation and ultraviolet pumping. The data form tests of the temperature structure and heating mechanisms of these clouds.

Key words: diffuse clouds; translucent clouds; photon-dominated regions (PDRs); molecules: H_2

1. INTRODUCTION

Early results from the Short Wavelength Spectrometer (SWS) on board the Infrared Space Observatory (ISO) have shown that the pure rotational lines of H_2 are readily detected in photon-dominated regions (PDRs) (Timmermann et al. 1996, Bertoldi 1997, see review by Draine & Bertoldi these proceedings). These observations refer to molecular clouds with densities n > 10^4 cm^{-3}, exposed to intense ultraviolet radiation from nearby bright stars with an enhancement factor $I_{\rm UV} \geq 100$ relative to the average interstellar background starlight (e.g., Draine 1978). Much less attention has been paid to the weakly illuminated clouds of lower density, which may contain a large fraction of the molecular gas in galaxies. This dilute molecular gas may fill much of the volume occupied by self-gravitating giant molecular clouds and includes the diffuse and translucent clouds that are not gravitationally bound. A good understanding of the physical conditions in the diffuse molecular gas is needed to determine their role in global star-forming activity and galactic evolution (e.g., McKee 1989, Li et al. 1997). The pure rotational lines of H_2 accessible with the ISO-SWS form an important new diagnostic tool of these regions.

We present here the first results of a deep survey of the H_2 J=2→0 S(0) and J=3→1 S(1) pure-rotational lines at 28.218 and 17.035 μm with the ISO-SWS in diffuse, translucent and high-latitude clouds. These clouds have densities n=n(H) + n(H_2) of 100–3000 cm^{-3} and are exposed to $I_{\rm UV} \leq 10$ (van Dishoeck et al. 1991). For comparison, results for the well-studied dense PDR IC 63 with n=5×10^4 cm^{-3} and $I_{\rm UV}$=650 are shown as well, together with those for the reflection nebula Cederblad 201 exposed to radiation with a lower color temperature (Kemper et al. 1999). The H_2 J=2 and 3 levels lie high in energy at 510 K and 1015 K respectively, and are thus excellent tracers of the warm $T \geq 100$ K gas component.

The objects are chosen to be well constrained by a wide variety of other observations. Specifically, the line-of-sight toward the bright O9.5 star ζ Oph is observed, for which a wealth of complementary optical absorption line data exist, including H_2 observations in the ultraviolet (e.g., Spitzer et al. 1974). Other objects include translucent and high-latitude clouds from the sample of Gredel et al. (1993, 1994) chosen to be free from contaminating emission of other clouds along the line of sight. Finally, H_2 has been observed along a cut through the outskirts of the molecular cloud S 140, for which complementary submillimeter data on CO isotopes and [C I] are available (Li 1997). The data will be compared with the available models for these regions.

2. OBSERVATIONS AND REDUCTION

The observations were performed with the SWS grating mode SWS02. The spectral resolving power and aperture for extended sources are 1500 and $20'' \times 27''$

Proceedings of the Conference "The Universe as seen by ISO", Paris, France, 20–23 October 1998 (ESA SP-427, March 1999)

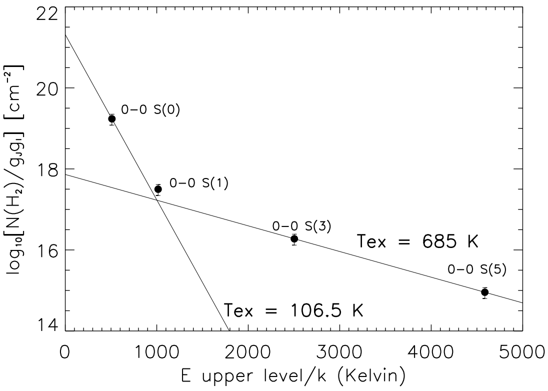

Figure 1. The H_2 excitation diagram toward IC 63 as derived from the ISO-SWS observations.

at the S(0) line, and 1800 and $14'' \times 27''$ at the S(1) line, respectively. Typical integration times range from 100 s per line for IC 63 to 2000 s per line for the diffuse clouds. These are among the deepest integrations performed with the SWS. Special software designed by Valentijn & Thi (1999) has been used to handle glitches and dark current fluctuations, together with the standard Interactive Analysis Package. The flux uncertainty is of the order of 30% for strong lines. The quality of the data varies from orbit to orbit due to the effects of "cosmic weather".

3. THE DENSE PDR IC 63

IC 63 is a small comet-shaped reflection nebula with $A_V \simeq 7$ mag situated at a distance of ~230 pc. It is exposed to far ultraviolet radiation ($I_{UV} \approx 650$) from the B0.5 star γ Cas located at a distance of 1.3 pc from the cloud. The observed molecular lines in the (sub)millimeter are narrow, $\Delta V \approx 1$ km s^{-1}, indicating the absence of shocks. The size of the cloud as mapped in ^{12}CO 3→2 is $40'' \times 20''$ or 0.04×0.02 pc. The fact that it is isolated and nearby makes it one of the simplest, best-characterized PDRs.

IC 63 has been studied intensively by Jansen et al. (1994, 1996), who observed a large variety of molecular lines to constrain the physical and chemical structure. One- and two-dimensional PDR models have been constructed by Jansen et al. (1995). The density is $\sim 5 \times 10^4$ cm^{-3} and the temperature is found to decrease from ~ 200 K at the edge to ~ 10 K in the center. This temperature profile reproduces well the ^{13}CO 6→5 data for this cloud. Using the IUE satellite, Witt et al. (1989) observed the ultraviolet fluorescence of H_2 and more recently, Luhman et al. (1997) detected three near-IR ro-vibrational H_2 emission lines. These lines are well fitted by the H_2 excitation model which takes ultraviolet pumping and collisional processes into account.

Pure rotational H_2 lines up to S(5) are detected with the ISO-SWS toward the peak of the CO map at RA (1950)=$0^h55^m58^s$, DEC(1950)=$60^o37'7''$. Although the density and radiation field are similar to those of the S 140 PDR observed by Timmermann et al. (1996), the lines in IC 63 are typically a factor of 10 weaker, 0.5–1.5 Jy (Thi et al. 1997). This suggests that geometrical and beam-filling effects play a role. The corresponding H_2 excitation diagram is shown in Figure 1. Because the S(2) line was not observed, no constraints on the ortho/para ratio can be obtained (Sternberg & Neufeld 1999).

The intensities of the four observed lines can be fit by two components of thermalized emission at temperatures of 106 and 685 K. The intensity of the S(1) line has nearly equal contributions from the two components. The inferred column density of warm H_2 at 106 K is 5.9×10^{21} cm^{-2}, while that of the hot component at 685 K is 1.2×10^{19} cm^{-2}. The total column of H_2 agrees well with the estimate of Jansen et al. (1994), $(5 \pm 2) \times 10^{21}$ cm^{-2}, although a temperature rather lower than 100 K was inferred in that analysis. The excitation temperatures characterizing levels J=0 to 2 and J = 3 to 7 are similar to those found in diffuse molecular clouds through ultraviolet absorption line observations (Spitzer & Jenkins 1975).

The results show that a very small column density of hot H_2 ($T \geq 500$ K) is sufficient to produce the observed intensities of the higher lines. The hot temperature is a factor of three higher than the maximum kinetic temperature of ~200 K at the edge given by the (2D) PDR models. It is comparable, however, to the temperatures of 500–600 K inferred from high-J H_2 lines for other dense PDRs (Timmermann et al. 1996, Bertoldi 1997). The PDR models of Jansen et al. (1995), which fit the H_2 ultraviolet and near-infrared observations, give fluxes in the pure rotational lines which are up to an order of magnitude too low compared with observations. Thus, even for this simple PDR the physical structure is not yet fully understood. Possible solutions for this discrepancy include an enhanced H_2 formation rate at high temperatures and/or a higher photoelectric heating efficiency (Bertoldi 1997).

4. THE 'COOL' PDR CEDERBLAD 201

Weak H_2 S(1) and S(3) emission at the level of 0.5–1.0 Jy has been detected toward the reflection nebula Cederblad 201 by Kemper et al. (1999). This cloud is illuminated by the B9.5 star BD+69^{o}1231 and is an example of a PDR around a cooler star (Spaans et al. 1994). The inferred density is $n \approx 5000$ cm^{-3}, and the intensity of the radiation is enhanced by a factor of 200. Because the radiation field lacks ultraviolet photons with short enough wavelengths to pump H_2, only collisions play a role in this source. The 1-D and 3-D models by Kemper et al. (1999), which include a detailed treatment of the heating and cooling, again fall short of the observed fluxes of the pure rotational lines. Since the density and ultraviolet radiation are too low in this source for heating due to H_2 collisional de-excitation to be important, it suggests that the discrepancy lies in other parameters controlling the heating. The absence of [O I] 63 μm emission indicates that shocks with velocities greater than 7 $km\,s^{-1}$ do not play a role.

Table 1. H_2 line fluxes toward diffuse and translucent clouds[a]

Source	Observing time (s)		Flux (Jy)	
	H_2 S(1)	H_2 S(0)	H_2 S(1)	H_2 S(0)
HD 94413	800	1800	<0.4	< 0.4
HD 149757N	n.a.	2000	n.a.	0.5
HD 149757	600	1200	0.4	< 0.3
HD 149757-OFF	600	1600	< 0.3	< 0.3
HD 154368	600	1400	< 0.5	< 0.4
MBM 55D	n.a.	2000	n.a.	< 0.3

[a]Upper limits are 2σ.

5. DIFFUSE AND TRANSLUCENT CLOUDS

The diffuse and translucent clouds were selected from the sample of Gredel et al. (1993, 1994) (see Table 1), and have been studied extensively by optical absorption and millimeter emission lines. MBM 55D is a high-latitude cloud, first detected by Magnani, Blitz & Mundy (1985). The objects were chosen to be isolated and well characterized, and to have a simple CO emission line profile with no evidence for other molecular clouds along the line of sight. For the well-known cloud toward ζ Oph (HD 149757), both the direction toward the star, as well as a position 30′ north have been observed. At the latter position, the CO 1–0 emission is two times stronger than at the position of the star (Liszt 1997). The OFF position was chosen as the location of lowest IR background intensity adjacent to ζ Oph that could be observed without an additional pointing of the spacecraft. The estimated densities range from 100–3000 cm^{-3} and the incident radiation field from $I_{\rm UV}\approx$0.5 for MBM 55D to $I_{\rm UV}\approx$1–2 for the other clouds.

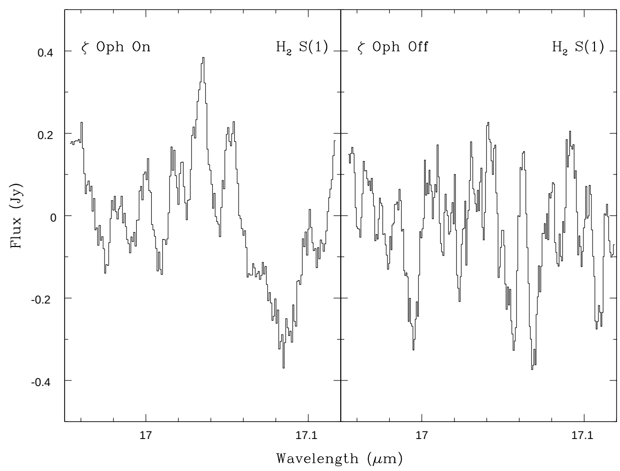

Figure 2. Examples of ISO-SWS spectra toward the diffuse cloud ζ Oph.

Examples of spectra are presented in Figure 2 and the results are summarized in Table 1. In general, the H_2 S(0) and S(1) lines are not detected down to 0.3 Jy (2σ). The only possible exception is ζ Oph which shows a marginal 2 σ detection of the S(1) line with a flux of $\sim$ 0.4 Jy on source. Assuming that the emission fills the beam, this implies an intensity

Table 2. Excitation temperatures and column densities of H_2 in peripheral regions of S 140[a]

22h17m24.5s			22h19m32.5s			22h20m36s		
-30″	0	+30″	-30″	0	+30″	-30″	0	+30″
I (10^{-5} erg s^{-1} cm^{-2} sr^{-1})								
0.6[b]	0.9	1.1	1.3	1.0	1.0	0.2	1.0	0.8
0.6[b]	2.3	1.3	0.9	1.0	1.4	0.6	0.8	0.3
$T_{\rm ex}$ (K)								
106	131	110	100	105	114	133	101	89
N (10^{21} cm^{-2})								
1.0	0.6	1.4	2.6	1.5	1.1	1.3	1.9	2.9

[a] All data are taken at DEC(1950)=+63°23′15.4″.
[b] The top entry at each position refers to the S(0) line, the lower entry to the S(1) line

of 4×10^{-6} erg s^{-1} cm^{-2} sr^{-1} and a J=3 column density a factor of $\sim$10 higher than derived from the ultraviolet observations toward the star (Spitzer et al. 1974).

Diffuse cloud models such as developed by van Dishoeck & Black (1986) predict typical S(0) and S(1) fluxes of 0.03–0.1 and 0.01–0.07 Jy, respectively. Most of the J=2 and 3 population is due to ultraviolet pumping, since the densities in these clouds, $n\approx150$ cm^{-3}, are below the critical densities for collisional excitation of the H_2 lines at $T\approx100$ K. Higher fluxes would require larger values of $I_{\rm UV}$. However, this would be in conflict with the detection of only weak ultraviolet absorption out of vibrationally excited levels of H_2, which indicates that the incident radiation field cannot be larger than $I_{\rm UV}$=1–2 for ζ Oph (Federman et al. 1995). If the S(1) line were real, there may be two possible explanations for this discrepancy. First, the J=2 and 3 column densities derived from the ultraviolet absorption line observations may have been underestimated due to saturation effects. The absorption lines from these levels lie on the flat and damped part of the curve of growth, and the derived column densities are very sensitive to the adopted line profiles. The velocity structure toward ζ Oph is known to be complicated, consisting of at least two components with narrow widths (Langer et al. 1987, Kopp et al. 1996).

The second possibility is that unresolved small-scale structure in the ISO-SWS beam is responsible for the H_2 emission, but does not contribute to the ultraviolet absorption, which arises in a very narrow pencil beam line of sight. Spaans (1995) and Joulain et al. (1998) have shown that the dissipation of turbulence can result in enhanced formation of molecules such as CH^+ and excitation of H_2. CH^+ is readily detected toward ζ Oph in optical absorption lines, so that the difference is unlikely to be due to line-of-sight effects. The possible S(1) intensity toward ζ Oph is within a factor of two of the value predicted by Joulain et al. (1998) for a cloud with n = 30 cm^{-3}. At densities typical of the ζ Oph cloud, $n\approx150$ cm^{-3}, the model intensity should be reduced significantly, however. The turbulent models of Joulain et al. do not take ultraviolet pumping into account, which will enhance the populations of the higher J levels.

The lack of detections in the other sources implies that H_2 emission at this level is not a common phenomenon, and that H_2 lines from cold translucent clouds such as MBM 55D and HD 94413 are weak. The HD 154368 cloud is thought to be similar in density to the ζ Oph cloud and to have a factor of 2–3 larger total column density (Snow et al. 1996). The absence of H_2 emission toward this cloud makes the possible detection toward ζ Oph more questionable.

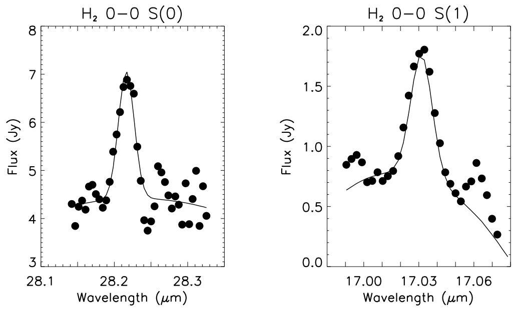

Figure 3. Examples of ISO-SWS H_2 S(0) and S(1) spectra in the outskirts of S 140. The spectra refer to RA(1950)=22^h 17^m 24.5^s, DEC(1950)=+63° 23′ 15″.

6. PERIPHERAL REGIONS OF S 140

The PDR S 140 ($d \approx$ 910 pc) has been studied extensively by ISO (e.g., Timmermann et al. 1996), but these observations have focused on the brightest emission at the interface. The peripheral regions, studied here at $\sim$ 20′ offset from the interface, are more representative of general GMC material. Typical conditions are A_V = 5–15 mag, I_{UV} = 40–100 and n = 500–3000 cm^{-3} derived from submillimeter lines and far-infrared continuum (Li 1997). Table 2 summarizes the results obtained at 9 positions in a cut across the cloud and Figure 3 shows examples of spectra. The lines are weak ($\sim$ 1 Jy) and indicate a column density of warm gas of (1–3) 10^{21} cm^{-2} at an excitation temperature of $\sim$ 100 K. Only PDR models with I_{UV} = 60–100 and $n \geq$3000 cm^{-3}, i.e., the upper range of parameters deduced from other diagnostics, can match the data.

7. CONCLUSION

We have presented the most sensitive ISO-SWS searches for the H_2 S(0) and S(1) lines from diffuse and translucent clouds down to 0.1 – 0.2 Jy rms. The lines are generally not detected until the density reaches $n \approx$3000 cm^{-3} and the radiation field $I_{UV} \geq$ 50. Where detected, the observed lines are stronger than computed in detailed PDR models which take collisional excitation in warm gas and UV pumping into account. This suggests that the photoelectric heating efficiencies and the H_2 formation rate at high temperatures need to be re-examined. The detection of H_2 emission from cool PDRs indicates that the discrepancy is unlikely to be due to an underestimate of the heating due to collisional de-excitation of vibrationally-excited H_2.

REFERENCES

Bertoldi, F. 1997, in 'First ISO Workshop on Analytical Spectroscopy', ESA SP-419, p.67

Draine, B.T. 1978, ApJS, 36, 595

Federman, S.R., Cardelli, J.A., van Dishoeck, E.F., Lambert, D.L., Black, J.H. 1995, ApJ, 445, 325

Gredel R., van Dishoeck E.F., Black J.H., 1993, A&A, 269, 477

Gredel R., van Dishoeck E.F., Black J.H., 1994, A&A, 285, 300

Jansen, D.J., van Dishoeck, E.F., Black, J.H. 1994, A&A, 282, 605

Jansen, D.J., van Dishoeck, E.F., Black, J.H., Spaans, M.C., Sosin, C. 1995, A&A, 302, 223

Jansen, D.J., van Dishoeck, E.F., Keene, J., Betz, A.L., Boreiko, R. 1996, A&A, 309, 899

Joulain, K., Falgarone, E., Pineau des Forêts, G., Flower, D. 1998, A&A, 340, 241

Kemper, C., Spaans, M., Jansen, D.J., Hogerheijde, M.R., van Dishoeck, E.F., Tielens, A.G.G.M. 1999, ApJ, in press

Kopp, M., Gerin, M., Roueff, E., Le Bourlot, J. 1996, A&A, 305, 558

Langer, W.D., Glassgold, A.E., Wilson, R.W. 1987, ApJ, 322, 450

Li, W. 1997, PhD Thesis, University of Texas

Li, W., Evans, N.J., Lada, E.A., 1997, ApJ, 488, 277

Liszt, H. 1997, A&A, 322, 962

Luhman, M.L., Luhman, K.L., Benedict, T., Jaffe, D., Fischer, J. 1997, ApJ, 480, 133

Magnani, L., Blitz, L., Mundy, L. 1985, ApJ, 295, 402

McKee, C.M. 1989, ApJ, 345, 782

Snow, T.P., Black, J.H., van Dishoeck, E.F. et al. 1996, ApJ, 465, 245

Spaans, M. 1995, PhD thesis, University of Leiden

Spaans, M., Tielens, A.G.G.M., van Dishoeck, E.F., Bakes, E.L.O. 1994, ApJ, 437, 270

Spitzer, L., Cochran, W.D., Hirschfeld, A. 1974, ApJS, 28, 373

Spitzer, L., Jenkins, E.B. 1975, ARAA, 13, 133

Sternberg, A., Neufeld, D.A. 1999, ApJ, in press

Thi, W.F., van Dishoeck, E.F., Jansen, D.J., Spaans, M., Li, W., Evans, N.J., Jaffe, D.T. 1997, in 'First ISO Workshop on Analytical Spectroscopy', ESA SP-419, p.299

Timmermann, R., Bertoldi, F., Wright C.M. et al. 1996, A&A, 315, 281

Valentijn E., Thi W.F. 1999, Exp. Astr., submitted

van Dishoeck, E.F., Black, J.H. 1986, ApJS, 62, 109

van Dishoeck, E.F., Black, J.H., Phillips, T.G., Gredel, R. 1991, ApJ, 366, 141

Witt, A.N., Stecher, Th.P., Boroson, T.A., Bohlin, R.C. 1989, ApJ, 336, 21

INTERSTELLAR CLOUDS AS SEEN IN THE ISOPHOT SERENDIPITY SURVEY

**L. V. Tóth[1,2], D. Lemke[1], O. Krause[1], S. Hotzel[1]
M. Stickel[1], U. Klaas[1], S. Bogun[3],
M.F. Kessler[4], R. Laureijs[4], M. Burgdorf[4], C.A. Beichman[5],
M. Rowan-Robinson[6], A. Efstathiou[6], G. Richter[7], & M. Braun[7]**

[1]Max–Planck–Institut für Astronomie, Königstuhl 17,
D–69117 Heidelberg, Germany
[2]Department of Astronomy, Loránd Eötvös University, Pázmány Péter sétány 1.
H–1117 Budapest, Hungary
[3]Data Management and Operations Division, ESO, Karl-Schwarzschild-Str. 2,
D–85748 Garching bei München, Germany
[4]ISO Data Centre, Astrophysics Division of ESA,
Villafranca, P.O. Box 50727, E–28080 Madrid, Spain
[5]Infrared Processing and Analysis Center, JPL, California Institute of Technology,
MS 100/22, Pasadena, CA 91125, USA
[6]Imperial College of Science, Technology and Medicine, The Blackett Laboratory,
Prince Consort Road, London SW7 2BZ, United Kingdom
[7]Astrophysikalisches Institut Potsdam, An der Sternwarte 16, D–14482 Potsdam, Germany

ABSTRACT

A galactic minisurvey was carried out at 170μm analyzing ISOPHOT Serendipity Survey (ISOSS) data of the Cepheus, Chamaeleon, and Rho Oph molecular cloud complexes. Colour temperatures of 170μm extended and point-like sources were derived using ISOSS and IRAS 100μm data covering first time the 10K$< T_{\rm dust} <$ 20K temperature range in a high resolution large area survey. A number of cold clouds, and very cold cloud cores were found in association with optical nebulosities and molecular clouds.

Key words: ISOPHOT; Serendipity; ISM: cold dust; ISM: individual (Chamaeleon), (Cepheus Flare), (Rho Oph)

1. INTRODUCTION

The main task of the present galactic serendipity minisurvey was locating and identifying cold clouds, and very cold cloud cores.

The knowledge of the distribution of cold interstellar matter in galaxies is important for the understanding of the overall dynamics or the star forming processes. While IRAS discovered the FIR cirrus, COBE proved the presence of cold dust in the Milky Way (see eg. Lagache et al. 1998), the distribution of the latter component was first surveyed with high enough angular resolution by ISOPHOT measurements. Indications for even colder dust clouds were found already on the basis of IRAS 60/100μm by Laureijs (1991), while finally a detection of $\approx$ 13K grain temperatures was possible with ISO (see eg. Lehtinen et al. 1998).

Besides identifying galaxies (see Stickel et al. these proceedings) the ISOPHOT Serendipity Survey (ISOSS) allowed us to observe galactic interstellar clouds containing cool ($\approx$ 17K) dust in cirrus, and cold ($<$ 15K) dust in dark clouds with a resolution of 2 arcminutes. By measuring at 170μm ISOSS can reveal colder regions than IRAS, and due to the high resolution the coldest cloud cores may be identified which were not resolved by the 40 arcmin DIRBE beam. Almost 15% of the sky was mapped in ISOSS covering most of the known molecular cloud complexes as shown in Figure 1. Thus the sample we may obtain is much larger than any of the previous FIR air-born (see, e.g., Keene, 1981), sub-mm range ground-based (see ,e.g., Launhardt et al. 1997), or balloon (see, e.g., Ristocelli et al. 1998) measurements.

ISOSS and IRAS data of three regions of altogether $\approx$ 75 deg^2 were analyzed. Our minisurvey included the Cepheus Flare, Rho Oph and Chamaeleon mid/high galactic latitude molecular complexes. These selected complexes are nearby star forming regions, located at distances of d(Cha) = 150pc, 120pc$<$ d(Oph) $<$ 160pc (Knude & Hog, 1998 using Hipparcos and Tycho Catalogues), and 200pc$<$ d(Cep) $<$ 450pc (Kun 1998). Thus the cloud structure of these large reservoirs of interstellar matter may be successfully resolved by the ISOPHOT Serendipity Survey.

The density distribution of the gas component towards the ISOSS identified cold, and very cold areas has already been surveyed using CO lines. Under-

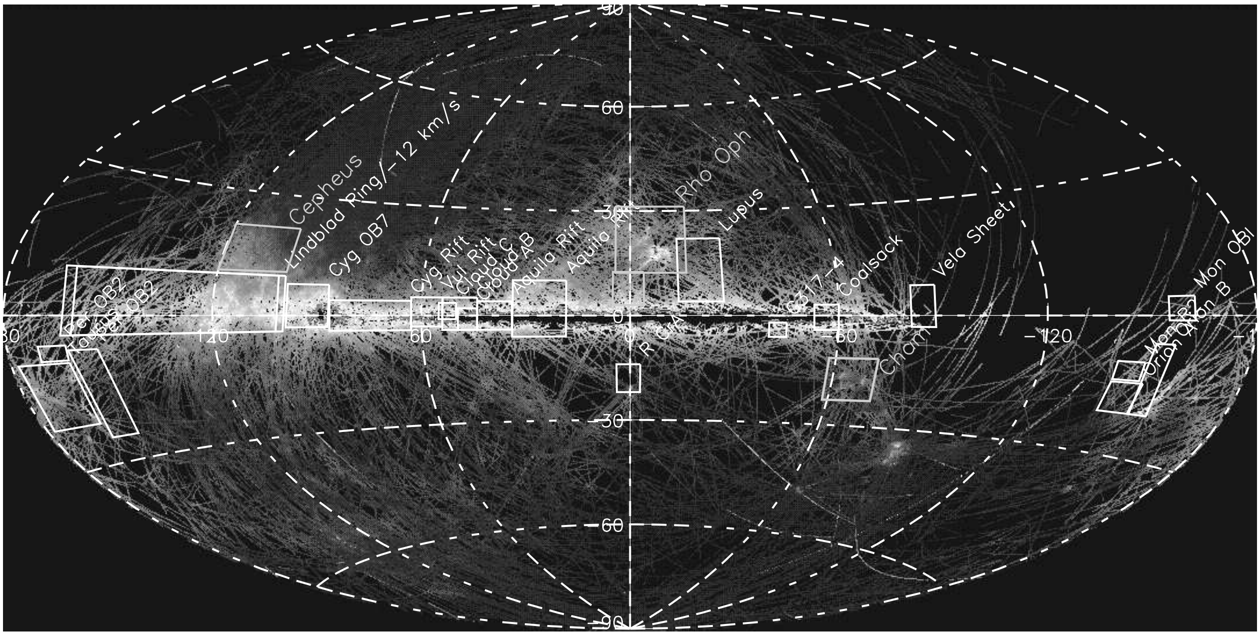

Figure 1. The 170μm sky brightness as seen by the ISOPHOT Serendipity Survey. Pixel size is 20'. Molecular complexes are marked with their boundaries, and names.

sampled ^{13}CO maps are available for all three regions from the Nagoya survey published by Yonekura et al. (1997), Nozawa et al (1991), and Mizuno et al. (1998), while the "CO webs" of Oph were mapped by Loren (1989) and a C^{18}O survey of Cha I was carried out by Haikala et al. (1998).

2. INPUT DATA AND DATA ANALYSIS

ISOPHOT Serendipity Survey (ISOSS) data was obtained with the C200 2x2 stressed GeGa pixel array (see Lemke et al., 1996) using the C_160 broad band filter. Details on the measuring mode and the standard signal derivation are given by Bogun et al. (1996), and Stickel et al. (these proceedings). The angular resolution perpendicularly to the slews is set by the Airy disk diameter ($d_{\rm Airy} = 2.2$') of the C200 camera, and the "in-slew" resolution is not significantly larger than that since the 1/8 second on-the-fly integration depending on the slewing speed corresponds to an in-slew sampling interval of at maximum 1 arcminute. An indication of the in-slew PSF is the detection of pointlike sources such as UGC 10953 shown in Figure 6 of Stickel et al. (these proceedings).

The positional accuracy is always better than 2' according to Stickel et al. (these proceedings). The absolute photometric accuracy of the surface brightness values calculated with the ISOPHOT Interactive Analysis software PIA [1] version 7.1 or later was found to be 20% (Klaas et al. 1998). The dynamical range covered is 10MJy/sr< $I(170)$ <500MJy/sr.

IRAS ISSA data was extracted along the ISOSS slews (see Hotzel et al. these proceedings). The ISSA 100μm surface brightness values were multiplied by 1.3 according to the COBE DIRBE/ISSA transformation found by Wheelock et al. (1994) which was confirmed by our own comparative analysis of the 100μm DIRBE and ISSA data.

Data analysis: The ISOSS data was smoothed to the ≈ 4.7 arcmin spacial resolution of the ISSA 100μm images. The smoothed 170μm composite image of the Chamaeleon region is shown in Figure 1 of Hotzel et al. (these proceedings). The data then was investigated in two steps. At first cold clouds were identified by their positive 170μm excess defined as $I(170)_{exc} = I(170) - 3.5 * I(100)$. Assuming an emissivity proportional to ν^2 a ratio of $\frac{I(170)}{I(100)} = 3.5$ corresponds to ≈ 15.5K color temperature. That is colder than the average color temperature of cirrus clouds (see eg. Lagache et al. 1998). Laureijs et al. (1991) used a similar relation to identify cold, 60μm deficient regions by their IRAS 100μm excess.

In the second step very cold spots ($T_{dust} < 13$K) were searched among the ISOSS peaks (see more details in Hotzel et al. these proceedings).

3. RESULTS

Some of the findings are summarized for our test regions below. The size of the studied regions in Rho Oph, Chamaeleon, and Cepheus were ≈ 20 deg^2, ≈ 35 deg^2, and ≈ 140 deg^2 respectively. Detailed results of the ISOSS galactic minisurvey will be given elsewhere listing all coordinates, and physical parameters derived.

Rho Oph: Extended $I(170)_{exc}$ is absent in the Rho Oph field. This is the warmest of the 3 studied regions. Only 8 very cold spots were found, which may

[1] The ISOPHOT Interactive Analysis (PIA) is a joint development by the ESA Astrophysics division and the ISOPHOT Consortium. Contributing ISOPHOT Consortium institutes are DIAS, RAL, AIP, MPIK, and MPIA

account for only a small fraction of the $0.3 \times 10^5 M_\odot$ total mass. All the very cold spots are in association with Loren (1989) CO clouds. Loren (1989) found 86 ^{13}CO condensations there, ISOSS observed at least partly 65 (73%) of them. Color temperature was derived for 54 (83%) of the observed clouds. The clouds of the Rho Oph field are among the most active star forming sites in the nearby interstellar matter as shown by a comparison of the young star content of the Cha, Cra, Lup, Oph, and Tau clouds by Chen et al. (1998). The high energy density interstellar radiation field may result the observed low number of very cold spots.

Chamaeleon: Seven extended cold clouds showed $170\mu m$ excess in the $0.1 \times 10^5 M_\odot$ ISM in Chamaeleon. These are all located inside large ^{12}CO clouds of Dame et al. (1987). We found 18 very cold spots, all associated with ^{13}CO clouds of Mizuno et al. (1998), and with optical nebulosities. Those 4 which were already measured in $C^{18}O$ (1-0) have low gas kinetic temperatures of 7 ± 1K. See also Hotzel et al. (these proceedings).

Cepheus: The cold clouds form 3 large associations at the eastern, northern, and western boundaries of the $2 \times 10^5 M_\odot$ Cepheus Flare giant molecular cloud, and one towards its center. As many as 105 very cold spots appear there. They are mostly associated with the extended cold regions, and are clustered. Two of the very cold spots of the Cepheus region were detected as ^{13}CO condensations by our dedicated follow-up measurements with the IRAM-30m telescope (Tóth et al. 1998). Investigations of the dark cloud L1168 (Lynds, 1962) are reviewed in Figure 2, where ISOSS, and IRAS sky surface brightness, and location of one of the serendipity slews, is displayed, and the associated molecular cloud is represented by ^{13}CO (1-0) line intensity map. The distribution of $C^{18}O$(1-0) and (2-1) line intensities are similar. The ISOSS detected very cold spot at the centre of L1168 was found to be a dense cold cloud core. A ring shaped CO core was revealed.

4. CONCLUSION AND OUTLOOK

The ISOSS data combined with IRAS 100μm images is a useful tool detecting galactic clouds, and differentiate among them according to their temperature in the 10K$< T_{\rm dust} <$ 70K range. Dust colder than 17K was not traced by IRAS, and clouds containing such cold dust were mostly not resolved by COBE DIRBE. The method used is capable of finding dense cloud cores of low gas kinetic temperature, thus is an effective way to locate these objects. Our mm-wavelength spectroscopic followup in Cepheus, and the $C^{18}O$ measurements of Haikala et al. (1998) and Vilas-Boas et al. (1994) in Chamaeleon demonstrates, that the very cold spots are actually cold molecular cloud cores

The very cold spot search will be extended to the Orion, Taurus, Cygnus, and the Southern Coalsack complexes. Based on the result of our galactic minisurvey we expect to detect few hundred very cold cloud cores in the Milky Way. A series of followup measurements in mm and sub-mm wavelengths has been started in order to derive the physical properties of the gas in the very cold cores.

ACKNOWLEDGMENTS

The ISOPHOT project was funded by the Deutsche Agentur für Raumfahrtangelegenheiten (DARA, now DLR), the Max - Planck - Gesellschaft, the Danish, British and Spanish Space Agencies and several European and American institutes.
Members of the Consortium on the ISOPHOT Serendipity Survey (CISS) are MPIA Heidelberg, ESA ISO SOC Villafranca, AIP Potsdam, IPAC Pasadena, Imperial College London.
This research has made use of the Digitized Sky Survey, produced at the Space Telescope Science Institute, NASA's Astrophysics Data System Abstract Service, and the NASA/IPAC Extragalactic Database (NED) which is operated by the Jet Propulsion Laboratory, California Institute of Technology, under contract with the National Aeronautics and Space Administration.

REFERENCES

Alton, P.B., et al. 1998, A&A, 335, 807.

Bogun, S., Lemke, D., Klaas, U., et al. 1996, A&A, 315, L71

Dame, et al. 1997, ApJ.,322, 706.

Haas, M., et al. 1998, A&A, 338, L33.

Haikala, L.K., Mattila, K., Lehtinen, K., Lemke, D. 1998, in "Star Formation with ISO", J.L. Yun & R. Liseau (eds.), ASP Conf. Ser. 132, p.147

Keene, J. 1981, ApJ, 245, 115.

Klaas, U., Laureijs, R., Radovich, M., Schulz, B. 1998, "ISOPHOT Calibration Accuracies", SAI/98-092/Dc Version 2.0 in 'ISO Explanatory Library'

Kun, M. 1998, ApJS, 115, 59.

Laureijs, R.J., Clark, F.O., Prusti, T. 1991, ApJ, 372, 185.

Launhardt, R., Ward-Thompson, D., Henning, T. 1997, MNRAS, 288, L45.

Lehtinen, K., Lemke, D., Mattila, K., Haikala, L.K. 1998, A&A, 333, 702

Lemke, D. et al. 1996, A&A, 315, L64.

Loren, ApJ, 338, 902.

Lynds, B.T., ApJS, 7,1.

Mizuno, A., et al. 1998, ApJ, 507, L83.

Nozawa, S., et al. 1991, ApJS, 77, 647.

Ristocelli, I., et al. 1998, ApJ, 496, 267.

Stickel, M., Bogun, S., Lemke, D., et al. 1998b, A&A, 336, 116

Tóth, L.V., Lisendfeld, U., Lemke, D., Stickel, et al. 1998, in prep.

Vilas–Boas, J.W.S., Myers, P.C., Fuller, G.A. 1994, ApJ, 433, 96

Yonekura, Y., et al. 1997, ApJS, 110, 21.

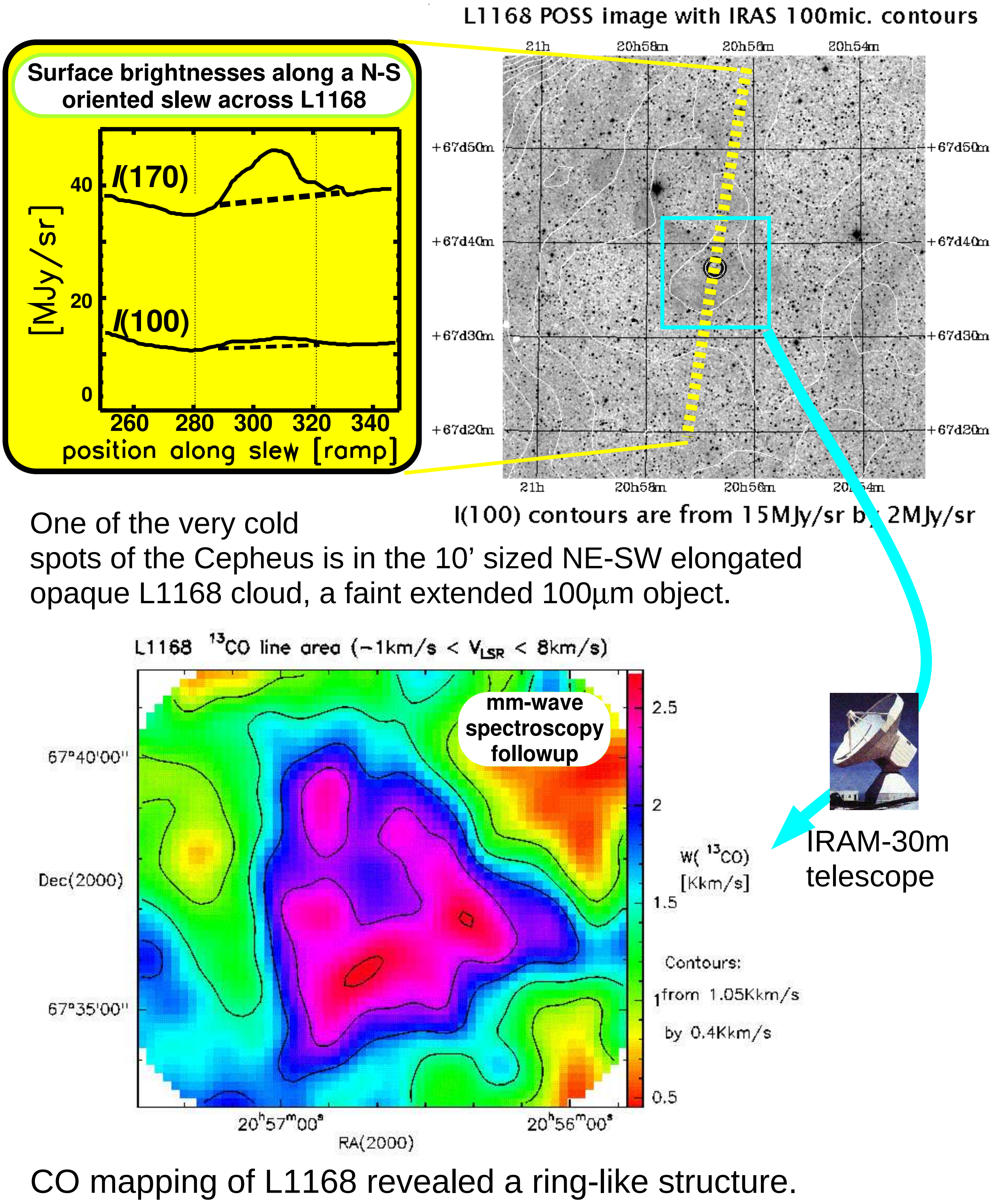

Figure 2. *The L1168 dark cloud is one of the coldest spots of Cepheus. The ISOSS, and IRAS sky surface brightnesses are shown along a serendipity slew crossing L1168 in the top left. The cloud appears as a moderate extinction region on POSS (top right), where the 100µm ISSA contours are overlaid. It's IRAS 100µm excess over the background is small compared to nearby objects. The color map in the bottom shows the distribution of* ^{13}*CO (1-0) line intensity as measured with the IRAM-30m telescope by Tóth, Lisenfeld et al. (1998).*

MID AND FAR INFRARED OBSERVATIONS OF TWO COMPACT H II REGIONS AND ONE COMPACT CO CLUMP

R.P. Verma, S.K. Ghosh, A.D. Karnik, B. Mookerjea & T.N. Rengarajan

Tata Institute of Fundamental Research, Homi Bhabha Road, Mumbai 400005, India

ABSTRACT

Three compact H II regions/ molecular clumps (IRAS 19181+1349, 20286+4105 and 20178+4046) have been observed at mid infrared wavelengths using ISO and at far infrared wavelengths using the TIFR 1 m balloon-borne telescope. ISO observations have been made in seven spectral bands (3.3, 3.7, 6.0, 6.75, 9.6 and 11.4 μm) using the ISOCAM instrument. Four of these bands cover the emission from Polycyclic Aromatic Hydrocarbon (PAH) molecules. Far infrared observations have been made in two bands with effective wavelengths of ~130 and ~210 μm. In addition, IRAS survey data for these sources in the four IRAS bands have also been processed using the HIRES routine. There are structural similarities between the images in the mid infrared bands and the large scale maps in the far infrared bands despite very different angular resolutions of the two. A comparison of the flux densities in different ISO bands clearly shows the importance of the PAH emission. Spectral energy distributions for these sources have been constructed by combining data from all these observations. Radiation transfer calculations through dust cloud have been made to understand these spectral energy distributions as well as the infrared morphologies of these sources.

Key words: Compact H II regions; Molecular clump; PAH.

1. INTRODUCTION

Ultracompact H II regions are a class of interesting astronomical sources as they represent early stages of deeply embedded high mass (O or early B) stars. Therefore their study can provide vital information about high mass star formation as well as their interaction with the parent molecular cloud. They are also often associated with OH/H_2O masers. Being deeply embedded in dust, almost all of their luminosity is emitted in the infrared wave band.

In this paper we report mid and far infrared observations of two ultracompact H II regions, IRAS 19181+1349 and IRAS 20178+4046. We also report observations of a compact molecular clump, IRAS 20286+4105. As a part of the study of Galactic star forming regions (Verma et al. 1994 and references therein) we have mapped these three regions simultaneously in two far infrared bands, using the TIFR 1 m balloon-borne telescope. These regions have also been imaged in seven mid infrared bands using the ISOCAM instrument onboard ISO. Besides these observations, we have processed IRAS data on these sources using the HIRES routine.

2. OBSERVATIONS

2.1. Mid infrared observations

Mid infrared observations have been made using the ISOCAM instrument. Images have been obtained in seven spectral bands– SW2 (3.3 μm), SW6 (3.72 μm), LW4 (6.0 μm), LW5 (6.75 μm), LW6 (7.75 μm), LW7 (9.62 μm) and LW8 (11.4 μm) filters. Of these, four filters (SW2, LW4, LW6 and LW8) cover the PAH bands whereas the remaining three filters serve as comparison to neighboring continuum. Areas of $3' \times 3'$ have been imaged for each source with a pixel field of view of 6 arcsec. The results presented here have been obtained from Auto Analysis Results (AAR) and have been processed with Off-Line Processing (OLP) pipeline (version 6.0).

2.2. Far infrared observations

Far infrared observations were made with the TIFR 1 metre telescope during a balloon flight made on February 20, 1994. The observations were made simultaneously in two bands with effective wavelengths of ~130 μm and 210 μm. The detectors consist of two arrays (2×3) of Si bolometers cooled to 0.3 K by closed cycle ^{3}He refrigerator. The field of view for each detector is 1.6 arcmin. Chopping is done by vibrating the secondary mirror at a frequency of 10 Hz and a throw of 3.6 arcmin. Areas of $\sim 20' \times 20'$ around each source were twice scanned in a raster mode. Data have been deconvolved using a Maximum Entropy Method (MEM). Jupiter was observed for flux calibration. The final resolution in the deconvolved maps is ~ 1 arcmin. The details of the telescope and the observational procedure are given in Ghosh et al. (1988) and that of the photometer in Verma et al. (1993).

Proceedings of the Conference "The Universe as seen by ISO", Paris, France, 20–23 October 1998 (ESA SP-427, March 1999)

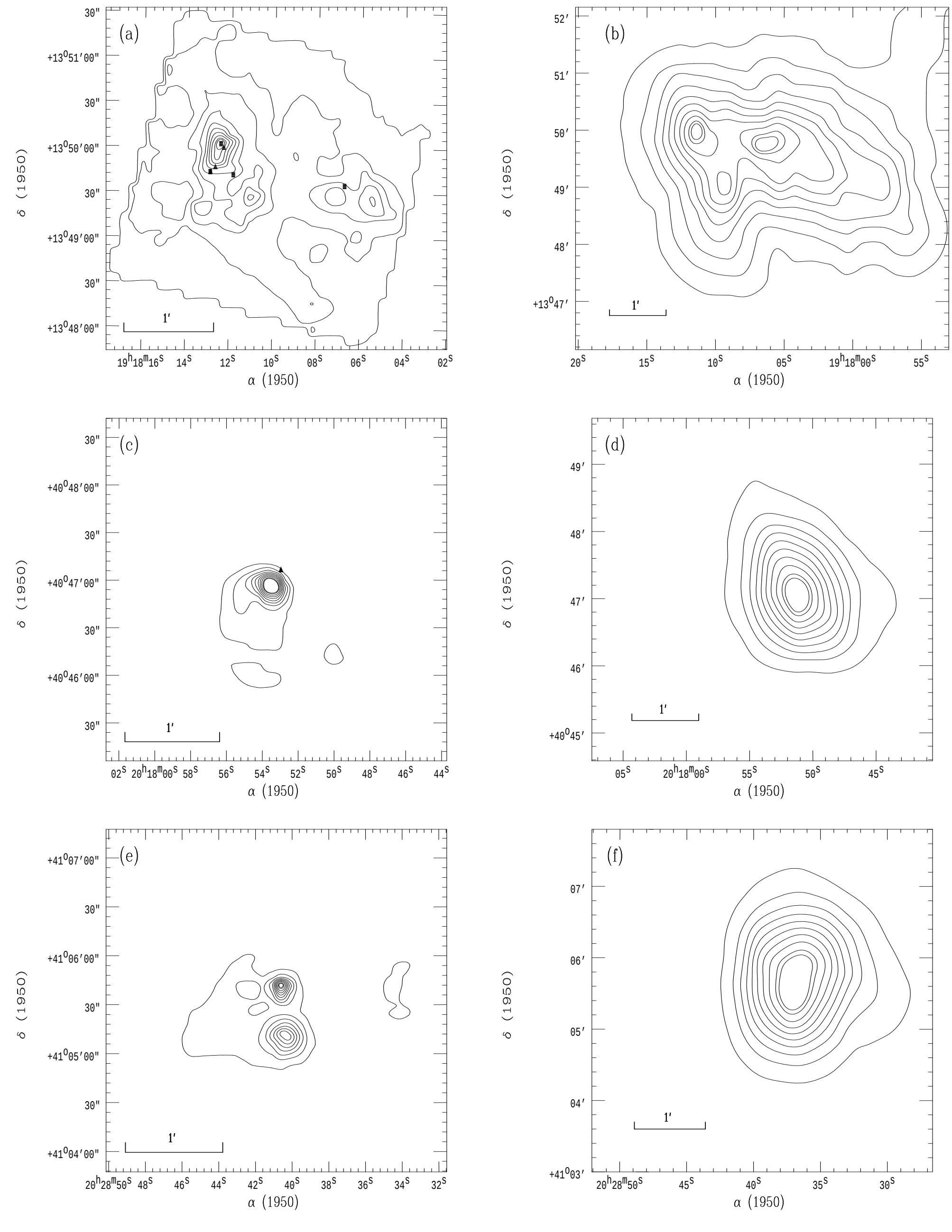

Figure 1. Maps of the sources in the mid and far infrared bands. In (a) and (b) (the top panel) we show the maps of IRAS 19181+1349 at 6.75 μm and 210 μm respectively; in (c) and (d) (the middle panel) we show the maps of IRAS 20178+4046; and in (e) and (f) (the bottom panel) the maps of IRAS 20286+4105. The contour levels are 10, 20, 30, 40, 50, 60, 70, 80, 90 and 95 per cent of the peak. In (a) and (c) the triangles and the squares represent the positions of small diameter radio sources from Kurtz et al. (1994) and Zoonematkermani et al. (1990).

IRAS survey data in the four bands have been processed using HIRES routine and intensity maps obtained.

3. RESULTS

Mid infrared images have been obtained for the three sources in the seven bands. IRAS 19181+1349 shows multiple structures in all the LW filters; in the SW filters only the main source can be seen. IRAS 20178+4046 shows only one component with a weak extension towards the south. IRAS 20286+4105 shows multiple structures in all the filters. The contour maps of the three sources in the LW5 filter (6.75 μm) are shown in Figure 1 (a, c and e). Flux densities of relatively strong sources in these images in various filters have been given in Table 1. It can be seen from this table that the flux densities are higher in the bands covering PAH emission as compared to those in the neighboring bands. This shows that PAH molecules play important role in these regions.

Table 1. Flux densities of strong sources in the ISO images

Source	RA (1950)	Dec. (1950)	Flux Density in Jy*						
			SW2 3.3 μm PAH	SW6 3.7 μm	LW4 6.0 μm PAH	LW5 6.7 μm	LW6 7.7 μm PAH	LW7 9.6 μm	LW8 11.4 μm PAH
19181+1349	19 18 12.3	+13 50 01	0.67	0.65	2.3	1.3	5.4	1.2	3.6
			(0.72)	(0.55)	(2.3)	(2.5)	(4.5)	(1.6)	(3.5)
	19 18 05.4	+13 49 19	–	–	(1.2)	(1.5)	(3.4)	–	–
	19 18 06.9	+13 49 24	–	–	(1.0)	(1.0)	(2.1)	(0.84)	(3.0)
20178+4046	20 17 53.1	+40 46 55	–	–	10.8	10.3	28.7	12.2	22.9
			–	–	(16.3)	(14.3)	(39.3)	(16.6)	(28.3)
	20 17 51.8	+40 47 16	0.86	0.53	–	–	–	–	–
			(1.8)	(0.7)					
20286+4105	20 28 40.2	+41 05 39	–	–	2.8	2.0	7.5	2.1	3.8
			–	–	(3.3)	(3.2)	(8.5)	(2.2)	(3.0)
	20 28 39.9	+41 05 09	–	–	3.2	2.6	7.3	2.1	4.5
			–	–	(5.3)	(5.1)	(13.7)	(4.0)	(7.3)

*For each source the first line gives the flux densities from Point Source List (CPSL) files whereas the second line gives (in parenthesis) the flux densities integrated over circles of 30 arcsec diameter.

Far infrared maps have been obtained for all the three sources in both the bands (130 μm and 210 μm). The maps in the 210 μm band are shown in Figure 1 (b, d and f). At this wavelength (also at 130 μm), IRAS 19181+1349 shows multiple structures very similar to those seen in the mid infrared; IRAS 20286+4105 shows elongation, roughly along the line joining the two sources at mid infrared and IRAS 20178+4046 shows only one component.

HIRES-IRAS maps of IRAS 19181+1349 at 12 and 25 μm show two sources separated along E-W but at longer wavelengths the two sources are not resolved. For the other two sources the IRAS maps show only a single source. The flux densities obtained from the far infrared maps are given in Table 2. Infrared spectral energy distribution (SED) for these sources, based on all the available observations (ISO, IRAS LRS, IRAS HIRES maps and TIFR), is shown in Figure 2.

4. DISCUSSION

In order to understand the infrared emission from these sources, radiation transfer calculations have been performed. As IRAS 19181+1349 shows two components in most of the bands, it has been modeled (Karnik & Ghosh 1998) as consisting of two sources. Each of these sources is represented by a star surrounded by a compact spherical dust clump. The radiation transfer calculations within these dust clumps have been made using the code CSDUST3 developed by Egan et al. (1988). These clumps are assumed to be surrounded by a cylindrical dust shell of uniform density. The distance of the source has been adopted as 9.7 kpc after Kurtz et al. (1994). The composition of the dust has been taken as a mixture of graphite, silicates and silicon carbide with ratios of different types of dust as parameters. The best fit to the SED has been obtained by varying different parameters of the model. Three types of radial density distributions (uniform, r^{-1} and r^{-2}) have been tried within the spherical clumps. The calculated SED for the best fit model is shown in Figure 2a. For this best fit model, the parameters are – luminosity of each star 6.3×10^5 $L_\odot$; inner radius of the spherical shell (r_{in}) 0.001 pc; outer radius (r_{out}) of the spherical shell 0.35 pc; $\tau_{100\,\mu m}$ for the spherical shell 0.01 for the E source and 0.02 for the W source; exponent of the radial density distribution in the spherical shell -2; $\tau_{100\,\mu m}$ for cylinder 0.013/pc; radius of the cylinder 4.0 pc and the dust composition C:Silicate:SiC as 40:60:0. The calculated radial distribution fits reasonably well the observed one.

IRAS 20178+4046 has been modeled as a single star surrounded by spherical dust shell. Its distance has been adopted as 3.3 kpc after Kurtz et al. (1994). The calculated SED for the best fit model is shown in Figure 2b. For this best fit model, the parameters are – luminosity of the star 9.7×10^4 $L_\odot$; r_{in} 0.001 pc; r_{out} 0.3 pc; $\tau_{100\,\mu m}$ 0.14; uniform density distribution; and the dust composition C:Silicate:SiC as 92:3:5.

IRAS 20286+4105 has presently been modeled as a single star (two source model for this source is being worked out) surrounded by a spherical dust shell. Its distance has been adopted as 3.7 kpc after Molinari et al. (1996). The calculated SED for the best fit model is shown in Figure 2. For this best fit model, the parameters are – luminosity of the star 3.2×10^4 $L_\odot$; r_{in} 0.016 pc; r_{out} 1.0 pc; $\tau_{100\,\mu m}$ 0.056; uniform density distribution; and the dust composition C:Silicate:SiC as 24:62:14.

ACKNOWLEDGMENTS

We thank the members of the Infrared Astronomy Group, TIFR for their help in instrumentation and support during the balloon flight campaign. We thank the members of the TIFR Balloon Facility, Hyderabad for conducting the balloon flight and the members of the Balloon Instrumentation Group for help during the balloon flight. We thank the Infrared Processing and Analysis Center (IPAC) for the HIRES processing of the IRAS data.

Table 2. Far infrared flux densities of the sources

Source	Flux Density in Jy (in 3 arcmin diameter circle)					
	HIRES-IRAS				TIFR	
	12 μm	25 μm	60 μm	100 μm	130 μm	210 μm
19181+1349(W)	68	403	4098	4246	3542	1223
19181+1349(E)	69	402				945
20286+4105	29	134	934	1240	1657	681
20178+4046	77	621	2318	2548	2932	910

REFERENCES

Egan, M.P., Leung, C.M., Spagna G.F. 1988, Computer Physics Communications, 48, 271

Ghosh, S.K., Iyengar, K.V.K., Rengarajan, T.N. et al. 1988, ApJ, 330, 928

Karnik, A.D., Ghosh, S.K. 1998, (in preparation)

Kurtz, S., Churchwell, E., Wood, D.O.S. 1994, ApJS, 91, 659

Molinari, S., Brand, J., Cesaroni, R., Palla, F. 1996, AA, 308, 573

Verma, R.P., Rengarajan, T.N., Ghosh, S.K. 1993, Bull. Astr. Soc. India, 21, 489

Verma, R.P., Bisht, R.S., Ghosh, S.K. et al. 1994, AA, 284, 936

Zoonematkermani, S., Helfand, D.J., White, R.L. et al. 1990, ApJS, 74, 181

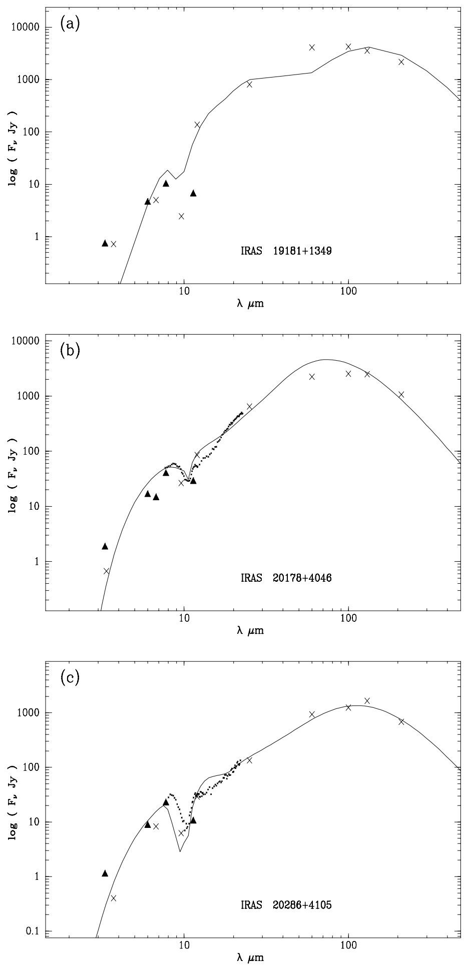

Figure 2. Infrared SED of (a) IRAS 19181+1349; (b) IRAS 20178+4046 and (c) IRAS 20286+4105. The triangles show the ISO fluxes in the PAH filters whereas crosses show continuum observations (from ISO, IRAS or TIFR) and dots represent the IRAS LRS data. The continuous lines represent the best fit model SEDs.

HOT CHEMISTRY IN THE DIFFUSE MEDIUM: SPECTRAL SIGNATURE IN THE H_2 ROTATIONAL LINES

L. Verstraete[1], E. Falgarone[2], G. Pineau des Forêts[3], D. Flower[4], & J.-L. Puget[1]

[1]Institut d'Astrophysique Spatiale, Orsay, France
[2] Radioastronomie Millimétrique, Ecole Normale Supérieure and Observatoire de Paris, Paris, France
[3] DAEC, Observatoire de Paris, Meudon, France
[4] Physics Department, The University, Durham, UK

ABSTRACT

Most of the diffuse interstellar medium is cold, but it must harbor pockets of hot gas to explain the large observed abundances of molecules like CH^+ and HCO^+. Because they dissipate locally large amounts of kinetic energy, MHD shocks and coherent vortices in turbulence can drive endothermic chemical reactions or reactions with large activation barriers. We predict the spectroscopic signatures in the H_2 rotational lines of MHD shocks and vortices and compare them to those observed with the ISO-SWS along a line of sight through the Galaxy which samples 20 magnitudes of mostly diffuse gas.

Key words: turbulence, chemistry, shocks, intermittency, H_2 rotational lines.

1. THE TRIGGER OF HOT CHEMISTRY IN THE COLD DIFFUSE MEDIUM

The large observed abundances of CH, CH^+, HCO^+, and OH in the (mainly cold) diffuse medium (T $\approx$ 50 K) imply that activation barriers and endothermicities of several 10^3 K are overcome. Pockets of hot gas must therefore exist. Large ion-neutral drift speeds, of several km s^{-1}, can equally contribute to triggering certain ion-neutral reactions in cold gas, such as the endothermic reaction $C^+ + H_2$ which forms CH^+ ($\Delta E/k$=4640 K). Two phenomena, operating on very different scales, are able to reproduce the observed abundances. These are MHD shocks (Flower & Pineau des Forêts, 1998 and references therein) and intense vortices, thought to be responsible for a large fraction of the viscous dissipation of supersonic turbulence (Joulain, Falgarone, Pineau des Forêts & Flower 1998).

In MHD shocks, the neutrals are heated by the ion-neutral drift which occurs in the magnetic precursor. The peak kinetic temperature of the neutrals depends on the shock velocity: it is $T_n \approx 10^3$ K for a 10 km s^{-1} shock propagating in a gas at n = 20 cm^{-3}. The hot layers have a thickness $\approx$ 0.1 pc or 20 000 AU and the time for a fluid particle to cross the hot layers $\approx 10^4$ yr.

In dissipative vortices with a magnetic field, the main heating mechanism is viscous dissipation in the layers of strong shear at the outer boundaries of the vortices. The streaming of the neutrals relative to the ions contributes no more than 10% of the total heating rate. The size of such vortices is ill-defined because no laboratory experiment is able yet to establish the dissipative scales in compressible MHD turbulence. For the sake of simplicity, and to allow an analytic description of these vortices with only two independent parameters, Joulain et al. (1998) adopted $r \approx 20$ AU, a radius close to the Kolmogorov scale (i.e. that of the viscous dissipation in the turbulent cascade). This radius corresponds to a balance between the stretching action of the large scales, which increases the vorticity, and the diffusion of the vorticity. In laboratory experiments on incompressible turbulence (Cadot et al. 1995; Belin et al. 1996), coherent vortices have been found to have radii which range between the Kolmogorov and the Taylor microscale. We assume that dissipative vortices in interstellar turbulence have radii $\approx$ 20 AU, and up to ten times larger. For a rotational velocity of 3.5 km s^{-1}, the temperature of the neutrals in the outer layers, which are heated by viscous dissipation, is $T_n \approx 10^3$ K and their thickness is comparable to the vortex radius. The timescale for a fluid particle to cross the hot layers is much shorter than for MHD shocks, a few 100 yr only in the case of the thinnest vortices.

The size and the crossing time are the main differences between MHD shocks and dissipative vortices. Non-equilibrium effects are therefore expected to be more pronounced in the latter. The column densities of molecules formed specifically in the hot layers (or layers with large ion-neutral drift) are consequently much larger in a single MHD shock than in a single vortex. The column densities of CH^+, for example, are compared in Table 1.

The column densities of CH and CH^+ observed in absorption in the direction of nearby stars tend to increase linearly with the total gas column density sampled by the line of sight (A_v). We have merged the data of Crane et al. (1995), which sample low

Proceedings of the Conference "The Universe as seen by ISO", Paris, France, 20–23 October 1998 (ESA SP-427, March 1999)

column densities, with those of Gredel (1997), which sample a larger range of A_v (up to 4.5 mag), and obtain the following scaling relation:

$$N(\mathrm{CH}^+) \approx 1.5 \times 10^{13} \left(\frac{A_v}{1\mathrm{mag}}\right) \mathrm{cm}^{-2}$$

This relation enables an estimate to be made of the number of shocks and/or vortices, per magnitude of diffuse gas, which are required to produce the observed column densities of CH^+ and CH. These numbers are also given in Table 1. It should be noted that 1000 vortices per magnitude correspond to only $\approx 1\%$ of the total column density of the gas, and 6 shocks of 10 km s^{-1} to 3%.

Table 1. Column densities of CH^+ produced in shocks and vortices

MHD shocks n_0=20 cm^{-3} B=7 μG		
V_s (km s^{-1})	N(CH^+) (cm^{-2})	number per magnitude
8	8.8×10^{10}	170
10	2.5×10^{12}	6
16	2.2×10^{13}	0.7
Vortices n=30 cm^{-3} B=10 μG		
v_D (km s^{-1})	N(CH^+) (cm^{-2})	number per magnitude
3.5	1.5×10^{10}	1000
4	3×10^{10}	500

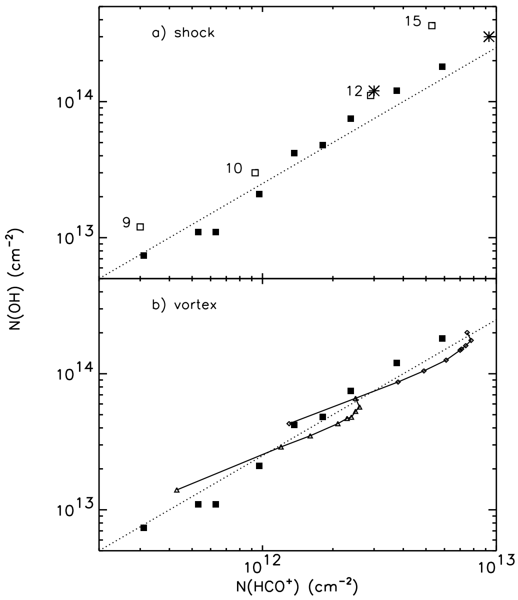

Figure 1. The correlation between the observed column densities of OH *and* HCO^+ *(filled squares are data from Lucas & Liszt,1996). The error bars are smaller than the size of the symbols. The dotted line corresponds* $N(\mathrm{OH})/N(\mathrm{HCO}^+) = 25$. *(a) Column densities predicted by the MHD shock model (open squares) for velocities of 9,10,12 and* 15 kms^{-1}. *The asterisks show the column densities for 10 shocks at velocities of 9 and* 10 kms^{-1} *which account better for the observed values. (b) Column densities predicted by the vortex model for* 10^3 *(connected triangles) and* 3×10^3 *standard vortices (connected diamonds) on the line of sight. Each point along these curves corresponds to a different value of the UV shielding, at the location of the vortex, from* 0.1 *to* 1 *mag.*

Figure 1 illustrates the good agreement between the column densities of OH and HCO^+ observed by Lucas & Liszt (1996) in absorption against extragalactic sources (i.e. on lines of sight which sample the diffuse galactic medium) and model predictions. In Fig. 1a, the predictions for MHD shocks of various velocities and various numbers on the line of sight are shown. In Fig. 1b, those for 1000 and 3000 vortices on the line of sight, and various degrees of shielding from the ambient UV field are shown.

It is not possible, solely on the basis of the abundances they produce, to distinguish between a few MHD shocks or a much larger number of small vortices. Whether the chemically active structures are shocks or vortices has yet to be established. The outcome has a bearing on the lifetimes of molecular clouds and their star formation efficiency: shocks dissipate the supersonic turbulent energy of a cloud on shorter time scales and larger distance scales than do vortices (Porter et al. 1994). If small-scale vortices are the main sites of the dissipation of interstellar turbulence, then the cascade occurs without much dissipation on intermediate scales, between 100 pc (the outer scale) and the size of a planetary system, or over more than five orders of magnitude.

2. ISO SWS OBSERVATIONS OF THE DIFFUSE GALACTIC MEDIUM

2.1. Characteristics of the selected line of sight

To test the existence and determine the characteristics of the small fraction of hot gas in the cold interstellar medium, we have searched for H_2 rotational lines on a long line of sight across the Galactic plane, avoiding star-forming regions and giant molecular clouds.

The selected target was a line of sight toward the inner Galaxy, characterized by a minimum of 5 GHz continuum emission (to ensure the absence of large star-forming regions associated with shocks on the line of sight), and a minimum in CO line emission. The CO(J = 1 - 0) line integrated area (W(CO) =60 K km s^{-1}) provides the column density of H_2 along this line of sight, $N(\mathrm{H}_2) = 1.2\times10^{22}$ cm^{-2}. The 100μm emission $I(100\mu\mathrm{m}) = 2080$ MJy sr^{-1} provides the column density of atomic and ionized gas $N(\mathrm{H}) + N(\mathrm{H}^+) = 1.3\times10^{22}$ cm^{-2}, using the IR luminosity per H nucleus $4\pi\nu I_\nu(100\mu m) = 6\times10^{-23}$ erg s^{-1} H^{-1} estimated above the molecular ring by

Pérault (1987). The total column density sampled by this line of sight is about 20 mag.

The 5 GHz-brightness temperature, $T_{cont}(5\mathrm{GHz}) = 0.5$ K, if due to free-free emission, may be converted into a flux of ionizing photons $N^{\star}_{Lyc} = 1.5 \times 10^{45}$ photon s^{-1}; this corresponds to a single main sequence star of type between B1 and B2, and to a local radiation field $\chi \approx 10$ times more intense than in the solar neighborhood, if the B star is 1 pc from the edge of the molecular cloud observed in CO.

2.2. The spectra

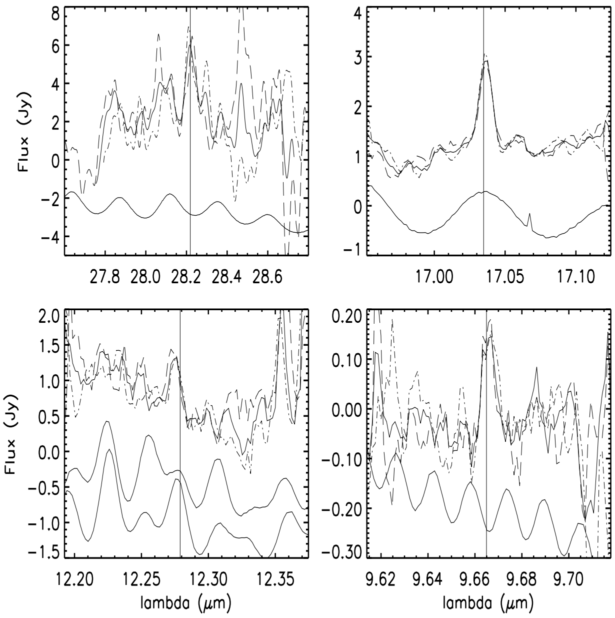

Figure 2. SWS spectra of the H_2 *rotational lines. The full scan (solid) is superposed on the UP (dot-dashed line) and DOWN (dashed) scans. At the bottom of each plot, we display (with an offset) the Relative Spectral Response Function (RSRF) of the instrument for a given detector. Below the S(2) line, we show the RSRF of the first (bottom) and last (top) detectors used in this spectral range. To obtain the best S/N, the low-frequency continuum of the S(3) line was removed: it has a value of* 0.2 *Jy at the line center.*

The line profiles presented here are all (but for the S(0) line) SWS-AOT2 spectra (resolving power $R \approx 2000$) taken during revolution 478 (March 8, 1997) of the ISO satellite. Each individual line has been observed with a succession of 200 seconds scans (17.02μm-S(1) and 12.23μm-S(2) lines: 9 scans each; 9.66μm-S(3) and 8.02μm-S(4) lines: 5 scans each). For the 28.22μm-S(0) line we used a SWS-AOT1 spectrum ($R \approx 800$) taken during revolution 516 (April 15, 1997).

Data reduction was performed within the SWS Interactive Analysis environment. In addition to standard pipeline reduction procedures, in-house tools were used to obtain the best signal-to-noise (S/N) ratio. Details on the data reduction will be given in Verstraete et al. (1999, in preparation).

Figure 2 shows all the detected lines. The UP (wavelength increasing with time during the scan) and the DOWN scans (wavelength decreasing with time) are also displayed. The DOWN scan is first performed, then comes the UP scan; each of these scans lasts 100 seconds. In all cases, the UP and DOWN scans are very similar: we are thus sure that the lines we detect are not due to transient artifacts. We do not show the S(4) line, which was not positively detected; we can estimate only an upper limit to the line flux from the root-mean-square noise at the line position (rms= 0.05 Jy). Our detection of the S(0) line is marginal owing to the poorer sampling of AOT 1; we therefore quote an upper limit to its line flux as well. In any case, the S(0) line emission traces predominantly the cold diffuse gas, which is not our concern here. The S(2) line is clearly detected but is blueshifted by about 100 km s^{-1}, i.e. half a resolution element. We are currently investigating the origin of this blueshift.

Line fluxes and errors have been estimated from gaussian fits to the line profiles shown in Fig. 2. We used the aperture sizes given in de Graauw et al. (1996) to convert to integrated brightnesses. The detected line intensities are $2.2(\pm 0.43) \times 10^{-5}$, $1.4(\pm 0.36) \times 10^{-5}$ and $5.6(\pm 1.68) \times 10^{-6}$ erg s^{-1} cm^{-2} sr^{-1} for the S(1), S(2) and S(3) lines respectively (the errors quoted include the absolute calibration error of the SWS from Schaiedt et al. 1996). Upper limits of 1.1×10^{-4} and 2.4×10^{-6} erg s^{-1} cm^{-2} sr^{-1} are found for the S(0) and S(4) lines respectively.

3. COMPARISON WITH MODEL PREDICTIONS

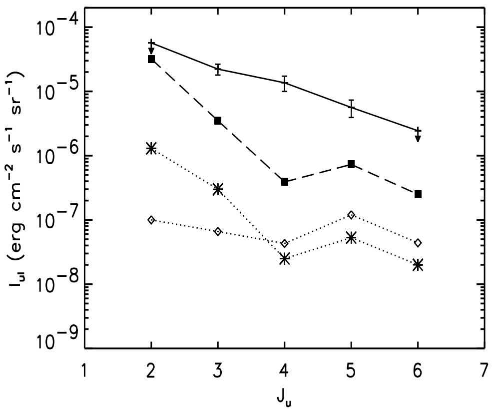

Figure 3. Comparison of the observed H_2 *line intensities (connected by a solid line) along the line of sight sampling the galactic diffuse medium to PDR model predictions, computed for* $\chi = 10$ *and* $n = 100$ *(asterisks) and* 10^4 *cm*$^{-3}$ *(diamonds). The estimated contribution of the cold ambient gas is shown by the solid squares.*

First, we have compared the observed H_2 line emission to that of the interface between the H II region of the B star and the molecular cloud (assuming they are contiguous). The line emission of such a PDR ($n = 100$ and 10^4 cm $^{-3}$ and $\chi = 10$) is shown in

Figure 3 together with the observed rotational line intensities. The expected emission from the 20 mag of cold diffuse gas is also shown on this Figure. To compute it, we have assumed that all the diffuse gas along the line of sight is PDR material i.e. the line of sight crosses a large number of edges of cold neutral clouds (n = 30 cm^{-3}) illuminated by the ambient ISRF (χ = 1). The adopted depth of each individual PDR is A_v = 0.3 mag, and the total number of interfaces along the line of sight is 20/0.3=67. Note that the H_2 line emission of the ambient gas depends only weakly on the above assumptions. The line intensities vary by less than a factor 2 if all the gas is assumed to be at A_v = 0.1 mag or if the adopted depth of each individual PDR is A_v = 0.5 mag. Except for the S(0) line, for which a non-negligible fraction arises in the cold diffuse gas, the observed higher transitions of H_2 are more than one order of magnitude more intense than the line fluxes expected from the interface between the H II region and the molecular cloud. Furthermore, all the observed lines but the S(0) line are significantly more intense than those expected from the ambient emission.

In Figure 4 we compare the H_2 line intensities (normalized to 1 mag of gas sampled by the line of sight) to those computed for the numbers of MHD shocks and vortices given in Table 1.

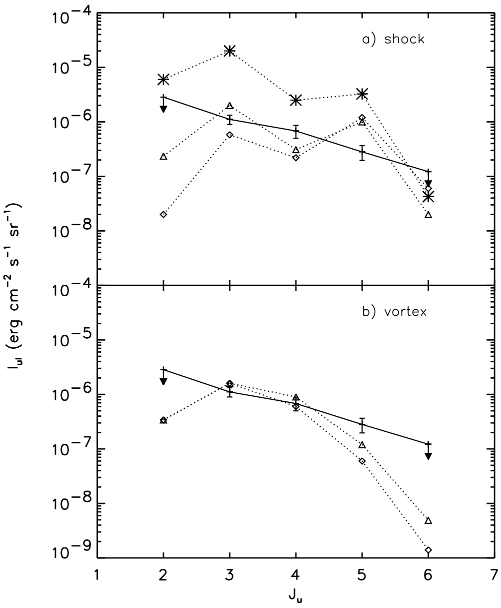

Figure 4. (a) Predictions of the H_2 *line intensities in the MHD shock models. The emission is that from* 170 *shocks (per magnitude) of* 8 *km s*$^{-1}$ *(asterisks),* 6 *shocks (per magnitude) of* 10 *km s*$^{-1}$ *(triangles) and* 0.7 *shocks (per magnitude) of* 16 *km s*$^{-1}$ *(diamonds), all of which are able to reproduce the observed* $N(CH^+)$ *per magnitude. (b) Predictions of the* H_2 *line intensities of the vortex model for* 1000 *isolated vortices per magnitude (triangles) or repeated impulsive heatings (diamonds), which are able to reproduce the observed* $N(CH^+)$ *per magnitude. For comparison purposes, the observed intensities (solid line) have been divided by* 20 *mag in both figures.*

4. CONCLUSION

The H_2 rotational emission of the diffuse medium detected along this line of sight across the Galaxy does not arise in the cold diffuse gas nor in the PDR possibly associated with the low brightness free-free emission and the small fraction of dense gas. On the other hand, the H_2 emission might be produced by a large number of localised hot regions (MHD shocks or dissipative vortices) which are the most plausible sites of formation of CH^+, CH, OH, HCO^+, C_2H ..., observed in the diffuse medium.

Further observations are necessary in order to distinguish the shocks from the vortices:
- high spectral resolution observations of molecular emission
- further tests of departures from equilibrium, which are more pronounced in the short-lived vortices.

ACKNOWLEDGEMENTS

We are grateful to John Black for useful comments on the fluorescent emission of molecular hydrogen from ambient gas.

REFERENCES

Belin, F., Maurer, J., Tabeling, P., Willaime, H. 1996 J. Physique II 6, 573

Cadot, O., Douady, S., Couder, Y. 1995 Phys. Fluids 7, 630

Crane, P., Lambert, D.L., Sheffer, Y. 1995 ApJS 99, 107

Flower, D.R., Pineau des Forêts, G. 1998 MNRAS 297, 1182

de Graauw, Th. et al. 1996 A&A 315, L49

Gredel R. 1997 A&A 320, 929

Joulain, K., Falgarone, E., Pineau des Forêts, G., Flower, D. 1998 A&A 340, 241

Lucas, R., Liszt, H.S. 1996 A&A 307, 237

Pérault M. 1987 PhD dissertation, Université Paris VII

Porter, D.H., Pouquet, A., Woodward, P.R. 1994 Phys. Fluids 6, 2133

Schaiedt, S.G. et al. 1996 A&A 315, L55

GRAIN DYNAMICS IN PHOTODISSOCIATION REGIONS

J.C. Weingartner[1] **& B.T. Draine**[2]

[1]Physics Department, Princeton University, Princeton, NJ, USA
[2]Princeton University Observatory, Princeton, NJ, USA

ABSTRACT

We discuss the forces on grains exposed to anisotropic radiation fields, including the usual "radiation pressure" force and also recoil forces due to photoemitted electrons, photodesorbed hydrogen atoms, and hydrogen molecules which form on the grain surface. We show that these forces can lead to grain dynamics in photodissociation regions which result in enhanced dust-to-gas ratios. Since the gas heating is probably dominated by photoelectric emission from dust, this might explain the unusually high gas temperatures inferred from ISO observations of molecular hydrogen in photodissociation regions.

Key words: dust; photodissociation regions.

1. INTRODUCTION

Far ultraviolet radiation incident on a cloud of molecular material dissociates molecules, giving rise to a surface layer of largely atomic material, called a photodissociation region (PDR). When a hot star is located near a molecular cloud, much of the star's radiant output is absorbed and reprocessed in the resulting PDR. Dust in the PDR efficiently absorbs UV photons, which results in thermal IR emission. The warm gas cools via forbidden transitions in metal atoms and ions and via rovibrational transitions in H_2. Thus, the conditions in PDRs are probed observationally by IR studies. Many theoretical PDR models have been developed, and include quantitative determinations of IR diagnostics (e.g. Tielens & Hollenbach 1985; Draine & Bertoldi 1996; see also the review by Hollenbach & Tielens 1997 and references therein). The detailed understanding of PDRs will yield information on the structure of molecular clouds and their interaction with young stars, and thus ultimately on the process of star formation.

As discussed by Draine & Bertoldi (these proceedings), observations with the ISO short wavelength spectrometer have yielded the H_2 rotational distribution functions in PDRs, from which surprisingly high values of gas temperature (500 – 1000 K) have been inferred. It is not yet clear what heating processes are able to maintain the gas at such high temperatures. Photoelectric emission from dust grains is expected to be a major mechanism, but calculated heating rates are inadequate. Here we consider the possibility of enhanced dust-to-gas ratios in PDRs, which would imply increased photoelectric heating rates.

2. GRAIN DYNAMICS

Enhanced dust-to-gas ratios can result when grains drift with respect to the gas. We will begin by describing the motion of the gas (see Figure 1). Ionizing radiation from the hot star located near the molecular cloud (MC) photoevaporates material at the cloud surface, which then expands into the intercloud medium in a photoevaporative flow (PF). Thus, the ionization front propagates into the cloud. In our analysis, we adopt the frame of reference in which the ionization front is stationary; in this frame material flows through the PDR.

If no other forces acted on the grains, they would simply be dragged along by the gas. However, there are forces associated with the anisotropic stellar UV radiation field. In addition to the usual "radiation pressure" force due to absorption and scattering ($F_{\rm rad}$), there are also recoil forces, due to photoemitted electrons ($F_{\rm pe}$) and due to photodesorbed adatoms and H_2 molecules which form on the grain surface ($F_{\rm pd}$). As a consequence of these "radiative" forces, the grains drift with respect to the gas, at speed $v_{\rm drift}$. If the gas moves at speed v_0 with respect to the ionization front then the grains move at speed $v_0 - v_{\rm drift}$. Deep within the PDR, where the stellar UV has been attenuated, $v_{\rm drift} = 0$. The grain overdensity near the ionization front is obtained using the continuity equation:

$$\frac{n_{\rm i}}{n_0} = \left(1 - \frac{v_{\rm drift,i}}{v_0}\right)^{-1}, \qquad (1)$$

where n_0 ($n_{\rm i}$) is the grain number density deep within the PDR (near the ionization front) and $v_{\rm drift,i}$ is the drift speed near the ionization front; we assume one-dimensional flow and ignore magnetic fields. Since the drag force is roughly proportional to the drift

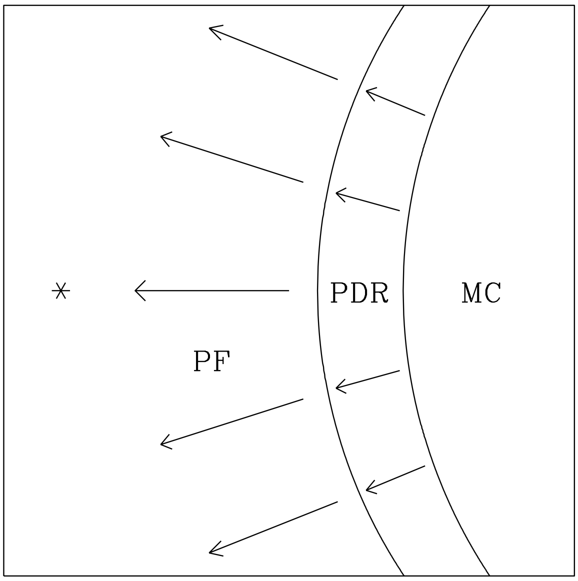

Figure 1. The physical picture.

speed, the overdensity is also given by

$$\frac{n_{\rm i}}{n_0} = \left(1 - \frac{F_{\rm tot}}{F_{\rm stop}}\right)^{-1}, \tag{2}$$

where $F_{\rm tot}$ is the sum of the radiative forces near the ionization front and $F_{\rm stop}$ is the magnitude of the radiative force which would result in $v_{\rm drift} = v_0$ (in which case the grains would be stopped near the ionization front).

3. EVALUATION OF RADIATIVE FORCES

Throughout, we assume spherical grains, so that Mie theory can be applied for the grain optics.

3.1. Radiation pressure force

The radiation pressure force is given by

$$F_{\rm rad} = \pi a^2 \int_0^{\nu_{\rm H}} d\nu\, u_\nu \left[Q_{\rm abs} + Q_{\rm sca}(1 - \langle\cos\theta\rangle)\right], \tag{3}$$

where a is the grain radius, $\nu_{\rm H} = 13.6\,{\rm eV}/h$, u_ν is the radiation energy density per frequency interval, and $\langle\cos\theta\rangle$ is the usual scattering asymmetry factor. We compute the absorption and scattering efficiency factors, $Q_{\rm abs}$ and $Q_{\rm sca}$ respectively, using a Mie theory code derived from BHMIE (Bohren & Huffman 1983) with dielectric functions as described by Draine & Lee (1984) and Laor & Draine (1993).

3.2. Photoelectric force

We adopt a physical model for the photoelectric emission process (see Bakes & Tielens 1994, Weingartner & Draine 1999a). Of course, the photoemission rate and the total energy of the emitted electrons depend on the grain's ionization potential, IP; for simplicity we take the electron energy $E_{\rm el} = (h\nu - IP)/2$, where $h\nu$ is the energy of the absorbed photon. The ionization potential depends on the grain charge; the charge distribution is determined by the rates of electron attachment by accretion from the gas and removal by photoemission. Thus, the average photoelectric force depends on the ambient conditions; including the spectrum and energy density of the radiation and the gas density, ionization, and temperature; through their effects on the charge distribution. For a fixed charge state, the force is given by

$$F_{\rm pe} = \pi a^2 \int_{\nu_{\rm Z}}^{\nu_{\rm H}} d\nu\, \frac{c u_\nu}{h\nu} A Y Q_{\rm abs} S \sqrt{2 m_e E_{\rm el}}, \tag{4}$$

where $\nu_{\rm Z} = IP/h$, Y is the photoelectric yield, the emission asymmetry factor $A(h\nu, a)$ measures the asymmetry in the emission of photoelectrons over the grain surface, the recoil suppression factor S accounts for electron emission in directions other than the surface normal, and m_e is the electron mass.

We follow the simple prescription of Kerker & Wang (1982) for determining the asymmetry factor A. The probability of photoemission from any site on the surface is taken to be proportional to the electric intensity $|\mathbf{E}|^2$ just below the surface at that point. Thus,

$$A(h\nu, a) = \frac{-\int_0^\pi \sin\theta\cos\theta |\mathbf{E}(\theta)|^2\, d\theta}{\int_0^\pi \sin\theta |\mathbf{E}(\theta)|^2\, d\theta}, \tag{5}$$

where θ is the polar angle with respect to the direction of the incident radiation. In Figure 2 we display $A(h\nu, a)$ as a function of incident photon energy for graphite grains of various sizes.

In determining the recoil suppression factor S we assume that the electrons emerge symmetrically with respect to the local surface normal, with a "cosine-law" angular distribution (i.e. the emission rate at angle ψ with respect to the surface normal $\propto \sin\psi\cos\psi$). For an uncharged grain, this would imply $S = 2/3$. When the grain is charged, the electron escapes on a hyperbolic trajectory, so that when it is at infinity its velocity vector makes an angle ψ_∞ with respect to the surface normal which differs from the corresponding angle at the surface, ψ. See Weingartner & Draine (1999b) for the detailed calculation.

3.3. Photodesorption force

In our simple model, we consider the exchange of hydrogen between the gas phase and the grain surface. We assume that the surface is entirely covered with chemisorption sites, as would be the case for bare graphite or silicate grains without ice mantles. When a gas phase H atom strikes the grain surface, it arrives either at an empty site or at a site which is already occupied by an adsorbed H atom. In the

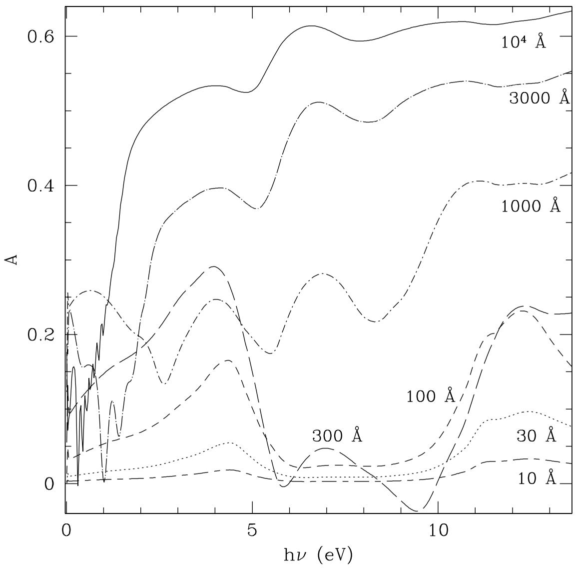

Figure 2. The emission asymmetry factor A as a function of the incident photon energy hν, for graphite grains. The grain radius is indicated for each curve.

former case, it occupies the site with some sticking probability; otherwise it reflects and remains in the gas phase. In the latter case, it recombines with the resident H with some recombination probability; otherwise it reflects and remains in the gas phase. We assume that H_2 formed on the grain surface is immediately ejected from the grain. Adatoms are removed from the grain surface via recombination and photodesorption.

Suppose that the grain's spin axis is aligned with the direction of the radiation anisotropy. Since the photodesorption rate is greater in the illuminated hemisphere than in the non-illuminated hemisphere, relatively more H leaves the surface as atoms in the former and as molecules in the latter. A net recoil force is expected, for two reasons. First, the total number of particles leaving the illuminated hemisphere exceeds that for the non-illuminated hemisphere. Second, the outgoing atoms likely carry a different momentum than the outgoing molecules. A net recoil force of zero is possible, but only if the momenta and sticking and recombination probabilities conspire to have the right values. The photodesorption force is greater when the spin axis makes a non-zero angle with respect to the radiation direction, since H which arrives at non-illuminated sites can be transported to illumination and photodesorbed. For a fuller discussion of the adopted values for relevant parameters and the details of the calculation, see Weingartner & Draine (1999b).

4. THE S140 PDR

Timmermann et al. (1996) studied the PDR associated with the S140 H II region using ISO and concluded that the gas temperature is $\gtrsim 500$ K. We have evaluated the radiative forces for graphite and silicate grains and the conditions in this PDR. To determine $F_{\rm stop}$, we employed the expression for $F_{\rm drag}$ in Draine & Salpeter (1979) and evaluated v_0 using a highly simplified model for the flow in the PDR; see Weingartner & Draine (1999b) for details. We display the ratios of the radiative forces to $F_{\rm stop}$, as a function of grain size, in Figures 3 and 4.

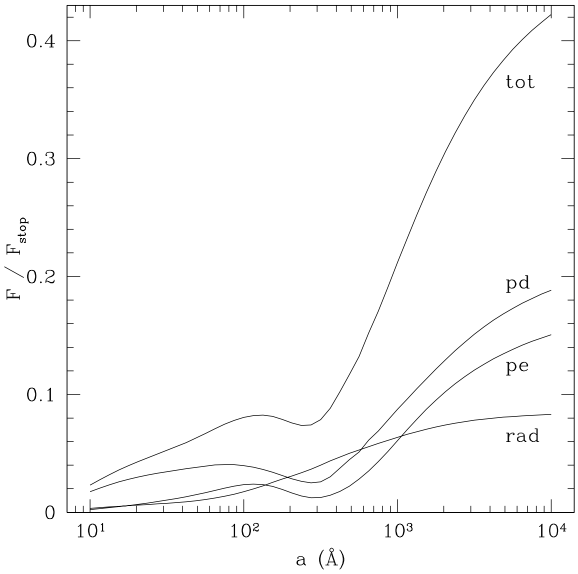

Figure 3. Ratios of the radiative forces to $F_{\rm stop}$, the force needed to stop graphite grains relative to the ionization front, near the ionization front.

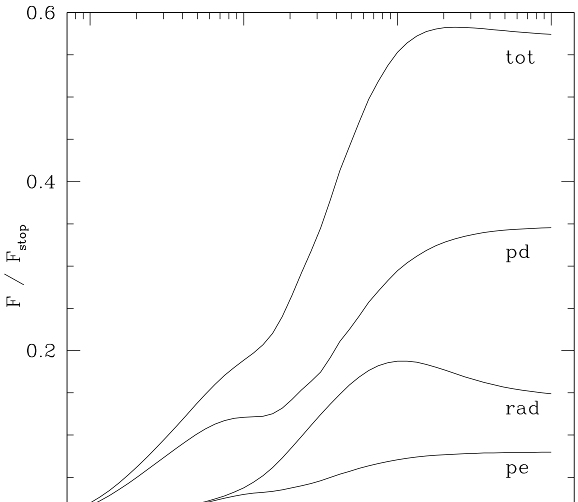

Figure 4. Same as Figure 3, but for silicate grains.

5. CONCLUSIONS AND FUTURE WORK

For the S140 PDR, the forces associated with the anisotropic radiation are apparently large enough to result in significant grain overdensities. It is important to note, however, that the total radiative force is highly uncertain, due to uncertainties in the microphysics of the photoemission and photodesorption processes.

Our program of study will include an examination of more PDRs and also simulations of the dynamics which result when $F_{\rm tot} > F_{\rm stop}$; i.e. when the grains near the ionization front are actually pushed deeper into the PDR. In this case, the further upstream a grain is pushed, the less effective the push, because the radiation is attenuated by other grains downstream. Also, we will add magnetic fields to the analysis. Finally, of course, we will estimate the implications for gas heating.

ACKNOWLEDGMENTS

This research was supported in part by NSF grants AST-9219283 and AST-9619429 and by an NSF Graduate Fellowship to JCW. We are grateful to R.H. Lupton for the availability of the SM plotting package.

REFERENCES

Bakes, E. L. O., & Tielens, A. G. G. M. 1994, ApJ, 427, 822

Bohren, C. F. & Huffman, D. R. 1983, Absorption and Scattering of Light by Small Particles (New York: Wiley)

Draine, B. T. & Bertoldi, F. 1996, ApJ, 468, 269

Draine, B. T. & Lee, H. M. 1984, ApJ, 285, 89

Draine, B. T. & Salpeter, E. E. 1979, ApJ, 231, 77

Kerker, M. & Wang, D.-S. 1982, J. Coll. Interface Sci, 85, 302

Laor, A. & Draine, B. T. 1993, ApJ, 402, 441

Hollenbach, D. J. & Tielens, A. G. G. M. 1997, ARA&A, 35, 179

Tielens, A. G. G. M. & Hollenbach, D. 1985, ApJ, 291, 722

Timmermann, R., Bertoldi, F., Wright, C. M., Drapatz, S., Draine, B. T., Haser, L., & Sternberg, A. 1996, A&A, 315, L281

Weingartner, J. C. & Draine, B. T. 1999a, submitted to ApJ

Weingartner, J. C. & Draine, B. T. 1999b, in preparation

THE GALACTIC CENTRE - A SPECTROSCOPIC AND IMAGING STUDY WITH THE LWS SPECTROMETER

G.J. White[1], **H.A. Smith**[2], **G.J. Stacey**[3], **J. Fischer**[4], **L. Spinoglio**[5], **J.-P. Baluteau**[6], **J. Cernicharo**[7], **& C.M. Bradford**[3]

[1]Physics Department, Queen Mary & Westfield College, London, UK
[2]Harvard Smithsonian Center for Astrophysics, MA 02138, USA
[3]Dept. of Astronomy, Cornell University, New York, USA
[4]Naval Research Laboratory, Washington DC, USA
[5]IFSI, CNR, Rome, Italy
[6]LAS, CNRS, Marseille, France
[7]CSIC, Madrid, Spain

ABSTRACT

We report observations of a fully sampled (spatially and spectrally) mapping of the central few arcminutes around the Galactic Centre, using the ISO LWS. The maps show the relative spatial distributions in about 20 different emission and absorption lines. The circumnuclear disc is clearly traced by some molecular lines, whilst the central region dominates in other atomic and ionised lines.

Spectra are also be shown of several other interesting sources within the Galactic Centre cloud ensemble, including Sgr A West and the 'Sickle' cluster.

Key words: galactic centre; far infrared astronomy; spectroscopy.

1. INTRODUCTION

The nucleus of our Galaxy is located $\sim$ 8.5 kpc from the Earth, more than 100 times closer than the nearest large external galaxy, or one thousandth of the distance to the nearest active Galaxy. Its relative proximity allows detailed views of the structure and physical conditions in the Galactic Nucleus, some of which almost certainly are present in the more distant galactic nuclei. The central regions are characterised by the distribution of stars formed in a past burst of starburst activity. The distribution of material in the central region of the Galaxy has been summarised by Genzel & Townes (1987), Genzel, Hollenbach & Townes (1994) and Zylka et al. (1994, 1995). An unusual compact ($\sim$ 1 AU - Krichbaum et al. 1993, Rogers et al. 1994) variable radio source close to the dynamical centre of the Galaxy, SgrA*, has been proposed to be a quiescent black hole, or a stellar cluster. Within 1 arcsec of SgrA* is a bright infrared complex, IRS16, which contains at least 15 components, and is probably the source of the strong stellar wind which has velocities of up to $\sim$ 700 km s^{-1}. Surrounding this is a cavity, which is dominated by atomic and ionised gas, which contains a total mass $\sim 1 - 3\ 10^6\ M_\odot$, and has a luminosity $\sim 7\ 10^6$ - $2.3\ 10^7\ L_\odot$. Almost all of this luminosity is absorbed by material lying close to the Centre, and then re-emitted as IR continuum, or via atomic and molecular line emission (A_ν to the Nucleus $\sim$ 30 mag). Zylka et al. (1995) show that the column density of warm (T $\sim$ 200 - 400 K) absorbing dust in the centre of the cavity is much lower from the surrounding Circum-Nuclear Disc (CND); a torus of dense and warm atomic and molecular gas and dust.

The CND is a ring of gas and dust, rotating around the central ionised cavity with a velocity $\sim$ 110 km s^{-1} and having a mass $\sim 10^4\ M_\odot$ of clumpy material. First recognised from the far-infrared observations by Becklin, Gatley & Werner (1982) it extends from a radius of 1.5 – 2 pc from the centre out to $\sim$ 6 - 8 pc, and may be connected to the gravitational potential of material in the Galactic Centre (Duschl 1989). Molecular line studies showed that the CND was composed predominantly of highly excited gas, corotating in the same general direction as the rest of the Galaxy (Fukui et al. 1977, Genzel et al. 1982, Harris et al. 1985, Sandqvist & Loren 1985, Serabyn et al. 1986, Gusten et al 1987 a,b). The neutral material in this ring is believed to be hot (T $\sim$ 150 - 450 K), dense ($n_{H_2} \sim 10^{3-7}$ cm^{-3}), and highly fragmented (Genzel et al. 1982, 1988 - filling factor $\sim$ 10 %, Zylka et al. 1995). This clumpy structure allows ultraviolet radiation from the central ionised region to penetrate into the neutral ring, heating and photo-ionising the gas. The likely source of this radiation is the cluster of hot, luminous stars, some of which are the HeI / HI stars detected by Krabbe et al. (1991). The presence of hot gas was independently inferred from the detection of near-IR H_2 emission, which suggested that the material was shock excited at the edge of the ionised region (Gatley et al. 1984).

Proceedings of the Conference "The Universe as seen by ISO", Paris, France, 20–23 October 1998 (ESA SP-427, March 1999)

The neutral gas in the ring appears to be dynamically coupled to the gas in the central cavity of ionised and atomic gas, and has its rotational axis close to that of the larger scale Galactic rotation. The sharp edge of the CND abuts directly against the ionised arc-like filaments (the Minispiral), which has led to speculation that material from the CND may be infalling towards the Centre along the ionised arms of the Minispiral. The submillimetre continuum data (Zylka et al. 1995) show that the central $\sim$ 30 arc second diameter cavity contains $\sim$ 400 $M_\odot$ of dust at T $\sim$ 40 K, 4 $M_\odot$ at $\sim$ 170 K and $\sim$ 0.01 $M_\odot$ at $\sim$ 400 K. The luminosity of the emitted radiation for these three phases is $\sim$ 2 10^6 $L_\odot$, 4 10^6 $L_\odot$ and 5 10^5 $L_\odot$ respectively. The hottest gas lies close to Sgr A*, whilst the brightest far-infrared emission comes from the transition region between the neutral CND and surrounding HII regions such as Sgr A East (a synchrotron shell-like source lying behind the central HII region (Pedlar et al. 1989), which has probably been formed as the result of and explosive event inside its core) and Sgr A West - the central HII region within which Sgr A* is embedded (Dent et al 1993). Lying further out are two molecular clouds, M-0.02-0.07 (also known as the 50 km s^{-1} cloud) and M-0.13-0.08 (also known as the 20 km s^{-1} cloud). These two clouds are believed to be connected together with the core of Sgr A East (Mezger et al. 1989, Okumura et al. 1991, Ho 1994). Recent ISO SWS spectroscopy of the Galactic Centre, and of nearby regions have been reported by Lutz et al. (1997). The excitation of material in the central regions is determined by a relatively soft radiation field, which is seen in the SWS spectrum by the low excitation fine structure line spectrum. (Lutz et al. 1996).

2. OBSERVATIONS

2.1. The Galactic Centre

Figure 1 shows the spectrum observed towards the Centre of the Galaxy. The spectrum is dominated by the 63 μm OI line. In total about 20 lines can be clearly distinguished, with a number of other likely detections which suffer from blending, or noise / baseline uncertainties. Several of the lines are seen in absorption against the continuum emission - notably the species OH, H_2O and CH. H_2O is a species which is already known to be ubiquitous towards many molecular clouds (Cernicharo et al. 1997). In this latter case, the absorption is believed to arise in the tenuous extended envelopes around the clouds.

Table 1 lists the fluxes of the bright lines measured towards SgrA*. These fluxes were obtained by fitting the baseline to adjacent parts of line-free emission, and then integrating under the line. In some cases (such as the CO 16–15 transition at 162.8 μm), there is the possibility of contamination from a nearby OH line. One prominent line that is seen in almost all of the spectra, but for which we have no identification, is the feature near 192.0 μm. In addition to the lines listed in the table, there is evidence for lines of OH (48.7, 163 μm), H_2O (47.9, 63.4, 125.3, 132.4μm), HD (112.0 μm) and CO lines extending up to $\sim$ J_{upper} 25.

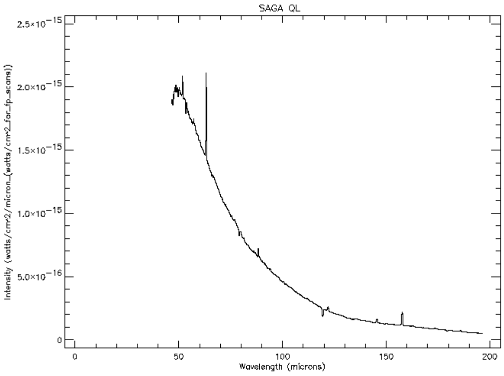

Figure 1. ISO LWS spectrum towards the Galactic Centre. A polynomial baseline has been fitted to the spectrum, to emphasise the relatively weak lines.

Figure 2 shows the continuum subtracted spectrum towards the Galactic Centre. About 20 individual lines can be distinguished above the noise level, including OI 63 and 145 μm. The lower panel has an expanded intensity scale to emphasise the weaker features. Although the spectra at many nearby locations appear similar, the deepest absorption lines relative to the continuum emission occur at the central position. There are a number of features whose presence is currently being worked on, where the baselines have some structure. The reality of such features will be reported later.

Figure 3 shows the maps made from the continuum subtracted spectra in the mapped area, for several of the lines reported here. The mapped area was uniformly mapped on a 20 arcsec grid, allowing full sampling of the region. The four lines shown are typical of the maps of other lines studied - in the case of the OI lines, emission is concentrated close to the centre. By contrast the CII and CO lines show a more pronounced double structure that is similar to the shape of the CND as traced in other molecular lines.

The circumnuclear ring can be clearly seem in a number of the maps, examples shown here include CII and CO. The two positions where the ISO lines peak are known to be strong emitters in molecular and atomic lines (White and Padman 1991, White 1996). It is believed that these two bright spots mark the sites where material is undergoing a strong tidal interaction with the central regions, which results in neutral and atomic gas being stripped off the edge of the circumnuclear ring before spiralling in towards the central mass. The molecular gas is very hot (T $\sim$ 300 - 500 K), and excited both by the effects of tidal stripping, as well as by photo-electric heating from the central ionised cavity. It is known that CO and CII emission is often very strong in warm photo-dissociated gas.

Table 1. Fluxes of the strong lines observed towards SgrA. The negative fluxes indicate lines that are seen in absorption against the continuum emission. The fluxes and identities of a number of other weaker lines will be reported separately.*

Line	Wavelength μm	Flux 10^{-17} W cm^{-2}
OIII	51.7	2.2
NIII	57.3	1.5
OI	63	14.2
OH	79.2	-1.28
OIII	88.3	1.8
OH	119.4	-4.5
NII	121.8	1.7
OI	145.6	1.1
CH	149.0	-6.1
CO 17–16	153.3	0.2
CII	157.7	6.7
CO 16–15 / OH	162.8	0.6
CO 15–14	173.6	0.4
H_2O	179.5	-0.6
CO 14–13	186.0	0.4
Unidentified	192.0	0.4

2.2. Other Galactic Centre sources

The Pistol is small region, with a diameter ~ 40 arc seconds whose radio continuum emission resembles the shape of a gun. A cluster of infrared sources (also known as 'The Quintuplet') lies about 10 - 20 arc seconds North of the Pistol (Okuda et al. 1990, Glass et al. 1990, Glass 1994, Moneti et al. 1993). The Pistol Star (Figer et al. 1998) is a luminous blue variable star, which may have been formed inside the associated nebulosity, and subsequently have been ejected. SWS spectroscopy of the nebulosity (Moneti et al. 1998) suggests a dust temperature of ~ 300 K. The presence of a number of (weak) high excitation lines suggests that the ionising source has an effective temperature of greater than 35000 K, a somewhat harder ionising field that that believed to be present at the Galactic Centre. However, the ISO beam includes not only this nebulosity, but also the emission from the quintupulet cluster, whose SED's are known to peak between 500 and 1000 K. A map of the CO $J=$ 2-1 CO, ^{13}CO and C^{18}O lines shows that the pistol is surrounded by a shell of molecular gas, with a diameter of about 6 arcmin. The Pistol cluster lies in the centre of this cavity, which appears to have been excavated by the effects of the radiation pressure from the luminous stellar cluster associated with the Pistol Nebula.

The lower panel shows a comparison between spectra observed towards the Centre, SgrA W and the Pistol source. The spectra of the first of these objects appear very similar to each other, because of their proximity on the sky. However the Pistol source has a quite different spectral appearance, with notably weak OI 145 μm emission. Lines such as the 179.5 μm H_2O line are again seen in all the spectra, showing it again to be an ubiquitous tracer of the widespread halo of molecular clouds

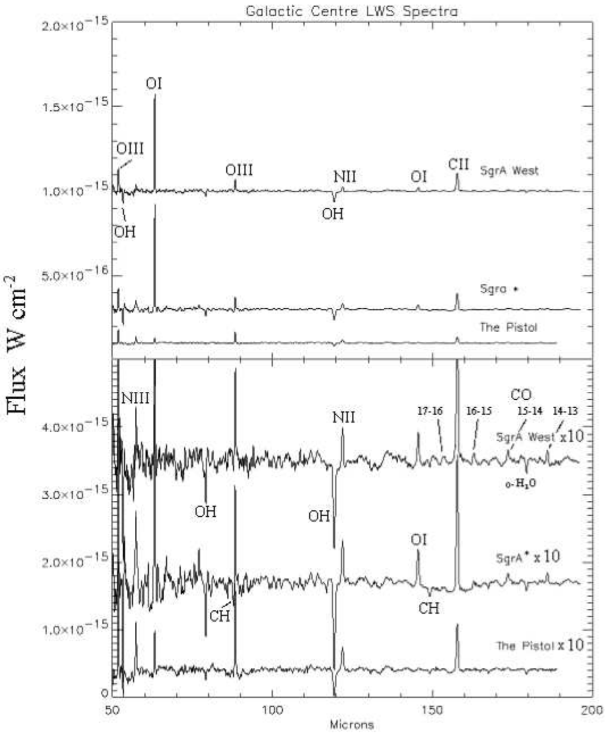

Figure 2. ISO LWS spectrum towards the Galactic Centre. A polynomial baseline has been fitted to the spectrum, to emphasise the relatively weak lines.

ACKNOWLEDGMENTS

We express our appreciation to the instrument construction teams, support staff at Vilspa, RAL and IPAC, to Sunil Sudha and Bruce Swinyard for help with the data, and to Emmanuel Caux for providing a Windows 95 version of ISAP 1.5.

REFERENCES

Becklin, E.E., Gatley, I. & Werner, M.W. 1982, ApJ, 258, 135

Cernicharo, J., Lim, T., Cox, P., Gonzalez-Alfonso, E., Caux, E., Swinyard, B., Martin-Pintado, J., Baluteau, J.P. & Clegg, P.E. 1997, A&A, 323, L25

Dent, W.R.F., Matthews, H.E., Wade, R. & Duncan, W.D. 1993, ApJ, 410, 650

Duschl, W.J. 1989, MNRAS, 240, 219.

Figer, D. et al. 1998, in press

Fukui, Y., Iguchi, T., Kaifu, N., Chikada, Y., Morimoto, M., Nagane, K., Miyazawa, K., Miyaji, T. 1977, PASJ, 29, 643

Genzel, R., Watson, D., Townes, C., Lester, D., Dinerstein, H., Werner, M., Storey, J. 1982, in The galactic center; Proceedings of the Workshop, Pasadena, CA, January 7, 8, 1982 (A83-40676 19-90). New York, American Institute of Physics, p. 72-76

Genzel, R., Hollenbach, D. & Townes, C.H. 1994, Rep. Prog. in Phys, in press

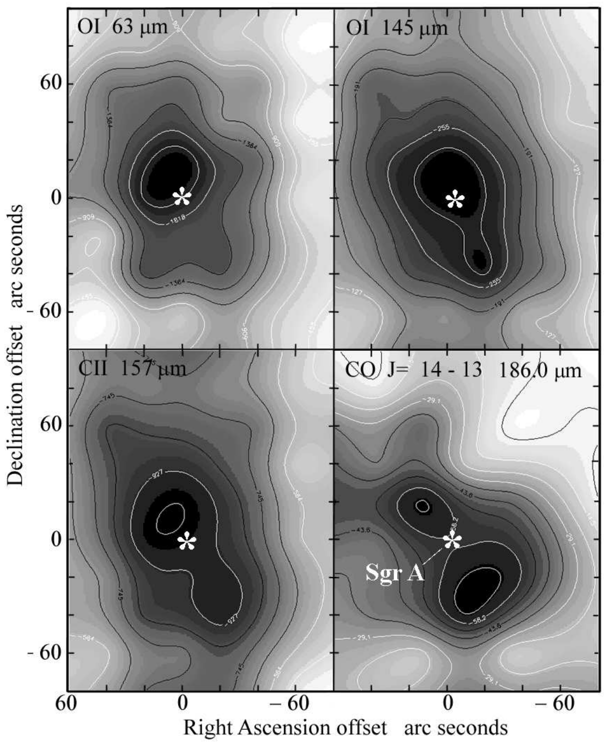

Figure 3. *Maps of the [OI] 63 and 145 μm, [CII] 157 μm and CO J = 4–3 emission lines.*

Genzel, R. and Townes, C.H. 1987, ARAA, 25, 377

Gusten, R., Genzel, R., Wright, M.C.H., Jaffe, D., Stutzki, J. and Harris, A.I. 1987, ApJ, 318, 124

Harris, A.I., Jaffe, D.T., Silber, M. & Genzel, R. 1985, ApJ Lett, 294, L93

Ho, P.T.P. 1994, in 'Astronomy with Millimeter and Submillimeter Wave Interferometry', IAU Colloquium 140, ASP Conference Series, vol. 59, eds. M. Ishiguro and W. J. Welch, p. 161.

Krabbe, A., Genzel, R., Drapatz, S. & Rotaciuc, V. 1991, ApJ, 382, L19

Krichbaum, E., et al. 1993, A&A, 274, L37

Lutz, D., Feuchtgruber, H., Genzel, R., Kunze, D., Rigopolou, D., Spoon, H.W.W., Wright, C.M., Egami, E., Katerloher, R., Sturm, E., Wieprecht, E., Sternberg, A., Moorwood, A.F.M., de Graauw, T. 1996, A&A, 315, L269

Mezger, P.G., Zylka, R., Salter, C.J., Wink, J.E., Chini, R., Kreysa, E. and Tuffs, R. 1989, A&A, 209, 337
Okumura, S. K., Ishiguro, M., Kasuga, T., Morita, K., Kawabe, R., Fomalont, E. B., Hasegawa, T., Kobayashi, H. 1991, ApJ, 378, 127O

Sandqvist, A., Wootten, A., Loren, R. B. 1985, A&A, 152 L25

Pedlar, A., Anantharamaiah, K.R., Ekers, R.D., Goss, W.M., van Gorkom, J.H., Schwarz, U.J. & Jun-Hui Zhao 1989, ApJ, 342, 796.

Rogers, A.E., et al. 1995, ApJ,

Serabyn, E. & Güsten, R., Walmsley, C.M., Wink, J.E., Zylka, R., 1986, A&A, 169, 85

White, G.J. & Padman, R.P. 1991, Nature, 354, 511

White, G. J. 1996, Astronomical Society of the Pacific Conference Series Volume 102, p171 - 178

Zylka, R., Mezger, P.G., Ward-Thompson, D., Duschl, W.J. & Lesch, H. 1995, preprint

Zylka , R., Mezger, P., Wilson, T.L. & Mauersberger, R. 1994, p 161, in The Nuclei of Normal Galaxies, edited by R. Genzel and A. I. Harris. Kluwer Academic Publishers

DUST DISTRIBUTION IN GALACTIC COMPACT H II REGIONS: AN ISOCAM VIEW

A. Zavagno & V. Ducci
Observatoire de Marseille, 2 Place Le Verrier, F-13248 Marseille Cedex 4, France

ABSTRACT

We present the first results of an Open Time ISOCAM program aiming to look at the distribution of the Infrared Emission Features (IEFs) and the associated continua between 3 and 12 μm in five galactic compact H II regions. The idea is to add new observational constraints on the IEF carriers.
The peak location of the IEFs is always found at the interface between ionized and neutral media. The continuum contribution is high near the main exciting star. The (band+continuum) intensity ratios show important variations. However, in all regions and for a given ratio, the same value is found at specific locations of the interface. This result points out the interface as a 'privileged' zone for the study of IEF properties. Finally, a strong rising continuum is observed between 10 and 12 μm. This continuum probably corresponds to the short wavelength part of the thermal emission from cold grains (T$\simeq$ 40 K) that peaks around 70 μm in compact H II regions.

Key words: compact H II regions; infrared emission features; dust; continuum.

1. INTRODUCTION

A series of band, the so-called Infrared Emission Features (IEFs), is seen in various astrophysical sources at 3.3, 6.2, 7.7, 8.6 and 11.3 μm. These bands are commonly attributed to carbonaceous compounds (Lǵer & Puget 1984, Allamandola et al. 1989). However, of the various candidates that have been proposed as carriers of these bands (and possibly part of the mid-infrared continuum), none has yet provided a fully satisfactory match to all the observed characteristics. More laboratory work together with astronomical observations (see Boulanger et al. 1998) are needed to better constrain the identification of the carriers. For this purpose, we selected a sample of five compact H II regions, spanning a large range of physical conditions (spectral type and evolution state of the exciting star, distance). IEFs are known to be strong in such regions (Roelfsema et al. 1998). With ISOCAM and the 3 arcsec pixel field of view, a mapping of the IEFs and associated continuum is done using the dedicated filters for the IEFs and the circular variable filter (CVF) for the continua.

Section 2 presents the ISOCAM observations and the data reduction. Results are presented and discussed in Section 3. Section 4 summarizes the main conclusions and presents the perspectives of this work.

2. OBSERVATIONS AND DATA REDUCTION

The observations have been made with the infrared camera ISOCAM on board of the Infrared Space Observatory. Five compact HII regions were observed, namely: Sh 61, Sh 138, Sh 152, Sh 156, Sh 186 (Sharpless 1959). The pixel field of view was 3 arcsec and the small field mirror was used. The covered field is (96 arcsec)^2 for Sh 61, Sh 152 and Sh 186 and 192 arcsec $\times$ 96 arcsec (2x1 raster in the right ascension direction) for Sh 138 and Sh 156. The fields are centered on the main exciting star's position. Observations using the SW2, LW4, LW6 and LW8 filters were obtained to look, respectively, at the distribution of the 3.3, 6.2, 7.7 and 11.3 μm emission band plus continuum. SW1 and five CVF observations were also obtained to estimate the associated continua. The CVF observations were made at 5.985, 6.911, 8.222, 10.52 and 12 μm with FWHM that varies between 0.156 and 0.295 μm. The presence of atomic fine-structure lines of [Ar II] at 6.9 μm and [S IV] at 10.5 μm also gives information about the physical conditions in these regions.
The data were analyzed using CAM Interactive Analysis (CIA) version 2. The standard procedure has been applied: dark correction, deglitching, flat field correction and calibration. The transient correction has been made using the IAS model. No deconvolution has been performed on the final images but it will be done in the next data reduction. The signal to noise ratio varies between 4 and 300.
In order to obtain the IEFs distribution, the continua have to be estimated. For the 3.3 μm continuum, the SW1 filter was used. Near the star, the presence of emission lines (like Brα at 4.05 μm) can lead to an overestimation of the continuum. However the contamination is expected to be low outside the ionized zone, where the IEF maximum is observed (see also Verstraete et al. 1996). A better continuum estimation in the ionized zone will be done using radio observations. The continuum emission associated with the 6.2 and 7.7 μm bands is relatively flat (see Fig. 1 in Roelfsema et al. 1996). Many test were performed using the 5.9, 6.9 and 10.5 μm CVF maps to determine the mean value of the continuum. The 11.3 μm

continuum is difficult to estimate as superimposed on a strong rising continuum observed in the 10-12 μm range. A continuum map has been created by interpolating the values obtained at 10.5 μm and 12 μm.

3. RESULTS

3.1. IEFs (band+continuum) distribution

Figure 1 presents the IEFs (band+continuum) distribution in Sh 138 observed with ISOCAM in the 3-12 μm range. This peculiar ionized region (Deharveng et al. 1998, Zavagno 1998) is partly hidden at optical wavelengths, due to the presence of a molecular cloud, southwards of the main exciting star (see Fig. 2). Emission peaks at 3 μm correspond to embedded young stars detected in the near IR. The IEFs peak is found at the interface between the ionized and neutral media. The conical shape of the dust 'depression' observed in Fig. 1 (LW4, LW6 and LW8 filters; see also Fig. 2) is probably due to a strong stellar wind associated with the main exciting star that has swept the dust in this region, making this part of the ionized region detectable at optical wavelengths. Note the rising continuum emission observed between 10 and 12 μm.

3.2. IEFs distribution, continuum subtracted

Figure 2 presents the distribution of IEFs centered at 3.3, 6.2, 7.7 and 11.3 μm. The continuum emission has been estimated as explained in Section 2 and then subtracted. The 6.2 μm emission is superimposed, in contours, on the other emission band maps. This shows that the bands distribution is very similar, indicating a common origin for the carriers. The 3.3 μm band is centered on embedded young stars detected in the near IR. All the continuum contributions are strong near the main exciting star. Note the large extension of the IEFs zone in this region, considering the distance of Sh 138 (5 kpc).

3.3. Intensity ratios

Figure 3 presents four intensity ratio maps obtained for Sh 152. These ratios are rband1=I(LW4)/I(LW6), rband2=I(LW6)/I(LW8), rband3=I(LW4)/I(LW8) and rband4=I(SW2)/I(LW8). The intensity, in each filter, is defined as $F_\nu \times \Delta\nu$ where F_ν represents the flux in mJy/pixel and $\Delta\nu$, the filter FWHM in Hz. The continuum is not subtracted but its contribution to the emission features is low outside the ionized zone, where we can obtain a good estimate of the IEF intensity ratios.
These maps confirm the location of the IEFs peak at the interface which is very well defined here (at the border of the ionized region), as in Sh 156.
The ratios exhibit important variations, indicating that the physical conditions probably influence the dust composition. The 6.2 to 7.7 μm intensity ratio is rather uniform over the whole region. Peaks are associated with two compact sources, probably of stellar origin.
The ratios exhibit different ranges of value in the different regions, probably depending on the physical conditions. However, at specific locations of the interface and for a given ratio, the same value is always found, in the five regions. This important result indicates that under specific physical conditions, the intensity ratio of two given IEFs is always the same, putting strong constraints on the carrier properties (survivance, composition). Indeed, whereas the global properties of IEF carriers are difficult to study under strong variations of the physical environment present in the different regions, the interface becomes a 'privileged' zone for such a study. Note that the typical values found at these locations, i.e. rband1=0.5, rband2=3.2, rband3=1.5 and rband4=0.15, are in good agreement with the values derived by Roelfsema et al. (1996) using a sample of six galactic compact H II regions.
The 11.3 μm feature is often superimposed on a strong rising continuum (see Figure 1 in Roelfsema et al. 1996). For this reason, the LW4 and LW6 to LW8 intensity ratios can also be used to study this continuum emission. We discussed this point in the next subsection.

3.4. 10-12 μm continuum emission

Figure 5 presents the 10-12 μm continuum emission observed in Sh 152. The CVF map obtained at 12 μm clearly shows an extension of this continuum emission towards the ionized zone, traced by the Hα emission. This emission, rising with wavelength, coincides with the extended red emission in Sh 152 (Darbon et al. these proceedings). In compact H II regions the long wavelength part of the spectrum is dominated by a continuum emission that peaks around 70 μm (see Figure 3 in Roelfsema et al. 1998), attributed to thermal continuum emission from cold grains (T$\simeq$40 K). ISOGAL images at 15 μm (see Copet et al. these proceedings) seem to confirm the origin of the 12 μm emission as due to cold grains thermal emission. Indeed, in Sh 152, 15 μm emission also extends towards the ionized region.

4. CONCLUSIONS

The main results of this study, obtained using a sample of five compact H II regions, can be summarized as follow:

- the IEFs are present and strong. The associated continuum contribution is important near the main exciting star.
- the IEFs peak at the interface between ionized and neutral media.
- intensity ratios of filters centered on the IEFs show important variations, spatially inside a given region and in the range of values from region to region.
- at specific locations of the interface and for a given ratio, the *same* value is found in all regions. This points out the interface as a 'privileged' zone to study the properties of IEF carriers.

- finally, a strong rising continuum is observed between 10 and 12 μm. This continuum probably corresponds to the short wavelength part of the strong thermal continuum of cold grains that dominates the 10-100 μm emission spectrum of compact H II regions.

The preliminary results show that the main goal of this proposal has been achieved: it will be possible to put new constraints on the IEF carriers especially using the feature and the feature to continuum ratios. A new CIA version together with a new stabilization program (see Coulais & Abergel these proceedings) will allow us to obtain a better final product for the data analysis. Finally, Sh 152 and Sh 156 present a well defined interface zone, allowing models of the mid-IR emission and comparisons with laboratory data.

ACKNOWLEDGMENTS

We thank Jean-Paul Baluteau for many fruitful discussions and the financial support of the GdR PCMI.

REFERENCES

Allamandola, L.J., Tielens, A.G.M.M, Barker, J.R. 1989, ApJS, 71, 733

Boulanger, F., Boissel, P., Cesarsky, D., Ryter C. 1998, A&A, 339, 194

Deharveng, L., Zavagno, A., Nadeau, D., Caplan, J., Petit, M. 1998, A&A submitted

Léger, A., Puget, J.-L. 1984, A&A 137, L5

Roelfsema, P.R., Cox, P., Tielens, A.G.G.M, et al. 1996, A&A, 315, L289

Roelfsema, P.R., Cox, P., Kessler, M., Baluteau, J.-P. 1998, ASP Conf. Series, 132, 76

Sharpless, S. 1959, ApJS, 4, 257

Verstraete, L., Puget, J.-L., Falgarone, E., Drapatz, S., Wright C.M., Timmermann, R. 1996, A&A, 315, L337

Zavagno, A. 1998, ASP Conf. Series, 132, 30

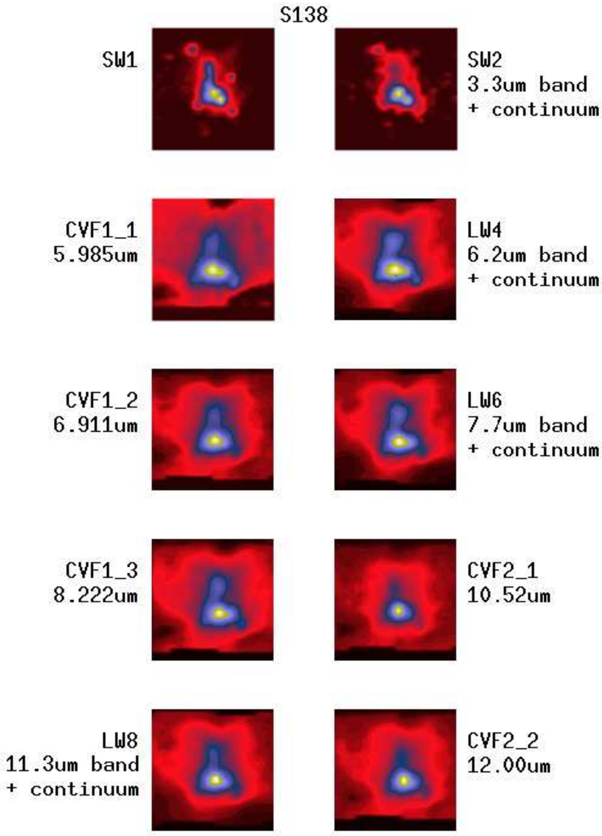

Figure 1. *3-12 μm ISOCAM (band+continuum) and continuum maps of Sh 138. North is up, east is left. An absolute flux scale, in mJy/pixel, is displayed for each image. The used filter name is written at the border of each corresponding image. Continuum images correspond to CVF observations, except for the 3.3 μm emission band (see text).*

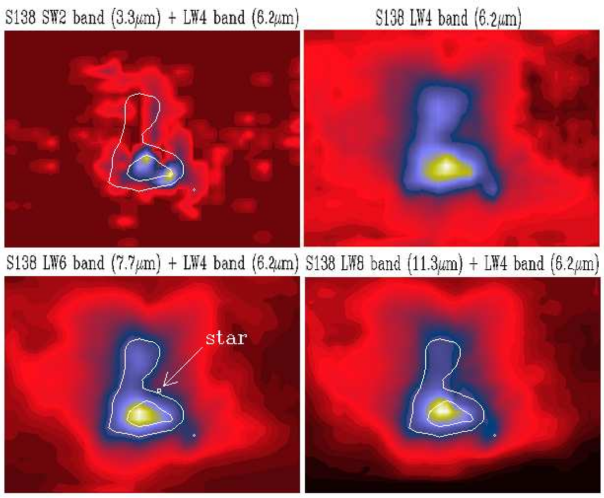

Figure 2. *3.3, 6.2, 7.7 and 11.3 μm IEF maps (continuum subtracted) of Sh 138. The 6.2 μm IEF (contours) is superimposed on the 3.3, 7.7 and 11.3 μm bands. An arrow points to the main exciting star.*

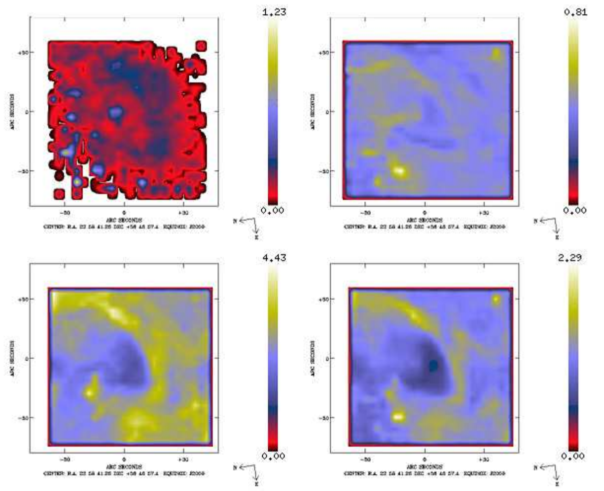

Figure 3. *Intensity ratios in Sh152. Upper left:* I(SW2)/I(LW8), *upper right:* I(LW4)/I(LW6), *lower left:* I(LW6)/I(LW8), *lower right:* I(LW4)/I(LW8).

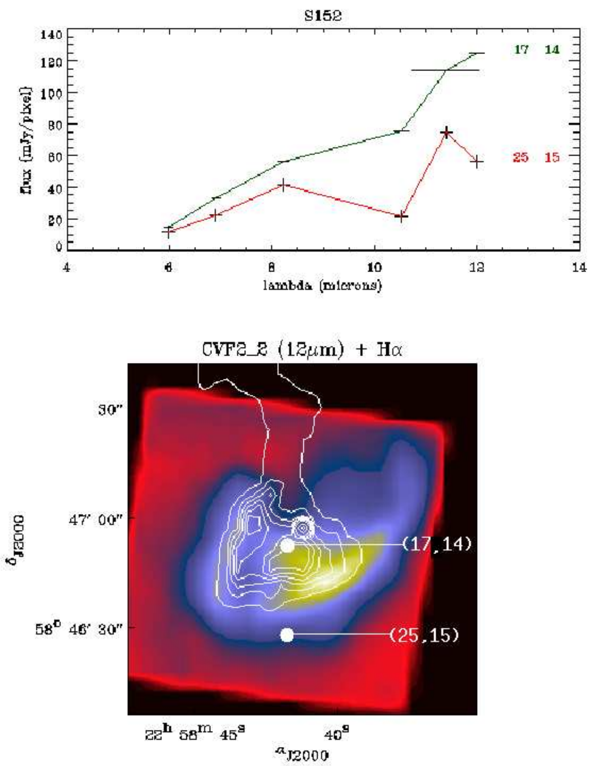

Figure 4. *10-12 μm continuum in Sh 152. Upper panel: flux distribution (in mJy/pixel) as a function of wavelength. The two selected pixels' location is shown on the lower panel. Lower panel: 12 μm CVF map (colors) and Hα emission (contours) of Sh 152.*

GALAXIES

THE ISO VIEW OF STAR FORMING GALAXIES

G. Helou
California Institute of Technology, Pasadena, California, USA

ABSTRACT

ISO studies of normal galaxies in the local Universe have revealed new basic properties with significant implications for the star formation process and cosmology. This paper will review the general results of a statistical nature, provide a glimpse of the profusion of results on individual objects, and explore some of the resulting insights.

Key words: normal galaxies; star formation; interstellar medium.

1. INTRODUCTION

The Infrared Space Observatory (ISO, Kessler et al. 1996) took infrared astronomy in space to new levels of sensitivity and a new realm of spectroscopy across the whole spectrum from 3 to 200μm. Its versatile instrumentation took to the rich and fascinating extragalactic infrared sky first revealed by IRAS, and moved our knowledge of that sky an order of magnitude further and deeper. The unfettered access to the spectrum in space and low thermal backgrounds gave ISO a tremendous advantage in studying galaxies regardless of redshift, and allowed it to tackle much lower surface brightness sources. The spectroscopic capabilities of all four instruments were especially valuable tools in characterizing the interstellar gas, dust and radiation field, and at constraining the overall energetics and star formation rate. It was thus able to extend the KAO studies of starburst nuclei to the less intense star formation in normal galaxies.

This article will review significant ISO contributions to understanding normal galaxies, defined as those systems whose energetics are dominated by nucleosynthesis with negligible contributions by an active galactic nucleus. Normal galaxies account for most of the star formation in the Universe, and therefore for the bulk of its chemical evolution. ISO data on normal galaxies should thus bridge the gap between the details of nearby systems and the cosmic history of star formation, one of the more prominent questions in cosmology today. Because of their diversity, understanding galaxies requires studying them as an ensemble, and in particular as a sequence with increasing levels of star formation activity, up to and including the most extreme. While this review will attempt to present the whole activity sequence, ultraluminous galaxies and nuclear starbursts are more extensively covered in Alan Moorwood's review (these proceedings).

2. THE MID-INFRARED SPECTRAL ENERGY DISTRIBUTION

In the integrated spectra of galaxies, the mid-infrared marks the transition from star-dominated emission to interstellar dust reradiation providing the luminosity. ISO has shown the details of this transition for the first time by providing continuous coverage, and filling in some crucial details as discussed in this and the next two sections. The relevant data were acquired with ISOPHOT, PHT-S module from 2.5 to 5 and from 5.7 to 11.6 μm (Lemke et al. 1996); with ISOCAM in the CVF (Circular Variable Filter) mode from 5 to 16.5 (Cesarsky et al. 1996); and with SWS from 2.5 to 45 μm (de Graauw et al. 1996).

The transition from stellar to interstellar emission is well illustrated by the spectra of Virgo Cluster galaxies collected by Boselli et al. (1998). Its precise location and therefore the interpretation to attach to mid-infrared fluxes can be parametrized by the ratio of far-infrared, say as measured by IRAS, to visible light fluxes. Interstellar dust emission takes over by 5 μm when this ratio exceeds 0.5, and at shorter wavelengths for higher ratios. As might be expected, Elliptical galaxies are dominated by stellar emission, both photospheric and from circumstellar dust shells, and therefore provide the templates that one subtracts to isolate the interstellar emission component in Spiral galaxies (Boselli, Lequeux & Contursi 1997; Madden, Vigroux & Sauvage 1997). In addition, ISO sensitivity has allowed us to study the small amounts of interstellar medium (ISM) contained in Elliptical galaxies, and to look into differences with the ISM of Spirals (Knapp et al. 1996; Fich et al. , Madden et al. & Malhotra et al. in these proceedings; note also the study of E+A galaxies in the Coma Cluster by Quillen et al. in preparation).

2.1. The aromatic features

IRAS data had already indicated (Beichman 1987; Puget & Léger 1989) that the mid-infrared emission from the ISM was dominated by small fluctuating grains and Aromatic Features in Emission (AFE). ISO has not only established into fact what had been hypothesis (Figure 1), but is also allowing us to address quantitatively the mid-infrared energy budget across various emission components, and to investigate the variation of this budget among various galaxies.

The AFE appear in two main groups, one stretching from 5.5 to 9 μm, with peaks at 6.3, 7.7 and 8.6, and the other one starting at 11 μm and extending to 12.5 μm (Lu et al. these proceedings; Helou et al. 1999). There is good evidence linking these features to Polycyclic Aromatic Hydrocarbons (PAH), but no rigorous spectral identification of specific molecules (Tielens these proceedings; Puget & Léger 1989; Allamandola et al. 1989). It is generally agreed that the emitters are small structures, no more than a few hundred atoms, transiently excited to high energy levels by single photons. The AFE together carry 5 to 20% of the "FIR" luminosity between 40 and 120 μm as defined in Helou et al. (1988), this percentage being generally smaller in more active galaxies (Lu et al. in these proceedings). Boselli et al. (1997 and 1998) have interpreted similar trends as evidence for the destruction of AFE carriers in more intense radiation fields (see also Helou, Ryter & Soifer 1991).

In addition to the AFE, there is a clear though weak continuum detection at $\lambda < 5\,\mu$m, and an apparently unrelated continuum component at $\lambda > 13\,\mu$m, which becomes dominant in active systems as discussed in section 3 below. The relation of the continua in these two spectral ranges is still unclear, making it hard to derive by interpolation a description of the continuum in $5 < \lambda < 13\,\mu$m where the Aromatic Features dominate.

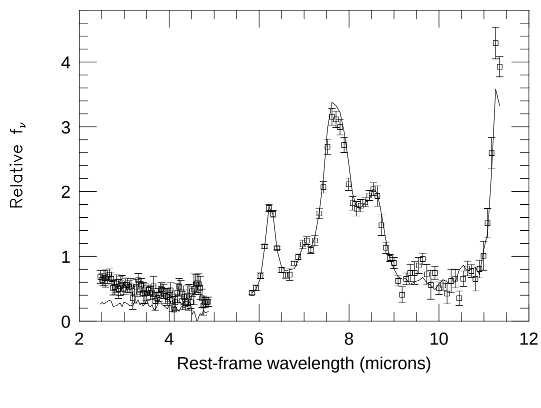

Figure 1. Two composite mid-infrared spectra, one for twelve FIR-cold galaxies (squares), and one for twelve FIR-warm ones (connected dots). Spectra were averaged after normalization to the 6.3 μm peak.

The relative fluxes in individual Aromatic Features depend very weakly on galaxy parameters such as the far-infrared colors, as illustrated in Figure 1. This is direct evidence that the emitting particles are not in thermal equilibrium. The strongest detectable effect in Figure 1 is the slightly stronger 11.3 μm feature in the colder galaxies. Since this feature is linked primarily to neutral PAHs as opposed to the shorter wavelength features which have a strong ionized PAH contribution (Tielens, these proceedings), one is tempted to interpret this trend as a result of the more active galaxies having a greater contribution to their luminosity originating in regions heated by harder radiation fields. The continuum at $\lambda < 5\,\mu$m is still subject to calibration uncertainties, but might amount to as much as three percent of the total infrared luminosity in some systems. It has a slope close to zero in f_ν *vs.* ν (connected dots in Figure 1), whose extrapolation to longer wavelengths would place it below the observed flux density even at $9-10\,\mu$m. It is almost certainly of non-stellar origin, and is probably due to fluctuating grains without aromatic features.

Rouan et al. (1996), Block et al. (1997) and Smith (1998) have combined ISOCAM and Brγ images with other broad-band and line images to estimate star formation rates, ISM parameters, obscuration and dust properties. These studies again point to Aromatic Feature carriers as a ubiquitous component of interstellar dust, to the likely destruction of these carriers by ionizing UV, and to dust heating in non-starburst disk galaxies being derived from both old stars and OB stars.

ISOCAM CVF studies between 5 and 17 μm are turning out to be powerful diagnostics of the radiation field in the disks of nearby galaxies, allowing us to disentangle the variations in heating intensity and hardness of interstellar radiation. The approach is to relate the intensity to the shape of the continuum, and the hardness to the ratios of ionic fine-structure lines (Tran 1998; Contursi 1998). See also, in these proceedings, the overview on ISOCAM studies of nearby galaxies by Vigroux et al., the studies of NGC 891 by Le Coupanec et al. and by Mattila et al., and of low-metallicity dwarf galaxies by Madden et al. (in preparation).

2.2. High-redshift applications

Since the spectral signature in Figure 1 applies to the majority of star-forming galaxies, it can be used as a template to obtain redshifts of highly extincted galaxies with the next infrared observatory, NASA's SIRTF (Space InfraRed Telescope Facility). For instance, a galaxy at a redshift z=3 with a flux density average of 0.5 mJy in the range $19-27\,\mu$m and a total infrared luminosity comparable to Mkn 231 at $\sim 3\times10^{12}\,L_\odot$ would be detected by the SIRTF IRS (Infrared Spectrometer; Roellig et al. 1998) in roughly 1000 seconds of integration (D.W. Weedman, private communication).

In surveys with fixed spectral bands, the Aromatic Features will result in a unique K-correction as redshift takes them in and out of the bands. The detection probability would be enhanced or lessened for certain redshift intervals, causing ripples in source counts as a function of flux; Xu et al. (1998) have modelled this effect for NASA's WIRE (Wide-Field InfraRed Explorer; Hacking et al. 1999) mission. However, this effect has already been manifested with ISO, in deep 15 μm imaging data in the direction of galaxy clusters. These observations were aimed at detecting background objects boosted by gravitational lensing, thus allowing the survey to penetrate further in space and time. In the Barvainis et al. (1999) survey, one out of every five galaxies detected in the direction of each of Abell 2218 and Abell 2319 turns out to be at a redshift near 1, the others being at redshifts of 0.3 or less. A redshift of 1 places the main clump of Aromatic Features squarely in the 15 μm band, enhancing the probability of detection. Similar results from a more extensive survey are reported by Metcalfe et al. (these proceedings), and by Fadda et al. (these proceedings).

As the early Universe opens up for mid-infrared exploration, the properties of low metallicity star-forming galaxies become more relevant as a template for high-redshift galaxies. ISO has provided the data for constructing such templates, both from studies of low metallicity dwarf galaxies (Madden et al., and Sauvage & Thuan in these proceedings), and the study of nearby galaxy disks with significant metallicity gradients such as M 101 (Vigroux et al. these proceedings).

2.3. Exceptions

The "standard" spectra described above characterize the integrated emission from normal galaxies, but exceptions arise at extreme conditions, and are easiest to detect in specific ISM phases of individual galaxies. At the smallest scales in the most intense parts of HII regions, Contursi (1998) and Tran (1998) report spectra which depart significantly from the standard ones in the location and strength of features. Similarly distorted spectra are also observed in NGC 4418 (Lu et al. 1999), and close to the Active Nucleus of Cen A (Vigroux et al. , these proceedings). This radical transformation in the spectrum must then result from extremely UV-rich heating radiation, and most likely reflects severe modification of the emitting grains, including the destruction of Aromatic Feature carriers. Significant distortions in the spectrum driven by a rising continuum but without radical changes in the Aromatic Features have also been reported by Lutz et al. (1998) in extremely active galaxies. The mid-infrared spectra of starbursts are relatively "standard", whereas galaxies with an active Black Hole nucleus have a continuum rising towards longer wavelengths with insignificant Aromatic Features. Ultra-Luminous Infrared Galaxies show intermediate spectra, modified in addition by large optical depths (Genzel et al. 1998).

At the other end of the heating sequence, Cesarsky et al. (1998) report that the 5–9 μm Aromatic Features are missing from the emission of the bulge and of the quiet parts of the bright infrared ring in M 31. The 11.3 and 12.7 μm features are present, perhaps a result of their originating primarily on neutral PAHs. The relatively weak and UV-poor heating radiation in these parts of M 31 cannot alone explain the absence of Aromatic Features, for other studies (e.g. Uchida et al. 1998) show that photons of a few eV are sufficient to generate the standard spectrum. It would appear that the dust properties are again modified, this time by prolonged shielding from UV processing in the astration cycle. Additional evidence of abnormal ISM properties in the same regions are found by Lequeux et al. (1999) in their study of the broad-band mid-infrared emission.

Another peculiar exception is provided by Sauvage & Thuan (these proceedings) in SBS 0335-052, a blue compact dwarf with a metallicity about 1/40 solar. None of the Aromatic Features are detected here, and the spectrum appears best fit by highly extincted blackbody emission. The authors propose the early chemical age of the system as the most likely reason behind the absence of the Aromatic Features, though one cannot rule out the possibility that the UV radiation from the intense star formation episode also plays a role in the destruction of the Aromatic Feature carriers. If this spectrum does indeed characterize all low metallicity objects, one would expect the "standard" spectrum to disappear gradually as a function of increasing redshift, thus making it harder to detect the Aromatic signature of dust and distinguish star formation from Black Hole activity as the energy source in the earliest systems.

3. THE 7-TO-15 μm COLORS

A large number of extragalactic broad-band measurements was collected by ISOCAM (Cesarsky et al. 1996) at wavelengths between 4 and 18μm, previously inaccessible with such sensitivity and versatility. Two photometric bands were most widely used for observations of nearby as well as distant and more luminous galaxies, namely the "LW2" band centered at 6.75 μm, and the "LW3" band centered at 15 μm. The LW2 filter was designed to capture mostly AFE emission, whereas LW3 was aimed at the continuum range beyond the bulk of the AFE, though it ends up with a small contribution from the last feature at 12.5 μm. The CVF mode of ISOCAM between 5 and 17 μm has also proven quite powerful in its ability to image both line and continuum emission. The overview by Vigroux et al. in these proceedings summarizes what has been learnt to date from these data, including the interpretation of the mid-infrared images and their relation to star formation rates.

The ISOCAM images of galaxies show dust emission in nuclear regions, in the inner barred disk, outlining the spiral arms, and tracing the disk out to the Holmberg radius and beyond (Malhotra et al. 1996, Sauvage et al. 1996, Vigroux 1997, Smith 1998, Roussel et al. in these proceedings). There are clear color variations within spiral galaxies, some of which have not yet found satisfactory explanations (Helou et al. 1996; Tran 1998).

The 6.75-to-15 μm color ratio formed from ISOCAM bands however has emerged as an interesting diagnostic of the radiation environment. This ratio remains relatively constant and near unity as the ISM of galaxies proceeds from quiescent to mildly active. As dust heating increases further, the 15 μm flux increases steeply compared to 6.75 μm, pointing to a significant contribution by dust at color temperature

100 K < T_{MIR} < 200 K, typical of a heating intensity up to 10^4 times that of the diffuse interstellar radiation field in the local Milky Way (Helou et al. 1997). While such a temperature could result from classical dust heated within or just outside HII regions, there is no decisive evidence as to the size of grains involved. It is simpler at this time to associate this component empirically with the observed emission spectrum of HII regions and their immediate surroundings (Tran 1998; Contursi 1998). This emission has severely depressed AFE, and is dominated by a steeply rising though not quite a blackbody continuum, consistent with mild fluctuations in grain temperatures, $\Delta T/T \sim 0.5$. This HII region hot dust component becomes detectable in systems where the color temperature from the 60-to-100 μm ratio is half T_{MIR}, demonstrating the broad distribution of dust temperatures within any galaxy. The combined data from ISO and IRAS on these systems are consistent with an extension of the "two-component model" of infrared emission, which describes galaxies as a linear combination of a quiescent medium and a star-forming medium, and where the mixing ratio determines the colors of each system (Helou 1986). This color behavior was observed in the sample of galaxies used for the Key Project on normal galaxies conducted under NASA Guaranteed Time (Helou et al. 1996), and confirmed in the sample of galaxies observed under ISOCAM Guaranteed Time (see figure in Vigroux et al. in these proceedings).

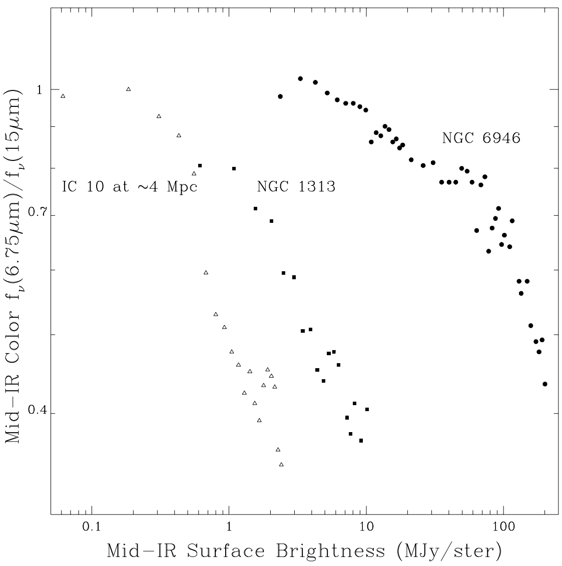

Figure 2. The mid-infrared color as a function of surface brightness for three disk galaxies well resolved by ISOCAM, and smoothed so the resolution corresponds to ≲200 pc in each case (Dale et al. 1999). All three data sets show roughly the same behavior, indicative primarily of how color and surface brightness evolve as heating intensity increases. The data are consistent with the expectation that a change in total ISM column density will shift the curves along the surface brightness axis: NGC 6946 does indeed have a total HI about an order of magnitude greater than the other two galaxies.

Similar behavior is observed within the disks of star forming galaxies, where the 6.75-to-15 μm color drops precipitously as the surface brightness exceeds a certain threshold (Dale et al. 1999). The point of inflexion in the color curve occurs at a variable surface brightness which is a function of the dust column density, whereas the shape of the curve seems invariant, and may result from a rise in both the hardness and intensity of the heating radiation (Figure 2). Dale et al. (1999) conclude that the mid-infrared surface brightness rise is driven primarily by column density while colors are determined mostly by heating intensity.

4. THE GLOBAL INFRARED SPECTRUM

Turning now to the long wavelength end of the spectrum, photometry at $120-200\,\mu$m using ISOPHOT is starting to constrain the distribution of dust temperatures at low heating levels, especially in nearby well resolved galaxies such as M31 (Haas et al. 1998, and in these proceedings), M51 or M101 (Hippelein et al. 1996), where cold dust dominates the luminosity. Similar analysis on more active galaxies is also under way (e.g., Klaas et al. 1997; Klaas, Haas & Schulz in these proceedings) to obtain the best possible estimates of the total infrared emission and therefore of the dust mass. Alton et al. (1998) have reported that the 200 μm emission is more extended than at shorter wavelengths in several galaxies. This result however hinges closely on a very precise knowledge of the beam shapes at various wavelengths, which was not yet achieved as of this writing.

A proper determination of the total infrared luminosity and the long-wavelength spectral shape in normal galaxies is critical to estimating the contribution of galaxies to the infrared and submm extragalactic background light, and thereby deriving the infrared term in the star formation history of the Universe. While work on the ISOPHOT calibration continues, one could estimate an improved infrared spectral energy distribution by combining the mid-infrared results described above with existing IRAS data. Such a rough estimation is presented in Table 1 for three different levels of activity in galaxies, parametrized by the 60-to-100 μm ratio. It should be noted that all information in Table 1 at $\lambda > 100\,\mu$m is based on modelling IRAS data using a power-law distribution of dust mass as a function of heating intensity. Table 1 illustrates the general trend, but also ignores variations in spectral shape at constant 60-to-100 μm ratio, including intrinsic scatter in the ratio of mid-infrared to far-infrared (Lu et al. in these proceedings). The 20 to 40 μm range appears to show the most significant growth in relative terms as the activity level increases, at the expense of the submillimeter. Even after ISO, our knowledge of the detailed shape of the spectrum in this range remains limited, and may not improve significantly until the launch of SIRTF.

5. MOLECULAR SPECTRAL LINES

One of the great achievements of ISO was the detection of the long-sought molecular hydrogen tran-

Table 1. Rough energy distribution across the infrared spectrum for galaxies with various levels of star formation activity, parametrized by the IRAS color in the first column. Each column heading gives the wavelength range over which the spectrum is integrated, and the table entries are the fractions of total infrared luminosity appearing in that range. The spectral range in column 6 corresponds to the "FIR" synthetic band (Helou et al. 1988).

$\frac{f_\nu(60\,\mu m)}{f_\nu(100\,\mu m)}$	F(3–5μm)	F(5–13μm)	F(13–20μm)	F(20–42μm)	F(42–122μm)	F(122–1100μm)
0.40	$\leq$0.02	0.12	0.04	0.10	0.40	0.29
0.72	$\leq$0.01	0.07	0.04	0.17	0.52	0.18
0.94	$\leq$0.01	0.04	0.04	0.22	0.56	0.13

sitions from rotationally excited states, and the realization of their promise as accurate tracers of the H_2 mass (e.g., Draine & Bertoldi in these proceedings), allowing for the first time a direct gauge of the dominant phase of the ISM. Most of the H_2 data were collected by the SWS (de Graauw et al. 1996). Several of these lines, especially S(0), S(1) and S(2) were detected in galaxies early in the ISO mission, permitting a detailed discussion of the gas phase conditions and heating mechanisms. Valentijn et al. (1996) for instance studied the nuclear star burst of NGC 6946. Because of their high excitation levels however, these lines tend to trace H_2 warmer than $\sim$ 100 K, and are therefore easier to detect in the more intense star formation environments (Kunze et al. 1996; Kunze et al. in these proceedings). Still, Valentijn & van der Werf (these proceedings) report the detection of H_2 emission from the extended disk of the edge-on galaxy NGC 891. They detect S(0) and S(1) at eight positions, tracing the emission out to 12 kpc from the nucleus of the galaxy, and derive H_2 temperature constraints and molecular mass estimates.

Hydroxyl (OH) was also detected in starburst galaxies, but in absorption rather than emission. A first report by Skinner et al. (1997) showed OH absorption at 35 μm in the spectrum of Arp 220, and confirmed for the first time pumping by infrared photons as the excitation mechanism behind OH megamasers. Bradford et al. (these proceedings) report OH in absorption at 35, 53 and 119μm in NGC 253, and resolve the line at 119μm with the LWS Fabry-Pérot mode. They estimate total column and excitation temperatures for the OH, and constrain the geometry of the molecular material and its relationship to the infrared-emitting dust. A similar study of NGC 4945 by Lord et al. (in preparation) finds consistency between the properties derived from OH data and [CII] 157.7 μm and [OI] 63.2 μm data. Lord et al. also report water vapor lines in absorption in the same object.

6. FAR-INFRARED FINE-STRUCTURE LINES

Far-infrared fine structure lines, [CII] 157.7 μm and [OI] 63.2 μm in particular, have long been used for estimating density and radiation intensity in photodissociation regions (PDR) (e.g., Hollenbach & Tielens 1997). ISO-LWS (Clegg et al. 1996) has provided for this topic a wealth of data, whose interpretation is creating controversy and challenging theoretical models. Malhotra et al. (1997) showed that while two thirds of normal galaxies have $\mathcal{L}$(CII)/$\mathcal{L}$(FIR) in the range $2-7\times10^{-3}$, this ratio decreases on average as the 60-to-100 μm or the $\mathcal{L}$(FIR)/$\mathcal{L}$(B) ratios increase, both indicating more active star formation (Figure 3). They linked this decrease to elevated heating intensities, which ionize grains and thereby reduce the photo-electric yield.

The same CII deficiency is also observed in ultraluminous infrared galaxies (Luhman et al. 1998), where optical depth effects have been proposed as the origin of the effect. This is hard to reconcile however with a similar deficiency effect observed for [NII] 121.9 μm, but not for [OI] 63.2 μm. Fischer et al., Luhman et al. and Malhotra et al. (these proceedings) give updated discussions of this topic, while Lord et al. and Unger et al. (in preparation) discuss PDR properties in NGC 4945 and Cen A.

Stacey et al. (these proceedings) present detailed maps of M 83 in several fine-structure lines, and point to the importance of low density HII regions as a source of [CII] emission. This same contribution by diffuse PDRs is invoked by Pierini et al. (these proceedings) in explaining the low [CII]-to-CO ratios in quiescent Virgo cluster galaxies. Using the same Virgo galaxies data, Leech et al. (in preparation) report a trend of decreasing [CII]/FIR ratios as galaxies become less active in star formation. Combining the results of Leech et al. with those of Malhotra et al. work leads to a picture where [CII]/FIR rises by an order of magnitude as galaxies move away from complete quiescence, reaches a broad maximum for normal galaxies actively forming stars, then decreases again by more than an order of magnitude as galaxies begin to approach the extreme properties of starbursts.

What could be behind this behavior? At the quiescent end, the relative lack of ionizing photons in the stellar spectrum could naturally explain the low values of [CII]/FIR. UV-poor heating would on one hand lower CII abundance, and on the other hand yield less energetic photo-electrons, so a less energetic CII excitation would be expected. At the starburst end, the extreme excitation conditions could generate lower photo-electric efficiency as proposed by Malhotra et al. (these proceedings). There is evidence however pointing in a different direction, namely that the relative drop in [CII] is due to a decrease in the concentration of the grains crucial for the photo-electric effect. It is well known (e.g. Hollenbach & Tielens 1997) that the smallest grains such as the carriers of AFE are responsible for the bulk of photo-electric yield in a PDR. Depletion of these carriers would weaken the coupling between radiation

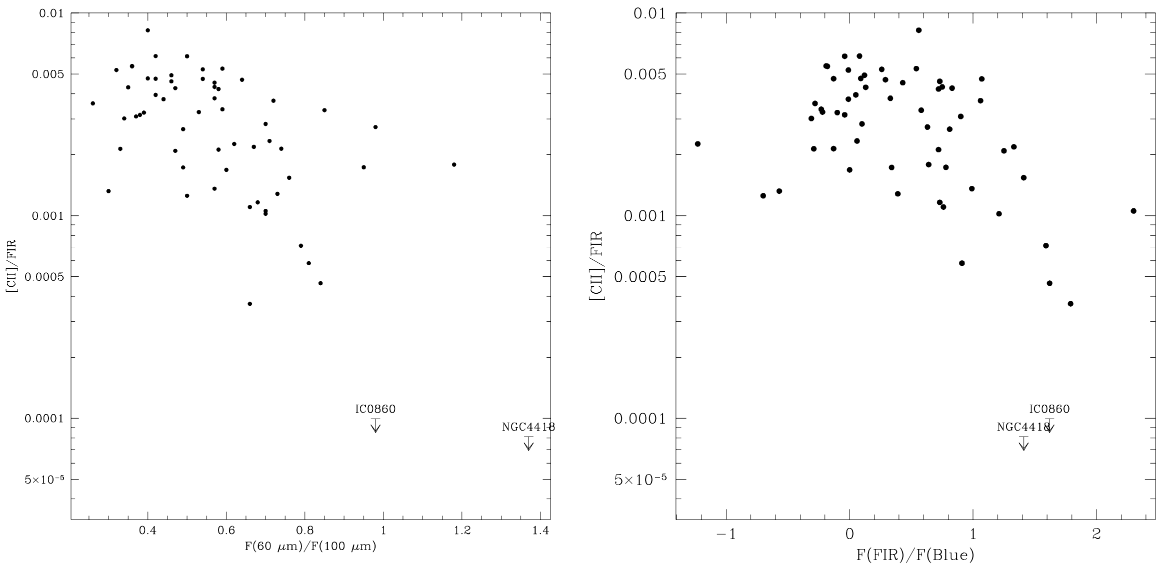

Figure 3. The CII deficiency in active star forming galaxies from Malhotra et al. (1997). See also Malhotra et al. (these proceedings).

field and gas, and lead to weaker fine-structure line emission compared to total dust re-radiation. The evidence in question is that unlike [CII]/FIR, the ratio of [CII] to AFE flux does not decrease in normal galaxies with increasing activity (Helou et al. 1999). This suggests that the emissions from [CII] and AFE originate in the same regions of the ISM, so their ratio is dictated by the physics of the photo-electric effect and remains constant, whereas [OI] and FIR originate from distinctly warmer and denser regions, so that the changing ratio [CII]/FIR, just like [CII]/[OI], reflects the systematic shift in density distribution of the ISM as galaxies approach star-burst conditions.

7. MORE STUDIES

In addition to the topics covered above, the ISO archive will soon offer a wealth of data on a wide variety of extragalactic subjects affecting our understanding of normal galaxies. Studies in galaxy clusters and groups for instance have targeted the population of medium-distant clusters at z=0.1–0.3 (Lémonon et al. , Fadda & Elbaz in these proceedings), or the location of enhanced infrared emission in compact groups (Latorre et al. in preparation). Stickel et al. (1998) have reported the detection of intracluster dust in Coma at 200μm, and related it to the cooling flows revealed by X-ray observations, while Xu, Sulentic & Tuffs (1999) have studied intergalactic star formation in Stefan's Quintet using mid-infrared data. Charmandaris et al. and Gallais et al. (these proceedings) have taken a detailed look at some of the nearest interacting galaxy systems in order to study collisionally induced star formation.

Beichman et al. (in preparation) and Gilmore & Unavane (in preparation) report on deep searches for mid-infrared haloes around edge-on galaxies, and place upper limits on the contribution to the missing mass by low-mass stars. Jarrett et al. (these proceedings) report on mid-infrared detection of a bridge of interstellar gas and magnetized plasma created between two galaxies after a collision which caused the two disks to pass through each other and entangle the interstellar media.

Observations of Local Group members allow detailed analysis of the ISM and star formation on the few pc scale, and are a crucial stepping stone to understanding the integrated emission in more distant objects. In these proceedings, such detailed studies of HII and star formation regions regions, or of the stellar population in the Magellanic Clouds are reported by Comeron & Claes, Henning et al. , Loup et al. , Missoulis et al. , and Vermeij & van der Hulst.

8. CONCLUSIONS

ISO studies of normal galaxies have already yielded major progress in our grasp of their phenomenology, especially in the areas of mid-infrared spectra and images, global spectral energy distribution, and far-infrared fine-structure lines. The improved phenomenology is reshaping our physical understanding of galaxies, in particular in terms of

1. better decomposition of the infrared luminosity into a distribution of dust mass as a function of heating intensity, based on the infrared spectrum and images;

2. more precise constraints on the density and intensity in the active ISM based on fine-structure lines, surface brightness, and the spectral decomposition above;

3. more accurate estimates of the molecular gas content based on H_2 data and other molecular lines.

The improved characterization and insights move us closer to formulating a dynamical model for star formation on the scale of galaxies, which would be a major step towards deriving the cosmological history of star formation in the Universe. In addition, they are key to understanding the extremely high luminosity objects, which are the beacons we must use in exploring the early Universe.

This progress leads to more informed planning for upcoming surveys or missions. SIRTF, SOFIA, FIRST and PLANCK will build on ISO, and eventually address the new puzzles that ISO will leave behind.

ACKNOWLEDGMENTS

I would like to thank all those colleagues who generously provided data and graphics for this review. Danny Dale and Nanyao Lu helped by providing customized plots and helpful discussions. I would like to acknowledge the patience of the editors, and their assistance with the manuscript, and Mary Ellen Barba for her negotiating skills. This work was carried out at the California Institute of Technology, under contract with the National Aeronautics and Space Administration, as part of the ISO Data Analysis Funding Program.

REFERENCES

Allamandola, L. J, Tielens, A. G. G. M., & Barker, J. R. 1989, ApJS, 71, 733

Alton, P.B. et al. 1998, A&A, 335, 807

Barvainis, R., Antonucci, A. & Helou, G. 1999, ApJ, submitted

Beichman, C.A. 1987, ARA&A, 25, 521

Block, D.L., Elmegreen, B.G., Stockton, A. & Sauvage, M. 1997, ApJL, 486, L95

Boselli, A., Lequeux, J. & Contursi, A. 1997, A&A, 324, L13

Boselli, A. et al. 1998, A&A, 335, 53

Cesarsky, C. et al. 1996, A&A, 315, L32

Cesarsky, D., et al. 1998, A&A, 337, L35

Clegg, P. et al. 1996, A&A, 315, L38

Contursi, A. 1998, *PhD Thesis*, Univ. de Paris

Dale, D. et al. 1999, in preparation

de Graauw, T. et al. 1996, A&A, 315, L49

Genzel, R. et al. 1998, ApJ, 498, 579

Haas, M., Lemke, D., Stickel, M. et al. 1998, A&A, 338, L33

Hacking, P. et al. 1999, *Astrophysics with Infrared Surveys: A Prelude to SIRTF*, PASP Conf Series, in press

Helou, G. 1986, ApJL, 311, L33

Helou, G. et al. 1988 ApJS, 68, 151

Helou, G., Ryter, C. & Soifer, B.T. 1991, ApJ, 376, 505

Helou, G. et al. 1996 A&A, 315, L157

Helou, G., Becklin, E., Stencel, R.E. & Wilkes, B. 1997, *ASP Conf Ser* 124, 393

Helou, G., Lu, N., Werner, M.W., Malhotra, S. & Silbermann, N. 1999, ApJ, submitted

Helou et al. 1999, in preparation

Hippelein, H. et al. 1996, A&A, 315, L79

Hollenbach, D.J. & Tielens, A.G.G.M. 1997, ARA&A, 35, 179

Kessler, M.F. et al. 1996, A&A, 315, L27

Klaas, U., Haas, M., Heinrichsen, I. & Schulz, B. 1997, A&A, 325, L21

Knapp, G.R., Rupen, M.P., Fich, M., Harper, D.A. & Wynn-Williams, C.G. 1996, A&A, 315, L75

Kunze, D. et al. 1996, A&A, 315, L101

Lemke, D. et al. 1996, A&A, 315, L64

Lequeux, J. et al. , A&A, submitted

Lu, N. et al. 1999, in preparation

Luhman, M.L. et al. 1998, ApJL, 504, L11

Lutz, D., Spoon, H.W.W., Rigopoulou, D., Moorwood, A.F.M. & Genzel, R., 1998, ApJ, 505, L103

Madden, S.C., Vigroux, L. & Sauvage, M. 1997, in *Extragalactic Astronomy in the Infrared*, ed. Mamon, Thuan & Van (Editions Frontières: Paris)

Malhotra, S. et al. 1996, A&A, 315, L161

Malhotra, S. et al. 1997, ApJ, 491, L27

Metcalfe, L. et al. 1996, A&A, 315, L105

Puget, J.-L. & Léger, A. 1989, ARA&A, 27, 161

Roellig, T.L., Houck, J.R., Van Cleve, J. et al. 1998, SPIE, in press

Rouan, D. et al. 1996, A&A, 315, L141

Sauvage, M. et al. 1996, A&A, 315, L89

Skinner, C.J., Smith, H.A., Sturm, E., Barlow, M.J., Cohen, R.J. & Stacey, G.J. 1997, Nature, 386, 472

Smith, B. 1998, ApJ, 500, 181

Smith, B.J. & Madden, S. C. 1997, AJ, 114, 138

Stickel, M. et al. 1998, A&A, 336, 116

Tran, D. 1998, *PhD Thesis*, Univ. de Paris

Uchida, K., Sellgren, K. & Werner, M., 1998, ApJ, 493, L109

Valentijn, E.A. et al. 1996, A&A, 315, L60

Vigroux, L. 1997, in *Extragalactic Astronomy in the Infrared*, ed. G. Mamon, T.X. Thuan & J.T.T. Van (Editions Frontières: Paris)

Xu, C. et al. 1998, ApJ, 508, 576

Xu, C., Sulentic, J.W. & Tuffs, R. 1999, in preparation

ISOCAM OBSERVATIONS OF GALAXIES

L. Vigroux, V. Charmandaris, P. Gallais, O. Laurent, S. Madden, F. Mirabel, H. Roussel, M. Sauvage, & D. Tran

CEA, Saclay, Service d'Astrophysique, 91191, Gif-sur-Yvette cedex, France

ABSTRACT

The current results of our ISOCAM Guaranteed Time observations of nearby galaxies demonstrate the wide variety of physical conditions and components that are present in mid infrared wavelengths. In the disks of normal galaxies, where the emission is dominated by the aromatic carbon particles, the mid-IR emission at 6 μm and 15 μm provides a useful star formation indicator, while the same is not true when the mid infrared emission is dominated by central HII regions, as in starburst galaxies. Early type galaxies show a variety of characteristics, from mostly photospheric emission to various degrees of dust emission, while some ellipticals are clearly dominated by strong non-thermal radio sources in the mid infrared. ISOCAM imaging spectroscopy provide strong and unique constraints on the nature of the infrared sources associated with luminous infrared galaxies.

Key words: ISO; IR astronomy; IR dust emission, galaxies.

1. INTRODUCTION

Observations of galaxies had been confined for a very long period of time to the visible and radio domains. Stellar content is probed by the galaxy emission in the visible, while the interstellar matter, HI or molecules are probed by emission in the radio domain. IRAS then brought to the fore the importance of the infrared (IR) domain in understanding the energy budget of galaxies. The infrared flux of galaxies is dominated by the radiation from dust heated by the interstellar radiation field. The shape of a galactic spectral energy distribution is determined by the fraction of the interstellar radiation field which is absorbed by the dust and radiated in the infrared, assuming a fixed dust composition and grain size distribution. IRAS observations have shown that the fraction of the interstellar radiation field which is absorbed by dust can be very large, ranging from 10% to almost 100% (Soifer et al. 1987). Therefore, observations at visible wavelengths alone cannot be used to determine the bolometric luminosity of a galaxy since they do not provide information about the absorbed energy that is emitted in the IR. The discovery of galaxies with luminosities 100 times larger in the infrared than in the visible was a major outcome of IRAS (Soifer et al, 1984). However, the lack of spatial resolution of IRAS has limited investigations to the integrated properties of galaxies, with the exception of the Magellanic Clouds, which were among the few galaxies that were well resolved by IRAS (Schwering 1989; Schwering & Israel 1989; Sauvage et al 1990). IRAS infrared color-color diagrams demonstrated that galaxies fall in a well defined sequence which has been interpreted in terms of different proportions of star forming regions, diffuse interstellar matter and active nucleus emissions (Helou 1986, Rowan-Robinson & Crawford 1989). The adequate separation of the various star forming complexes from the diffuse interstellar medium was difficult, if not impossible, before ISOCAM (Cesarsky et al. 1996a), which provided a spatial resolution of 6 arcsec, 20 times higher than IRAS, corresponding to a linear size of a few 100 pc in nearby galaxies.

About 50 nearby galaxies, spanning a wide range of morphological types, luminosities and activity levels, have been completely imaged in various ISOCAM Guaranteed Time programs. Most of the observations were done with the two main ISOCAM filters: LW2, from 6 to 8 μm and LW3, from 12 to 17 μm. The limiting surface brightness of most of these maps is 2 μJy arcsec^{-2} with a spatial resolution of 6 arcsec. The brightest galaxies have also been observed with the Circular Variable Filter (CVF) from 5 to 16.5 μm with spectral resolution of R=35. The limiting surface brightness of most of these CVF scans is 100 μJy arcsec^{-2}. The LW2 wavelength domain can be dominated by the emission of the Unidentified Infrared Bands (UIBs), at 6.2, 7.7, and 8.6 μm, carriers of which are proposed to be particles with an aromatic hydrocarbon component and stochastically heated to high temperatures (for example, PAHs: Léger & Puget 1984; Allamandola et al. 1989; coal grains: Papoular et al. 1991). Emission from hot very small carbon grains (VSGs; Desert et al. 1990) is responsible for the underlying continuum that is often present in the LW3 filters, but there can also be a significant contribution from a pseudo continuum and a wide band at 12.7 μm, which seems to be due to the same carriers which are responsible for the UIBs at shorter wavelengths.

Proceedings of the Conference "The Universe as seen by ISO", Paris, France, 20–23 October 1998 (ESA SP-427, March 1999)

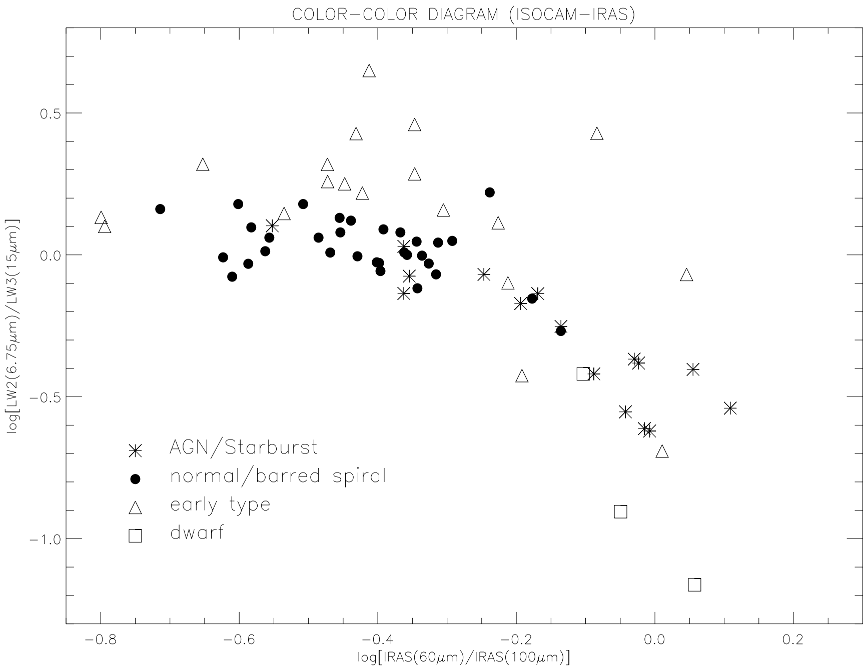

Figure 1. ISOCAM color-IRAS color diagram for galaxies in our program. The programs are separated into active galaxies, barred and normal galaxies, early-type galaxies and dwarf galaxies. Note the turn over for IRAS 60/100 flux ratios > 0.5, in the domain occupied predominately by the AGN/starbursts and dwarf galaxies. The can be explained by the destruction of the UIBs (LW2 band) in the intense radiation field, as the emission from very small hot grains (LW3) increases.

2. OBSERVATIONS OF NORMAL SPIRAL GALAXIES

From our program of normal galaxies, we find that throughout the galaxies, the mid infrared integrated colors of normal galaxies are relatively constant, with a LW2/LW3 flux ratio of the order of 1 with a large dispersion. In a LW2/LW3 flux density ratio versus IRAS 60μm/100μm flux density ratio, the sequence defined by our sample of normal galaxies is flat for galaxies with IRAS 60/100 ratios below 0.5 and decreases for the most active galaxies (Figure 1).

This result, first obtained by Helou (these proceedings) on a sample of galaxies selected to cover the whole range of IRAS colors, is confirmed for our larger sample. Early type galaxies do not follow the main trend, while blue compact dwarf galaxies are located in the region populated by the most active starburst galaxies and AGNs. Observations of Galactic nebulae (e.g. Cesarsky et al, 1996b) have shown that LW2/LW3 flux density ratios of the order of 1 are typical in the neutral interstellar medium and in photodissociation regions (PDRs), where the 2 filters at 7 and 14 μm are dominated by the aromatic bands and pseudo continuum. This ratio is much lower (<0.5) in the HII regions, where the carriers of the aromatic bands are destroyed and the 14 μm emission is dominated by the strong continuum due to hot VSGs. The mid IR colors of normal and mildly active galaxies demonstrate that their mid IR flux is dominated by the neutral ISM and PDRs. A detailed analysis of a sample of nearby spiral galaxies has shown that the emission from galaxies is dominated in the mid IR by PDRs with only a minor contribution from the neutral ISM which never represents more than 30% of the total emission at 7 μm (Roussel et al. 1999). The 7 μm maps of two well-known spiral galaxies, M51 and M83, are good illustrations of the importance of PDR emission in the disk of spiral galaxies (Figure 2).

The spiral arms are the most prominent features in these maps. At the resolution of ISOCAM, there is a good correlation between the spiral arms as seen in H_α, and the spiral arms discernible by the 7 μm emission. Color maps of 7μm/14μm flux density ratios show very small variations around the mean value of 1 observed for the disk as a whole. Since in the core of HII regions this ratio is much smaller than 1, this means that the mid IR emission is dominated by PDRs, and not the HII regions themselves. These results hold only in the disks of normal spirals. There are two noticeable exceptions to this rule. In the most active regions where strong starbursts are present, the 7μm/14μm flux density ratios decrease below 0.5 (Figure 1). In these cases, the mid IR emission is dominated by ionized regions with strong contributions from hot VSGs. On the other hand, in low star formation galaxies like M31, (Cesarsky et al., these proceedings) the 7 μm emission does not coincide with the star formation complexes, mainly due to extinction effects. It follows, instead, the neutral gas distribution and traces the gas density.

The tight correlation between star formation complexes and mid IR emission in the disks of spiral galaxies indicates that the mid IR emission should be a good star formation efficiency indicator. Cer-

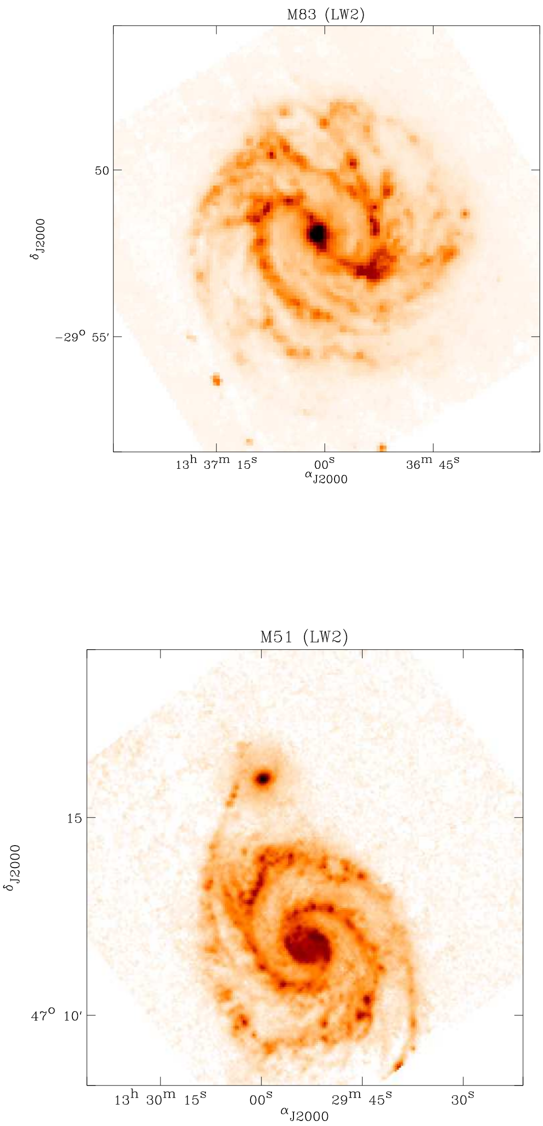

Figure 2. ISOCAM 7 μm images of M83 (upper) and M51(lower) using 6" pixel field of view

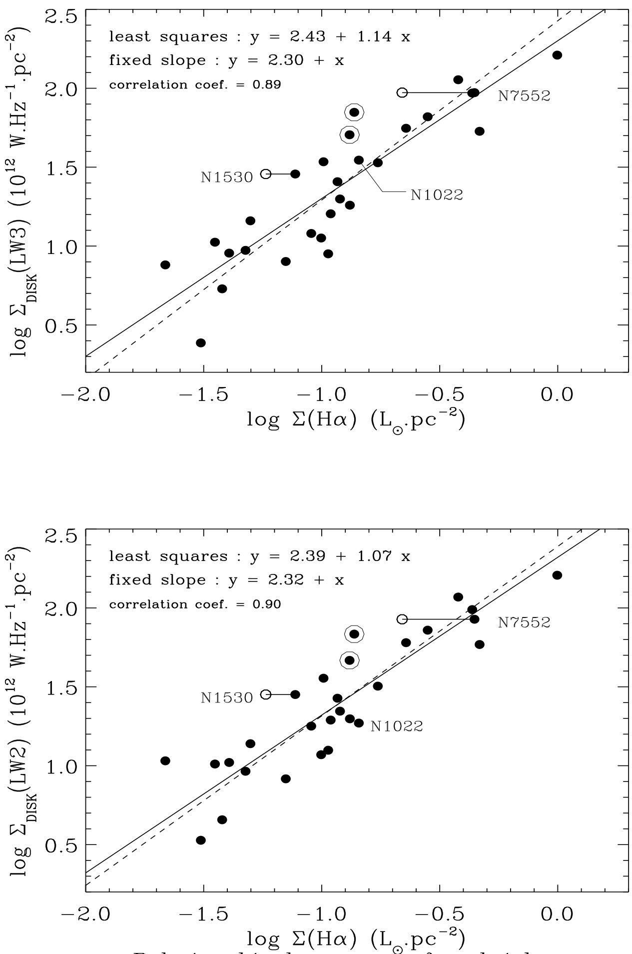

Figure 3. Relationship between surface brightnesses averaged over the whole disk of Hα and : (upper) LW3 (12 to 18 μm) ; (lower) LW2 (5 to 8.5 μm). The dashed line is the best least squares fit and the linear correlation is shown as the solid lines.

tainly, mid IR emission is less prone to absorption than Hα or Hβ. However, the conversion mechanism between the amount of young stars formed and the 15 μm flux densities is less straightforward than for hydrogen recombination lines. The Hα energy can be computed with a simple set of parameters such as density and ionizing photon fluxes, while mid IR calculations require a detailed model of dust composition and radiation transfer. Such a model does not exist at the level which is needed to derive a star formation rate from mid infrared fluxes in galaxies. But, a calibration of mid infrared fluxes can be performed using other well established indicators. Roussel et al, (1999) have shown that, in the disks of spiral galaxies, a good correlation exists between mid IR fluxes, at 7 and 15 μm and Hα (Figure 3).

This correlation holds when the total emission remains dominated by PDRs, which is the case as long as the star formation rate integrated over the disk remains < 0.1 M$_\odot$ yr^{-1} kpc^{-2}. At larger star formation rates, this relationship does not hold since the mid IR emission is dominated by the central HII regions where Hα is strongly absorbed. This is the case in central regions of barred galaxies where a high star formation rate is induced by gas mass transfer along the bar (Martinet & Friedlich 1998), or in interacting galaxies which have experienced a strong starburst due to shocks in the colliding gaseous disks (Vigroux et al. 1996). The mid IR luminosity of spiral galaxies is a combination of the luminosity of the disk and the central regions. The ratio of the central region luminosity over the disk luminosity ranges from a few percent in normal spirals to a factor 2 or more in early type barred spirals or AGN. The integrated mid IR luminosity cannot be used to derive star formation rates without knowing what the relative fractions of the disks and central regions are.

The integrated mid IR luminosity of galaxies is tightly correlated with the IRAS far infrared (FIR) luminosity (Figure 4) (Roussel et al. 1999). In recent years, the FIR luminosity has been proposed to be a reliable indicator of star formation (Devereux & Young, 1990), despite the fact that the relationship between SFR and FIR luminosity is not linear (Lonsdale & Helou, 1987, Sauvage and Thuan, 1992). The ISOCAM observations confirm that the integrated FIR luminosity is not a good indicator of star formation in normal or mildly active galaxies, since it is proportional to the integrated mid IR luminosity which, itself, is not a good star formation indicator. However, the reason for the non linearity is not the relative variation of a diffuse component and star forming complexes. It is rather due to the variation of the bright hot central regions with respect to the cold disks. FIR luminosity can be used as a good star formation indicator only in strong starburst galaxies, as has been done in the past, but not in normal or mildly active galaxies, where two mechanisms of infrared emission exist, disks where the emission is dominated by the PDRs and central regions where it is dominated by the hot continuum of grains. The long standing interpretation of the IRAS color-color diagram as due to the variation of a cold cirrus like component with respect to active star forming complexes (Helou, 1986), is no longer valid in light of ISOCAM results. The relevant parameters are the proportion of star formation in the disk and in the central regions. It is only at wavelengths longer than 100 μm that the coldest cirrus like component can take a major role in the integrated light of a galaxy.

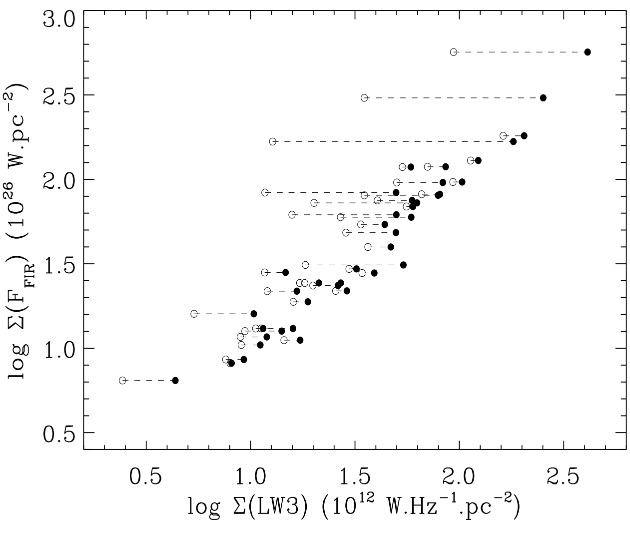

Figure 4. Proportionality between far-infrared and mid-infrared surface brightnesses. Far-IR fluxes are a combination of 60 and 100 μm IRAS fluxes as defined in Helou et al. 1988. Filled circles represent total fluxes and empty circles show the effect of taking into account only bare disks (this was possible only for LW3, since galaxies are not resolved by IRAS). The best least-squares fit gives a slope of 1.04 ($^{+0.14}_{-0.12}$ at a 3 σ confidence level) with a correlation coefficient of 0.97. The relationship with LW2 fluxes is very similar.

3. OBSERVATIONS OF EARLY-TYPE GALAXIES

IRAS has shown that up to 50% of early type galaxies can have a significant infrared emission (Knapp et al. 1989; 1992; Jura et al, 1996). This emission has been attributed to dust released by stellar winds of metal rich stars and heated by the strong interstellar radiation fields prevailing in the core of elliptical galaxies. However, some of these galaxies have strong 10 μm emission excess, the origin of which was still a matter of debate. Some authors attributed this MIR excess to photosphere emission of AGB stars (Jura et al. 1987; Knapp et al. 1992), some others to the presence of interstellar hot dust (Sauvage and Thuan, 1994). The distribution and origin of the mid infrared emission in early-type galaxies has been difficult to ascertain with IRAS data, due to the lack of spatial resolution. To address this question, we have observed a sample of 20 nearby early type galaxies spanning a large range of properties, regular ellipticals, dusty ellipticals and radio sources (Madden et al., these proceedings). The galaxies were observed through three filters, LW1 at 4.5 μm, LW2 at 7 μm and LW3 at 15 μm. The central cores were observed with the 3 arcsec lens at 7 and 15μm, and the complete galaxies at 6 arcsec with the 4.5, 7, and 15 μm filters. The results of this sample are not reconcilable with a single explanation; instead they demonstrate a wide variety of behavior in the mid IR. Stellar photospheric emission dominates the mid IR in normal ellipticals, such as NGC 1399 and NGC 2300 and, more surprisingly, also in the HI rich star forming S0 galaxies NGC 5102. These galaxies which have progressively less dust lie above the relatively flat slope of the disk galaxies in the color-color diagram of Figure 1. Low level residual dust may also be present in these galaxies, as suggested by the spectrum of NGC 1399, which also hints of a silicate emission feature. Strong 7 μm emission is found in the dusty galaxies of our sample like NGC 5266, NGC 5363 and NGC 5866, enhanced well above the 4.5 and 15 μm emission - an unambiguous signature of the presence of the aromatic bands which are ubiquitous in the photodissociation regions in Galactic sources and other galaxies. The presence of UIBs is also demonstrated by a CVF spectrum obtained toward NGC 5173 where the 11.3 microns band is detected (M.Sauvage, private communication). However, the band structure may be different from that observed in spiral galaxy disks where the 7 μm to 15 μm flux density ratio is always less than 1, in contrast to most of the ellipticals in our sample. This may be due to a difference in excitation mechanism: if UV photons, usually attributed to the heating of the carriers of the UIBs in spiral galaxies, prove to be insufficient in exciting these particles in early-type galaxies, visible photons may well be the excitation agents. Finally, some other sources have mid infrared colors which cannot be interpreted without a non-thermal continuum, as in the case of strong radio sources such as M87, Abell 426 and NGC3928.

4. INTERACTING GALAXIES

Since IRAS, interacting galaxies are known to have very large infrared emission (Soifer et al, 1984, 1987). In the most extremes cases, the Ultra Luminous Infrared Galaxies (ULIRG), almost 100% of the galaxy energy is emitted in the far infrared with a flux density peak between 60 and 100μm. IRAS observations were limited to integrated fluxes in four bands which did not provide sufficient constraints to determine the origin of the infrared emission. The two mechanisms which have been proposed are emission due to starbursts (e.g. Joseph & Wright 1985) or that due to dust shrouded active galactic nuclei (e.g. Sanders et al. 1988). Several ground-based observations have shown that most AGNs are surrounded by starburst regions, such as in NGC 1068, for example (Telesco et al, 1988; Condon et al. 1991; Downes & Solomon, 1998), yet the origin of the large IR emission of these galaxies remains a source of discussion. ISO provided the first opportunity to perform detailed studies of these galaxies offering spatial resolution with ISOCAM, and spectral resolution with SWS and LWS adequate to provide constraints on the different models. Spectral diagnostics have been obtained by Genzel et al., (1998) to separate the AGN from the starburst region. They are based on emission line flux ratios of ions, like NeII, NeIII and NeV, which provide a measure of the hardness of the ionizing photon energy spectrum, combined with the intensity of aromatic bands. These bands are absent in AGN, but dominate the mid IR emission in starburst regions. However, the spatial resolution of SWS (20 x 40 arcsec^2), and LWS (3 arcmin diameter) were not sufficient to resolve the regions which are at the origin of the infrared emission. ISOCAM, with its CVF mode, also provides a unique tool to survey the origin of this infrared emission.

Interactions between two large spiral galaxies can be observed at different stages: from weakly interacting systems like the Antennae Galaxies (NGC 4038/4039), to almost totally merged systems, like Arp 220. In the Antennae, the interaction has created the conditions for intense star formation in the region where the two disks overlap. Cold dust (Evans et al. 1998), molecular gas (Stanford et al. 1990) and CII emission (Fischer et al. 1996; Nikola et al. 1998) all peak in the overlap region. The overlap region radiates 50% of the total 15$\,\mu$m flux density of the whole system (Vigroux et al, 1996). The structure of the overlap regions in the mid infrared is very similar to the complex patches observed in radio continuum (Hummel & van der Hulst 1986). The brightest of these mid IR sources, which is not very conspicuous at optical wavelengths, radiates about 15% of the total 15$\,\mu$m flux density of the two galaxy system (Mirabel et al, 1998). All these observations demonstrate that, in this interacting system, most of the star formation takes place in the overlap region, and not in the two nuclei of the parent galaxies. A similar result has been observed in the more advanced merging system, Arp 299. In this case, the structure is even more complex than in the Antennae (Gallais et al. this volume). Two bright infrared knots dominate the mid infrared emission. But, if the west knot coincides with one of the galaxy nuclei as seen in J band, the east IR knot is displaced by 500 pc with respect to the other nucleus. The spectra of the different knots of Arp 299 can be interpreted in view of a starburst origin with varying degrees of intensity and extinction. In contrast, the mid IR spectrum of the interacting pair IRAS 19254-7245 is dominated by only one of the two nuclei, which hides a dusty AGN (Laurent et al. these proceedings). These interacting galaxies have complex structures, with starburst regions not necessarily coincident with galactic nuclei and dusty AGNs. The large beam of the two ISO spectrographs encompass a complex structure of knots with different infrared spectral energy distributions. The modeling of these observations in term of physical conditions, electron temperatures, densities, radiation flux, etc. is hampered by the complexity of the geometry of the emitting region given the SWS and LWS beam sizes. Despite its poor spectral resolution, ISOCAM CVF observations provides strong constraints on the nature of the infrared sources associated with luminous infrared galaxies (Laurent et al., these proceedings).

Radio galaxies are thought to be giant elliptical galaxies powered by accretion of interstellar matter onto a supermassive black hole. Interactions with gas rich galaxies may feed them with cold interstellar matter, but a major problem is to understand how the fueling gas finds its way from typical galactic radii of several kiloparsecs down to a few parsecs from the center, and at the rates required to power the AGN. Bar structures have been proposed in theoretical models but prove to be very difficult to observe. Centaurus A may serve as a template to investigate these questions (Mirabel et al, 1999, and references therein). Figure 5 shows the 7$\,\mu$m ISOCAM image and the 20 cm radio contours (Condon et al. 1996), overlaid on an optical image of Centaurus A. The 7 μm emission from dust reveals a bisymmetric structure of 5$'$ ($\sim$5 kpc for a distance of 3.5 Mpc) in total length. In contrast to the optical dark lanes which show a wide and somewhat chaotic distribution, the structure of the mid-infrared emission is remarkably thin, smooth and bisymmetric. The central structure corresponds to a bar 3 kpc long rotating as a solid body. This gaseous disk and its associated bar are thought to be the result of the capture of a gas rich galaxy, the gas of which settled into a disk. As the disk lies in a plane which is not aligned with the main axis of the galaxy, it is subject to a large torque (Barnes & Hernquist 1992), forcing it to warp. However, the low temperature of the gas make this disk self-gravitating and stable. A bar can develop over a few rotation period. The CVF spectra shows two main components: a central active nucleus surrounded by starburst complexes found in the central regions of the bar. These ISOCAM observations provide the first direct evidence for the mechanism which transport the material toward the central region and ultimately, to the central active nucleus.

5. CONCLUSIONS

ISOCAM observations are helping to elucidate the nature of the mid-IR emission of nearby galaxies. In doing so, we see that ISOCAM can probe the large variety of physical phenomena present in galaxies at mid infrared wavelengths, something that was motivated by IRAS, yet was not possible to constrain until ISO. Yet, despite the power that we now possess in the mid infrared to understand the physical phenomena prevailing in galaxies, one of the critical links in the picture remains the absence of comparable high spatial resolution in the far infrared. This

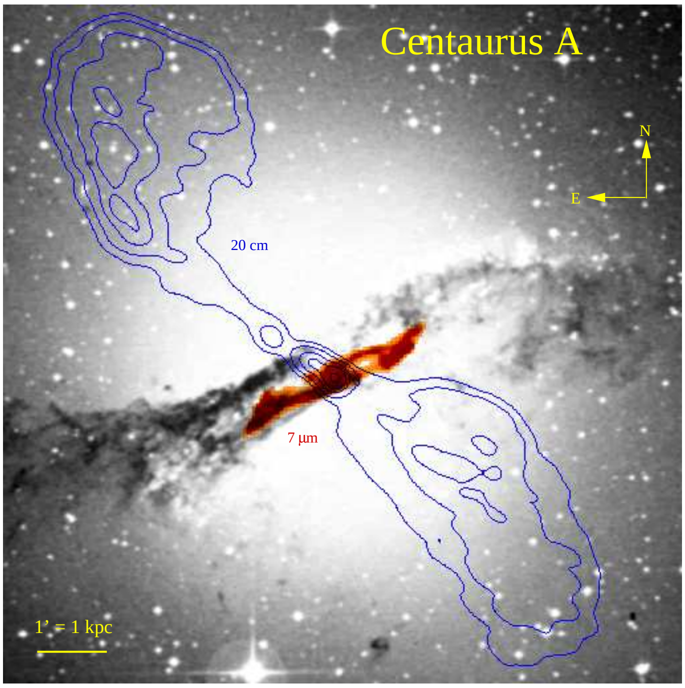

Figure 5. ISOCAM 7µm image (red) and 20 cm continuum contours (Condon et al. 1996) superposed on an optical image of Centaurus A (Mirabel et al. 1998).

aspect will await future missions which will provide far infrared measurements at the same spatial resolution as the ISOCAM maps in the mid-IR. As incentive for future missions, it should be noted that the interpretation of the emission mechanisms in nearby galaxies would have been misunderstood without the information obtained with the spectral imaging capability provided by the ISOCAM CVF. Unfortunately, such a mode does not exist in the SIRTF payload. In this respect, the interpretation of SIRTF observations will have to rely on ISOCAM CVF results for interpretation. Space-borne imaging spectroscopy will be achievable in the FIR on FIRST with the SPIRE and PACS instruments. SPIRE is based on an imaging FTS with a field of view of 2.5 x 2.5 arcmin^2 and a pixel field of view of 18 arcsec, while the grating spectrometer, PACS, will have a field of view of 1 x 1 arcmin^2 and 9 arcsec pixels. Thus SPIRE and PACS together will complement the ISOCAM observations in the far infrared.

REFERENCES

Allamandola, L. J., Tielens, A.G.G.M. & Barker, J.R., 1989, ApJS 71, 733

Barnes, J.E.. & Hernquist, L., 1992, ARA&A 30, 705

Cesarsky, C. et al. , 1996a, A&A 315, L32

Cesarsky, D, et al. , 1996b, A&A 315, L309

Condon, J.J., Huang, Z.-P., Yin, Q.F. & Thuan, T.X., 1991, ApJ 378, 65

Condon, J.J., Helou, G., Danders, D.B. & Soifer, B.T., 1996, A&ASS 103, 81

Désert, F-X., Boulanger, F. & Puget. J.L., 1990, A&A 237, 215

Devereux, N.D. & Young, J., 1990, ApJ 350, L25

Downes, D. & Solomon, P.M. 1998, ApJ, 507, 615

Evans, R., Harper, A. & Helou, G. 1997, in "Extragalactic Astronomy in the Infrared", eds G.A. Mamom, T,X, Thuan, J.T.T. Van, Editions Frontiers

Fischer, J. et al. 1996, ApJ 315,

Genzel, R. et al. 1998, ApJ, 498, 579

Helou, G., 1986, ApJ 311, L33

Helou, Khan, I.R., Malek, L. & Boehmer, L., 1988, APJS 68, 151

Hummel, E & van der Hulst, J.M., 1986, A&A 155, 151

Joseph, R.D. & Wright, G.S., 1985, MNRAS, 214, 87

Jura, M., Kim, D.-W., Knapp, G. R. & Guhathakurta, P., 1987, ApJL 312, L11

Jura, M., 1996, ApJ, 472, 806

Knapp, G.R., Guhathakurta, P., Kim, D.-W. & Jura, M., 1989, ApJ, 70, 320

Knapp, G.R., Gunn, J.E. & Wynn-Williams, C.G., 1992, ApJ 399, 76

Léger, A. & Puget, J.-L., 1984, A&A 137, L5

Lonsdale-Persson, C.J. & Helou, G., 1987, ApJ 314, 513

Martinet, L. & Friedlich, D., 1998, A&A 323, 363

Mirabel, I.F., Vigroux, L., Charmandaris, V., Sauvage, M., Gallais, P., Tran, D., Cesarsky, C., Madden, S.C., Duc, P.-A. 1998, A&A 333, L1

Mirabel, I.F., Laurent, O., Sanders, D.B., Sauvage, M., Tagger, M., Charmandaris, V., Vigroux, L., Gallais, P., Cesarsky, C. & Block, D.L., 1999, in press

Nikola, T., Genzel, R., Herrmann, F., Madden, S.C., Poglitsch, A., Geis, N., Townes, C.H. & Stacey, G.J., 1998, ApJ 504, 749

Papoular, R., Reynaud, C., Nenner, I., 1991, A&A 247, 215

Roussel, H., Sauvage & Vigroux, L., 1999, submitted to A&A

Rowen-Robinson, M. & Crawford, J., 1989, MNRAS 238, 523

Sanders, D.B., Soifer, B.T. et al. 1988, ApJ, 325, 74

Sauvage, M., Thuan, T.X. & Vigroux, L., 1990, A&A, 237, 296

Sauvage, M. & Thuan, T.X., 1992, ApJ 396, L69

Sauvage, M. & Thuan, T., 1994, ApJ 429, 153

Soifer, B.T. et al. , 1984, ApJ 278, L71

Soifer, B.T., Houck, J.R. & Neugebauer, G., 1987, ARA&A 187

Schwering, P.B.W & Israel, F.P., 1989, A&AS 79,79

Schwering, P.B.W., 1989, A&AS 79, 105

Stanford, S.A., Sargent, A.J., Sanders, D.B. & Scoville, N.Z. 1990, ApJ 349, 492

Telesco, C.M. & Drecher, R. 1988, ApJ 334, 573,

van der Hulst, J.M. & Hummel, E.,1985, A&A 150, L7

Vigroux, et al. , 1996, A&A 315, L93

FAR-INFRARED SPECTROSCOPY OF NORMAL GALAXIES WITH ISO LWS

S. Malhotra[1,2,3], G. Helou[1], D. Hollenbach[4], M. Kaufman[4,5], S. Lord[1], J.R. Brauher[1], D. Dale[1], N.Y. Lu[1], C. A. Beichman[1], H. Dinerstein[6], D. A. Hunter[7], K. Y. Lo[8], R. H. Rubin[4], N. Silbermann[1], G.J. Stacey[9], H. A. Thronson Jr.[10], & M. W. Werner[11]

[1] I.P.A.C., Caltech, Pasadena
[2] N.O.A.O, Tucson
[3] Hubble Fellow
[4] NASA Ames Research Center, Moffett Field
[5] S.J.S.U
[6] U. Texas, Astronomy Department, Austin
[7] Lowell Observatory
[8] University of Illinois
[9] Cornell University, Ithaca
[10] NASA, Headquarters, Washington
[11] JPL, Pasadena

ABSTRACT

The deficiency of [CII] (158 μm) line emission in many normal and ultraluminous galaxies is one of the major surprises from ISO-LWS observations. We show that this is not an isolated phenomenon: there is a smooth decline in $L_{[CII]}/L_{FIR}$ ratio with increasing dust temperature (as indicated by far-infrared colors $F_\nu(60\mu m)/F_\nu(100\mu m)$, i.e. F60/F100) and star-formation activity (indicated by L_{FIR}/L_B), independent of their luminosity or morphology. In a sample of 60 normal galaxies, these trends span a factor of 100. Of the numerous explanations proposed for the $L_{[CII]}/L_{FIR}$ variation the leading ones are (a) optical depth and extinction, (b) softer radiation field from old stellar populations (c) inefficient photoelectric heating by charged grains when the UV radiation density per gas atom (G_0/n) is high.

We can rule out hypothesis (a) with the observations that the [OI]/[CII] line ratio increases for galaxies with higher F60/F100. This is contrary to the expectation that [OI] at 63 μm should be more severely affected by extinction because it is at a shorter wavelength. Optical depth should also affect [OI] 63 μm line more strongly because OI exists deeper (to $A_v = 10$) in the interior of clouds than [CII]. Hypothesis (b) explains the slight decrease in $L_{[CII]}/L_{FIR}$ seen in early type galaxies with low rates of star-formation and the lowest L_{FIR}/L_B in the sample. The dramatic fall in $L_{[CII]}/L_{FIR}$ for the warmest and most actively star-forming galaxies is best explained by hypothesis (c). In galaxies with warmer dust, there is less cooling via the [CII] line, while [OI] remains a major coolant. This trend is qualitatively explained in PDR models by an increase in radiation field G_0, which raises the dust temperature and the [OI]/[CII] line ratio.

1. INTRODUCTION AND SAMPLE

The [CII] (158 μm) and [OI] (63 μm) are dominant coolants of the neutral ISM, radiating typically 0.1 – 1% of the FIR luminosity and about 1500-4000 times more energy than the CO(1-0) line. The [CII] and [OI] (63μm) lines are able to cool the gas because C and O are abundant in neutral gas and because the excitation energy is low ($\Delta E/k$ = 91K for C^+ and $\Delta E/k$ = 224K for O). The [OI] line becomes effective at higher gas densities and temperatures. Comparing line strengths to models one can constrain physical conditions in the ISM (e.g., Tielens & Hollenbach 1985, Wolfire et al. 1990). Gas heating is dominated by photoelectron ejected from dust grains, following UV absorption (Watson 1972).

These lines arise in PDRs (Photon Dissociation Regions) including diffuse HI, and UV illuminated surface of molecular clouds; and in case of [CII], also ionized gas. For normal galaxy nuclei and star formation regions in the spiral arms, most of the observed [CII] arises from PDRs on molecular cloud surfaces (Crawford et al. 1985). However, integrated over the disks of normal spiral galaxies, a substantial fraction (up to 50%) may also arise from 'standard' atomic clouds, i.e. the cold neutral medium (CNM) (Madden et al. 1993) or from extended, low density HII regions (Heiles 1994).

The sample in the ISO key-project on ISM in normal galaxies consists of galaxies whose luminosity is dominated by star-formation and excludes AGNs (Helou et al. 1996). Sixty distant galaxies, for which all the FIR emission is within one LWS beam, and 9 nearby, resolved galaxies were observed with LWS (Clegg et al. 1996) aboard ISO (Kessler et

Proceedings of the Conference "The Universe as seen by ISO", Paris, France, 20–23 October 1998 (ESA SP-427, March 1999)

al. 1996). The sample spans a range of morphologies (irregular, spiral, S0 and ellipticals), far-infrared luminosity (Log($L_{FIR}/L_{\odot}$)=7.7-11.2), FIR color ($F_\nu(60\mu m)/F_\nu(100\mu m)$), and ratio of the luminosities in far-infrared and B band (L_{FIR}/L_B). We observed up to 7 atomic and ionic fine structure lines for each galaxy: [CII] (158μm), [OI] (145μm), [NII] (122μm), [OIII] (88μm), [OI] (63μm), [NIII] (57μm) and [OIII] (52μm). The most common lines observed are [CII] (158μm), [OI] (63μm), and [NII] (122μm).

2. [CII]/FIR RATIO

The [CII] observations were designed to have (1σ) sensitivity of $5 \times 10^{-5} \times L_{FIR}$. This value should be compared to that of the $L_{[CII]}/L_{FIR} = 3\times10^{-3}$ in the Milky Way (Wright et al. 1991) and $L_{[CII]}/L_{FIR} = 1-3\times10^{-3}$ for normal and starburst galaxies (Lord et al. 1996, Stacey et al. 1991).

Theoretically, little variation in $L_{[CII]}/L_{FIR}$ ratio is expected because it is a measure of the fraction of energy absorbed by dust that goes into heating the gas via photoelectron ejection. There are two physical conditions that could change this ratio and both the effects are seen in the present sample. The first is positive charge on grains which raises the work function of the grains so the photoelectrons carry a smaller fraction of the incident energy. Second, a softer radiation also leads to lower $L_{[CII]}/L_{FIR}$ as only UV photons produce photoelectrons while both optical and UV photons heat the dust.

Most galaxies in the sample have [CII]/FIR in the range of $0.1-1\%$, consistent with previous observations and the models of PDRs where the gas is heated by the photoelectrons from dust. The $L_{[CII]}/L_{FIR}$ flux ratios observed in the present sample span a factor of 100. Galaxies with warmer infrared colors (i.e. higher $F_\nu(60\mu m)/F_\nu(100\mu m)$ ratio) and higher FIR/Blue luminosity have smaller flux ratio (Figures 1 and 2). The $L_{[CII]}/L_{FIR}$ shows little dependence on FIR luminosity, most of which may be due to correlation between far-infrared color ($F_\nu(60\mu m)/F_\nu(100\mu m)$) and FIR luminosity. Two galaxies, NGC 4418 and IC 0860, were not detected in [CII], [OI] or any other lines, and we show their 3σ upper limits for the [CII] flux.

3. REASONS FOR [CII] DEFICIENCY

(a) [CII] line could be optically thick or self-absorbing. For NGC 4418 this implies $N(H) = 4\times10^{22}$ and $A_v \simeq 20$ for $\tau = 1$. The total extinction towards the nucleus of NGC 4418 is $A_v > 50$. This implies a high ratio of PDR to cold molecular gas. Self-absorption by cooler foreground gas is a possibility, and has been seen towards Sgr B2 (Cox et al. these proceedings).

(b) High extinction: $\tau_{dust} = 1$ at 150 μm implies $A_v = 1,500$. This is insufficient to explain the [CII] deficiency and is unlikely even for very obscured starbursts like Arp220 (Fischer et al. these proceedings).

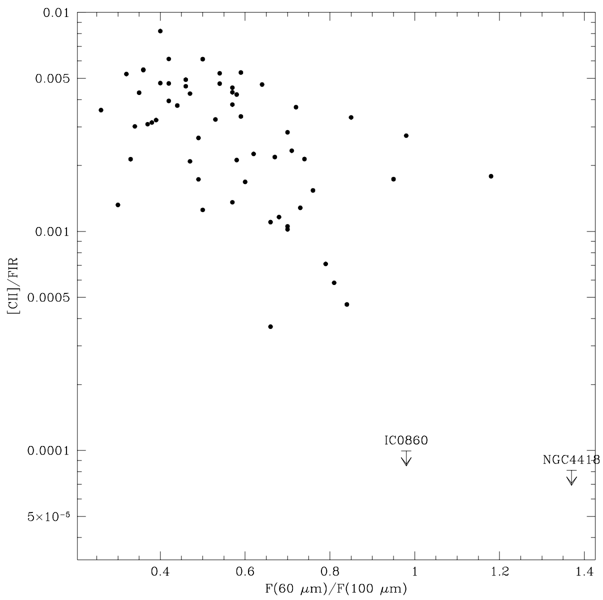

Figure 1. The ratio $L_{[CII]}/L_{FIR}$ *is plotted against the ratio of flux densities at* 60μm *and* 100μm *measured by IRAS. There is a trend for galaxies with higher* $F_\nu(60\mu m)/F_\nu(100\mu m)$ *(i.e. warmer dust) to have lower* $L_{[CII]}/L_{FIR}$. *Two galaxies in a sample of 60 have no detected [CII], for these the upper limit symbols show 3*σ *limits*

(c) Softer radiation from older/less massive stellar populations could lead to lower [CII]/FIR ratios (Luhman et al. 1998). This hypothesis also naturally explains the absence of FIR lines from ionized gas (Satyapal et al. in preparation).

(d) An extraneous FIR source, e.g. an obscured AGN, can lead to both a higher FIR/Blue luminosity and a lower $L_{[CII]}/L_{FIR}$. This hypothesis is supported by the observed compactness of the [CII] deficient sources in the mid-IR emission. A buried AGN could produce a lot of FIR without much [CII] since the UV field will be inefficient at making [CII] both due to its hardness (higher ionization states for C will be common) and due to its strength as discussed next.

(e) For high levels of UV radiation (G_0/n), the dust grains are positively charged and are less efficient at heating the gas because of a higher potential barrier to photoelectric ejection (Tielens & Hollenbach 1985).

4. THE [OI]/[CII] LINE RATIO

The line ratio [OI](63 μm)/[CII] increases with $F_\nu(60\mu m)/F_\nu(100\mu m)$, showing a tight correlation (Figure 4) (Malhotra et al. 1999), which is qualitatively explained by PDR models (Kaufman et al. 1999). The line ratio [OI]/[CII] and the dust temperature $F_\nu(60\mu m)/F_\nu(100\mu m)$ both increase with the UV radiation density G_0. However, PDR models underpredict [CII]/[OI] ratios observed. That is

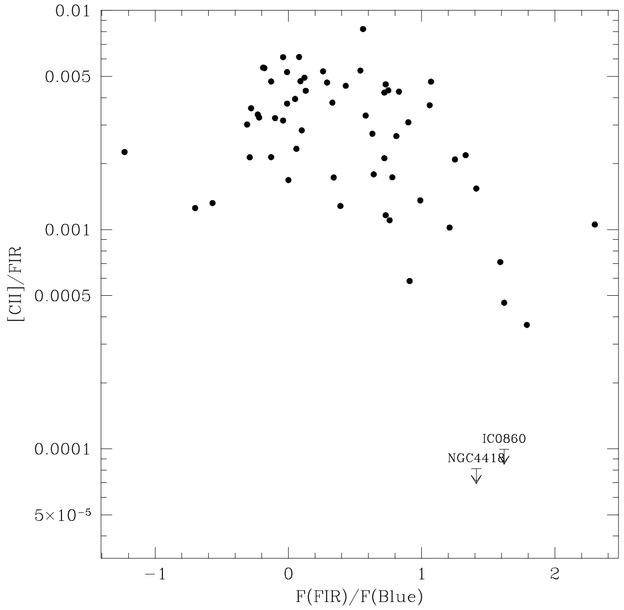

Figure 2. *The ratio* $L_{[CII]}/L_{FIR}$ *also decreases with higher ratio of FIR/Blue luminosity, which is a good estimator of star-formation activity. Galaxies at the low end of star-formation activity also show a less dramatic decrease in* $L_{[CII]}/L_{FIR}$. *The three galaxies with the lowest* L_{FIR}/L_B *are early type galaxies with a high proportion of old stars which produce softer radiation, leading to low* $L_{[CII]}/L_{FIR}$.

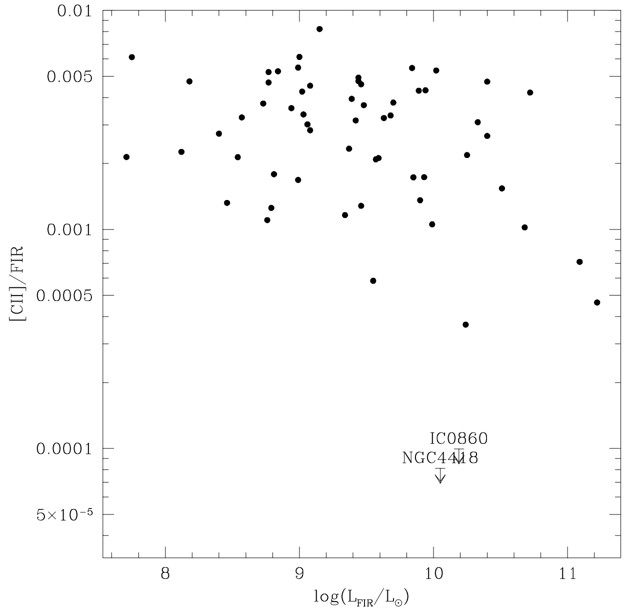

Figure 3. $L_{[CII]}/L_{FIR}$ *does not depend on the total FIR Luminosity. There is a weak tendency for the more luminous galaxies to be [CII] deficient, but that is probably due to a weak correlation between* $F_\nu(60\mu m)/F_\nu(100\mu m)$ *and* L_{FIR} *in the sample.*

because [CII] arises from ionized regions as well as neutral PDRs. Quantitative agreement between observations and PDR models of [OI]/[CII] line ratio is obtained by subtracting the [CII] emission due to ionized gas, estimated from the [NII] (122 μm) line (Malhotra et al. 1999).

This trend also rules out many of the hypothesis for [CII] deficiency listed in the last section.

(a) Since [OI] is present in the interiors of clouds ($A_v < 10$) whereas C^+ is confined to surface layers ($A_v < 4$), [OI] is more likely to go optically thick. Towards the Galactic center a deeper absorption profile is seen in the [OI] (63 μm) line (Keene et al. and Cox et al. in these proceedings) than the [CII] line (Cox et al. these proceedings).

(b) At a shorter wavelength [OI] 63 μm should be more sensitive to dust extinction than [CII] at 158 μm, contrary to the trends seen.

(c) It seems counterintuitive that the warmest and the more actively star-forming galaxies should have softer radiation fields and older stellar populations. However, no connection between the hardness of the radiation field and the far-infrared colors have been drawn. We think that softer radiation fields are responsible for the slight deficiency seen in the three early type galaxies NGC 6958, NGC 1052 and NGC 5866 with the lowest ratios of L_{FIR}/L_B in Figure 2. While optical light is absorbed by the dust grains and heats the dust, dust photoelectric heating of the gas is only possible when UV photons with energy greater than work function of the grain (E > 6eV) are available.

(d) The AGN hypothesis may explain the deficiency of [CII] but does not easily explain the trends in the $L_{[CII]}/L_{FIR}$ with L_{FIR}/L_B and $F_\nu(60\mu m)/F_\nu(100\mu m)$ ratios unless a significant fraction of galaxies have obscured active nuclei.

(e) An increase in [OI]/[CII] ratio is expected when radiation density G_0 increases, gas temperatures go up and more of the cooling is done via the [OI] (63 μm) line. As G_0/n increases further, grains get positively charged and there is less photoelectric heating of the gas, hence there is less total cooling relative to the FIR continuum emitted by grains.

5. CONCLUSIONS

In a study of 60 normal star-forming galaxies it is seen that the [CII] line gets increasingly weaker with respect to FIR continuum for galaxies with warmer dust and more active star formation. At the extreme end of that sequence we find two galaxies with no [CII] detected, and $L_{[CII]}/L_{FIR} < 10^{-4}$, roughly a factor of a 30-100 smaller than expected. The oxygen line at (63 μm) [OI]/FIR is constant to a factor of 7 where it is detected but [OI] is not detected for the [CII] deficient galaxies. The most favored explanation for [CII] variation and deficiency is positively charged grains at high UV radiation densities found in warm and active galaxies. This hypothesis explains the decreasing trend in $L_{[CII]}/L_{FIR}$ with increasing F60/F100 and L_B/L_{FIR}, the non-detection of [CII] and the increase in [OI]/[CII] ratio.

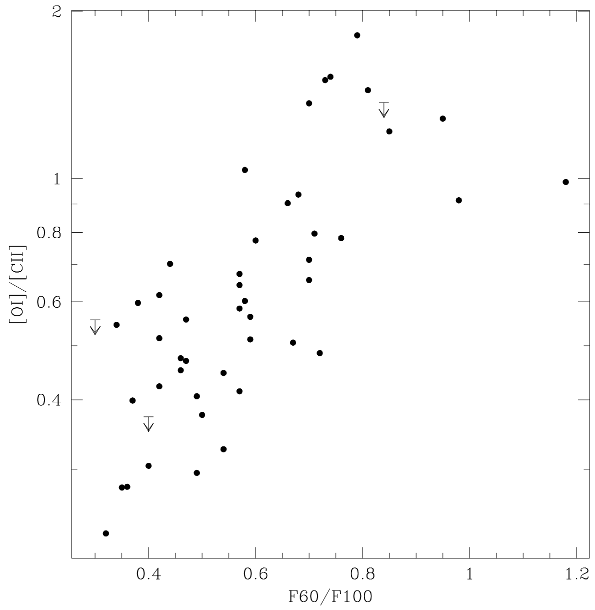

Figure 4. The ratio of [OI](63μm)/[CII] correlates very well with the IRAS colors F60/F100. This figure shows only the galaxies for which [CII] was observed, and the upper limits are 3-sigma non-detections of [OI]. The two [CII] deficient galaxies have no detections of [OI] and are not shown in this figure.

[CII] deficiency is also expected in galaxies with lower ratios of UV to optical radiation due to older or less massive stars. We see this effect in early type galaxies at the lowest end of the FIR/Blue ratio in this sample (Malhotra et al. these proceedings).

The [CII] and [OI] are among the brightest lines emitted by star-forming galaxies. About 0.2-0.7 % of the total FIR luminosity of a galaxy emerges in these lines. Normally, they are not affected by extinction, and are less affected by low metallicity than the CO lines. So, these lines have all that one might wish for in tracers of star-formation, except that we now have evidence that they are suppressed for some galaxies. The [CII]/FIR ratio does not depend on galaxy luminosity or morphology. This implies that high redshift searches for [CII] emitters will be most efficient at finding cool but luminous galaxies. Since [OI] is brighter for more active systems, [OI] searches for starbursts at high redshift may be more efficient.

ACKNOWLEDGEMENTS

This work was supported by ISO data analysis funding from NASA, and carried out at the IPAC and JPL (Caltech).

REFERENCES

Clegg, P.E., et al. 1996, A&A, 315, L38.

Crawford, M.K. et al. 1985, ApJ, 291, 755.

Heiles, C, 1994, ApJ, 720.

Helou, G., Malhotra, S., et al. 1996, A&A, 315, 157.

Kessler, M.F. et al., 1996, A&A, 315, L27.

Kaufman, M. et al., 1999 in preparation.

Lord, S., Malhotra, S. et al. 1996. A&A, 315, 117.

Luhman, M. et al. 1998, ApJ, 504, L11.

Madden, S.C., et al. 1993, ApJ, 407, 579.

Malhotra, S. et al. 1997, ApJ, 491, L27.

Malhotra, S., et al. 1999, in preparation.

Stacey, G. et al. 1991, ApJ, 373, 423.

Tielens, A.G.G.M., & Hollenbach, D., 1985, ApJ, 291, 722

Watson, W.D., 1972, ApJ, 176, 103.

Wolfire, M., Tielens, A.G.G.M., Hollenbach, D., 1990, ApJ, 358, 116.

Wright, E.L., et al. 1991, 381, 200.

AN LWS SPECTROSCOPIC SURVEY OF INFRARED-BRIGHT GALAXIES

J. Fischer[3], S.D. Lord[4], S.J. Unger[5], C.M. Bradford[3], J.R. Brauher[4], P.E. Clegg[5], J.W. Colbert[6], P. Cox[7], M.A. Greenhouse[2], V. Harvey[8], M.A. Malkan[6], G. Melnick[9], H.A. Smith[9], L. Spinoglio[10], V. Strelnitski[8], & J.-P. Suter[8]

[1]Naval Research Laboratory, Washington, DC, USA
[2]NASA Goddard Space Flight Center, Greenbelt, MD, USA
[3]Cornell University, Astronomy Department, Ithaca, NY, USA
[4]California Institute of Technology, IPAC, Pasadena, CA, USA
[5]Queen Mary & Westfield College, Univ. of London, London, UK
[6]Univ. of California, Dept. of Astronomy, Los Angeles, CA, USA
[7]Institut d'Astronomie Spatiale, Orsay, France
[8]Maria Mitchell Observatory, Nantucket, MA, USA
[9]Harvard-Smithsonian, CfA, Cambridge, MA, USA
[10]Istituto di Fisica dello Spazio Interplanetario-CNR, Roma, Italy

ABSTRACT

We present a comparative observational overview of the results of a far-infrared (43 - 197 μm) spectroscopic survey of a small sample of relatively nearby infrared-bright galaxies using the Infrared Space Observatory (ISO) Long Wavelength Spectrometer (LWS). The survey reveals a dramatic progression in emission and absorption line characteristics in these galaxies extending from strong [O III] 52, 88 μm and [N III] 57 μm fine-structure line emission to detection of only faint [C II] 158 μm line emission from gas in photodissociation regions. The several ultraluminous galaxies (ULIGs) included in the full spectral sample have the weakest emission line characteristics and show strong molecular absorption lines. We suggest that the variation in apparent excitation is not due to variation in density or far-infrared extinction, but rather may be due to differences in radiation hardness. The molecular absorption spectra show varying excitation as well, extending from galaxies in which the molecular population mainly occupies the ground state to galaxies in which there is significant population in higher levels. The origin of the [C II] 158 μm deficit in ultraluminous galaxies remains uncertain.

Key words: infrared-bright galaxies; ultraluminous galaxies; far-infrared spectra; starbursts; photodissociation regions; interstellar medium.

1. INTRODUCTION

In order to elucidate the evolutionary status, energetics, obscuration, and physical conditions of the nuclear regions of dusty, infrared-bright galaxies with minimal sensitivity to extinction, we have used the grating mode of the ISO Long Wavelength Spectrometer (LWS) (Clegg et al. 1996) to carry out (1) a full far-infrared spectral survey of a small sample of nearby IR-bright galaxies and (2) a fine-structure line survey of more distant galaxies, including a survey of ultraluminous galaxies in the [C II] 158 μm fine-structure line. The observations allow us to analyze the dust continuum, to put constraints on the radiation hardness of the illuminating source(s) and the intensity of the radiation as it impinges upon the surrounding clouds of gas and dust, and ultimately on the nature of the power sources. Analyses of the spectra of the individual galaxies are presented in these proceedings (Bradford et al., Harvey et al., Spinoglio et al.) and elsewhere (Fischer et al. 1996, Fischer et al. 1997, Colbert et al. 1999, Satyapal et al. 1999, and Unger et al. 1999). Here we present a comparative overview of these spectra.

2. THE LWS FULL SPECTRA OF INFRARED-BRIGHT GALAXIES

We present full, high signal-to-noise LWS spectra of six infrared-bright galaxies in Figure 1. The LWS aperture is $\sim 70''$ (Swinyard et al. 1998) and the spectral resolution is $\lambda/\Delta\lambda \sim 200$ in grating mode. The spectra are presented in sequence extending from strong [O III] 52.88 μm and [N III] 57 μm fine-structure line emission in the galaxies Arp 299 and M 82, to only faint [C II] 158 μm line emission from gas in photo-dissociation regions in the prototypical ultraluminous galaxy Arp 220. The far-infrared spectrum of Arp 220 is dominated by absorption lines of OH, H_20, CH, and [O I]. Intermediate in the sequence are Cen A, NGC 253, and NGC 4945, showing weak [O III] and [N III] lines while their PDR

Proceedings of the Conference "The Universe as seen by ISO", Paris, France, 20–23 October 1998 (ESA SP-427, March 1999)

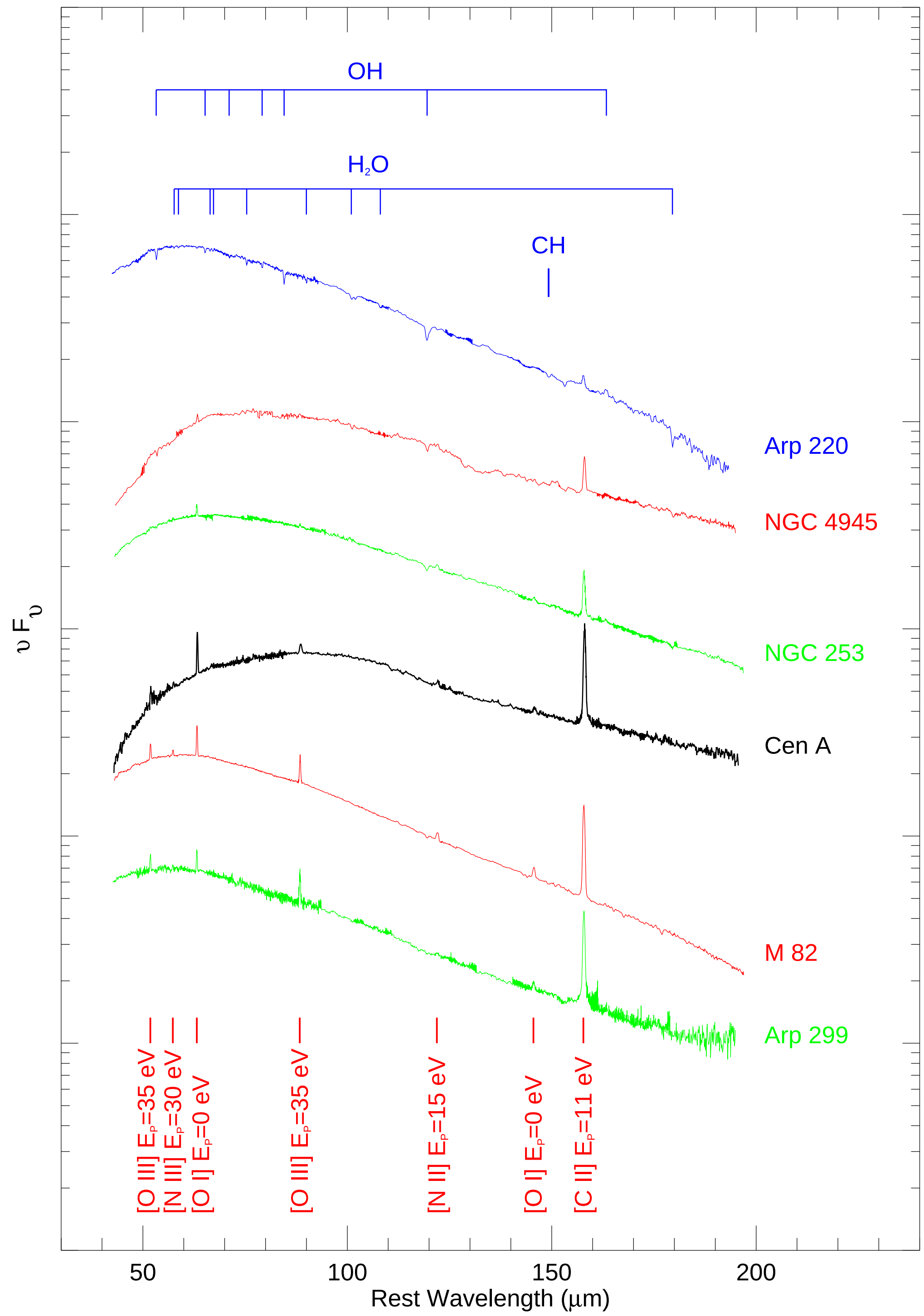

Figure 1. The full ISO Long Wavelength Spectrometer spectra of six IR-bright galaxies. The spectra have been shifted and ordered vertically according to apparent excitation (Fischer et al. 1999).

emission lines remain moderately strong. Interestingly, the strength and richness of the molecular absorption spectra is anti-correlated with the equivalent widths of the fine-structure emission line. For example, M 82 shows faint OH absorption from the ground level at 119 μm (Colbert et al. 1999), while NGC 253 shows absorption from the ground-state in three cross-ladder transitions and an emission line cascade at 79 μm and 163 μm (Bradford et al. these proceedings). In NGC 4945 and Arp 220, OH absorption from both ground and excited rotational levels is present (Fischer et al. 1997). In Arp 220, although the existence of a downward cascade is suggested by the presence of emission at 163 μm, absorption from rotational levels as high as 416 K and 305 K above the ground state is seen for OH and H_2O, respectively, and the [O I] 63 μm line is seen in absorption.

It is of interest to compare the far-infrared spectra of the archetypical Seyfert 2 galaxy NGC 1068 (Spinoglio et al. these proceedings) and that of the Galactic Center (White et al. these proceedings) with the spectra presented in Figure 1. The equivalent widths of the far-infrared fine-structure line emission in NGC 1068 resemble those in the starburst galaxy M 82. In addition to its Seyfert 2 nucleus, NGC 1068 hosts a starburst in its circumnuclear ring, that is possibly as young as the youngest clusters in M 82 (Davies et al. 1998). This starburst may be responsible for much of the far-infrared emission, as suggested by Telesco et al. (1984). A notable difference is that in NGC 1068 the OH lines are observed in emission suggesting unique excitation conditions possibly related to its Seyfert 2 nucleus (see discussion in Spinoglio et al. these proceedings), while in M 82 OH is observed in absorption (Colbert et al. 1999). We note here that for Cen A (Unger et al. 1999; Figure 1), also known to harbor an AGN, the weakness of the far-infrared [O III] lines may indicate that the AGN is not the dominant source powering the far-infrared luminosity. The far-infrared spectrum of the Galactic Center (White et al. these proceedings) would fall toward the upper end of the sequence shown in Figure 1, with an added emission line component due to warm, perhaps shock-excited, neutral gas.

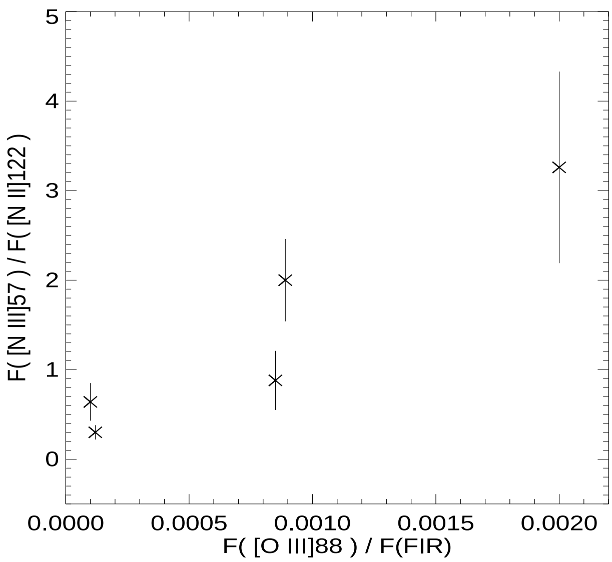

Figure 2. The [N III]57 μm/[N II]122 μm line ratio versus the [O III]88 μm line to integrated far-infrared continuum flux ratio for the sample galaxies.

3. THE FAR-INFRARED SPECTRA OF THE ULTRALUMINOUS INFRARED GALAXIES

The far-infrared spectrum of the second brightest ultraluminous galaxy Mkn 231 (Harvey et al. these proceedings) is surprisingly similar to that of Arp 220. It is dominated by molecular absorption, with similar OH absorption line ratios, and only faint PDR line emission is present. A single component absorption layer is inconsistent with the observed line ratios and fluorescent components do not alleviate the problem. The observed OH line ratios probably result from independent absorption and emission components (Suter et al. 1998). Of the ultraluminous galaxies, Genzel et al. (1998) find that Mkn 231 has the largest AGN component while the far-infrared luminosity of Arp 220 is powered by a starburst, so the similarity of the far-infrared spectra of these two ultraluminous galaxies is interesting.

The ultraluminous galaxies have fainter [C II] 158 μm equivalent widths than in normal and less luminous IR-bright galaxies by an order of magnitude (Luhman et al. 1998, Luhman et al. 1999). This has been interpreted as an indication of a lower interstellar radiation field G_o in Arp 220, where the [O I]145/[C II]158 ratio is unexpectedly low (Fischer et al. 1997, Luhman et al. 1998). Implicit in this interpretation is the assumption that the [O I] 145 μm line flux is not lowered by self-absorption, a reasonable assumption since its lower level is 228 K above the ground state. If self-absorption is responsible for the apparent faintness of the [O I] 145 μm line, then very high values of G_o are possible, as has been suggested by Malhotra et al. (1998) for a small percentage of their sample of normal galaxies. We note that analysis of the relative [C II] and [O I] lines in the mid-sequence galaxies Cen A, NGC 253, and NGC 4945 yields lower values of the interstellar radiation field G_o compared with Arp 299 and M 82. These galaxies also have colder dust temperatures.

The low fine-structure line equivalent widths in ultraluminous galaxies are probably not due to extinction. Despite the inferred high column density of dust, the estimated extinction to the ionized gas in Arp 220 is $A_v \sim$ 25-50 (Fischer et al. 1997, Genzel et al. 1998). We address this further in the next section.

4. PARAMETERIZATION OF THE FAR-INFRARED SPECTRAL SEQUENCE OF IR-BRIGHT GALAXIES

The sequence shown in Figure 1 may be caused by variation of many parameters, but it is of interest to examine whether a single parameter or evolutionary effect can play the dominant role in the progression, and in particular to try to understand what conditions cause the ultraluminous galaxies to appear at the extreme end of the sequence.

High extinction ($A_v \sim 50$) has been invoked to explain the weakness of the near-infrared recombination lines in ULIGs (Genzel et al. 1998). However, significantly higher extinction ($A_v \geq 1000$) would be necessary to explain the weakness of the far-infrared fine-structure lines by extinction effects. To further investigate whether far-infrared extinction plays a dominant role in the spectral sequence, we examined the temperature-insensitive [O III]52/[O III]88 line ratio as a function of the [O III]88/F_{FIR} ratio for the galaxies in Figure 1 in which [O III] line emission was detected. No dependence was found for our small sample and all of the measured [O III] line ratios fall within the range 0.6 - 1.2, consistent with electron densities between 100 - 250 cm^{-3} (Fischer et al. 1999). These results suggest that neither density nor far-infrared extinction in the form of a single screen model appear to be single dominant parameters in the observed sequence.

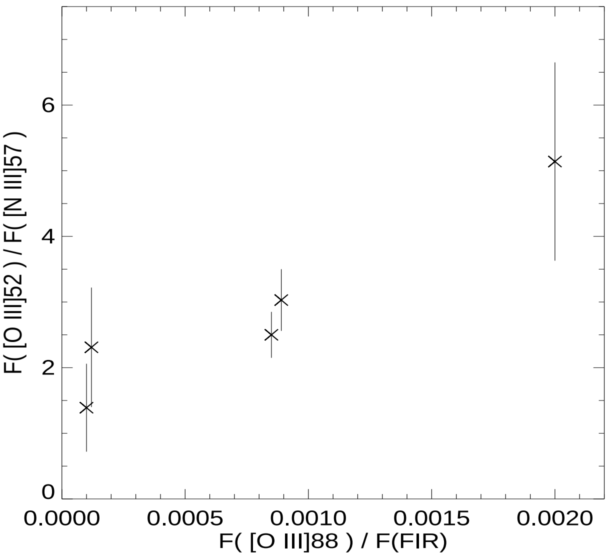

Figure 3. *The [O III]52 μm/[N III]57 μm line ratio versus the [O III]88 μm line to integrated far-infrared continuum flux ratio for the sample galaxies.*

In Figures 2 and 3 we plot the [N III]57/[N II]122 and [O III]52/[N III]57 line ratios as a function of the [O III]88/F_{FIR} ratio for galaxies from Figure 1 (where these lines were detected). The excitation potentials of [N II], [N III], and [O III] are 14.5, 29.6, and 35.1 eV, respectively. Thus for constant metallicity, both Figures 2 and 3 indicate that with progression to low relative emission line strength is a progression to lower excitation. The ionization parameter, defined as the ratio of ionizing photons to hydrogen atoms at the inner face of the cloud, plays a key role in determining ionization structure of clouds surrounding a source of ionizing radiation. It is equal to $Q(H)/4\pi r^2 n_H c$, where Q(H) is the Lyman continuum rate and n_H is the hydrogen density at the inner radius, r, of the cloud. Thus if density effects alone do not appear to explain the sequence, effects such as larger inner cloud radii, lower $Q(H)/L_{Bol}$ due to dust within the HII regions or softer radiation fields due to starburst evolution may be responsible for the apparent excitation progression seen in Figures 2 and 3. If the latter is the case, and if starbursts are the source of the excitation, then an aging starburst or one with an IMF with a low upper mass limit could be present in the ultraluminous galaxies and other low excitation galaxies. It is difficult to reconcile the aging starburst interpretation with the high luminosity of the ultraluminous galaxies, since older starbursts have lower luminosities than their younger counterparts. Soft radiation fields may explain the prominent molecular absorption due to the presence of ubiquitous molecular material in these galaxies. Although dusty H II regions or metallicity effects may play a role, our simple photoionization modelling suggests that these effects would not produce the observed progression of line ratios.

ACKNOWLEDGMENTS

This work was supported in part by the Office of Naval Research and the NASA ISO grant program. We appreciate the skill and dedication of the LWS instrument and data analysis teams at Vilspa, RAL, and IPAC.

REFERENCES

Clegg, P.E., Ade, P.A.R., et al. 1996, A&A, 315, L38

Colbert, J.W., Malkan, M.A., et al. 1999, ApJ, February 1 issue

Davies, R.I., Sugai, H., & Ward, M.J. 1998, MNRAS, 300, 388

Downes, D. & Solomon, P.M. 1998, ApJ, 507, 615

Fischer, J., Shier, L.M., et al. 1996, 315, L97

Fischer, J., Satyapal, S., et al. 1997, in "First ISO Workshop on Analytical Spectroscopy" SP-419, eds. Heras, A.M. et al. ESA Publications Division, Noordwijk, Netherlands, p. 149.

Fischer, J., Luhman, M.L., et al. 1998, in "Astrophysics with IR Surveys: A Prelude to SIRTF", ASP Conf. Ser., ed. Bicay, M., in press

Genzel, R., Lutz, D., et al. 1998, ApJ, 498, 579

Luhman, M., Satyapal, S., et al. 1998, ApJ,, 504, L11

Luhman, M. et al. 1999, in prep.

Malhotra, S., Helou, G. et al. 1998, ApJ., 491, L27

Satyapal, S., Luhman, M.L., et al. 1999, in prep.

Suter, J-P., Harvey, V., et al., 1998, BAAS, 30, 1383

Swinyard, B.M., Burgdorf, M.J., Clegg, P.E. et al. 1998, in "Infrared Astronomical Instrumentation", Proc. of SPIE, ed, Fowler, A.M., 3354, 888

Telesco, C., Becklin, E., et al. 1984, ApJ, 282, 427

Unger, S.J., Clegg, P.E., et al. 1999, in prep.

THE ISO SWS SURVEY FOR MOLECULAR HYDROGEN IN GALAXIES

E.A. Valentijn[1] **& P.P. van der Werf**[2]

[1]SRON and Kapteyn Institute, Groningen, The Netherlands
[2] Sterrewacht Leiden, The Netherlands

ABSTRACT

ISO SWS has made the first extragalactic direct detection of the H_2 molecule in pure rotational lines in the nucleus of NGC 6946. Here we focus on the interstellar medium in the *disks* of spiral galaxies. Our detection (Valentijn & van der Werf 1999, hereafter VW99) of the two lowest pure rotational lines of molecular hydrogen at 28.2 (S(0)) and 17.0 μm (S(1)) at 8 positions throughout the stellar disk of NGC 891 provides new insight in atomic to molecular hydrogen ratios and the physical state of the interstellar medium in the disks of late-type galaxies. H_2 has been detected out to 12 kpc from the center of NGC 891. The data indicate relatively warm ($T = 150 - 230$ K) molecular clouds scattered throughout the disk, in addition to a massive cooler ($T = 80 - 90$ K) component which dominates in the outer regions. For H_2 ortho-para ratios of 2–3 the cool component has typical edge-on surface densities of about $3000\,M_\odot/pc^2$, in which case it outweighs the atomic hydrogen by a factor 10. This factor raises the gas masses within the optical disks sufficiently to account for the observed rotation curves in these regions.

Key words: Molecular Hydrogen; ISM.

1. INTRODUCTION

Molecular gas masses in spiral galaxy disks are notoriously difficult to measure, and usually depend on indirect measurements based on other tracers such as the CO molecule or dust. Figure 1 schematically highlights some of the key issues in this field. The principal components of the interstellar medium (ISM) are HI, H_2, and dust. The HI content is well known and its distribution is more extended than that of the stars. Applying the Galactic "extinction to HI ratio" (A_V/N(HI)) to HI images of galaxies, a relatively high dust content in the outer regions is found, as is also concluded from optical extinction studies using inclination tests (e.g., Valentijn 1990).

This dust was not detected by IRAS, which was only sensitive to warmer, more centrally located dust. It is, however, now detected by ISOPHOT, as testified by several papers in these proceedings reporting $T = 10 - 20$ K dust, with masses 10–20 times higher than detected by IRAS. Most importantly, Alton et al. (1998a) find a $200\,\mu$m scalelength almost a factor two larger than the IRAS scalelength. This indicates a *cold* dust component more extended than the stellar component, which is also the case for the HI distribution. This is confirmed by recent SCUBA observations (Alton et al. 1998b). Thus both recent far-infrared and submillimetre photometry and optical extinction studies appear to indicate a dust component with a radial scalelength larger than that of the stars, such as is also the case with the HI. The question arises how this compares to the molecular gas component. ISO allows a direct measurement of molecular hydrogen through its purely rotational transitions, without having to resort to indirect tracers such as CO, which rely on a standard "CO to H_2 conversion ratio" (determined for an ensemble of *Galactic* giant molecular clouds) and hence are fraught with uncertainties. Characterizing the H_2 component independent of CO data was the principal goal of the ISO-SWS survey for molecular hydrogen in galaxies.

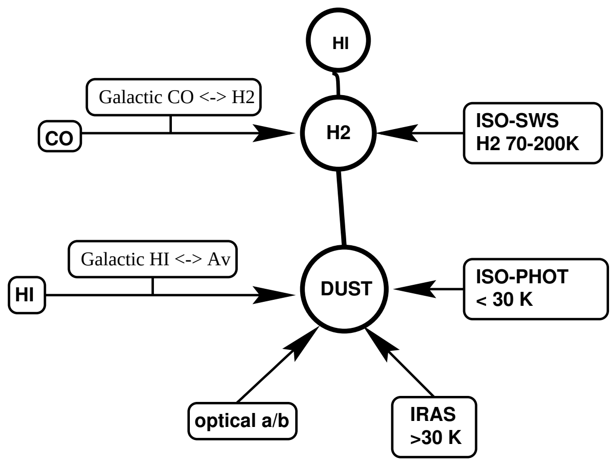

Figure 1. Components of the interstellar medium and their tracers.

Proceedings of the Conference "The Universe as seen by ISO", Paris, France, 20–23 October 1998 (ESA SP-427, March 1999)

2. OBSERVING H_2 IN GALAXIES WITH ISO-SWS

2.1. H_2 rotational lines

Since the H_2 molecule is homonuclear with no permanent dipole moment, transitions with $\Delta J = \pm 1$ are strictly forbidden, and the rotational ladder of H_2 consists of an ortho (J odd) and a para (J even) series of weak quadrupole transitions. ISO's SWS (de Graauw et al. 1996) provides a unique possibility to observe moderately warm H_2 directly in the lowest purely rotational transitions S(0): $J_\mathrm{u} - J_\mathrm{l} = 2 - 0$ at 28.2188 μm (para) and S(1) : $J_\mathrm{u} - J_\mathrm{l} = 3 - 1$ at 17.0348 μm (ortho). The ortho/para ratio (hereafter o/p) will be three if set by the ratio of statistical weights.

2.2. NGC 6946

The first extragalactic detection of these lines was obtained in the central, relatively warm and star forming region of the nearby face-on spiral galaxy NGC 6946 (Valentijn et al. 1996), and in fact this paper contains the first published spectrum of the lowest (S(0), 28 μm) transition of H_2 in any object outside the solar system; we refer to this paper for further details of our survey. Observed line ratios (S(0)/S(1)$\sim$ 0.15) indicate a temperature of this gas component of 170 K for an ortho/para ratio of 3, corresponding to the ratio of statistical weights. When combined with the observed line flux this leads to a mass of $5 \times 10^6\,\mathrm{M}_\odot$. A significant upper limit on the S(2) (12.3 μm- para) line flux was used to constrain the o/p ratio to ≥ 2, a value which is also commonly found for PDRs. The warm gas is confined to a $\sim$5$''$ (135 pc) diameter region where a moderate nuclear starburst accounts for the elevated temperature. Depending on the assumed CO/H_2 conversion factor, the warm component contains of the order of 5–10% (with formal lower and upper limits of 2 and 20%) of the total molecular mass in this region. CO data had indicated the presence of this warm gas, but did not provide a mass measurement. The ISO results can fully account for the warm component indicated by the CO data. The CO/H_2 conversion factor for the ^{12}CO $J = 1 \rightarrow 0$ line is not strongly affected by the presence of the warm component.

Since this paper was published, we have surveyed NGC 6946 at one more position, about 4 kpc East of the nucleus. We have detected both S(0) and S(1) with a significantly higher line ratio (S(0)/S(1)$\sim$ 1), and a flux of $\sim 5 \cdot 10^{-17}\,\mathrm{W\,m^{-2}}$ for both lines (see Fig. 2). Assuming local molecular gas densities based on other molecular tracers we derive a temperature around $130 - 170$ K, which is similar to the relative warm component detected in the disk of NGC 891 (see next Section).

2.3. H_2 in the disk of NGC 891

In the nearby edge-on galaxy NGC 891 we observed the S(0) and S(1) lines at the centre and at 7 positions

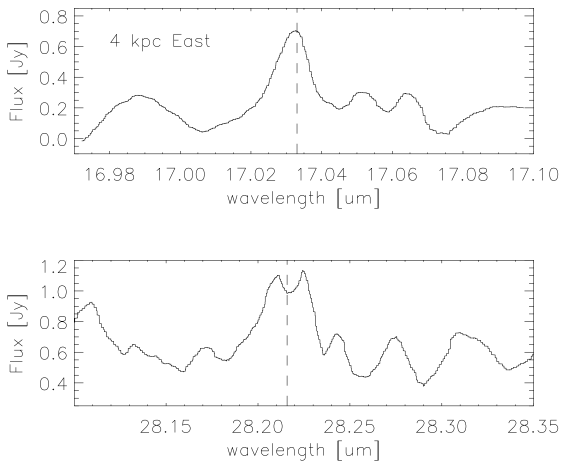

Figure 2. ISO-SWS detection of H_2 S(0) and S(1) in the disk of NGC 6946, 4 kpc East of the nucleus. The dashed lines indicate the expected wavelength of the line, given the radial velocities determined from CO data.

along the galaxy major axis, out to a radius of 11 kpc (assuming a distance to NGC 891 of 9.5 Mpc). We integrated for about 1500 sec on each line, except at the position at 11 kpc North where we integrated in total for $\sim$ 4 hours. We have detected both lines at each of the surveyed positions, even at the outermost position at 11 kpc, where CO is barely detected.

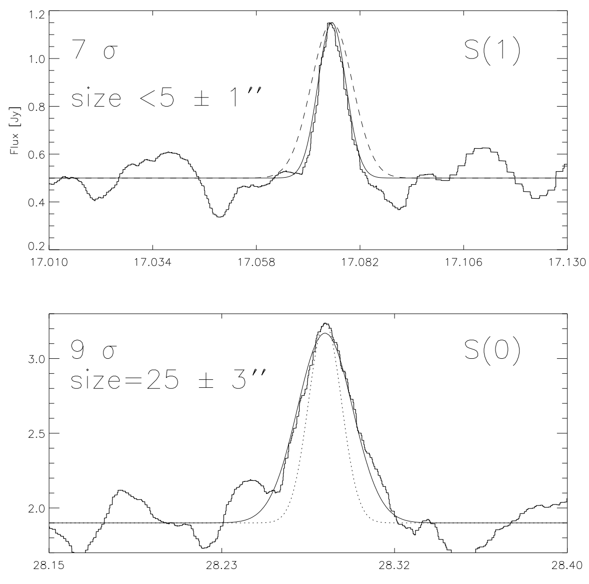

Figure 3. ISO-SWS line profiles of H_2 S(0) and S(1) in the disk of NGC 891, 8 kpc South of the nucleus, together with Gaussian fits to the profiles (solid lines). The dotted line represents the theoretical line profiles for a source extent $\leq 5''$ perpendicular to the slit, identical to the fit for S(1). The long dashed line represents the theoretical profile for a source extent filling the slit (identical to fit for S(0)).

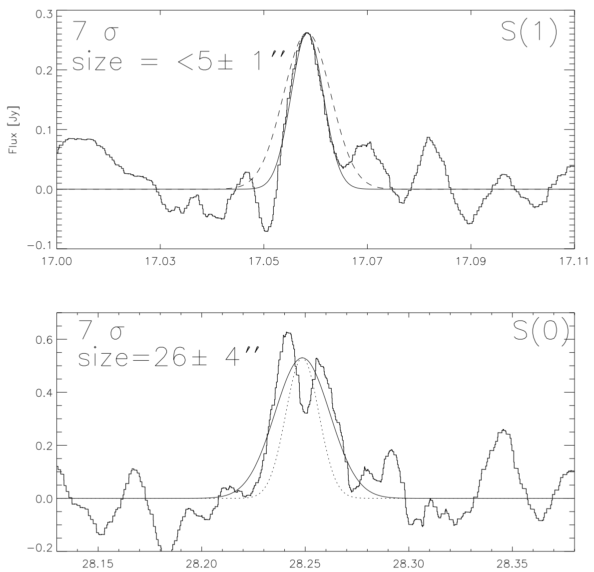

Figure 4. ISO-SWS line profiles of H_2 S(0) and S(1) in the disk of NGC 891, 11 kpc North of the nucleus. Line profiles are coded as in Fig. 3. Also here the S(1) profile matches to that of a point source, while the S(0) profile corresponds to that expected from a slit filling source.

In Figs. 3 and 4 we show our observations at some of the outer positions. In Fig. 5 (from VW99) the rotation curve in H_2 of NGC 891 is compared with CO data. The accuracy of the wavelength calibration corresponds to about $20\,\mathrm{kms}^{-1}$. Since the SWS slitwidth of 20″ at S(0) and 14″ at S(1) is a factor 2–3 larger than the diffraction beam, an offset of a point source of 4″ on the slit causes a wavelength shift corresponding to $41\,\mathrm{kms}^{-1}$ at S(1) and $53\,\mathrm{kms}^{-1}$ at S(0). When allowing for such small shifts the observed rotational velocities match well to the CO data.

In Fig. 5 we also compare the radial H_2 S(0) and S(1) profiles with the CO profile. Remarkably, the S(1) line follows more or less the CO profile, while the S(0) line shows an excess at larger radii, indicating a larger radial scale length, like the HI gas and the cool dust detected with SCUBA. At the outer positions, the S(1) lines originate from unresolved compact sources; this is not the case for the S(0) line: Figs. 3 and 4 indicate that the S(0) emission originates from extended (slit filling) regions. These line profiles imply that S(1) traces unresolved warm regions scattered throughout the disk, but more common in the inner regions, while S(0) traces a cooler and more pervasive component (see VW99 for details).

We have compared these results with models of the collisional excitation of H_2 as well as information from other tracers. We conclude that at $r < 6$ kpc the H_2 emission is dominated by relatively warm clouds ($T = 130 - 230$ K) with $n_{\mathrm{H}_2} \sim 200 - 2000\,\mathrm{cm}^{-3}$ and $N_{\mathrm{H}_2} \sim 10^{22}\,\mathrm{cm}^{-2}$, with a factor 3 times higher N_{H_2} in the nuclear region. Interpolating our measurements and integrating over the whole $r < 6$ kpc region, these values correspond to $\sim 2{\cdot}10^9\mathrm{M}_\odot$ of warm H_2, roughly half of the mass deduced from CO data (e.g., Sakomoto et al., 1997) in the same region. Given its temperature and density, this large amount of warm gas can be identified with UV-heated outer layers of molecular clouds throughout the inner disk of NGC 891, where CO may be photodissociated. This interpretation is in agreement with the detection of extended [CII] 158 μm emission in NGC 891 (Madden et al., 1994) originating in warm extended photodissociation regions (PDRs). These PDRs thus contain a significant fraction of the gas mass in the inner disk of NGC 891.

For the outer positions, the observations require a cooler ($80-90$ K) and pervasive (i.e., slit filling) component, which is also radially more extended than the warm component and the stellar distribution in NGC 891 (see VW99 for details). A total edge-on column density in the range $1 - 3 \times 10^{23}\,\mathrm{cm}^{-2}$ (i.e., $1600 - 5500\,\mathrm{M}_\odot/\mathrm{pc}^2$) is implied, with n_{H_2} around a few hundred cm^{-3} and temperatures in the range $80 - 90$ K. For these computations we used o/p=2, resulting in about a factor two lower mass than for o/p=3. Thus, our data indicates a massive H_2 component in the disk of NGC 891 and in the next Section we further discuss our observations of this cooler $80 - 90$ K component.

3. DISCUSSION

3.1. Robustness of results

A crucial step in our analysis is the conclusion that the S(0) and S(1) lines trace separate components of the ISM. If instead a 1-component solution was adopted (accounting for both the S(0) and S(1) emission), the derived temperature would be $100-130$ K, density $n_{\mathrm{H}_2} \sim 200\,\mathrm{cm}^{-3}$ and the implied masses significantly lower, although still substantial. In this case we would identify this gas with the photodissociated outer layers of molecular clouds also detected in [CII] 158 μm emission and indeed the derived masses agree well with those derived from the [CII] data of Madden et al. (1994). However, the disparity of the line profiles indicate that this model is too simple and suggest a 2-component solution with a warm component dominating S(1) and a cool component dominating S(0), with parameters and implications as discussed in the previous section. Given that this conclusion ultimately depends on the quality of the line profiles, we discuss below the robustness of these results.

The significance of the disparity in line profiles is well illustrated by Figs. 3 and 4. We have built special filter routines to remove the effect of the cosmic rays near the noise level (Valentijn & Thi 1999), which resulted in nearly gaussian noise, a factor of 3–4 lower than obtained with the standard pipeline routines. Our results have been checked for stability when applying different filter values. Furthermore, the result at the outer positions of NGC 891, of unresolved S(1) and slit-filling S(0), has consistently been obtained at all three positions. Finally, the SWS line profile has been extensively characterized in the laboratory and in orbit on both extended sources and point sources, and fully support the adopted theoretical profiles as used in Figs. 3 and 4. We thus conclude that these results are robust and are not affected by uncertain or poorly characterized instrumental effects.

3.2. Relation to other ISM components

Since the temperature of the gas detected here ($T \sim 80$ K) is close to the upper level temperature (91 K) of the [CII] 158 μm transition, this molecular gas should emit strongly in [CII] if most of the carbon was in the form of C^+. Remarkably, the observed [CII] emission (Madden et al. 1994) is a factor 5–10 too low. This discrepancy is in line with other reports of underluminous [CII] emission at this conference and in the recent literature. An interesting possibility is that a lower C^+ abundance, or alternatively optically thick [CII], might account for the existence of the $80-90$ K gas: the absence of effective [CII] cooling would lead to an elevated temperature. We also note that unlike the Milky Way, radio synchrotron radiation from the disk of NGC 891 is intense, and the resulting enhanced cosmic ray heating may also be responsible for the elevated temperatures derived here.

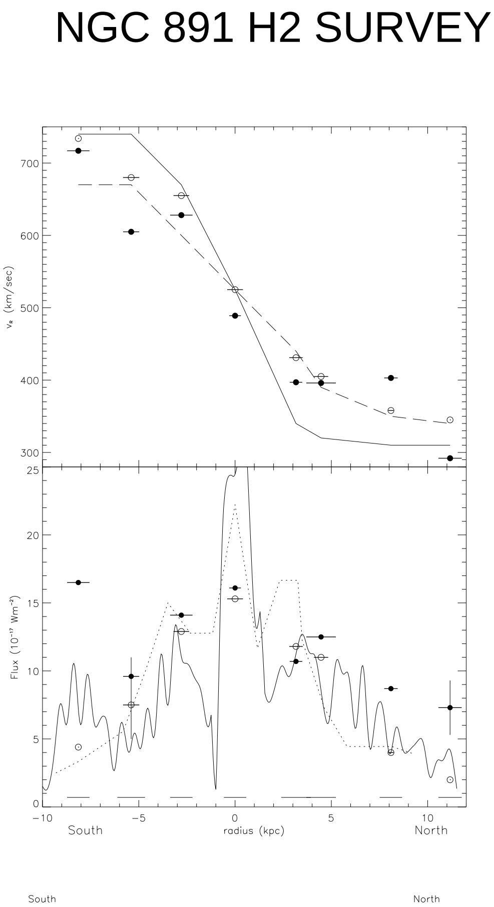

Figure 5. Observations of H_2 S(0) (filled circles) and S(1) (open circles) at various positions along the major axis of NGC 891. The size of the emitting regions, projected along the major axis, are indicated by horizontal bars through the data points. The horizontal bars at the bottom of the figure indicate the size of the SWS aperture (for S(0)) projected along the major axis. Top panel: heliocentric radial velocities, the lines indicate the approximate maximum and minium rotational velocities from ^{12}CO (Sakamoto et al. 1997). Bottum panel: total linestrength, with ^{12}CO intensity profiles (drawn line from Sakamoto et al. 1997, dashed line from Scoville et al. , 1993) arbitrary scaled to best fit the S(1) data in the disk (nuclear point excluded). The exceptionally large errors of two S(0) lines, observed late in the ISO mission with aged detectors, are indicated by a vertical bar.

Our data are confined to the stellar disk of NGC 891, and do not extend into the outer regions of the HI disk, where the mass discrepancy indicated by the rotation curve is most prominent. However, the cooler H_2 component detected here has a scale length which is more extended than the CO or the stellar component, like the HI and the cold dust component. Furthermore, within the outer stellar disk analysis of high-quality rotation curves indicates that a mass discrepancy also exists also in these regions, and Burkert & Silk (1997) propose that this matter could be in the form of unseen baryons, in agreement with our results.

We finally note that Alton et al. (1998b) deduce a total cold (15 K) dust mass at $r < 11$ kpc of 5×10^7 $M_\odot$, which is only a factor 10 less than the HI mass found from 21 cm line work (Swaters et al. 1998). However, when the H_2 mass derived here is taken into account, the total gas to dust ratio is $\sim$200, close to the Galactic value.

REFERENCES

Alton, P.B., Trewhella, M., Davies, J.I., Evans, R. et al. 1998a, A&A, 335, 807

Alton, P.B., Bianchi, S., Rand, R.J., Xilouris, E.M. et al. 1998b, ApJ, 507, L125

Burkert, A., & Silk, J. 1997, ApJ, 488, L55

Graauw, de Th. et al. 1996, A&A.315, L49

Madden, S.C., Geis, N., Genzel, R., Herrmann, F. et al. 1994, Infrared Phys. Technol., 35, 311

Sakamoto, S., Handa, T., Sofue, Y., Honma, M. & Sorai K. 1997, ApJ, 475, 134

Scoville, N.Z., Thakkar, D., Carlstrom, J.E. & Sargent, A.I. 1993, A&A, 404, L59

Swaters, R.A., Sancisi, R., & van der Hulst, J.M. 1998, ApJ, 491, L114

Valentijn, E.A. 1990, Nature, 346, 153

Valentijn, E.A., Van der Werf, P.P., Graauw, Th., & de Jong, T. 1996, A&A 315, L145

Valentijn, E.A. & Thi, W.F. 1999, Experimental Astronomy. in press

Valentijn, E.A. & Van der Werf, P.P. 1999, submitted

ISO OBSERVATIONS OF ACTIVE GALAXIES

A.F.M. Moorwood

European Southern Observatory, Karl-Schwarzschildstr. 2, D-85748 Garching bei München, Germany

ABSTRACT

ISO observed essentially all classes of active galactic nuclei (AGN), providing more sensitive, extensive and detailed photometry than IRAS plus images and the first high quality spectra over the complete 2.5-200 μm range. In this brief review I will focus on a few selected scientific topics where early results indicate that ISO has or is likely to make a significant impact. These include i) the nature of the far infrared emission of quasars, radio galaxies and Seyfert galaxies, ii) origin of the hot dust continuum and PAH emission features in Seyfert galaxies, iii) use of fine structure lines to determine the shape of the photoionizing continuum and to investigate the origin of the line asymmetries in Seyferts, iv) the pumping mechanism in OH megamasers, and v) the use of infrared diagnostics to distinguish between starburst and AGN activity in Ultraluminous Infrared and other highly obscured galaxies.

Key words: active galaxies

1. INTRODUCTION

Active galactic nuclei (AGN) range from objects as seemingly diverse as highly luminous and variable quasars, exhibiting broad emission lines and roughly power law non-thermal continua over the complete X-ray to radio range, to type Seyfert 2 galaxies whose emission line ratios sometimes provide the only evidence that their nuclei cannot be powered solely by stars. Their commonality is provided by the 'standard model' which proposes that all such objects are powered by a black-hole plus accretion disc 'engine' which generates both high energy photons and particles. In order to account for the wide range of observed properties the standard model requires a large anisotropy of the central radiation, created by adding a thick obscuring torus, and of intrinsic beaming of the particle jets so that the observed properties become strongly dependent on viewing angle. Additional differences are related to nature of the surrounding media with which the radiation and particles interact and hence the nature of the host galaxies.

Much of current AGN research is still centered on testing the standard model and, in particular, various specific unification schemes, e.g, between quasars and radio galaxies and between the different Seyfert types. AGN research is probably the most multi-wavelength discipline in astronomy and ISO can potentially complement X-ray, optical and radio studies in a number of areas. For example, if dust tori exist, they are expected to be heated by UV radiation producing infrared emission which should be anisotropic in the mid-infrared (hottest dust emission obscured when viewed edge-on) but become increasingly isotropic to longer wavelengths whereas at essentially all other wavelengths the radiation is highly anisotropic. As discussed in more detail below, therefore, continuum spectral energy distributions observed with ISO are relevant for testing both for the presence of tori and orientation dependent unification schemes.

With its extensive spectroscopic capabilities, ISO has also observed a wide range of fine structure emission lines in Seyfert galaxies. These lines are produced by ions with ionization potentials from a few to a few hundred eV and hence provide information on the shape of the EUV photoionizing continuum - of interest for testing accretion disc models and differences between the Seyfert types.

Other hot topics in AGN research include the formation and evolution of AGNs which, again, ISO is well equipped to address. In particular, the possible evolutionary association between AGN and starburst activity and, specifically, whether or not the Ultraluminous Infrared Galaxies detected by IRAS contain AGNs as expected if they are the pre-cursors of quasars which only become directly visible once the obscuring dust in these objects has been expelled by radiation pressure (Sanders at al. 1988).

ISO observed all known types of AGN yielding images, continuum spectral energy distributions, low and medium resolution spectra and some polarimetry. Some programmes (particularly within the Central Programme) targeted carefully selected and statistically significant samples of objects of a given type. Others were directed to more detailed studies of individually selected objects using several and sometimes all of the ISO instruments. As the data is still proprietary and its analysis and interpretation at a relatively early stage, a comprehensive review is impossible at this time and the full impact of ISO is yet to be seen. Based on published results; material kindly provided by various people and what has been presented at this conference, however, I hope

Proceedings of the Conference "The Universe as seen by ISO", Paris, France, 20–23 October 1998 (ESA SP-427, March 1999)

to show in the following sections that ISO data has the quality required to address some of the these key issues in the field of AGN research. In line with the brief background sketched in this Introduction I have featured selected results on quasars, radio galaxies and Seyfert galaxies which appear relevant to testing the Standard Model and Unification Schemes. I have also included work on OH megamasers which I think represents a beautiful example of a long standing prediction cleanly confirmed by ISO. I have also drawn attention to the new ISO spectral diagnostics for distinguishing starburst and AGN activity e.g in Infrared Ultraluminous Galaxies without, I hope, infringing too much on Dimitra Rigopoulou's specific review of these objects.

2. QUASARS AND RADIO GALAXIES

2.1. Infrared SEDs and Unification

At the extreme end of the AGN range, ISOPHOT observations have been made of around 70 quasars and radio galaxies within the European Central Quasar Programme (P.I Rolf Chini) plus another 70 quasars extending to higher redshifts in the US Central Programme (P.I Belinda Wilkes) and a selection of matched quasar/radio galaxy pairs (P.I Peter Barthel) as well as a number of BL Lacs and other related objects in several smaller central and open time programmes. In addition to clarifying the, still uncertain, nature of the far infrared emission in these objects and its relation to other properties, one of the aims is to test the proposed unification of flat/steep-spectrum quasars and possibly radio galaxies and radio loud quasars. As mentioned in the Introduction, such schemes attribute differences in their non-thermal radio properties to beaming which produces a strong viewing angle dependence of their observed spectra, fluxes, polarization and variability (roughly, quasars are viewed along and radio galaxies perpendicular to the particle jets). In contrast, dust emission from an optically thin torus should be more or completely isotropic and universally present in the extreme case of complete unification to a single parent population.

Results for a sub-sample of 10 objects from the European Central Quasar programme have recently been presented by Haas et al. (1998). They find that the radio-quiet and steep-spectrum quasars show a bump around 60 μm and a decline longward of 100 μm which is steeper than expected for self absorbed synchrotron radiation and is attributed to emission from dust at a wide range of temperatures from $\simeq$30K to 600K. The hottest component, which is absent in starburst galaxies and most ULIRGs, is identified with dust heated by the AGN. Of significance for unification schemes is the fact that the radio galaxy CygA shows a similar spectrum to the steep spectrum radio quasar 3C48 and the radio-quiet quasars - consistent with thermal emission associated with a hidden quasar. In contrast the energy distributions of the flat spectrum radio quasars exhibit a smooth continuation from the radio to the infrared suggestive of synchrotron emission alone. Of particular interest, however, is the flat spectrum radio source 3C 279 which was observed at different times during the mission. Although Klaas et al. (1998) measured variable polarization up to $\simeq$ 20% around 170 μm - consistent with non-thermal synchrotron emission, Haas et al. (1998) found a thermal bump emerging when the variable non-thermal emission was in a low state. This thus provides an indication that thermal components may be more generally present but swamped by the more dominant synchrotron emission. Steep spectra more consistent with thermal rather than non-thermal emission have also been seen in some of the quasars observed in the US programme (Wilkes et al. and Hooper et al. these proceedings) and in samples studied by Andreani et al. (1998) who also draw the significant conclusion in relation to galaxy formation that the inferred dust abundance is essentially constant from z = 1 to 5.

Observations of matched (radio power, distance etc.) pairs of quasars and radio galaxies made specifically to test the unification scheme reveal that quasars are actually more luminous than radio galaxies in the far-infrared - contrary to the predictions of the simple unification schemes described above (van Bemmel & Barthel 1998). After subtracting the estimated non-thermal emission the quasars are still more luminous implying that they do not belong to the same parent population as the radio galaxies or that the source of dust emission (torus?) is optically thick even in the far-infrared.

In summary, therefore, these different programmes provide evidence for thermal dust contributions to the far infrared emission of both quasars and radio galaxies but also that it is probably not isotropic due to additional infrared synchrotron emission and/or the possibility that the dust emitting region/torus is optically thick.

2.2. Centaurus A

The nearby radio galaxy Cen A deserves special mention as it has been studied with all 4 ISO instruments. In particular, spectacular images made with CAM by Mirabel et al. (1998) show not the large elliptical galaxy crossed by a prominent dust lane familiar from optical pictures but a small, barred, spiral centred at the origin of and perpendicular to the radio jets feeding the two large radio lobes. The authors argue that this spiral has formed within the elliptical from material accreted during one or more interactions in the past and that it is responsible for feeding the central engine and hence generating the radio jets. The SWS spectrum shows high excitation lines typical of an AGN (Genzel et al. 1998). SWS and PHT-S spectra, however, also show PAH and silicate features and, together with other data, have been modelled by Alexander et al. (1998) who claim that the overall continuum contains contributions from an $\simeq$ 3.6 pc diameter AGN torus plus a nuclear starburst and cooler, more extended, cirrus components which are presumably associated with the spiral 'galaxy'. An obvious question is whether or not Cen A is a special case or whether similar spiral structures are responsible for fuelling the black hole in other radio galaxies and also contributing to their far-infrared emission.

3. INFRARED SEDs OF SEYFERT GALAXIES

The energy distributions of a large fraction of the 48 CfA Seyferts have also been measured out to 200 μm using ISOPHOT. In contrast to the quasars, any non-thermal components here appear to be weak or absent and the overall thermal energy distributions are generally well fitted with two thermal emission components corresponding to dust temperatures around 170 and 30 K. The hotter component is again attributed to AGN heated dust and the cooler, which has also been measured to be more spatially extended, to dust heated by stars in the disk (Rodríguez Espinosa & Pérez García, 1998; Pérez García et al. 1997; Pérez-García & Rodríguez Espinosa, 1998).

4. HOT DUST AND PAH EMISSION FEATURES IN SEYFERTS

Although spectra of Seyferts have previously been obtained from the ground in a limited region around 10 μm the SWS, PHT-S and CAM-CVF spectrometers on ISO brought large gains in both sensitivity and wavelength coverage which allowed the first observations of the strongest of the 'PAH' features at 7.7 μm and proved to be important for determining the overall continuum shape necessary to establish the presence or not of 9.7 μm silicate absorption. These points are well illustrated by the complete SWS + LWS spectrum of the Circinus galaxy (nearby Seyfert 2 at 4Mpc) shown in Fig. 1. which exhibits strong mid-infrared continuum from hot dust, 9.7 μm silicate absorption and the PAH emission features at 3.3, 6.3, 7.7, 8.6, 11.3 and 12.6 μm (Moorwood et al. 1996).

Follow-up spectral imaging observations of this galaxy from 5 to 16 μm have also been obtained at lower spectral resolution using CAMCVF in order to establish the previously unknown spatial distribution of the PAH emission (Moorwood et al. 1998). Around 6.3 μm (where the spatial resolution is highest) our images show that the continuum arises in an unresolved source whereas emission in the 6.3 μm feature extends over about 30$''$ (600 pc). For the continuum, higher spatial resolution has in fact been achieved in ground-based observations which indicate that the emitting region is only a few pc in size (Siebenmorgen et al. 1997). This, together with its spectral distribution and silicate absorption is qualitatively consistent with emission from a torus although detailed radiation transfer modelling shows that an isotropic dust distribution cannot be excluded (Siebenmorgen et al. 1997). The observed PAH feature distribution is a new result which clearly excludes the AGN itself as the excitation source. As shown by the overlay on Hα in Fig. 2, however, there is also no spatial correlation between the PAH feature emission and the starburst 'ring' containing the most recently formed hot stars (the Brγ distribution is similar to Hα). Its distribution is, in fact, more similar to that of the near IR stellar continuum and [FeII] and H_2 line emission suggesting that it is excited by the somewhat older starburst activity (B and A stars) for which there is other evidence in this galaxy.

In a large statistical study, low resolution PHT-S spectra of 26 Seyfert 1's and 28 Seyfert 2's obtained by Clavel et al. (1998) show marked differences between the two types. Seyfert 2's generally exhibit a weak and ill-defined continuum but prominent PAH feature emission whereas Seyfert 1's are characterized by a strong continuum and no or less pronounced PAH emission features. On average, the Seyfert 1's are about a factor of 7 more luminous in the continuum around 7.7 μm whereas their 7.7 μm PAH feature equivalent widths are a similar factor smaller and the distribution of PAH feature luminosities is essentially identical for the two types. The apparent weakness of the PAH features in Seyfert 1's is thus simply due to dilution by the stronger continuum. These results are qualitatively consistent with models of the expected infrared emission from a torus which predict that they should be brighter when viewed face rather than edge-on due to radiation transfer effects (c.f. Pier & Krolik 1992). The authors note that, assuming zero face-on extinction, the luminosity ratio observed between Seyfert 1's and 2's would imply an average extinction for the type 2's of 2.1 magnitudes at 7.7 μm, i.e $A_v \simeq 100$ magnitudes or an X-ray absorbing column of $N_H \simeq 2.3 \times 10^{23}\, cm^{-2}$ which is not untypical of the values deduced from X-ray observations of some Seyfert 2's but much lower than required to suppress the hard X-rays in many others. The infrared values may be underestimates, however, in cases where the hot dust emission is completely suppressed by absorption within the torus. Another prediction of torus models is that the 9.7 μm silicate feature can appear in emission when viewing face-on whereas it should be in absorption when observing edge-on. As already shown, silicate absorption is observed in the Seyfert 2 Circinus galaxy which is extremely bright because of it closeness. The Seyfert 2 continua are too weak in the Clavel et al sample to detect silicate absorption but a weak and rather narrow emission feature at 9.7 μm is claimed in their average Seyfert 1 spectrum. No evidence of silicate emission, however, has been found in the few Seyfert 1's observed with PHT-S within the MPE Central Galaxy programme (P.I Reinhard Genzel). Amongst those galaxies in which 7.7 μm PAH features have been detected the Seyfert 1's are also an order of magnitude more luminous than the Seyfert 2's. Debates on the interpretation of these data within the framework of tori and unification models is therefore set to continue!

5. IONIZING CONTINUUM SHAPE IN SEYFERTS

The first complete high sensitivity access to spectroscopy over the 2-200 μm range achieved with the SWS and LWS spectrometers on ISO resulted in the detection of a large suite of fine structure, hydrogen recombination and molecular hydrogen emission lines in Seyfert galaxies. Complete spectra obtained of a few bright galaxies such as NGC1068 and that of the Circinus galaxy shown in Fig. 1 contain about 30 fine structure lines emitted by species with ionization energies in the range 8 - 300eV (c.f. Moorwood 1997) which provide important diagnostic information for a range of physical regimes, e.g., photodissociation regions ([OI], [CII]); starbursts ([FeII], [SiII], [OIII], [NeII], [NeIII], [SIII],

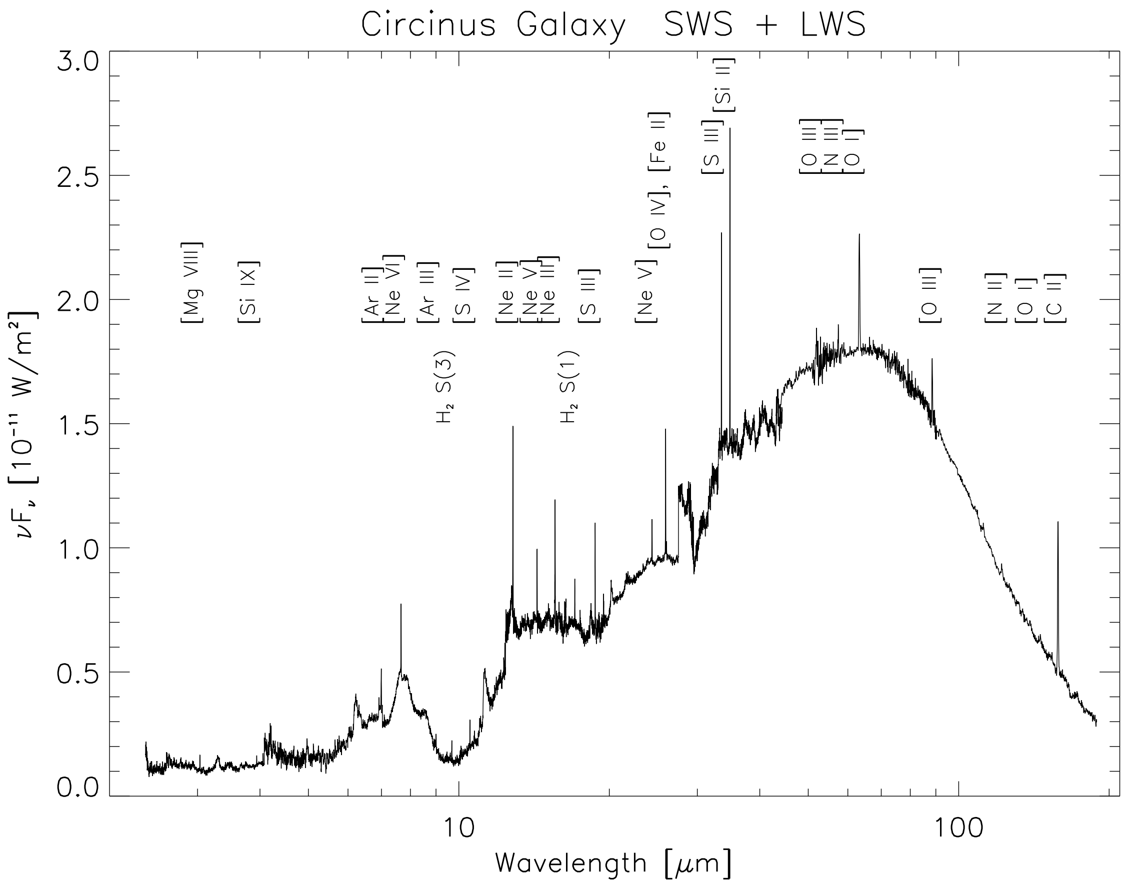

Figure 1. Combined SWS+LWS spectrum of the Circinus galaxy showing the overall continuum arising from dust at a wide range of temperatures; solid state and PAH features; molecular hydrogen, hydrogen recombination and ionic fine structure lines from species with IP of around 8 - 300eV.

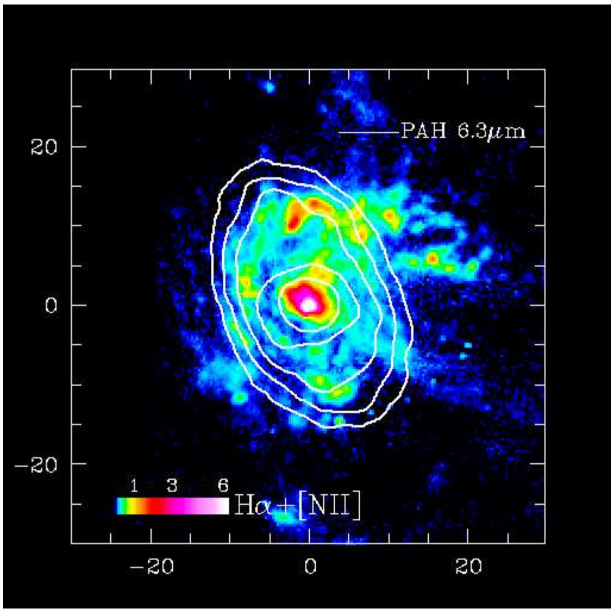

Figure 2. PAH 6.3 μm emission feature contours overlaid on an Hα image showing the starburst 'ring' in the Circinus galaxy.

[SIV]); NLR ([OIII], [OIV], [NeV]) and the 'coronal' line region ([NeV], [NeVI],[MgV], [MgVII], [MgVIII], [SiVII], [SiIX], [CaVIII]). The series of lines emitted by ions of the same element e.g O, Ne, S and Mg offer abundance independent probes of the obscured ionizing continua in AGN while [OIII], [SIII] and [NeV] provide important density sensitive line pairs. Although complete spectra have only been obtained for a few galaxies, selected sets of lines have been measured additionally on several tens of Seyferts.

The first detailed modelling made was of the Seyfert type 2 Circinus galaxy (Moorwood et al. 1996). Fig. 3 shows the derived EUV continuum together with that observed by IRAS in the infrared. Assuming ionization bounded clouds, the main conclusions were that the EUV (few hundred eV) ionizing continuum is extremely hard ($\simeq \nu^{-0.5}$) and that a significant (order of magnitude) 'bump' or break is required around 70 eV. This shape is in fact similar to that expected both from accretion disc models (Laor 1990) and interpolations of UV/X-ray observations of Seyfert 1's and quasars (Walter et al. 1994). The predicted X-ray emission is also consistent with that subsequently measured with the ASCA satellite (Matt et al. 1997). More recent and independent modelling based on similar assumptions gives essentially the same result for the Circinus galaxy but, surprisingly, requires a photon deficit rather than a bump around 70 eV in the case of the prototypical Seyfert 1 NGC 4151 (Alexander et al 1998; Sturm et al. 1998). The overall conclusion, however, is that a bump in the intrinsic spectrum is also probably present in this case but suffers absorption by neutral hydrogen between the BLR and NLR for which there is additional evidence from UV absorption lines. Without this intrinsic bump it is also difficult to account for the line flux from the BLR. The EUV continuum in NGC4151 is also found to be softer than in the lower luminosity Circinus galaxy. Based simply on line ratios relative to Circinus rather than detailed modelling of other, more luminous Seyferts, this appears to be a general trend which is also qualitatively consistent with the accretion disc models whose continua also tend to soften with increasing luminosity.

With regard to the reality of the bump or break in the UV continuum, however, an uncertainty has been introduced by Binette et al. (1997) who have shown that the same ISO spectrum of the Circinus galaxy can be reproduced with a simpler power law photoionizing spectrum if the emitting clouds are assumed to be density rather than ionization bounded. Although this possibility cannot be excluded, more recent attempts to model the optical emission from extranuclear clouds in Circinus suggests that including density bounded clouds reduces but does not eliminate the need for the UV bump (Oliva et al. 1998).

5.1. Shock excitation in Seyferts?

It has been suggested by various authors that photoionization associated with high velocity shocks driven by mass outflow could provide an alternative source of some or all of the emission from the so-called narrow line region in Seyfert galaxies. Detailed models show that shocks with velocities of a few $\times 10^2\, kms^{-1}$ could indeed generate an AGN like ionizing continuum and moderately high excitation lines by photoionization of the pre-cursor gas (Dopita & Sutherland, 1996). The models so far are not able to produce the highest excitation 'coronal' lines, arising from species with ionization potentials above 100eV, which include [FeVII, X, XI and XIV] in the visible and [NeVI], [SiVI,VII,IX], [MgVII,VIII] in the ISO range (Moorwood et al. 1997). Recent ISO spectra of galactic supernova remnants also cast some doubt on the importance of this mechanism for producing lower excitation lines in Seyferts. A complete SWS+LWS spectrum of the SNR RCW103 for example is found to be dominated by low excitation lines and shows particularly strong [FeII] emission, attributed to grain destruction by the shock which increases enormously the gas phase Fe abundance (Oliva et al. 1998). It is quite different to that observed in Seyferts and its detailed analysis provides no evidence for line emission from a photoionized precursor. Comparison with the spectra of other SNRs observed with ISO is still required, however, in case RCW103 is exceptional due to the fact that it is interacting heavily with a dense molecular cloud.

6. LINE ASYMMETRIES IN SEYFERTS

It has been known for more than 20 years that the optical lines in Seyfert spectra are often shifted and/or show asymmetries towards the blue but rarely the red. This has generally been attributed to the combination of outflowing emitting clouds combined with moderate optical extinction whose effect is largest on the emission from the the receding clouds. A slightly more complex variant assumes dusty infalling clouds. If either of these models were correct, however, it is clear that such shifts and asymmetries should completely disappear in the mid-infrared where any extinction corresponding to the moderate amount required in the visible would be vanishingly small. It has therefore come as a surprise that the fine structure lines observed with ISO in the prototype Seyfert 1 galaxy, NGC4151, do show blue asymmetries which are essentially identical to those seen in the visible. Rather than moderate, extended, extinction therefore it has been proposed by Sturm et al. (1998) that the extinction to the receding clouds could be produced by a geometrically thin but optically thick obscuring screen of sub-arcsec extension (sufficient to block about 20% of the redshifted light at optical and infrared wavelengths) containing $\geq 5 \times 10^6\, M_\odot$ of hydrogen which may be molecular.

7. OH MEGAMASERS IN ULTRALUMINOUS INFRARED GALAXIES

A number of Ultraluminous Infrared galaxies are also sources of intense OH maser emission at radio wavelengths and it has been long suspected that the required population inversion results from excitation of the OH radicals by absorption of infrared photons in transitions at 35 and 53 μm followed by a radiative cascade. ISO has provided clear confirmation of this through its detection, with SWS, of the expected 35 μm absorption feature in the prototypical galaxy of this type, Arp220 (Skinner et al. 1997). The number of photons absorbed is consistent with the maser power and the velocity width matches that of the radio emission lines as expected. More detailed modelling also requires that the infrared photons be emitted from a warm, extended region i.e suggesting that the infrared luminosity is dominated by a massive starburst rather than an obscured AGN.

OH maser emission is also observed from stars and it is interesting to note here that SWS+LWS spectra of the F-type hypergiant IRC+10420 show both absorption in the 35 μm doublet plus emission in the rotational cascade lines at 79, 98.7 and 163 μm predicted by the detailed infrared pumping model (Sylvester et al. 1997).

8. ISO SEARCHES FOR AGNs IN ULIRGs

ISO has provided clear spectroscopic diagnostics for distinguishing between starburst and AGN activity. Analogously to the long used visible line ratio diagrams, high excitation lines such as [OIV](26 μm) and [NeV](14 and 24 μm) require the hard spectrum of an AGN while photoionization by hot stars in starbursts is sufficient to produce extremely bright lower excitation lines such as [NeII](12.8 μm). The potential advantage of the infrared lines is their much lower sensitivity to extinction when probing for AGNs in dust enshrouded galactic nuclei. Uniquely infrared is

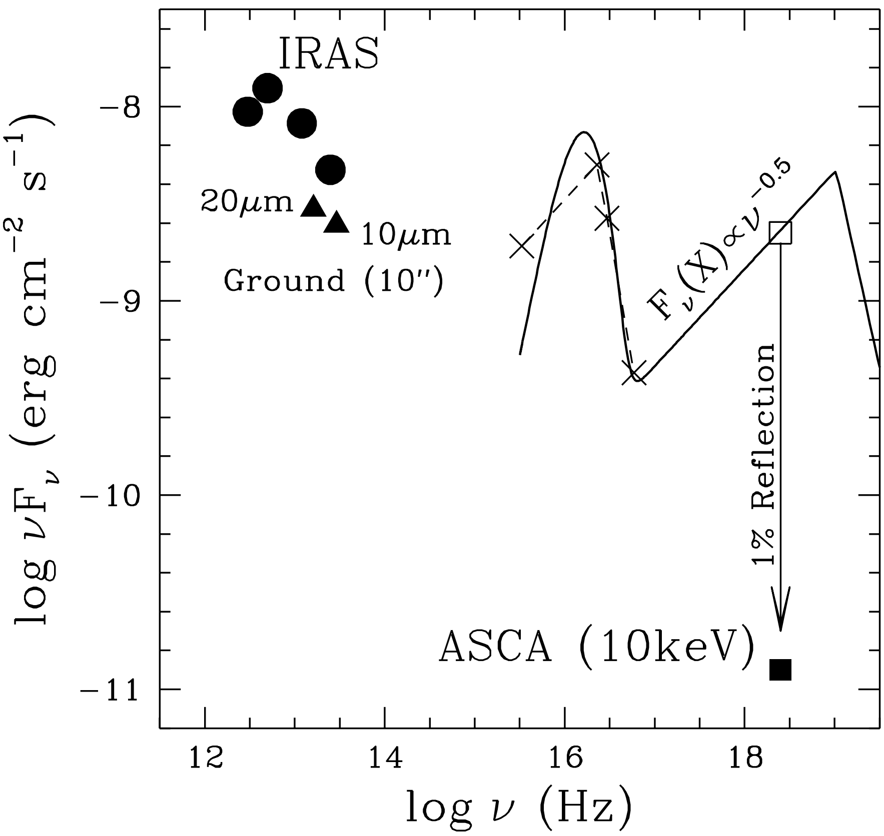

Figure 3. X-ray to far-infrared SED of the Circinus galaxy including the intrinsic UV-X-ray continuum derived from modelling of the infrared fine structure lines (Moorwood et al. 1996).

the additional possibility of using the PAH 7.7 μm/ continuum ratio which is large in starburst galaxies but small in AGNs (except Seyfert 2s) due to dilution by the hot dust continuum.

Genzel et al. (1998) have shown that known starburst galaxies and AGNs are well separated in a combined [OIV]/[NeII] versus PAH 7.7/continuum plot. A sample of 15 ULIRGs plotted on the same diagram appear to be intermediate between the AGNs and starbursts but with most in the region where a starburst is expected to dominate the luminosity. Whereas the PAH feature is clear in most, only one or two clearly show high excitation emission lines. Within a smaller sample observed with the CAM-CVF, Laurent et al. (these proceedings) also confirm the separation of starburst and AGN activity based on the PAH feature to continuum ratios and conclude that 3 out of their 4 ULIRGs (including Arp220 and NGC6240) are starburst powered.

In order to extend the study of ULIRGs to fainter (but more luminous) examples, a much larger sample of $\simeq$ 70 objects has been observed with PHTS (Lutz et al. 1998, Rigopoulou et al. 1998). A PAH 7.7 μm/ continuum versus 6 μm/60 μm continuum ratio diagram, which is sensitive to a hot dust continuum, supports the earlier results that the lower luminosity ULIRGs are predominantly starburst powered but also suggests that the fraction of AGNs increases with luminosity and that about half the ULIRGs with luminosities above 2×10^{12} L$_\odot$ may be AGN powered.

ACKNOWLEDGMENTS

I am indebted above all to my various collaborators, particularly Reinhard Genzel and Dieter Lutz at the MPE, Tino Oliva in Florence and Ralf Siebenmorgen at VILSPA. I am also extremely grateful to R. Chini, D. Lemke, M. Haas, J. Clavel, J. Rodríguez Espinosa, U. Klaas, E. Sturm and P. Barthel for sending me results prior to publication.

REFERENCES

Alexander, T., Sturm, E., Lutz, D., Sternberg, A., Netzer, H., Genzel, R. 1998, ApJ (in press) and these proceedings

Binette, L., Wilson, A.S., Raga, A., Storchi-Bergmann, T. 1997, A&A, 327, 909

Clavel, J., Schultz, B., Altieri, B., Barr, P., Claes, P., Heras, A., Leech, K., Metcalfe, L., Salama, A. 1998 to appear in Structure and Kinematics of

Quasar Broad Line Regions (C.M. Gaskell, W.N. Brandt, M. Dietrich, D. Dultzin-Hacyan, eds.), PASP Conference Series

Dopita, M.A., Sutherland, R.S. 1996, ApJS 102, 161

Genzel, R., Lutz, D., Sturm, E., Egami, E., Kunze, D., Moorwood, A.F.M., Rigopoulou, D., Spoon, H.W.W., Sternberg, A., Tacconi-Garman, L.E., Tacconi, L., Thatte, N. 1998, ApJ, 498, 579

Haas, M., Chini, R., Meisenheimer, K., Stickl, M., Lemke, D., Klass, U., Kreysa, E. 1998, ApJ, 503, L109 and these proceedgins

Klaas, U.,Laureijs, R., Clavel, J. 1998, ApJ (in press)

Laor, A. 1990, MNRAS, 246, 369

Lutz, D., Spoon, H.W.W., Rigopoulou, D., Moorwood, A.F.M., Genzel, R. 1998, ApJ, 505, L103

Matt, G. et al. 1996, MNRAS,281, L69

Mirabel, I.F., et al. 1998, A&A, 333, L1

Moorwood, A.F.M., Lutz, D., Oliva, E., Marconi, A., Netzer, H., Genzel, R., Sturm, E., de Graauw, Th. 1996, A&A, 315, L109

Moorwood, A.F.M. 1997, Extragalactic Astronomy in the Infrared, XVIIth Rencontres de Moriond (G.A. Mamon, Trinh Xuân Thuân, J. Trân Thanh Vân eds.), Editions Frontiéres Paris, 301

Moorwood, A.F.M., Marconi, A., van der Werf, P.P., Oliva, E. 1997, Ap&SS. 248, 113

Moorwood, A.F.M. et al. 1998 (in preparation)

Oliva, E., Drapatz, S., Lutz, D., Sturm, E., Moorwood, A.F.M. 1998, Ap&SS, 255, 211 and A&A submitted

Oliva, E., Marconi, A., Moorwood, A.F.M. 1998, A&A in press

Pérez García, A.M., Rodríguez Espinosa, J.M., Santolaya Rey, A.E. 1998, ApJ,500,685

Pérez García, A.M., Rodríguez Espinosa, J.M. 1998, ApJ submitted

Pier, E.A., Krolik, J.H. 1992, ApJ, 401, 99

Rodríguez Espinosa, J.M., Pérez García, A.M., Lemke, D., Meisenheimer, K. 1996, A&A, 315, L129

Rodríguez Espinosa, J.M., Pérez García, A.M. 1998, ApJL, 487, L33

Sanders, D.B. et al. 1988, ApJ, 325, 74

Siebenmorgen, R., Moorwood, A.F.M., Freudling, W., Käufl, H.-U. 1997, A&A, 325, 450

Skinner, C. et al. 1997, Nature, 386, 472

Sturm, E., Alexander, T., Lutz, D., Sternberg, A., Netzer, H., Genzel, R. 1998, ApJ in press

Sylvester, R. et al. 1997, MNRAS 291, L42

Walter, R., Orr, A., Courvoisier, T.J.-.L., Fink, H.H., Makino, F., Otani, C., Wamsteker, W. 1994, A&A., 285, 119

ULTRALUMINOUS IRAS GALAXIES AS SEEN WITH ISO

D. Rigopoulou[1], R. Genzel[1], D. Lutz[1], D. Kunze[1], A.F.M. Moorwood[2], H.W.W. Spoon[1], E. Sturm[1], M. Thornley[1], & D. Tran[1]

[1]MPE, Postfach 1603, 85740 Garching, Germany
[2]ESO, Karl-Schwarzschildstr. 2, 85748 Garching, Germany

ABSTRACT

We review the results of a major spectroscopic survey of nearby Starbursts and moderate redshift Ultraluminous IRAS Galaxies (ULIRGs) using ISO-SWS, ISOPHOT-S and ISOCAM (CVF) on board ISO. Detailed modeling reveals that massive stars, $M_{upper} \geq$ 100 $M_\odot$ are formed in most Starbursts in relatively short bursts (one or a few O star lifetimes). In the area of ULIRGs we address the main question of the dominant energy source as well as their evolution. We have found that the combination of mid-infrared fine structure line ratio with the strength of the PAH feature provides an excellent tool for discriminating between starburst and AGN activity. Our studies indicate that, on average, ULIRGs are mainly powered by Starbursts. The strength of the PAH feature is also used to probe for evolutionary effects. We find no evidence that ULIRGs found in advanced stages of merging are more AGN-like, as postulated by the classical evolutionary scenario. We suggest that local conditions (related to the energetics of the AGN) determine the dominance of the starburst or AGN.

Key words: Starbursts; Ultraluminous Galaxies; mergers.

1. INTRODUCTION

The nature and evolution of Ultraluminous Infrared Galaxies has remained unclear since their discovery by IRAS more than a decade ago. With luminosities in excess of 10^{12} $L_\odot$ ULIRGs are the dominant population of extragalactic objects in the local Universe, outnumbering optically selected Seyferts and QSOs (Soifer et al. 1986). The disturbed optical appearance of most ULIRGs implies that these galaxies have undergone strong interactions leading to a complete merger. A commonly accepted interpretation is that during a galaxy collision the interstellar medium is transported inwards, resulting in prodigious star formation events on scales of less than a few kiloparsec. As the merger advances, gas falls into the nucleus proper and accretes onto the central massive black hole.

Although this scenario is plausible, the question of *what dominates the luminosity of ULIRGs and how ULIRGs evolve* has remained fairly unanswered. On the one hand optical spectroscopy reveals signs of AGN activity in ULIRGs (e.g Sanders et al. 1988, Veuilleux, Kim et al. 1994), on the other hand radio (Condon 1991), submillimetre (Rigopoulou et al. 1996a, Rowan-Robinson & Crawford 1989) and millimetre observations (e.g. Rigopoulou et al. 1996b) imply that ULIRGs show characteristics very similar to those of starbursts. Since it is likely that both an AGN as well as a starburst are both present, the question to be pursued is *which, if any, of the two dominates on average.*

With the advent of the Infrared Space Observatory (ISO) (Kessler et al. 1996) it has been possible to take a fresh look in the issue of energetics and evolution of ULIRGs. The availability of sensitive mid-infrared spectroscopy capable of penetrating the obscuring dust, gave new insight into the nucleus of ULIRGs where all the activity takes place. Mid-infrared fine structure lines observed with the Short Wavelength Spectrometer (SWS), polycyclic aromatic hydrocarbon (PAH) observed with the ISOPHOT-S and the ISOCAM-CVF, are used as discriminators between AGN and starburst activity and to probe for evolutionary effects.

Here we review the results of a major spectroscopic survey of Ultraluminous galaxies using ISO-SWS, ISOPHOT-S and ISOCAM-CVF spectroscopy. The observations of ULIRGs are compared to a number of template Starbursts and AGN in order to establish differences and/or similarities. A summary of the properties of AGNs as observed with ISO can be found in Moorwood et al. (these proceedings). A brief summary of the properties of Starbursts is given here, followed by a detailed presentation of the results on ULIRGs.

2. SWS SPECTROSCOPY OF STARBURSTS

Starburst galaxies contribute a large fraction of the star-formation rate in the local Universe. High-mass star formation events appear to take place almost everywhere, from galactic sources, to nearby galaxies, to ULIRGs and out to high-redshift systems.

Proceedings of the Conference "The Universe as seen by ISO", Paris, France, 20–23 October 1998 (ESA SP-427, March 1999)

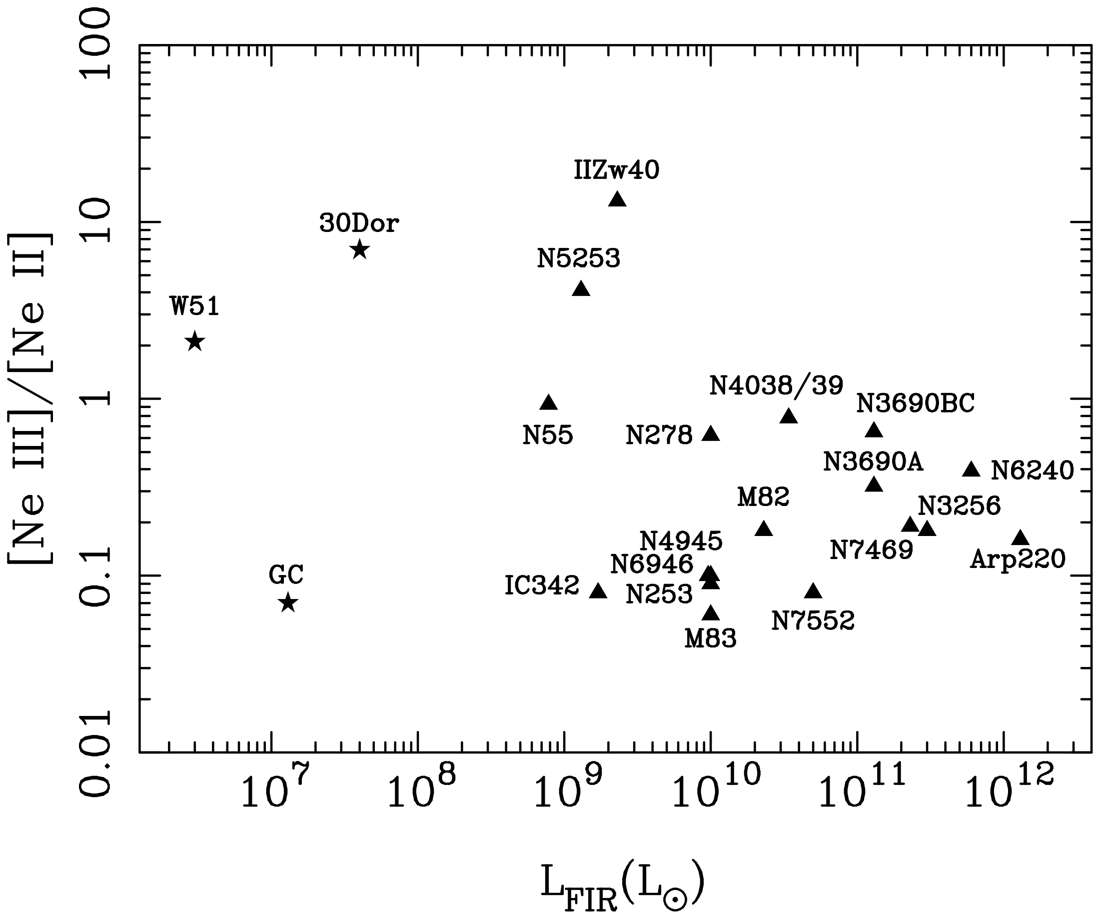

Figure 1. The [NeIII]/[NeII] ratio as a function of far infrared luminosity (L_{FIR}) for the starburst templates (filled triangles) and a handful of nearby "template" star-forming sources (filled stars).

Thus understanding the properties of dusty starbursts is important in studies of the most powerful star-forming events in the Universe.
In conjunction with the studies of ULIRGs we have carried out an extensive program of spectroscopic studies on 20 nearby Starbursts as part of the MPE ISO-Guaranteed time program. Detailed modeling of the observations enables us to understand the formation and evolution of massive stars.

In Figure 1 we have plotted the [NeIII]/[NeII] line ratio as a function of far-IR luminosity. We concentrate on the Ne ratio as a tracer of massive star population. The ratio is sensitive to the spectral shape of the UV field and the properties of the massive stars present. The information from the line ratios is then folded into the modeling to provide constraints on various star formation parameters, including the upper mass cutoff M_{upper} of the Initial Mass Function (IMF) and the age and duration of the starburst.

Based on fine structure lines observed with ISO (in particular the [NeII] 12.8 μm and [NeIII] 15.6 μm lines) we model the evolution of the high mass stellar population. We use the evolutionary synthesis code STARS (Kovo, Alexander and Sternberg 1998) to model the integrated properties from individual stellar clusters. The code is based on the most recent Geneva tracks. The SEDs assigned to each location of the log T_{eff} – log(g) diagram are taken from Pauldrach et al. (1997) and Kurucz models. To predict the nebular emission from the evolving stellar clusters the SEDs produced by stars are then fed into the photoionization code CLOUDY (Ferland et al. 1993).

The results of the detailed modeling (Thornley et al. 1998) show that massive stars with $M_{upper} \geq 100\,M_\odot$ are present in the entire sample in agreement with observations of massive stars in galactic starburst templates (e.g., R136: Brandl et al. 1996, Galactic Centre: Eckart et al. 1995). Moreover, we find that starburst events are consistent with short bursts (t$\simeq$10 Myr) of star formation which produce massive stars which exhibit soft line ratios as a result of the rapidly ageing stellar population.

3. THE NATURE OF ULTRALUMINOUS INFRARED GALAXIES

The fine structure lines observed by ISO span a wide range of ionizing energies, from a few eV, 8eV for Si^{++}, to 55 eV for [OIV] and 97 eV for [NeV]. Since these lines are mainly insensitive to variations of the extinction and electron temperature, they provide excellent probes of the photoionized gas. Such mid-infrared fine structure lines have been observed in a

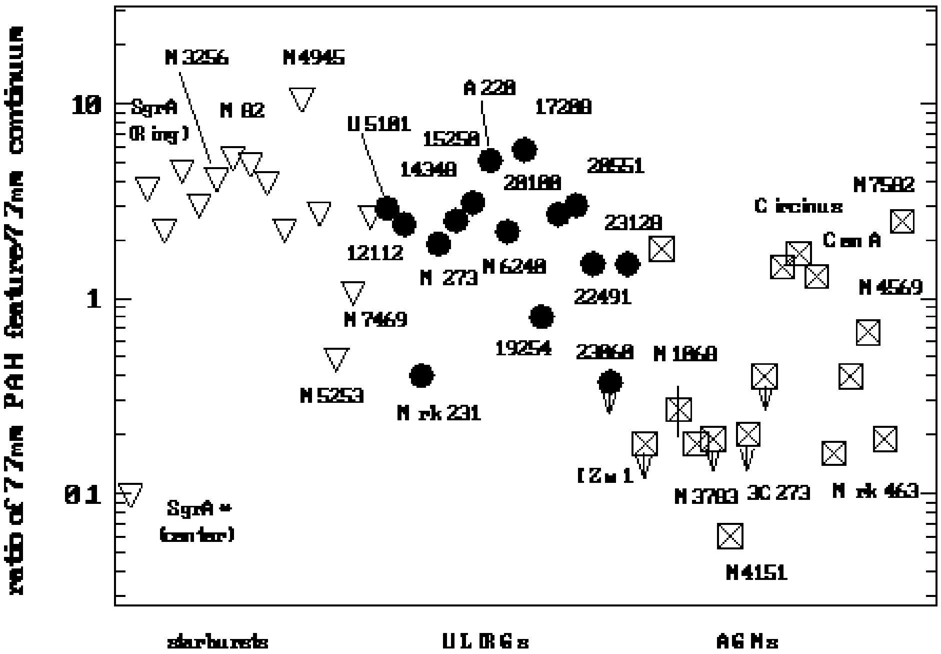

Figure 2. PAH 7.7μm feature line-to-continuum for different sources. Starburst templates are marked as open triangles, ULIRGs as filled circles, and AGNs as crossed rectangles. The "PAH" emission feature is most prominent in the integrated spectra of star forming regions and starburst galaxies, but faint in AGN spectra or very close to stars because the carriers are destructed due to the extremely intense radiation field.

number of ULIRGs as well as template Starbursts and AGNs. Detailed description of the observations and the analysis can be found in Genzel et al. (1998).

We find that the ratio of low-to-high excitation lines is an excellent tool for probing the hardness of the UV radiation field. Comparison studies between a classical starburst NGC 3256 (Rigopoulou et al. 1996), and a typical AGN galaxy NGC 4151 (Alexander et al. 1998) have shown that high excitation lines like [OIV] are strong in typical AGNs but very weak or absent in Starbursts which only show low excitation fine structure lines. When compared to the SWS spectroscopy of the prototypical ULIRG Arp 220 (Sturm et al. 1996) we find that none of the high excitation lines seen in typical AGN were detected. We have extended such studies to a larger sample of 13 ULIRGs all observed with ISO-SWS. We find that, on average, the ULIRG line ratios exhibit values more similar to those of Starbursts. Among the ULIRGs observed only Mrk273 shows a detection of [OIV] and possibly [NeV].

4. A NEW TOOL: PAH FEATURES

It has been known for sometime (Puget and Léger 1989, Roche et al. 1991) that unidentified emission bands at 3.3, 6.2, 7.7, 8.7 and 11.2 microns are probably emitted by large, carbon-rich molecules (PAHs) or very small grains that are exposed to moderately intense UV radiation. Recent observations in galactic sources show that PAH features originate in a number of environments like HII regions and dense molecular clouds (e.g. Verstraete et al. 1996), diffuse cirrus (Mattila et al. 1996) etc.

Using ISOPHOT we have obtained low-resolution spectra for the 13 ULIRGs with SWS observations as well as classical Starbursts and AGNs. Figure 2 is a plot of the 7.7 strength of the PAH feature for the 15 SWS ULIRGs and the AGN and Starbursts.

We find that among ULIRGs all but MRK 231, IRAS 23060, and IRAS 19254 have 7.7 μm features resembling those of Starbursts, in accordance with the trend found from ISO-SWS spectroscopy.

By combining the two diagnostic tools, the fine structure line ratios from the SWS spectroscopy (probing

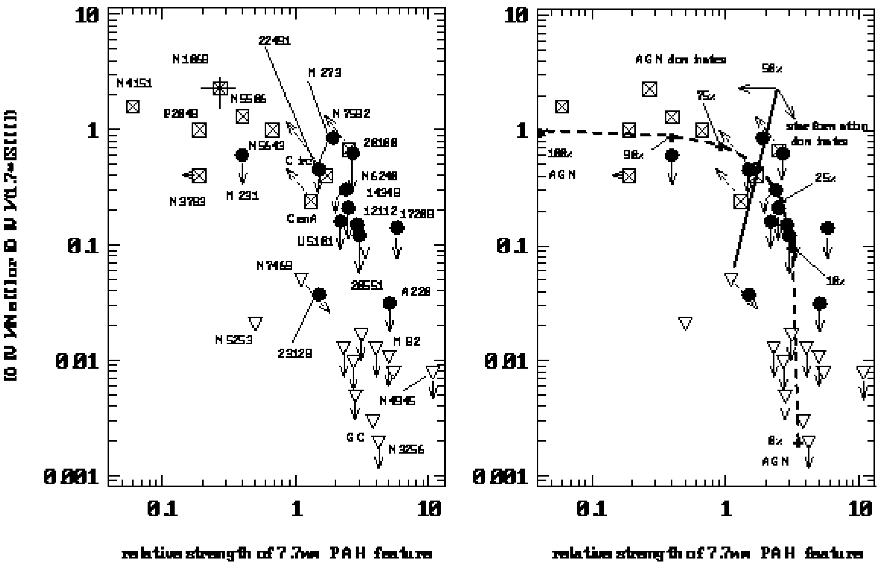

Figure 3. *ISO Diagnostic diagrams. The extinction corrected line ratio of high to low excitation fine structure lines [OIV]/[NeII] measured from the SWS spectra are combined with the PAH 7.7 μm feature-to-continuum strength measured from the ISOPHOT-S spectra. left: data with individual sources marked, ULIRGs (filled circles), template Starbursts (triangles), AGNs (squares). Right: a simple "mixing model". The dashed curve has been obtained by assigning various fractions of total luminosity to an AGN and the rest to a starburst. The "starburst" and "AGN" dominated areas are indicated.*

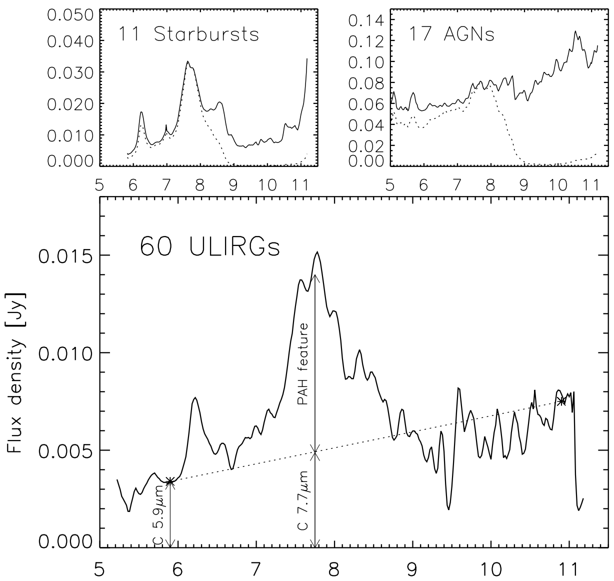

Figure 4. *Average ISOPHOT-S spectrum of all ULIRGs observed. The spectra of each galaxy have been individually scaled to S_{60}=1Jy. Top panels show average spectra of starburst galaxies (left) and AGNs (right) for comparison. Dashed lines: same spectra after applying additional A_V=50 foreground extinction.*

the ionized gas), and the PAH line-to-continuum ratios (probing the UV radiation field) we construct a new diagnostic diagram. Figure 3 shows the results for the ULIRGs together with template Starbursts and AGNs. Such diagrams are best for empirically separating AGNs and Starbursts. From the fine structure [OIV]/[NeII] line ratios and the PAH 7.7 μm feature to continuum strength we deduce that the vast majority of ULIRGs are predominantly powered by star formation. However, there are few examples of AGN dominated ULIRGs (like Mrk 273), whereas co-existence of a low luminosity AGN with a dominant starburst is also possible.

5. A NEW LARGE SAMPLE OF ULIRGS

We have extended the small SWS sample of ULIRGs (Genzel et al. 1998) and obtained ISOPHOT-S spectra for a new bigger sample (Lutz et al. 1998). The new sample of 60 ULIRGs is drawn from the 1.2 Jy sample of Strauss et al. (1992). No infrared color criteria were applied to avoid biasing the sample towards AGNs. The averaged spectrum of all 60 ULIRGs (individually scaled to S_{60}=1Jy to give all sources equal weight) is shown in Figure 4. The spectrum clearly shows the PAH features at 6.2 , 7.7 and 8.6 μm but it also shows a relatively low continuum. A comparison of the ULIRG average spectrum to the Starburst and AGNs template spectra (also shown in the same Figure) provides a first direct indication that ULIRGs are more starburst-like.

Using the strength of the 7.7 μm feature-to-continuum ratio, L/C, (for a definition see Genzel et al. 1998) we classify the sample ULIRGs as AGN or Starbursts. We use this definition in sections 6, 7 and 8.

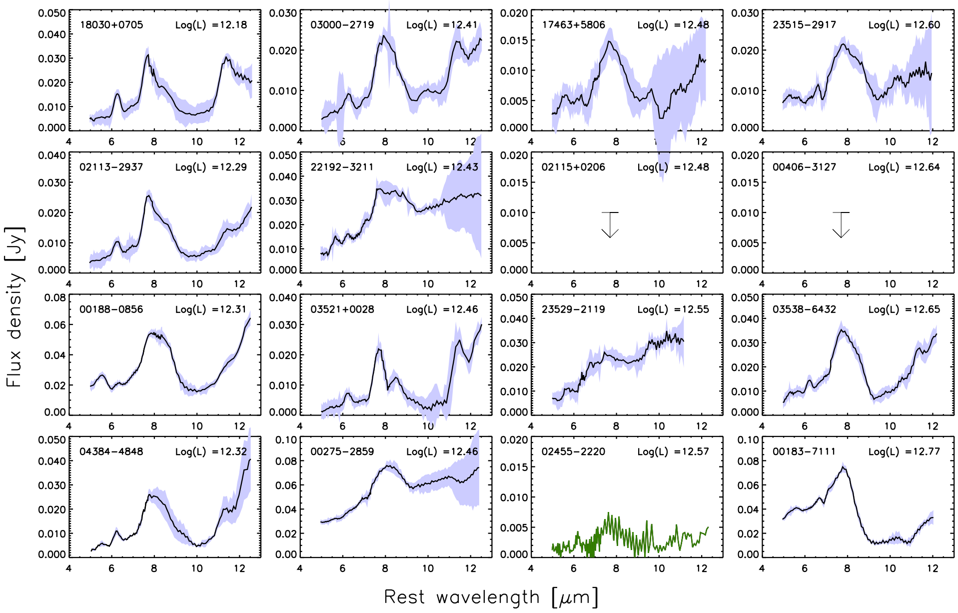

Figure 5. ISOCAM-CVF spectra of the faintest ULIRGs. PAH features are detected in all but 3 cases. The error bars shown are not statistical errors but refer to the specific reduction analysis.

We note that since ULIRGs are heavily obscured silicate absorption can seriously influence the spectra beyond about 8 μm and affect the continuum. Therefore, it is not possible to constrain the silicate optical depth from our PHOT spectra alone.

The ISOPHOT-S sample of ULIRGs has been extended to even fainter and more distant ULIRGs with ISOCAM-CVF observations of the fainter members of the ULIRG class (part of the ZZULIRG consortium). Figure 5 shows the ISOCAM-CVF spectra obtained. We stress that PAH features are detected even in the most distant members of the ULIRG class (Tran et al. 1998).

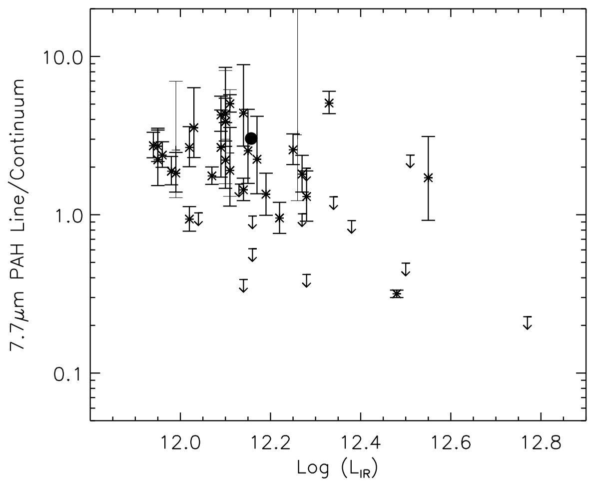

Figure 6. PAH 7.7 μm feature line-to-continuum ratio as a function of infrared luminosity. Thick symbols refer to PAH detections, thin symbols denote galaxies with significant PAH but with a 2σ continuum. The filled circle denotes the location of the average spectrum of 14 ULIRGs that were to faint to be analyzed individually.

6. LUMINOSITY VS. ACTIVITY

How does the activity change with luminosity? In Figure 6 the measured L/C is plotted as a function of the infrared luminosity. We find that the average L/C value for Starbursts is 3 whereas AGNs have an L/C of 0.3. We then classify as AGNs those ULIRGs with L/C <1 (plus some with upper limits slightly above 1) and the rest as Starbursts. We find that the fraction of AGN-like ULIRGs rises with luminosity. Assuming two luminosity bins, separated at log (L_{IR})=12.3 and using the above definitions we find that the fraction of AGN in the low luminosity bin is low, 8 out of 51, while for the high luminosity bin we find 5 AGNs out of 9 objects.

The above statistical results confirm the earlier conclusions drawn from the smaller sample (Genzel et al. 1998) presented in Section 4, that ULIRGs are predominantly starburst-powered. On the other hand our results are in perfect agreement with the results from optical spectroscopy (Veilleux et al. 1998) that the fraction of AGN powered ULIRGs increases with increasing luminosity. However, we stress that even at high luminosities one may still find Starbursts (see Figure 6) and also that even objects which exhibit optical Seyfert-like spectra may still be predominantly powered by starbursts (see case of UGC 5101, Genzel et al. 1998).

7. THE EFFECTS OF DUST

Since ULIRGs are highly obscured objects it is instructive to see how dust affects their spectrum. We find that:

The PAH feature-to-continuum ratio is anticorrelated with the ratio of feature-free 5.9μm continuum to the IRAS 60μm continuum, in agreement with suggestions that strong 5.9μm continuum is a sign of AGN activity. Thus warm ULIRGs are AGN dominated while cold ULIRGs are starburst powered.

Those ULIRGs with starburst-like PAH feature-to-continuum tend to have a weaker 5.9 μm continuum. We interpret this result as the effect of the very high extinction even in the mid-infrared for the dust-rich ULIRGs, in agreement with previous ISO-SWS spectroscopy.

The effects of dust extinction deserve more attention. As we showed in Figure 4, extinction can suppress the 6.2, 8.6 and 11.3 features in comparison to the 7.7 μm one. Lutz et al. (1998) found an anticorrelation between the 6.2/7.7 feature vs extinction, which proves that indeed the suppression of these features is due to the very strong extinction. We conclude that the unusual PAH features observed in ULIRGs are the combined effect of strong extinction and intense radiation fields.

8. EVOLUTION OF ULIRGS

In the grand picture of the evolution of ULIRGs, the proposed Sanders (1988) scenario predicts that interaction and merging of the ULIRG parent galaxies triggers starburst activity which later subsides giving way to the emerging AGN. Through the various stages of interactions the separation between the two nuclei is constantly decreasing, until the merger is complete. Therefore, we would expect that advanced mergers should, on average, be more AGN-like, whereas those galaxies at earlier stages of interactions should appear starburst-powered.

A direct test of the above scenario is presented in Figure 7. The PAH line-to-continuum, which is an indication of the AGN activity in ULIRGs is plotted as a function of the nuclear separations as measured from high resolution near-infrared imaging. The bulk of the nuclear separations were measured from recent near-infrared observations (Rigopoulou et al. 1998). From Figure 7 it is obvious that the expected correlation following the Sanders evolutionary scenario is not seen. Instead we find starbursts at even the smallest nuclear separations. We suggest therefore, that the dominance of AGN or starburst depends on local parameters such as the fueling of the AGN in addition to the global stage of the merger.

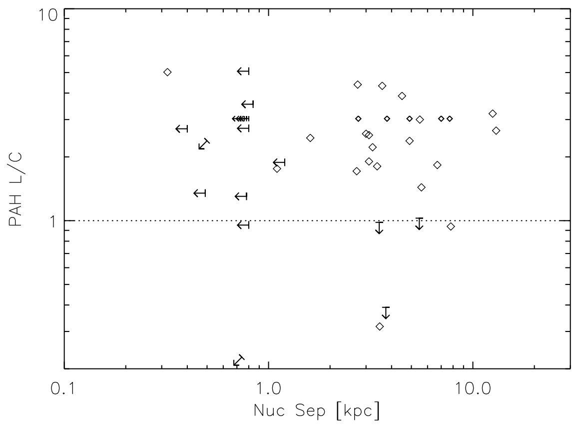

Figure 7. PAH 7.7μm feature line-to-continuum as a function of nuclear separation of the interacting parts of a ULIRG. Small symbols denote sources with noisy spectra. Most nuclear separations are from Rigopoulou et al (1998). The dotted line indicates the adopted separation L/C=1 (see text) between starbursts and AGNs.

REFERENCES

Alexander, T., et al. 1998 ApJ in press

Brandl, B., et al. 1996, ApJ 466, 254

Condon J.J., Anderson, M.L., and Helou, G. 1991, ApJ 376, 95

Eckart A., et al. 1995, ApJ 445, 23

Ferland, G., 1993, Internal Report Dept. of Physics, Univ. of Kentucky

Genzel, R., et al. 1998, ApJ 498, 579

Kessler, M.F. et al. 1996, A&A 315, L27

Kim, D.C., Sanders, D.B., Veilleux, S., Mazarella, J.M., and Soifer, B.T. 1995, ApJS 98, 129

Kovo, O. Alexander, T., and Sternberg, A. 1998 in prep.

Lutz, D., Spoon, H.W.W., Rigopoulou, D., Moorwood, A.F.M., and Genzel, R. 1998, ApJ 505, L103

Mattila, K. et al. 1996 A&A 315, L353

Puget, J.-L., and Léger, A., 1989, ARA&A, 27, 161

Rigopoulou, D., Lawrence, A., & Rowan-Robinson, M. 1996, MNRAS 278, 1049

Rigopoulou, D., et al. 1996, A&A 305, 747

Rigopoulou, D., et al. 1996, A&A 315, L125

Roche, P.F., Aitken, D.K., Smith, C.H., and Ward, M.J., 1991, MNRAS, 248, 606

Rowan-Robinson, M., & Crawford, J. 1989, MNRAS 248, 606

Sanders, D.B., Soifer, B.T., Elias, J.H., Madore, B.F., et al. 1988, ApJ, 325, 74

Soifer, B.T., Sanders, D.B., Neugebauer, G., Danielson, G.E., et al. 1986, ApJ, 303, L41

Strauss, M., et al. 1992, ApJS, 83, 29

Sturm, E. et al. 1996 A&A 315, L133

Sturm, E., et al. 1998 ApJ in press

Thornley M.D., et al. 1998 in prep.

Veilleux, S., Sanders, D.B., and Kim, D.C. 1997, ApJ, 484, 92

Verstraete, L., et al. 1996 A&A 315, L337

THE ISOPHOT SERENDIPITY FAR-INFRARED SKY SURVEY: A STATUS REPORT

M. Stickel[1], D. Lemke[1], L.V. Tóth[1,2], S. Hotzel[1], U. Klaas[1], S. Bogun[3], M.F. Kessler[4], R.J. Laureijs[4], M. Burgdorf[4], C.A. Beichman[5], M. Rowan-Robinson[6], A. Efstathiou[6], G. Richter[7], & M. Braun[7]

[1]Max–Planck–Institut für Astronomie, Königstuhl 17, D–69117 Heidelberg, Germany
[2]Department of Astronomy, Loránd Eötvös University, Ludovika tér 2., H–1083 Budapest, Hungary
[3]Data Management and Operations Division, ESO, Karl-Schwarzschild-Str. 2, D–85748 Garching bei München, Germany
[4]ISO Data Centre, Astrophysics Division of ESA, Villafranca, P.O. Box 50727, E–28080 Madrid, Spain
[5]Infrared Processing and Analysis Center, JPL, California Institute of Technology, MS 100/22, Pasadena, CA 91125, USA
[6]Imperial College of Science, Technology and Medicine, The Blackett Laboratory, Prince Consort Road, London SW7 2BZ, United Kingdom
[7]Astrophysikalisches Institut Potsdam, An der Sternwarte 16, D–14482 Potsdam, Germany

ABSTRACT

The ISOPHOT Serendipity Survey utilized the slew time between ISO's pointed observations with strip scanning measurements of the sky in the far-infrared at $170\,\mu$m. The slews contain information about two fundamentally different types of objects, namely (almost) unresolved galactic and extragalactic far-infrared sources as well as extended regions of galactic cirrus emission. Initial software development and data analysis emphasizes the detection of point sources. First results from an investigation of a high galactic latitude field near the North Galactic Pole indicate that the detection completeness with respect to previously known IRAS sources will be almost 100 per cent for sources with $f_{100\mu m} > 2$ Jy. Nevertheless, even faint sources down to a level of $f_{170\mu m} \approx 1$ Jy can be detected. Since the majority of the detected point sources are galaxies, the Serendipity Survey will result in a large database of ≈ 2000 galaxies. The calibration will be based on photometric observations of 12 galaxies covering a large brightness range. Follow-up observations of three highly interesting cold galaxies were carried out with ISO.

Key words: galaxies; surveys.

1. OBSERVATIONAL CONCEPT

ISO's primary observing mode was pointed observations of selected celestial targets with a single instrument (Kessler et al. 1996). The sequence of scheduled observations required the slewing of the telescope between individual measurements, which could have been quite long and thereby cross a significant part of the sky. To maximize the scientific return of the mission, the ISOPHOT team proposed that the otherwise unused slewing time should also be utilized for scientific purposes (Lemke & Burgdorf 1992).

The ISOPHOT C200 array (Lemke et al. 1996), which is sensitive up to 200 μm, was selected as the most useful instrument for such a slewing survey. A broad band filter at a wavelength of 170 μm has the prospect of delivering data serendipitously beyond the IRAS $100\,\mu$m limit not only for cold point or marginally extended sources but also for extended cold FIR emitting material distributed on large scales in the Galaxy.

At the long wavelength observed, the mostly unresolved sources consist of galaxies, a small fraction of galactic sources, and a few solar system objects such as asteroids. A special type of point-like sources are compact knots embedded in more extended cirrus regions, and highly elongated narrow cirrus ridges, which have been crossed almost perpendicular to their major axis. The separation of the latter two sources from genuine galactic or extragalactic point sources on the basis of the Serendipity slew data alone is likely difficult since a full sky coverage will not be achieved and a second crossing of a particular source was unlikely to happen. In this case, the IRAS $100\,\mu$m maps can be used to clarify the nature of detected sources.

The galactic cirrus emission and the diffuse FIR background in the slews are sampled on all spatial scales, allowing for the first time its detailed study over large areas of the sky at a wavelength beyond the IRAS

Proceedings of the Conference "The Universe as seen by ISO", Paris, France, 20–23 October 1998 (ESA SP-427, March 1999)

limit. By comparison with IRAS 60 μm and 100 μm data, cold regions or spots within the galactic cirrus can be identified and the color temperatures as a function of galactic coordinates studied.

In the following, emphasis is put on the Serendipity Slew processing with respect to the detection and extraction of point or marginally resolved sources. The analysis of extended galactic molecular cloud regions is described by Tóth et al. (these proceedings), while the search for the coldest galactic objects is described by Hotzel et al. (these proceedings).

2. OBSERVATIONAL DATA AND STANDARD REDUCTION

The ISOPHOT C200 detector (2×2 pixel array, pixel size of 89.4 arcsec) was used in conjunction with the C_160 broad band filter (central wavelength 170 μm, equivalent widths 89 μm) to obtain the Serendipity Survey slew data. To cope with the high dynamic range of brightness between the galactic planes and the galactic poles in conjunction with the varying slew speed of the telescope (max. $\approx$ 8 arcmin/sec), the fastest read-out rate of the C200 camera of 1/8 sec was chosen, during which 4 detector readouts take place.

During the slewing phase, the sky positions as a function of time were delivered by the on-board gyros alone. The gyro positions show a drift away from the correct sky positions and only at the end of a slew, after activation of the star-trackers close to the target position, the positions are again precisely known. Methods to partially correct the gyro drift are being developed and will be applied. The final slew position error is expected not to exceed $\approx$ 2 arcmin even for the longest slews with a length of $\approx 150\,^\circ$.

For each detector pixel, the raw data consist of detector voltages as a function of readout time. Signals are derived by fitting a straight line to these four point integration ramps. The signals are converted to surface brightnesses [MJy/sr] using for short slews the default detector responsivities or for long slews (> 75 sec) the responsivities derived from a measurement of the on-board Fine Calibration Source preceding the acquisition of slew data. This standard signal derivation makes use of the ISOPHOT Interactive Analysis[1].

3. EXTRACTION OF POINT SOURCES

The first step to extract the astrophysically relevant information for point sources lying on the slews (Figure 1a) is the determination and subtraction of the large scale background from diffuse galactic emission. Particularly during long slews crossing the galactic plane, the background estimation method has to cope with strongly varying surface brightnesses ranging from a few to several hundred MJy/sr. Moreover, a slew may also contain parts, where the detector was saturated.

[1]The ISOPHOT Interactive Analysis (PIA) is a joint development by the ESA Astrophysics Division and the ISOPHOT consortium. Contributing ISOPHOT Consortium institutes are DIAS, RAL, AIP, MPIK, and MPIA.

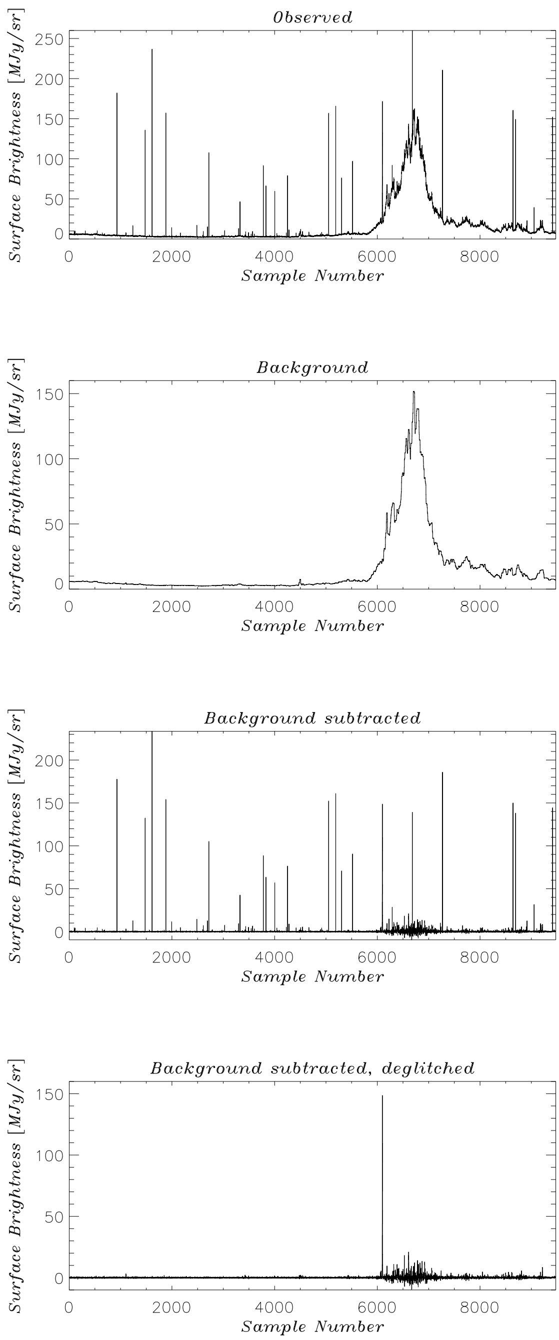

Figure 1. Top to bottom : (a) Data stream of one detector pixel for a long (> 130°) Serendipity slew crossing the galactic plane. (b) Estimated Background. (c) Background subtracted slew data showing strong glitches and increased noise near the Galactic Plane. (d) Glitches removed from (c). The remaining high peak is the nearby galaxy NGC 6946.

To avoid loss of resolution, the flux calibrated data streams of the four pixels are not rebinned, but kept as a function of signal number. After denoising with a non-linear filter (Smith & Brady 1997), a morphological rolling ball algorithm (Sternberg 1986) is applied to remove all peaks up to a width somewhat larger than that of point sources, resulting in the slew background (Figure 1b). The full width at zero intensity for point sources is taken to be five times the FWHM of the C200 170 μm beam profile. Because of the variable slew speed, the radius of the rolling ball, measured in number of signals, changes along the slew.

Cosmic ray hits (glitches) are removed from the individual background subtracted data streams of the four pixels (Figure 1c) by using a noise peak elimination filter (Imme 1991), where data points are replaced only if they are confined to one signal and exceed the local noise level by a factor of three. Very strong signals in the center of sources may erroneously be removed by this procedure, but this can be undone by copying back the signals in question once a source region has been identified. Faint glitches can hardly be recognized, because they resemble genuine noise peaks, yet may have an accompanying faint glitch in a second detector pixel. Occasionally, extremely strong glitches mimic real sources in showing several high signals in sometimes more than one detector pixel.

The background subtracted and deglitched signals (Figure 1d) of the four pixels are phase-shifted according to the rollangle of the detector and a signal-to-noise ratio weighted mean signal is derived. This resulting mean is again slightly filtered (Smith & Brady 1997), from which regions of source candidates are selected by setting a cut on the filtered mean surface brightness. This cut is usually rather low, 3 σ of the local noise level, which in turn is non-constant due to crossing of the regions with different background levels such as the galactic plane. No other criterium such as a detection with a predefined signal-to-noise ratio in several pixels is required for the definition of a source candidate region. The low threshold for the source candidate selection guarantees that even faint sources will be found. On the other hand, this obviously leads to a quite a number of false faint source candidates, mostly unremoved detector hits by cosmic rays, which, however, can easily be recognized because their widths are well below those expected for unresolved point sources.

To decouple the determination of the source position from the derivation of the source flux, the ratio of the four peak fluxes to the highest flux among the four pixels is used in comparison with the expected ratios from a gaussian source model to estimate the minimal source distance perpendicular to the slew direction. It should be noted that the slew offset is a particularly critical parameter for the total source flux, and it is foreseen to improve its derivation by including the ISOPHOT beam profile. For each source candidate region, a non-linear least-squares fit of a two-dimensional circular symmetric gaussian with fixed slew offset together with a tilted plane is then applied to the data from the four background subtracted data streams.

This results in source widths and peak fluxes, and total fluxes derived thereof. The used two-dimensional gaussian is only a first approximation to the real point source profile and ignores important effects such as detector drifts, which lead to asymmetric profiles along the slew direction. As a result, the

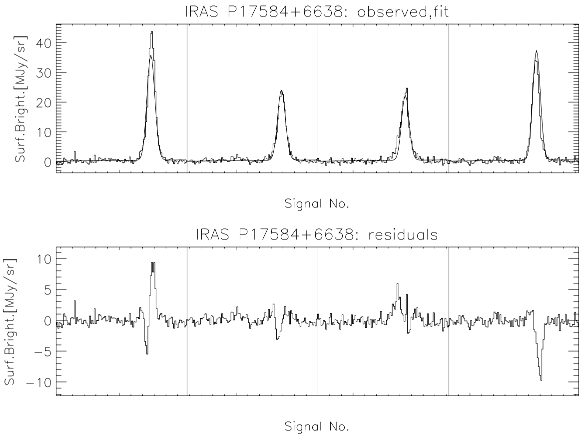

Figure 2. Serendipity Slew data for NGC 6543. Each panel shows for all four detector pixels the source region side-by-side. The upper panel shows the background subtracted data (histogram) together with the fit results (continuous line), while the lower panel shows the residuals after subtraction of the fit.

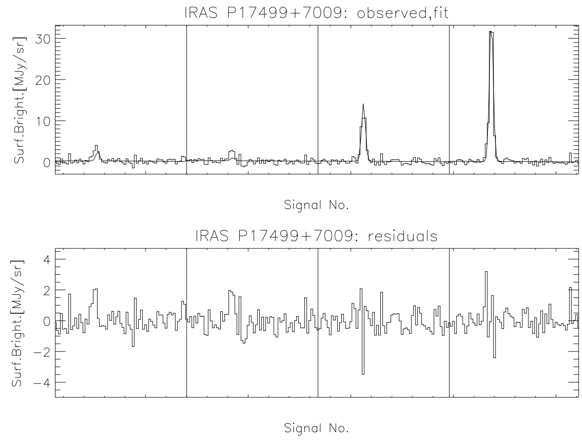

Figure 3. Same as Fig. 2 for NGC 6503.

fit residuals for the brightest sources exceed by far the local noise levels.

The derivation of source parameters will in any case be hampered and the result less accurate if only one or two pixels have a high signal-to-noise ratio, i.e. if a slew touches a sources, but do not cross it almost centrally. The information content of the brightness profiles of the four detector pixels is also significantly reduced if the detector moves parallel to its edges and not with some odd rollangle. In this case each of the two detector pixels having the same distance to a sources show an almost identified brightness profile.

Each fitted source candidate is eventually cross-checked against the IRAS Point Source and Faint Source catalogs and searched for in the NED database. Detailed results of the batch processing are written to log and plot files to allow the selection of subgroups from the source candidates found.

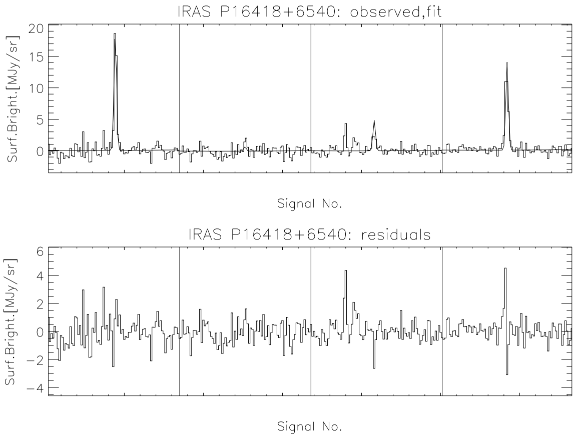

Figure 4. Same as Fig. 2 for IC 1228.

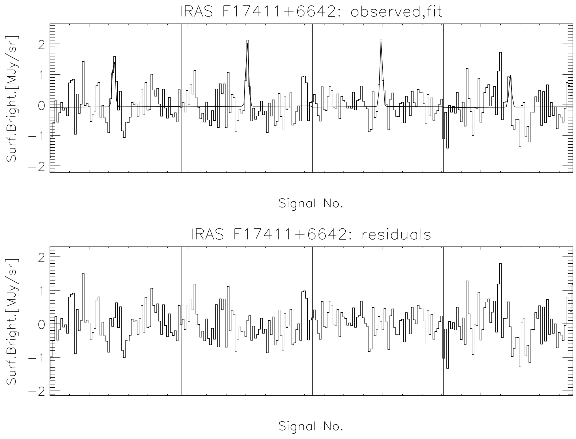

Figure 6. Same as Fig. 2 for UGC 10953.

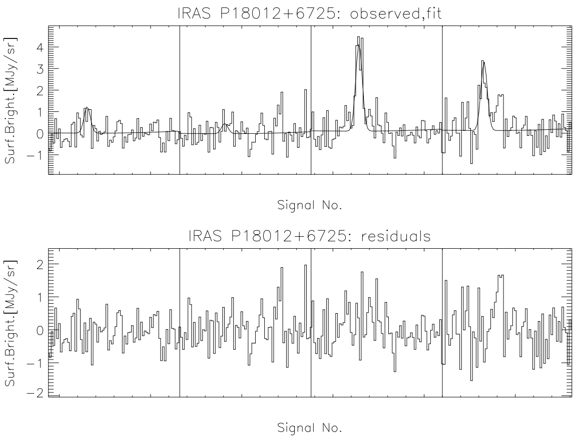

Figure 5. Same as Fig. 2 for UGC 11099.

4. CURRENT PROCESSING STATUS

During almost 800 revolutions, Serendipity data have been taken along $\approx$ 12500 slews. About 75 per cent have a preceding FCS calibration measurement while the rest are rather short slews calibrated with ISOPHOT default responsivities. The total on-sky integration time is $\approx$ 500 hours, the total slew length $\approx 150000\,^{\circ}$. The total amount of raw ERD level data is $\approx$ 6.5 GBytes.

The first bulk processing of the complete slew database with a initial version of the above described extraction software has been carried out in summer 1998. The resulting data amount to $\approx$ 20 GBytes. The results are used to get first experiences with such a large database, to improve the used processing methods and to select subsets for detailed analysis of the achievable accuracy in total flux and position, particularly for the calibration sources.

5. EXAMPLES OF PROCESSING RESULTS

The slew processing is illustrated with the fit results to sources covering a wide range in fluxes. Two of the brightest Serendipity Sources are the planetary nebula NGC 6543 (IRAS 17584+6638, Figure 2) having an IRAS 100 μm flux of $\approx$ 63 Jy and the galaxy NGC 6503 (IRAS P17499+7009, Figure 3) having an IRAS 100 μm flux of $\approx$ 25 Jy. It should be noted that NGC 6543 appears rather wide as measured in number of signals, since it lies at the end of a slew with already decelerating slew velocity. It is moreover one of ISO's calibration sources having repeated observations. The residuals after subtraction of the fit from the background subtracted data in the case of NGC 6543 are clearly much larger than the noise in the adjacent regions and show a systematic pattern, indicating that the source profile for this bright source is not a simple gaussian. This could be due to the slightly extended nature of this source or because of detector drifts. The Serendipity fluxes derived for both NGC 6543 and NGC 6503 is $\approx$ 20 Jy. Both fluxes are rather uncertain, as judged from the fluxes derived from repeated crossings of both sources, and are expected to be improved once a more accurate source profile is used.

For the fainter source IC 1228 (IRAS P16418+6540, Figure 4) with $f_{100\mu m}$ = 7.4 Jy, a much better fit result is obtained, where the residuals hardly exceed the noise in the regions adjacent to the source. This is also demonstrated with the derived fluxes from three crossings, agreeing within 20 per cent and yielding $f_{170\mu m} \approx$ 7 Jy. UGC 11099 (IRAS P18012+6725, Figure 5) shows that even sources with $f_{100\mu m} \approx$ 1 Jy can not only be detected, but also a useful flux ($f_{170\mu m} \approx$ 0.9 Jy) be derived. A second example is UGC 10953 (IRAS F17411+6642, Figure 6), which does not appear in the IRAS Point Source catalog but was crossed twice yielding a consistent 170 μm flux of $\approx$ 1 Jy. For these faint sources, the two-dimensional gaussian is clearly adequate, since noise will play a dominant role, particularly if only two or three detector pixels show a significant signal. At such low flux levels, also distortions due to glitches not completely removed become important, as can be seen in the residuals of detector pixel four (rightmost) for UGC 11099 (Figure 5).

6. DETECTION COMPLETENESS : THE NORTH ECLIPTIC POLE MINISURVEY

To test the software under development, and to gain experience with the bulk data processing already before the end of the ISO mission, the Consortium on the ISOPHOT Serendipity Survey (CISS) had selected a 100 square degrees large high galactic latitude field, ($16^h28^m00^s \leq \alpha_{2000} \leq 18^h12^m00^s$, $+64°00'00'' \leq \delta_{2000} \leq +75°00'00''$), close to the north ecliptic pole, the so-called Minisurvey field. It has the advantage that the foreground emission due to galactic cirrus is rather low, thereby reducing the possible confusion with compact galactic FIR sources.

The investigation of this field was carried out with 336 slews, which had crossed the Minisurvey field before August 14, 1997, totaling 1263° inside the Minisurvey field, corresponding to 4.2 hours of observing time. It emphasized the detection and completeness of point sources in comparison with previously known IRAS sources (4). In view of the early stage of the data analysis at that time, the derived fluxes as well as the reliability of sources found on the slews were used to assess necessary improvement in the processing of the slews.

As a measure for the completeness of the Serendipity processing, the number of IRAS sources expected to be seen on the Minisurvey slews was used. All IRAS point sources lying closer than 2 arcmin to one of the slews crossing the Minisurvey area were selected, but only sources with an IRAS 100 μm quality flag greater than 1 were considered to be potential serendipity sources.

Table 1. Cumulative statistics of the source detection completeness in the Minisurvey field for IRAS sources nominally closer than 2 arcmin to any Serendipity slew.

Flux range IRAS 100 μm	# expected sources	# found sources	percentage completeness
> 10 Jy	11	11	100%
5 - 10 Jy	5	5	100%
2 - 5 Jy	10	9	90%
1.5 - 2 Jy	12	6	50%
total	38	31	82%

Table 1 summarizes the cumulative statistics in several IRAS 100 μm flux bins, where each crossing of a particular source has been counted separately. Since the majority of IRAS point sources are galaxies the spectral energy distribution of which peaks in the wavelength range between 100 μm and 200 μm, their expected 170 μm flux will be close to the IRAS 100 μm flux. Most IRAS 100 μm sources therefore are expected to be detectable also at 170 μm. On the other hand, one star with $f_{100} > 2$ Jy lying in the surveyed region has been excluded because its intensity is steeply falling towards longer wavelengths and is therefore not expected to be seen at 170 μm. For sources brighter than 5 Jy, all expected sources have been found. Only one source is missing in the flux region between 2 - 5 Jy, namely IRAS 16452+6418. An inspection of the IRAS 100 μm showed that this source sits on top of an extended cirrus region, and in fact, the Serendipity processing did detect the cirrus structure but an automatic separation of the point source from the cirrus was not possible.

Below 2 Jy the percentage of detected objects drops, which is easily understood since only sources which are almost centrally crossed are expected to show up in more than 1 pixel with a sufficiently high signal-to-noise ratio. Moreover, since the pointing information of the ISO satellite is still preliminary, IRAS sources that are nominally close enough to be seen on the slews might actually be more than 2 arcmin away and hence not detected. Therefore, the completeness is expected to be improved in the near future, when better ISO slew pointing data will be available. Consequently, sources with $f_{100\mu m} < 1.5$ Jy have currently not been used for the statistical assessment.

7. FLUX CALIBRATION

The two aspects of importance concerning source fluxes are the reproducibility, i.e. the agreement of the fluxes derived from repeated crossings of a particular source, and the external accuracy, i.e. the agreement between the fluxes derived from dedicated photometric measurements and the serendipity slews. The former is mainly determined by the Serendipity data structure and quality of source crossings and can be derived from the scatter of the Serendipity fluxes for a particular source. For the latter, it is expected that due to the fast slew velocity and the finite response time of the detector only a fraction of the total source signal is seen, which requires a rescaling of all flux values derived directly from the slew data.

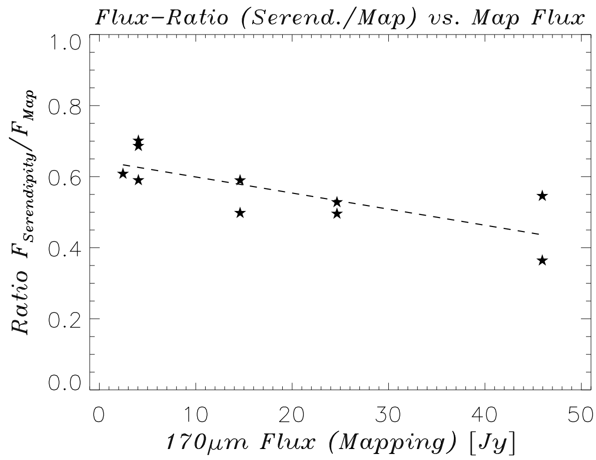

Figure 7. The ratio of derived Serendipity and photometric fluxes from dedicated calibration maps vs. the map fluxes for 5 sources with good Serendipity slew data.

To link the Serendipity fluxes to the absolute photometric flux level at 170 μm, a total of 12 repeatedly crossed galaxies have been mapped in a dedicated Serendipity Calibration programme. For 5 sources crossed almost centrally, i.e. with a signal-to-noise of a least 5 in at least three pixels, the ratio between the Serendipity and the photometric flux vs.

the photometric flux is given in Figure 7. The ratio under standard high speed condition is ≈ 0.5 and appears to be slightly flux dependant. NGC 6543 has been crossed several times near the end of slews at lower slew velocities. These measurements indicate that a larger signal is seen by slower slews. The calibration for the conversion to absolute fluxes will be updated once a better method for the determination of the source offset position, the most critical parameter for the derivation of the total source flux, and the ISOPHOT beam profile is implemented.

8. ISOPHOT FOLLOW-UP OBSERVATIONS OF SELECTED SOURCES

Already before the end of the ISO mission, interesting candidates for follow-up observations with ISOPHOT have been selected late 1997 from a subset of gyro-drift corrected slews. Eventually, observing time was granted for 3 cold galaxies, where the combined Serendipity and IRAS data had suggested a high $170\,\mu$m / $100\,\mu$m flux ratio. Photometric mapping was carried out at $100\,\mu$m and $170\,\mu$m with ISOPHOT in Spring 1998. While for normal galaxies, this ratio is ≈ 1, the Serendipity findings of ratios > 2 could be confirmed for all sources. In fact, one galaxy showed a very high $170\,\mu$m / $100\,\mu$m ratio of 5, indicating a very low overall temperature of ≈ 14K. Follow-up observations have been initiated to investigate this cold galaxy in more detail.

9. CONCLUDING REMARKS

The assessment of the Serendipity Minisurvey field yielded a frequency of source detections of $\approx 0.025/°$ or one detected source along a slew length of 40°, which is equivalent to a surface density of 0.5/square degree. The IRAS database of cataloged galaxies and quasars gives an extragalactic source density of 0.5/square degree for the Minisurvey field which exactly coincides with the measured source density along Serendipity slews. Taking these values one can estimate that with a total sky coverage of $\approx 15\%$ ≈ 4000 galaxies have been seen on all Serendipity slews, which is in agreement with previous estimations (Bogun 1995). However, the derivation of accurate positions and fluxes will be very difficult for sources lying far off the slews. A more conservative estimate can be obtained under the assumption that a source has to lie not more than about half a detector pixel ($45''$) away from the detector center in order to derive reliable flux values. This would bring the effective sky coverage down to ≈ 10 per cent, and also decrease the number of galaxies for which reliable fluxes can be obtained from the Serendipity slews. For a large fraction of the sources, a photometric accuracy of about 30 per cent can eventually be expected. This will provide a large database of $170\,\mu$m fluxes mostly for galaxies.

ACKNOWLEDGMENTS

The ISOPHOT project was funded by the Deutsche Agentur für Raumfahrtangelegenheiten (DARA, now DLR), the Max - Planck - Gesellschaft, the Danish, British and Spanish Space Agencies and several European and American institutes.
Members of the Consortium on the ISOPHOT Serendipity Survey (CISS) are MPIA Heidelberg, ESA ISO SOC Villafranca, AIP Potsdam, IPAC Pasadena, Imperial College London.
This research has made use of the Digitized Sky Survey, produced at the Space Telescope Science Institute, NASA's Astrophysics Data System Abstract Service, and the NASA/IPAC Extragalactic Database (NED) which is operated by the Jet Propulsion Laboratory, California Institute of Technology, under contract with the National Aeronautics and Space Administration.

REFERENCES

Bogun S. 1995, Dissertation, University of Heidelberg, Germany

Imme M. 1991, CVGIP: Graphical Models and Image Processing 53, 204

Kessler M. F., Steinz J. A., Anderegg M. E., Clavel J., Drechsel G. et al. 1996, A&A 315, L27

Lemke, D. Burgdorf M. 1992, Infrared Astronomy with ISO. T. Encrenaz, M. Kessler (eds.), Nova Science Publishers, Commack, New York, p. 69

Lemke D., Klaas U., Abolins J., Abraham P., Acosta-Pulido J. et al. 1996, A&A, 315, L64

Smith S.M., Brady J.M. 1997, Int. Journal of Computer Vision, 23, 45

Sternberg S. 1986, Computer Vision, Graphics and Image Processing 35, 333

Stickel M., Bogun S., Lemke D., Klaas U., Toth L. V. et al. 1998, A&A 336, 116

THE FAR-INFRARED CONTINUUM OF QUASARS

B.J. Wilkes[1], **E.J. Hooper**[1], **K.K. McLeod**[2], **M.S. Elvis**[1], **C.D. Impey**[3], **C.J. Lonsdale**[4], **M.A. Malkan**[5], **& J.C. McDowell**[1]

[1]Smithsonian Astrophysical Observatory, 60 Garden St., Cambridge, MA 02138, USA
[2]Astronomy Department, Wellesley College, Wellesley, MA 02481, USA.
[3]Steward Observatory, University of Arizona, Tucson, AZ 85721, USA
[4]IPAC, Caltech, Pasadena, CA 91125, USA
[5]Department of Astronomy, University of California, Los Angeles, CA 90095, USA

ABSTRACT

ISO provides a key new far-infrared window through which to observe the multi-wavelength spectral energy distributions (SEDs) of quasars and active galactic nuclei (AGN). It allows us, for the first time, to observe a substantial fraction of the quasar population in the far-IR, and to obtain simultaneous, multi-wavelength observations from 5–200 μm. With these data we can study the behavior of the IR continuum in comparison with expectations from competing thermal and non-thermal models. A key to determining which mechanism dominates, is the measurement of the peak wavelength of the emission and the shape of the far-IR–mm turnover. Turnovers which are steeper than $\nu^{2.5}$ indicate thermal dust emission in the far-IR.

Preliminary results from our ISO data show broad, fairly smooth, IR continuum emission with far-IR turnovers generally too steep to be explained by non-thermal synchrotron emission. Assuming thermal emission throughout leads to a wide inferred temperature range $\sim 50 - 1000$ K. The hotter material, often called the AGN component, probably originates in dust close to and heated by the central source, e.g. the ubiquitous molecular torus. The cooler emission is too strong to be due purely to cool, host galaxy dust, and so indicates either the presence of a starburst in addition to the AGN or AGN-heated dust covering a wider range of temperatures than present in the standard, optically thick torus models.

Key words: quasars.

1. INTRODUCTION AND ANALYSIS

The energy output of quasars and AGN is comparable throughout the far-IR to X-ray spectral regions, so studies of their emission mechanisms require observations throughout this range. Prior to ISO, the far-IR continuum was observed by IRAS, providing our first look at quasars in this wavelength range and showing them to be strong emitters from 12–100 μm. The poor spatial resolution and limited wavelength range of IRAS restricted observations to the IR-brightest subsets of quasars and AGN and left open many questions as to the range of behavior present and the emission mechanisms responsible in the various types of AGN. With ISO we are now able to address some of these limitations by studying a large number of different kinds of AGN and quasars.

We observed 72 quasars and AGN covering a full range of redshift and luminosity and many different types of SEDs. The observations were made with ISOPHOT (Lemke et al. 1996) and cover 5–200 μm in 8 bands. The status of this project, including a description of the sample and global comparisons of our results with those of IRAS, is summarised elsewhere (Hooper et al. these proceedings). Here we discuss our preliminary results in the context of the scientific questions we wish to address, with particular emphasis on the high-redshift objects in the sample.

The data were processed with PIA[1] (Gabriel et al. (1997)) through the AAP level, from which custom scripts (originating with M. Haas & S. Mueller at MPIA) were used to determine source fluxes and uncertainties. Default vignetting values from PIA were applied to the chopped data, and the flux scale was set by FCS observations. Sky noise estimates based on Herbstmeier et al. (1998) were included in the error budget. For further details of the data reduction please refer to Hooper et al. (these proceedings).

2. SPECTRAL ENERGY DISTRIBUTIONS (SEDs).

Figure 1 shows typical examples of the SEDs of a radio-loud (upper, RLQ) and radio-quiet (lower, RQQ) quasar (Elvis et al. 1994). Throughout the far-IR–ultraviolet (UV) spectral region, the SEDs are remarkably similar, showing the big blue bump in the

[1]PIA is a joint development by the ESA Astrophysics Division and the ISOPHOT Consortium

optical-UV, the broad IR bump, and an inflection between the two centered at $\sim 1\,\mu$m. The differences between the two radio classes are evident in the radio region where, by definition, the RLQs are several orders of magnitude more luminous, and in the soft X-ray region where the RLQs are a factor of ~ 3 brighter and have a harder spectrum. This latter difference is generally ascribed to an additional synchrotron self-Compton component linked to the radio emission - see Wilkes 1999 for a review of quasar SEDs.

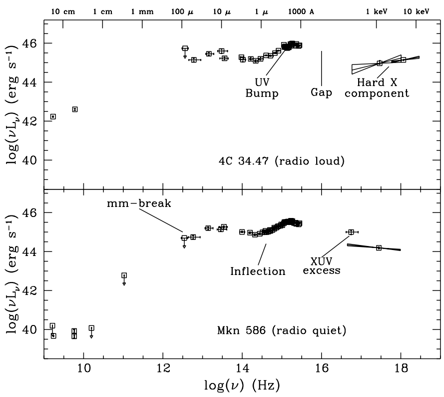

Figure 1. Rest-frame radio–X-ray spectral energy distributions (SEDs) for low-redshift radio-loud (upper, RLQ) and radio-quiet (lower, RQQ) quasars (Fig.1 from Elvis et al. 1994). These are typical examples of SEDs in the current literature. The display of νL_ν vs ν highlights the energy output and the structure of the SED.

The radio–IR SEDs of core-dominated RLQs are generally smooth while in both RQQs and lobe-dominated RLQs the far-IR cutoff is steep and does not extrapolate into the radio. This difference has resulted in the general belief that the IR emission in core-dominated RLQs is dominated by beamed, non-thermal and in RQQs by thermal emission mechanisms - see Wilkes 1999 for a review. The median RLQ SED in Figures 2,3, and 4 was generated from a combination of lobe- and core-dominated RLQs. In a unification scenario (see Barthel (1999) for a review) the beamed IR component is expected to be weaker in lobe-dominated sources where the beam is in the plane of the sky. Thus it may not be surprising that the RLQ SED, formed by combining SEDs from the two radio subclasses, is similar to that of the RQQs. A detailed comparison of the SEDs of core- and lobe-dominated RLQs is required to confirm this scenario. Such a transition from non-thermal to thermal emission with decreasing core-dominance is demonstrated in the preliminary ISOPHOT results of the European Core Program on Quasars (Haas et al. 1998, also these proceedings).

The main questions we wish to address with our ISO sample are (i) to better understand the interplay between thermal and non-thermal emission in the various types of source (ii) to investigate the relative contributions of cool (galactic/starburst) and warm (AGN-related) dust (iii) to characterize and measure the continua in order to constrain models (iv) to study the evolution of the IR SEDs.

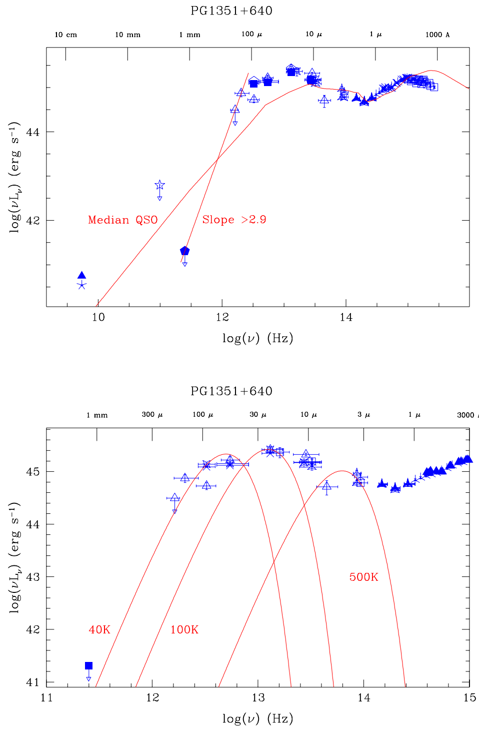

Figure 2. The rest-frame SED of the low-redshift (z=0.088), RQQ PG1351+640 from Elvis et al. (1994) with the ISO data points (open triangles) added. Upper: the radio–UV SED showing a steep ($\alpha_{fir} > 2.9$) far-IR cut-off; Lower: the IR–optical SED with representative grey body (assuming $\beta = 2$) curves superposed.

2.1. Low redshift quasar: PG1351+640

Figure 2 shows the rest-frame SED of a low-redshift (z=0.088), RQQ PG1351+640. The ISO data points are shown as open triangles and the remainder of the multi-wavelength data are from Elvis et al. (1994). This SED is typical of the low-redshift RQQs in our sample and compares well with the low-redshift median. The current limit on the far-IR turnover is $\alpha_{fir} > 2.9$, too steep to be due to non-thermal synchrotron emission, for which $\alpha_{fir} < 2.5$ is required and $\alpha < 1$ is more typical (Gear et al. 1994). We thus conclude that the far-IR emission in this quasars is dominated by thermal emission from dust.

The IR SED is smooth and indicates a wide and probably continuous range of temperatures: 40–500 K. In a purely thermal scenario this smooth continuum can be explained by a combination of cool host galaxy dust, warm (~ 100 K) starburst-related dust (e.g., Rowan-Robinson 1995) and hot ($T_{eff} \sim 800 - 1300$ K) AGN-related dust (e.g., from a torus, Pier & Krolik 1993). Alternatively the emission could originate in AGN-related dust which is sufficiently optically thick and/or geometrically arranged (e.g., the warped disk model of Sanders et al. (1989) or a patchy torus) to produce comparable emission over the wide range of observed temperatures. This latter scenario is supported by the results of van Bemmel & Barthel (these proceedings) which demonstrate that RLQs have significantly brighter far-IR emission than radio galaxies in samples which were matched so that the only difference should be one of orientation.

Table 1. The Broad-band IR luminosities of the High redshift Quasars.

Name	Redshift	L(7–25 μm)[1]	L(2–25 μm)[1]	L(2–200 μm)[1]	# ISO det'ns
1107+48	3.010	1.7E+47	6.9E+47	-	2
BR 1202−0727[2]	4.690	1.7E+48	8.5E+48	8.9E+48	3
1407+265	0.944	7.5E+46	1.2E+47	-	2
1413+1143	2.551	8.8E+47	1.6E+48	2.0E+48	7
1718+481	1.084	2.7E+46	8.2E+46	-	3
HS 1946+7658	3.030	4.2E+47	1.1E+48	2.1E+48	4
3C422	0.942	7.6E+46	1.4E+47	-	2
1351+640	0.088	2.5E+45	3.1E+45	5.2E+45	6

1: Luminosity over indicated bandpass, assuming H_o=50 km s^{-1} Mpc^{-1} and q_o=0 (erg s^{-1})
2: Probably a gravitationally lensed source (Omont et al. (1996))

We also note that, with these data alone, we cannot rule out a significant contribution from a non-thermal component in the mid- and near-IR.

3. HIGH REDSHIFT QUASARS

Our sample includes 9 quasars with redshift > 0.9. The 7 for which we have reliable ISO detections are listed in Table 1 along with their redshifts, preliminary estimates of several broad-band IR luminosities and the number of ISO detections used in this determination. The luminosities were determined via linear interpolation between the data points and are not tabulated where there were insufficient data to provide useful constraints. The IR-band luminosities, determined assuming H_o=50 km s^{-1} Mpc^{-1} and q_o=0, are high, ranging from 10^{46-49} erg s^{-1} ($\sim 10^{13-16}$L$_\odot$). For comparison, the low-redshift RQQ, PG1351+640 (Table 1) has luminosities $\sim 10^{45}$ erg s^{-1} ($\sim 10^{12}$L$_\odot$).

The rest-frame, radio–UV SED of BR 1202−0727, the object with the highest luminosity, L(2–200 μm) $\sim 10^{49}$ erg s^{-1}, is displayed in Figure 3. Our ISO fluxes and upper limits are shown as open triangles and our ground-based near-IR photometry, obtained at the Steward Observatory 61" telescope in March 1996, as open squares. Multiwavelength data are from Isaak et al. (1994) and McMahon et al. (1994). The median, low-redshift, RQQ SED (Elvis et al. 1994), normalised at $\sim 2\,\mu$m, is superposed for comparison. Relative to the rest-frame optical emission, the IR emission in this object is $\sim$ 2 orders of magnitude stronger than is typical. This is a complex source. It is a luminous (dust $\sim 10^{11}$M$_\odot$, Ohta et al. 1996), double (Omont et al. 1996), CO source with a Lyα emission line companion (Hu et al. 1996). Given its unprecedentedly strong mm and IR luminosities and double nature it seems highly likely that the source is gravitationally lensed and so amplified by $\sim\times 10$. However lensing cannot explain the unusual SED of BR 1202-0727, since partial lensing would boost the smaller, optical/UV source rather than the probably extended IR emitting region.

Two extreme temperature grey-body curves (assuming an emissivity index, $\beta = 2$) are also superposed in Figure 3 (upper) for illustration. Again a wide range of temperature is present, 50 − 1000 K although the upper limits in the mid-IR prevent any constraint on the emission at intermediate temperatures in this source. In Figure 3 (lower) an SED representing a ULIRG with the maximum H-band host galaxy luminosity based on low redshift quasars (McLeod 1997) is superposed. This comparison illustrates that the far-IR emission is comparable or in excess of that expected from a ULIRG and far exceeds that expected from the host galaxy (see also Wilkes 1997).

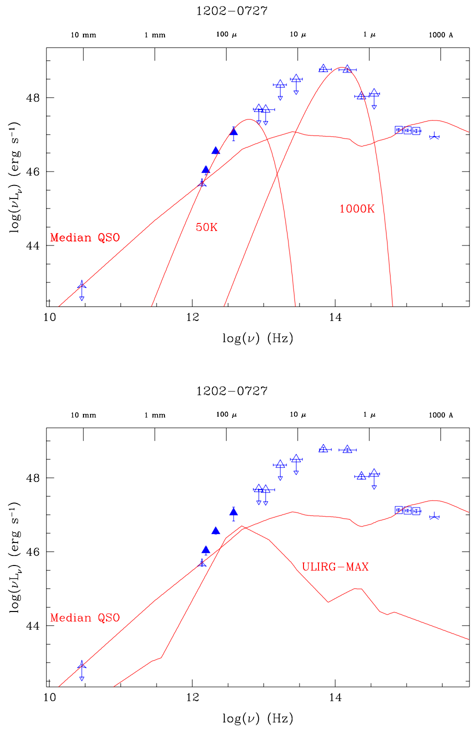

Figure 3. The rest-frame, radio–UV SED of the high-redshift, RQQ BR 1202−0727 including the ISO data points (open triangles). The median SED for low redshift RQQs (Elvis et al. 1994), normalised to the optical SED, is superposed for comparison. Upper: grey-body curves (assuming β=2) at two extreme temperatures are superposed. Lower: the SED of an ULIRG is superposed, normalised to the highest H-band luminosity host galaxy observed in low redshift sources (McLeod 1997).

The rest-frame, radio–UV SED of HS 1946+7658 is displayed in Figure 4. Our ISO fluxes and upper limits are shown as open triangles and the remainder of the multiwavelength data were taken from Kuhn et al. (1994) and Kuhn (1996). We also superpose grey-body curves (assuming dust with emissivity index, $\beta = 2$) at two extreme temperatures to illustrate the range of temperature present in the data. The SED of HS 1946+7658 is remarkably similar to the low redshift, RQQ median, extending the conclusion of Kuhn et al. (1994) based on the optical SED for this source. As with the low redshift RQQ PG1351+640, the IR continuum appears smooth. In a pure thermal scenario, this suggests the presence of dust covering a continuous range from $< 80 - 500$ K rather than two distinct low and high temperature components. The low temperature limit is determined by the longest wavelength at which we have data rather than a real cut-off in the source.

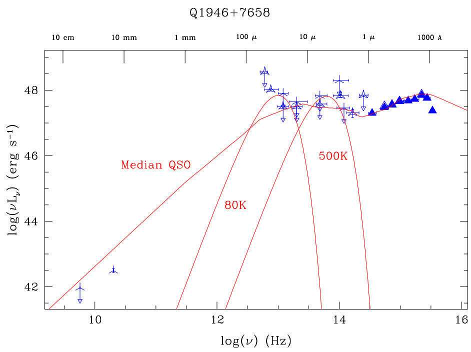

Figure 4. The rest-frame, radio–UV SED of the high-redshift, RQQ HS 1946+7658 including the ISO data points shown as open triangles. The median SED for low redshift RQQs (Elvis et al. 1994) is superposed for comparison. Grey-body curves (assuming β=2) at two temperatures are superposed to illustrate the range of temperature present in a pure thermal emission scenario.

In summary, the broad-band IR luminosities, ranging from 10^{46-48} erg s^{-1} ($\sim 10^{13-15}$L$_{\odot}$, assuming BR 1202-0727 is lensed), are $\sim$ 2 orders of magnitude higher than those of Ultraluminous IR galaxies (ULIRGs) whose SEDs peak in the IR with luminosities $\sim 10^{11-13}$L$_{\odot}$ (e.g. Sanders & Mirabel (1996)), even allowing for the different assumed Hubble constant (Sanders & Mirabel 1996) use $H_o = 75$ km s^{-1} Mpc^{-1}). In the far-IR these luminosities are too high to be due to the host galaxy. As for the low redshift sources (2.1.), the inferred temperature ranges are generally too broad to be fit by standard, AGN molecular torus models (Pier & Krolik 1993), which can reproduce the higher temperature emission. Thus more complex models or a strong starburst component are required to provide the lower temperature emission.

ACKNOWLEDGMENTS

We wish to thank the staff at the ISOPHOT data center in Heidelberg, in particular Martin Haas, for their help and hospitality while working on these data. We also thank the ISO staff at IPAC for their continual support and help both during visits and remotely. This work is supported by NASA grant NAGW-3134.

REFERENCES

Barthel, P. 1999 in "Quasars and Cosmology", Gary Ferland and Jack Baldwin, Eds, ASP Conf. Proc. in press

Elvis, M. S., Wilkes, B. J., McDowell, J. C., Green, R. F., Bechtold, J., Willner, S. P., Cutri, R., Oey, M, S., & Polomski, E. 1994, ApJS, 95, 1

Gabriel, C. et al. 1997 in Proceedings of ADASS VI, ASP Conf. Ser. 125, G. Hunt & H.E. Payne, eds., [ASP], p. 108

Gear, W., Stevens, J.A., Hughes, D.H., Litchfiueld, S.J., Robson, E.I., Terasanta, H., Valtaoja, E., Steppe, H., Aller, M.F., & Aller, H.D. 1994, MNRAS, 267, 167

Haas, M., Chini, R., Meisenheimer, K., Stickel, M., Lemke, D., Klaas, U. & Kreysa, E. 1998 ApJL, 503, 109

Herbstmeier, U., Abraham, P., Lemke, D., Laureijs, R. J., Klaas, U., Mattila, K., Leinert, C., Surace, C. & Kunkel, M. 1998, AA, 332, 739

Hu, E.M., McMahon, R.G. & Egami, E. 1996, ApJ, 459, L53

Isaak, K.G., McMahon, R.G., Hills, R.E. & Withington, S. 1994, MNRAS, 269, L28

Kuhn, O. 1996, PhD Thesis, Harvard University

Kuhn, O., Bechtold, J., Cutri, R., Elvis, M. & Reike, M. 1994, ApJ, 438, 643

Lemke, D. *et al.* 1996, AA 315, L64

Mcleod, K.K. 1997 in "Quasar Hosts", D.L. Clements & I. Perez-Fournon eds., Springer, p. 45

McMahon, R.G., Omont, A., Bergeron, J., Kreysa, E. & Haslam, C.G.T. 1994, MNRAS, 267, L9

Ohta, K., Yamada, T., Nakanishi, K., Kohno, K., Akiyama, M. & Kawabe, R. 1996, Nature, 382, 426

Omont, A., Petitjean, P., Guilloteau, S., McMahon, R.G., Solomon, P.M. & Pecontal, E. 1996, Nature, 382, 428

Pier, E.A. & Krolik, J.H. 1993, ApJ, 418, 673

Rowan-Robinson, M. 1995, MNRAS, 272, 737

Sanders, D.B. & Mirabel, I.F. 1996, ANRAA, 34, 749

Sanders, D., Phinney, E.S., Neugebauer, G., Soifer, B.T., & Matthews, K. 1989, ApJ, 347, 29

Wilkes, B.J. 1999 in "Quasars and Cosmology", Gary Ferland and Jack Baldwin, Eds, ASP Conf. Proc. in press

Wilkes, B.J. 1997 in "Quasar Hosts", D.L. Clements & I. Perez-Fournon eds., Springer, p. 136

THE STARBURST GALAXY NGC 6090: AN ISO VIEW

J.A. Acosta-Pulido[1,2,3], **U. Klaas**[2], **& R.J. Laureijs**[1]

[1]ISO Data Centre, Astrophysics Division, ESA, Villafranca, Spain
[2]Max–Planck–Institut für Astronomie, Heidelberg, Germany
[3]Instituto de Astrofísica de Canarias, E-38200 La Laguna, Spain

ABSTRACT

We present ISOCAM and ISOPHOT observations of the galaxy pair NGC 6090. The SED derived from all ISO measurements is typical for strong starbursts which were triggered by the tidal interaction. With ISOCAM observations we could resolve the two nuclei of NGC 6090 separated by 6″ in the MIR. The NE nucleus is the more active one, both in the optical and in the MIR.

Key words: galaxies; starburst; NGC 6090.

1. INTRODUCTION

NGC 6090 is a strongly interacting galaxy pair. The separation between the two nuclei is 6.4″, which corresponds to a projected distance of 3.6 kpc (at a distance of 117 Mpc). It is classified as a Bright IRAS source, with an IR luminosity $\geq 10^{11}$L$_\odot$ (Soifer et al. 1987). The two nuclei show HII region like emission line spectra in the optical with similar extinction (E[B-V]$\sim$ 0.5) as determined from Balmer line ratios (Kim et al. 1995). The NE nucleus appears to be more active than the SW one: 2.2 and 3.7 times brighter in the B band and in Hα emission, respectively.

2. OBSERVATIONS

NGC 6090 was observed with ISOPHOT (Lemke et al. 1996) covering the full accessible wavelength range of this instrument (from 2.5 to 200 μm). The ISOPHOT data were reduced using the ISOPHOT Interactive Analysis (version 7.0). Results from the ISOPHOT data set were published earlier (Acosta-Pulido et al. 1996, hereafter paper I), here we present the data with improved calibration. Photometry in the 2.5-5.5 μm range was obtained by binning the ISOPHOT-SS channels to four wavelengths.

NGC 6090 was also observed with ISOCAM (Cesarsky et al. 1996) using 10 filters from 4.5 to 15.5 μm, including two narrow band filters with the

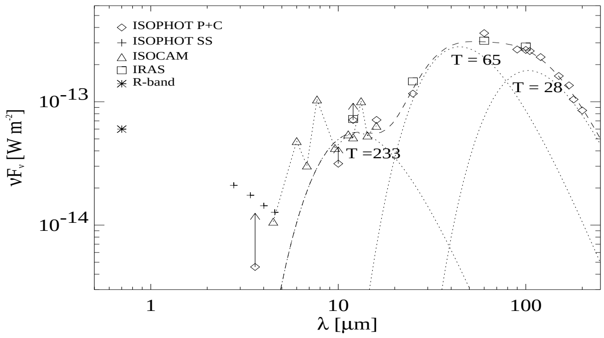

Figure 1. Spectral energy distribution of NGC 6090. All ISO photometric data points are presented. The dashed line represents a composite model including three modified blackbody components. Photospheric stellar emission dominates at $\lambda \leq 4\mu m$.

CVF in fixed mode. Our motivation for the ISOCAM observation was to provide spatial resolution to the feature emission we observed in the ISOPHOT-S spectrum. We performed a 3×3 microscanning raster using a step of 1/3 of a pixel in order to oversample the PSF. The pixel field of view was 3″. Dark current subtraction and deglitching was done using standard CIA routines. A transient correction was performed using a procedure developed by ourselves based on the Fouks–Schubert transient model (Fouks et al. 1995). Different raster positions were combined using the drizzle algorithm (Hook & Fruchter 1997), followed by a PSF deconvolution using the Lucy–Richardson algorithm within STSDAS/IRAF. We have used the theoretical PSFs provided within CIA (version 3.0).

3. RESULTS

3.1. Broad band photometry

The spectral energy distribution (SED) is shown in Fig. 1. The shape of the SED is well constrained by our multi-filter photometry, which sets strong requirements for modelling. From Fig. 1 it becomes clear that a substantial fraction (32%) of the IR energy is emitted at wavelengths shorter than 40 μm,

Proceedings of the Conference "The Universe as seen by ISO", Paris, France, 20–23 October 1998 (ESA SP-427, March 1999)

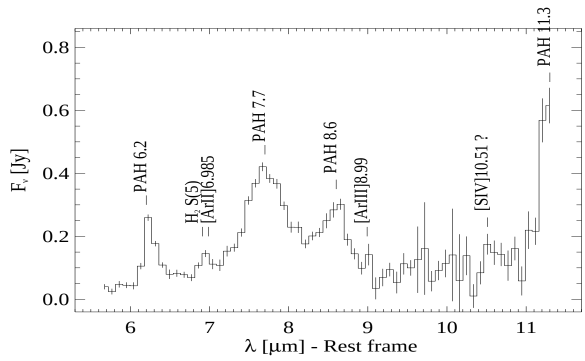

Figure 2. ISOPHOT-SL spectrum of NGC 6090.

not only in the form of continuum but emission in the broad features, as shown in Fig. 2. This emission is generally attributed to small grains and PAH emission. At $\lambda \leq 4$ μm the stellar photosphere emission dominates, as confirmed by the smooth transition from R–band ground based measurements (Huchra 1977) to ISOPHOT-SS data points (see Fig. 1).

We find that the IR continuum can be modelled in a first approach as the emission from three different temperature modified blackbody (emissivity $\propto \lambda^{-1}$) emission: a cold component of T$\sim$ 28 K, a warmer component of T$\sim$ 65 K and a hot component of T$\sim$ 233 K. This result is compatible with that found for other more luminous starburst galaxies (Klaas et al. 1997), and more surprisingly for Seyfert galaxies (Pérez García, Rodríguez Espinosa & Santolaya Rey 1998). The hot component was fitted to the estimated underlying continuum, which makes it rather uncertain given the presence of emission features (see Fig. 2). In paper I we have shown that improved models containing PAH molecules are able to explain the observed SED in great detail (Krügel & Siebenmorgen 1994).

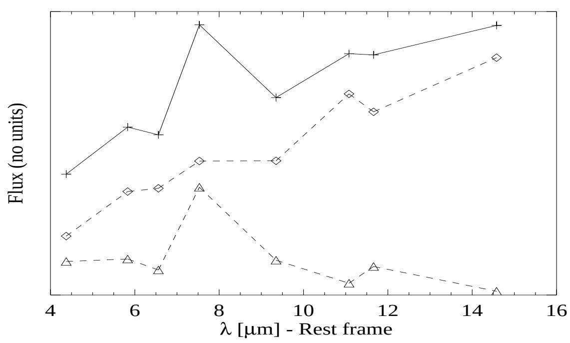

Figure 3. NGC 6090 broad band spectra (F_ν) as measured through ISOCAM filters. The integrated spectrum is represented as crosses joined by a continuous line. Individual spectra corresponding to the NE and SW nuclei are represented by diamonds and triangles, respectively.

3.2. Line Emission

We present in Fig. 2 our flux calibrated ISOPHOT-SL spectrum. In addition to the prominent PAH emission features, there is a clear detection of the following atomic lines: [ArII] 6.98 μm + $H_2S(5)$, [ArIII] 8.99 μm, and less clear [SIV] 10.5 μm. Emission from [NeII] 12.81 μm and [NeIII]15.56 μm was measured using narrow band imaging (CAM-CVF), after continuum subtraction.

We have measured line ratios [NeIII]/[NeII] = 0.14 and [ArIII]/[ArII] = 0.56. These ratios are compatible with photoionization by photospheric emission of $T_{eff} \sim 38000$ K (Sellmaier et al. 1996), and also typical of starburst galaxies (Spinoglio & Malkan 1992).

3.3. MIR imaging

The separation of the two optical nuclei is very close to the maximum spatial resolution which can be achieved with ISOCAM. Our MIR imaging after mosaicing shows an elongated structure in all measured filters, however the two nuclei could be clearly resolved only after PSF deconvolution (see Fig 4).

Most of the MIR emission coincides with the nuclei, contrary to what was found for the Antennae galaxy (Vigroux et al. 1996), which likely reflects different evolutionary stage in the two systems. The two nuclei show different MIR spectrum: the NE nucleus becomes dominant towards long wavelength, whereas the the SW one shows mostly PAH emission (see Figs. 3 and 5).

4. CONCLUSIONS

We present ISO photometry from 2.5 to 200 μm and MIR mapping of the starburst galaxy NGC 6090. The most remarkable results are the following:

- The SED is roughly the composition of 3 modified blackbody components with temperatures 233, 65 and 28 K.
- Small grains and PAH molecules contribute to almost one third of the IR luminosity.
- Using ISOCAM the MIR emission from NGC 6090 could be resolved into two components (6$''$ apart), corresponding to the location of the two optical nuclei.
- Most of the MIR emission is confined to the two optical nuclei. The NE nucleus is always dominant, whereas the SW nucleus becomes brighter at short wavelengths (4.5 μm) and when sampling PAH emission.

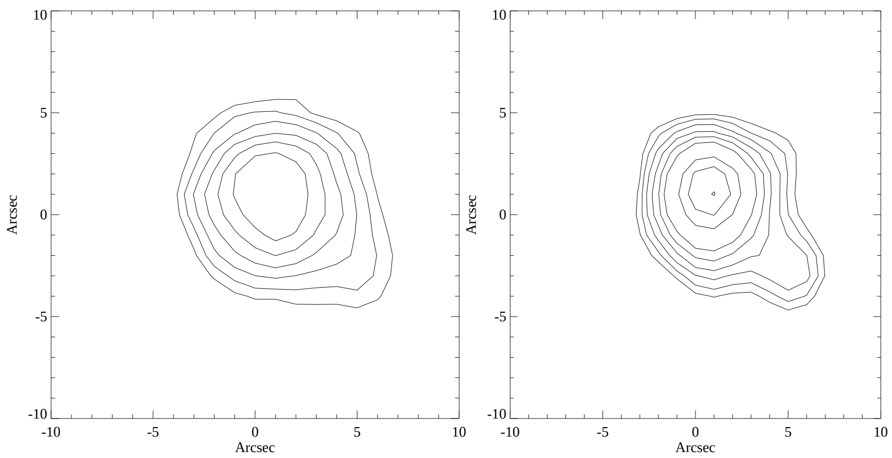

Figure 4. *NGC 6090 image corresponding to filter LW4 - 6 μm before (left panel) and after (right panel) PSF deconvolution. The orientation is N up and E to the left.*

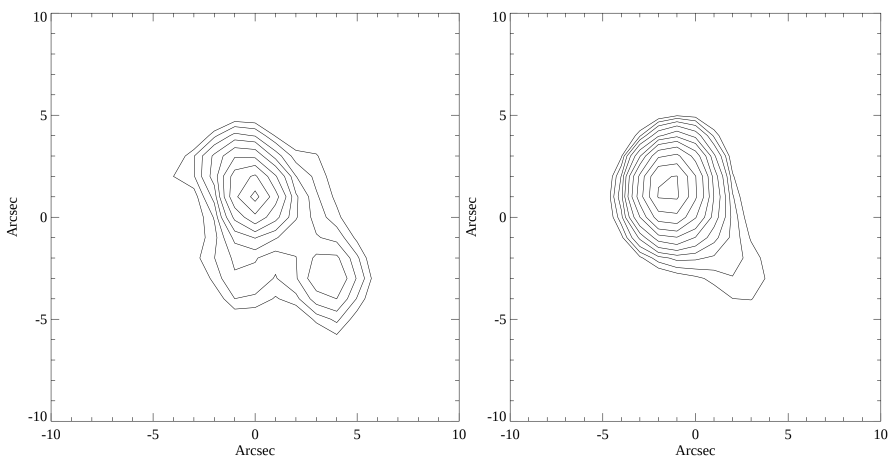

Figure 5. *NGC 6090 deconvolved images corresponding to filters LW1 - 4.5 μm (left panel) and LW3 - 14.3 μm (right panel). The orientation is N up and E to the left. The two nuclei contribute differently depending on the wavelength (see Fig. 3).*

ACKNOWLEDGEMENTS

It is a pleasure to acknowledge A. Biviano and B. Altieri for helping with the ISOCAM data analysis. The ISOPHOT data were reduced using PIA, which is a joint development of ESA Astrophysics Division and the ISOPHOT consortium. The ISOCAM data were reduced using CIA, which is a joint development of ESA Astrophysics Division and the ISOCAM consortium.

REFERENCES

Acosta-Pulido, J.A., Klaas, U., Laureijs, R.J. et al. 1996, A&A, 315, L121

Cesarsky, C.J. et al. 1996, A&A, 315, L32

Fouks, B.I. & Schubert J. 1995, Proc. SPIE, 2552, 421

Huchra, J.P. 1977, ApJSS, 35, 171

Hook, R. & Fruchter, A. 1997, ST-ECF Newsletter, 24, 9

Klaas, U. et al. 1997, A&A, 325, L21

Kim, D-C. et al. 1995, ApJSS, 98, 129

Krügel, E. & Siebenmorgen, R. 1994, A&A, 282, 407

Lemke, D., Klaas, U., Abolins J. et al. 1996, A&A, 315, L64

Pérez Garcia A.M., Rodríguez Espinosa J.M. & Santolaya Rey A.E. 1998, ApJ, 500, 685

Sellmaier, F.H., Yamamoto, T., Pauldrach, A.W.A. & Rubin, R.H., 1996, A&A, 305, L37

Soifer B.T. et al. 1989, AJ, 98, 766

Spinoglio L. & Malkan M. 1992, ApJ, 399, 504

Vigroux L. et al. 1996, A&A, 315, L93

MODELLING THE INFRARED CONTINUUM OF CENTAURUS A

D.M. Alexander[1], **A. Efstathiou**[2], **J.H. Hough**[3], **D. Aitken**[3], **D. Lutz**[4], **P. Roche**[5], **& E. Sturm**[4]

[1]SISSA, via Beirut 2-4, 34013 Trieste, Italy
[2]Astrophysics Group, Imperial College, London, UK
[3]Department of Physical Sciences, University of Hertfordshire, Hatfield, Hertfordshire, UK
[4]Max-Planck-Institut fur extraterrestrische Physik, Garching, Germany
[5]Department of Astrophysics, Oxford University, Oxford, UK

ABSTRACT

We present ISOPHOT-S, ISOSWS and 8 to 13$\,\mu$m ground based observations of Centaurus A that show prominent PAH and silicate features. These and other data are used to construct a model for the infrared continuum. We find that in a nuclear sized aperture ($\sim$4 arcsec, $\sim$60 pc) the SED is characteristic of emission from a starburst and AGN torus; in larger apertures an additional component of cirrus emission is required. Based on our model, the torus diameter is estimated to be 3.6 pc and the best fitting inclination angle of the torus is 45 degrees. This result has implications for the detectability of tori in low power AGN and in particular for the use of the IRAS 60/25$\,\mu$m flux ratio as an indicator of the torus inclination.

Key words: active-galaxies; individual; Cen A; nuclei-galaxies; galaxies-radiative transfer.

1. INTRODUCTION

Rowan-Robinson and Crawford (1989) attribute the infrared (IR) spectra of galaxies to a mixture of up to 3 components: i) general disc emission from grains heated by the interstellar radiation field (cirrus), ii) a Seyfert component peaking in the mid-infrared and iii) a starburst component peaking at about 60$\,\mu$m. Essentially all of these sources arise from the thermal reprocessing of ultra-violet and other high frequency photons by the dust within these objects. The dust grains re-radiate the absorbed energy in the IR, with the resultant spectrum dependent on the distribution of dust grain temperatures. For the starburst and Seyfert components, the clouds of dust are optically thick, even to IR photons, so radiative transfer effects are important.

Centaurus A, the famous southern radio (FRI) counterpart to NGC5128, identified by Bolton, Stanley and Slee (1949), at a distance of approximately 3.1 Mpc (Tonry and Schechter 1990) is the closest active galaxy to us. It is a multi-faceted object, showing evidence of a merger (Mirabel et al. 1998), starburst and AGN activity, with HII regions, shells, jets, optical filaments and a warped dust lane.

Evidence of star formation is most apparent in the dust lane that intersects the host galaxy NGC5128. Marston & Dickens (1988) found that their 12$\,\mu$m IRAS DSD observations followed the Hα emission, along the dust lane, and hence the regions of star formation. They modelled their 12, 25, 60 and 100$\,\mu$m observations as a cirrus spectrum of small and large grains heated by the interstellar radiation with two grain temperatures - hot (240 K) small grains and cooler (30 K) large grains. Evidence of starburst activity comes from enhanced far-IR and sub-mm nuclear emission that shows a structure offset from the dust lane (e.g. Hawarden et al. 1993) and from the high star formation rate, which is typical of a starburst galaxy (Eckart et al. 1990). Evidence of AGN activity comes from the radio jets/lobes (e.g. Clarke, Burns & Norman 1992) and variable x-ray emission (e.g. Morini, Anselmo & Molteni 1989) whilst evidence of a Seyfert-like dusty torus comes from the high optical depth to the nucleus (e.g. Blanco, Ward & Wright 1990).

2. OBSERVATIONS AND DATA

The observations used to constrain the models are an array of published and unpublished data, taken from a variety of sources and grouped into 3 aperture sizes: a small nuclear aperture of $\sim$4 arcsec, an intermediate aperture of $\sim$20 arcsec and a large aperture of $\sim$90 arcsec.

The ISOPHOT-S observations (intermediate aperture) have not been presented before, see Figure 1. The observations have been reduced with PIA without additional modifications. The zodiacal light contributions have been removed using a chopped measurement. The ISOPHOT-S spectrum consists of two parts - PHT_SL (6 to 12$\,\mu$m) and PHT-SS (2.5 to 5.5$\,\mu$m). Clearly seen in the spectrum are the deep 9.7$\,\mu$m silicate absorption feature and PAH emission features, however importantly, PAH emission at 3.3$\,\mu$m is not clearly detected.

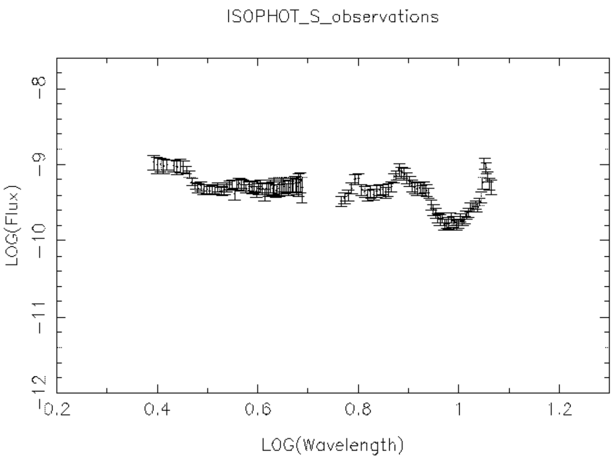

Figure 1. ISOPHOT-S observations. The flux units are $ergs^{-1}cm^{-2}$. The wavelength units are LOG(microns).

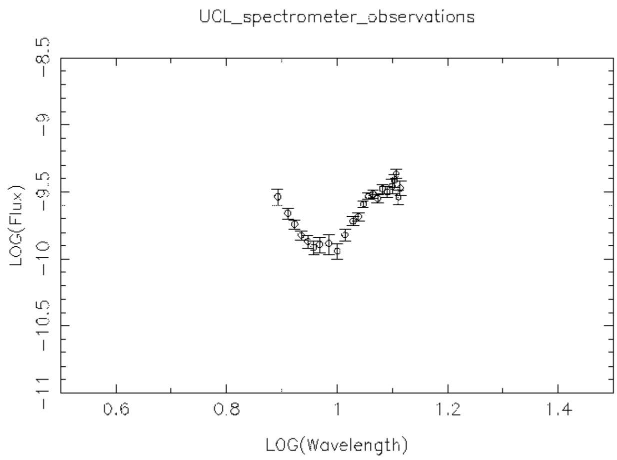

Figure 2. UCL spectrometer observations. The units are the same as in figure 1.

The ISOSWS observations (intermediate aperture) presented here are the continuum points. The emission line spectrum, details of the observations and data reduction will be presented in Sturm et al (in preparation). The continuum points were determined by a second order polynomial fit to the line free regions of the data. The error bars represent the uncertainty in flux calibration - the RMS noise level is insignificant by comparison. No correction has been made for the different aperture sizes at the different wavelengths.

Due to the problem of starlight contamination, and some uncertainty in the flux levels at the short wavelength end of these ISO spectra, the data shortward of 6 μm are not used in the model fitting.

The UCL spectrometer observations (nuclear aperture) have not been presented before, see Figure 2. The silicate feature at 9.7 μm is clearly detected. In addition there appears to be a component of 11.3 μm PAH and 12.8 μm [NeII] emission.

Additional data was obtained from the literature. The near-IR points (nuclear aperture) were taken from Packham et al (1996) and have had the stellar contribution removed. The sub-mm points (intermediate and large aperture) were taken from Hawarden et al (1993) and have been corrected for non-thermal contributions. The 12, 25, 60 and 100 μm large aperture points were taken from Marston and Dickens (1988) and are IRAS DSD observations.

3. THE MODEL COMPONENTS

The proposed model for Centaurus A is a combination of a number of components. The first component is the AGN dusty torus, based on the NGC1068 tapered disc infrared model of Efstathiou, Hough and Young (1995) which assumed a quasar-like central continuum source illuminating an optically and geometrically thick dusty torus. The main model parameters are: opening half-angle of the toroidal cone (θ), ratio of the inner and outer radii (r1/r2), ratio of the height to outer radius (h/r2), equatorial optical depth ($e_{\tau uv}$), dust sublimation temperature (T1) and radial dependence of the density distribution ($r^{-\beta}$). The second and third components are the starburst and cirrus models of Efstathiou, Rowan-Robinson & Siebenmorgen (1998). The cirrus spectrum is assumed to arise from 12,000 K stars centrally illuminating a diffuse optically and geometrically thin dust shell. The starburst is modelled as an ensemble of giant molecular clouds centrally illuminated by hot stars. The stellar population is modelled in terms of the population synthesis models of Bruzual and Charlot (1993) and the giant molecular clouds evolve with time due to the expansion of the HII regions. Additional information on the model components is given in Alexander et al. (1998).

To take into account of dust lane absorption, radiation from the torus and starburst are visually extincted by 10 mags, essentially the same as the value adopted by Packham et al (1996). The cirrus is not extincted since it is itself associated with the dust lane. The extinction model used assumes the grain model and interstellar extinction curve of Rowan-Robinson (1992).

4. THE CENTAURUS A MODEL

For small apertures, and at IR wavelengths below 12 μm, it was assumed that the SED would be dominated by radiation from the torus, seen through the dust lane. Therefore the torus model is fitted to this wavelength range, which includes the 9.7 μm silicate feature. In fitting to larger apertures, a contribution from the smaller apertures is included and any additional components required.

The torus parameters were set to be the same as those in the Efstathiou, Hough & Young (1995) model for NGC1068 (θ=30 degrees, r1/r2=0.01, h/r2=0.1, $e_{\tau uv}$=1,200, T1=950 and β=-1) and the SED was calculated for different values of inclination (the angle between the polar axis and the line of sight). No value of inclination gave a simultaneously good fit to both the near-IR continuum and the silicate feature, with the former best fit by 40 degrees and the latter by 70 degrees. The observed silicate feature shows a feature at 11.3 μm which is probably PAH emission, therefore a component of starburst was added. This provided an excellent fit to the silicate feature, with roughly equal components of torus and starburst for wavelengths less than 60 μm, with the torus at an inclination of 45 degrees, see Figure 3.

For larger apertures a component of cirrus emission was required. For completeness, the contribution this would make in the nuclear aperture is shown in Figure 3 (the cirrus component was determined assuming constant surface brightness, as implied from the fits to the larger apertures).

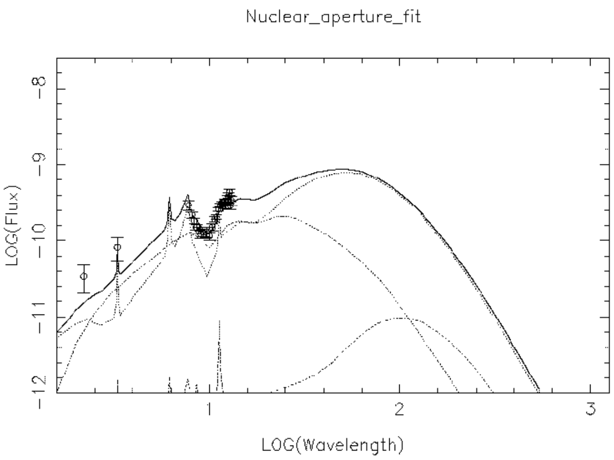

Figure 3. The model fit to the nuclear aperture data points. At the 100 μm wavelength: the lowest intensity model component is the cirrus, the highest intensity component is the starburst and the component in between is the torus. The units are the same as in Figure 1.

In the intermediate aperture, the torus component is kept fixed and an additional contribution from the starburst is added, producing a reasonable fit to the intermediate aperture data points for the silicate feature and IR continuum below 25 μm. The PAH features and the continuum at longer wavelengths showed that an additional component was required. Observations (e.g. Marston & Dickens 1988) suggest that this additional component is cirrus emission from stars within the dust lane. By slightly reducing the contribution from the starburst and adding a component of cirrus, an excellent fit to all the data points is obtained, see Figure 4.

The observed size of the starburst component (e.g., Hawarden et al. 1993) limits the contribution it should have in the large aperture. Whilst there should be an additional contribution from the starburst, the cirrus emission, which is associated with the dust lane, and so is widespread, should contribute

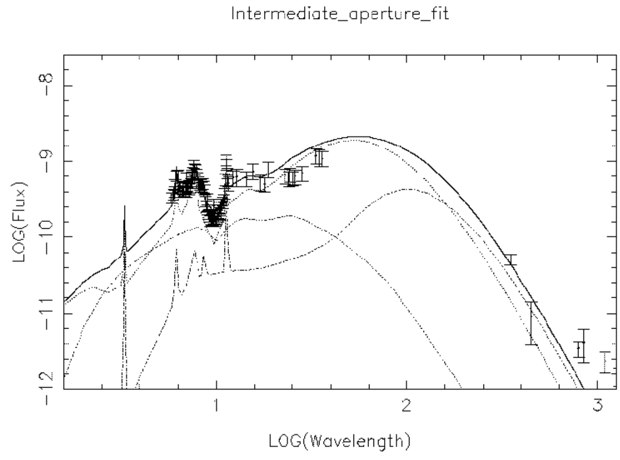

Figure 4. The model fit to the intermediate aperture data points. The model components and units are the same as in Figure 3.

significantly more. The best fit is obtained with a relatively small increase in the starburst contribution and a significant increase in the cirrus contribution, see Figure 5.

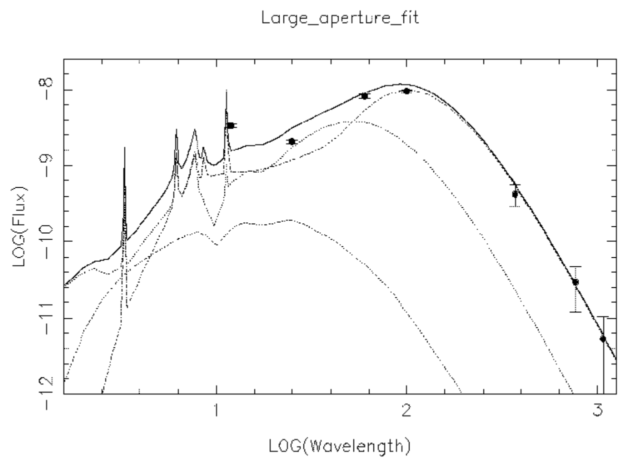

Figure 5. The model fit to the large aperture data points. The model components and units are the same as in Figure 3.

5. DISCUSSION

The complete model includes contributions from torus, starburst and cirrus in all apertures. The model fit in the nuclear aperture is quantitatively similar to that found by Laurent et al. (these proceedings), with ISOCAM CVF observations and AGN and starburst observational templates.

The opening half-angle of the torus cone is very similar to that of the 'cones' in the recently published HST nuclear Paα image (Schreier et al. 1998), and if it is assumed that these observations are of ionisation cones, rather that the suggested warped accretion disc, the cone opening half-angle is constrained between 30 and 40 degrees. Extinction to the 2.2 μm region can be estimated by comparing the flux for the face-on torus to the 45 degree inclined torus and is 2.6 mags, equating to a visual extinction of 23 mags. This degree of extinction is consistent with the analysis of Meadows & Allen (1992) and suggests that the near-IR emission region is considerably less extincted than the x-ray region (70 mags, Blanco, Ward & Wright 1990).

Based on this model, the torus diameter is calculated to be 3.6 pc, assuming a distance of 3.1 Mpc, placing it easily within the nuclear aperture. This is significantly smaller than that actually observed in other galaxies (e.g., $\sim$1 kpc for MG0414+0534 (Oya et al. these proceedings), $\sim$200 pc for NGC1068 (Young et al. 1996), $\sim$100 pc for NGC4261 (Jaffe et al. 1993) and $\sim$50 pc for NGC4151 (Mundel et al. 1995). However, although of a small diameter, this model does not support the even smaller diameter tori of the Pier & Krolik (1992) model.

Possible observational support for the small torus size estimate comes from the 2.3 GHz radio observations of the nuclear sub-arcsecond scale jet and counter jet (Jones et al, 1996). These images show the core to be completely absorbed between the jet and counter jet, attributed to a gaseous disc or torus of 0.4 to 0.8 pc. The model torus, with an inclination of 45 degrees would present a 1.4 pc absorption band; very similar to the size of the radio core absorption.

Within the context of unified theories the inclination of the torus is a crucial parameter in determining whether an AGN is a Type 1 or Type 2. Various studies have suggested that the IRAS 60/25 μm flux ratio is an indicator of torus inclination with high or low ratios implying edge-on to face-on torus inclinations. The combination of all the model components gives a 60/25 μm flux ratio of 9.4, although the actual torus 60/25 micron flux ratio is only 0.7. The torus inclination implied from this study is identical to that found for NGC1068 (Efstathiou, Hough & Young 1995) and yet the IRAS 60/25 μm flux ratio for NGC1068 is only 2.1. If the torus was as powerful as that in NGC1068, or a smaller 'nuclear' sized aperture was used, the 60/25 μm flux ratio would be more indicative of the torus inclination but within the large IRAS sized aperture, the torus is dominated by other more powerful IR emitting components.

A comparison of the mean IRAS 60/25 μm flux density ratios of the extended 12 μm sample of galaxies, which is considered statistically complete on 12 μm flux, gives a mean of 4.1$\pm$2.9 for the Seyfert 1s and 4.5$\pm$3.0 for the Seyfert 2s (Andy Thean, private communication). This suggests that this colour ratio cannot distinguish between Type 1 and Type 2 AGN and so cannot be a reliable indicator of the torus inclination.

The IRAS 60/25 μm flux density ratio is more likely to provide a ratio of the AGN to star formation components. Evidence for this comes from the 60 μm to 6 cm flux correlation (Wilson 1988) which works only if the radio jet/lobe AGN emission is removed (Peter Bartel, private communication), thereby strongly suggesting that the 60 μm flux is coming from star formation and starburst regions. Additional evidence comes from the ISOLWS observations of NGC1068 (Spinoglio et al. these proceedings) where the far-IR continuum is almost indistinguishable to that of the archetypal starburst galaxy M82.

REFERENCES

Alexander, D.M., Efstathiou, A., Hough, J.H. et al. 1998, MNRAS, in press

Blanco, P.R., Ward, M.J., Wright, G.S. 1990, MNRAS, 242, 4P

Bolton, J.G., Stanley, G.J., Slee, O.B. 1949, Nature, 164, 101

Bruzual, G., Charlot, S. 1993, ApJ, 405, 538

Clarke, D.A., Burns, J.O., Norman, M.L. 1992, ApJ, 395, 444

Eckart, A., Cameron, H., Rothermal, H. et al. 1990, ApJ, 363, 451

Efstathiou, A., Hough, J.H., Young, S. 1995, MNRAS, 277, 1134

Efstathiou, A., Rowan-Robinson, M., Siebenmorgan, R. 1998, MNRAS, in press

Hawarden, T.G., Sandell, G., Matthews, H.E. et al. 1993, MNRAS, 260, 844

Jaffe, W., Ford, H.C., Ferrarese, L. et al. 1993, Nature, 364, 213

Jones, D.L. et al. 1996, ApJ, 466, L63

Marston, A.P., Dickens, R.J., 1988, A&A, 193, 27

Meadows, V., Allen, D., 1992, Proc.ASA, 10(2), 104

Mirabel et al. 1998, A&A, 333, L1

Morini, M., Anselmo, F., Molteni, D., 1989, ApJ, 347, 750

Mundel, C.G., Pedlar, A., Baum, S.A. et al. 1995, MNRAS, 272, 355

Packham, C., Hough, J.H., Young, S. et al. 1996, MNRAS, 278, 406

Pier, E., Krolik, J. 1992, ApJ, 401, 99

Rowan-Robinson, M. 1992, MNRAS, 258, 787

Rowan-Robinson, M., Crawford, J. 1989, MNRAS, 238, 523

Schreier, E.J., Marconi, A., Axon, D.J. et al. 1998, ApJ, 499, 143

Tonry, J.L., Schechter, P.L. 1990, AJ, 100, 1794

Wilson, A.S. 1988, A&A, 206, 41

Young, S., Packham, C., Hough, J.H., et al. 1996, MNRAS, 283, L1

ISO PHOTOMETRY OF A QUASAR SAMPLE

Paola Andreani[1,2]
[1]Università di Padova, Dip. Astronomia, Padova, Italy
[2]MPI für Extraterrestrische Physik, Garching, Germany

ABSTRACT

We used PHOT to carry out photometry at wavelengths of 11.5, 60 and 160 μm of a complete subsample of optically selected bright quasars taken from two complete multicolour (U,B,V,R,I) quasar surveys. A preliminary analysis shows that 70 per cent of the objects are detected at least in one band, suggesting that a quite large percentage of optically selected quasars show thermal emission.
The aim of our projects is to use these data to investigate the following. (1) Construction of the spectral energy distribution (from UV to radio) of the population to address issues on the relative importance of thermal and non-thermal emission: the inference of the amount of dust in these objects will have profound impact into the torus model and the unification scheme of the Active Galactic Nuclei. (2) Estimation of the bivariate luminosity function: this will tell us how the optical-infrared relation for quasars changes as a function of both luminosity and redshift.

Key words: Quasars; Luminosity Function; Spectral Energy Distribution.

1. THE AIM OF OUR PROJECT

A complete sub-sample of bright quasars was selected from two complete optical multicolour (U,B,V,R,I) quasar surveys: the Edinburgh Bright Quasar Survey (Goldschmidt et al. 1992) and the ESO Key-Programme 'A Homogeneous Bright Quasar Survey' (HBQS: Cristiani et al. 1995) in a total sky area of 888 sq. deg. The optical fluxes are in the range 15 < B < 17, partially overlapping those of the PG survey, but with a much better photometric accuracy (σ_B ~0.1mag). Our samples show that the true surface density of optically-selected quasars in the range $15 < B < 16.5$ is significantly higher (a factor 3) with respect to the PG survey. No other complete quasar surveys sample such bright fluxes.

Before the advent of these two new surveys, the PG survey was the only one probing the magnitude/redshift plane with magnitudes brighter than B=16.5 and redshifts less than z=1. No other existing complete quasar surveys sample such bright fluxes and that therefore our surveys are unique in this sense. Up to date, at low redshifts (z<1) and bright magnitudes (B<16), all the statistical analysis on the QSO Spectral Energy Distribution (SED) and multivariate luminosity function have been mainly based on the multi-wavelength observations (VLA, IRAS, EINSTEIN) of the PG QSOs. Because of sensitivity limits, quite often, the PG QSOs have been the only objects for which detections was possible. In this way the observed properties have been extrapolated to the entire QSO population. However, it is now widely accepted that the PG survey suffers incompleteness and any statistical analysis is affected therefore by large uncertainties. Our bright subsample of QSOs was designed to cover the magnitude/redshift plane in a way to a) partially overlap the PG sample in order to address the problem of the PG incompleteness, and b) partially extend at fainter magnitudes and higher redshifts in order to better address any redshift or magnitude dependence.

Very little is known about the optical-infrared properties of quasars, and almost all is derived from the IRAS detections of the PG sample (Neugebauer et al. 1986; Sanders et al. 1989; Rowan-Robinson 1995). However, in addition to the problems discussed above, this sample only picks up a narrow range of fluxes and consequently a narrow range of luminosities at any one redshift. Therefore, at the moment, it is impossible to disentangle the twin effects of luminosity and redshift correlations. The aim of this project is to estimate from the new space density of optically selected quasars, the bivariate luminosity function. This will tell us how the optical-infrared relation for quasars changes as a function of both luminosity and redshift. Using this relation we can derive the relative strengths of the different components responsible for far infrared (FIR) emission (Rowan-Robinson 1995; Sanders et al. 1989).

Observing in the FIR/submillimetre bands can provide crucial information about the physical mechanisms driving the AGN emission. For radio-loud compact objects the spectral turnover of the most compact core regions has to lie in this domain. For radio-quiet objects, representing the majority amongst AGN, the interest is to determine the nature of their FIR/submm emission and try to understand why they lack radio fluxes although their UV-O-IR emission appears so similar to radio-loud objects.
Though there has been an active discussion during the past several years about two alternative interpre-

Proceedings of the Conference "The Universe as seen by ISO", Paris, France, 20–23 October 1998 (ESA SP-427, March 1999)

tations, either a synchrotron radiation from the AGN itself or emission by circum-nuclear dust, the more recent tendency was to clearly favour the latter, at least for radio-quiet objects.

Furthermore, the FIR SED is fundamental to test the structure and anisotropy of the obscuring-reprocessing torus as predicted by unification models of AGN and to check the existence of a so-called 'quasar 2' population (in analogy with the Seyfert 2 galaxies). In particular, knowledge of the spectral region where the dust emission peaks and starts to become optically thick (50-100 μm again for redshifted objects) is needed to constrain the nature of the torus and its geometrical and physical parameters (dimensions, dust temperature and optical depth).
Indeed, dust organized in a toroidal structure surrounding the central engine and with a wide temperature distribution up to ~ 1500 K (where grains begin to sublimate), re-radiates thermally at $\lambda \geq 1\,\mu$m photons absorbed from the primary source (Neugebauer et al. 1986, Sanders et al. 1989). This interpretation naturally accounts for the basic observed features of the long-wavelength spectrum of AGN. In particular, it explains the very steep spectral indices for AGN in the sub-mm as grey-body emission of thermal dust with absorption coefficients depending on frequency as $\alpha(\nu) \propto \nu^{1-2}$. It also nicely explains the minimum in the SED often observed in AGNs at $\lambda \sim 1\,\mu$m and due, in this framework, to the cross-over of the primary or stellar continuum with the emission spectrum from dust at the sublimation temperature (e.g., Sanders et al. 1989, Granato & Danese 1994). Thermal emission at these wavelengths is also supported by the detections of CO emission from low and high-z radio-quiet quasars (see the review by Barvainis 1997).

An important outcome of this research will be the comparison between our determination of the space density of quasars in the infrared with that of ultraluminous IRAS galaxies (ULIRGs) with similar bolometric luminosities. A hot debated question is the presence of AGN activity in a significant fraction of these ULIRGs (see Genzel et al. 1998 and Rigopoulou et al. in these proceedings). Comparing the space density of optically selected quasars to that of the ULIRGs with AGN activity as a function of bolometric luminosity and redshift, strong constrains on the torus model can be found. For instance, the size of the opening angle of the obscuring torus, (within which the object appears as a Seyfert 1 type AGN, like the optically selected QSOs) and its dependence on luminosity and redshift. On the other hand, it is possible to explain the high luminosity seen in ULIRGs with AGN activity as due to thermal radiation from hot dust of the torus which lies on the line of sight. In this case any AGN activity in these objects is heavily obscured by dust. By comparing the relative numbers of objects of the different types we can constrain the covering factor of the dust and estimate the opening angle of the torus.

2. OBSERVATIONS WITH ISO

The final sample consists of 34 quasars observed with the ISOPHOT instrument (Lemke et al 1996) in the following bands 11.5, 60 and 160 μm, 13 objects also in the 7.5, 25 and 100 μm bands. The originally preferred technique for observing faint sources, chopping between the source and the sky, was abandoned due to concerns about uncertainties in estimating and calibrating fluxes. Our programme was switched then from chopping to small raster scans but this changing together with the reduced in-flight sensitivities resulted in a halving of the originally planned sample.

Data were reduced with the ISOPHOT Interactive Analysis Tool (PIA V7.2) (Gabriel, Acosta-Pulido, Heinrichsen 1998) and additional software kindly provided by Ilse van Bemmel (see also these proceedings). Data were corrected for electronics nonlinearity, cosmic particle glitches, signal losses for chopper offset and aperture size and were calibrated using associated measurements of the thermal fine calibration source on board.

70% of the objects were detected at least in one band. The missed objects were probably undetected because of the shorter integration time: to estimate the on-source integration time required for detection the adopted criterium was to scale the expected FIR flux according the B-band magnitude (the smaller the magnitude the shorter the integration time) but as shown below this criterium does not hold for quasars, since there is no relation among the B luminosity and the FIR ones.

3. FIRST RESULTS

3.1. Optical/FIR properties

Our preliminary results can be briefly summarized in the following:

(1) There is no correlation between the blue magnitude and the ISOPHOT fluxes. Our adopted criterium to estimate the integration time obviously failed. This probably means that there is no obvious link between the power of the nuclear source and the emission of the putative dusty torus.

(2) It appears that no further link between FIR fluxes and redshift exists. The detection probability remains constant in the redshift 0.2-2.2. The large and negative K-correction implied by a thermal spectrum peaking around 30-100 μm in the object rest frame makes the FIR flux rather constant for a wide redshift range.

(3) Colour-colour diagrammes indicate that, while the 7.5/12 μm flux is unrelated to that at 60, 100, 160 μm, the three latter fluxes seem to be well tied suggesting that different spectral components in the quasar SED are present.

(4) Among the four radio-loud quasars, quite unexpected is the non-detection of two objects. This could be due to the peculiar steep spectrum of the non-thermal emission.

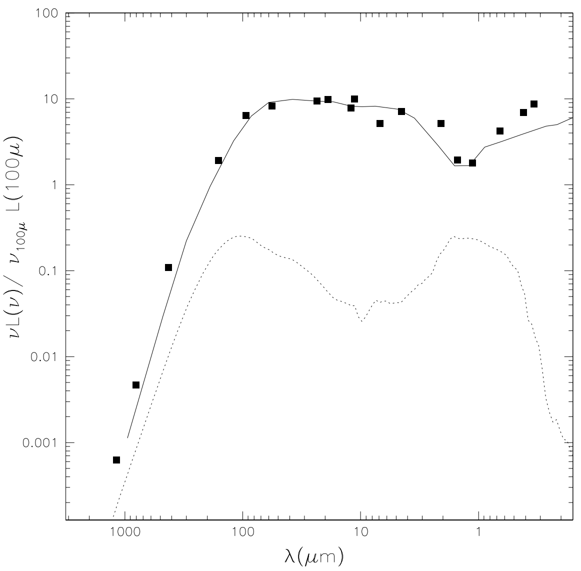

Figure 1. The SED as νL_ν versus ν in the rest-frame of a quasar at $z = 0.1$. Filled-squares are the observed data in the optical and NIR bands (U,B,R,J,H,K), IRAS and ISO data and sub-mm data at 450, 850 and 1250 μm. The spectrum is normalized at the 100 μm datum. The solid curve represents the SED predicted by the model of Granato & Danese (1994), while the dashed line is the spectrum of a nearby spiral for comparison.

3.2. Fitting the SED with a torus model

As stated above, one of the aim of the present work is to gain deeper insights into the physical mechanisms driving the AGN emission. A way to achieve this task is to compare the observed SED from the UV to the mm region of the quasars with that predicted by models. We have chosen the torus model developed by Granato & Danese (1994) (see Andreani, Franceschini, Granato 1998) in the framework of the unified scheme of AGN. A dusty gaseous torus surrounds the central source (black hole plus the accreting disc) and thermally emits from the near IR to the mm region. As an example of our work, Figure 1 shows the SED as νL_ν versus ν in the object's rest-frame of a quasar at $z = 0.1$. This object was detected by IRAS and ISO (see Haas et al. 1998) and observed in the sub-mm as well. The spectrum is normalized at the 100 μm datum. The solid curve represents the best-fitted SED as predicted by Granato & Danese's (1994) model. The best-fit suggests the presence of a torus with a dust mass of $\sim 10^7 M_\odot$ with an extension of ~ 2 kpc. In this case, however, the extension of the torus may be well due to the presence of the hosting galaxy.

4. CONCLUSIONS

Quite unexpected a large number of optically selected quasars are detected with ISOPHOT in at least one of the following bands 7.5, 11.5, 60, 100, 160 μm. Because of the faintness of the observed sources, calibration of these data is not, at present, secure and further work has to be done on the on-board performance of the fine calibration source. Different techniques for estimating the source flux are being explored and in general other issues for the reduction strategy are being investigated.

ACKNOWLEDGEMENT

The author warmly thanks Ilse van Bemmel for her help during the data analysis and for her permission of using her software.

REFERENCES

Andreani P., Franceschini A., Granato G.L. 1998 MNRAS submitted

Barvainis R. 1997, in 'Quasar Hosts' ESA/IAC Conference, Tenerife, eds. Clements D., Perez-Fournon I., Springer Verlag.

Cristiani et al., 1995 A&A Sup. 112, 347

Gabriel, C., Acosta-Pulido J., Heinrichsen I., 1998, Proc. of ADASS VII conf. ASP Conf. Series 145, eds R. Albrecht, R.N. Hook H.A. Bushouse (San Francisco), p.165

Genzel, R., et al. 1998, ApJ 498, 579

Goldschmidt, P., et al., 1992 MNRAS, 256, 65p

Granato, G.L., & Danese L., 1994, MNRAS 268, 235

Haas, M., et al. 1998, ApJ 503, L109

Neugebauer, G., et al. 1986, ApJ, 308, 815

Rowan-Robinson, M. 1995 MNRAS 272, 737

Sanders, D.B., Phinney, E.S., Neugebauer, G., Soifer, B.T., Matthews, K. 1989, ApJ 347, 29

ISO SPECTROSCOPY OF OH IN THE STARBURST GALAXY NGC 253

C.M. Bradford[1], G.J. Stacey[1], J.A. Fischer[2], H.A. Smith[3], R.J. Cohen[4], M.A. Greenhouse[5], S.D. Lord[6], D. Lutz[7] R. Maiolino[8], M.A. Malkan[9], & N. Rieu[10]

[1]Cornell University, Ithaca, NY, USA
[2]Naval Research Laboratory, Washington D.C., USA
[3]Harvard-Smithsonian, CfA, Cambridge, MA USA
[4]Jodrell Bank, U. of Manchester, Cheshire, UK
[5]NASA Goddard Space Flight Center,
[6]IPAC, Cal. Inst. of Tech., Pasadena, CA, USA
[7]MPE, Garching, Germany
[8]Osservatorio Astronomico di Arcetri, Firenze, Italy
[9]University of California, Los Angeles, CA, USA
[10]Observatoire de Paris, Paris, France

ABSTRACT

Using the ISO LWS and SWS gratings we have detected five far-IR rotational transitions of the OH molecule in the starburst galaxy NGC 253. These detections, including all four transitions connecting to the ground state, allow a determination of the OH column density and abundance, and constrain the distributions of molecular gas and warm dust in NGC 253's nuclear starburst. A simple radiative excitation-deexcitation scheme approximately reproduces the observed fluxes in emission and absorption for the 4 optically thin transitions. For the optically thick $119\,\mu$m doublet, we have obtained a velocity-resolved profile with the LWS Fabry-Perot, which shows both absorption, and a high velocity component in emission, possibly related to a large molecular cloud distinct from the nucleus.

Key words: galaxies: starburst – galaxies: individual: NGC 253 – galaxies: ISM – molecules: OH.

1. INTRODUCTION

NGC 253 is a nearby (D $\sim$ 3Mpc) edge-on ($i = 78°$) IR bright spiral galaxy and our best example of a massive nuclear starburst (Engelbracht et al. 1998). Star formation tracers such as radio continuum (from SNR and HII regions), mid- and far-infrared (FIR) continuum (warm dust), and near- and mid-infrared spectral lines (from HII regions and PDRs) trace a region of size $\leq 10''$ in which most of the luminosity is generated (see Ulvestad & Antonucci 1997, Telesco et al. 1993, Smith & Harvey 1996)). The raw material for this nuclear starburst is the $4-6\times10^{10}\mathrm{M}_\odot$ of molecular gas, observed to be distributed over a $\sim 35''\times10''$ region around the nucleus (Mauesberger et al. 1996). The mutual interaction between the molecular gas ring or bar and the intense nuclear starburst is not entirely clear. To study this molecular gas–starburst relationship, we have observed the FIR rotational transitions of OH with the spectrometers on the ISO observatory.

2. DATA

The observations of the rotational transitions of NGC 253, along with the inferred optical depths are listed in Table 1. We will publish the line fluxes, photon rates, and other intermediate analysis step in a subsequent paper. The reduced data were binned without smoothing, and all but the $79\,\mu$m doublet were fit with two gaussian components centered at the wavelengths appropriate for the systemic velocity of NGC 253, 240 km s^{-1}. Uncertainties are estimated via the fluctuations in the final data points, or where systematics appear to be important, by fitting bumps in the

Table 1. Observed Far-IR OH Rotational Transitions

Absorption λ	$\tau_{apparent}$	$\mathrm{N}_{\mathrm{OH},implied}$ (cm^{-2})	τ_{actual}
34.mm	.05	1.02×10^{17}	.05
53.3mm	.12	0.39×10^{17}	.32
$119\,\mu$m	.27	0.017×10^{17}	17
Emission λ		$\frac{\text{Observed}}{\text{Predicted}}$ Photon Rate	
$79.1\,\mu$m		2.0 +/- 0.5	
$163\,\mu$m		1.15 +/- 0.1	

Proceedings of the Conference "The Universe as seen by ISO", Paris, France, 20–23 October 1998 (ESA SP-427, March 1999)

spectrum. The Fabry-Perot profile of the 119 μm line (see Figure 2) is scaled and offset so that both the total line flux and the continuum flux density are equal to those measured with the grating.

3. ANALYSIS

3.1. Column density of OH

In typical molecular clouds associated with star formation, OH resides predominantly in the ground state. The two processes which excite OH, collisions with H_2 and stimulated absorption of the FIR continuum, are much slower than spontaneous emission. As shown in Table 2, critical densities for the FIR transitions of OH are $\sim 10^{10}\mathrm{cm}^{-3}$, so collisions will excite a fraction $f_u \simeq \frac{n_{H_2}}{n_{crit}} < 10^{-4}$ for $n_{H_2} < 10^6$. Stimulated absorption to the upper levels is more effective, but still slower than spontaneous emission by the factor $(e^{\frac{h\nu}{kT}} - 1)^{-1}$ which is $\sim 10^{-1}$ for a 35 K radiation field. Thus the ground state column density is a good measure of the total OH column density.

Table 2. Physical Parameters of the Far-IR Transitions of OH

λ (μm)	$A^{\dagger}$ (s^{-1})	$n^{\dagger}_{crit}$ (cm^{-3})	B (10^{15} cgs)
34.60, .63	0.0174	1.1×10^{10}	6.5
53.25, .34	0.0456	2.5×10^{9}	41
79.10, .17	0.0356	3.6×10^{10}	53
98.71, .73	0.353	5.5×10^{9}	3100
119.22, .42	0.139	3.4×10^{10}	2100
163.11,.38	0.0648	1.9×10^{9}	3400

† A coefficients and critical densities are from Destombes et al. (1977) and Dewagan et al. (1987)

However, as shown in Table 1, the equivalent widths (EWs) of the three ground state absorptions imply different OH column densities. In particular, the 119 μm doublet suggests an $N_{OH} \sim 2\%$ of that implied by the 34 μm transition, and in fact the 79 μm line is in emission. This is due to the reemission of absorbed 119 μm and 79 μm photons by excited OH. Because the nuclear FIR emission excites much more molecular gas than just the fraction which absorbs along our line of sight to the continuum, and this excited OH decays radiatively (see Table 3, Figure 1), we should see much of the total absorption along our line of sight cancelled by reemission from other lines of sight. Indeed, if the both the FIR emitting dust and molecular gas are distributed symmetrically and completely contained within the LWS beam, there will be no net absorption in the 119 μm and 79 μm lines (dust opacity and velocity effects neglected), regardless of the true OH column.

Fortunately, excitations in the cross-ladder transitions at 34 and 53 μm decay through multiple pathways (see Table 2, Figure 1), and are optically thin (see Table 1), thus they can meaningfully constrain N_{OH}. Only 4% of all 34 μm absorptions result in

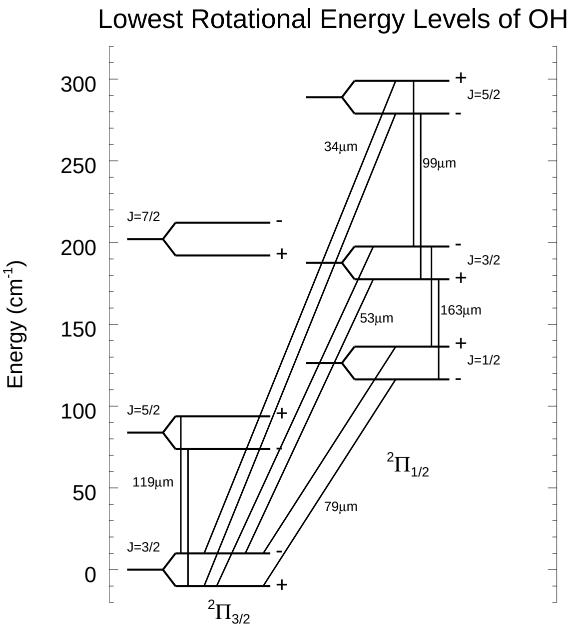

Figure 1. The lower rotational energy levels of the OH molecule, including the fine structure splitting which gives rise to the doublets. An excitation by a 79 μm or 119 μm photon results in a reemission of this photon in the absence of collisional deexcitation

reemission at 34 μm, so the transition is a reliable measure of total OH column. The observed EW implies an optically thin transition, $\tau_{34} = 0.05$, and a column density $N_{OH,34} = 1.0 \times 10^{17}$ cm^{-2}. Since a 53 μm absorption results in 31.5 % reemission at 53 μm , the observed equivalent width (EW) corresponds to a range in N_{OH}. In the unlikely case that a negligible fraction of reemitted 53 μm photons enter the beam, the observed EW exactly measures N_{OH}; this is a lower limit to the true column density. More likely, there is significant reemission in the profile, the measured absorption will be smaller, that is, the true column density is higher than measured with the EW. A plausible assumption is that the molecular gas is symmetrically distributed with respect to the FIR source(s); in this case, the profile includes the full 31.5% of the absorbed flux reemitted, and the column density should be increased by $(1 - .315)^{-1} = 1.46$. Thus we have the range in column density, $3.9 \times 10^{16}\mathrm{cm}^{-2} < N_{OH,53} < 5.7 \times 10^{16}\mathrm{cm}^{-2}$. Evidently $N_{OH,53}$ is a factor of 2-3 smaller than $N_{OH,34}$.

3.2. Velocity resolved 119 μm profile

Figure 2 plots the 119 μm OH doublet observed in NGC 253. The optical depth as measured by this profile is about 0.7, but based on the column density measured by the optically thin 34 μm line, the optical depth in each of the 119 micron lines is ~ 16. As an initial guide to the velocity structure, we have overplotted the data with a fit of three gaussian components in each line (6 total). For each line, two components are in absorption and one, at $v \simeq 350\mathrm{km\,s}^{-1}$, is in emission.

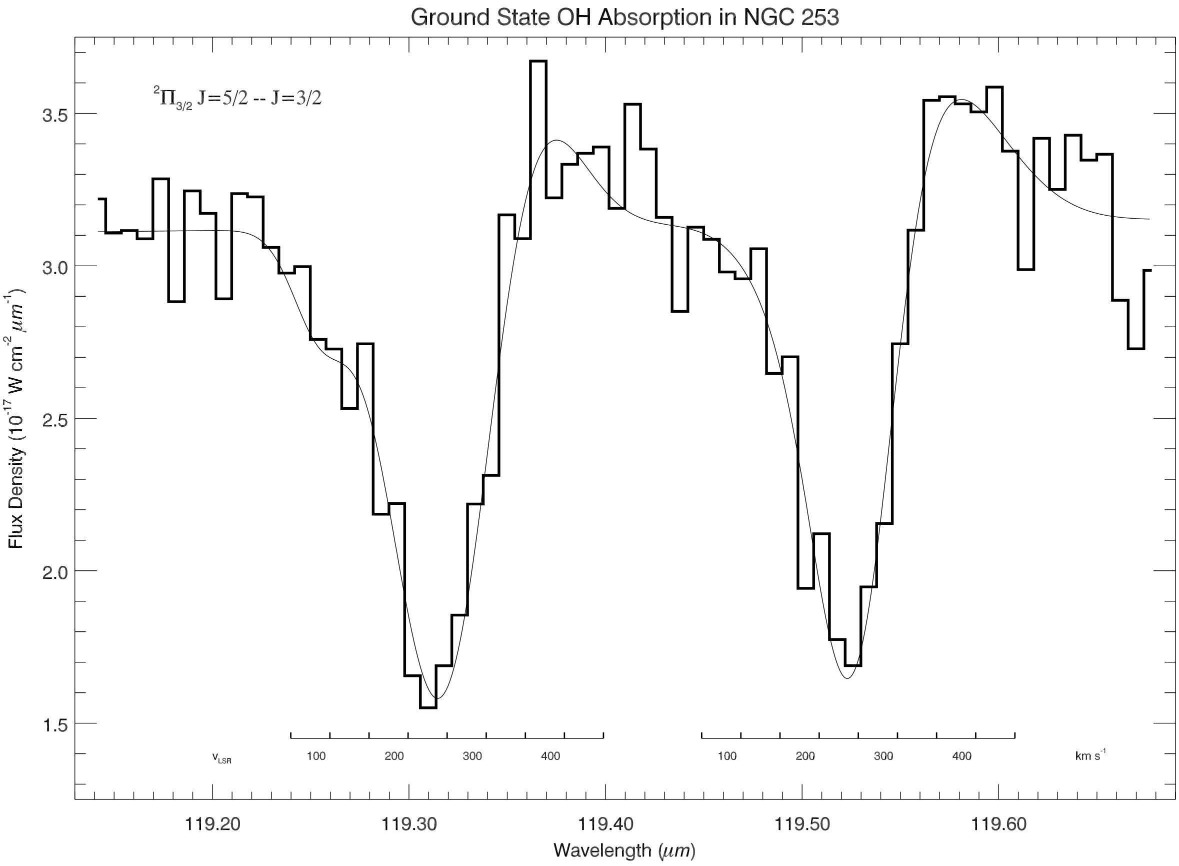

Figure 2. *Velocity-resolved profile of the 119 μm doublet of OH in NGC 253. The data were obtained with the ISO LWS Fabry-Perot, and were scaled and shifted to match the LWS grating measurement of the transition.*

Table 3. *Radiative Decay Pathways for Excited OH*

Absorption from Ground State	Radiative Branching Ratios
34.6 μm	4% @ 35 μm, 13% @ 48 μm, 25% @ 53 μm, 36% @ (163 & 79 μm), 1% @ (115 & 84 μm), 20% @ 96 μm, 34% @ 119 μm
53.3 μm	31% @ 53 μm, 44% @ (79 & 163 μm), 24% @ (96 & 119 μm)
79.1 μm	100% @ 79 μm
119 μm	100% @ 119 μm

4. DISCUSSION

4.1. Distribution of gas and FIR emitting dust

The importance of reemission is demonstrated by the absorption transitions. The photon rates in emission at 163 μm and 79 μm are predicted to within a factor of two by simply counting the photons observed in absorption and following the branching ratios. This implies that either the distributions of the far-IR emitting dust and molecular gas are roughly spherically symmetric and/or the dust and gas are largely coextensive, both reasonable for a starburst galactic nucleus.

The discrepancy between $N_{\rm OH,53}$ and $N_{\rm OH,34}$ suggests that the two absorption profiles trace different components of NGC 253's molecular gas. A plausible explanation is that averaged over the beam, the 34 μm continuum originates in warm dust closer to the nucleus than the 53 μm continuum, and hence it passes through a larger column of OH. The same argument applies locally to star formation regions, the warmer dust is likely more deeply embedded, and thus shorter wavelengths will trace a larger molecular column density. If the foreground dust is sufficiently cool, it will not emit appreciably at 34 μm, and thus not affect the EW or the implied column density.

4.2. OH abundance

Integrated over the $34'' \times 11''$ region containing most of the molecular gas traced by CO (2-1) (Mauesberger et al. 1996), $N_{\rm OH,34}$ implies an OH abundance, $X_{\rm OH} \sim 1.4\times10^{-7}$. This is more than the value estimated for quiescent molecular clouds ($\sim 5\times10^{-8}$) (Prasad & Huntress 1980), but less than the value observed in the shocked gas of Orion ($\sim 5 \times 10^{-7}$) (Watson et al. 1985). This is not surprising, ro-vibrational H_2 emission in the nucleus of NGC 253 indicates the presence of some shocked gas (Rieke et al. 1998), but globally, the shock conditions will be less intense than in Orion. Using these OH data, and the results of the LWS A01 scan, we are in the process of constructing a model of the dust and gas distribution and the radiative transfer in the nucleus of NGC 253.

4.3. Interpretation of the 119 μm profile

Because of the high optical depth in the 119 μm transition ($\tau \sim 16$), very low collisional deexcitation, and the lack of additional decay pathways other than reemission, the transfer in the line is essentially scattering. With $\tau \sim 16$, then, a 119 μm photon will scatter ~ 250 times, and traverse a distance $\sim 16\times$ the size of the region before escaping. Since the continuum dust opacity at 119 μm across the region may approach unity, this scattering quickly makes the effective continuum opacity significant (~ 16), and the profile that we observe must trace material only in the outer portion of the dust / molecular gas region. If the gas and dust were well mixed and isothermal, the profile might appear as a $\tau \sim$ a few absorption, since this is the depth in OH that would, through scattering, achieve a dust opacity of about unity. In reality, however, the outer regions contain cooler dust, which will decrease the observed absorption. Thus the weak absorption is qualitatively plausible, although the details of the transfer are complex and require modelling to address.

The velocity structure of the 119 μm absorption profile resembles the large beam (36$''$) CS (1-0) and 12$''$ CO (2-1) emission profiles which trace dense and warm gas (see Paglione et al. 1995 and Mauesberger et al. 1996). This is not surprising; although the 119 μm absorption does not reliably trace column density, it may indirectly trace excitation. If the dust and gas are distributed together, the deepest absorption will occur in the gas associated with the warmest dust.

The emission component in the two lines is at about 350 km s^{-1}, roughly the same as a cloud distinct from the nucleus seen in interferometric CS (2-1) (Peng et al. 1996). This is possible if the cloud itself if relatively weak in the far-IR continuum, but contains a lot of gas which is illuminated from the side by the nuclear continuum. Since it is easy to get unity optical depths in the 119 μm transition, an emission component with intensity of order the continuum level is feasible. As a part of our global galaxy model, we are in the process of estimating the OH emission that might arise from such a clump, and constraining the geometry of the system.

5. SUMMARY

We have observed five far-IR rotational transitions of OH in NGC 253. The OH level populations are determined radiatively, and the reemission of absorbed photons through various decay pathways must be accounted for in the analysis. To within a factor of two, the radiative scheme predicts the two emission lines fluxes based on the photons in absorption, and we conclude that our line of sight has about the same molecular column to the far-IR continuum as the average line of sight in the galaxy.

Of the three absorption transitions, two are suitable as measures of the column density of OH. Their discrepancy strongly suggests multiple temperature dust components with the warmer dust behind more molecular gas, a plausible scenario for starburst-heated dust.

Due to its high optical depth and tendency to be reemitted, the 119 μm OH transition traces only a fraction of the total molecular gas. In the doublet profile of NGC 253, there is an interesting emission feature at high velocity which may be associated with an isolated cloud or complex to the SW of the nucleus.

REFERENCES

Destombes, J.L., Marliere, C., Baudry, A., Brillet, J. 1977, A&A, 60, 55

Dewangan, D.P., Flower, D.R., Alexander, M.H. 1987, MNRAS, 226, 505

Engelbracht, C.W., Rieke, M.J., Rieke, G.H., Kelly, D.M., Achtermann, J.M. 1998, ApJ, 505, 639

Mauersberger, R., Henkel, C., Wielebinski, R., Wiklind, T., Reuter, H.P. 1996, A&A, 305, 421

Paglione, T.A.D, Jackson, J.M., Ishizuki, S., Rieu, N.-Q. 1995, AJ, 109, 1716.

Peng, R., Zhou, S., Whiteoak, J.B., Lo, K.Y., Sutton, E.C. 1996, ApJ, 470, 821

Prasad, S.S., Huntress, W.T. 1980, ApJ Suppl., 43, 1

Rieke, G., Lebofsky, M., Walker, C. 1998, ApJ, 325, 679

Smith, B.J. & Harvey, P.M. 1996, ApJ, 468, 139

Telesco, C.M., Dressel, L.L., Wolstencroft, R.D. 1993, ApJ, 414, 120

Ulvestad, J.S. & Antonucci, R.R.J. 1997, ApJ, 488, 621

Watson, D.M., Genzel, R., Townes, C.H., Storey, J.W.V. 1985, ApJ, 298, 31

RADIO AND INFRARED ACTIVITY OF BLUE GALAXIES

O. Cardona[1], N.M. Lipovka[2], A.A. Lipovka[2] E. Chavira[1], & O.V. Verkhodanov[3]

[1]Instituto Nacional de Astrofisica Optica y Electronica, MEXICO
[2]St. Petersburg branch of Special Astrophysical Observatory RAS, RUSSIA
[3]Special Astrophysical Observatory RAS, N. Arkhiz, RUSSIA

ABSTRACT

In this paper, we study the galaxies published in the catalogue of Serrano et al. (1996). More than 10 percent of the optical objects show radio emission at frequency 1.4 GHz. 70 percent of them are active galaxies characterized by a colour excess in the blue. These sources are rather faint at radio wavelengths and identified with bright galaxies (11m - 13m). These galaxies have compact nucleus and spiral arms or irregular filaments. More than half of them are identified with infrared sources. The radio emission of the central part of these galaxies has been observed.

Key words: Blue galaxies.

1. INTRODUCTION

During recent years, Blue Galaxies have been under active investigation, because they are unique objects to study starburst evolution. These galaxies are characterized by low radio emission and an excess of colour in the blue. Their spectra show pronounced stellar continuum with narrow emission lines. In most cases there is evidence that the recent star formation was of a short duration (the metallicity of these objects is 2 orders of magnitude less than in our Galaxy). There are two possible ways to explain this fact. The first deals with galaxy-galaxy interactions (merging) that leads to starbursts (Zabludoff et al. 1996). The second explanation invokes a delayed active star formation due to the high UV background which prevails before $z = 1$ (Babul & Ferguson 1996).

2. RADIO AND INFRARED PROPERTIES

The field of the sky under investigation is characterized by an excess of blue galaxies. The coordinates of the galaxies were measured on Palomar glass plates using the blink-comparator at Tonantcintla (INAOE) and following the method described in Chavira et al. (1992). The r.m.s. of the coordinates calculated with the reference stars taken from PPMN catalogue is typically 1.5 - 2.0 arcsec. The complete catalogue of the galaxies and faint diffuse objects up to 18 m for this field of sky has been published by Serrano et al. (1996). More than 10 percent of these objects show radio emission at 1.4 GHz, and approximately 80 percent of this number are active galaxies with excess colour in the blue. These sources are rather weak at radio wavelength (F < 10 mJy) and are identified with bright galaxies 11m - 13m, spirals or galaxies with irregular filaments and blue compact nuclei.

Table 1 lists the optical objects, that show radio emission at 1.4 GHz (Verkhodanov et al. 1997, Condon et al. 1996). Column 1 gives the number by order.
Columns 2 and 4 list the equatorial coordinates (1950.0), line 1 - data from Serrano et al. (1996) and line 2 - data from Condon et al. (1996).
Columns 3 and 5 give the r.m.s of the coordinate measurements.
Column 6 lists the 1.4 GHz flux densities with the r.m.s errors in Column 7 (Condon et al. 1996)
Column 8 gives the type of the galaxy - 'b' means blue.

The elliptical galaxy N 14 (PGC 10175) is located at $z = 0.004$. It is the only powerful radio source in this field, and has spectrum which resembles that of a Seyfert galaxy. This galaxy seems to have an active nucleus because there is a strong difference between the flux densities measured before 1974 (Bolton et al. 1975, Ekers & Ekers 1973, Kazes et al. 1970, Cameron 1971, Kellermann et al. 1970, Condon et al. 1977, Condon et al. 1978, Lequeux 1971, Cohen et al. 1971, Pilkington & Scott 1965, Rogstad & Ekers 1969, Haynes et al. 1975, Heeschen 1961, Heeschen 1970, Humason et al. 1956) and after 1974 (Condon et al. 1996, Kuhr et al. 1979, Parkes Catalogue 1990).

In Table 2 the infrared galaxies (more than half of our list) are listed (Fullmer & Lonsdale 1989). The precision of the coincidence of our coordinates and the IRAS coordinates is typically $2.4'' \times 5.0''$. This is better than for other optical catalogues. Column 1 is the number as taken in Table 1. Column 2 gives the name of galaxy and column 3 the galaxy type. Column 4 lists the magnitude, Column 5 the velocity. Column 6 lists the size (Fullmer & Lonsdale 1989),

Proceedings of the Conference "The Universe as seen by ISO", Paris, France, 20–23 October 1998 (ESA SP-427, March 1999)

Table 1. Optical objects, that show radio emission at 1.4 GHz

N	RA(1950) h m s	RMS s	DEC(1950) deg min sec	RMS sec	P mJy	RMS mJy	Type
1	2	3	4	5	6	7	8
1	02 16 17.08		-06 52 05.0				G b
	02 16 16.18	0.56	-06 52 08.4	7.8	3.5	0.4	
2	02 19 06.26		-05 44 58.4				G b
	02 19 04.80	0.34	-05 44 42.5	3.8	11.8	2.1	
3	02 20 42.57		-04 44 38.6				Irr b
	02 20 42.57	0.5	-04 44 30.2	7.6	3.3	0.5	
4	02 22 14.85		-08 10 21.1				Sc b
	02 22 12.20	0.53	-08 10 09.0	5.3	3.9	0.4	
5	02 23 06.22		-06 04 43.1				G b
	02 23 06.24	0.42	-06 04 56.1	6.3	2.8	0.4	
6	02 23 14.74		-06 00 14.0				G b
	02 23 15.07	0.52	-06 00 01.6	5.1	2.8	0.5	
7	02 25 41.61		-06 03 43.1				G b
	02 25 41.67	0.38	-06 04 16.8	8.5	3.2	0.5	
8	02 27 20.86		-06 12 11.9				G b
	02 27 21.10	0.33	-06 12 18.1	4.5	2.5	0.4	
9	02 32 20.37		-07 54 03.4				G b
	02 32 20.63	0.12	-07 54 07.3	1.6	10.4	1.0	
10	02 33 04.30		-07 22 16.7				G b
	02 33 04.50	0.61	-07 22 30.1	8.2	8.2	2.0	
11	02 34 28.66		-05 33 55.0				G b
	02 34 28.63	0.20	-05 33 59.9	3.8	13.3	2.0	
12	02 36 03.86		-06 53 30.4				G b
	02 36 03.98	0.03	-06 53 35.2	0.4	48.9	1.7	
13	02 37 00.85		-08 20 39.9				G b
	02 37 01.58	0.08	-08 20 53.4	1.2	32.8	2.0	
14	02 38 36.67		-08 28 10.8				G b
	02 38 37.34	0.02	-08 28 09.4	0.3	926.1	29.2	

Column 7 the distance (in Mpc). Column 8 gives the size of the galaxy in Kpc for the IRAS sources and Column 9 the size as taken from Condon et al. (1996). Column 10 indicates the size of the radio emission. The optical data (Columns 2 to 5) were chosen from the catalogue of de Vaucouleurs et al. (1991).

One can see from Table 2 that the radio emission for the main part of the galaxies is emitted from the central nuclear region. This result of our investigation is in agreement with the statistical study of Condon & Broderick (1986) and Condon et al. 1990. A consequence of their results is that the sample of extragalactic sources under investigation are weak radio sources which are identified with spiral galaxies and of which more than 50 percent are IRAS sources. Less than 1% of the infrared sources are radio loud sources. In our catalogue this class of galaxies is represented by the powerful radio source, the galaxy N 14 (Table 1).

3. CONCLUSION

The sample of blue galaxies under investigation are bright nearby galaxies, which have velocities between 1000 and 6000 $\mathrm{km\,s^{-1}}$. The remarkable feature of them is the blue compact nucleus and thin spiral arms or irregular filaments. The main part of the radio emission comes from the central parts of the galaxies and have flux densities less than 10 mJy. More than 50 percent of the infrared sources have been identified with blue galaxies with weak radio emission at 1.4GHz.

Table 2. The IR galaxies with measurable radio emission.

N	Name	Type	mv m	v km/s	2R(IRAS) arc sec	D Mpc	2R Kpc	2R(VLA) arc sec	
1	2	3	4	5	6	7	8	9	10
2	NGC 895	SAS6 b	13.2	2289	210	30.5	31	71.8 x 47.3	34
7	PGC9390	S..3P b	13.5	5835	72	77.8	27.2	≤108 x 69.9	≤100
9	PGC9822	G b	12.85		60			35.1 x 36	58
10	PGC9846	.SXT5 b	12.28	1308	168	17.4	14.2	≤109 x 14.1	≤65
11	PGC9923	SASs5P b	13.09		78			63 x 48	81
12	PGC10010	PSBS1 b	12.00	1275	132	17	11	16 x ≤16.5	≤12
13	PGC10065	.SAS5S b	12.8	1021	120	13.6	7.9	61.9 x 37.7	52
14	PGC10175	.E.4...b	11.4	1285	90	17	7.5	10.8 x 12.3	11

REFERENCES

Babul, A., Ferguson, H.C. 1996, ApJ, 458, 100

Bolton, J.G., Shimmins, A.J., Wall, J.V. 1975, Australian J. Phys. Astrophys. Suppl., 34, 1

Cameron, M.J. 1971, MNRAS, 152, 403

Chavira, E., Kijaeva, O.V., Lipovka, N.M., et al. 1992, Preprint N 81 SPb

Cohen, M.H., Cannon, W., Purcell, G.H., et al. 1971, AJ, 170, 207

Condon, J.J., Broderick, J.J. 1986, AJ, 92, 94

Condon, J.J., Cotton, W.D., Greisen, E.W., et al. 1996, The NRAO VLA Sky Survey (available on the WWW at http://www.nrao.edu/NVSS/NVSS.html)

Condon, J.J., Helou, G., Sanders, D.B., et al. 1990, ApJS, 73, 359

Condon, J.J., Hicks, P.D., Jauncey, D.L. 1977, AJ, 82, 692

Condon, J.J., Jauncey, D.L., Wright, A.E. 1978, AJ, 83, 1036

Ekers, R.D., Ekers, J.A. 1973, A&A, 24, 247

Fullmer, L., Lonsdale, C. 1989, Catalogue of Galaxies and Quasars observed in the IRAS survey, V.2

Haynes, R.F., Huchtmeier, W.K.H., Siegman, B.C. et al. 1975, Printed by CSIRO, Melbourne

Heeschen, D.L. 1961, Publ. Nat. Radio Astron. Obs., 1, 129

Heeschen, D.S. 1970, AJ, 75, 523

Humason, M., Mayall, N.U., Sandage, A. 1956, AJ, 61, 97

Kazes, I., Le Squeren, A.M., Nguyen-Quang-Rieu. 1970, Astrophys. Lett., 6, 193

Kellermann, K.I., Clark, B.G., Jauncey, D.L., et al. 1970, ApJ, 161, 803

Kuhr, H., Nauber, U., Pauliny-Toth, I.I.K. et al. 1979, Max-Planck- Institut fur Radioastronomie, Preprint N 55

Lequeux, J. 1971, A&A, 15, 30

Parkes Catalogue, Special pre-update Edition. 1990

Pilkington, J.D., Scott, P.F. 1965, Memoirs Roy. Astron. Soc., 69, 183

Rogstad, D.H., Ekers, R.D. 1969, ApJ, 157, 481

Serrano, A.,Cardona, O., Chavira, E., et al. 1996, Preprint N 116 SPb

de Vaucouleurs, G., de Vaucouleurs, A., Corwin, G., et al. 1991, Third Reference Catalogue of Bright Galaxies, Springer-Verlag

Verkhodanov, O.V., Trushkin, S.A., Andernach, H., et al. 1997, ASP Conference Series, 125, 322

Zabludoff, A.I., Zaritsky, D., Lin, H., et al. 1996, ApJ, 466, 104

MID-IR IMAGING OF COLLISIONAL RING GALAXIES WITH ISOCAM

V. Charmandaris[1,2], O. Laurent[2], I.F. Mirabel[2], P. Gallais[2], L. Vigroux[2], & C.J. Cesarsky[2]

[1]Observatoire de Paris, DEMIRM, France
[2]CEA/DSM/DAPNIA, Service d'Astrophysique, Gif-sur-Yvette, France

ABSTRACT

We present mid-IR images and spectra of three collisional ring galaxies observed as part of the ISO GT program CAMACTIV (P.I.: I.F. Mirabel) by ISOCAM. The observations, reveal the distribution of hot dust in the galaxies and enable us to probe the mechanisms responsible for the heating of the ISM. Even though the mid-IR colors of Arp 10 were typical of those found in spiral arms of late type spirals, the Cartwheel (AM 0035-33) galaxy revealed a surprisingly strong mid-IR emission from the nucleus which we attribute to a previously undetected star formation activity. The third ring of the sample, Arp 118, harbours a Seyfert 2 nucleus which exhibits a clearly detected hot continuum in the [5.1-6.7] μm range.

Key words: interacting galaxies; starburst.

1. INTRODUCTION

Collisional ring galaxies, of which the Cartwheel is the "prototypical" candidate, are believed to form when an "intruder" galaxy passes through the center of a rotating disk of a larger "target" galaxy (Lynds & Toomre 1976; Theys & Spiegel 1976; Appleton & Struck-Marcell 1996 and references therein). The perturbation triggers a radially expanding ring-like density wave on the disk, causing massive star formation in the ring (see Appleton & Marston 1997). The symmetry and well defined dynamical history of ring galaxies has made them ideal candidates for studies of the phase transition of the interstellar medium due to collisionally induced star formation.

2. OBSERVATIONS

The Cartwheel group was observed with ISOCAM in a 2×2 raster mode using two broad band filters centered at 6.75 μm (LW2), and 15 μm (LW3) and a 6 arcsec pixel field of view. The mid-IR maps cover the Cartwheel galaxy and the two nearby companions G1 and G2. Arp 10 was observed in a similar configuration using though a 3 arcsec PFOV. On the other hand, Arp 118 was sufficiently bright in the mid-IR so that we could obtain a full mid-IR spectrum of a 96 $\times$96 arcsec^2 region centered on the galaxy using the circular variable filter (CVF) and a 3 arcsec PFOV.

The standard data reduction procedures described in the ISOCAM[1] manual were followed. Dark subtraction was performed using a model of the secular evolution of ISOCAM's dark current. Cosmic rays were removed using a multi-resolution median filtering method while the memory effects of the detector were corrected using the so-called IAS transient correction algorithm which is based on an inversion method. The final raster was constructed after using the instrumental flat fields and correcting for the lens field distortion. These methods and their consequences are discussed in detail in Starck et al. (1998).

3. THE SAMPLE

3.1. Arp 10

Arp 10 (= VV 362) is a collisional ring galaxy (distance = 122 Mpc) containing a bright ring, an off-center nucleus and a faint bar. Deep Hα images by Charmandaris et al. (1993) revealed, in addition to the bright outer ring, a very small inner ring and traces of outer ring arcs. A study of its atomic hydrogen content (see Charmandaris & Appleton 1996 and references therein) suggests that the HI disk consists of two main parts: a very irregular outer structure, and a more regular inner disk associated with the main bright optical ring. Evidence for optical shells or ripples in the outer isophotes of the galaxy reminiscent of the ripples seen in some early type systems are present.

Our ISOCAM images (see Fig. 1) clearly show that the mid-IR emission is associated with the bright outer star forming ring and the nucleus. Due to our limited resolution, the small inner ring could not be

[1]The ISOCAM data presented in this paper were analyzed using "CIA", a joint development by the ESA Astrophysics Division and the ISOCAM Consortium. The ISOCAM Consortium is led by the ISOCAM PI, C. Cesarsky, Direction de Sciences de la Matière, C.E.A., France.

discriminated from the nucleus and the mid-IR counterparts of the star formation threshold effects discovered by Charmandaris et al. 1993 could be put in stringent tests. The mid-IR flux from the nucleus (18 mJy in the LW2 filter and 20 mJy in the LW3 filter) represents almost 65% of the total flux in both filters. This is in agreement with the star formation activity on the galaxy since most of the Hα flux originates from the inner ring and nucleus (Charmandaris et al. 1993). The mid-IR color ratio LW3/LW2$\sim$1.1, a value typical in star forming regions of late type galaxies, almost everywhere in Arp 10.

3.2. The Cartwheel

The Cartwheel galaxy was discovered by Zwicky at a distance of 121 Mpc (H_o=75 km s^{-1} Mpc^{-1}). It has a bright outer ring and an inner ring which is connected to the outer one with a series of "spokes" (see Fig. 1 in Higdon 1996). Three small companion galaxies located north and north-east of the ring complete the group. It is still unclear which of the companions is the culprit for the creation of the Cartwheel ring, but it is likely that each of them contains sufficient mass to trigger the generation of the star forming ring (see discussion by Appleton & Struck-Marcell 1996). On-going efforts to simulate the dynamics of the system have been focused on the nearby companion G2 (Bosma priv. comm.) and on the most distant one, G3, (Horellou priv. comm.) which seems to be connected to the Cartwheel with a plume of HI gas (Higdon 1996).

Our ISOCAM observations reveal that one-third of the circumference of Cartwheel's outer ring is detected in the LW2 band (see Fig. 2a). The detected segment of the ring corresponds to the brightest part of the optical ring as defined in the Hα. About 1.4 mJy (60% of the LW2 flux from the outer ring) comes from a hot-spot in the ring, unresolved to our observations, which corresponds to the position of two large HII region complexes.

Interestingly, in the LW3 filter, only the hot-spot is detected (at 7.5 mJy) in the outer ring (Fig. 2b), and the only other emission from the Cartwheel is from the central regions (3.8 mJy in LW3 and 3.6 mJy in LW2). The LW3/LW2 flux ratio, often used as a diagnostic of the intensity of the radiation field, of the hot-spot is 5.2, a value which is among the highest detected in all interacting galaxies of the CAMACTIV sample. For comparison, the highest LW3/LW2 flux ratio detected in the interacting galaxy NGC 4038/39 is only 2.6 and it is found in the region where the two disks overlap (Mirabel et al. 1998).

A clue as to why the hot-spot is different comes from a comparison with radio and optical observations (Higdon 1996). The hot-spot coincides with the peak of the 20 cm and 6 cm radio continuum emission from the ring, and, unlike the rest of the outer ring, shows a sudden drop in HI surface density at that point. Assuming that the HI absorption is not responsible for the drop in surface density, this suggests that most of the cool gas in the hot-spot region is either ionized and/or has already been converted into stars. The very powerful UV radiation field in the hot-spot implied by its radio and Hα emission – the Hα surface density is at least a factor of 3 times higher there compared with the other regions of the ring – would be expected to illuminate a *larger volume* of interstellar grains, thereby boosting the thermal continuum at longer wavelengths sampled by the LW3 filter relative to the shorter wavelength PAH-dominated LW2 emission. For an ideal spherical HII region of radius R, its volume is proportional to R^3 while the volume of the associated photo-dissociation-region (PDR) which has a shell shape would vary as R^2. Hence, the filling factor of the HII regions in a given giant molecular cloud of the ISM would increase with a higher rate than the corresponding PDRs. Moreover, in a strong UV environment, the dissociation of PAH molecules would further diminish their contribution to the LW2 flux.

Although centrally concentrated, the emission from the central regions is resolved and a faint filament of LW2 emission extending to the west of the nucleus follows one of the "spokes" seen in optical images. However, it was initially a surprise for us to detect such a strong signal from the center of the Cartwheel, which had previously been believed to be almost devoid of nuclear activity (Fosbury & Hawarden 1977; Higdon 1995). The center of the Cartwheel exceeds the outer star-forming ring by a factor of 1.6 in LW2 while it has 0.4 times the flux of the outer ring in LW3. The nuclear region has mid-IR colours similar to those of late type galaxies (LW3/LW2 = 1.1), although optically, it has very red colours suggestive of an older stellar population (Struck et al. 1996). As a result of this discovery, follow up CO observations revealed the presence of 1.5$\times$10^9 M$_\odot$ of H_2 in the nuclear regions in agreement with the collisional scenarios (Horellou et al. 1998).

The morphological types of the two nearby companions of the Cartwheel are distinctly different. The eastern companion (G2) is an early type S0 galaxy. This explains the contrast on the LW2 over LW3 emission from the two companion galaxies since in early type galaxies the mid-IR emission is dominated by the old stellar population. The LW2 flux is typically 6 times stronger than the LW3 emission which is consistent with temperatures of $\sim$5000 K. Since the LW2 emission of G2 is just $\sim$4 times stronger than the rms noise of the LW3 emission any expected stellar contribution to the LW3 filter measurement would be below our detection limit. The ratio of LW3 to LW2 flux of G1 is $\sim$1.4, a value found in most normal late type galaxies (see Charmandaris et al. 1999 for more details).

3.3. Arp 118

Arp 118 is one of the three collisional rings which host an identified Seyfert nucleus. Its IR luminosity is L_{IR}=2.5$\times$10^{11} L$_\odot$, almost 10 times higher than other ring galaxies. Moreover, a recent study of its molecular gas (Gao et al. 1995) revealed an extremely disturbed system with the nucleus being displaced off-center suggesting that the elliptical companion which led to the ring formation is a considerable fraction of its mass. The CO luminosity is twice that of Arp 220 and its velocity width (650 km s^{-1}) is 2-3 times higher than most ring galaxies.

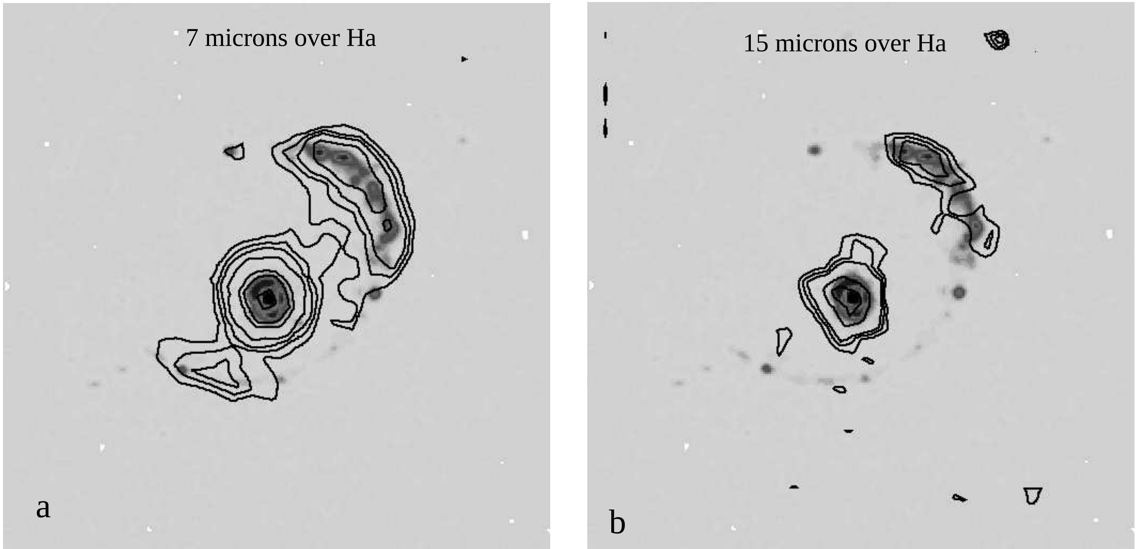

Figure 1. *Arp 10: a) Contour map of the ISOCAM LW2 emission overlayed on an Hα image (Fig. 3 of Charmandaris et al. 1993). The contour levels are 0.2, 0.25, 0.3, 0.4, 0.8, 1 and 1.5 mJy/pixel. b) Contour map of the ISOCAM LW3 emission overlayed on the same Hα image. The contour levels are 0.3, 0.4, 0.5, 1 and 1.5 mJy/pixel. North is up and East is left in both images.*

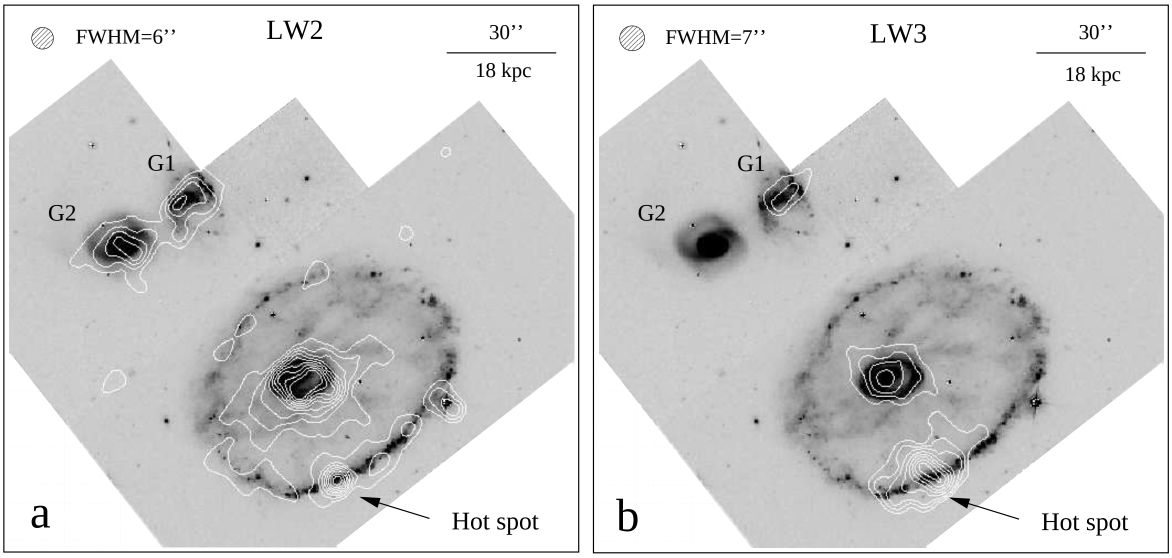

Figure 2. *The Cartwheel: a) Contour map of the ISOCAM LW2 emission overlayed on an HST wide I band image. The contour levels are from 0.1 to 0.5 mJy/pixel with a step of 0.05 mJy/pixel. b) Contour map of the ISOCAM LW3 emission overlayed on the same HST image. The contour levels are 0.2, 0.3, 0.4, 0.6, 0.8, 1, 1.2 and 1.4 mJy/pixel. North is up and East is left in both images.*

Since its mid-IR emission is very strong, this is the only ring galaxy studied with ISOCAM for which a complete CVF scan has been performed. The analysis and interpretation of the data is still in progress. However, we present here one of the most interesting results, that is the identification in the mid-IR of the AGN signature from the Seyfert nucleus. The details of this method are discussed in Laurent et al. (these proceedings) and the application to Arp 118 is presented in Fig. 3.

4. CONCLUSIONS

Our analysis of a sample of these three ring galaxies suggests that:

1) Most of the mid-IR emission (the nucleus of the Cartwheel being the only exception) is associated with the star forming regions of the galaxies.

2) The broad band mid-IR colors of Arp 10 are typical of those found is star forming regions of late type spirals. There is a one to one correspondence between the Hα and mid-IR emission.

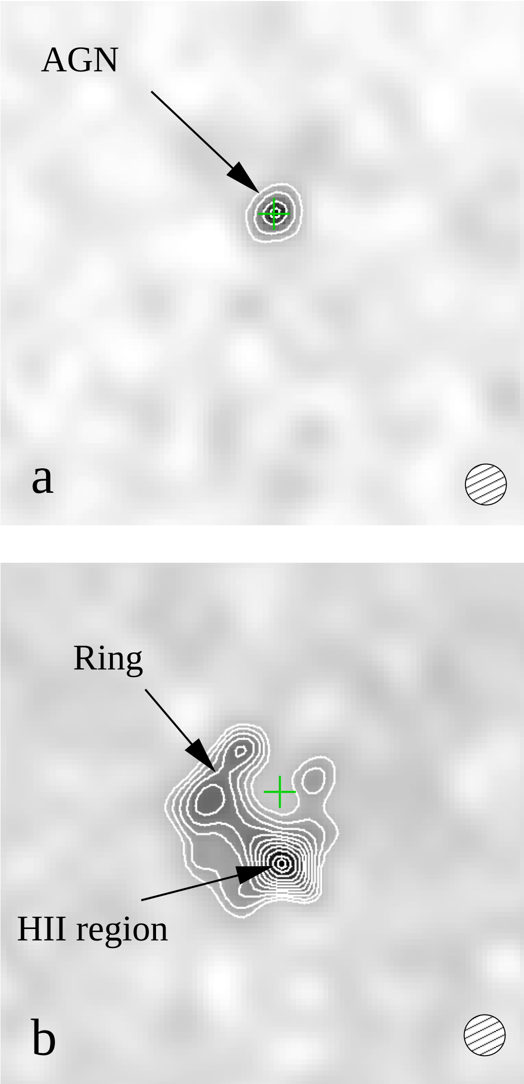

Figure 3. *Arp 118: a) Intensity map of the ISOCAM CVF [5.1-6.7]μm continuum emission. Only one source is detected and it coincides with the Seyfert 2 nucleus of the galaxy marked with a cross. b) Intensity map of the PAH emission in the same range as before with the hot AGN continuum subtracted. The peak emission coincides with the giant extranuclear HII region (see Gao et al. 1997 for more details and images).*

3) A large fraction of the mid-IR emission of the Cartwheel, is associated with the inner ring and nucleus, in stark contrast to that expected from optical emission-line studies (where most of the line emission originates from the outer ring). Recently faint Hα emission has been detected from the inner ring and it is possible that this may be due to a low-level star formation which heats the grains. However, in order to explain why the nuclear emission is so powerful compared with that of the outer ring at ISOCAM wavelengths, it seems that the dust in the outer ring must be spatially distributed very differently. One possibility is that the grains in the outer ring experience a significantly diluted UV radiation field because they are lifted out of the disk by stronger stellar winds. Alternatively, the nuclear regions may be heated by a very different process than the outer, for example shock waves from infalling clouds (Struck et al. 1996). Recent detection of molecular gas (Horellou et al. 1998) further strengthens the probability of this scenario.

4) The CVF spectrum of Arp 118 clearly suggests that the UIB features are associated with the massive star forming regions of the ring. A hot continuum emission [5.1–6.7]μm from the Seyfert nucleus is detected in agreement with the classification scheme proposed by Laurent et al. (these proceedings).

ACKNOWLEDGMENTS

V.C. is grateful to P.N. Appleton and C. Struck (Iowa State Univ.), F. Combes (Obs. de Paris) and C. Horellou (Onsala Space Obs.) for useful comments and discussions.

REFERENCES

Amram, P., Mendes de Oliveira, C., Boulesteix, J., Balkowski, C., 1998, A&A 330, 881

Appleton, P.N., Struck-Marcell, C., 1996, Fund. of Cos. Phys. 16, 111

Appleton, P.N., Marston, A. 1997, AJ 113, 201

Charmandaris, V., Appleton, P.N., Marston, A. 1993, ApJ 414, 154

Charmandaris, V., Appleton, P.N. 1996, ApJ 460, 686

Charmandaris, V., Laurent, O., Mirabel, I.F et al. 1999, A&A, 341, 69

Fosbury, R., Hawarden, T. 1977, MNRAS 178, 473

Gao, Y., Solomon, P.M., Downes, D., Radford, S.J.E. 1997, ApJ 481, L35

Higdon, J. 1995, ApJ 455, 524

Higdon, J. 1996, ApJ 467, 241

Horellou, C., Charmandaris, V., Combes, F. et al., 1998, A&A, 340, L51

Lynds, R., Toomre, A., 1976, ApJ 209, 382

Mirabel, I.F., Vigroux, L., Charmandaris V. et al. 1998, A&A 333, L1

Starck, J.-L., Abergel, A., Aussel, H. et al. 1998, A&AS 133, (in press)

Struck, C., Appleton, P.N., Borne, K.D., Lucas, R.A. 1996, AJ 112, 1868

Theys, J., Spiegel, E. 1976, ApJ 212, 616

ISOCAM OBSERVATIONS OF COMPACT HII REGIONS IN THE LARGE MAGELLANIC CLOUD

F. Comerón[1] & P. Claes[2]

[1]European Southern Observatory, Garching bei München, Germany
[2]ESTEC, European Space Agency, Noordwijk, The Netherlands

ABSTRACT

ISOCAM images at 15 μm are presented of five fields in the Large Magellanic Cloud, suspected to contain ultracompact HII regions from the existence of IRAS point sources with typical colors of these objects. The dramatic improvement in angular resolution provided by ISOCAM has allowed us to identify true compact objects in some of the fields, and to assess the reliability of IRAS-based criteria. The resolution of ISOCAM at the distance of the Magellanic Clouds does not allow to discern between compact and ultracompact HII regions. However, comparison to aperture synthesis radio surveys can be used to discriminate between both kind of objects. In this way, we show that two of the three bright point sources seem indeed to be ultracompact. Our observations provide a first sample of objects suitable for studies of early stages of the life of massive stars in an environment of much lower metallicity than that of our Galaxy.

Key words: massive star formation; ultracompact HII regions; Magellanic Clouds

1. INTRODUCTION

Ultracompact HII regions are the first observational manifestations of recently born massive stars (Churchwell 1990). Their sizes are below 0.1 pc across, and the high densities of associated warm dust make them the brightest point sources of the Galaxy in the mid- and far-infrared. In turn, the high density of ionized gas produces HII regions optically thick even at frequencies as high as 5 GHz. Besides their intrinsic interest as astrophysical objects, they are important to understand the intermediate stages of the process by which a massive protostellar core turns into an emerged bright star, the accompanying dynamical processes of accretion, the chemical transformations that follow the onset of a powerful ultraviolet radiation field in the interior of the parental molecular core, and the role of massive stars in the destruction of molecular clouds. They are probes of the ongoing large scale star forming activity of a galaxy and of the initial mass function at the high mass end. However, observational studies of ultracompact HII regions are usually hampered by the need of high spatial resolution, which so far has restricted the studies of these objects to our own Galaxy, and by the fact that they are bright only at mid- and far-infrared wavelengths and in the radio domain.

ISOCAM imaged at 15 μm five fields in the Large Magellanic Cloud (LMC) suspected to contain ultracompact HII regions. The selection of fields was based on the existence of sources unresolved by IRAS with far-infrared colors typical of galactic ultracompact HII regions. Given the small linear size of these objects, the IRAS beam was heavily contaminated by unrelated LMC sources, making color selection criteria much less reliable than in our Galaxy. The dramatic improvement in angular resolution provided by ISOCAM has allowed us to identify true compact objects in some of the fields, yielding important clues on their nature and morphology. Unfortunately, the angular resolution of ISOCAM at 15 μm is still insufficient to discern between compact and ultracompact HII regions. However, we show here that much more insight can be gained when combining our ISOCAM observations with published aperture synthesis radio surveys, enabling us to establish the ultracompact nature of two of the detected sources and an assessment on the spectral types of the sources embedded in them. The reader is referred to Comerón & Claes (1998) for a more detailed description of the present work.

2. SOURCE SELECTION AND ISOCAM OBSERVATIONS

In an analysis of the IRAS Point Source Catalog, Wood & Churchwell (1989) found mid-infrared color criteria allowing the construction of very complete and uncontaminated samples of galactic ultracompact HII regions. Therefore, we used those criteria to select our list of targets in the LMC, centering our pointings at the positions of the brightest sources in the IRAS Point Source Catalog in the direction of the LMC with colors consistent with them being ultracompact HII regions. The observations were carried out between July and November 1997. The ISOCAM filter LW9 (15 μm) was used. Each observation consisted of a microscan using the $1.5'' \times 1.''5$ pixel field of view, with six exposures of 2.1 s taken on each of

Proceedings of the Conference "The Universe as seen by ISO", Paris, France, 20–23 October 1998 (ESA SP-427, March 1999)

the 4 microscan positions. The data were reduced using the ISOCAM Interactive Analysis package. Transients in the detector response were corrected using the Saclay model. Five fields were observed, with three bright point sources detected.

3. RESULTS

3.1. How to tell ultracompact HII regions from other objects?

Although we used the color-color criteria of Wood & Churchwell (1989) to select a suitable target list, it is doubtful that these criteria can be applied to Magellanic Cloud sources, because much more extended objects at their distance would be unresolved as well. With ISOCAM, it is possible to resolve at 15 μm parsec-sized structures in the Magellanic Clouds, but this resolution is not enough to separate compact from ultracompact regions. Fortunately, high resolution radiosurveys at centimeter wavelengths (Marx et al. 1997) can complement mid-infrared observations in order to recognize true ultracompact HII regions in the Magellanic Clouds, based on their high turnoff frequencies. Therefore, we will consider as likely ultracompact HII regions sources that fulfil these conditions:

- Appearing as bright point sources at 15 μm.
- Having no compact radio counterpart at frequencies below 5 GHz, or having a compact radio counterpart with spectral index close to 2 (i.e., optically thick) at those wavelengths.

3.2. Are the sources that we detect ultracompact HII regions?

Figures 1 shows the fields where bright point sources were detected. Scaling the typical spectral energy distribution of a galactic ultracompact HII region to the observed flux at 15 μm, the three point sources in LI-LMC 1501 and 1518 (object designation from Schwering & Israel 1990) have luminosities typical of HII regions excited by O type stars. LI-LMC 1518 has a compact radio counterpart, appearing as a point source at our 3$''$ resolution, with a slightly negative spectral index between 1.4 and 2.4 GHz, and a flux ratio (15 μm / 2.4 GHz) of 125, characteristic of compact HII regions: we do *not* consider it to be ultracompact. However, none of the components of LI-LMC 1501 is detected at either 1.4 or 2.4 GHz in the survey of Marx et al. (1997), implying flux ratios (15 μm / 2.4 GHz) larger than 250 and 150 for the bright and faint components, respectively. LI-LMC 1501 is detected at lower resolution (about 8$''$) in another survey at similar frequencies (Hunt & Whiteoak 1994), but with positive spectral index between 1.4 and 4.8 GHz. We interpret this as an indication of the emission being produced in a moderately extended HII region (undetectable in higher resolution observations) with optically thick embedded point sources. We therefore consider that the two point sources in LI-LMC 1501 are likely to be true ultracompact HII regions.

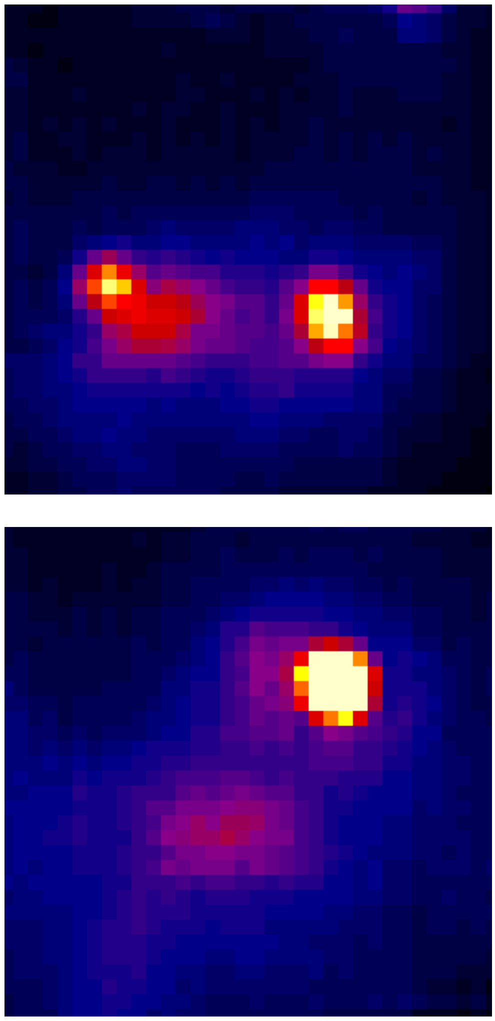

Figure 1. The three compact HII regions observed by ISOCAM at 15 μm, in the area of the LMC Complex N159. The LMC 1501 sources (top figure) do not have a compact counterpart detected down to a level of 6 mJy at 2.4 GHz, what suggests that they are ultracompact HII regions. This is not the case for LI-LMC 1518, which seems to be a compact (but not ultracompact) HII region. The imaged areas are 51$''\times$ 51$''$, i.e., 12.5 pc $\times$ 12.5 pc at the distance of the LMC.

3.3. The ionizing stars

Although they are not directly observable, something can be said about the ionizing stars of the compact HII regions. We assume that:

- Practically all the luminosity of the star is ultimately reemitted by the surrounding dust;
- The spectral energy distributions of all the compact HII regions are similar to those of typical galactic HII regions;
- Practically all the luminosity input of the region is provided by a single star.

Under these assumptions, it is possible to estimate the luminosity and spectral type of the embedded star. In this way, we obtain:

LI-LMC 1518: ionized by a star with luminosity 1.3×10^5 L$_\odot$, spectral type O6V.

LI-LMC 1501-E (left component): ionized by a star with luminosity 5.9×10^4 L$_\odot$, spectral type O7.5V.

LI-LMC 1501-W (right component): ionized by a star with luminosity 1.0×10^5 L$_\odot$, spectral type O7V.

3.4. What about the other fields?

The other three fields observed are presented in Figure 2. They do not contain any bright point sources within the $51'' \times 51''$ field of view. Interpreting the non-detections is not straightforward, but we believe that they may be due to the field size being comparable to the IRAS error box. This is supported by the fact that the (IRAS 12 μm / ISO 15 μm) flux ratio (the latter integrated over the whole frame) is several times larger for the fields without detected bright sources, suggesting that such bright sources may be found just outside the imaged areas.

4. CONCLUSIONS

Three bright, unresolved sources appear in two of our ISOCAM fields. They belong to the HII complex N159, near the 30 Doradus region. One of them is identified with a known compact radiosource, while for the other two no compact radio counterpart has been detected. The lack of radio continuum emission from a point source at 2.4 GHz indicates an infrared to radio continuum flux ratio much higher than in typical compact HII regions, especially considering that the lower metallicity of the LMC, and consequently lower dust contents, should reduce that ratio with respect to typical values in our Galaxy. This large ratio suggests that the two point sources in question are true ultracompact HII regions. The lack of point source emission at 2.4 GHz can be explained by a very high electron density of the emitting region, characteristic of ultracompact HII regions, making them optically thick at frequencies above $\sim$5 GHz. The non-detection of compact radio continuum sources at the positions of the bright infrared point sources, despite of their brightness at 15 μm, can thus be taken as an indication of them being optically thick at that frequency.

The angular resolution of the radio and infrared observations separately is insufficient to reliably pinpoint bona-fide ultracompact HII regions at the distance of the LMC. Nevertheless, our observations demonstrate how their combination can provide insight on the physical conditions of the emitting volume. In this way, the two radio-quiet bright point sources detected by ISOCAM can be considered as the best ultracompact HII region candidates identified so far in a galaxy different from ours. This provides a first sample of objects suitable for future studies of the early stages of massive star formation in an environment of much lower metallicity than that of our Galaxy.

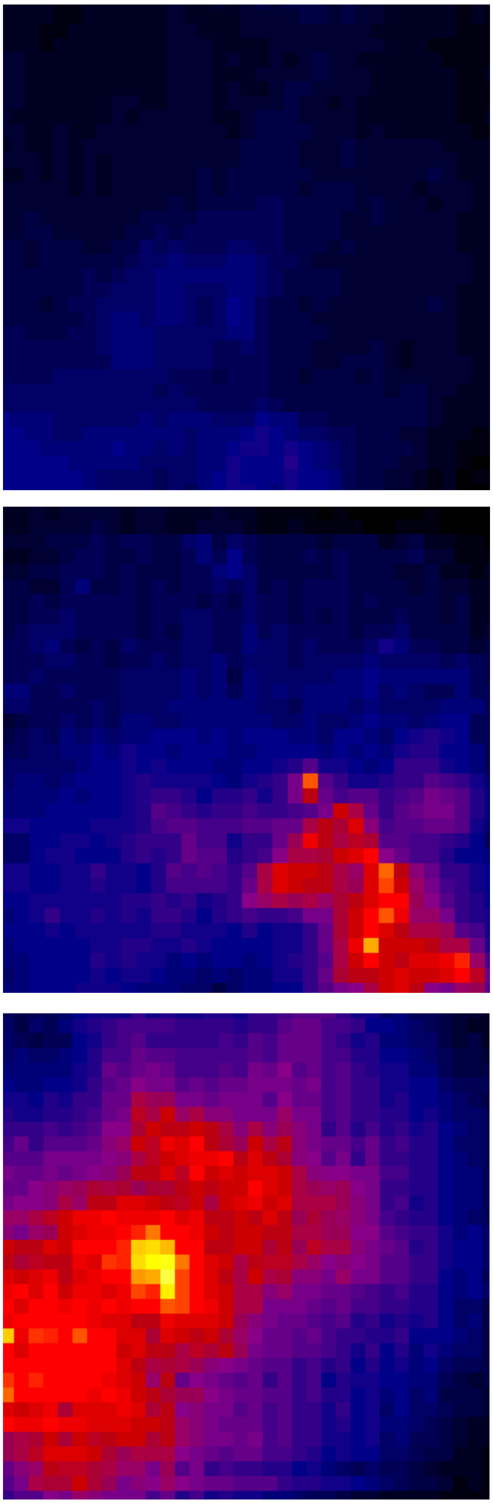

Figure 2. Other fields selected on the basis of IRAS color-color criteria, but where no bright point source was detected. The intensity levels were compressed with respect to those in Figure 1 to enhance structure.

ACKNOWLEDGMENTS

We are pleased to thank the support received at ESTEC and VILSPA during the data entry and the data reduction stages of the work presented here.

REFERENCES

Churchwell, E. 1990, A&AR, 2, 79.

Comerón, F., Claes, P. 1998, A&A, 335, L13.

Hunt, M.R., Whiteoak, J.B. 1994, PASAu, 11, 68.

Marx, M., Dickey, J.M., Mebold, U. 1997, A&AS, 126, 325.

Schwering, P.B.W., Israel, F.P. 1990, "Atlas and catalogue of infrared sources in the Magellanic clouds", Kluwer Acad. Press.

Wood, D.O.S., Churchwell, E. 1989, ApJ, 340, 265.

ISO OBSERVATIONS OF DUST IN ELLIPTICAL GALAXIES

M. Fich[1], **M.P. Rupen**[2], **G.R. Knapp**[3], **L. Malyshkin**[3], **D.A Harper**[4], **& C.G. Wynn-Williams**[5]

[1] Observatoire de Paris, DEMIRM and University of Waterloo, Canada
[2] National Radio Astronomy Observatory
[3] Princeton University
[4] University of Chicago
[5] Institute for Astronomy, University of Hawaii

ABSTRACT

We have mapped 15 elliptical galaxies with ISO using ISOCAM and ISOPHOT at wavelengths from 4.5 to 200 μm. In this paper we will highlight results from CAM (4.5, 6.75 and 15 μm) and PHT-04 (21 μm). These observations should enable us to discern if the dust in the centers of these galaxies is distributed in the same way as the stars or is in discrete clumps at the nucleus. This is crucial to understanding the origin of the 12 and 25 μm IRAS emission and deciding if it is associated with stellar or circumstellar dust as opposed to truly interstellar dust.

Key words: Elliptical Galaxies, Dust

1. INTRODUCTION

Twenty years ago, elliptical galaxies were considered to be devoid of interstellar matter and to consist of an old coeval stellar population established at the time of galaxy formation. As observational sensitivities have improved, it has been found that typical elliptical galaxies contain small amounts of interstellar matter in all its familiar phases, and to have varied and complex star formation histories. IRAS detected weak infrared emission from a significant fraction of nearby elliptical galaxies, allowing the typical global cold interstellar dust (and by inference gas) content to be characterized in these galaxies, its relationship with star formation to be investigated, and the current rate of gas injection via mass loss from evolving stars to be measured (Jura et al. 1987; Knapp et al. 1989). The flux densities emitted by these galaxies are generally very weak, only a few times the r.m.s. noise of the IRAS observations, and are almost always of low statistical significance (see Bregman et al. 1998): also, the IRAS data provide little information on the spatial distribution of the emitting material. The ISO observations described herein were made to measure and map the broad-band emission of a sample of elliptical galaxies from short (4.5μm) to long (200μm) wavelengths to allow the contributions of evolved stars, hot interstellar dust, active nuclei and cold, extended dust to be measured. The much improved sensitivity and mapping capability of ISO are of particular importance to this work.

These observations were obtained under the ISO Guest Investigator Programme. Our goal was to observe as many elliptical galaxies as possible with a wide range of intrinsic properties (blue/red colors; low/high luminosity; detected/not detected by IRAS; with/without a bright AGN; in regions of low and high galaxy spatial density; with relatively strong and weak diffuse X-ray emission; etc.). The strategy was to provide complete wavelength coverage of several galaxies of interest and to provide complementary wavelength coverage for others which were being observed by CAM or PHOT as part of the ISO Core Programme, with the eventual goal of providing maps with complete wavelength coverage for a significant number of elliptical galaxies.

2. OBSERVATIONS AND DATA REDUCTION

2.1. ISOPHOT observations

The ISOPHOT observations were made in two modes. The broadband emission at 60, 100, 135 and 200 μm was measured by the long wavelength arrays to search for cold extended dust (e.g., Haas et al. 1998). These data are not yet in a state of analysis that they can be discussed further here; almost all observed galaxies were detected, including at the longest wavelengths. Observations were also made at 20 μm using the multiaperture photometer (Klaas et al. 1994). Six apertures, from 23″ to the largest, 180″, were used.

Fifteen galaxies were successfully observed: NGC 807, NGC 855, NGC 1052, NGC 1172, IC 2006, NGC 3998, NGC 4261, NGC 4374, NGC 4486 (M87), NGC 4552, NGC 5173, NGC 5363, NGC 5666, IC 1459 and NGC 7768. The data were reduced using the ISOPHOT Interactive Analysis tool PIA (Gabriel et al. 1998). The processing included: subtraction of dark current, deglitching, and correction of the

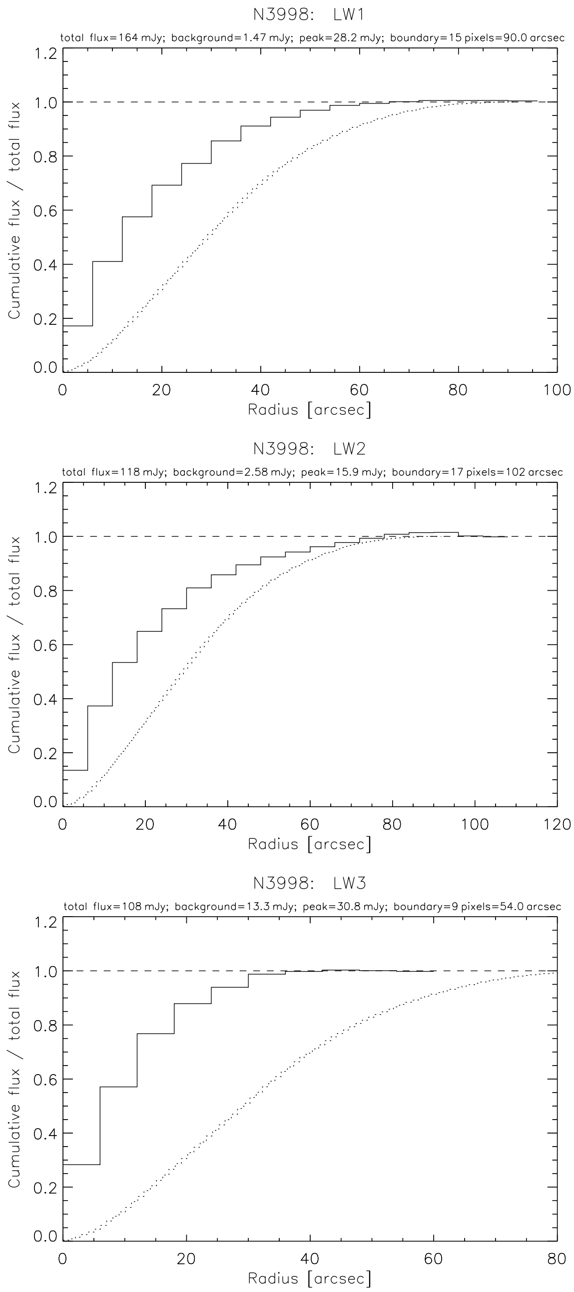

Figure 1. Aperture photometry results for NGC 3998 from ISOCAM. The total flux in each panel is shown at the top of each plot and the horizontal dashed line marks the point at which the cumulative flux reaches this level. The solid line gives the cumulative flux within the specified radius for the ISOCAM filter specified in the title for each panel. The dotted line shows the cumulative flux seen at optical wavelengths.

largest apertures for vignetting. The median differential surface brightness counts were calculated for each aperture.

The photometer is internally calibrated. As a check on the calibration and pointing, we observed three isolated stars with no (known) circumstellar dust: ι Gru, γ Tuc and HR 13. Form these calibration observations we conclude that the instrumental PSF is as measured before launch, and that the flux calibration and pointing of the instrument are good. However, we found evidence of hysteresis, rendering the observations through the smallest aperture relatively low and making the source appear extended on this scale - this is probably due to the weakness of the sources and the brightness of the background (mostly zodiacal light) at this wavelength. The data reduction is described in detail by Knapp et al. (1998).

2.2. ISOCAM observations

The ISOCAM observations were made with three broad-band filters: LW1 (4.5μm central wavelength), LW2 (6.75 μm) and LW3 (15μm). Small galaxies (D_{25} < 2 arcminutes) were observed at a scale of

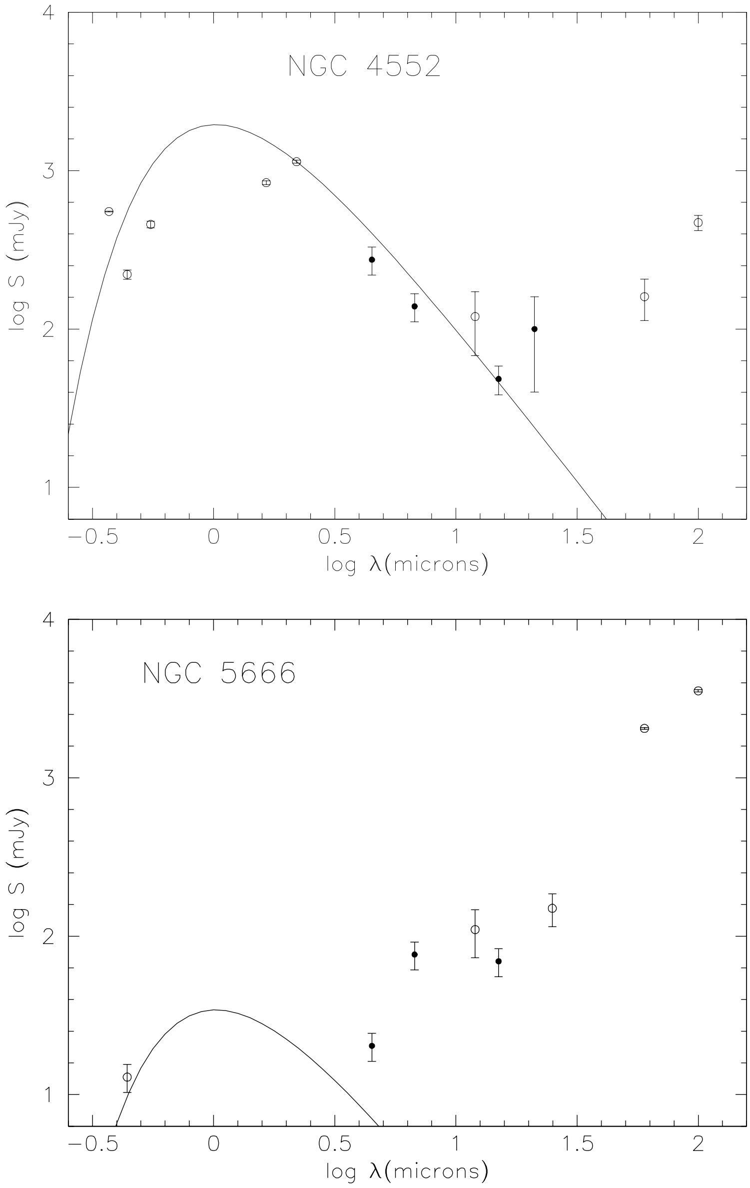

Figure 2. The spectral energy distribution for two quite different cases. Open circles: photometry from NED and Knapp et al. (1989). Filled circles: total fluxes measured by ISOCAM. The solid line shows a 5000 K blackbody spectrum normalized to the 2.2 μm flux density. The top panel shows NGC 4552 which has only a small amount of (cold) interstellar dust. The bottom panel shows the spectral energy distribution for NGC 5666 which is dominated by dust at all infrared wavelengths.

3″ per pixel and a total unvignetted field of about 1.5 arcminutes; larger galaxies at 6″ per pixel and the largest, NGC 4472 and IC 1459, by scans across the galaxy. Although observations were programmed for all three filters, not all of the observations were made. The observed galaxies are: NGC 807 (LW2 only): NGC 855, IC 2006 (LW1 only), NGC 2293 (LW1 only), NGC 2328 (LW3 only), NGC 3998, NGC 4472 (LW1 only), NGC 4552, NGC 5061 (LW2 only), NGC 5666 and IC 1459.

The data were reduced using the ISOCAM Interactive Analysis (CIA) package running under IDL (Ott et al. 1998). Standard instrumental flat fields obtained by the ISOCAM team were used. The sky background was calculated assuming that the corner pixels of the images are free of emission from the galaxy. The preliminary analysis discussed in this paper does not take account of the instrumental point spread function, and the emission centroid is presently determined only as the brightest pixel. The total flux densities were found by performing aperture photometry on the data.

3. RESULTS

Our results are still preliminary. However we have detected at least 10 of the 15 galaxies observed, most of which show evidence of *extended warm/hot dust.* Our ISOCAM data are in good shape, with relatively small uncertainties in the final fluxes and are consistent with prior observations. *Our ISOPHOT-04 data are not yet well understood.* We will refine these observations and continue to work on other relevant ISO data we obtained in this program. We will also continue our program of ground-based submillimeter observations to compare the cold dust content of these galaxies to the warmer dust seen with ISO.

The $20\,\mu$m ISOPHOT observations detected NGC 807, NGC 855, NGC 1052, NGC 3998, NGC 4486, NGC 5666, and IC 1459. The emission for NGC 1052 and NGC 3998 appears to be centrally concentrated and anomalously strong, and likely much of it arises from the active nucleus. The emission from NGC 4486 is extended (almost certainly more than the largest aperture, 180″) and shows no central concentration, i.e. the AGN is not detected. The extension, and the total flux density (2.4 ± 0.8 Jy) shows that this emission arises from the stellar population - it is probably mostly emitted by the circumstellar dust shells produced by mass loss.

Preliminary examination of the ISOCAM data shows that the total flux densities are in reasonable agreement with those expected from the IRAS data. The infrared colors of the galaxies show a wide range, due to the different strengths of different components. The emission from NGC 3998 becomes more concentrated with increasing wavelength (Figure 1) and is a superposition of two components: a hotter component which is distributed like the stars and a cooler unresolved component which may be due to hot dust associated with the active nucleus. NGC 2293 is weakly detected, if at all, but there are several point sources in the field (probably due to the low latitude of this galaxy) which may be confusing the emission. In Figure 2 we show the spectral energy distributions of two of the galaxies we observed, combining IRAS, optical and ISOCAM data. The emission from NGC 4552 is typical of that from a galaxy with little interstellar dust (Figure 2, top panel): the emission observed by ISOCAM arises almost entirely from the starlight, and there is little or no excess emission which can be attributed to interstellar dust. This galaxy shows weak emission at the longer IRAS wavelengths suggesting the possible presence of small amounts of interstellar dust; we should be able to check this with our observations with ISOPHOT. The spectrum of the dusty galaxy NGC 5666 is shown in Figure 2 (bottom). The emission at all wavelengths longer than about 2 μm is dominated by interstellar dust.

As might be expected, given the wide range of galaxy properties our sample contains, we have found a wide range of infrared properties in these galaxies. We expect that, over the next year, we will be able to make significant progress in sorting out the meaning of all of these.

ACKNOWLEDGEMENTS

We wish to express our deepest gratitude to the European Space Agency ESA, to the ISO team and to IPAC for the observing time and data reduction support. This work was partly supported by NASA via grant NAG-3364 to Princeton University.

REFERENCES

Bregman, J.N., Snider, B.A., Grego, L., & Cox, C.V. 1998, ApJ, 499, 670

Gabriel, C., Haas, M., Heinrichsen, I., & Tai, W.M. 1998, ISOPHOT PIA, Version 7.1

Haas, M. 1998, A&A, 337, L1

Jura, M., Kim, D.-W., Knapp, G.R., & Guhathakurta, P. 1987, ApJ, 312, L11

Klaas, U., Krüger, H., Heinrichsen, I., Heske, A., Laurijs, R., & The ISOPHOT Consortium 1994, ISOPHOT Observer's Manual

Knapp, G.R., Guhathakurta, P., Kim, D.-W., & Jura, M. 1989, ApJS, 70, 329

Knapp, G.R., Rupen, M.P., Fich, M., Harper, D.A., & Wynn-Williams, C.G. 1999, in preparation

Ott, S., Delany, M., et al. 1998, CIA Users' Manual V5.0

ISOCAM OBSERVATIONS OF THE INTERACTING GALAXY SYSTEM MRK 171

P. Gallais[1], O. Laurent[1], V. Charmandaris[2,1], D. Rouan[3], I.F. Mirabel[1], M. Sauvage[1], D. Tran[4], & L. Vigroux[1]

[1]CEA/DSM/DAPNIA Service d'Astrophysique, 91 191 Gif-sur-Yvette, France
[2]Observatoire de Paris, DEMIRM, 61 av. de l'Observatoire, 75 014 Paris, France
[3]DESPA, Observatoire de Paris-Meudon, 92 195 Meudon Cedex, France
[4]MPI für Extraterrestrische Physick, Postfach 1603, 85740 Garching, Germany

ABSTRACT

We present mid-infrared observations of Mrk 171, a system of at least two interacting galaxies, which has been observed with the ISOCAM camera in the spectral range 5–16 μm. The comparison of the mid-infrared morphology with that at shorter wavelengths, as well as the overall variation of the spectral energy distribution of the different components leads us to conclude that i) the system is the result of the interaction of ONLY two galaxies, ii) there is no evidence of an active galactic nucleus in the system and iii) intense star formation occurs outside the nucleus of NGC 3690. Mid-infrared observations appear then to be a powerful tool to probe deeply obscured regions harboring either star forming regions or AGNs.

Key words: galaxies: individual: Mrk 171, Arp 299; galaxies: interactions; star: formation

1. INTRODUCTION

At a distance of 42 Mpc, Mrk 171 (Arp 299 = IC 694 + NGC 3690) is one of the nearest interacting galaxies. Because of its proximity, and its intrinsic size (8 kpc), it provides good conditions to explore the effects of star formation activity triggered by an interaction. This system is in a stage of interaction where the main components are close enough to suggest that the outer part of their galactic disks are overlapping/merging (see Angonin et al. 1996) even though the individualities of the galaxies are still conserved.

Mrk 171 has been studied extensively in optical (Augarde and Lequeux 1985), infrared (Gallais 1991; Wynn-Williams et al. 1991; Shudong Zhou et al. 1993; Gehrz et al. 1983; Keto et al. 1997), and radio wavelengths (Gehrz et al. 1983; Zhao et al. 1997; Aalto et al. 1997; Casoli et al. 1998). Based on those observations the overall morphology (see Fig. 1 for details) is characterized by: i) the nuclear region of IC 694 (source A) at the east, ii) the nuclear region of NGC 3690 (source B = B1 + B2) at the south-west and iii) two regions of emission (sources C and C') at the north-west. The nuclear region of NGC 3690 has been resolved in two components, B1 and B2, which have distinct spectral behaviours. At short near-infrared wavelengths (I, J, H bands), the emission from B2 is dominant. On the other hand, the flux of B1 becomes increasingly stronger at longer wavelengths (K, L bands) as well as in the radio while B2 is hardly or not detected (see Fig. 2). It has been suggested that source C could be the nucleus of a third galaxy in the interacting system but this hypothesis is questioned by the location of this source on the [J-H]/[H-K] color-color diagram (Gallais 1991), far from the nuclei locus, and by recent CO observations (Aalto et al. 1997; Casoli et al. 1998) which suggest that this source, associated to the source C', could be attributed to star forming complexes in the overlap region of the two galactic disks.

High resolution HST observations in the visible revealed a clumpy distribution in NGC 3690 at a very small spatial scale, showing emission from at least 4 components in the B region. Adaptive optics near-infrared imaging reveals even more (a dozen) unresolved ($\theta < 0.3$ arcsec) knots at K (Lai et al. 1998). Source C is also resolved in several sources of emission. Moreover, while component A is characterized by a flat spectrum at radio wavelengths, its optical spectrum does not show evidence of the presence of an active galactic nucleus (AGN) (Gehrz et al. 1983).

Several questions regarding Mrk 171 are still open to debate:

- how many galaxies are really involved in the interaction ?
- what is the exact position of the nucleus of NGC 3690 ?
- what is the nature of sources C and C' ?
- does the system host any deeply embedded active nuclei ?

Using its capabilities to probe dusty regions, new sensitive mid-infrared (mid-IR) observations of Mrk 171 have been performed with the ISOCAM instrument on-board the ISO spacecraft (Kessler et al. 1996). The preliminary results of these observations are presented in the following sections.

2. OBSERVATIONS AND DATA REDUCTION

Mrk 171 has been observed with ISOCAM (Cesarsky et al. 1996) with the Continuously Variable Filter (CVF), resulting in a full coverage of the spectral range from 5 to 16 μm with a spectral resolution of 40. The pixel size was 1.5 arcsec giving a total field of view of 48 arcsec $\times$ 48 arcsec. The system is then fully mapped with an angular resolution ranging from 3 to 4.5 arcsec. The data reduction and analysis were performed using the CAM Interactive Software (CIA)[1].

Even though the pointing of ISO in the CVF mode has proven to be fairly reliable, we verified the relative astrometry after identification and detailed comparison of all main features of our mid-IR images with those found in a series of existing near-IR and optical images. The shape of their spectral energy distribution as well as possible effects of absorption were taken into account. Absolute astrometry uses the HST WFPC2 archive images as reference.

In order to make a first order estimate for the principal characteristics of the different components of Mrk 171 and compare it with other extragalactic sources of our sample, we use the CVF data set to construct the equivalent images at LW2 and LW3, two of the most commonly used ISOCAM broad band filters. The LW2 [5–8.5 μm] filter is dominated by the PAH-like emission features while the LW3 [12–18 μm] filter mainly samples the thermal signature of hot dust as well as emission from high excitation forbidden lines (i.e. [NeII], [NeIII]). The resulting contours in these filters are presented in Fig. 1, overlaid on HST red images.

3. DISCUSSION

In Fig. 1, we indicate the naming convention adopted by previous authors. Region A corresponds to the central region of IC 694, (the eastern part of Mrk 171), B corresponds to the central region of NGC 3690 at the south-western part, and the 2 northern components of NGC 3690 are addressed as C and C'. The mid-IR fluxes have been measured and are reported in Table 1.

All main components in the system exhibit both high fluxes in both filters and extremely red colors. The flux ratios LW3/LW2, ranging from 2.5 to 6.6, are quite high in regards to the ones measured in other objects such as normal galaxies in which it takes values from 0.7 to 1.2 (Roussel et al. these proceedings) or in the Antennae galaxies in which the brightest spot has a ratio of 2.6 (Mirabel et al. 1998). In Mrk 171, all the components present a very large excess of emission at 15 μm which can be interpreted as an important concentration of hot dust heated by young massive stars and/or as due to a still important extinction at 6 μm, also pointing to a high concentration of dust.

[1]The ISOCAM data presented in this paper were analysed using "CIA", a joint development by the ESA Astrophysics Division and the ISOCAM Consortium. The ISOCAM Consortium is led by the ISOCAM PI, C. Cesarsky, Direction des Sciences de la Matière, C.E.A., France.

If we derive an equivalent IRAS 12 μm flux assuming a power-law SED in the 5–18 μm range, we find that 86% of the overall IRAS 12 μm flux is accounted for by the 4 sources, with A and B1 contributing dominantly (respectively 28 and 44%). If we assume that for each region, the ratio of the 12 μm flux to the bolometric luminosity is the same as for the whole system, then we derive luminosities ranging from 0.3 to $2.\,10^{11}\,L_\odot$, implying that those sources are extraordinary brighter (up to 3 orders of magnitude) than any star forming region in the local universe (for instance, the brightest complexes in M82 exhibit luminosities of "only" $1.5 \times 10^8\,L_\odot$). The star formation mechanism in Mrk 171 is obviously of a remarkably high efficiency; Rouan et al. (1998) reach a same conclusion, based on near-IR adaptive optics observations.

Table 1. Integrated fluxes in the LW2 and LW3 broad band filters. Fluxes are corrected for dilution due to the size of the point spread function.

Source	LW2 (Jy)	LW3 (Jy)	LW3/LW2
A	0.25	1.66	6.6
B	0.57	2.17	3.8
C	0.13	0.52	4.0
C′	0.11	0.28	2.5

3.1. The nuclear region of IC 694

The central region of IC 694 (region A) is clearly recognized in our images. It appears as an unresolved bright source, corresponding to the radio peak observed at 6 and 20 cm by Gehrz et al. (1983). However, in the optical image, there is no such source at this position, indicating a high absorption in the visible, and indeed, an important dust lane crosses A. The observed emission in the optical HST images shows a "patchy" pattern suggesting that what we actually sample is the star forming complexes in the outskirts of an obscured central source. High resolution near-IR imaging confirms this interpretation (Lai et al. 1998).

3.2. The nature of sources C and C'

The nature of source C is not clear. Casoli et al. (1989) had proposed that this source could be associated with the nucleus of a third galaxy while other authors (Keto et al. 1997, Casoli et al. 1998, for instance) support the hypothesis of an extraordinary extra-nuclear starburst. The mid-IR diagnostic flux ratio LW3/LW2 (see Table 1) for region C agrees with the latter interpretation, since it is similar to values found in regions dominated by young massive stars rather than in a post-starburst population. This is also supported by the shape of the full mid-IR spectrum of this region (Gallais et al. 1999).

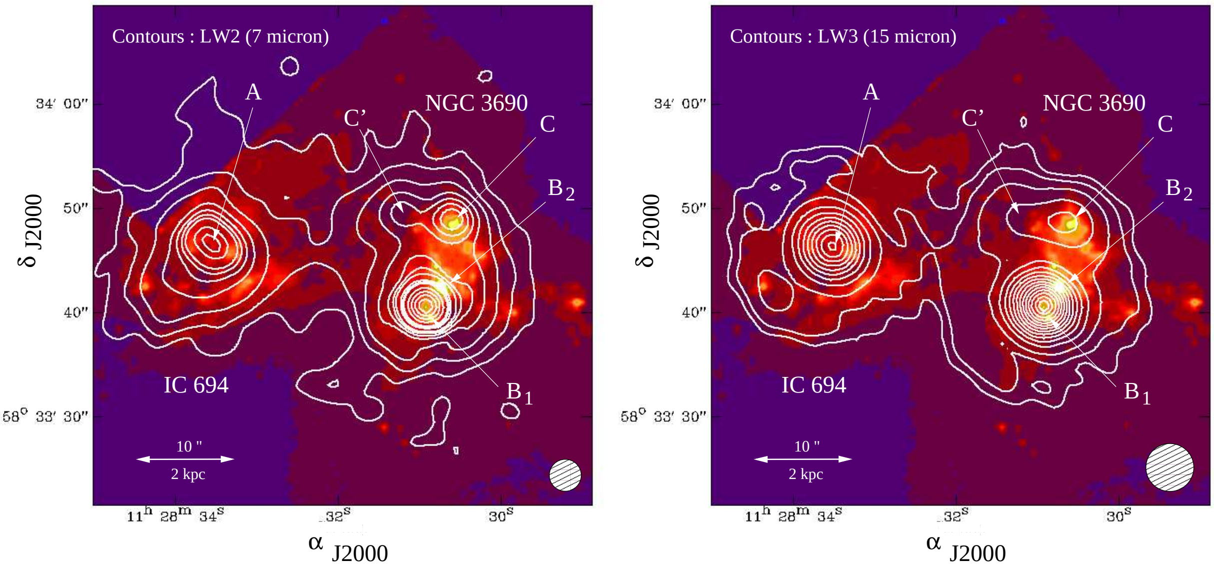

Figure 1. Mid-IR emission in the LW2 and LW3 bands in contours superimposed to the HST WFPC2 red image (593.5 nm). The different regions in the two galaxies are clearly marked.

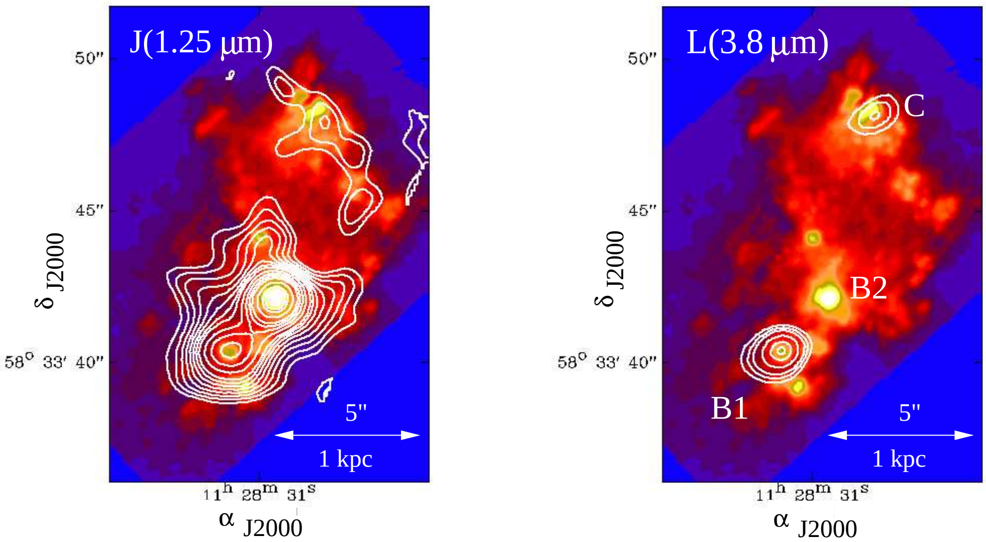

Figure 2. Near-IR J and L band contours (Gallais 1991) of NGC 3690 superimposed on the same HST image. One can clearly see that the flux of region B1 dominates at longer wavelengths, while B2 having a spectral signature of an old stellar population practically disappears.

3.3. The nature of source B

The southern part of NGC 3690 is quite complex:

- HST observations, as well as Adaptive Optics imaging have revealed that the southern part of NGC 3690 is very clumpy and hosts many sources (see Figure 1).
- in the near-infrared, ground-based observations (see Fig. 2), have shown that the bulk of the emission is coming from 2 main sources: B1 and B2 (Gallais 1991, Wynn-Williams et al. 1991). The northern source B2 coincides with an extended source in the HST image, and its near-infrared colour indices indicate an emission typical of an old stellar component while the southern one is very reddened.
- the brightest mid-IR emission coincides very well with near-infrared source B1 which is rather faint and unresolved at optical wavelengths and is not detected in the UV band (see Fig. 3).

These points support the hypothesis that the nucleus of NGC 3690 is located at the position B2 (Gallais 1991, Wynn-Williams et al. 1991), while B1 is an extremely powerful highly obscured star forming region, located at a projected distance of 500 pc from the nucleus. Such a region has already been observed with ISOCAM in the Antennae (NGC 4038/39), where the brightest mid-IR knot is located at about 2 kpc from the nucleus of the galaxy, in a very clumpy region (see Fig. 1 of Mirabel et al. 1998).

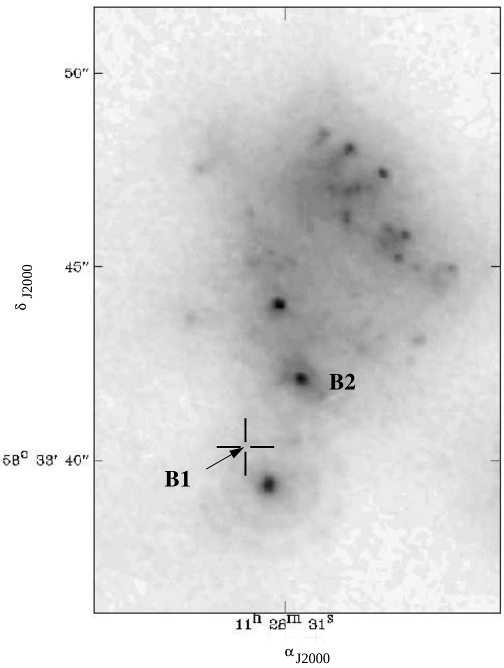

Figure 3. We present a UV image (200 nm) of NGC 3690 taken with the FOC on-board the HST. The position of B1 and B2 are marked. One can see that no emission is associated with B1 confirming its highly obscured nature.

4. CONCLUSIONS

Based on these morphological and qualitative considerations, we can conclude that:

- the intrinsic luminosities of any of the identified source is extremely high, compared to star forming regions in classical nearby starburst galaxy;
- the nucleus of NGC 3690 is located at the position of source B2;
- the emission from region B originates from several sources, of which B1 appears to be an extraordinary active region of star formation ($L_{bol} > 10^{11}\,L_\odot$);
- the emission from sources C and C' can be explained by star formation occurring in tidally distorted regions of the galactic disks;
- there is no evidence of an active nucleus, based on the individual spectra of sources that does not correspond to typical AGN spectra: for instance, all SED exhibit the whole set of PAH-like features.

ACKNOWLEDGMENTS

We thank HST team and PIs of the proposals which provided the WFPC2 and FOC images made with the NASA/ESA Hubble Space Telescope and obtained from data archive at the Space Telescope Science Institute. STScI is operated by the Association of Universities for Research in Astronomy, Inc. under the NASA contract NAS 5-26555.

REFERENCES

Aalto, S., Radford, S.J.E., Scoville, N.Z., Sargent, A.I. 1997, ApJ 475, L107

Angonin-Willaime, M.-C., Casoli, F., Gerin, M., Rouan, D. 1996, CFHT bull 34, 8

Augarde R., Lequeux J. 1985, A&A 147, 273

Casoli, F., Combes, F., Augarde, R., Fignon, P., Martin, J.-M. 1989, A&A 224, 31

Casoli, F., Willaime, M.-C., Viallefond, F., Gerin, M. 1998, submitted to A&A

Cesarsky, C.J., Abergel, A., Agnese P. et al. 1996, A&A 315, L32

Gallais, P., 1991, Thèse de Doctorat de l'Université Paris VII

Gallais, P., Laurent, O., Charmandaris, V., et al. 1999, (in preparation)

Gehrz R.D., Sramek R.A., Weedman D.W., 1983, ApJ 267, 551

Kessler, M.F., Steinz, J.A., Anderegg M.E. et al. 1996, A&A 315, L27

Keto E., Hora J.L., Deutsch L. et al., 1997, ApJ 485, 598

Lai, O., Rouan, D., Alloin, D. 1998, in proceedings of the conference *Astronomy with Adaptive Optics*, Sonthofen, Sep. 1998

Mirabel, I.F., Vigroux, L., Charmandaris, V., Sauvage, M., Gallais, P., Tran, D.Q., Cesarsky, C.J., Madden, S.C., Duc, P.-A. 1998, A&A 333, L1

Rouan, D., Clenet, Y., Lai, O. 1998, in proceedings of the conference *Astronomy with Adaptive Optics*, Sonthofen, Sep. 1998

Vigroux, L. Mirabel, I.F., Altiéri, B. et al. 1996, A&A 315, L93

Wynn-Williams, C.G., Eales, S.A., Beklin, E.E., Hodapp, K.-W., Joseph, R.D., McLean, I.S., Simons, D.A., Wright, G.S. 1991, ApJ 377, 426

Zhao J.-H., Anantharamaiah K.R., Goss W.M., Viallefond F., 1997, ApJ 482, 186

Zhou S., Wynn-Williams C.G., Sanders D.B. 1993, ApJ 409, 149

COLD DUST IN THE ANDROMEDA GALAXY MAPPED BY ISO

M. Haas[1], **D. Lemke**[1], **M. Stickel**[1], **H. Hippelein**[1]
M. Kunkel[1], **U. Herbstmeier**[1], **& K. Mattila**[2]
[1] Max-Planck Institut für Astronomie, Königstuhl 17, 69117 Heidelberg
[2] Helsinki University Observatory, P.O. Box 14, SF-00014 Helsinki, Finland

Figure 1. ISO 175μm map of M31, north is up, east is left. The emission is dominated by a ring structure at 10 kpc radius (50′ along the major axis at PA 39°), with numerous bright condensations and a faint outer ring at 14 kpc. At 175μm - sensitive to cold emission - the warm nucleus is faint as well.

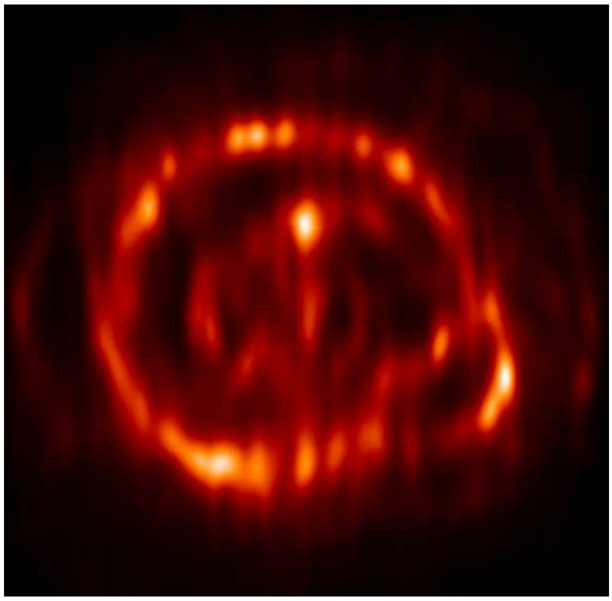

Figure 2. Face-on deprojection of the 175 μm image of M31, adopting a thin disk and an inclination of 75.5°. The major axis lies horizontally, i.e. northeast is on the left. The structure is dominated by the cold ring at 10 kpc radius. No clear spiral pattern is recognisable. The perturbations in the southwest might be caused by the companion galaxy M32.

A complete 175μm map of the Andromeda galaxy (M31) at 1.′3 resolution shows the distribution of cold dust (Fig. 1). It is dominated by a ring at 10 kpc radius supplemented by a faint outer one at 14 kpc. No clear spiral pattern is recognisable (Fig. 2). The azimuthally averaged radial brightness profile is rather flat within the 10 kpc ring and decreases exponentially outside thereof, discernible down to a brightness of 0.07 MJy/sr at a distance of 22 kpc. Since the ring comprises a large reservoir for star formation, as an evolutionary conjecture M31 might be in a transition phase changing its classical optical Sb type spiral morphology towards that of a ringed galaxy. The bulk of the dust has a temperature of only 16 K (Fig. 3), considerably colder than the 21-22 K previously inferred from the IRAS data and also colder than the 19 K found for the Milky Way. The cold dust is accompanied by warm dust, formally described by a component at about 45 K. At the common resolution of 2.′5 the triplet 60/100/175 μm flux ratio varies only little across the rings as well as the disk, thus everywhere in M31 at least two dust components are required to fit the far-infrared spectral energy distribution. This provides a direct evidence in M31 for the existence of two dust populations - small and large grains - similar to what had been found in the Milky Way. For the cold dust component around 16 K we can now estimate the corresponding mass from its emission yielding $3 \cdot 10^7\,M_\odot$, dust mass about a factor of ten higher than inferred from the IRAS 60/100 μm data alone. The new cold dust mass - if evenly distributed in the plane of the galaxy - would be sufficient to make the disk of M31 moderately opaque in the optical (face-on: $0.1\,M_\odot\,pc^{-2}$ corresponding to $\tau_V \approx 0.5$) - see Haas et al. (1998) A&A 338, L33.

Proceedings of the Conference "The Universe as seen by ISO", Paris, France, 20–23 October 1998 (ESA SP-427, March 1999)

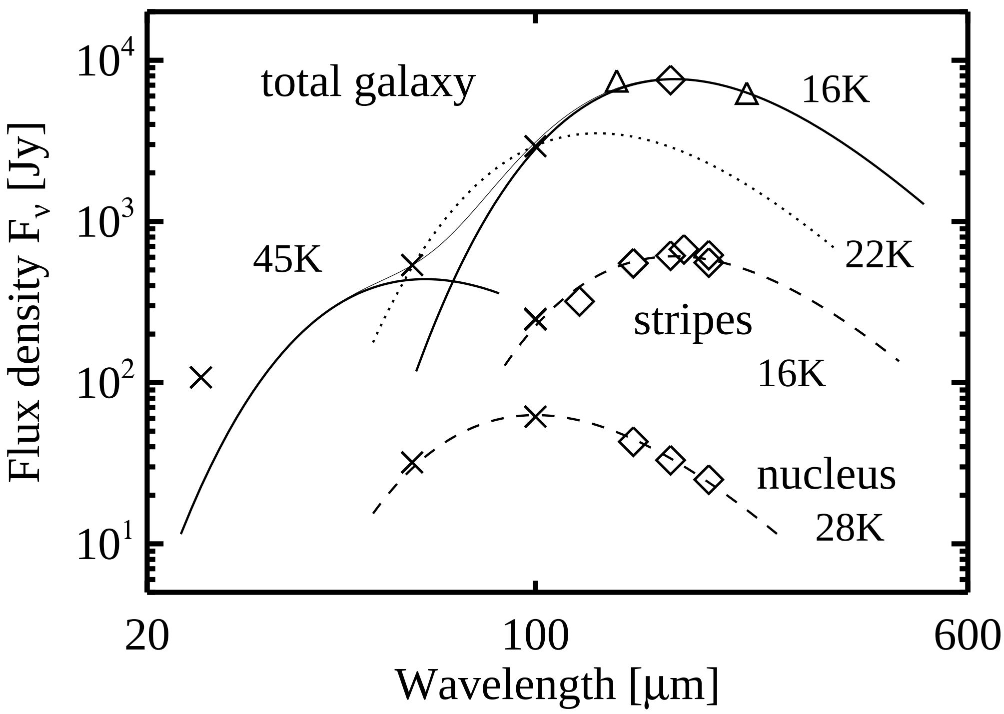

Figure 3. Infrared spectral energy distribution of M31. The data are shown by symbols (diamonds ISO, crosses IRAS, triangles DIRBE) with the size being larger than the errors. The blackbody curves with emissivity proportional to λ^{-2} are shown by lines. The dotted line with T = 22 K through the IRAS 60 and 100 µm data points indicates what one would extrapolate from this wavelength range alone without any further assumptions. The data obtained from the map stripes at various wavelengths clearly determine the shape of the energy distribution. They show that there is actually a maximum around 175µm corresponding to a temperature of 16 K which fits the total flux as well. With respect to the dominating 16 K curve the flux shows an excess at 60 µm, indicating the presence of accompanying warm dust which is here formally described by a 45 K blackbody. The nucleus (4.′5 x 4.′5, 1×4 kpc*) - after subtraction of the disk contribution - has a temperature of 28 K.*

ON THE FAR-INFRARED EMISSION OF QUASARS

M. Haas[1], **R. Chini**[2], **K. Meisenheimer**[1], **M. Stickel**[1],
D. Lemke[1], **U. Klaas**[1], **E. Kreysa**[3], **& S. Müller**[2]

[1] Max-Planck Institut für Astronomie, Königstuhl 17, 69117 Heidelberg
[2]Astronomisches Institut, Ruhr-Universität Bochum, 44780 Bochum, Germany
[3] Max-Planck Institut für Radioastronomie, Auf dem Hügel, 53121 Bonn, Germany

ABSTRACT

As part of the ISO European Central Quasar Programme we obtained the spectral energy distributions between 4.8 and 200 μm for a sample of 71 quasars and radio galaxies, the sample consisting of radio quiet quasars from the PG-catalog, quasars and radio galaxies from the 3C-catalog, flat and steep spectrum radio loud quasars and high redshift radio quasars. First results on bright representative objects are presented.

Key words: quasars; radio galaxies.

1. INTRODUCTION

Unified schemes (Orr & Browne 1982, Barthel 1989) try to explain quasars and radio galaxies as intrinsically similar sources where the observed differences are due to aspect-angle effects: a quasar with flat radio spectrum is observed nearly pole-on so that a beamed jet with superluminal motion causes the bright radio and far-infrared (FIR) appearance; a quasar with steep spectrum is seen at an intermediate angle between pole-on and edge-on; a radio galaxy is viewed nearly edge-on, whereby the nucleus contains an "optical quasar" which is obscured behind a dust torus. Radio quiet quasars share the thermal properties of the radio loud ones, but the lack of magnetic fields near the central engine prohibits the development of a powerful jet which seems to be the origin of the strong synchrotron emission. A check of these schemes is offered via the FIR: If the FIR emission of the dust torus is optically thin and isotropic, then it should show up in the SEDs of all members of a unified class, irrespective of aspect angle.

2. RESULTS

The SEDs (Figure 1) reveal signatures of thermal dust as well as synchrotron emission. In most cases one of the two components is so dominant that the other remains hidden. The SEDs of the radio quiet (e.g. PG 0050+124) and steep spectrum quasars (e.g. 3C48) show a bump around 60μm and a decline longward of 100μm. These spectra provide an impressive confirmation of the hypothesis that the SED of a typical steep spectrum and radio quiet quasar contains a strong far infrared bump due to thermal emission by dust. It can be described as a superposition of several modified blackbodies, showing the broad variety of temperatures from hot ($\approx$600 K) to cool ($\approx$ 30K) dust present in these objects. Ultraluminous IR galaxies are generally cooler and provide much less IR power than quasars, this argues against the interpretation of ULIGs as hidden quasars.

Unification between flat spectrum and steep spectrum quasars: While the FIR spectrum of the steep spectrum quasar 3C48 closely resembles that of other quasars in our sample, the FIR emission of the flat spectrum quasars (e.g. FR 0234+28) is dominated by a strong synchrotron component, smoothly concatenating the mm flux to that observed in the mid-infrared. In one flat spectrum radio quasar we might see thermal and synchrotron emission with similar FIR strength: for the source 3C279 a bump around 20-100μm is prying above the synchrotron spectrum interpolated between the mm and near-infrared range. The upper limits for thermal emission are such that the dust emission of any but the brightest quasars could lie underneath the dominating synchrotron spectra. Therefore Doppler boosted synchrotron emission of a relativistic jet seen almost end-on is consistent with our observed FIR spectra of flat spectrum quasars and does not contradict this unification.

Unification between strong radio galaxies and radio loud quasars: The detection of a strong thermal component in Cyg A similar to 3C48 is evidence of a hidden quasar in this key radio galaxy. On the other hand, 3C20 belongs to the same class of powerful radio galaxies, but could not be detected by ISOPHOT to a level which is at least 2 times lower than that of 3C48. On a one to one base this would argue

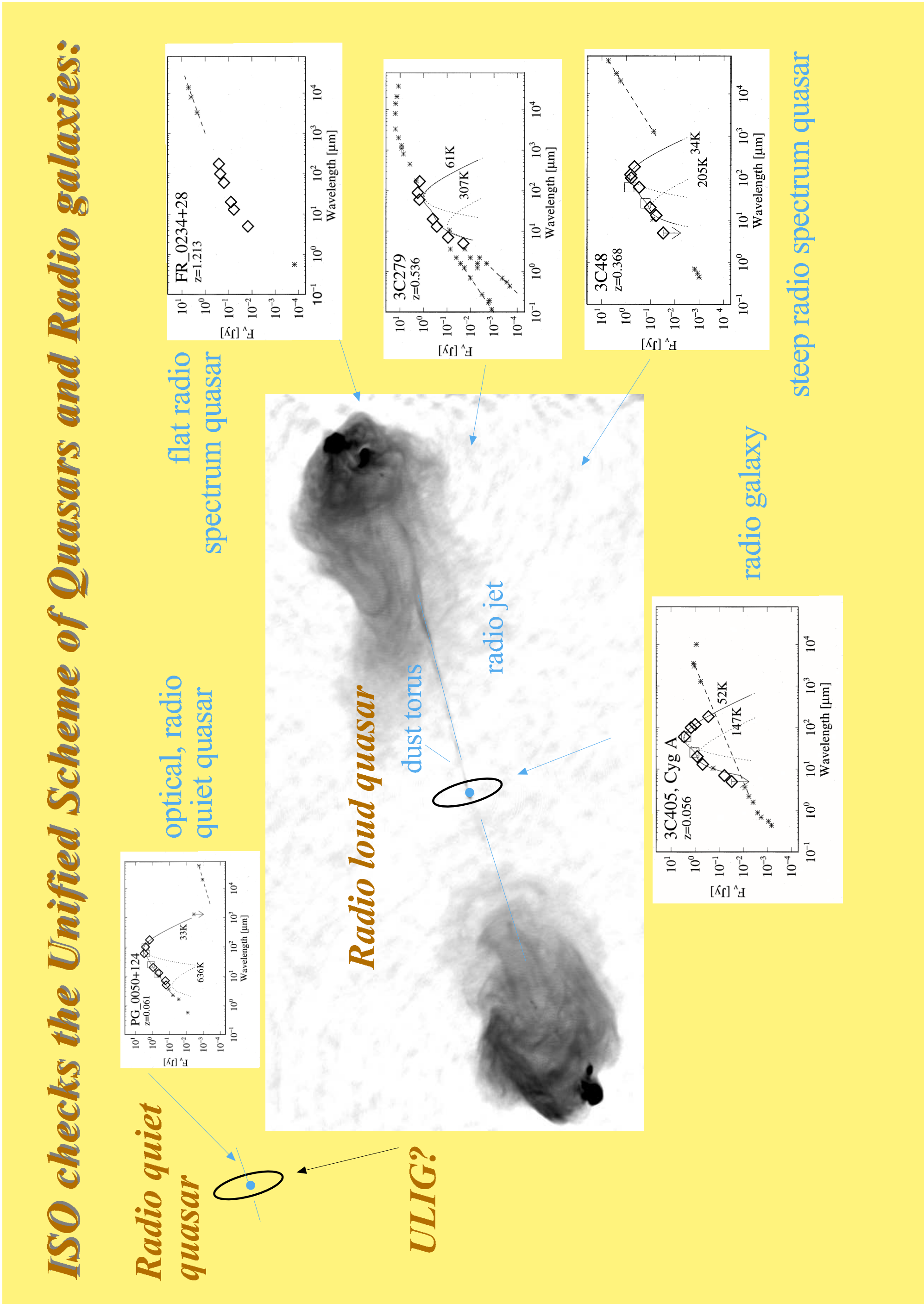

Figure 1. Illustration of the unified schemes and the SEDs

against this general unification scheme. Much better statistics on the correlation of extended radio power and L_{dust} is required before final conclusions from the FIR view about the unification between radio galaxies and quasars can be drawn. The completion of the ISO Central Quasar Programme should provide a sufficiently broad statistical basis to settle this important issue. Further reading: Haas et al. (1998).

REFERENCES

Barthel, P. 1989, ApJ, 336, 606

Haas, M. et al. 1998, ApJ, 503, L109

Orr, M.J.L. & Browne, I.W.A. 1982, MNRAS, 200, 1067

FAR-INFRARED SPECTROSCOPY AND NEAR-INFRARED IMAGING OF THE ULTRALUMINOUS SEYFERT 1 GALAXY MRK 231

V.I. Harvey[1], S. Satyapal[2], M.L. Luhman[3], J. Fischer[3], P.E. Clegg[4], P. Cox[5], M.A. Greenhouse[2], S.D. Lord[6], M.A. Malkan[7], H.A. Smith[8], L. Spinoglio[9], G.J. Stacey[10], & S.J. Unger[4]

[1]University of Nevada, Las Vegas/NASA Goddard
[2]NASA Goddard Space Flight Center, Greenbelt, MD, USA
[3]Naval Research Laboratory, Washington, DC, USA
[4]Queen Mary & Westfield College, Univ. of London, London, UK
[5]Institut d'Astronomie Spatiale, Orsay, France
[6]California Institute of Technology, IPAC, Pasadena, CA, USA
[7]Univ. of California, Dept. of Astronomy, Los Angeles, CA, USA
[8]Harvard-Smithsonian, CfA, Cambridge, MA, USA
[9]Istituto di Fisica dello Spazio Interplanetario-CNR, Roma, Italy
[10]Cornell University, Astronomy Department, Ithaca, NY, USA

ABSTRACT

We present far-infrared spectroscopy of the ultraluminous infrared Seyfert 1 galaxy Mrk 231 obtained with the ISO Long Wavelength Spectrometer. These far-infrared observations reveal a far-infrared spectrum different from classical starburst galaxies and lower luminosity infrared bright galaxies. Like the prototypical ultraluminous infrared galaxy Arp 220, the far-infrared spectrum shows weak or absent far-infrared emission lines and many strong absorption lines. Near-infrared $3.3\,\mu$m dust feature observations for this source also reveal a $L_{FIR}/L_{3.3\mu m}$ ratio that is higher than that of M82, the prototypical starburst galaxy. We combine these near-infrared imaging observations with the ISO spectroscopy and discuss the origin of the dominant luminosity source in the galaxy.

Key words: galaxies: starburst, active; infrared: galaxies; infrared: ISM: lines and bands.

1. INTRODUCTION

Ultraluminous infrared galaxies (ULIGs) are an important constituent of the local Universe, with luminosities and space densities comparable to those of optically selected quasars (e.g., Soifer et al., 1984, 1987; Sanders & Mirabel 1996). The luminosity in the far-infrared is thought to be a result of dust absorption and subsequent thermal re-radiation of high energy photons. These high energy photons may come from two sources: an active galactic nucleus (AGN) or a compact energetic starburst. Both phenomena are believed to be triggered by the influx of gas into the nuclear region of the galaxy brought about by galaxy interactions. Determining the dominant energy input mechanism in the dust enshrouded nuclear regions of ULIGs has been the focus of much debate.

Mrk 231, at a distance of 253 Mpc (H_0=50 km s^{-1} Mpc^{-1}) is one of the most luminous and best studied nearby ULIGs, with a luminosity of $3.3\times10^{12}\ L_\odot$. This system, considered an advanced merger (Sanders et al. 1987), reveals signatures of both AGN and starburst activity. It has a compact, stellar-like nucleus which is unresolved, and an optical spectrum consisting of broad allowed emission lines and narrow forbidden lines classifying it as a Seyfert 1 (Boksenberg et al. 1977, Lipari et al. 1994). Its optical spectrum is dominated by strong FeII emission features similar to those found in low redshift absorption line quasars (Boroson & Meyers 1992). On the other hand, the detection of blue circumnuclear stellar clusters (Hutchings & Neff 1987), the presence of a circumnuclear structure of hot molecular gas 2.5 kpc in diameter revealed by near-infrared H_2 observations (Krabbe et al. 1997), and the detection of CO absorption bands in the nucleus (Krabbe et al. 1997) suggest the coexistence of energetic starburst activity. In addition, no fine structure lines from highly ionized species, a standard signature of AGN-dominated activity, are detected in the near- (e.g., [SIV]; Krabbe et al. 1997) or mid-infrared (e.g., [OIV], [NeV]; Genzel et al. 1998).

We present ISO far-infrared observations of Mrk 231. Using these observations and $3.3\,\mu$m dust feature imaging observations, we discuss the origin of the dominant luminosity source in this galaxy.

Proceedings of the Conference "The Universe as seen by ISO", Paris, France, 20–23 October 1998 (ESA SP-427, March 1999)

2. OBSERVATIONS AND DATA REDUCTION

2.1. ISO observations

As part of the ISO LWS Consortium's extragalactic guaranteed-time program on infrared-bright galaxies, we obtained a full 43 to 197 μm low resolution (R$\sim$200) spectrum of Mrk 231 on 1996 May 15. The position of the ISO $\sim$70 arcsec beam was $\alpha(2000)=$ 12h56m14.2s; $\delta(2000)=$ 56^{o}52m24.9s. Two data sets were obtained. Removal of cosmic ray glitches, dark current subtraction, wavelength and flux calibration, and correction for instrumental responsivity variations was carried out using the ISO LWS Pipeline 7 (Swinyard et al. 1996). Subsequent data processing, including co-addition and spectral line-fitting, was carried out using the ISO Spectral Analysis Package (ISAP). The absolute flux calibration error, determined by comparing overlapping data in neighboring detectors was 25 per cent. The total integration time for the full grating scan was 3,000 seconds.

2.2. Near-infrared dust feature observations

Narrowband (R=50) imaging observations of Mrk 231 were obtained on 1998 April 24 and 25 at the NASA Infrared Telescope Facility (IRTF) 3 m telescope. The NSFCAM 256$\times$256 InSb array camera was used with the circular variable filter (CVF) centered on the redshifted 3.29 μm dust feature and two neighboring continuum wavelength positions. The data set consisted of 48 images at the online wavelength and 24 images at each of the continuum wavelengths. The integration time per image was 1 second, with 20 coadds per frame. The platescale was 0.148 arcsec per pixel and the FWHM of the point spread function was $\sim$ 0.8. The images were calibrated using the standard star ρ Virgo (spectral type A0 V; $M_{3.3\,\mu m}$=4.68 magnitudes).

The Image Reduction and Analysis Facility (IRAF) was used to reduce the data. All images were background-subtracted, divided by flat fields at the corresponding wavelengths, and flux calibrated. Images at the same wavelengths were spatially registered with the XREGISTER package using a discrete cross-correlation function and coadded using the IMCOMBINE routine. An image of the feature flux was generated by subtracting the average continuum image from the final online image.

3. RESULTS

The far-infrared spectrum of Mrk 231 is shown in Figure 1 (top). Also included is the far-infrared spectrum of M82 (Colbert et al. 1999), the prototypical starburst galaxy. As seen from the figure, the spectrum of Mrk 231 is significantly different from that of M82. While the spectrum of M82 is characterized by several fine structure emission lines, there is a dearth of these emission lines in the spectrum of Mrk 231. However, the Mrk 231 spectrum exhibits many molecular absorption features. Particularly prominent is the OH radical. Also noticeable is the [CII] 158 μm fine structure line (redshifted to 165 μm) and the [OI] 63 μm emission line (redshifted to 65 μm) emission line, both of which are weaker than in the starburst galaxy.

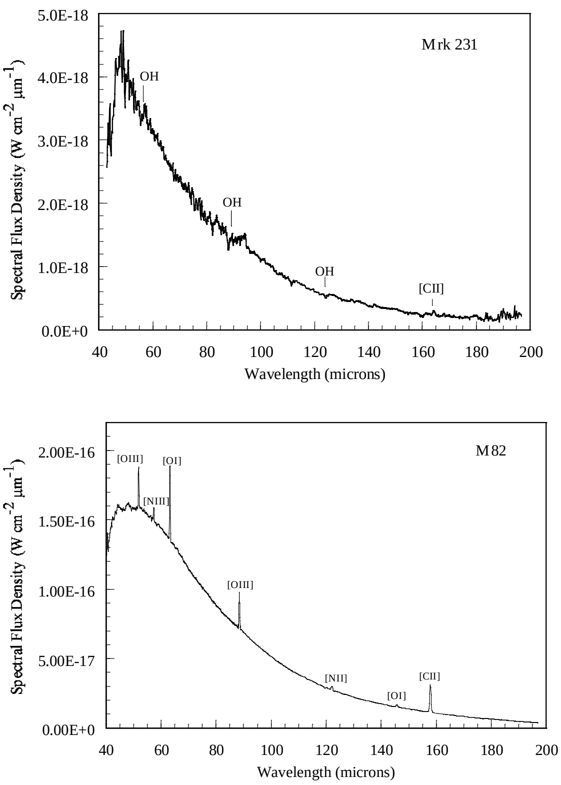

Figure 1. ISO LWS spectrum of Mrk 231 (this paper) and M82 (Colbert et al. 1999).

Our 3.29 μm dust feature observations are displayed in Figure 2. Using the total flux in a 5 arcsec aperture from the online and offline images, no dust emission feature was detected. The 3 σ upper limit for the flux gives a ratio $L_{FIR}/L_{3.3\,\mu m} > 3.0 \times 10^4$. This value is much greater than that found for the prototypical starburst galaxy M82, where $L_{FIR}/L_{3.3\,\mu m} = 1.8 \times 10^3$ (Satyapal et al. 1995).

4. DISCUSSION

4.1. Dust feature observations

The 3.29 μm dust feature is a member of a family of near-infrared dust features at 3.3, 6.2, 7.7, 8.7, and 11.3 μm. Though the emission is not well understood, it is believed to come from hydrogenated carbon grains (Léger & Puget 1984), called polycyclic aromatic hydrocarbons (PAHs), undergoing vibrational transitions due to UV photons impinging upon the grains (Dennefeld & Désert 1990). These grains are about 10 Angstroms in size and consist of approximately 50 atoms. Imaging in the 3.29 μm emission feature can be used as a tool to discriminate between

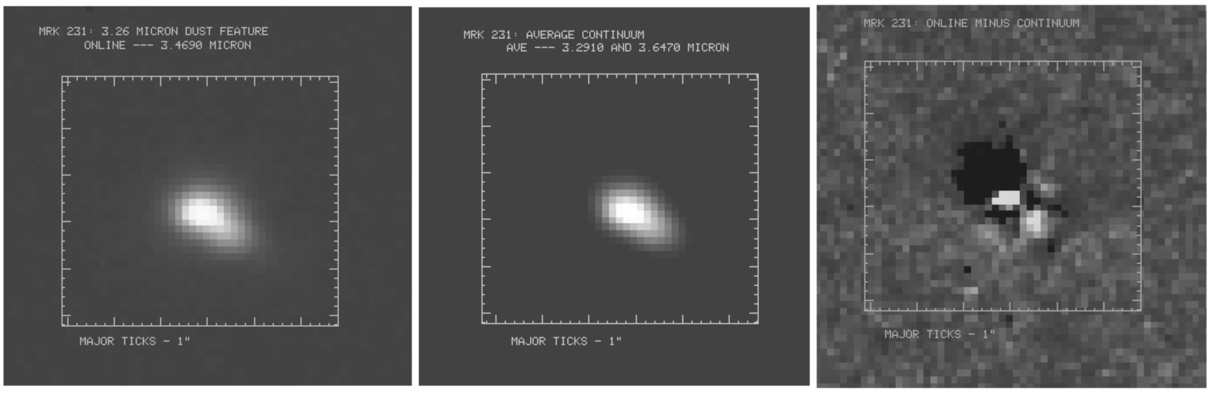

Figure 2. Online + continuum, continuum, and continuum-subtracted 3.29μm dust feature observations of Mrk 231. Major tick separation–1 arcsec.

star formation activity and the effects of an active nucleus. This feature has been widely observed in starburst galaxies but rarely in AGNs, suggesting that the presence of this feature is associated with star formation activity in the nuclear regions of galaxies (Aitken & Roche 1985). Empirically, the ratio of the total far-infrared luminosity to the 3.29μm feature luminosity has been found to be roughly constant for a number of starburst galaxies (e.g., Dennefeld & Désert 1990, Mouri et al. 1990), suggesting that the feature emission is a measure of star formation activity in starburst galaxies, where the large far-infrared luminosities are generally attributed to young stars. High spatial resolution imaging in this feature reveals a striking similarity with the Brγ emission in the prototype starburst, M82 (Satyapal et al. 1995), suggesting that the feature emission can be used as a high resolution probe of the regions of active star formation in galaxies in which the hydrogen recombination line emission may be contaminated by the effects of an AGN. Near-infrared imaging (Mazzarella et al. 1994) as well as mid-infrared imaging (Miles et al. 1994) of the Seyfert galaxy NGC 7469 reveal an extended annular region of 3.29μm and 11.3μm feature emission around the nucleus. Since this galaxy is known to possess circumnuclear star formation activity (e.g., Heckman et al. 1986, Wilson et al. 1986), this morphology suggests that the 3.29μm feature carriers are destroyed in the harsh radiation field near the AGN, and that the detection of the feature may indicate starburst activity in galaxies harboring an AGN.

We did not detect the dust feature in a 5 arcsec aperture centered on the nucleus of Mrk 231. If the implied high $L_{FIR}/L_{3.3\mu m}$ in Mrk 231 is due to extinction, and the intrinsic ratio is similar to that found in M82, the required extinction would be $A_v > 70$ magnitudes, assuming a foreground screen extinction geometry and a 1.85 dust emissivity power law (Landini et al. 1984).

4.2. Photodissociation region (PDR) gas

In an effort to determine the physical properties of the ensemble PDR component in Mrk 231, we compared the relative strengths of the observed [OI] 63μm and [CII] 158μm lines and total FIR continuum flux to the model predictions of the Kaufman et al. (1998) PDR code. The Kaufman et al. code is an updated version of earlier works stemming from the study by Tielens & Hollenbach (1985). Among other updates to the input physics, the code includes the effects of gas heating associated with the photoelectric ejection of electrons from very small grains (< 15 angstroms) and polycyclic aromatic hydrocarbons (Bakes & Tielens 1994). Comparing the observations to model grids depicting the behavior of [CII] 158μm / [OI] 63μm and ([CII] 158μm + [OI] 63μm) / FIR as a function of gas density n and incident UV flux G_o, we derive an extremely low implied gas density, where $n < 50$ cm^{-3}. This density is lower than that of any extragalactic medium observed to date and is much less than the interstellar gas density implied by CO observations of Mrk 231, e.g., $n \sim$700 cm^{-3} (Solomon et al. 1997). The disagreement with previous observations suggests that an upward correction to the observed [OI] 63μm line is necessary before comparing with the PDR models. Although effects such as very high extinction ($A_v > 1000$) can decrease the observed [OI] 63μm to [CII] 158μm line ratio, self-absorption of the [OI] 63μm line, as seen in the prototypical ULIG Arp 220 (Fischer et al. 1998), is the most likely explanation for a low observed [OI] line flux. To match the density derived from CO data, an upward correction to the [OI] line flux of 2-3 times is required. From the PDR models, correcting the [OI] line flux by this amount corresponds to an incident UV flux G_o of $\sim$3000 times the average interstellar radiation field in the solar neighborhood for $n \sim$700 cm^{-3}. These values of n and G_o resemble those of other ULIGs. In particular, the high ratio of G_o/n (> 1 cm^3) is likely common among ULIGs,where the resultant reduced photoelectric heating has been posed as an explanation for the observed [CII] deficit in ULIGs (Luhman et al. 1998,1999; Malhotra et al. 1997).

4.3. Ionized gas

Our ISO observations reveal that none of the lines from ionized gas seen prominently in the spectrum of M82 (Figure 1) are detected in Mrk 231. The far-infrared spectrum is similar to that seen in the prototypical ULIG, Arp 220 (see Fischer et al. these proceedings), and the low [CII] 158 μm /FIR line flux ratio from Mrk 231 is similar to that found in a sample of ~15 ULIGs studied by Luhman et al. (1998, 1999). However, unlike many of the other ULIGs studied in our program, Mrk 231 is generally considered to be a dust-enshrouded quasar. As mentioned earlier, it shares many characteristics with quasars including a broad, Seyfert 1 optical emission spectrum, optical and radio variability, and a broad-absorption-line spectrum. What fraction of the luminosity is powered by this AGN? The lack of 3.29 μm dust feature emission and the low 7.7 μm dust feature strength found by Genzel et al. (1998) suggest that Mrk 231 is predominantly powered by a hard, AGN-like radiation field. However, such a radiation field should produce strong emission lines from the ionized gas but no such lines are seen in the mid-infrared (Genzel et al. 1998) or the far-infrared. Moreover, not only do we find that Mrk 231 is characterized by small line-to-continuum ratios, but the upper limits on the far-infrared [OIII] lines indicate that the [OIII]/[CII] ratio in Mrk 231 is substantially smaller than that found in the lower luminosity starbursts, M82 and Arp 299, indicating that the radiation field is softer than that found in the prototypical starbursts studied in our program. The line flux deficit in Mrk 231 can be the result of substantial dust absorption of ionizing photons in the central regions of the galaxy. This scenario may explain the warm 25/60 μm IRAS colors of Mrk 231. However, whether the effect of an increased dust-to-gas ratio in Mrk 231 also results in an effective softening of the radiation field needs to be investigated.

5. CONCLUSIONS

The ISO spectrum of Mrk 231 is characterized by the following features: (1) there are only two positive identifications of fine structure emission lines ([OI] 63 μm and [CII] 158 μm) with line strengths much weaker relative to the total infrared luminosity than that seen in the lower luminosity galaxies in our program studied by ISO, and (2) strong molecular absorption lines (OH) are detected. These features show that the far-IR spectrum of Mrk 231 is very different from that of the prototypical starburst galaxy, M82. These differences may be due to dust absorption of ionizing photons, reducing the line fluxes from the ionized and photodissociated gas and softening the radiation field.

Near-infrared dust feature observations reveal that the ratio, $L_{FIR}/L_{3.3\,\mu m} > 3.0 \times 10^4$, is substantially larger than the ratio found in M82. If this high ratio is due to extinction, and the intrinsic ratio is similar to that seen in M82, the visual extinction would be greater than 70 magnitudes, assuming a foreground screen geometry for the obscuring material.

REFERENCES

Aitken, D.K., Roche, P.F. 1985, MNRAS, 213, 777

Bakes, E.L.O., & Tielens, A.G.G.M. 1994, ApJ, 427, 822

Boksenberg, A. and Carswell, R.F., Allen, D.A., Fosbury. A.E., and Penston, M.V., Sargent, W.L.W. 1977, MNRAS, 178, 451

Boroson, T.A., Meyers, K.A. 1992, ApJ, 397, 442

Colbert, et al. 1999, in press

Dennefeld, M., and Désert, F.X. 1990, A&A, 227, 397

Fischer, J., et al. 1998, this conference

Genzel, R., Lutz, D., Sturm, E., Egami, E., Kunze, D., Moorwood, A.F.M., Rigopoulou, D., Spoon, H.W.W., Sternberg, A., Tacconi-Garman, L. E., Tacconi, L., Thatte, N. 1998, ApJ, 498, 579

Heckman, T.M., Beckwith, S.; Blitz, L.; Skrutskie, M., Wilson, A. S. 1986, ApJ, 305, 157

Hutchings, J.B., Neff, S.G. 1987, AJ, 92, 14

Kaufman, M., Wolfire, M.G., Hollenbach, D.J., & Luhman, M.L. 1998, in preparation

Krabbe, A., Colina, L., Thatte, N., Kroker, H. 1997, ApJ, 476, 98

Landini, M., Natta, A., Salinari, P., Oliva, E., Moorwood, A.F.M. 1984, A&A, 134, 284

Léger, A., Puget, J.L. 1984, A&A, 137, L5

Lipari, S., Colina, L., Macchetto, F. 1994, ApJ, 427, 174

Luhman, M.L., et al. 1999, in preparation

Luhman, M.L., et al. 1998, ApJ, 504, L11

Mazzarella, J.M, Voit, G.M., Soifer, B.T., Matthews, K., Graham, J.R., Armus, L., Shupe, D. 1994, AJ, 107, 1274

Malhotra, S., et al. 1997, ApJ, 491, L27

Miles, J.W., Houck, J.R., Hayward, T.L. 1994, ApJ, 425, 37

Mouri, H., Kawara, K., Taniguchi, Y., Nishida, M, 1990, ApJ, 356, L39

Sanders, D.B., Mirabel, I.F. 1996, ARA&A, 34, 749

Sanders, D.B., Young, J.S., Scoville, N.Z., Soifer, B.T., Danielson, G.E. 1987, ApJ, 312, L5

Satyapal, S., Watson, D.M., Pipher, J.L., Forrest, W.J., Coppenbarger, D., Raines Nicholas, S., Libonate, S., Piche, F.; Greenhouse, M.A.; Smith, H.A., Thompson, K.L.; Fischer, J. 1995, ApJ, 448, 611

Soifer, B.T., et al., 1987, ApJ, 320, 238

Soifer, B.T., et al., 1984, ApJ, 278, 71

Solomon, P.M., et al. 1997, ApJ, 478, 144

Swinyard, B.M. et al. 1996, A&A, 315, L43

Wilson, A.S., Baldwin, J.A., Sun, S.-D., Wright, A.E. 1986, ApJ, 310, 121

Tielens, A.G.G.M., & Hollenbach, D. 1985, ApJ, 291, 722

THE US KEY PROJECT ON AGN SPECTRAL ENERGY DISTRIBUTIONS (CHARACTERISTICS OF THE ISO DATA)

E. Hooper[1], B. Wilkes[1], K.K. McLeod[2], M.S. Elvis[1], C. Impey[3], C. Lonsdale[4], M. Malkan[5], & J. McDowell[1]

[1] Harvard-Smithsonian Center for Astrophysics, Cambridge, MA, USA
[2] Wellesley College, Wellesley, MA, USA
[3] Steward Observatory, Tucson, AZ, USA
[4] IPAC, Caltech, Pasadena, CA, USA
[5] UCLA, Los Angeles, CA, USA

ABSTRACT

The US ISO Key Project on quasar spectral energy distributions seeks to better understand the very broad-band emission features of quasars from radio to X-rays. A key element of this project is observations of 72 quasars with the ISOPHOT instrument at 8 bands, from 5 to 200$\,\mu$m. The sample was chosen to span a wide range of redshifts and quasar types. This paper presents an overview of the analysis and reduction techniques, as well as general trends within the data set (comparisons with IRAS fluxes, uncertainties as a function of background sky brightness, and an analysis of vignetting corrections in chopped observing mode). A more detailed look at a few objects in the sample is presented in Wilkes et al. (these proceedings).

Key words: ISOPHOT; infrared astronomy; quasars; spectral energy distributions.

1. INTRODUCTION

A substantial fraction of the bolometric luminosity of many quasars emerges in the infrared (Elvis et al. 1994), from synchrotron radiation and dust. Which of these emission mechanisms is dominant depends on quasar type and is an open question in many cases. Two major ISO observing programs have obtained broad-band photometry for large samples of quasars: a European Central program which focused on low-redshift, predominantly radio-loud quasars; and a US Key Project to examine quasars spanning a wide range of redshifts and SEDs, e.g., X-ray and IR-loud, plus those with unusual continuum shapes.

The final sample for the US Key Project consists of 72 quasars observed with the ISOPHOT instrument (Lemke et al. 1996) in most or all of the following bands: 5, 7, 12, 25, 60, 100, 135, and 200$\,\mu$m. Ninety percent of the quasars in the sample have redshifts $z < 1$, while the remaining 10% lie in the range $2 < z < 4.7$ (see Hooper et al. 1999 for a plot of absolute blue magnitude vs. redshift for the sample). More than half of the sample consists of luminous X-ray sources, 25% are strong UV emitters, and smaller subgroups contain strong infrared sources, X-ray-quiet objects, red quasars, and BALQSOs. The infrared data points will be combined with all available fluxes at other wavebands to generate a comprehensive atlas of broadband SEDs (see Wilkes et al. in these proceedings for some examples).

Most of the sources (53 of 72) were observed in a rectangular chop mode, the point source detection technique preferred at the beginning of the ISO mission. Concerns about calibrating and interpreting chopped measurements, particularly at long wavelengths, led us to switch to small raster scans. We reobserved 18 of the chopped fields in raster mode and added 19 new targets. The change in observing strategy, combined with lower than expected instrumental sensitivity, has resulted in a halving of the originally planned sample. However, we now have the added benefits of data from both observing modes for a subset of the targets and better information about background variations from the raster maps.

In this paper we present an overview of the analysis and reduction strategies and give an update of the status of the data products. Reduction of faint object data taken with the ISOPHOT instrument has been complex and somewhat uncertain, and the techniques are still in a state of development. Comparisons of our results with independent checks, such as IRAS, and an overlap of the raster and chopped observing methods help establish the validity of our data set, and the large size of the sample provides a convenient testbed for a variety of analysis procedures.

2. POINT SOURCE FLUXES

The bulk of the data reduction, including most instrumental calibrations and corrections, is done with PIA, the standard software for ISOPHOT reductions

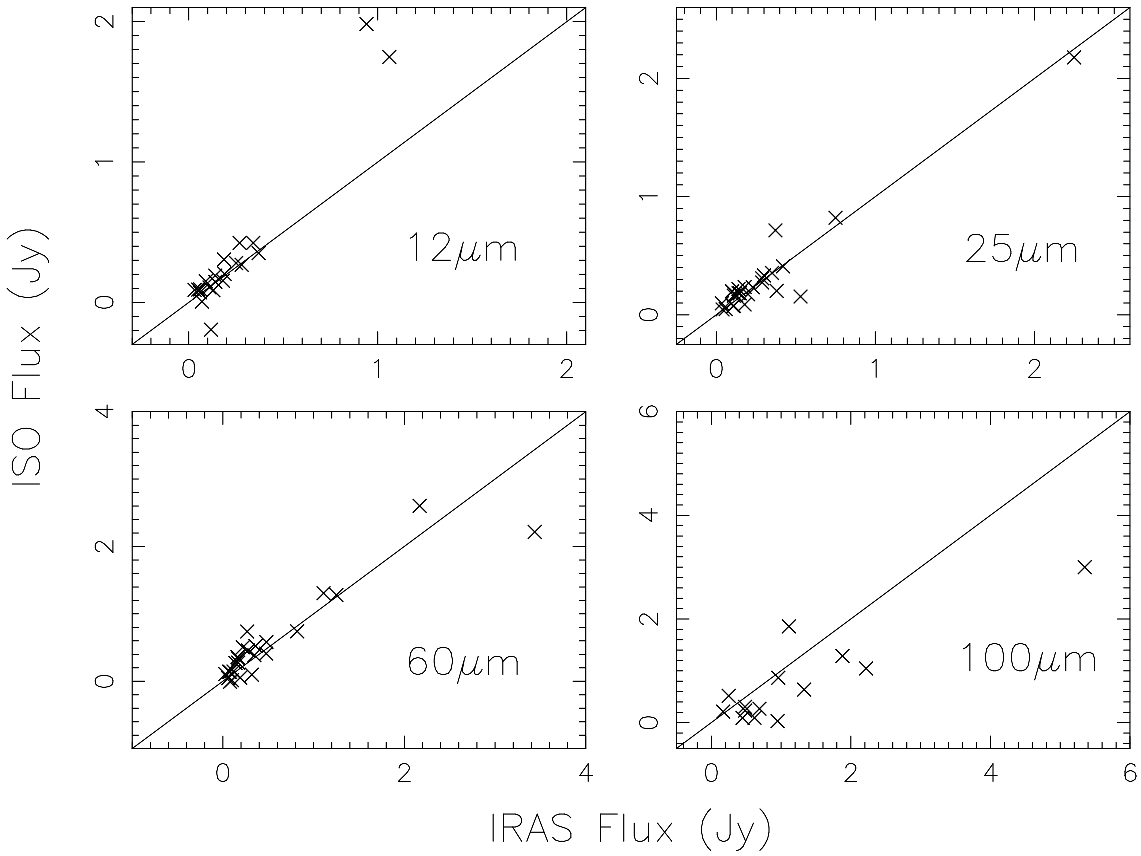

Figure 1. Comparison of ISO and IRAS fluxes for chopped measurements reduced with a Fourier transform code. Lines corresponding to equal flux observed with both telescopes are provided to guide the eye and do not represent any kind of fitting.

(Gabriel, Acosta-Pulido, & Heinrichsen 1998). Basic steps are typically run in batch mode, including ramp subdivision into 8 points per pseudo-ramp, two-threshold deglitching, orbitally dependent dark current subtraction, and flux calibration with the internal fine calibration sources, to produce AAP-level files. Standard instrumental drift corrections have not been employed in chopped data, as there are too few points per chopper plateau. We have not yet explored the use of drift corrections in raster data. The AAP files are left without vignetting corrections or sky subtraction, as these steps are done with external custom scripts.

The final reduction steps, extracting the source flux and estimating uncertainties, is an area of ongoing work, with multiple techniques being explored. To maintain flexibility, IDL scripts outside of PIA, written by Martin Haas & Sven Müller and modified by us, are used for both chopped and raster data. We currently employ three main techniques: a traditional source minus the average of adjacent backgrounds for chopped data, from which are derived numerous statistics; a Fourier analysis of the sequence of chopped measurements, which is generally less affected by residual glitches than the traditional approach but is more difficult to interpret; and a simple average background subtraction in the raster maps to obtain source flux and uncertainty estimates. Many on-the-fly options are available, including altering the vignetting values, finding and correcting gaps in the chopper sequence, discarding part of the sequence, flat fielding, background subtraction, plus plots of any aspect of the data.

Fluxes derived using the Fourier transform analysis of chopped measurements of relatively bright sources are compared to IRAS values in Figure 1. The agreement is generally good; possible explanations for the few large deviations include residual glitches or flux calibration errors in ISO, errors in IRAS fluxes, or intrinsic source variation. A similar plot was presented in Hooper et al. (1999) based on an earlier stage of the analysis techniques. An improvement in the agreement of the ISO and IRAS fluxes in the current version is particularly apparent at 60 μm.

3. BACKGROUND ESTIMATES

Intrinsic sky structure noise can dominate instrumental uncertainties in ISOPHOT measurements at wavelengths $\lambda \geq 100\mu$m (Herbstmeier et al. 1998). Background fluctuations are particularly problematic for simple chopped measurements with the four-pixel C200 array, where they contribute a systematic error that is difficult to determine directly from the observations. One possibility is to estimate the structure noise using the results of Herbstmeier et al. (1998), along with the prescription of Helou & Beichman

(1990) to adjust for the observed sky brightness and selected wavelength.

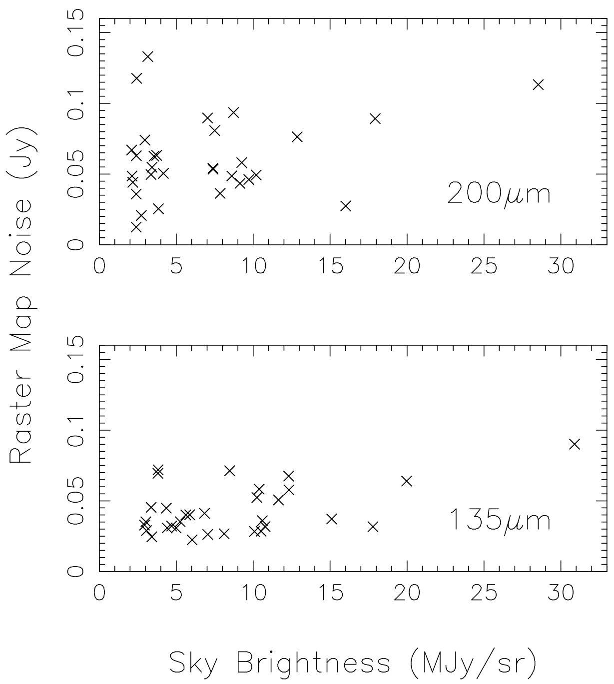

Figure 2. Rms noise vs. sky brightness for the C200 array raster data, calculated from off-source positions in the same manner as the flux for the source. Includes contributions from both the instrumental noise and the sky structure noise.

We measure the background variations more directly where possible from 2×4 raster scans with the C200 array, using the same technique as the source flux determination. The difference between the flux at a sky position in the raster sequence and the average of the preceding and following pointings (cases in which the source is centered on the pixel in any of these three positions are excluded) for each pixel forms a sequence of 12 measurements from which to estimate the total noise contribution, including structure noise and instrumental effects. These noise figures are plotted against measured sky brightness in Figure 2 for most of the raster maps in our sample. A weak trend of increasing noise with sky brightness is evident at 200 μm. The results are generally consistent with Herbstmeier et al. (1998), given that extrapolations of the structure noise between different fields and brightness levels can differ from the measured values by a factor of 5 or more.

4. VIGNETTING CORRECTIONS

Vignetting corrections are important parameters for chopped faint source observations, as relatively small errors can produce large changes in the computed source flux. Working with Martin Haas, we derived vignetting corrections from our C200 chopped data (135 & 200 μm) to compare with the default values.

The first step was to calculate average flat fields for the array in the on and off-source positions separately. Given the large sample size, we expect that any observed differences in the measured flat fields reflect changes in the vignetting between the two chopper positions. With proper vignetting corrections applied, the values should be close for each pixel. This was not the case for the default corrections; the flat fields differed by a similar or larger factor than with no correction applied at all.

The ratios of the on and off-source flat fields were used to estimate vignetting corrections, a process aided by the geometry of the array and the chopper motion. All of the observations had a rectangular chopping pattern of ± 90 arcsec, a total throw approximately equal to the projected angular size of the array. The spacecraft pointed halfway between the source and the background field. In this configuration, one half of the array imaged the central field of view of the spacecraft in each chopper position. Assuming that the central field had relatively uniform low-level vignetting (in the calculations it is set to 1.0, the same value used for the central field with no chopper movement), the flat field ratios directly gave the vignetting correction factors for the outer part of the chopping pattern. The derived corrections, listed in Table 1, are smaller and more uniform than the standard values, which range from 1.01 to 1.10. In addition, the new numbers are smaller at the longer wavelength, whereas many but not all of the default corrections follow the opposite trend. We are still evaluating whether the new or standard vignetting corrections are closer to the true values.

Table 1. Vignetting corrections for the C200 array with a total chopper throw of 180 arcsec. Derived from the average flat fields of each pixel in the on-source (+90 arcsec chopper position) and off-source (-90 arcsec chopper position) configurations.

λ & chop position	Pixel 1	Pixel 2	Pixel 3	Pixel 4
135 μm on source	1.018	1.000	1.000	1.024
135 μm off source	1.000	1.026	1.015	1.000
200 μm on source	1.009	1.000	1.000	1.010
200 μm off source	1.000	1.022	0.999	1.000

ACKNOWLEDGMENTS

Martin Haas, Sven Müller, Mari Poletta, and Ann Wehrle provided invaluable help with the data reduction. We benefited greatly from discussions with Thierry Courvoisier, Péter Ábrahám, Ilse van Bemmel, Rolf Chini, and Bill Reach. The IDC, IPAC, and the INTEGRAL Science Data Center were very hospitable during visits to work on this project. The financial support of NASA grant NAGW-3134 is gratefully acknowledged.

REFERENCES

Gabriel, C., Acosta-Pulido, J., & Heinrichsen, I. 1998 Proc. of the ADASS VII conference, ASP Conf. Ser. 145, ed. R. Albrecht, R.N. Hook, & H.A. Bushouse (San Francisco: ASP), 165

Helou, G., & Beichman, C. A. 1990, in "From Ground-Based to Space-Borne Sub-mm Astronomy," Proc. of the 29th Liége Internat. Astroph. Coll. (ESA), 117

Herbstmeier, U. et al. 1998, A&A, 332, 739

Hooper, E., Wilkes, B., McLeod, K., McDowell, J., Elvis, M., Malkan, M., Lonsdale, C., & Impey, C. 1999, in "Astrophysics with Infrared Surveys: A Prelude to SIRTF," ed. M. Bicay, R. Cutri, & B. Madore (San Francisco: ASP), in press

Lemke, D. et al. 1996, A&A, 315, L64

INFRARED STUDY OF THE INTERACTING GALAXY PAIR UGC 12914/5 - "TAFFY"

T.H. Jarrett[1], G. Helou[1], D. Van Buren[1], E. Valjavec[1], & J. Condon[2]

[1]Infrared Processing and Analysis Center, Caltech/JPL, Pasadena CA, USA
[2]National Radio Astronomy Observatory, Charlottesville, Va, USA

ABSTRACT

We are conducting an infrared wavelength study of the nearby interacting spiral galaxy system, UGC 12914/12915 (VV 254), using ground-based near infrared and mid-infrared imaging and spectral observations using ISOCAM and PHT-S on the Infrared Space Observatory (ISO). VV 254 is one of the closest examples of a rarely occurring sub-class of interacting systems consisting of two counter-rotating spirals having suffered a nearly face-on collision only $\sim 10^7$ years past. Our ISOCAM imaging data spatially resolves the system, revealing two morphologically disturbed spiral galaxies, large scale dynamical ring and a connecting intergalactic bridge. The total mid-IR emission is dominated by the nucleus of the more compact companion, UGC 12915 (northern galaxy), having nearly double the mid-infrared photons as compared to the ringed UGC 12914 (southern galaxy). The total mid-infrared flux density is $\sim$1.3 Jy, or about 5% of the total far-infrared flux density (IRAS bands).

The near-/mid-infrared in conjunction with radio continuum data indicate that UGC 12915 is now undergoing vigorous star formation in or near its nucleus while UGC 12914 is more quiescent (possibly in a pre-starburst phase), and thus the off-center collision has influenced the ISM evolution unequally in the two galaxies. A large-scale ring, resonantly induced by the nearly face-on collision, is identified in LW2 (6 μm) and LW8 (11 μm) bands. Finally, the connecting bridge between the two spirals does contain dust in correct proportion to the observed atomic gas column density assuming the radiation field transiently heating the small dust grains is similar in intensity to what is observed in the solar neighborhood and high galactic latitude cirrus clouds. The detailed nature of colder dust (T<100 K) is still uncertain owing to lack of resolution in the far-infrared.

Key words: galaxies: individual (UGC 12914/12915, VV254); interactions; ISM.

1. INTRODUCTION

The nearby interacting galaxy-galaxy VV 254 possesses a number of favorable (and combined, unique) characteristics toward study of spiral galaxy collisions. Extensive study of the system in the radio (Condon et al. 1993) reveals that the galaxies are: (1) normal (pre-collision) spiral galaxies, (2) nearly parallel ($< 11°$) in orientation of their respective disks, (3) in contra-rotation to each other, and (4) orbiting roughly in the plane of the sky. The orbit and disk orientation facilitates clean separation on the sky of the disk and post-collision environment. Two newly formed large angular-size structures from the encounter are distinguished: the disk of UGC 12914 (southern most galaxy) appears to have a stellar ring (roughly centered about the nucleus) and the system is joined by a very bright radio synchrotron "bridge" sandwiched between the two spiral galaxies (Figs. 1 & 2). The bridge is composed of disk stripped gas (neutral and ionized) and a strong magnetic field stretched like 'taffy' from the collision, which Condon et al. (1993) deduce occurred only $\sim 10^7$ years ago. The bridge is even more remarkable in that it contains nearly one-quarter of the total hydrogen gas mass of the VV 254 system.

Not surprisingly the violent encounter has probably induced a burst of star formation in the disks, particularly UGC 12915, clearly evident in optical and near-infrared. The bridge should contain, in addition to the atomic hydrogen, both molecular hydrogen gas and interstellar dust stripped from the parent galaxy(s), assuming the molecular gas/dust has not been destroyed by shocks from the interaction. Cold dust, representing the bulk of the total dust mass, is traced by in the far-infrared, but unfortunately the VV254 system is not large enough in angular size to be fully resolved by IRAS. In order to understand the energetics of the bridge ISM, it is important that the dust column density be measured. ISO does have the required spatial resolution, sensitivity and spectral coverage to measure the mid-infrared emission presumably originating from small, hot dust grains and molecules associated with small carbonaceous grains. ISO observations can not only belie the presence of dust in the connecting bridge, but also allow comparison of the mid-infrared energetics with the atomic hydrogen column density to help decode the effect of the recent galaxy-galaxy interaction on the intergalactic medium of the bridge and interstellar medium of the disks and nuclear regions.

2. DATA

The near-infrared J ($1.3\,\mu$m), H($1.7\,\mu$m), and Ks ($2.2\,\mu$m) imaging data was acquired with the Hale 200" telescope and Palomar prime-focus infrared camera (PFIRCAM; see Jarrett et al. 1994) on Sept. 10 1998 under ideal photometric conditions. PFIRCAM employs a 256×256 HgCdTe array with 0.495 arcsec pixels, giving a total field of view $\sim 2.1\times2.1$ arcmin. The resulting surface brightness sensitivity is 21.3 mag per arcsec^2 at K-band and 22.5 mag per arcsec^2 at J- band.

The ISOCAM data consists of four individual observations. Each set consists of observations with LW1 (4.1 - $5.0\,\mu$m), LW2 (5.5 - $8.5\,\mu$m), LW8 (10.9 - $11.9\,\mu$m) and LW3 (12.2 - $17.0\,\mu$m) with raster scanning and 6 arcsec pixels. The PHT-S data consists of one individual AOT centered on UGC 12914 and centered on UGC 12915, with a 24×24 arcsec aperture. The relative (channel-channel) calibration is estimated to be good to 10 - 20%, while the absolute calibration is probably only good to 30% (mainly due to the absence of flux correction for underestimation induced by the finite chopping frequency).

3. RESULTS

The reduced near-infrared (NIR) JHKs images are shown in Fig 1 with linear grey-scale and contour rendering. In addition, the lower panel is a map of the K-band ($2.2\,\mu$m) continuum overlaid with atomic hydrogen column density contours to illustrate the large concentration of gas in the intergalactic medium and well beyond the outer low surface brightness NIR isophotes. The NIR is sensitive to light coming from the older stellar population and from red supergiants associated with massive star formation. Stellar light reveals the overall system morphology to be widely disturbed. The nuclei of UGC 12914/5 dominate the total near-IR emission, with prominent "red" dust lanes evident in the brighter nucleus, UGC 12915, and an H II knot $\sim$30 arcsec southwest of the nucleus (spatially correlated with H α line emission). A tidal- warped spiral arm of UGC 12915 is seen to the northwest of the nucleus following the radio continuum. The disk of UGC 12914 is characterized by a bright nucleus, dust lanes extending 20-30 arcsec from the nucleus and bright "warp" features anchoring the north-south ends of the disk. A spiral arm extending above the northern "warp" feature appears to be tidally stretched by the interaction with UGC 12915. Moreover, a large-scale ring or branch of the tidal-wrapped spiral arm encircles UGC 12914, with the brightest section passing through the southwestern bridge region. In spite of the ring presence, most of the connecting bridge region is devoid of near- infrared light.

The final super-coadded (sum of four sets) mid-infrared (MIR) images for the ISOCAM bands,

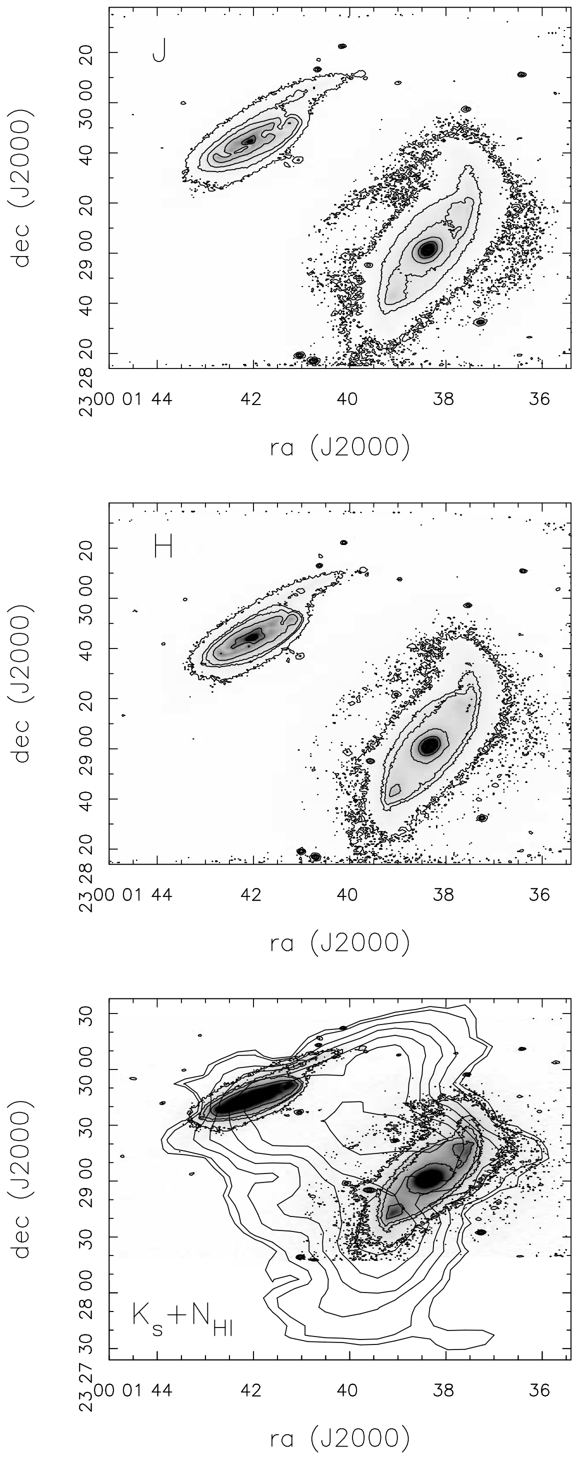

Figure 1. VV254 as seen in the near-infrared. Panels are gray-scale/contour overlays of J band ($1.3\,\mu$m), H band ($1.6\,\mu$m), & Ks band ($2.2\,\mu$m). Bottom panel shows the Ks image overlaid with contours of atomic hydrogen column density.

LW1($4.5\,\mu$m), LW2($6.75\,\mu$m), LW8($11.4\,\mu$m), and LW3 ($15.0\,\mu$m), are shown in Fig 2. Radio continuum contours are included with the LW3 grey-scale image. The total 'effective' field of view is about 3 arcmin, with 2 arcsec pixels. The nucleus of UGC 12915 is the brightest object in the field, approximately 50-60% brighter than the combined nucleus and adjacent knots (spatially coincident with the NIR 'warp' knots) comprising the disk of UGC 12914. The total integrated flux density of the system, UGC 12914/5 + bridge is ~1.3 Jy, which is about 20% of the total IRAS 60 μm flux density (6.3 Jy) and 10% of the 100 μm flux density (13.4 Jy). The UGC 12914/5 nuclei supply the bulk of the MIR emission; nonetheless, the 'bridge' is easily seen in LW2, LW8 and LW3 images. The MIR bridge, presumably originating from hot dust (T~150 K), which emits both continuum and PAH line emission. The line emission peaks at 6.2 and 11.4 μm, spatially coincident with the 1.49 GHz radio and the H I line emission. The integrated flux of the bridge is between 10 and 40 times fainter than the nucleus of UGC 12915. There is no evidence of a stellar population in the bridge based on the LW1 image which should trace stellar photosphere emission from late-type stars and photoionization from hard UV photons via the hydrogen recombination line Brα at 4.1 μm. Warm dust emitting from the bridge region and abutting large-scale ring can be clearly seen in LW2.

The detailed composition of the MIR emission spectrum (shortward of 12 μm) coming from the nuclear regions is revealed with PHT-S spectroscopy (Fig 3). The PAH line emission is clearly seen at 6.2, 7.7 and 11.3 μm for the disk/nucleus of UGC 12915, dominating the total 6 to 12 μm band emission. For comparison, a composite spectrum (Lu et al. 1998; Helou et al. 1998) comprised of many quiescent (normal) spiral galaxies is overlaid in black (dashed line) to illustrate the aromatic emission features and underlying continuum shortward of 6 μm. The presence of PAH line emission is strongly correlated with star formation in normal galaxies (as the composite nicely demonstrates) and in infrared-luminous starburst galaxies, but is generally not found near AGNs (the hard UV radiation destroys the small grains and UIB carriers; cf. Boulanger 1998; Boselli et al. 1998). The integrated flux density of the 7.7 μm band is 0.2 Jy and the 6.2 μm band 0.03 Jy for UGC 12915, comparable to the ISOCAM LW flux densities (the estimated uncertainty is 30%). At the short end, the 2.5 to 4.5 μm spectrum is dominated by noise, while no Brα recombination or PAH emission line at 3.3 μm is discernible.

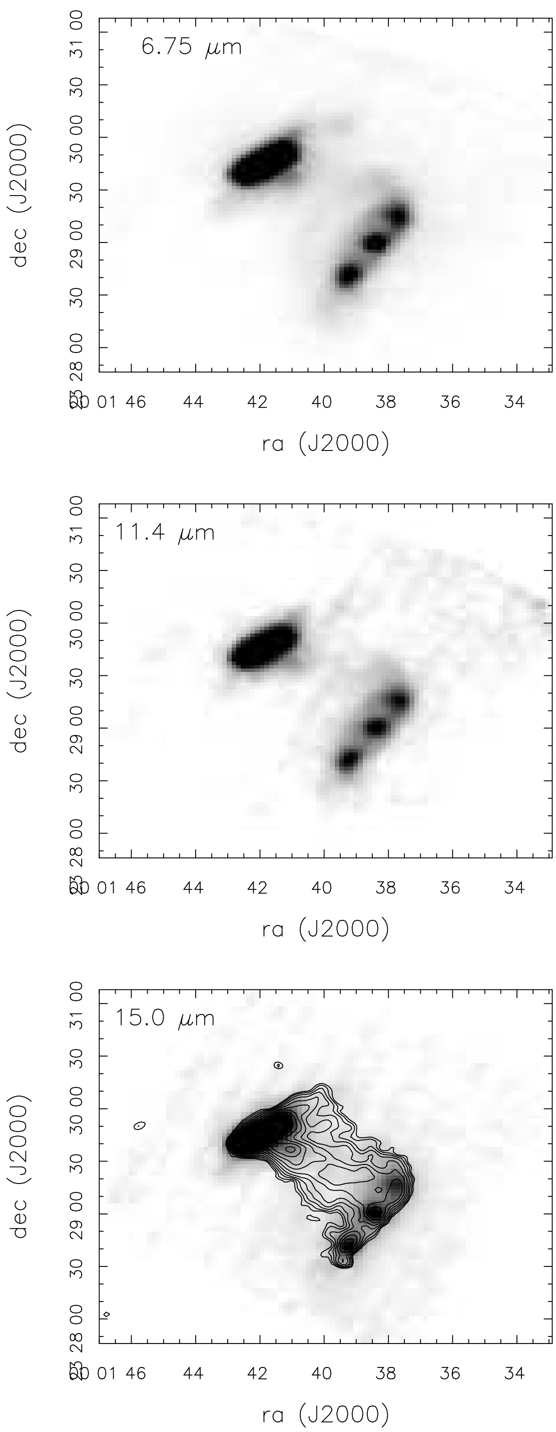

Figure 2. VV254 as seen in the mid-infrared. Panels are gray-scale/contour overlays of ISOCAM LW2 (5.5 - 8.5 μm), LW8 (10.9 - 11.9 μm), and LW3 (12.2 - 17.0 μm). Bottom panel (LW3 image) includes contours of the 1.49 GHz radio continuum, ranging from 0.1 to 7 mJy/beam (5 arcsec FWHM).

4. DISCUSSION

Infrared imaging reveals that the UGC 12914/5 system can be decomposed into three principal morphological components (size ~10 kpc): two multi-peaked nuclear regions (dominating the total MIR flux), large-scale ring or tidal-wrapped spiral arm of UGC 12914, and connecting bridge. The energetics and general ISM environment are vastly different, with the nuclear regions subject to a vigorous starburst (UGC 12915) or normal/pre-starburst phase (UGC 12914), the ring/arms modified by an expanding shock wave (from the collision), and the connecting bridge constrained by strong magnetic fields trapping electrons stripped in the encounter and channelling energetic cosmic rays from massive star formation regions (source of the non-thermal radio emission) and diffuse UV stellar radiation from the galactic disk regions. Given the relatively brief evolution from the initial encounter to the present state of the system, these regions are likely to evolve dramatically in the next 10^8 years. The connecting bridge region of VV 254 is unique in that it contains a significant atomic gas column density, accounting for nearly a one-quarter of the total H I mass of the system. The MIR emission suggests that there is a significant dust content in the bridge – as traced by the warm/hot dust emission, including the gap between the H II region and the ring. These observables are consistent with the 'splash' bridge formation mechanism (cf. Struck 1977) in which the counter-rotating inter-penetrating disks (at small impact radius) of UGC 12914/5 have reduced the rotational angular moment of diffuse gas in the disks, thus leaving remnant gas (but not stars) behind as the disks pass through.

The origin of the MIR emission is probably warm/hot dust grains re-radiating in the 5 - 25 μm window. The likely candidate is heating due to the interstellar UV radiation field local to the bridge. Comparing observed atomic hydrogen column density with the ISOCAM flux densities, the LW2 and LW8 values agree within a factor of two with the model predictions (and observations centered at 11 μm) dominated by the PAH line emission, while LW3 (mostly free of line emission) agrees well with predicted continuum emission from very small grains (cf. Désert et al. 1990). The LW1 upper limit is slightly higher ($2\times$) than the predicted continuum emission, but is consistent to within the measurement uncertainty. We may conclude that the intensity of dust emission coming from the VV 254 bridge region is consistent with the observed atomic gas column density – assuming that the 21-cm line emission is optically thin, dust emission associated with molecular gas in the bridge is relatively minor and that the interstellar radiation field is comparable to that observed in the solar neighborhood and in high galactic latitude cirrus clouds. Sensitive isotopic CO observations are needed to measure the total H_2 mass fraction in the bridge region and estimate the contribution of the MIR emission from molecular gas.

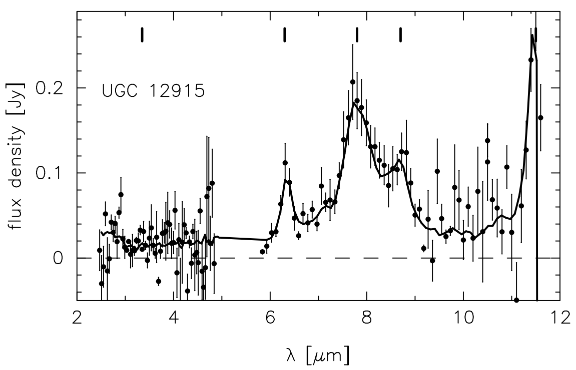

Figure 3. Mid-infrared spectrum of UGC 12915. The relative uncertainties in the pixel values are denoted by the 1σ errorbars. The absolute uncertainty is estimated to be 30%. A composite mid-IR spectrum (from Lu et al. 1998; generated from a linear combination of spectra from 28 normal galaxies) is denoted with dashed line (redshift-corrected to the VV 254 frame of reference).

ACKNOWLEDGMENTS

We would like to thank the ISO staff at IPAC for their help, particularly, Ken Ganga and Nanyao Lu. We thank Joe Mazzerella for useful discussions and Jim Cordes (Cornell U) for help with obtaining the Palomar data. This work would not have been possible without the help of M. Kessler who rescheduled our ISO observations to accommodate visibility restrictions. This work was supported in part by the Jet Propulsion Laboratory, California Institute of Technology, under a contract with NASA.

REFERENCES

Boselli, A., Lequeux, J., Sauvage, M., Boulade, O., Boulanger, F. 1998, A&A, 335, 53

Boulanger, F. 1998, IAU Symposium n.179, p. 153

Bushouse, H.A., Werner, M.W. 1990, ApJ, 359, 72

Condon, J.J., Helou, G., Sanders, D.B., Soifer, B.T. 1993, AJ, 105, 1730

Désert, F.X., Boulanger, F., & Puget, J.L. 1990, A&A, 237, 215

Helou, G., Lu, N.Y., Werner, M.W., Malhotra, S., Silberman, N. 1998, ApJL, in press.

Jarrett, T.H., Beichman, CA., Van Buren, D., Gautier, N., Jorquera, Bruce, C. 1994, Infrared Astronomy with Arrays, ed. I.S. McLean, Kluwer, p. 293.

Lu, N.Y. 1998, ApJ, in preparation.

Struck, C. 1997, ApJS, 113, 269.

ULTRA-LUMINOUS INFRARED GALAXIES: FAR-INFRARED SPECTRAL ENERGY DISTRIBUTIONS

U. Klaas[1], **M. Haas**[1] **& B. Schulz**[2]

[1]Max-Planck-Institut für Astronomie, Heidelberg, Germany
[2]ISO Data Centre, Astrophysics Division, ESA, Villafranca, Spain

ABSTRACT

We have obtained the most complete data set of far-infrared photometry of a sample of 37 archetypal and bright ultra-luminous galaxies. For the first time the maximum in their spectral energy distribution can be clearly seen. Assuming a grain emissivity proportional to λ^{-1}, the spectral energy distributions can be described in first order by a superposition of two dust components with temperature ranges between 100 and 165 K and between 30 and 55 K, respectively. No very cold dust component of temperatures $\sim$ 15 K, as found in more normal galaxies, is needed. There is no correlation between the temperatures of both components, implying that the heating mechanisms are independent.

Key words: Infrared: galaxies; Galaxies: photometry; fundamental parameters; starburst; AGN.

1. INTRODUCTION

One of the major discoveries of the IRAS mission was the finding of galaxies which emit the bulk of their energy in the far-infrared (FIR). The class of ultra-luminous IR galaxies is defined by $L_{FIR} > 10^{12}\ L_\odot$. Because of the relatively high fraction of AGN type objects (from optical emission lines) and powerful radio galaxies Sanders et al. (1988a) suggested that the ULIRGs form an evolutionary link between starburst galaxies and quasars.

In order to probe this hypothesis in more depth the ISO Central Programme comprises several observational projects to provide the most complete photometric and spectroscopic data set of this object class, see contributions by Luhman et al. and Rigopoulou et al. in these proceedings.

We have performed broad band photometry in 10 filters between 10 and 200 μm of a flux limited sample of the brightest ULIRGs in order to:

- answer the fundamental question: How much flux is emitted beyond the IRAS 100 μm long wavelength limit?
- determine accurately the shape of the IR spectral energy distribution (SED);
- determine the main heating constituents and their average temperatures;
- determine global parameters such as luminosity, emissivity, and dust mass;
- identify sub-groups in this sample with respect to spectral shape (e.g. relative ratio of thermal components), morphological and excitation parameters and look for criteria for possible evolutionary trends.

2. THE SAMPLE

We used the QMW IRAS galaxy catalogue (QIGC, Rowan-Robinson et al. 1991) in the version of Sept. 1991, comprising 17711 entries, as the data base for selection of the sample. We selected all sources with $L_{FIR} > 10^{12}\ L_\odot$ and $f_{60} > 3$ Jy. This yielded a sample of 48 sources. Though this criterion does not discriminate between normal and the so-called warm ULIRGs (Sanders et al. 1988b), the sample contains only a few of the latter ones. 37 out of the 48 sample sources, i.e. 77 per cent, could be observed. In co-ordination with the other ISO Central Programme projects we included the two objects NGC 6240 and Mrk 463 which are somewhat less luminous.

All objects were observed with ISOPHOT in the following filter sequence: 10, 12, 16, 25, 60, 90, 120, 150, 180, and 200 μm. The measurements from 10 to 25 μm were performed in chopped mode, the FIR photometry was performed in the sparse map off-on mode.

Proceedings of the Conference "The Universe as seen by ISO", Paris, France, 20–23 October 1998 (ESA SP-427, March 1999)

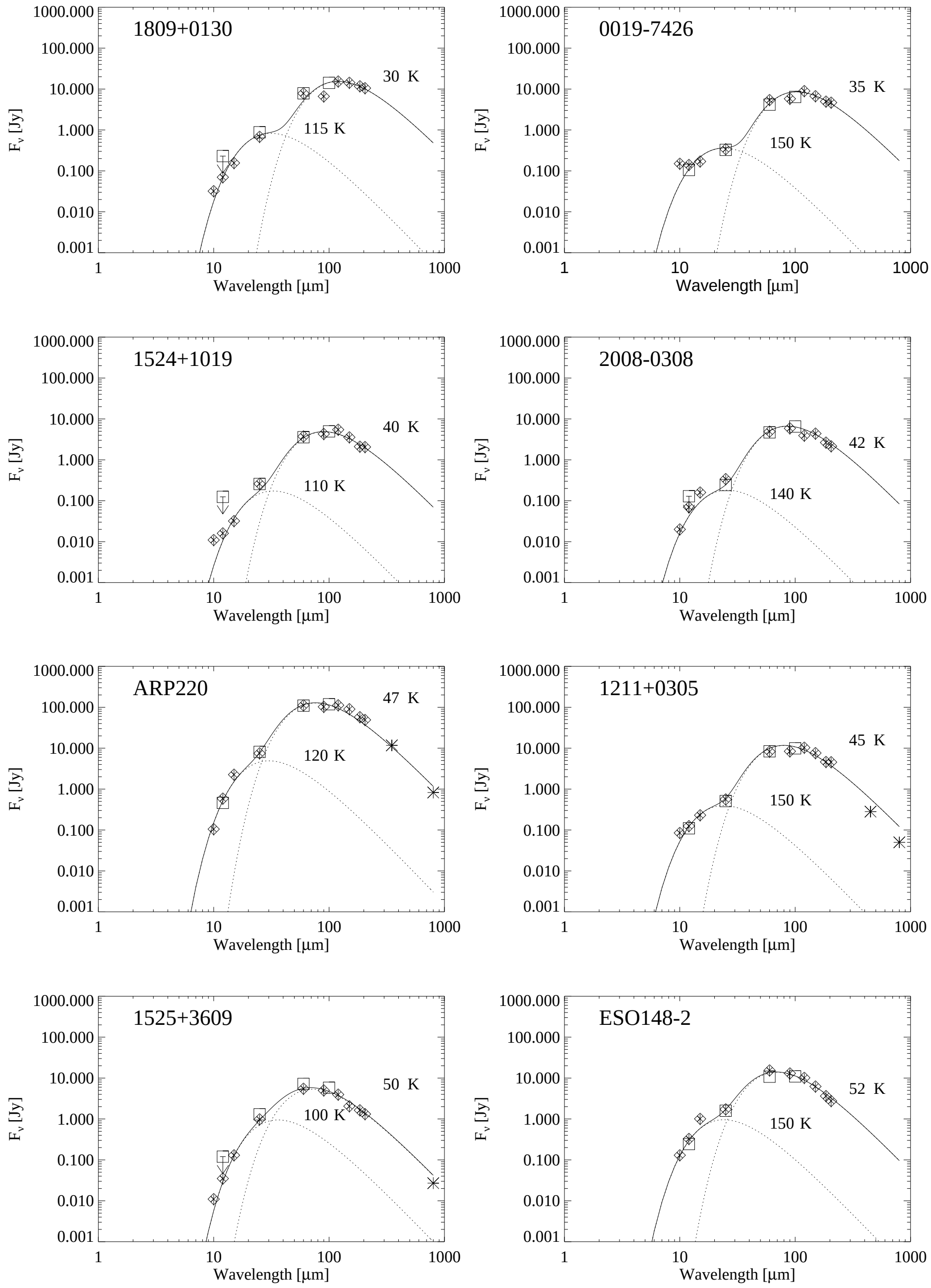

Figure 1. FIR SEDs of eight ULIRGs showing the range of possible shapes of all objects in the bright ULIRG sample. IRAS photometry and available sub-millimeter measurements from Rigopoulou et al. (1996) have been included: diamonds: ISOPHOT, squares: IRAS, asterisks: sub-mm. Two modified BBs with emissivity $\propto \lambda^{-1}$ have been fitted to the data. Their temperatures are shown in the plots. The left column displays objects with a low temperature of the warm component, the right column shows those with the temperature of the warm component at the upper end. The temperature of the cold component increases from top to bottom.

3. SPECTRAL ENERGY DISTRIBUTIONS OF ULIRGS

In Figure 1 we present the SEDs of eight of our objects. We have selected those which demonstrate the variety of spectral shapes in our full sample. In order to assess the variations quantitatively we have fitted two modified black bodies with emissivity $\propto \lambda^{-1}$ (according to the description by Hildebrand 1983) to the photometric points.

The remarkable features of the SEDs are:

- For each galaxy the maximum of the SED can now be clearly determined. It lies between 60 and 100 μm, and the 4 new photometric points beyond 100 μm clearly show the first part of the Rayleigh-Jeans branch.

- For many sources the 10 – 20 μm SEDs could be measured for the first time, since IRAS provided only upper limits.
- The SEDs can be fitted by two λ^{-1} modified BBs. We call them "warm" ($\sim$ 7 – 30 μm) and "cold" ($\sim$ 30 – 200 μm) components:
  - The temperature of the warm component varies between 100 and 165 K.
  - The temperature of the cold component varies between 30 and 55 K.
- The overall shape of the SEDs varies from exhibiting a pronounced "knee' at about 20–30 μm to one single BB-like envelope.
- The sequence in Figure 1 implies that a wide range of combinations of cold and warm components are possible.

The non-correlation between the temperatures of both components and all possible combinations of temperatures within the ranges outlined above strongly argues for the fact that the heating mechanisms and the relative contributions of dust components are independent of each other.

Two aspects need more detailed work:

- A fit by modified BBs with emissivity $\propto \lambda^{-2}$ gives lower temperatures and allows to introduce a very cold component of approximately 15 K, similar to what is found for normal spiral galaxies. This possible alternative is currently being investigated in more detail including further sub-mm/mm observations. Although the contribution to the total luminosity by this very cold component would be minor, it would alter the derived dust masses considerably due to the strong dependence of the dust mass on temperature ($M \propto T^{-6}$).
- No extinction correction has been performed. Such a correction would flatten the SED in the MIR and shift the peak of the warm component to higher temperatures.

4. LUMINOSITY OF COLD COMPONENT VERSUS LUMINOSITY OF WARM COMPONENT

In Fig. 2 we plot the luminosities of the warm versus those of the cold component. The following can be found:

- The luminosity of the cold component dominates in all objects the total energy output.
- The distribution of luminosities of the cold component is quite homogeneous with a pronounced peak at $1.3{\cdot}10^{12}$ $L_\odot$.
- The distribution of luminosities of the warm component is more scattered and shows several local peaks. This is again an argument for the independence of the heating mechanisms of warm and cold component.
- There is some trend that the luminosity of the warm component is higher for those objects which have also a higher luminosity of the cold component, though there is a large scatter.

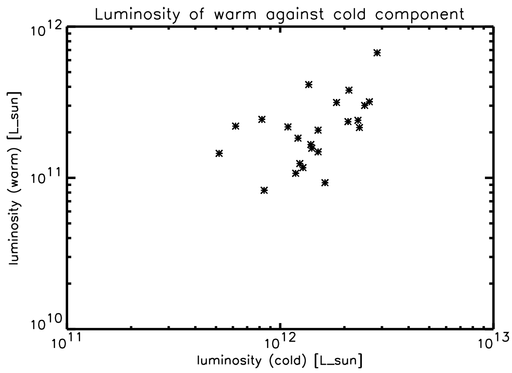

Figure 2. Luminosity of the warm component versus luminosity of the cold component for 22 ULIRGs.

5. PHOTOMETRIC TEMPLATES OF ULIRGS

Besides our statistical ULIRG sample observations we have obtained photometry in all 23 ISOPHOT filters from 3.3 to 200 μm for the well known objects Arp 220 and NGC 6240. These data have been published in Klaas et al. (1997).

REFERENCES

Hildebrand, R.H. 1983, QJRAS, 24, 276

Klaas, U., Haas, M., Heinrichsen, I., Schulz, B. 1997, A&A, 325, L21

Rigopoulou, D., Lawrence, A., Rowan-Robinson, M. 1996, MNRAS, 278, 1049

Rowan-Robinson, M., Saunders, W., Lawrence, A., Leech, K. 1991, MNRAS, 253, 485

Sanders, D.B., Soifer, B.T., Elias, J.H., et al. 1988, ApJ, 325, 74

Sanders, D.B., Soifer, B.T., Elias, J.H., et al. 1988, ApJ, 328, L35

INFRARED PROPERTIES OF STAR-FORMING REGIONS AND LINKS WITH STARBURST GALAXIES

M. Kontizas[1], **V. Missoulis**[2], **E. Kontizas**[3], **S. Oliver**[2], **A. Dapergolas**[3], **& F. Maragoudaki**[1]

[1]Section of Astronomy, Astrophysics & Mechanics, Department of Physics, University of Athens, Greece
[2]Physics Department, Imperial College, U.K.
[3]Astronomical Institute, National Observatory of Athens, Greece

ABSTRACT

Four stellar complexes (star forming regions) in the LMC have been investigated using IRAS observations and starcounts in the optical region (U magnitude). The optical data allow us to detect such structures and give information on the age range of their stellar component. Under the assumptions of this age range, a Salpeter IMF and two different mechanisms of star formation rate (instantaneous and constant), we derived the expected flux in the optical and infrared wavelengths in order to compare them with the observed ones.

The expected flux at the U magnitude (in the optical window) for the adopted range of ages ($10^{6.5} - 10^{8.5}$ years) has been found comparable to the one derived from our starcounts within the errors. However, the infrared luminosity has been found to exceed systematically at least 10 times the U luminosity. We suggest that the excess far-infrared energy must be searched to the far UV radiation wavelengths.

Key words: star-forming regions; infrared properties; star-burst galaxies.

1. INTRODUCTION

Stellar complexes are the major large scale structures in a galaxy where very recent star formation occurs (Efremov & Chernin 1994). These regions have dimensions from 250-1200 pc, and they contain very young stellar component in the form of stars, stellar associations and clusters with ages not exceeding a few $\times 10^8$yr (Kontizas et al., 1996). The optical image of these regions is dominated by the most massive stellar component of O and B SpT main sequence stars and possibly the few M supergiants and Carbon stars. The infrared fluxes detected comes from dust, pre-main sequence stars and protostars.

From a search of such regions on the wide field photographic plates (direct and objective prism plates) taken with the 1.2m U.K. Schmidt Telescope in Australia, it is found that the stellar complexes can be revealed as concentrations of enhanced stellar number density compared to their surrounding regions (Kontizas et al. 1996, Maragoudaki et al. 1998).

Four of the LMC stellar complexes which have been detected from direct and objective prism plates (Kontizas et al. 1996, Maragoudaki et al. 1998) are discussed here. The stellar content was found from the distribution of spectral types down to $M_v \approx 0.0$ whereas the morphology and extension of these complexes was determined for star counts down to $M_v \approx +2.5$mag. The far infrared (FIR) properties of Shapley I has been investigated in the past by Meaburn & Laspias (1991). The estimated (from IRAS observations) number of O5 and earlier supergiants is in agreement with the results of Kontizas et al. (1994) obtained from the spectral classification.

In the present investigation we will compare the properties of the four selected complexes in the infrared from the IRAS images with those properties derived from the optical observations (star count and spectral classification). The regions studied by Kontizas et al. (1996) and Maragoudaki et al. (1998) will be used as characteristic star forming regions in a galaxy and their properties will be compared with those of starburst galaxies. Therefore, criteria of starburst galaxies in the FIR (without active nuclei) and stellar evolutionary models with an IMF are used to provide the connection of starburst regions to starburst galaxies.

2. OBSERVATIONAL MATERIAL

We combine data in the optical and IR wavelengths for four stellar complexes in the LMC.

2.1. Optical data

The observational material and the derived properties of the four selected complexes are described in detail by Kontizas et al. (1996) and Maragoudaki et al. (1998).

Proceedings of the Conference "The Universe as seen by ISO", Paris, France, 20–23 October 1998 (ESA SP-427, March 1999)

Direct plates taken from the U.K. Schmidt Telescope were used in order to perform star counts and reveal enhancements of number density of stars above 2-3 σ the average local background, down to $V \approx 21.0mag$. Objective prism plates from the same telescope were used in order to classify the stars in the complexes and derive the distribution of spectral types within the defined area down to $V \approx 18.5mag$. Comparison with nearby fields allow us to derive the actual number of stars per spectral type and the total number of stars down to the detection limit.

2.2. Infrared data

IRAS data at 12, 25, 60 and 100 μm have been used, in order to derive the IR fluxes for the selected regions. The derived infrared flux corresponds to the IRAS data of the optically defined complex.

3. METHODOLOGY

The procedure of our investigation implies the following steps:

- Derivation of the observed flux in the optical waveband.
- Derivation of the observed IR flux from the IRAS images.
- Derivation of the predicted total flux in the optical from the available data under the appropriate assumptions.

3.1. Total observed flux in the optical waveband

It is known that the dominant stellar component of the complexes are the O, B stars, therefore the optical flux of these regions is very well represented by the flux in the U magnitude.

Having found the boundaries of the selected complexes (Kontizas et al. 1996, Maragoudaki et al. 1998) we derive the total number of stars down to the detection limit after subtraction of the superimposed field stars. The adopted complex region of Shapley-I and the two nearby regions which were used to represent the local background for the subtraction of field stars (normalized to the same area) is illustrated as an example, in Figure 1. This procedure was performed for various magnitude ranges and therefore the total number of stars provides the total U flux of the complex.

3.2. Total observed flux in the infrared

In order to calculate the IR flux we used IRAS observations at 12, 25, 60 and 100 μm for the regions corresponding to the selected complexes. A value of the background flux has been derived from the mean IR flux of the whole LMC IRAS image per unit area.

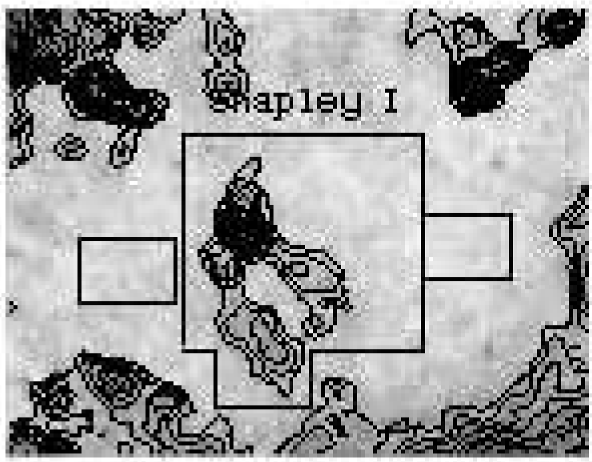

Figure 1. The complex region of Shapley I, as it was revealed from the isopleth maps on star counts in the U waveband. The nearby regions which were adopted as representative of the local background, are also shown.

The total IR fluxes (background subtracted) for the selected complexes are given in Table 1.

Table 1. The observed infrared fluxes (Jy) of the selected complexes and the ratio f_{60}/f_{100}

Complex	12 μm	25 μm	60 μm	100 μm	f_{60}/f_{100}
Shapley I	52	160	1451	2463	0.59
Shapley IV	7.8	2.4	139	560	0.24
Shapley IX	30	43	546	1430	0.38
Shapley X	207	1412	7527	7722	0.97

3.3. Predicted flux

The optical data provide basic information on the age of the stellar complexes and a total number of stars at certain magnitudes. Assuming a set of stellar ages, an IMF and two star formation rates we can find the total flux at the required optical and IR wavelengths.

In an extended search for the detection of stellar complexes in the LMC it is found that the main stellar component involved cannot be older than a few times $10^8 yr$ (Maragoudaki et al. 1998). Thus, we have used models of stellar evolution at ages $10^{6.5} yr$ (for the very young and the most massive stellar component) and $10^{8.5} yr$ (for the older stellar population). Moreover, Massey (1998) has found that the slope of the IMF for LMC, SMC and our Galaxy's massive stellar component in clusters and associations is ~ 1.3 despite their large metallicity differences. Thus, we accepted a Salpeter IMF slope for the four stellar complexes. This assumption is in agreement

Table 2. Total fluxes in U and IR waveband of the selected complexes. The fluxes are measured in 10^{40}erg.s^{-1}

Complex	Observed U	Predicted U for $t = 10^{6}.5$yrs	Predicted U for $t = 10^{8}$yrs	Observed IR.
Shapley I	0.13	0.22	0.034	2.6
Shapley IV	0.98	0.14	0.021	0.38
Shapley IX	0.42	0.033	0.005	1.9
Shapley X	0.25	0.084	0.013	11

with the observed LF of the studied complexes for the range of magnitudes corresponding to the brightest stars ($14.0 < U_{mag} < 17.0$) within the observational errors.

We have also taken into consideration two different models of star formation rate, one corresponding to constant $\dot{M}$, and one for instantaneous star formation.

Following the above assumptions, we derived the predicted flux with normalising point at the number of stars for $U_{mag} \sim 16.5$.

4. RESULTS AND DISCUSSION

According to Heckman (1990, 1996) one criterion for star-burst galaxies is based on the ratio of $\frac{f_{60}}{f_{100}} > 0.5$. This criterion is fulfilled for Shapley I and Shapley X and this could be also a criterion for a starburst region in a galaxy. Those ratios are shown in Table 1.

The total fluxes in the optical and FIR wavelength for the four selected regions are given in Table 2. The total FIR luminosity is estimated as $L_{IR} = 3.65 \times 10^{5}(2.58f_{60} + f_{100})D^{2}L_{\odot}$ (Devereux & Eales 1989).

We can also see that the FIR luminosity is systematically larger than the U luminosity of this region (Table 2). Thus, we suggest that the excess FIR luminosity should be searched to the far UV radiation.

Grosso et al. (these proceedings) combined the IR and X-ray deep surveys to study the young population in extremely young cluster embedded in the nearby star-forming clouds and confirmed that essentially all IR sources are X-ray emitters.

From the isochrones and the number of stars with $U < 18.5$ we can estimate also the total mass of the young stellar component. Specifically we obtain that 100 $M_{\odot}$ correspond to 4 such luminous stars if the age is $10^{6.5}$yrs and to 2 stars if the age is 10^{8}years. On the other hand we can estimate the star formation rate from the total IR radiation as $\dot{M} = 26L_{IR,11}M_{\odot}.yr^{-1}$ (Hunter et al. 1986) where $L_{IR,11}$ is the total IR luminosity in $10^{11}L_{\odot}$.

According to Hunter et al. (1986) the above relation is valid for the situation when all the UV radiation is absorbed by the dust. If only a fraction is absorbed, then the star formation rate should be multiplied by q=(total UV radiation)/(absorbed UV radiation). If the star formation rate is underestimated, then the age is overestimated. In the present situation it is safe to assume that q is not much larger than unity and also there is nothing to indicate that the star formation rate was constant.

For Shapley I we have $L_{IR} = 6.85 \times 10^{6}L_{\odot}$ and for Shapley X we have $L_{IR} = 3 \times 10^{7}L_{\odot}$. Consequently we obtain star formation rates $\dot{M} = 1.8 \times 10^{-3}M_{\odot}.yr^{-1}$, $\dot{M} = 7.8 \times 10^{-3}M_{\odot}.yr^{-1}$ for Shapley I and Shapley X respectively. In table 3 the total masses of the complexes are presented by the assumption of age equal to 10^{8}yrs. The mass becomes twice as small if the age is $10^{6.5}$yrs. Finally, the age listed in Table 3 is calculated under the assumption that the star formation rate was constant and the mass is the corresponding to age 10^{8}yrs (Table 3). We do not give any estimation of the age of Shapley IV, Shapley IX because they do not satisfy the conditions of a starburst region and also the contrast in luminosity between them and the field is very small. So the IR radiation possibly is not related to a recent starburst.

The estimated ages of Shapley I, Shapley X show a very good agreement with the results of (Kontizas et al. 1996).

Table 3. The total stellar mass and the estimated ages.

Complex	Observed Total Mass $M_{\odot}$	Predicted Age yr
I	2×10^{5}	2×10^{8}
IV	1×10^{5}	-
IX	5×10^{4}	-
X	6×10^{4}	8×10^{6}

We will try to estimate the temperature of the dust. We expect that we have cold and hot dust. The temperature of the cold dust is estimated from the luminosities at 60, 100 μm. We assume an emission coefficient proportional to ν. From $f_{60} = 990$ Jy, $f_{100} = 1815$ Jy (Meaburn & Laspias 1991) we obtain $T_d = 37$ K. From $f_{60} = 1451$ Jy, $f_{100} = 2463$ Jy we obtain $T_d = 38$ K. From $f_{60} = 7527$ Jy, $f_{100} = 7722$ Jy we obtain $T_d = 48$ K.

In all the above situations the radiation of the dust at 12, 25 μm is much smaller than that we observe so we ignore its radiation at the smaller IRAS wavelengths. The luminosity of the stars at 12, 25 μm is also very small so the only possible candidates for that radiation are the hot dust and the HI clouds. If we assume that the contribution of the HI clouds is small, then the temperature of the dust should be 150 K for Shapley I, 130 K for Shapley X (130 and 110 in case of emission coefficient proportional to ν^2). If we ignore the role of the dust and assume black-body clouds, from the fluxes at 12, 25 μm we obtain T=190, 150 K, respectively. The estimation of the temperature of the hot dust is in agreement with the predictions of the hot dust model (Bernlohr 1993) in Shapley X and Shapley I for the ν^2 case whereas the estimation of the temperature of the HI clouds is higher than the temperature of the HI clouds of our galaxy. Nevertheless in Shapley I the error due to the background is large. The enormous resulted temperature of the HI clouds means either that the role of the radiation of the HI clouds is negligible, or that they have been heated by the radiation of ionization fronts due to the UV radiation of OB-stars or shock waves due to supernova explosions. Another important factor is the HII regions. According to Wainscoat et al. (1992) $f_{12}/f_{25} \simeq 0.13$. This ratio corresponds to temperature equal to 126 K when the emission coefficient is proportional to ν so the resulted temperature of the dust, slightly depends on any assumption about the importance of the IR radiation of HII regions. From the above discussion we understand that the predicted temperature of the hot dust is in agreement with the hot dust grains model.

ACKNOWLEDGMENTS

The authors would like to thank the U.K. Schmidt Telescope Unit for loan of the optical observational material. They would also like to express their thanks to the General Secretariat of Research & Technology, to PPARC (grant number GR/K98728) and to the EC TMR Network programme (FMRX-CT96-0068) for their financial support.

REFERENCES

Bernlohr, 1993, A&A 268, 25

Devereux, N.A., Eales, S.A. 1989, ApJ, 340, 708

Efremov, Yu, N, Chernin, A.D. 1994, Vistas in Astronomy, 38, 165.

Heckman, T.M., Armus, L., Milley, G.K. 1990, ApJS, 74, 833

Heckman, T.M., Dahlem, M., Eales, S.A., Fabbiano, G., Weaver, K. 1996, ApJ, 457, 616

Hunter D.A., Gillett F.C., Gallagher III J.S., W.L.Rice, Low F.J. 1986, ApJ. 303, 171

Kontizas, M., Kontizas, E., Dapergolas, A., Argyropoulos, S., Bellas-Velidis, I. 1994, A&AS, 107, 77.

Kontizas, M., Maravellias, S.E., Kontizas, E., Dapergolas, A., Bellas-Velidis, I. 1996, A&A, 308, 40.

Maragoudaki, F., Kontizas, M., Kontizas, E., Dapergolas, A., Morgan, D.H. 1998, A&A, 338, L29.

Massey, P. 1998, IAU Symp. 190 on "New Views of the Magellanic Clouds".

Meaburn, J., Laspias, V.N. 1991, A&A, 245, 635.

Rowan-Robinson, M., Mann, R.G., Oliver, S.J. et al. 1997, MNRAS, 289, 490.

Wainscoat, R.J., Cohen, M., Völk, K., Walker, H.J., Schwartz, D.E. 1992, ApJS 83, 111

THE ISO-SWS SURVEY OF MOLECULAR HYDROGEN LINES IN ACTIVE GALAXIES

D. Kunze[1], **D. Rigopoulou**[1], **R. Genzel**[1], **& D. Lutz**[1]

[1]Max-Planck-Institut für extraterrestrische Physik, Garching, Germany

ABSTRACT

We present a survey of molecular hydrogen line emission in nearby starburst and Seyfert galaxies. Excitation temperatures and gas masses for low-lying energy levels of H_2 are derived from the observed pure rotational lines. The H_2 (0-0) S(1) line in Seyferts is emitted by a "warm" gas at temperature of 120–140 K. This component accounts for 0.2–20 per cent of the total gas content. In starbursts the temperature of the S(1) emitting gas is somewhat higher (up to 210 K) and contributes typically a few per cent to the total gas mass (up to 9 per cent in M 82). The S(5) and S(7) lines trace a "hotter" gas component at temperatures of about 1100 K (up to 1700 K in IC 342) both in Seyfert and starburst galaxies. The excitation of the molecular hydrogen in starbursts and some of the Seyfert galaxies is dominated by UV-fluorescence. However it cannot be excluded that a part of the "warm" H_2 gas is thermally excited. For some of the Seyferts indications for shock excitation are found.

Key words: interstellar medium; molecular hydrogen; starburst galaxies; Seyfert galaxies; infrared galaxies.

1. INTRODUCTION

Molecular hydrogen is one of the major constituents of the interstellar medium. With ground-based and airborne observations however only its near-infrared ro-vibrational transitions around 2.1 μm can be detected. These lines typically trace molecular hydrogen gas of masses around $\sim 10^{4-5}\,M_\odot$ and temperatures of about 4000 K. The H_2 gas at this temperature is a very small fraction (as small as 10^{-6}) of the total amount of H_2. Since the ro-vibrational lines tend to get faint at lower temperatures, most of our knowledge about the H_2 content of galaxies comes from CO observations using a CO/H_2 conversion factor derived from galactic molecular cloud observations.

With the advent of the Infrared Space Observatory (ISO: Kessler et al. 1996) it was for the first time possible, to observe the pure rotational line emission of molecular hydrogen in external galaxies. These lines probe directly the gas in low-lying energy states of H_2. Detections of such lines with the Short Wavelength Spectrometer (SWS: de Graauw et al. 1996) on board ISO have been reported, e.g. for NGC 3256 (Rigopoulou et al. 1996), NGC 4038/39 (Kunze et al. 1996), NGC 6946 (Valentijn et al. 1996) and the Circinus galaxy (Moorwood et al. 1996).

In this paper we present a survey of molecular hydrogen line emission in starburst and Seyfert galaxies. The sample contains in total 21 objects (see Tables 1 and 2). Almost all nearby starburst galaxies and Seyferts are included. The objects represent a variety of different galaxy types and show a wide spread in gas content and luminosity. In the following Section 2 we describe briefly the observations and data analysis. In Section 3 gas masses and excitation temperatures are derived. A comparison with the gas mass, as derived from CO observations, is presented in Section 4. The origin of the H_2 emission is being investigated in Section 5. Final conclusions are drawn in Section 6.

2. OBSERVATIONS

The observations for this survey have been carried out as part of the MPE ISO Guaranteed Time Programme "Bright Galactic Nuclei". The measurements have been made throughout the ISO mission. Some of the observations have already been published in previous papers (Rigopoulou et al. 1996, Kunze et al. 1996, Moorwood et al. 1996). Additionally we have included flux measurements for NGC 6946 by Valentijn et al. (1996).

The SWS grating line profile scan mode (SWS02) was used to investigate the molecular hydrogen lines. Typically the H_2 (0–0) S(0), S(1), S(2), S(5), S(7) and the H_2 (1–0) Q(3) have been observed (see Figures 1 and 2). The aperture sizes range from 14×20 to $20 \times 27\,\mathrm{arcsec}^2$. The spectral resolution of the SWS of $\lambda/\Delta\lambda \approx 1000-2000$ is well matched to the typical velocity dispersion of galaxies.

Data reduction has been performed with the SWS Interactive Analysis System. Special routines for high quality dark subtraction, detector signal jump and cosmic ray hit removal, flat-fielding and defringing have been used. Dark subtraction is a critical item in SWS data analysis for extragalactic objects, because the flux levels are usually low. Defringing is very im-

Proceedings of the Conference "The Universe as seen by ISO", Paris, France, 20–23 October 1998 (ESA SP-427, March 1999)

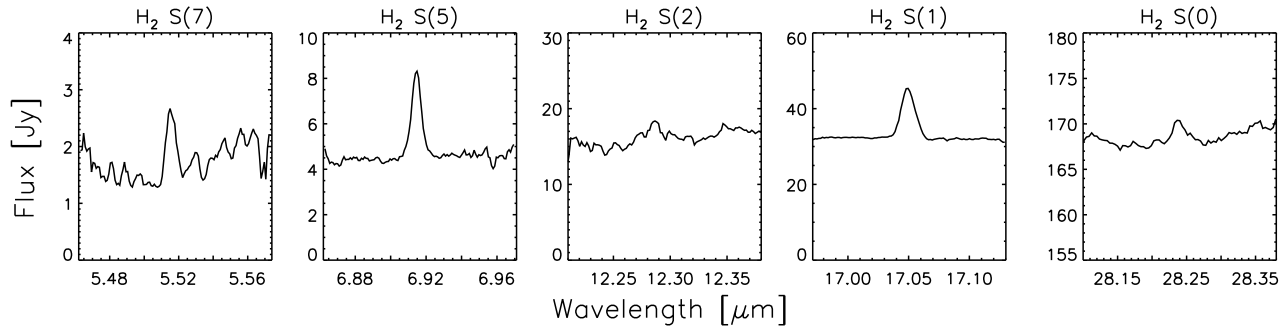

Figure 1. Pure rotational lines of molecular hydrogen in NGC 253.

portant for the H_2 S(0), S(1) and S(2) line. These lines are observed in SWS band 3, which is mostly affected by fringes. Especially in case of low line-to-continuum ratio the fringes have to be removed before measuring line fluxes. For the resulting line fluxes we claim an accuracy of about 30 per cent (see Schaeidt et al. 1996 and Salama et al. 1997). In some objects some of the lines could not be detected. For these lines we have determined 3σ upper limits for the line flux.

3. GAS MASSES AND EXCITATION TEMPERATURES

The observed line fluxes and their ratios can be used to get estimates for the gas mass and excitation temperature of molecular Hydrogen in its low-lying energy levels. In case of spontaneous emission the column density N_i of the upper level of a transition can be calculated from the observed line flux $F_L(i)$ according to:

$$N_i = \frac{F_L(i)}{A_i \times h \times \nu_i} \times \frac{4\pi}{beam} \qquad (1)$$

with A_i being the Einstein-coefficient and ν_i the frequency of the transition. h is Planck's constant and *beam* the solid angle of the beam size. To determine the actual gas mass in a level its column density is multiplied by the physical area of the object according to the aperture and the mass of a H_2-molecule.

Excitation diagrams are used to derive excitation temperatures for the molecular hydrogen gas (see Figures 3 and 4). In these diagrams the column density divided by the statistical weight of the upper level $ln(N_i/g_i)$ of each transition is plotted against the upper level energy T_i.

In case of local thermodynamical equilibrium (LTE) the column density N_i of the i-th state of the H_2 gas would follow the Boltzmann equation:

$$\frac{N_i}{N} = \frac{g_i}{Z(T_{ex})} \times exp(-\frac{T_i}{T_{ex}}) \qquad (2)$$

with g_i and T_i beeing the statistical weight and energy of level i. N is the total column density of the molecular hydrogen gas, T_{ex} the excitation temperature (corresponding to the LTE kinetic temperature) and $Z(T_{ex})$ the partition function at T_{ex}. Plotting $ln(N_i/g_i)$ against T_i would then give a straight line with the slope $(1/T_{ex})$.

Assuming thermal emission, it is apparent that the level population of the molecular Hydrogen cannot be described with a single excitation temperature (see Figures 3 and 4). For individual pairs of lines however the slopes in the excitation diagrams can be used to determine LTE equivalent excitation temperatures. The detections of the S(1) and S(0) lines (or upper limits of the latter whenever not detected) are used to constrain the temperature of a “warm” line emitting H_2 gas, while the S(5) and S(7) lines are

Table 1. The starburst sample galaxies.

Galaxy Name	Distance	Type
M 82	3.3	Irr
NGC 253	3.5	Sc
IC 342	3.6	Scd
NGC 5236	3.7	SB pec
NGC 4945	4.1	SBcd
NGC 5253	4.1	Im pec
NGC 6946[a]	5.7	Sbc
II Zw 40	10.5	BCD
NGC 4038	21.0	SBm
NGC 7552	21.2	SBbc
NGC 3256	36.6	SB pec
NGC 3690	42.0	SBm pec

Distance in [Mpc], $H_0 = 75 Mpc/km/s$
[a]: Valentijn et al. (1996)

Table 2. The Seyfert sample galaxies.

Galaxy Name	Distance	Type
Circinus	4	S2
Cen A	4	RG
NGC 1068	14	S2
NGC 4151	20	S1.X
NGC 7582	20	S1
NGC 1365	22	S1
NGC 5506	23	NLXG
NGC 7469	66	S1+SB
NGC 1275	70	Scd

Distance in [Mpc], $H_0 = 75 Mpc/km/s$

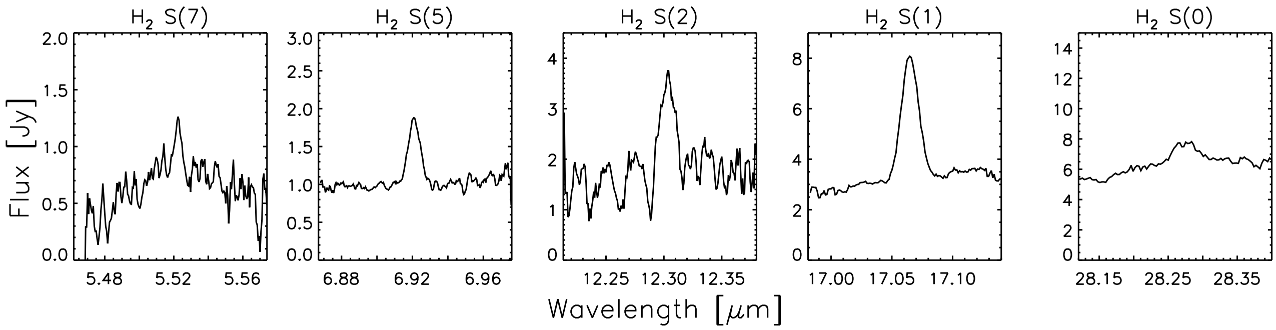

Figure 2. Pure rotational lines of molecular hydrogen in Cen A.

used to determine the temperature of a "hotter" gas component.

We find that on average the excitation temperature of the S(1) line emitting gas in Seyferts is about 120–140 K, somewhat lower than the average value for the starbursts which is found to be $\sim$ 190 K (up to 210 K in NGC 253). The derived excitation temperature is affected by the ortho-to-para conversion rate of H_2. The ortho-to-para ratio in turn, depends on the actual H_2 excitation mechanism. In the case of UV fluorescence the ortho-to-para ratio is 3 in LTE, however it drops rapidly below 3 for low temperatures ($T \leq 200$ K). In the case of shocked H_2 emission the situation is more difficult since the pre-shock gas is colder ($T \sim 50$ K) than the postshock gas. From the S(5) and S(7) lines we derive excitation temperatures for the "hotter" gas component in Seyferts and starburst galaxies in of about 1100 K (up to 1700 K in IC 342).

4. COMPARISON WITH CO DATA

Most of the knowledge about the molecular content of galaxies has so far relied on observations of CO emission, assuming a certain CO/H_2 conversion factor. However, CO probes successfully gas lying at really low temperatures of a few tens hardly up to a hundred K. And although the cool gas comprises the bulk of the gas content in a galaxy, it provides no information on the "warmer" gas, which might be more directly linked to the source of activity.

As shown in Section 2, the gas mass in individual energy levels of the H_2 molecule can be directly derived from the observed line fluxes. Assuming a standard ortho-to-para ratio of 3 (see Valentijn et al. 1996), we have determined estimates for the gas masses in the "warm" and "hotter" gas component of H_2 probed with the pure rotational lines. We find that the "warm" gas ($T \sim 120 - 200$ K) mass constitutes up to a few per cent of the total mass in the galaxies as derived from CO observations.

In particular the "warm" gas mass in starbursts was found to account for about 9 per cent in M82, whereas it can be as low as 0.1 per cent as it is the case for NGC 7552. On the other hand, in Seyferts, the mass of the "warm" gas ranges between 20 per cent in NGC 7469 to 0.2 per cent in NGC 7582. For the mass of the "hotter" gas component we find that it accounts for a lot less, in the order of at most a few 10^{-5} in both starburst and Seyfert galaxies.

5. H_2 EXCITATION MECHANISMS

The molecular hydrogen gas can be excited by various excitation mechanism: UV fluorescence and shock

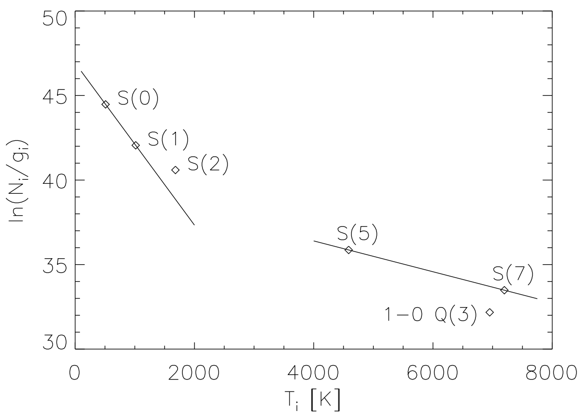

Figure 3. Excitation diagram for NGC 253.

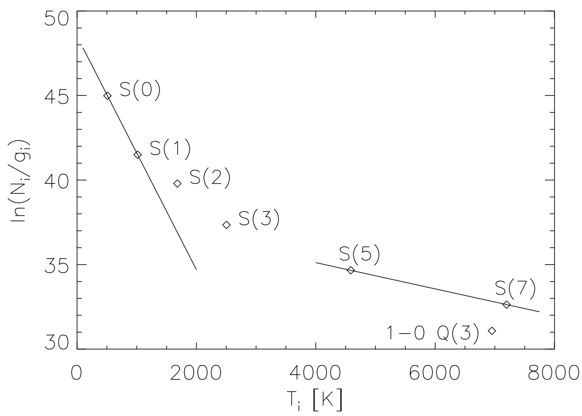

Figure 4. Excitation diagram for Cen A.

excitation. For the "warm" gas we additionally cannot exclude that part of the radiation we observe is emitted by thermally excited gas. To distinguish between the different excitation mechanisms we compare observed H_2 line ratios S(1)/S(0), S(1)/S(2), S(1)/S(3) and S(5)/S(7) with predictions from PDR and shock models as well as with ISO observations of galactic templates, like S 140 (Timmermann et al. 1996) or Cep A (Wright et al. 1996).

Comparison of measured line ratios and predictions from PDR models by Burton, Hollenbach and Tielens (1992) and Black & van Dishoeck (1987) show, that the excitation of molecular hydrogen in starbursts and some of the Seyferts (NGC 7582 and possibly NGC 5506, Cen A and NGC 4151) is dominated by UV fluorescence. For the Seyferts also a combination of the two mechanisms is a plausible scenario.

Rotational as well as ro-vibrational H_2 lines can also arise in gas heated by molecular shock waves. Both types of molecular shocks, C- and J-shocks, produce significant H_2 emission (see e.g. Draine 1980 and Hollenbach & McKee 1989).

We have compared our observed H_2 line ratios S(1)/S(0), S(1)/S(2), S(1)/S(3) and S(5)/S(7) with shock models calculated by Brand et al. (1988), Hollenbach & McKee (1989), Draine et al. (1983) and Kaufmann & Neufeld (1996). A direct comparison of the ratios for Seyferts shows that just a single speed shock model cannot fit the observations. Moreover, almost all shock codes predict a quite low 0-0 S(0) emission, much lower than the observed one (in cases where the S(0) line is detected). It might be, that part of the S(0) emission comes from thermally excited molecular hydrogen. From a comparison of the observed and predicted line ratios we find, that a combination of C-shocks of relatively low velocity could fit the observations of NGC 1275, NGC 7469 and possibly NGC 1068. None of the starburst galaxies is a clear case candidate for shock excited H_2 emission.

6. CONCLUSIONS

A survey of molecular hydrogen emission in starburst and Seyfert galaxies was presented. The observed pure rotational lines trace a "warm" and "hotter" H_2 gas component at temperatures of 120-210 K and $\sim$ 1100 K, respectively. The "warm" component accounts on average for a few per cent of the total H_2 gas mass as derived from CO observations. There is evidence, that UV fluorescence is the dominating excitation mechanism for molecular hydrogen in many of the galaxies of our sample. However we cannot dismiss the possibility that a combination of PDR emission plus shocked emission and for the "warm" component also thermal emission contributes to the observed line fluxes. In some of the Seyferts indications for shock excitation have been found.

ACKNOWLEDGMENTS

ISO-SWS and the ISO Spectrometer Data Centre at MPE are supported by DARA under grants 50 QI 8610 8 and 50 QI 9402 3.

REFERENCES

Black J.H., van Dishoeck E.F. 1987, ApJ, 322, 412

Brand P.W.J.L., Moorhouse A., Burton M.G., Geballe T.R., Bird M., Wade R. 1988, ApJ, 334, L103

Burton M.G., Hollenbach D.J., Tielens A.G.G.M. 1992, ApJ, 399, 563

Draine B.T. 1980, ApJ, 241, 1021

Draine B.T., Roberge W.G., Dalgarno A. 1983, ApJ, 264, 485

de Graauw Th., Haser L.N., Beintema D.A., et al. 1996, A&A, 315, L49

Hollenbach D., McKee C.F. 1989, ApJ, 342, 306

Kaufmann M.J., Neufeld D.A. 1996, ApJ, 456, 611

Kessler M.F., Steinz J.A., Anderegg M.E., et al. 1996, A&A, 315, L27

Kunze D., Rigopoulou D., Lutz D., et al. 1996, A&A, 315, L101

Moorwood A.F.M., Lutz D., Oliva E., et al. 1996, A&A, 315, L109

Rigopoulou D., Lutz D., Genzel R., et al. 1996, A&A, 315, L125

Salama, A., Feuchtgruber H., Heras A., et al. 1997, ESA SP-419, 17

Schaeidt S.G., Morris P.W., Salama A., et al. 1996, A&A, 315, L55

Timmermann R., Bertoldi F., Wright C.M., et al. 1996, A&A, 315, L281

Valentijn, E.A., van der Werf P.P., de Graauw Th., et al. 1996, A&A, 315, L145

Wright C.M., Drapatz S., Timmermann R., et al. 1996, A&A, 315, L301

THE MID-INFRARED SPECTRAL PROPERTIES OF STARBURST GALAXIES AND AGNS SEEN BY ISOCAM

O. Laurent[1], I.F. Mirabel[1], V. Charmandaris[2], P. Gallais[1], L. Vigroux[1], & C.J. Cesarsky[1]

[1]CEA/DSM/DAPNIA, Service d'Astrophysique, Gif-sur-Yvette, France
[2]Observatoire de Paris, DEMIRM, France

ABSTRACT

We present a new diagnostic tool based on mid-IR spectra (5-16 μm) to distinguish the emission triggered by an active galactic nucleus (AGN) from that associated with star formation activity. Mid-IR emission in galaxies integrated over large regions (from 100 pc to several kpc) can be understood as a mixing of three components (HII regions, diffuse/photodissociation regions (PDRs), and AGN). We show that AGN spectra, contrary to starburst spectra, present an important continuum below 9 μm emitted by hot dust and an absence of Unidentified Infrared Bands (UIBs) probably destroyed by photodissociation mechanism in the AGN radiation field. The diagnostic diagram derived from these features can be used to detect obscured AGNs embedded in a large concentration of dust.

Key words: galaxy; mid-infrared; active galactic nucleus; starburst

1. INTRODUCTION

Since the discovery of ultraluminous infrared galaxies (L(8-1000μm) > 10^{12}L$_\odot$) which emit the bulk of their energy in the infrared, different studies have shown that intense star formation regions as well as AGNs are necessary to explain these high luminosities (see Sanders & Mirabel 1996 for a review). Since a great amount of molecular gas is needed for fuelling nuclear starbursts and/or AGNs, these regions are usually embedded in a large concentration of dust producing a heavy obscuration. Consequently, the absorption makes the distinction between starburst and AGN activities difficult and the main problem, not yet fully resolved, concerns the estimation of their relative contributions to the total infrared luminosity. We have observed at mid-IR wavelengths ($A_V/A_{8\,\mu m}$~50) for penetrating obscured regions not visible at optical wavelengths (Mirabel et al. 1998a). In addition, at these wavelengths (5-16 μm), we detect dust emission heated preferentially by AGNs or young stars (Mirabel et al. 1998b). We address the question of the distinction between AGNs and starbursts by presenting a new diagnostic for estimating the relative importance of these two main energy sources found in galactic centers.

2. OBSERVATIONS

A sample of 22 nearby active/interacting galaxies was observed in spectro-imaging mode with the ISOCAM camera on board the Infrared Space Observatory (ISO) (Cesarsky et al. 1996a, Kessler et al. 1996). The standard data reduction was applied using the CAM Interactive Analysis (CIA)[1] software. Each galaxy was fully mapped in the wavelength band covering 5-16 μm.

3. AGN AND STARBURST SPECTRA

The imaging capabilities of the camera, which provides an angular resolution of 5 arcsec, have been fully operated in observing nearby prototype active galaxies: NGC 5128 (Mirabel et al. 1998b) and NGC 1068. Thanks to the good spatial resolution obtained at these wavelengths (~100-400 pc with FWHM = 5 arcsec), we have been able to differentiate the mid-IR emission produced by the AGN from the one produced by the circumnuclear star forming regions (see Figure 1). In addition, observations of nearby star forming galactic regions were used to identify the typical mid-IR emission of a pure ionized region (HII) heated by OB stars in M17 (Cesarsky et al. 1996b) as well as that of the interface called photo-dissociation region (PDR) between HII regions and molecular clouds in NGC 7023 (Cesarsky et al. 1996c). Assuming that galaxy spectra are composed over large spatial scales of a mixing of HII region, PDR and (if it exists) AGN spectra which are similar to these three mid-IR templates, we can decompose the emission originating from larger regions observed in our galaxy sample.

3.1. Distinction between AGN, HII and PDRs

The UIBs at 6.2, 7.7, 8.6, 11.3 and 12.7 μm presented in Figure 1 are probably emitted by complex 2-dimensional molecules with C-C and C-H bonds that have been commonly called polycyclic aromatic hydrocarbons (PAHs) (see Puget & Léger 1989 for a

[1]CIA is a joint development by the ESA Astrophysics Division and the ISOCAM consortium. The ISOCAM consortium is led by the ISOCAM PI, C. Cesarsky, Direction des Sciences de la Matière, C.E.A. France.

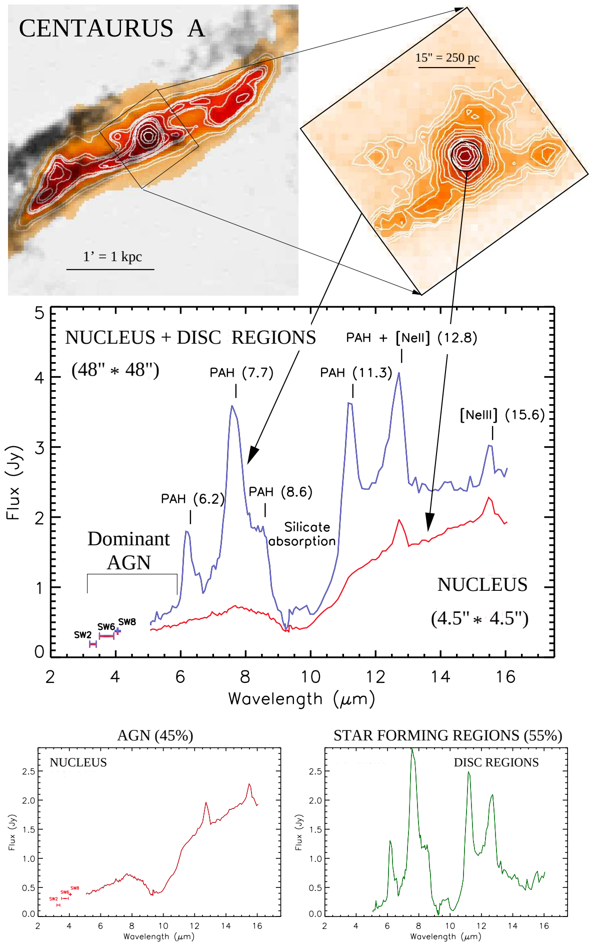

Figure 1. Upper left panel: Distribution of dust in the inner region of CenA observed at 7 μm (contours) with optical dark lanes superimposed. Upper right panel: Map between 8.2 and 8.7 μm of the nuclear region observed in spectro-imaging mode with the CVF (Circular Variable Filter) where we observe the nucleus as well as a part of the disc structure. The spatial resolution achieved is 100 pc (FWHM = 5 arcsec). Middle panel: The lower curve represents the mid-IR spectrum covering the nuclear region (100 pc in diameter) whereas the upper curve shows the spectrum integrated over a larger region (800 pc in diameter) including both disc structures and the nucleus. Bottom panel: The AGN spectrum (left) represents 45 % of the energy between 5 and 16 μm and is highly dominant at short wavelengths between 3 and 6 μm. The emission associated with star formation regions (right) is not detected with the three narrow band filters at 3-4 μm. The absence of PAH bands is clearly observed in a region of 50 pc in radius containing the AGN whereas PAH bands dominate the emission outside the nucleus. In addition, the high [NeIII]/[NeII] ratio detected in the AGN reveals the presence of a hard radiation field.

review). Mid-IR observations of nearby galactic regions revealed that UIBs originate from PDRs and diffuse regions (Verstraete et al. 1996, Mattila et al. 1996, Tran 1998). Statistical studies have already shown that AGNs present faint UIBs contrary to starburst galaxies (Roche et al. 1991, Genzel et al. 1998). We confirm this result with ISOCAM observations of nearby prototypical active galaxies (NGC 5128 and NGC 1068) for which UIBs are absent in nuclear regions of several hundred parsecs. This absence of UIBs could be the result of their destruction by photodissociation mechanisms produced by the intense UV-X radiation field in AGNs (Léger et al. 1989, Allain et al. 1996). In addition, a noticeable continuum at short wavelengths [5-9 μm] commonly attributed to hot dust is present in our sample of AGN spectra (see also Barvainis 1987). In the light of these results, the UIB(6.2 μm)/continuum[5-6.7 μm] ratio can be used as a tool for distinguishing between AGNs and PDRs/diffuse regions. The combined effects of an increased continuum associated with an absence of UIBs in AGNs make this diagnostic very efficient. In Figure 2, we present in detail the method used to calculate this ratio.

We now use the information given by the mid-IR continuum shape between short(5-6 μm) and long(14-15 μm) wavelengths. In the upper panel of Fig. 3, the spectrum of a "pure" HII region presents an absence of UIBs as for AGN spectra. Nevertheless, unlike in the AGN spectra, the continuum at short wavelengths is very faint. Assuming these continuum behaviors, we can estimate the HII/AGN ratio just using the warm continuum[14-15μm]/hot continuum[5-5.6 μm] indicator.

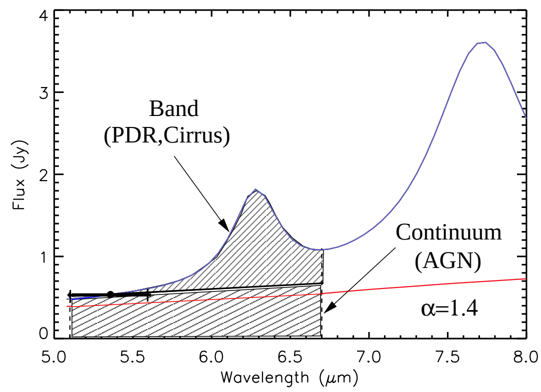

Figure 2. The spectrum between 5.1 μm and 6.7 μm is divided into two different parts. The flux above the thick line (power law with a spectral index α∼1.4 fitting the AGN spectral continuum and scaled to the average flux between 5.1 μm and 5.6 μm) estimates the flux arising from the UIB at 6.2 μm and traces the star formation activity. The flux below the line mainly selects the continuum from the AGN. The band/continuum indicator varies similarly to the (PDRs, diffuse regions)/AGN ratio.

3.2. Mid-IR diagram

In Figure 3, we present a diagram combining the strength of the UIB(6.2 μm) feature with the continuum[14-15μm]/[5-5.6 μm] ratio. We have used the three mid-IR spectra as templates for identifying the contribution of each component in our galaxy sample. In HII regions, UIBs are absent or faint and there is a strongly rising continuum associated with emission lines : [ArIII](9 μm), [SIV](10.5 μm), [NeII](12.8 μm) and [NeIII](15.6 μm). Regions dominated by PDRs, observed in galactic discs, present strong UIBs largely dominating the total emission

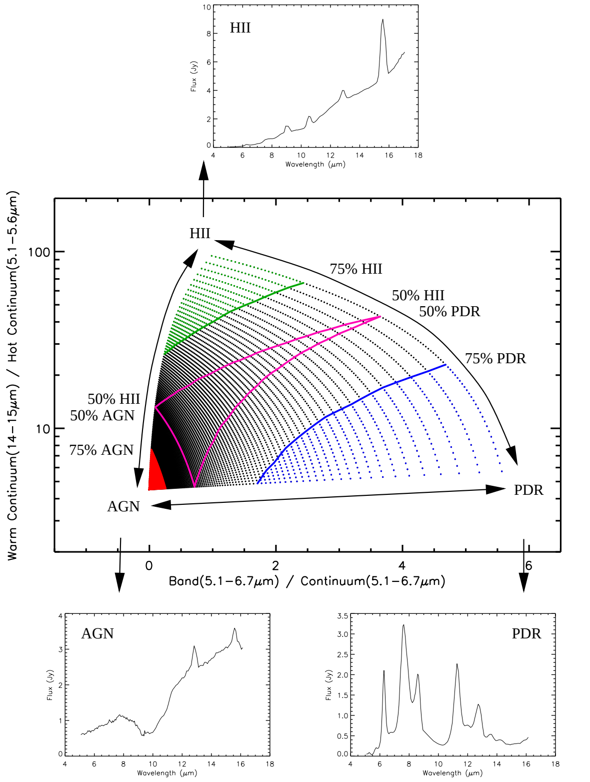

Figure 3. Based on synthetic spectra containing variable fractions of three mid-IR templates observed in a pure HII region (M17), a PDR (NGC 7023) and an AGN (NGC 5128), the diagnostic diagram defines three distinct areas. In the upper part, we select spectra dominated by HII regions (intense starbursts). On the left, AGN spectra are dominant in a very small region, and finally, PDR spectra fall in the right part. The percentages indicate the fraction of each mid-IR contribution used in the composite spectra.

with a faint continuum. Finally, AGN mid-IR emission is mainly characterized by a strong continuum at 5-6 μm without UIBs. Assuming that spectra integrated over the whole galaxy are composed of the mixing of spectra originating from HII regions, PDRs and an AGN, we have built composite spectra from the three mid-IR templates. This diagram can be decomposed into three different regions where we preferentially select AGN (bottom left), HII (top) and PDR spectra (bottom right).

Figure 5 includes in the same diagram 35 spectra containing star forming regions and/or AGNs. The starburst galaxies such as Arp 220 and Mrk 171(A) present a large fraction of pure HII regions compared to PDRs. The AGN detected for nearby objects are located in the bottom left part of the diagram. The star forming regions observed in galactic discs are situated in the region dominated by PDRs.
Using this diagram, we conclude that well-known ultraluminous galaxies like IRAS 23128-5919 and NGC 6240 have mid-IR spectra which are dominated by a strong starburst contribution. The AGN contribution is detected only in nearby objects for which we are able to separate nuclear regions from the galactic disc.

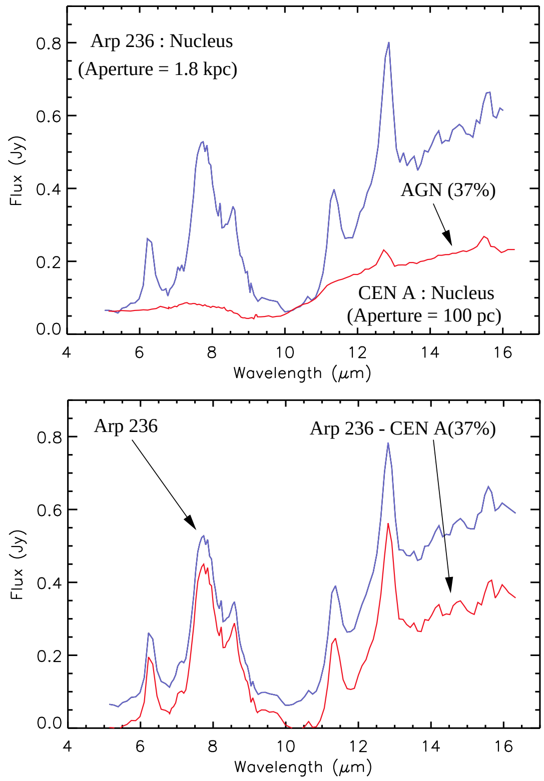

Figure 4. Indication of the presence of an optically hidden AGN in Arp 236 (IC 1623, VV114). Upper panel: the mid-IR spectrum of the more luminous region (1.8 kpc in diameter) is shown in the top curve. On the bottom, we have assumed that the AGN spectrum of CenA (100 pc in diameter) can approximately reproduce the main characteristics of any obscured AGN spectrum. The non-negligible continuum at short wavelengths may be due to an AGN contribution which amounts to ~40% of the total mid-IR flux. Lower panel: The AGN contribution is removed from the initial spectrum. The result is consistent with a typical starburst spectrum.

We have attempted to use this diagnostic diagram to find new AGNs hidden by a large column density of dust. On the diagram, the nucleus of Arp 236 (IC 1623, VV114) is close to the AGN region and as a consequence may contain a non-negligible AGN fraction. This IR luminous system ($L_{IR}=10^{11.62}\,L_\odot$) which is composed of several nuclei and/or compact starburst regions is classified as an early-stage gas-rich merger ($M(H_2) = 5.1\times10^{10}\,M_\odot$, Yun et al. 1994). Previous near-IR and radio studies showed no evidence for an AGN. Nevertheless, we could find an obscured AGN in the eastern region (knot A) observed by Doyon et al. (1995). Knot A is the brightest source in the near-IR, the reddest and also the most compact source (not resolved at 3.7 μm with a FWHM of 0.3 arcsec). In Figure 4, we present the mid-IR spectrum of the eastern nucleus including source A which comprises most of the flux at 3.7 μm (Knop et al. 1994). We estimate that ~40% of the mid-IR emission originates from an AGN (assuming the AGN spectrum of CenA).

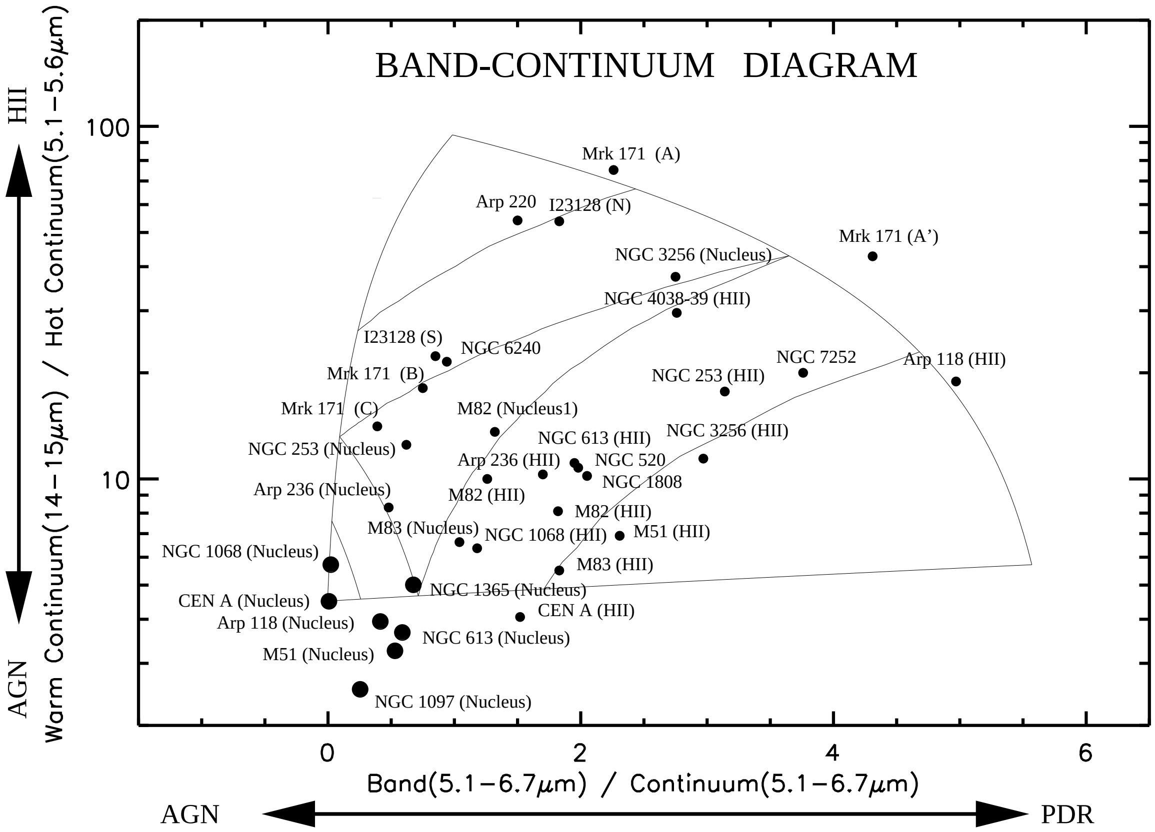

Figure 5. Diagnostic diagram including 35 spectra covering a large sample of mid-IR emission (nuclear regions, extra-nuclear star forming regions marked HII and unresolved galaxies). Galaxies hosting an intense starburst are in the upper part. The central regions of galaxies (size of several kpc) hosting an AGN (big circles) are all located in the bottom left part of the diagram. Spectra of galactic discs lie near the PDR region. The curves demarcate the AGN, PDR and HII contributions according to Figure 3.

4. CONCLUSIONS

We have obtained a new AGN/Starburst diagnostic using the strength of the UIB at $6.2\,\mu$m and the mid-IR continuum. This diagnostic is based on two independent points:
1) The presence, in “pure” AGN spectra, of a non-negligible continuum below 9μm which we attribute to emission from hot dust directly heated by the central engine.
2) The absence, in “pure” AGN spectra, of UIBs whose carriers are presumably destroyed by photodissociation in the strong UV-X radiation field.

ACKNOWLEDGMENTS

We thank H. Roussel and D. Tran for providing data in advance of publication as well as S. Madden for her help on different aspects of this work.

REFERENCES

Allain, T., Leach, S. *et al.* 1996, A&A, 305, 602

Barvainis, R. 1987, ApJ, 320, 537

Cesarsky, C., Abergel, A. *et al.* 1996a, A&A, 315, L32

Cesarsky, D., Lequeux, J. *et al.* 1996b, A&A, 315, L305

Cesarsky, D., Lequeux, J. *et al.* 1996c, A&A, 315, L309

Doyon, R., Nadeau, D. *et al.* 1995, ApJ, 450, 111

Genzel, R., Lutz, D. *et al.* 1998, ApJ, 498, 579

Kessler, M.F., Steinz, J.A. *et al.* 1996, A&A, 315, L27

Knop, R.A., Soifer, B.T. *et al.* 1994, AJ, 107, 920

Léger, A., Boissel, P. *et al.* 1989, A&A, 213, 351

Mattila, K., Lemke, D. *et al.* 1996, A&A, 315, L353

Mirabel, I.F., Vigroux, L. *et al.* 1998a, A&A, 333, L1

Mirabel, I.F., Lauren,t O. *et al.* 1998b, A&A, in press

Puget, J.L., & Léger, A. 1989, ARAA, 27, 161

Roche, P.F., Aitken, D.K. *et al.* 1991,MNRAS,248, 606

Sanders, D.B., & Mirabel, I.F. 1996, ARAA, 34, 749

Tran, D. 1998, PhD thesis, University of Paris XI

Verstraete, L., Puget, J.L. *et al.* 1996, A&A, 315, L337

Yun M.S., Scoville N.Z. *et al.* 1994, ApJ

ISM IN THE EDGE-ON GALAXY NGC 891: THE PAH COMPONENT AS SEEN BY ISOCAM

P. Le Coupanec[1], **D. Rouan**[1], **P. Gallais**[2], **A. Léger**[3], **M. Giard**[4], **F. Lacombe**[1], **& D. Tiphène**[1]

[1]DESPA, Observatoire de Paris-Meudon, Meudon, France
[2]CEA/DSM/DAPNIA Service d'Astrophysique, 91 191 Gif sur Yvette, France
[3]Institut d'Astronomie Spatiale, Orsay, France
[4]CESR, Université de Toulouse, Toulouse, France

ABSTRACT

In this paper, we present preliminary results of mid-infrared observations of the "normal" edge-on galaxy NGC 891. The whole plane of the galaxy was mapped through the ISO-CAM broad-band filters from 4.5 μm (LW1) to 15 μm (LW9) and the central 8 kpc have been observed with the spectro-imaging mode of the camera. The mapping of the so-called Unidentified Infrared Bands, UIBs (6.2, 7.7, 8.6 and 11.3 μm), is clearly done with a high signal to noise ratio in the whole galactic plane, providing the distribution of PAH-like molecules in the diffuse interstellar medium (ISM) of this galaxy. Correlation is established between the distribution of PAHs in terms of abundance and excitation state, mapped by these aromatic infrared bands ratios, and the galactic structure (distribution of gas and radiation field) showing an obvious weakening of the 11.3 μm band in central regions.

Key words: galaxies: individual: NGC 891; Unidentified features; ISM.

1. INTRODUCTION

The carriers of the Unidentified Infrared Bands (UIB) seem to be an important component of the galactic interstellar medium since those bands are detected in many different regions in the Milky Way. The UIB bands carriers can largely contribute to the emission of the galactic plane in the 12 μm IRAS band (Boulanger et al. 1985). In a first time, detection of the infrared bands was made essentially in regions rich in UV, like reflection nebulae or edges of HII regions. Then these features were observed in low density medium (Giard et al. 1988, Ristorcelli et al. 1994, Mattila et al. 1996) and even when UV density is as low as 10 times the mean ISRF (Boulanger et al. 1996), demonstrating the presence of the UIB carriers in the diffuse medium of our galaxy. Indeed, the bands have been observed since many years in the spectra of external galaxies inhabited by a strong starburst but exciting only a very small fraction of the medium. Confirmation of the presence of UIB carriers even in the diffuse medium of external quiet galaxies is important to prove that it is not only in few star forming complexes that the UIBs form, but that the whole ISM is involved. A study of processes of formation, excitation and destruction of these molecules in galaxies similar to ours and at a large spatial scale is then possible. Some important effects like protection of the molecules from the UV radiation field by the dust or sticking and ejection of PAH from the ice mantle of grains can be searched for.

Detection of the unidentified infrared bands in the diffuse interstellar medium of external normal spiral galaxies and then mapping of their relative strength were the purpose of an ISO program. The aim was to confirm the abundance of a PAH component (assumed to be the carrier) and to study conditions of excitation of these carriers at a large spatial scale in the diffuse interstellar medium. However, the surface brightness of a "normal" galaxy is low and the specific idea of this program was to look at edge-on galaxies where the column density is much larger than in face-on galaxies (Rouan et al. 1996).

The Sb galaxy NGC 891 appears to be a very good candidate for this study. Located at a distance of 9 Mpc, it is seen nearly face-on (inclination angle of 88.3°), displays characteristics of a "normal" spiral galaxy and is considered to be very similar to the Milky Way.

2. OBSERVATIONS

The whole galactic plane was mapped using a raster scan in all large CAM filters: LW1(4.5 μm) to LW9 (15 μm) (see Cesarsky et al. 1996, for a description of the instrument). The pixel field of view was 6 arcsec and the integration time about 140 sec per position. A CVF scan was made on regions centred on the galactic nucleus. The standard data processing has been followed, consisting mainly in dark current substraction, glitches correction, removal of all images affected by a strong transient effect. The zodiacal background contribution has been estimated on

Proceedings of the Conference "The Universe as seen by ISO", Paris, France, 20–23 October 1998 (ESA SP-427, March 1999)

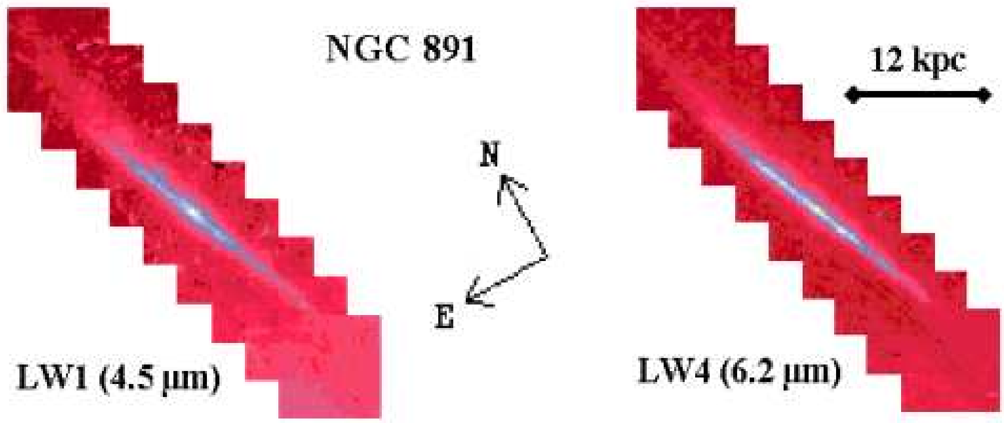

Figure 1. Images of the edge-on galaxy NGC891 obtained at 4.5 µm (LW1) and at 6.2 µm (LW4). The emission in the band appears present at all location in the disk.

blank parts of the image and subtracted to the signal. Both the CVF and LW raster were reduced with the CAM Interactive Analysis package (Ott et al. 1998). Images in LW1 and LW4 filters are presented in Figure 1. The effects of the transient appear as a tail at the north-east side of the galaxy. We took care of this remnant feature and did not consider it in the analysis.

3. RESULTS AND DISCUSSION

3.1. Link with molecular gas and UV field

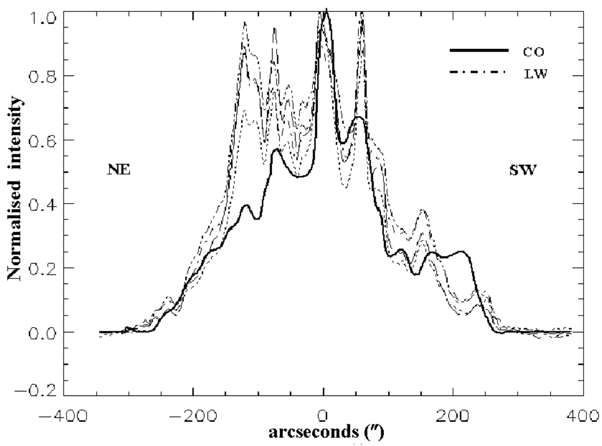

Figure 2. Comparison of galactic profiles in CO (Sofue & Nakai 1993) and in the PAH bands at 6.2, 7.7 and 11.3 µm.

An obvious result is that the infrared bands (6.2, 7.7 and 11.3 µm) are clearly detected with a high signal to noise ratio along the whole galactic plane, including in peculiar regions like in the bulge and spiral structures (see Figure 1). It is a confirmation of presence of UIB carriers in the diffuse medium of a "normal" spiral galaxy which was already known since the NGC 5907 observations (Rouan et al. 1996). An interesting thing is the comparison of the UIB bands distribution with other interstellar components like CO molecules. In Figure 2, galactic profiles in the UIBs are compared to the CO profile (Sofue & Nakai 1993) which represent the distribution of molecular clouds. A good correlation exists between structures in CO and those of the excited UIB carriers. A conclusion is that UIB carriers are bound to the molecular gas distribution, this is easy to understand since it traces stellar formation regions where young stars are able to excite aromatic molecules around them.

The CO distribution shows a strong asymmetric profile of the galaxy where the southern-west side has a lower level of intensity compared to the northern-east side. This characteristic, which can be due to the spiral structure, is confirmed by the UIB bands profiles observed and it is more obvious at wavelengths greater than 5 µm.

The radio galactic profile obtained by Sukumar & Allen (1991) at 6 cm is also compared to the infrared profile at 4.5 µm revealing a fairly good correlation (see Figure 3). The 6 cm emission is likely in majority free-free emission and can be considered as a good tracer of ionised matter in HII regions. The ratio between the fluxes received at 4.5 µm and 6 cm indeed agrees with the expected intensity ratio. Both the spatial and intensity correlation lead to suppose that the 4.5 µm measured flux is a good tracer of the ionised matter, even if it is still affected by photospheric stellar emission. Then, searching for a distribution of the energy source in the galaxy, a stellar distribution was modelized by an exponential disk, with a scale length $h_s = 3.9$ kpc and a scale height $z_s = 400$ pc and with a stellar bulge distribution as already described by Xilouris et al. (1998). This stellar distribution is integrated along the line of sight and fitted with a good agreement on the smooth component of the 4.5 µm galactic profile. It represents then a mean galactic profile of young stars distribution which is exciting matter in local emission features.

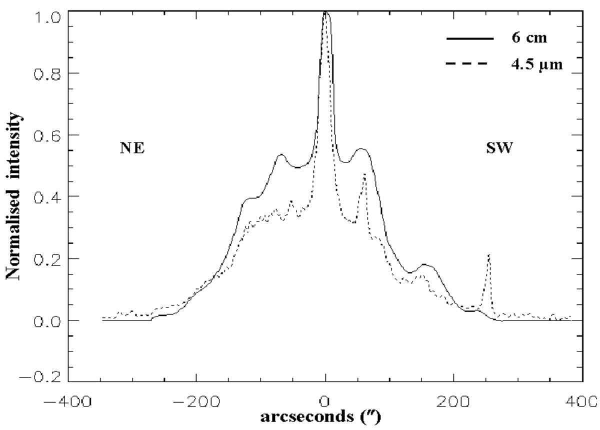

Figure 3. Comparison of normalised galactic profiles in radio at 6 cm (Sukumar & Allen 1991) and at 4.5 µm in the LW1 filter.

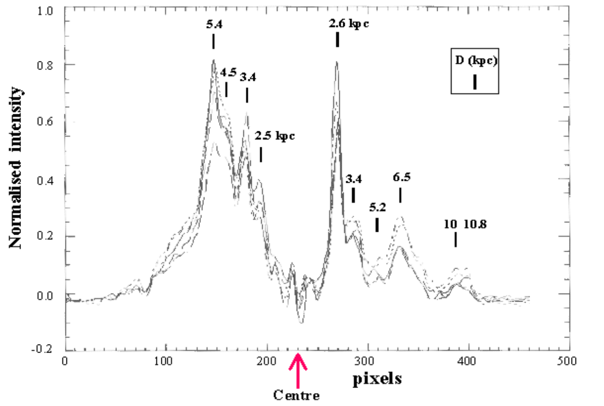

Figure 4. A spiral structure: substraction of the smooth inter-arms stellar distribution to the galactic profiles in all LW filters. The galactic centre is indicated and each peak is annotated by its distance to the centre.

3.2. Excitation efficiency and galactic structure

To explain the emission profiles observed beyond $5\,\mu$m, a function describing a UV photon absorption probability and/or an excitation efficiency of UIB carriers is introduced as a factor of the previous stellar distribution and this new function is adjusted so that the product [source $\times$ efficiency] fits the infrared bands profiles. The obtained agreement shows that this efficiency function is quite constant outside the bulge. There is a clear *deficiency of carriers excitation in the bulge* which can be related either to the high density of molecular clouds in the centre, PAH being stuck on the ice mantle of grains, or to an actual destruction of carriers by the UV field. Ratios of UIB 6.2, 7.7 and $11.3\,\mu$m to the flux measured at $4.5\,\mu$m show several peaks which correspond to CO peaks tracing molecular gas in the arms: the excitation of carriers seems to be very efficient in the arms. The ratio profiles confirm the reduced UIB carriers excitation in the bulge.

The difference between the galactic profiles in all LW filters and the fitted stellar distribution, assumed to be representative of the smooth inter-arms component was done. Then, several structures are clearly showing up for all filters (see Figure 4): these structures are not symmetrical in intensities but they appear to be symmetrical in position with respect to the galactic centre. They are likely linked to the spiral structure and two clumps of emission standing at about 3 kpc and 3.5 kpc on both sides of the centre can be due to the supposed bar structure and ring of matter in the galaxy seen in CO (Sofue & Nakai 1993). One important structure at about 2.6 kpc is may be contaminated by the supernova SN1986J.

3.3. Relative intensity of UIB bands

The CVF scan gives a spectrum for regions around 4 kpc from the galactic centre from $5\,\mu$m to $12\,\mu$m (see Figure 5). It is quite uniform along the whole galactic plane and is typical of spectra observed in diffuse medium of our galaxy with prominent infrared

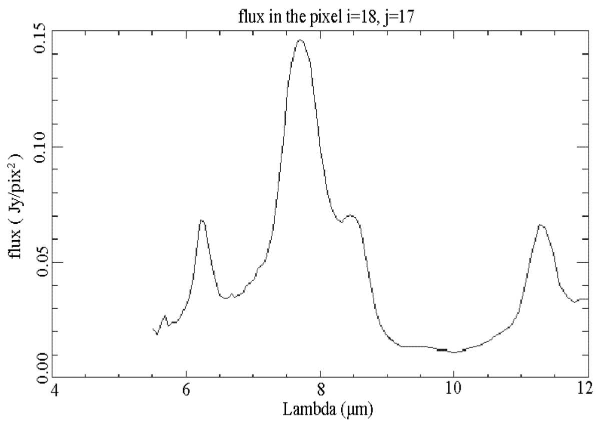

Figure 5. The CVF spectrum on regions in the center of NGC 891.

bands and a rather low continuum. The only particular characteristic is *a 11.3 µm band significantly low* compared to typical spectra in our galaxy and the ratio of UIB bands after substraction of a linearly fitted continuum which contains the $11.3\,\mu$m band confirms this trend. Indeed, we checked that the continuum underlying UIBs is proportional to the intensities of the bands. Then the study of the bands profiles ratios with large LW filters makes sense and gives information along the galactic plane (see Figure 6).

The ratio 6.2 to $7.7\,\mu$m is quite *constant* in very different regions as the bulge, spiral arms or diffuse regions. On the other hand, ratios as $6.2/11.3\,\mu$m and $7.7/11.3\,\mu$m show clearly a strong increase of the $11.3\,\mu$m band intensity in more diffuse regions outside the centre where energy density is lower. To explain this $11.3\,\mu$m band behaviour, two propositions come to mind. First, the absorption along the line of sight of the galactic centre in NGC 891 can be more important for the $11.3\,\mu$m band (located within the "$10\,\mu$m" silicate band) than for the other bands and it can explain the weakening of its intensity towards the centre but this is in conflict with the usual behaviour of the dust extinction versus wavelength, unless the silicate band becomes very strong. Secondly, we can think of the modification of the physical state of the carrier. Indeed, this band is the only one observed here that involve a C-H band vibration and then a strong inhibition of this band can be due to a possible PAH dehydrogenation effect in regions with higher energy density.

The other interesting ratios are those of the UIBs flux to the one of the VSG continuum measured in the LW9 filter at 15 μm. The main conclusion is that there is no particular variation of the ratios along the galactic plane between very small grains heating and PAH excitation. The UIB intensities and the VSG continuum are proportional: either, both are related or, the VSG heating does not depend with the galactic structure. Such a behaviour can support results of Boulanger et al. (1998) who reproduce the infrared bands spectrum by a fitted sum of lorentzian functions, considering that the underlying continuum is the wing of the bands.

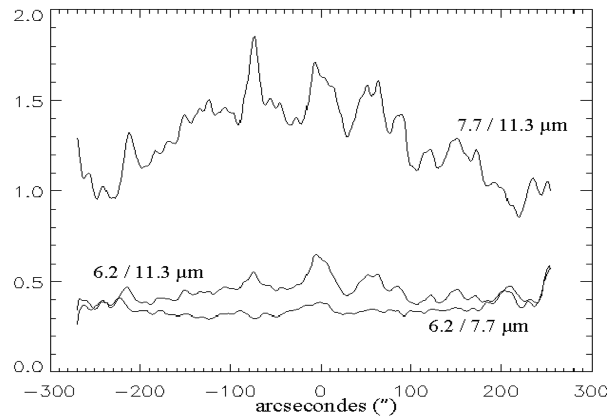

Figure 6. Ratios of galactic profiles in the PAH bands 6.2/7.7 μm, 6.2/11.3 μm and 7.7/11.3 μm. The 11.3 μm band intensity decrease in the galaxy centre.

3.4. Supernova and the UIB bands

The supernova SN1986J is an important contribution to the brightness of the galactic profile. For the only south-west side, the ratio between the UIBs and the flux at 4.5 μm was plotted as a function of the injected flux at 4.5 μm. The ratio increases strongly at the position where the supernova explosion occurred and so there is a direct relation between the star explosion and the increase of UIB carriers excitation efficiency. Observations with ISO of the supernova Cassiopeia A show a correlation between the gas and the dust emission (Lagage et al. 1996) and prove that formation of complex molecules is possible in the cores. One possible process which can be invoked is the heating of PAH by electrons (Bakes et al. 1994) and it will be useful to check if this hypothesis is efficient here.

4. CONCLUSION

Observing a quiet edge-on spiral galaxy gives the confirmation that UIBs are clearly detected in the whole diffuse medium in external galaxies similar to ours, implying presence of aromatic compounds, as PAH, and confirming the necessity of a transiently heating mechanism. The maps of infrared bands in NGC 891 show that the excited matter distribution follows the molecular gas distribution and star forming regions. The measured flux at 4.5 μm is shown to be a tracer of ionised matter and thus of the primary source of UIB excitation, the young hot stars. The galactic emission profiles in the different bands can be adjusted by the product of the derived stellar distribution by an efficiency factor. We demonstrate clearly a deficiency of excitation of UIB bands carriers in the bulge which could be due to a sticking of PAH on the ice mantle of grains in the numerous molecular clouds present in the galactic centre. When the stellar distribution is subtracted to the galactic profiles of PAH bands, the spiral structure appears clearly as symmetric peaks relative to the nucleus, with may be, the presence of a ring of matter and a bar structure. The PAH bands intensities ratios along the galactic plane show a very particular behaviour of the 11.3 μm band. The inhibition of this band near the galactic centre can be an effect of an important absorption towards the centre, or to PAH dehydrogenation in these regions.

REFERENCES

Allen, C. 1973, Astrophysical quantities, Athlone Press

Bakes, E., Tielens, A.G.G.M., 1994, ApJ, 427, 822

Boulanger, F., Band, B., van Albada, G.D. 1985, A&A, 144, L9

Boulanger, F., Boissel, P., Cesarsky, D., Ryter, C. 1998, A&A, 339, 194

Boulanger, F., et al. 1996, A&A, 315, L325

Cesarsky, C.J., Abergel, A., Agnese P., et al. 1996, A&A, 315, L32

Giard, M., Pajot, F., Lamarre, J.M., et al. 1988, A&A, 201, L1

Lagage, P.O., Claret, A., Ballet, J., et al. 1996, A&A, 315, L273

Mattila, K., Lemke, D., Haikala, L.K., et al. 1996, A&A, 315, 353

Ristorcelli, I., Giard, M., Meny, C., et al. 1994, A&A, 286, L23

Rouan, D., Le Coupanec, P., Gallais, P., Lacombe, F., Tiphène, D., Léger, A. 1996, ISAS Conf *Diffuse Infrared Radiation and the IRTS*, Nov 11-14 1996, Kanagawa, Japan

Sofue, Y., Nakai, N. 1993, PASJ, 45, 139

Sukumar, S., Allen, R.J. 1991, ApJ, 382, 100

Xilouris, E.M., Alton, P.B., Davies, J.L., et al. 1998, A&A, 331, 894

[C II] 158 μm OBSERVATIONS OF A SAMPLE OF LATE-TYPE GALAXIES FROM THE VIRGO CLUSTER

K. J. Leech[1], H.J. Völk[2], I. Heinrichsen[1], H. Hippelein[3], L. Metcalfe[1], D. Pierini[2], C.C. Popescu[2], R.J. Tuffs[2] & C. Xu[4]

[1] ISO Data Centre, Astrophysics Division, ESA, Villafranca, Spain.
[2] Max-Planck-Institut für Kernphysik, Heidelberg
[3] Max-Planck-Institut für Astronomie, Heidelberg
[4] IPAC, Caltech, USA

ABSTRACT

We have observed 19 Virgo cluster spiral galaxies with the Long Wavelength Spectrometer (LWS) onboard ESAs Infrared Space Observatory (ISO) obtaining spectra around the [C II] 157.741 μm fine structure line. These 19 galaxies are relatively quiescent in star forming activity compared to previous studies from airborne observatories.

Fifteen of the nineteen galaxies were detected in the [C II] line. Any influence of the Virgo cluster environment on the [C II] emission was found to be small compared with the strong dependence of the line emission on basic measurables such as morphology. These relatively quiescent galaxies exhibit a smaller range of [CII] to FIR ratios compared to other galaxy surveys, yet there is a good correlation between the strength of the [C II] line and the far-infrared flux, as measured by IRAS.

Key words: Galaxies: clusters: general; Galaxies: general; Galaxies: ISM; Infrared: galaxies

1. INTRODUCTION

The ISO (Kessler et al. 1996) Guaranteed Time programme VIRGO (Völk et al. in prep) is a study of a complete volume-limited, unbiased sample of spiral, irregular and BCD galaxies from the Virgo cluster, selected from the Virgo Cluster Catalogue (VCC) of Binggeli et al. (1985), as described in Boselli et al. (1997). While the VIRGO proposal is primarily photometric, we wished to observe many of these galaxies spectroscopically. Various constraints limited observations to the [C II] 157.741 μm cooling line. This line should probe photodissociation regions (cf. Stacey et al. 1991) associated with massive star formation, and also the diffuse components of the Interstellar Medium (e.g. Nakagawa et al. 1998). It fact, it has been observed not only in "compact" regions of the Galaxy like HII regions, OB associations, reflection nebulae, and planetary nebulae, but also in "diffuse" regions, as well as for entire galaxies. [C II] emission is thought to be the most important gas cooling process in late type galaxies, balancing the photoelectric heating from grains.

In field galaxies the [C II] line has a luminosity of the order of 10^{-3} to 10^{-2} that of the total FIR flux of a galaxy (e.g. Malhotra et al. 1997). The present sample, selected from the Virgo cluster, better represents the properties of the [C II]-line emission in galaxies less active in star-forming activity (even at the top end of the luminosity range observed) than the sample of Malhotra et al. (1997).

At the distance of the Virgo cluster (taken to be 21 Mpc), the 80 arcsec beam of LWS, Clegg et al. (1996), covers an area of approximately 7 kpc in diameter – optical images of the Virgo galaxies by Sandage & Tammann (1985) indicate that the LWS beam covers out to the observed spiral arms. The extended [C II] emission detected at this distance in NGC 6946 by Madden et al. (1993) accounted for 70% of the total [C II] emission. Observation of Virgo galaxies with LWS therefore detects not only [C II] emission from the dense nucleus but, assuming Virgo galaxies are similar to NGC 6946, will primarily sample the [C II] emission from diffuse regions in and between the spiral arms.

This paper presents a preliminary reduction, analysis and discussion of the [C II] data. The full data will be presented in Leech et al. in prep. A companion paper at this conference (Pierini et al., these proceedings), extended in Pierini et al. (1999), discusses the [C II]-line emission in more detail and its relation to other measures of the star-forming activity.

2. SAMPLE SELECTION AND OBSERVATIONS

The galaxies observed in the [C II] 158 μm line are a subsample of a large complete sample of late-type galaxies selected from the Virgo Cluster catalogue of Binggeli et al (1985) for observations with the ISOPHOT (Lemke et al. 1996) and ISOCAM (Cesarsky et al. 1996) instruments. The parent sam-

Proceedings of the Conference "The Universe as seen by ISO", Paris, France, 20–23 October 1998 (ESA SP-427, March 1999)

Table 1. Sample galaxies and positions of selected reference fields.

Target	Alternate name	RA (J2000)	DEC (J2000)	Core or Periphery	60 μm flux (Jy)	100 μm flux (Jy)	B_T
VCC 66	NGC 4178	12 12 46.9	10 52 07.0	P	2.8	9.0	11.9
VCC 92	NGC 4192,M98	12 13 48.4	14 54 07.2	P	6.5	21.5	10.9
VCC 460	NGC 4293	12 21 13.2	18 23 03.6	P	4.6	10.6	11.2
VCC 857	NGC 4394	12 25 56.0	18 12 47.6	P	1.0	4.3	11.8
VCC 873	NGC 4402	12 26 06.8	13 06 47.6	C	5.4	17.4	12.6
VCC 1003	NGC 4429	12 27 26.2	11 06 30.3	C	1.4	4.3	11.1
VCC 1043	NGC 4438	12 27 45.7	13 00 30.4	C	3.7	13.1	10.9
VCC 1110	NGC 4450	12 28 29.5	17 05 06.8	P	1.4	7.6	10.9
VCC 1158	NGC 4461	12 29 03.0	13 11 07.1	C	<0.2	<0.8	12.1
VCC 1253	NGC 4477	12 30 02.9	13 38 07.7	C	0.5	1.0	11.3
VCC 1326	NGC 4491	12 30 57.2	11 29 02.1	C	2.8	3.3	13.4
VCC 1412	NGC 4503	12 32 05.5	11 10 38.8	C	<0.2	1.0	12.1
VCC 1690	NGC 4569,M90	12 36 49.9	13 09 53.8	C	8.8	25.0	10.2
VCC 1727	NGC 4579	12 37 43.5	11 49 06.4	C	4.9	19.6	10.6
VCC 1813	NGC 4596	12 39 56.3	10 10 38.0	P	0.4	1.0	11.5
VCC 1869	NGC 4608	12 41 13.6	10 09 14.9	P	<0.2	<0.5	12.0
VCC 1972	NGC 4647	12 43 32.4	11 34 46.7	P	4.9	15.9	12.0
VCC 1987	NGC 4654	12 43 57.2	13 07 35.1	P	13.4	33.4	11.1
VCC 2070	NGC 4698	12 48 23.2	8 29 14.9	P	<0.2	1.6	11.5
VBACK01		12 13 30.9	15 30 47.2				
VBACK03		12 13 52.4	8 29 12.2				
VBACK04		12 25 05.9	17 43 52.1				
VBACK12_1		12 43 08.5	9 47 34.4				
VBACK12_2		12 43 08.5	9 47 34.4				
VBACK13		12 48 14.5	12 58 38.7				

ple, which is defined in Völk et al. in prep (see also Boselli et al. 1997), was selected from a cluster as this represented the most convenient way of ensuring completeness in a wide variety of intrinsic properties, embracing a large dynamic range in star-formation activity. We chose Virgo cluster member galaxies because of the high level of completeness of the VCC, (to B_T 18), because at the distance to the cluster the typical angular sizes of the infrared emitting regions are well matched to the angular resolution of ISO, the distance of this cluster was optimum for the detection of dwarf galaxies with ISOPHOT and because galaxies in the peripheral regions are thought to be freshly infalling from the field (Tully & Shaya 1984) and therefore less representative of the cluster environment. In order to provide a statistical check of the influence of the cluster environment on the far-infrared properties, the selection was made from two contrasting regions, i.e. cluster core and cluster periphery.

LWS was capable of detecting a large fraction of the spiral galaxies in the parent sample (based on predictions from the IRAS fluxes and the average [CII]-line to far-infrared continuum ratios of late-type galaxies observed with KAO), but constraints on the available observing time restricted us to a sample of 21 spirals earlier than Scd and complete to B_T=12.3 mag. Of these 21 targets, the interacting pair VCC1673 – 1676 was not included because the LWS beamwidth was not able to separate the individual emissions and VCC 836 was not observed due to conflicts with another programme. These final 18 giant Virgo spirals nevertheless provide a sample of relative quiescent galaxies in comparison to other samples of normal spiral galaxies selected for ISO observations (i.e., Malhotra et al. 1997).

One other optically faint core galaxy, VCC 1326, was observed to serve as a cross-calibration target between the LWS measurements and the ISOPHOT measurements of the larger VIRGO programme.

Information on all these galaxies is given in Table 1, together with the positions of sky background reference fields (denoted VBACK in the following tables and figures) to check for foreground [C II] emission from the Milky Way.

The observing log was given in Leech et al. (1998). All observations carried out were standard grating range scans (AOT 2's), and sets of observations were used to observe several galaxies in sequence (in ISO terminology, the observations were concatenated), with one sky background position used for each set.

3. DATA REDUCTION AND RESULTS

The Auto Analysis Results from Off-Line Processing (OLP) version 6 were processed further using the ISO Spectral Analysis Package (ISAP) by: reading data in; discarding bad LWS data points; averaging scans for detector 8 (the one covering the 158 μm region); and finally fitting continua and gaussians to any lines seen in the data to obtain flux and central wavelength.

Of the 19 galaxies observed, 15 were detected. Of the six background positions used, five had no detectable emission at galactic [C II] wavelengths and one was repointed to VCC 873 (confirming the line flux and wavelength for that galaxy). In several galaxy observations (e.g. VCC 1110) galactic [C II] emission was observed, and in all such cases was measured and

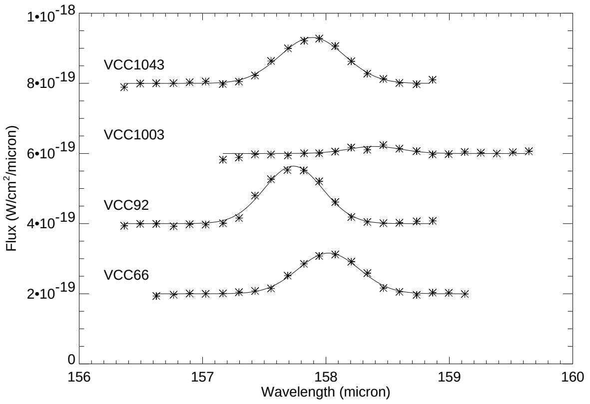

Figure 1. Example Virgo galaxy observations. The level of the baselines is arbitrary.

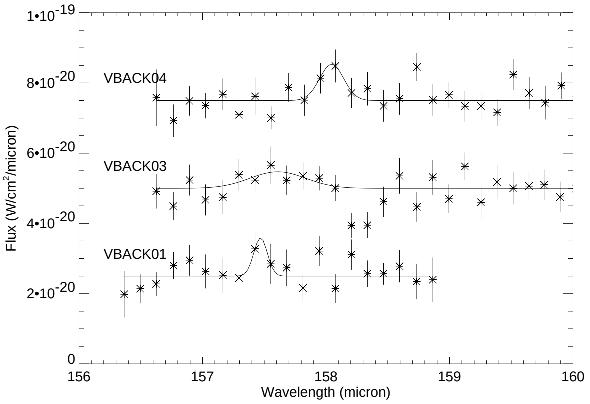

Figure 2. Example Background observations. The level of the baselines is arbitrary.

noted. In only one case do we think there may be confusion between emission from galactic [CII] and the target Virgo galaxy (VCC 1326).

Example [CII] line wavelength regions are shown in Figure 1, and example background positions are shown in Figure 2. In cases where no line was present the strongest feature in the spectral region was taken to be the upper limit of detectability. A few of the observations suffer from memory effects and/or glitches that cause the first few short-wavelength datapoints to be systematically lower than the continuum. These points were not used when deriving the line or continuum fluxes.

Line fluxes, central wavelengths and continuum fluxes will be presented in Leech et al. (in preparation).

4. DISCUSSION

Figure 3 shows the relation between the [CII] flux and the far-infrared (FIR) flux from IRAS measurements given by FIR = 1.26×10^{-18} ($2.58 \times F_\nu(60\mu m) + F_\nu(100\mu m)$) Wcm^{-2} (Helou et al. 1988). Despite the spatial mis-match between the LWS 80 arcsec diameter circular aperture and the larger IRAS square

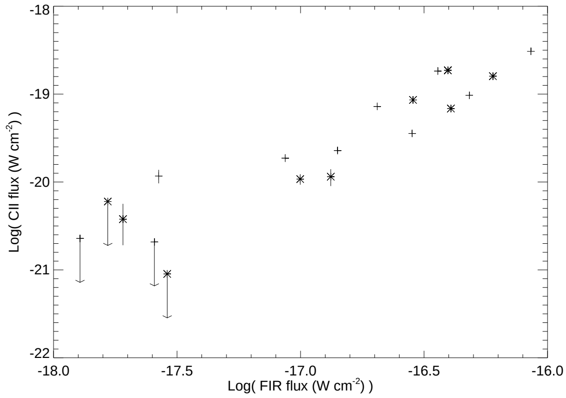

Figure 3. [C II] flux against FIR flux. Error bars are marked in the vertical, where they are larger than the symbol size, and upper limits are marked. Core galaxies are marked by '', periphery by '+'.*

apertures, there is a good correlation between these observed quantities despite the approximately two orders of magnitude range in both observable quantities.

This correlation is consistent with the LWS [C II] measurements in 5 Sc or later Virgo spirals by Smith & Madden (1997). Galaxies which have higher continuum and line brightnesses tend to have later Hubble types, consistent with the increase in star formation activity with increasing lateness, e.g., Kennicutt et al. (1994). The tendency for the correlation to flatten off with increasing brightness, as observed by Stacey et al. (1991) for a sample embracing starburst and ultraluminous galaxies, is not apparent for the relatively quiescent Virgo sample.

The range of the [C II] to the total IRAS FIR flux ratio is from 0.1% to 0.5%. It covers the ranges expected for compact sources (0.2%), such as active star-forming regions, to the diffuse component of the ISM (0.6%), Nakagawa et al. (1998). Galaxies observed by Stacey et al. (1991) cover the range 0.15 – 0.6%, and in NGC 5713 the ratio is 0.7% (Lord et al. 1996).

The [C II]/FIR ratio increases with the current star formation rate (measured by the Hα EW) in quiescent galaxies till a "plateau" value, typical of gas-rich and starburst galaxies – see Pierini et al. (these proceedings).

Figure 4 shows the [C II] to FIR ratio against the dust temperature, as measured by the ratio of the IRAS flux densities at 60 and 100 μm. We note that galaxies with higher f(60)/f(100) have lower values of [C II]/FIR, in agreement with Malhotra et al. (these proceedings). There is no apparent relation between the [CII] line/dust colour ratio and position in the cluster or HI mass surface density in the galaxian disks. Therefore, any relation of the [CII] emission to the diffuse HI component of the ISM is not obvious, at least for the central regions of the disks observed. [CII] emission was, however, found to have a strong dependence on basic measurables such as morphology – this will be discussed more in Leech et al. (in preparation).

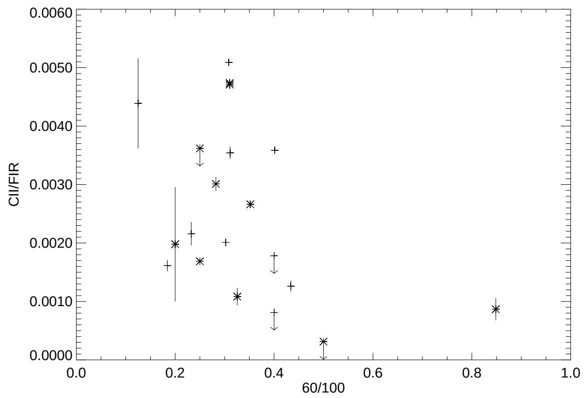

Figure 4. [C II]/FIR ratio against dust temperature, indicated by 60/100 μm ratio. Error bars and upper limits are marked. Core galaxies are marked by '', periphery by '+'.*

5. SUMMARY

We have observed 19 normal high surface brightness late-type galaxies from the Virgo cluster with the LWS spectrometer onboard the ISO satellite around the [C II] fine structure line, detecting 15 of these. A good correlation is found between the strength of the [C II] and the FIR flux. Both fluxes increase significantly with later Hubble types. Conversely, no difference can be found in the [C II] properties between the core and periphery galaxies.

REFERENCES

Binggeli, B., et al. 1985, AJ 90, 1681

Boselli, A., et al. 1997, A&AS 121, 507

Cesarsky, C.J., et al. 1996, A&A 315, L32

Clegg, P.E., et al. 1996, A&A 315, L38

Helou, G., et al. 1988, ApJS 68, 151.

Kennicutt, R.C., Tamblyn, P., Congdon, C., 1994, ApJ 435, 22

Kessler, M.F., et al. 1996, A&A 315, L27

Leech, K.J. et al. 1998, 'First ISO Workshop on Analytical Spectroscopy', Eds Heras, Leech, Trams & Perry, ESA SP-419, p279.

Leech, K.J., et al. in prep.

Lemke, D., et al. 1996, A&A 315, L64.

Lord, S.D., et al. 1996 A&A, 315, L117.

Madden, S.C., et al. 1993, ApJ 407, 579.

Malhotra, S., et al. 1997 ApJ 491, L27.

Nakagawa, T., et al. 1998 ApJS 115, 259.

Pierini, D., et al. 1999 MNRAS 303, L29.

Sandage, A., Binggeli, B., Tammann, G.A. 1985, AJ 90, 395.

Smith, B.J., Madden, S.C. 1997 AJ 114, 138

Stacey, G.J., et al. 1991, ApJ 373, 423

Tully, R.B., Shaya, E.J. 1984 ApJ, 281, 31

Völk, H., et al. in prep

MEDIUM-DISTANT CLUSTERS OF GALAXIES SEEN BY ISO

L. Lémonon, M. Pierre, C.J. Cesarsky, D. Elbaz & L. Vigroux
DAPNIA/SAp, CEA Saclay, France

ABSTRACT

We present a comprehensive study of ISO cluster galaxies in connection with other wavelengths. First results show that infrared galaxies detected by ISO-CAM concentrate on the edge of clusters. Surprisingly, they are not emission lines galaxies but very luminous elliptical, merging or interacting ones, which suggests non-trivial connections between star formation rate, optical and mid-IR properties. However, no correlation has been found between the MIR/optical star formation properties of the galaxies, so that the exact origin of the IR emission remains unclear.

Key words: galaxy clusters.

1. INTRODUCTION

Until recently, detailed cluster studies were restricted to nearby clusters ($z < 0.1$). Nowadays, new imaging as well as spectroscopic capabilities (visible, X-ray, IR, radio) have considerably improved our view of the distant universe. In this context, clusters at redshift ~ 0.2–0.3 are about the most distant objects for which extensive resolved multi-wavelength studies are possible within reasonable observing times. Moreover, they offer the unique advantage, compared with more nearby objects, of being observable together with their surroundings in a single field of view by most of the modern instruments (at $z = 0.2, 30' = 7.6$Mpc, with $H_0 = 50, q_0 = 0.5$). In this context, we have selected a sample of ten bright objects, expected to be rich clusters, from the *ROSAT All Sky Survey* (RASS) in the $z = 0.15 - 0.3$ range in order to investigate issues ranging from cluster formation and evolution down to a local phenomenon such as the enrichment of the inter-cluster medium (ICM) (Pierre et al. 1994). We have undertaken a detailed high-resolution multi-wavelength follow-up including ROSAT HRI and PSPC, ASCA pointings, radio images at 3, 6, 13, 20 and 36 cm and extensive photometry and spectroscopy in the optical. Seven of them were included in the ISO Central Programme (DEEPXSRC, 30 hours, P.I.: C.J. Cesarsky; Collaborator: M. Pierre), in order to study the influence of the environment on the galaxy evolution. We present here the analysis which allowed us to statistically determine properties of IR emitting galaxies in our clusters.

2. OBSERVATIONS

Seven objects extracted from the RASS have been observed by ISO, at 6.75 and 15 μm with ISO-CAM and at 90 μm with ISOPHOT. From our X-ray/radio/optical, four clusters turned out to be very rich objects ranging from $z = 0.165$ (Abell 1111) to $z = 0.307$ (Abell 1300), and three objects appeared to be small groups with a central AGN (see Table 1) (Lémonon 1999). All observations were made with a pixel size of 6 arcsec, and each sky position as observed four times. The various environmental conditions are represented in those seven objects, fully described in several papers, and can be summarized as follows:

- Abell 1300: a post merging cluster containing a radio halo and a relic radio source (Lémonon et al. 1997, Reid et al. 1998)
- RXJ1104-2330: a strong AGN of BL-Lac type possibly embedded in a small cluster or a large group of galaxies (Lémonon 1999)
- Abell 1732 and Abell 1111: two cooling flow clusters respectively large and small (Lémonon 1999)
- RXJ1032-2607: probably a strong AGN in a small group of galaxies (Lémonon 1999)
- RXJ1314-2516: a new very interesting merging cluster of galaxies, containing probably a relic radio source (Lémonon 1999)
- RXJ1315-4236: a more nearby ($z = 0.105$) AGN of BL-Lac type, in a group of galaxies (Lémonon 1999)

3. IR EMISSION IN ISOCAM FILTERS

As discussed by Fadda & Elbaz (these proceedings), the k-correction for distant clusters is a very important point when we look in the mid-IR wavelength. In our redshift range ($0.165 < z < 0.307$), LW2 always includes only the 6.2 μm Unidentified Infrared Band (UIB) feature, but is more and more (with the redshift) contaminated by the Rayleigh-Jeans tail of red stars. The LW3 filter is less and less sensitive to the warm dust but is always contaminated by the 11.3μm

Proceedings of the Conference "The Universe as seen by ISO", Paris, France, 20–23 October 1998 (ESA SP-427, March 1999)

Table 1. DEEPXSRC ISOCAM observations. The column are : (1) the object name from the ACO catalogue (Abell et al. 1989) when existing or the ROSAT All Sky Survey number. (2) the redshift of the object. (3) the size of the side of the maximum sensitivity box area. (4) the sensitivity in the LW2 (6.75 μm) CAM filter. (5) the sensitivity in the LW3 (15 μm) CAM filter (RXJ1314−2516 was not observed in the LW3 band).

Object name	z	Field of View	LW2 μJy	LW3 μJy
Abell 1300	0.307	6.4′	500	1400
RXJ1104−2330	0.187	6.4′	450	1000
Abell 1732	0.193	6.4′	400	1000
Abell 1111	0.165	6.4′	500	1300
RXJ1032−2607	0.247	4.8′	750	1500
RXJ1314−2516	0.244	4.8′	500	-
RXJ1315−4236	0.105	9.6′	750	1100

UIB feature and the 9.7μm silicate absorption. Unfortunately, the interpretation of mid-IR properties is turning into a maze by this mixity of IR contributions.

4. RESULTS

4.1. What kind of objects did we detect?

First, two thirds of the objects detected by ISOCAM are optically identified as stars. On about 70 remaining galaxies, since we had optical spectra for 35 of them, we were able to evaluate the contamination by field galaxies. One third of the 35 appeared not to belong to the clusters, so by extrapolation, we expect that some 50 out of 70 are really clusters members. At our depth, 20 fields galaxies on the total area covered by our ISOCAM observation are in a good agreement with deep 15 μm count at 1 mJy from ELAIS (Rowan-Robinson et al., these proceedings). We detect as many galaxies at 6.75 μm as at 15 μm although very few of them are detected in both filters (about 15%). Detected galaxies are bluer (V-I $\sim$ 1.2) than the mean cluster galaxy (V-I $\sim$ 1.5, which corresponds to "normal" early-type galaxies at those redshifts) but their spectrum look like elliptical galaxies.

4.2. Radial distribution of ISOCAM galaxies in clusters

Figure 1 shows the radial distribution of a composite cluster made of all detected galaxies. The density in the center is only due to the central dominant (cD) galaxies which are 10-100 times more luminous in the optical that normal elliptical galaxies and thus expected to be more luminous also in the mid-IR. The main observation is that most of detected galaxies concentrate on the edge of the cluster. Below 750 kpc, only one galaxy is detected in both band (cD galaxies excluded) although about 20 galaxies are detected at 6.75 μm or 15μm. This may suggests that 6.75 and 15 μm galaxies are two different populations of galaxies. To the contrary, beyond 750 kpc, more than 50% of them are detected in both bands, so galaxies in this range may be a different population. The seven galaxies detected in both bands are bluer than the mean detected galaxies with an optical color of V-I $\sim$ 0.95, corresponding to Scd type.

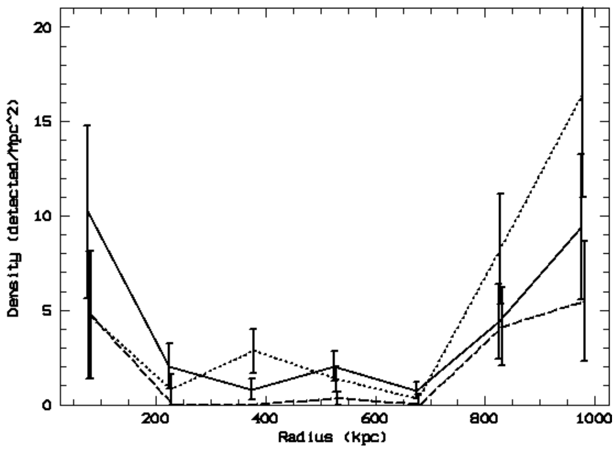

Figure 1. Radial distribution of ISOCAM galaxies in a composite cluster made of all detected galaxies in each cluster. Solid and dotted lines show 6.75 and 15μm galaxies, respectively, dashed line shows galaxies detected in both bands.

4.3. Galaxies detected only at 6.75 μm

This population may be the signature of the Rayleigh-Jeans tail of an old stars population, as :

1. all cD galaxies are detected, and they are the most luminous galaxies of each clusters,
2. there is likely a correlation between LW2 and I flux (see Figure 2),
3. the mean V-I color ($\sim$ 1.4) is closer of 'normal' elliptical galaxy than others detected objects,
4. regarding our 15 μm completeness, we can be sure that most of galaxies detected at 6.75 μm have a 15 μm flux *below* the 6.75 μm one, excluding intense star formation activity.

Even if many galaxies seen only at 6.75 μm are detected beyond 750 kpc where elliptical galaxy density is much lower than in center, the low total number of them is fully compatible with the statistically normal density of early-type in outskirt regions.

4.4. Galaxies detected at 15 μm

It is well known that spiral galaxies in clusters are more concentrated in the external regions (Dressler 1980). Figure 1 shows that galaxies detected at 15 μm are preferentially seen beyond 750 kpc, and much more than 6.75 μm ones. Half of them are detected also at 6.75 μm with flux ratio typical of photo-dissociation regions or star formation activity. Their optical colors are bluer than mean cluster galaxies.

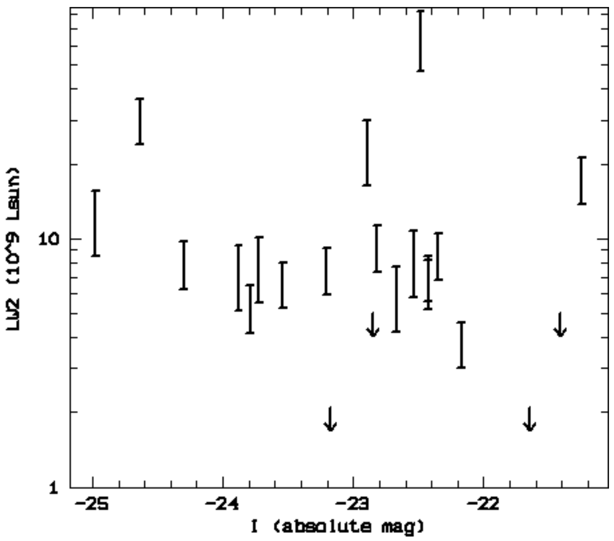

Figure 2. The 6.75 μm (μJy) luminosity in function of the I absolute magnitude for objects detected only at 6.75 μm. Four galaxies are well outside the general trend, they must be field galaxies or dusty/star-forming objects.

4.5. Effects of the environmental conditions

It could be a correlation between the number of detect galaxies at 6.75 μm and the X-ray luminosity in the [0.1-2.4 keV] band (Lémonon 1999). Since the X-ray luminosity is related to the richness of the clusters, this corroborates the suggestion of section 4.3. as most LW2 galaxies are luminous early-type galaxies. Other effects of environmental conditions are very hard to point out because of our low statistic (between 4 and 15 galaxies detected by ISOCAM per cluster).

4.6. Optical correlations with star-forming galaxies

In the course of our optical follow-up, we have discovered that detected ISOCAM galaxies in medium distant clusters (at a sensitivity of $\sim$ 1 mJy) are not emission lines galaxies but very luminous elliptical, merging or interacting ones, which suggests non-trivial connections between star formation rate, optical and mid-IR properties (see Figure 3). However, the spectral resolution at which the redshift of these galaxies were measured (15 Å) does not allow us to identify any peculiar signature in the optical spectra of these objects, so that the exact origin of the IR emission remains unclear. This observation became a very scheming subject since IR deep surveys claim the existence of a population of galaxies with great IR fluxes in the past ($0.6 < z < 1$) with no peculiar optical signature (Elbaz et al. 1998, Aussel et al. 1999) and could be a new starting point to the comprehension of the stars formation history.

ACKNOWLEDGMENTS

The ISOCAM data presented in this paper was analysed using 'CIA', a joint development by the ESA Astrophysics Division and the ISOCAM Consortium. The ISOCAM Consortium is led by the ISOCAM PI, C. Cesarsky, Direction des Sciences de la Matière, C.E.A., France.

REFERENCES

Abell, G.O., Corwin, H.G., Olowin, R.P. 1989, ApJS 70, 1

Aussel, H., Cesarsky, C., Elbaz, D., Starck, J.L. 1999, A&A, 342, 313

Dressler, A. 1980, ApJ 326, 351

Elbaz, D. et al. 1998, "NGST" 34th Liege Astrophysics Colloquium, eds. Benvenuti P. et al. ESA Pub., astro-ph/9807209

Lémonon, L., Pierre, M., Hunstead, H., Reid, A., Mellier, Y., Böhringer, H. 1997, A&A 326, 34

Lémonon, L., Pierre, M., Cesarsky, C.J. et al. 1999, in preparation

Lémonon, L. 1999, PhD. thesis, University of Paris XI, France

Pierre, M., Böhringer, H., Ebeling, H., Voges, W., Schuecker, P. et al. 1994, A&A 290, 725

Pierre, M., Aussel, H., Altieri, B. et al. 1996, A&A 315, L297

Reid, A.D., Hunstead, R.W., Lémonon, L., Pierre, M. 1998, MNRAS accepted

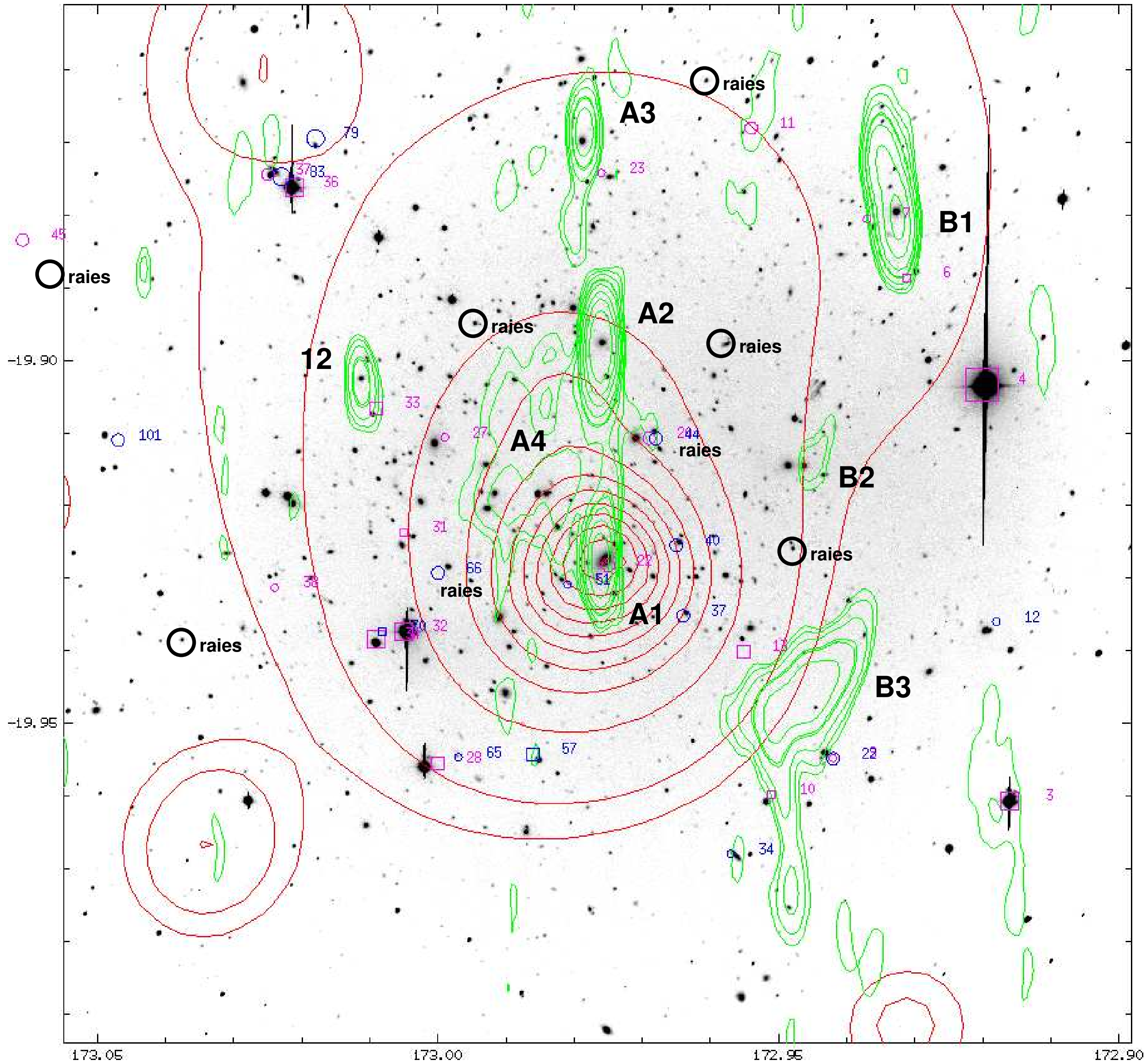

Figure 3. Abell 1300, a post-merging cluster (Lémonon et al. 1997, Reid et al. 1998). On the R band image taken on the CFHT are overlaid in red contours X-ray [0.4-2.4 KeV] PSPC levels (8.3×10^{-4}, and 1.8×10^{-3} to 6×10^{-2} by step of 5.76×10^{-3} counts/s/arcmin^2)and in green radio (1.4 GHz) ATCA levels ($0.2, 0.3, 0.5, 0.9, 1.6, 3.2$ and 6 mJy/beam). It confirms that detected ISOCAM galaxies (in magenta and blue for respectively $6.75\,\mu m$ and $15\,\mu m$ bands, circle for galaxies and squares for point-like objects, with size proportional to emitting fluxes) in clusters above a limited flux are not galaxies with emission lines but very luminous elliptical, merging or interacting galaxies (Pierre et al. 1996). Line-emitting galaxies are pointed by the "RAIES" label. Abell 1300 contains the most distant radio halo known (A4) and a relic radio source (B3). This is one out of our seven objects, others are available in Lémonon (1999).

INFRARED EMISSION OF NORMAL GALAXIES FROM 3 TO 12 μm

N. Y. Lu[1], G. Helou[1], N. Silbermann[1], S. Malhotra[1], M. W. Werner[2], C. A. Beichman[1], R. H. Rubin[3], & H. Thronson[4]

[1]IPAC, MS 100-22, Caltech, Pasadena, CA 91125, U.S.A.
[2]Jet Propulsion Laboratory, MS 233-303, 4800 Oak Grove Road, Pasadena, CA 91109, U.S.A.
[3]NASA/Ames Research Center, MS 245-6, Moffett Field, CA 94035, U.S.A.
[4]Code SE, NASA HQs, Washington DC 20546, U.S.A.

ABSTRACT

We report infrared spectra over wavelength ranges from 2.5 to 5 μm and from 6 to 11.6 μm on a sample of 45 disk galaxies whose bolometric luminosities are derived predominately from stellar sources. The vast majority of the sample spectra look "alike" and can be modelled by a set of emission features (EFs or UIR bands) including those at 6.2, 7.7, 8.6 and 11.3 μm and their associated emission plateaux, superposed on a low-level continuum that possibly extends to and mixes with a photospheric continuum at near-infrared (IR) wavelengths. These continua, which dominate the near-IR part of the spectrum, and the EFs, which dominate the mid-IR part, contribute about equally to the total spectral energy between 3 and 12 μm that in turn carries a luminosity equivalent to about 10% to 40% of the far-IR luminosity for a normal galaxy. From the most quiescent to the most active galaxies in the sample, we found (i) little systematic trend in the relative strengths of the mid-IR features, except for the 11.3 μm feature that could be depressed relative to the other features by up to a factor of 2 or so; and (ii) the ratio of the EF flux to the far-IR flux drops by about 60% on average.

Key words: infrared: lines and bands; ISM: general.

1. INTRODUCTION

The wavelength range of 3 to 12 μm contains a number of important spectral signatures from the ISM, including the so called UIR bands or broad emission features (hereafter EFs) centered around 3.3, 6.2, 7.7, 8.6 and 11.3 μm (Gillett, Forrest & Merrill 1973) and a possible near-infrared continuum (Sellgren 1984; Bernard et al. 1994). Spectra over various parts of this wavelength range have been obtained on a few dozens of infrared bright galaxies using ground-based observations or IRAS (e.g., Roche et al. 1991). But high-S/N spectra were not available before ISO on more normal galaxies. Such data are needed in order to characterize the mid-IR emission of galaxies in an unbiased way.

With its unprecedented sensitivity and continuous wavelength coverage, ISO made it possible for the first time to study spectroscopically in the mid-IR a large number of normal galaxies. As part of the ISO Key Project on Normal Galaxies (Helou et al. 1996), we obtained low-resolution spectra over 2.5 to 12 μm for a sample of 45 galaxies. By covering a broad range of parameters such as optical luminosity, the shape of the far-infrared (FIR) dust continuum emission, the FIR-to-blue luminosity ratio and the optical morphology, the sample was selected to represent the population of normal, star-forming galaxies in the local universe. In this short report, we concentrate on characterizing the observed mid-IR spectra and a few correlations of the EF strengths with galactic parameters at other wavelengths.

2. SPECTRA

The spectra were taken in the PHT-S spectroscopic mode of ISOPHOT (Lemke et al. 1996) whose two 64-element detector arrays cover respectively the wavelength ranges of 2.5 to 4.9 μm with 0.04 μm per element (or pixel), and of 5.9 to 11.7 μm with 0.1 μm per pixel. The aperture size is $24'' \times 24''$ per pixel. We used a chopping mode with sky positions placed at 150 arcsec on either side of each galaxy position. The final sky-subtracted spectra were derived from the Edited Raw Data using the PHOT Interactive Analysis (PIA, Version 7) in a standard way, but with the flux scale determined by a detector responsivity derived directly from calibration observations of standard stars in a similar chopping mode (Acosta-Pulida private communication). ISOCAM imaging data in the LW2 filter (centered at 6.7 μm; Cesarsky et al. 1996a) are available from Silbermann et al. (1996) on 2/3 of our sample galaxies. The flux scales of these two independent data sets agree with each other within $\sim 20\%$ over the wavelength range of LW2. The CAM images also show that the PHT-S aperture contains, on average, about half of the total mid-IR luminosity of a galaxy.

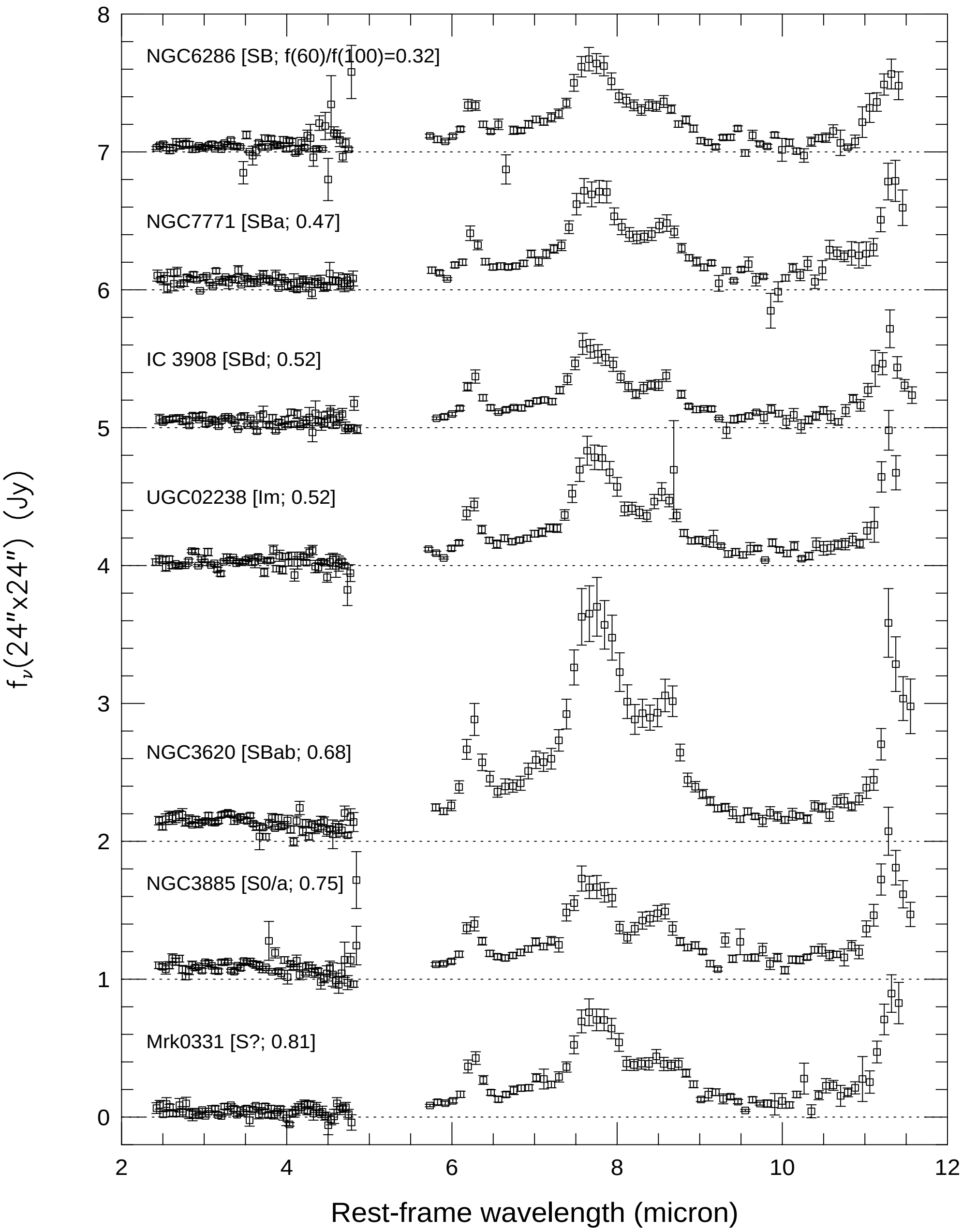

Figure 1. PHT-S spectra of 7 sample galaxies. The ordinate is the flux density within the PHT-S aperture and the abscissa is the rest-frame wavelength. Each spectrum has been vertically shifted by a constant shown by the corresponding dotted line. For each galaxy, its optical morphological type and IRAS 60μm-to-100μm flux density ratio are indicated next to the galaxy name.

The vast majority of the sample galaxies look "alike" over this wavelength range. Figure 1 displays 7 sky-subtracted, rest-frame spectra representative of the majority of galaxies in the sample. The spectra can be characterized by a set of broad EFs with relative intensities similar to those of Type-A spectra of Galactic sources (e.g., Geballe 1997), superposed on a possible low-level continuum that can be visually identified in most individual spectra at near-IR wavelengths away from those bright EFs. The wavelength dependence of this continuum seems to be significantly shallower than the power law of $f_\nu \propto \lambda^{-2.5}$ which describes the long-wavelength tail of stellar photospheres as observed in a number of elliptical galaxies (e.g., Boselli et al. 1998), suggesting a possible non-stellar continuum that could become brighter than the photospheric continuum at wavelengths longer than about $4\,\mu$m. We defer a quantitative analysis of this continuum till the flux calibration at these wavelengths is better understood. To estimate roughly the energetics of the EFs and the underlying continuum, we approximate the combined (stellar and non-stellar) continuum by a power-law function fitted to the sections of the spectrum in the rest frame between 3.5 and $5\,\mu$m and between 9.5 and $10.5\,\mu$m. On average, the fitted continuum contributes to about 50% of the total spectral energy between 3 and $12\,\mu$m.

The overall spectral similarity among galaxies of quite different optical and FIR properties implies either (i) the carriers of the mid-IR emission are not in thermal equilibrium, or (ii) the emission arises only from the part of the ISM under a *certain narrow* range of physical conditions if (i) is not true. Spectra of the EFs similar to those in Figure 1 have been seen toward various Galactic sources, suggesting that (i) should be the correct explanation here.

3. MID-IR EMISSION FEATURES

We consider here only the brightest EFs in mid-IR that are unambiguously detected in individual spectra. The $3.3\,\mu$m feature and other weak features that show up clearly only when we average over a number of sample spectra are analyzed elsewhere.

In order to compare our results later on with those of sources of other types (e.g., AGNs and HII regions) where a strong mid-IR continuum may be present, we derived a continuum-subtracted flux for each EF using the continuum fit defined above. The flux of the $6.2\,\mu$m feature, EF(6.2), is a spectral integration from 6 to $6.6\,\mu$m in wavelength, EF(7.7) from 7.2 to $8.2\,\mu$m, EF(8.6) from 8.2 to $9.2\,\mu$m, and EF(11.3) is twice the flux integrated from 10.9 to $11.3\,\mu$m. Note that these fluxes only include part of the emission plateau between 6 and $9\,\mu$m. Taking into account the full extent of this plateau as well as the $12.7\,\mu$m feature and its associated plateau (see Boulanger et al. 1996; Cesarsky et al. 1996b), the total flux would be roughly 1.25 times the combined EF fluxes defined here.

Using these fluxes, we show various relative feature strengths in Figure 2 as functions of $f(60)/f(100)$, IRAS 60μm-to-100μm flux density ratio; and in Figure 3 as functions of $\log(L_{FIR}/L_B)$, the FIR-to-blue luminosity ratio. L_{FIR}, as defined in Helou et al. (1988), approximates the total dust emission between 42 and $122\,\mu$m. In these figures, we use only the 36 brightest sample galaxies with a heliocentric redshift below 0.03. The filled circles in the figures are the subset of 22 galaxies for which a PHT-S aperture correction has been derived from the CAM imaging data at $6.7\,\mu$m and is less than 75%. In spite of the large ranges in both $f(60)/f(100)$ and L_{FIR}/L_B that our sample covers, the relative strengths among EF(6.2), EF(7.7) and EF(8.6) remain largely unchanged. Relative to these 3 features, the strength of EF(11.3) however decreases by a factor of $\sim$ 2 from quiescent galaxies [i.e., f(60)/f(100) $\sim$ 0.3 or $L_{FIR}/L_B \sim 1$] to galaxies of somewhat starburst characteristics [i.e., f(60)/f(100) $\sim$ 0.8 or $L_{FIR}/L_B > 30$]. If the EFs arise from the so-called polycyclic aromatic hydrocarbon mole-

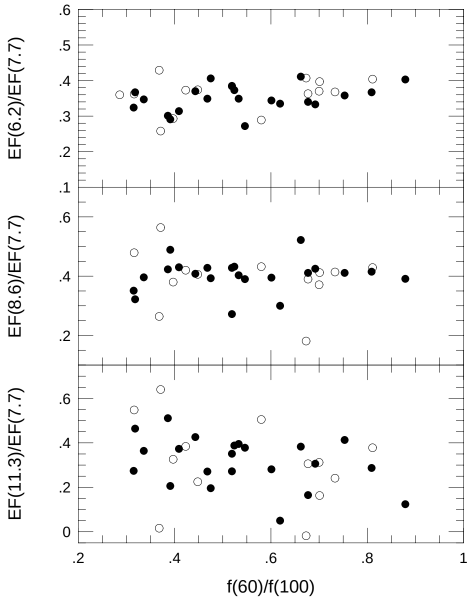

Figure 2. Plots of the relative strengths between the brightest mid-IR EFs as a function of IRAS 60μm-to-100μm flux density ratio for the 36 brightest sample galaxies at heliocentric heliocentric redshifts below 0.03. The filled circles are for the subset of 22 galaxies for which a PHT-S aperture correction is available and is less than 75%.

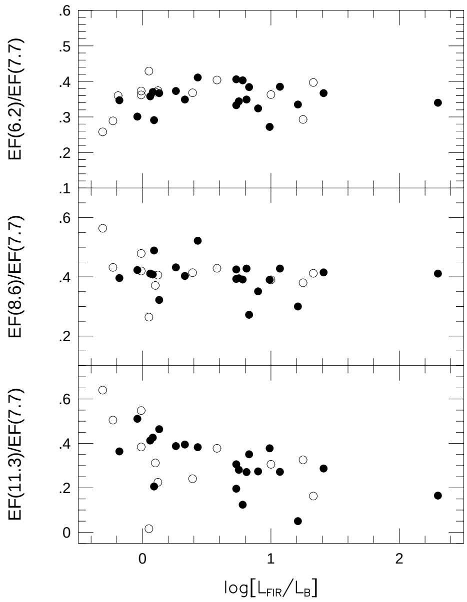

Figure 3. The same as Figure 2, but with the abscissa being the FIR-to-blue luminosity ratio.

cules (PAHs; Léger & Puget 1984; Allamandola, Tielens, & Barker 1985) and the observed variation of EF(11.3)/EF(7.7) arises from a changing percentage of ionized PAHs (cf. Langhoff 1996), it is then surprising to see that EF(6.2)/EF(7.7) remains roughly constant over the entire sample (see, for example, Lu 1998).

Figures 4 and 5 show that the ratio of the combined flux of the 4 mid-IR EFs to that of the FIR emission from dust grains of much larger sizes decreases as f(60)/f(100) or L_{FIR}/L_B increases. In these plots, we show only those 22 galaxies with an available PHT-S aperture correction that is less than 75%. For star-forming galaxies, an increase in f(60)/f(100) or L_{FIR}/L_B is usually attributed to an increasing contribution to the total dust emission from the warm dust in star-forming regions. Therefore, these trends could be a result of the EF carriers being preferentially destroyed in HII regions, a phenomenon that has been known in our own Galaxy (e.g., Helou, Ryter, & Soifer 1991). Also note that the flux ratio of EFs/FIR could become only a few percent for starburst galaxies, a factor that needs to be taken into account when one plans to use the mid-IR features to determine the redshifts of distant, FIR-selected galaxies.

ACKNOWLEDGMENTS

We would like to thank J. Acosta-Pulida for providing us with a copy of the new cal-g table. The data presented here were reduced in part with PIA, which is a joint development by the ESA Astrophysics Division and the ISOPHOT consortium. This work was supported in part by the Jet Propulsion Laboratory, Caltech, under a contract with NASA.

REFERENCES

Allamandola, L.J., Tielens, A.G.G.M., & Barker, J. R. 1985, ApJ, 290, L25.

Bernard, J. P., et al. 1994, A&A, 291, L5.

Boselli, A., et al. 1998, A&A, 335, 53.

Boulanger, F., et al. 1996, A&A, 315, L325.

Cesarsky, C. J., et al. 1996a, A&A, 315, L32.

Cesarsky, D., et al. 1996b, A&A, 315, L305.

Geballe, T. R. 1997, in *From Stardust to Planetesimals: Contributed Papers*, ed. M.E. Kress, A.G.G.M. Tielens, & Y.J. Pendleton, NASA Conference publication 3343, Moffett Field: NASA ARC), p. 119.

Gillett, F. C., Forrest, W. J., & Merrill, K. M. 1973, ApJ, 183, 87.

Helou, G., Khan, I., Malek, L., & Boehmer, L. 1988, ApJS, 68, 151.

Helou, G., Ryter, C., & Soifer, B. T. 1991, ApJ, 376, 505.

Helou, G., et al. 1996, BAAS, 189, 6704.

Langhoff, S. R. 1996, J. Phys. Chem., 100, 2819.

Léger, A., & Puget, J. L. 1984, A&A, 137, L5.

Lemke, D. et al. 1996, A&A 315, L64.

Lu, N. Y. 1998, ApJ, 498, L65.

Roche, P.F., Aitken, D.K., Smith, C.H., & Ward, M.J. 1991, MNRAS, 248, 606.

Sellgren, K. 1984, ApJ, 277, 623.

Silbermann, N., et al. 1996, BAAS, 189, 6701.

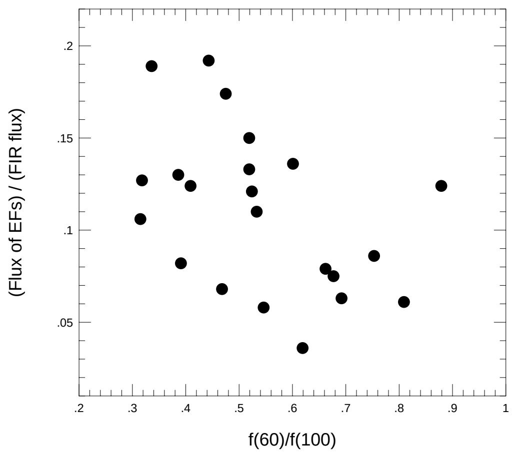

Figure 4. The ratio of the combined flux of the four mid-IR features to the FIR flux is plotted as a function of IRAS 60μm-to-100μm flux density ratio for the 22 sample galaxies for which a PHT-S aperture correction is available from CAM imaging data at 6.7μm and is less than 75%.

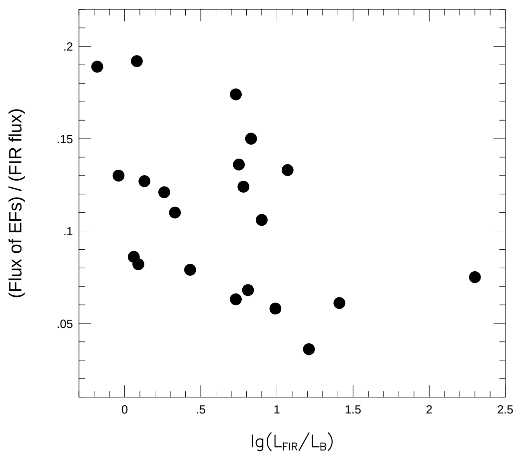

Figure 5. The same as Figure 4, but with the abscissa being the FIR-to-blue luminosity ratio.

THE MID-INFRARED EMISSION FROM EARLY-TYPE GALAXIES

S.C. Madden, L. Vigroux, & M. Sauvage
CEA Saclay, Service d'Astrophysique

ABSTRACT

We have conducted a survey of E and S0 galaxies using ISOCAM's imaging broad band filters covering 4.5 to 18 μm, to probe the dust content of early-type galaxies. While emission from the evolved stellar population can be dominant in the mid-infrared, dust in the form of either small hot grains and/or UIBs can also be shown to be present in some cases. Several galaxies in our sample are dominated in the mid-infrared by non-thermal nuclear activity. Due to the high sensitivity and high resolution of ISO, we can begin to comprehend the origin and distribution of the mid-infrared emission from early-type galaxies.

Key words: mid-infrared astronomy; elliptical galaxies; dust.

1. INTRODUCTION

Early-type galaxies contain a diversity of interstellar media, consisting largely of hot (10^6 to 10^7 K) gas (Sarazin 1997; Brown & Bregman 1998) and to a lesser degree, cold gas in the form of CO and HI (see Henkel & Wiklind 1997 and Knapp 1999 for reviews). Since the stellar distribution of early-type galaxies is often dominated by the evolved red giant population, the presence of dust, apriori, should not be unexpected. Mass-losing red giants expel dust through stellar winds into circumstellar envelopes and subsequently into the ISM. Several analyses of IRAS observations of early-type galaxies confirm the presence of cold (on the order of 30 K) dust, with 60 and 100 μm detections as high as 50 % of E and S0 galaxies (Knapp et al. 1989, 1992; Jura et al. 1987), or much lower, when applying more stringent criteria and excluding galaxies harboring AGNs and peculiar systems (Bregman et al. 1998). While dust masses from IRAS observations are of the order of 10^5 to 10^6 $M_\odot$, colder dust emitting at submillimeter wavelengths has been detected with masses up to an order of magnitude greater (Fich and Hodge 1993). Dust patches and lanes observed from optical obscuration provide further evidence for cold dust (eg. Ebneter and Balick 1985; Goodfrooij & de Jong 1995; van Dokkum & Franx 1995).

The question of the presence of hot dust grains (of order of 100's K) was brought to the fore with 12 μm IRAS observations (Knapp et al. 1992; Sauvage & Thuan 1994). The distribution and origin of dust in early-type galaxies has been difficult to ascertain with IRAS data, due to the lack of resolution and the fact that some of the 12 μm emission may arise from evolved stars at 4000 to 6000 K.

Possible origins of dust include: (1) merging events resulting in galaxies donating large amounts of dust and gas, often seen in dust patches and dust lanes; (2) cooling flow condensations (eg. Fabian et al. 1991), often accounting for dust centrally concentrated; and (3) mass loss from late-type stars (Knapp et al. 1992), which would result in dust more widely distributed throughout the galaxy. Although the presence of dust in early-type galaxies may not be surprising, the quantity of dust seems high relative to expected life-times in the hot ISM (Draine & Salpeter 1979; Tsai & Matthews 1996). Knowledge of the properties of dust in local elliptical galaxies is an essential step in understanding the cosmological star formation rate since the lack of knowledge of dust remains one of the outstanding uncertainties in the models (Franceschini et al. 1998).

Given the imaging capabilities and the unrivaled sensitivity and spatial resolution of ISOCAM, we have conducted a survey of the mid-infrared emission of a sample of early-type galaxies using 3 broad-band filters centered at 4.5, 6.7, and 15.0 μm. We can interpret the contributions from the MIR broad-band filters in light of what we have deduced from other ISOCAM observations of spiral galaxies (see reviews by Vigroux et al. 1998, and, Helou et al. and Vigroux et al. in these proceeding). Noteworthy characteristics of the MIR filters are:

- 4.0 to 5.0 μm (LW1): The Rayleigh-Jeans tail emission of the evolved stellar population.
- 5.0 to 8.5 μm (LW2): The UIB carriers of 6.3, 7.7, 8.6 μm, if present and excited, can dominate the emission in this filter. These bands are proposed to be of carbonaceous origin, stochastocally heated to high temperatures (for example, PAHs: Léger & Puget 1984; Allamandola et al. 1989; coal grains: Papoular et al. 1991).

Proceedings of the Conference "The Universe as seen by ISO", Paris, France, 20–23 October 1998 (ESA SP-427, March 1999)

- 12.0 to 18.0 μm (LW3): Continuum emission in the LW3 15 μm band is seen in HII regions and IR luminous galaxies, thought to originate in very small grains (VSGs) which are transiently heated to high temperatures, i.e. 100 to 200 K (Désert et al. 1990). The UIBs at 11.3 and 12.8 μm can also be present in the LW3 15 μm filter. Non-thermal emission associated with AGNs and central radio sources can dominate the emission of the LW3 band.

If no dust were present, the 6.7 and 15 μm bands would contribute only to the diminishing emission of the old stellar population.

2. DISCUSSION

One example of ISOCAM images is shown for NGC 5266 in Figure 1. The 4.5 μm stellar emission traces the optical extent of the galaxy, while the 15 μm emission is confined to an obvious dust lane. This dust lane is also seen in the optical and is probably a remnant of a merging event, as is thought to be the case for the gas (Morganti et al. 1997). The 6.7 μm band contains emission from both components.

The various spectral energy distributions can be discussed with a color-color diagram constructed with the 3 ISOCAM bands (Figure 2). Regions dominated by various MIR emission origins are delineated in the diagram by dashed lines. Galaxies falling in the left hand side of the diagram, such as NGC 4486, Abell 426, NGC 1052 and NGC 3928, appear to be dominated in the overall emission from the galaxy, by non-thermal emission processes from AGNs and radio sources. Those dominated by their evolved stellar emission such as, for example, NGC 2300, and NGC 1399, are located near the line marked in the upper right quadrant, which indicates 4000 to 5000 K. To verify this, the CVF spectrum of NGC 1399 is shown in Figure 3, with a 4700 K blackbody continuum fit. The spectrum is relatively featureless and ostensibly has some excess dust emission toward the long wavelength part of the spectrum and a very speculative broad feature around 10 μm that may be amorphous silicate. In any case, the dominant MIR emission is stellar in this case. Progressively dustier galaxies move in the color-color diagram (Figure 2), from the stellar continuum line toward the left and below. In the bottom right quadrant lie galaxies exhibiting excess in the 6.7 μm band, above the 4.5 and 15 μm emission levels - clear evidence for the presence of UIB features in the 6.7 μm band. Galaxies located in the upper right quadrant may also contain smaller amounts of UIBs in addition to VSGs, but NGC 5866, NGC 5266 and NGC 5363 unequivocally contain UIBs. The presence of UIBs in early-type galaxy environments may help constrain the nature and excitation of UIBs, the PAHs hypothesis of which requires UV photons to excite. (Sellgren 1984). We can determine whether there is sufficient UV energy to excite the UIBs in these sources, or if other sources, such as optical photons, are necessary (Sellgren et al. 1990; Uchida et al. 1998).

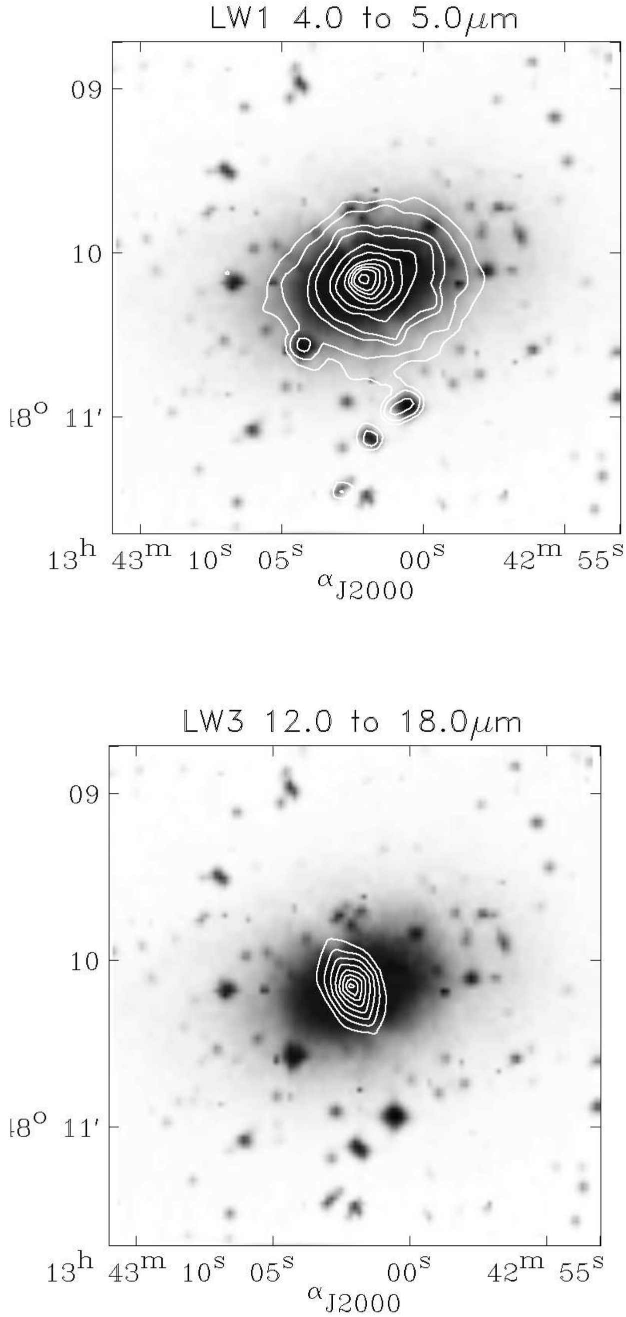

Figure 1. ISOCAM MIR emission distribution (white contours) from NGC 5266 superimposed on the optical. (top): LW1 covering 4.0 to 5.0 μm; (bottom): LW3 covering 12.0 to 18.0 μm. A dust lane is apparent in the 15 μm band while the 4.5 μm band is dominated by the stellar continuum.

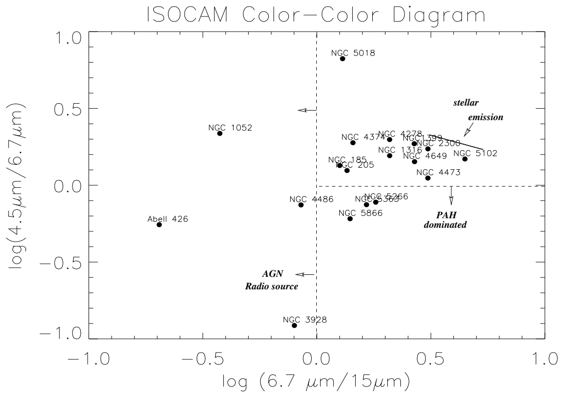

Figure 2. ISOCAM color-color diagram for early-type galaxies. The dashed lines delineate regions of characteristic dominant emission processes: left: nonthermal emission from AGNs and radio sources dominate the emission; bottom right: UIBs dominate in the 6.7 μm band; top right: a progression of mostly stellar emission (indicated by line) to dustier galaxies (to the left and below).

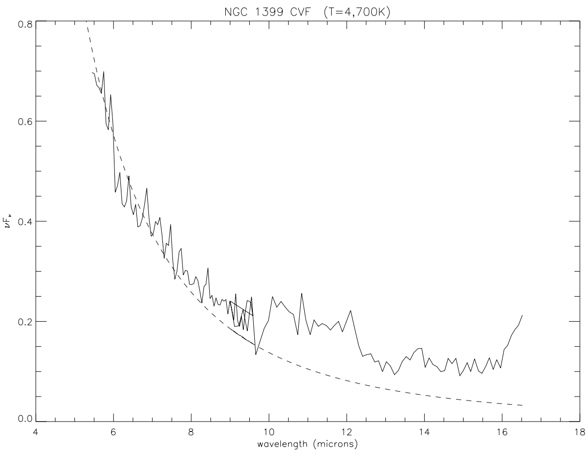

Figure 3. CVF spectrum of NGC 1399. The dashed line is a black body fit to stellar emission of 4700 K). The spectrum is relatively featureless, and shows some excess dust emission toward long wavelengths. There is some speculation that a broad 10 μm emission feature is present, in the form of amorphous silicate.

We are fitting model spectral energy distribution profiles for our sample where the UV to NIR data exist with consistent apertures. One example of such a model derived from the PEGASE population synthesis model (Fioc & Rocca-Volmerange 1997) is shown in Figure 4 for NGC 4473 with our 3 MIR ISOCAM data points along with the UBVRIJHK. The ISOCAM points fill in critical wavelength regimes in the fitting of the SED. The data are fit with a synthetic spectrum of a 13 Gyr old instantaneous star formation burst. While most of the MIR emission, arising from the central 36 arcsec, is consistent with an origin dominated by a population of evolved AGB stars, there is some residual emission in the MIR.

The behavior of the MIR emission in the early-type galaxies is compared to other types of galaxies in the ISOCAM color- IRAS color diagram in Figure 5. Galaxies from a variety of other CEA Saclay guaranteed time surveys are indicated by the filled circles, while early-type galaxies are the open triangles. Spiral and barred galaxies, for the most part, show relatively little variation in the ratio of the 6.7 μm/15 μm bands for f60/f100 ranging from 0.2 to 0.5 (Roussel et al., these proceedings). As the radiation field increases beyond this, the subsequent increase of the temperature of the small grains, in addition to the possible destruction of the UIBs in the more intense radiation fields, results in the decrease of the 6.7 μm/15 μm ratio. This turnover begins the regime typifying AGNs, starbursts and blue compact dwarf galaxies (Charmandaris et al. and Laurent et al., these proceedings). Most of the early-type galaxies do not contain as much dust as diskier late-type galaxies and are, therefore, located above these galaxies in the diagram, while some galaxies which have evidence for recent star formation, such as, NGC 185 and NGC 205 (the 2 left most points in the diagram), resemble the disk galaxies. Those which lie well above this horizontal branch in the ISOCAM color - IRAS color diagram are progressively more and more dust-free. AGN-dominated early-type galaxies are evident as they occupy the space beyond the turn-over, as do other well-known galaxies containing AGNs (Note: As the IRAS FIR values for some of the early-type galaxies are upper limits or not very firm values, some of these galaxies can shift along the f60/f100 axis in this diagram. Nevertheless, noteworthy characteristics of the early-type galaxies in this diagram are still apparent.)

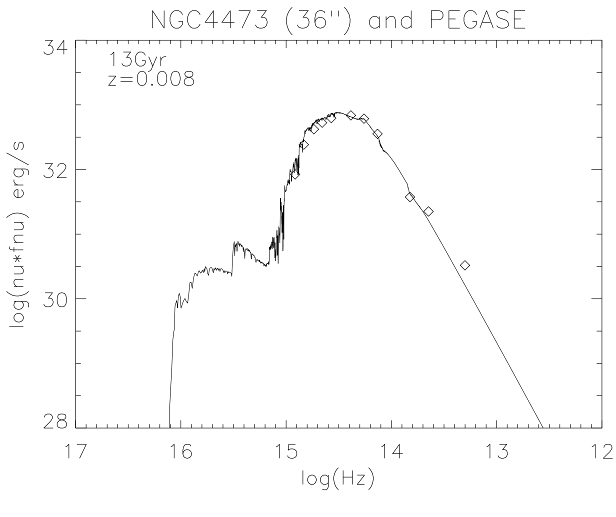

Figure 4. Spectral Energy Distribution for NGC 4473 with observed UBVRIJHK points and ISOCAM 4.5, 6.75, 15 μm observations indicated by the open boxes and the synthetic spectrum for a 13 Gy instantaneous burst of star formation stellar population modelled by PEGASE (Fioc & Rocca-Volmerange 1997). Errors for the observed data are contained within the boxes.

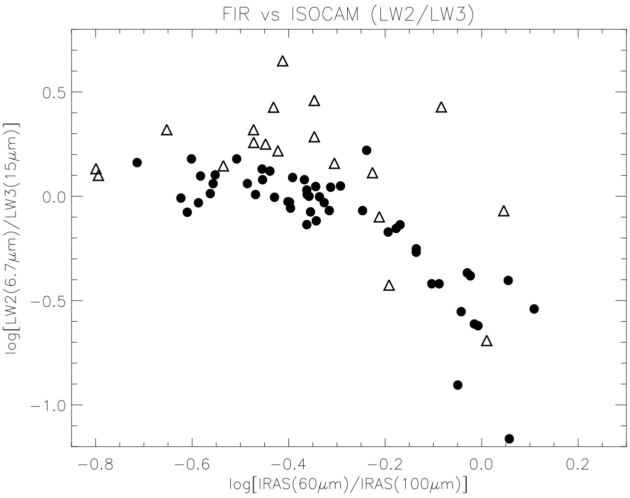

Figure 5. ISOCAM LW2(6.7 μm)/LW3(15 μm) and FIR emission for early-type galaxies (open triangles) compared with that for a variety of other types of galaxies from the CEA guaranteed time programs (filled circles).

3. CONCLUSIONS

From our survey of early-type galaxies with ISOCAM, we find a variety of characteristics in the spectral energy of the 3 MIR broad bands. Using diagnostic color-color diagrams, we can delineate the different MIR emission origins from mostly stellar emission to non-thermal emission from AGNs/radio sources, and galaxies with a range of dust contributions. From SEDs, we determine that about 1/2 of the sample have some measurable MIR excess originating from the heating of small grains, and UIBs, which have been widely attributed to aromatic bonds in molecules or large particles. Several galaxies show no observable evidence for infrared dust excess, with MIR emission arising solely from a population of cool evolved stars. This evidence in early-type galaxies for the presence of the UIBs will provide further constraints on the nature and excitation of the UIBs. The ISOCAM 6.7 μm/15 μm ratio, in conjunction with FIR observations, may also be used as a tool to differentiate dusty galaxies from from those which are dust-free. These conclusions will be further refined through modelling of the spatial distribution of the MIR emission.

ACKNOWLEDGMENTS

We are grateful to M. Fioc for his advice in the modelling of the stellar population of our galaxies using PEGASE.

REFERENCES

Allamandola, L. J., Tielens, A.G.G.M. & Barker, J.R. 1989, ApJS, 71, 733

Brown, B.A. & Bregman, J.N., 1998 ApJ, 497, L75

Bregman, J.N., Snider, B.A., Grego, L. & Cox, C. 1998, ApJ, 499, 670

Désert, F-X., Boulanger, F. & Puget. J.-L. 1990, A&A, 237, 215

Draine, B.T. & Salpeter, E.E. 1979, ApJ, 231, 77

Ebneter, K & Balick, B. 1985, ApJ, 90, 183

Fabian, A., Nulsen, P.E.J, & Canizares, C.R. 1991, A&ARev, 2, 191

Fich, M. & Hodge, P. 1993, ApJ, 415, 75

Fioc, M. & Rocca-Volmernage, B. 1997, A&A, 326, 950

Franceschini, A., Sliva, L., Fasano, G., Granato, L., Bressan, A., Arnouts, S. & Danese, L. 1998, ApJ, 506, 600

Jura, M., Kim, D.-W., Knapp, G. R. & Guhathakurta, P. 1987, ApJL, 312, L11

Goudfrooji, P. & de Jong, T. 1995, A&A, 298, 784

Henkel, C. & Wiklind, T. 1997, SSRv, 81, 1

Knapp, G.R., Guhathakurta, P., Kim, D.-W. & Jura, M. 1989, ApJS, 70, 320

Knapp, G.R., Gunn, J.E. & Wynn-Williams, C.G. 1992, ApJ, 399, 76

Knapp, G.R. 1999, in Star Formation in Early-Type Galaxies, eds P. Carral & J. Cepa (San Francisco:PASP). in press

Léger, A. & Puget, J.-L. 1984, A&A, 137, L5

Morganti, R., Sadler, M.E., Oosterloo, T.A., Pizzella, A. & Bertola, F. 1997, AJ, 113, 937

Papoular, R., Reynaud, C. & Nenner, I. 1991, A&A, 247, 215

Sarazin,C.L. 1997, in The Nature of Elliptical Galaxies, eds. M. Arnaboldi, G.S. Da Costa & P. Saha (San Francisco:PASP)

Sauvage, M. & Thuan, T. 1994, ApJ, 429, 153

Sellgren, K. 1984, ApJ, 277, 623.

Sellgren, K., Luan, L. & Werner, M. 1990, ApJ, 359, 384

Tsai, J.C. & Mathews, W.G. 1996, ApJ, 468, 571

Uchida, L.I., Sellgren, K. & Werner, M. 1998, ApJ, 493, L109

van Dokkum, P.G. & Franx, M. 1995, AJ, 110, 2027

Vigroux, L. 1998, in Extragalactic Astronomy in the Infrared, eds G.A. Mamon, T.X. Thuan, & T.V. Tran, Moriond Series in Astrophysics, p. 509, Editions Frontières.

ISO OBSERVATIONS OF THE INTERSTELLAR MEDIUM IN ELLIPTICAL GALAXIES

S. Malhotra[1,2,3], D. Hollenbach[5], G. Helou[1], E. Valjavec[1], D. Hunter[4], D. Dale[1], N. Lu[1], N. Silbermann[1], S. Lord[1], H. Dinerstein[6], & H. A. Thronson[7]

[1] I.P.A.C., Caltech, Pasadena
[2] N.O.A.O, Tucson
[3] Hubble Fellow
[4] Lowell Observatory
[5] NASA, Ames Research Center, Moffett Field
[6] University of Texas, Astronomy Department, Austin
[7] NASA, Headquarters, Washington

ABSTRACT

Three IRAS-detected elliptical galaxies were observed with ISO-LWS and PHT, and two of them were observed with CAM. The mid-IR images of NGC 1155 and NGC 6958 at 7 and 15 μm show extended emission which follows a de Vaucouleurs profile. The ratio of 15/7 μm flux decreases with radius in both galaxies, approaching the values empirically observed for purely stellar systems.

All three galaxies are detected in the [CII](158 μm) line, and NGC 1155 in the [OI] (63 μm) line. The ISO-LWS observations of the [CII] line are more sensitive measures of cool ISM than HI and CO; the only previous detection of cool gas was of HI in NGC 1052. The observed $L_{[CII]}/L_{FIR}$ ratio in ellipticals follows the same trends seen in other (spiral and irregular) galaxies wherein $L_{[CII]}/L_{FIR}$ decreases with increasing $F_\nu(60\mu m)/F_\nu(100\mu m)$. These trends indicate similar local physical conditions in the ISM in spirals and ellipticals.

The UV radiation from old stellar populations is insufficient, by a factor of 2-30, to produce enough photoelectric heating of gas to account for the cooling via the [CII] and [OI] lines. Heating by X-rays is also insufficient in NGC 6958 and NGC 1155. Given the observed variations in the optical-UV colors and the uncertainties in modelling the UV from old stellar populations, we can make a clear case for young stellar populations in NGC 1155.

Key words: Elliptical galaxies; mid-IR; Far-IR spectroscopy, ISM.

1. MID-INFRARED IMAGING

In spiral galaxies the mid-IR emission is dominated by small grains transiently heated to high temperatures and aromatic features of small grains in the ISM. For ellipticals the ISM-to-stellar ratio is generally low so photospheres and circumstellar dust may contribute significantly to the mid-infrared (Knapp, Gunn & Wynn-Williams 1992), although Sauvage & Thuan (1994) have argued that the same IRAS color-color relation (Helou 1986) holds for early and late type galaxies indicating a similar origin from the ISM. CAM imaging at 7 and 15 μm has enough sensitivity and resolution to yield the spatial distribution of the mid-IR emission. The interpretation is complicated by the dependence of mid-IR emission on both dust and heating source distributions.

The mid-IR emission of both NGC 6958 and NGC 1155 is extended in nature and follows de Vaucouleurs radial profile (Figure 1). To gain signal-to-noise in the outer parts of the galaxies we average the emission in annuli after subtracting the background determined at radii greater than 90″. The LW3/LW2 ratio decreases going from the center of the galaxy outwards (Figure 1) approaching a value of 0.5. This is lower than the ratio found in other (i.e. spiral) galaxies in the sample (cf Helou et al. these proceedings). In NGC 1155 the effective radius for the mid-IR emission is intermediate between those of B-band and Hα light (Figure 2), indicating that both ionizing and non-ionizing radiation heat the dust. A similar result was found for the spiral galaxy NGC 6946 (Malhotra et al. 1996).

From the change in the mid-IR color we infer that the dust in the ISM dominates in the inner parts of the galaxies, and the dust associated with stars becomes dominant in the outer parts. The decrease in LW3/LW2 in the outer parts of the galaxy is then due to different proportions of photospheric and ISM contributions, with the photospheres having a lower LW3/LW2 ratio. The LW3/LW2 ratio of 0.3-0.2 is observed in ellipticals devoid of ISM (Madden et al. 1997).

Proceedings of the Conference "The Universe as seen by ISO", Paris, France, 20–23 October 1998 (ESA SP-427, March 1999)

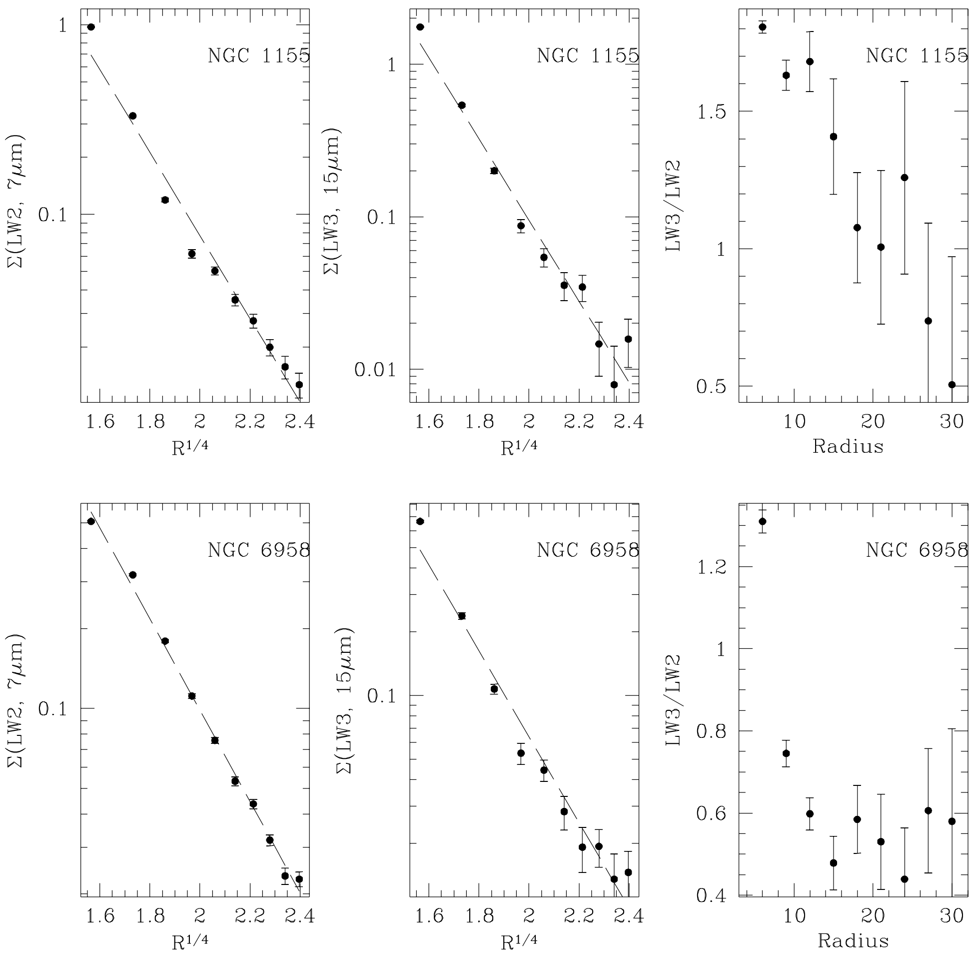

Figure 1. The left and middle panels show surface brightness profiles of NGC 1155 and NGC 6958 at 7 and 15μm *respectively. The mid-IR emission follows a de Vaucouleurs radial profile. The right panels show the mid-IR color variation with radius. The ratio of LW3 (15* μm*) and LW2 (7* μm*) light decreases towards the outer parts of the galaxies, and reaches an asymptotic value of 0.5, characteristic of old stellar populations in galaxies devoid of ISM.*

2. FAR-INFRARED SPECTROSCOPY

We detect the [CII](158μm) line in all three galaxies, albeit at low (3σ) S/N for NGC 6958. The other major fine structure cooling line, [OI] (63 μm), is detected in NGC 1155 and undetected in NGC 6958 at uninteresting upper limits. In Table 1 we summarize what is known about the ISM in the three ellipticals: HI (21 cm) is detected in NGC 1052 (van Gorkom et al. 1986) and Hα is detected in all three. [CII] detections imply a minimum mass in H (assuming $T \gg 91$K and $n_H > 10^4 cm^{-3}$) which is 10-100 times smaller than the HI detections and upper limits.

2.1. Trends in line strengths

The 3 elliptical galaxies lie within the broad correlation between $L_{[CII]}/L_{FIR}$ and $F_\nu(60\mu m)/F_\nu(100\mu m)$ (cf. Malhotra et al. 1997 and these proceedings). There is a also a trend of decreasing $L_{[CII]}/L_{FIR}$ with increasing L_{FIR}/L_B. The two ellipticals NGC 6958 and NGC 1052 along with the S0 galaxy NGC 5866 lie at the lowest extreme of L_{FIR}/L_B, indicating a low rate of current star-formation. There is an indication that the $L_{[CII]}/L_{FIR}$ ratio is lower for low values of L_{FIR}/L_B. This is expected in galaxies with low rates of current star-formation since only the UV photons ($\lambda < 2000 Å$) contribute to photoelectric heating of gas, while dust is heated by optical as well as UV photons. In early type galaxies which have less active star-formation rate per blue luminosity, we should see a decrease in $L_{[CII]}/L_{FIR}$ and [CII]/CO(1-0).

2.2. Origin of [CII]

With limited knowledge of the phases of the ISM in these galaxies and without assuming Galactic values of temperature and density, it is hard to constrain with what phases of the ISM [CII] is associated. The [CII] emission could be from ionized gas in HII regions, or PDRs (photo dissociation regions) includ-

Table 1. The properties of the ISM in the elliptical galaxies studied in this paper.

Name	Morphology	Distance	M(HI) Mass	$M(H_2)$ in	M(HII) $M_\odot$	$M_H(C^+)$
NGC 1052	E4	14 Mpc	0.7×10^7	$< 3 \times 10^8$	3×10^4	$> 4 \times 10^5$
NGC 6958	E+	28 Mpc	$< 3 \times 10^8$	?	?	$> 8 \times 10^5$
NGC 1155	EL	45 Mpc	?	?	?	$> 1 \times 10^7$

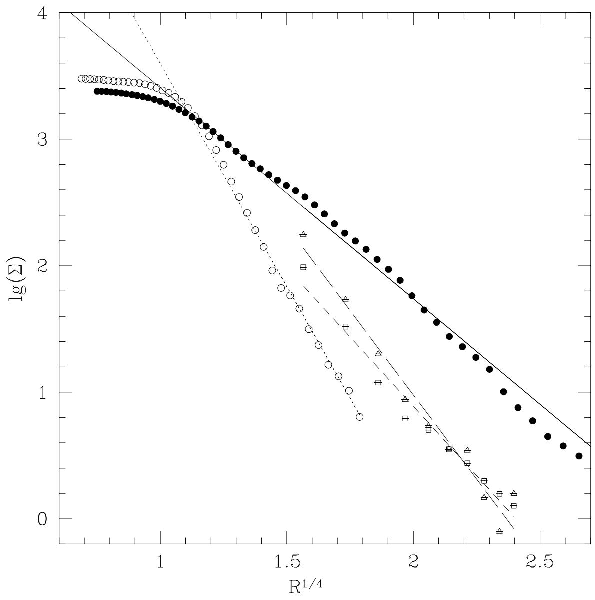

Figure 2. The radial profile in optical B band (filled circles), the Hα (open circles), and the mid-infrared (LW2: open squares, LW3: triangles) in NGC 1155 is plotted along with the best fit de Vaucouleurs profile for each wavelength. The mid-infrared light shows a radial distribution intermediate to the B band and the Hα.

ing neutral atomic medium and UV irradiated surfaces of molecular clouds. Assuming case B recombination ($T = 10^4$ K) and a carbon abundance of $X_C = 3 \times 10^{-4}$ in the HII regions (i.e. solar metallicity with all the C existing as C^+) the upper limit on [CII] emission from HII regions is

$$\frac{L([CII])}{L(H\alpha)} < 0.18 \frac{X_{C^+}}{3 \times 10^{-4}} \left(\frac{1}{1 + n_e/n_{crit}}\right)$$

where n_e is the density of electrons in the HII region and n_{crit} is the critical density for [CII] excitation, which is $84\,cm^{-3}$ for 10^4 K ionized gas. For NGC 1155 and NGC 6958 the observed ratio $L([CII])/L(H\alpha)$ is 2.5 and 58 respectively indicating that most of the [CII] is not associated with HII regions. For NGC 1052 the observed $L([CII])/L(H\alpha) = 0.16$. Taking $n_e = 10^3\,cm^{-3}$, inferred from the ratio of SII lines (Kim 1989) the contribution of HII regions to [CII] emission is still negligible $L([CII])/L(H\alpha) < 0.015$. Thus not a lot of the [CII] emission arises from the HII regions, even if the Hα flux is underestimated by factors of a few due to extinction.

A fair amount of [CII] emission could be from diffuse HI. For a cold neutral medium (CNM) with typical Galactic values T=80K and $n_H = 90\,cm^{-3}$, $M(HI)/L([CII]) = 20\,(3 \times 10^4/X_C^+) M_\odot / L_\odot$. For NGC 1052 the observed $M(HI)/L([CII]) = 14$ which can be accommodated with higher gas density or temperature, or some contribution from molecular medium. Comparing the [CII] and [OI] (63μm) line flux measurements of NGC 1155 with PDR models by Kaufman et al. (1999), we infer density $n \simeq 10^2\,cm^{-3}$ and UV radiation density $\simeq 10^2\, G_0$, where G_0 is the UV radiation density in the solar neigborhood.

2.3. Gas energetics

In spirals, [CII] and [OI] are the major coolant of neutral gas and most of the heating is by photoelectrons from dust grains. The potential barrier to photoejection from neutral grains is 6 eV (Bakes & Tielens 1994) or higher, which means that only photons with $\lambda \leq 2000 \mathring{A}$ contribute to gas heating. Old stellar populations (PNe, PAGB stars) in ellipticals produce enough ionizing flux to explain the Hα emission seen in the ellipticals (Rose & Tinsley 1974, Binnette et al. 1994). So it is possible that at least some of the photoelectric heating is by old stars.

We use GISSEL (Bruzual and Charlot 1993) stellar population models of instantaneous burst of ages 1 Gyr, 10 Gyr and 13 Gyr to calculate the UV spectra of elliptical galaxies. The mass of each galaxy is normalised to match the B-band flux. The UV heating flux is calculated by assuming that the work function of the grains is 6 eV and the efficiency of overall photoelectric heating process is $\gamma = 0.1$ (Tielens & Hollenbach 1985). The total power that goes into heating the gas is given by:

$$L_{PE} = (\gamma\, f_{abs}\, \int (h\nu - 6eV)\, N_\nu\, d\nu)$$

where N_ν is the number of photons at frequency ν and f_{abs} is the fraction of photons absorbed by the dust. f_{abs} can be estimated from the observed values of L_B/L_{FIR} and using a standard extinction curve with the spectral energy distribution from stellar population models. Table 2 lists the photoionizing luminosity available to heat the gas in old stellar populations, compared to the luminosity of the [CII] and [OI] lines; for NGC 1052 and NGC 6958 the [OI] line strength is estimated using the correlation between [OI]/[CII] and $F_\nu(60\mu m)/F_\nu(100\mu m)$ (Malhotra et al. these proceedings).

The UV heating produced by the old stellar populations fails to account for the [CII] and [OI] emission by factors of 2 or 3 in NGC 1052, NGC 6958 and clearly fails for NGC 1155 by a factor of 30. The theoretical estimates of UV production by old

Table 2. Photoionization luminosity vx luminosity of the [CII] and [OI] lines.

Name	L([CII])	L([OI]) (Luminosity	L(CII+OI) in	L(Hα) $L_\odot$)	L_{PE}(1 Gyr)	L_{PE}(10 Gyr)	L_{PE}(13 Gyr)
NGC 1052	0.5×10^6	(0.25×10^6)	0.75×10^6	3.2×10^6	0.1×10^6	0.06×10^6	0.2×10^6
NGC 6958	1.6×10^6	(0.66×10^6)	2.3×10^6	2.5×10^4	0.4×10^6	0.3×10^6	0.9×10^6
NGC 1155	20×10^6	20×10^6	40×10^6	8.1×10^6	0.8×10^6	0.5×10^6	1.7×10^6

populations are uncertain and vary significantly with age and metallicity (cf. Magris and Bruzual 1993). The observed optical-UV colors (1550-V) of ellipticals vary by a factor of 10 for active and quiescent galaxies (Burstein et al. 1988). IUE spectra, between 1250 and 1850 Å, exist only for NGC 1052 (Burstein et al. 1988). Extrapolating the IUE spectrum to 912 Å and estimating from the FIR/Blue colors that $f_{abs} = 0.04$, we recalculate that $L_{PE} = 0.07 \times 10^6 M_\odot$, about a tenth of the UV luminosity implied by [CII] and [OI] observations. The extra UV could come from very obscured source(s).

These sources could be young stars or X-rays from hot gas and active nuclei. Both the x-ray luminosity and temperature of NGC 1052 indicate that the x-ray emission is dominated by the seyfert nucleus (Davis and White 1996). The X-ray luminosity of NGC 1052 is $\simeq 3 \times 10^6 L_\odot$ of which about 10% could be used up for heating in atomic medium and about 40% in molecular medium in the low ionization case (Maloney et al. 1996). But in XDRs one expects a higher line to continuum ratio as the X-rays are equally efficient at heating the gas and the dust, whereas the UV radiation in PDRs heats dust much more efficiently. Because NGC 1052 follows similar trends in $L_{[CII]}/L_{FIR}$ as the other (spiral) galaxies in the sample, significant X-ray heating of gas is not a favored scenario. NGC 1155 and NGC 6958 were not detected by Einstein or ROSAT. We estimate the X-ray luminosity from the $L_X - L_B$ relation (Fabbiano et al. 1992) to be $\simeq 10^5 L_\odot$ and $\simeq 0.7 \times 10^5 L_\odot$ for NGC 6958 and NGC 1155 respectively. That is simply not sufficient to heat the gas to produce the [CII] flux seen (Table 2).

3. SUMMARY

(1) The Mid-IR emission from elliptical galaxies arises both from ISM and stars. 7/15 μm ratio varies with radius indicating that ISM dominates at the centers. In NGC 1155 the dust emission extends to 10 kpc.

(2) [CII] (158 μm) and [OI] (63 μm) lines are detected in galaxies where HI and CO detections were difficult, making ISO-LWS one of the two most sensitive probes of small quantities of warm ISM. Hα was detected in all. [CII] does not arise in classical HII regions, and is associated with HI in NGC 1052.

(3) The fluxes in the cooling lines, [CII] and [OI], provide fairly stringent lower limits on the UV flux between 912 and 2100Å. With all the uncertainties in modelling, UV from evolved stellar populations is insufficient by at least a factor of 2-3 for NGC 1052 and NGC 6958 and a clear factor of 30 for NGC 1155. In NGC 1155 and NGC 6958 X-ray gas heating is also insufficient.

ACKNOWLEDGEMENTS

We thank Sue Madden and John Mulchaey for helpful comments. This work was supported by ISO data analysis funding from the US NASA, and carried out at IPAC and the JPL of the California Institute of Technology.

REFERENCES

Bakes, E.L.O., Tielens, A.G.G.M. 1994, ApJ, 427, 822

Binnette, L., et al. 1994, A&A, 292, 13

Burstein, D., et al 1988, ApJ, 328,440

Davis, D.S, White, R. 1996, ApJ, 470, L35

Helou, G 1986, ApJ, 311, L33

Kim, D.W. 1989, ApJ, 346, 653

Knapp, G.R., et al. 1992, ApJ, 399,76

Madden, S. et al 1997, in Extragalactic Astronomy in the Infrared.

Magris, G., & Bruzual, G. 1993, ApJ, 417, 102

Malhotra, S., et al. 1996, A&A, 315, 161

Malhotra, S. et al. 1997, ApJ, 491, L27

Rose, J.A. & Tinsley, B.M. 1974, ApJ, 190, 243

Sauvage, M. & Thuan, T. 1994, ApJ, 429, 123

Tielens, A.G.G.M. & Hollenbach, D. 1985, ApJ, 291, 722

van Gorkom, J.H. et al., 1986, AJ, 91, 791

DETECTION OF WIDELY-DISTRIBUTED UIR BAND EMISSION IN THE DISK OF NGC 891

K. Mattila[1], **K. Lehtinen**[1] **& D. Lemke**[2]

[1]Observatory, P.O. Box 14, FIN-00014 University of Helsinki, Finland
[2]Max-Planck-Institut für Astronomie, Königstuhl 17, D-69117 Heidelberg, Germany

ABSTRACT

The spectrum of the unidentified infrared emission bands (UIRB) between 5.8 and 11.6 μm has been observed for the first time in the disk of an external galaxy where the interstellar radiation field (ISRF) is quite low as compared to the nuclear regions. We used PHT-S, the low-resolution spectrometer of the ISOPHOT instrument (PHT) aboard ISO. The UIRBs at 6.2, 7.7, 8.6, and 11.3 μm have absolute intensities which are similar to the values observed for the diffuse emission of our own Galaxy. The UIRBs between 5.9 and 11.7 μm contribute ~9% of the total IR radiation of NGC 891. The intensity ratios and band widths in the NGC 891 disk emission are similar to the galactic nebulae and diffuse emission, pointing to a common carrier for the UIRBs in the two galaxies. However there are some notable variations of the band ratios along the major axis of the galaxy.

Key words: ISM: UIR emission; ISM: galaxies.

1. INTRODUCTION

Strong UIRB emission has been detected in HII region type galactic nuclei showing vigorous star formation activity (Moorwood 1986, Roche et al. 1991). With the Infrared Space Observatory (ISO) large surveys and several detailed individual studies have been performed of the UIRBs in the nuclear or starburst regions of galaxies (see, e.g., Lutz et al. 1998).

In the case of disks of external galaxies no spectra have been obtained for the UIRBs so far. In this paper we present results of an ISOPHOT low resolution spectrometer (PHT-S) observing project aimed at studying the UIRBs in the disk of the galaxy NGC 891. NGC 891 is an Sb spiral closely similar to our own Galaxy, thus motivating a comparison with spectrophotometry of the diffuse galactic UIR emission (Mattila et al. 1996). NGC 891 is seen almost exactly edge-on (inclination 89°). This is an essential condition in order to have a sufficiently large column density of ISM along the line of sight to enable spectrophotometric analysis with PHT-S.

2. RESULTS

The main UIRBs at 6.2, 7.7, 8.6, and 11.3 μm are clearly present in the disk of NGC 891 at least to a distance of 10 kpc, both North and South of the centre. The spectra look very similar to those observed for the diffuse emission of the disk of our Galaxy as well as for bright galactic objects, such as reflection nebulae and HII regions (see Fig. 1).

Comparison with IRAS 12 μm flux density shows that at least 50 - 60 %, and possibly all of the IRAS 12 μm emission of NGC 891 is due to the UIR bands plus the weak underlying continuum seen in our spectra. The energy emitted (and absorbed) by the UIRB carriers is ca. 14 % relative to the large grains. This is nearly the same fraction (10 %) as found for the diffuse emission of our Galaxy (Mattila et al. 1996).

The line intensities for the four UIR bands plotted along the major axis show the following characteristic features (see Fig. 2).

- A central peak.
- A ring of minimum intensity between 1-2.5 kpc.
- A ring of maximum intensity between 3.5-6 kpc.
- The profiles are not symmetric: the minimum appears deeper and the maximum broader and stronger on the northern (right hand) side.

Comparison of the UIRB distribution with other ISM components shows that (see Fig. 3):

- the UIRB carriers have a distribution very similar to CO and large dust grains (1.3 mm emission)
- a large-scale association of the UIRB emission with neutral hydrogen is not present
- the UIRB emission does not follow the ionized gas distribution (H_α, [CII] 158 μm); thus an essential part of the UIRB emission must come from the non-ionized ISM component.

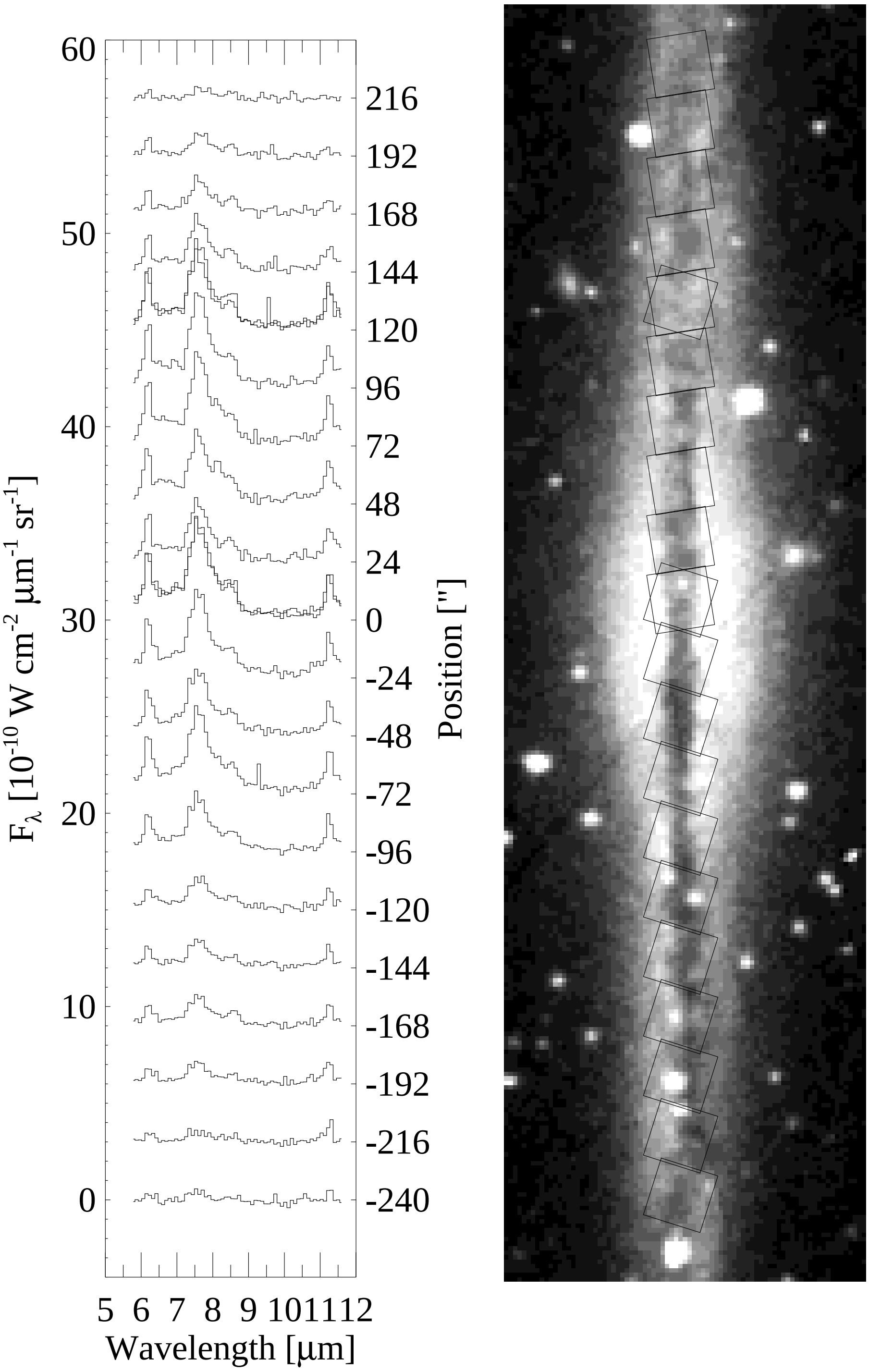

Figure 1. (left panel) PHT-SL spectra along the major axis of NGC 891. (right panel) Optical B band image of NGC 891 from the Digital Sky Survey with the observed $24'' \times 24''$ areas superposed. For the central and the $+120''$ positions two spectra and two different aperture orientations corresponding to ISO orbits 656 and 788 are shown. The position angle of the major axis is 24 deg. In this figure the NE end of the axis with positive offsets is at the top and the SW one at the bottom

There are significant trends and differences of the line ratios between the different parts of NGC891 (see Fig. 4).

- On the southern axis, outside the molecular ring the 11.3/7.7 μm ratio increases with increasing offset. The 8.6/7.7 μm ratio shows the same tendency, but the 8.6/11.3 μm ratio decreases slightly over this range.

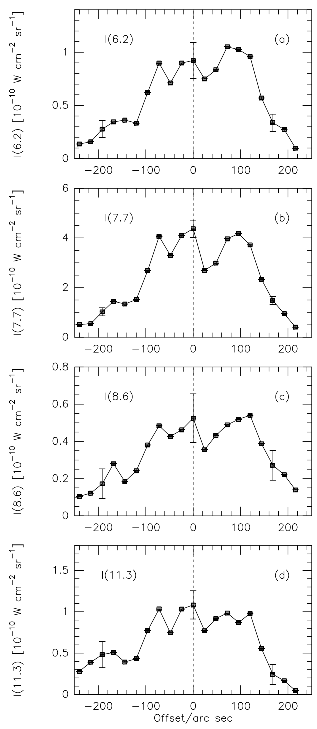

Figure 2. Distribution of the UIR band intensities along the major axis of NGC 891. X-axis is the offset from the centre of the galaxy, positive offsets refer to the NE, negative to the SW part. Representative statistical *error bars for three positions are shown. The relative point-to-point calibration errors are ~10% and the absolute overall calibration accuracy is ~30%*

- On the northern axis, outside the molecular ring, the 8.6/7.7 μm ratio increases. Over the same range there is a modest decrease in the 11.3/7.7 μm ratio. As a result the 8.6/11.3 μm ratio shows an even stronger increase than the 8.6/7.7 μm ratio.
- The line ratios for the central position do not differ from the values of the inner galactic disk.
- The line ratios for the inner disk of NGC 891 are very similar to those in the diffuse disk emission of the Milky Way Galaxy (Mattila et al. 1996).

3. DISCUSSION

We have made an attempt to interpret the observed band ratios and their variations in NGC 891 in terms of the PAH model. There are several possible mechanisms which influence the PAH band ratios and can explain the different types of band ratio variations as observed in NGC 891:

- Hydrogenation/dehydrogenation of PAHs
- The fraction of PAH cations, [PAH$^+$]/[PAH]
- The fraction of compact and non-compact species in the PAH ion mixture
- Size distribution of the PAH mixture

The strength of the C–C vibration bands (6.2 and 7.7 μm) depends only on the PAH skeleton structure, whereas the C–H band strengths (8.6 and 11.3 μm) depend on the number of H atoms in the molecule. For strong dehydrogenation it is thus possible to obtain a small intensity ratio of the 11.3 μm to the 6.2 and 7.7 μm bands, corresponding to the galactic and NGC 891 ISM observations. The dehydrogenation is thought to occur through UV photodissociation, thus becoming monotonically weaker when the ISRF weakens.

A probable solution to the band ratio problem has emerged from recent laboratory and theoretical results for PAH cations (for a review see Allamandola et al. 1995): the 6.2, 7.7, and 8.6 μm band cross sections for PAH$^+$s are typically a factor of 10 larger than for neutral PAHs whereas the 11.3 μm band is much less influenced. The ISM 11.3/7.7 μm ratio could thus be understood if a substantial fraction of the PAHs are ionized.

Absorption spectra of a number of compact and non-compact PAH cations were measured by Hudgins et al. (1994) and Hudgins & Allamandola (1995). Roelfsema et al. (1996) inspected these results especially in view of the large variation of the 8.6/7.7 μm band ratio they observed in compact HII regions

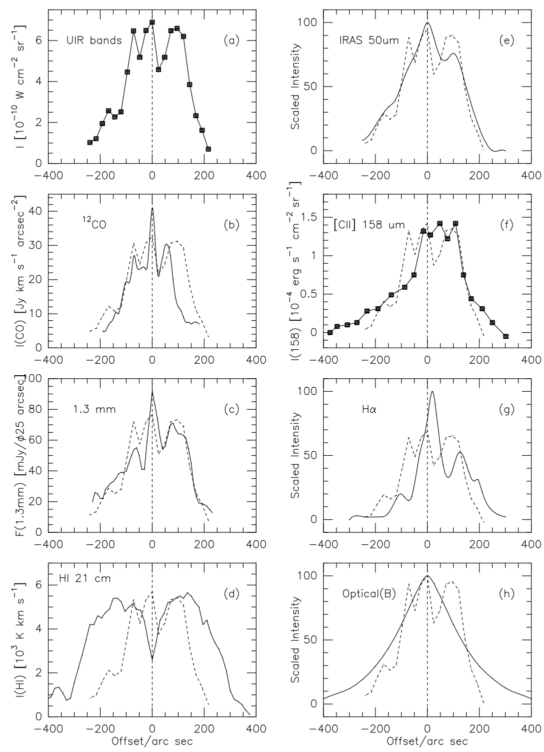

Figure 3. Distributions of different ISM components along the major axis of NGC 891. X-axis is the offset from the centre of the galaxy, positive offsets refer to the NE, negative to the SW part. The sum of the four UIR band intensities (6.2, 7.7, 8.6, and 11.3 μm) is shown in panel (a) and, arbitrarily scaled, as dotted line in panels (b)-(h)

Table 1. UIR band ratios as observed in different parts of NGC 891 (present study) and other objects (from literature).

Object (1)	$\frac{I(6.2)}{I(7.7)}$ (2)	$\frac{I(8.6)}{I(7.7)}$ (3)	$\frac{I(11.3)}{I(7.7)}$ (4)	$\frac{I(8.6)}{I(11.3)}$ (5)	Reference
NGC 891 Southern end -168" to -240"	0.263±10	0.195±12	0.52±8	0.40±5	Present study
NGC 891 Inner disk South -24" to -120"	0.217±3	0.130±8	0.26±3	0.51±2	Present study
NGC 891 Inner disk North +24" to +120"	0.260±6	0.132±5	0.26±2	0.52±6	Present study
NGC 891 Northern end +144" to +192"	0.250±18	0.191±20	0.19±2	1.04±18	Present study
Milky Way Diffuse radiation ($l=-5°, -30°; b=0$)	0.215	0.159	0.238	0.676	Mattila et al.(1996)
G300.2-16.8 Cirrus			0.33-0.43		Lemke et al. (1998)
ρ Oph Bright rim	0.32	0.17	0.30	0.57	Boulanger et al.(1996)
Twelve galaxy nuclei(starburst)				0.73±0.25 (0.40 – 1.44)	Aitken & Roche(1984)
Six Compact HII Regions	0.10-0.50	0.11-1.7	0.09-0.20	0.7-10	Roelfsema et al.(1996)
NGC 1333 $r=1''-11''$				0.65-0.27	Joblin et al.(1996)

(see Table 1). They found that the addition of less-condensed PAHs to the mixture enhances the 8.6 μm region relative to the 7.7 μm region.

The band ratios as observed in NGC 891 suggest:

- a low dehydrogenation degree of the PAHs at the southern end of the major axis,
- an increase of the fraction of PAH cations, especially the non-compact ones, along the northern major axis of NGC 891.

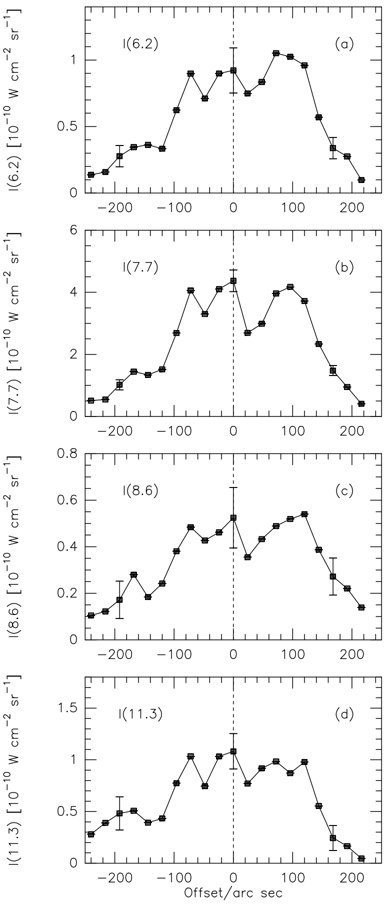

Figure 4. UIR band intensity ratios along the major axis of NGC 891. X-axis is the offset from the centre of the galaxy, positive offsets refer to the NE, negative to the SW part. Statistical error bars are shown

REFERENCES

Aitken D.K., Roche P.F. 1984, MNRAS 208, 751

Allamandola L.J., Sandford S.A., Hudgins D.M., Witteborn F.C. 1995, PASP Conf. Ser. 73, 23

Boulanger F., Reach W.T., Abergel A. et al. 1996, A&A 315, L325

Hudgins D.M., Allamandola L.J. 1995, J.Ph.Chem. 99, 3033

Hudgins D.M., Sandford S.A., Allamandola L.J. 1994, J.Ph.Chem. 98, 4243

Joblin C., Tielens A.G.G.M., Geballe T.R., Wooden D. 1996, ApJ 460, L119

Lemke D., Mattila K., Lehtinen K. et al. 1998, A&A 331, 742

Lutz D. et al., 1998, ApJ 505, L103

Mattila K., Lemke D., Haikala L. et al. 1996, A&A 315, L353

Moorwood A.F.M., 1986, A&A 166, 4

Roche P.F., Aitken D.K., Smith C.H., Ward M.J. 1991, MNRAS 248, 606

Roelfsema P.R., Cox P., Tielens A.G.G.M. et al. 1996, A&A 315, L298

ISO OBSERVATIONS OF THE HIGH-REDSHIFT LENSED QUASAR MG 0414+0534

S. Oya, J. Iwai, F. Iwamuro & T. Maihara
Department of Physics, Kyoto University, Kyoto, Japan

ABSTRACT

Far-infrared ISOPHOT observations of a gravitationally lensed quasar, MG 0414+0534 are presented. Observations using the raster mapping mode in the three bands at 60, 100 and 170 μm have provided the spectral energy distribution (SED) in the mid- to far-infrared regions in the quasar-rest frame. We discuss the geometrical characteristics of the postulated dusty torus by comparing the absorption-corrected, overall SED from the optical to the far-infrared with model predictions.

Key words: high redshift; quasar; gravitational lens; dust torus.

1. INTRODUCTION

MG 0414+0534 is known as a gravitationally lensed QSO, first found by Hewitt et al. (1989) from the samples of MIT-Green Bank 5 GHz radio survey (Bennett et al. 1986). The object was quite unique in that the optical spectrum was extremely steep without any emission feature having a very red optical-to-infrared color, i.e., $R-K \sim 7.2$ (Annis and Luppino 1993). There was no secured knowledge about the lensed source until Lawrence e al. (1995) detected Hα emission line of the source identifying it as a highly reddened quasar at a redshift of 2.64. More recently McLeod et al. (1998) made an estimate of the redshift of the lensing galaxy to be in the range from $z=$ 0.45 to 0.60 based on high resolution images and photometric data including near-infrared measurements.

In this report, we describe far-infrared ISOPHOT observations of MG 0414+0534, and present preliminary discussions on the nature of the rest-frame mid-infrared emission presumably attributed to the thermal radiation from a dusty torus around a powerful central source.

2. OBSERVATIONS AND RESULTS

2.1. ISOPHOT data

The observations of MG 0414+0534 with the ISOPHOT (AOT of PHT22) were made on February 1, 1998 using the raster mapping method. The telescope was pointed consecutively towards the 3 $\times$ 3 grid points for photometric measurements in the 60 μm (C_60) and 100 μm (C_100) bands, while in the 170 μm (C_160) band, the grid was 4 $\times$ 4. The offset between the grid points was one pixel pitch, i.e. 46 arcsec for the two shorter bands and 92 arcsec for the 170 μm band.

Originally, we planned to make four-band photometry dividing the observation using C200 into two bands, C_135 and C_200. Since the chopping method might be fatally inadequate in ISOPHOT observations due to the detector anomaly as well as the irregular nature of the cirrus emission in spatial variation, we chose the raster mapping method following the advice of Kawara (private communication), and in consequence, we had to use the C_160 band instead of the two band.

Data analyses of the three-band photometry data were made at the Astronomical Data Analysis Center of NAO-J (National Astronomical Observatory, Japan) using PIA version 7.2 (Gabriel et al. 1997) with IDL version 5.1. Specific procedures were essentially identical to the pipeline processing of the ISO Data Center. The mapped images of these three bands were shown in Figure 1. Since the C_160 image was affected by cirrus emission which appeared to have a noticeable gradient of the background brightness, we made a background-subtracted image assuming a homogeneous gradient of the background, as shown in the last panel of the figure.

Flat fielding was applied in reference to a set of calibration frames in FCS1, which were taken before and after the raster mapping observations, and also flux calibrations were made to the created images with the same FCS1 data. For the photometric measurement, we utilized the IRAF software package. The object fluxes were determined by assuming that the object was a point source, and that the source brightness was concentrated on the central pixel. The reduced photometry data are presented in Table 1 together with the estimated uncertainties.

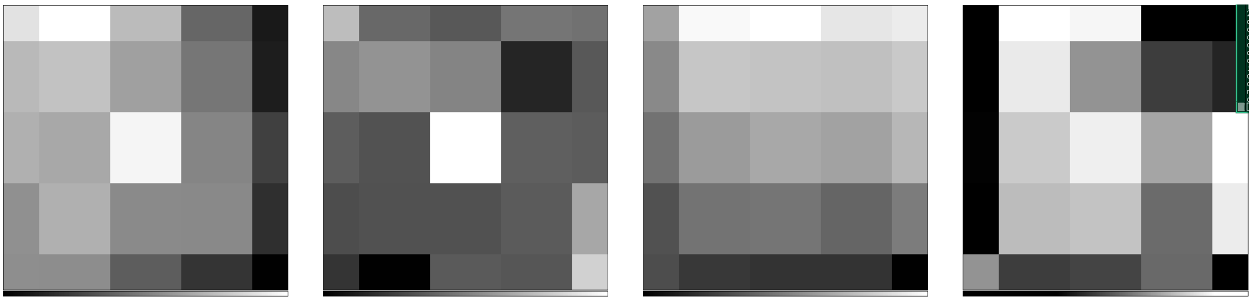

Figure 1. *The reduced maps of C_60, C_100, and C_160, from the left to the right, respectively. The North is nearly up with a tilt of 15 degrees, and the East is nearly left. The gradient-corrected C_160 image is shown in the last map to the right. See text.*

Table 1. *Calibrated fluxes of MG 0414+0534 and the uncertainties.*

Band	Wavelength (μm)	Flux (mJy)	Uncertainty (mJy)
C_60	60.8	107	21
C_100	103.5	161	31
C_160	174.0	92	62
IRAS25	25.0	53	13

2.2. Near-infrared and optical data

Low resolution ($R \sim 100$) spectrophotometric data taken by the OH-airglow suppressor spectrograph (OHS: Iwamuro et al. 1994) mounted on the University of Hawaii 2.2m telescope were adopted for the near-infrared continuum in the 1.1 to 1.7 μm region, for the purpose of an SED study of MG 0414+0534 in the following discussion. The estimated flux density of the observation contained all four split images, and the error was about 10% of the flux. (The OHS observations made on October 14 and 17, 1993, will be described in Oya et al. 1999.) Lawrence et al. (1995) reported the detection of the broad Hα emission line at 2.385 μm in the K-band. The redshift of z=2.639 was determined, and the nature of the lensed object was identified as a luminous type 1 quasar. Optical spectroscopic data are cited from Hewitt et al. (1992).

2.3. IRAS data

We also analyzed IRAS data around the present target. An image of the IRAS 25 μm band was produced using the HIRES and the photometric intensities of the source were evaluated using IRAF. The result of the IRAS 25 μm band are given in Table 1.

3. DISCUSSION

3.1. SED

The data obtained by ISO observations are plotted in Figure 2 as filled circles, and the IRAS (HIRES) data as filled squares. The data at $\log\nu \sim 14.5$ are taken from Annis & Luppino (1993). The near-infrared spectrophotometric data in the $14.5 < \log\nu$ range are obtained using OHS. The optical and radio data are from Hewitt et al. (1992). The ordinate of $\log(\nu L\nu)$ in units of ergs s^{-1} is based on the following cosmological parameters: $H_0 = 50\,\mathrm{kms}^{-1}\,\mathrm{Mpc}^{-1}$ and $q_0 = 0.5$.

The plotted optical to near-infrared data were corrected for absorption, assuming $A_V = 5.5$ mag in the lens galaxy as estimated by Lawrence et al. (1995). A noticeable excess emission feature around 0.3 μm could be attributed to the small blue bump usually interpreted as FeII line complex (e.g. Lawrence et al. 1995). Note that absorption in the quasar host galaxy might also be the case as suggested by Falco, Lehár & Shapiro (1997), and this should be examined further.

Of course, we had to be careful to the possibility of time variation of the source when the overall SED was treated. However, the variation was found to be small: less than 0.5 mag in the I-band (McLeod et al. 1998), less than 0.3 mag at near-infrared wavelengths during two years (Lawrence et al. 1995 and Oya et al. 1999), and 3% rms at 15 GHz for six months (Falco, Lehár, & Shapiro 1997).

3.2. Relationship to the lens galaxy

An optically faint source in the center of the MG 0414+0534 system was studied by Falco, Lehár & Shapiro (1997), which was deemed to be a fairly massive galaxy with a mass $2.1 \times 10^{11}\, M_\odot$, responsible for the lensing and presumably located at around z=0.5. It was unlikely, however, that the far-infrared emission measured in the present ISO observations was from this lens galaxy. The total far-infrared luminosity amounting to more than $10^{12}\, L_\odot$ in the assumed location at z=0.5 should be in the ULIRG category, but the observed peak wavelength (in F_ν)

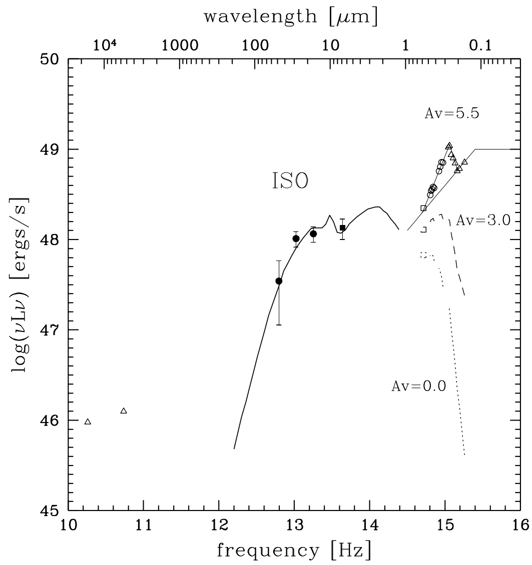

Figure 2. The overall SED of MG 0414+0534. The data obtained with ISO are plotted by filled circles; IRAS (HIRES) data by the filled square; OHS data by open circles; and the data of Hewitt et al. (1992) by open triangles; the data of Anis & Luppino (1993) by the open square. The optical to near-infrared data are absorption-corrected by $A_V = 5.5\,mag$. The thick solid line represents a best fit model SED of the dusty torus. The thin solid line is a primary power-low continuum in the UV to optical range.

at about 40 μm (in the rest frame) was short for this type of galaxies.

3.3. Interpretation: the dusty torus

The overall rest-frame SED of MG 0414+0534 in the optical to far-infrared regions was obtained, under the assumptions that most of the absorption occurs in the lens galaxy, that the lens effect is the same for the entire spectrum from the optical to the far-infrared, and that the distance to the lens galaxy is z=0.5. Later, we shall show the difference of the effective magnification factor for fluxes at different wavelengths due to the geometrical source configuration.

Based on the observed SED from the optical to the far-infrared, we compared it with model SEDs calculated by assuming a face-on torus around the luminous quasar ($L_{total} = 6.0 \times 10^{47}$ erg s^{-1}, if the magnification factor of 55 by lensing was assumed). We employed the optically thick dusty torus model proposed by Granato & Danese (1994). The detailed explanation will be presented in Oya et al. (1999). Note that the magnification factor by the lens effect would not be the same between the central optical source and the surrounding torus. However, as shown in the following subsection, the difference of the factor is less than 3, if the configuration of the lens geometry provided by Hewitt et al. (1992) is assumed. In Table 2, we list the typical model parameters which fit well to the present overall SED, comparing to that for lower luminosity AGN of the Seyfert 1 type. Basically, the model was specified by two geometrical parameters. The first parameter is the covering factor f_c, which has an almost direct relation with the total flux ratio of the far-infrared torus emission to the central optical one. The second parameter is the ratio of the outermost radius to the innermost radius of the torus. It was assumed that the innermost radius is set by the luminosity of the central UV source and the sublimation temperature of the dust.

Table 2. Parameters for a tuned dusty torus model.

Parameters	MG 0414+0534	Seyfert 1 galaxies
$\log L_{UV}$(erg s^{-1})	47.8	45.1
r_0 [a] (pc)	7.9	0.37
r_m/r_0	100	1500
r_m [b] (pc)	790	550
f_c [c]	0.14	0.8

Notes:
a) The innermost radius of the torus.
b) The outermost radius of the torus.
c) The covering factor of the torus which means the solid angle ratio viewed from the center.

3.4. Magnification by the lens effect

It was necessary to check whether the magnification factor of the torus might be different from that of the central optical source. We made calculations of the magnification by adopting the simple singular-isothermal potential model, basically the same as that of Hewitt et al. (1992). The outer radius of the torus in our model is about 1 kpc, which corresponds to a linear scale of 0.13 arcsec. With this condition, the emission from a circular ring would have a magnification of about 20, while the magnification of the central source would be about 55. Since the effective radius of the mid- to far-infrared emissions would be smaller than the outermost radius assumed, the magnification difference could smaller than that. Therefore, the covering factor in the model shown in Table 2 might be a little larger, but not differ so much from that of the present model.

4. CONCLUSION

Even if the magnification factor is 55, the lensed quasar MG 0414+0534 is one of the highest luminosity class objects in the high redshift region. The mid- to far-infrared emissions have been measured by ISO, although not very easily. We have analyzed the raster mapping images of the ISOPHOT 60, 100, and 170 μm bands, and have found positive detections in all bands. The observed mid- to far-infrared emission of the lensed quasar, MG 0414+0534 can be interpreted by the thermal emission of the hypothetical dusty torus. The ratio of the far-infrared emission to the optical is rather small, meaning that the covering factor of the torus is fairly small.

ACKNOWLEDGMENTS

The authors would like to thank Kimiaki Kawara and Yasunori Sato for plenty of helpful advice, and also to the ISO staff for extensive support to the present observations. The ISOPHOT data presented in this paper were reduced using PIA, which is a joint development by the ESA Astrophysics Division and the ISOPHOT Consortium. We were able to use IDL version 5.1 by courtesy of the Astronomical Data Analysis Center of the National Astronomical Observatory, Japan. The data processed using HIRES were provide by IPAC (the Infrared Processing and Analysis Center).

REFERENCES

Annis J., Luppino G. A. 1993, ApJL 407, L69

Bennett C. L., Lawrence C. R., Burke B. F., Hewitt J. N., Mahoney J. H. 1993, ApJS 61, 1

Falco E. E., Lehár J., Shapiro I. I. 1997, AJ 113, 540

Gabriel, C., Acosta-Pulido, J., Heinrichsen, I., Morris, H. Tai, W. M. 1997, Proc. of the ADASS VI Conference, eds. G. Hunt & H.E. Payne, pp. 108.

Granato G.L., Danese L. 1994, MNRAS 268, 235

Hewitt J. N., Burke B. F., Turner E. L., Schneider D. P., Lawrence C. R., Langston G. I., Brody J. P. 1989, Lecture Notes in Physics, 330, Gravitaional Lenses, eds. J. M. Moran, J. N. Hewitt & K. Y. Lo (Belrin:Springer-Verlag), pp. 147

Hewitt J. N., Turner E. L., Lawrence C. R., Schneider D. P., Brody J. P. 1992, AJ 104, 968

Iwamuro F., Maihara T., Oya S., Tsukamoto, H., Hall D.N.B., Cowie L.L., Tokunaga A.T., Pickles A. 1994, PASJ 46, 515

Lawrence C. R., Elston R., Januzzi B. T., Turner E. L. 1995, AJ 110, 2570

McLeod B. A., Bernstein G. M., Rieke M. J., Weedman D. W. 1998, AJ 115, 1377

Oya, S., Iwai, J., Iwamuro, F., Maihara, T. 1999, in preparation

[CII] EMISSION AND STAR-FORMATION IN LATE-TYPE GALAXIES

D. Pierini[1], K.J. Leech[2], R.J. Tuffs[1] & H.J. Völk[1]

[1]Max-Planck-Institut für Kernphysik, Heidelberg, Germany
[2]ISO Data Centre, Astrophysics Division, ESA, Villafranca, Spain

ABSTRACT

We demonstrate the existence of a linear correlation between the ratio of the [CII($^2P_{3/2} \rightarrow ^2 P_{1/2}$)] ($\lambda$ 158 μm) fine structure cooling line intensity to the [^{12}CO(J : 1 $\rightarrow$ 0)] (λ 2.6 mm) line emission, I_{CII}/I_{CO}, and the Hα (λ 6563 Å) equivalent width (EW), over the range 2-71 Å in Hα EW, for a sample of 21 late-type galaxies. The latter is comprised of an optically selected sample of 12 normal Virgo cluster spiral galaxies with [CII] detections obtained by us with LWS onboard ISO, plus 9 galaxies with higher star-formation rates (SFRs), for which [CII] data and, especially, Hα EW data are available in the literature. As a result we infer I_{CII}/I_{CO} to be a reliable diagnostic of the current normalized global SFR for non-starburst spiral galaxies. Moreover we find that the ratio of the [CII] line to the total far-infrared (FIR) continuum intensity, I_{CII}/I_{FIR}, decreases from $\sim 0.5\%$ to $\sim 0.1\%$ with decreasing SFR which we propose is due to a "[CII]-quiet" component of I_{FIR} from dust heated by the general interstellar radiation field (ISRF). The more "quiescent" galaxies in the sample have I_{CII}/I_{CO} different from those observed in "compact" Galactic interstellar regions. Therefore their [CII]-emission is interpreted to be dominated by diffuse regions of the Interstellar Medium (ISM). For normal "star forming" galaxies the diffuse component of the [CII]-emission is estimated to account for at least 50% of the total.

Key words: galaxies; interstellar medium; star-formation; infrared.

1. INTRODUCTION

The physical state of the interstellar gas is regulated by several fine structure cooling lines, among which the [CII($^2P_{3/2} \rightarrow ^2 P_{1/2}$)] ($\lambda$ 158 μm) line transition of singly ionized carbon C^+ often dominates (Tielens & Hollenbach 1985). Its luminosity, I_{CII}, typically amounts to a few $\times 10^{-3}$ of the total FIR continuum emission, I_{FIR}, for galaxies; at the same time the [CII] line is up to 6600 times more intense than the [^{12}CO(J : 1 $\rightarrow$ 0)] (λ 2.6 mm) rotational line (Crawford et al. 1985).

For starbursts there is a good correlation between the [CII] line intensity and the emission from the [CO] line, probing the molecular gas component. This correlation holds also for a large sample of Galactic HII regions, OB associations, reflection nebulae, planetary nebulae, i.e. "compact" interstellar regions, and has suggested to earlier observers a physical association of the [CII]-emitting regions with molecular clouds; for non-starburst galaxies and non-OB star-forming molecular clouds the line ratio is typically a factor of 3 lower (e.g., Stacey et al. 1991 - S91). The correlation has been interpreted as evidence that the [CII]-emission from galaxies is being originated from warm dense gas from an ensemble of photodissociation regions (PDRs), forming the boundaries between HII regions and molecular clouds (Crawford et al. 1985; Tielens & Hollenbach 1985; Wolfire et al. 1989; S91; Hollenbach et al. 1991).

Recent studies, on the other hand, have emphasized other phases of the ISM, i.e., an Extended Low-Density Warm Ionized Medium (ELDWIM) (Heiles 1994) and a Cold Neutral Medium (CNM) (Madden et al. 1993; Bennett et al. 1994), as the main sources of the [CII] line.

In view of the difference between starburst and non-starburst galaxies, Stacey et al. (1991) concluded that I_{CII}/I_{CO} was a diagnostic of the global star-formation activity in galaxies.

Here we study the properties of the [CII]-emission of 21 late-type galaxies with a large range in star-formation activities (as probed by the Hα EW - Kennicutt et al. 1994) in order to: i) sample the behaviour of relatively quiescent galaxies; and ii) estimate the contributions of the different ISM phases.

2. THE SAMPLE

The galaxies observed by us with the Long Wavelength Spectrometer (LWS) (Clegg et al. 1996) are a subsample of targets of the ISO Guaranteed Time program VIRGO, an ISOPHOT (Lemke et al. 1996) 40 - 220 μm study of a deep optically complete sample of spiral, irregular and BCD galaxies, selected from the Virgo Cluster Catalogue (VCC) of Binggeli et al. (1985) (Völk et al. in preparation).

Nineteen normal spiral galaxies were selected from the parent ISOPHOT sample by Leech et al. (these proceedings - L98) within a limiting magnitude of $B_T \leq 12.5$ and observed with LWS (80$''$ HPBW),

onboard ESA's Infrared Space Observatory (ISO) (Kessler et al. 1996), in the spectral region around the [CII] line. Here we consider only those 12 of the 15 detected galaxies, which have Hα EWs from Kennicutt & Kent (1983) and from Gavazzi (private communications), [^{12}CO(J : 1 → 0)] line emission from Kenney & Young (1988) (at the 45″ resolution of the 14 m FCRAO telescope) and IRAS FIR fluxes (Thuan & Sauvage 1992).
In order to investigate the [CII]-emission properties over a large dynamic range in SFRs, we extend the L98 sample of "quiescent" (as defined in Section 3) Virgo spirals to late-type galaxies more active in star-forming, which have [CII], [CO], FIR and, in particular, Hα measurements as well. Therefore we add 3 low-mass VCC spiral galaxies (Smith & Madden 1997 - SM97), with LWS [CII] line intensities and [CO] line observations taken at the 12 m NRAO telescope, with a resolution (beamsize FWHM = 55″) similar to FCRAO. The sources of the FIR and Hα data are the same as for the L98 sample.
We consider, without introducing any morphological or luminosity bias, in addition 3 gas-rich galaxies and 3 starbursts, taken from S91 (see S91 for the sources of the data).

3. RESULTS

We explore the dependence of I_{CII}/I_{CO} on the Hα EW. We divide non-starburst galaxies into "quiescent" and normal "star-forming" galaxies according to their values of Hα EW < 10 Å and ≥ 10 Å, respectively, which have consistently a stellar birthrate parameter b of Scalo (1986) < 0.1 and ≥ 0.1 (see Kennicutt et al. 1994), where b is defined as the ratio of the SFR at the current time to the past SFR averaged over the age of the disk.
Moreover, we study the dependence of I_{CII}/I_{FIR} on the Hα EW. For the Virgo cluster galaxies IRAS integrated fluxes are used, as a definitive calibration of the ISOPHOT data is not yet available. Given the low resolution of IRAS, we assume that the bulk of the FIR (Helou et al. 1985) emission originates within the LWS beam in order to determine I_{CII}/I_{FIR}.
Finally we compare the parameter ranges occupied by entire galaxies with those occupied by compact Galactic sources.

3.1. I_{CII}/I_{CO} and the current SFR

Figure 1a shows the existence of a reasonably tight linear relation between I_{CII}/I_{CO} and the Hα EW. The [CII]-to-[CO] line intensity ratio increases from 1.6×10^2 to $\sim 6.3 \times 10^3$, varying by more than a factor of 35, with Hα EW increasing from 2 to 71 Å (see SM97 for the case of NGC 4299).
Therefore I_{CII}/I_{CO} is indeed a reliable diagnostic of the global SFR, at least in normal late-type galaxies.

3.2. I_{CII}/I_{FIR} and the current SFR

Figure 1b shows that I_{CII}/I_{FIR} roughly ranges between 1.1×10^{-3} and a mean "plateau" value of $\simeq 4\times10^{-3}$ (defined by the normal star-forming galaxies), which is between the average values $(I_{CII}/I_{FIR})_{Gc} \simeq 0.2\%$ and $(I_{CII}/I_{FIR})_{Gd} \simeq 0.6\%$ for compact and diffuse regions of the Galactic ISM, respectively (Nakagawa et al. 1998 - N98).

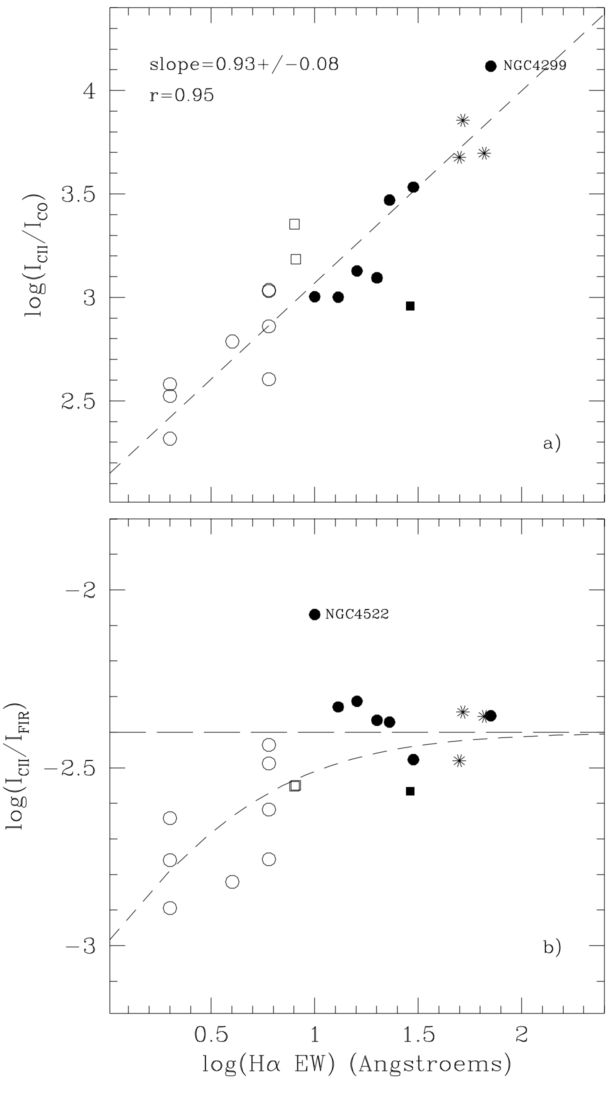

Figure 1. log(I_{CII}/I_{CO}) *vs.* log(Hα EW) *(a) and* log(I_{CII}/I_{FIR}) *vs.* log(Hα EW) *(b) for the sample. Circles/squares denote VCC/gas-rich spirals. Filled/open symbols denote objects with* Hα EW ≥ 10 Å/< 10 Å*. Asterisks denote starbursts. The short-dashed line in (a) shows the least-squares fit of* I_{CII}/I_{CO} *vs.* Hα EW*, while the long-dashed line in (b) represents the mean "plateau" value of* I_{CII}/I_{FIR} *for the normal star-forming galaxies (NGC 4522 excluded - see Pierini et al. 1999).*

We find in addition a positive trend of the value of I_{CII}/I_{FIR} with increasing Hα EW for the quiescent galaxies, reproduced by the model-curves of Völk et al. (in preparation), one of which is shown as the short-dashed line in Figure 1b.

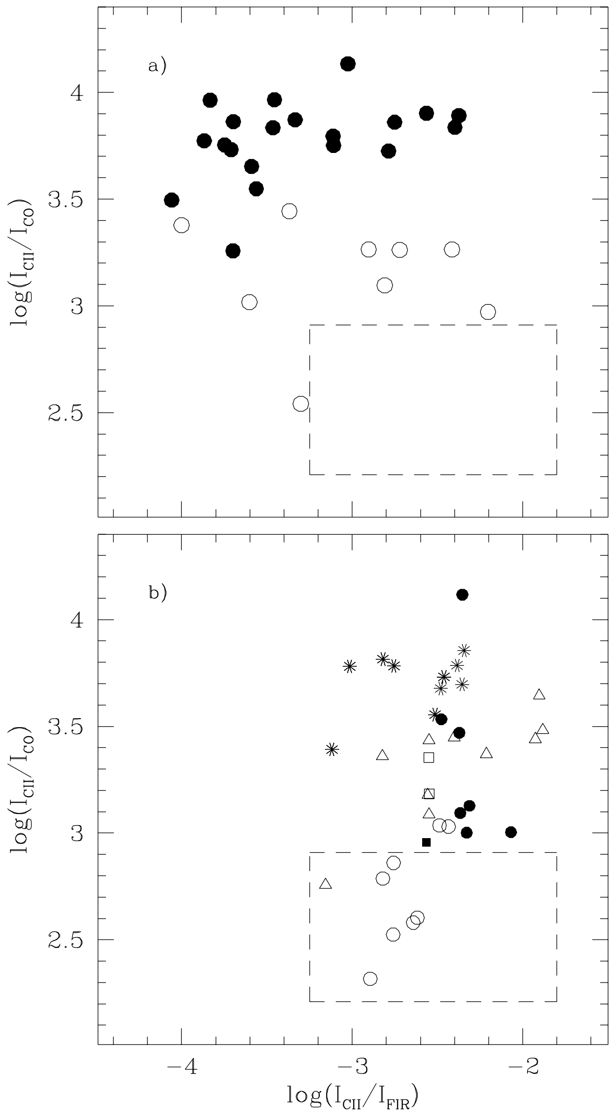

Figure 2. *$\log(I_{CII}/I_{CO})$ vs. $\log(I_{CII}/I_{FIR})$ (a) for Galactic sources (S91), with big filled/open circles denoting star-forming regions/molecular clouds; (b) for the galaxies shown in Figure 1 (with the same symbols) plus all other galaxies in S91 as in the text (gas-rich systems without Hα EWs are represented by empty triangles). Boxes denote a range in parameter space for galaxies without compact Galactic counterparts.*

3.3. The [CII] line emission from compact Galactic sources and from the global ISM of external galaxies

Galactic molecular clouds and HII regions/OB associations (Figure 2a) span a much wider (2 decades cf. S91) range in I_{CII}/I_{FIR} than galaxies and cluster at two definite values of I_{CII}/I_{CO} ($\sim$ 3.3 and $\sim$ 3.8 in log respectively), while galaxies go from 2.3 to $\sim$ 3.8 in log. This is seen by comparison with Figure 2b, where our galaxy sample is plotted, together with all the other galaxies in S91 that lack Hα EW. The compact Galactic regions leave the rectangular box empty (within 1σ) which is filled by our low-Hα EW-galaxies.

4. DISCUSSION

For moderate values of I_{CII}/I_{CO}, its correlation with the Hα EW is interpreted as the global, *mass-normalized* [CII]-emission from a galaxy, increasing about linearly with the *mass-normalized* present SFR. Mass-normalization is for [CII] in terms of I_{CO}, and for Hα in terms of the stellar continuum I_R in the red (see Pierini et al. 1999). The [CO]-normalization however, while very interesting in itself, has the great advantage that we can make use of existing I_{CII}/I_{CO} data for compact Galactic regions in a comparison with those for our galaxy sample.

The linear correlation implies that all the non-ionizing UV-flux from intermediate-mass stars ($5 \leq$ M ≤ 20 M$_\odot$), that is not primarily absorbed in dense HII regions, is used for the production of [CII], independent of how large the SFR per unit mass is. Since most of the non-ionizing UV-flux is from B stars, whereas Hα is due to massive stars in OB associations producing mainly Lyman continuum radiation, the correlation implies in addition a rather tight coupling of the stellar initial mass function between these two stellar populations (e.g., Güsten & Mezger 1983; Larson 1986). For a low normalized SFR this is a significant result, and is equally consistent with the [CII]-emission coming from PDRs or from low-density diffuse galactic regions.

For high SFRs the [CII]-emission might be dominated by (high-density) PDRs. At very high UV-fluxes the [CII]-emission from PDRs becomes saturated due to grain charging and dust absorption, and I_{CII}/I_{CO} takes the value of $\sim$ 6300 found for starburst galaxies (cf. S91).

I_{CII}/I_{FIR} is fairly constant within $10 \leq$ Hα EW $\leq$ 50 Å. It should decrease for larger Hα EWs or, equivalently, higher values of I_{FIR}, as demonstrated observationally by, e.g., S91, Malhotra et al. (1997; and these proceedings) and N98, and theoretically by e.g. Tielens & Hollenbach (1985) in the PDR picture.

Thus the interesting *new* phenomenon in our data is the *opposite* range $2 \leq$ Hα EW ≤ 10 Å, where I_{CII}/I_{FIR} tends to rapidly decrease with Hα EW. It can be shown quantitatively (cf. Xu et al. 1994) that this range corresponds to galaxies which are close to becoming, or are in fact already "radio-quiet" (Condon et al. 1991) in the sense that their dust heating is increasingly dominated by the general ISRF due to stars which are not Supernova progenitors due to their low mass and which therefore cannot produce Cosmic Ray electrons and nonthermal radio emission (Xu et al. 1994). It is physically clear that these stars cannot produce any substantial photoelectric grain heating either, increasingly rendering such galaxies also "[CII]-quiet"! Within this framework, in Figure 1b we plot a characteristic curve, selected from the model curves of Völk et al. (in preparation), which gives a synthetic interpretation of the data.

Compact interstellar [CII] sources do not appear to represent the galaxies with a low normalized SFR in our sample. We interpret this as a tentative indication that such relatively quiescent galaxies are *dominated* in their [CII]-emission by diffuse regions of the ISM (i.e., an ELDWIM or a CNM), whose integrated emission might be considerable indeed (Heiles 1994; Madden et al. 1994; Bennett et al. 1994; SM97). A crucial test of such an interpretation would be a successful search for low I_{CII}/I_{CO} Galactic compact regions which fill the empty rectangular region in Fig-

ure 2a. If such compact objects were to exist, then the PDR mechanism could partially also hold for quiescent galaxies. If not, then a diffuse origin is indicated.
For normal "star-forming" galaxies the mean value of I_{CII}/I_{FIR} is about 4×10^{-3} (cf. Figure 1b and Figure 2b). If we assume this result to be due to a linear combination of compact and diffuse regions as they exist in our Galaxy, then the diffuse component is given by $x \cdot (I_{CII}/I_{FIR})_{Gd}$, where $x = I_{FIRd}/I_{FIR}$ and $1 - x$ define a diffuse and a corresponding compact fraction of I_{FIR}, respectively. With our above mean value, and using the above-mentioned results of N98, we obtain for the "plateau galaxies" $x \simeq 0.5$ and $x \cdot (I_{CII}/I_{FIR})_{Gd} \simeq 3 \times 10^{-3}$, with $(1-x) \cdot (I_{CII}/I_{FIR})_{Gc} \simeq 1 \times 10^{-3}$ for the remaining compact component. This corresponds to a 75% diffuse and 25% compact I_{CII}/I_{FIR} fraction, respectively. Thus, for normal galaxies, i.e. non-starburst galaxies, the diffuse [CII]-emission is on average *at least as strong as the compact one.*
For starburst galaxies (e.g. S91), on the other hand, I_{CII}/I_{FIR} decreases with I_{FIR} below the plateau value. The above simple model then implies a corresponding decrease of the diffuse fraction consistent with an increasing dominance of an ensemble of bright compact PDRs. However it remains to be investigated whether the model and its numerical parameters are applicable to such extreme cases.

5. SUMMARY

We use LWS detections of the [CII] (λ 158 μm) fine structure cooling line in 12 VCC normal spiral galaxies to define a sample of 21 late-type galaxies, having [CII], Hα, [CO] and far-IR measurements, with the largest range in star-formation activity available at present in the literature. We find that:
1) The ratio between the [CII] and [CO] line intensities has a reasonably tight positive correlation with the Hα EW. Therefore, we demonstrate that I_{CII}/I_{CO} is a reliable tracer of the global current normalized SFR below the saturation level of I_{CII}/I_{CO}, i.e. up to Hα EW ~ 50 Å.
2) The ratio of the [CII] line to total FIR intensity has a narrow range of $(1.1 - \sim 5) \times 10^{-3}$. Its decrease toward H$\alpha$ EW $\simeq 10$ Å can be readily explained by a "[CII]-quiet" component of the FIR continuum emission at lower SFRs.
3) The lack of compact Galactic [CII]-emission regions as counterparts to the low-SFR galaxies is tentatively interpreted in terms of a dominant [CII]-emission from the diffuse components of the ISM of such galaxies.
4) For starburst galaxies a simple theoretical model gives further indications that the compact fraction dominates the [CII]-emission.
5) The same model demonstrates that for *normal galaxies* the diffuse fraction of the [CII]-emission is *at least as strong as the compact fraction.*

ACKNOWLEDGMENTS

We are grateful for the support of this work by project 50-OR-9501B of DARA (Deutsche Agentur für Raumfahrt Angelegenheiten).

REFERENCES

Bennett, C.L., Fixsen, D.J., Hinshaw, G. et al. 1994, ApJ, 434, 587
Binggeli, B., Sandage, A., Tammann, G.A. 1985, AJ, 90, 1681 (VCC)
Clegg, P.E., Ade, P.A.R., Armand, C. et al. 1996, A&A, 315, L38
Condon, J.J., Anderson, M.L., Helou, G. 1991, ApJ, 376, 95
Crawford, M.K., Genzel, R., Townes, C.H., Watson, D.M. 1985, ApJ, 291, 755
Güsten, R., Mezger, P.G. 1983, Vistas Astr., 26, 159
Heiles, C. 1994, ApJ, 436, 720
Helou, G., Soifer, B.T., Rowan-Robinson, M. 1985, ApJ, 298, L7
Hollenbach, D.J., Takahashi, T., Tielens, A.G.G.M. 1991, ApJ, 377, 192
Kenney, J.D., Young, J.S. 1988, ApJS, 66, 261
Kennicutt, R.C., Kent, S.M. 1983, AJ, 88, 1094
Kennicutt, R.C., Tamblyn, P., Congdon, C.W. 1994, ApJ, 435, 22
Kessler, M.F., Steinz, J.A., Anderegg, M.E. et al. 1996, A&A, 315, L27
Larson, R.B. 1986, MNRAS, 218, 409
Lemke, D., Klaas, U., Abolins, J. et al. 1996, A&A, 315, L64
Madden, S.C., Geis, N., Townes, C.H. et al. 1993, ApJ, 407, 579
Malhotra, S., Helou, G., Stacey, G. et al. 1997, ApJ, 491, L27
Nakagawa, T., Yui, Y.T., Doi, Y. et al. 1998, ApJS, 115, 259 (N98)
Pierini, D., Leech, K.J., Tuffs, R.J., Völk, H.J. 1999, MNRAS, in press
Scalo, J.M. 1986, Fund. Cos. Phys., 11, 1
Smith, B.J., Madden, S.C. 1997, AJ, 114, 138 (SM97)
Stacey, G.J., Geis, N., Genzel, R. et al. 1991, ApJ, 373, 423 (S91)
Thuan, T.X., Sauvage, M. 1992, A&AS, 92, 749
Tielens, A.G.G.M., Hollenbach, D. 1985, ApJ, 291, 722
Wolfire, M.G., Hollenbach, D., Tielens, A.G.G.M. 1989, ApJ, 344, 770
Xu, C., Lisenfeld, U., Völk, H.J., Wunderlich, E. 1994, A&A, 282, 19

ISOPHOT OBSERVATIONS OF NARROW LINE SEYFERT 1 GALAXIES

M. Polletta[1] **& T. J.-L. Courvoisier**[1,2]
[1] Geneva Observatory, Ch. des Maillettes 51, CH-1290, Sauverny, Switzerland
[2] INTEGRAL Science Data Centre, Ch. d' Ecogia 16, CH-1290, Versoix, Switzerland

ABSTRACT

The Narrow Line Seyfert 1 Galaxies (NLSy1s) are characterized by optical, ultraviolet, and X-ray properties that differ from those observed in normal Seyfert galaxies. The proposed models attribute their peculiarity to an orientation effect (pole-on model) or to an intrinsic property (low mass black hole). In both cases their infrared emission will be the same as observed in normal Seyfert 1, if it is thermal radiation from an optically thick disk. Some NLSy1 galaxies are also characterized by a strong infrared continuum, probably due to a bright starforming region.
We obtained four broad infrared spectra of NLSy1 galaxies with the imaging photo-polarimeter (ISOPHOT) on-board of the Infrared Space Observatory (ISO). A non-standard procedure of data reduction has been applied and it is presented. The spectral energy distributions are modeled to derive the temperature distributions and compared with those of normal Seyfert 1 galaxies. The ratios between the infrared and the optical and soft X-ray luminosities are also derived, and compared with those of Seyfert 1 galaxies. The obtained infrared spectra of NLSy1s and the ratio L_{SX}/L_{IR} are consistent with those of normal Seyfert 1 galaxies, but the ratios between the infrared and optical luminosities are higher than in normal Seyfert galaxies. On the basis of these results we conclude that the presence of bright starforming regions is not a general property of NLSy1 galaxies, and that the infrared emission in NLSy1s is due to re-radiation of their soft X-ray component.

Key words: ISOPHOT; Seyfert galaxies; starformation; spectral energy distribution.

1. INTRODUCTION

NLSy1s are defined by their optical emission line properties (Osterbrock & Pogge 1985; Goodrich 1989) : permitted lines are only slightly broader than the forbidden lines, and narrower than in typical Seyfert 1 galaxies (FWHM (H_β) $\simeq$ 500 - 2000 km s^{-1}); forbidden lines emission is relatively weak ($[OIII]/H_\beta < 3$); and strong emission features from FeII, and high-ionization optical lines are observed. Although the emission lines widths and ratios have given a designation to the class long ago, it is only recently that the singular nature of these objects has been discovered thank to X-ray observations. The soft X-ray spectra are systematically steeper than in typical Seyfert 1 galaxies; the soft X-ray emission shows rapid and/or large amplitude variations; and at higher energies ($>$ 2 keV) NLSy1s show spectra described by a relatively weak power law steeper than observed in Seyfert 1 galaxies (Brandt et al. 1997). Some NLSy1s have exceptionally strong EUV/soft X-ray excesses, many times more than un-reddened Seyfert 1s, when normalized by the optical continuum. Some NLSy1s are also characterized by red optical continuum spectra and relatively strong infrared (IR) emission that dominates their luminosity (Halpern and Oke 1987). However, no complete or large samples of NLSy1 have been studied in the infrared and IRAS data are insufficient to define the multiple components which make up their infrared spectral energy distributions (SEDs), therefore it is not yet clear if NLSy1s show peculiar properties also at infrared energies. This question is being addressed by the Infrared Space Observatory (ISO; Kessler et al. 1996) that observed in total 16 NLSy1s at several wavelengths with a better sensitivity and spatial resolution than available with IRAS. The ISO data are essential to properly model the infrared SED, and to determine temperatures and contributions of the various IR components.
Preliminary results obtained with the Imaging Photo-Polarimeter (ISOPHOT; Lemke et al. 1996) on board ISO for four NLSy1 galaxies are here presented.

2. ISOPHOT OBSERVATIONS AND DATA REDUCTION

We observed 4 NLSy1 galaxies (TONS180, RXJ0323-49, IRAS13224-3809, PG1404+226) with ISOPHOT using the P1, P2, C100, and C200 detectors in chopper mode at 9 wavelengths between 3.6 and 200 μm. Raw data have been processed with version 7.0 of the Off-Line Processing. The first part of the data reduction has been performed using the version 7.2.2(e) of the PHT Interactive Analysis (PIA) tool (Gabriel et al. 1996). The reduction procedure starts with the Edited Raw Data (ERD): a sequence of detector readouts distributed in several sets of 4 response curves or

Proceedings of the Conference "The Universe as seen by ISO", Paris, France, 20–23 October 1998 (ESA SP-427, March 1999)

ramps, according to the integration time. Each set of four ramps represents a chopper position (on- and off-source). Each ramp is corrected for the non-linearity of the detector response, and for contamination of cosmic particle events (glitches). After having applied these corrections a straight line is fitted to each ramp, in order to determine its slope or Signal per Ramp Data (SRD). The SRD are corrected for highly discrepant points still contaminated by glitches, for the orbital dependent dark current, for the signal dependence on the ramp integration time (reset time interval), and for the signal loss outside the beam of the telescope (vignetting) to obtain an average Signal per Chopper Plateau (SCP). The average SCP data are further processed by performing the power calibration to obtain the Standard Processed Data (SPD). The SPD of the C100 and C200 detector, that collect the signal on respectively 9, and 4 pixels are also corrected for the flat fielding by taking PIA correction values.

Because the detector response varies with time, the actual response is determined at the time the source is observed by measuring the flux emitted by two thermal Fine Calibration Sources (FCS1 and FCS2) on board. We use the FCS1 because it is the best calibrated. After the flux calibration, data are a sequence of off- and on-source flux values each associated to a chopper plateau. The data reduction from this level to final results was performed interactively. During the interactive procedure several operations have been performed (background subtraction, correction for transient effect, source flux determination). They do not follow the standard reduction method, therefore a description is given.

The background to be subtracted to each on-source measurement has been estimated by taking the weighted mean of the values measured in the previous and in the next background position of each on-source position in order to remove long term drift effects. In Fig. 1 an example of this procedure applied to P2 detector data of TONS180 is shown. The data are two series of four on-source ($\diamond$), and four off-source ($\times$) measurements. The last pair of on- and off-source values is obtained with the weighted mean of the two last on-source measurements, and the flux observed in the last off-source position for the background. The background values (B) that are subtracted to the on-source values (S) are indicated with filled squares. The source flux, measured by each pixel, is the weighted mean of subtracted values obtained for each on-source position.

In case of the C100 detector only the central pixel pointed on the source was considered to derive the flux density; since the border pixels contain only a small fraction of the central point source; summing these values would therefore only increase the noise. In case of C200 detector the source flux is equally distributed on the four pixels of the array, therefore the final source flux has been computed adding the values measured by each pixel.

A correction for the signal loss due to transient effects depending on the time for chopper plateau is applied, because short integration times do not permit to the detector to reach the correct value when it receives a signal.

Since all the differences between on- (S) and off-source (B) measurements should give the same value for each pixel, all the pairs S-B that give a signal that differs from the average difference more than a certain number of standard deviations according to the number of available S-B pairs are rejected (Chauvenet's criterion in Taylor 1982). In Fig. 2 we report an example showing the data obtained with the central pixel of the C100 camera for RXJ0323-49. The symbols have the same meaning than in Fig.1. Selected pairs of on- (S) and off- (B) measurements, after deletion of discrepant points, are indicated by filled symbols. In this case five pairs S-B have been selected (solid line), and three have been discarded (dashed line). The final source flux is the weighted mean of the differences given by each pair, and the associated uncertainty is the standard deviation of the weighted mean σ_S. We assume to detect a source when the measured flux is higher than $3\sigma_S$, otherwise an upper limit to the flux equal to 3 times the standard deviation associated to the whole of differences is given.

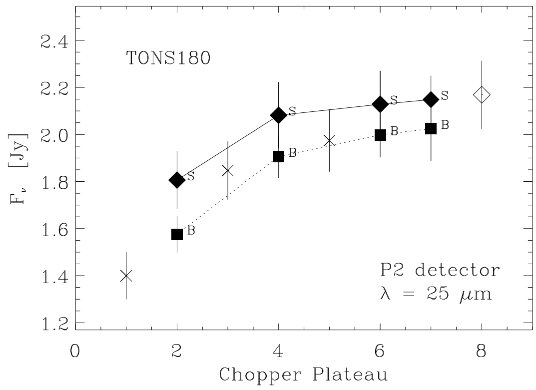

Figure 1. P2 detector data of TONS180 at 25 μm. $\diamond$ represent on-source measurements, $\times$ off-source measurements, $\square$ weighted means of each couple of consecutive off-source measurements. Filled symbols represent the selected on- and off-source values per chopper plateau.

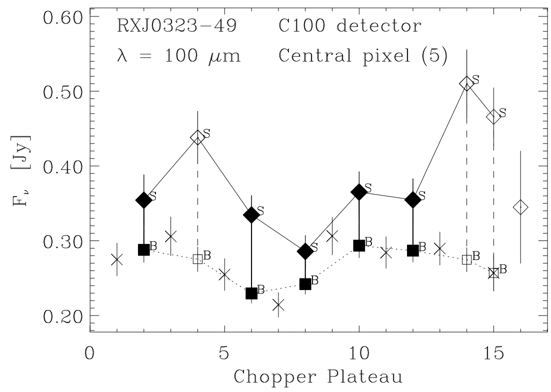

Figure 2. C100 central pixel data of RXJ0323-49 at 100 μm. Selected pairs after deletion of discrepant points are indicated by filled symbols (see text). For the meaning of others symbols see caption of Fig. 1.

During the data reduction only statistical errors are taken into account, however the accuracy of the absolute photometric calibration depends mainly on systematic errors, and it is currently known to be better than 30 % (Klaas & Radovich 1998). Therefore we associate to the measured flux an uncertainty of 30%.

3. IS IRAS 13224-3809 A DOUBLE SOURCE ?

At long wavelengths (60, and 100 μm) both IRAS and ISO detected IRAS 13224-3809, but consistent values are obtained only if all the pixels of the C100 detector are taken into account. The flux measured by the central pixel is indeed only ~45% of the total ISOPHOT and IRAS flux at both wavelengths. Looking at the signal obtained by each pixel of the C100 camera an excess in pixel 2 is observed, as shown in Fig. 3. An estimation of the cirrus contamination obtained from IRAS measurements is less than 20 mJy at 100 μm, therefore it can not explain the observed difference. Moreover, an excess in the same sky region is observed in the C200 detector. The presence of a bright infrared source far from the center, but included in the IRAS beam is probably the cause of this excess. A research in galactic and extra-galactic databases did not reveal the presence of a known source in the position corresponding to the observed excess. In the following analysis of the infrared emission of IRAS 13224-3809 we will use only the fluxes where the contribution of the second infrared source is negligible. They are the fluxes obtained with the central pixel of the C100 detector, and with the P detector because their field of view is of maximum 52" of diameter.

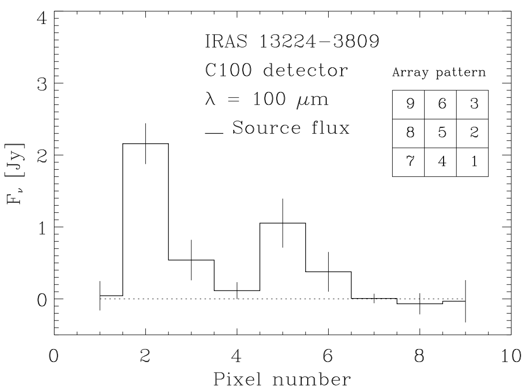

Figure 3. Measured source fluxes by each pixel of the C100 detector of the observation of IRAS 13224-3809 at 100 μm. The dotted line represents the zero level flux.

4. SPECTRAL FITS

The thermal nature of the mid- and fir-infrared emission from Seyfert galaxies is well established, even if it is not yet clear which is its origin: an accretion disk, a molecular torus, stars, HII regions, dust, or clouds of gas. Detailed models have been developed that take into account the different processes occurring in each scenario, but we did not compare them with the obtained spectral energy distributions (SEDs), because our purpose was to present the results less dependent than possible on models. We chose the simplest model for thermal emission : a sum of isothermal grey body components. The flux density of an isothermal grey body is expressed by the following law : $F_\nu = \Omega \cdot B(\nu, T) \cdot (1 - e^{-\tau})$ (Gear 1988), where Ω is the solid angle subtended by the source, $B(\nu, T)$ is the Planck function for a blackbody of temperature T, and τ is the optical depth that depends on the frequency at which the source becomes optically thin, and on the dust emissivity. We fitted ISOPHOT data of each object converted to the rest frame luminosity (H_0 = 75 km s^{-1} kpc^{-1}) using one or more grey body components at different temperatures, assuming a dust emissivity $\propto \nu^{1.5}$ that is reasonable dependence at the considered wavelengths ($<$ 200 μm) (Hildebrand 1983), and we left to vary the solid angle Ω, the temperature T, and the optical depth τ. The best fitting curves of the observed SEDs are shown in Figs. 4-7. All the spectra require at least two different temperatures.

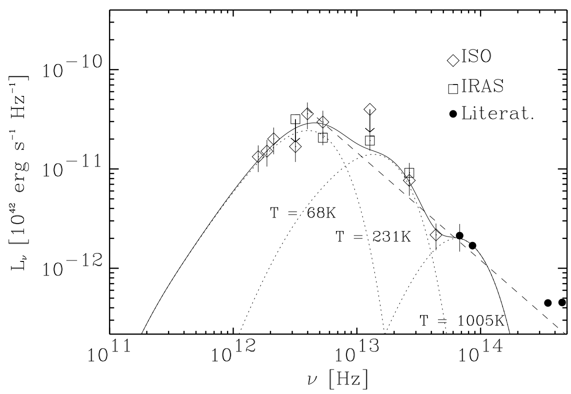

Figure 4. Spectral energy distributions of TONS180. Dotted lines represent single grey body components at the indicated temperature, and solid line the composite spectrum obtained summing each single component. The dashed line represents the power law obtained fitting ISOPHOT data at $\lambda <$ 100 μm. Arrows indicate 3σ upper limits.

5. RESULTS

Previous works on NLSy1s have suggested the presence of a starburst in NLSy1s because of their high infrared luminosities, and spectra (Halpern and Oke 1987). However in our sample no object is an ultraluminous IR galaxy : two sources are luminous infrared galaxies ($L_{IR} > 10^{11} L_\odot$), and two have infrared luminosities lower than $10^{11} L_\odot$. Moreover their spectral distributions are typical of Seyfert 1 galaxies, and rather different from star-formation dominated galaxies (Mas-Hesse et al. 1994), and their temperature distribution is also similar to that

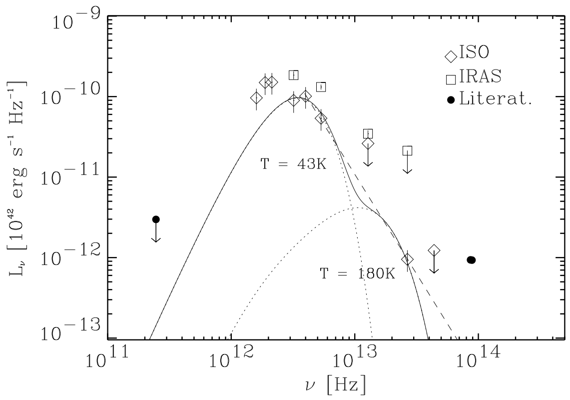

Figure 5. Spectral energy distributions of IRAS 13224-3809. See caption of Fig. 4 for the meaning of lines.

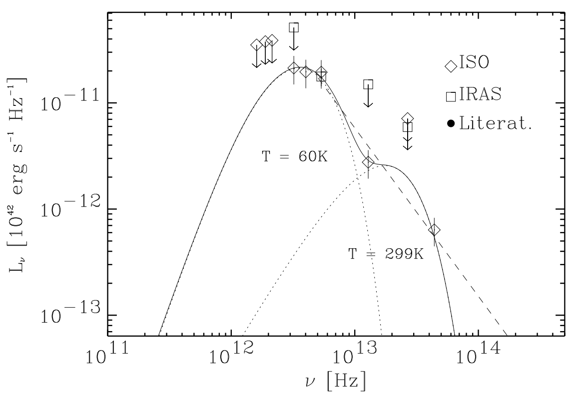

Figure 6. Spectral energy distributions of RXJ0323-49. See caption of Fig. 4 for the meaning of lines.

observed in Seyfert galaxies. These results do not exclude the presence of bright starforming regions in NLSy1s, indeed in IRAS 13224-3809 the steep mid-IR spectrum is probably due to the presence of a starburst emitting at longer wavelengths. However the presence of a bright starforming region is not always required for explaining the infrared emission of NLSy1 galaxies.
This result is also supported by L_{SX}/L_{IR} ratios similar to those observed in normal Seyfert 1 galaxies (Green et al. 1992). However, the L_{FIR}/L_B ratios are higher in NLSy1s than in normal Seyfert galaxies. Within the framework of the unified schemes involving a dusty torus, this result suggest that the infrared emission in NLSy1s is due to re-radiation of the EUV-soft X-ray component, as observed in normal Seyfert 1 galaxies, and any starforming region contribution is required to explain it. The origin of the EUV/soft X-ray excess in NLSy1s is still an open question, but its relationship with the infrared component is probably the same as in normal Seyfert 1 galaxies.

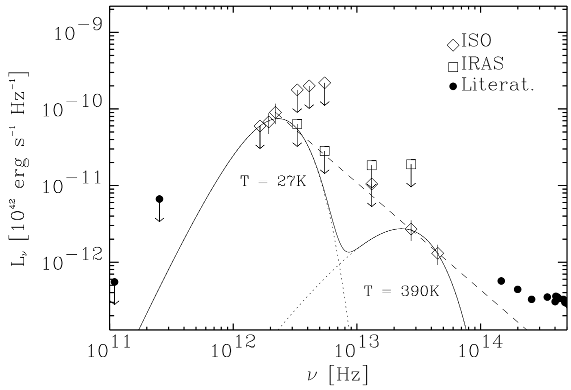

Figure 7. Spectral energy distributions of PG 1404+226. See caption of Fig. 4 for the meaning of lines.

ACKNOWLEDGMENTS

We thank Martin Haas, Péter Ábrahám, B. Wilkes, and Eric J. Hooper for help in the data reduction. The ISOPHOT data presented in this paper were reduced using PIA, which is a joint development by the ESA Astrophysics Division and the ISOPHOT consortium.

REFERENCES

Boller, T., Brandt, W. N., and Fink, H. 1996, A&A, 305, 53

Boroson, T. A. and Green, R. F. 1992, ApJS, 80, 109

Brandt, W. N., Mathur, S., Elvis, M. 1997, MNRAS, 285, L25

Gabriel, C. et al. 1996, the PIA Users Manual

Gear, W. K. 1988, Millimetre and Submillimetre Astronomy, R. D. Wolstencroft and W. B. Burton (eds.)

Goodrich, R. W. 1989, ApJ, 342, 224

Green, P. J., Anderson, S. F., and Ward, M. J. 1992, MNRAS, 254, 30

Halpern, J. P., and Oke, J. B. 1987, ApJ, 312, 91

Hildebrand, R.H. 1983, QJRAS, 24, 267

Kessler, M. et al. 1996, A&A, 315, L27

Klaas, U. and Radovich, M. 1998, Report on the ISOPHOT Sci. Val. for OLP V7.0, (SAI/98-049/rp)

Lemke, D. et al. 1996, A&A, 315, L64

Mas-Hesse, J. M. et al. 1994, ApJS, 92, 599

Osterbrock, D. E., and Pogge, R. W. 1985, ApJ, 287, 166

Taylor, J. R. 1982, An introduction to Error Analysis, The Study of Uncertainties in Physical Measurements 1997, University Science Books

Ulvestad, J. S., Antonucci, R. R. J., and Goodrich, R. W. 1995, AJ, 109, 81

BARRED SPIRALS OBSERVED IN THE MID-INFRARED

H. Roussel[1], L. Vigroux[1], M. Sauvage[1], C. Bonoli[2], A. Bosma[3], P. Gallais[1], T. Hawarden[4], S. Madden[1], & P. Mazzei[2]

[1]DAPNIA/Service d'Astrophysique, CEA/Saclay, 91191 Gif-sur-Yvette cedex, France
[2]Osservatorio Astronomico, Vicolo dell'Osservatorio 5, 35122 Padova, Italy
[3]Observatoire de Marseille, 2 Place Le Verrier, 13248 Marseille cedex 4, France
[4]Joint Astronomy Center, 660 N. A'ohoku Place, Hilo, Hawaii 96720, USA

ABSTRACT

Using ISOCAM observations, we compare the properties of barred and non-barred normal spirals from the point of view of their dust emission in the mid-infrared. In this paper, our aim is to infer some statistical trends in their star formation activities. We have found that a fraction of barred galaxies show an excess of emission around 15 μm, which is never the case for their unbarred counterparts, and that this is to be found only among early-type systems. Concentrating our analysis on central regions, we interpret such an excess as being due to impulsively heated dust grains, excited to high temperatures by a recent star formation increase triggered by bar-driven gas inflows.

Key words: bars; spirals; dust; star formation.

1. INTRODUCTION

It is now well established that orbit perturbations induced by a strong bar potential cause the gas from the inner disk to flow inwards and reach the nucleus or a circumnuclear ring located at an inner resonance; there, it can provide fresh material for enhanced star formation. For instance, a kinematical study of NGC 1530, which shows a high concentration of molecular gas in the nucleus, has evidenced such inward motions caused by shocks along the bar (Reynaud & Downes 1998), and numerous barred galaxies are known to harbour starburst rings or hot spots, like NGC 1097, NGC 1365 and NGC 1672 (which belong to our sample), all three also having an active nucleus probably fed by the same mechanism. Martinet & Friedli (1997), with their hydrodynamical simulations including stars, gas and star formation, have shown that strongly barred spirals undergo a starburst episode coupled with an evolution of the bar and disk structure. The main motivation for carrying out observations in the infrared range resides in avoiding the substantial extinction which usual star formation indicators such as far-UV and optical recombination line fluxes are likely to suffer from in dense central regions of galaxies. Previous studies with IRAS data could not distinguish between the emission arising from the disk and from the inner parts, a drawback which is suppressed in the present sample, due to the proximity of its members and the angular resolution of the instrument. We therefore have the possibility to further examine important results of IRAS-based analyses: Hawarden et al. (1986) have evidenced an emission excess at 25 μm, attributed to warm dust heated by starburst activity, in a large fraction of their optically selected SB and SAB spirals; Huang et al. (1996), using an optically selected sample and an IR-bright one, have examined the presence of a 25 μm excess in the light of galactic type (early or late) and relative infrared brightness; the 25 μm excess is correlated with the mid-IR emission compactness (Devereux 1987). In this paper, we interpret mid-IR properties of barred spirals with respect to what goes on in their central regions, a study which will be developed in Paper I.

2. THE SAMPLE

Galaxies were selected according to the following criteria:

- nearby and extended enough to allow a good resolution mapping with a 3 or 6 arcsec pixel field of view;
- moderate inclinations on the line of sight;
- spanning the whole de Vaucouleurs spiral sequence, from S0/a to Sdm;
- extended range of relative IR-brightnesses, with $0.25 < L_{\rm FIR}/L_{\rm B} < 5$.

We supplemented this initial sample by a large part of the Virgo cluster sample of Boselli et al. (1998), in order to broaden it and to gather a reference subset of unbarred galaxies of size comparable to the SB one. The final sample comprises 23 barred and 19 comparison spirals: 12 SABs (weakly barred) and 7 SAs (unbarred). Due to observing time constraints, our sample is by no means statistically complete, but spans a reasonable range of properties; the $L_{\rm FIR}/L_{\rm B}$ distribution, though extended, is however similar to those of optically selected samples.

All the galaxies were mapped in the two broadband filters LW2 and LW3 (respectively 5-8.5 μm and 12-18 μm) with a 3 or 6 arcsec pixel field of view and the observations homogeneously reduced using the CIA package; in addition, five low resolution CVF spectra were also secured between 5 and 15 μm. Fluxes are thought to be reliable within 30%, due to camera memory effects.

3. LINKS BETWEEN MORPHOLOGICAL TYPE AND MID-IR ACTIVITY

3.1. The mid-IR color

We have first investigated the morphological dependence of the global LW3/LW2 color, i.e. derived from fluxes integrated over the whole galaxy. The LW2 filter covers the emission from the so-called UIBs (unidentified infrared bands, due to carbonaceous compounds) at 6.2, 7.7 and 8.6 μm, while LW3 mainly collects a composite of the hot tail of a continuum attributed to VSGs (very small grains) and of the UIBs at 11.3 and 12.7 μm. Both components are impulsively heated by high energy radiation. From observations of distinct emission sites in our Galaxy, the VSG continuum has been shown to rise and get steeper in HII regions and UIBs to be predominant in photodissociation shells surrounding ionized regions or hot stars (Tran 1998). The fact that both LW3 and LW2 fluxes are linked with star formation in some way is a serious drawback for the interpretation of the LW3/LW2 color. Nevertheless, beyond some level of exciting radiation density, it shows the behavior that was expected before the launch of the satellite, i.e. it increases with star formation activity.

3.2. The role of central regions

We show in Figure 1 the variation of this indicator as a function of morphological type and bar feature. Whereas unbarred as well as weakly barred spirals have a relatively constant color whatever their type, of the order of 1 (between 0.7 and 1.2), strongly barred ones can exhibit hot colors, and the higher the excess which can be reached the earlier the type. Since in our few spectra the UIB component is ubiquitous and fairly constant in shape, the only varying feature being the VSG continuum, the LW3/LW2 rise has to be due to an increased contribution from very hot dust. The observed dependence with morphological type suggests that the bulge-to-disk ratio is an important parameter in the star formation triggering efficiency of bars. However, only a fraction of SB0/a-SBb galaxies have a hot LW3/LW2 ratio, which may be related to the details of bar strength, availability of gas and duration of the bar-induced star formation enhancement.

In view of the previous finding, we have tried to quantify the part of the central condensation in the global emission for each sufficiently resolved galaxy. The extent of this condensation was chosen by eye, the effects of the point spread function (PSF) making any systematic criterium hazardous, and the measured fluxes were corrected for PSF dilution. This results

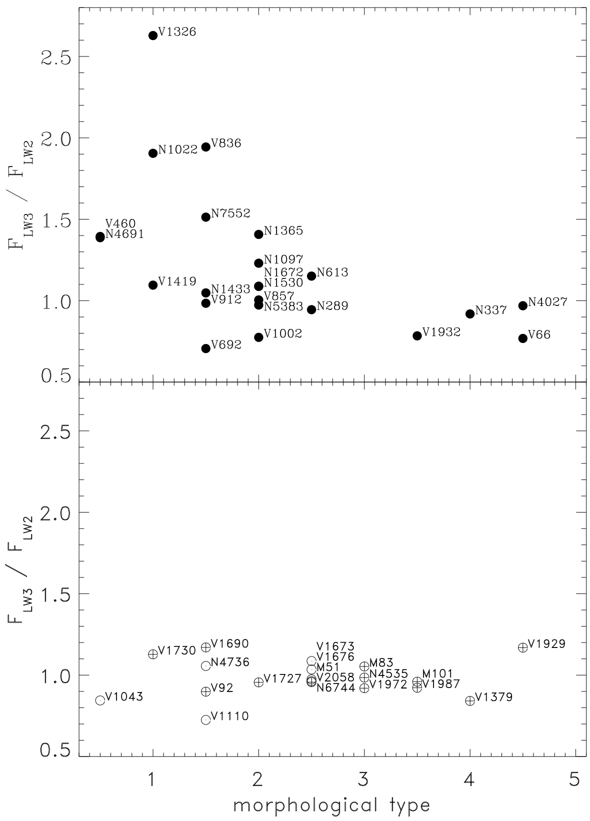

Figure 1. Mid-IR color versus de Vaucouleurs type, for SB galaxies on top and SA/SAB galaxies bottom (SAs appear as empty circles and SABs as crossed circles). Types (coming from the RC3) are coded with 1 for Sa, 2 for Sb, etc. Galaxies are identified by their NGC number, or their VCC number for the Virgo subsample. The barred morphology of V836, seen edge-on, comes from the boxy bulge indication of Maiolino et al. (1997).

in the distribution displayed in Figure 2. SA and SAB galaxies (which from their mid-IR properties are undistinguishable) are in all cases dominated by their

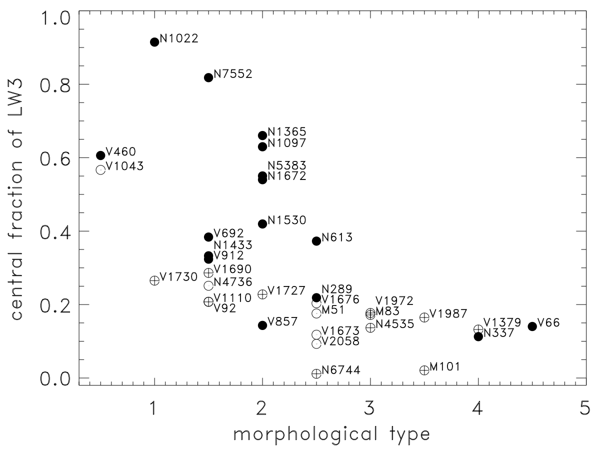

Figure 2. Contribution of central regions to the total 15 μm flux along the de Vaucouleurs sequence. Symbols are the same as in Figure 1.

disk (by more than 70%). On the contrary, early-type barred spirals are almost always relatively brighter in their central regions than their unbarred counterparts of the same type, including those with no global LW3/LW2 excess; the ones with a detectable excess (i.e. N1097, N1365, N7552 and N1022) are dominated in their total emission by their central parts (60 to 90% of the 15 μm flux). N1097 and N1365 shelter an active nucleus, but examining their CVF spectra, we conclude that its contribution to the broad central region emission is negligible, since their spectra are very similar to those of normal spirals and are dominated by UIBs in the short-wavelength part; as to N7552 and N1022, they present no sign of an active nucleus.

Now, considering Figure 3, from which it is clear that colors in central regions are systematically hotter than in disks, the trend observed in Figure 1 is explained in view of the flux fraction contributed by central condensations. The rise of LW3/LW2 colors is not due to UIB features falling down, but really to a higher excitation of VSGs causing the continuum longward of 13 μm to take off, as is evidenced by our spectra (Figure 4). Looking more closely at the behavior of LW3/LW2 as a function of the 15 μm surface brightness (Figure 5), a correlation can be seen between the excess at 15 μm and the energy density as traced by dust emission, itself related to the density of young stars. It can be noticed that in this diagram, galaxies with the highest color excess are located in the upper right part (those lacking either have not been observed with enough angular resolution to identify a nucleus or are seen edge-on).

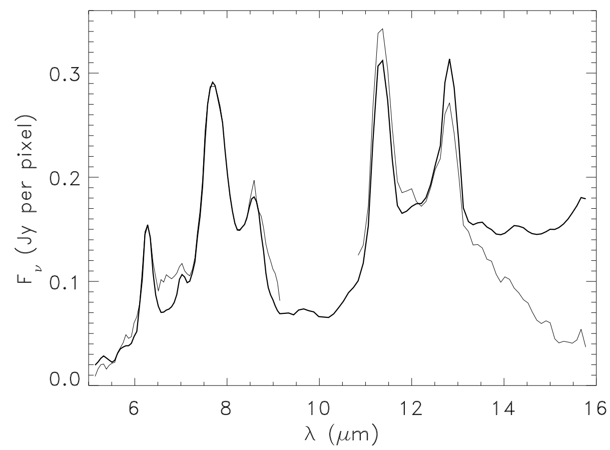

Figure 4. Low resolution spectra of M83 in the nucleus (thick line) and in the disk. The disk spectrum has been rescaled by a factor of 16.

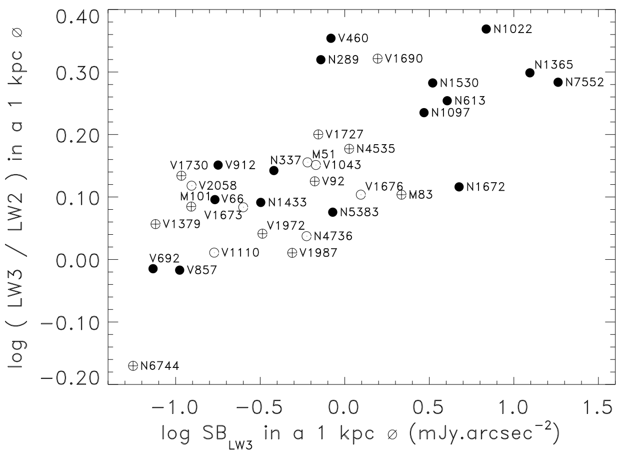

Figure 5. Variation of the mid-IR color inside a fixed physical aperture with the interstellar radiation density, whose effect is to increase the dust emission surface brightness (both at 7 and 15 μm).

4. DISCUSSION

We have seen that only some fraction of early-type barred galaxies show an abnormal LW3/LW2 color, though their central regions tend to be more energetic than in unbarred spirals of the same type. This fact is a hint that either the importance of the bulge is not the only governing parameter for producing bar-induced star formation enhancements, or early-type SBs with no LW3 excess have indeed undergone such a bursting episode, but which has now faded. According to the simulations of Martinet & Friedli (1997), the timescale for the full development of a strong bar, star formation boosting and return to a quiet state is of the order of 2 Gyr. Thus, the only sign of this past activity may be a prominent bulge, swollen by gas flows, and the evolution of bars may be accompanied by a shift towards an earlier Hubble stage. The amount of available gas in the disk and the gas-to-star conversion efficiency in bars, before the gas can reach the nucleus, must also play an important role. An analysis of dust emission inside bars is under way.

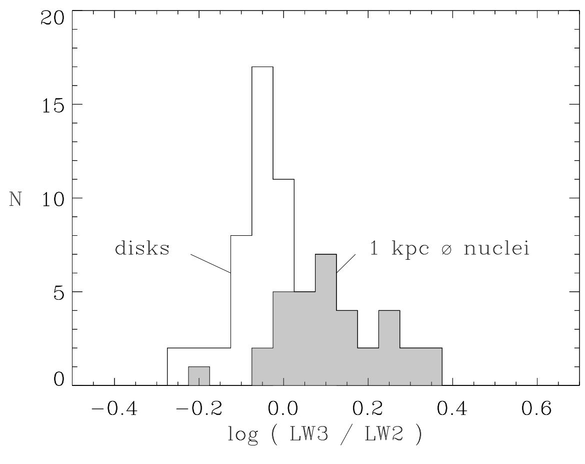

Figure 3. Compared histograms of the mid-IR color in disks and in 1 kpc diameter central regions.

Another interesting aspect is that many active nuclei are found to lie on the top of their morphological type bin in Figure 1: this is the case of V836, N1365, N1097, N613 and N1672. Even if the contribution of the AGN to dust emission on kpc scales is probably weak in our objects, this fact is certainly significant

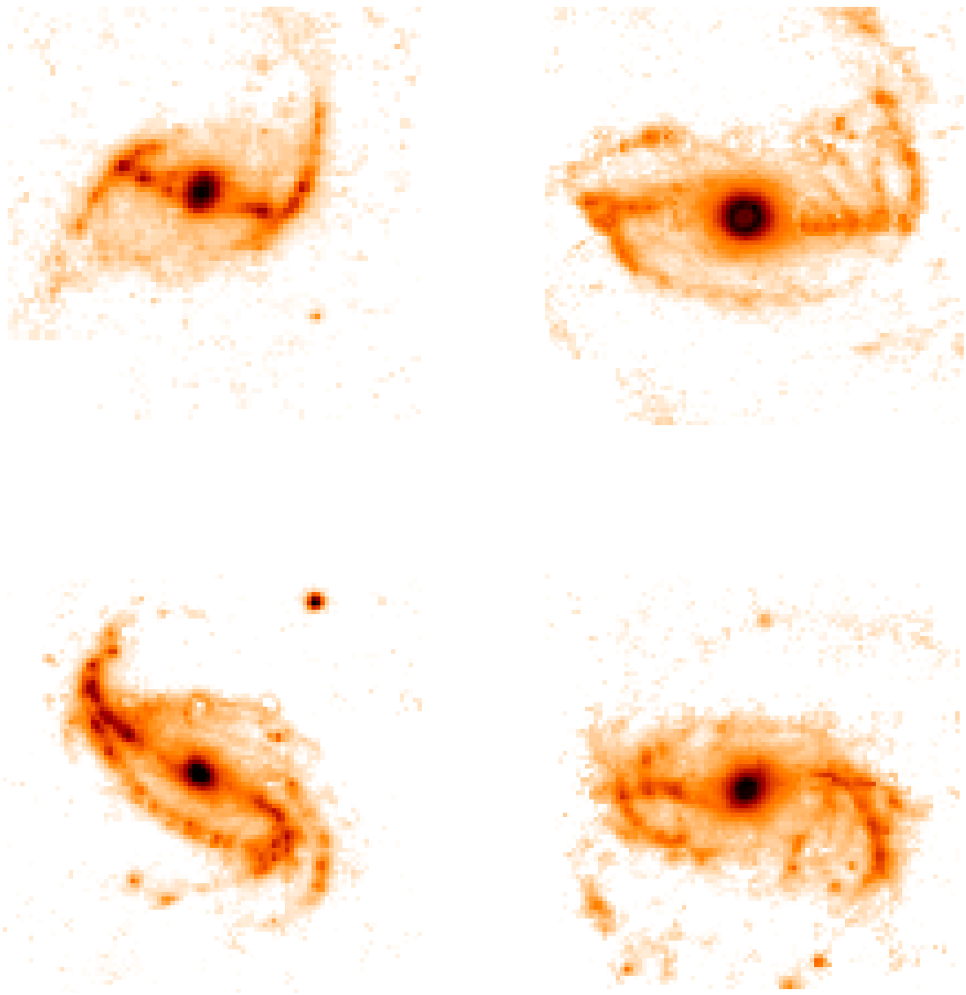

Figure 6. Four specimens among our 7μm maps (N1530 and N1097 on top, N613 and N1672 bottom). Note that the starburst ring in N1097 is quite well resolved.

and suggests that the same mechanism that produces a (circum)nuclear starburst also allows the AGN to be fed. In this respect, it is noteworthy that the first three objects cited above are known to possess a nuclear bar.

REFERENCES

Boselli, A., Lequeux, J., Sauvage, M. et al. 1998, A&A, 335, 53

Devereux, N. 1987, ApJ, 323, 91

Hawarden, T., Mountain, C., Leggett, S., Puxley, P. 1986, MNRAS, 221, SC41

Huang, J., Gu, Q., Su, H. et al. 1996, A&A, 313, 13

Maiolino, R., Ruiz, M. et al. 1997, ApJ 485, 552

Martinet, L., Friedli, D. 1997, A&A, 323, 363

Reynaud, D., Downes, D. 1998, A&A, 337, 680

Roussel, H., Vigroux, L., Sauvage, M. 1999, in prep. (Paper I)

Tran, D. 1998, PhD thesis, University of Paris XI

DUST IN AN EXTREMELY METAL-POOR GALAXY: MID-INFRARED OBSERVATIONS OF SBS 0335−052

M. Sauvage[1], **S. Madden**[1], **& T.X. Thuan**[2]
[1]CEA/DSM/DAPNIA/Service d'Astrophysique, CE-Saclay, 91191 Gif sur Yvette cedex, France
[2]Astronomy Department, University of Virginia, P.O. Box 3818, University station, Charlottesville, VA 22903-0818

ABSTRACT

The metal deficient (Z = $Z_\odot/41$) Blue Compact Dwarf Galaxy (BCD) SBS 0335−052 was observed with ISOCAM between 5 and 17 μm. With a $L_{12\mu m}/L_B$ ratio of 2.15, the galaxy is unexpectedly bright in the mid-infrared. The spectral energy distribution (SED) is dominated by a very strong continuum which makes the ionic lines of [SIV] and [NeIII] very weak. From 5 to 17 μm the SED can be fitted with a grey-body spectrum, modified by an extinction law similar to that observed toward the Galactic Center, with an optical depth of A_V $\sim$19-21 mag. Such a large optical depth implies that a large fraction (as much as $\sim$ 75%) of the current star-formation activity in SBS 0335−052 is hidden by dust with a mass between $3\times10^3\,M_\odot$ and $5\times10^5\,M_\odot$. It is remarkable that such a nearly primordial environment contains as much dust as galaxies which are 10 times more metal-rich. If the hidden star formation in SBS 0335−052 is typical of young galaxies at high redshifts, then the cosmic star formation rate derived from UV/optical fluxes would be underestimated.

1. INTRODUCTION

Galaxy formation is one of the most fundamental unsolved problems in astrophysics. Much effort has gone into the search for primeval galaxies (hereafter PGs), i.e. galaxies undergoing their first major burst of star formation, at redshifts larger than ∼2. Several objects have been put forward as possible PGs, ranging from high-redshift radio-galaxies to Lyα emitters. However, most of these candidate PGs appear to already contain a substantial amount of heavy elements (as indicated for example by the presence of P Cygni profiles), implying previous star formation and metal enrichment.

SBS 0335−052 is a relatively nearby Blue Compact Dwarf Galaxy (hereafter BCD) with an absolute magnitude M_B= -16.7 and which appears to be undergoing its first burst of star formation. With a metallicity of only $Z_\odot/41$ (Izotov et al. 1997), it is the second most metal-deficient galaxy known, after I Zw 18 ($Z_\odot/50$). With a redshift of 0.0136 and a Hubble constant of 75 km s^{-1} Mpc^{-1}, it is at a distance of 54.3 Mpc ($1'' = 263$ pc). Thuan et al. (1997) have found that the stars in SBS 0335−052 are not older than $\sim$ 100 Myr, making it a truly young galaxy. Yet, despite its youth and extremely low metallicity, HST images of SBS 0335−052 clearly show dust patches mixed in with the six super-star clusters where most of the star formation is occurring (Thuan et al. 1997). We have therefore obtained MIR observations of SBS 0335−052 with the Infrared Space Observatory (ISO) to study the properties of dust and star formation in a truly metal-deficient environment, similar to those prevailing at the epoch of galaxy formation.

2. OBSERVATIONS AND DATA REDUCTION

The observations were obtained with ISOCAM (Cesarsky et al. 1996a), the MIR imaging instrument aboard ISO (Kessler et al. 1996). They consist of two different sets: a set of broad-band filter maps, and a set obtained by imaging spectroscopy.

The broad-band maps were obtained with a spatial sampling of 3″ per pixel and in a 3×3 raster mode with a 3-pixel displacement in each direction. We used the LW9, LW10, LW8, LW6 and LW2 filters, centered respectively at 14.9, 12.0, 11.3, 7.7 and 6.7 μm. Note that the LW10 filter is identical to the IRAS 12 μm filter. Total on-source times were 860 s for LW10 and 1540 s for the other filters. Imaging spectroscopy was performed using the Circular Variable Filter (CVF) facility of ISOCAM with a sampling of 6″ per pixel and a spectral resolution $\lambda/\Delta\lambda$ of $\simeq 40$. Due to the faintness of the source we obtained observations only in the 8.78- 17.34 μm wavelength range. The total on-source time was 4800 s.

The various steps of ISOCAM data reduction[1] are detailed in Stark et al. (1998) and we will only describe

[1]We used the software package "CIA", a joint development by the ESA Astrophysics Division and the ISOCAM consortium. The ISOCAM consortium is led by the ISOCAM PI, C. Cesarsky, Direction des Sciences de la Matière, C.E.A, France.

Proceedings of the Conference "The Universe as seen by ISO", Paris, France, 20–23 October 1998 (ESA SP-427, March 1999)

here aspects that depart from the methods discussed in that paper: dark current subtraction and transient correction.

The dark current is known to show secular trends which depend on the position of the satellite in its orbit and on the time elapsed since launch. These trends can be accurately modelled (see Biviano et al. 1998), allowing nominal dark subtraction.

Transient corrections using the inversion algorithm of Abergel et al. (1996) were applied successfully to the broad-band observations. For the CVF observations, the known oversimplification of the method combined with the intrinsic faintness of the source results in errors of similar magnitude for both corrected and uncorrected CVF data. Synthesis of the LW8 and LW9 flux densities from corrected or uncorrected spectra gives flux densities 1.3 times larger than the observed ones. Thus we have adopted for the remaining discussion the CVF spectrum uncorrected for transient effects and scaled down by a factor of 1.3. Figure 1 displays the spectral energy distribution of SBS 0335−052. Flat-fielding and photometry for the CVF scan were made following Aussel et al. (1998). Conversion from camera units to mJy was performed using the calibration factors given in the *ISOCAM Cookbook*[2]. Most of the star formation in SBS 0335−052 occurs within a region of ~2.5" in size, so that the individual super-star clusters in SBS 0335−052 are not resolved by ISOCAM.

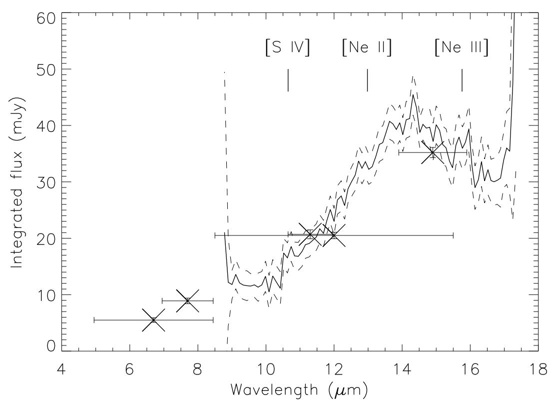

Figure 1. The spectral energy distribution of SBS 0335−052. Crosses represent broad-band observations with horizontal bars showing the width of the filters. 1σ errors bars are smaller than the symbols. Broad-band flux densities have been integrated over the point spread function. The thick line is the CVF spectrum with the effects of varying point spread function with wavelength taken into account. The dashed lines show ±1σ errors. Expected positions of the [SIV]λ10.5μm, [NeII]λ12.8μm, and [NeIII]λ15.6μm emission lines are indicated.

[2] *http://www.iso.vilspa.esa.es/manuals/iso_cam/.*

3. DISCUSSION

3.1. Global properties

Since the ISOCAM LW10 filter is equivalent to the IRAS 12 μm filter, it is interesting to see how the integrated properties of SBS 0335−052 compare with those of other BCDs and irregular galaxies. We have thus compiled IRAS and Hα data for the Thuan & Martin (1981) catalog of BCDs, hereafter TM81, as well as for the sample of BCDs and irregular galaxies in Sauvage et al. (1990) to perform the comparison.

With a 12 μm to blue luminosity ratio L_{12}/L_B of 2.15±0.06, SBS 0335−052 is comparable to the most MIR-bright objects in the TM81 catalog. In that sample the mean L_{12}/L_B ratio ($<\log L_{12}/L_B> = -0.12\pm0.27$), while already twice as high as that for spiral galaxies in the CfA catalog (Sauvage & Thuan 1994), is a factor of 3 smaller than the ratio for SBS 0335−052. This shows that even though the BCD is ∼ 10 times more metal-poor than the galaxies in TM81, it nevertheless contains a significant amount of dust heated by an intense UV radiation field.

If we compare the 12 μm luminosity to a tracer of star formation such as the Hα luminosity, SBS 0335−052 appears to be normal. Although total Hα fluxes are scarce for BCDs, the available data give $<\log L_{12}/L_{H\alpha}> = 0.96\pm0.70$ for the above samples, as compared to 0.65±0.03 for SBS 0335−052. Thus, even though the metallicity of the BCD is exceptionally low, and the galaxy unusually MIR-bright, its star-forming properties appear to be normal when compared to other BCDs.

3.2. The Mid-infrared spectrum

When the MIR spectral energy distribution of SBS 0335−052 (Figure 1) is compared to MIR spectra of other star-forming galaxies (see e.g. Vigroux 1997), two facts stand out : (1) there is no emission from the so-called Unidentified Infrared Bands (hereafter UIBs, usually attributed to carbon-based dust, see e.g. Puget & Léger 1989; Papoular et al. 1996); and (2) there are no evident fine structure ionic lines, even though neon as well as sulfur lines are usually quite bright in starburst galaxies.

In Figure 1, a hint of the [SIV]λ10.5μm and [NeIII]λ15.6μm lines can be seen. The quality of our spectrum prevents us from actually measuring line fluxes. Instead we compute upper limits as twice the local rms noise times the instrumental profile width at 20% of peak intensity at the line location. We obtain upper limits of 5.6×10^{-14} erg s^{-1} cm^{-2} for [SIV], 4.5×10^{-14} erg s^{-1} cm^{-2} for [NeII], and 5.4 $\times10^{-14}$ erg s^{-1} cm^{-2} for [NeIII]. These upper limits are completely consistent with the prediction of the photoionization model of Stasinska (1990). We conclude, therefore, that the weakness (or absence) of ionic fine-structure lines in SBS 0335−052 can be explained by a very strong continuum which decreases the equivalent widths of the lines, making them difficult to detect.

None of the usual UIB features are seen, suggesting that their carbonaceous carriers are absent or have been destroyed. As the star-forming region, 660 pc in diameter, contains 5000 equivalent O7 stars (Izotov et al. 1997), the average energy density is $\gtrsim 10\,\mathrm{eV\,cm^{-3}}$. Puget & Léger (1989) suggest that at this stage, the abundance of the band-emitting dust is reduced by a factor of ~10. Therefore the absence of the bands can be understood as a destruction effect. The origin of the continuum emission is more problematic. We observe what could be interpreted as either a broad emission feature at around 14 μm, or a broad absorption feature at $\lambda \gtrsim 16\,\mu$m. As we know of no candidate which would show such an emission feature we favor the second interpretation. Indeed silicate absorption bands at 9.7 and 18 μm could provide an explanation for the strange shape of the MIR spectrum of SBS 0335−052.

Testing this is not straightforward as the expected shape of the dust emission spectrum in this wavelength range is difficult to constrain. Apart from the stochastic heating of macromolecules giving rise to the UIBs, MIR emission is thought to be produced by very small grains in a thermal regime intermediate between equilibrium and stochastic heating (see e.g. Désert et al. 1990). We have therefore attempted to fit the spectral energy distribution (SED) of SBS 0335−052 with different screen models where the emission spectrum was successively: (1) a black-body modified by an emissivity law of the form $f_\nu \propto B_\nu(T)\,\nu^{1-2}$; (2) a power-law spectrum; and (3) the continuum MIR spectrum of the Galactic HII region M17 with UIBs and ionic lines removed (Cesarsky et al. 1996b). The free parameters of the underlying spectra include in all cases a scaling factor, in addition to the temperature in case (1) and the power-law slope in case (2). A further uncertainty comes from the extinction curve to be used. We have tried two different laws, the standard MIR extinction law of Draine (1989), and that observed in the direction of the Galactic Center by Lutz et al. (1996). The latter differs from the previous one by its much higher A_λ/A_V in the range 2-8 μm. This difference is ascribed to ice coating on grains. The free parameter associated with the extinction curve is simply the absolute extinction at a reference wavelength. Our fitting procedure searches for best fits to the CVF scan data only. There is no attempt to fit the broad-band data outside of the CVF range. However, a successful model will be one that also accurately predicts them.

Both a power law and the M17 spectrum fail to reproduce the observed SED. Power laws overproduce emission shortward of 8 μm while the M17 spectrum overestimates emission longward of 14 μm. On the contrary, a black-body spectrum modified by an emissivity law proportional to $\nu^{1.5}$ and extinguished by a screen of dust, gives an excellent fit to the SED of SBS 0335−052 (Figure 2). The fit is very sensitive to the shape of the extinction law. It is impossible to obtain a good fit for the LW2 and LW6 bands with the standard extinction curve of Draine (1989). On the contrary, excellent fits of these bands can be obtained with the Lutz et al. (1996) extinction curve. The temperature obtained for the black-body curve probably carries little physical meaning since the MIR-emitting grains are not likely to be in thermal equilibrium.

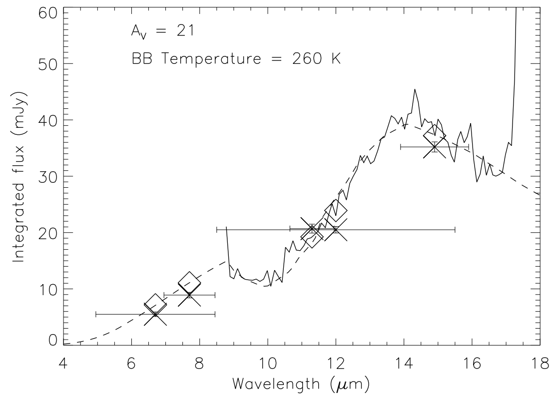

Figure 2. The best-fit model (dashed line) for the spectral energy distribution of SBS 0335−052. It consists of a black-body of temperature 260 K, with an exponent of 1.5 for the emissivity law, and A_V = 21 mag. The extinction curve of Lutz et al. (1996) gives the best results. Open diamonds show the prediction of the best-fit spectrum for broad-band measurements. The agreement with the observations is satisfactory for all filters.

The information we derive concerning the dust extinction is more physical. Given the uncertainties in our data, we obtain an equivalent A_V of 19-21 mag. Such a high value of extinction is in sharp contrast to the values ($A_V \leq 0.6$ mag) derived by Izotov et al. (1997) from optical spectrophotometric observations. The large difference between the optical and infrared extinctions implies that the heating sources responsible for the infrared emission detected by ISO are probably too deeply embedded in dust to be detected in the visible and that most of the infrared emission is powered by invisible star clusters. Indeed, correcting the Hα flux for 20 mag of visible extinction would lead to unrealistically high star formation rates which would be incompatible with the non-detection of SBS 0335−052 in the far-infrared by IRAS.

The LW10 luminosity of $2.5\times10^8\,L_\odot$ is equivalent to the bolometric luminosity of 2500 O7 stars, i.e. half the equivalent number of stars in the visible super-star clusters. Given that in the BCD sample of TM81, $\langle \log L_{12}/L_{FIR} \rangle = -0.85\pm0.09$, it is probable that in fact some 18000 equivalent O7 stars are required to power the total infrared emission. This implies that even in very low-metallicity environments such as those characterizing PGs, a significant fraction, i.e. ~ 3/4, of the total star formation activity of a galaxy can be effectively hidden from UV/optical observations.

From the extinction derived in the MIR, we can estimate the dust mass. As MIR extinction is essentially due to silicates (Draine & Lee 1984), this result will likely be a lower limit as some carbon-based dust can also be present. Using the dust model of Draine & Lee (1984), we obtain a dust surface density of 1.5 $M_\odot\,\mathrm{pc^{-2}}$. To derive a dust mass, we need to estimate lower and upper bounds to the dust spatial extent. For a lower bound, we assume that the dust is only associated with hidden super-star clusters (SSCs). O'Connell et al. (1994) found that SSCs typically have a very compact core with a half-light radius of ~ 3 pc, embedded in considerably more extended halos with diameters ~ 30 pc. If we adopt the latter value, and consider that at least 3 SSCs are hidden (they have the power of 2500 equivalent O7 stars needed to power the LW10 luminosity), we derive a dust mass of $\sim 3.2 \times 10^3\,M_\odot$. A likely upper limit to the spatial extent of the dust is the size of the region where reddening is observed by HST (Thuan et al. 1997), i.e. 660 pc. This gives a dust mass of $5{\times}10^5\,M_\odot$.

With the HI mass given in Thuan et al. (1997), the gas-to-dust mass ratio of SBS 0335−052 is then between $\sim 2 \times 10^3$ and $\sim 3 \times 10^5$, i.e. much higher than in the Galaxy, which is not too surprising for such a low metallicity object. More extraordinary is the fact that the dust mass in SBS 0335−052 can be of the same order of magnitude as that in BCDs which are on average ~ 10 times more metal-rich ($<\log M_{dust}> = 4.4{\pm}0.6\,M_\odot$ in the TM81 BCD sample).

Because stars in SBS 0335−052 are not older than $\sim$100 Myr, there is not enough time for the silicate dust to be made in the envelopes of red giant stars. Rather silicate grains probably condensed out of supernova ejecta (see e.g. Dwek et al. 1992). Adopting the supernova silicate dust mass input rate of $0.5\,M_\odot\,pc^{-2}\,Gyr^{-1}$ obtained by Dwek (1998) for the Galactic Center at 0.1 Gyr, the age of SBS 0335−052, and assuming the diameter of the dust-forming region to be 660 pc, we derive a silicate dust mass of $\sim 2{\times}10^4\,M_\odot$, i.e. in the range of the above estimates.

4. CONCLUSIONS AND IMPLICATIONS

Although SBS 0335−052 is one of the most metal-deficient galaxies known, it is unexpectedly bright in the MIR range, implying a silicate dust mass in the range 10^3–$10^5\,M_\odot$. The SED shows pronounced extinction, $A_V \sim 20$ mag. Given that the total MIR luminosity already requires the bolometric luminosity of 50% more young stars than are seen in the galaxy, the star formation rate (SFR) as derived from the optical or UV luminosities must underestimate the true star formation rate by at least 50%, and more likely by a factor of 4 as argued above. Thus if SBS 0335−052 is a representative example of PGs, the cosmic star formation rate will be systematically underestimated if based only on UV and optical fluxes.

ACKNOWLEDGEMENTS

T.X.T. has been partially supported by NASA grant JPL961535. We acknowledge useful conversations with Yuri Izotov.

REFERENCES

Abergel, A., et al. 1996, A&A, 315, L329

Aussel, H., Gerin, M., Boulanger, F., Désert, F. X., Casoli, F., Cutri, R. M., & Signore, M. 1998, A&A, 334, L73

Biviano, A., Sauvage, M., Roman, P., Boulade, O., Gallais, P., & Okumura, K. 1998, "The ISOCAM dark current calibration report", ESA Technical report

Cesarsky, C., et al. 1996a, A&A, 315, L32

Cesarsky, D., Lequeux, J., Abergel, A., Perault, M., Palazzi, E., Madden, S., & Tran, D. 1996b, A&A, 315, L309

Desert, F. X., Boulanger, F., & Puget, J. L. 1990, A&A, 237, 215

Draine, B. T. 1989, in Infrared spectroscopy in astronomy, ed. B. H. Kaldeich, (Noordwijk:ESA), 93

Draine, B. T., & Lee, H. M. 1984, ApJ, 285, 89

Dwek, E., Moseley, S. H., Glaccum, W., Graham, J. R., Loewenstein, R. F., Silverberg, R. F., & Smith, R. K. 1992, ApJ, 389, L21

Dwek, E. 1998, ApJ, 501, 643

Izotov, Y., Lipovetsky, V. A., Chaffee, F. H., Foltz, C. B., Guseva, N. G., & Kniazev, A. Y. 1997, ApJ, 476, 698

Kessler, M. F., et al. 1996, A&A, 315, L27

Lutz, D., et al. 1996, A&A, 315, L269

O'Connell, R. W., Gallagher, J. S., & Hunter, D. A. 1994, ApJ, 433, 65

Papoular, R., Conard, J., Guillois, O., Nenner, I., Reynaud, C., & Rouzaud, J. N. 1996, A&A, 315, 222

Puget, J. L., & Leger, A. 1989, ARA&A, 27, 161

Sauvage, M., & Thuan, T. X. 1994, ApJ, 429, 153

Sauvage, M., Thuan, T. X., & Vigroux, L. 1990, A&A, 237, 296

Starck, J. L., et al. 1998, A&A, in press

Stasinska, G. 1990, A&AS, 83, 501

Thuan, T. X., & Martin, G. E. 1981, ApJ, 247, 823

Thuan, T. X., Izotov, Y. I., & Lipovetsky, V. A. 1997, ApJ, 477, 661

Vigroux, L. 1997, in Extragalactic astronomy in the infrared, ed. G. Mamon, T. X. Thuan, & J. T. T. Van, (Paris: Editions Frontières), 63

SPECTROPHOTOMETRY AND IMAGING OF AGNs FROM 2.5 TO 11.6 μm

B. Schulz, J. Clavel, B. Altieri,
P. Barr, P. Claes, A.M. Heras, K. Leech, L. Metcalfe, & A. Salama

ISO Data Centre, Astrophysics Division, ESA, Villafranca, Spain.

ABSTRACT

We present low resolution spectrophotometric and imaging ISO observations of a sample of 58 AGN's over the 2.5–11.6 μm range. The data strongly support unification schemes and set new constraints on models of the molecular torus.

Key words: AGN, Seyfert Galaxies, Infrared, Spectroscopy.

1. INTRODUCTION

According to the "unified model" of Active Galactic Nuclei (AGN), Seyfert 1 and Seyfert 2 galaxies (hereafter Sf1 and Sf2) are the same objects viewed at a different angle: Sf1's are observed close to face-on such that we have a direct view to the Broad emission Line Region (BLR) and the accretion disk responsible for the strong UV-Optical-X-ray continuum, whereas Sf2's are seen at an inclination such that our view is blocked by an optically thick dusty torus which surrounds the disk and the BLR (e.g. Antonucci 1993). This model makes specific predictions. In particular, the UV photons from the disk which are absorbed by the grains in the torus should be re-emitted as thermal radiation in the IR. Several arguments constrain the torus inner radius to be of the order of $\sim$ 1 pc in which case the dust temperature should peak to about 700–1000 K and give rise to an emission "bump" between$\simeq$ 2 and 15 μm (Pier & Krolik 1992). The model also predicts that the silicate 9.7 μm feature should appear preferentially in absorption in Sf2's and in emission in Sf1's. In order to test these predictions and better constrain the model, we initiated a programme of mid-IR observations of a large sample of AGN's. Throughout we use $H_0 = 75\,\mathrm{km\,s^{-1}}$; $q_0 = 0$.

2. OBSERVATIONS

A sample of 57 AGNs and one non active "normal" SB galaxy was observed with the PHT and CAM instruments on board the Infrared Space Observatory (ISO; Kessler et al. 1996). The sample is drawn from the CfA hard X-ray flux limited complete sample but lacks the most well known objects (e.g. NGC 4151) which were embargoed by ISO guaranteed time owners. On the other hand, the sample was enriched in bright Sf2's. We caution that our sample is therefore not "complete" in a statistical sense. It is about equally divided into Sf1's (28 sources, including 2 QSO's) and Sf2's (29), where we define Sf1's as all objects of type ≤ 1.5 and Sf2's those whose type is $>$ 1.5. The mean and r.m.s. redshift are 0.047 ± 0.083 and 0.016 ± 0.013 for Sf1's and Sf2's.

For each object, the data-set consists of CAM images obtained through filters at 6.75 and 9.63 μm, together with 2.5–11.6 μm spectra obtained immediately before with the PHT-S low resolution ($3000\,\mathrm{km\,s^{-1}}$) spectrograph. The images consist of arrays of 32×32 pixels (i.e. 96×96 arcsec) with an effective resolution (FWHM) of 3.8 and 4.5 arcsec, for the 6.75 and 9.63 μm filters, respectively. The exposure times were 200 s, sufficiently long to ensure stabilisation of the detectors. For the spectra, on-source measurements were alternated with sky measurements at a frequency of 1/256 Hz, with a chopper throw of 300 arcsec. The on-source exposure times varied between 512 s and 2048 s, depending on the source brightness. The spectrograph aperture is 24×24 arcsec^2.

3. CALIBRATION AND DATA REDUCTION

The CAM images were reduced and calibrated using standard procedures of the CAM Interactive Analysis (CIA) package. Nuclear fluxes were obtained by integrating all the emission in a circle of 5–6 pixels radius (15–18 arcsec). Their accuracy, mainly limited by flat-fielding residuals, is ± 10 per cent. Radial profiles were also computed and compared to that of point-like calibration stars. For all sources but 4, the AGN are unresolved at the $\simeq 4$ arcsec resolution of ISOCAM. Because PHT-S was operating close to its sensitivity limit, special reduction and calibration procedures had to be applied. After a change of illumination, the responsivity of the Si:Ga photoconductors immediately jumps to an intermediate level. This initial jump is followed by a characteristic slow transient to the final level. At the faint flux limit, this time constant is extremely long, and in practice only the initial step is observed in chopped-mode. The spectral response function for this partic-

Proceedings of the Conference "The Universe as seen by ISO", Paris, France, 20–23 October 1998 (ESA SP-427, March 1999)

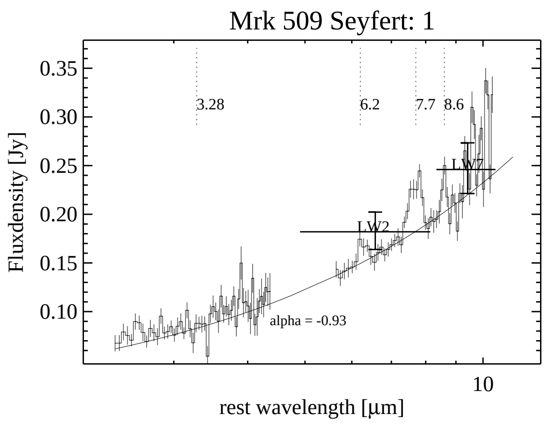

Figure 1. A representative Sf1 spectrum with error bars. The two data-points marked LW2 and LW7 indicate the flux from the CAM images with its error and the filter wavelength range. The best-fit power-law continuum is also shown.

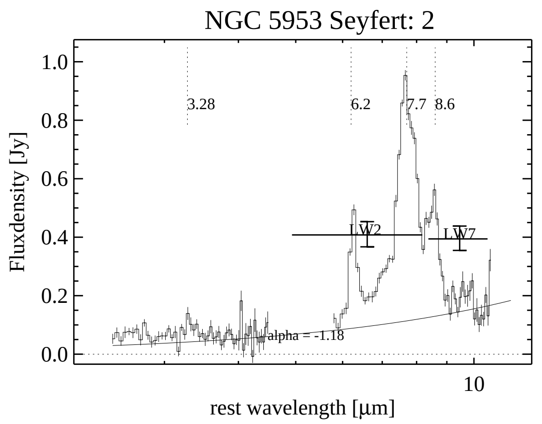

Figure 2. A representative Sf2 spectrum.

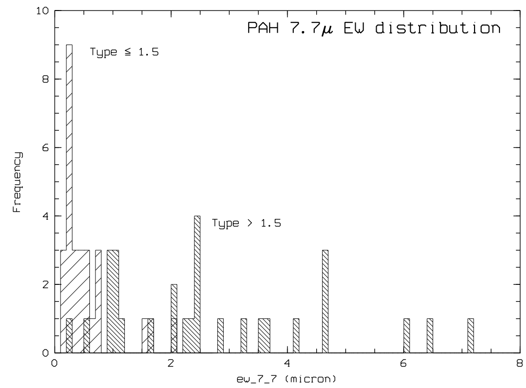

Figure 3. Distribution of PAH 7.7μm EW for Sf1 (spaced hatching at +45 °) & Sf2 (fine hatching, -45 °).

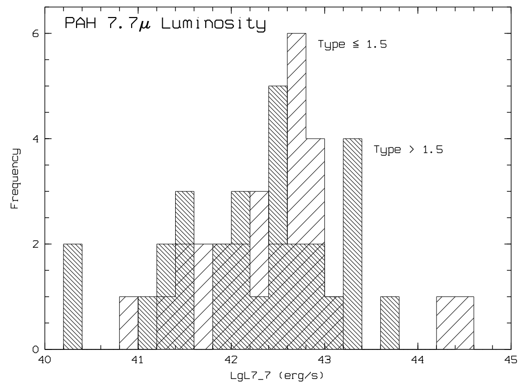

Figure 4. Distribution of PAH 7.7μm luminosities for Sf1 (spaced hatching at +45 °) & Sf2 (fine hatching, -45 °).

ular mode and flux-level was derived directly from observations of a faint standard star HD 132142 whose flux ranges from 0.15 to 2.54 Jy. The calibration star observation was performed with the same chopper frequency and readout-timing as the AGN observations. The S/N of the PHT-S spectra was considerably enhanced by two additional measures: *i*) the 32-s integration ramps were divided into sub-ramps of 2 sec and no de-glitching (removal of cosmic ray hits) was performed at ramp-level *ii*) after slope-fitting and de-glitching at slope-level, the maximum of the distribution of the slopes was determined by fitting a gaussian to the histogram. The resulting PHT-S fluxes should be accurate to within ±10 per cent.

For all sources but 4, the agreement between the CAM and the PHT-S flux is excellent which confirms the reliability of our calibration. The 4 slight mismatches occur for the 4 spatially resolved sources.

4. THE DIFFERENCE BETWEEN SF1 AND SF2

As illustrated in Figure 1, the mid-IR spectrum of a typical Sf1 (Mrk 509) is markedly different from that of a Sf2 (NGC 5953, Figure 2): Sf1's have a strong continuum well approximated by a power-law ($F_\nu \propto \nu^\alpha$) of average index and r.m.s. dispersion $\langle\alpha\rangle = -0.84 \pm 0.24$ and weak emission features. By contrast, most Sf2's display only a weak continuum together with very strong emission features. These features have well defined peaks at at 6.2, 7.7 and 8.6 μm, usually ascribed to Polycyclic Aromatic Hydrocarbon (PAH) bands. In many galaxies of adequate S/N and redshift, the blue side of the strong 11.3μm PAH feature is also detected as a sharp rise in flux toward the long wavelength end of the PHT-S array (see e.g. Figure 7). The mean spectral index of the Sf2's, $\langle\alpha\rangle = -0.75 \pm 0.56$ is consistent with that of Sf1's. The EW distribution of the strongest PAH band at 7.7 μm is shown in Figure 3. It clearly illustrates that PAH's are systematically weaker in Sf1's than in Sf2's where EW's extend up to $\sim$ 7μm. A two-tail KS test confirms that Sf1's and Sf2's have statistically different EW distributions at the $4 \cdot 10^{-8}$ confidence level. The mean ($\pm$r.m.s) 7.7 μm PAH equivalent width of Sf1's is $\langle EW_{PAH} \rangle = 0.53 \pm 0.47\,\mu$m, 5 times smaller than that of Sf2's, $\langle EW_{PAH} \rangle = 2.72 \pm 1.83\,\mu$m. As can be seen from Figure 4, the distribution of the 7.7 μm PAH *luminosity* is however the same in Sf1's and Sf2's, at the 52 per cent confidence level (KS test). The mean ($\pm$r.m.s) PAH luminosity of Sf1's is $\langle \log L_{PAH} \rangle = 42.44 \pm 0.80$ erg s^{-1}, not statistically different (at the 26 per cent confidence level) from that of Sf2's, $\langle \log L_{PAH} \rangle = 42.22 \pm 0.87$ erg s^{-1}.

5. IMPLICATION FOR UNIFICATION SCHEMES

The continuum flux at a fiducial wavelength of 7 μm was read-out from the best-fit power-law. The resulting mean ($\pm$r.m.s.) continuum logarithmic luminosities for Sf1's and Sf2's are $\langle \log \nu L_{\nu,7} \rangle = 43.73 \pm 0.86$ and 42.80 ± 0.79 erg s^{-1}, respectively, implying that the mid-IR continuum of Sf2's is $\sim$ 9 times less luminous, on the average, than that of Sf1's. Together with the difference in PAH EWs, these results imply that *the prime distinguishing feature of Sf2's in the mid-IR is that their continuum is depressed relative to that of Sf1's.*

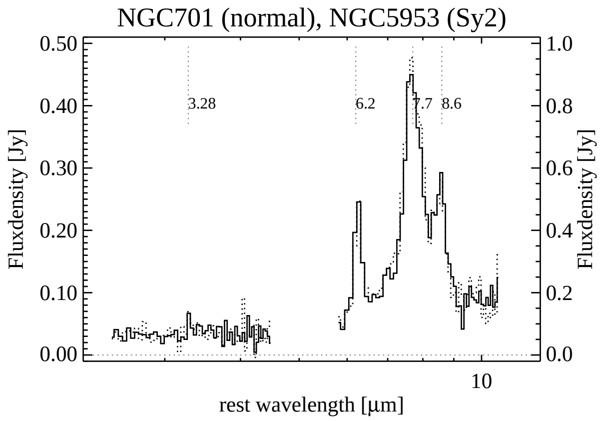

Figure 5. The spectra of the non-active galaxy NGC 701 (heavy line) and of the Sf2 galaxy NGC 5953 (dotted-line).

The above result is broadly consistent with unification schemes as illustrated in Figure 6, where the mid-IR continuum, which is directly visible in face-on objects (i.e. Sf1's), is largely extinguished in edge-on objects (i.e. Sf2's). It further implies that the torus is opaque to its own mid-IR radiation. Assuming that face-on objects suffer zero extinction, one can use the average PAH EW ratio $\langle R \rangle$ in Sf1's and Sf2's to infer the mean Sf2 extinction. The average ratio for the strongest PAH band at 7.7 μm is $\langle R \rangle = 5.2 \pm 3.5$, where the error quoted reflects the r.m.s. dispersion of Sf2 EW's. This implies that the Sf2 continuum suffers on the average from 1.8 ± 0.7 magnitudes of extinction at 7.7 μm, i.e. $A_v = 89 \pm 37$ magnitudes (Rieke & Lebofsky 1985). For a normal gas to dust

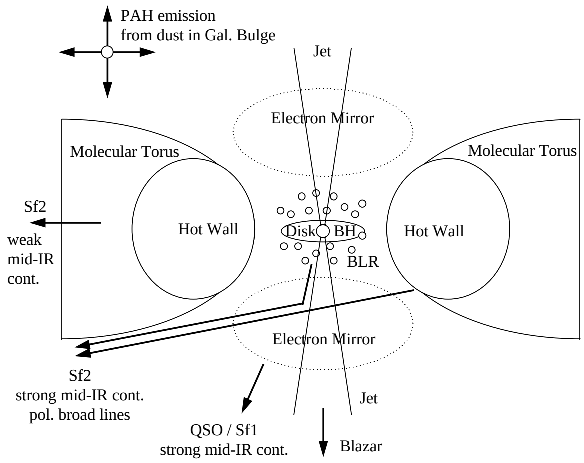

Figure 6. A graphical illustration of a unification scheme for Seyferts. Sf1 types are seen face-on, Sf2 types are seen edge-on. Sf2 types with "hidden" BLR are seen at a grazing angle. The PAH emission is not related to the AGN.

ratio, this corresponds to an average X-ray absorbing column, $N_H = 2.0 \pm 0.8 \cdot 10^{23}$ cm^{-2} (Gorenstein 1975). The latter is in good agreement with the mean Sf2 absorbing column as measured directly from X-ray data by Mulchaey, Mushotzky & Weaver (1992), $N_H = 1.6^{+8.6}_{-1.3} \cdot 10^{23}$ cm^{-2} or Smith & Done (1996), $N_H = 1.0 \pm 1.3 \cdot 10^{23}$ cm^{-2}. The large dispersion in A_v and N_H presumably reflects the spread in Sf2 torus viewing angles, i.e. from grazing incidence to completely edge-on.

It also suggests that PAH emission is isotropic and arises from outside the torus, either in the Narrow Line Region or in the ISM of the bulge. To check the origin of the PAH features, we have observed the nucleus of the "normal" (i.e. non active) SB galaxy NGC 701. Its PHT-S spectrum is plotted in Figure 5 together with that of the Sf2 nucleus NGC 5953. The mid-IR spectrum of NGC 701 – fairly typical of a "normal" galaxy (Helou et al. 1998) – is virtually indistinguishable from that of NGC 5953. As a matter of fact, the 7.7 μm PAH EW in NGC 701, $5.88 \pm 0.05\,\mu$m and luminosity, $\log L_{PAH} = 42.048 \pm 0.009$ erg s^{-1}, are well within the range spanned by Sf2's. We therefore conclude that the *PAH emission is unrelated to the active nucleus and arise from the ISM in the bulge.*

As can be seen from Figure 5, also the continuum of NGC 5953 is indistinguishable from that of NGC 701. This further suggests that in Sf2's with 7.7 μm PAH EW's in excess of $\simeq 5\,\mu$m, the torus emission is totally suppressed, at least up to 11.6 μm, and the faint residual mid-IR continuum arises entirely from outside the active nucleus, i.e. from stars shortward of $\sim 3\,\mu$m and from very small ISM dust particles at longer wavelengths. In such objects, the PAH EW only provides a lower limit to A_v and N_H. From the 29 Sf2's, only 3 have $EW_{PAH} \geq 5\,\mu$m. This suggests that about 10 per cent of Sf2's suffer from extinction in excess of 125 visual magnitudes, sufficient to block-out the mid-IR continuum. These extreme Sf2's are

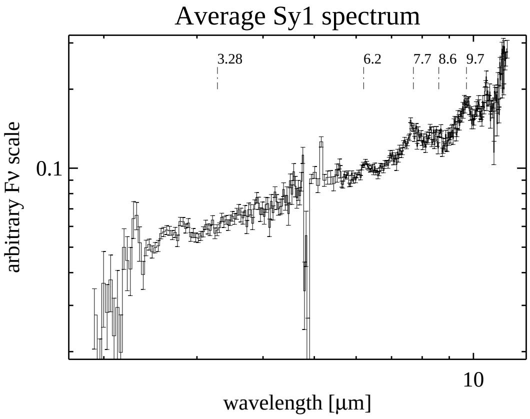

Figure 7. The average Sf1 spectrum of the 28 type ≤ 1.5 *galaxies in the sample.*

presumably those where the torus symmetry axis lies in the plane of the sky.

Ten Sf2 galaxies have $7.7\,\mu$m PAH EW $\leq 1.6\ \mu$m, in the range occupied by Sf1's (Figure 3). Among these, four have been observed in spectropolarimetry and *all 4 display broad-lines in polarized light*. These are Mrk 3, NGC 7674, IRAS 05189-2524 and NGC 4388 (Heisler et al. 1996). Conversely, none of the three Sf2's with $7.7\,\mu$m PAH EW $> 1.6\ \mu$m for which spectropolarimetric or IR spectroscopic data exist (Mrk 266, NGC 5728, NGC 1097) have "hidden" broad lines. This confirms the suggestion by Heisler et al. that those Sf2 which have "hidden" BLR (seen in spectropolarimetry or in direct IR spectroscopy) are those for which our line of sight (LOS) grazes the torus upper surface such that we can see the reflecting mirror but not the BLR. The mid-IR continuum most likely originates from thermal emission by hot dust grains located on the inner wall of the torus. Hence, the fact that the "hidden" BLR Sf2's are the same sources which display a Sf1-like mid-IR continuum further constrains the mirror and the torus inner wall to be in neighbouring regions. It is conceivable that the mirror is the wall itself or a wind of hot electrons boiled-off the torus. Mrk 3 has an X-ray absorbing column of $10^{24}\,\mathrm{cm}^{-2}$ (Turner et al. 1997) corresponding to an extinction of 125 magnitudes, sufficient to block the mid-IR radiation. The fact that it is nevertheless visible up to $11.6\,\mu$m indicate that the X-ray source is embedded further down the throat of the torus than the mirror and the wall emitting the mid-IR continuum.

6. THE SILICATE $9.7\,\mu$m FEATURES AND FURTHER CONSTRAINTS ON THE TORUS

Figure 7 shows the weighted mean Sf1 spectrum obtained by averaging the rest wavelength spectra of all 28 type ≤ 1.5 AGN's. The Silicate $9.7\,\mu$m feature appears *in emission* with an equivalent width $\langle \mathrm{EW}_{9.7} \rangle = 0.254 \pm 0.009\,\mu$m. This immediately *rules out models with very large torus optical depths.* In the model of Pier & Krolik (1992) for instance, the strength of the Silicate feature is calculated as a function of inclination i and of the vertical and radial Thomson optical depth τ_z and τ_r, respectively. Reading from their Figure 8, models with $\tau_z \geq 1$ and/or $\tau_r \geq 1$ are ruled-out as they would predict the Silicate feature in absorption. For an average Sf1 inclination $\cos i = 0.8$, the best fit to $\langle \mathrm{EW}_{9.7} \rangle = 0.254 \pm 0.008\,\mu$m suggests $\tau_r \simeq 1$ and $0.1 \leq \tau_z \leq 1$. A unit Thomson optical depth corresponds to a column density $\mathrm{N_H} \simeq 10^{24}\,\mathrm{cm}^{-2}$. While these figures are somewhat model dependent, it is reassuring that they agree with our independent estimate of $\mathrm{N_H}$ based on the PAH EW ratio. The PAH bands are so strong in Sf2's that placing the continuum at $9.7\,\mu$m becomes a subjective decision. The mean Sf2 spectrum shows a weak maximum at $9.7\,\mu$m and a shallow minimum near 10 μm. In the absence of longer wavelengths data, one can only set a provisional upper limit of $0.32\,\mu$m to the Silicate EW in Sf2's, whether in absorption or in emission.

REFERENCES

Antonucci, R. 1993, ARAA., 31, 473

Gorenstein, P. 1975, ApJ, 198, 95

Helou, G. et al. 1998, preprint

Heisler, C.A. et al. 1996, Nature, 385, 700

Kessler, M.F., Steinz, J.A., Anderegg, M.E., et al. 1996, A&A, 315, L27

Mulchaey, J.S., Mushotzky, R.F. & Weaver, K.A. 1992, ApJ, 390, L69

Oliva, E. et al 1998, A&A 329, 210

Pier, E.A. & Krolik, J.H. 1992, ApJ, 401, 99

Rieke, G.H. & Lebofski, M.J. 1985, ApJ, 288, 618

Roche, P.F. et al. 1991, MNRAS, 248, 606.

Smith, D.A. and Done, C. 1996, MNRAS, 280, 355

Turner, T.J. et al 1997, ApJ 488, 164

THE ISO LWS SPECTRUM OF THE SEYFERT GALAXY NGC 1068

L. Spinoglio[1], J.-P. Suter[2], M.A. Malkan[3], P.E. Clegg[4], J. Fischer[5], M. Greenhouse[6], H.A. Smith[7], D. Péquignot[8], G.J. Stacey[9], Nguyen-Q-Rieu[8], S.J. Unger[4], & V. Strelnitski[2]

[1] Istituto di Fisica dello Spazio Interplanetario-CNR, Roma, Italy
[2] Maria Mitchell Observatory, Nantucket, MA, USA
[3] Physics and Astronomy Department, UCLA, Los Angeles, USA
[4] Queen Mary and Westfield College, London, UK
[5] Naval Research Laboratory, Washington, USA
[6] NASA Goddard, Greenbelt, USA
[7] Harvard-Smithsonian Center for Astrophysics, Cambridge, USA
[8] Observatoire de Paris-Meudon, France
[9] Dept. of Astronomy, Cornell University, New York, USA

ABSTRACT

The prototypical Seyfert type 2 galaxy NGC 1068 has been observed with the LWS (Long Wavelength Spectrometer) on board the ISO (Infrared Space Observatory, ESA) satellite from 43 to 197μm. All the expected ionic fine structure lines have been detected. Also present are OH rotational lines in emission, at 79, 119 and 163 μm.

The ionic line intensities and ratios in NGC 1068 are discussed in the context of photoionization models of nonthermal (AGN) and thermal (starburst) origin and photodissociation regions models of the host-galaxy interstellar medium.

Emission in the low-lying rotational lines of OH seems to be due to rotational or ro-vibrational radiative pumping in an optically thick layer illuminated by a warm continuum source.

Key words: infrared: galaxies, lines; galaxies: Seyfert, active nuclei, starburst, ISM; galaxies: individual: NGC1068; photoionization models; ISM: molecules

1. INTRODUCTION

NGC 1068 is the prototypical Seyfert type 2 galaxy, also considered to contain the archetypal hidden Seyfert type 1 nucleus (Antonucci & Miller 1985). Because of its relatively small distance (14.4 Mpc) and high brightness ($L_{IR} = 2 \times 10^{11} L_{\odot}$, Bland-Hawthorn et al. 1997) NGC 1068 has been extensively observed at all wavelengths and studied in detail (see the proceedings of the NGC 1068 Workshop 1997). Infrared mapping of NGC 1068 soon revealed that the infrared emission was due to both a Seyfert nucleus (dominating the 10μm emission) and to a disk of 3kpc in diameter (emitting most of the luminosity at $\lambda > 30\mu m$) (Telesco et al. 1984). A recent $Br\gamma$ imaging study (Davies, Sugai & Ward 1998) indicates that a short burst of star formation occurred throughout the circumnuclear ring (15-16 arcsec in radius) within the last 4-40 Myr.

Current mid- to far-infrared spectroscopic observations from space or airborne platforms suffer from poor spatial resolution, and are not able to spatially separate the different regions emitting infrared lines: the active nucleus, the starburst and the interstellar medium. However detailed modeling using photoionization codes are able to spectroscopically distinguish the different emission components (e.g., Spinoglio & Malkan 1992).

2. OBSERVATIONS

NGC 1068 has been observed with the LWS (Long Wavelength Spectrometer, Clegg et al. 1996) on board the Infrared Space Observatory (Kessler et al. 1996), as part of the Core Programme of the LWS instrument team. The full low resolution spectrum (43-197μm) of NGC 1068 was collected during orbit 605 (July 13, 1997). Two on-source full scans (15,730 seconds of total integration time) and two off-source (6′ N) scans of the [CII]158μm line (3,390 seconds of total integration time) were obtained. On- and off-source scans had the same integration time per spectral step. Because of the design of the LWS spectrometer, simultaneously with the 158μm data, a short spectral scan of equal sensitivity to the on-source spectrum was obtained at sparsely spaced wavelengths across the LWS range.

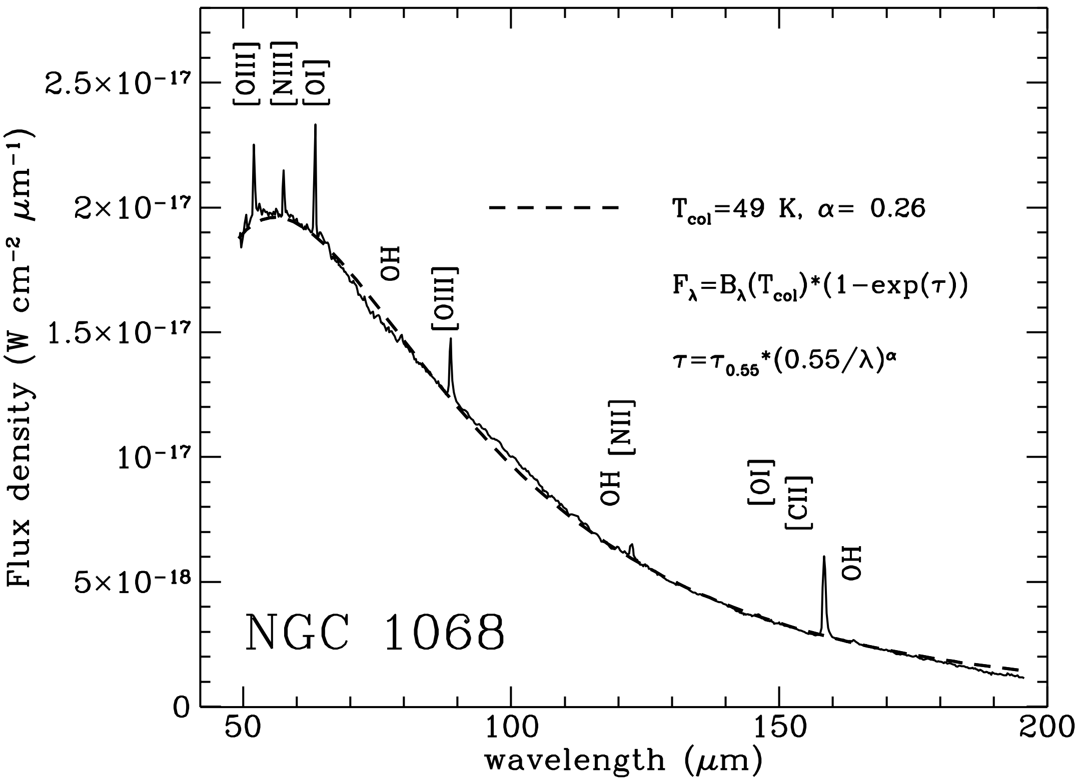

Figure 1. LWS spectrum of NGC 1068. The dashed line represents the black-body fit to the data. The line identifications are also shown.

The LWS beam is roughly independent of wavelength and equal to 80 arcsec. The spectra were calibrated using Uranus, resulting in an absolute accuracy better than 30% (Swinyard et al. 1996). The data analysis has been done with ISAP (ISO Spectral Analysis Package), starting from the auto-analysis results processed through the LWS Version 7-8 pipeline (July 1998). To increase the signal-to-noise ratio, all the full grating scans taken on the on-source position have been coadded, as well as the two sets of data on the off-source position. No signal was detected in the off-source position.

In Fig. 1 the complete far-infrared spectrum of NGC1068 is shown, together with a black-body fit. The best fit parameters (obtained with ISAP) resulted in a color temperature of T=49 ± 2.6 K and a dust emissivity index of α=0.27±0.15, where $\tau = \tau_{0.55} * (0.55/\lambda)^\alpha$, with $\tau_{0.55} = 0.15 \pm 0.13$.

Colbert et al. (1998) found a similar value of 48 K, fitting the LWS spectrum of M 82, whose shape is very similar to that of NGC 1068.

3. THE IONIC FINE STRUCTURE LINES

We have combined our far-infrared spectrum (Fig.1) with infrared spectroscopic data from the literature (Lutz et al. 1997, Greenhouse et al. 1998, Marconi et al. 1996, Thompson 1996). We find that a single model cannot satisfactorily explain these data. We identify three components:

- a starburst component, originated in the circumnuclear environment of the galaxy (e.g. Davies et al. 1998) that produces most of the emission of the intermediate ionization lines;
- an AGN component exciting the high ionization lines and contributing to the low-to-intermediate ionization lines;
- a photo-dissociation region (PDR), in the interstellar medium of the galaxy, which excites only the low ionization lines.

Detailed modeling is currently in progress and will be reported in a future paper (Spinoglio et al. 1998). Here we present a possible approach to successfully fit the mid- to far-infrared line emission spectrum.

Spinoglio & Malkan (1992) combined a narrow-line region model (NLR) with typical parameters (with log U = −2.5, log n = 4, $\alpha = -1.5$, where U is the ionization parameter, n is the Hydrogen number density and α is the slope of the power law ionizing continuum) with a coronal line region model (CLR) (with log U = 0, log n = 1, $\alpha = -1.5$) to predict the infrared fine-structure lines in NGC 1068. Comparing the observations with these model predictions, we find that the intermediate ionization lines typical of AGNs with ionization potential greater than $\sim$ 60eV and critical density greater than $\sim 10^4$cm^{-3} (e.g., [OIV], [NeIII], [NeV], [SIV], [MgV]) are in agreement within a factor two, while both the highest ionization lines (typically [NeVI] and some of the infrared coronal lines) and the “HII region lines” with either low critical density or low ionization ([NII], [NIII], [OIII], [NeII], [ArII]) disagree by more than a factor two. As expected, the PDR lines are observed to be much brighter, because that model did not consider the emission from the gas external to the HII regions in the galaxy.

The intrinsic nuclear spectrum of NGC 1068 has been inferred by Pier et al. 1994. Using this as input ionizing continuum for the photoionization models, for both the NLR and the CLR, instead of the softer spectrum ($\alpha = -1.5$) adopted in Spinoglio & Malkan (1992), we are able to better reproduce the observed high ionization lines.

Moreover, for the 'HII region lines', we will use a low density starburst model using the synthetic properties of starburst galaxies (e.g. Leitherer & Heckman 1995), to reproduce a short burst of star formation, like the 'instantaneous model' adopted to explain the far-infrared ionic lines in the Antennae and in M82 (Fischer et al. 1996, Colbert et al. 1998).

Finally, the low ionization lines can be accounted for by photodissociation region models (e.g. Kaufman et al. 1999). The [OI]63μm/[CII]158μm versus [OI]63μm/145μm line diagram (Fig.2) shows that both PDR and HII region (denoted as 'starburst') components are revealed by our data.

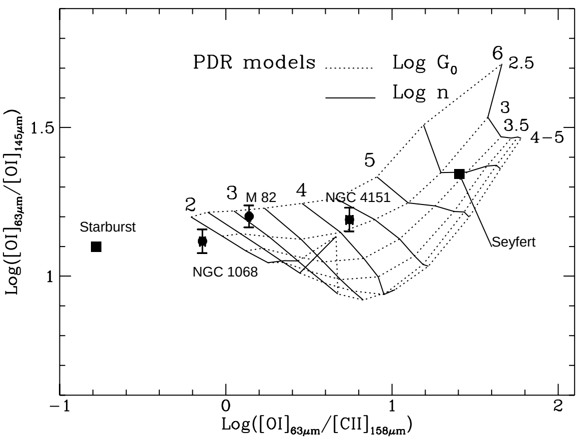

Figure 2. Line ratio diagram showing the position of NGC 1068 relative to the PDR models (Kaufman et al. 1999), where G_0 is the incident far-ultraviolet flux in units of 1.6×10^{-3} erg cm^{-2}s^{-1} *(Habing 1968) and n is the density. For comparison are also shown the "Starburst" and "Seyfert" models of Spinoglio & Malkan (1992), the position of NGC 4151 (Spinoglio et al. 1997) and M82 (Colbert et al. 1998).*

4. THE OH LINES

In NGC 1068 the OH rotational lines are seen in emission, in contrast with other bright infrared galaxies, such as Arp 220 (Fischer et al. these proceedings), Mrk231 (Harvey et al. these proceedings), NGC 4945 (Lord et al. in preparation), M 82 (Colbert et al. 1998), where these lines are seen mostly in absorption.

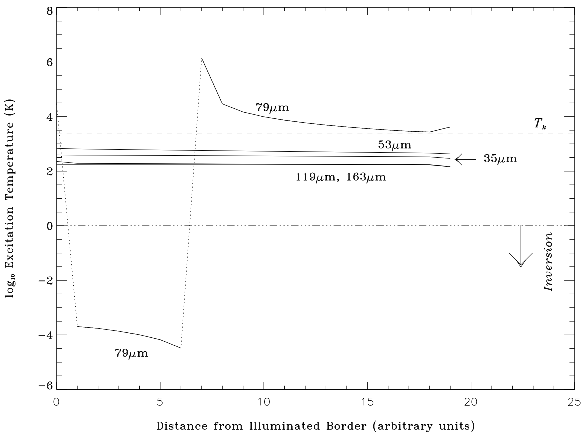

Figure 3. Excitation temperatures of the lowest rotational transitions of OH within a layer illuminated by a source of black-body continuum, as a function of the distance within the layer from the illuminated boundary. Continuum brightness temperature $T_{\rm B} = 4,000$ K; dilution factor $\Omega = 0.15$; gas kinetic temperature within the layer $T_{\rm k} = 2,500$ K; hydrogen number density $n_{\rm H} = 10^7$ cm^{-3}; OH column density $n_{\rm OH} \times L = 2 \times 10^{16}$ cm^{-2} (this corresponds to the total optical depth of the layer in the 119μm line $\tau_{119} = 110$). It is seen that the 79μm transition is inverted ($T_{\rm x} < 0$) in the front part of the illuminated layer and overheated ($T_{\rm x} > {\rm T_k}$) deeper in the layer. Other transitions in this layer are cooler than $T_{\rm k}$. Overheating and inversion of a transition make it a good emitter.

In order to try to use the OH lines to probe the source and conditions responsible for the excitation of these lines, we performed a simple modeling of radiative transfer in low-lying rotational lines of OH, in an optically thick layer illuminated by a warmer source of continuum. The result was that all the three transitions in question (79, 119 and 163μm) tend to be overheated or inverted by this rotational radiative pumping. The 79μm line and the pair of 119μm and 163μm lines require somewhat different parameters for overheating and inversion. This can be interpreted in terms of different layers of the same gas/dust envelope of a continuum source.

Color temperatures $\sim$ 4,000 K for the central source and kinetic temperatures $\sim$ 2,000 K for the pumped layer were typical values we used. Typical optical depths were several tens. We got a strong effect for the 79μm transition and, at somewhat higher values of the temperatures, for the pair 119 and 163μm (see Figs.3 and 4).

We have not exhausted the parameter space as yet, but rather have demonstrated the strong tendency of just these three transitions to appear in emission due to rotational radiative pumping of optically thick, warm gas, is obvious. It is tempting to connect the source of the emission with that of the radio megamasers.

An article discussing the pattern of absorption and emission in the rotational lines of OH detected by ISO in several infrared bright galaxies is currently

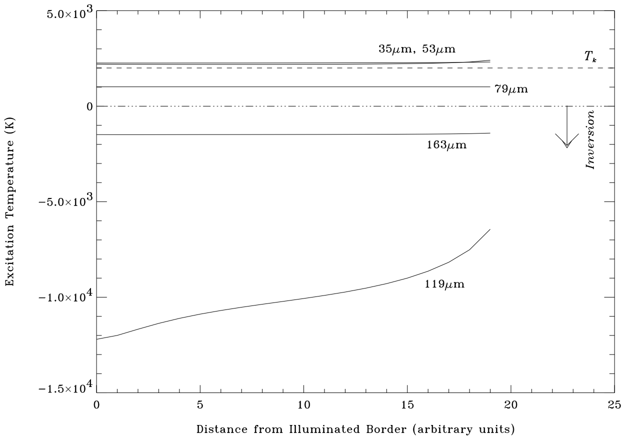

Figure 4. Same as Fig. 3 but: $T_{\rm B} = 8,000\,K$*;* $\Omega = 0.004$*;* $T_{\rm k} = 2,000\,K$*;* $n_{\rm H} = 10^9\,cm^{-3}$*;* $n_{\rm OH} \times L = 2 \times 10^{15}\,{\rm cm}^{-2}$*. It is seen that in such a layer the 163μm and 119μm lines are inverted throughout the layer, whereas* $T_{\rm x}$ *of the other transitions is not far from* $T_{\rm k}$*.*

in preparation (Suter et al. 1998). Both the observed OH emission in NGC1068, or the probable hidden emission (inseparable from the absorption with the available spectral resolution) in Arp220, Mrk231 or NGC4945, probably arises in compact, dense envelopes of young stars or in the envelope of a single compact source, as a result of fluorescence or weak laser amplification supported by rotational or ro-vibrational radiative-radiative pumping.

ACKNOWLEDGEMENTS

The authors acknowledge the LWS Consortium for having built the LWS instrument and solved many instrumental and data reduction problems. The ESA staff at VILSPA is also acknowledged for the ISO mission operations. This research was supported in Italy by the Italian Space Agency (ASI).

REFERENCES

Antonucci, R.R.J, & Miller,J.S. 1985, ApJ, 297,476

Bland-Hawthorn, J., et al. 1997, Ap&SS,248,9

Clegg, P.E., et al. 1996, A&A, 315, L28.

Colbert, J., et al. 1998, ApJ, in press.

Davies, R.I., Sugai,H., and Ward,M.J. 1998, MNRAS, in press.

Fischer, J., et al. 1996, A&A, 315, L97

Greenhouse, M., et al. 1998, ApJ, submitted.

Habing, H.J. 1968, Bull.Astr.Inst.Netherlands, 19, 421.

Kaufman, M. et al. 1999, ApJ, submitted.

Kessler, M.F. et al. 1996, A&A, 315, L27.

Leitherer, C., and Heckman, T.M. 1995, ApJS, 96, 9.

Lutz, D. et al. 1997, Ap&SS,248,217.

Marconi, A., et al. 1996, A&A, 315, 335.

Pier, E.A., et al. 1994, ApJ, 428, 124.

Spinoglio, L. & Malkan, M.A. 1992, ApJ,399,504.

Spinoglio, L., et al. 1997, in Extragalactic Astronomy in the Infrared, ed. G.A. Mamon, Trin Xuan Thuan, J Tran Thanh Van (Gif-sur-Yvette, Editions Frontières),333.

Spinoglio, L., et al. 1998, in preparation.

Suter, J.-P., et al. 1998, in preparation.

Swinyard, B.M., et al. 1996, A&A, 315, L43.

Telesco, C.M., et al. 1984, ApJ, 282, 427.

The NGC 1068 Workshop, 30 October - 2 November 1996, Ringberg Castle, 1997, Ap&SS,248,1

Thompson, R.I. 1996, ApJ, 459, L61.

FAR-INFRARED SPECTROSCOPIC IMAGES OF M83

G.J. Stacey[1], M.R. Swain[1], C.M. Bradford[1], M.J. Barlow[2], P. Cox[3], J. Fischer[4], S.D. Lord[5], M.L. Luhman[4], N.Q. Rieu[6], H.A. Smith[7], S.J. Unger[8], & M.G. Wolfire[9]

[1]Cornell University, Ithaca, NY, USA
[2]University College, London, UK
[3]Institute d'Astrophysique Spatiale, Paris,France
[4]Naval Research Laboratory, Washington D.C., USA
[5]IPAC, Cal. Inst. of Tech., Pasadena, CA, USA
[6]Observatoire de Paris-Meudon, France
[7]Harvard-Smithsonian Center for Astrophysics, Cambridge, USA
[8]Queen Mary and Westfield College, London, UK
[9]University of Maryland, College Park, MD, USA

ABSTRACT

We have mapped the nearby face on barred spiral galaxy, M83 in the bright [CII] 158 μm, [OI] 63 and 146 μm, [NII] 122 μm, and [OIII] 88 μm fine-structure lines with the Long Wavelength Spectrometer (LWS) on ISO. The maps are nearly fully sampled, and cover the inner $6.75' \times 6'$ region - essentially the entire optical disk. We also obtained a full LWS grating scan of the nucleus. The lines are detectable over the entire disk, and enhanced at the nucleus, where the [OI] 63 μm and [NII] lines are particularly strong. At the nucleus, the line ratios indicate a strong starburst headed by O9 stars. Surprisingly, the [OI] and [CII] line emission (from photodissociation regions) is not enhanced relative to [NII] (from low density HII regions) on the spiral arms. The line ratios are the same for the spiral arms and interarm regions. We find very strong emission in the [OIII] 88 μm, [OI] 146 μm, and [CII] lines at the intersection of the bar and spiral arm to the SW indicating particularly strong star formation activity there. The [OI] 63 μm/146 μm line ratio is quite small there likely the result of self absorption in the 63 μm line by enveloping clouds. The total luminosity of this emission peak is $\sim 1.2 \times 10^9 L_\odot$

Key words: galaxies: starburst – galaxies: individual: M83 – galaxies: ISM – infrared: galaxies

1. INTRODUCTION

The far-infrared (far-IR) fine structure lines that arise from abundant atoms and ions provide unique probes of the physical conditions of the interstellar medium in galaxies. Until ISO, most far-IR astronomical spectroscopy was performed using airborne, or balloonborne observatories. Unfortunately, the high background associated with these observatories prevented the detection of the far-IR lines from all but the brightest extragalactic sources. The cryogenic telescope on ISO dramatically changed this situation enabling for the first time detection of many of the lines from fairly large, systematically selected galaxy samples (e.g., Malhotra et al. 1997, Luhman et al. 1998). These studies demonstrate how the lines and far-IR continuum constrain the physical conditions of the ambient gas clouds, and the hardness and strength of the ambient interstellar radiation fields, thereby telling us much about the star formation history of these galaxies.

Galaxies are complicated beasts, and far-IR line emission can arise from a wide variety of regions - some currently forming stars, some not - within the galaxy. Therefore, to properly interpret spectra obtained from distant galaxies, it is important to examine as best we can the far-IR properties of various regions in nearby, resolved star forming galaxies. A fine example of such a galaxy is the nearby barred spiral galaxy M83. M83 has high surface brightness, is presented to us nearly face on ($i \sim 24°$) and has both well defined spiral arms and an optical bar that are resolvable at the spatial resolution of ISO's long wavelength spectrometer (LWS). At the distance of M83 ($d \sim 3.7$ Mpc), the 80 $''$ LWS beam subtends 1.5 kpc.

The highest priority project in the LWS Core Program 'The ISM in Normal Spiral Galaxies' was to map the brightest far-IR fine structure lines from M83. We used the LWS grating to map nearly the entire optical disk in the five brightest far-infrared fine structure lines: the [OI] (63 and 146 μm), [OIII] 88 μm, [NII] 122 μm, and [CII] 158 μm lines. The map is laid out on a rectangular 8×7 point grid that is nearly fully sampled ($45''$ step size), and covers nearly the entire optical disk. We also obtained a complete LWS grating scan (43 to 196 μm) at the nucleus, and deeper, separate integrations for the [OIII] 52 μm and [NIII] 57 μm lines there. The total integration time for the project was $\sim$ 5 hours.

2. RESULTS AND DISCUSSION

2.1. Overall properties

The lines are all detected over much of the optical disk (Figures 1 to 5). The [CII], and [OI] 63 μm maps have particularly high signal to noise (S/N) ratios. The bright optical bar is apparent in each of the line maps, and the spiral arms are obvious in all but the lowest S/N [OIII] 88 μm and [OI] 146 μm maps. The integrated flux in all of the lines is $\sim 2.1 \times 10^8 L_\odot$, or $\sim$ 0.68% of the total far-IR flux from the galaxy ($L_{far-IR} \sim 3.1 \times 10^{10} L_\odot$). Over half of the line flux comes out in the bright [CII] 158 μm line, and 60% of the remaining flux comes out in the [OI] 63 μm line. These ratios are typical for spiral galaxies (cf. Stacey et al. 1991, Lord et al. 1996). For the discussion that follows, we will refer to several regions apparent in optical images of M83: the bright central nucleus, the bar extending about 2′ to the NE and SW of the nucleus, the spiral arms (especially the western arm prominent in Figures 3 and 5, and the intersection of this spiral arm and the southwestern bar.

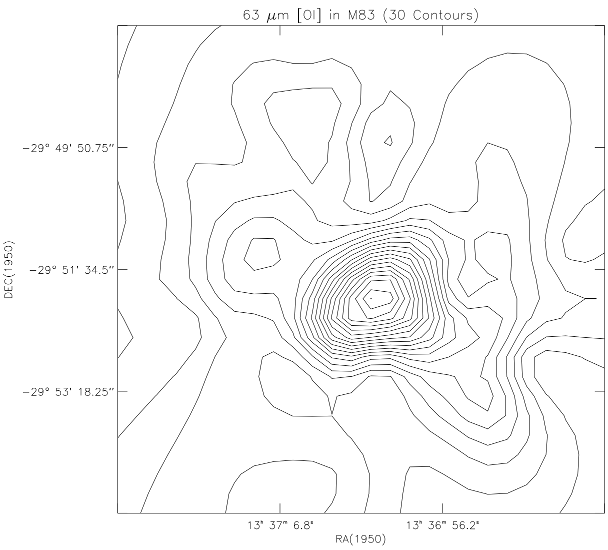

Figure 1. 63 μm [OI] map of M83. Contour intervals (1.5 σ) are 3.3% of the peak flux: 1.24 $\times 10^{-18}$ W cm^{-2} per 80′ beam.

2.2. Origins of the far-IR lines

It takes 14.5 and 35.1 eV photons to form N^+ and O^{++} respectively, so that the [NII], [NIII], and [OIII] line emission arises exclusively from ionized gas regions. Oxygen has nearly the same ionization potential as hydrogen (13.6 eV), so that the [OI] emission traces exclusively neutral gas clouds. However, since the ionization potential of carbon (11.4 eV) is

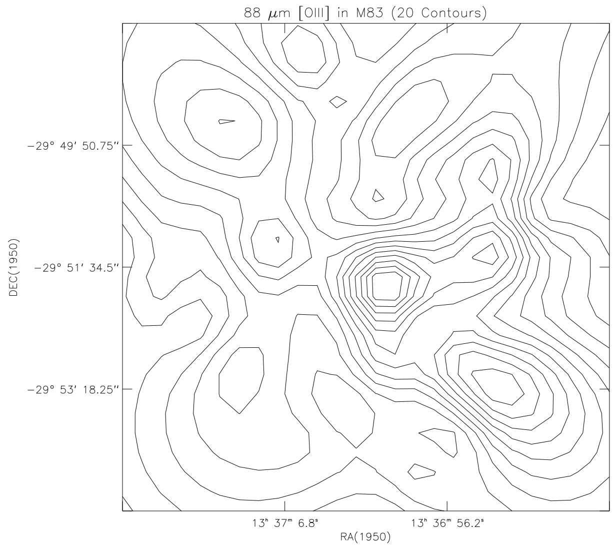

Figure 2. 88 μm [OIIII] map of M83. Contour intervals (1.5 σ) are 5% of the peak flux: 3.33 $\times 10^{-19}$ W cm^{-2} per 80′ beam.

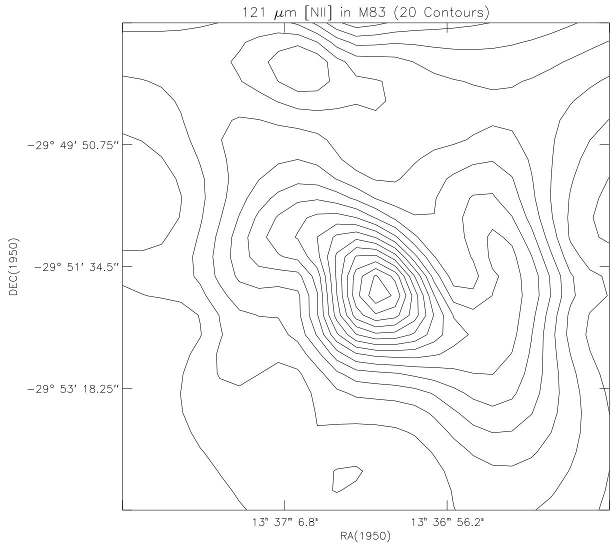

Figure 3. 122 μm [NII] map of M83. Contour intervals (2 σ) are 5% of the peak flux: 2.65 $\times 10^{-19}$ W cm^{-2} per 80′ beam.

less than that of hydrogen, C^+ is found both in ionized and neutral hydrogen gas regions. Furthermore, the [CII] emitting level has low excitation requirements so that the [CII] line is an important coolant for three major gas reservoirs (1) warm, dense, photodissociation regions (PDRs) on the surfaces of UV exposed molecular clouds (2) atomic clouds (T $\sim$ 100 K, n $\sim$ 30 cm^{-3}), and (3) extended, low density (ELD) HII regions (also know as the warm ionized medium, WIM). In galactic nuclei, it is clear that most of the observed [CII] emission arises from PDRs (Stacey et al. 1991). Integrated over the disks of normal spiral galaxies, however, [CII] likely arises from each component in roughly equal proportions (Madden et al. 1993, Geis et al. 1998). However,

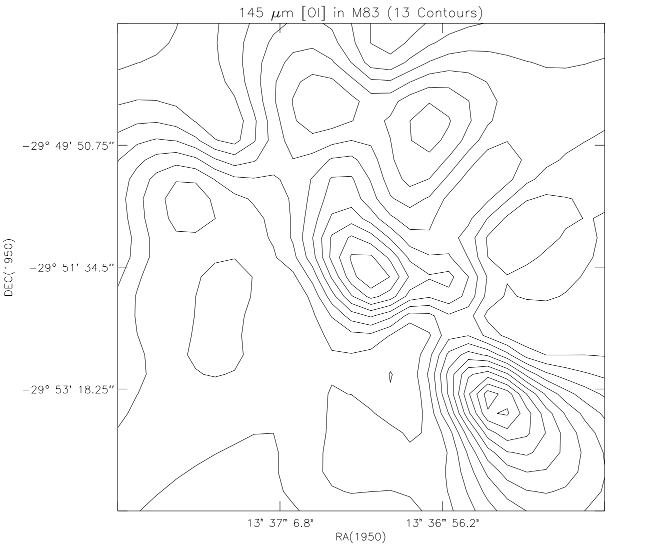

Figure 4. 146 μm [OI] map of M83. Contour intervals (1 σ) are 7.7% of the peak flux: 8.5 $\times 10^{-20}$ W cm^{-2} per 80′ beam.

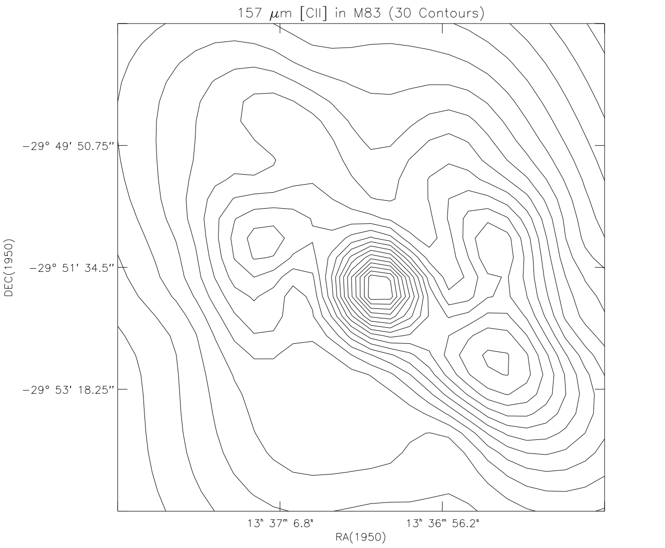

Figure 5. 158 μm [CII] map of M83. Contour intervals (3 σ) are 3.3% of the peak flux: 1.72 $\times 10^{-18}$ W cm^{-2} per 80′ beam.

it is possible to model the [CII] emission as arising from any of the three ISM components by modestly changing assumed cloud parameters, especially cloud density.

This situation can be ameliorated somewhat by comparing [NII] and [CII] emission. Since N^+ is only found in HII regions, and the critical density for the 122 μm line is similar to that of the 158 μm [CII] line in ionized gas regions, the [CII]/[NII] line ratio can be used to delineate the fraction of the observed [CII] emission that arises from the ELD/WIM subject only to an assumed N/C abundance ratio. We have made this calculation for the various regions of M83, and find that roughly 37% (nucleus), 30% (spiral arms), and 27% (interarm regions) of the observed [CII] emission arises from ELD/WIM HII regions in M83. Furthermore, the strength of the [OI] lines relative to [CII] indicates that little [CII] arises from 'atomic clouds'. Most of the remaining [CII] emission (that not arising from ELD/WIM) arises from the classic dense PDRs on molecular cloud surfaces.

2.3. The nucleus

The strongest line (and continuum) emission arises from the nuclear starburst region. The nucleus is especially prominent in the [OI] 63 μm, and [NII] 122 μm line emission for which the nuclear emission is twice as bright as any other region of the galaxy. The total line flux (dominated by the [CII] and [OI] 63 μm lines) is 1.8 $\times 10^7 L_\odot$ or $\sim 0.5\% L_{far-IR}$.

The complete LWS L01 spectrum reveals weak [OIII] 51.8 and [NIII] 57.4 μm line emission. The ratio of the [OIII] lines is insensitive to gas temperature, but gas density sensitive in the regime 100 $\leq n_e \leq 10^4$ cm^{-3}. For the nucleus, the line ratio, I[OIII] 52 μm/I[OIII] 88 μm $\sim$ 1.05, so that $n_e \sim$ 250 cm $^{-3}$ - comparable to diffuse HII regions in M82 (Lord et al. 1996), but much larger than those in the Galaxy (ne $\sim$ 3 cm^{-3}, Pettuchowski & Bennett 1993). The ratio of the [NIII] to [NII] lines is sensitive to the hardness of the ambient stellar UV radiation field. For the nucleus, I[NIII]/I[NII] $\sim$ 0.9. This is much smaller than that for M82 ($\sim$ 2.1, Colbert et al. 1998) which means that the main sequence is headed by later type stars (Teff $\sim$ 35,000 K, O9, (Rubin 1985) in M83 than for M82 (Teff $\sim$ 37,000, O8). Assuming the same initial mass function (IMF), the starburst must be older in M83. If a single starburst occurred, it occurred about 10^7 years ago. Since the lines have similar excitation requirements, I[NIII]/I[OIII] is largely an N/O abundance indicator. For M83, I[NIII]/I[OIII]52 μm $\sim$ 0.67 which means that N/O $\sim$ 2.4 solar (Rubin 1985) - similar to the abundance ratios in the inner Galaxy (Lester et al. 1987). Enhanced N/O indicates more processing of the ISM.

The ratio of the two [OI] lines is sensitive to gas pressure. By factoring in the [CII] line emission that likely arises from PDRs we can decouple temperature and density. The observed line ratios are I[OI]63μm/I[OI]146μm $\sim$ 17, and I[CII]/I[OI]63μm$\sim$ 0.9. Using the PDR models of Wolfire, Tielens, and Hollenbach (WTH 1991) we find that the emitting clouds must be dense ($n_H \sim$ 3000 cm^{-3}), and exposed to high UV radiation fields, $G_o \sim$ 5000 times the local interstellar radiation field. Surprisingly, the derived UV field is larger than that derived for M82: $G_o \sim$ 1000 (Lord et al. 1996).

2.4. Spiral arms/interarm regions

The eastern and western spiral arms are discernible in all lines, but especially prominent in the (higher signal to noise ratio) [CII], [OI] 63 μm, and [NII] maps. The arm/interarm contrast is highest for the [OIII] 88 μm line suggesting that the earliest type stars reside in the spiral arms, consistent with their formation there. Somewhat unexpectedly, the [CII]/[NII]/[OI] line intensity ratios are roughly the same for the spiral arms and the interarm regions: there is no evidence for enhancement of PDR line emission on the spiral arms. This is surprising since one would expect relatively enhanced [OI] line emission on the spiral arms from the UV exposed molecular clouds in the arm star formation regions. Similarly, it is also surprising that the [CII] and [NII] line intensity ratio is the same on the spiral arms as it is in the interarm region. One might expect enhanced [CII] relative to [NII] due to spiral arm PDR emission. The star forming spiral arms are not distinguishable from the interarm regions by their line ratios. At the spatial resolution of ISO, the components of the ISM that give rise to the [OI], [NII], and [CII] lines must be well mixed. The [OI] line intensity ratio, I[OI] 63/I[OI] 146 μm is about 20 - consistent with rather high UV radiation fields ($G_o \sim 3000$, WTH). Subtracting off the ELD/WIM [CII] emission (30%), the [CII]/[OI] 63 μm ratio is 1.3 so that PDR models indicate rather dense clouds as well ($n_H \sim 3000\,\mathrm{cm}^{-3}$).

2.5. Bar/spiral arm interface

The bright NE-SW optical bar is apparent in the fine structure line maps. Particularly intriguing is that the [OI], [CII], and [OIII] lines are all strongly enhanced at the bar-spiral arm intersections (at $\sim$ 2' NE and SW of the nucleus), suggesting enhanced star formation activity in these regions. The [OI] 146 μm, [OIII], and [CII] lines are particularly strong at the SW bar-spiral arm interface (SW peaks in Figures 2, 4 and 5), where the lines are about as strong as they are at the nucleus! The far-IR continuum is $\sim$ 3 times weaker there so the line to continuum ratio is enhanced in this region: $\sim 0.7\%$. The I[OI] 63 μm/I[OI] 146 μm ratio is very small ($\sim 8 \pm 1.5$). Normally this suggests very strong UB radiation fields ($G_o \sim 10^5$), and very high gas densities ($n_H \sim 10^4$ cm^{-3}, WTH). However, the I[CII]/[OI] 63 ratio is unusually large (~ 1.3, subtracting off the [CII] emission from ELD/WIM), and if the UV fields and gas densities are as large as indicated, the line to continuum ratio should be small, $\leq 0.1\%$ - a factor of seven smaller than the observed ratio. The combined data are therefore inconsistent with any single component PDR model (WTH).

Optical depth effects in the 63 μm [OI] line may cause these unusual ratios. The 63 μm [OI] line has long been known to have appreciable optical depth (cf. Stacey et al. 1983, Stacey et al. 1993, Poglitsch et al. 1996), and ISO has shown that the [OI] line is often self absorbed towards massive, embedded star formation regions in the Galaxy (cf. Baluteau et al. 1998). The bright [OIII] emission at the SW bar-spiral arm intersection indicates a young massive star formation site there, so it is reasonable to expect the star clusters will still be embedded in their nascent molecular clouds. The [OI] 63 μm emission from these embedded star formation sites is then easily absorbed by neutral oxygen in the cooler blanketing clouds. The [CII] line is not affected by this mechanism since ionized carbon will not be found in these dark clouds, and the [OI] 145 μm line is not affected since it is a transition between excited states. If we assume that the self absorption has reduced the [OI] 63 μm line flux by a factor of 2.5 then a self consistent model can be made with ($G_o \sim 10^{3.3}$) and gas densities ($n_H \sim 10^4$ cm^{-3}, WTH). The SW bar region is strong in other indicators of star formation particularly in its Hα (de Vaucouleurs et al. 1983), and CO rotational line emission (e.g. Kenney & Lord 1991). Kenney & Lord (1991) have suggested that orbit crowding at the bar-spiral arm transition may have triggered a massive burst of star formation there. The bright far-IR fine structure line we observe there is consistent with this scenario.

REFERENCES

Baluteau, J.-P, et al. 1998, A&A 322, L33

Colbert, J.W., Malkan, M.A., Fischer, J., Lord, S., Luhman, M., Satyapal, S., Smith, H.A., Spinoglio, L., & Stacey, G.J. 1998, to appear in ApJ

Geis, N. et al. 1998 in prep.

Kenney, J.D.P., & Lord, S.D. 1991, ApJ 381, 118

Lester, D.F., Dinerstein, H.L., Werner, M.W., Watson, D.M., Genzel, R., & Storey, J.W.V. 1987, ApJ 320, 573

Lord, S.D., Hollenbach, D.J, Haas, M.R., Rubin, R.H, Colgan, S.W.J., & Erickson, E.F. 1996, ApJ 465, 703

Luhman, M.L., Satyapal, S., Fischer, J., Wolfire, M.A., Cox, P., Lord, S.D., Smith, H.A., Stacey, G.J., & Unger, S.J. 1998, ApJ 504, L11.

Madden, S.C., Geis, N., Genzel, R., Herrmann, F., Jackson, J.M., Poglitsch, A., Stacey, G.J., & Townes, C.H. 1993, ApJ 407, 579

Malhotra, S., Helou, G., Stacey, G.J., Hollenbach, D. Lord, S., Beichman, C.A., Dinerstein, H., Hunter, D.A., Lo, K.Y., Lu, N.Y., Rubin, R.H., Silbermann, N., Thronson, H.A. Jr., & Werner, M.W. 1997, ApJ 491, L27

Petuchowski, S.J. & Bennett, C.L. 1993, ApJ 405, 591

Poglitsch, A., Herrmann, F., Genzel, R., Madden, S.C., Nikola, T., Timmermann, R., Geis, N., & Stacey, G.J. 1996, ApJ 462, L43.

Rubin, R.H. 1985, ApJ S 57, 349

Stacey, G.J., Smyers, S.D., Kurtz, N.T., & Harwit, M. 1983, ApJ 268, L99

Stacey, G.J. Genzel, R., Lugten, J.B., Poglitsch, A., Sternberg, A., & Townes, C.H. 1991, ApJ 373, 423

Stacey, G.J, Jaffe, D.T., Geis, N., Genzel, R., Harris, A.I., Poglitsch, A.,Stutzki, J., & Townes, C.H. 1993, ApJ 404, 219

de Vaucouleurs, G., Pence, W.D., & Davoust, E. 1983, ApJ S, 53, 17

Wolfire, M.G., Tielens, A.G.G.M., & Hollenbach, D. 1990, ApJ 358, 116

ISO SPECTROSCOPY OF NGC 4151

E. Sturm[1], **T. Alexander**[1,2,3], **D. Lutz**[1], **A. Sternberg**[2], **H. Netzer**[2], **& R. Genzel**[1]

[1]Max-Planck-Institut für Extraterrestrische Physik, Garching, Germany
[2]Tel Aviv University, Tel Aviv, Israel
[3]Institute for Advanced Study, Princeton, USA

ABSTRACT

We discuss ISO-SWS and ISOPHOT-S spectra of the Seyfert Galaxy NGC 4151. The spectral features in the mid-infrared are ideal tracers of the physical conditions in the narrow line emitting region (NLR), and of the spectral energy distribution (SED) of the central ionizing source. The analysis of mid-IR line profiles and the modelling of mid-IR line strengths with photoionization models are therefore powerful new tools for the study of active galactic nuclei (AGNs).

We find that the mid-IR fine-structure line profiles in NGC 4151 display blue asymmetries which are very similar to those observed in the optical lines produced in the narrow line region. Because the mid-infrared lines are much less sensitive to extinction than are the optical lines this similarity places strong constraints on scenarios which have been invoked to explain the optical line asymmetries. For example, we are able to rule out the simplest radial-motion-plus-dust scenarios for the production of the line asymmetries. Our preferred model is that of a central, geometrically thin but optically thick, obscuring screen.

The mid-IR line fluxes, together with a compilation of UV to near-IR narrow emission line data are used to reconstruct the spectral shape of the obscured extreme-UV continuum of the central ionizing source. We find a best-fit model - consisting of a clumpy, optically thick (ionization bounded) gas distribution - that reproduces the observed line fluxes, and which is consistent with the observed geometry of the optical NLR. The best fitting SED does not display a 'Big Blue Bump', which would be the expected signature of an accreting black hole. This is in contrast to our detection of such a bump in the SED of the Circinus Galaxy. Our analysis suggests that in NGC 4151 such a component may be absorbed by material located between the NLR and the central ionizing source.

Key words: active galaxies.

1. INTRODUCTION

NGC 4151 is one of the brightest, closest, and best studied Seyfert galaxies (see e.g. Boksenberg et al 1995, or Knop et al. 1996 and references therein). Nevertheless, the nature and physical conditions of its active nucleus are not yet well understood. Mid-infrared spectroscopy, obtained with ISO, is an important new diagnostic tool to investigate the active nuclei in Seyfert/active galaxies. This wavelength regime offers a large number of diagnostically important lines and features, which are relatively insensitive to extinction. Here we will concentrate on two major topics: the kinematics and structure in the narrow line region, and the spectral energy distribution of the central ionizing source. More details of the methods we used and of the results (e.g. electron temperatures and densities, and a discussion of possible contributions from circumnuclear starburst regions) can be found in Sturm et al. (1999) and Alexander et al. (1999).

Many studies of Seyfert galaxies have attempted to investigate the structure and kinematics of the narrow-line gas by an analysis of the emission-line profiles of these objects (e.g., Heckman et al. 1981, Pelat and Alloin 1982, Veilleux 1991 a,b,c). These studies have shown that in many cases the emission-lines exhibit blueward asymmetry and are blueshifted with respect to the galaxies' systemic velocity. One of the most widely adopted models to explain the observed asymmetry in the optical profiles has been an outflow of line-emitting clouds, which are embedded in pervasive obscuring dust (see Figure 1). Alternatively, dusty infalling clouds embedded in a relatively transparent environment could also produce the observed asymmetries and velocity shifts. In any case, if the asymmetry of the optical forbidden lines were produced by radial motion plus dust, one would expect that *infrared* lines do not or only marginally show such asymmetries, because they are much less affected by extinction. Here we present the first study of mid-IR line profiles of a Seyfert galaxy (NGC 4151).

The ionizing SED of the central source is of particular interest in the ultraviolet, where many models predict the so-called 'Big Blue Bump', i.e. thermal radiation from an accreting disk around a central black

Proceedings of the Conference "The Universe as seen by ISO", Paris, France, 20–23 October 1998 (ESA SP-427, March 1999)

hole. Unfortunately, the ultraviolet SED - and thus the blue bump - of AGN continua cannot be directly observed due to galactic and intrinsic absorption (see Figure 4). However, many emission lines in the ISO range have ionization energies which cover exactly this gap in the observable SED (Figure 5). Hence, by fitting a photoionization model to the observed lines, it is possible to constrain the SED. We present a new method to determine the best fitting photoionizing continuum and emission line cloud model.

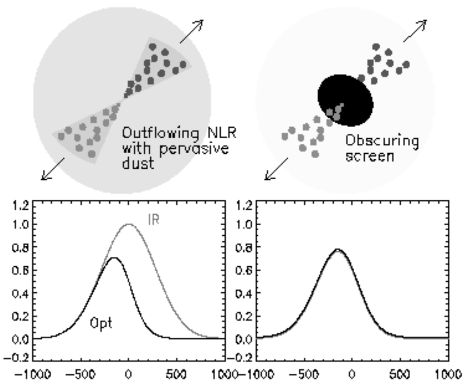

Figure 1. Sketch of a biconical NLR with outflowing clouds. Top left: The clouds are embedded in a dusty environment. The redshifted clouds are further away from the observer, hence, are more affected by extinction, causing a blueshifted line profile with a blue excess (bottom left). In an alternative model (top right) an obscuring screen, optically thick also in the mid-IR, obscures part of the redshifted, high velocity clouds very close to the nucleus. In this case both optical and mid-IR lines show the same asymmetry (bottom right).

2. NLR STRUCTURE AND LINE PROFILES

Recent HST imaging and spectral imaging observations unveiled the biconical structure of the NLR in NGC 4151 and were able to assign radial velocities to the individual cloud components in these cones. The NLR clouds are most probably outflowing (see, e.g., Hutchings et al. 1998). This geometry of systems of outflowing clouds in a biconical structure is used in Figure 1 to illustrate one of the radial-motion-plus-dust scenarios which could explain the blue asymmetries in the line profiles. As noted above, in these scenarios the line profiles of mid-infrared lines should be much more symmetric, since extinction in the mid-IR is about a factor of 50 smaller than in the optical. However, an inspection of the mid-infrared line profiles measured by ISO shows, that these lines show the same blue excess and blue shift than the optical lines (see Figure 2, 3, and Sturm et al. 1999). Hence, the shifts and asymmetries cannot be explained by simple radial-motion-plus-dust pictures.

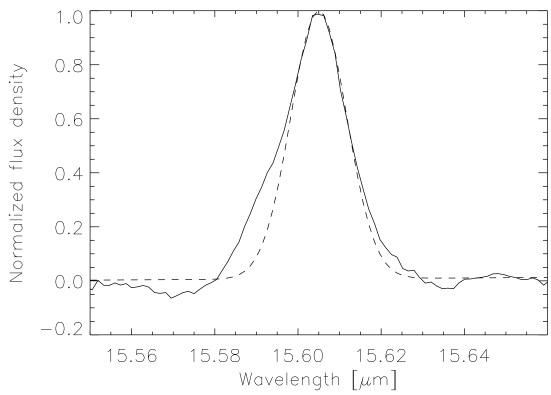

Figure 2. The [Ne III] 15.5 μm line (solid). Overplotted (dashed) a gauss fit to the core of the profile, illustrating the asymmetry and blue excess.

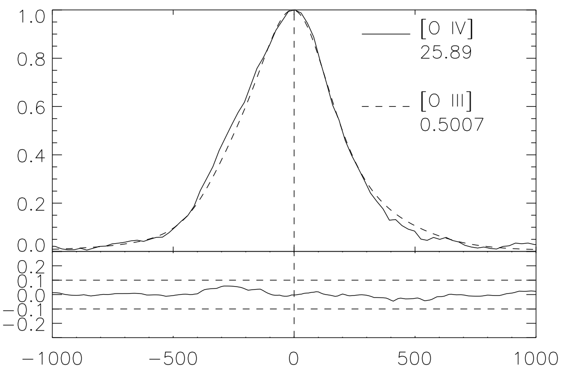

Figure 3. Comparison of the ISO SWS line profile of [O IV] (solid lines) with the optical counterpart [O III] convolved with the SWS instrumental profile (dashed). The optical line is taken from Veilleux (1991a). The lower part of the panel shows the difference (ISO - optical) of the two profiles. +10 per cent and -10 per cent margins in the residual plots are shown as horizontal dashed lines. Units are: velocity (kms^{-1}) with respect to the peak (x-axis), and normalized flux densities (y-axis).

The apparent anisotropic distribution of the line emitting clouds could be real, i.e. there could be more bright, blue shifted clouds close to the nucleus than red shifted ones. While this explanation is perfectly plausible for a single source it is hard to believe, that it would also be tenable for a larger sample, because of the preferential blueshift and blueward asymmetry found in these samples.

Alternatively, there could be an occulting component near the center of the NLR which is opaque at both optical and mid-IR wavelengths, and which fully blocks some of the more distant NLR emission from view (see Figure 1). This possibility is consistent only with outflowing gas. Hutchings et al. (1998) found strong evidence for such an outflow. They also found that the clouds with the highest radial velocities are the ones closest to the nucleus. The line profile shown in Figure 2 suggests, that it are indeed these high velocity clouds, whose red counterparts are missing. The line profiles can hence be explained by a central, geometrically thin, but optically thick obscuring screen of sub-arcseconds (tens-of-parsec) extension - see Sturm et al. (1999) for more details.

3. PROBING THE OBSCURED AGN CONTINUUM

The December 1993 multi-wavelength campaign to monitor the variability in the continuum emission of NGC 4151 (see e.g. Edelson et al. 1996, and references therein) yielded a simultaneous SED extending from the optical to γ-rays. The combined data are shown in Figure 4 (together with additional data from the literature, see Alexander et al. 1999 for details). This figure also illustrates the expected 'Big Blue Bump' in the gap, where the SED cannot be observed directly. In Figure 5 we have indicated some of the ISO (and optical) lines that arise in this gap. This makes it possible to reconstruct the ionizing SED in the EUV, by fitting a photoionization model to the observed line fluxes. For calculating the models the gas (or 'cloud') properties, i.e. geometrical models of the NLR, have to be specified as well. Our new method to determine the best fitting photoionizing continuum and emission line cloud model is described in detail in Alexander et al. 1999. It parametrizes the gap by a grid of different luminosities at several energies (see Figure 7). Different cloud geometries are taken into account. For NGC 4151 we find a best fit model consisting of a clumpy, optically thick gas distribution, that reproduces the observed line fluxes, and which is consistent with the observed geometry of the optical NLR.

The best fitting SED (see Figure 6) does not display a Big Blue Bump, in contrast to our detection of such a bump in the SED of the Circinus Galaxy (see Figure 7 and Moorwood et al. 1996 - also these proceedings). Our analysis suggests, that in NGC 4151 such a component may be absorbed by material located between the NLR and the central ionizing source. Such an absorber was already predicted by independent observations of UV absorption lines (Kriss et al. 1995).

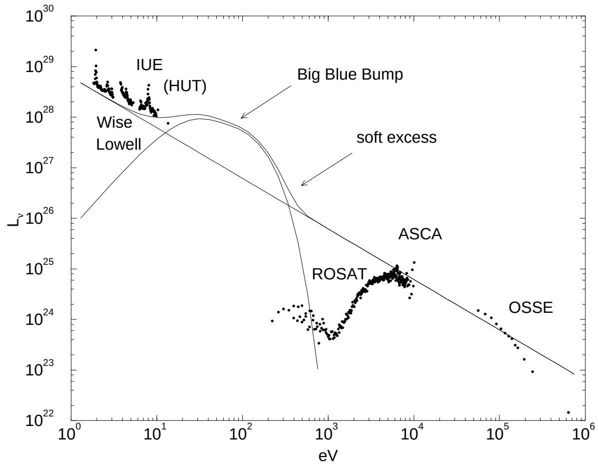

Figure 4. A nearly simultaneous SED of NGC 4151 from the optical to γ-rays (points) (from Edelson et al 1996; HUT result from Kriss et al. 1995). A sketch of a bump superimposed on a power-law is presented for illustration purposes (line).

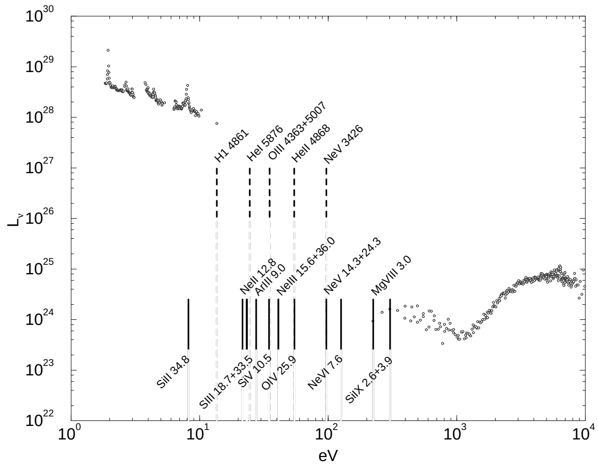

Figure 5. The strong observed IR emission lines (full lines) and some of the optical emission lines (dashed lines) plotted on the energy axis according to the ionization energy required to produce the emitting ion from the preceding ionization stage. Also shown (again) is the observed SED of NGC 4151 (points).

REFERENCES

Alexander, T., Sturm, E., Lutz, D., Sternberg, A., Netzer, H., Genzel, R., 1999, ApJ, 512, in press

Boksenberg A., et al. 1995, ApJ, 440, 151

Edelson, R., et al. 1996, ApJ, 470, 364

Heckman, T.M., Miley, G.K., van Breugel, J.M. and Butcher, H. 1981, ApJ, 247, 403

Hutchings, J.B., Crenshaw, D.M., Kaiser, M.E., et al. 1998, ApJ, 492, L115

Knop, R.A., Armus, L., Larkin, J.E. et al. 1996, AJ, 112, 81

Kriss, G.A., Davidsen, A.F., Zheng, W., Kruk, J.W., Espey, B.R., 1995, ApJ, 454, L7

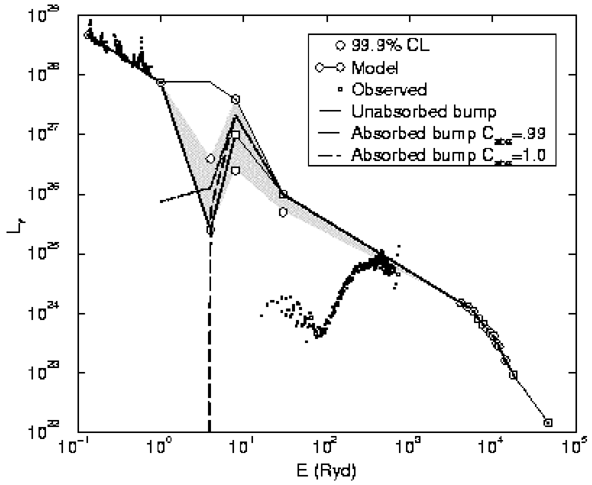

Figure 6. *The best-fit SED for NGC 4151 (fat solid line). The shaded area is the 99.9% confidence limit on the SED. Superimposed is an example of a quasi-thermal bump absorbed by 5×10^{19} cm^{-2} of neutral hydrogen. Shown are: the unabsorbed bump (thin solid line), and the absorbed bump with a covering factor of the absorbing material of 0.99 (dotted) and 1 (dashed).*

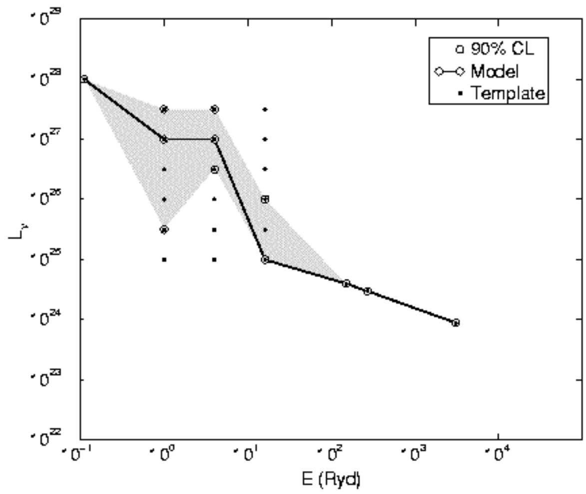

Figure 7. *The best-fit SED for the Seyfert 2 galaxy Circinus (see Moorwood et al. 1996, and Alexander et al. 1999). The dots illustrate the parametrization of the gap in the observable SED.*

Moorwood A. F. M., et al. 1996, A&A, 315, L109

Pelat, D., Alloin, D. 1982, A&A, 105, 335

Sturm, E., Alexander, T., Lutz, D., Sternberg, A., Netzer, H., Genzel, R., 1999, ApJ, 512, in press

Veilleux S., 1991a, ApJS, 75, 357

Veilleux S., 1991b, ApJS, 75, 383

Veilleux S., 1991c, ApJS, 369, 331

INFRARED EMISSION FROM RADIO-LOUD ACTIVE NUCLEI

I. M. van Bemmel[1], **P. D. Barthel**[2], **& Th. de Graauw**[3]

[1]European Southern Observatory, Garching bei München, Germany
[2]Kapteyn Astronomical Institute, Groningen, The Netherlands
[3]Dutch Space Research Organisation, Groningen, The Netherlands

ABSTRACT

In order to test the unification scheme for double-lobed radio sources, the far-infrared properties of a matched sample of radio-galaxies and radio-loud quasars were studied using ISOPHOT. The quasar data were complemented with nearly simultaneous submillimeter and centimeter radio data. The results show that quasars are generally brighter than radio-galaxies in their far-infrared output and that beamed non-thermal radiation must be excluded as source for this infrared excess. However, non-thermal flares or optically thick tori can still reconcile these results with the unification scheme.

Key words: active galactic nuclei; unification; spectral energy distributions

1. INTRODUCTION

The unified theory for radio-loud active galaxies (Barthel, 1989; Urry & Padovani 1995) predicts the existence of a dusty torus surrounding the central engine. Models for the reprocessing of the hard non-thermal nuclear radiation by this torus show that at wavelengths longward of 60 μm the torus will be optically thin (Pier & Krolik 1992; Granato & Danese 1994). However, in the IRAS observations quasars are two to four times brighter at 60 μm than radio galaxies (Heckman et al. 1994). In some special geometries of the torus, models can account for this infrared excess. Also the torus could still be optically thick at 60 μm, or there could be a significant amount of angle dependent non-thermal contamination in quasars. Non-thermal beamed radiation has been proposed as a possible solution (Hes et al. 1995).

In order to discover the true cause of the infrared excess in quasars, observations are needed at longer wavelengths. All current torus models predict that beyond 80 μm the thermal emission will be isotropic. According to unified schemes, the output of quasars should then equal that of matched radio-galaxies at these long far-infrared wavelengths. ISOPHOT observations of quasars and radio-galaxies have been obtained to test this hypothesis. To quantify any possible non-thermal contamination in quasars, the latter were in addition observed with SCUBA at the JCMT, and the NRAO Very Large Array (VLA).

2. SAMPLE SELECTION AND OBSERVATIONS

The target sample is selected using several criteria. First of all the objects must have the double-lobed radio structure typical for Fanaroff & Riley class II sources (Fanaroff & Riley 1974). Six matched pairs were constructed, containing one quasar and radio-galaxy each, having the same redshift, radio-lobe power and angular size. Lobe radio power is a reasonably good measure of the active nucleus power, and is furthermore independent of the orientation of the objects.

Observations were carried out with ISOPHOT at three wavelengths, during the period October 1996 to April 1998. We made raster-mode mini-maps with C100 and C200 (AOTs P3 and P22). The rasters have a size of 3×3 (C100) and 4×2 (C200) in Y$\times$Z direction. The filters used were the 60 μm, 90 μm (C100) and 160 μm (C200). Observations of only four pairs were completed during the lifetime of ISO; for the other two pairs only the radio-galaxy was observed. For the quasars these data were complemented with nearly simultaneous VLA[1] A-array data at 6, 2, 1.2 and 0.7 cm (April 17, 1998) and JCMT[2] SCUBA data at 450 μm and 850 μm (May 28, 1997), addressing their non-thermal radio core strengths. These observations were made in order to detect possible non-thermal contamination of the far-infrared emission. Since the effect of non-thermal emission in radio-galaxies is negligible (Hoekstra et al. 1997), these objects were not observed with the VLA and SCUBA.

[1]The National Radio Astronomy Observatory is a facility of the National Science Foundation operated under cooperative agreement by Associated Universities, Inc.

[2]The James Clerk Maxwell Telescope is operated by The Joint Astronomy Centre on behalf of the Particle Physics and Astronomy Research Council of the United Kingdom, the Netherlands Organisation for Scientific Research, and the National Research Council of Canada.

3. DATA REDUCTION

3.1. ISO data reduction

All ISO data have been processed with OLP version 6.11 and raw data have been reduced using the Phot Interactive Analysis tool (PIA[3]) version 7.2(e). The steps from ERD to AAP level were all done using the default procedures. Deglitching at ERD level was done with the two-threshold method, setting sigmas of 3.0 (flagging) and 0.5 (reacceptance). At SRD level reset interval correction was applied, as well as dark current subtraction per raster point. Afterwards the data were deglitched again with a sigma of 2.5 (source measurements) or 0.5 (FCS measurements). At SCP level no significant corrections were applied. The signal of the FCS was in most cases outside the hard extrapolation limits of PIA, therefore it was decided to use only default responsivities for all sources at all wavelengths.

3.2. ISO flux determination

The final flux was determined using an IDL program called ana_mini_map, developed by the PHOT support center in Heidelberg. This program uses each pixel of the detector as a scan across the source. Thus no map is made, instead it determines the background flux from the two off-source raster positions immediately before and after the on-source raster position. This off-source flux is compared to the on-source flux. If a signal is present, all pixels will show a positive difference between on- and off-source positions. However, due to the faint flux levels, noise caused a lot of false results for some pixels. To avoid using noisy data, an IDL tool was developed to determine the noise on the pixels used by ana_mini_map. Pixels with extremely high noise on either one of the off-source positions or the on-source position were excluded from the flux determination. This produced a reliable flux for all the detections (errors are generally less than 10 per cent).

Tests were conducted by comparing the results to DIRBE background measurements and IRAS detections of our sources. Both DIRBE and IRAS reproduced our results within a 10 per cent error limit. However, due to the large calibration errors for faint sources, the fluxes presented here are to be taken with errors of about 30 per cent (Lemke et al. 1996). In order to present the results as clearly as possible, only the statistical errors are given by the error bars in the plots, thus providing better insight into the real meaning of the detection.

3.3. VLA and SCUBA data reduction

The VLA data were reduced using the AIPS version of 15 April 1998. Calibration was done using the standard flux calibrators and nearby phase calibrators. After calibration the maps were cleaned using CLEAN and the core flux density values were determined using the MAXFIT procedure. 3C 351 caused some problems at 6 cm and 2 cm, because of the strong hotspots in this source. The exact flux of the core in these bands has not yet been determined. The 6 cm core flux of Bridle et al. 1994 was plotted instead, since no strong variations have been reported of this source at cm wavelengths. For all sources the errors are smaller than the symbols in the plots.

The SCUBA data were reduced using the SCUBA Data Reduction Facility (SURF) and Kernel Application Package (KAPPA). Not all sources were observed at all bands. Only sources with an observation have a SCUBA upperlimit, and only 3C 334 has been marginally detected ($\sim 2\sigma$), be it in both bands.

[3]PIA is a joint development by the ESA Astrophysics Division and the ISOPHOT consortium.

4. RESULTS

The resulting broad band spectra are plotted for each pair in Figure 1. It is immediately clear that in most cases the quasar is still brighter than the radio-galaxy, even up to the longest ISOPHOT wavelengths, with only one exception. The quasars are detected at all ISOPHOT bands, whereas in only one out of four observations the radio-galaxy was detected. From the additional VLA and SCUBA data it is evident that the quasar cores do not contribute significantly to the far-infrared emission observed with ISO, since the sub-mm points and VLA Q-band data would have to be much higher in that case.

From the simple black-body fits to the ISO data it is also clear that two of the four radio-galaxies need a lower temperature than the quasars. This could imply that in radio-galaxies we observe a cooler dust component, which is in agreement with the unification theory, assuming a dust distribution with a temperature gradient. In one case the black-body temperature could not be determined, because there is no detection of the radio-galaxy at any wavelength (3C 19). In the final case the far-infrared spectra of the quasar and radio-galaxy are identical, which is surprisingly enough the pair with compact sources.

5. DISCUSSION

5.1. Non-thermal contamination

Radio-quiet and radio-loud quasars show remarkable similarities in their broad band spectra. The similar infrared to submillimeter slope and far-infrared turnover frequency point to an identical source of infrared emission. Since radio-quiet quasars have no significant non-thermal component, the infrared emission must be thermal (Sanders et al. 1989). Assuming the models for thermal torus emission show the correct trends, an aspect angle dependent non-thermal contamination must be present in radio-loud quasars to reconcile the observed infrared excess in these objects with the unification theory. There are two possibilities: continuous beaming, or flaring, which requires a rapidly varying beamed component.

Continuous beaming is in most cases not more than a 30 per cent effect (Hoekstra et al. 1997) and has been

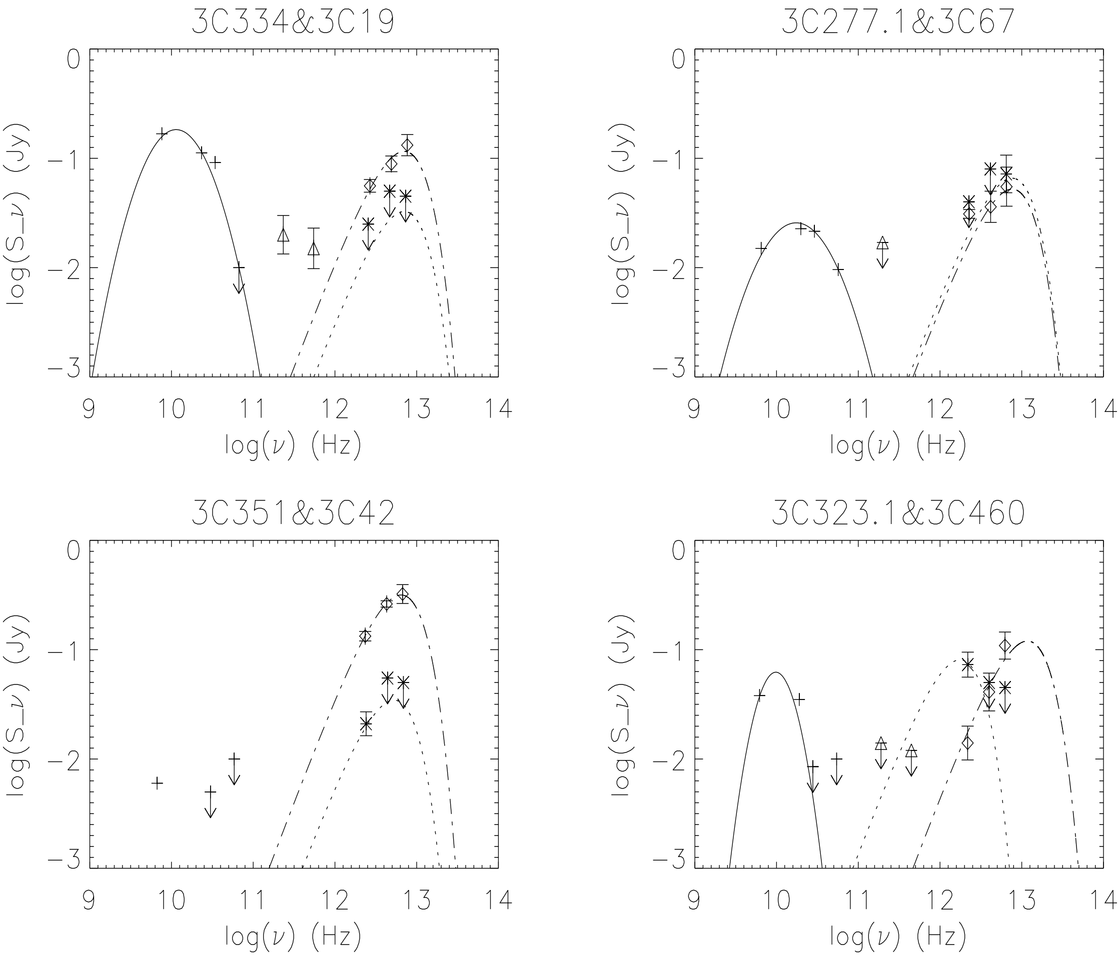

Figure 1. The complete spectra for the four pairs observed with ISO. For the quasars: plusses are VLA data, triangles are SCUBA data, red diamonds are ISO data. The solid line is an empirical fit to the radio-core spectra, the dash-dotted line is a black body fit to the ISO data. For the radio-galaxies: asterisks are ISO data and the dotted line is a black-body fit.

solidly ruled out for causing the excess in at least two quasars (van Bemmel et al. 1998). Here, only one quasar is detected at 7 mm and the detections with SCUBA are marginal at best. In our results continuous non-thermal contamination of the far-infrared is negligible, as can also be seen from the fits to the radio data in Figure 1. It is important to use only core flux densities, as this is the only source of beamed non-thermal radiation in active galaxies. When using the total radio flux densities as done by Haas et al. (1998), the centimeter flux densities will be dominated by emission from the radio lobes. These have generally steep spectra and are not beamed, thus they do not contribute significantly to the infrared emission in these sources.

A varying component can easily be missed. Strongly beamed radiation from non-thermal flares has been observed in blazars (Brown et al. 1989); such flares are both very strong and short-lived, with typical timescales of several days. They could be observed in quasars due to the small aspect angle of these objects. In previous work two out of three quasars showed high 3 mm fluxes, which could not be fitted with a radio core model and were suggestive of flaring (van Bemmel et al. 1998). In radio-galaxies beamed flare radiation is much less likely to be observed, because of the larger aspect angles in these sources. Strong flares can cause large differences in far-infrared output, whilst being missed in the non-thermal core spectra.

5.2. Optically thick torus

The persistence of the infrared-excess at longer wavelengths can also be explained if the torus is optically thick up to 140 μm at least. Arguing in favour of this concept is the fact that a lower temperature is needed for the black-body fit in at least two of the radio-galaxies. Here maybe only the cooler edge of the torus is seen, while in quasars the hot inner parts dominate the infra-red output. This is in contradiction with the present models for dusty tori, but in broad agreement with predictions from the unified models. Since changing the models for the torus also has implications for the X-ray spectra observed in these sources, new modelling has to be done to study this possibility in more detail.

5.3. Evolution between types

Evolution has been proposed as a solution to the infrared-excess (van Bemmel et al. 1998). This would then imply that quasars are younger and still contain more dust in their host galaxy, whereas radio-galaxies are older and have processed their dust and gas into stars. A link with the ultra-luminous galaxies has been made in this respect as these being very young quasars who are in the phase of birth (Sanders et al. 1988). However, during a recent conference on this topic, most evidence showed that these so-called ULIRGs are in many cases driven by strong starbursts and not by a central active nucleus (Monsters or Babies: What powers ultra-luminous infrared galaxies?, Ringberg Castle, 1998). The fact that we find one pair in which the far-infrared spectra are identical, also argues against evolution between the types. Any evolutionary model is obviously in conflict with orientation based unification concepts.

6. CONCLUSIONS

Observations of matched pairs of quasars and radio-galaxies show that the previously reported infrared-excess is still present in quasars, up to 140 μm rest-frame wavelength. This cannot be accounted for by current torus models, without causing a contradiction with unified schemes. Continuous beaming has to be excluded in our objects, but non-thermal flares can explain the excess, without necessary adjustments to either theory. Also the models for the torus have to be examined in more detail to explain observed temperature differences between quasars and radio-galaxies. This is currently under investigation and will be described in future publications.

Future work will also include the search for flares in 3C 334 with SCUBA and the investigation of orientation dependence of optical emission lines in a sample of double-lobed active galactic nuclei.

ACKNOWLEDGEMENTS

Our thanks to all people who helped us during the hard reduction process, especially Martin Haas who provided a lot of useful tips and advice. Also thanks to Ronald Hes for initial involvement. And thanks to Eric Hooper, Mari Poletta, Belinda Wilkes, Thierry Courvoisier and Rolf Chini for advice and discussions. Thanks to Xander Tielens for useful comments and advice while making this manuscript.

REFERENCES

Barthel, P.D., 1989, ApJ, 336, 606

Bridle, A.H., Hough, D.H., Lonsdale, C.J., Burns, J.O., Laing, R.A., 1994, AJ, 108, 766

Brown, L.M.J., Robson, E.I., Gear, W.K., et al., 1989, ApJ, 340, 129

Fanaroff, B.L., Riley, J.M., 1974, MNRAS, 167, 31P

Granato, G.L., Danese, L., 1994, MNRAS, 268, 235

Haas, M., Chini, R., Meisenheimer, K., et al., 1998, ApJ, 503, L109

Heckman, T.M., O'Dea, C.P., Baum, S.A. Laurikainen, E., 1994, ApJ, 428, 65

Hes, R., Barthel, P.D., Hoekstra, H., 1995, A&A, 303, 8

Hoekstra, H., Barthel, P.D., Hes, R., 1997, A&A, 319, 757

Lemke, D., Klaas, U., Abolins, J., et al., 1996, A&A, 315, L64

Pier, E.A., Krolik, J.H., 1992, ApJ, 401, 99

Sanders, D.B., Phinney, E.S., Neugebauer, G., Soifer, B.T., Matthews,K., 1989, ApJ, 347, 29

Sanders, D.B., Soifer, B.T., Elias, J.H., et al., 1988, ApJ, 325, 74

Urry, C.M., Padovani, P., 1995, PASP, 107, 803

van Bemmel, I.M., Barthel, P.D., Yun, M.S., 1998, A&A, 334, 799

THE PHYSICAL STRUCTURE OF MAGELLANIC CLOUD H II REGIONS

R. Vermeij & J.M. van der Hulst
Kapteyn Institute, PO Box 800, NL-9700 AV Groningen, The Netherlands

ABSTRACT

This paper presents some of the first results of a project aimed at determining in detail the physical conditions of star-forming regions. The project uses spectroscopic data obtained of 17 H II regions in the SMC and LMC. The data set consists of ISO-SWS, ISO-LWS and optical spectroscopic data covering a spectral range from 0.35 μm to 198 μm. The combination of optical and infrared data makes it possible to derive the detailed physical structure of an H II region. Quantities derived from this structure, e.g. improved chemical abundances and excitation source, will provide a link to the star-forming properties of these regions.

Key words: Magellanic Clouds; interstellar medium; elemental abundances.

1. INTRODUCTION

Insight in the physical structure of H II regions is important for many astrophysical applications. Studies of H II regions can give information about the star formation rate in a galaxy. In addition, H II regions can be used to probe the structure of the local interstellar medium (ISM) which can teach us something about the environments in which stars are formed. Furthermore, the nebular abundances which can be derived provide constraints on the chemical evolution of a galaxy.

Thus far, most studies of H II regions have relied on optical spectroscopy only. The physical parameters needed to determine the elemental abundances (the electron temperature and density) are derived by using the optical lines originating from the lowest levels in the ground state of an ion. Usually, the electron temperature T_e is determined by using the [O III] λ5007,4959 and λ4363 optical lines, while the electron density n_e is found by using the [S II] λ6717,6730 doublet (Osterbrock 1989). The physical parameters thus derived are then combined with the line fluxes to obtain the *ionic* abundances and from that the *total* abundances.

The method of deriving the abundances as described above, however, is not without problems. There are several reasons why the abundances derived in this way are to be used with caution. First of all, the electron temperature and density are derived using lines from different ions which do not necessarily occupy the same part of the nebula. As is shown by photoionization models (e.g. Garnett 1992), doubly-ionized oxygen is mainly confined to the central parts of the nebula while S II is more concentrated towards the edge. If the temperature and density do not vary through the nebula the [O III] temperature and [S II] density can be used for the derivation of the abundances, but in more realistic cases, that is, with gradients present, this procedure will give erroneous abundances. Secondly, not all ionic species have lines in the optical. In order to derive the total elemental abundances one has to make corrections for the unseen ions. These Ionization Correction Factors (ICFs) are often based on coincidences in the ionization potentials for different ions (Peimbert & Torres-Peimbert 1977) but they are not always reliable (e.g. see Pagel 1978 for sulfur). Finally, temperature variations through the nebula tend to bias the temperature sensitive lines, like [O III] λ4363, towards the regions with higher T_e. This leads to an overestimate of the electron temperature and an underestimate of the abundances. Models by Stasińska (1980) show that this problem can occur in metal-rich nebulae. The way one usually counters this problem is by using the t^2-method as developed by Peimbert (1967), where t^2 is the fluctuation around a mean temperature T_0. The right value of t^2 to use in different cases, however, can not easily be determined.

Table 1. The infrared lines observed with SWS and LWS. Some of the complementary optical lines are also given. The wavelength unit is μm.

OI	63.0	Ne II	12.8	S II	0.67	Ar II	6.98
OII	0.37	Ne III	0.39	S III	0.63	Ar III	0.71
OIII	0.43	Ne III	15.6	S III	0.91	Ar III	0.77
OIII	0.50	Ne III	36.0	S III	18.7	Ar III	8.99
OIII	51.8	C II	158	S III	33.5	Brα	4.05
OIII	88.4	Fe II	26.0	S IV	10.5	Brβ	2.63
OIV	25.9	Si II	34.8	N II	122	Pfα	7.46

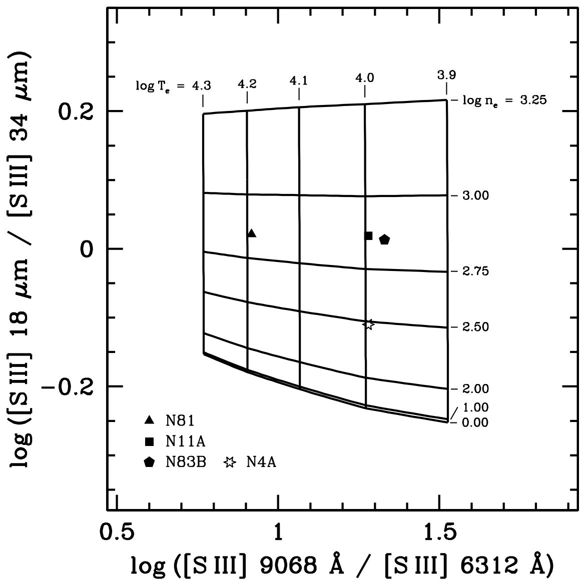

Figure 1. An example of a diagnostic diagram used to derive the temperature and density. Similar diagrams can be made for species like O III and Ne III. Shown are the first results for T_e([S III]) *and* n_e([S III]) *for four program objects.*

2. COMBINING OPTICAL WITH INFRARED SPECTROSCOPY

Many of the problems described in the introduction can be solved by combining optical with infrared spectroscopy. This is possible because many of the ions with forbidden lines in the optical have a triplet of low-lying fine-structure levels from which infrared lines originate. These lines are, due to the small energy difference between the fine-structure levels, very sensitive to changes in the electron density which makes them an excellent tracer of n_e. Combining the density-sensitive infrared lines with the temperature-sensitive optical lines makes it possible to determine unambiguously the physical conditions using lines from the same ion (Dinerstein 1983). One is thus sure to probe the same nebular material which solves the problem of the possible 'incompatibility' of the [O III] temperature and [S II] density. Given enough optical and infrared lines from various ions one can trace the temperature and density structure throughout the nebula. An example of how the physical conditions can be derived from these lines is shown in Figure 1 for [S III]. Given the physical structure, improved ionic abundances can then be derived.

The problem of deriving the total abundances from ionic abundances can be alleviated with IR spectroscopy because many ionic species without lines in the optical do have lines in the infrared. Examples of these are the [S IV] 10.5 μm and [Ar II] 6.98 μm lines which can serve to constrain the necessary ionization correction factors. The combination of optical and infrared spectroscopy makes it also possible to address the problem of temperature fluctuations. If one can find, for one and the same ion, two temperature-sensitive line ratios, a value for t^2 can be derived. An example of two of these ratios is given by the [O III] λ5007/4363 and [O III] λ5007/52 μm line ratios. This has been done by Dinerstein et al. (1985) for a set of planetary nebulae.

3. THE ISO LMC/SMC H II REGION PROGRAM

The spectrometers on board ISO have now given us access to a wide range of IR fine-structure lines of all astrophysically important elements. As part of the SWS Guaranteed Time Program for H II regions observations were made of a set of 17 H II regions in the Magellanic Clouds (Van der Hulst & Vermeij 1997). The SWS (de Graauw et al. 1996) observations are complemented by LWS (Clegg 1996) data from the program of Baluteau et al. (1997). Optical spectroscopic data obtained in 1995 and 1996 with the B&C spectrograph at the ESO 1.5 m telescope complete the data set. The optical data consist of longslit spectra at various positions in the program H II regions as well as driftscan spectra. The lines observed with ISO are given in Table 1 together with some of the optical lines.

The main goal of the H II region program is to derive, in detail, the temperature, density and ionization structure of the program H II regions, and from these, a set of improved elemental abundances for the Magellanic Clouds. For the interpretation of the data the photoionization code CLOUDY (Ferland 1993) will be used.

4. SOME FIRST RESULTS

At this moment the SWS line scans and all the optical data have been reduced and analysis has begun. In general, the [Ne II] 12.8 μm, [Ne III] 15.6, 36.0 μm, [S III] 18.7, 33.4 μm and [S IV] 10.5 μm have been detected as well as Brα and Brβ. To give an idea of the quality of the SWS data, some of the line scans for the H II region N160A1 are shown in Figure 2.

In Figure 1 a diagnostic diagram is given for the temperature and density of the [S III] emitting zone. The results for four H II regions are shown. For the LMC objects N11A, N83B and N4A the electron temperature lies around 10^4 K while N81 in the SMC shows a higher temperature of about 16 000 K. The electron densities lie between 300 cm^{-3} and 650 cm^{-3}. To combine the SWS with the optical data the driftscan spectra have been used. For the density dependent IR/IR line ratio the standard aperture correction has been applied.

Fig. 3 shows the [Ne III]/[Ne II] and [Ne III]/[S III] line ratios versus the [S IV]/[S III] line ratio for eight of the program objects. The objects show a wide range in excitation. The electron temperatures for [S III] reflect the differences in excitation with N83B having the lowest excitation and N81 the highest excitation. Not shown in this figure are the results for SMC N88A which is even more highly excited than N81 (with [S IV]/[S III] $\approx$ 6 and [Ne III]/[S III] $\approx$ 3). Note the tight correlation between the [Ne III]/[Ne II] and [S IV]/[S III] line ratios in the left panel of

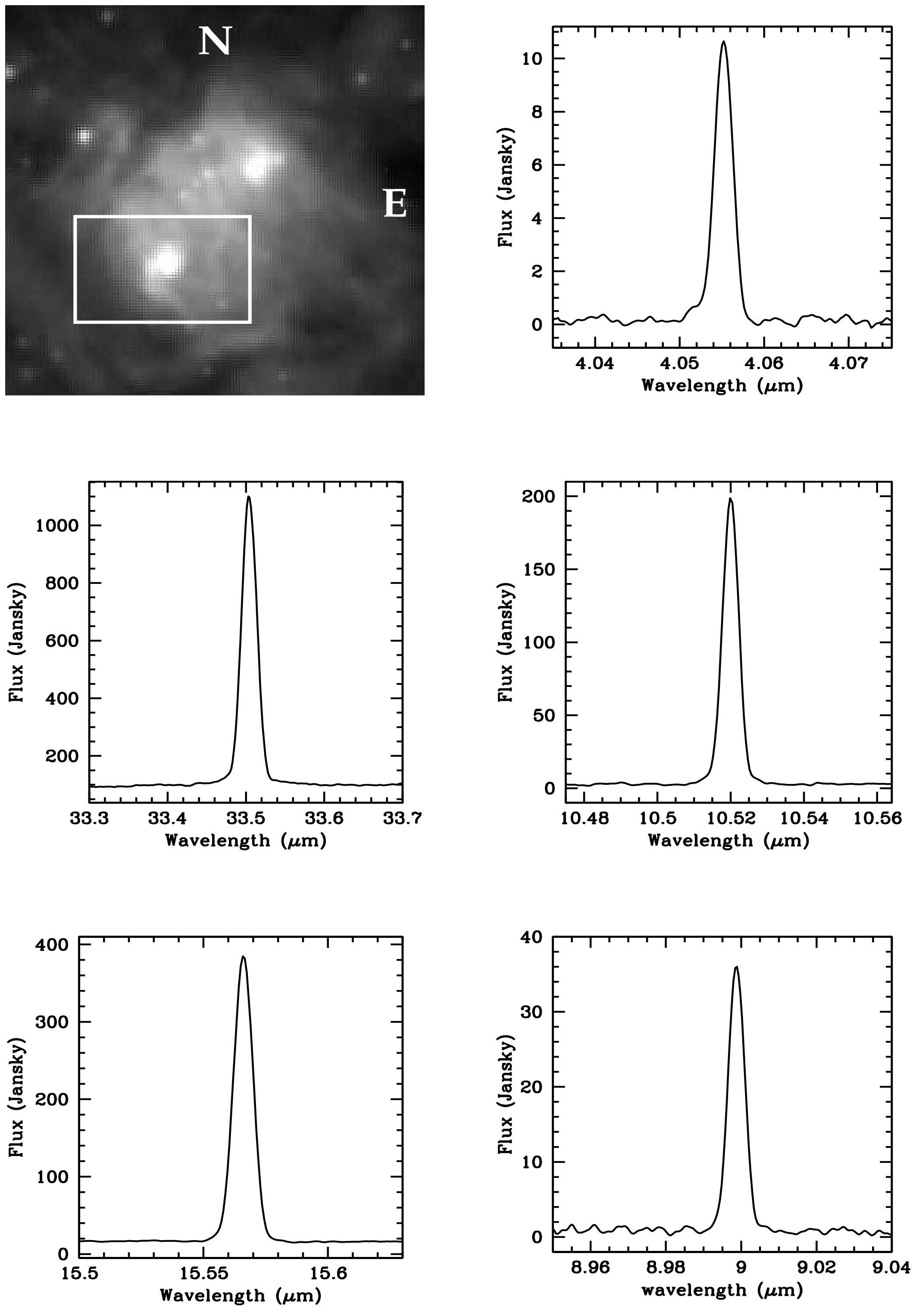

Figure 2. The LMC object N160A1. Shown are a few of the fully reduced SWS line scans of this region. From top to bottom, left to right, the lines shown are Brα, [S III] *33.5 μm,* [S IV] *10.5 μm,* [Ne III] *15.6 μm and* [Ar III] *8.98 μm. Given in the top-left corner is an Hα image of the H II region N160A with the position of the SWS band 4 aperture.*

Fig. 3. The correlation between the [Ne III]/[S III] and [S IV]/[S III] line ratios in the right panel of Fig. 3 shows some scatter. This is probably due to different relative values for the neon and sulfur abundances between various objects. All lines used in these ratios are observed with the same aperture except for [S IV] 10.5 μm.

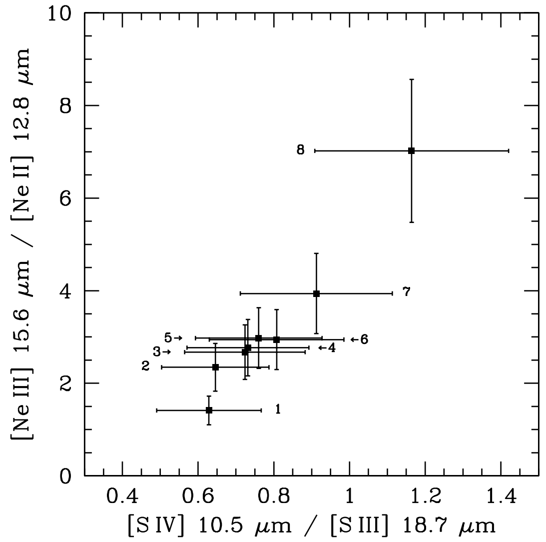

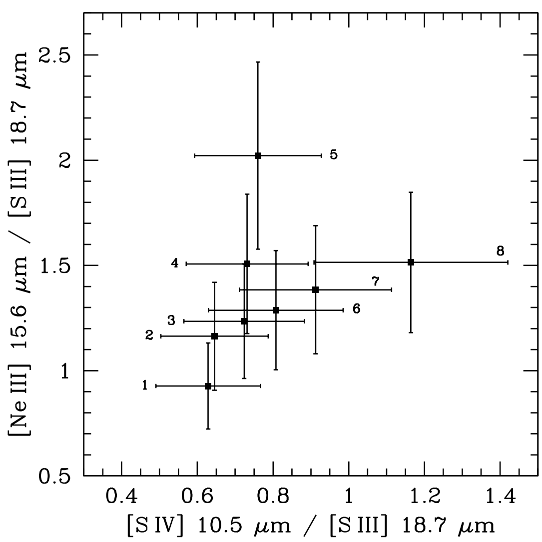

Figure 3. The [Ne III]/[Ne II] *and* [Ne III]/[S III] *line ratios versus the* [S IV]/[S III] *line ratio. These line ratios are used to constrain the nature of the source ionizing the nebula. The differences in the excitation are clearly visible. Object legenda : 1 = N83B, 2 = N11A, 3 = N160A2, 4 = N160A3, 5 = N159-5, 6 = N4A, 7 = N160A1, 8 = N81.*

ACKNOWLEDGEMENTS

SWS is a joint project of SRON and MPE (DARA grants no. 50 QI 9402 3 and 50 QI 8610 8) with contributions from KU Leuven, Steward Observatory and Phillips Laboratory.

REFERENCES

Baluteau, J.-P., Joubert, M., Cox, P., Roelfsema, P., Caux, E., Emery, R. 1997 *New ISO/LWS results on the Magellanic Cloud HII regions*, ESA SP-419, p. 99

Clegg, P.E. 1996, A&A, 315, L38

Dinerstein, H.L. 1983, *IAU Symposium 103, Planetary Nebulae*, ed. D. Flower (Dordrecht : Reidel), p. 79

Dinerstein, H.L., Lester, D.F., Werner, M.W. 1985, ApJ, 291, 561

Ferland, G.J. 1993, University of Kentucky Physics Department, Internal Report

Garnett, D.R. 1992, AJ, 103, 1330

de Graauw, Th. et al. 1996, A&A, 315, L49

Van der Hulst, J.M., Vermeij, R. 1997 *SWS Observations of HII regions in the Magellanic Clouds*, ESA SP-419, p. 105

Osterbrock, D.E. 1989, *Astrophysics of Gaseous Nebulae and Active Galactic Nuclei*, University Science Books, Mill Valley Ca.

Pagel, B.E. J. 1978, MNRAS, 183, 1P

Peimbert, M. 1967, ApJ, 150, 825

Peimbert, M., Torres-Peimbert, S. 1977, MNRAS, 179, 217

Stasińska, G. 1980, A&A, 85, 359

DOUBLE-BARRED STARBURST GALAXIES VIEWED BY ISOCAM

H. Wozniak[1], D. Friedli[2], L. Martinet[2] & D. Pfenniger[2]

[1]IGRAP/Observatoire de Marseille, France
[2]Geneva Observatory, Switzerland

ABSTRACT

We present broad band 6.75 μm (LW2) and 15 μm (LW3) images that have been obtained with ISOCAM for two double-barred galaxies (NGC 1097 and NGC 4321) extracted from our global project WMFP15. These galaxies have both a large-scale stellar bar and a $\sim$1 kpc scale nuclear bar surrounded by a circumnuclear ring. In the case of NGC 4321 both bars are aligned while they are misaligned in the case of NGC 1097. The comparison of their mid-infrared properties reveals that star formation is differently taking place in these objects.

Key words: ISOCAM; double-barred galaxies.

1. INTRODUCTION

Double-barred galaxies have gained strong new interests through observations (e.g., Wozniak et al. 1995; Friedli et al. 1996), numerical simulations (e.g. Friedli & Martinet 1993; Friedli 1996) and theory (e.g. Shlosman et al. 1989). Indeed, systems with bars within bars might play a crucial role in fueling central activity of galaxies and shaping circumnuclear starbursts. Moreover, double-barred galaxies and galaxies with central non-axisymmetric deformations are very common, especially in early-type disk galaxies (Erwin & Sparke 1998).

An example of still open problems on such double-barred galaxies is the number of distinct bar patterns of rotation. Indeed, if both bars rotate at the same speed they should be aligned to survive otherwise the gravitational torque from the secondary bar on the primary one would destroy the latter. A single pattern speed could exist in NGC 4321 (Knapen et al. 1995). However, for this object, the hypothesis of two different pattern speeds cannot be completely excluded (García-Burillo et al. 1998). We might be just looking at a peculiar moment when both bars are aligned. The bars of NGC 1097 have probably distinct rotation speeds since they are misaligned by 63 degrees, the secondary bar being tipped behind the primary one. The number of pattern speeds should have also an effect on the way star formation is triggered in the circumnuclear regions. It is thus worthwhile to compare how star formation is taking place in the circumnuclear rings of these two objects.

The present study is devoted to the comparison of the double-barred galaxies NGC 1097 and NGC 4321 (M 100). It is a part of the global project WMFP15 intended to clarify the interplay between central starburst activity and the non-axisymmetric dynamics of barred galaxies. A full report is given in Wozniak et al. (1999)

2. NGC 1097

NGC 1097 is a SB(s)b galaxy which hosts a LINER (Phillips et al. 1984) or Seyfert 1 nucleus (Storchi-Bergmann et al. 1996). This object is also a starburst galaxy whose star formation rate is significant ($SFR_{FIR} \approx 5\,M_\odot\,yr^{-1}$). Near-infrared observations have clearly shown the existence of a nuclear bar misaligned with the large-scale one. Both bars are separated by a prominent circumnuclear ring (CNR) of star formation. Images at 15 μm (see Figure 2) reveal six major distinct peaks regularly spaced along the CNR, distributed two by two with respect to the nucleus. At 6.75 μm two of them show sub-structures. This symmetry clearly suggests that star formation is organised at large-scales along the CNR.

3. NGC 4321

NGC 4321 (M 100) is a late-type giant, moderately barred spiral galaxy in Virgo, located at roughly the same distance as NGC 1097 ($\sim$17 Mpc). Its inner region has been extensively studied at several wavelengths. Optical, Hα, near-infrared, and CO images have revealed many intricate features associated with its mild star formation activity in the central kpc ($SFR_{FIR} \approx 3\,M_\odot\,yr^{-1}$). A nuclear bar almost perfectly aligned with the large-scale bar occupies the region inside the CNR. Several H II regions lie on a 1 kpc circumnuclear ring crossing the long stellar bar. The LW2 and LW3 images (see Figure 3) show an inhomogeneous emission resulting in an incomplete ring-like distribution. Two bright spots near the nuclear bar ends dominate the emission in both bands. We have recently suggested that the high LW2/LW3 ratio in these two star forming region could be due to Wolf-Rayet stars (Wozniak et al. 1998).

Table 1. Comparison of MIR properties.

Region	Properties	NGC 1097	NGC 4321
Nucleus	Surface brightness	Fainter than ring	∼ same as ring
	Colour ($F_{6.75\,\mu m}/F_{15\,\mu m}$) in central pixel	0.88	0.80
Nucleus< R <Ring	Surface brightness	Same for both (1.0–1.2 mJy arcsec^{-2})	
	Extreme colour	0.94 (max)	0.70 (min)
Ring	Structure	6 spots at 15 μm	2 spots + 2 extended regions
	Mean [max] colour	0.65 [0.85]	0.85 [1.05]
	Positions of max colour	=min(15 μm)	not correlated to extrema
	Colour of star-forming regions	∼0.6 (=minima)	≥0.95 (=maxima)

4. COMPARISON OF MIR PROPERTIES

Radial profiles have been obtained by averaging the surface brightness in 1.5 arcsec wide annuli centred on the nucleus. The profiles displayed in Figure 1 clearly show the luminosity bump due to the CNR. The surface brightness maximum is located at 9 arcsec for NGC 1097 and 6 arcsec for NGC 4321. The azimuthal profiles displayed in Figure 1 have been obtained by averaging the surface brightness in 7.5 arcsec (i.e. 3 pixels) wide annuli centred at the radius of maximum brightness. The bin size is 10°. A summary of the main features is given in Table 1.

4.1. From the nucleus to the CNR

The nucleus of NGC 1097 has roughly the same colour as any region of star formation located in the CNR. It is also much fainter than any other Seyfert galaxy of our sample (e.g. NGC 1808, NGC 7469). However, ISOCAM spectra at 3 arcsec (H. Roussel, private communication) unambiguously show the Unidentified Infrared Bands (UIBs) in the nuclear region although they should have disappeared because of the radiation field of the Active Galactic Nucleus (AGN). These spectra are rather similar to photodissociation regions than AGN ones (see Genzel et al. 1998 for example). On the other hand, Laurent et al. (these proceedings) classify the nucleus as an AGN on the basis of the 5–6 μm continuum. The AGN however does not dominate the emission because of the rough resolution; star-forming regions could be included in the same pixel as the nucleus. These results emphasize the ambiguity of the power source of LINERs (Huang et al. 1998). The old LINER classification could be due to star forming regions (Maoz et al. 1998) while the Seyfert 1 characteristics appear only with high resolution observations. There was often some confusion about the nature of nuclear activity (e.g. NGC 6764, Contini et al. 1997).

The region between the nucleus and the CNR has roughly the same surface brightness in both objects. However, this region is bluer in NGC 1097 ($F_{6.75\,\mu m}/F_{15\,\mu m}$∼0.94) than in NGC 4321. It is moreover one of the bluest parts of the radial profile of NGC 1097 while it is the reddest for NGC 4321. This region is however not associated to star formation activity since Hα and K images do not reveal any H II regions.

4.2. The ring (CNR)

In NGC 1097, the minimal colours of the CNR correspond to the regions of star formation ($F_{6.75\,\mu m}/F_{15\,\mu m}$∼0.6). These low colours could be easily explained by the presence of strong optical and UV radiation fields which destroy the UIB carriers. Thus, $F_{6.75\,\mu m}$ decreases while these high radiation fields heat and excite big grains so that $F_{15\,\mu m}$ increases. Indeed, the colours of these regions are similar to those of mild starbursts (L. Vigroux, private communication).

However, the colours of star forming regions of the CNR of NGC 4321 does not conform to this simple interpretation: the star forming regions fit to maximal colours (≥ 0.95) contrary to NGC 1097. This may mean that UIB carriers dominate the 6.75 μm luminosity. Wozniak et al. (1998) put forward that these carriers may be amorphous carbon grains created in Wolf-Rayet stellar winds. This could be particularly the case for the two spots at the end of the nuclear bar ($1.0 \leq F_{6.75\,\mu m}/F_{15\,\mu m} \leq 1.2$), confirming the suggestion by Knapen et al. (1995) that these regions might be young and powered by OB stars.

Part of the 6.75 μm luminosity could also be due to H_2 heated by shocks. This assumption remains to be confirmed by ground-based IR spectroscopy as no SWS or CAM–CVF spectra are available.

The CNR of NGC 1097 is also brighter and redder ($F_{6.75\,\mu m}$<$F_{15\,\mu m}$) on the whole than NGC 4321.

ACKNOWLEDGMENTS

We are grateful to O. Laurent, D. Tran, and L. Vigroux for enlightening discussions during this meeting. We also acknowledge H. Roussel for showing us NGC 1097 CVF spectra prior to publication, and the Swiss National Science Foundation (FNRS) for its support.

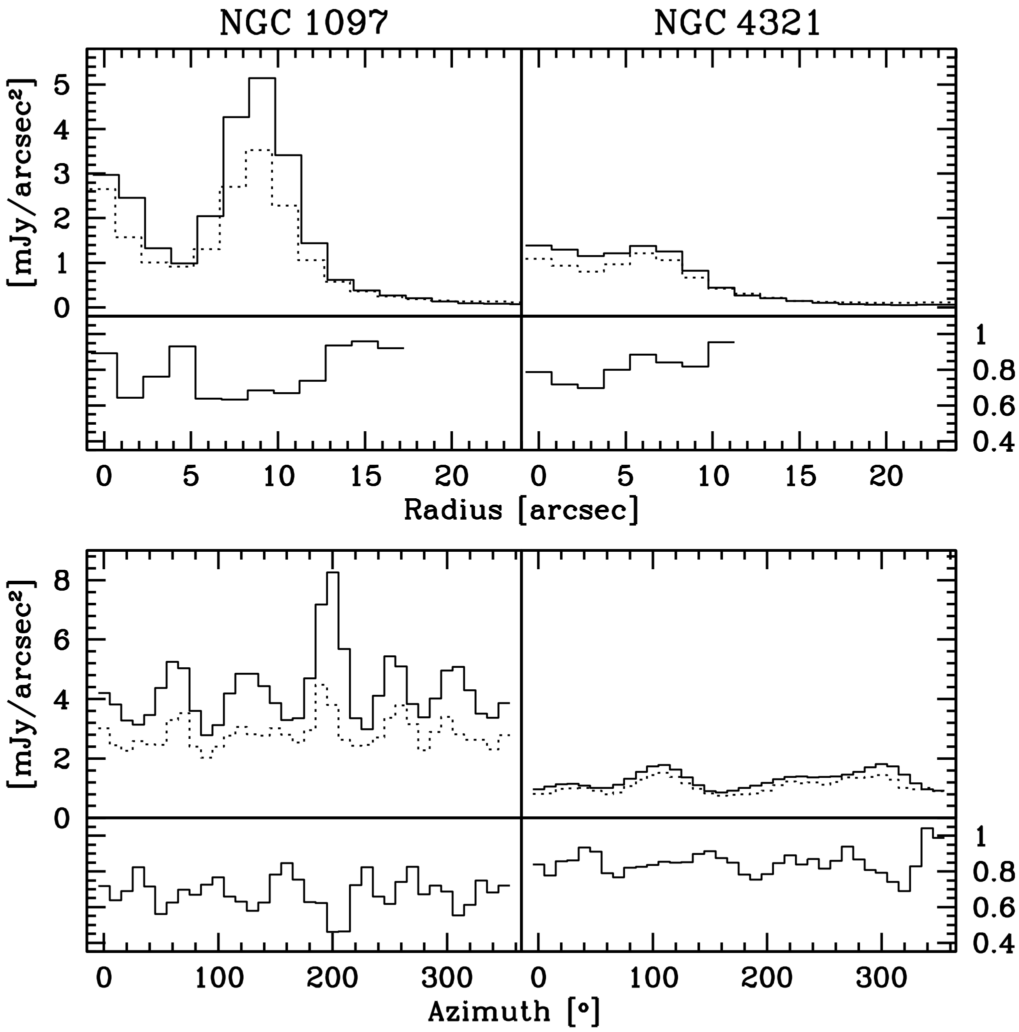

Figure 1. Top panels: radial profiles obtained with deconvolved images. Full lines are 15 μm profiles, dotted lines are 6.75 μm ones. The lower sub-panels show the colour profiles obtained by the ratio of LW2 to LW3 radial profiles. Bottom panels: azimuthal profiles along the ring. The lower sub-panels show the colour profiles obtained by the ratio of LW2 to LW3 azimuthal profiles. North is at 0 degree.

REFERENCES

Contini, Th., Wozniak, H., Considère, S., Davoust, E. 1997, A&A, 324, 41

Erwin, P., Sparke, L.S. 1998, in: Galaxy Dynamics, ASP Conf. Ser., eds. D.R. Merritt, M. Valluri, and J.A. Sellwood, ASP, San Francisco, in press

Friedli, D. 1996, A&A, 312, 761

Friedli, D., Martinet, L. 1993, A&A, 277, 27

Friedli, D., Wozniak, H., Rieke, M., Martinet, L., Bratschi, P. 1996, A&AS, 118, 461

García-Burillo, S., Sempere, M.J., Combes, F., Neri, R. 1998, A&A, 333, 864

Genzel, R., Lutz, D., Sturm, E., et al. 1998, ApJ, 498, 579

Huang, J.H., Chen, Y., Gu, Q.S. 1998 (astro-ph/9811401)

Knapen, J.H., Beckman, J.E., Heller, C.H., Shlosman, I., de Jong, R.S. 1995, ApJ, 454, 623

Maoz, D., Koratkar, A., Shields, J.C., et al. 1998, AJ, 116, 55

Phillips, M. M., Pagel, B. E. J., Edmunds, M. G., Diaz, A. 1984, MNRAS, 210, 701

Shlosman, I., Frank, J., Begelman, M.C. 1989, Nature, 338, 45

Storchi-Bergmann, T., Wilson, A., Baldwin, J. 1996, ApJ, 460, 252

Wozniak, H., Friedli, D., Martinet, L., Martin, P., Bratschi, P. 1995, A&AS, 111, 115

Wozniak, H., Friedli, D., Martinet, L., Pfenniger, D. 1998, A&A, 330, L5

Wozniak, H., Friedli, D., Martinet, L., Pfenniger, D. 1999, in preparation

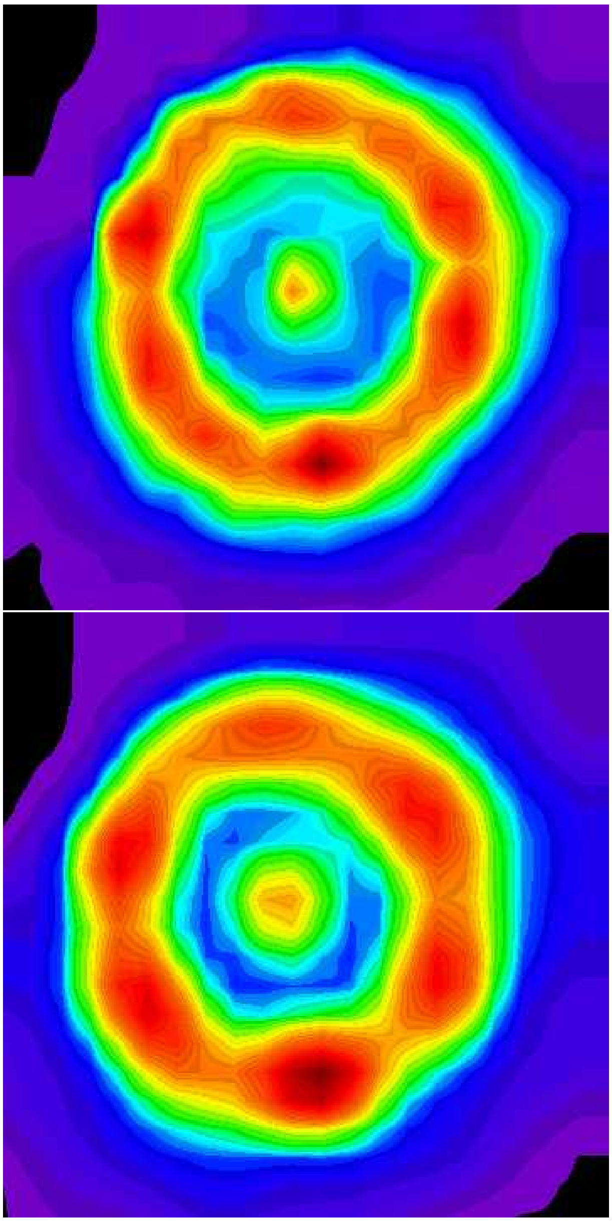

Figure 2. *Deconvolved ISOCAM images of NGC 1097 in broad band filters LW2 (top) and LW3 (bottom) obtained in beamswitching mode. Pixel scale is 1.5 arcsec. Field of view is 31.5 arcsec×31.5 arcsec. Surface brightness scales from 0 to 6.85 mJy arcsec^{-2} for the LW2 image and 0 to 11.05 mJy arcsec^{-2} for the LW3 one. North is up.*

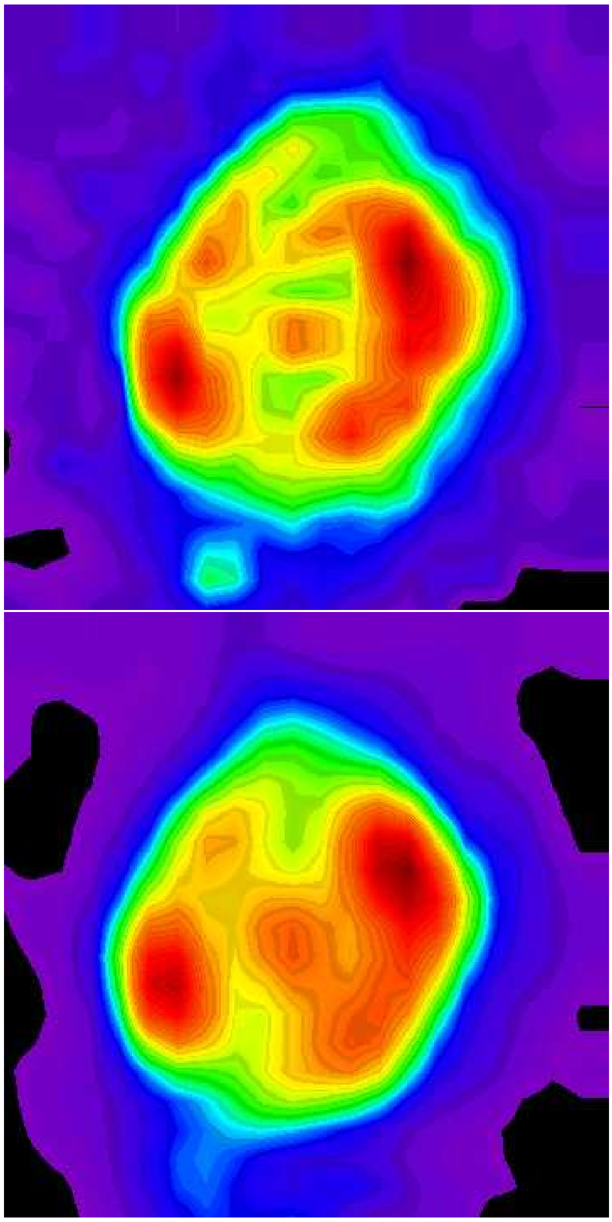

Figure 3. *As Figure 2 but for NGC 4321. Surface brightness scales from 0 to 2.12 mJy arcsec^{-2} for the LW2 image and 0 to 2.40 mJy arcsec^{-2} for the LW3 one.*

ARE SPIRAL GALAXIES OPTICALLY THIN OR THICK?

E.M. Xilouris[1,2], N.D. Kylafis[2,3], & J. Papamastorakis[2,3]

[1]University of Athens, Physics Department, 157 83 Athens, Greece
[2]Foundation for Research and Technology-Hellas, P.O. Box 1527, 711 10 Heraklion, Crete, Greece
[3]University of Crete, Physics Department, P.O. Box 2208, 710 03 Heraklion, Crete, Greece

ABSTRACT

We compare optical and near-infrared surface photometry of seven edge-on spiral galaxies with corresponding surface photometry calculated from a realistic model of spiral galaxies which takes into account both absorption and scattering by the interstellar dust. For the stars and the dust in the disk we use exponential distributions in both directions, radially and perpendicular to the plane of the disk, while the de Vaucouleurs ($R^{1/4}$) profile is used for the description of the bulge. From this analysis we were able to determine all the parameters of the axisymmetric 3D distributions of stars and dust that best fit the surface photometry of the galaxies and thus obtain some general conclusions, the most significant of which are:
1) The face-on central optical depth is less than one in all optical bands, indicating that typical spiral galaxies like the ones that we have modelled would be completely transparent if they were to be seen face-on.
2) The dust scaleheight is about half that of the stars, which means that dust is more concentrated near the plane of the disk.
3) The dust scalelength is about 1.4 times larger than that of the stars and dust is more radially extended than the stars.
4) The gas-to-dust mass ratio calculated, with the dust mass derived from the model, is close to the value derived for our Galaxy.
5) The derived extinction law matches quite well with the Galactic extinction law, indicating a universal dust behaviour.

Key words: galaxies; dust; extinction.

1. INTRODUCTION

The amount and the way that dust is distributed within spiral galaxies as well as its extinction effects on the galactic starlight has been a matter of debate over the last few years. Since Disney, Davies and Phillipps (1989) proposed that spiral galaxies may be optically thick, a long series of papers has been published by different authors with conclusions that often differ widely.

In our studies we perform detailed modelling of spiral galaxies, aiming at the determination of the parameters that describe the three-dimensional dust distribution in these galaxies (see Xilouris et al., 1997, 1998a and 1998b, hereafter Paper I, II and III, respectively).

In Sect. 2 we describe the observations, in Sect. 3 we briefly discuss the model and in Sect. 4 we present the model results followed by some general conclusions.

2. OBSERVATIONS

Optical observations of all the galaxies except for IC 2531 were made at Skinakas observatory in Crete, using the 1.3 m telescope. Exposures were made through B, V, I broad band filters. The optical and near-infrared observations of IC 2531 were made by Y.I. Byun using the Australian National University (ANU) 1 m and 2.3 m telescopes respectively. Near-infrared observations of NGC 891 were made by M. Trewhella using the 2.5 m telescope at the Wyoming Infrared Observatory.

3. MODEL

The stellar emissivity (luminosity per unit volume) that we use consists of an exponential (in both radial and vertical directions) disk and a bulge which produces an $R^{1/4}$ law, namely

$$L(R,z) = L_s \exp\left(-\frac{R}{h_s} - \frac{|z|}{z_s}\right) + L_b \exp(-7.67 B^{1/4}) B^{-7/8}, \qquad (1)$$

with h_s and z_s being the scalelength and scaleheight of the disk and

$$B = \frac{\sqrt{R^2 + z^2 (b/a)^2}}{R_e}, \qquad (2)$$

with R_e being the effective radius of the bulge and a and b the semi-major and semi-minor axis respectively. Here L_s and L_b are the normalization constants for the stellar emissivity of the disk and the bulge respectively.

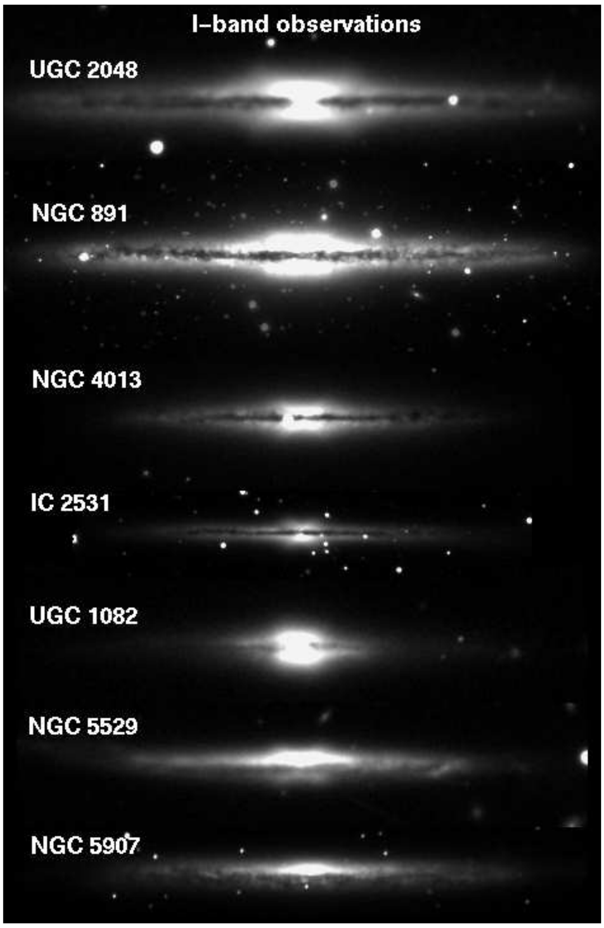

Figure 1. I-band observations of the galaxies UGC 2048, NGC 891, NGC 4013, IC 2531, UGC 1082, NGC 5529 and NGC 5907 (top to bottom).

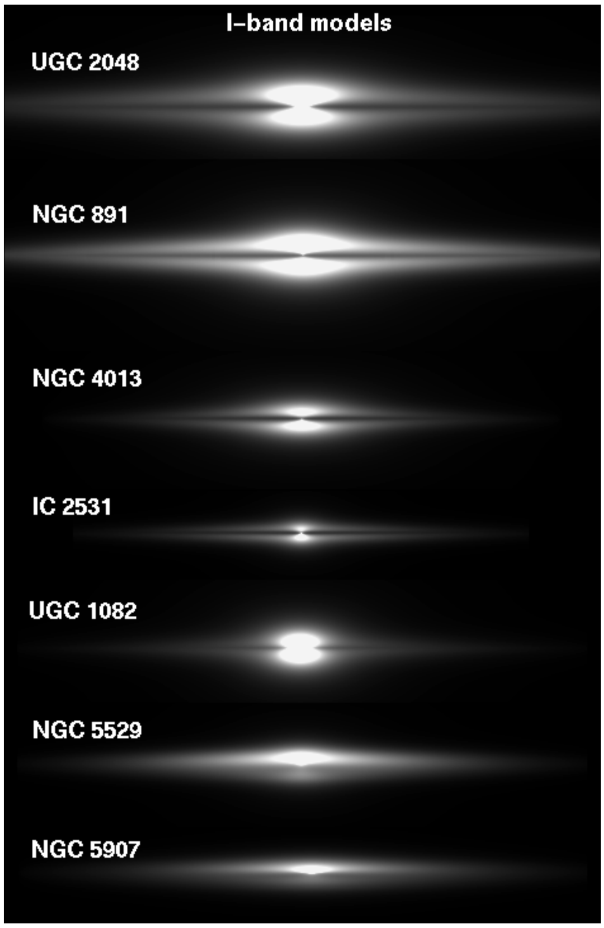

Figure 2. I-band models of the galaxies UGC 2048, NGC 891, NGC 4013, IC 2531, UGC 1082, NGC 5529 and NGC 5907 (top to bottom).

For the extinction coefficient we use a double exponential law, namely

$$\kappa_\lambda(R,z) = \kappa_\lambda \exp\left(-\frac{R}{h_d} - \frac{|z|}{z_d}\right), \tag{3}$$

where κ_λ is the extinction coefficient at wavelength λ at the center of the disk and h_d and z_d are the scalelength and scaleheight respectively of the dust. The central optical depth of the model galaxy seen face-on is

$$\tau_\lambda^f = 2\kappa_\lambda z_d. \tag{4}$$

The radiative transfer model that we have used is that described in Kylafis & Bahcall (1987) - see also Paper I.

4. RESULTS

Through three-dimensional axisymmetric modelling of the dust and the stars, we have been able to determine the parameters that describe the distribution of stars and dust in seven late-type galaxies. Using the values of these parameters we have created model images and compared them with the observed images. We do so in Figs. 1 and 2. In Fig. 1 the I-band observations of all seven galaxies are presented (UGC 2048, NGC 891, NGC 4013, IC 2531, UGC 1082, NGC 5529 and NGC 5907 from top to bottom). In Fig. 2 we show the model images of these galaxies in the I-band with the same scale and sequence as in Fig. 1 so that a direct comparison can be made between the two figures. All the values of the parameters as well as a detailed description of the comparison between model and observations are given in Papers I, II and III.

We have quantified the opacity of the galaxies in terms of their central face-on optical depth τ^f. *For all the galaxies we have found central face-on optical depths with values less than one in all the bands that we analyzed, indicating that they would appear to be transparent when seen face-on, despite their obvious dust lane in their almost edge-on orientation seen in the observations.* The values of the optical depth in all bands are plotted in Fig. 3 for each galaxy. Different symbols indicate different bands. In particular, open circles correspond to the B-band, open squares to the V-band, open triangles to the I-band, solid squares to the J-band and solid triangles to the K-band.

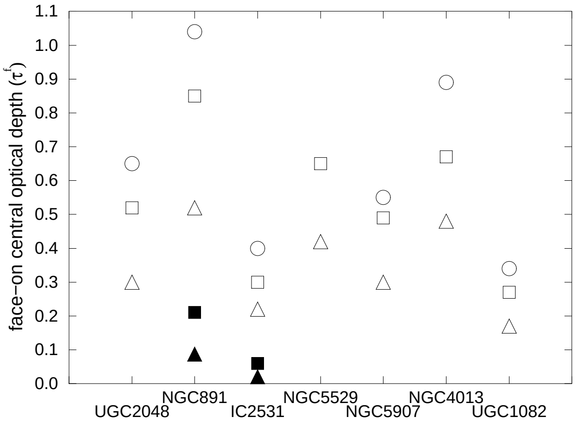

Figure 3. Values of the face-on central optical depth in all the bands that were modelled for each galaxy. Different symbols are for different bands. Open circles correspond to the B-band, open squares to the V-band, open triangles to the I-band, solid squares to the J-band and solid triangles to the K-band.

It is of interest to see how the scaleheight of the stars is related to that of the dust. We show this in Fig. 4, where the parameters z_s and z_d (in kpc) as well as their ratio are plotted for each galaxy. The symbols have the same meaning as in Fig. 3. For the case of UGC 2048 (analyzed in Paper I), we give half of the derived scaleheight values since, as mentioned in Paper I, its distance has probably been overestimated by a factor of 2. Doing the statistics in the V-band data we derive a mean ratio of $z_s/z_d = 1.8 \pm 0.6$ implying that the dust is more concentrated to the plane of the disk with respect to the stars. This was, of course, evident from the prominent dust lanes. This mean value of z_s/z_d is plotted as a horizontal dashed line.

Of particular interest is the extended distribution of dust in the radial direction relative to the stars, as can be seen from the values that were derived for the scalelengths. In order to have a better view of how the scalelengths of the stars and the dust are related we give a plot (Fig. 5) similar to that of the scaleheights described above. The symbols here have exactly the same meaning as that in Fig. 3. As with the scaleheights of UGC 2048, we adopt half the values of the scalelengths derived from the model. The statistics that were done in the V-band, give a mean ratio of $h_d/h_s = 1.4 \pm 0.2$. This value is shown as a dashed horizontal line. *In all seven galaxies we have found that the dust is radially more extended than the stars. This is a prediction of our model.* The extended radial distribution of the dust has recently been confirmed for our Galaxy using COBE/DIRBE data (Davies et al. 1997a). Analysis of ISO data for several galaxies (Davies et al. 1997b, Alton et al. 1998a), as well as SCUBA observations of NGC 891 in 450 and 850 μm (Alton et al. 1998b) also indicate a more extended radial distribution for the dust than for the stars. Another work that also supports this is that of Lequeux & Guelin (1996), where a systematic reddening of background galaxies is found in the outer regions of the galaxy M 31 suggesting the existence of dust even beyond the optical disk.

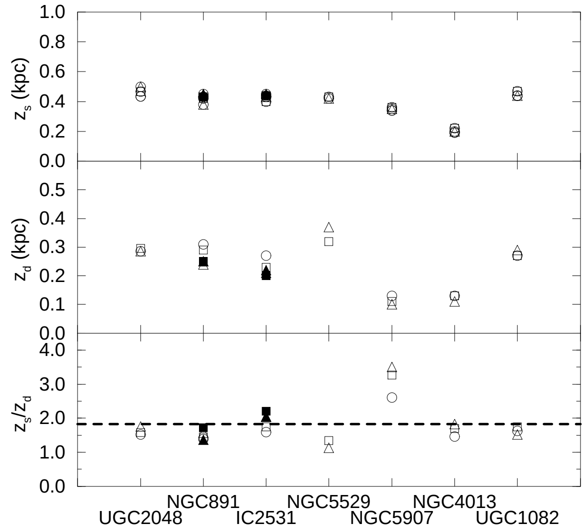

Figure 4. The values of z_s (top graph), z_d (middle graph) and z_s/z_d (bottom graph) for each galaxy. All lengths are given in kpc. For the explanation of the symbols see Fig. 3. The dashed line in the last graph gives the mean value of the ratio calculated by using the V-band data.

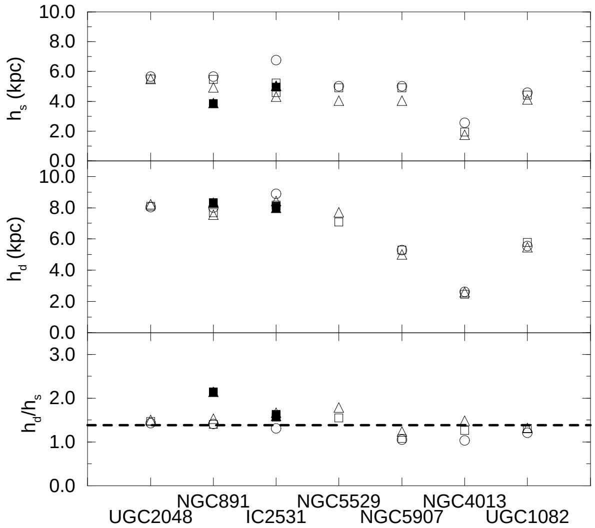

Figure 5. The values of h_s (top graph), h_d (middle graph) and h_s/h_d (bottom graph) for each galaxy. All lengths are given in kpc. For the explanation of the symbols see Fig. 3. The dashed line in the last graph gives the mean value of the ratio calculated by using the V-band data.

Another interesting result that comes out of our model analysis is the dust mass calculation. For all galaxies analyzed, we find a dust mass which gives a gas-to-dust mass ratio close to that derived for our Galaxy. A better picture of this is given in Fig. 6, where the gas mass (top graph) and the dust mass (middle graph) are plotted (in units of $M_\odot$) for each galaxy. For the dust mass (middle graph) we give the model calculations (filled circles) as well

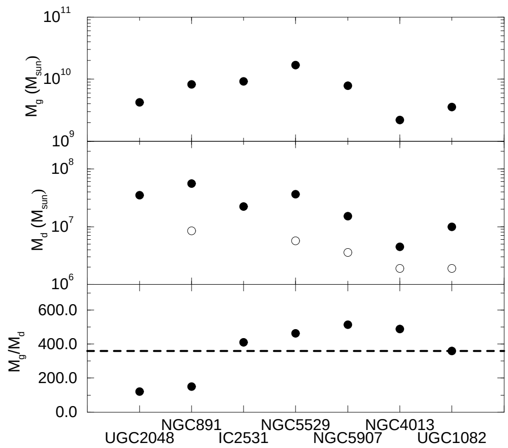

Figure 6. *The values of M_g (top graph), M_d (middle graph) and M_g/M_d (bottom graph) for each galaxy. All the masses are in units of $M_\odot$. For M_d we give a direct comparison between the values as calculated by our model (filled circles) and those calculated using the IRAS fluxes (open circles) wherever IRAS data were available. The dashed line in the last graph gives the mean value of the gas-to-dust mass ratio.*

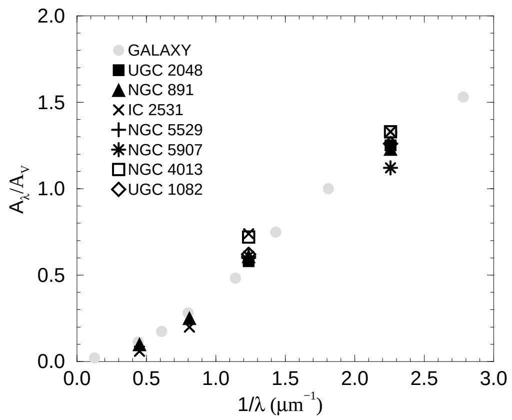

Figure 7. *The observed (gray circles) values of A_λ/A_V for our Galaxy and the values calculated for all the galaxies analyzed. The symbols are explained inside the plot.*

as the calculations using the IRAS data (open circles). The gas-to-dust mass ratio (using the dust mass derived from the model) is also given for each galaxy (bottom graph). A mean value of this ratio is $M_g/M_d = 360 \pm 160$ (close to the value of ~ 160 adopted for our Galaxy, see Spitzer 1978; Sodroski et al. 1994) and is plotted as a horizontal dashed line in the last graph. *For all the galaxies we have found a dust mass about an order of a magnitude more than that calculated using the IRAS fluxes, which proves the existence of a cold dust component that has gone undetected by IRAS.* This is evident from the middle graph of Fig. 6, where the two dust masses (the one calculated from our model and the other calculated using the IRAS fluxes) are directly compared. Our extinction model, being independent of the dust temperature (both warm and cold dust contribute to the extinction of light), is able to calculate the whole amount of dust contained within the galaxies. Strong support to this argument (that vast amounts of cold dust exists in spiral galaxies) is now given by recent far infrared observations in longer wavelengths, where the cold dust is now seen in emission (Alton et al. 1998a, 1998b; Bianchi et al. 1998; Haas et al. 1998; Krügel et al. 1998).

Having calculated the values of A_λ/A_V for all the galaxies we are able to show how the values of the relative extinction in each band is compared with the values derived for our Galaxy (Rieke & Lebofsky 1985). This is done in Fig. 7, where the values of the extinction ratios A_λ/A_V are plotted as a function of the inverse wavelength ($1/\lambda$). Each symbol here represents a different galaxy as shown inside the graph. One can see that *the extinction law derived for all the galaxies is in very good agreement with that measured for our Galaxy indicating a universal dust behaviour.*

REFERENCES

Alton P.B., Trewhella M., Davies J.I. 1998a, A&A, 335, 807

Alton P.B., Bianchi S., Rand R.J., Xilouris E.M., Davies J.I., Trewhella M. 1998b, ApJ, 507, L125

Bianchi S., Alton P.B., Davies J.I., Trewhella M. 1998, MNRAS, 298, 49

Davies J.I., Trewhella M., Jones H., et al. 1997a, MNRAS, 288, 679

Davies J.I., Alton P. B., Trewhella M., Bianchi S. 1997b, MNRAS, submitted

Disney M.J., Davies J.I., Phillipps S. 1989, MNRAS, 239, 939

Haas M., Lemke D., Stickel M., et al. 1998, A&A, 338, L33

Krügel E., Siebenmorgen R., Zota V., Chini R. 1998, A&A, 331, L9

Kylafis N.D., Bahcall J.N. 1987, ApJ, 317, 637

Lequeux J., Guélin M. 1996, New extragalactic perspectives in the New South Africa, Kluwer Academic Publishers

Rieke G.H., Lebofsky M.J. 1985, ApJ, 288, 618

Sodroski T.J., Bennett C., Boggess N., et al. 1994, ApJ, 428, 638

Spitzer L. 1978, Physical Processes in the Interstellar Medium, New York, Wiley-Interscience

Xilouris E.M., Kylafis N.D., Papamastorakis J., Paleologou E.V., Haerendel G. 1997, A&A, 325, 135 (Paper I)

Xilouris E.M., Alton P.B., Davies J.I., et al. 1998a, A&A, 331, 894 (Paper II)

Xilouris E.M., Byun Y.I., Kylafis N.D., Paleologou E.V., Papamastorakis J. 1998b, A&A, submitted (Paper III)

COSMOLOGY

ISOCAM EXTRAGALACTIC MID-INFRARED DEEP SURVEYS UNVEILING DUST-ENSHROUDED STAR FORMATION IN THE UNIVERSE

D. Elbaz[1], H. Aussel[1], C.J. Cesarsky[1], F.X. Désert[2], D. Fadda[1], A. Franceschini[3], M. Harwit[4], J.-L. Puget[2], & J.L. Starck[1]

[1]Service d'Astrophysique, CEA/DSM/DAPNIA Saclay, 91191 Gif-sur-Yvette Cedex, France
[2]Institut d'Astrophysique Spatiale, Bât 121, Université Paris XI, F-91405 Orsay Cedex, France
[3]Osservatorio Astronomico di Padova, Italy
[4]511 H.Street S.W., Washington, DC 20024-2725; also Cornell University

ABSTRACT

ISOCAM extragalactic mid-infrared deep surveys have detected a population of strong infrared emitters ten times more numerous than expected if there were no evolution from z $<$ 0.2 (IRAS) up to the maximum redshift of these galaxies (z$\simeq$1.5). The mid-infrared cosmic background produced by these galaxies ($\simeq 2.35 \pm 0.8$ nW m^{-2} sr^{-1}, at 15 μm above 50 μJy) is larger than 30 per cent of the energy radiated in the I band by the optical galaxies detected in the HDF, which are two orders of magnitude more numerous. This fraction is much higher than in the local universe (z<0.2) as probed by IRAS, where all integrated infrared emission from 8 to 1000 μm makes 30 per cent of the optical starlight (Soifer & Neugebauer 1991). Even assuming a conservative spectral energy distribution (SED), they produce a major contribution to the 140 μm DIRBE background measured by Hauser et al. (1998, $\simeq 25.1 \pm 7$ nW m^{-2} sr^{-1}) and Lagache et al. (1999, $\simeq 15.3 \pm 9.5$ nW m^{-2} sr^{-1}). This is both a confirmation of the strong infrared cosmic background that was first detected by Puget et al. (1996) and the first identification of the galaxies responsible for a large fraction of this background at 140 μm. We were able to identify the galaxies responsible for this strong infrared emission in the region of the Hubble Deep Field (HDF plus its flanking fields) due to the large number of ground-based observations of HDF galaxies. We find that these bright (several times $10^{11}\ L_\odot$) and massive ($<M> \simeq 1.5 \times 10^{11}\ M_\odot$) infrared galaxies have a typical redshift of z$\simeq$0.7 and optical colors similar to field galaxies. The fraction of galaxies with morphological signs of interactions is larger at higher redshift. This is consistent with the nature of local luminous infrared galaxies (LIGs, with $L_{bol} \simeq L_{IR} > 10^{11}\ L_\odot$) found by IRAS, which often exhibit evidence of galaxy interaction or merging (Sanders & Mirabel 1996) and indicates that interactions should play a crucial role in the evolution of galaxies as expected from bottom-up scenarios.

Keywords: cosmological surveys; mid-infrared; galaxy evolution.

1. INTRODUCTION

Early-type galaxies and the central bulges of spirals are expected to have rapidly converted most of their primordial gas into stars as indicated by their red colors, typical of old stellar populations, and the lack of remaining fuel to entertain new star formation. The bulk of these stars was therefore expected to have formed during a major episode of star formation and the distant galaxies which should have experienced this process were called 'primeval' galaxies. The failure of optical searches for such primeval galaxies, expected to exhibit strong Ly-α emission lines (Djorgovski & Thompson 1992), was interpreted with the help of two scenarios which are not mutually exclusive. On one hand, the predictions of bottom-up cosmological scenarios of galaxy formation (White & Frenk 1991) and the observational evidence for merging galaxies, suggest that primeval galaxies simply do not exist, because galaxy formation is a continuous process. On the other hand, strong dust extinction could have masked these major episodes of star formation so that primeval galaxies should be found in infrared surveys (Franceschini et al. 1991, 1994).

Optical surveys found a strong evolution of the population of blue galaxies as a function of redshift for galaxies below z=1 (Canada-France Redshift Survey, CFRS, Lilly et al. 1995, Hammer et al. 1997). At larger redshifts, Steidel et al. (1996) used the U and B drop out technique to select galaxies at redshifts 3 and 4 from their broad-band colors. Madau et al. (1996) translated these observations into a famous plot showing the average star formation history of the universe, which could also be seen as the universal history of an ideal galaxy. In this plot, the formation of stars per cubic megaparsec of the universe was expected to peak at a redshift close to 1 and then decrease at larger redshifts. However, when observed spectroscopically, the drop-out galaxies were found to exhibit a flat spectrum in the UV, indicative of a strong dust extinction which could lead to an underestimation of the associated star formation rates (SFR) of these galaxies by a factor of three and maybe even as much as ten (Pettini et al. 1997, Meurer et al. 1997).

In the local universe, direct infrared observations from IRAS (Soifer & Neugebauer 1991) showed that the infrared luminosity from 8 to 1000 μm of galaxies is about 30 per cent of that from starlight. The population of LIGs only produce about 6 per cent of this integrated infrared emission. Hence, although the detection by IRAS of LIGs, which appeared to be the strongest starbursts ever detected, was legitimately considered as a breakthrough, it was not supposed to change our understanding of the history of star formation because of the marginal proportion of stars born in these galaxies. However, analyses of IRAS extragalactic source counts showed evidence for strong evolution at low flux levels for ULIGs (ultra-LIGs, $L_{bol} \simeq L_{IR} > 10^{12}\ L_{\odot}$, Hacking et al. 1987, Lonsdale & Hacking 1989, Lonsdale et al. 1990). More recently, Kim & Sanders (1998) found a very strong density evolution for ULIGs with a 60 μm flux between 0.5 Jy and 1.5 Jy of the form $\Phi(z) \simeq (1+z)^{7.6\pm3.2}$. This result was only tentative because of the small redshift range sampled by IRAS luminous galaxies (z<0.27), but it is an indication that ULIGs and maybe also LIGs should have played a stronger role in the past. The second argument in favor of such an evolution was found by Puget et al. (1996) who detected a strong cosmic infrared background (CIRB) in the 300 μm to 1 mm range in the COBE-FIRAS data. This result was then confirmed by Guiderdoni et al. (1997) and by a positive detection at lower wavelength using another instrument on-board COBE, DIRBE. The exact value of the COBE-DIRBE CIRB at 140 μm is still a matter of debate (Hauser et al. 1998, find a value of 25 ± 7 nW m^{-2} sr^{-1}, while Lagache et al. 1999, find 15 ± 9 nW m^{-2} sr^{-1}), but most importantly its existence is now confirmed by independent teams and suggests that the rest-frame infrared emission of galaxies is much higher at high redshift than estimated locally (z<0.2) by IRAS.

Several cosmological surveys have been performed with ISOCAM, on-board ISO, in directions of low zodiacal and Galactic cirrus mid-infrared emission, ranging from large and shallow ones (several square degrees, complete down to $\simeq$ 2 mJy) to narrow and very deep ones (a few square arc-minutes, complete down to 50 μJy). These surveys were performed in the two main broad-band filters of ISOCAM: the 6.75 μm LW2 filter and the 15 μm LW3 filter, respectively centered on the rest-frame parts of the SED which are dominated by aromatic features (7 μm band) and by the thermal emission of very small dust grains (VSGs). We will show in the following that with a thousand times better sensitivity and sixty times better spatial resolution than IRAS, ISOCAM mid-infrared extragalactic surveys have unveiled most of the star formation in the universe below z$\simeq$1 and identified most of the galaxies contributing to the COBE-FIRAS 140 μm cosmic background. The galaxies responsible for most of the mid-infrared light are located at z$\simeq$0.7 and have a bolometric luminosity larger than $10^{11}\ L_{\odot}$. We will discuss this result considering the role of interactions and comparing the relative roles of star formation and Active Galaxy Nuclei (AGN) activities.

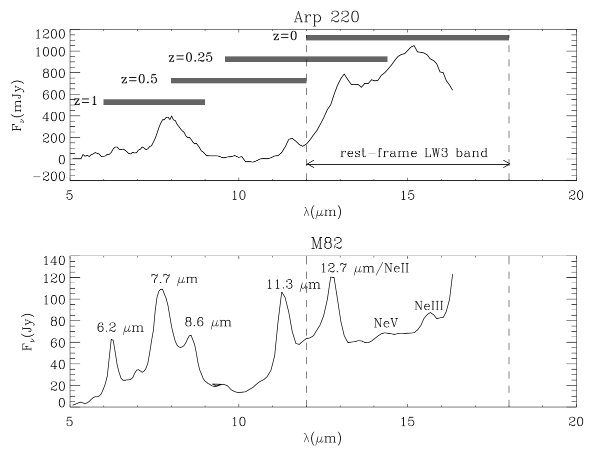

Figure 1. SEDs from ISOCAM Circular Variable Filter. The displacement of the 12-18 μm (LW3) bandpass is plotted as a function of redshift. Upper plot: Arp 220 (Charmandaris et al. 1998), high LW3 over LW2 ratio. Lower plot: M82 (Tran 1998), showing strong UIB features and low ratio of the 12-18 μm over the 5-8.5 μm band.

2. ORIGIN OF THE MID-IR EMISSION AND K-CORRECTION

The rest frame mid-IR emission of galaxies can be divided into three components:

- *UIBs:* the Unidentified Infrared Bands (UIBs), detected at 6.2, 7.7, 8.6, 11.3 and 12.7 μm as well as their underlying continuum, dominate the mid-IR emission below 12 μm (see Figure 1). The carriers of these UIBs are proposed to be aromatic carbon species such as PAHs (Polycyclic Aromatic Hydrocarbons, Léger & Puget 1984, Puget & Léger 1989, Allamandola et al. 1989) or coal grains (Papoular 1991). Below 12 μm, where the SED is dominated by the UIBs, the intensity of the interstellar radiation field produces only small changes in the shape of the spectrum. This is strong indication that the carriers of the UIBs are transiently heated by the absorption of individual photons (Boulanger 1998).
- *Warm dust (T>150 K):* Very Small Grains (VSGs) of dust heated by optical-UV photons emitted by stars produce a continuum at $\lambda >$ 10 μ**m** (Désert et al. 1990).
- *Forbidden lines of ionized gas:* NeII (12.8 μm), NeIII (15.6 μm), SIV (10.5 μm), ArII (7 μm). These lines are good indicators of the star formation activity, particularly the NeIII/NeII ratio, which is correlated to the temperature of the stars ionizing the ISM.

For local galaxies, the LW2 (5-8.5 μm) and LW3 (12-18 μm) filters measure respectively the MIR emission due to UIBs and to VSGs (emission lines are negligible in these broad-band filters). The LW3 band becomes more and more dominated by UIBs with increasing redshift, due to k-correction (see Figure 1). At z$\simeq$1, the effective LW3 band corresponds to the rest-frame LW2 band typically, so it probes UIBs, not hot dust, and above z$\simeq$1.5, dust emission (UIBs + VSGs) becomes too faint to be detected by ISOCAM.

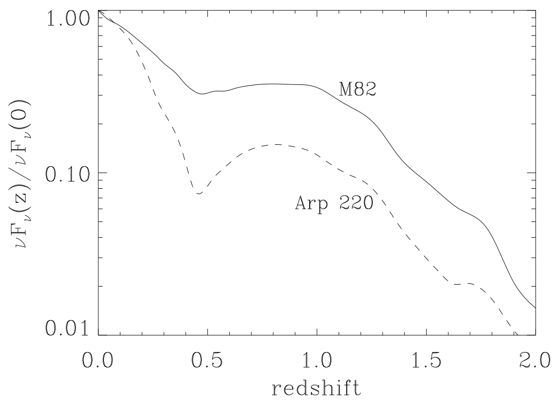

Figure 2. K-correction for the SED of M82 (plain line) and Arp 220 (dashed line) in the LW3 band (12-18 μm).

The k-corrections for the SED of M82 and Arp 220 have been plotted in Figure 2. A galaxy with an SED like M82, or Arp 220, will be fainter in νF_ν with increasing redshift up to a redshift of typically z≃0.4-0.5. Above this redshift, however, the k-correction will become negative, i.e. the galaxy will appear brighter, due to the entrance of the UIBs into the LW3 band, with a maximum around z≃0.7. Indeed, in very deep ISOCAM surveys, like in the HDF field, we will see that most of the galaxies are located above z=0.4, with a mean redshift of z=0.7. Above a redshift of z≃1.4, the k-correction falls rapidly, which explains why there is a cut-off in the redshift distribution of ISOCAM galaxies.

The MIR emission of a galaxy is correlated with its star formation activity as illustrated by the case of the Antennae galaxy (Vigroux et al. 1996, Mirabel et al. 1998). Most of the star formation in this system, as probed by ISOCAM, takes place in a source lying in the overlapping region of the two interacting galaxies, NGC 4038/4039. This source is optically faint and most of the optical emission arises from the two galactic nuclei. In this case, one would underestimate the SFR when using only the optical-UV part of the SED. It is not straightforward, however, to estimate a star formation rate in starburst regions with good precision using only the MIR flux of a galaxy. Indeed, the MIR results from a mixture of stochastic heating (UIBs) and thermal emission at high temperature (VSGs), while the FIR results from thermal emission of big grains at lower temperature. However, assuming that the physics of local galaxies is representative of that of more distant ones, one can still compare the properties of local and distant galaxies in order to quantify the evolution of galaxies.

3. DESCRIPTION OF THE ISOCAM EXTRAGALACTIC SURVEYS

Before the launch of ISO, there was a great deal of discussion about the best strategy that would both optimize the instrument capabilities and the scientific outcome of the ISOCAM mid-infrared extragalactic surveys. Large surveys would have to be shallow because they are time consuming. They would probe the brightest objects at large distances and would otherwise give good statistics for nearby objects. Pencil beams could go much deeper, although limited by the confusion limit of a 60-cm telescope, and could probe a comparable volume of the universe, with a large extent over redshift or time. Because there was no obvious answer to this question, Guaranteed Time deep surveys were divided into a shallow survey, a deep survey and an ultra-deep survey, and in order to be less biased by large-scale structures, it was decided to perform these two types of surveys in the northern (Lockman Hole) and in the southern (Marano Field) hemispheres. These fields were obviously chosen because of their low foreground Galactic emission (low zodiacal and cirrus emission) but also because they were already covered at other wavelengths and in particular in the X-ray by ROSAT and now other satellites. We will see in the next section that this choice was beneficial. It allowed us to achieve good statistics over a large flux range and in particular around 1 mJy where we found a rapid change in the slope of the number counts. The use of the lensing magnification of galaxies in the line of sight of galaxy clusters, like A2390 (Altieri et al. 1998, see also Metcalfe et al., these proceedings), allowed us to complete the number counts below 100 μJy.

These surveys were complemented by other surveys from the ISO Open Time. The European Large Area Infrared Survey (ELAIS, european consortium of 19 institutes lead by M.Rowan-Robinson, see these proceedings), for sources above ≃ 2 mJy, and the ISOCAM-HDF (P.I. M.Rowan-Robinson, Rowan-Robinson et al. 1997, Aussel et al. 1999, Désert et al. 1999) which improved the log N-log S and allowed us to identify the galaxies responsible for the infrared excess (Aussel et al. these proceedings).

Finally, the combination of all surveys is statistically significant from 50 μJy up to 50 mJy and even 300 mJy, including IRAS (see Table 1). Hence they cover four orders of magnitude in flux and therefore give a very strong constraint on the evolution of galaxies in the universe below typically z≃1.4 (upper limit due to k-correction). We have only mentioned in Table 1 those surveys used to derive the log N-log S presented in this paper. Column 3 gives the total area covered by each survey. The depth of the surveys is not homogeneous over this total area but the variation of the signal-to-noise ratio as a function of the position in the mosaic was taken into account in the source detection and in the determination of the number counts. Column 4, [F_{min},F_{max}], gives the flux range over which the number of detections is statistically significant. Column 5, t_{exp}, gives the exposure time per sky position, i.e. after co-addition of all pixels which observed the same position on the sky. This exposure time depends on the number of redundancies for this given position and was summarized with two numbers when a large fraction of the image is seen at very different depths. The last column gives the integrated contribution of the sources detected in each survey to the 15 μm cosmic background, i.e. 2.35±0.8 nW m^{-2} sr^{-1} above the 0.05 mJy level, or the less statistically significant value of *3.3±1.3 nW m^{-2} sr^{-1}* above *0.03 mJy*. Other ISOCAM extragalactic surveys were performed during ISO lifetime: Taniguchi et al. (1997) made an

Table 1. Description of the ISOCAM extragalactic surveys. We have only mentioned here those surveys used to derive the log N-log S presented in this paper.

Region	Name	area	[F_{min},F_{max}] (mJy)	t_{exp} ksec	CIRB $nW\ m^{-2}\ sr^{-1}$
A2390	Ultra-Deep Survey	6.8 arcmin^2	[0.05,0.2]	5-25	1±0.4 (43 %)
			[0.03,0.2]	*5-25*	*2±0.9 (60 %)*
HDF-North	Ultra-Deep Survey	27.4 arcmin^2	[0.1,0.3]	6.4-19.2	0.7±0.3 (30 %)
Marano Field	Ultra-Deep Survey	49 arcmin^2	[0.1,1.0]	5.4-9.7	1.35±0.5 (57 %)
Lockman Hole	Deep Survey	484 arcmin^2	[0.4,1.5]	0.9	0.5±0.2 (21 %)
Lockman Hole	Shallow Survey	0.45 deg^2	[1.2,5]	0.18	0.2±0.1 (9 %)
ELAIS fields	Very Shallow Survey	12 deg^2	[2,50]	20 sec	0.2±0.1 (9 %)

ultra-deep survey of the Lockman Hole in the LW2 7 μm band, a new ISOCAM-HDF observation was performed on the southern HDF field (P.I. M. Rowan-Robinson, Oliver et al. 1999) and both a deep and a second ultra-deep survey were also performed on the Marano Field (P.I. C. Cesarsky). Finally, one of the CFRS fields at 1415+52 was also covered by ISOCAM at 7 μm (Flores et al. 1998a) and 15 μm (Flores et al. 1998b). With a sensitivity close to the Lockman Hole Deep Survey on a smaller area, it allowed us to identify some ISOCAM detections (see Section 5).

4. DATA ANALYSIS

The data analysis of ISOCAM images appeared to be more complex than expected. The main culprits for this major difficulty are the cosmic ray impacts inducing memory effects on the detectors. It was therefore decided to develop two different techniques which were used independently on the same datasets. The resulting source lists with position and photometry were compared in order to check the robustness of the two tools. We also decided to perform some Monte-Carlo simulations in order to estimate the level of incompleteness and the photometric accuracy as a function of the source fluxes. The two techniques have been applied to the ISOCAM-HDF ultra-deep survey and published in the same issue of A&A (see Desert et al. 1999, for the 'three-beam technique', and Aussel et al. 1999, for the 'PRETI technique').

ISOCAM data are subject to standard gaussian noise (photon and readout noises) and to errors associated with the flat-fielding and dark current substraction. But the main limitation of ISOCAM deep surveys comes from its thick and cold pixels:

- because they are **thick**, ISOCAM pixel detectors are very sensitive to cosmic ray impacts (4.5 pixels receive one glitch per second). The behaviour of these glitches can be divided into three families:
  - "normal glitches": the more common ones, which correspond to electrons and last only one or two readouts. They are easily removed with a median filtering (the combination of several scales for the median allows the best correction).
  - "faders": these glitches as well as the following ones are probably associated with protons and alpha particles. They induce positive peaks in the detector response, which can last several readouts. Since ISOCAM is best used in the raster mode, a real source will look like these glitches, i.e. a positive response over the number of readouts spent on a given position of the sky.
  - "dippers": some glitches are followed by a trough extended over more than one hundred readouts.
- ISOCAM pixels are **cold**, so that electrons move very slowly within them and therefore induce a transient behaviour: a pixel will take several hundred readouts to stabilize when moving from the background to the position of a source on the sky and inversely. Because of time limitation, one is therefore limited to non stabilized signals which results in an uncertainty on the photometry. This uncertainty is strongly reduced by the partial correction of the transient behaviour and by the use of simulations to define a statistical distribution of measured fluxes for any given input flux. The final uncertainty on ISOCAM deep survey fluxes is on the order of 20 per cent.

In order to facilitate the separation of sources from cosmic ray impacts, ISOCAM surveys were performed using the raster mode with a redundancy (number of different pixels falling successively on a given sky position) ranging from 2 for the shallowest survey (ELAIS) to 88 for the deepest surveys (Marano Field Ultra-Deep survey; 64 for the HDF field).

4.1. Data reduction techniques

Four different techniques applied to the ISOCAM-HDF (North) image have been compared: the 'Saclay technique', called PRETI (Starck et al. 1998), the 'Orsay technique', called three-beam technique (see Désert et al. 1999), the 'Imperial College technique' (see Serjeant et al. 1997) and the 'Carlo Lari technique' (Lari 1999). After comparison, all four techniques reach the same result at 15 μm, and find a small difference at 7 μm. This will be discussed in a common paper that will be submitted soon. The use of simulated ISOCAM images was of great help in this work.

In the following, we give a brief description of the tool that we have developed at Saclay, PRETI. This tool is based on a multi-resolution wavelet transform which separates the temporal history of each individual pixel into several timelines, each associated with a given frequency in the variation of the signal. This technique developed by J.L.Starck consists in searching for patterns in the wavelet space (or frequency space), which correspond to the 'bad' glitches, namely the faders and the dippers. Indeed, being extended, a bad glitch will be detected over several successive scales and appear as a pattern in the wavelet, or frequency, space. After having isolated this pattern, one can then subtract it from the original signal, which in fact means subtracting a smooth function without the high-frequency contribution corresponding to the gaussian noise of the detector and where faint sources are hidden. When the data cubes have been cleaned of their glitches, they can be co-added to produce a mosaic image on which standard source detection techniques can be applied. This final step was done using again a multi-resolution wavelet transform, applied spatially instead of temporally. The techniques (1) and (2) were applied to all surveys: they agree on the photometry at the 20 per cent level and the differences in astrometry are less than the pixel size.

4.2. Simulations

We performed simulations in order to quantify the sensitivity limit (minimum detected flux, below the completeness limit), the completeness limit (flux above which all sources are detected) and the photometric accuracy. These simulations were performed with real datasets (in order to simulate realistic glitches) in which we introduced fake sources including the PSF and their modelled transient. For this, we used a long staring observation of more than 500 readouts and analyzed it as if it was a mosaic. In a raster observation, a real source will only be detected when the camera points toward its direction, while the sources present in a staring observation will remain present over the whole observation and hence will be removed as part of the low frequency component of the signal. We added to this simulated raster containing real ISOCAM noise some simulated sources with their PSF and transient behavior and then analyzed the data with the different techniques described above. The simulations were used to set the parameters of the data reduction technique and then to estimate the rate of detections of sources per flux bin as well as the error bar on the photometry. We used them to calculate the 90 per cent confidence level error bars shown in the log N-log S (Figure 4).

5. NATURE OF THE GALAXIES DETECTED IN ISOCAM EXTRAGALACTIC SURVEYS

The detailed study of the properties of ISOCAM galaxies is only beginning but with the help of the large number of multi-wavelength observations of the HDF (Williams et al. 1996) and of the CFRS field at 1415+52 (Lilly et al. 1995), the second most observed field at all wavelengths after the HDF, one can already begin this work.

In the CFRS field, Flores et al. (1998b) have found that two thirds of the galaxies detected by ISOCAM at 15 μm down to a flux density of 250 μJy were starburst galaxies as probed by their radio emission at 6 and 21 cm. They recalculated the history of the metal production or star formation per unit volume of the universe, plotted by Madau (1996) and Lilly (1995) using only the optical and UV information on CFRS galaxies, for the dust extinction and found a correction factor of about three. Hence, optical-UV light would only probe 25 per cent of the star formation in the universe below z=1. This strong uncertainty on this correction factor needs to be reduced by more statistics not only on infrared galaxies but also on template SEDs of local galaxies, since the database of Schmitt et al. (1998) that they used only contains 59 galaxies. However, the excess that we find in the number counts (see Section 6) and the strong 15 μm cosmic background (see Section 7), confirm that this plot should indeed be corrected by a non negligible factor for dust extinction.

In the ISOCAM-HDF, we identified 36 sources, among the 44 detections at 15 μm, with an optical counterpart from the catalog of Barger et al. (1999) limited to I<22.5. The mean redshift of these galaxies is $< z > \simeq 0.7$ and most of them are located between z=0.4 and 1.4 (as expected from the k-correction, see Section 2). The mean ratio of their effective fluxes at 15 μm over the K band is close to that found for M82, if it was redshifted at z=0.7. Hence, we used the SED of M82 to determine the rest-frame 15 μm flux of these galaxies, although we are aware of the strong uncertainty associated with this estimate. The mean 15 μm luminosity of ISOCAM-HDF galaxies, is about ten times larger than that of M82 so this assumption should be quite conservative since ISOCAM-HDF galaxies should be even more active than M82 and closer to LIGs and ULIGs. Assuming that ISOCAM-HDF galaxies present SEDs similar to that of M82, their mean infrared luminosity would be of the order of $3 \times 10^{11}\ L_{\odot}$ and they would be classified as LIGs (Sanders & Mirabel 1996). For a typical ratio of M/L_K of about 1.5 (Charlot, private communication), they would have a mean mass of $1.5 \times 10^{11}\ M_{\odot}$.

5.1. Origin of the infrared emission: star formation versus AGN

The major source for the huge energy radiated by these galaxies should be star formation activity. Indeed, only a few per cent of AGNs have been identified optically, in the radio or in the X-ray in our sample of ISOCAM galaxies (see also Aussel et al., these proceedings). Genzel et al. (1998) found that only 20-30 per cent of the energy radiated by local ULIGs is powered by AGN activity, and this fraction should be even lower for our galaxy sample since they are mainly LIGs. However, the fraction of galaxies harboring an AGN (but not dominated by its radiation) should be much larger: Genzel et al. (1998) detected the presence of an AGN in at least 50 per cent of the ULIGs that they studied. It was recently suggested by Fabian & Iwasawa (1999) that if the hard X-ray background detected around 30 keV by HEAO1 were produced by dusty AGNs (Seyferts 2) as indicated by its flat slope, then these dusty AGNs should produce a contribution to the CIRB of $\simeq 3\ \mathrm{nW\,m^{-2}\,sr^{-1}}$, i.e. between 10 and 20 per cent of the CIRB measured by COBE-DIRBE. Such a contribution of AGNs to the CIRB would be reasonable if most of it was produced by LIGs and ULIGs and ISOCAM surveys seem to favor this option.

5.2. Optical properties of the faint 15 μm galaxies

Using available data on the HDF, especially in the optical and NIR from Barger et al. (1999), we find that the optical colors of the galaxies detected above 100 μJy (ISOCAM-HDF completeness limit, Aussel et al. 1998) do not strongly differ from field galaxies (see Aussel et al., these proceedings). Hence it would not have been possible to discriminate the ISOCAM galaxies from their optical colors only.

The study of the spectroscopic properties of these galaxies is still underway (spectra made available to the community by the group of the University of Hawaii, Barger et al. 1999). However, we have already found that a large fraction of ISOCAM-HDF galaxies exhibit weak emission lines and strong Balmer H_δ absorption lines characteristic of the presence of a large number of A stars with an age of typically one Gyr. On the other hand, galaxies with strong emission lines detected in the field are not detected at 15 μm. We also found the same result in the list of spectra obtained after a multi-spectroscopic follow-up of 15 μm ISOCAM detections in the field of a nearby galaxy cluster, A1689 (P.I. P.A.Duc, see Fadda et al., these proceedings). Flores et al. (1998b) had already found the same result on the CFRS field at 1415+52 and interpreted this result as a proof that the galaxies with dust-enshrouded star formation detected by ISOCAM have been forming stars during the last few 10^8 years. The lack of detection by ISOCAM of emission line galaxies was suggested to be due to the low metallicity of these galaxies. A completely independent spectroscopic survey of post-starburst galaxies in clusters of galaxies located at redshifts z=0.4-0.5 seems to already confirm this result (Dressler et al. 1999, Poggianti et al. 1999). They propose that galaxies with weak or no emission lines but strong Balmer H_δ absorption lines, that they call e(a), are most probably dust-enshrouded starbursts using only optical arguments based, for example, on the ratio of the OII over H_α equivalent widths. A possible scenario for the origin of these dusty starbursts galaxies, found both in ISOCAM extragalactic surveys and in the optical spectroscopic surveys of distant clusters, could be linked to the effects of galaxy interactions. Indeed, Poggianti & Wu (1999) find an exceptionally high fraction of e(a) spectra among local LIGs where the fraction of interacting galaxies is very high. ISOCAM detections of CFRS galaxies also present morphological signatures of interactions and we find a morphological segregation with increasing redshift in the ISOCAM-HDF with more interacting galaxies with increasing redshift (see Figure 3).

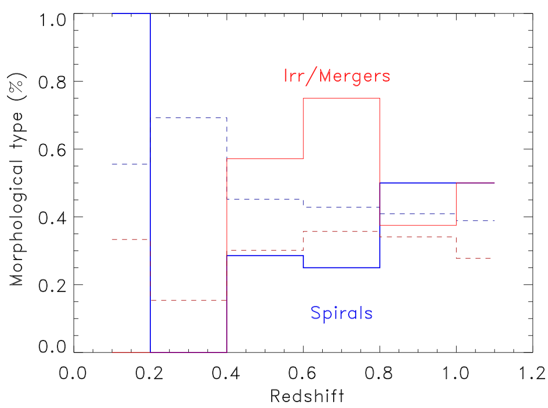

Figure 3. Fraction of Peculiar versus Spiral galaxies in the HDF+Flanking fields for galaxies detected at 15 µm (plain lines) and all galaxies (dashed lines). Above z≃0.4, peculiar galaxies dominate the distribution of galaxies detected with ISOCAM while optically selected galaxies are mainly spirals. This population of peculiar galaxies may produce the rapid evolution below the 1 mJy level found in the 15 µm number counts.

6. NUMBER COUNTS

The most impressive result after three years of data analysis and calibration is the consistency of all different surveys as shown by the log N-log S plot over four orders of magnitude in flux density when including the IRAS point (Figure 4). The number counts are perfectly fitted by a no-evolution model normalized to IRAS (Franceschini 1998) above the 1 mJy level typically, while they strongly diverge from this law below 1 mJy, with an increasing difference which reaches a factor of 10 at the faintest fluxes (around 50 μJy). Although k-correction can be negative as shown in Figure 2 and therefore could explain a part of the excess at low fluxes, it can certainly not reproduce an excess of a factor of 10 as we find here. The detailed modelling of this evolution is quite complex and a paper will be devoted to this subject (Franceschini et al., 1999). However, the increasing fraction of interacting galaxies as a function of redshift detected in the ISOCAM-HDF (Figure 3) may explain the behavior of the log N-log S, if LIGs were to begin to dominate the number counts above z≃0.4 and completely dominate them at z≃0.7. There was already a hint of such a strong evolution of LIGs and ULIGs in the analysis of local ULIGs by Kim & Sanders (1998, see Section 1).

We learned from the previous section about the nature of the galaxies that were detected in ISOCAM surveys that this excess is produced by a few LIGs, two orders of magnitude less numerous than optical galaxies detected in the HDF (see Aussel et al. 1998). Hence, the luminosity function of galaxies should be different at z≃0.7, the mean redshift of ISOCAM-HDF galaxies, than locally, favoring luminous galaxies. The flattening of the log N-log S at low fluxes implies that we are not far from having identified most of the galaxies producing the mid-infrared background and indicates that we should be able to give a good constraint on the cosmic background produced by these sources.

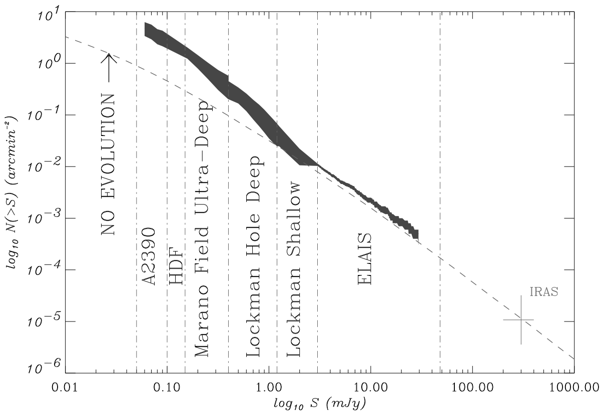

Figure 4. log N(S)- Log S: number of objects, N, detected at 15 μm above a given flux level, S(mJy). The data are consistent although they come from 6 different origins (see Table 1). Dashed line: no evolution from IRAS (Franceschini et al. 1998).

7. COSMIC INFRARED BACKGROUND

Integrating the 15 μm number counts over the whole flux range, one finds a conservative value of about 2.35 ± 0.8 nW m^{-2} sr^{-1} above 50 μJy and 3.3$\pm$1.3 nW m^{-2} sr^{-1} above 30 μJy, with less confidence. This corresponds to 30-45 per cent of the cosmic background seen with the HST in the I-band (7 nW m^{-2} sr^{-1}, Lagache et al. 1999). This fraction is very high since locally IRAS showed that it is the total infrared luminosity of galaxies, i.e. from 8 to 1000 μm, which is about 30 per cent of that from starlight (Soifer & Neugebauer 1991). Assuming a conservative SED one would then expect these galaxies to emit at least as much energy in the far infrared than in the optical. In particular, one can estimate the effective ratio of their 140 μm over 15 μm energy densities at the mean redshift of 0.7 and compare it to the COBE-DIRBE value. A conservative ratio would be of the order of three, like for M82, although a more realistic one would be higher than that. In this conservative case, they would produce more than 50 per cent of the COBE-DIRBE CIRB found by Lagache et al. (1999, $\simeq 15.3 \pm 9.5$ nW m^{-2} sr^{-1}) and about 30 per cent of the value found by Hauser et al. (1998, $\simeq 25.1 \pm 7$ nW m^{-2} sr^{-1}). This is only a lower limit since a ratio of 3 is probably too conservative and since the number counts have not completely flattened yet. The minimum ratio of the energy densities at 140 μm over 15 μm is about 10, hence if the faint 15 μm galaxies were moderate ULIGs, they would produce the whole COBE-DIRBE background.

8. CONCLUSION

ISOCAM extragalactic surveys are nearly four orders of magnitude more sensitive than IRAS in the 15 μm range. They teach us that a few luminous and massive infrared galaxies located at a mean redshift of 0.7 produce most of the 15 μm and probably also DIRBE-140 μm cosmic background. Assuming a conservative spectral energy distribution for these galaxies, one finds that they emit as much energy in the infrared than the two orders of magnitude more numerous optical galaxies detected in the HDF. The galaxies producing this infrared excess present morphological signs of interaction. Hence, both dust extinction and galaxy interactions played a major role in galaxy evolution since z$\simeq$1.

Additional conclusions will be reached only after having collected a statistically larger sample of optical counterparts to ISOCAM galaxies, in particular, in the ultra-deep surveys performed in the Marano Field where we have detected hundreds of very faint 15 μm galaxies. The large amount of energy released by these galaxies will be one of the key questions for the next spatial telescopes, like SIRTF and FIRST, and at larger redshifts for the ground-based submillimeter interferometer LSA-MMA. The Next Generation Space Telescope (NGST) would give a unique insight into the origin of their activity, and in particular the proportion of the energy due to AGN activity, if it were to observe up to 25-30 μm.

ACKNOWLEDGMENTS

We would like to thank Suzanne Madden for very fruitful scientific discussions and for her advises in the redaction of this paper.

REFERENCES

Allamandola, L.J., Tielens, A.G.G.M., Barker, J.R., 1989, ApJS 71, 733

Altieri B., Metcalfe L., Kneib J.P. 1998, A&A, in press, astro-ph/9810480

Aussel H., Cesarsky C., Elbaz D., Starck, J.L. 1998, A&A 342, 313

Barger A. J., Cowie L. L., Trentham N., Fulton E., Hu E. M., Songaila A., Hall D. 1999, AJ 117, 102

Boulanger, F. 1998, *Star Formation with the Infrared Space Observatory, Lisbon, Portugal*, J.Yun & R.Liseau (Eds.), ASP Conf. Ser., Vol.132, p.15.

Charmandaris, V., Mirabel, I.F., Tran, D., et al., 1998, in *Extragalactic Astronomy in the Infrared*, T.Thuan, G. Mamon, J.T.T.Van (eds), XVIIth Moriond Astr. Meeting, Ed. Frontière, p.283

Désert F.-X., Boulanger F., Puget J.-L. 1990, A&A 237, 215

Désert, F.-X., Puget, J.-L., Clements, D.L., Pérault, M., Abergel, A., Bernard, J.-P., Cesarsky, C.J. 1999, A&A 342, 363

Djorgovski, S., Thompson, D. 1992, in IAU Symp. 149, 'The Stellar Populations of Galaxies', ed. B.Barbuy and A.Renzini (Dordrecht: Kluwer), p.337

Dressler, A., Smail, I., Poggianti, B.M., 1999, ApJS, in press, astro-ph/9901263

Fabian, A.C., Iwasawa, K., 1999, MNRAS in press, astro-ph/9901121

Flores H., Hammer F., Désert F.-X. et al. 1998a, A&A, in press, astro-ph/9811201

Flores H., Hammer F., Thuan T. et al. 1998b, ApJ, in press, astro-ph/9811202

Franceschini A., Toffolatti L., Mazzei P., Danese L., De Zotti G., 1991, A&A Suppl.Ser. 89, 285

Franceschini A., Mazzei P., de Zotti G., Danese L. 1994, ApJ 427, 140

Franceschini, A. 1998, in *Extragalactic Astronomy in the Infrared*, T.Thuan, G. Mamon, J.T.T.Van (eds), XVIIth Moriond Astr. Meeting, Ed. Frontière, p.509.

Franceschini, A. et al. 1999, in preparation

Genzel R., Lutz D., Sturm E., Egami E., Kunze D. et al. 1998, ApJ 498, 579

Guiderdoni B., Bouchet F.R., Puget J.-L., Lagache G., Hivon E. 1997, Nature 390, 257

Hacking, P.B., Houck, J.R., 1987, ApJS 63, 311

Hammer F., Flores H., Lilly S.J., et al. 1997, ApJ 481, 49

Hauser, M.G., Arendt, R.G., Kelsall, T., 1998, ApJ 508, 25

Hughes D. H., Serjeant S., Dunlop J., Rowan-Robinson M., Blain A. et al. 1998, Nature 394, 241

Kim, D.C., Sanders, D.B. 1998, ApJS 119, 41

Lagache G. et al. 1999, A&A, in press.

Lari, C. 1999, in preparation

Léger A., Puget J.L. 1984, A&A 137, L5

Lilly S. J., Le Fèvre O., Hammer F., Crampton D. 1995, ApJ 460, L1

Lonsdale, C.J., Hacking, P., 1989, ApJ 339, 712

Lonsdale, C.J., Hacking, P., Conrow, T.P., Rowan-Robinson, M., 1990, ApJ 358, 60

Madau P., Ferguson H. C., Dickinson M. E., Giavalisco M., Steidel C. C., Fruchter A. 1996, MNRAS 283, 1388

Meurer G. R., Heckman T. M., Lehnert M. D., Leitherer C., Lowenthal J. 1997, AJ 114, 54

Mirabel I.F., Vigroux L., Charmandaris V., Sauvage M., Gallais P. *et al.* 1998, A&A 333, L1

Oliver S. J. et al. , 1996, In *Wide-Field Spectroscopy and the Distant Universe*, ed. SJ Maddox, Singapore World Sci., p.264

Oliver S. J. et al. , 1998, IAP workshop on Wide-Field Surveys.

Papoular, R., Reynaud, C., Nenner, I., 1991, A&A 247, 215

Pettini M., Steidel C. C., Adelberger K. L., Kellogg M., Dickinson M. et al. 1997, to appear in 'ORIGINS', ed. J.M. Shull, C.E. Woodward, and H. Thronson, (ASP Conference Series), astro-ph/9708117

Puget J.-L. Léger, A. 1989, Ann.Rev.Ast.Ap. 27, 37

Poggianti, B.M., Smail, I., Dressler, A., 1999, ApJ, in press, astro-ph/9901264

Poggianti, B.M., Wu, 1999, in preparation

Puget J.-L. , Abergel A., Bernard J.-P., Boulanger F., Burton W. B. *et al.* 1996, A&A 308, L5

Puget, J.-L. *et al.* 1999, these proceedings

Scoville, N.Z., Soifer B.T. 1991, in *Massive Stars in Starbursts*, ed. Leitherer C., Walborn N., Heckman T., Norman C., Cambridge Univ. Press, p.233

Searjeant, S.B.G., Eaton, N., Oliver, S.J., et al. 1997, MNRAS 289, 457

Soifer B.T., Neugebauer G. 1991, AJ 101, 354

Spinoglio L., Malkan M.A., Rush B., Carrasco L.,Recillas-Cruz E. 1995, ApJ 453, 616

Starck J.-L., Aussel H., Elbaz D., Cesarsky C. J., 1998, in *Extragalactic Astronomy in the Infrared*, T.Thuan, G. Mamon, J.T.T.Van (eds), XVIIth Moriond Astr. Meeting, Ed. Frontière, p.509.

Steidel C.C., Giavalisco M., Pettini M., Dickinson M., Adelberger K.L. 1996, ApJ 462, L17

Rowan-Robinson M., Mann R. G., Oliver S. J., Efstathiou A., Eaton N. et al., 1997, MNRAS 289, 490

Sanders, D.B., Mirabel, I.F., 1996, *Ann. Rev. Astron. Astrophys.* 34, 749

Saunders W., Rowan-Robinson M., Lawrence A., Efstathiou G., Kaiser N. et al. 1990, MNRAS 242, 318

Schmitt, H., Kinney, A., Calzetti, D., Storchi-Bergmann, T., 1997, AJ 114, 592

Serjeant, S.B.G., Eaton, N., Oliver, S.J. 1997, MNRAS 289, 457

Smail I., Ivison R. J., Blain A. W. 1997, ApJL 490, 5

Taniguchi, Y., Cowie, L.L., Sato, Y. 1997, A&A 328, L9

Tran D. 1998, PHD thesis, Université de Paris XI.

Vigroux L., Mirabel I. F., Altieri B., Boulanger F., Cesarsky C. J. et al. 1996, A&A 315, L93

White, S. D. M., Frenk, C. S. 1991, ApJ 379, 25

Williams, R.E., Blacker, B., Dickinson, M. et al. 1996, AJ 112, 1335

LONG WAVELENGTH COSMOLOGICAL SURVEYS WITH ISO

J-L. Puget & G. Lagache
Institut d'Astrophysique Spatiale, Orsay, France

ABSTRACT

We review ISO deep surveys at wavelengths longer than 100 μm beyond which the redshift of the peak emission of starburst galaxies (at 60 to 80 μm) tends to favour distant sources. The number counts of sources at 175 μm show a very steep slope between 100 mJy and 1 Jy implying a strong cosmological evolution. It is also shown that deep surveys in low cirrus regions show the structure of the background with a large signal to noise ratio. The anisotropies of the background are dominated at angular scales close to the angular resolution by the structure of the extragalactic background which will, thus, be a very useful tool for cosmological studies until large passively cooled telescopes in space become available.

Key words: Far-infrared; cosmology.

1. THE FAR INFRARED SKY AT HIGH LATITUDE

One of the important results brought by the IRAS survey has been the discovery of a population of galaxies radiating most of their energy in the far infrared. These galaxies are often ultraluminous and in fact there is a tendency for starburst galaxies to have the infrared to optical luminosity correlated with the bolometric luminosity (Sanders and Mirabel 1996). It is also well established that these ultraluminous galaxies are often associated with interacting or merging galaxies. These discoveries raised three crucial questions for galaxy formation and evolution: i) what is the fraction of the stellar radiation in galaxies which has been absorbed by dust and reradiated in the infrared and the evolution of this fraction with redshift? ii) what fraction of the integrated infrared luminosity is coming from normal $L_\star$ spirals with respect to the fraction coming from mergers? iii) is the infrared the tool to trace the history of merging in the formation of galaxies?

A typical ultraluminous infrared galaxy (ULIRG) has a spectral energy distribution (SED) peaking around 60 to 80 μm but radiates a significant fraction of its energy in the mid infrared (10 to 20 % of the energy between 6 to 15 μm) in form of aromatic features (at 6.2, 7.7, 8.6, 11.3 and 12 μm). When such a spectrum is redshifted strong non monotonous K-corrections will affect the observed flux as a function of redshift. Figure 1 illustrates this point. The flux density from a typical 10^{12}L$_\odot$ ULIRG is displayed for redshifts between 0.1 and 10. In the submillimetre range the K-correction (defined as the ratio of the rest-frame flux density over the redshifted one) is larger than unity: the decrease of the flux with redshift is compensated by the increase due to the shift of the peak emission towards the observed wavelength band. This effect is strongest at wavelengths longer than 1 mm. The longest wavelength observable with ISO with a broad filter and a good sensitivity is centred on 175 μm (the C-160 filter). At this wavelength the K-correction increases up to about 2.8 at a redshift of about 1.2 and is larger than 2 for redshifts from 0.5 to 2 (see Dole et al. in these proceedings). At 90 μm the K-correction factor starts to decrease for redshifts larger than 0.2. Observations at 175 μm are thus much more powerful for cosmological studies than 90 μm ones. This conclusion is reinforced by the behaviour of the C-200 detector, which does not present the difficulties associated with the use of the C-100 detector: strong memory effects, spontaneous spiking,...

The far infrared sky at high latitudes has essentially three components: the zodiacal background, the emission from Galactic cirrus and the emission from infrared galaxies at all redshifts.

The zodiacal emission at long wavelengths has a minimum brightness at high ecliptic latitudes

$$B_{zod} = 0.7 \left(\frac{\lambda}{175\mu m}\right)^{-3} \quad MJy/sr.$$

The average cirrus emission is given by

$$B_{cirrus} = 1.2 \left(\frac{N_H}{10^{20}cm^{-2}}\right) \quad MJy/sr$$

at 175 μm falling to 0.5 at 90 μm . The cirrus has a filamentary structure, which exhibits a spatial power spectrum, which has been established from the IRAS data by Gautier et al. (1992) and is given by:

$$P(k) = 1.4\,10^{-12} B_0{}^{-3} \left(\frac{k}{k_0}\right)^{-3} \quad Jy^2/sr$$

with $k_0 = 10^{-2} arcmin^{-1}$.

Proceedings of the Conference "The Universe as seen by ISO", Paris, France, 20–23 October 1998 (ESA SP-427, March 1999)

The cosmologically interesting component is the emission from distant infrared galaxies. In a deep survey, this component can be separated into galaxies detected individually and a background of unresolved objects either because of the sensitivity limit of the survey or because individual sources cannot be properly isolated and their flux measured because of confusion. The integrated cosmic background has been detected at long wavelengths with the FIRAS and DIRBE instruments aboard the COBE satellite (Puget et al. 1996; Schlegel et al. 1997; Fixsen et al. 1998; Hauser et al. 1998; Lagache 1998; Lagache et al. 1999). Using the FIRAS data and the 140 and 240 μm DIRBE data, we can derive the value of the cosmic background at 175 μm: 0.8 MJy/sr. The main uncertainty is due to the difficulty to properly evaluate the emission from interstellar dust associated with the ionised gas. Hauser et al. (1998) finds it to be zero when Lagache et al. (1999) finds a non negligible contribution.

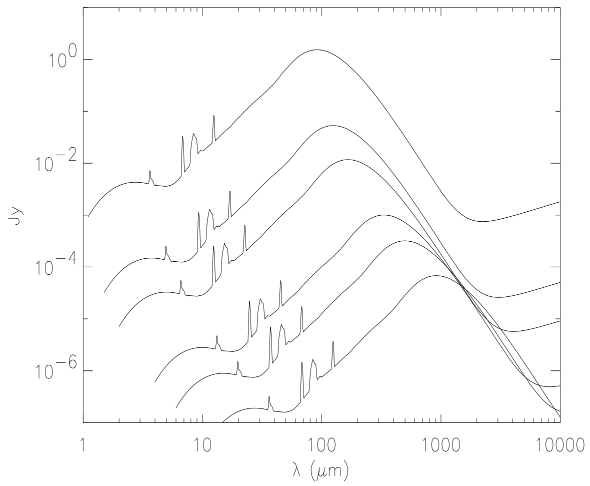

Figure 1. Observer-frame model spectra of a $10^{12}\,L_\odot$ galaxy at increasing redshift 0.1, 0.5, 1., 3., 5, 10., for a cosmology $\Omega_0 = 1$ and h=0.5 (from Maffei 1994)

2. ISO OBSERVATIONS

This section will review only observations at wavelengths longer than 100 μm. Several groups have carried out deep surveys. Kawara et al. (1998) made a deep survey at 175 μm in the Lockman hole with a sensitivity limit of 100 mJy and detected 45 sources in a 1.1 square degree field. The most extensive cosmological deep survey at long wavelength was carried out by the FIRBACK collaboration (Puget et al. 1999). In the initial region surveyed (roughly a quarter of a square degree in the Marano field) 24 sources were found with fluxes larger or equal to 100 mJy. The complete survey covered about one square degree in the same region and 3 square degrees in the Northern hemisphere in the ELAIS N1 and N2 fields (this Northern survey is partially observed together with the ELAIS collaboration - see M. Rowan-Robinson et al. these proceedings). Source counts have now been done in the whole survey. The results are presented by Dole et al. (1999).

The photometric calibration for point sources used by the FIRBACK collaboration is nearly equivalent to the PHOT calibration. Nevertheless the FIRBACK team have calibrated the extended background using the DIRBE results and use the beam pattern measurements done using Saturn (Toth et al. 1997). Table 1 gives the values of the background in the field derived when different values of the beam pattern integral are used to calibrate the extended emission. Flux received by a pixel to brightness in the same pixel are related by:

$$B(MJy/sr) = F(Jy)/\Omega(sr)$$

With the larger values of the solid angle given by Saturn measurement, the value of the background found in this field agrees with the DIRBE estimate for the same wavelength within the uncertainties (about 0.4 MJy/sr). We adopt the value derived from the Saturn measurements for our studies of the structure of the background. This has important astrophysical implications. The background in the Marano field can be decomposed into its three components:

Zodiacal emission: 0.7 MJy/sr

Extragalactic background: 0.8 MJy/sr

The remaining Cirrus emission is also given in Table 1. Using the Gautier et al. (1992) calibration of the power spectrum of the fluctuations of the Cirrus brightness gives a good agreement with the observations only if the Cirrus brightness is around 1.7 MJy/sr (Lagache 1998). Gautier et al. (1992) have found that the normalisation of the power spectrum scales with the third power of the brightness. A value of the cirrus brightness of 6 MJy/sr would lead to a cirrus fluctuation 50 times larger and thus much larger than the observed one.

Table 1. Derived Values of the cirrus contribution using different beams

beam	Ω sr	B MJy/sr	cirrus MJy/sr
PIA 6.5	$1.88\,10^{-7}$	7.90	6.40
PIA 7.2	$2.75\,10^{-7}$	5.30	3.80
Puget et al.	$4.07\,10^{-7}$	3.65	2.15
DIRBE		3.16	1.66

Using the Gautier et al. (1992) prediction of the cirrus fluctuations, the extrapolation of the source counts and the measurement noise, we can interpret the background fluctuations observed with ISOPHOT. The measurement noise can be estimated rather accurately from the comparison of the 4 independent rasters carried out exactly in the same way. Such an observation strategy does not provide proper sampling of the sky but was used in the first FIRBACK observation (first quarter of a square degree in the Marano field) to establish the feasibility of the observations of the extragalactic background fluctuations with ISO. Many people working in this field contested the feasibility of such an observation. The observations in the other fields were carried out with rasters shifted with respect to each other by half a pixel to provide proper sampling.

The interpretation of the background fluctuations power spectrum with its three components is summarised in Figure 2 (Lagache 1998). The observed power spectrum is in good agreement with the observations when we use for the cirrus component an average brightness of 1.7 MJy/sr. The power spectrum of the cirrus fluctuations would rise by a factor 70 if we would use the PIA 6.5 calibration and 14 if we would use the PIA 7.2 calibration. The level of fluctuation is thus, although more indirect, another indication that the extended source calibration at 175 μm provided by PIA is too low by a factor of order 1.5.

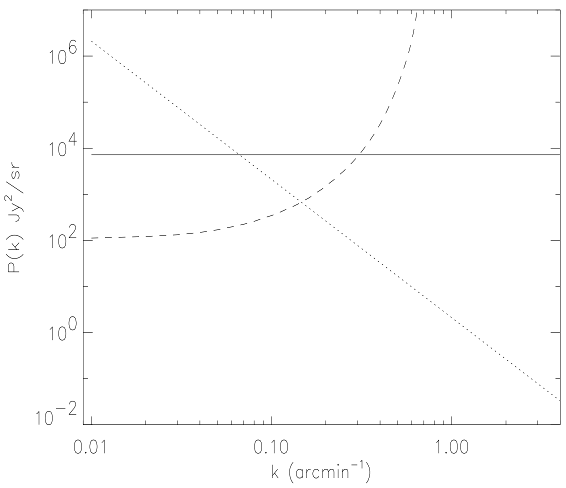

Figure 2. Predicted power spectra for the FIRBACK Marano1 field; line: source confusion noise; dash-dash: instrumental noise; dot-dot: cirrus confusion noise

Other deep observations have been carried out with ISOPHOT at long wavelengths. Stickel et al. (1998) made two long scans through the Coma cluster at 120 and 185 μm. They observe fluctuations of the background. This is demonstrated by strong correlation between the pattern of fluctuations observed at the two wavelengths. The amplitude of these fluctuations are typically 0.5 MJy/sr peak to peak on a total flux of 4 to 5 MJy/sr. Color ratios ($\frac{120}{185}$) of these observations present a maximum centred on the Coma cluster. The statistical significance of this maximum is weak but this excess is an interesting hint for the presence of dust in the cluster, which would have a colour ratio slightly warmer than the other components of the background fluctuations.

Herbstmeier et al. (1998) compiled a rather inhomogeneous set of observations of fields with no strong source but with different levels of cirrus content. The integration time per sky pixel and thus the measurement noise in these observations vary by large factors and the absence of exactly repeated observations makes the precise estimate difficult. Nevertheless these observations form a useful set to check if the two components of the background fluctuations identified in the FIRBACK observations (cirrus and extragalactic background) are present in these fields as expected. The calibration adopted by Herbstmeier et al. in this paper is based on the DIRBE brightness and thus consistent with the FIRBACK one.

Two results emerge from this study. They study the background fluctuations as a function of the average brightness. They find a dependence similar to the one found by Gautier et al. (1992) when they use a DIRBE calibration for the brightness. Nevertheless we now know that for regions with low cirrus content, the extragalactic background and cirrus emission contribute about equally to average brightness. Furthermore, the extragalactic background contributes very significantly to the fluctuations especially at high spatial frequencies. A direct comparison of total level of brightness and fluctuations is not any more the right approach to this question except in the Cepheus field where the interstellar emission is clearly dominant. The second set of results is composed of power spectra of fluctuations in the different fields and is reproduced in Figure 3.

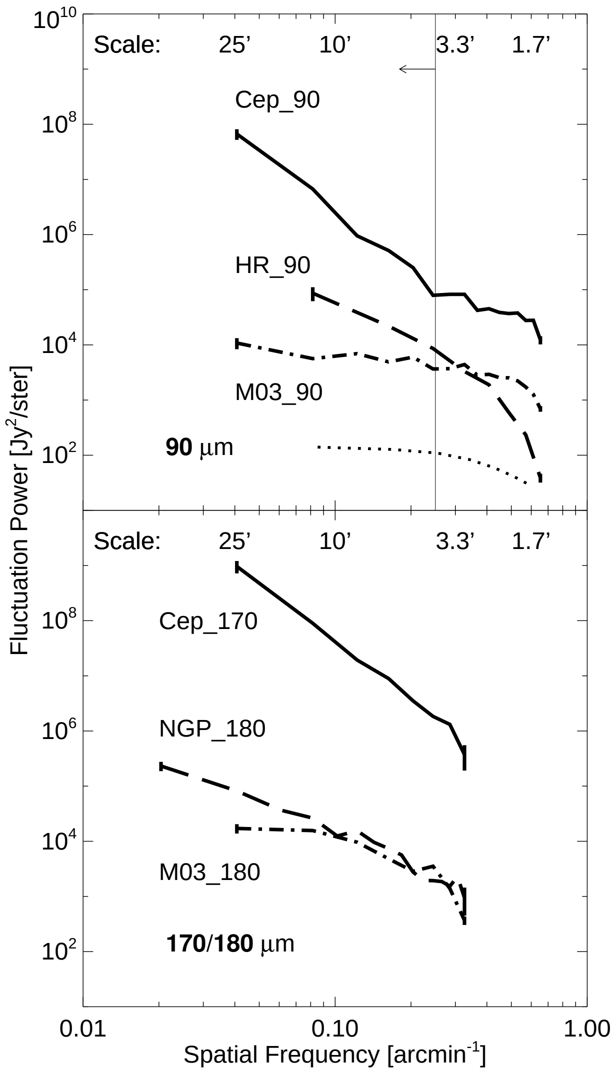

Figure 3. Measured total power spectra (from Herbstmeier et al. 1998)

A trend is clearly observable in this plot: the power spectrum is flatter for low brightness regions. This is predicted because the extragalactic background fluctuations are expected to give a more or less white noise, i.e. a flat power spectrum when the cirrus power spectrum is steep (k^{-3}). As already mentioned the measurement noise is not homogeneous in these observations and not easily measured. The flattening at high spatial frequencies in the Cepheus power spectrum is due to measurement noise. The M03 and NGP fields have a much lower measurement noise. The level of the rather flat power spectrum observed is around $10^4 \mathrm{Jy}^2 \mathrm{sr}^{-1}$ in the 3 to 10 arc minutes angular scale range as expected for the extragalactic component in Figure 2. We thus conclude that these observations exhibit fluctuations dominated by the extragalactic background.

3. COSMOLOGICAL IMPLICATIONS

Models for Galaxy evolution including the effect of extinction and the radiation coming out in the far infrared and extreme objects where this radiation becomes dominant have been developed in the last few years (Franceschini et al. 1998, Guiderdoni et al. 1998). The discovery of an intense far infrared background using the COBE data suggested that observations of galaxy evolution and of the star formation history in the universe using ultraviolet and optical emission as observed with large ground based telescopes and the Hubble Space Telescope might be missing an important part of the story.

The standard model for the development of structures and galaxies starts from a scale free power spectrum of initial density fluctuations in the early universe. It then assumes that gravitational instability leads to the appearance of cold dark matter halos in which baryonic matter condenses to form first small galaxies and later by merging larger galaxies and clusters. Although many questions remain unresolved, this model links together many observations in a globally coherent picture. In this picture merging is a very important mechanism to build galaxies as we see them at present. A critical but unanswered question is how much of the star formation takes place during quiescent phases of galaxy evolution versus the star formation associated with the merging process itself.

At present interacting and merging galaxies are known to be often ultraluminous starburst galaxies radiating mostly in the infrared. Observations in the far infrared are needed for two reasons. The first one is to establish what fraction of the nucleosynthesis energy radiated by stars has been absorbed by dust and thus is not observable in the UV and optical ranges. The second is to find out what fraction of stars in a massive galaxy have been formed during the mergers undergone by this galaxy. If mergers and interacting galaxies make most of the ULIRG not only today but also in the past we expect that their relative density will increase in the past like the square of the density of galaxies. We thus expect a very strong evolution of ULIRGs at least at low and moderate redshifts. The intensity of the far-infrared background at its peak and its rather flat spectrum at long wavelengths ($B_\nu \propto \nu^2$ for $300 \mu m < \lambda < 1 mm$) implies such a strong evolution (Gispert et al. 1999). The far-infrared production rate increases by a factor 30 from redshift 0 to redshift 2 and stays almost constant up to redshift 4. The ISO deep surveys at 15 μm (Aussel 1999) and 175 μm give very steep number counts which can be explained only by strong cosmological evolution. These counts are in excellent agreement with predictions of semi-empirical models for galaxy formation and evolution, which accounts for the far-infrared extragalactic background. It is thus likely that the faint infrared sources observed with ISO are the brighter end of the population of sources making the background.

4. SUMMARY AND CONCLUSIONS

Limited sensitivity but even more confusion limit due the limited size of cryogenically cooled telescopes (60 cm for ISO, 85 cm for SIRTF) will not allow to observed deep and faint enough sources in the mid and far infrared before large passively cooled space telescopes with low emissivity and cryogenically cooled instruments are flown about 10 years from now (FIRST and NGST) to fully answer these questions.

The ISO observations have shown nevertheless that the structure of the background due to faint sources beyond the confusion limit will be a very useful tool.

ACKNOWLEDGEMENTS

We thank the ISOPHOT team for many useful discussions.

REFERENCES

Aussel, H. 1999, PhD thesis, Paris XI University

Dole, H. et al. 1999, to be submitted to A&A

Fixsen, D.J. et al. 1998, ApJ, 508, 123

Franceschini, A. et al. 1998, MNRAS 296, 709

Gautier, T.N.III et al. 1992, AJ 103, 1313

Gispert, R., Lagache, G. & Puget, J.L., 1999, to be submitted to A&A

Guiderdoni, B. et al. 1998, MNRAS 295 , 877

Hauser, M.G. et al. 1998, ApJ, 508, 25

Herbstmeier, U. et al. 1998, A&A 332, 7

Kawara, K. et al. 1998, A&A 336, L9

Lagache, G. 1998, PhD thesis, Paris XI University

Lagache, G. et al. 1999, A&A, in press

Maffei, B., 1994, PhD thesis, Paris XI University

Puget, J.L. et al. 1996, A&A 308, L5

Puget, J.L., Lagache, G. et al. 1999, A&A, in press

Sanders, W. & Mirabel, I.F. 1996, ARAA 34, 749

Schlegel, D.J. et al. 1998, ApJ 500, 52539

Stickel et al. 1998, A&A 329, 55

Toth, L.V., Abraham, P., Stickel, M. 1998, internal ISOPHOT report

THE EUROPEAN LARGE AREA ISO SURVEY: ELAIS

M. Rowan-Robinson[1], S. Oliver[1], A. Efstathiou[1], C. Gruppioni[1], S. Serjeant[1], C.J. Cesarsky[2], L. Danese[3], A. Franceschini[4], R. Genzel[5], A. Lawrence[6], D. Lemke[7], R. McMahon[8], G. Miley[9], I. Pérez-Fournon[10], J-L. Puget[11], B. Rocca-Volmerange[12], P. Ciliegi[4], P. Héraudeau[7], C. Surace[7], F. LaFranca[4], & ELAIS consortium

[1]Imperial College of Science Technology and Medicine, Astrophysics Group, London, UK
[2]Service d'Astrophysique, DSM/DAPNIA, CE-Saclay, France
[3]SISSA, Trieste, Italy
[4]Osservatorio Astronomica di Padova, Padova, Italy
[5]MPE, Garching, Germany
[6]Institute for Astronomy, University of Edinburgh, Edinburgh, UK
[7]Max-Planck-Institut für Astronomie, Heidelberg, Germany
[8]Institute of Astronomy, Cambridge, UK
[9]Sterrewacht, Leiden, The Netherlands
[10]Instituto de Astrofisica de Canarias, Tenerife, Canary Islands, Spain
[11]Institut d'Astrophysique Spatiale, Orsay, France
[12]Institut d'Astrophysique de Paris, Paris, France

ABSTRACT

The European Large Area ISO Survey (ELAIS) has surveyed $\sim$ 12 square degrees of the sky at 15 and 90 μm and subsets of this area at 6.75 and 175 μm using the Infrared Space Observatory (ISO). This project was the largest single open time programme executed by ISO, taking 375 hours of data. A preliminary catalogue of more than 1000 galaxies has been produced. In this paper we describe the goals of the project, describe the follow-up programmes that are in progress, and present some first scientific results including a provisional number count analysis at 15 and 90 μm.

Key words: surveys; starburst galaxies; AGN.

1. INTRODUCTION

The European Large Area ISO Survey (ELAIS) is a collaboration involving 19 European institutes (in addition to the authors and others at their institutes the following people and others at their institutes are involved: I. Gonzalez-Serrano, E. Kontizas, R. Mandolesi, J. Masegosa, K. Mattila, H. Norgaard-Nielsen, M. Ward) and is the largest open time project being undertaken by ISO.

In this paper we describe some of the key scientific goals of ELAIS and give a brief description of the survey, comparing it with other ISO surveys. We give a preliminary discussion of the 15 and 90 μm source-counts and describe the follow-up programme now under way at a wide range of wavelengths, giving some first scientific results.

2. KEY SCIENTIFIC GOALS

In this section we highlight some of the principal scientific motivations for this programme, though naturally there are many other goals which we do not have space to discuss.

- The main extra-galactic population detected by IRAS was galaxies with high rates of star formation. These objects are now known to evolve with a strength comparable to AGN. The sensitivity of ISO allow us to detect these objects at much higher redshifts and thus obtain greater understanding of the cosmological evolution of star formation. This is directly complementary to studies of star-formation history in the optical and UV. Comparison of the star-formation rates determined in the FIR with that determined from the UV will give a direct estimate of the importance of dust obscuration, vitally important for models of cosmic evolution.
- If elliptical galaxies underwent a massive burst of star-formation between $2 < z < 5$, they would be observable in the far infrared and may look like IRAS F10214+4724. This survey will provide a powerful discrimination between such a top-down scenario and any hierarchical bottom-up merging model whose components are individually too faint to detect.

Proceedings of the Conference "The Universe as seen by ISO", Paris, France, 20–23 October 1998 (ESA SP-427, March 1999)

- Unified models of AGN suggest that the central engine is surrounded by a dusty torus. The mid and far infrared emission from the torus is much less sensitive to the viewing angle than the optical. Thus a mid and far infrared selected sample of AGN will place important constraints on unification schemes.

- IRAS uncovered a population with enormous far infrared luminosities, $L_{\rm FIR} > 10^{12}L_{\odot}$. While many of these objects appear to contain an AGN it is argued that star formation could provide most of the energy. Interestingly, most of these objects appear to be in interacting systems, suggesting a triggering mechanism. Exploration of this population to higher redshift will have particular significance for models of AGN/galaxy evolution.

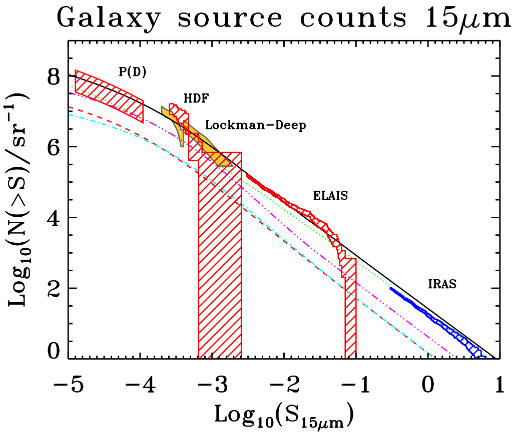

Figure 1. Preliminary 15 μm integral source counts from the ELAIS survey (Serjeant et al. 1999), together with counts from ISO HDF (Oliver et al. 1997, hatched, Aussel et al. 1999, shaded), and CAM Deep survey (Elbaz et al. 1998, shaded), with IRAS 12 μm counts (hatched) at bright end, (IRAS data shifted to 15 μm using cirrus spectrum - Verma 1999). Models are from Pearson & Rowan-Robinson (1996): all components solid; spiral galaxies dotted; star-bursts dash-dot-dot-dot; AGN-dash. Faint end constraints (hatched) come from the ISO HDF P(D) analysis.

3. THE ELAIS SURVEY

The ELAIS observations began on 12th March 1996 and ended on 8th April 1998, shortly before the exhaustion of the Helium coolant. The total survey area covered in blank fields is 6, 11, 12, & 1 sq. deg. at 6.75, 15, 90 and 175 μm, and an additional 2 sq. deg. within the ELAIS survey areas has been surveyed at 175 μm by the FIRBACK team (Puget et al. 1999). Table 1 specifies the main survey areas. A full description of the survey will be given by Oliver et al. (1999).

As part of the follow-up programme described below, we have embarked on surveys of these same areas at X-ray, ultraviolet, visible, near infrared, submillimetre and radio wavelengths. Table 2 shows the wavelengths and areas covered (or planned to be covered in allocated observing time) across the whole electromagnetic spectrum. The surveys at 2-10 keV, U, K, 850 μm and 21 cm will be among the largest area surveys in these wavebands, to these sensitivities, being undertaken. Thus ELAIS has developed from its original concept as a survey at 15 and 90 μm into a powerful multiwavelength survey across the entire electromagnetic spectrum.

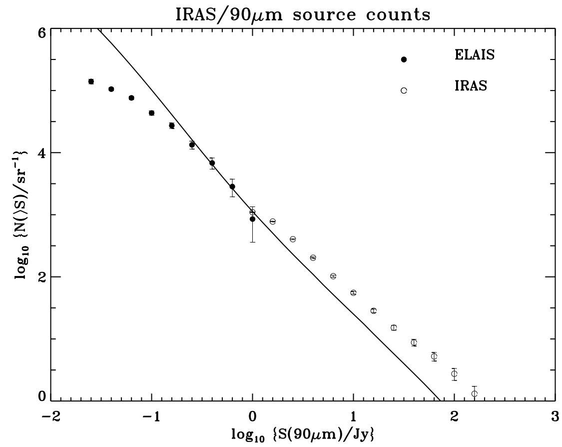

Figure 2. Preliminary 90 μm integral source counts from the ELAIS survey (filled circles), together with counts interpolated from IRAS *60 and 100 μm data (open circles) (Verma 1999). Model is from Rowan-Robinson (1999).*

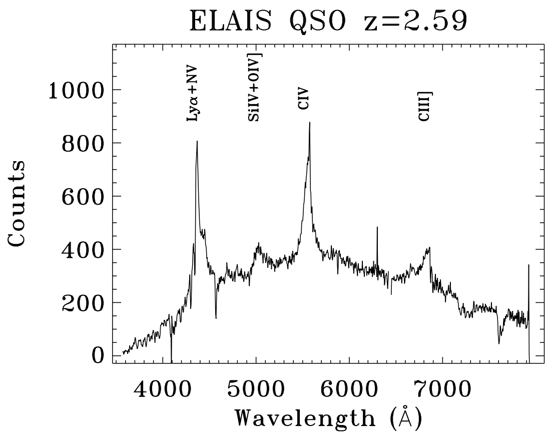

Figure 3. Spectrum of a z=2.59 QSO associated with an ELAIS 15 μm source, taken with the 2dF on the AAT (Gruppioni et al 1999).

4. COMPARISON WITH OTHER ISO SURVEYS

ISO carried out a variety of surveys exploring the available parameter space of depth and area (cf the review by Oliver 1998). Table 3 summarizes the main ISO extra-galactic blank-field surveys. It is clear that information will be available at a wide range of ISO wavelengths, and to a wide range of sensitivities, and that together these surveys will provide a powerful probe of the infrared sky. The ELAIS survey will play a key role because of its large area and the numbers of sources detected (see Table 2 for numbers found in our Quick-Look Analysis).

Table 1. Summary of ELAIS Survey Areas. These areas were selected primarily for having low Cirrus contamination, specifically $I_{100} < 1.5 MJy/sr$ from the IRAS maps of Rowan-Robinson et al. (1991). For N1-3, S1 and all X areas we also restricted ourselves to regions of high visibility > 25% over the mission lifetime. For low Zodiacal background we required $|\beta| > 40$ and to avoid saturation of the CAM detectors we had to avoid any bright IRAS 12μm sources. 6 additional small ($0.3° \times 0.3°$) rasters (X1-6) were centred on well studied areas of the sky or high-z objects

Name	Nominal Coordinates J2000		M (°)	N (°)	ROLL (°)	$\langle I_{100} \rangle$ (MJysr^{-1})
N1	$16^h10^m01^s$	$+54°30'36''$	2.0	1.3	20	1.2
N2	$16^h36^m58^s$	$+41°15'43''$	2.0	1.3	30	1.1
N3	$14^h29^m06^s$	$+33°06'00''$	2.0	1.3	330	0.9
S1	$00^h34^m44^s$	$-43°28'12''$	2.0	2.0	20	1.1
S2	$05^h02^m24^s$	$-30°35'55''$	0.3	0.3	290	1.1

5. PRELIMINARY NUMBER COUNTS

Source catalogues have been extracted from the ELAIS data at all wavelengths and preliminary source count analyses have been performed at 15 and 90 μm. The 15 μm results are shown in Fig. 1, where we have included results from our HDF-N survey (Oliver et al. 1997, Aussel et al. 1999), from the ISO Deep survey in the Lockman hole (Elbaz et al. 1998) and extrapolated from IRAS 12 μm counts (Verma 1999). The models shown are from Pearson & Rowan-Robinson (1996) and agree well with the data. Similar agreement is found for the models of Franceschini et al. (1997). As can been seen these counts confirm the strong evolution detected in the *ISO HDF* analysis (Oliver et al. 1997). A more detailed analysis of the 15 μm counts will be presented shortly (Serjeant et al. 1999).

The counts at 90 μm are extremely preliminary, since there are still major uncertainties in the calibration and there is so far no detailed correction for incompleteness due to the variable effects of cosmic rays. However they show reasonable consistency at the bright end with counts at 90 μm interpolated from IRAS 60 and 100 μm data and demonstrate that we should be reasonably complete at least to 100 mJy (Figure 2). A more detailed discussion of the 90 μm counts will be given by Efstathiou et al. (1999).

Results from our northern and southern 21 cm surveys have already been published (Ciliegi et al. 1999, Gruppioni et al. 1999) and show good consistency with earlier sub-mJy radio surveys. These radio surveys represent a very substantial expansion of the area of the sky surveyed to sub-mJy sensitivities and the follow-up of these radio surveys will be a very interesting project in its own right.

6. FOLLOW-UP

An extensive follow-up programme is being undertaken, including measurements at all wavelengths from X-ray to radio (Tables 2 and 4). This programme will provide essential information for identifying the types of objects detected in the infrared, their luminosities, energy budgets and other detailed properties. As well as studying the properties of the objects detected by ISO a number of the follow-up surveys will provide independent source lists which will be extremely valuable in their own right, not least because we can investigate why some objects emit in the infrared and others do not. As we emphasized above ELAIS has become a deep multi-wavelength survey of these 12 sq degrees of sky, which will have impacts on a wide range of extragalactic astrophysics. The wealth of multi-wavelength information will make ELAIS areas a natural focus for future surveys, for example with WIRE, SIRTF, XMM and FIRST.

Preliminary optical identifications have already been made for several hundred 15 and 90 μm and 21 cm sources and these have been the subject of several spectroscopic runs (see Table 4). Results from spectroscopy of 90 μm galaxies with R < 18 in the south using FLAIR and the ESO/Danish 1.5m telescope will be published shortly (Linden et al. 1999). As expected the galaxies tend to be normal spirals or starbursts. We will also be reporting the first results from spectroscopy of 15 μm and 21 cm galaxies using 2dF and the ESO 3.6m and NTT telescopes (Gruppioni et al. 1999, La Franca et al. 1999). Fig. 3 shows the spectrum of a z=2.59 quasar found in our first 2dF run. Taking into account those galaxies which are too faint for their spectra to be classifiable, about 20-40 % of the 15 μm galaxies for which we have spectra so far are AGN (QSO, Sey 1, Sey 2 or NELG), broadly consistent with expectations of the models of Pearson & Rowan-Robinson (1996) and Franceschini et al. (1998).

In conclusion it is clear that the ELAIS project will not only meet its original scientific goals, but will also provide the basis for a series of powerful multiwavelength surveys over the next decade.

ACKNOWLEDGEMENTS

This work was in part supported by PPARC grant no. GR/K98728 and EC Network is FMRX-CT96-0068.

REFERENCES

Aussel, H., et al. 1999, A&A, 342, 313

Bogun, S., et al. 1996, A&A 315, L71

Ciliegi, P., et al. 1999, MNRAS in press

Clements, D., et al. 1999, in preparation

Clements, D., et al. 1998, in *Astrophysics with Infrared Surveys: A Prelude to SIRTF* ed. M. Bicay et al. (in press)

Efstathiou, A., et al. 1999, in preparation

Elbaz, D., 1997, *Taking ISO to the Limits* Laureijs R. & Levine D. (eds) ESA Publications

Elbaz, D., et al. 1998, in Proc. of 34th Liege International Astrophysics Colloquium on the "Next Generation Space Telescope"

Franceschini, A., Mazzei, P., De Zotti, G, Giann, F., Danese, L. et al. 1994, ApJ, 427, 140

Franceschini, A., et al. 1998, ApJ in press

Gruppioni, C., et al. 1999, in preparation

Hammer, F., Flores, H. 1998, in Proceedings of the XVIIIth Moriond astrophysics meeting "Dwarf Galaxies and Cosmology", Les Arcs, March 1998

Kawara, K., et al. 1998, A&A 336, 9

LaFranca, F., et al. 1999, in preparation

Linden, M., et al. 1999, in preparation

Mattila, K., et al. 1999, in preparation

Nørgaard-Nielson, H.U., et al. 1997, *Taking ISO to the Limits* Laureijs R. & Levine D. (eds) ESA Publications

Oliver, S.J., et al. 1997, MNRAS, 289, 471

Oliver, S. 1998, in *Highlights of the ISO Mission* Special scientific session of the IAU General Assembly, Kyoto', D.Lemke et al. (eds) (Kluwer) in press

Oliver, S.J., et al. 1999, in preparation

Pearson, C., & Rowan-Robinson, M. 1996, MNRAS, 283, 174

Puget, J.-L., et al. 1999, A&A, in press

Rowan-Robinson, M., et al. 1991, MNRAS, 249, 729

Serjeant, S.B.G., et al. 1997, MNRAS, 289, 457

Serjeant, S.B.G., et al. 1999, in preparation

Siebenmorgen, R., et al. 1996, A&A, 315, L169

Taniguichi, Y., et al. 1997, *Taking ISO to the Limits* Laureijs R. & Levine D. (eds) ESA Publications

Verma, A., 1999, in preparation

Table 2. Field Surveys within the ELAIS regions, the vast majority carried out as part of the ELAIS collaboration.

Band	2-10keV	U	B, V, I	R	H/K	6.7	15	90	175	850	21cm
Area (sq degs)	0.15	6	1	13	1	6	11	12	3	0.1	8.2
Depth	1×10^{-14}	22.5	23	23.5	19.5	1	3	100	100	8	0.1-0.4
Units	CGI	mag	mag	mag	mag	mJy	mJy	mJy	mJy	mJy	mJy
Galaxies		30000			3000	1104	1618	390	100		1448
Stars		15000									

Table 3. Field Surveys with ISO

Survey Name	[e.g. Reference]	Wavelength (μm)	Integration (s)	Area (sqdeg)
PHT Serendipity Survey	Bogun et al. 96	175	0.5	7000
CAM Parallel Mode	Siebenmorgen et al. 96	7	150	33
ELAIS		7,15,90,175	40, 40, 24, 128	6, 11, 12,1
CAM Shallow	Elbaz et al. 98	15	180	1.3
FIR Back	Puget et al. 99	175	256, 128	1, 3
IR Back	Mattila et al. 99	90, 135,180	23, 27, 27	1, 1, 1
SA 57	Norgaard-Nielsen et al. 97	60, 90	150, 50	0.42,0.42
CAM Deep	Elbaz et al. 98	7, 15, 90	800, 990, 144	0.28, 0.28, 0.28
Comet fields	Clements et al. 99	12	302	0.11
CFRS	Hammer & Flores 98	7,15,60,90	720, 1000, 3000,3000	0.067
CAM Ultra-Deep	Elbaz et al. 98	7	3520	0.013
ISOHDF South	Oliver et al. 99b	7, 15	$> 6400, > 6400$	4.7e-3, 4.7e-3
Deep SSA13	Taniguchi et al. 97	7	34000	2.5e-3
Deep Lockman	Kawara et al. 98	7, 90, 175	44640, 48, 128	2.5e-3, 1.2 , 1
ISOHDF North	Serjeant et al. 97	7, 15	12800, 6400	1.4e-3, 4.2e-3

Table 4. ELAIS Follow-up Programme Summary

Telescope	shifts/nights	Projects
AXAF	150ks	X-ray Survey in N1, N2
ESO 3.6m	3	Optical Imaging
		Optical Spectroscopy
ESO NTT	9	NIR Photometry
		Optical Spectroscopy
ESO 2.2m	13	NIR Photometry
ESO/Dan. 1.5m	35	Optical Survey
		Optical Photometry
		Optical Spectroscopy
AAT	2	Optical Spectroscopy (2dF)
		NIR Spectroscopy
INT	13	Optical Survey
		NIR Survey
CFHT	1	Integral Field Spectroscopy
Calar Alto 3.6m	8	Optical Spectroscopy
		NIR Photometry
Calar Alto 2.2m	2	Optical Spectroscopy
UK Schmidt	2	Optical Spectroscopy (FLAIR)
Mt.Hopkins	12	NIR Photometry
ITRF	5	NIR Photometry
IAC 0.8m	28	Optical Photometry
ESA OGS 1.m	4	Optical photometry
ATNF CA	10	21 cm Survey
VLA	6	21 cm Survey

ISO DEEP FAR-INFRARED SURVEY IN THE LOCKMAN HOLE A SEARCH FOR OBSCURED OBJECTS AT HIGH REDSHIFT

K. Kawara[1], Y. Sato[2,3], H. Matsuhara[2], Y. Taniguchi[4], H. Okuda[2], Y. Sofue[1] T. Matsumoto[2], K. Wakamatsu[5], L.L. Cowie[6], R.D. Joseph[6], & D.B. Sanders[6]

[1]Institute of Astronomy, The University of Tokyo, 2-21-1 Osawa Mitaka, Tokyo, 181, Japan.
[2]Institute of Space and Astronautical Science (ISAS), 3-1-1 Yoshinodai, Sagamihara, Kanagawa, 229, Japan.
[3]ISO Data Centre, ESA Astrophysics Division, Villafranca del Castillo, Spain.
[4]Astronomical Institute, Tohoku University, Aoba, Sendai 980-77, Japan.
[5]Department of Physics, Gifu University, Gifu 501-11, Japan.
[6]Institute for Astronomy, University of Hawaii, 2680 Woodlawn Drive, Honolulu, HI 96822, USA.

ABSTRACT

Two $44' \times 44'$ fields in the Lockman Hole were mapped at 95 and 175 μm using ISOPHOT. A simple program code combined with PIA works well to correct for the drift in the detector responsivity. The number density of 175 μm sources is 3 - 10 times higher than expected from the no-evolution model. The source counts at 95 and 175 μm are consistent with the cosmic infrared background.

Key words: Galaxies; evolution, Galaxies; formation, quasars; general, Galaxies; starburst, Cosmology; observations, Infrared; galaxies.

1. INTRODUCTION

As part of the Japan/UH cosmology program using the ISAS guaranteed time, 95 and 175 μm surveys were conducted in the Lockman Hole to search for obscured infrared galaxies at high redshift. The first results and preliminary discussion were presented by Kawara et al. (1998). This paper presents observations, image processing, and discussion on the nature of far-infrared sources. Point source extraction from the maps and source counts will be presented in a forthcoming paper (Kawara et al. 1999).

2. OBSERVATIONS

We have carried out a deep far-infrared survey at 95 and 175 μm by using ISOPHOT (Lemke et al. 1996) which is an imaging photopolarimeter on board the Infrared Space Observatory (ISO; Kessler et al. 1996). Two fields named LHEX and LHNW, each extending approximately $44' \times 44'$, were selected in the "Lockman Hole", a region with the smallest HI column density in the sky (Lockman et al. 1986), to minimize confusion noise due to infrared cirrus. The combinations of the filters and the detector arrays which were used for the observations are given in Kawara et al. (1998).

Raster mapping was performed with the AOT PHT22 staring raster map mode using 35.4 hours, which were executed between revolutions 194 and 215 (May 28 and June 19, 1996). Each of the two fields is made up of four sub-fields having an approximately $22' \times 22'$ area each. The parameters used for raster mapping of a single sub-field and details of the read-out settings are given in Kawara et al. (1998).

3. DATA REDUCTION

The PHT Interactive Analysis (PIA) - Gabriel et al. (1997) - version 6.4 was used with the default settings to reduce the edited raw data created in November, 1996 via the off-line processing version 5.1 or 5.2. Maps of 95 μm created from the PIA's Astronomical Analysis Processing (AAP) are dominated by noise due to drift in the detector responsivity. The AAP created maps are thus cleaned by a median smooth routine developed by Kawara et al. (1998).[1] The photometric error introduced from this correction is 4% or better and no extended brightness structures recognized within a $22' \times 22'$ area are affected.

The flux calibration can be made using either the COBE background measurements or the IRAS point source fluxes. Note that the intensity of interplanetary dust emission varies little at such high ecliptic latitude ($\beta \sim 45°$) as the solar elongation changes. The fields contain only one IRAS source (F10507+5723). This is the brightest source detected in our survey and identified with a Sb galaxy UGC 06009 (Thuan & Sauvage 1992). The IRAS fluxes are 533 mJy at 60 μm and 1218 mJy at 100 μm (IRAS FSC). Its flux ratio f(100 μm)/f(60 μm) =

[1]This routine is now included in PIA and called "Median Filtering."

2.29 is fitted to a combination of the infrared cirrus and starburst spectra given by Pearson & Rowan-Robinson (1996), if 76% of the 100 μm flux comes from the cirrus component. This predicts f(175 μm) = 1133 mJy from f(175 μm)/f(100 μm) = 0.93 which is comparable to that in the inner arm of a Sc galaxy M101 (Hippelein et al. 1996). The COBE based scaling yields 347 mJy at 95 μm and 451 mJy at 175 μm, implying that the COBE based scaling may underestimate point source fluxes by 3.5 at 95 μm and 2.5 at 175 μm. The origin of these differences is unclear. In the following discussion, the ISO fluxes are scaled based on the IRAS measurements.

4. DISCUSSION

There are numerous spots in the 95 and 175 μm maps presented by Kawara et al. (1998). Bright spots cannot be attributed to peaks of the infrared cirrus. The total HI column density N_H in our fields is approximately 6×10^{19} cm^{-2} (Jahoda et al. 1990). The correlation between N_H and the infrared cirrus brightness indicates $B_{cirrus}(95\mu\mathrm{m}) = 0.41$ MJy sr^{-1}and $B_{cirrus}(175\mu\mathrm{m}) = 0.81$ MJy sr^{-1}(Table 2 in Boulanger et al. 1996). Using the models by Gautier et al. (1992) with $\alpha = -2.9$ for the index of the spatial power spectrum of the infrared cirrus, $\sigma_{cirrus}(95\mu\mathrm{m}) \sim 0.14$ mJy and $\sigma_{cirrus}(175\mu\mathrm{m}) \sim 1.7$ mJy are obtained for one sigma cirrus confusion noise. The 3 σ flux levels reached in our survey are tentatively estimated to be $\sim 45 \pm 20$ mJy at 95 μm and $\sim 45 \pm 25$ mJy at 175 μm. Hence, a probability of having a cirrus peak brighter than the detection limits is so low that most of spots are likely to be galaxies.

In the two fields LHEX and LHNW, covering 1.1 square degrees in total, there are 36 and 45 sources brighter than 150 mJy at 95 and 175 μm, respectively. Out of 45 175 μm sources, 36 sources are within the area which was observed at both wavelengths. 31 of the 36 sources have the 95 μm counterparts within 40″ that were detected above the 3 σ flux level. The completeness down to 150 mJy is estimated to be almost 100%, because of the low probability of cirrus confusion and the high SNR (signal to noise ratios) detection (typical SNR $\sim$ 10). The cumulative counts down to 150 mJy are thus 1.1×10^5 sources sr^{-1} at 95 μm and 1.3×10^5 sources sr^{-1} at 175 μm. Fig. 1 compares the 95 and 175 μm counts with the models developed by Guiderdoni et al. (1997, 1998). The number density of 175 μm sources brighter than 150 mJy are ten times higher than that expected from the no-evolution model. The counts both at 95 and 175 μm counts are consistent with the models containing a strongly evolving component which is required to account for the cosmic infrared background found by Puget et al. (1996).

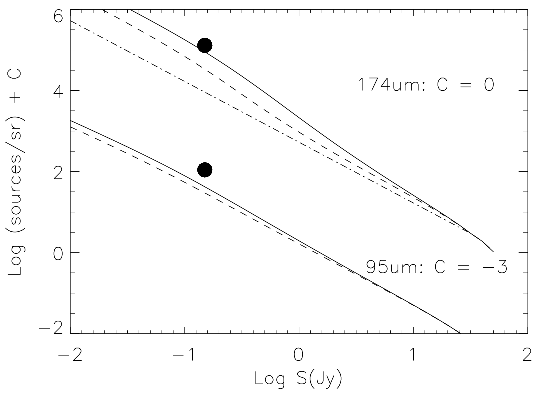

Figure 1. The cumulative number counts at 95 and 175 μm down to 150 mJy which are compared with the models by Guiderdoni et al. The no-evolution model is plotted with the dash-dot line, and scenarios E and A with the solid and dash lines, respectively.

ACKNOWLEDGEMENTS

The ISOPHOT data presented in this paper was reduced using PIA, which is a joint development by the ESA Astrophysics Division and the ISOPHOT consortium. The ISOPHT consortium is led by the Max Plank Institute for Astronomy (MPIA), Heidelberg.

REFERENCES

Boulanger, F., Abergel, A., Bernard, J.-P., et al. 1996, A&A 312, 256.

Gabriel, C., et al. 1997, Proc. of the ADASS VI Conference, G. Hunt & H.E. Payne (eds), pp. 108

Gautier, T.N., Boulanger, F., P, Pérault, M., & Puget, J.L. 1992, AJ, 103, 1313

Guiderdoni, B., Bouchet, F.R., Puget, J.-L., Guilaine, G., & Hivon, E. Nature, 390, 257

Guiderdoni, B., Hivon, E., Bouchet, F.R., & Maffei, B. MNRAS, 295, 877

Hippelein, H., Lemke, D., Haas, M., et al. 1996, A&A, 315, L82

IRAS FSC, version 2.0, 1990, Joint IRAS Science Working Group, U.S. Government Printing Office, Washington D.C.

Jahoda, K., Lockman, F.J., & McCammon, D. 1990, ApJ, 354, 184

Kawara, K., Sato, Y., Matsuhara, H. et al. 1998, A&A 336, L9

Kawara, K. et al. 1999, in preparation.

Kessler, M.F., Steinz, J.A, Anderegg, M.E. et al., 1996, A&A 315, L27

Lemke, D., Klaas, U., Abolins, J., et al. 1996, A&A 315, L64

Lockman, F.J., Jahoda, K., & McCammon, D. 1986, ApJ, 302, 432

Pearson, C. & Rowan-Robinson, M. 1996, MNRAS, 283, 174

Puget, J.L. et al. 1996, A&A, 308, L5

Thuan, T.X., & Sauvage, M. 1992, A&AS, 92, 749

A DEEP AND ULTRA-DEEP ISOCAM COSMOLOGICAL SURVEY THROUGH GRAVITATIONALLY LENSING CLUSTERS OF GALAXIES

L. Metcalfe[1], B. Altieri[1], B. McBreen[2], J-P. Kneib[3], M. Delaney[2], A. Biviano[4], M.F. Kessler[1], K. Leech[1], K. Okumura[5], B. Schulz[1], D. Elbaz[6] & H. Aussel[6]

[1]ISO Data Centre, Astrophysics Division, ESA, Villafranca, Spain.
[2]Physics Department, University College Dublin, Stillorgan Road, Dublin 4, Ireland
[3]Observatoire Midi-Pyrenees, 14 Av. E. Belin, 31400 Toulouse, France
[4]Osservatorio Astronomico di Trieste, via G.B. Tiepolo 11, 1-34131 Trieste, Italy
[5]Institut d'Astrophysique Spatiale, Bat. 121, Universite Paris-Sud, F-91405 Orsay, France
[6]DSM/DAPNIA/Sap, CEA-Saclay, 91191 Gif-sur Yvette Cedex, France.

ABSTRACT

We present imaging results and source counts from an ISOCAM deep and ultra-deep cosmological survey through gravitationally lensing clusters of galaxies at 7 and 15 μm. A total area of about 53 arcmin^2 was covered in maps of three clusters. The lensing increases the sensitivity of the survey. A large number of luminous mid-infrared (MIR) sources were detected behind the lenses, and most could be unambiguously identified with visible counterparts. Thanks to the gravitational amplification, these results include the faintest MIR detections ever recorded, extending source counts to an unprecedented level. The source counts, corrected for cluster contamination and lensing distortion effects, show an excess by a factor of 10 with respect to the prediction of a no-evolution model, as we reported for A2390 alone in Altieri et al. (1999). These results support the A2390 result that the resolved 7 and 15 μm background radiation intensities are $(1.7\pm0.5)\times10^{-9}$ and $(3.3\pm1.3)\times10^{-9}$ W m^{-2} sr^{-1} respectively, integrating from 30 μJy to 50 mJy.

Key words: gravitational lensing; galaxy clusters; number counts; morphology.

1. INTRODUCTION

Following the identification of the first cosmological gravitational lens by Young et al. (1980) the theoretical and observational exploitation of the lensing phenomenon developed rapidly. In 1987 luminous giant arcs were discovered in the fields of some galaxy clusters by Lynds and Petrosian (1986), and independently by Soucail et al. (1987), and these were soon recognised to be Einstein rings (Paczyński 1987). Since then observations of cluster-lenses have been extended to wavelengths other than the visible (e.g. Smail et al. (1993) for the NIR, and Smail et al. (1997) for the sub-mm region). At the same time models describing the lensing have been refined (Kneib et al. 1996) to the point where source counts made through a cluster lens can be corrected to yield the counts which would be found in the absence of the lens.

We report key results of a deep-survey programme, initiated almost a decade ago as part of the 'Central Programme' of the ISO mission, and which has extended the exploitation of the gravitational lensing phenomenon to the Mid-infrared (MIR) for the first time by using ISOCAM (Cesarsky et al. 1996) on ESA's ISO spacecraft (Kessler et al. 1996).

The programme achieved deep and ultra-deep (ISOCAM) imaging through a sample of gravitationally lensing clusters of galaxies, benefiting from the lensing to search for background objects to a depth not otherwise achievable. Lensing amplifies sources and, for a given apparent flux limit, suppresses confusion, due to the apparent surface area dilation. To the flux-limits of this sample, even rich foreground galaxy clusters are essentially transparent at 15 μm.

2. OBSERVATIONS, DATA-REDUCTION AND DATA-ANALYSIS

2.1. Observations

We observed the fields of the well-known gravitationally lensing galaxy clusters Abell 370, Abell 2218 and Abell 2390. A total area of about 53 arcmin^2 was covered. Table 1 lists the observational parameters of the survey which used CAM's 6.7 μm (LW2) and 14.3 μm (LW3) filters. By employing the CAM 3 arcsec per-pixel field-of-view (PFOV) and raster step sizes which were multiples of 1/3 pixel, over many raster steps, we achieved a final mosaic pixel size of 1 arcsec. The diameter of the PSF central maximum is, in arcseconds, $0.84\times\lambda(\mu m)$, and the FWHM is about half that. The final 1 arcsec pixel

Proceedings of the Conference "The Universe as seen by ISO", Paris, France, 20–23 October 1998 (ESA SP-427, March 1999)

size improved source separation and allowed a better cross-identification with observations at other wavelengths. This strategy differs from many other CAM deep surveys which used the 6 arcsec per-pixel field-of-view. The 5σ sensitivity limits are given in Table 1 and depend on the lensing cluster in question. These limits refer to apparent source brightness *before* correction for the effects of lensing. For the clusters observed, the highest-magnification regions of the lenses give amplifications of 5 to 10 - so with this method we could in principle make 5σ detections in LW2 and LW3, of sources with intrinsic brightnesses as low as 6μJy and 13μJy, respectively, if any such faint background source falls in the regions of strongest lensing. Typical magnifications are about 2 over the central few square-arcmin of the clusters.

Lensing also causes a surface dilation effect over the area probed. This spatial dilation is stronger towards the core of the cluster and increases with source-plane redshift. These effects need to be corrected during analysis in order to compare results with *blank* sky counts (e.g. in the Hubble Deep field and Lockman Hole – Rowan-Robinson et al. 1997; Taniguchi et al. 1997; Aussel et al. 1999; Elbaz et al. 1998).

2.2. Data reduction and analysis

The reduction of ISO faint source data is extremely challenging and many work-years have been invested in developing effective and reliable techniques. The ultimate performance is particularly sensitive to the effectiveness with which the detector's global responsive transient and cosmic-ray-induced glitches can be removed from the data. Two substantially independent data reduction approaches were applied. These are described in detail in the ISOCAM Faint Source Report (Altieri et al. 1998 - available on the ISO www page). We particularly refer to Sections 3.3 and 3.4 of that document, and related sections. Key techniques employed to perform photometry and to extract source-lists and sensitivity limits are described in Section 5 of the report and also in Altieri et al. (1999).

Detailed lensing models of the three clusters used have been produced by Kneib et al. (1996) and (1999), and Bezecourt et al. (1999). By correcting for the lens magnification and surface dilation effects, contamination by cluster galaxies (mainly at $7\,\mu$m), and non-uniform sensitivity of our maps, we can derive number counts to compare with blank sky counts. The object density per flux bin was computed using magnification-dependant surface areas derived from the lensing models so dividing the maps into sets of sub-maps. The unreliable data at the boundaries of the maps were discarded.

3. RESULTS

In Section 2.1. the potential limiting sensitivity of this survey was described (6 and $13\,\mu$Jy at 5σ in LW2 and LW3 respectively). Achieving this potential is a matter of luck with respect to source distribution behind the lens. In practice, the faintest $15\,\mu$m source detected was intrinsically an $18\,\mu$Jy source amplified to $80\,\mu$Jy (a 6σ detection).

Fake-source simulations are described in Altieri et al. (1999), and show that our 80% completeness levels in LW3 (for which we report source counts here) before accounting for lensing are : 500, 250 and 100μJy for A370, A2218 and A2390, respectively. Our simulations for A370 and A2218 are still preliminary so their associated completeness levels may be adjusted slightly when the full analysis is finished. Lensing has a variable effect over the field so it is not possible to state a global completeness level after correction for lensing. Rather, we stopped counting at the 50% completeness flux level in the highest magnification bins we could use. This was an intrinsic $33\,\mu$Jy at $15\,\mu$m for A2390, corresponding to a 5σ threshold for counting a source.

3.1. Cluster images at $15\,\mu$m

Overlays onto visible images of ISOCAM LW3 ($15\ \mu$m) deep images through the three clusters can be found in figures 1, 2 and 3. (See also Barvainis et al. (1999) for additional ISO data on A2218.)

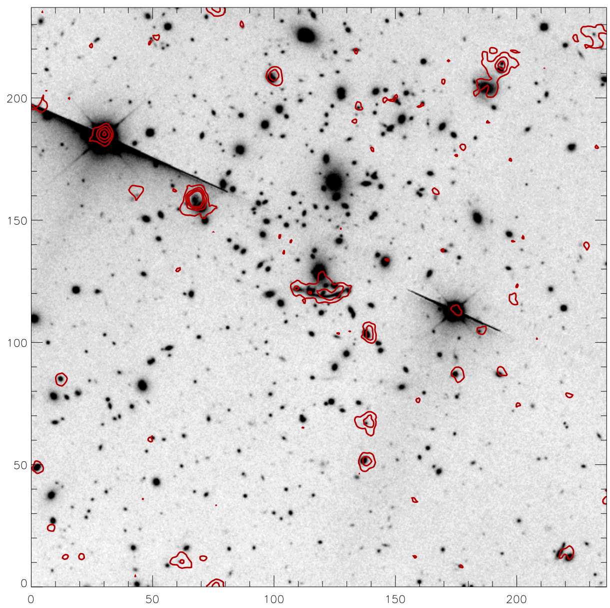

Figure 1. Contours of an ISOCAM $15\,\mu m$ image of Abell 370 over a deep CFHT I-band image. The giant arc is well detected by ISO, along with a number of other MIR sources in the field, some with quite faint optical counterparts. (All axes are arcseconds.)

From these images we can remark that we generally do not see the optical arc(lets) at $15\,\mu$m. We see a Large Number of MIR sources, shown from spectroscopic, photometric or lensing redshifts to be behind the lens. These are, in effect, IR arc(let)s.

Thanks to our high-resolution images we have been able to unambiguously identify 90% of sources with (sometimes extremely faint) counterparts in deep NIR and visual (HST/WFPC2 and ground-based) images. Spatial resolution is good enough to allow recognition of IR correlations with the visual morphology of objects, e.g., the ISO detection peak

Table 1. Observational parameters and lensing clusters of galaxies used for the survey. On-chip integration time (t_{int}) was always 5.04 seconds and the 3 arcsec per-pixel field-of-view was used.

FIELD	FILTER †	Readouts per step	Raster steps X	Raster steps Y	dm arcsec	dn arcsec	area (sq.arcmin)	depth 5σ (μJy)	No. of times repeated	Tot. time (sec.)
Abell 2390	LW2	13	10	10	7	7	5.3	33	4	29300
	LW3	13	10	10	7	7	5.3	67	4	29300
Abell 2218	LW2	14	12	12	16	16	16	*	2	22000
	LW3	14	12	12	16	16	16	150	2	22000
Abell 370	LW2	10	14	14	22	22	31.3	*	2	22688
	LW3	10	14	14	22	22	31.3	330	2	22688

(*) in Metcalfe et al. (1999). (†) LW2 and LW3 filters have reference wavelengths 6.7 and 14.3 μm, respectively.

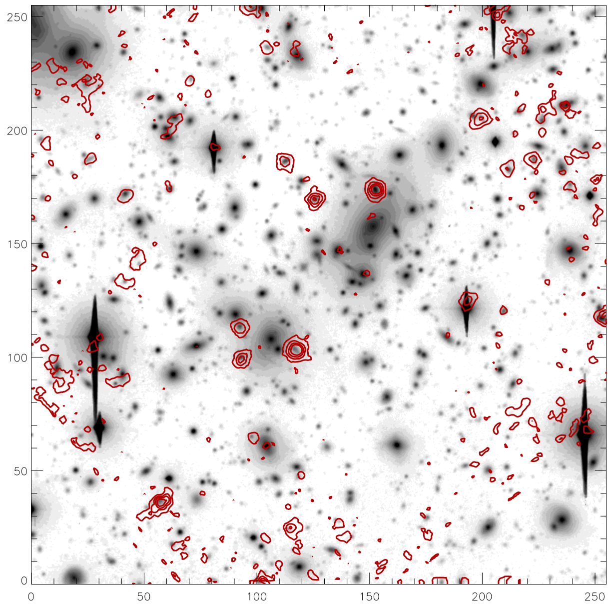

Figure 2. Contours of the inner 4×4 square arcmin of an ISOCAM 15 μm image of Abell 2218 over a deep Palomar 5m I-band image (Smail, private communication). Note the strong ISO detection of the giant arc at (117,105), the several MIR sources corresponding to faint optical counterparts [e.g. (200,205), (45,140), (105,240)] and the fact that the IR "arclets" are generally not from the same population as the known visual arclets.

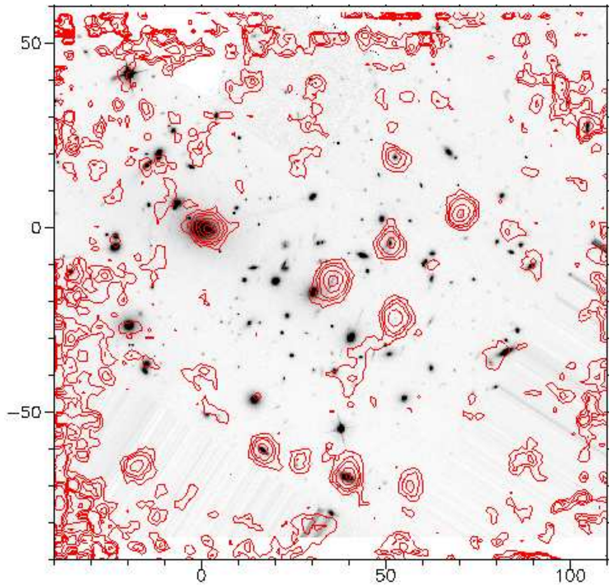

Figure 3. Contours of an ISOCAM 15 μm image of Abell 2390 over an HST (F814W) I-band image. Note the ISO detection of part of the straight arc near the centre of the image (35,-15), and the two strong ISO detections (spectroscopic redshift unknown) at (53,-25) and (70,05). These objects have extremely red colours and very faint visual fluxes. Their colours, if interpreted as due to redshift, imply photometric redshifts greater than 3.

matches the bright visual knot in the straight arc (Pelló et al. 1991) near the centre of the A2390 map.

We found that at 7 μm about half the sources are cluster galaxies, the other half are lensed background sources. We infer that almost all 15 μm sources are lensed background galaxies because this is the case for most sources for which we have spectroscopic redshifts. In addition the photometric and lensing-inversion redshifts for the remaining sources are consistent with locations beyond the cluster. This indicates that, at 15 μm, the cluster-core becomes transparent, similar to the Sub-mm case (Smail et al. 1997).

Some ISO targets have extremely red optical and NIR colours. It appears that 15 μm imaging favours selection of star-forming galaxies and dusty AGNs that are not evident in UV/optical surveys.

3.2. Number counts and source properties

We have extracted 15 μm source counts for the three clusters taking only 5σ detections into account for statistical studies. The analysis performed for A370 and A2218 is provisional, and is being refined. It is expected, however, that the final results will differ only in detail. We find a total of 71 sources within our survey area (see Table 1), with 30, 23 and 18 from A2390, A2218 and A370 respectively.

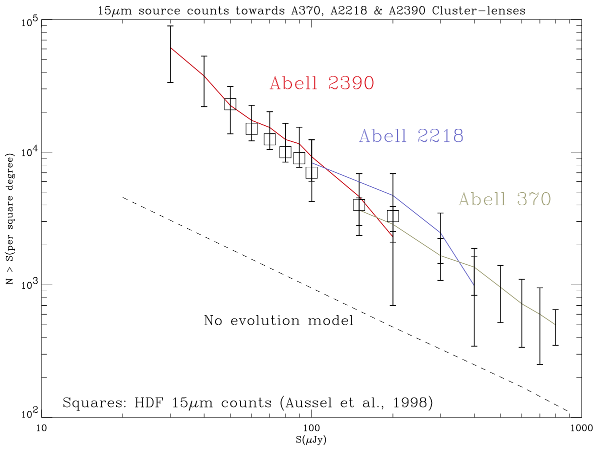

Figure 4. ISO 15 μm source counts for three clusters. The slope from A2390 is -1.5 $\pm$ 0.3 and N_{15}(>30 μJy) = 13 $\pm$ 5 arcmin^{-2} at 15 μm. Counts for A2390 are fully corrected for lensing. Counts for A370 and A2218 have only been roughly corrected. Planned final corrections are not expected to significantly alter the slope, but could move A370 and A2218 datapoints slightly along the curve towards lower flux.

The 15 μm counts show a steadily increasing excess by a factor of order 10 over no-evolution models (see Figure 4, and Franceschini et al. 1994). These results confirm the Lockman hole result of Elbaz et al. (1998), and agree with the HDF counts of Aussel et al. (1999). There is no sign of flattening of the counts at the faintest levels. The slope stays close to -1.5 $\pm$ 0.3 down to the 30 μJy limit. These source densities favour extreme evolution models.

Integrating the number counts over our A2390 flux range (30 μJy to 200 μJy) and over other ISOCAM surveys (Elbaz et al. 1998) up to 50 mJy we find that the resolved background light is $(3.3\pm1.3)\times10^{-9}$ and $(1.7 \pm 0.5) \times 10^{-9}$ W m^{-2} sr^{-1} at 15 μm and 7 μm, respectively. The 15μm lower limit is close to the upper limit from the gamma-CMBR photon-photon pair production (Stanev and Franceschini 1997).

4. CONCLUSIONS

The method of looking through gravitational lenses served to extend ISO coverage of background sources to the deepest levels, especially at 15 μm. The results suggest that abundant star formation occurs in very dusty environments at z$\sim$1. Caution must be employed to take account of the effects of dust in inferring global star formation history from UV or optical luminosities of high-z galaxies. We will present a more complete description of these MIR observations, including 7 and 15 μm photometry in a forthcoming paper (Metcalfe et al. 1999). A detailed study of the optical properties of the MIR galaxies may reveal the nature of the evolving or new population of luminous IR sources.

ACKNOWLEDGMENTS

The ISOCAM data presented in this paper was analysed using 'CIA', a joint development by the ESA Astrophysics Division and the ISOCAM Consortium. The ISOCAM Consortium is led by the ISOCAM PI, C. Cesarsky, Direction des Sciences de la Matière, C.E.A., France.

REFERENCES

Altieri, B., Metcalfe, L., Ott, S. et al. 1998, `http://www.iso.vilspa.esa.es/users/expl_lib/CAM_list.html`

Altieri, B., Metcalfe, L., Kneib, J-P. et al. 1999, A&A, in press, astro-ph/9810480

Aussel, H., Cesarsky, C.J., Elbaz, D., Starck, J.-L. 1999, A&A, 342, 313

Barvainis., R., Antonucci R., Helou., G. 1999, in preparation.

Bezecourt., J., Kneib, J.-P., Soucail, G., Ebbels, T. 1999, submitted to A&A, astro-ph/9810199

Cesarsky, C.J., Abergel, A., Agnese, P. et al. 1996, A&A 315, L32

Elbaz, D., Aussel, H., Cesarsky, C. J. et al., 1998, Proc. of 34th Liege Int. Astr. Coll. on the NGST, astro-ph/9807209

Franceschini, A., Mazzei, P., De Zotti, G., Danese, L. 1994, ApJ 427, 140

Kessler, M.F., Steinz, J.A., Anderegg, M. et al. 1996, A&A 315, L27

Kneib, J-P., Ellis, R.S., Smail, I., Couch, W.J., Sharples, R.M. 1996, ApJ 471, 643

Kneib, J-P., et al. 1999, in preparation

Lynds, R., Petrosian, V. 1986, Bull. Am. Astr. Soc. 18, 1014

Metcalfe, L., et al. 1999, in preparation

Paczyński, B. 1987, Nature 325, 572

Pelló, R., LeBorgne, J.F., Soucail, G., Mellier, Y., Sanahuja, B., 1991, ApJ 366, 405

Rowan-Robinson, M., Mann, R., Oliver, S. et al. 1997, MNRAS 289, 490

Smail, I., Ellis, R., Aragoń-Salamanca, A. et al. 1993, MNRAS 263, 628

Smail, I., Ivison, R.J., Blain, A.W. 1997, ApJ 490, L5

Soucail, G., Mellier, Y., Fort, B., Mathez, G., Cailloux, M. 1987, The Messenger, 50, 5

Stanev, T., Franceschini, A. 1997, ApJ 494, L159

Taniguchi, Y., Cowie, L., Sato, Y. et al. 1997, A&A, 328, L9

Young, P., Gunn, J.E., Oke, J.B., Westphal, J., Kristian, J. 1980, ApJ 241, 507

THE NATURE OF THE GALAXIES RESPONSIBLE FOR THE EXCESS IN THE 15 μm NUMBER COUNTS

H. Aussel[1], D. Elbaz[1], C.J. Cesarsky[1], & J.L. Starck[1]

[1]Service d'Astrophysique, DSM/DAPNIA, CE-Saclay, France

ABSTRACT

We have used a complete flux limited sample of sources detected at 15 μm in the Hubble Deep Field area to investigate the mid–infrared, optical and spectroscopic properties of the galaxies responsible for the excess in the number counts at this wavelength. We show that these galaxies are large spirals and irregular or merging systems, with colors typical of normal spiral. We estimate their mid–infrared luminosity and show that they are of the order of local ULIRGs. Using the 15 μm luminosity as an indicator of star formation, we show that the classical [OII] tracer is extincted in these galaxies. Finally, we discuss the implication of our results on the picture of galaxy evolution.

Key words: Cosmology; Number Counts ; Galaxy : evolution

1. INTRODUCTION

Several extragalactic surveys have been performed with ISOCAM (Cesarsky et al. 1996), on various area and at various depths. Two broad–band filters have been mainly used, the LW2 filter that covers the 5 to 8.5 μm wavelength range and the LW3 filter that covers the 12 to 18 μm range. In this last band, as it is shown by the review from Elbaz et al. (these proceedings), the number counts display a strong departure from the predictions of a model without evolution below a flux of 1 mJy. On the contrary, the number counts measured above 1 mJy are in good agreement with this model over more than two orders of magnitude in flux. This behavior of the number counts has been confirmed with the observations of different fields at similar depth, and is interpreted as the sign of a strong evolution of a population of field galaxies (Elbaz et al. these proceedings).

Very deep observations reaching a flux limit of 100 μJy at 15 μm allow to study the galaxies undergoing this strong evolution, because the number of sources in excess with respect to the predictions of a no-evolution model is roughly a factor of five above the underlying non evolving population at this flux level. The statistical properties of the sources detected in such an observation will therefore be dominated by the evolving population. From this point of view, the observation of the Hubble Deep Field (Williams et al. 1996) with ISOCAM (Rowan–Robinson et al. (1997) and reference therein), recently reanalyzed by Aussel et al. (1999) and Désert et al. (1999) provides a sample large enough at such depth to allow a statistical study of the properties of the sources detected at 15 μm. Moreover, numerous observations at other wavelengths of this area as well as spectroscopic follow–ups allow for a detailed analysis of the properties of this sample.

2. THE SAMPLE

The recent reanalysis by Aussel et al. (1999) of the ISOCAM observation of the Hubble Deep Field led the authors to produce two lists of sources : a main list has been derived by setting strong constraints on the detections criteria, and a supplementary source list was obtained by relaxing the detection criteria and by a deblending by hand of some confused sources in the main list. This sample is difficult to handle for a detailed analysis, because it is not a flux limited sample: since the observing time is not the same on all the observed area, the sensitivity of the ISOCAM observation varies strongly from one point to the other. Moreover, it was not possible at the time the paper was written to assess the reliability of the supplementary source list. New calibration observations obtained within the last months of the ISO mission have allowed us to perform simulations of ISOCAM deep observations, starting from raw data that do not contain any source. Adding simulated sources to this dataset has allowed us to study more precisely the reliability of the source lists produced so far and their completeness (Aussel 1999). We have applied these simulations to the ISO–HDF observations at 15 μm and shown that : 1) the main source list does contain statistically 0.5 false detections at 99.9 per cent confidence level, 2) the supplementary source list, limited to a flux limit of 100 μJy contains statistically 1 false detection at 99.0 per cent confidence level, 3) the completeness over the whole observed area is of 99.3 per cent of detected sources above a flux of 100 μJy. We have therefore merged the two source lists of the Aussel et al. (1999) paper with a limiting flux of 100 μJy. This gives us a complete and flux limited catalog of 44 sources over the whole ISO–HDF area detected at 15 μm. We present here the study of the properties of this mid-IR selected sample.

3. OPTICAL PROPERTIES

3.1. Optical counterparts

We have used for the identification of the optical counterparts of the ISOCAM sample the catalog of Barger et al. (1999), complete to a limiting magnitude of I=24.5, that also contains the B, V, and HK' magnitude of the object, as well as a compilation of all the measured redshifts published so far on the HDF and its flanking fields. The astrometric accuracy of the ISO–HDF appears to be very good since most of the 15 μm sources have a counterpart within a radius of 3 arcsec of their position, while the ISOCAM observations were performed with the 6 arcsec pixel field of view lens. The mean distance between the nearest neighbours in the catalog of Barger et al. (1999) being of 6.3 arcsec, this ensures that the correct identification has been obtained. For six of the ISOCAM sources, it was not possible to assign an optical counterpart. For two sources, this is due to confusion. In the four other cases, a counterpart is detected in the flanking field exposures taken by the HST, but at a level too faint to be in the flux limited catalog from Barger et al. (1999).

A redshift is available for 27 out of the 38 identified ISOCAM sources. Since our goal is to investigate the properties of the mid–infrared selected sample with respect to the optically selected field galaxies, it is important to define a reference sample for which the redshift information is also known. We have carefully checked (Aussel 1999) that a subsample of the Barger et al. (1999) catalog limited to I=22.5 has the following properties : 1) out of the 251 galaxies of the sample, 152 have a redshift measured. 2) The magnitude distribution in B, V, I, and K of the galaxies with known redshifts are the same than the ones of the complete sample. 3) The B-I, V-I and I-K color distributions of the galaxies with measured redshift are the same than the one of the complete sample. Thus, the sample defined by all galaxies with I $\leq$ 22.5 and with a known redshift should not be biased and have the same optical properties than the complete sample flux limited to I=22.5 and can be used as a reference sample.

36 out of 44 ISOCAM sources have an optical counterpart with I $\leq$ 22.5. Since the excess in the counts is a factor of 5 above the predictions of a no–evolution model, most of the 15 μm with optical counterparts do belong to the excess sources. Redshifts are known for 26 sources out of the 36 identified. The distribution of the fluxes at 15 μm of the sources with known redshift is similar to the distribution of the fluxes of the whole ISOCAM complete sample, thus indicating that no strong bias should be introduced in restricting the study to the sources with known redshifts. We can therefore compare the optical properties of the mid–infrared selected sample to the properties of the optical selected reference sample.

3.2. Redshifts, colors, morphologies and luminosities

We have compared the redshifts distribution of the reference sample and of the mid-IR selected sample. A Kolmogorov–Smirnov test applied to the two distributions does not allow to distinguish them with a reliable confidence level, indicating that they are very similar. 85 per cent of the 15 μm are above redshift 0.4, up to z=1.275. The mean redshift is $< z >$=0.697, the median redshift being z=0.761.

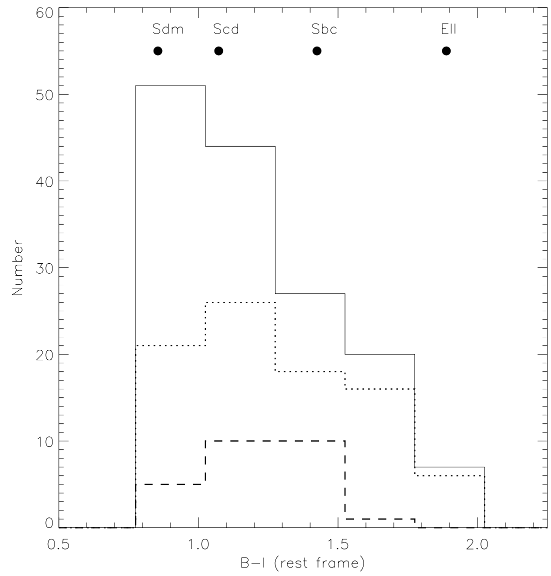

Figure 1. Rest frame B–I color distribution of the 15 μm (dash) selected sample and of the reference sample (solid). The dotted line is the histogram of a subsample of the reference sample, selected with I$\leq$ 21.5. The four data points are the B–I colors of the four template spectra from Coleman et al. (1980).

We have used a method similar to the one used by Lilly et al. (1991) to compute the rest–frame B, V, I and K colors of the galaxies of the reference sample from their observed colors and redshifts, using the template spectra of Coleman et al. (1980) and their extension in the near–IR by Fernández-Soto et al. (1999). Figure 1 shows the B–I color distribution of the ISOCAM selected sample and of the reference sample. The rest–frame color of the four templates (Ell, Sbc, Scd and Sdm) of Coleman et al. (1980) have also been plotted. The bulk of the 15 μm sources exhibits colors typical of spirals (Sbc to Scd). The only elliptical detected by ISOCAM contains an AGN. The proportion of galaxies with colors typical of blue irregulars (Sdm) is very low in the ISOCAM sample, in comparison with the reference sample.

A crude study of the morphology of the galaxies detected at 15 μm shows that roughly half of them are disk dominated galaxies, while the other half are interacting systems or irregular galaxies.

Most of the ISOCAM galaxies are intrinsically luminous objects, their absolute K magnitude being between -22 and -25 for the objects above z=0.4, that is of the order of or more luminous than a M^* galaxy. This is coherent with the lack of Sdm galaxies in the ISOCAM sample, because most of these blue galaxies are fainter than M^*. This effect is illustrated on Figure 1 where the B–I color distribution of a subsample of the reference sample selected at I=21.5 is depleted blue galaxies (dotted line) with respect to the color distribution of the reference sample.

This comparison of the optical properties of the sources detected at 15 μm demonstrate clearly that the galaxies responsible for the excess in the counts at these wavelength do not belong to the faint blue population responsible for the excess observed in the B band number counts (Ellis 1997).

4. MID-INFRARED PROPERTIES

The knowledge of the redshift of the sources detected at 15 μm allows us to estimate their luminosity at 15 μm. This computation depends on the K–correction assumed for the objects. We have obtained a range of luminosity by using the smallest and the largest K–correction measured with the mid-IR spectra of various templates of galaxies, from elliptical to ULIRGs (Aussel 1999). The typical uncertainty in the luminosity is about a factor of 10, depending on the choice of the K–correction but allows for a comparison with local objects observed at the same wavelength with ISOCAM. We find that a large spiral galaxy like M51 can only be detected up to a redshift of 0.3 in the ISO–HDF observations. An ultraluminous galaxy like Arp 220 can be detected up to a redshift of 1.6 of our ISOCAM sources are brighter by factors 2 to 20 than Arp 220, depending on the K–correction.

The galaxies detected at 15 μm are therefore very luminous objects in the mid-IR, with 85 per cent of the galaxies having luminosities of the order of or brighter than $5 \times 10^{10} L_{\odot}$. In the local universe, Fang et al. (1998) have shown that the 12 μm luminosity function is dominated by AGNs at such level. This could not be the case in our sample for 3 reasons : 1) our galaxies are observed at high redshift ($< z >= 0.7$) where the LW3 filter is shifted in the wavelength range where the aromatic bands play a major role. For an AGN, where no bands are observed, the K-correction effect leads to a loss of 80 per cent of the local flux in the filter, while for a spiral dominated by the bands, it leads to a gain of 40 per cent, thus favoring the detection of band dominated objects. 2) The evolution of AGNs in the radio and IRAS faint counts is well described by a luminosity evolution in $(1+z)^3$ (Pearson & Rowan-Robinson 1996). This evolution is much too weak to account for the excess observed in the deep 15 μm, that is made by the sources analyzed here. 3) 9 ISOCAM sources have been detected by deep radio integrations. Their measured spectral index led Richards et al. (1998) to classify 3 of them as AGNs and the remaining 6 as star formation dominated. The same ratio is observed in the radio sample alone, indicating that the mid-IR selection does not favor AGNs.

It therefore seems that the galaxies responsible for the excess in the 15 μm counts are dominated by star–formation process. However, the possibility that they are dominated by a dust enshrouded AGN that would not appear neither at radio wavelength nor in spectroscopy is still left open to more detailed follow–up. Deep observations in the LW2 band can help to identify the contribution from AGNs at redshifts below 0.5 or above 1. by using the mid-IR colors, but the ISO-HDF observation in this band is not sensitive enough to allow for this study. Our team is performing a similar study on a larger area of the southern hemisphere where very deep LW2 data have also been obtained.

5. SPECTROSCOPIC PROPERTIES

Part of the spectra used to measure the redshifts of the sources of the Barger et al. (1999) catalog have been made available to the community by the group of the University of Hawaii. We have measured on these spectra the equivalent width of the [OII] line (3727 Å), which is an indicator of star formation (Kennicutt 1992). Surprisingly, the 15 μm sources for which the spectra were available do not belong to the higher [OII] emitters, in contrary to what their star–forming or AGN activity is indicating from the mid-IR luminosity. The equivalent width of the [OII] line is the ratio of the flux in the [OII] line which is a direct measure of the star formation rate, to the continuum level under the line which is dominated at this wavelength by stellar emission. The flux at 15 μm of the ISOCAM sources is due to dust heated by young stars. It is therefore related to the star-forming activity of the galaxy. The ratio of the luminosity at 15 μm over the luminosity in the K band of a galaxy is therefore the ratio of a measure of its star formation rate over a measure of its stellar content, in the same way than the [OII] equivalent width (hereafter EW([OII])). A correlation is therefore expected if one plots EW([OII]) versus the $L_{15\,\mu m}/L_K$ for all the ISOCAM detected galaxies for which a spectrum is available, because when $L_{15\,\mu m}/L_K$ rises, it means that the star formation activity of the galaxy rises, and therefore the EW([OII]) should also rise.

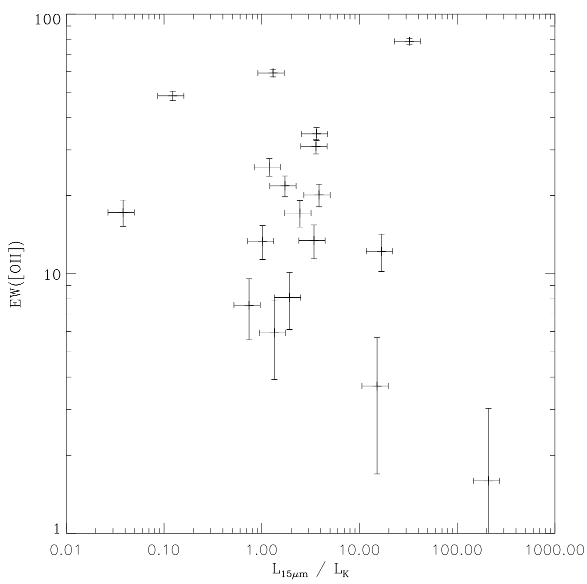

Figure 2. [OII] equivalent width as a function of the ratio $L_{15\,\mu m}/L_K$ for the subsample of the ISO-HDF sources for which the spectrum is available.

Figure 2 presents such plot for the part of the 15 μm sample for which spectra are available. We have used here a K-correction of spiral to compute the 15 μm luminosity, but the results do not qualitatively change when we use a K–correction of a more active galaxy. A weak anti-correlation is found when a correlation was expected. We interpret this result as the effect of dust extinction on the [OII] : if star formation occurs in dust enshrouded regions, this line will be strongly extincted, due to the short wavelength where it sits, while the stellar continuum at this wavelength will remain unaffected, because most of the emitting stars are outside the dust clouds where stars are forming. This leads to a decrease of the EW([OII]). On the contrary, the 15 μm flux is much less affected by extinction and remains a good tracer of star formation.

This result demonstrates how dangerous it is to derive star–forming activity from UV data alone, the wavelengths used (1200 and 2600 Å) being even blueward than the [OII] line, and therefore even more sensitive to extinction. It appears that in the HDF, a significant fraction of the star formation can be missed if one does not correct for the absorption of UV and visible photons by dust.

6. CONCLUSIONS

Our results so far show that the galaxies responsible for the excess of the number counts at 15 μm are : 1) Luminous galaxies in the mid-IR at redshifts between 0.4 and 1.2) Large spirals and merging systems whose colors are not bluer or redder than usual spiral galaxies, 3) These galaxies show signs of extinction of the usual [OII] line diagnostic for star formation. Whether the mid-IR emission of these systems is dominated by a dust enshrouded AGN or by star formation is still an open question. However, if an AGN dominates in all the sources, it has to be completely buried in order to remain spectroscopically undetected, as well as radio quiet.

The measure of the cosmic infrared background at various wavelength gives more constraints on the nature of these galaxies. At 15 μm in the ISO–HDF observation, the slope of the integrated number counts is of 1.3 (Aussel et al. 1999). This indicates that the faintest sources dominate in the integral that leads to the measure of the cosmic infrared background (CIB) at this wavelength, and that it has not yet been resolved into discrete sources. Integrating the number counts obtained with ISOCAM down to the depth of the ISO–HDF observation leads to a lower limit of the CIB of 1.15 nW/m^2/sr, that is dominated by the faintest sources, i.e. the galaxies responsible for the excess in the counts that are studied here. These galaxies are at a median redshift of 0.75, and thus emit the observed contribution to the background at 8.5 μm. They also emit at longer wavelength in the far-infrared. Their rest–frame emission at 80 μm will contribute to the CIB at 140 μm. The measured value of the CIB at this wavelength by Hauser et al. (1999) is of 25 nW/m^2/sr. We deduce from this that if the ratio of the energy emitted at 140 μm over the one emitted at 8.5 μm by the galaxies detected by ISOCAM cannot be greater than 25/1.2$\sim$21. This sets very strong constrains on the shape of the spectral energy distribution (SED) of the ISOCAM sources. Galaxies like Arp 220 with a SED strongly peaking around 80 μm have a ratio of the order of 100 in the energy emitted at 80 and 8.5 μm and are therefore excluded. The ISOCAM sources are therefore luminous infrared galaxies, as indicated by their mid–IR luminosity, that should have a flatter SED in the far–infrared.

The observation of the Hubble Deep Field at mid–infrared wavelength thus reveals an important sample of star forming galaxies that would have remained unnoticed with optical data alone. We are now extending the size of our sample with other observations in the southern hemisphere to confirm and extend our results.

ACKNOWLEDGEMENTS

We are grateful to Len Cowie for having given us access to the Barger et al. (1999) catalog before its publication as well as for his help for handling the spectra of the Hawaii group.

REFERENCES

Aussel, H. 1999, PhD Thesis, Université de Paris–VII.

Aussel, H., Cesarsky, C.J., Elbaz, D. et al. 1999, A&A, in press

Barger, A.J., Cowie, L.L., Trentham, N. et al. 1999 AJ in press

Cesarsky, C.J., Abergel, A., Agnèse, P. et al. 1996, A&A, 315, L32

Coleman, G.D., Wu, C.C., Weedman, D.W. 1980, AJSS, 43, 393

Désert, F.-X., Puget, J.-L., Clements, D.L. et al. 1999, A&A, in press

Ellis, R.S. 1997, ARA&A, 35, 389

Fang, F., Shupe, D.L., Xu, C., et al. 1998, ApJ, 500, 693

Fernández-Soto, A., Lanzetta, K. M., et Yahil, A. 1999, ApJ in press

Hauser, M.G., Arendt, R.G., Kelsall, T. et al. 1998, ApJ, 508, 25

Kennicutt, R.C. 1992, ApJ, 388, 310

Lilly, S., Cowie, L.L., Gardner, J.P., 1991, AJ, 369, 79

Pearson, C., Rowan-Robinson, M. 1996, MNRAS, 283, 174

Richards, E.A., Kellermann, K.I., Fomalont, E.B. et al. 1998, AJ,116 , 1039

Rowan–Robinson, M., Mann, R.G., Oliver, S.J. et al. 1997, MNRAS, 289, 490

Williams, R.E., Blacker, B., Dickinson, M. et al. 1996, AJ, 112, 1335

ISO IMAGING OF GAMMA-RAY BURST LOCATIONS

M. Delaney[1], L. Hanlon[1], L. Metcalfe[2], B. McBreen[1], R. Laureijs[2], F. Quilligan[1], N. Smith[10], B. Altieri[2], A. Castro-Tirado[3], E. Costa[4], M. Feroci[4], F. Frontera[5], T. Galama[6], J. Gorosabel[3], P. Groot[6], J. Heise[7], C. Kouveliotou[8], E. Palazzi[9], J. van Paradijs[6], & L. Piro[4]

[1]Department of Experimental Physics, University College Dublin, Belfield, Dublin 4, Ireland
[2]ISO Data Centre, ESA Astrophysics Division, Villafranca del Castillo, Spain
[3]Laboratorio de Astrofisica Espacial y Fisica Fundamental, Villafranca del Castillo, Spain
[4]Istituto di Astrofisica Spaziale CNR, Frascati, Italy
[5]Dipartimento di Fisica, Universita di Ferrara, Italy
[6]Astronomical Institute "Anton Pannekoek", University of Amsterdam, The Netherlands
[7]SRON Laboratory for Space Research, Utrecht, The Netherlands
[8]NASA Marshall Space Flight Center, Huntsville, Alabama, USA
[9]Istituto Tecnologie e Studio Radiazione Extraterrestrie CNR, Bologna, Italy
[10]Cork Institute of Technology, Cork, Ireland

ABSTRACT

We present results from the ISO Target of Opportunity (TOO) program to observe gamma-ray burst (GRB) locations with the CAM and PHOT instruments. The error circles of GRB 970228, GRB 970402, GRB 970508 and GRB 980329, obtained by the X-ray instruments aboard the Italian-Dutch *BeppoSAX* satellite, were observed on timescales ranging from days to months after the GRB events. These observations, awarded under Discretionary time, represent the first prompt GRB counterpart searches at far-infrared wavelengths. A list of observations made in this TOO program, and details of the analysis and results of CAM observations of GRB 970508 are presented. A tentative CAM detection of a source at this GRB position has been made at 12 μm.

Key words: gamma-ray bursts.

1. INTRODUCTION

Gamma-ray bursts (GRBs) were first discovered more than 25 years ago by the Vela satellites (Klebesadel et al. 1973). The vast majority of the more than 2000 observed bursts have been detected in the last seven years by the Burst and Transient Source Experiment (BATSE) (Meegan et al. 1996) aboard the Compton Gamma-Ray Observatory (CGRO). The continuum emission from GRBs generally peaks at a few hundred keV and extends with a power law shape up to MeV energies. Emission up to GeV energies has been seen in a few rare cases. At energies below a few hundred keV the spectra rapidly turn over, to the extent that only $\sim$ 2 per cent of the emission observed during the burst is detected below 10 keV. Despite 20 years of intensive searches, until recently no convincing flaring or fading counterparts had been detected. The rapid localization capability of the two Wide Field Cameras (WFC) (Jager et al. 1993) aboard *BeppoSAX* (Boella et al. 1997) precipitated the ground-breaking discoveries of X-ray (Costa et al. 1997a), optical (van Paradijs et al. 1997) and radio afterglows (Frail et al. 1997) to a number of GRBs. Redshifted spectroscopic lines in the optical afterglows of a handful of GRBs have now confirmed the cosmological nature of this phenomenon (Metzger et al. 1997). The appearance of the multiwavelength afterglows is broadly consistent with the model in which an adiabatically expanding blast wave accelerates synchrotron emitting relativistic electrons, a significant fraction of which may cool rapidly (Waxman et al. 1998; Sari et al. 1998; Galama et al. 1998a). However, the nature of the underlying emission mechanism, which must provide about 10^{52} ergs of energy to power the GRB, remains unknown. Compact stellar remnant progenitors, such as supernovae (Berezinsky et al. 1996; Woosley 1993) or hypernovae (Paczynski 1998) could produce the required energy. Consequently it might be expected to find GRBs in or near star forming regions and with probable associated emission at infrared (IR) wavelengths.

Schaefer (1981) carried out a major study of far IR emission from 23 well-localized GRBs (detected between 1979 to 1981) using the IRAS faint source catalog. Though IRAS sources were detected in 2 error boxes, these were attributed to chance associations. As IRAS flew during 1983, this search suffered from the significant disadvantage of not being a rapid follow-up study. Compared to IRAS, ISO had a wider wavelength coverage, better spatial resolution, greater sensitivity and a longer lifetime (Kessler et al. 1996). ISO also had the added benefit in that its operational lifetime overlapped with that of *BeppoSAX*. With its Wide Field Cameras *BeppoSAX* made it possible to promptly localize the position of a GRB. In August 1996, *BeppoSAX* localized its first GRB about 6 weeks after the burst event. By January 1997, the time delay had been reduced to 10 hours and a TOO program was awarded to make the rapid follow-up observations of *BeppoSAX* localized GRBs with ISO.

Table 1. GRB locations observed by ISO. Those GRBs with detected optical transients (OT) and X-ray and radio afterglows are indicated. The TOO delay is the response time of ISO to the initial GRB detection. Those locations that did not appear in ISO's visibility window for some time after the initial GRB detection are marked with †.

GRB	z	Optical	X-ray	Radio	TOO delay
970228		Y	Y		7 months†
970402			Y		2.3 days
970508	0.83	Y	Y	Y	12 days†
980329		Y	Y	Y	3.8 days†

Out of 12 *BeppoSAX* localized GRBs that occurred between the beginning of the TOO program (February 1997) and the end of the ISO mission (April 1998) only 2 bursts, GRB 970402 and GRB 970828, immediately met ISO's visibility criteria. An ISO follow-up observation of the former was made within 55 hours, while an observation of the latter was not conducted due to unavoidable scheduling delays and the absence of an optical transient (OT). A further 3 burst locations from the sample of 12 became visible *after* the burst event. Limited observations of the GRB 970508 and GRB 980329 locations were conducted within days, but there was a considerable delay of 7 months before the location of GRB 970228 was observed. Table 1 lists the GRBs observed by ISO and the delay time of each follow-up observation.

2. OBSERVATIONS AND DATA ANALYSIS

A total of 4 GRB locations have been observed by ISO (Table 1). Here we report on the results of CAM observations of GRB 970508 and give a brief description of the observations of the remaining 3 GRBs. A log of all ISO observations of GRB locations is presented in Table 2.

2.1. GRB 970228

The *BeppoSAX* detection of this burst, and its subsequent decaying X-ray afterglow (Costa et al. 1997a), led to the detection of of the first GRB optical counterpart (van Paradijs et al. 1997). CAM and PHOT observations of the X-ray error box were conducted on 2 October 1997 – this delay of 7 months was due to ISO visibility constraints. The CAM observation was made with the LW3 filter (Heske et al. 1994). PHOT observations were made with the C100 detector (C_60 and C_90 filters) and the C200 detector (C_160 filter) (Klaas et al. 1994). Results are in preparation (Groot et al. 1998).

Table 2. Log of ISO observations of GRB locations. The CAM filters LW2, LW3, and LW10 cover the wavelength ranges 5–8.5 μm, 12–18 μm and 8–15 μm. The PHOT filters C_60, C_90 and C_160 are centered on the wavelengths 60.8 μm ($\Delta\lambda$ = 60.8 μm), 95.1 μm ($\Delta\lambda$ = 95.1 μm) and 174 μm ($\Delta\lambda$ = 174 μm).

GRB	UT Start – End	Instrument	Filter
970228	Oct 02.906 – 02.955	CAM	LW3
	Oct 02.955 – 02.982	PHOT	C_60
	Oct 02.955 – 02.982	PHOT	C_90
	Oct 02.983 – 02.990	PHOT	C_160
970402	Apr 05.179 – 05.232	CAM	LW10
	Apr 05.233 – 05.287	CAM	LW10
	Apr 05.246 – 05.307	PHOT	C_160
	Apr 13.157 – 13.219	CAM	LW10
	Apr 13.220 – 13.279	CAM	LW10
	Apr 13.280 – 13.323	CAM	LW10
	Apr 13.324 – 13.366	CAM	LW10
970508	May 21.057 – 21.087	CAM	LW10
	May 24.050 – 24.094	CAM	LW10
	May 24.095 – 24.106	PHOT	C_60
	May 24.107 – 24.114	PHOT	C_160
	Nov 11.021 – 11.065	PHOT	C_60
	Nov 11.021 – 11.065	PHOT	C_90
	Nov 11.066 – 11.070	PHOT	C_160
980329	Apr 01.972 – 01.982	CAM	LW3
	Apr 01.983 – 01.992	CAM	LW2
	Apr 04.962 – 04.975	CAM	LW3
	Apr 04.975 – 04.988	CAM	LW2

2.2. GRB 970402

The *BeppoSAX* error box of GRB 970402 was the first to be rapidly surveyed at far-infrared wavelengths (Castro-Tirado et al. 1998a). In total, 8 ISO observations were made of this error box. Two consecutive observations with CAM LW10 and a PHOT C_160 observation on 5 April 1997, about 2.3 days after the event, and a further 4 consecutive CAM LW10 observations on 13 April. Though about 50 sources (including the variable star BL Cir) were detected by CAM in a 2 arcmin field centered on the GRB error box, no new transient sources down to a 5 σ limit of 0.14 mJy in the LW10 filter and 350 mJy in the C_160 filter were identified (Castro-Tirado et al. 1998a).

2.3. GRB 970508

This burst triggered the *BeppoSAX* GRB monitor on May 8, 1997 (Frontera et al. 1997; Costa et al. 1997b). It was simultaneously detected by BATSE as a weak, classical GRB event (Kouveliotou et al. 1997). Initially localized to within a 3 arcmin radius error circle by the *BeppoSAX* WFC2 detector (Heise et al. 1997), the detection of a fading X-ray source by the narrow-field instrument (NFI) further localized the GRB 970508 location to within a 50 arcsec circle (Piro et al. 1997). Within this error circle an OT was discovered whose flux increased for the first two days post-burst and then subsequently decayed (Bond 1997; Djorgovski et al. 1997). The decay phase was characterized by a power law dependence with time ($f(t) \propto t^{-1.14}$ days), similar to that observed for GRB 970228 (Castro-Tirado et al. 1998b; Galama et al. 1998b; Garcia et al. 1998; Sokolov et al. 1998; Galama et al. 1997). Near IR (2.2 μm) emission was also observed from the OT source between May 13.25 (K_s = 18.2±0.2 mag) and May 20.21 (K_s = 19±0.3 mag) (Chary et al. 1998). Spectra of the OT exhibit evidence that the source is at a redshift of 0.835, providing the first direct measurement of the distance to a GRB (Metzger et al. 1997). Radio afterglow was also detected from the OT position, reaching a plateau flux of $\sim$ 600 μJy at 4.86 and 8.46 GHz (Frail et al. 1997), and with a time-averaged (May 17–22) flux of 1.62 ± 0.25 mJy (Bremer et al. 1998) at 86.2 GHz. More than 50 days after the GRB event, 1.4 GHz emission with an average flux of 228 ± 30 μJy was detected (Galama et al. 1998a).

The GRB 970508 error circle was not visible with ISO immediately after the burst, but became visible for seven short windows lasting from 3000 to 8500 seconds between May 20 and May 26. Observations were made with CAM on May 21 and 24 and with PHOT on May 24. A second window was available from October 25 to November 21 1997 and follow-up observations of the field were made with PHOT on November 11 1997. A log of the observations is presented in Table 2. All May observations were centred at $\alpha(2000) = 6^h\ 53^m\ 46.7^s$, $\delta(2000) = +79^\circ\ 16'\ 02''$, the centre of the X-ray afterglow error circle (Piro et al. 1997). All November observations were centred at $\alpha(2000) = 6^h\ 53^m\ 49.2^s$, $\delta(2000) = +79^\circ\ 16'\ 19''$, the position of the OT (Bond 1997).

Raster maps of the NFI 50 arcsec radius error circle were obtained with the PHOT C_60, C_90 and C_160 filters. Further details of the PHOT observations and data reduction will be given in Hanlon et al. 1998. Micro-scan raster observations of the same field were carried out with CAM using the LW10 filter (8–15 μm, reference wavelength 12 μm assuming a $1/\lambda$ spectrum), the 3 arcsec PFOV and a raster step-size of 7 arcsec (Heske et al. 1994). This configuration has a PSF with FWHM of $\sim$ 4 arcsec. Due to the non-integral pixel step size the pixels in the resulting CAM mosaic have a resolution of 1 arcsec. The 6×6 raster on May 21 covered an area of 131×131 arcsec and achieved deepest coverage (total integration time of 2379 s) in a 60×60 arcsec area at the centre of the mosaic where all 36 points of the raster overlap. The 8×8 raster on May 24 covered a 145×145 arcsec mosaic, with deepest coverage (total integration time of 3432 s) in the central 45×45 arcsec area. All data processing steps, including dark current subtraction, cosmic ray *glitch* removal and flatfielding, were performed with the CAM Interactive Analysis system (CIA) (Ott et al. 1997). Persistent glitch residuals and severe detector transients were removed manually. Point source photometry was performed by integrating the signal in a 4×4 arcsec aperture (approximately equal to the PSF FWHM) positioned on the centroid of the source. The measured flux was background subtracted and corrected for the flux attenuation due to the familiar lag in detector response (the responsive transient) and flux lost outside the aperture due to the size of the PSF. The overall error was derived by combining the uncertainty from all of the above effects with the error on the background. The latter was estimated by selecting a source-free region of the mosaic with sensitivity matching that of the source region, rebinning the pixels in this region into 4×4 arcsec bins (to match the aperture size used in the photometry) and then calculating their RMS.

2.4. GRB 980329

This very bright burst, with a variable radio counterpart (Taylor et al. 1998) and a fading OT (Palazzi et al. 1998), is the 10th GRB localized by *BeppoSAX*. Though not immediately visible to ISO, the location of this burst became visible for a limited period on 4 April 1998, 3.8 days after the burst event. The very short visibility window made it necessary to observe with CAM using an unorthodox *chopping* observation technique. Further details of this technique can be found in Ali et al. (these proceedings). A paper detailing the results of the CAM observations of GRB 980329 is in preparation (Metcalfe et al. 1999).

3. RESULTS AND DISCUSSION

Of the observations listed in Table 2 the results of the CAM observations of GRB 970508 are presented here. The results of PHOT observations of this burst are to appear in Hanlon et al. 1998. Of the 3 remaining bursts, the results of observations of GRB 970402 have been published (Castro-Tirado et al. 1998a) and the analysis and interpretation of the data from the observations of GRB 970228 and GRB 980329 is still ongoing (Groot et al. 1998; Metcalfe et al. 1999).

The central 45×45 arcsec region of the May 24 CAM LW10 mosaic image of the GRB 970508 location is shown in Figure 1. The CAM contours are overlaid on the June 2 HST STIS image (Pian et al. 1998). The most significant ($\sim 3.6\ \sigma$) source is coincident with the OT to within a few arcseconds. Since this matches the ISO pointing accuracy (estimated from the coincidence of several sources in the combined May 21 and May 24 CAM mosaics with optical sources) it is very unlikely that this IR source is one of the faint galaxies, G1 and G2, that have been identified by Pian et al. 1998. No OT coincident sources appear in data from the earlier May 21 observation. The *a posteriori* probability of detecting a source with the measured flux in a CAM pixel is less than 1 per cent, based on estimation of source counts derived from CAM observations of the Hubble Deep Field (Oliver et al. 1997). Assuming a decay proportional to $t^{-1.1}$ days (as was seen in the R band) the flux on May 21 can be inferred by extrapolating the flux observed on May 24. This yields an expected May 21 flux 79 ± 35 μJy. Since this is not inconsistent with the measured 3 σ upper limit of 60 μJy for the May 21 observation, we cannot rule out the possibility that the origin of this 8–15 μm flux is constant rather than transient.

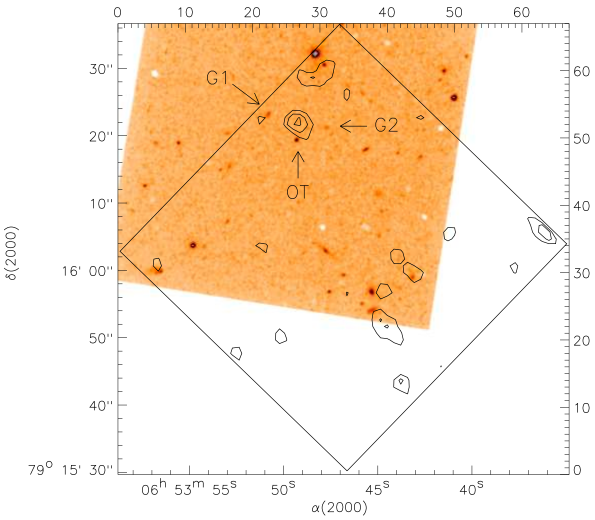

Figure 1. The central 45 × 45 *arcsec region of the CAM LW10 mosaic image taken on May 24 overlaid with the HST STIS image from June 2. The OT and two nearby galaxies, G1 and G2, are indicated. The orientation is North up and East left. CAM LW10 pixel scaling are shown on the top and right axes. The white 'divets' are due to a flatfielding error in the STIS standard processing pipeline. The contour levels are: 2, 3 and 4* μ*Jy arcsec*$^{-2}$.

4. CONCLUSIONS

The ISO observations of GRB 970508 place unique limits on the level of far-infrared emission in the weeks and months following the burst event. Associated emission in the CAM LW10 filter (8–15 μm) has been tentatively detected from this GRB source on May 24. This emission is consistent with the extrapolated optical to radio synchrotron spectrum which has been modelled as arising from relativistic electrons which are accelerated by an adiabatically expanding blast wave (Galama et al. 1998a). Though no conclusive detection of IR emission from a GRB source has been made, it is important to note that only a preliminary result is reported here. The analysis and interpretation of much of the data has yet to be completed.

ACKNOWLEDGMENTS

The ISOCAM data presented in this paper was analysed using 'CIA', a joint development by the ESA Astrophysics Division and the ISOCAM Consortium. The ISOCAM Consortium is led by the ISOCAM PI, C. Cesarsky, Direction des Sciences de la Matiére, C.E.A., France.

REFERENCES

Berezinsky, V. et al. 1996, ApJ 469, 311

Boella, G. et al. 1997, A&AS 122, 299

Bond, H. 1997, IAU Circular 6654

Bremer, M. et al. 1998, A&A 332, L13

Castro-Tirado, A. et al. 1998a, A&A 330, 14

Castro-Tirado, A. et al. 1998b, Science 279, 1011

Chary, R. et al. 1998, ApJ 498, L9

Costa, E. et al. 1997a, Nature 387, 783

Costa, E. et al. 1997b, IAU Circular 6649

Djorgovski, S. et al. 1997, Nature 387, 876

Frail, D. et al. 1997, Nature 389, 261

Frontera, F. et al. 1997, A&AS 122, 357

Galama, T. et al. 1997, Nature 387, 479

Galama, T. et al. 1998a, ApJ 500, L101

Galama, T. et al. 1998b, ApJ 497, L13

Garcia, M. et al. 1998, ApJ 500, L105

Groot, P. et al. 1998, in preparation

Hanlon, L. et al. 1998, in preparation

Heise, J. et al. 1997, IAU Circular 6654

ISOCAM Observer's Manual: 1994, ESA

Jager, R. et al. 1993, Adv. Space Res. 13, 315

Kessler, M. et al. 1996, A&A 315, L27

Klaas, U. et al. 1994, ISOPHOT Observer's Manual, ESA

Klebesadel, R. et al. 1973, ApJ 182, L85

Kouveliotou, C. et al. 1997, IAU Circular 6660

Meegan, C. et al. 1996, ApJS 106, 65

Metcalfe, L. et al. 1999, in preparation

Metzger, M. et al. 1997, Nature 387, 878

Oliver, S. et al. 1997, MNRAS 289, 471

Ott, S. et al. 1997, in G. Hunt and H. Payne (eds.), *Astronomical Data Analysis Software and Systems VI*, Vol. 125 of *ASP Conf. Series*, p. 34

Paczynski, B. 1998, ApJ 494, 45

Palazzi, E. et al. 1998, A&A 386, L95

Pian, E. et al. 1998, ApJ 492, L103

Piro, L. et al. 1997, IAU Circular 6656

Sari, R. et al. 1998, ApJ 497, 17

Schaefer, B. 1981, Nature 294, 722

Sokolov, V. et al. 1998, A&A 334, 117

Taylor, G. et al. 1998, ApJ 502, L115

van Paradijs, J. et al. 1997, Nature 386, 686

Waxman, E. et al. 1998, ApJ 497, 288

Woosley, S. 1993, ApJ 405, 273

FIRBACK FAR INFRARED SURVEY WITH ISO: DATA REDUCTION, ANALYSIS AND FIRST RESULTS

H. Dole[1], **G. Lagache**[1], **J-L. Puget**[1], **R. Gispert**[1], **H. Aussel**[2,7], **F.R. Bouchet**[3], **C. Ciliegi**[4], **D.L. Clements**[5], **C.J. Cesarsky**[2], **F.-X. Désert**[6], **D. Elbaz**[2], **A. Franceschini**[7], **B. Guiderdoni**[3], **M. Harwit**[8], **R. Laureijs**[9], **D. Lemke**[10], **R. McMahon**[11], **A.F.M. Moorwood**[12], **S. Oliver**[13], **W.T. Reach**[14], **M. Rowan-Robinson**[13], **M. Stickel**[10]

[1]Institut d'Astrophysique Spatiale, Orsay, France
[2]Service d'Astrophysique, CEA/DSM/DAPNIA Saclay, France
[3]Institut d'Astrophysique de Paris, France
[4]Osservatorio Astronomico di Bologna, Italy
[5]Cardiff University, UK
[6]Laboratoire d'Astrophysique, Observatoire de Grenoble, France
[7]Osservatorio Astronomico di Padova, Italy
[8]511 H.Street S.W., Washington, DC 20024-2725
[9]ISOC ESA, VILSPA, Madrid, Spain
[10]MPIA, Heidelberg, Germany
[11]Institute for Astronomy, University of Cambridge, UK
[12]ESO, Garching, Germany
[13]Imperial College, London, UK
[14]IPAC, Pasadena, CA, USA

ABSTRACT

FIRBACK is one of the deepest cosmological surveys performed in the far infrared, using ISOPHOT. We describe this survey, its data reduction and analysis. We present the maps of fields at $175\,\mu m$. We point out some first results: source identifications with radio and mid infrared, and source counts at $175\,\mu m$. These two results suggest that half of the FIRBACK sources are probably at redshifts greater than 1. We also present briefly the large follow-up program.

Key words: ISOPHOT; far infrared survey; cosmology; galaxy evolution

1. INTRODUCTION

The discovery of the Cosmic Far Infrared Background Radiation (CFIBR) (Puget et al. 1996, Fixsen et al. 1998, Hauser et al. 1998, Lagache et al. 1999) using COBE data and constraints on its spectrum, demonstrates that about two thirds of the light emitted by galaxies integrated over all redshifts has been processed by dust and released at FIR and submm wavelengths. This background is in line with models using strong evolution of galaxies.
Studying the population of galaxies radiating mostly at long wavelengths as a function of redshift is thus one of the important but difficult observational tasks of today in the field of galaxy formation and evolution (see Puget & Lagache, these proceedings).
In this context, FIRBACK, which is a cosmological survey dedicated to a study of the Cosmic Far Infrared Background and galaxies contributing to it, is one important step.

2. DATA SET

FIRBACK is a survey of 3 main fields (described in Table 1) covering 4 square degrees using ISOPHOT. All fields have been observed in raster mode (AOT P22) with the `C200` detector and `C_160` filter centered at $\lambda = 175\,\mu m$. We have also additional ISO observations with ISOPHOT and ISOCAM (see below).

Table 1. Fields of the FIRBACK survey.

Field Name	α_{2000}	δ_{2000}	l	b	area
	h min	deg min	deg	deg	sq deg
Marano	03 11	-54 45	270	-52	1
ELAIS N1	16 11	+54 25	84	+45	2
ELAIS N2	16 36	+41 05	65	+42	1

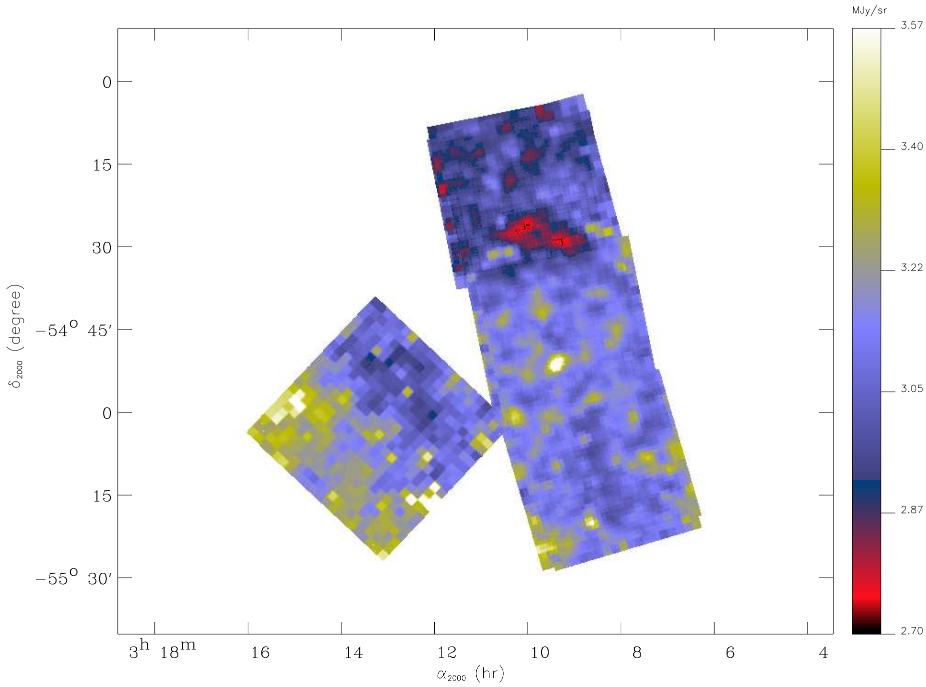

Figure 1. Map of FIRBACK Marano fields

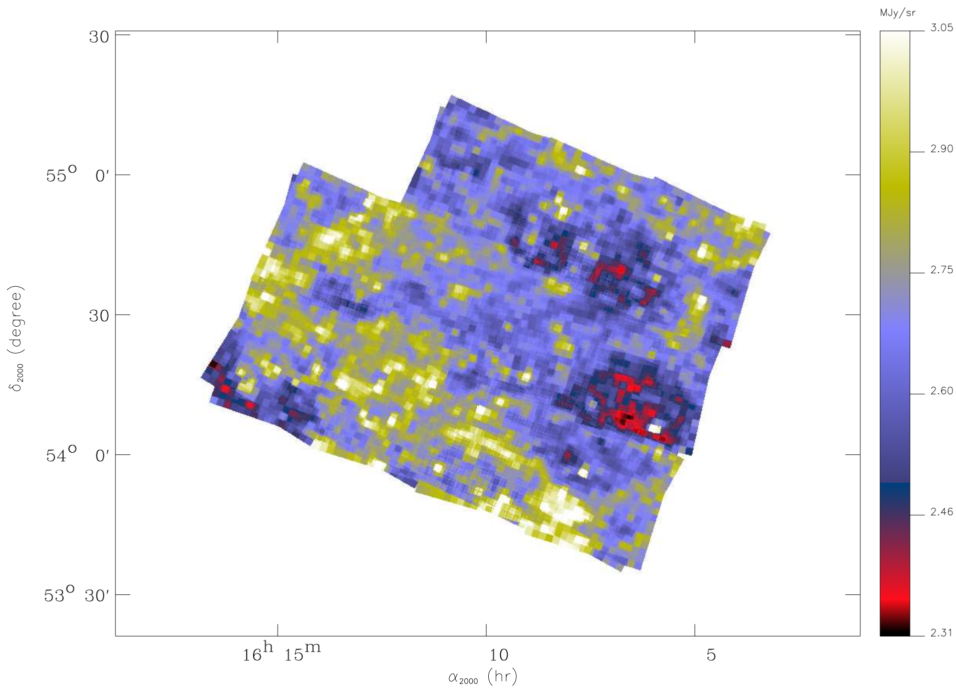

Figure 2. Map of FIRBACK ELAIS N1 field

FIRBACK Marano

This area (map Figure 1) is composed of four individual fields, called Marano 1, 2, 3 and 4, which have been observed four times. The redundancy goes from 32 (in overlapping regions) to 1 (on the edges) with an average of 16, and the oversampling is optimal in both Y and Z directions in Marano 2, 3 and 4 (half pixel offset between rasters). Marano 1 covers $31.5' \times 31.5'$, and Marano 2, 3 and 4 about $77' \times 26'$. Integration time per sky pixel is 256 s on average. *Additional observations:* in Marano 1 we have one P25 absolute measurement, five small rasters at $90\,\mu m$ (not yet reduced); in the complete Marano field, we have a $15\,\mu m$ ISOCAM survey.

FIRBACK ELAIS N1

This area (map Figure 2) is composed of eleven individual fields, observed 2 times with an offset of less than a pixel, and the redundancy goes from 16 (in overlapping regions) to 1 (on the edges) with an average of 8. ELAIS N1 covers about 2 square degrees. Integration time per sky pixel is 128 s on average. Note that the northern FIRBACK fields have been chosen to cover some corresponding ELAIS fields at other wavelengths (see Rowan-Robinson et al., these proceedings).

FIRBACK ELAIS N2

This area (map Figure 3) is composed of nine individual fields, observed 2 times with an offset of one pixel, so the redundancy is 8 on average, without oversampling. ELAIS N2 covers about $57' \times 57'$.

3. DATA REDUCTION

3.1. From raw data to AAP

We used PIA[1] version 7.2.2 (PHT Interactive Analysis, Gabriel et al. 1997) to reduce data from ERD (Edited Raw Data, the lowest level) to AAP (Auto Analysis Product Data, level where flux density and positions are available):
- ERD to SRD (Signal per Ramp Data): linearisation, deglitching, fit ramps to first order
- SRD to SCP (Signal per Chopper Plateau Data): deglitching, no drift correction
- SCP to AAP: no reset interval correction (reset times are identical), subtraction of dark current, power calibration using interpolation between 2 FCS.

We then used our own IDL routines to correct for transients induced by strong glitches, and to perform a flat correction using observational redundancies.

[1]PIA is a joint development by the ESA Astrophysics Division and the ISOPHOT Consortium

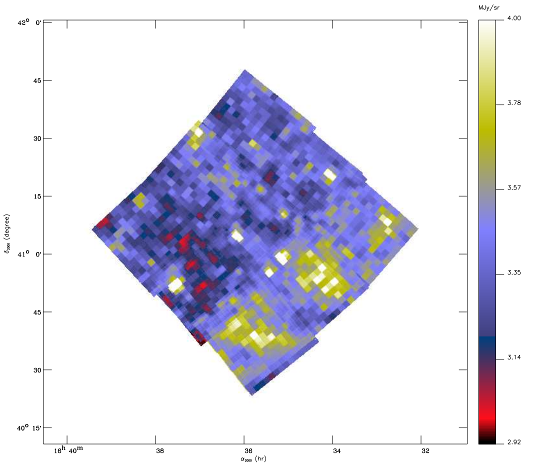

Figure 3. Map of FIRBACK ELAIS N2 field

3.2. Map projection

Our basic data projection is performed in two steps: (1) geometrical grid computation and (2) projection of the signal.
- The first step is the most time consuming. We read all AAP data of one complete field, and create a large grid in (α, δ) with tunable pixel sizes (usually 10 arcsec); this step has to be performed just one time.
- The second step just acts to restore the grid, to coadd individual raster data onto the grid by distributing the pixel signal in the area of one pixel, and by updating a weighting map.

This method is well-suited to large amounts of data, in terms of sky surface or number of co-added rasters with different roll angles. Figures 1, 2 and 3 show such maps.

4. RESULTS

4.1. Source detection

Source detection is directly performed on final co-added maps, using eye recognition to discriminate point sources from cirrus structure. We then computed the flux by aperture photometry with radii chosen to minimize noise in source detection $R_{min} = 60''$ and $R_{max} = 92''$ (Puget et al. 1999).

4.2. Catalogs and identifications

Sources in our catalog have a S/N ratio greater than 3, and photometric accuracy is about 30 %. Fluxes are in the range 75 mJy to 1.6 Jy, with an average of 252 mJy and a median of 175 mJy.

In order to constrain both Spectral Energy Distribution (SED) and position of these sources, we looked for identifications: Table 2 gives a summary of detected sources and identifications with ISO or ground-based radio telescopes.

In the *Marano Field*, we performed a smaller $15\,\mu m$ survey using ISOCAM (Désert et al. 1998), which covers about 50 % of the $175\,\mu m$ survey surface. Radio identifications are performed using Australia Telescope Compact Array available data (Gruppioni et al. 1997) or preliminary data of our program being reduced, that is why 8 identifications is a lower limit.

The situation is different in northern fields *ELAIS N1 & N2* because the ELAIS consortium performed observations using ISO at $\lambda = 15\,\mu m$, $\lambda = 90\,\mu m$ (Rowan-Robinson et al., these proceedings), using the VLA at $\lambda = 20\,cm$ (Ciliegi et al. 1998), and at other wavelengths. Most of the 31 sources with $90\,\mu m$ counterpart have a color ratio $\frac{F_{175\,\mu m}}{F_{90\,\mu m\,PHOT}} \geq 2$, which has to be compared to local sources ($z \leq 0.1$) where $\frac{F_{175\,\mu m}}{F_{100\,\mu m\,IRAS}} \simeq 1$ (Stickel et al. 1998), suggesting that a significant proportion of FIRBACK sources are large-redshift sources (see discussion below). Most of NED[2] identifications are FIRST (Becker et al. 1995) or IRAS sources.

[2]The NASA/IPAC Extragalactic Database (NED) is operated by the Jet Propulsion Laboratory, California Institute of Technology, under contract with the National Aeronautics and Space Administration

Table 2. Number of FIRBACK sources and identifications

Field Name	175 μm	15 μm	90 μm	20 cm
$F_\nu(mJy) \geq$	75	1	60	0.2
Marano	78	29	no data	≥ 8
ELAIS N1	113	19	18	20
ELAIS N2	85	no data	13	22

4.3. Source counts

We present raw source counts in Figure 4, using sources coming from FIRBACK ELAIS N1, N2 and Marano 2 3 4 fields (208 sources brighter than 100 mJy in less than 3 square degrees). Raw counts means here that *counts are not corrected for incompleteness.* For $log(S \geq 300\, mJy)$, counts are not expected to change a lot due to incompleteness correction, so the steep slope of 2.20 is a minimum. We also plotted Marano 1 raw counts (Puget et al. 1999) which are higher by a factor 2 but compatible within uncertainties, probably because based on 22 sources in a smaller area (0.25 square degree), Kawara et al. (1998) data in the Lockman Hole (difficult to see in the plot because their count at 150 mJy gives the same number as ours), models with and without evolution from Franceschini et al. (1998), and model E from Guiderdoni et al. (1998). Compared to extrapolated IRAS counts, FIRBACK counts are about 20 times higher at 200 mJy. Our counts are not compatible with non-evolution models and need strong evolution. Model with evolution from Franceschini et al. (1998) predicts smoother slopes than observed, whereas model E from Guiderdoni et al. (1998) fits roughly the slope even if lower than observed.

5. FOLLOW-UP [3]

An intensive multiwavelength follow-up program is being performed.
In the *Marano field*, we are following-up at $\lambda = 20$ cm using the Australia Telescope Compact Array in compact configurations (data being reduced) and extended configuration (program to submit)(Dole). In the optical range, one source has been observed with the NTT (Dennefeld).
In the *ELAIS N1 & N2 fields* at millimetre wavelengths, we are following-up using the IRAM 30 m antenna and Plateau de Bure Interferometer (Omont & Guiderdoni). Submillimetre observations in N1 are scheduled at JCMT (Scott) and in April at CSO (Lagache), and optical follow-up of sources is performed at Palomar (Reach).

[3] extended FIRBACK collaboration for follow-up also includes: D. Benford, P. Cox, M. Dennefeld, G. Helou, R. Mac Mahon, A. Omont, F. Pajot, T. Phillips, D. Scott, F. Viallefond

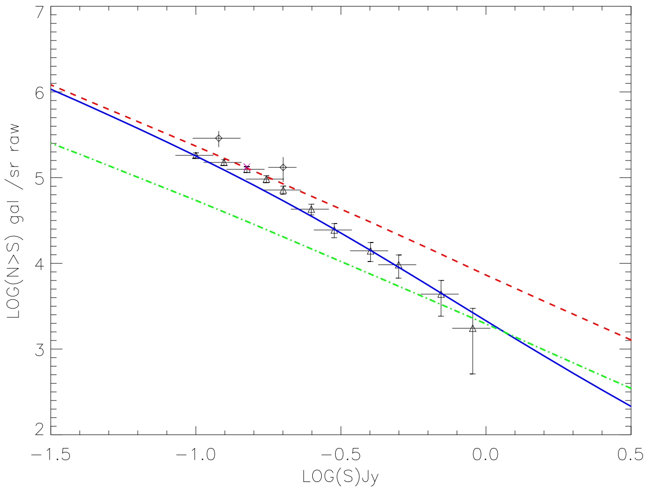

Figure 4. Source counts with FIRBACK data in Marano 1, 2, 3, 4, ELAIS N1 and ELAIS N2. These counts are not corrected for incompleteness. Data: diamonds: Marano 1 (Puget et al. 1999); triangles: ELAIS N1, N2 and Marano 2 3 4; Lockman Hole data (Kawara et al. 1998): purple star at 150 mJy, superimposed on our counts. Models: Guiderdoni et al. 1998: blue line: model E; Franceschini et al. 1998: red dash-dash: with evolution; green dash-dot: without evolution

6. DISCUSSION ON COSMOLOGICAL IMPLICATIONS

6.1. Population

The steep slope of the number counts (≥ 2.2) cannot be accounted for by the effect of the K-correction (ratio, at a given wavelength, of the emitted flux and the observed flux with a spectral redshift) if no cosmological evolution is present as can be seen in Figure 4. The Guiderdoni et al. (1998) model which gives rather a good fit to our counts presents a strong evolution for the star burst component ($\propto (1+z)^5$) and an ULIRG (Ultra Luminous Infrared Galaxies) component. In this model, the far infrared background comoving luminosity per unit volume increases by a factor of 20 from $z = 0$ to $z = 2.5$.
This model also predicts a redshift distribution for sources brighter than 100 mJy at 175 μm. The redshift distribution peaks at $z = 0.9$ with a median of $z = 1.0$, about half of the sources lie at redshift between 1 and 2, and about 10% above $z = 2$. Furthermore, this model is compatible with the far infrared background detected in the COBE data. Sources detected in our survey account for 3% of this background at 175 μm, and the model predicts that 90% of the background is made of sources brighter than 2 mJy; this predicted value is probably too low, because our slope is higher than the model, and our counts are not yet corrected for incompleteness.

6.2. Identifications

If these galaxies are star burst galaxies with a SED peaking at 75 μm, a typical source observed close to

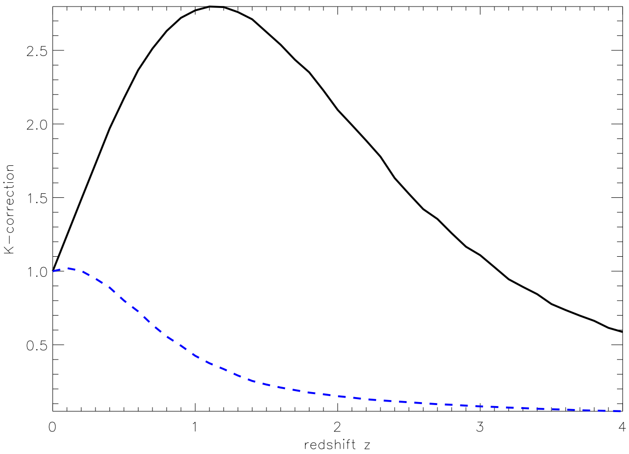

Figure 5. K-correction at 175 μm (black line) and 90 μm (blue dash-dash line) as a function of redshift for a starburst galaxy whose SED peaks at 75 μm

our detection limit ($F_{175\,\mu m} = 100\,\mathrm{mJy}$) has a luminosity $1.2 \times 10^{12} L_\odot$ (in a $h = 0.5$ and $\Omega_0 = 1$ cosmology).
The same source will have $F_{15\,\mu m} \simeq 1\,\mathrm{mJy}$ and thus is easily detectable with ISOCAM. One of the differences between mid- and far-infrared observations is that the K-correction allows observation of galaxies with redshifts in general below 1.4 (because of the PAH feature's cutoff) in the mid infrared; no such strong limit exists in the far infrared. We have only 25% detections at 15 μm, implying that more than half of the sources are at $z > 1.4$ (redshift at which 15 μm flux drops sharply).
The expected 90 μm flux for this source is $F_{90\,\mu m} \simeq 40\,\mathrm{mJy}$, and thus not easily detectable in the ELAIS survey. Furthermore, the K-correction at 90 and 175 μm as function of redshift (Figure 5) shows that between redshifts $z = 1$ and $z = 2$ the ratio $\frac{K-corr_{175\,\mu m}}{K-corr_{90\,\mu m}}$ grows from 6 to 14: at $z = 2$ a similar galaxy has 14 times more flux at 175 μm than at 90 μm.
The non-thermal emission is known to be strongly correlated with the FIR emission for starburst galaxies (e.g Helou et al. 1985), even if Sanders & Mirabel (1996) show an important scatter in the correlation. With ELAIS VLA identifications (42 sources), we compute $q = \log(F_{\nu\,FIR}) - \log(F_{\nu\,1.4GHz})$ (we take $F_{175\,\mu m}$ for $F_{\nu\,FIR}$ and not a combination of $F_{60\,\mu m}$ and $F_{100\,\mu m}$) the FIR to 1.4 GHz log ratio. For 70 % of our sample $q < 2.3$, and $2.3 \leq q < 3$ for 30 %; the dispersion is significant and must be taken into account for deep radio observations.

7. CONCLUSION

We presented the FIRBACK 175 μm survey, data reduction and analysis. Identifications of sources at various wavelengths, color ratios and source counts suggest that half of the sources are at redshifts greater than 1. Following-up these sources in order to have better positional accuracies, and SED constraints is now the key for understanding this population of dust enshrouded galaxies.
Additional information, images and papers are available online at `http://wwwfirback.ias.fr`

ACKNOWLEDGMENTS

We would like to thank M.A. Miville-Deschênes for his courtesy in permitting use of his image printing program, and C. Gabriel for fruitful discussions at ESA's ISO Data Centre (IDC) at Vilspa, Spain.

REFERENCES

Becker, R.H., et al. 1995, ApJ, 450, 559
Ciliegi, C. et al. 1998, astro-ph/9805353
Condon, J.J., 1992, ARA&A. 30, 575
Désert, F-X., et al. 1998 A&A, astro-ph/9809004
Elbaz, D., et al. 1998, astro-ph/9807209
Fixsen, D.J., et al. 1998, ApJ, 508, 123
Franceschini, A., et al. 1998, MNRAS 296, 709
Gabriel, C., et al. 1997, Proc. of the ADASS VI conf., ASP Conf. Ser., Vol.125, p108
Gruppioni, C., et al. 1997, MNRAS, 286, 470
Guiderdoni, B., et al., 1998, MNRAS 295, 877
Hauser, M.G., et al. 1998 ApJ, 508, 25
Helou, G., et al. 1985, ApJ, 298, L7
Kawara, K., et al. 1998, A&A 336, L9
Lagache, G., et al. 1999, A&A, in press, astro-ph/9901059
Puget, J.L., et al. 1996, A&A 308, L5
Puget, J.L., et al. 1999, A&A, in press, astro-ph/9812039
Sanders, D.B., Mirabel, I.F., 1996, ARA&A 34, 749
Stickel M., et al. 1998, A&A, 336, 116

DEEP ISOCAM OBSERVATIONS OF GALAXY CLUSTERS

D. Fadda & D. Elbaz
Service d'Astrophysique - CEA Saclay, F91191 Gif-sur-Yvette, France

ABSTRACT

Ten galaxy clusters, with redshift ranging from 0.2 to 1, have been observed with the ISO camera in the two bands LW2 and LW3 (centered respectively at 6.75 and 15 μm). We present a first analysis for three of these clusters at redshifts 0.2, 0.5 and 1.

Key words: galaxy clusters.

1. INTRODUCTION

Galaxy evolution is strongly influenced by the environment. The galaxy morphology is related to the density of its environment (Dressler 1980) and, in the case of galaxy clusters, elliptical galaxies are more common than spirals with respect to the field. If we look to distant clusters we detect some evolution effects as Butcher-Oemler effect (1984) or a variation in the morphological content with the redshift (Dressler et al. 1997) .

In this observational program of galaxy clusters at medium and high redshift (P.I.: A. Franceschini; collaborators: C. Cesarsky, P.A. Duc, A. Moorwood and A. Biviano), we are interested in studying the galaxy evolution with respect to their distance from the cluster center, in observing active galaxies in clusters and finally, in comparing the behavior of galaxies in clusters and in the field. This is really interesting especially after the results of IR deep surveys which claim the existence of a population of galaxies with great IR fluxes in the past ($0.6 < z < 1.$), which does not present any peculiar optical signature (Elbaz et al. 1998, Aussel et al. 1998).

2. OBSERVATIONS

Ten rich galaxy clusters, with redshift ranging from 0.2 to 1, have been observed with the ISO camera in the two bands LW2 and LW3 (centered respectively at 6.75 and 15 μm). Three of them were observed very deeply (see Tables 1 and 2).

Optical follow-up's of the observed clusters are scheduled in the next months. Only that of A1689 has already been carried out in May 1998 with EMMI on the NTT at La Silla (P.I.: P.A. Duc). A total of about 120 spectra have been obtained in a field of 3×5 square arcminutes centered on Abell 1689. The observed objects were mostly the optical counterpart candidates of the sources detected in the ISOCAM bands and the data are in course of reduction.

Table 1. Shallow observations

Cluster Name	z	Field of View	Pix. FoV	Time (sec)
A1689	0.19	$5.6' \times 5.6'$	$6''$	4506
GHO1600+412	0.3	$7.4' \times 7.4'$	$6''$	4546
3C295	0.46	$4.0' \times 4.0'$	$3''$	5413
3C330	0.55	$7.4' \times 7.4'$	$6''$	4536
CL0016+1609	0.55	$5.6' \times 5.6'$	$6''$	4476
J1888.16CL	0.56	$5.6' \times 5.6'$	$6''$	4506
CL1322+3029	0.7	$2.2' \times 2.2'$	$3''$	5373
GHO1322+3027	0.75	$4.0' \times 4.0'$	$6''$	2732
GHO1603+4313	0.895	$2.2' \times 2.2'$	$3''$	5373
CL1603+4329	0.92	$4.0' \times 4.0'$	$6''$	2732
CL1415+5244	...	Failed	...	...

Table 2. Deep observations

Cluster Name	z	Band	Field of View	Pix. FoV	Time (sec)
3C330	0.55	LW3	$15.2'\times3.3'$	$6''$	20584
J1888.16CL	0.56	LW2	$13.7'\times3.35'$	$6''$	20967
J1888.16CL	0.56	LW3	$15.2'\times3.3'$	$6''$	20624
GHO1603+4313	0.895	LW2	$13.7'\times3.35'$	$6''$	20967
GHO1603+4313	0.895	LW3	$15.2'\times3.3'$	$6''$	20604

3. IR EMISSION IN ISOCAM FILTERS

The part of the galaxy spectrum seen by each ISOCAM filter is a function of the redshift (K correction). The galaxy spectrum is the sum of three different components: UIBs, warm dust and forbidden lines of ionized gas. In the case of nearby clusters, the LW3 band is centered on the warm dust emission and the LW2 band is dominated by the contribution of the UIBs.

Proceedings of the Conference "The Universe as seen by ISO", Paris, France, 20–23 October 1998 (ESA SP-427, March 1999)

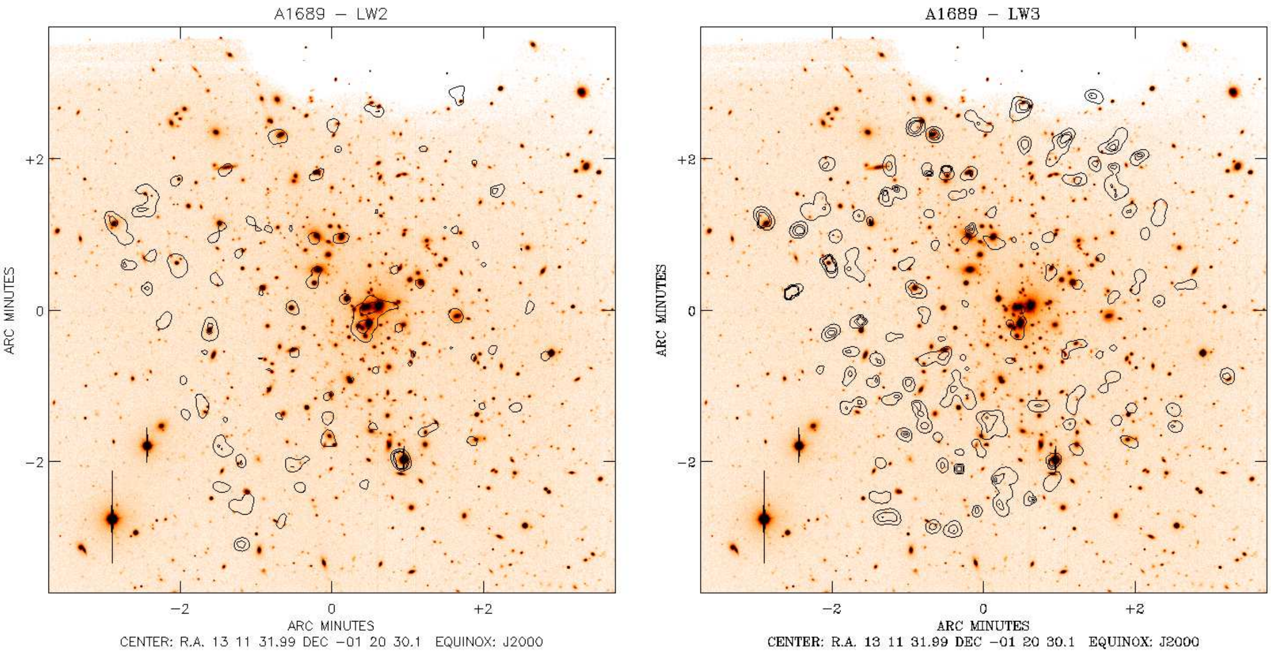

Figure 1. A1689 in the LW2 (left) and LW3 (right) bands superposed on a NTT image (PI: P.A. Duc)

When we consider distant clusters ($0.5 < z < 1.0$), the LW3 band is more and more contaminated by the UIBs, while in the LW2 band the contribution of the stellar continuum, especially from old population stars, overtakes the UIB features (see Fig. 2).

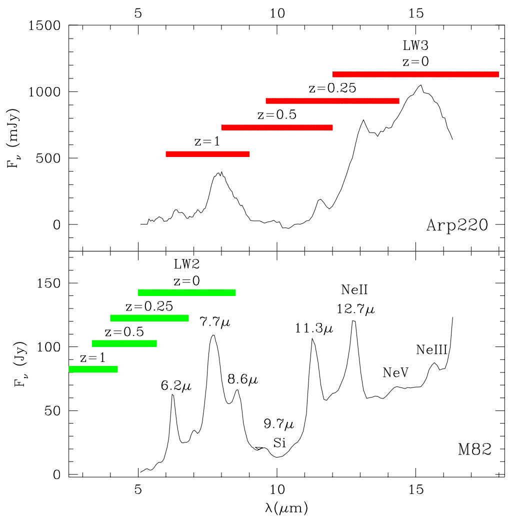

Figure 2. The figure shows the spectra of two known starburst galaxies observed by ISO (courtesy of D. Tran and V. Charmandaris) and the LW2 and LW3 bands at different redshifts.

4. DISCUSSION

We detect a spatial segregation in the distribution of ISOCAM sources. In the A1689 field (Fig. 1) we can

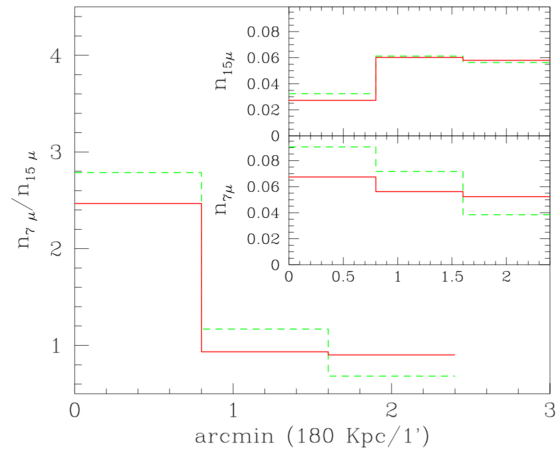

Figure 3. Source number density for A1689. Shaded and solid lines refer respectively to $5\tau_W$ and $7\tau_W$ thresholds in the wavelet detections of sources (Starck et al. 1998).

remark an overdensity of LW2 sources in the cluster center, while LW3 sources seem to avoid the central region. There are more detections associated to the dust (LW3 band) in the outskirts than in the central region, likely because galaxies which are far from the cluster center are generally more active than central galaxies (see Fig. 3).

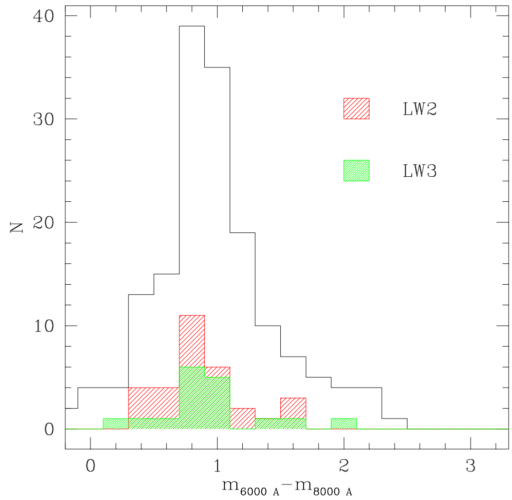

Figure 4. Color distribution for A1689.

If we compare the distribution of colors for the galaxies (Gudehus & Hegyi 1991) with the analogous distributions for galaxies detected in the two bands (Fig. 4), we note that these distributions do not differ significantly, as in the case of ISOCAM observations of the Hubble Deep Field (Aussel et al. 1998). This shows that the activity unveiled by the mid-infrared images is hidden in the optical, corroborating the observation of the Antennae galaxy by Mirabel et al. (1998).

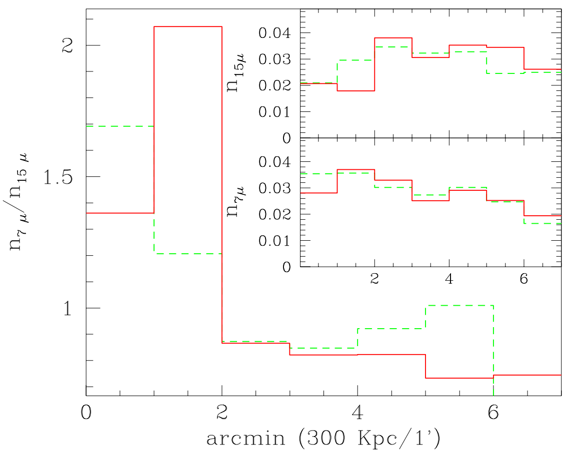

Figure 5. Source number density for J1888.16CL. Shaded and solid lines refer respectively to $5\tau_W$ and $7\tau_W$ thresholds in the wavelet detections of sources (Starck et al. 1998).

The segregation effect is more clearly visible in the cluster J1888.16CL at a redshift of 0.5 (Fig. 5). This effect could be due to a more intense activity of galaxies or to a favored detection of arclets at 15 μm as in the case of A2390 (Altieri et al. 1998). For the cluster GHO 1603+4313 at $z = 1$ we find an uniform distribution for the LW2 band and an overdensity of galaxies at the cluster center for the LW3 band (Fig. 6). This

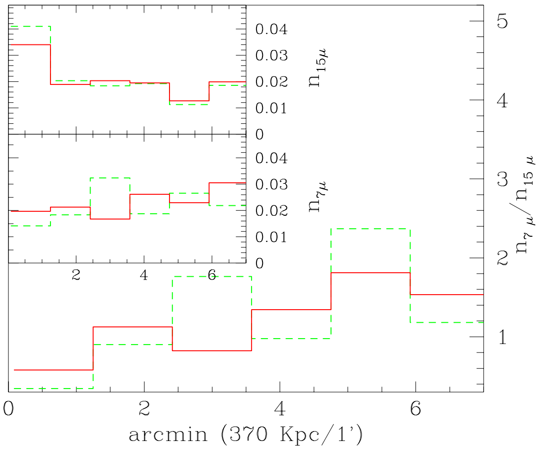

Figure 6. Source number density for GHO 1603+4313. Shaded and solid lines refer respectively to $5\tau_W$ and $7\tau_W$ thresholds in the wavelet detections of sources (Starck et al., 1998).

is consistent with previous cases, since LW3 at $z = 1$ corresponds to LW2 band at rest ($z = 0$), due to K-correction, but may be also associated to a stronger star formation activity at higher z.

ACKNOWLEDGMENTS

We thank H. Aussel for his helpful advise.
The ISOCAM data presented in this paper was analyzed using 'CIA', a joint development by the ESA Astrophysics Division and the ISOCAM Consortium. The ISOCAM Consortium is led by the ISOCAM PI, C. Cesarsky, Direction des Sciences de la Matiere, C.E.A., France.

REFERENCES

Altieri, B., Metcalfe, L., Kneib, J.P., & Mc Breen, B. 1998, 'NGST' - 34th Liège Astrophysics Colloquium, eds. Benvenuti, P. et al, ESA Publication, SP-431 (astro-ph 9808131)

Aussel, H., Cesarsky, C., Elbaz, D. & Starck, J.L. 1998, A&A, 342, 313

Butcher, H. & Oemler, A. 1984, ApJ, 285, 426

Charmandaris, V. et al. 1998, in preparation

Dressler, A. 1980, ApJ, 236, 351

Dressler, A. et al. 1997, ApJ, 450, 591

Elbaz, D. et al. 1998, 'NGST' 34th Liege Astrophysics Colloquium,eds. Benvenuti, P. et al. ESA Pub. (astro-ph 9807209)

Gudehus, D. H., & Hegyi, D., J. 1991, AJ, 101, 18

Mirabel, F. et al. 1998, A&A, 333, L1

Starck, J.-L., et al. 1998, "Extragalactic Astronomy in the Infrared", 1997, G.A.Mamon et al. eds.

Tran, D., 1998, Ph.D. Thesis

THE EUROPEAN LARGE-AREA ISO SURVEY (ELAIS) NEAR-INFRARED OBSERVATIONS OF THE SOUTHERN FIELDS

P. Héraudeau[1], **C. Surace**[1], **D. Lemke**[1], **S. Oliver**[2], **M. Rowan-Robinson**[2], **& the ELAIS consortium**[3]

[1] Max-Planck Institut für Astronomie, Heidelberg, Germany
[2] I. C. S. T.M., London, United Kingdom
[3] European consortium involving 19 countries

ABSTRACT

The European Large Area ISO Survey (ELAIS) is a survey of 4 main regions of the sky at 15 and 90 μm. The follow-up programmes from the ground are summarized. We present preliminary results from near-infrared (K-band) observations in the southern ELAIS fields. We show the histogramme distribution of the K-band magnitude for all objects in the observed regions. The "stellarity" index derived from the source extraction is also shown. We roughly find that 2/3 of the objects detected in the fields are elongated (i.e. galaxies). For a small sample of ISOPHOT detections, the corresponding NIR sources are classified as follows: a) 20% of stars: b) 70% of galaxies and c) 10% of interacting systems.

Key words: deep survey; follow-up; near-infrared.

1. INTRODUCTION

The European Large Area ISO Survey (ELAIS, P.I.: M. Rowan-Robinson) is a consortium of several European institutes whose goal is to study the infrared objects and the infrared background in 4 areas in the sky, using ISO and several ground-based telescopes. The 4 areas have been chosen to have the faintest Infrared background from IRAS data and at high ecliptic latitude, in order to avoid contamination by the zodiacal light. Observations have been performed with ISO at 90 and 175 μm (with ISOPHOT) and 7.5 and 15 μm (with ISOCAM). The 4 fields (3 in the northern hemisphere and 1 in the south) were observed by ISO for almost 1,300,000 seconds (~360 hours). The fields all together cover about 13 deg^2 on the sky. That makes ELAIS the most important ISO programme (considering the awarded observation time) and one of the most exciting projects in studying the Galactic and extragalactic universe. For more information about ELAIS, please see Oliver et al. (1997), Rowan-Robinson et al. (these proceedings) and our web site *http://athena.ph.ic.ac.uk/*.

2. FOLLOW-UP PROGRAMMES

The most significant results from ELAIS will come from the linking of ISO data with follow-up observations. A vast programme of observations has been undertaken with ground-based and space telescopes to survey the ELAIS fields or to do pointing observations on ELAIS sources. This will include mainly:

- R-Band optical CCD data over all ELAIS fields to provide optical identifications for spectroscopic and related follow-up;
- Spectroscopy of all or the vast majority of optical candidates for all ELAIS sources. This involves a two pronged attack using multi-object spectroscopy (e.g. MOSCA at Calar-Alto) for the brightest objects and single object spectroscopy using 4m class telescopes (and soon with the VLT) on the faintest objects. This will be principally to obtain the redshifts and thus luminosity but also for classification and for assessment of star-formation rates;
- Radio data to sub mJy level over the entire survey areas (see Ciliegi et al. 1998). This will allow identification of some of the most interesting objects which are expected to be optically very faint but to have detectable radio fluxes assuming the usual radio/FIR correlation;
- Multi-wavelength surveys at other wavelengths to allow broad band photometry and the study of bi-variate luminosity functions or pointed photometry observations of ELAIS sources.

For the first 2 years of the ELAIS project, we have been very successful in getting observing time since more than 150 nights were awarded to the project (see Rowan-Robinson et al. these proceedings).

Proceedings of the Conference "The Universe as seen by ISO", Paris, France, 20–23 October 1998 (ESA SP-427, March 1999)

3. ISOPHOT DATA PROCESSING AND SOURCE DETECTION

We used the ISOPHOT Interactive Analysis software (PIA, developed by ESA) to reduce the raw data and dedicated routines have been developed to detect ISOPHOT sources. We assigned each detection a probability and several people classified all good candidates into 5 classes of detections from bright, obvious sources (classified as one) to glitches (classified as 5).
We then ended with about 400 'true' ISOPHOT sources out of 900 detections over the whole area covered by the 4 ELAIS fields. About 110 PHOT sources have been detected in the S1 field we proposed to observe in the near-infrared (see next section)

For details about PHOT data reduction and detections see also Surace et al. (these proceedings).

4. PRELIMINARY RESULTS FROM NIR PHOTOMETRY

4.1. Observations

All 110 ISOPHOT sources of the S1 field have been observed in the near-infrared, which represents a total of 180 detections by CAM, PHOT or both detectors. A 20×20 arcmin survey has also been done on the S2 field. Observations were made using IRAC2 on the ESO/MPIA 2.2m telescope at La Silla in October 1997, June 1998 and SOFI on the NTT in October 1998. With its larger field of view and higher sensitivity, SOFI allowed us to increase noticeably the number of observed sources.

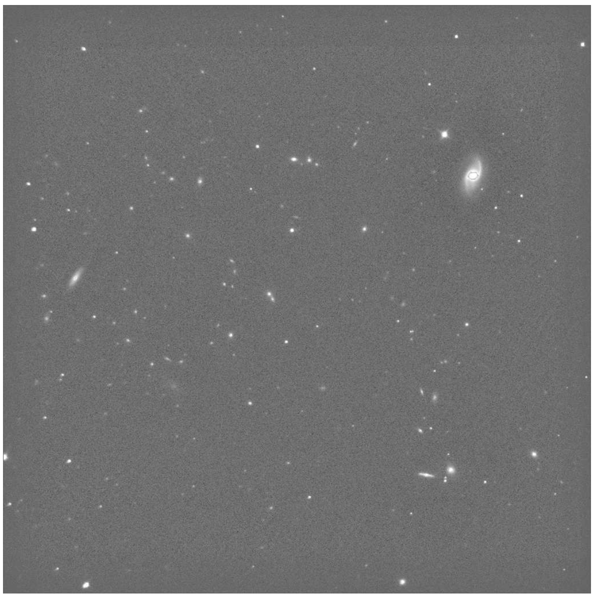

Figure 1. A SOFI image of an ISOPHOT source (the merger close to the centre). The field of view is 5 arcmin.

4.2. Star/galaxy identification

We used the Source Extractor software *SExtractor* (Bertin & Arnouts 1996) to measure the magnitudes of all the objects in the K images (not only ISOPHOT sources). SExtractor is well adapted to our purpose and in particular concerning deblending of merging objects. A total of 6400 sources have been extracted in the 850 arcmin^2 of the whole area covered during the observations ($\sim$42 SOFI fields). The histogramme distribution of the K magnitude is shown in Figure 2. Note that SOFI allows us to go down to the 20th magnitude with an uncertainty of about 0.25 mag. The stellarity as a function of K magnitude is also shown (Figure 3). The 'stellarity' index is used as a star/galaxy classifier. It is computed from the isophotal areas and the peak intensity of sources together with the seeing of the image. The stellarity index equals 0 for stars and 1 for galaxies, intermediate values correspond to more ambiguous objects (see Bertin and Arnouts 1996 for more details). An average seeing FWHM of $0.8''$ has been used for the classification of all images. Dividing roughly the sample into two with a stellarity index > 0.8 for stars, we get 2000 stars and 4400 elongated objects in our preliminary survey.

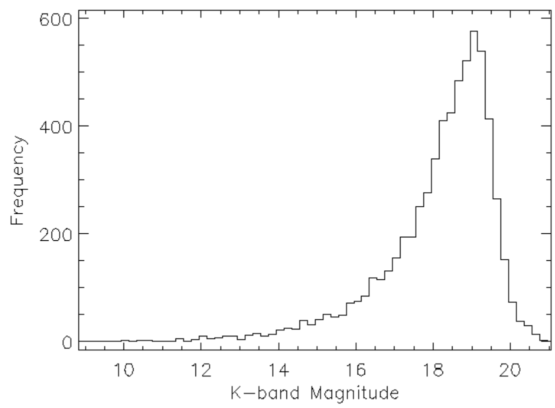

Figure 2. Histogramme distribution of the K magnitude for 6400 objects detected in the ELAIS fields observed in the near infrared.

4.3. ISOPHOT sources identification

We first used the R-band images of the Digital Sky Survey to identify some of the sources which are visible both in the NIR and in the *R*-band. We then got the coordinates from the COSMOS catalog (Yentis et al. 1992) to accurately compute the positions of all sources in the field. For ISOPHOT detections we over plotted the pixel (45 arcsec) to the IRAC2 or SOFI field in order to identify the FIR emission in the NIR Figure 4 shows some examples of the ISOPHOT detections, plotted with their near infrared and optical counterpart. One must note that whereas in some cases the identification is easy, other detections are associated with blank fields (objects with no or faint counterpart in the NIR). We usually end up with more than one object corresponding to a PHOT

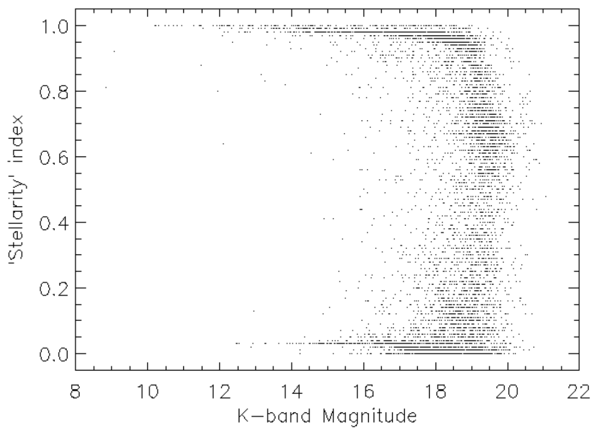

Figure 3. The stellarity index as a function of the total K-magnitude for all detections in the NIR. An average seeing FWHM of 0.8" has been used for the classification.

source. We thus need more information to identify the source without ambiguity (ISOCAM data, redshift...). For example, we found 100 objects corresponding to a subsample of 57 ISOPHOT detections at 90 microns. Out of these 100 objects we found the following distribution: a) 20% of stars, b) 70% of galaxies and c) 10% of interacting systems.

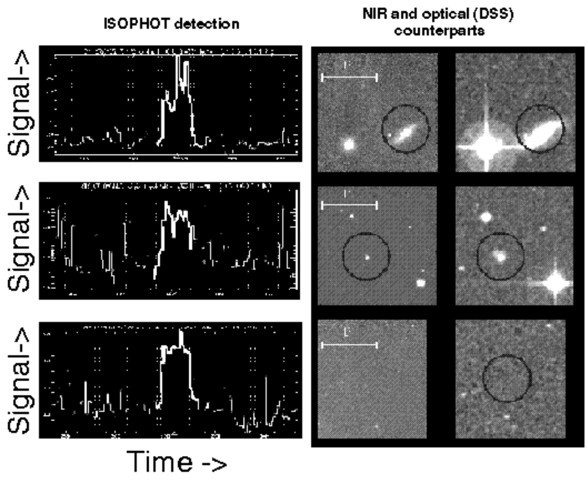

Figure 4. 3 examples of ISOPHOT detection (left) with their near infrared (centre) and optical (right) counterpart).

5. PERSPECTIVES

Using the complete radio, ISO, near-IR, optical and X-ray data on the S1 field, we will have the unprecedented possibility to:

- constrain the full spectral energy distributions of almost all the objects in S1, and thus probe the bolometric luminosity function of galaxies;
- address the emission processes, dust content and evolution of these obscured objects;
- to test AGN unification models;
- to search for ultraluminous infrared galaxies and protogalaxies;
- to search for close companions, as many of these galaxies may be mergers that have been missed in the optical due to dust obscuration, and
- to compare the properties of galaxy populations selected at different wavelengths.

Finally, the nature and the distance of the objects detected will allow to constrain cosmological scenarios and will lead to a better understanding of the cosmological evolution of star formation.

After getting positions and distances for all ELAIS sources, we will also be able to examine clustering as a function of the redshift and so test the gravitational instability picture of structure formation test.

REFERENCES

Bertin, E., Arnouts, S. 1996 A&AS, 117, 393.

Ciliegi, P., McMahon, R., Miley, G., Gruppioni, C., Rowan-Robinson, M., Cesarsky, C., Danese, L., Franceschini, A., Genzel, R., Lawrence, A., Lemke, D., Oliver, S., Puget, J-L., Rocca-Volmerange, B. 1998 MNRAS (in press)

Oliver, S., Rowan-Robinson, M., Cesarsky, C., Danese, L., Franceschini, A., Genzel, R., Lawrence, A., Lemke, D., McMahon, R., Miley, G., Puget, J-L., Rocca-Volmerange, B., in "New Horizons from Multi-Wavelength Sky Surveys", IAU 179, 1996, Kluwer Academic Publishers, edited by Brian J. McLean, Daniel A., Golombek, Jeffrey J. E. Hayes, and Harry E. Payne, p. 112. "The European Large Area ISO Survey: ELAIS"

Yentis, D.J., Cruddace, R.G., Gursky, H., Stuart, B.V., Wallin, J.F., Mac Gillivray, H.T., Collins, C.A. 1992 in Digitised Optical Sky Surveys, Mac Gillivray, H.T., and Thomson, E.B. (Eds), Kluwer, Dordrecht, 67.

A STUDY OF THE SPATIAL FLUCTUATIONS OF FIR BRIGHTNESS IN THE LOCKMAN HOLE

H. Matsuhara[1], K. Kawara[2], Y. Sato[1,3,5], Y. Taniguchi[3], H. Okuda[1], T. Matsumoto[1], Y. Sofue[2], K. Wakamatsu[4], L. L. Cowie[6], R. D. Joseph[6], & D. B. Sanders[6]

[1]The Institute of Space and Astronautical Science
[2]Institute of Astronomy, the University of Tokyo
[3]Astronomical Institute, Tohoku University
[4]Department of Physics, Gifu University
[5]ISO Science Operations Centre
[6]Institute for Astronomy, University of Hawaii

ABSTRACT

Two 44×44 arcmin^2 fields in the Lockman Hole were surveyed at 95 and 175 μm using ISOPHOT as a part of Japan/UH cosmology program using the ISAS guaranteed time (Kawara et al. 1998). In this paper we investigate the spatial characteristics of FIR brightness distribution in the Lockman Hole. We first calculated the angular correlation function of each 44×44 arcmin^2 field and then its Fourier transform (the angular power spectral density: PSD) over the spatial frequency range of $0.05 \sim 1$ arcmin^{-1}. The power law index of the 95 μm PSD is $-1 \sim 0$, unlike that of the IR cirrus: -3 (Gautier et al. 1992). We conclude that the fluctuation due to the IR cirrus is not dominant in the Lockman Hole. On the other hand, the power law index of the 175 μm PSD is about -2, and the IR cirrus may contribute at low spatial frequencies. However, the faint galaxy fluctuation must contribute significantly as proposed by Guiderdoni et al. (1997).

Key words: IR cirrus; galaxy evolution; diffuse radiation.

1. INTRODUCTION

The diffuse sky emission in the far-infrared (FIR) is dominated by emission from the interstellar dust. At high Galactic latitude, it is known as "IR cirrus", which has a complex spatial distribution (Low et al. 1984). The spatial structure of IR cirrus at 100 μm measured by IRAS was extensively studied by Gautier et al. (1992). From a Fourier analysis of the brightness distribution, the authors found a power spectral density (PSD) of the brightness fluctuation $P(f)$, written as

$$P(f) = P_0\Big(\frac{f}{f_0}\Big)^{\alpha} \qquad (1)$$

where f is spatial frequency (inverse of the angular scale length d) and $\alpha \simeq -3$ below the spatial frequency corresponding to the IRAS beam size $d_{\rm beam}$ ($f_{\rm max} = d_{\rm beam}^{-1} \sim 0.25$ arcmin^{-1}). They also found a relation $P_0 \propto B_0^3$, where B_0 is the mean brightness of the IR cirrus in the sky area concerned. Assuming these power spectral characteristics are valid for higher spatial frequency and for all FIR wavelengths, Helou & Beichman (1990) predicted that the detectivity of 1m-class space FIR telescopes would be limited by the noise due to the fluctuation of the IR cirrus ("cirrus confusion noise") even at high Galactic latitude.

ISOPHOT (Lemke et al. 1996) on-board the Infrared Space Observatory ISO (Kessler et al. 1996) is capable to observe the IR cirrus at wavelengths longer than 100 μm, with a better spatial resolution than that of IRAS. Recently Herbstmeier et al. (1998) analyzed the spatial characteristics of four fields measured by ISOPHOT, and obtained the characteristics of the power spectra roughly consistent with the above power spectrum (Equation 1) for bright cirrus regions.

In this paper we investigate the spatial characteristics of FIR brightness distribution in the Lockman Hole, a region with a uniquely low HI column density (Lockman et al. 1986), and thus the IR cirrus contribution to the fluctuation is expected to be minimal among many FIR deep surveys executed using ISOPHOT. We expect that the detectivity of the ISOPHOT observations in the Lockman Hole is not limited by the cirrus confusion noise, but by the confusion noise by the faint, distant galaxies, as discussed by Helou & Beichman (1990). The fluctuation analysis of FIR brightness in the Lockman Hole can thus give unique information on the FIR galaxy counts of distant galaxies below its confusion limit.

Proceedings of the Conference "The Universe as seen by ISO", Paris, France, 20–23 October 1998 (ESA SP-427, March 1999)

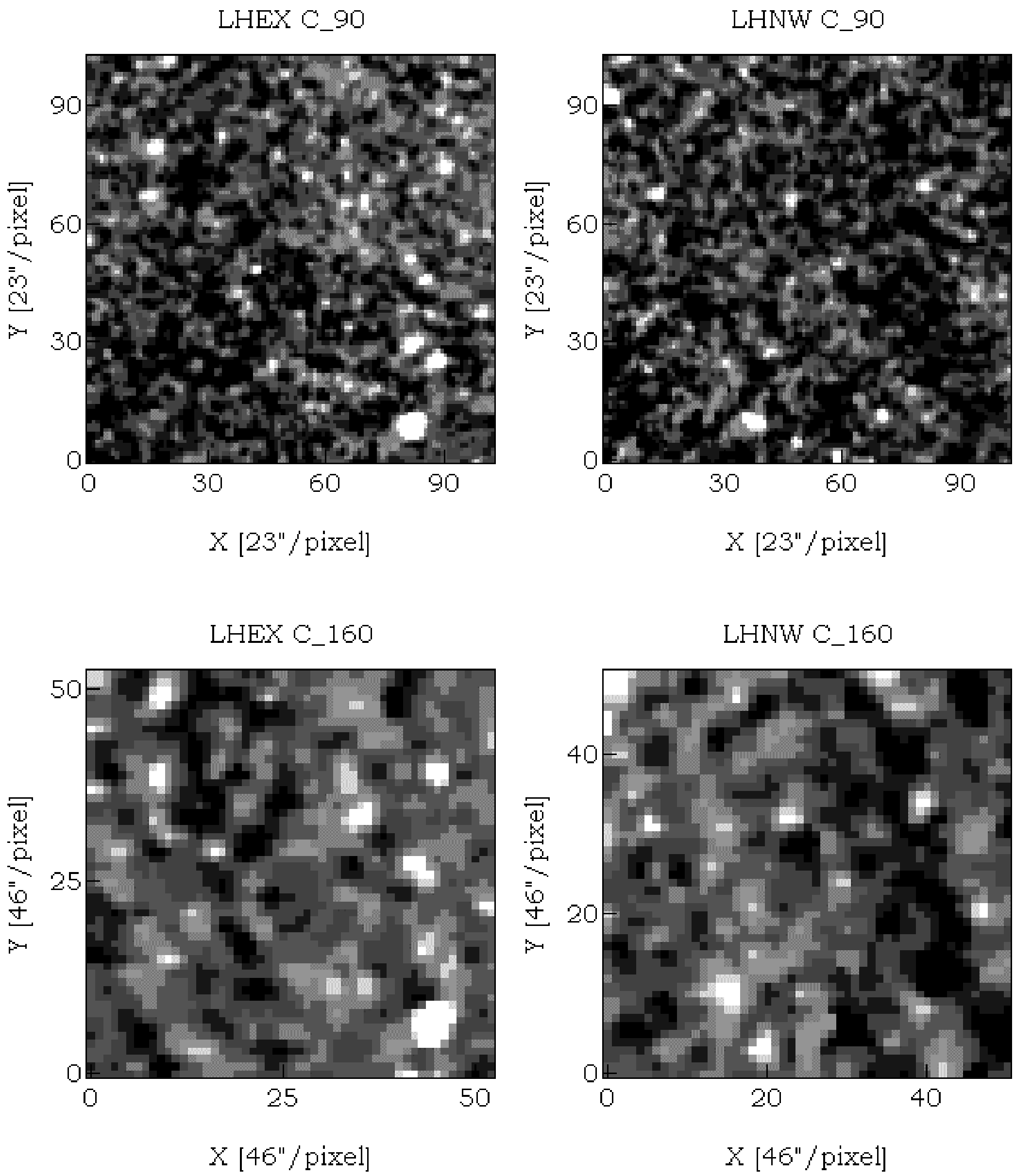

Figure 1. (top)95 μm images of LHEX (left) and LHNW (right), made of four 22×22 *arcmin*^{2} *sub-fields, and rebinned into* 103×103 *pixels (23 arcsec/pixel). Roughly the north is left and the west is top. (bottom) 175 μm images rebinned into* 53×53 *(LHEX) or* 51×51 *(LHNW) pixels (46 arcsec/pixel).*

2. OBSERVATIONS AND DATA PROCESSING

The FIR survey of the Lockman Hole, which was executed as a part of Japan/UH cosmology program using the ISAS guaranteed time, is described in Kawara et al. (1998) (see also Kawara et al. in these proceedings). Two 44×44 arcmin^2 fields named LHEX and LHNW were mapped with two filters: `C_90` (centered at 95 μm) and `C_160` (175 μm). Each of the two fields is made up of 4 sub-fields.

Each sub-field map was produced from the edited raw data by the PHT Interactive Analysis (PIA) version 7.1 or 7.2, and is hereafter called as an AAP (Astronomical Analysis Processing of PIA) map. Each AAP map is either 58×58 pixels (23 arcsec/pixel) for a 95 μm sub-field, or 31×31 pixels (46 arcsec/pixel) for a 175 μm sub-field. To correct the drift in the responsivity of the detectors, we applied the median filter smoothing (see Kawara et al. 1998 for details) onto the AAP data.

For flux calibration we used one of two FCS1 measurements, which was obtained just after the raster mapping of each sub-field. Based on this calibration, we found the mean brightness of both 95 μm and 175 μm images is consistent with the DIRBE/COBE brightness within 25 per cent. However, the IRAS point source (F10507+5723) flux obtained from the LHEX 95 μm image (see Figure 1) is about a factor of two smaller than the IRAS 100 μm flux.

On the other hand, the 175 μm flux of the IRAS source is consistent with the estimated flux assuming $f(175\mu m)/f(100\mu m) = 0.93$ (Kawara et al. 1998) within 20 per cent. Hence the adopted flux calibration is probably reliable within 25 per cent for 175 μm images while for 95 μm images the flux could be a factor of two larger if the ISO fluxes are scaled based on the IRAS flux.

Figure 1 shows the images of LHEX and LHNW used for the fluctuation analysis, each of which is the largest square area extracted from the mosaiced map made up from four sub-field AAP maps. Each image is rebinned into 103×103 pixels^2 (`C_90`), 53×53 pixels^2 (`C_160` LHEX), or 51×51 pixels^2 (`C_160` LHNW). The plate scale is 23 arcsec/pixel for 95 μm maps, and 46 arcsec/pixel for 175 μm maps.

3. POWER SPECTRA OF THE FIR IMAGES

For each image shown in Figure 1, the 2-dimensional angular correlation function $C(x, y)$ was calculated from the brightness distribution $B(x_0, y_0)$:

$$C(x,y) = \; < (B(x_0,y_0) - \bar{B})(B(x_0+x, y_0+y) - \bar{B}) > \quad (2)$$

where bracket $<>$ represents the average over the whole area in each image shown in Figure 1, and $\bar{B} =< B >$. Then, the coordinates were expressed in polar coordinates as $C(r, \theta)$, and the Fourier transforms in various radial directions were calculated (*i.e.* θ is fixed for each transform), giving one-dimensional power spectral densities (PSDs) of the map. Finally, the PSDs were averaged with respect to θ and are shown in Figure 2. The small error bars of PSDs represent the deviations with respect to θ, showing that the PSDs are almost independent of θ. The PSDs at high frequencies ($f \geq 0.8$ arcmin^{-1} for 95 μm, and $f \geq 0.4$ arcmin^{-1} for 175 μm) suffers from smoothing by the instrumental beam, hence they are not real spatial characteristics of the sky.

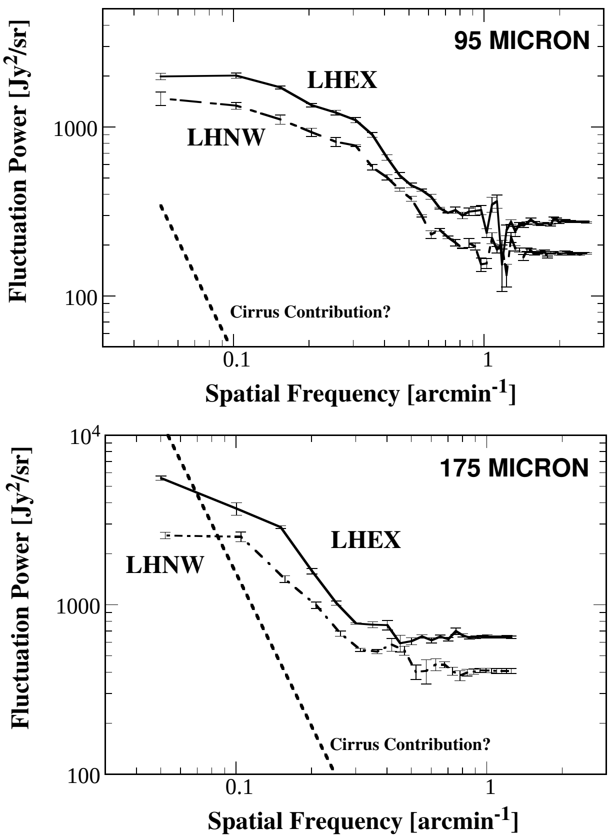

Figure 2. Fluctuation power spectrum densities (PSDs) of 95 μm (top) and 175 μm (bottom) images. Solid lines represent power spectra of LHEX, and dash-dotted lines represent power spectra of LHNW. The PSDs of LHEX are larger than those of LHNW due to the existence of an IRAS point source F10507+5723. Dotted line shows the estimated IR cirrus contributions based on the formula of Gautier et al. (1992).

4. DISCUSSION

In Figure 2 contributions by the IR cirrus fluctuation are also shown (dotted lines). This estimate is based on Equation 1 using the mean brightness B_0 of the IR cirrus, which is estimated from the atomic hydrogen column density towards the Lockman Hole of 6×10^{19} atoms cm^{-2}. Using the FIR emissivity of the cirrus dust given by Kawada et al. (1994), we obtain $B_0 = 0.32$ MJy/sr at 95 μm and $B_0 = 1.0$ MJy/sr at 175 μm.

At low spatial frequency, the 95 μm PSDs are nearly flat ($\alpha = -1 \sim 0$), and the value of the PSDs is comparable with those of the M04 and the Draco Nebula: $4 \sim 7 \times 10^3$ Jy^2/sr (Herbstmeier et al. 1998), even though the IR cirrus contribution to the PSD of the Lockman Hole should be much smaller than those to the PSDs of the above regions. Thus, as for the 95 μm images, we conclude that the IR cirrus fluctuation is not dominant at all spatial frequencies.

On the other hand, the 175 μm PSDs represent power-law with $\alpha \simeq -2$ at low frequency ($f \sim 0.1$ arcmin^{-1}), which may indicate the presence of IR cirrus contribution. However, as proposed by Guiderdoni et al. (1997), the contribution of faint galaxies located at $z = 0.5 \sim 2.5$ is probably important. As shown in Kawara et al. (1998), the cumulative counts of detected point sources at 175 μm down to 150 mJy are much higher than those expected from the no-evolution model, indicating the existence of an additional population, such as the ultraluminous infrared galaxies (scenario E of Guiderdoni et al. 1998). Such an evolutional scenario predicts the 175 μm PSD of $\simeq 10^3$ Jy^2/sr (Guiderdoni et al. 1997), which is comparable with the observed PSD at low frequencies. Further detailed study based on such a model of the FIR galaxy counts, however, requires the knowledge of point spread functions of the ISOPHOT detectors up to angular length $d \sim 10$ arcmin, and is still ongoing.

REFERENCES

Gautier, T.N., Boulanger, F., Pérault, M., Puget, J.-L. 1992, AJ, 103, 1313

Guiderdoni, B., Bouchet, F.R., Puget, J.-L, Guilaine, G., Hivon, E. 1997, Nature, 390, 257

Guiderdoni, B., Hivon, E., Bouchet, F.R., Maffei, B. 1998, MNRAS, 295, 877

Helou, G., & Beichman, C.A. 1990, in *From Ground-Based to Space-Borne Sub-mm Astronomy* Proc. of the 29th Liége International Astrophysical Coll., ESA Publ., p.117

Herbstmeier, U., Abraham, P., Lemke, D. et al. 1998, A&A, 332, 739

Kawada, M., Bock, J.J., Hristov, V.V. et al. 1994, ApJ, 425, L89

Kawara, K., Sato, Y., Matsuhara, H. et al. 1998, A&A, 336, L9

Kessler, M.F., Steinz, J.A., Anderegg, M.E. et al. 1996, A&A, 315, L27

Lemke, D., Klaas, U., Abolins, J. et al. 1996, A&A, 315, L64

Lockman, F. J., Jahoda, K., McCammon, D. 1986, ApJ, 302, 432

Low, F.J., Beintema, D.A., Gautier, F.N. et al. 1984, ApJ, 278, L19

MOLECULES AT HIGH REDSHIFTS

D. Puy[1,2] **& M. Signore**[3]

[1]Laboratory for Astrophysics, Paul Scherrer Institute, Villigen, Switzerland
[2]Institute of Theoretical Physics, University of Zurich, Switzerland
[3]Laboratoire de Radioastronomie, Observatoire de Paris, France.

ABSTRACT

After the recombination of Hydrogen, primordial molecules such as H_2, HD can be formed.The formation of structures in the post-recombination gaseous medium is commonly explained by primordial density fluctuations. In a self-gravitating collapsing cloud, temperature tends to increase with contraction. In this context molecular line emissions can play an important role in the thermal balance of collapsing molecular clouds and in the dynamics of collapsing proto-clouds.
We calculate analytically the molecular cooling due to H_2 and HD. Our analysis is done under the hypothesis that we consider only the first two excited levels of the H_2 and HD molecules. The potentiality of fragmentation of collapsing protoclouds through the thermal instability is discussed. Finally we suggest that this study could also be extended to the CO molecule.

Key words: Cosmology.

1. INTRODUCTION

Primordial molecules can play a role in observational cosmology, and can offer interesting perspectives for Cosmology. In the framework of the standard Big Bang model, the nucleosynthesis of the light elements took place at $t_{nuc} \sim 10^2$ sec after the Big Bang. Cosmologists compute and predict the abundances of deuterium, helium-3, helium-4 and lithium-7 as a function of the ratio of nucleons to photons η and predict also very tiny abundances of heavier elements. In standard Big Bang Theory, chemistry took place around the epoch of recombination. The chemistry of the primordial gas after the recombination epoch has been studied by several groups (Lepp & Shull 1984, Dalgarno & Lepp 1987, Puy et al. 1993). More recently Stancil et al. (1996) have developed a new model of lithium chemistry in the early Universe. They include, in particular, new quantal rate coefficients for the radiative association of lithium and hydrogen (Dalgarno, Kirby, & Stancil 1996).
The study of primordial chemistry of molecules addresses a number of interesting questions pertaining to the thermal balance of collapsing molecular protoclouds. In numerous astrophysical cases molecular cooling and heating influence dynamical evolution of the medium, see for example the review done by Dalgarno and Mc Cray (1972) who present molecular cooling and heating in HI regions, or Shu (1997) who discusses the influence of molecules in star formation. The existence of a significant abundance of molecules can be crucial on the dynamical evolution of collapsing objects. Because the cloud temperature increases with contraction, a cooling mechanism can be important for the structure formation, by lowering pressure opposing gravity, i.e. by allowing continued collapse of Jeans unstable protoclouds. This is particularly true for the first generation of objects. Many authors have examined this problem (Bodenheimer 1968, Hutchins 1976, Palla et al. 1983, Villere & Bodenheimer 1987, Tegmark et al. 1997) introducing molecular coolants, mainly H_2 molecules. From Fall and Rees (1985) we know that H_2 molecules are important cooling agents and can lead, sometimes, to the fragmentation process of the object and thus provide a possible scenario of globular cluster formation for collapsing galaxies.
The cosmological fractional abundance HD/H_2 is small (Lepp and Shull 1984, Puy et al. 1993). Nevertheless, the presence of a non-zero permanent electric dipole moment makes HD a potentially more important coolant than H_2 at modest temperatures, although HD is much less abundant than H_2. Recently Puy and Signore (1997) showed that during the early stages of gravitational collapse, for some collapsing masses, HD molecules were the main cooling agent when the collapsing protostructure had a temperature of about 200 K.

We consider here only the transition between the ground state and the first state. Thus in section 2 we describe briefly the molecular cooling in the context of gravitational collapse then in section 3 we discuss the possibilities of thermal instability and the outlooks of these studies.

2. MOLECULAR COOLING AND GRAVIATIONAL COLLAPSE

The excitation of rotational levels of molecules are radiative and collisional. Molecular heating corre-

Proceedings of the Conference "The Universe as seen by ISO", Paris, France, 20–23 October 1998 (ESA SP-427, March 1999)

sponds to a radiative excitation followed by collisional excitation when molecular cooling describes a collisional excitation followed by radiative de-excitations (spontaneous and induced). We consider only the molecular cooling which is the dominant term in the cooling function as we have shown for a collapsing cloud (Puy & Signore 1996, 1998a). If we compare the temperature of the first transition (H_2 and HD) with the temperature of the cosmological radiation between the redshifts [5,20] and the temperature of a collapsing protocloud at the same range of turn-around redshift (Padmanabhan 1993), it is possible to approximate the total molecular cooling Λ_T (see Puy & Signore 1998b). We find

$$\Lambda_T \;=\; \Lambda_{H_2} + \Lambda_{HD} \tag{1}$$

where

$$\Lambda_{H_2} \;=\; 1.23\times 10^{-20} n_{HD}^2 \exp(-\frac{512}{T_m}) \frac{\sqrt{T_m}}{5\times 10^{-4} + n_{HD}\sqrt{T_m}\Big[1+3\exp(-\frac{512}{T_m})\Big]} \tag{2}$$

H_2 molecular cooling, and

$$\Lambda_{HD} \;=\; 2.66\times 10^{-21} n_{HD}^2 \exp(-\frac{128.6}{T_m}) \frac{\sqrt{T_m}}{1 + n_{HD}\sqrt{T_m}\Big[1+3\exp(-\frac{128.6}{T_m})\Big]} \tag{3}$$

HD molecular cooling.
We have chosen the same model of gravitational collapse developed in Puy & Signore (1996) from Lahav (1986). The evolution equations for a collapsing cloud, characterized by the mass M, are:

$$\frac{dn}{dt} \;=\; -3\frac{n}{r}.\frac{dr}{dt} + (\frac{dn}{dt})_{chem} \tag{4}$$

$$\frac{dT_m}{dt} \;=\; -2\frac{T_m}{r}.\frac{dr}{dt} + \frac{2}{3nk}.\Lambda_T \tag{5}$$

$$\frac{d^2r}{dt} \;=\; \frac{5k}{\mu m_H}.\frac{T_m}{r} - \frac{GM}{r^2} \tag{6}$$

respectively the conservation of the matter, the evolution of the temperature T_m of the collapsing cloud and the evolution of the radius r, where n is the density, t the time, $(\frac{dn}{dt})_{chem}$ the chemical contribution, k the Boltzmann constant, μ the mean molecular weight, m_H the mass of hydrogen and G the gravitational constant. All these equations are coupled with the equations of the chemical kinetics due to the chemical network (see Puy & Signore 1997). The calculations of the thermal function (molecular and chemical) are well-described in Puy & Signore (1998b) which deals with the thermal analysis of this gravitational collapse.

3. DISCUSSION

At the beginning of the gravitational collapse the matter temperature increases, then due to the very important efficiency of the molecular cooling, the temperature decreases. We consider here the *transition regime* i.e. the point where the temperature curve has a horizontal asymptote (see Puy & Signore 1997): $dT_m/dt = 0$ and where the cooling due to molecules can exceed the heating resulting from the collapse.
In this context, we can ask if a thermal instability can be developed. Many studies have focused on the problem of thermal instability since the appearance of the pioneer work of Field (1965). Field has given a criterion describing the condition of instability. Thus with a cooling Λ_T and in a case of isobaric perturbation, the Field's criterion leads to

$$\frac{\partial \ln\Lambda_T}{\partial \ln T_m} < 0 \tag{7}$$

In our case the logarithmic differential of the total molecular cooling function is

$$\frac{\partial \ln\Lambda_T}{\partial \ln T_m} \;=\; \frac{7T_m + 7T_m\xi_o e^{-\frac{\Delta T_o}{T_m}}}{2+2\xi_o e^{-\frac{\Delta T_o}{T_m}}} - \frac{5T_o + 5T_o\xi_o e^{-\frac{\Delta T_o}{T_m}} + 5\xi_o \Delta T_o e^{-\frac{\Delta T_o}{T_m}}}{1+\xi_o e^{-\frac{\Delta T_o}{T_m}}} \tag{8}$$

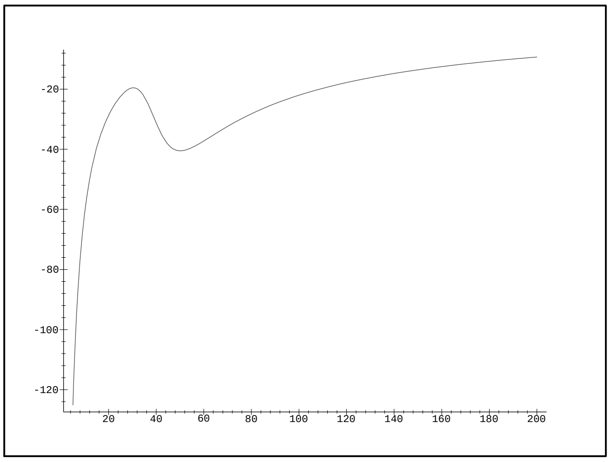

Figure 1. $\partial ln\Lambda_{Total}/\partial lnT_m$ in y-axis and temperature of the matter in x-axis (in Kelvins).

In Figure 1, we have plotted the function $y(T_m) = \frac{\partial \ln\Lambda_T}{\partial \ln T_m}$ which shows that $y(T_m) < 0$ corresponding to a thermal instability. Thus by maintaining the same pressure in its surroundings, such a blob would get cooler and cooler and denser and denser until it could separate into miniblobs. This possibility is very interesting and could give a scenario of formation of primordial clouds. However a quantitative study is necessary to evaluate the order of magnitude of the mass and the size of the clouds. This last point can be crucial particularly concerning the composition of the molecular clouds at high redshift such as the Lyman-α absorbers in order to evaluate the possible signature of the primordial clouds.
In the very early Universe the components of the primordial molecular medium are formed from the elements of the primordial nucleosynthesis. Later, as

soon as stellar processes occur in proto-objects, other molecular species appeared such as CO, CI, HCN. Therefore, their line emission can be seen as an excellent probe of physical conditions of very high redshift objects. Among them, the diatomic molecule CO has the strongest lines at radio wavelengths, the rotational transitions being spaced by 115 GHz in the rest frame at $z = 0$ (this separation, at a redshift z, becomes compressed by a factor $1/(1+z)$). Moreover, the carbon monoxide line emission had already been detected in a few high redshift objects, e.g.:

1. CO$(3-2)$, CO$(4-3)$ and CO$(6-5)$ in the ultraluminous IR galaxy F10215+4724 at the redshift $z = 2.28$ (Brown and Van den Bout 1992, Solomon et al. 1992).
2. CO$(3-2)$, CO$(4-3)$, CO$(5-4)$ and CO$(7-6)$ in the cloverleaf quasar at the redshift $z = 2.56$ (Barvainis et al. 1994, Barvainis et al. 1997).
3. CO$(5-4)$ in the quasar BR1202−0725 at the redshift $z = 4.69$ (Ohta et al. 1996, Omont et al. 1996).
4. CO$(5-4)$ in the quasar BRI1335−0418 at the redshift $z = 4.41$ (Guilloteau et al. 1997).

One must also add that, at least for the first three objects, their detectability in molecular transitions may be due to high emissivity of the gas and above all magnification from gravitational lensing rather than an extremely large mass of gas. Moreover, there is no a priori evidence of gravitational lensing for BRI1335-0418. Therefore, if this absence of strong gravitational magnification is confirmed, the fourth object could have a large mass of molecular gas which could be associated with the presence of some huge starburst. However, if there is no doubt about the reality of the CO detection in these objects, it is more difficult to definitively determine the CO to H_2 conversion factor in these objects.
Let us also remark that, here, we study *protostructures* in the mass range $10^8 - 10^{10}$ $M_\odot$ i.e. in the mass range of dwarf galaxies. Recently, Verter & Hodge (1995) estimated the CO to H_2 conversion factor for the very low metallicity dwarf irregular galaxy GR8. They found $X > 80 \times 10^{20}$ molecules cm^{-2} (Km s^{-1})$^{-1}$ which is a factor 30 larger than for our Galaxy ($X = N(H_2)/W_{CO}$ where $N(H_2)$ is the column density of molecular hydrogen gas and W_{CO} is the integration of CO antenna temperature over the velocity profile).
Thus the calculations of molecular functions could, in principle, be extended to the CO molecules for collapsing protoclouds at $z < 5$. The CO molecules could even be a better cooling agent than H_2 and HD. This extended study is beyond the scope of our paper.

ACKNOWLEDGMENTS

The authors gratefully acknowledge Stéphane Charlot, Lukas Grenacher, Philippe Jetzer, Bianca and Francesco Melchiorri, Flavia Svara for valuable discussions on this field. Part of the work of D. Puy has been conducted under the auspices of the *D^r Tomalla Foundation*.

REFERENCES

Barvainis R., Tacconi L., Alloin D., Antonucci R., Coleman P. 1994 Nature 371, 586

Barvainis R., Maloney P., Alloin D., Antonucci R. 1997 ApJ 484, 695

Bodenheimer P., 1968, ApJ 153, 483

Brown R. L., Van den Bout P.A. 1992 ApJ 397, L19

Dalgarno A., Mc Cray 1972 Ann. Rev. Astron. Ap. 10, 375

Dalgarno A., Lepp S. 1987, in: *Astrochemistry*, eds Vardya-Tarafdar, p109

Dalgarno A., Kirby K., Stancil P.C. 1996 Ap. J. 458, 397

Fall M., Rees M., 1985 ApJ 298, 18

Field G., 1965 ApJ 142, 531

Guilloteau S., Omont A., Mc Mahon R.G., Cox P., Petitjean P. 1997 A&A 328, L1

Hutchins J. 1976 ApJ 205, 103

Lahav O. 1986, MNRAS 220, 259

Lepp S., Shull M.J. 1984, ApJ 280, 465

Ohta K., Yamada T., Nakanishi K., Kokno K., Akiyama M., Kawabe R. 1996 Nature 382, 426

Omont A., Petitjean P., Guilloteau S., Mc Mahon R.G., Solomon P.M. Pecontal E. 1996 Nature 382, 428

Padmanabhan T. 1993 in *Structure Formation in the Universe* Cam. Univ. Press

Palla F., Salpeter E., Stahler S. 1983 ApJ 271, 632

Puy D. et al. 1993 A&A 267, 337

Puy D., Signore M. 1996 A&A 305, 371

Puy D., Signore M. 1997 New Astronomy 2, 299

Puy D., Signore M. 1998a New Astronomy 3, 27

Puy D., Signore M. 1998b New Astronomy 3, 2

Shu F. 1997, in *Molecules in Astrophysics: Probes and Processes*, Van Dishoeck, p 19

Stancil P.C., Lepp S., Dalgarno A. 1996 Ap. J. 458, 401

Tegmark M., Silk J., Rees M., Blanchard A., Abel T., Palla F. 1997 ApJ 474,1

Verter F., Hodge P. 1995 ApJ 446, 616

Villere K., Bodenheimer P. 1987, in: *Astrochemistry*, Vardya-Tarafdar, p121

THE ESO-SCULPTOR REDSHIFT SURVEY WITH ISO

B. Rocca-Volmerange[1], V. de Lapparent[1], C. Surace[2] & the ELAIS consortium

[1]Institut d'Astrophysique de Paris, Paris, France
[2]Imperial College of Medecine Science and Technology, London, UK

ABSTRACT

The ESO-Sculptor deep redshift survey (de Lapparent et al. 1997), nearly complete down to $R = 20.5$, contains $\simeq$ 700 galaxies in the configuration of a thin strip $\simeq$ 0.2×1 square degrees, reaching out to a redshift of $\simeq 0.5$. In order to build an IR luminosity function, to detect possible traces of ultraluminous galaxies as well as to analyze the far-IR properties of normal galaxies, the European Large Area ISO Survey (ELAIS) Survey observed a small ($24' \times 24'$) region of the ESO-Sculptor survey with ISOPHOT. About 14 infrared sources have been detected with a flux > 30mJy . With an error box of one pixel, the cross-correlation requires an improved data processing of the source extraction pipeline and complementary data.

Key words: cosmology; galaxies.

1. INTRODUCTION

Through the far-infrared emission of galaxies, a large fraction of the energy balance is released in periods of intense activity. Therefore our understanding of the physics of galaxy evolution and formation mainly depends upon the knowledge of the multi-spectral energy distributions of field galaxies. The ESO-Sculptor redshift survey, initially proposed by de Lapparent et al. (1997) to map the large-scale galaxy distribution at high redshifts, is simultaneously an exemplary sample for spectrophotometric evolution of galaxies. Reliable redshifts have been measured for $\simeq$ 700 galaxies with $R \leq 20.5$ (Bellanger et al. 1995) in a 0.2 degree^2 area. Recently, an additional $\simeq$300 galaxies with $20.5 \leq R \leq 21.5$ have measured redshifts on the same area. The ESO-Sculptor survey also provides deep B,V,R photometry for $\simeq$12000 galaxies down to V=24 on 0.4 degree^2 (Arnouts et al. 1997). The spectral classification of the galaxy sample has been performed using a principal component analysis (PCA) by Galaz et al. 1998. To complete the multi-spectral emission of this sample, two ISO surveys were performed on the ESO-Sculptor area. One is a small field ($24' \times 24'$) of the ELAIS survey (P.I.: M. Rowan-Robinson), observed with ISOPHOT (90 μm) and ISOCAM (15μm) cameras: The PHOT results are presented here. A deeper survey (P.I.: B. Rocca-Volmerange) was observed with ISOCAM and the data are being processed.

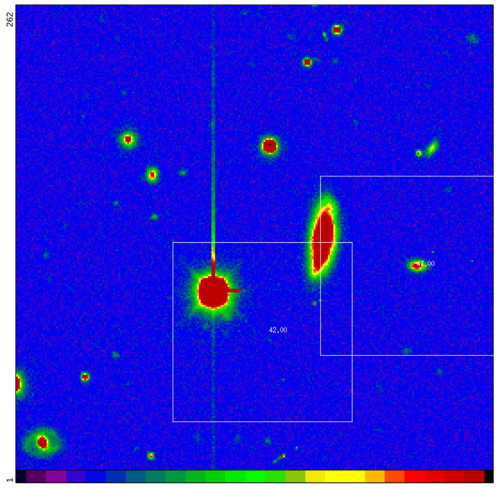

Figure 1. An example of the correspondence between the ISOPHOT detection (the white square represents a PHOT pixel size) and the corresponding ESO-Sculptor field observed in the R band

2. THE ISOPHOT OBSERVATIONS

The mapping-mode of ISOPHOT and the C-100 detector were used through the filter centred on 90 μm. The area was covered by a 12×12 raster map with an overlapping step of $120''$. The exposure time is 25 sec per pixel, significantly deeper than the large ELAIS survey (Oliver et al. 1998). The area has been selected from the ESO-Sculptor field to minimize the low cirrus background and to avoid the presence of strong nearby sources. The data processing was carried out with the ISOPHOT MPIA data extraction pipeline (Surace et al. 1998) and the extracted sources were compared to the optical counterparts of the survey.

Proceedings of the Conference "The Universe as seen by ISO", Paris, France, 20–23 October 1998 (ESA SP-427, March 1999)

Table 1. PHOT sources detected in a small part of the ESO-Sculptor redshift survey area, observed with the ISOPHOT camera (90 μm). The flux threshold is 30 mJy.

Detection	α (2000)	δ (2000)	Flux (mJy)	σ (mJy)
1	0 22 12.99	-30 20 57.41	83.2	31.1
2	0 21 53.54	-30 08 37.8	45.7	27.0
3	0 21 41.97	-29 59 31.56	32.9	25.1
4	0 21 40.27	-29 58 11.04	65.6	24.9
5	0 22 02.29	-30 04 25.09	58.4	27.7
6	0 22 15.58	-30 17 45.05	33.3	24.8
7	0 22 05.04	-30 04 15.26	50.1	22.7
9	0 22 04.09	-30 03 30.44	61.7	23.3
9	0 22 07.38	-30 00 15.57	40.7	25.1
10	0 22 33.92	-30 04 46.59	57.4	16.9
11	0 23 01.44	-30 15 48.79	41.2	16.3
12	0 23 15.39	-30 10 28.64	35.8	17.5
13	0 23 37.56	-30 16 41.69	70.8	16.9
14	0 23 32.97	-30 07 58.39	59.1	22.1

3. DETECTIONS AND OPTICAL COUNTERPARTS

Table 1 presents the ISOPHOT detections in the ESO-Sculptor field with the help of the MPIA pipeline. 14 sources are identified with fluxes superior to the 30 mJy detection limit by pixel. Surace et al. (1998) give uncertainties between 20 and 60 mJy. In Figures 1 and 2, two examples of the optical counterparts in the *R* band are presented. The error box of one pixel size is centred on each ISO source, as listed in table 1. To interpret these data, the first difficulty is to integrate the total emission of sources. An improved data processing is needed on the example of Figure 1 where the spiral giant galaxy simultaneously contributes to the emission of two different pixels. The second difficulty arises when several galaxies are identified within the PHOT error box (Figure 2). To evaluate the emission of each galaxy in the far-infrared requires additional information. On the ESO-Sculptor field, a better analysis is possible because the redshift and the spectral type of each galaxy were determined from the redshift survey catalogue (de Lapparent et al. in preparation).

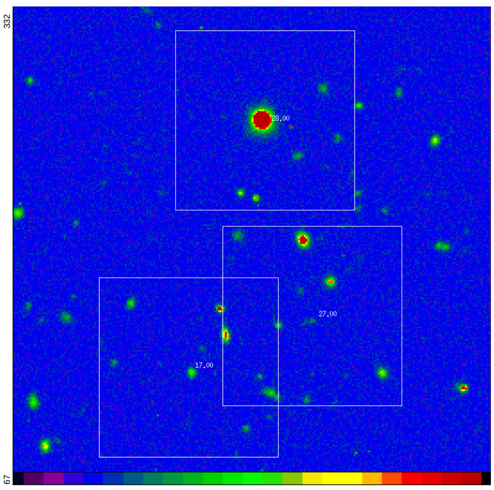

Figure 2. See caption of Figure 1

ISOCAM observations were also performed on the ESO-Sculptor field. One survey was observed at the depth of the ELAIS survey. Another one reaches the sensitivity of the guarantee time deep survey. Both are being processed with the ISOCAM/CEA software at Saclay.

REFERENCES

Arnouts , S., de Lapparent, V., Mathez, G., Mazure, A., Mellier, Y., Bertin, E. Kruszweski, A. 1997, AASS, 124, 163

Bellanger, C., de Lapparent, V., Arnouts, S., Mathez, G., Mazure, A., Mellier, Y. 1995, AASS, 110, 159

de Lapparent, V., Arnouts, S., Bardelli, S., Ramella, M. 1997, The Messenger, 89, 21

Galaz, G. & de Lapparent, V. 1998, AA, 332, 459

Oliver, S., Rowan-Robinson, M., Cesarsky, C., Danese, L., Franceschini, A., Genzel, R., Lawrence, A., Lemke, D., McMahon, R., Miley, G., Puget, J-L., Rocca-Volmerange, B. 1998, in "Wide Field Surveys in Cosmology" Colombi et al. (eds.) Publisher: Editions Frontières, p. 165

Surace C., Abraham, P., Herbstmeier, U. 1997, in *ISOPHOT Interactive Analysis reports*

A MID-INFRARED DEEP GALAXY SURVEY IN THE SSA13 FIELD

Y. Sato[1,2,3], L.L. Cowie[4], Y. Taniguchi[3], D.B. Sanders[4], K. Kawara[5], H. Okuda[2], K. Wakamatsu[6], T. Matsumoto[2], R.D. Joseph[4], Y. Sofue[5] & H. Matsuhara[2]

[1]ISO Data Centre, ESA Astrophysics Division, Villafranca del Castillo, Spain
[2]Institute of Space and Astronautical Science (ISAS), Sagamihara, Japan
[3]Astronomical Institute, Tohoku University, Sendai, Japan
[4]Institute for Astronomy, University of Hawaii (UH), Honolulu, United States
[5]Institute of Astronomy, The University of Tokyo, Mitaka, Japan
[6]Department of Physics, Gifu University, Gifu, Japan.

ABSTRACT

We have executed a deep ISOCAM LW2 (7 μm) imaging survey in the SSA13 field. So far 26 sources are detected down to 10 μJy in the area of 16.8 arcmin^2. We could find optical counterparts of these sources in many cases. But some sources are only found in the LW2 band. Their nature should be investigated further.

Key words: survey; cosmology; galaxies

1. INTRODUCTION

We have executed deep cosmological surveys using Japan/ISAS Guaranteed Time (Principal Investigator: Y. Taniguchi). ISO gave us two new windows for searching the distant universe. One is in the mid-infrared where dust extinction for stellar continuum emission is negligible, and the other is in the far-infrared where energy generated in stars is transferred to dust and we can see its re-radiated emission directly. We use these windows to explore dusty star-forming galaxies which had not been found yet.

Results of the far-infrared part of this program, carried out in the Lockman Hole, is reported in Kawara et al. 1998a, Kawara et al. and Matsuhara et al. (in these proceedings).

For the mid-infrared, we have done two deep imaging surveys in the Lockman Hole and the SSA13 as the Japan/UH cosmology program. The former one is reported in Taniguchi et al. (1998). Here we report initial results gained in the SSA13 field.

2. FIELD

The SSA13 field, one of the UH selected area to search general properties of field galaxies, was chosen as the second and final target for our deep ISOCAM LW2 ($\lambda_c = 6.75\,\mu$m) imaging survey.

This field is located at high ecliptic and Galactic latitudes ($\beta \sim 46°$ and $b \sim 74°$) and has very small atomic hydrogen (HI) column density (N(HI) $= 1.5 \times 10^{20}$ cm^{-2}).

In addition to these quite good conditions to explore the distant universe, high quality data are available such as deep optical (B and I bands) and near-infrared (K band) images and spectroscopic redshifts (Cowie et al. 1996). Recently we have got a deep submillimeter image as well (Barger et al. 1998).

3. OBSERVATIONS

Our SSA13 observation is very similar to that which was executed in the Lockman Hole. The fundamentals are: ISOCAM, LW2 filter, 6 arcsec pixel-field-of-view (PFOV) lens and a concatenated chain of micro-scans with their center positions defined to sample the PFOV.

The observations were executed in revolutions 560, 561, 610, 612, 613 and 614 using almost all time available for the SSA13 field. Roughly three hours for each of the first two and four hours for the remains; summing up about 23 hours. This implies we could not release any longer lasting observations. This limitation required to change some observational parameters used in the Lockman Hole.

We noticed that accurate registration of ISOCAM frames is critical to detect faint sources. Thus we decided to use non-integer pixel size offsets in micro-scans and a fundamental integration time of 20 seconds hoping to go even deeper in a short chain of micro-scans.

4. DATA REDUCTION

Use of the same program developed for the Lockman Hole image failed due to increased impacts by cosmic rays. Their rates themselves and following transients are the main reasons.

After dark subtraction, we corrected long timescale trends with median and smooth filtered pixel history. A width of more than 2 $\times$ the number of readouts in each pointing was used.

Then short timescale glitches were removed inside each pointing. Deviant readouts from the median were masked out iteratively.

The flatfield was constructed after removing readout frames which will be flatfielded.

After subtracting the median sky, all the images were summed up into fine grids aligned with the North-East direction. We performed field distortion correction using calibration files in the CIA, determined by Aussel (1998).

The final image is shown in Figure 1 as a signal-to-noise (SN) image to express statistical significance adequately.

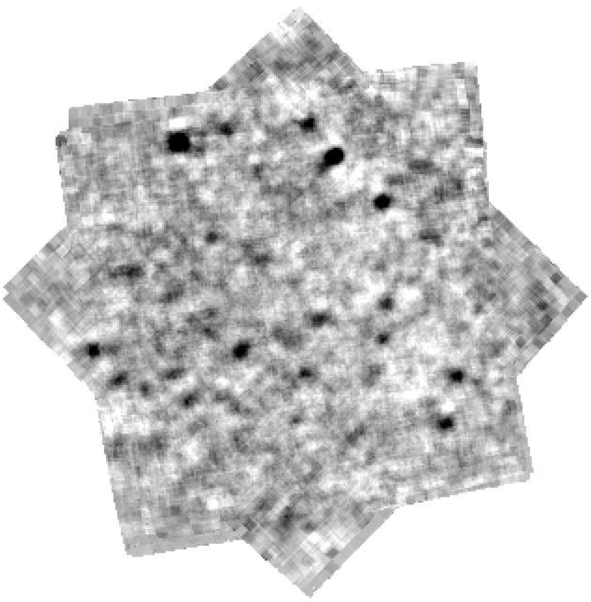

Figure 1. ISOCAM LW2 (7 μm) signal-to-noise image of the SSA13 field. Darker in the image is brighter in surface brightness. North is up and east is to the left. Map size is 5.4 arcmin in Right Ascension and 5.5 arcmin in Declination. The area covered is 16.8 arcmin^2.

5. PHOTOMETRY

Smoothing by Boxcar filtering with width of 5 was used both in the signal and the noise images. All the areas which exceed a signal-to-noise (SN) ratio = 1 were regarded as sources. We have got 26 such sources.

The photometry was done using this area. In order to account for flux below SN = 1, we padded some pixels to this. Note that we applied statistical transient correction for faint point sources; namely we just divided signals by 0.6 (initial response). We assumed there were no significant signal growth due to quite large time constants for such faint sources. We used an initial response of 0.6 reported in Abergel et al. (1996).

SN was calculated from a sum over the same area but on the SN image. Noise was estimated as a ratio between the two measurements.

Measured flux spans from roughly 10 to 100 μJy, while the SN ranges between 6 to 40. Noise marks 1.2 μJy (1σ) but raises up to 7 times due to small integration in the peripheries.

6. OPTICAL COUNTERPARTS

We used ground-based B, I, K and HST I band images to find optical counterparts of detected 7 μm sources. Five bright 7 μm sources are used for registration on optical images, and it gave quite good results: the root-mean-square error was around one arcsec.

Using this transformation, we could find many optical counterparts within the used PFOV of 6 arcsec. They are ranging from star, elliptical, spiral, irregular galaxies and a combination of them. Actually some sources are confused with several sources and it would be difficult to pick up only one of them.

Several sources have no or quite faint optical counterparts. Some are located in peripheries of the map and thus might be spurious ones. But the others are nearer to the center. These could consist of a new population which has not yet been discovered.

Here we show some examples of optical counterparts (Figure 2).

7. SURFACE DENSITY AND REDSHIFTS

Mobasher et al. (1996) shows that 9 sources would be detected down to 10 μJy in the Hubble Deep Field (HDF) with an area of 5 arcmin^2, if most of the galaxies detected in the HDF are undergoing a strong starburst. Scaling to our area just gives 31. It is very close to our current result of 26. Note that we could not detect fainter sources in map peripheries. Thus most of the detected sources could be star-forming galaxies.

Cowie et al. (1996) gives results of redshift measurements for eleven of the 26 sources. Highest is 1.305, though one measurement failed to determine redshift. This source is located very close to an antenna-like galaxy at z = 1.038. They appear to be interacting with each other. Assuming this has $z > 1$, we get a median redshift of $z \sim 0.5$, though these measurements may not be representative for our whole sample.

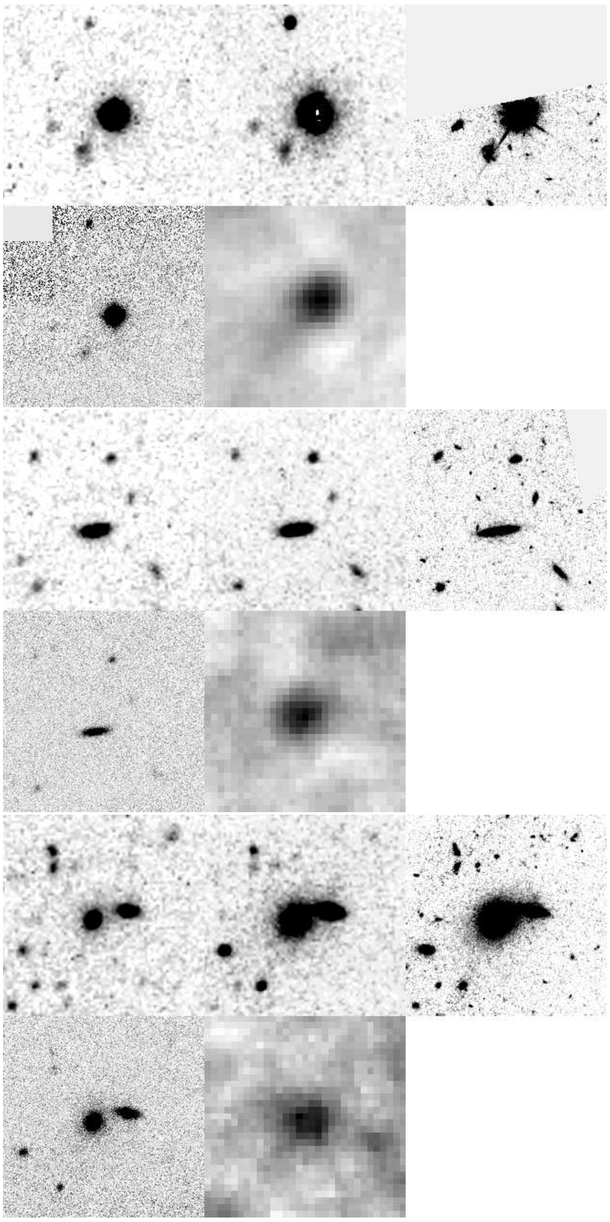

Figure 2. Some ISOCAM LW2 sources detected in the shorter wavelengths. Five images for each object. Upper row from the left are B, I, I(HST) band images and lower row are K and LW2 ones. Map size is 30 arcsec in both directions.

ACKNOWLEDGMENTS

We wish to thank the ISOCAM team in Saclay, Orsay and the CIDT team in VILSPA. After the execution of our Lockman Hole survey, we got useful advice for designing our SSA13 observation, especially from D. Elbaz and F.-X. Désert.

REFERENCES

Abergel, A., Bernard, J.P., Boulanger, F. et al. 1996, A&A 315, L329

Aussel, H., 1998, ISOCAM LW Channel Field of View Distortion, Ver 0.9

Barger, A.J., Cowie, L.L., Sanders, D.B. et al. 1998, Nat 394, 248

Cowie, L.L., Songaila, A., Hu., E.M. et al. 1996, AJ 112, 839

Kawara, K., Sato, Y., Matsuhara, H. et al. 1998a, A&A 336, L9

Mobasher, B., Rowan-Robinson, M., Georgakakis A. 1996, MNRAS 282, 7

Taniguchi, Y., Cowie, L.L., Sato, Y. et al. 1998, A&A 328, L9

THE LARGE EUROPEAN AREA ISO SURVEY ISOPHOT RESULTS USING THE MPIA-PIPELINE

C. Surace[1,2], P. Héraudeau[1], D. Lemke[1], S. Oliver[2], M. Rowan-Robinson[2] & the ELAIS consortium[3]

[1] Max Planck Institut für Astronomie, Heidelberg, Germany
[2] Imperial College of Medicine Science and Technology, London, UK
[3] European consortium involving 19 countries

ABSTRACT

The European Large Area ISO Survey (ELAIS) will provide infrared observations of 4 regions in the sky with ISO. Around 2000 Infrared sources have been detected at 7 and 15 μm (with ISOCAM), 90 and 175 μm (with ISOPHOT)) over 13 square degrees of the sky. We present the source extraction pipeline of the 90 μm ISOPHOT observations, describe and discuss the results obtained and derive the limits of the ELAIS observation strategy.

Key words: ISOPHOT; Survey; Methods: data-analysis.

1. INTRODUCTION

ELAIS (P.I.: M. Rowan-Robinson) is a consortium involving 19 European institutes. The project consists of an ISO survey of 13 square degrees of the sky distributed mainly in 4 areas (3 in the northern hemisphere, 1 in the southern one). These areas have been chosen to be at high ecliptic latitude, to have low cirrus background, and to avoid the presence of strong 12 μm sources close by (Oliver et al. 1998). We used the mapping mode of ISOPHOT and the C_100 detector. Each area was initially planned to be covered by a 20×10 raster map without overlapping. Details on the observing modes and the characteristics of the survey can be found in Oliver et al. (1997).
Because ELAIS is the largest open time project (around 360 hours) being undertaken by ISO, the regions observed will be one of the most well studied at several wavelengths and will be some of the most adequate regions to explore the extragalactic universe.

To treat the large amount of data several data extraction pipelines have been set-up at Imperial College (London), IAS and CEA (Paris) and MPIA (Heidelberg). These pipelines provide the basic data for ground based telescope follow-ups at different wavelengths (Héraudeau et al. these proceedings, Ciliegi et al. (1998) - for a review, see Rowan-Robinson et al. these proceedings) and essential information to constrain the spectral energy distribution in the mid- and far-infrared band.
In the following sections we will describe the ISOPHOT MPIA data extraction pipeline and discuss quantitatively the results obtained.

More information about the status of the survey and ELAIS ground-based follow-ups is available at the WEB address: *http://athena.ph.ic.ac.uk/*.

2. DATA ANALYSIS

2.1. Data raw analysis

The raw data have been analyzed using the ISOPHOT Interactive Analysis tool (Gabriel et al. 1996) (PIA[1] Version 7.2.2). We use PIA to reduce the raw data from the "Edited Raw Data (ERD)" level to the "Auto Analysis Product (AAP)" level, keeping the integrated values during the ISO slewing mode. For deglitching we used the very low sigma value of 1.5 for the sigma-deglitching in order to get rid of the fluctuations of the detector after being hit by a glitch. We use the FCS measurements to calibrate the data. The calibration was checked using dedicated measurements (see section 2.2.) We used private routines (Surace et al. 1997) to reduce the pixel-to-pixel response fluctuations and to derive the final surface brightness values and fluxes of the objects.

2.2. Calibration

The calibration step of the ISOPHOT data is still under discussion despite of the constant progress in building good calibration files. We decide to check the quality of the FCS calibration of the survey observing calibration stars and sources detected in the

[1] PIA is a joint development by the ESA Astrophysics Division and the ISOPHOT consortium

Proceedings of the Conference "The Universe as seen by ISO", Paris, France, 20–23 October 1998 (ESA SP-427, March 1999)

ELAIS survey. The strategy is to observe alternatively a standard star and an ELAIS source, in each field and to compare the fluxes obtained in these measurements with theoretical values (Schulz, B. private communication) and the flux values derived previously from the survey. The measurements have been performed using the ELAIS observing mode for better consistency. Fig. 1 shows examples of observations performed for that purpose.

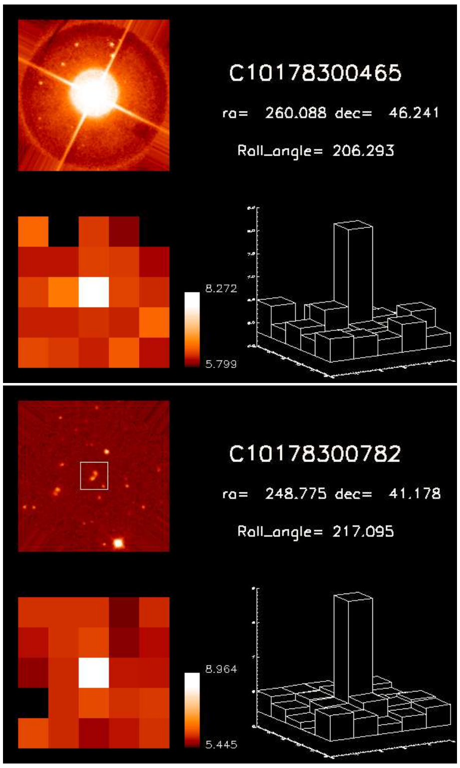

Figure 1. Two calibration dedicated measurements. Each frame is composed by the DSS image (upper left, rotated by the value of the roll angle) the ISOPHOT C100 image (lower left, intensity range is display besides in MJy/sr) the 3D view of the total map (lower right corner). The upper frame is the standard star, the lower one is one ISOPHOT source.

We found that the fluxes derived in our pipeline where in relatively good agreement for the point-like sources:

- The fluxes derived using the FCS calibration and the theoretical values agree within 15% of the total fluxes.
- The fluxes derived during calibration measurements agree within 5% with those derived from the survey

2.3. Target detection

The non overlapping mapping mode of the ELAIS survey makes impossible the use of the built-up map for detection purpose. The noise resulting in building the map will not allow an efficient detection. The detection of the ISOPHOT sources is based directly on the time sequence analysis of the AAP files. The analysis process is summarized in Fig. 2. The basic idea of the pipeline is to detect the maximum of objects by a 1.5 sigma threshold search over the time sequence of the ratio of one pixel over the other 8 pixels of the C100 detector. The spurious detections are rejected by a second threshold search on the redundancy. The pipeline can be summarized by the different steps:

- ratio by raster point of each pixel over the 8 others of the C100 pixels (8 values for 1 pixel)
- 1.5 sigma threshold detection over the time sequence of a pixel (median over 5 raster points)
- 1.5 sigma threshold detection over the time sequence of the ratio for each pixel (median over 5 raster points and fit of the background over 5 raster points)
- selection of the pixels the sum of the detections of which is greater than 4.
- computation of the flux of the detection (flux of the detection pixel - median(flux of 26 surrounding pixels))
- computation of the coordinates of the detections

The detections are visually inspected by 5 different people and classified in 5 groups defined as follows :

- class 1: Clear detection of a bright source
- class 2: Clear detection of a source
- class 3: Probable detection of a source
- class 4: Affected by glitches, not a source
- class 5: Spurious detection

A final classification is given to the detections. In the following we will only consider the detections belonging to the classes 1, 2 and 3. These detections represent approximatively 10% of the total number of detections.

The close by (separation $< 50''$) "real" detections are grouped and the corresponding fluxes are added. The data are saved in an IDL structure format and included in an IDL database. An ASCII table is also provided, with:

- *num:* number of the detection in the raster
- α*:* right ascension (J2000)
- δ*:* declination (J2000)
- *flux:* flux in mJy
- *sigma:* uncertainty in mJy
- *det:* detection level ($1 < det < 10$)
- *time:* central time of the detection in seconds
- *pix:* pixel number ($0 < pix < 8$)
- *rp:* raster point ID of the detection
- *classif:* classification given to the detection.

See Table 1 for an example.

The optical identification is performed on the DSS images, and R-band survey when available, using a maximum likelihood method.

Table 1. Example of table generated by the MPIA pipeline.

num	α (2000)	δ (2000)	flux	sigma	det	time	pix	rp	classif.
13	0 31 44.77	-42 32 50.07	117.2823	31.6307	4	601.930	2	19	2/2/2/2/2/
26	0 31 34.37	-42 44 20.68	214.7283	41.2120	9	1066.973	2	34	1/2/1/1/1/—1
27	0 31 35.27	-42 45 6.11	132.6574	41.3140	9	1066.973	5	34	2/2/2/2/1/—1
56	0 30 52.44	-42 43 10.48	8.4550	22.1327	5	1966.065	7	63	3/3/3/3/3/

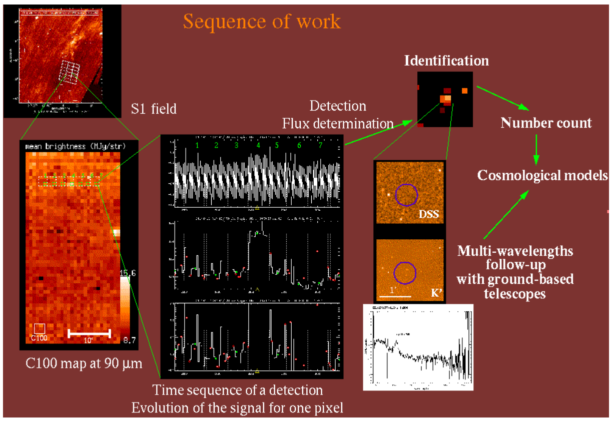

Figure 2. Summary of the data extraction procedure. From the ISO observation, the detection is performed on the time sequence. This gives the basic information for the identification of the sources and the follow-ups.

3. RESULTS AND LIMITS

3.1. Detection limit

Figure 3 shows the distribution of the fluxes derived from our pipeline. Even if some sources have been detected down to 10 mJy. The uncertainties of the fluxes is found between 20 and 60 mJy, depending on the observation itself. The detection of some sources with a signal to noise value less than one is due to the fact that the detection and the computation of the flux and uncertainties are based on two different processing modes. While the detection is performed on each individual pixel the computation of the flux is derived on all the pixels of the detector. The sigma values on the fluxes include also the pixel-to-pixel fluctuations.

Nevertheless, some rasters have been lost due to the fact that they have been observed during the end of the orbit. Indeed the resulting noise is too high to be able to detect any source contribution.

The drop off of the histogramme indicates a detection limit at 60 mJy. While the median is 80 mJy and the completeness of the survey is reached for a limit of 100 mJy (Rowan-Robinson et al. these proceedings).

One has to be aware that due to this detection limit, some objects which are brighter than 100 mJy could be missed by the survey. Indeed if, due to the position of an object in the field, its flux could be distributed among at least two neighbouring pixels, and then not be detected by the pipeline. We estimate to miss 20% of these objects in the survey. This situation improves when using the overlapping observational (overlap 3/2 pixels) mode.

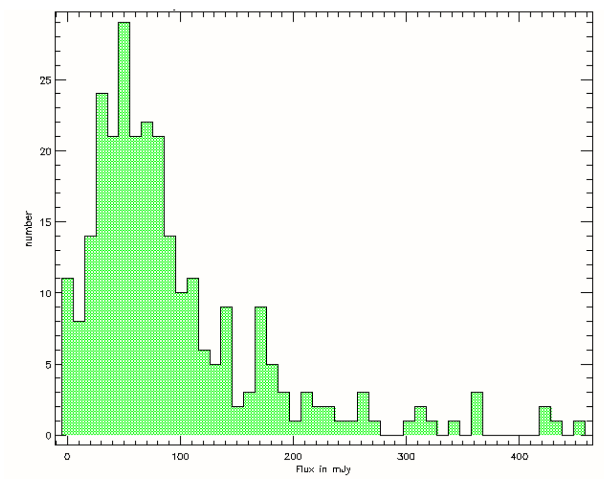

Figure 3. Distribution of the fluxes of the detections, derived using the pipeline.

3.2. Spatial distribution

Up to now 45 fields have been analyzed leading to a total of 8164 detections that have been eye-balled. The observers have agreed on a number of 274 "reliable detections" (class 1 or 2)) and 642 "probable sources" (class 3). One has to remind however that a bright object could be detected several times. This leads to a density of 30 detections by square degrees. The large number of "class 3" object is due to the behaviour of the C_100 detector, when hit by glitches. A forthcoming new deglitching method will improve the reliability of the sources.

Figure 4 shows the spatial distribution of the detections on the N2 ELAIS field. The light crosses show the detections by the pipeline. The dark filled circles are the so-called "class 3" detections while the light filled circles are the "class 2" detections.

The overdensity of the detections in some area is an artificial effect due to the overlapping regions between two rasters. There is no clear evidence of some 2D clustering properties of the "real sources". They look smoothly distributed in the field. However the

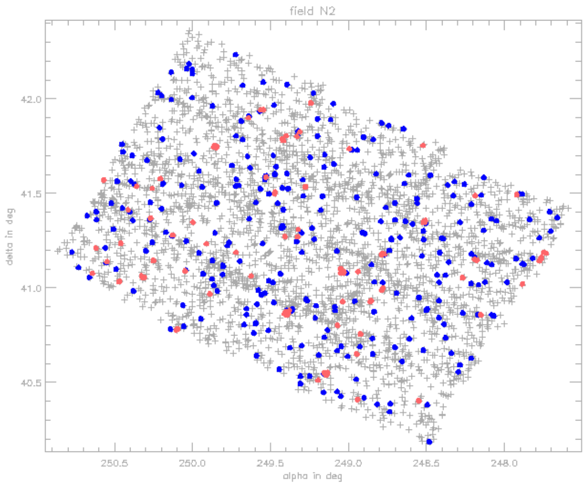

Figure 4. Spatial distribution of the ISOPHOT detections. The light crosses are the detections of possible sources. The dark filled circles are the "class 3" detections, the light filled circles are the "class 2" detections

"class 3" detections are often linked to the "class 2" detections.

This could be explained by the facts that:

- the source could have a morphology leading to a bright center and fainter outer parts
- the source is not centered in the pixel so part of the flux is in the neighbouring pixels
- the beam profile of bright sources could affect as well the neighbouring pixels.

A more elaborate analysis taking into account the signal to noise ratio of each raster as well as the overlapping regions is ongoing.

4. CONCLUSION

In this contribution we have presented the MPIA ISOPHOT ELAIS pipeline. The results from this pipeline will be cross checked with those obtained with other pipelines in order to get a complete source list to deliver to the scientific community. We have cross-checked the ELAIS calibration using some dedicated measurements of standard stars and ELAIS sources. We claim that the MPIA ELAIS fluxes are calibrated with an accuracy better than 20%. We listed 274 reliable detections and 642 probable detections. A 2D and 3D spatial correlation analysis is on-going.

ACKNOWLEDGMENTS

C. S. would like to thank U. Herbstmeier for his contribution to this study, the ISOPHOT group in Heidelberg, C. Gabriel for valuable discussions and B. Schulz for providing calibration data.

REFERENCES

Ciliegi P. & the ELAIS consortium 1998, MNRAS, in press

Gabriel C. et al. 1996, PIA Users Manual, available from ESA/ISO Ground Observatory VILSPA or MPIA Heidelberg

Oliver S. and the ELAIS consortium , 1997 in *New Horizons from Multi-Wavelength Sky Surveys*, Ed: Brian McLean Pubs: Kluwer IAUS 179, 112

Oliver, S. & the ELAIS consortium 1998, MNRAS, in press

Surace C., Abraham P., Herbstmeier U. *New flatfielding correction method for ISOPHOT C100/C200 detector* June 1997, ISOPHOT Interactive Analysis Reports

LIST OF PARTICIPANTS

M. Abada-Simon, Observatoire de Paris-Meudon, 5 place J. Janssen, 92195 Meudon Cedex, France, abada@obspm.fr

A. Abergel, Institut d'Astrophysique Spatiale, Bât 121, Université Paris XI, 91405 Orsay Cedex, France, abergel@ias.fr

P. Abraham, Max-Planck-Institut für Astronomie, Koenigstuhl 17, D-69117 Heidelberg, Germany, abraham@mpia-hd.mpg.de

J. Acosta Pulido, ISO Science Operations Centre Astrophysics, Division of ESA, Villafranca P.O. Box 50727, 28080 Madrid, Spain, jap@ll.iac.es

N. Aghanim, Institut d'Astrophysique Spatiale, Bât 121, Université Paris XI, 91405 Orsay Cedex, France, aghanim@ias.fr

D. Alexander, Department of Physical Sciences, University of Hertfordshire, Hatfield, Hertfordshire, United Kingdom, dma@star.herts.ac.uk

B. Ali, University of Rochester, Dept. of Physics & Astronomy, Rochester, 14627 New-York, United States of America, babar@rocky.pas.rochester.edu

R. Allen, Space Telescope Science Institute, 3700 San Martin Drive, Head Research Programs Office, MD 21218 Baltimore, United States of America, rjallen@stsci.edu

B. Altieri, ESA Villafranca, Villafranca del Castillo, P.O. Box 50727, E-28080 Madrid, Spain, baltieri@iso.vilspa.esa.es

M. Anderegg, ESA/ESTEC, Astrophysics Division, Keplerlaan 1, P.O. Box 299, NL-2200 AG Noordwijk, The Netherlands

P. André, CEA/dsm/dapnia/sap, C.E. Saclay, 91191 Gif Sur Yvette, France, pandre@rosetta.saclay.cea.fr

P. Andreani, Max-planck-institut für Extraterrestrische Physik, Giessenbachstrasse, Postfach 1603, 85740 Garching, Germany, andreani@pd.astro.it

B. Aringer, Institut für Astronomie, Univ. Wien, Tuerkenschanzstr. 17, A-1180 Wien, Austria, aringer@astro1.astro.univie.ac.at

S. Atreya, University of Michigan, Space Research Building, 2455 Hayward Street, MI 48109-2143 Ann Arbor, United States of America, atreya@umich.edu

H. Aussel, CEA Dsm/dapnia/Service d'Astrophysique, 91191 Gif Sur Yvette, France, aussel@discovery.saclay.cea.fr

A. Bacmann, CEA Dsm/dapnia/Service d'Astrophysique, 91191 Gif Sur Yvette, France, bacmann@discovery.saclay.cea.fr

J.-P. Baluteau, Laboratoire d'Astronomie Spatiale, Traverse du Siphon, Les 3 Lucs, BP 8, 13376 Marseille Cedex 12, France, baluteau@astrsp-mrs.fr

P. Barthel, Kapteyn Astronomical Institute, P.O. Box 800, NL-9700 AV Groningen, The Netherlands, pdb@astro.rug.nl

M. Barucci, Observatoire de Paris-Meudon, 5 place J. Janssen, 92195 Meudon Cedex, France, barucci@obspm.fr

E. Becklin, UCLA Astronomy & Astrophysics Division, 8105C Mathematical Sciences Bldg., 405 Hilgard Avenue, CA 90095-1562 Los Angeles, United States of America, becklin@sofia.astro.ucla.edu

C. Beichman, IPAC/Caltech, Mail Code 100-22, 770 South Wilson Avenue, CA 91125 Pasadena, United States of America, chas@ipac.Caltech.edu

D. Beintema, SRON, Postbus 800, NL-9700 AV Groningen, The Netherlands, douwe@sron.rug.nl

M. Benedettin, Ist. Di Fisica Dello Spazio Interplanetario, Consiglio Nazionale delle Ricerche, Area di Ricerca, Tor Vergata, via Fosso del Cavaliere, 00133 Roma, Italy, elisa@orion.ifsi.rm.cnr.it

G. Benedetto, Fisica Cosmica, Via Bassini 15, 20133 Milano, Italy, pdibene@ifctr.mi.cnr.it

J.-P. Bernard, Institut d'Astrophysique Spatiale, Bât 121, Université Paris XI, 91405 Orsay Cedex, France, bernard@ias.fr

F. Bertoldi, Max-Planck-Institut für Radioastronomie, Auf dem Hügel 69, D-53121 Bonn, Germany, bertoldi@mpifr-bonn.mpg.de

B. Bézard, Observatoire de Paris-Meudon, 5 place J. Janssen, 92195 Meudon Cedex, France, Bruno.Bezard@obspm.fr

J. Blommaert, ESA Villafranca, Villafranca del Castillo, P.O. Box 50727, E-28080 Madrid, Spain, jblommae@iso.vilspa.esa.es

R.M. Bonnet, European Space Agency, 8-10 rue Mario Nikis, F-75738 Paris Cedex 15, France

H. Bonnet, Alcatel, 26 avenue Jean-Francois Champollion, BP 1187, 31037 Toulouse Cedex, France

S. Bontemps, Observatoire de Bordeaux, rue de l'Observatoire, BP 89, 33270 Floirac, France, bontemps@astro.su.se

C.M. Bradford, Department of Astronomy, Space Sciences Building, Cornell University NY 14853 Ithaca, United States of America, bradford@astrosun.tn.cornell.edu

A. Brahic, CEA/dsm/dapnia/sap, C.E., Saclay, 91191 Gif Sur Yvette, France

B. Brandl, Cornell University, 220 Space Sciences Bldg, 14850 Ithaca Ny, United States of America, brandl@astrosun.tn.cornell.edu

M. Burgdorf, ESA Villafranca, Villafranca del Castillo, P.O. Box 50727, E-28080 Madrid, Spain, mburgdor@iso.vilspa.esa.es

S. Cabrit, DEMIRM, Observatoire de Paris, 61 avenue de l'Observatoire, 75014 Paris, France, sylvie.cabrit@obspm.fr

J. Cami, SRON, Laboratory for Space Research, P.O. Box 8009, 700 AV Groningen, The Netherlands, cami@astro.rug.nl

A. Castets, Laboratoire d'Astrophysique de l'Observatoire de Grenoble, 414 rue de la Piscine, Domaine Universitaire de Grenoble, BP 53, 38041 Grenoble Cedex 09, France, Alain.Castets@obs.ujf-grenoble.fr

E. Caux, Centre d'Etude Spatiale des Rayonnements, 9 avenue du Colonel Roche, BP 4341, 31029 Toulouse Cedex, France, caux@cesr.fr

C. Ceccarelli, Laboratoire d'Astrophysique de l'Observatoire de Grenoble, 414 rue de la Piscine, Domaine Universitaire de Grenoble, BP 53, F-38041 Grenoble Cedex 09, France, Cecilia.Ceccarelli@obs.ujf-grenoble.fr

J. Cernicharo, Consejo Superior De Investigaciones Cientificas Instituto de Estructura de la Materia, Dpto Fisica Molecular, C/Serrano 121, 28006 Madrid, Spain, cerni@astro.iem.csic.es

C. Cesarsky, C.E.A.-Saclay DSM/DIR, Orme des Merisiers, 91191 Gif Sur Yvette, France, cesarsky@ariane.saclay.cea.fr

D. Cesarsky, Institut d'Astrophysique Spatiale, Bât 121, Université Paris XI, 91405 Orsay Cedex, France, cesarsky@ias.fr

P. Chanial, CE Saclay, SAp, Orme des Merisiers, 91190 Saclay, France, chanial@elbereth.obspm.fr

V. Charmandaris, DEMIRM, Observatoire de Paris, 61 avenue de l'Observatoire, 75014 Paris, France, vassilis.charmandaris@obspm.fr

J. Chieze, CEA, Dsm/dapnia/service d'Astrophysique, 91191 Gif Sur Yvette, France, chieze@cea.fr

A. Claret, CEA, Dsm/dapnia/service d'Astrophysique, 91191 Gif Sur Yvette, France, claret@discovery.saclay.cea.fr

P.E. Clegg, Queen Mary And Westfield College, Physics Department, Mile End Road, E1 4NS London, United Kingdom, p.e.clegg@qmw.ac.uk

M. Cohen, Radio Astronomy Laboratory, 601 Campbell Hall, University of California, CA 94720 Berkeley, United States of America, mcohen@astro.berkeley.edu

D. Coia, University of Padova, Vicolo dell'Osservatorio 5, 35122 Padova, Italy, coia@pdmida.pd.astro.it

P. Colom, Observatoire de Paris-Meudon, 5 place J. Janssen, 92195 Meudon Cedex, France, colom@obspm.fr

F. Comeron, ESO Garching, Karl-Schwarzschild-Strasse 2, D-85748 Garching bei München, Germany, fcomeron@eso.org

A. Contursi, CEA, Saclay, Bât 522, 91191 Gif Sur Yvette, France

E. Copet, DESPA - Observatoire de Paris-Meudon, 5 place J. Janssen, 92195 Meudon Cedex, France, copet@deniseyg.obspm.fr

P. Corporon, Université de Montréal, Dept de Physique, CP 6128 Succursale Centre ville, H3C 3J7 Montreal, Canada, corporon@astro.umontreal.ca

J. Correia, Queen Mary And Westfield College, Physics Department, Mile End Road, E1 4NS London, United Kingdom, J.C.Correia@qmw.ac.uk

A. Coulais, Institut d'Astrophysique Spatiale, Bât 121, Université Paris XI, 91405 Orsay Cedex, France, coulais@ias.fr

A. Coustenis, Observatoire de Paris-Meudon, 5 place J. Janssen, 92195 Meudon Cedex, France, coustenis@mesiob.obspm.fr

P. Cox, Institut d'Astrophysique Spatiale, Bât 121, Université Paris XI, F-91405 Orsay Cedex, France, cox@ias.fr

E. Crété, Centre d'Etude Spatiale des Rayonnements, 9 avenue du Colonel Roche, BP 4341, 31029 Toulouse Cedex, France, crete@cesr.fr

J. Crovisier, ARPEGES, Observatoire de Paris-Meudon, 92195 Meudon, France, crovisie@mesiob.obspm.fr

A. Cudell, University of Heidelberg, Rosenbergweg 7, 69121 Heidelberg, Germany, aarnoldt@ix.urz.uni-heidelberg.de

G. Davis, Institute of Space and Atmospheric Studies, University of Saskatchewan ,116 Science Place, S7N5E2 Saskatoon, Canada, G.R.Davis@usask.ca

L. di Caprio, Laboratory for Ice Research, 1906 Titanic ave., CA 91125 Pasadena, United States of America, leonardo@iceberg.edu

T. De Graauw, SRON, Laboratory for Space Research, P.O. Box 8009, 700 AV Groningen, The Netherlands, Thijsdg@sron.rug.nl

T. De Jong, SRON, Sorbonnelaan 2, 8584 CA Utrecht, The Netherlands, t.dejong@sron.ruu.nl

G. Decin, Institut Voor Sterrekunde Katholieke, Universiteit Leuven, Celestijnenlaan 200, BB-3001 Heverlee, Belgium, greet.decin@ster.kuleuven.ac.be

M. Delaney, Physics Department, University College Dublin, Stillorgan Road, Belfield Dublin 4, Ireland, mdelaney@bermuda.ucd.ie

K. Demyk, Institut d'Astrophysique Spatiale, Bât 121, Université Paris XI, ,91405 Orsay Cedex, France, demyk@ias.fr

L. d'Hendecourt, Institut d'Astrophysique Spatiale, Bât 121, Université Paris XI, 91405 Orsay Cedex, France, ldh@ias.fr

H. Dole, Institut d'Astrophysique Spatiale, Bât 121, Université Paris XI, 91405 Orsay Cedex, France, dole@ias.fr

C. Dominik, Sterrewacht Leiden, P.O. Box 9513, NL-2300 Ra Leiden, The Netherlands, dominik@strw.leidenuniv.nl

E. Dotto, Observatoire de Paris-Meudon, 5 place J. Janssen, 92195 Meudon Cedex, France, dotto@megasx.obspm.fr

T. Douvion, CEA, Dsm/dapnia/service d'Astrophysique, 91191 Gif Sur Yvette, France, douvion@discovery.saclay.cea.fr

B. Draine, Dept. of Astrophysical Sciences, 113 Peyton Hall, Princeton University Observatory, NJ 08544-1001 Princeton, United States of America, draine@astro.princeton.edu

P. Drossart, Observatoire de Paris-Meudon, 5 place J. Janssen, 92195 Meudon Cedex, France, drossart@mesiob.obspm.fr

D. Dubreuil, CEA, Dapnia, Orme des Merisiers, Bât 709, 91191 Gif Sur Yvette Cedex, France, dubreuil@discovery.saclay.cea.fr

V. Ducci, Observatoire de Marseille, 2 place Leverrier, 13248 Marseille, France, ducci@obmara.cnrs-mrs.fr

E. Dwek, Laboratory for Astronomy and Solar Physics, Code 685 NASA / Goddard Space Flight Center, MD 20771 Greenbelt, United States of America, edwek@stars.gsfc.nasa.gov

M. Egan, Air Force Research Laboratory, 29 Randolph, RD AFRL/VSBC Hanscom AFB MA, 01731-3010 Hanscom AFB, United States of America, egan@pldac.plh.af.mil

D. Elbaz, CEA/DAPNIA, Orme des Merisiers, 91191 Gif Sur Yvette Cedex, France, elbaz@discovery.saclay.cea.fr

R. Emery, Rutherford Appleton Laboratory, Chilton Didcot, OX 11 OQX, Oxfordshire, United Kingdom, R.J.EMERY@RL.Ac.UK

Th. Encrenaz, DESPA, Observatoire de Paris-Meudon, 5 place J. Janssen, 92195 Meudon Cedex, France, therese.encrenaz@obspm.fr

P. Encrenaz, DEMIRM, Observatoire de Paris, 61 avenue de l'Observatoire, 75014 Paris France

N. Evans, Department of Physics, Keele University, Keele ST5 5BG, Staffordshire, United Kingdom, ae@astro.keele.ac.uk

S. Eyres, Department of Physics, Keele University, Keele ST5 5BG, Staffordshire, United Kingdom spe@astro.keele.ac.uk

D. Fadda, CEA, Dsm/dapnia/service d'Astrophysique, 91191 Gif Sur Yvette, France, fadda@discovery.saclay.cea.fr

E. Falgarone, DEMIRM,Observatoire de Paris, 61 avenue de l'Observatoire, 75014 Paris, France, edith@ensapb.ens.fr

H. Feuchtgruber, Max-Planck-Institut für Extraterrestrische Physik, Giessenbachstrasse, Postfach 1603, 85740 Garching, Germany, fgb@mpeia.mpe-garching.mpg.de

M. Fich, DEMIRM, Observatoire de Paris, 61 avenue de l'Observatoire, 75014 Paris, France, fich@astro.uwaterloo.ca

J. Fischer, Naval Research Laboratory, 4555 Overlook av sw, 20375-5351 Washington DC, United States of America, jfischer@irfp8.nrl.navy.mil

W. Forrest, University of Rochester Dept. of Physics & Astronomy, Rochester, 14627 New-York, United States of America, forrest@rocky.pas.rochester.edu

T. Fouchet, Observatoire de Paris-Meudon, 5 place J. Janssen, 92195 Meudon Cedex, France, fouchet@megasn.obspm.fr

V. Frey, OrsayTerre, Bat. 509, Université Paris-Sud, 91405 ORSAY cedex, France, frey@geol.u-psud.fr

Y. Fuchs, CEA/dsm/dapnia/sap, Orme des Merisiers, Bât 709, 91191 Gif Sur Yvette, France, yfuchs@discovery.saclay.cea.fr

M. Fulchignoni, Observatoire de Paris-Meudon, 5 place J. Janssen, 92195 Meudon Cedex, France, fulchignoni@obspm.fr

C. Gabriel, ESA Villafranca, Villafranca del Castillo, P.O. Box 50727, E-28080 Madrid, Spain, cgabriel@iso.vilspa.esa.es

P. Gallais, CEA, Dsm/dapnia/service d'Astrophysique, 91191 Gif Sur Yvette, France, gallais@discovery.saclay.cea.fr

Y. Gallant, Sterrenkunding Instituut Universiteit Utrecht, Postbus 80.00 03508 TA Utrecht, The Netherlands, gallant@astro.uu.nl

S. Ganesh, Institut D'Astrophysique de Paris, 98 bis boulevard Arago, 75014 Paris, France, shashi@iap.fr

K. Ganga ,IPAC/Caltech, Mail Code 100-22, 770 South Wilson Avenue CA 91125 Pasadena, United States of America, kmg@ipac.Caltech.edu

P. Garcia-Lario, ISO Science Operations Centre, P.O. Box 50727, 28080 Madrid, Spain, pgarcia@iso.vilspa.esa.es

R. Gehrz, University of Minnesota, 116 Church St., SE Minneapolis, 55455 Minnesota, United States of America gehrz@astro.spa.umn.edu

R. Genzel, Max-Planck-Institut für Extraterrestrische Physik, Giessenbachstrasse, Postfach 1603, 85740 Garching, Germany, genzel@mpe-garching.mpg.de

M. Gerbaldi, Institut d'Astrophysique de Paris, 98 bis boulevard Arago, 75014 Paris, France, gerbaldi@iap.fr

M. Gerin, Laboratoire de Radioastronomie, ENS, 24 rue Lhomond, 75231 Paris Cedex 05, France, maryvonne.gerin@physique.ens.fr

T. Giannini, Osservatorio Astronomico di Roma, Via Frascati 33, Monte Porzio, 00040 Roma, Italy, teresa@coma.mporzio.astro.it

M. Giard, Centre d'Etude Spatiale des Rayonnements, 9 avenue du Colonel Roche, BP 4341, 31028 Toulouse Cedex, France, giard@cesr.fr

R. Gispert, Institut d'Astrophysique Spatiale, Bât 121, Université Paris XI, 91405 Orsay Cedex, France, gispert@ias.fr

E. Gonzáles-Alfonso, Consejo Superior De Investigaciones Cientificas, Instituto de Estructura de la Materia, Dpto Fisica Molecular, C/Serrano 121, 28006 Madrid, Spain, gonzalez@astro.iem.csic.es

S. Gravano, Physics Dept,Keele University, Keele ST5 5BG, Staffordshire, United Kingdom sg@astro.keele.ac.uk

I. Grenier, Service d'Astrophysique, CEA Saclay, Orme des Merisiers, 91191 Gif Sur Yvette, France, isabelle.grenier@cea.fr

M. Griffin, Physics Department, Queen Mary and Westfield College, London E1 4Ns, United Kingdom, m.j.griffin@qmw.ac.uk

C. Griffith, North Arizona, United States of America, griffith@bohr.phy.nau.edu

M. Groenewegen, Max-Planck-Institut für Astrophysik, Karl Schwarzchildstr.1, Postfach 1523, 85740 Garching, Germany, groen@mpa-garching.mpg.de

N. Grosso, Service d'Astrophysique du CEA, Orme des Merisiers, Bât 709, 91191 Gif Sur Yvette, France, grosso@discovery.saclay.cea

E. Grün, Max-Planck Institut für Kernphysics, Saupfercheckweg 1, 69117 Heidelberg, Germany, Eberhard.Gruen@mpi-hd.mpg.de

C. Gry, Laboratoire d'Astronomie Spatiale, Traverse du Siphon, Les 3 Lucs BP 8, 13376 Marseille Cedex 12, France, cgry@iso.vilspa.esa.es

M. Guélin, IRAM, 300 rue de la Piscine, 38406 St Martin d'Hères, France, guelin@iram.fr

O. Guillois, CEA, CE Saclay - SPAM DRECAM, Bât 522, 91191 Gif Sur Yvette, France, guillois@droopy.saclay.cea.fr

M. Haas, Max-Planck-Institut für Astronomie, Koenigstuhl 17, 69117 Heidelberg, Germany, haas@mpia-hd.mpg.de

E. Habart, Institut d'Astrophysique Spatiale, Bât 121, Université Paris XI, 91405 Orsay Cedex, France, habart@ias.fr

H. Habing, Sterrewacht Leiden, P.O. Box 9513, NL-2300 Ra Leiden, The Netherlands, habing@strw.leidenuniv.nl

L. Haikala, ESO, Alonso de Cordova 3107, Casilla 19001, Santiago, Chile, lhaikala@eso.org

L. Hansen, Niels Bohr Inst., Juliane Maries Vej 30, DK-2100 Copenhagen, Denmark, leif@astro.ku.dk

V. Harvey, University of Nevada, Las Vegas, United States of America, harvey@stars.gsfc.nasa.gov

P. Harvey, University of Texas, Astronomy Dept., 78712 Austin, United States of America, pmh@zeke.as.utexas.edu

M. Harwit, Cornell University, 511 H Street SW, 20024-2725 Washington DC, United States of America, martin.harwit@ibm.net

I. Heinrisrichen, Max-Planck-Institut-für-Kernphysik, Postfach 103980, 69029 Heidelberg, Germany, heinrich@iso.vilspa.esa.es

G. Helou, IPAC/Caltech, Mail Code 100-22, 770 South Wilson Avenue, CA 91125 Pasadena, United States of America, gxh@ipac.Caltech.edu

Th. Henning, Astrophysical Institute and University, Schillergaesschen 3, D-07743 Jena, Germany, henning@astro.uni-jena.de

A. Heras, ISO Science Operations Centre, P.O. Box 50727, 28080 Madrid, Spain, aheras@iso.vilspa.esa.es

P. Heraudeau, Max-Planck-Institut für Astronomie, Koenigstuhl 17, D-69117 Heidelberg, Germany, Heraudeau@mpia-hd.mpg.de

E. Hooper, Harvard-Smithsonian Center for astrophysics, 60 Garden Steet, MS 83MA, 02138 Cambridge, United States of America, ehooper@as.arizona.edu

M. Hopwood, Physics dept., Keele University, Keele ST5 5BG, Staffordshire, United Kingdom, meh@astro.keele.ac.uk

J. Hora, Smithsonian Astrophysical, Observatory, 60 Garden Steet, MA 02138 Cambridge, United States of America, jhora@cfa.harvard.edu

S. Hotzel, Max-Planck-Institut für Astronomie, Koenigstuhl 17, 69117 Heidelberg, Germany, hotzel@mpia-hd.mpg.de

L. Houziaux, Academie Royale de Belgique, 12 avenue des Villas, 4180 Hamoir, Belgique, leo.houziaux@ulg.ac.be

D. Hutsemekers, Institut d'Astrophysique, 5 avenue de Cointé, B-4000 Liége, Belgium, hutsemek@astro.ulg.ac.be

R. Huygen, Institut Voor Sterrekunde, Katholieke Universiteit Leuven, Celestijnenlaan 200B, B-3001 Heverlee, Belgium, rik.huygen@ster.kuleuven.ac.be

D. Imbault, CEA/dsm/dapnia/sap, C.E. Saclay, Bât 774, 91191 Gif Sur Yvette, France, imbault@dsmdir.cea.fr

T. Jacq, Observatoire de Bordeaux, rue de l'Observatoire, 33270 Floirac, France, jacq@observ.u-bordeaux.fr

T. Jarrett, IPAC/Caltech, Mail Code 100-22, 770 South Wilson Avenue CA 91125 Pasadena, United States of America, jarrett@ipac.Caltech.edu

N. Jenkins, ESA Villafranca, Villafranca del Castillo, P.O. Box 50727, E-28080 Madrid, Spain, njenkins@iso.vilspa.esa.es

A. Jones, Institut d'Astrophysique Spatiale, Bât 121, Université Paris XI, 91405 Orsay Cedex, France, ant@ias.fr

A. Jorissen, Institut d'Astronomie et d'Astrophysique, Université Libre de Bruxelles, C.P. 226 Boulevard du Triomphe, B-1050 Bruxelles, Belgium, ajorisse@astro.ulb.ac.be

M. Joubert, CNES Toulouse, 18 avenue Edouard Belin, 31055 Toulouse Cedex, France, Martine.Joubert@cnes.fr

J. Juillet, Alcatel, 26 avenue Jean-Francois Champollion, BP 1187, 31037 Toulouse Cedex, France

K. Justtanont, Stockholm Observatory, S-13336 Saltsjobaden, Sweden, kay@astro.su.se

A. Kaas, Stockholm Observator,y 13336 Saltsjobaden, Sweden, amanda@astro.su.se

I. Kamp, Institut für Theoretical Physik and Astrophysik, Universitt Kiel, D-24098 Kiel, Germany, kamp@astrophysik.uni-kiel.de

K. Kawara, Institute of Astronomy, The University of Tokyo, Japan, kkawara@mtk.ioa.s.u-tokyo.ac.jp

J. Keane, Kapteyn Astronomical Institute, SRON, P.O. Box 800 NL-9700 AV Groningen, The Netherlands, jacquie@astro.rug.nl

J. Keene, California Institute of Technology, Observational Cosmology, Mail Stop 320-47, 1200 E. California Blvd, CA 91125 Pasadena, United States of America, jbk@medoc.Caltech.edu

M.F. Kessler, ESA Villafranca, Villafranca del Castillo, P.O. Box 50727, E-28080 Madrid, Spain, mkessler@iso.vilspa.esa.es

U. Klaas, Max-Planck-Institut für Astronomie, Koenigstuhl 17, D-69117 Heidelberg, Germany, klaas@mpia-hd.mpg.de

R. Klein, Friedrich-Schiller Universitaet Jena, Astrophysikalisches Institut and Universitaets-Sternwarte, Schillergässchen 2-3, D-07745 Jena Germany, rklein@astro.uni-jena.de

A. Klotz, Centre d'Etude Spatiale des Rayonnements, 9 avenue du Colonel Roche, BP 4341, 31029 Toulouse Cedex, France , klotz@cesr.fr

E. Kontizas, Astronomical Institute, National Observatory of Athens, Greece

M. Kontizas, Section of Astronomy, Astrophysics & Mechanics, Department of Physics, University of Athens, Greece, mkonti@titan.astro.noa.gr

D. Kunze, Max-planck-Institut für Extraterrestrische Physik, Giessenbachstrasse, Postfach 1603, 85740 Garching, Germany, kunze@mpe.mpg.de

N. Kylafis, University of Crete, Physics Department, P.O. Box 2208, 710 03 Heraklion Crete, Greece, kylafis@physics.uch.gr

G. Lagache, Institut d'Astrophysique Spatiale, Bât 121, Université Paris XI, 91405 Orsay Cedex, France, lagache@ias.fr

P. Lagage, CEA DSM/DAPNIA/Service d'Astrophysique, Orme des Merisiers, 91191 Gif Sur Yvette Cedex, France, lagage@cea.fr

W. Langer, Jet Propulsion Laboratory, 4800 Oak Grove Drive, MS 169-506, CA 91109 Pasadena, United States of America, langer@nimba.jpl.nasa.gov

C. Lari, Istituto di Radioastronomica, CNR, Via Gobetti 101, 40129 Bologna, Italy, lari@artbo1.bo.cnr.it

B. Larsson, Stockholm Observatory, 13336 Saltsjobaden, Sweden, bem@astro.su.se

R. Laureijs, ESA Villafranca, Villafranca del Castillo, P.O. Box 50727, E-28080 Madrid, Spain, rlaureij@iso.vilspa.esa.es

O. Laurent, CEA Dsm/dapnia/service d'Astrophysique, France, olaurent@discovery.saclay.cea.fr

Th. Le Bertre, DEMIRM, Observatoire de Paris, 61 avenue de l'Observatoire, 75014 Paris, France, lebertre@obspm.fr

A. Le Bras, Observatoire de Paris-Meudon, 5 place J. Janssen, 92195 Meudon Cedex, France, lebras@astem.obspm.fr

P. Le Coupanec, Observatoire de Paris-Meudon, 5 place J. Janssen, 92195 Meudon Cedex, France, patricia.lecoupanec@obspm.fr

B. Le Floch, CSIC-IEM, Serrano 121, 28006 Madrid, Spain, lefloch@astro.iem.csic.es

K. Leech, ESA Villafranca, Villafranca del Castillo, P.O. Box 50727, E-28080 Madrid, Spain, kleech@iso.vilspa.esa.es

S. Leeks, Queen Mary And Westfield College, Physics Department, Mile End Road, E1 4NS London, United Kingdom, S.J.leeks@qmw.ac.uk

A. Léger, Institut d'Astrophysique Spatiale, Bât 121 Université, Paris XI, 91405 Orsay Cedex, France, leger@ias.fr

K. Lehtinen, University of Helsinki Observatory, Tahtitorninmaki P.O. Box 14, 00014 Helsinki, Finland, kimmo.lehtinen@helsinki.fi

E. Lellouch, Observatoire de Paris-Meudon, 5 place J. Janssen, 92195 Meudon Cedex, France, lellouch@obspm.fr

J. Lemaire, Observatoire de Paris-Meudon, 5 place J. Janssen, 92195 Meudon Cedex, France, lemaire@obspm.fr

D. Lemke, Max-Planck-Institut für Astronomie, Koenigstuhl 17, D-69117 Heidelberg, Germany, lemke@mpia-hd.mpg.de

L. Lemonon, CEA Dsm/dapnia/service d'Astrophysique, 91191 Gif sur Yvette, France, lemonon@discovery.saclay.cea.fr

P. Lena, Observatoire de Paris-Meudon, 5 place J. Janssen, 92195 Meudon Cedex, France, lena@obspm.fr

M. Lepintre, Institut d'Astrophysique Spatiale, Bât 121 Université, Paris XI, 91405 Orsay Cedex, France, lepintre@ias.fr

D. Levine, SIRTF Science Center, MS 100-22, Caltech, 1201 E California Blvd, CA 91125 Pasadena, United States of America, deblev@ipac.Caltech.edu

D. Lis, California Institute of Technology, George W. Downs Laboratory of Physics, Mail Stop 320-47, 1200 E. California Blvd, CA 91125 Pasadena, United States of America, dcl@medoc.Caltech.edu

R. Liseau, Stockholm Observatory, SE-13336 Saltsjobaden, Sweden, rene@astro.su.se

X.-W. Liu, Dept of Physics and Astronomy, University College London, Gower Street, London, WC2E 6BT, UK xwl@star.ucl.ac.uk

S. Lord, IPAC/Caltech, Mail Code 100-22, 770 South Wilson Avenue, CA 91125 Pasadena, United States of America, lord@ipac.Caltech.edu

D. Lorenzetti, Osservatorio Astronomico di Roma, Via Frascati 33, Monte Porzio, 00040 Roma, Italy, dloren@coma.mporzio.astro.it

C. Loup, Institut d'Astrophysique de Paris, 98 bis boulevard Arago, 75014 Paris, France, loup@caha.es

N. Lu, IPAC/Caltech, Mail Code 100-22, 770 South Wilson Avenue, CA 91125 Pasadena, United States of America, lu@ipac.Caltech.edu

D. Lutz, Max-Planck-Institut für Extraterrestrische Physik, Giessenbachstrasse Postfach 1603, 85740 Garching, Germany, lutz@mpe.mpg.de

S. Madden, Service d'Astrophysique CEA, Saclay, Orme des Merisiers, 91191 Gif Sur Yvette, France, madden@discovery.saclay.cea.fr

T. Maihara, Kyoto University, Dept. Physics, Kitashirakawa, 606-8502 Kyoto, Japan, maihara@cr.scphys.kyoto-u.ac.jp

J.-P. Maillard, Institut d'Astrophysique de Paris, 98 bis boulevard Arago, 75014 Paris, France, maillard@iap.fr

K. Malfait, Institut Voor Sterrekunde, Leuven Universiteit, Celestijnenlaan 200B, B-3001 Heverlee, Belgium, Koen.Malfait@ster.kuleuven.ac.be

S. Malhotra, IPAC/Caltech, Mail Code 100-22, 770 South Wilson Avenue, CA 91125 Pasadena, United States of America, san@ipac.Caltech.edu

J. Martin, Observatoire de Paris, 61 avenue de l'Observatoire, 75014 Parism Francem jmmartin@obspm.fr

L. Martin-Hernandez, Kapteyn Astronomical Institute, SRON, P.O. Box 800 NL-9700 AV Groningen, The Netherlands, leticia@astro.rug.nl

J. Martin-Pintado, Osservatorio Astronomico Nacional, Campus Universitario Alcala de Hénares, 28800 Alcala De Hénares, Spain, martin@oan.es

J. Matagne, ESA Villafranca, Villafranca del Castillo, P.O. Box 50727, E-28080 Madrid, Spain, jmatagne@iso.vilspa.esa.es

J. Mather, NASA Goddard Space Flight Center, Code 685, MD 20771 Greenbelt, United States of America, john.mather@gsfc.nasa.gov

H. Matsuhara, Infrared Astrophysics Division, The Institute of Space and Astronautical Science, Yoshinodai, 3-1-1229-8510 Sagamihara, Japan, maruma@astro.isas.ac.jp

K. Mattila, Observatory, University of Helsinki, Tahtitornimaki, FIN-00014 Helsinki, Finland, mattila@cc.helsinki.fi

B. Mc Breen, Physics Department, University College Dublin, Stillorgan Road, Dublin 4, Ireland, bmcbreen@ollamh.ucd.ie

G. Meeus, Katholieke Universiteit Leuven, Instituut voor Sterrenkunde, Celestijnenlaan 200B B-3001 Heverlee, Belgique, gwendolyn@ster.kuleuven.ac.be

P. Mennebelle, DEMIRM, Observatoire de Paris, 61 avenue de l'Observatoire, 75014 Paris France

L. Meny, Centre d'Etude Spatiale des Rayonnements, 9 avenue du Colonel Roche, BP 4341, 31029 Toulouse Cedex, France, meny@cesr.fr

L. Metcalfe, ISO Science Operations Centre, Astrophysics Division, Space Science Department of ESA, Villafranca, P.O. Box 50727, 28080 Madrid, Spain, lmetcalf@iso.vilspa.esa.es

F. Mirabel, CEA/dsm/dapnia/sap, C.E. Saclay, 91191 Gif Sur Yvette, France, mirabel@discovery.saclay.cea.fr

V. Missoulis, Imperial College of Science Technology and Medecine, Prince Consort Road, SW7 2BZ London, United Kingdom ,v.misoulis@ic.ac.uk

M. Miville-Deschênes, Institut d'Astrophysique Spatiale, Bât 121, Université Paris XI, 91405 Orsay Cedex, France, mamd@ias.fr

M. Mizutani, Department of Astronomy, Kyoto University, 7-3-1 Hongo Bunkyo-ku, 113-0033 Kyoto, Japan, mizutani@astron.s.u-tokyo.ac.jp

A. Moneti, ISO Science Operations Centre, P.O. Box 50727, 28080 Madrid, Spain, amoneti@iso.vilspa.esa.es

T. Montmerle, CEA/dsm/dapnia/sap, C.E. Saclay, 91191 Gif Sur Yvette, France, montmerle@cea.fr.

A. Moorwood, ESO Garching, Karl-Schwarzschild-Strasse 2, D-85748 Garching bei München, Germany, amoor@eso.org

T. Morel, Astrophysics Group, Imperial College of Science Technology and Medicine, Blackett Laboratory, Prince Consort Road, London SW7 2BZ, United Kingdom, t.morel@ic.ac.uk

M. Morris, UCLA, Astronomy& astrophysics Division, 8105C Mathematical Sciences Bldg., 405 Hilgard Avenue, CA 90095-1562 Los Angeles, United States of America, morris@astro.ucla.edu

P. Morris, SRON, Laboratory for Space Research, P.O. Box 800, 9700 AV Groningen, The Netherlands, patrickm@sron.ruu.nl

C. Moutou, Observatoire de Haute Provence du CNRS, 04870 Saint Michel l'Observatoire, France, claire@obs-hp.fr

T. Müller, ISO Science Operations Centre, P.O. Box 50727, 28080 Madrid, Spain, tmueller@mpia-hd.mpg.de

F. Najarro, Instituto de Estructura de la Materia, CSIC, C/Serrano 121, 28006 Madrid, Spain, najarro@isis.iem.csic.es

A. Natta, Osservatorio Astrofisico di Arcetri, Largo E. Fermi 5, I-50125 Firenze, Italy, natta@arcetri.astro.it

R. Nguyen Quang, Observatoire de Paris, 61 avenue de l'Observatoire, F-75014 Paris, France, rieu@obspm.fr

L. Nordh, Stockholm Observatory, 13336 Saltsjobaden, Sweden, nordh@astro.su.se

A. Noriega-Crespo, IPAC/Caltech, Mail Code 100-22, 770 South Wilson Avenue CA 91125 Pasadena, United States of America, alberto@ipac.Caltech.edu

Y. Oasa, Department of Astronomy, University of Tokyo 2-21-1 Osawa, Mitaka, Tokyo, 181-8588, Japan, yummy@pavane.mtk.nao.ac.jp

H. Okuda, Laboratory of Infrared Astrophysics, ISAS, Yoshinodai Sagamihara, Kanagawa, Japan, okuda@astro.isas.ac.jp

K. Okumara, Institut d'Astrophysique Spatiale, Bât 121, Université Paris XI, 91405 Orsay Cedex, France, okumara@ias.fr

G. Olofsson, Stockholm Observatory, 13336 Saltsjobaden, Sweden, olofsson@astro.su.se

A. Omont, Institut d'Astrophysique de Paris, 98 bis boulevard Arago, 75014 Paris, France, omont@iap.fr

T. Onaka, Department of Astronomy, Tokyo University of Tokyo, Bunkyo-ku 113-032, Tokyo, Japan, onaka@astron.s.u-tokyo.ac.jp

D. Osip, University of Florida, Department of Astronomy, 211 Bryant Space Science Center, 32611-2055 Gainesville, Florida, United States of America, osip@astron.mit.edu

T. Owen, University of Hawaii, Institute for Astronomy ,2680 Woodlawn Drive, Honolulu 96822 Hawaii, United States of America, owen@ifa.hawaii.edu

L. Pagani, Observatoire de Paris, 61 avenue de l'Observatoire, 75014 Paris, France, laurent.pagani@obspm.fr

F. Pajot, Institut d'Astrophysique Spatiale, Bât 121, Université Paris XI, 91405 Orsay Cedex, France, pajot@ias.fr

M. Palumbo, Osservatorio Astrofisico di Catania, Viale Andrea Doria 6, I-95125 Catania, Italy, mepalumbo@alpha4.ct.astro.it

E. Pantin, CEA/dsm/dapnia/sap, CE Saclay, 91191 Gif Sur Yvette, France, pantin@discovery.saclay.cea.fr

P. Papadopoulous, Sterrewacht Leiden, Niels Bohrweg 2, NL-2333 Ca Leiden, The Netherlands, papadop@strw.leidenuniv.nl

R. Papoular, CEA, Ce Saclay Spam, Bât 522, 91191 Gif Sur Yvette, France, papoular@spam.saclay.cea.fr

E. Peeters, SRON, Groningen Laboratory for Space Research, P.O. Box 800, 9700 AV Groningen, The Netherlands, peeters@astro.rug.nl

D. Péquignot, Observatoire de Paris-Meudon, 5 place J. Janssen, 92195 Meudon Cedex, France, Daniel.Pequignot@obspm.fr

S. Pérez-Martinez, CSIC-IEM, Instituto de Estructura de la Materia, Dpto Fisica Molecular, C/Serrano 121, 28006 Madrid, Spain, sonia@astro.iem.csic.es

P. Persi, Istituto Astrofisica Spaziale, CNR, Via del Fosso del Cavaliere, I-00133 Roma, Italy, persi@saturn.ias.rm.cnr.it

S. Peschke, Max-Planck Institut für Kernphysik, Postfach 103 980, D-69029 Heidelberg, Germany, peschke@orion.mpia-hd.mpg.de

S. Pezzuto, Ist Di Fisica Dello Spazio Interplanetario, Consiglio Nazionale delle Ricerche, Area di ricerca, Tor Vergata, via Fosso del Cavaliere, 00133 Roma, Italy, pezzuto@le.infn.it

T. Pickering, Kapteyn Astronomical Institute, SRON, P.O. Box 800, NL-9700 AV Groningen, The Netherlands, tim@astro.rug.nl

D. Pierini, Max-Planck Institut für Kernphysics, Saupfercheckweg 1, 69117 Heidelberg, Germany, daniele.pierini@mpi-hd.mpg.de

G. Pineau des Forêts, DAEC, Observatoire de Paris, 92195 Meudon Principal, France, forets@obspm.fr

M. Polleta, Geneve Observatory, Chemin des Maillettes 51, S-1290 Sauverny, Switzerland, Maria.Polletta@obs.unige.ch

T. Prusti, ESA Villafranca, Villafranca del Castillo, P.O. Box 50727, E-28080 Madrid, Spain, tprusti@iso.vilspa.esa.es

J.-L. Puget, Institut d'Astrophysique Spatiale, Bât 121, Université Paris XI, 91405 Orsay, Cedex, France puget@ias.fr

D. Puy, Paul Scherrer Institute, 5232 Villigen-PSI, Switzerland, puy@physik.unizh.ch

P. Querre, CEA, Dapnia, Orme des Merisiers, 91191 Gif Sur Yvette Cedex, France, pquerre@cea.fr

A. Quillen, Steward Observatory, University of Arizona, 933 N. Cherry St., AZ 85721 Tucson, United States of America, aquillen@as.arizona.edu

C. Reynaud, CEA, Ce Saclay Spam, Bât 522, 91191 Gif Sur Yvette, France, creynaud@cea.fr

P. Richards, CLRC, RAL Rutherford Appleton Laboratory, Chilton, OX11 OQX Didcot, United Kingdom, pjr@sdc1.bnsc.rl.ac.uk

M. Rieke, Steward Obsservatory, University of Arizona, 933 N. Cherry St., AZ 85721 Tucson, United States of America, mrieke@as.arizona.edu

G. Rieke, Steward Obsservatory, University of Arizona, 933 N. Cherry St. AZ 85721 Tucson, United States of America, grieke@as.arizona.edu

D. Rigopoulou, Max-Planck-Institut für Extraterrestrische Physik, Giessenbachstrasse, Postfach 1603, 85740 Garching, Germany, dar@mpe.mpg.de

M. Robberto, Max-planck-institut für Astronomie, Koenigstuhl 17, D-69117 Heidelberg, Germany, robberto@mpia-hd.mpg.de

B. Rocca-Volmerange, Institut d'Astrophysique de Paris, 98 bis boulevard Arago, 75014 Paris, France, rocca@iap.fr

N. Rodriguez-Fernandez, Osservatorio Astronomico Nacional, Apartado 1143, Alcala de Hénares, 28800 Alcala De Hénares, Spain, nemesio@oam.es

P. Roelfsema, SRON, Postbus 800, NL-9700 AV Groningen, The Netherlands, pjotr@sron.rug.nl

D. Rosenthal, Max-planck-institut für Extraterrestrische Physik, Giessenbachstrasse, Postfach 1603, 85740 Garching, Germany, rosenthal@mpe-garching.mpg.de

F. Rostas, Observatoire de Paris-Meudon, 5 place J. Janssen, 92195 Meudon Cedex, France, rostas@obspm.fr

D. Rouan, Observatoire de Paris-Meudon, 5 place J. Janssen, 92195 Meudon Cedex, France, daniel@isolde.obspm.fr

E. Roueff, Observatoire de Paris-Meudon, DAEC, 5 place J. Janssen, 92195 Meudon Cedex, France, roueff@obspm.fr

H. Roussel, CEA/dsm/dapnia/sap, CE Saclay, 91191 Gif Sur Yvette, France, hroussel@discovery.saclay.cea.fr

M. Rowan-Robinson, Imperial College, Astrophysics Group, Blackett Laboratory, Prince Consort Rd, 5W7 2BZ London, United Kingdom, m.robinson@ic.ac.uk

R. Russell, The Aerospace Corporation, M2-266, P.O. Box 92957CA, 90009-2957 Los Angeles, United States of America, Ray.W.Russell@aero.org

A. Salama, ESA Villafranca, Villafranca del Castillo, P.O. Box 50727, E-28080 Madrid, Spain, asalama@iso.vilspa.esa.es

M. Salez, DEMIRM, Observatoire de Paris, 61 avenue de l'Observatoire 75014 Paris, France, Morvan.Salez@obspm.fr

P. Saraceno, Ist. di Fisica dello Spazio Interplanetari, Consiglio Nazionale delle Ricerche, Area di ricerca, Tor Vergata, via Fosso del Cavaliere,00133 Roma, Italy, saraceno@ifsi.rm.cnr.it

Y. Sato, ISO Science Operations Centre, ESA Satellite Tracking Station, Villafranca del castillo, P.O. Box 50727, 28080 Madrid, Spain, ysato@iso.vilspa.esa.es

S. Satyapal, NASA, Goddard Space Flight Center, United States of America, satyapal@stars.gsfc.nasa.gov

M. Sauvage, CEA/DSM/DAPNIA/SAp, CE Saclay, 91191 Gif Sur Yvette, France, msauvage@cea.fr

D. Schaerer, Observatoire Midi-Pyrènées, 14 avenue Edouard Belin, 31400 Toulouse, France, schaerer@obs-mip.fr

H. Schild, Institut für Astronomie, ETH Zentrum, CH 8092 Zuerich, Switzerland, hschild@astro.phys.ethz.ch

N. Schneider, I. Physik Institut University of Cologne, Zülpichev Str. 77, 50937 Köln, Germany, schneider@ph1.uni-koeln.de

M. Schultheis, Institut d'Astrophysique de Paris, 98 bis boulevard Arago, 75014 Paris, France, schulthe@iap.fr

B. Schulz, ISO Science Operations Centre, Astrophysics Division of ESA, Villafranca, P.O. Box 50727, 28080 Madrid, Spain, bschulz@iso.vilspa.esa.es

M. Sempere, Consejo Superior De Investigaciones Cientificas Instituto de Estructura de la Materia, Dpto Fisica Molecular, C/Serrano 121, 28006 Madrid, Spain, sempere@astro.iem.csic.es

R. Shipman, Air Force Research Laboratory ,29 Randolph, RD AFRL/VSBC, Hanscom AFB, MA 01731-3010 Hanscom AFB, United States of America, shipman@plh.af.mil

F. Sibille, Observatoire de Lyon, 69230 Saint Genis Laval, France, sibille@obs.univ-lyon1.fr

S. Sidher, Space Science Department, Rutherford Appleton Laboratory, Chilton Didcot OX11 OQX, Oxfordshire, United Kingdom, s.d.sidher@rl.ac.uk

R. Siebenmorgen, ESA Villafranca, Satellite Tracking Station, Villafranca del Castillo, P.O. Box 50727, E-28080 Madrid, Spain, rsiebenm@iso.vilspa.esa.es

M. Silverstone, UCLA Astronomy& Astrophysics, Division 8105C, Mathematical Sciences, Bldg. 405, Hilgard Avenue, CA 951562 Los-Angeles, United States of America, murray@astro.ucla.edu

C. Singer, Alcatel, 26 avenue Jean-Francois Champollion, BP 1187, 31037 Toulouse Cedex, France

J.-P. Sivan, Observatoire de Haute Provence du CNRS, 04870 Saint Michel l'Observatoire, France, sivan@obs-hp.fr

H. Smith, NASA Headquarters, 300 E. Street SW, DC 20546 Washington,, United States of America, hsmith1@hq.nasa.gov

B. Smith, Institute for Astronomy University of Hawaii, 2680 Woodlawn Drive, HI 96822 Honolulu, United States of America, smith@ifa.hawaii.edu

C. Spangler, California Institute of Technology, Mail Stop 105-24, 1200 E. California Blvd, CA 91125 Pasadena, United States of America, ecs@astro.Caltech.edu

L. Spinoglio, Ist Di Fisica Dello Spazio Interplanetario, Consiglio Nazionale delle Ricerche, Area di ricerca, Tor Vergata, via Fosso del Cavaliere, 00133 Roma, Italy, luigi@lupus.ifsi.rm.cnr.it

G. Stacey, Cornell University 220 Space Sciences Bldg, 14850 Ithaca Ny, United States of America, stacey@astrosun.tn.cornell.edu

K. Stapelfeldt, Jet Propulsion laboratory, 4800 Oak Grove Drive, Mail Stop 183-900, CA 91109 Pasadena, United States of America, krs@wfpc2-mail.jpl.nasa.gov

J.-L. Starck, CEA - DAPNIA/SEI-SAp, Orme des Merisiers, 91191 Gif Sur Yvette, France, jstarck@cea.fr

B. Stepnik, Institut d'Astrophysique Spatiale, Bât 121, Université Paris XI, 91405 Orsay Cedex, France, stepnik@ias.fr

M. Stickel, Max-Planck-Institut für Astronomie, Koenigstuhl 17, D-69117 Heidelberg, Germany, stickel@mpia-hd.mpg.de

G. Stringfellow, CASA, University of Colorado, Campus Box 3898, 0309-0389 Boulder, United States of America, guy@casa.colorado.edu

E. Sturm, Max-Planck-Institut für Extraterrestrische Physik, Giessenbachstrasse Postfach 1603, 85740 Garching, Germany, sturm@mpe.mpg.de

C. Surace, Max-Planck-Institut für Astronomie, Koenigstuhl 17, 69117 Heidelberg, Germany, Surace@mpia-hd.mpg.de

G. Swarup, National Centre for Radio Astrophysics, Tata Institute of Fundamental Research, Pune University Campus, Post Bag No 3, Ganeshkhind, 411007 Pune, India, gswarup@ncra.tifr.res.in

R. Sylvester, Department of Physics and Astronomy, Gower Street, WC1E 6BT London, United Kingdom, rjs@star.ucl.ac.uk

T. Tanabe, Institute of Astronomy, The University of Tokyo, Oosawa-cho, 2-21-1, Mitaka, 181-8588 Tokyo, Japan, ttanabe@mtk.ioa.s.u-tokyo.ac.jp

W. Thi, Leiden Observatory, P.O. Box 9513, 2300 RA Leiden, The Netherlands, thi@strw.leidenuniv.nl

H. Thronson, NASA Headquarters, 300 E. Street SW, DC 20546 Washington, United States of America, Harley.Thronson@hq.nasa.gov

A. Tielens, SRON. Kapteyn Astronomical Institute. P.O. Box 800. 9700 AV Groningen. The Netherlands, tielens@astro.rug.nl

R. Timmermann, Universität Köln, I. Physikalisches Institut, Zuelpicher Str.77, 50937 Köln, Germany, timmer@ph1.uni-koeln.de

L.V. Toth, Max-Planck-Institut für Astronomie, Koenigstuhl 17, D-69117 Heidelberg, Germany, lvtoth@mpia-hd.mpg.de

Q. Tran, Max-Planck-Institut für Extraterrestrische Physik, Giessenbachstrasse, Postfach 1603, 85740 Garching, Germany, dantran@mpeia2.mpe-garching.mpg.de

T. Tsuji, Institute of Astronomy, School of Science, The University of Tokyo, Mitaka, Tokyo, 181-8588 Japan, ttsuji@mtk.ioa.s.u-tokyo.ac.jp

R. Tuffs, Max-Planck-Institut für Kernphysik, Saupfercheckweg 1, Postfach 10398, 069117 Heidelberg, Germany, rjt@taurus.mpi-hd.mpg.de

S. Turck-Chièze, CEA/dsm/dapnia/sap, CE Saclay, 91191 Gif Sur Yvette, France, turck@cea.fr

S. Unger, Queen Mary and Westfield College, Physics Department, Mile End Road, E1 4NS London, United Kingdom, s.j.unger@qmw.ac.uk

E. Valentijn, Kapteyn Astronomical Institute, SRON, P.O. Box 800, NL-9700 AV Groningen, The Netherlands, valentyn@sron.rug.nl

I. Van Bemmel, ESO Garching, Karl-Schwarzschild-Str.2, D-85748 Garching bei München, Germany, ivbemmel@eso.org

E. Van Dishoeck, Sterrewacht Leiden, P.O. Postbus 9513, NL 3300 RA Leiden, The Netherlands, ewine@strw.Leidenuniv.nl

W. Van Driel, USN, Observatoire de Paris, 5 place J. Janssen, 92195 Meudon, France, vandriel@mesioq.obspm.fr

P. Van Hoof, University of Kentucky, Dept. of Physics and Astronomy, 177 CP building, Lexingtom, Kentucky, United States of America, vanhoof@cita.utoronto.ca

C. Van Kerckhoven, Institute of Astronomy, K U Leuven ,Celestijnenlaan 200 B, B-3001 Leuven, Belgium, caroline@ster.kuleuven.ac.be

B. Vandenbussche, Institute of Astronomy, K.U. Leuven, Celestijnenlaan 200 B, B-3001 Leuven, Belgium, Bart.Vandenbussche@ster.kuleuven.ac.be

L. Vannier, Observatoire de Paris-Meudon, DAMAP, 5 place J. Janssen, 92195 Meudon Cedex, France, laurence.vannier@obspm.fr

C. Vastel, Centre d'Etude Spatiale des Rayonnements, 9 avenue du Colonel Roche, BP 4346, 31029 Toulouse Cedex 04, France, vastel@cesr.fr

R. Verma, Tata Institute of Fundamental Research, Homi Bhabha Road, Colaba, 400005 Mumbai, India, vermarp@tifr.res.in

R. Vermeij, Kapteyn Astronomical Institute, SRON, P.O. Box 800, NL-9700 AV Groningen, The Netherlands, ronald@astro.rug.nl

L. Verstraete, Institut d'Astrophysique Spatiale,Bât 121, Université Paris XI, 91405 Orsay Cedex, France, verstra@ias.fr

F. Viallefond, DEMIRM, Observatoire de Paris, 61 avenue de l'Observatoire, F-75014 Paris, France, fviallef@maat.obspm.fr

L. Vigroux, CEA/dsm/dapnia/sap, CE Saclay, 91191 Gif Sur Yvette, France, vigroux@discovery.saclay.cea.fr

A. Vogler, CEA, Saclay Service d'Astrophysique, Orme des Merisiers, Bât 709, 91191 Gif Sur Yvette, France, ajv@discovery.saclay.cea.fr

S. Volonté, European Space Agency, 8-10 rue Mario Nikis, 75738 Paris Cedex 15, France, svolonte@hq.esa.fr

C. Waelkens, Institut voor Sterrekunde Katholieke Universiteit Leuven, Celestijnenlaan 200B, B-3001 Heverlee, Belgium, christoffel@ster.kuleuven.ac.be

H. Walker, Rutherford Appleton Laboratory, Chilton Didcot, OX 11 OQX Oxfordshire, United Kingdom, h.j.walker@rl.ac.uk

M. Walmsley, Osservatorio Astrofisico di Arcetri, Largo E. Fermi 5, I-50125 Firenze, Italy, walmsley@arcetri.astro.it

W. Wamsteker, ESA Villafranca, Villafranca del Castillo, P.O. Box 50727, E-28080 Madrid, Spain, wwamstek@notes.vilspa.esa.es

Z. Wang, Smithsonian Astrophysical Observatory, 60 Garden Steet, MS66, MA 02138 Cambridge, United States of America, zwang@cfa.harvard.edu

D. Ward-Thompson, University of Wales, Department of Physics, 5 Parade, CF2 3YB Cardiff, United Kingdom, D.Ward-Thompson@astro.cf.ac.uk

R. Waters, Astronomical Institute "Anton Pannekoek", University of Amsterdam, Kruislaan 403, NL-1098 SJ Amsterdam, The Netherlands, rensw@astro.uva.nl

J. Weingartner, Princeton University, Physics Departme, Washington Road, Stillorgan Road, 08544 Princeton NJ, United States of America, josephw@astro.princeton.edu

M. Werner, Jet Propulsion Laboratory, 4800 Oak Grove Drive, CA 91109 Pasadena, United States of America, mww@ipac.Caltech.edu

P. Wesselius, SRON, P.O. BOX 800, 9700 AV Groningen, The Netherlands, p.r.wesselius@sron.rug.nl

G. White, Queen Mary And Westfield College, Physics Department, Mile End Road, E1 4NS London, United Kingdom, G.J.White@qmw.ac.uk

H. Wiesemeyer, Institut de Radio Astronomie Millimétrique, 300 rue de la Piscine, 38406 St Martin d'Hères Cedex, France, wiesemey@iram.fr

B. Wilkes, Smithsonian Astrophysical Observatory, 60 Garden Steet, MA 02138 Cambridge, United States of America, belinda@cfa.harvard.edu

J. Winters, Technische Universität, Berlin Inst. für Astronomie & Astrophysik Sekr., PN 8-1 Hardenbergstr. 36, D-10623 Berlin, Germany, winters@physik.tu-berlin.de

L. Woltjer, Observatoire de Haute Provence du CNRS, 04870 Saint Michel l'Observatoire, France

C. Woodward, University of Wyoming, Department of Physics & Astronomy, U. Wyoming, 82071-3095 Laramie, United States of America, chelsea@kaya.uwyo.edu

H. Wozniak, Observatoire de Marseille, 2 place Verrier, 13248 Marseille, France, wozniak@observatoire.cnrs-mrs.fr

E. Young, University of Arizona, Steward Observatory, AZ 85721 Tucson, United States of America, eyoung@as.arizona.edu

M. Yun,National Radio Astronomy Observatory, 1003 Lopezville Rd, 87801 Socorro NM, United States of America, myun@nrao.edu

A. Zavagno, Observatoire de Marseille, 2 place Verrier, 13248 Marseille, France, zavagno@obmara.cnrs-mrs.fr

OBJECT INDEX

AUTHOR INDEX

D

E

F

G

H

I

J

K

L

M

N

O

P

Q

R

S

T

U

V

W

X

Y

Z